

*The 8th US-Japan Seminar on
Dielectric and Piezoelectric Ceramics*

**PROGRAM SUMMARY
and
EXTENDED ABSTRACTS**

19990429 001

General Chairmen: Raj Gururaja, Hewlett Packard, USA
Noboru Ichinose, Waseda University, Japan

Program Chairmen: Thomas R. Shrout, Penn State University, USA
Takashi Yamamoto, National Defense Academy, Japan

Local Arrangements: Brian Pazol, Materials Systems Inc., USA

October 15-18, 1997
Plymouth, Massachusetts

DISTRIBUTION STATEMENT A
Approved for Public Release
Distribution Unlimited

**8th U.S.-JAPAN SEMINAR
DIELECTRIC AND PIEZOELECTRIC CERAMICS
October 1997**

SCHEDULE SUMMARY

| | Morning | Afternoon | Evening |
|--------------------------------|---|--|--|
| <u>Wednesday</u> October 15 | — | | 6:00 Registration & Cocktail Party |
| <u>Thursday</u> October 16 | 8:00–8:15 Opening Remarks --- 8:15 – 8:45 Special Talk -- 8:45 – 9:45 Session I (Invited) -- 9:45 – 12:00 Session I (Oral & Poster) | 1:30 – 2:30 Session II (Invited) --- 2:30 – 5:00 Session II (PM) (Oral & Poster) | 6:00 – 10:00 Banquet Dinner |
| <u>Friday</u> October 17 | 8:30–9:30 Session III (Invited) --- 9:30 – 12:00 Session III (Oral and Poster) | 1:30 – 2:30 Session IV (Invited) --- 2:30 – 5:00 Session IV (Oral & Poster) | --- |
| <u>Saturday</u> October 18 | 8:30 – 10:30 Session V (Invited) --- 10:30 – 11:30 Discussion (U.S./Japan) | A. Golf Tournament B. Whale Watching C. Plimouth Plantation | |

The Eighth US - Japan Seminar on Dielectric and Piezoelectric Ceramics

October 15-18, 1997

*Sheraton Inn
Plymouth, Mass.*

PROGRAM

Wednesday, October 15

6:00 p.m. Registration and Reception

Thursday, October 16 (morning)

8:00-8:15 Opening Remarks: Naboru Ichinose, *Waseda University, Japan*
Raj Gururaja, *Hewlett Packard, USA*

8:15-8:45 Prof. Okazaki Memorial Lecture; *L.E. Cross, Penn State University, USA*

8:45-12:00 Session I—Basic Science

Session Chairs: Ahmad Safari, *Rutgers University, USA*
Tadashi Shiosaki, *Kyoto University, Japan*

PAGE

Invited Papers

- My Life with Dielectric Ceramics, *K. Wakino, Murata Manufacturing Co., Japan* 1
- Are Domains Taking a Rest, or Do They Go Somewhere?, *J. Fousek, Penn State University (on leave from Technical University, Liberec, Czech Republic), USA* 6

Contributed Papers

Domains

- I-1 Domain Configuration and Ferroelectric Related Properties of Relaxor Based Single Crystals, *S. Wada, S.-E. Park, L.E. Cross, and T.R. Shrout, Penn State University, USA* 11
- I-2 Domain Structure of PbTiO_3 and $\text{Pb}(\text{Zn}_{1/2}\text{Nb}_{1/2})_{0.91}\text{Ti}_{0.09}\text{O}_3$ Single Crystals by Atomic Force and Kelvin Force Microscopy, *T. Yamamoto, K. Kawano, M. Saito, and S. Omika, National Defense Academy, Japan* 16
- I-3 Nanoscale Imaging of Domain Dynamics and Retention in Ferroelectric Thin Films, *A. Gruverman, A.S. Prakash*, S. Aggarwal*, B. Yang*, M. Wuttig*, H. Tokumoto, O. Auciello**, T. Venkatesan*, and R. Ramesh*; Joint Research Center for Atom Technology (Japan), * University of Maryland, and **Argonne National Laboratory, USA* 20

| | PAGE |
|--|------|
| I-4 Domain Wall Mobility and Stress Effects in Piezoelectric Thin Films, <u>S. Trolier-McKinstry</u> , <u>F. Chu</u> , <u>J.L. Lacey</u> , <u>J.F. Shepard, Jr.</u> , <u>T. Su</u> , <u>F. Xu</u> , <i>Penn State University</i> ; <u>G. Zavala</u> and <u>J. Fendler</u> , <i>Syracuse University</i> | 24 |
| I-5 The Application of Acoustic Emission (AE) Method for Ferroelectric Devices and Materials, <u>H. Aburatani</u> and <u>K. Uchino</u> , <i>Penn State University, USA</i> | 28 |
| <u>Defects and Interfaces</u> | |
| I-6 The Influence of Mobile vs. Randomly Quenched Impurities on Ferroelectric Phase Transformations, <u>Q. Tan</u> , <u>J.F. Li</u> , and <u>D. Viehland</u> , <i>University of Illinois at Urbana-Champaign, USA</i> | 32 |
| I-7 Thermochemical Interactions at Electrode Interfaces in Electroceramic Applications, <u>D.P. Cann</u> and <u>C.A. Randall</u> , <i>Penn State University, USA</i> | 36 |
| I-8 Resistivity Anomaly of (Ba,Ca,Sr,Pb)TiO ₃ Semiconducting Ceramics Fired by Reduction-Reoxidation Method, <u>S. Tashiro</u> , <u>A. Osonoi</u> , and <u>H. Igarashi</u> , <i>National Defense Academy, Japan</i> | 40 |
| <u>BaTiO₃ Fundamentals</u> | |
| I-9 Hypothesis on Rare Earth Doping of BaTiO ₃ Ceramic Capacitors, <u>A. Hitomi</u> , <u>X. Liu</u> , <u>T.R. Shrout</u> , and <u>C.A. Randall</u> , <i>Penn State University, USA</i> | 44 |
| I-10 Grain Size Effects in Dielectric Barium Titanate, <u>S.P. Ostrander</u> and <u>W.A. Schulze</u> , <i>Alfred University, USA</i> | 48 |
| I-11 Processing, Characterization and Modeling of BaTiO ₃ Glass Ceramics Showing Finite Size Effects, <u>C. Randall</u> , <u>D.L. McCauley</u> , and <u>X. Liu</u> , <i>Penn State University, USA</i> | 52 |
| <u>Crystal Growth</u> | |
| I-12 Crystal Growth and Characterization of New Piezoelectric Materials: Langasite and its Related Compounds, <u>T. Fukuda</u> , <u>K. Shimamura</u> , and <u>H. Takeda</u> , <i>Tohoku University, Japan</i> | 57 |
| I-13 Growth and Properties of Tungsten-Bronze Ferroelectric Potassium Lithium Niobate (KLN) Single Crystals, <u>Z. Chen</u> , <u>K. Miyashita</u> , <u>M. Adachi</u> , and <u>A. Kawabata</u> , <i>Toyama Prefectural University, Japan</i> | 61 |
| I-14 Growth and Characterization of KLN Fiber Crystals by μ -PD Method, <u>M. Takahashi</u> , <u>R. Komatsu</u> , and <u>S. Uda</u> , <i>Mitsubishi Materials Corp., Japan</i> | 64 |
| <u>Miscellaneous</u> | |
| I-15 Effect of Calcium Zirconate Addition to Ca Doped LaMnO ₃ Ceramics, <u>K. Abe</u> and <u>J.R. Zen</u> , <i>Sakai Chemical Industry Co. Ltd., Japan</i> | 68 |
| I-16 Processing and Induced-Phase Transformation in Sr-Doped PZT Ceramics, <u>Y. Yu</u> and <u>R.N. Singh</u> , <i>University of Cincinnati, USA</i> | 70 |

10:30–12:00 Break and Poster Review

Thursday, October 16 (afternoon)

1:30-5:00 Session II—Thin Films

Session Chairs: Bruce Tuttle, *Sandia National Laboratory, USA*
Yukio Sakabe, *Murata Electronics, Japan*

PAGE

Invited Papers

- Fatigue Mechanism of PZT Thin-Film Capacitors, K. Aoki, Y. Fukuda, K. Numata, and A. Nishimura, *Texas Instruments, Japan* 74
- CVD of Thin Perovskite Films, P.C. Van Buskirk, M.W. Russell, S.T. Johnston, and S.M. Bilodeau, *Advanced Technology Materials, Inc., USA* 80

Contributed Papers

Review

- II-1 Comparative Assessment of Electronic Ceramics R&D in the U.S. and Japan, S. Swartz, *NexTech Materials, USA*; T.R. Shrout, *Penn State University, USA*; and Tadashi Takenaka, *Science University of Tokyo, Japan*. 84

BaTiO₃ & Ba,SrTiO₃

- II-2 Dielectric Behavior of (Ba,Sr)TiO₃ Thin Films and its Correlation with Oxygen Defect Density, Y. Fukuda and K. Aoki, *Texas Instruments Tsukuba R&D Center*; H. Haneda and I. Sakaguchi, *National Institute for Research in Inorganic Materials, Japan*; K. Numata and A. Nishimura, *Texas Instruments Memory R&D Center, USA*. 88
- II-3 Preparation of BaTiO₃ and SrTiO₃ Thin Films for Communications Applications, R. W. Schwartz, *Clemson University*; and P.G. Clem and D. Dimos, *Sandia National Laboratories, USA* 92
- II-4 Phase Transition and Ferroelectric Properties of BaTi_{0.91}(Hf_{0.5}Zr_{0.5})_{0.09}O₃ by a Laser Ablation Method Using the Fourth-harmonic Wave of a YAG Laser, Y. Masuda, S. Fujita, and A. Baba, *Hachinohe Institute of Technology*; H. Matsumoto and T. Hirai, *Tohoku University*; and K. Nagata, *National Defense Academy, Japan* 96
- II-5 The Effect of Oxygen on the Barium Titanate Film Capacitor, B.H. Tsao and R.L.C. Wu, *K Systems Corp.*; and S. Fries Carr and J.A. Weimer, *Wright Laboratory, Wright-Patterson Air Force Base, USA* 100

PbTiO₃

- II-6 Electrical Properties of (Pb,Ca)TiO₃ Thin Films by Multiple-Cathode Sputtering, H. Maiwa, *Shonan Institute of Technology*; and N. Ichinose, *Waseda University, Japan* 104

| | PAGE |
|--|-------------|
| II-7 Effect of Niobium on Some Electrical Properties of Nb-doped PbTiO ₃ Thin Films, <u>T. Shiosaki</u> , R.C. Ibrahim, T. Horiuchi, and K. Matsushige, Kyoto University, Japan | 108 |
| II-8 Electrical and Structural Analysis of Epitaxial Lanthanum Modified PbTiO ₃ Thin Films Exhibiting a-Oriented Domains, <u>J.P. Maria</u> and S. Trolier-McKinstry, Penn State University, USA | 112 |
| <u>PZT/Devices</u> | |
| II-9 Bioanalytical MEMS Based on Piezoelectric Materials, <u>D.L. Polla</u> , R.C. McGlennen, and L.T. Furcht, University of Minnesota, USA | 116 |
| II-10 Effect of Thickness and Texture on the Ferroelectric Properties of Lead Zirconate Titanate Thin Films by Sol-Gel Processing, <u>F. Chu</u> , T. Su, and S. Trolier-McKinstry, Penn State University, USA | 120 |
| II-11 Properties of Sputtered Ir and IrO ₂ Electrodes for PZT Capacitors, <u>M. Shimizu</u> , S. Hyodo, S. Nakashima, H. Fujisawa, and H. Niu, Himeji Institute of Technology; and H. Okino and T. Shiosaki, Kyoto University, Japan | 124 |
| II-12 The Low-Field Biaxial Stress Response and Transverse Piezoelectric Coefficients of Sol-Gel PZT Thin Films, <u>J.F. Shepard, Jr.</u> and S. Trolier-McKinstry, Penn State University, USA | 128 |
| <u>Optical/SAW/Miscellaneous</u> | |
| II-13 Theoretical Study on SAW Characteristics of LiNbO ₃ /Sapphire Structures, <u>T. Shiosaki</u> , T. Nishida, T. Horiuchi, and K. Matsushige, Kyoto University, Japan | 132 |
| II-14 Fabrication and Electrical Properties of LiTaO ₃ /ZnO/Al ₂ O ₃ Hexagonal Heterostructure, <u>T. Tsurumi</u> , Y. Ma, H. Kimura, and N. Ohashi, Tokyo Institute of Technology, Japan | 136 |
| II-15 Synthesis and Properties of K(Sr _{0.5} Ba _{0.5}) ₂ Nb ₅ O ₁₅ Thin Films by Chemical Solution Deposition Method, <u>W. Sakamoto</u> , A. Kawase, T. Yogo, and S. Hirano, Nagoya University, Japan | 140 |
| II-16 Crystal Orientation and Dielectric Properties of Sol-Gel Derived SrBi ₂ Ta ₂ O ₉ Thin Films, <u>T. Hayashi</u> and T. Hara, Shonan Institute of Technology, Japan | 144 |

3:30–5:00 Break and Poster Review

Friday, October 17, 1997 (morning)

8:30-12:00 Session III—Capacitors and Dielectrics

Session Chairs: Walter Schulze, *Alfred University, USA*
Tadashi Takenaka, *Science University of Tokyo, Japan*

PAGE

Invited Papers

- Recent Topics in Multilayer Ceramic Capacitor Technology, T. Nomura,
T. Arashi, A. Sato, Y. Nakano, and S. Sato, *TDK Corp. Japan* 148
- Changing the Equilibrium in MLCC Manufacturing, A. Rae, J. Bultitude,
S. Butcher, M. Chu, and V. Ganine, *TAM Ceramics, USA* 155

Contributed Papers

Base Metal Systems

- III-1 Mechanism of Improvement in Resistance Degradation in Y-doped BaTiO₃
Based Multilayer Ceramic Capacitors with Ni Electrodes Under Highly
Accelerated Life Testing, S. Sato, Y. Nakano, A. Sato, and T. Nomura,
TDK Corp., Japan 161
- III-2 Microstructure and Reliability Study of MLCs with Ni Electrodes, M. Chu,
J. Bultitude, V. Ganine, and A. Rae, *TAM Ceramics Inc., USA* 165
- III-3 Electron Microscopy Study of Dislocation Loops in Stoichiometric
BaTiO₃ and Nonstoichiometric (Ba,Ca)TiO₃, T. Suzuki, M. Ueno, Y. Nishi,
K. Arai, and M. Fujimoto, *Taiyo Yuden Co. Ltd., Japan* 168
- III-4 Ca Ion Selective Site Occupation at Ruddlesden-Popper-Type Faults and the
Resultant Dielectric Properties of A-site-excess (Sr,Ca) TiO₃ Ceramics,
M. Fujimoto, T. Suzuki, Y. Nishi, and K. Arai, *Taiyo Yuden Co. Ltd.*; and
J. Tanaka, *National Institute for Research in Inorganic Materials, Japan* 172
- III-5 Effects of Heat Treatment on Dielectric Properties of X7R Designated MLCs
with Ni Internal Electrodes, H. Shoji, H. Matsushita, Y. Nakano, H. Ogawa,
and A. Onoe, *Nippon Chemi-con Corp.*; and Y. Yamashita and H. Kanai,
Toshiba Corp., Japan 176

Thin Layers/X7R

- III-6 Electrical and Physical Characteristics of Low-Fire X7R MLCCs with $\leq 3 \mu\text{m}$
Active Layers and 70 Ag-30 Pd Electrodes, J.J. Beeson and L. A. Mann,
Kemet Electronics Corp.; S. Venigalla and S.A. Costantino, *Cabot Performance
Materials; USA* 180
- III-7 Effect of AC Signal Field on the Electrical Properties of Thin Layer MLC's
with X7R Characteristics, G.H. Maher, V. Bheemineni, and
T.I. Prokopowicz, *MRA Laboratories Inc., USA* 184
- III-8 High Energy Storage X7R Dielectrics, W. Huebner, S.C. Zhang, M. Pennell,
X.M. Ding, *University of Missouri -Rolla, USA* 188

Synthesis and Manufacturing

- III-9 Dielectric Properties of PMN Based Ceramic Under D.C. and A.C. Fields, *U. Kumar, J. Hock, B. Rawal and M. Randall, AVX Corporation, USA* 193
- III-10 Manufacturing of Barium Titanium Powder by Oxalate Process, *M. Nishido and K. Harada, Fuji Titanium Ind. Co. Ltd., Japan* 197
- III-11 Use of Low Fire BaTiO₃ Dielectrics in the Manufacture of MLCCs, *S.P. Gupta and L.A. Mann, Kemet Electronics Corp., USA* 201
- III-12 Preparation of Barium Strontium Titanates by Vapor Phase Hydrolysis of Precursors Via Modified Alkoxide Route, *T. Hayashi, K. Sunaga, S. Satoh, and H. Satoh, Shonan Institute of Technology,; and K. Sasaki, former Research Associate, DuPont, Japan* 205

Microwave/Miscellaneous

- III-13 The Effect of Calcining Sequence and Dopant Addition on the Densification and Microwave Properties of Zirconium Tin Titanate, *J. Wilson, P. Pruna, and M. Megherhi, Ferro Transelco Division, USA* 209
- III-14 Dielectric Properties of Ba(Zn_{1/3}Ta_{2/3})O₃ - KTaO₃ Ceramics, *H. Yokoi, A. Tosa, and K. Ohbayashi, NGK Spark Plug Co., Ltd., Japan* 212
- III-15 Development of the Varistor/Capacitor Co-fired Multilayer Device, *T. Sogabe, TDK Corp., Japan* 216
- III-16 Dielectric Properties of Ta₂O₅ Based Ceramics, *N. Ichinose and T. Ukai, Waseda University; and Y. Yamashita, Toshiba R&D Center, Japan* 220
- III-17 Effect of Poling on Conducting Barium Titanate, *R.D. Roseman, University of Cincinnati, USA* 223
- III-18 Effect of pH and Cation Concentration on PMN Powders Prepared by a Coprecipitation Method, *D.-Y. Jeng, C.J. Chen, and S.R. Chaudhuri, YTC America, Inc., USA* 227

10:30–12:00 Break and Poster Review

Friday October 17 (afternoon)

1:30-5:00 Session IV—Piezoelectrics, Actuators, and Sensors

Session Chairs: Wayne Huebner, *University of Missouri-Rolla, USA*
Toshio Ogawa, *Shizuoka Institute of Science and Technology, Japan*

PAGE

Invited Papers

- Mechanical Loss in Piezoceramics Under High Vibration Level, S. Takahashi and Y. Sasaki, *NEC Corp.*; and S. Hirose, *Yamagata University, Japan* 231
- Relaxor Based Ferroelectric Single Crystals with High Piezoelectric Performance, S.-E. Park and Thomas R. Shrout, *Penn State University, USA* 235

Contributed Papers

Single Crystals

- IV-1 Growth of Single Crystal PMN-PT, P. Bridenbaugh, J. Rottenberg, and G.M. Loiacono, *Crystal Associates Inc., USA* 242
- IV-2 Relaxor Single Crystals from Polycrystalline Precursors, M.P. Harmer, H.M. Chan, T. Li, F. Meschke, and A.M. Scotch, *Lehigh University, USA* 244
- IV-3 Templated Grain Growth of Ferroelectric Materials, B. Brahmaroutu, P. Rehrig, S.H. Hong, S. Trolier-McKinstry, and G.L. Messing, *Penn State University, USA* 248
- IV-4 Effect of Electrode Material on the Physical and Electrical Properties of a PZN Relaxor-PT Single Crystal, J.Y. Yamashita, K. Harada, T. Kobayashi, S. Shimanuki, and S. Saito, *Toshiba Corp., Japan* 252
- IV-5 Intelligent Engineering of Hydrothermal Reactions, R.E. Riman, B.L. Gersten and S.B. Cho, *Rutgers University*; M.M. Lencka and A. Anderko, *OLI Systems Inc.*; and L.E. McCandlish, *Ceramare Corp., USA* 256

Polycrystalline Ceramics

- IV-6 Dielectric and Piezoelectric Properties of Ceramics in the Lead Indium Niobate-Lead Titanate Solid Solution, E.F. Alberta and A.S. Bhalla, *Penn State University, USA* 260
- IV-7 Preparation and Electric Properties of $\text{Pb}(\text{Yb}_{1/2}\text{Nb}_{1/2})\text{O}_3\text{-PbTiO}_3\text{-PbZrO}_3$ Ceramics, H. Ohuchi, T. Sanada, M. Ueda, and T. Hashimoto, *Shonan Institute of Technology, Japan* 264
- IV-8 Ferroelectric Properties and Crystal Orientation in Rhombohedral PZT Ceramics, T. Ogawa and A. Yamada, *Shizuoka Institute of Science and Technology, Japan* 268
- IV-9 High Power Ceramic Materials for Piezoelectric Transformer, Y. Fuda, M. Katsuno, and M. Tamura, *Tokin Corp., Japan* 272

| | PAGE |
|---|------|
| IV-10 Temperature Stable Piezoelectric Ceramics for Cylindrical Vibrators of Vibratory Gyroscopes, <u>M. Tamura</u> , <u>K. Satoh</u> , <u>O. Ise</u> , and <u>E. Otsuki</u> , <u>Tokin Corp., Japan</u> | 276 |
| IV-11 The Influence of the Heat Treatment Conditions on the Temperature Stability of the Piezoelectric Properties and Absolute Values of the Lead Titanate Ceramics, <u>K. Miyabe</u> , <u>K. Tachimoto</u> , <u>K. Horino</u> , <u>T. Tsukada</u> , and <u>M. Takada</u> , <u>TDK Corp., Japan</u> | 280 |
| IV-12 Non-Lead Piezoelectric Ceramics Based on $(\text{Bi}_{1/2}\text{Na}_{1/2})\text{TiO}_3$, <u>T. Takenaka</u> and <u>H. Nagata</u> , <u>Science University of Tokyo, Japan</u> | 284 |
| <u>Electromechanical Properties</u> | |
| IV-13 Effect of Grain Size on the Electromechanical Properties of Antiferroelectric-to-Ferroelectric Phase Switching PLSnZT Ceramics, <u>M.-J. Pan</u> and <u>S. Yoshikawa</u> , <u>Penn State University, USA</u> | 288 |
| IV-14 Technique for Measuring Electromechanical Coupling in Electrostrictors and Piezoelectrics, <u>S.P. Leary</u> and <u>S.M. Pilgrim</u> , <u>Alfred University, USA</u> | 292 |
| IV-15 Flexural Failure in Navy Type III PZT, <u>L. Ewart</u> , <u>Naval Undersea Warfare Center, USA</u> | 295 |
| IV-16 Electromechanical Fatigue of Lead Zirconate Titanate Ceramics, <u>H. Makino</u> and <u>N. Kamiya</u> , <u>Toyota Central R&D Lab. Inc., Japan</u> | 299 |
| IV-17 Electromechanical Properties of High Temperature Piezoelectric Materials, <u>Y. Sakabe</u> , <u>M. Kimura</u> , <u>K. Ogiso</u> , and <u>A. Ando</u> , <u>Murata Manufacturing Co. Ltd., Japan</u> | 303 |
| <u>Composite Fabrication</u> | |
| IV-18 Solid Freeform Fabrication (SFF) of Novel PZT Ceramic/Polymer Composites, <u>A. Safari</u> , <u>S.C. Danforth</u> , <u>R.K. Panda</u> , <u>T.F. McNulty</u> , and <u>A. Bandyopadhyay</u> , <u>Rutgers University, USA</u> | 307 |
| IV-19 PZT MicroRod Composite Ultrasonic Transducers, <u>M.T. Strauss</u> and <u>M.V. Parish</u> , <u>CeraNova Corp., USA</u> | 311 |
| IV-20 Preparation of Fine Scale PZT Fibers and Their 1-3 Composite Properties, <u>R.J. Meyer, Jr.</u> , <u>T.R. Shrout</u> , and <u>S. Yoshikawa</u> , <u>Penn State University, USA</u> | 313 |
| IV-21 Anisotropic Piezoceramic (3-3) Composites, <u>V.S. Venkataramani</u> , <u>P.C. Schaefer</u> , and <u>L.S. Smith</u> , <u>GE Corporate R&D, USA</u> | 317 |
| <u>Actuators/Transducers</u> | |
| IV-22 Fine Grain Piezoelectric Ceramics for Transducer and Actuator Applications, <u>W. Hackenberger</u> and <u>J. Helgeland</u> , <u>TRS Ceramics Inc.</u> ; <u>M. Zipparo</u> , <u>C. A. Randall</u> , and <u>T.R. Shrout</u> , <u>Penn State University; USA</u> | 323 |
| IV-23 Piezocomposite Materials for Ultrasonic Imaging Applications, <u>B. Pazol</u> , <u>H. Pham-Nguyen</u> , <u>J. Hollenbeck</u> , <u>M. Callahan</u> , <u>K. Gabriel</u> , and <u>G. Schmidt</u> , <u>Materials Systems Inc., USA</u> | 326 |

| | | |
|-------|---|-----|
| IV-24 | Computer Simulation of Piezocomposite Transducers, <u>W. Cao</u> , <i>Penn State University, USA</i> | 329 |
| IV-25 | Medical Ultrasonic Transducers with Switchable Frequency Bands Centered About f_0 and $2f_0$, <u>T.R. Gururaja</u> and <u>J. Chen</u> , <i>Hewlett Packard Co.; and A. Shurland, University of Pennsylvania; USA</i> | 333 |
| IV-26 | Bimorph and Pseudo Shear Mode Actuation, <u>L.E. Cross</u> , <i>Penn State University, USA</i> | 337 |
| IV-27 | Capped Ceramic Underwater Sound Projector, <u>J.F. Tressler</u> , <u>W. J. Hughes</u> , <u>W. Cao</u> , <u>K. Uchino</u> , and <u>R.E. Newnham</u> , <i>Penn State University, USA</i> | 340 |
| IV-28 | Piezocomposite SmartPanels™ for Active Surface Control Applications, <u>D. Fiore</u> , <u>R. Torri</u> , and <u>R. Gentilman</u> , <i>Materials Systems Inc., USA</i> | 344 |

3:30–5:00 Break and Poster Review

Saturday, October 18 (morning)

8:30–11:30 Session V—Ferroelectric and Related Materials

Session Chairs: Clive Randall, *Penn State University, USA*
Y. Yamashita, *Toshiba Corporation, Japan*

Invited Papers

| | |
|---|-----|
| Piezoelectric Properties of PNN-PT-PZ Ceramics, <u>N. Kamehara</u> , <u>M. Kondo</u> , <u>M. Hida</u> , and <u>K. Kurihara</u> , <i>Fujitsu Laboratories, Japan</i> | 348 |
| Structure-Property Relationships of Antiferroelectric $\text{Pb}(\text{Zr,Ti})\text{O}_3$ Based Materials: Hydrostatic Depoling Characteristics, <u>B.A. Tuttle</u> , <u>J. Voigt</u> , <u>D. Zeuch</u> , <u>R. Moore</u> , <u>J. Glass</u> , <u>J. Michael</u> , <u>T. Garino</u> , and <u>W. Olson</u> , <i>Sandia National Laboratory, USA</i> | 353 |
| Diffusion Phenomena Along Grain and Interphase Boundaries in Electroceramics, <u>H. Haneda</u> , <i>National Institute for Research in Inorganic Materials, Japan</i> | 359 |
| Smart Skis and Other Applications of Piezo Control Technology, <u>A. Bogue</u> , <i>Active Control eXperts, Inc., USA</i> | 366 |

10:30–11:30 Break and Discussion

Session I—Basic Science

PAGE

Invited Papers

- | | |
|---|---|
| My Life with Dielectric Ceramics, <u>K. Wakino</u> , <i>Murata Manufacturing Co., Japan</i> | 1 |
| Are Domains Taking a Rest, or Do They Go Somewhere?, <u>J. Fousek</u> , <i>Penn State University (on leave from Technical University, Liberec, Czech Republic), USA</i> | 6 |

Contributed Papers

Domains

- | | |
|---|----|
| I-1 Domain Configuration and Ferroelectric Related Properties of Relaxor Based Single Crystals, <u>S. Wada</u> , <i>S.-E. Park, L.E. Cross, and T.R. Shrout, Penn State University, USA</i> | 11 |
| I-2 Domain Structure of PbTiO_3 and $\text{Pb}(\text{Zn}_{1/2}\text{Nb}_{1/2})_{0.91}\text{Ti}_{0.09}\text{O}_3$ Single Crystals by Atomic Force and Kelvin Force Microscopy, <u>T. Yamamoto</u> , <i>K. Kawano, M. Saito, and S. Omika, National Defense Academy, Japan</i> | 16 |
| I-3 Nanoscale Imaging of Domain Dynamics and Retention in Ferroelectric Thin Films, <i>A. Gruverman, A.S. Prakash*, S. Aggarwal*, B. Yang*, M. Wuttig*, H. Tokumoto, Q. Auciello**, T. Venkatesan*, and R. Ramesh*</i> ; <i>Joint Research Center for Atom Technology (Japan), * University of Maryland, and **Argonne National Laboratory, USA</i> | 20 |
| I-4 Domain Wall Mobility and Stress Effects in Piezoelectric Thin Films, <u>S. Trolier-McKinstry</u> , <i>F. Chu, J.L. Lacey, J.F. Shepard, Jr., T. Su, F. Xu, Penn State University; G. Zavala and J. Fendler, Syracuse University</i> | 24 |
| I-5 The Application of Acoustic Emission (AE) Method for Ferroelectric Devices and Materials, <u>H. Aburatani</u> and <i>K. Uchino, Penn State University, USA</i> | 28 |

Defects and Interfaces

- | | |
|---|----|
| I-6 The Influence of Mobile vs. Randomly Quenched Impurities on Ferroelectric Phase Transformations, <i>Q. Tan, J.F. Li, and D. Viehland, University of Illinois at Urbana-Champaign, USA</i> | 32 |
| I-7 Thermochemical Interactions at Electrode Interfaces in Electroceramic Applications, <u>D.P. Cann</u> and <i>C.A. Randall, Penn State University, USA</i> | 36 |
| I-8 Resistivity Anomaly of $(\text{Ba,Ca,Sr,Pb})\text{TiO}_3$ Semiconducting Ceramics Fired by Reduction-Reoxidation Method, <u>S. Tashiro</u> , <i>A. Osonoi, and H. Igarashi, National Defense Academy, Japan</i> | 40 |

BaTiO₃ Fundamentals

- I-9 Hypothesis on Rare Earth Doping of BaTiO₃ Ceramic Capacitors, A. Hitomi,
X. Liu, T.R. Shrout, and C.A. Randall, Penn State University, USA 44
- I-10 Grain Size Effects in Dielectric Barium Titanate, S.P. Ostrander and W.A. Schulze,
Alfred University, USA 48
- I-11 Processing, Characterization and Modeling of BaTiO₃ Glass Ceramics Showing Finite
Size Effects, C. Randall, D.L. McCauley, and X. Liu, Penn State University, USA 52

Crystal Growth

- I-12 Crystal Growth and Characterization of New Piezoelectric Materials: Langasite and its
Related Compounds, T. Fukuda, K. Shimamura, and H. Takeda, Tohoku University,
Japan 57
- I-13 Growth and Properties of Tungsten-Bronze Ferroelectric Potassium Lithium Niobate
(KLN) Single Crystals, Z. Chen, K. Miyashita, M. Adachi, and A. Kawabata,
Toyama Prefectural University, Japan 61
- I-14 Growth and Characterization of KLN Fiber Crystals by μ -PD Method, M. Takahashi,
R. Komatsu, and S. Uda, Mitsubishi Materials Corp., Japan 64

Miscellaneous

- I-15 Effect of Calcium Zirconate Addition to Ca Doped LaMnO₃ Ceramics, K. Abe and
J.R. Zen, Sakai Chemical Industry Co. Ltd., Japan 68
- I-16 Processing and Induced-Phase Transformation in Sr-Doped PZT Ceramics,
Y. Yu and R.N. Singh, University of Cincinnati, USA 70

My Life with Dielectric Ceramics

Kikuo Wakino

Murata Manufacturing Co., Ltd.

2-26-10, Tenjin, Nagaokakyo-shi, Kyoto 617, Japan

I joined Murata Manufacturing Co., Ltd. in the beginning of 1952 and retired in 1992. During these 40 years, I have been engaging and conducting the research and development of dielectric, ferroelectric and semi-conductive ceramics and some their applications. In this brief report, I would like to describe the major memorable events from the technical and industrial interest point of view. This report may include personal prejudices and/or misjudgments, but I would be very happy, if this report is of value for historical reference and useful for new comers in these field.

TiO₂ and Titanate Ceramic Capacitor

The first application of Titanium Dioxide and solid solution of MgTiO₃ and CaTiO₃ as a ceramic capacitor material was started in Germany in the 1920's. Epoch making BaTiO₃ was found and it's family have been recognized as the indispensable material for high K ceramic capacitor. Small parasitic inductance due to the small size and simple structural electrode of ceramic capacitor is the most important deature for the high frequency application. Because of this advantage, ceramic capacitor is only type of capacitor for microwave circuit.

Ilmenite, the main mineral resource of titanium dioxide, includes 0.1 to 0.5 % of Nb₂O₅ as an impurity depending on the mine. This Niobium is not removed through conventional sulfuric acid process for titanium dioxide manufacturing, which used to be most popular in Japan on that time.

Around 1950, at the very beginning of Murata, Murata had been faced with a very serious problem of insulation resistance (IR) degradation of titanium dioxide capacitor during operation. After severe straggling, Murata finally found that addition of Manganese (Mn) ion is the very effective counter measure to prevent the degradation of IR. This phenomenon was found accidentally at Murata.

One day of 1947-8 the stock of TiO₂, which was purchased around 1944, had run out and the TiO₂ source was therfore switched to new type product. Then the IR degradation problem started and Murata faced with a serious situation and forced to stop the delivery of products. After several tries, Murata found that warm flesh colored TiO₂ did not degrade in IR and pale white colored TiO₂ did and that warm flesh colored one included a small amount of Mn as an impurity with the help of the Chemical Laboratory of Kyoto University. Since then, at Murata, 0.2 to 0.7 wehight % of MnO₂ have been added into all Titanate formulation as a reduction inhibitor even though the reason is not clear in a scientific manner. This fact has been keeping me itchy (wondering) for almost 40 years. However the detailed studies of the role of Mn-ion in TiO₂ ceramics have scarcely been presented. Just before my retirement from Murata, I started the study to clarify the this longtime pending question with the help of many of my colleagues; the role of Mn-ion in Titanates and the quantitative relation between Mn-ion and Nb-ion which comes from ilmenite ore.

Based on several independent measurements, it became clear, that less than 1.0% of Nb₂O₅ acts as donor (Nb⁺⁵) and accelerates the reduction of TiO₂ and other Titanate; Mn-ion exists as Mn³⁺ and compensates the excess electron supplied from Nb⁺⁵ and prevents the reduction of TiO₂ and other Titanate. The tremendous improvement of the insulation resistance degradation is based on the critical balance between donor (Nb⁺⁵) and acceptor (Mn⁺³) concentrations. [1]

Why BaTiO₃ was not found in Germany

When I joined Murata, 1952, BaTiO₃ was already in production for ceramic capacitor and

underwater ultrasonic transducer (fish finder). It was for many years, a question for me that, whereas Germany was the first country which found and had been producing TiO_2 and MgTiO_3 - CaTiO_3 solid solution ceramics as capacitor, why BaTiO_3 was not found in Germany?

I raised this question with Professor L. E. Cross of The Pennsylvania State University, but clear answer could not be heard. Still I repeated several times the same questions and finally one day he told me as follows.

"Professor Bussem, who used to be a research engineer and group leader of the electronics ceramics in Siemens, had moved to USA after 1945. He was professor at The Penn. State University and then at Rutgers University. He told me, Siemens had already been working on BaTiO_3 , but no good insulating ceramics was made. All products were blacked colored and conductive, and dielectric properties were not measurable. And then, finally Siemens gave up the research of BaTiO_3 ."

If this is true, my guess rather understanding on BaTiO_3 discovery story is as follows. One of the TiO_2 manufacturing process in Japan (Kronos Brand) was transferred from Germany and was based on the sulfuric acid process and shows pale white color. TiO_2 used in Siemens would also be from sulfuric route and might be including 0.2 to 0.5 % Nb_2O_5 as an impurity which comes from Ilmenite ore and cause the reduction of BaTiO_3 . On the other hand, in the USA, the biggest TiO_2 manufacturer, duPont, was employing TiCl_4 rout which distils out Nb in process and includes only a trace of Nb. In Japan, fortunately, Dr. Ogawa and Waku might have used chloride rout products or impure TiO_2 in their research work and thus have had no reduction problem. Fate had not smiled on Siemens!

Deviation Problem of A/B ratio of BaTiO_3

In 1954, Murata started the import of BaTiO_3 from the BT powder manufacturer of USA to expand HiK ceramic capacitor production. With the first few lots of BaTiO_3 , the production was carried out successfully, but after finishing 4 or 5 lots, we encountered a serious problem of imperfect sintering even at higher isntering temperature than before. After bothersome trial and error and testing, we found that the cause of this trouble came from the large upward deviation of molar ratio A/B compared with the former batches. The trouble was solved by fine tuning the molar ratio but we could not get such consistent characteristics as the first few lots. In spite of our strong request to keep narrow deviation of molar ratio, the supplier could not give us good answer. Then, finally we decided to produce BaTiO_3 by ourselves. We established stable mass production facility in 1960, using a precise weighing and mixing system and automated rotary kiln, and then achieved very narrow controlled condition of approximately 0.1 % standard deviation of A/B ratio. This technology attracted the interest of one chemical company of the USA and the process was transferred to them together with equipment.

Semi-conductive BaTiO_3

As mentioned before, our TiO_2 is including a small amount of Nb, so TiO_2 and BaTiO_3 ceramics made from this TiO_2 are easily reduced and became semi-conductive. But in Murata, we were interested in only good insulator and have had the magic ingredient in hand, and by passed this problem with Mn-ion addition. Then we failed to measure the resistance, temperature characteristics of resistance etc. other than insulation resistance, dielectric properties and others. Surprisingly, one day of 1954, the big news from Phillips regarding the abnormal increase of resistance value at around Curie temperature was introduced through Professor Kiyoshi Abe of Kyoto University. Triggered by Professor Abe's suggestion, the strong R&D team for semi

conductive BaTiO_3 ceramics was organized under the leadership of Dr. Osamu Saburi. Murata succeeded in development and production of BC (Class III capacitor) and PTC products in short time but we missed the honor of being the first finder of peculiar characteristics of the semi conductive BaTiO_3 . This is the good reason that, R&D engineers should have a broad understanding and strong curiosity even about unexpected or unwanted phenomena.

My contribution on this subject is concentrated mainly on establishment of mass production condition and line.

PZT

The basic research on the phase diagram, structural analysis, anti-ferroelectric and ferroelectric behavior of PbZrO_3 (PZ) and $\text{PbZr}_3\text{-PbTiO}_3$ solid solution (PZT) were derived and intensively performed by Professor Y. Takagi and his group of Tokyo Institute of Technology in the beginning of 1955, but since they were basic scientist and would not be interested in practical applications, any piezoelectric measurements were not made. The piezoelectric properties were investigated widely by Dr. Hans Jaffe and Bernald Jaffe of NBS (presently NIST). The most significant results are the discovery of large piezoelectric behavior at Morphotropic Boundary (MPB) composition, soft piezoelectric characteristics with the doping of some rare earth element and hard piezoelectric characteristics with the doping of chromium, cobalt and some other transition element. Again we missed the first discovery of large piezoelectricity of PZT family even Murata already was producing BaTiO_3 piezoelectric devices. But based on the mass production and product design technique of BaTiO_3 ceramics, Murata succeeded to develop and mass produce the ceramic filter, ceramic resonator, transducer etc. and made contributions for the temperature stabilization, miniaturization, tuning less assembling for IF circuit, timing device for CPU and cost reduction of the electronic equipment.

DR. S. Fujishima and his group had engaged in the development of piezoelectric devices and put them into production and my group was responsible to develop and produce PZT ceramics.

Dielectric Resonator

The basic research of extremely low loss and temperature stable microwave ceramics at Murata was started in the beginning of 1970, triggered by the request of Professor Yoshio Kobayashi of Saitama University who was studying the electromagnetic mode analysis of dielectric resonator. In the beginning, we started with Class I ceramic capacitor material and then extended the coverage of material to other types. During this work, we have gotten following results; [2]-[17]

- The infra red and far infrared reflectivity data are well fit by the classical dispersion theory based on rigid sphere model lattice vibration and Frenel's relation.
- The complex dielectric constant at microwave are predictable by the help of the above mentioned scheme.
- This method is useful for selection of the candidate material for the microwave application without laborious microwave measurement.
- Dielectric loss tangent closely relates not only to the intrinsic harmonicity of crystal field but also to the purity of constituting material and perfection of crystal structure.
- It is possible to design higher Q, smaller and temperature stable resonator compared to conventional air cavity.
- Using a very high pure and well-sintered dielectric resonator, we can achieve very low distortion less than -160 dBm, which is good enough for high power microwave mixing device.

- Most significant miniaturization of microwave filter is achieved by using TEM mode with somewhat large degradation of Q but is good enough for practical use.

In 1975, we reported the first practical 4.8 GHz filter. [18] Since then, every year Murata have developed several new type devices. We are contributing tremendously to the miniaturization of components used in the cellular telephone system for both base station and hand held set.

Acknowledgement

These results are the total output by all of the people supported by Mr. Akira Murata whoes strong leadership on originality, challenge and curiosity about new things made his company to prosper. I would like to express my heartfelt thanks to Mr. Akira Murata for his support, Professors Emeritus Kiyoshi Abe (passed a way) and Tetsurou Tanaka of Kyoto University, Professor Yoshihiro Konishi of Tokyo Technical Institute and Professor Yoshio Kobayashi of Saitama University for their excellent guidance and support in technical direction. Moreover I would like to express my sincere thanks to Dr. Satoru Fujishima, Dr. Toshio Nishikawa, Dr. Youhei Ishikawa, Mr. Yukio Sakabe, Dr. Haruo Matsumoto, Dr. Hiroshi Tamura, Dr. Kenji Tanaka and many others of my excellent colleagues at Murata for their constant and warm support to me.

References

- [1] K. Wakino, H. Takagi, H. Sano, K. Nishida, K. Tomono and Y. Sakabe, "Behavior of Mn-Ion on Electrical Conductivity of Nb-Doped TiO_2 -Based Ceramics", *Ceramic Trans.* Vol. 32, pp. 129-137, 1993
- [2] K. Wakino and H. Tamura, "Relations between Microwave Dielectric losses and Micro Structure of $(\text{ZrSn})\text{TiO}_4$ Dielectric Ceramics," *J. Ceramic Society of Japan*, Vol. 88, No. 8, pp. 475-482 (1980) (in Japanese)
- [3] K. Wakino and H. Tamura, "Relations between Microwave Dielectric losses and Micro Structure of $(\text{ZrSn})\text{TiO}_4$ Dielectric Ceramics," *J. Ceramic Society of Japan*, Vol. 88, No. 8, pp. 475-482 (1980) (in Japanese).
- [4] K. Wakino, K. Minai and H. Tamura, "Microwave Characteristics of $(\text{ZrSn})\text{TiO}_4$ and $\text{BaO-PbO-Nd}_2\text{O}_3\text{-TiO}_2$ Dielectric Resonators," *J. Am. Ceram. Soc.* Vol. 67, No. 4, pp. 278-281, (April 1984)
- [5] H. Tamura, T. Konoike, Y. Sakabe and K. Wakino, "Improved High Q Dielectric Resonators with Complex Perovskite Structure," *J. Am. Ceram. Soc.* Vol. 67, No. 4, C59-61, (April 1984)
- [6] K. Wakino, D. A. Sagara and H. Tamura, "Far Infrared Reflection Spectra of $\text{Ba}(\text{ZnTa})\text{O}_3\text{-BaZrO}_3$ Dielectric Resonator Material," *Proceedings of the 6th International Meeting on Ferroelectricity Kobe 1985. Japanese Journal of Applied Physics* Vol. 24, pp. 1042-1044, (1985).
- [7] K. Wakino, M. Murata and H. Tamura, "Far Infrared Reflection Spectra of $\text{Ba}(\text{ZnTa})\text{O}_3\text{-BaZrO}_3$ Dielectric Resonator Material," *J. Am. Ceram. Soc.* Vol. 69, No. 1, pp. 34-37, (1986).
- [8] H. Tamura, D.A. Sagala and K. Wakino, "Lattice Vibration of $\text{Ba}(\text{Zn}_{1/3}\text{Ta}_{2/3})\text{O}_3$ Crystal with Ordered Perovskite Structure," *Jpn. J. Appl. Phys.*, Vol. 25, No. 6 June, pp. 787-791, (1986).
- [9] K. Wakino and H. Tamura, "Microwave Characteristics and Infra-red Reflection Spectra of TiO_2 Single Crystal," *The Amer. Ceram. Society, Annual Meeting*, (1988).
- [10] K. Wakino and H. Tamura, "Microwave Dielectric Materials," *Ceramic Transaction*, Vol.8, pp. 305-314, (1990).
- [11] H. Matsumoto, H. Tamura and K. Wakino, " $\text{Ba}(\text{Mg,Ta})\text{O}_3\text{-BaSnO}_3$ High-Q Dielectric Resonator," *Jpn. J. Appl. Phys.*, Vol. 30, No. 9B, September, pp. 2347-2349, (1991).
- [12] T. Nishikawa, K. Wakino, H. Tamura, H. Tanaka and Y. Ishikawa, "Precise Measurement Method for Temperature Coefficient of Microwave Dielectric Resonator Material," *IEEE MTT-S International Microwave Symposium Digest* (Cat. No. 87CH2395-2) J-6, pp. 277-280, Las Vegas Nevada, (June 9-11, 1987).
- [13] K. Wakino (invited), "High Frequency Dielectrics and Their Applications," *ISAF '86-Proceedings of the 6th IEEE Inter-national Symposium on Applications of Ferroelectrics*, Bethlehem PA, (June 1986).
- [14] K. Wakino, "Recent Development of Dielectric Resonator Materials and Filters in Japan," *ECAPD-1/ISAF '88* (1988/9/1).
- [15] K. Wakino, "Ultra fine Particle and Microwave Dielectric Materials," *91st The American Ceramic Society Annual Meeting*, (1989/04/26).
- [16] H. Tamura, J. Hattori, T. Nishikawa and K. Wakino, "Third Harmonic Distortion of Dielectric Resonator Materials," *Jpn. J. Appl. Phys.*, Vol. 28, No.12, December, pp. 2528-2531, (1989).

- [17] K. Wakino T. Nishikawa Y. Ishikawa and H. Tamura, "Dielectric Resonator Materials and their Applications for Mobiles Communication Systems," Br. Ceram. Trans. J., Vol. 89, No. 2, pp. 39-43, (1990).
- [18] K. Wakino, T. Nishikawa, S. Tamura and Y. Ishikawa, "Microwave Bandpass Filters Containing Dielectric Resonators with Improved Temperature Stability and Spurious Response," 1975 IEEE MTT-S International Microwave Symposium, IEEE Cat. No.75CH0955-5, pp.63-65 (1975).
- [19] K. Wakino and Y. Konishi, "Bandpass Filter with Dielectric Materials used for Broadcasting Channel Filter," IEEE Trans. Broadcasting, Vol. BC-26, No.1, pp.1-6 (March 1980).
- [20] K. Wakino (invited), "High Frequency Dielectrics and Their Applications," '86-Proceedings of the 6th IEEE International Symposium on Applications of Ferroelectrics, Bethlehem PA. June 1986.
- [21] K. Wakino (invited), "Recent Development of Dielectric Resonators and Filters in Japan," 1987 SBMO International Microwave Symposium Proceedings (IEEE Cat.No.87THO 183-4), pp.681-688, July 27-30, 1987.
- [22] K. Wakino, T. Nishikawa, H. Matsumoto and Y. Ishikawa, "Miniaturized Band Pass Filters using Half Wave Dielectric Resonators with Improved Spurious Response," 1978 IEEE MTT-S International Microwave Symposium Digest, pp.230-232, 27-29 June 1978.
- [23] K. Wakino, T. Nishikawa, H. Matsumoto and Y. Ishikawa, "Quarter Wave Dielectric Transmission Line Diplexer for Land Mobile Communications," 1979 IEEE MTT-S International Microwave Symposium Digest (IEEE Cat. No.79CH1439-9), pp.278-280, 30 April-2 May 1979.
- [24] K. Wakino, T. Nishikawa, and Y. Ishikawa, "Miniaturized Diplexer for Land Mobile Communication using High Dielectric Ceramics," 1981 IEEE MTT-S International Microwave Symposium Digest (Cat. No.0149-645X/81), pp.185-187, June 15-19, 1981.
- [25] K. Wakino, T. Nishikawa, Y. Ishikawa and H. Matsumoto, "400 MHz Band Elliptic Function Type Miniaturized Diplexer using Dielectric Resonators," 32nd IEEE Vehicular Technology Conference, pp.303-5, 23-26 May 1982.
- [26] K. Wakino, T. Nishikawa, S. Tamura and H. Tamura, "An X-band GaAs FET using a Dielectric Resonator," Proceedings of the 37th Annual Frequency Control Symposium, pp. 481-4, Philadelphia, PA, U.S.A., (1983).
- [27] T. Nishikawa, K. Wakino and Y. Ishikawa, "800 MHz Band Channel Dropping Filter using TM_{010} mode Dielectric Resonator," 1984 IEEE MTT-S International Microwave Symposium Digest Expanding Microwave Horizons (Cat.No.84CH2034-7, pp.199-201, 29 May-June 1984).
- [28] T. Nishikawa, K. Wakino, H. Wada and Y. Ishikawa, "800 MHz Band Dielectric Channel Dropping Filter Using TM_{110} Triple Mode Resonance," 1985 IEEE MTT-S International Microwave Symposium Digest (Cat.No.85CH2163-4), pp.289-92, 4-6 June 1985.
- [29] K. Wakino, T. Nishikawa, Y. Ishikawa and H. Tamura, "800 MHz Band Miniaturized Channel Dropping Filter Using Low Loss Dielectric Resonator," Denshi Tokyo, No.24, pp.72-75 (1985), IEEE Tokyo Section.
- [30] T. Nishikawa, K. Wakino, J. Hattori and Y. Ishikawa, "800 MHz Band Face-Bonding Filter Using Dielectric B.D.L.S.," 1986 IEEE MTT-S International Microwave Symposium Digest (Cat.No. 86CH2031-0), pp.403-406, June 2-4, 1986.
- [31] T. Nishikawa, K. Wakino, K. Tsunoda and Y. Ishikawa, "Dielectric High-Power Bandpass Filter Using Quarter-Cut TE_{01d} Image Resonator for Cellular Base Stations," IEEE Transactions on Microwave Theory and Techniques, Vol.MTT-35, No.12, pp.1150-1155 (Dec.1987).
- [32] T. Nishikawa, K. Wakino, T. Hiratsuka and Y. Ishikawa, "800 MHz Band High-Power Bandpass Filter Using TM_{110} Mode Dielectric Resonators for Cellular Base Station," 1988 IEEE MTT-S International Microwave Symposium Digest.

Are Domains Taking A Rest Or Do They Go Somewhere?

Jan Fousek^{*)}

Materials Research Laboratory
The Pennsylvania State University
University Park, PA 16802 USA

Abstract—In the introduction, we classify applications of ferroelectric materials from the point of view of significance of domain phenomena. Present status of domain imaging methods is described, followed by a short overview of new observations on static and dynamic properties of domains. Recently suggested possibilities of applications based on domain properties are then enumerated. Important unanswered domain-related material properties are specified and some new research areas suggested. The field of domain investigations is very much alive and promising in both new basic ideas and practical use.

I. INTRODUCTION

Ferroic materials in general and ferroelectrics in particular are characterized by two principal features. First, it is the existence of a structural phase transition from the parent phase to the ferroic phase in which the structure of the material has a lower symmetry. In many materials, this leads to high and temperature dependent values of basic material characteristics such as thermal expansion, dielectric permittivity or piezoelectric coefficients. Second, it is the fact that in the ferroic phase the medium can exist in 2 or more *domain states* differing in spatial orientation. This feature is reflected in the existence of domains: regions representing domain states which are distinguished by the orientation of spontaneous polarization (in ferroelectrics) and of spontaneous strain (in ferroelastics).

The significant property of ferroelectrics and ferroelastics is that applied electric field and mechanical stress can change the relative volumes of domains. It is this phenomenon which is responsible for huge nonlinearities, hysteretic response but even for substantial increase of already pronounced linear properties. Practical applications of ferroelectrics can be divided into two groups. In some of them, those properties are important that characterize single domain samples and the presence of domains is highly undesired. In others, domain phenomena are fundamental or may increase figures of merit. Tab. 1 gives a survey of both; it also indicates the present market status of these applications.

Research into static and dynamic characteristics of domains in ferroelectric and (often simultaneously) ferroelastic materials has been going on for fifty years. Which particular subjects of research have been moving forward in recent years? Is there anything left to be discovered? Can we reliably predict the behaviour of commonly studied and applied materials? What are the most pressing issues to be addressed

in forthcoming research, and what could be, perhaps, the target domain properties? This lecture offers a few comments to these questions.

II. RECENT ADVANCES IN DOMAIN IMAGING METHODS; NEW OBSERVATIONS AND APPLICATIONS

Of several kinds of ferroelectric systems (single crystals, ceramics, glass-ceramics, polymers, thin films) here we shall pay preferential attention to domains in single crystals where all basic concepts on the behaviour of domains originate, being however aware of consequences for the properties of ceramics and thin films. Understandably, in this short talk only a very partial selection of issues can be made - with the aim to comment on the questions asked above.

A. Domain Imaging

Imaging domains, their shapes and sizes, is a fundamental task. Nature offers a variety of approaches since the symmetry relations dictate that neighbouring domains differ in the orientation of structure and in tensorial properties. In addition, some methods provide contrast of domain walls. Since the sixties there has been a constant progress in imaging methods and increasing sophistication and sensitivity of techniques have brought us from optical microscopy and classical surface methods (etching and decoration) through X-ray topography and pyroelectric mapping into the realm of scanning electron microscopy, second harmonic scattering, photorefractive two-beam coupling, high resolution transmission electron microscopy, electron holography and atomic force microscopy.

Let us shortly mention just some important new observations. *HRTEM* is now able to measure the widths of domain walls and verifies that they are just one or a few lattice constants [1]. The width may depend on what we are watching: a wall in KNbO_3 is characterized by ionic displacements within 15 Å but significant changes of electron density extend over a band 50 Å wide [2]. Chemical nanodomains have been identified in relaxor-type ferroelectrics [3]. Also new *optical techniques* prove to be very powerful. A method based on photorefractive properties made it possible [4] to image 180° domains optically in large BaTiO_3 crystals; this

TABLE I
APPLICATIONS OF FERROELECTRICS

| Physical property | Example of device | C.A. |
|-------------------|-------------------|------|
|-------------------|-------------------|------|

DOMAINS PLAY AN ESSENTIAL ROLE

| | | |
|------------------------------------|---|--------------|
| piezoelectricity of poled ceramics | transducers | yes |
| | sensors, actuators | yes |
| | positioners, motors | yes |
| | resonators, filters | yes |
| permittivity of ceramics | capacitors | yes |
| polarization bistability | nonvolatile memories | yes |
| dielectric nonlinearity | variable capacitors | no |
| single domain wall motion | analog recording | no |
| electron emission | ferroelectric cathodes | yes |
| switchable birefringence | displays | no |
| | optical memories | no |
| | image processors | no |
| electro-optics | diffraction gratings | no |
| nonlinear optics | frequency multipliers based on quasi-matching structure | close to yes |
| photorefractive | image processors | no |
| | optical memories | |

DOMAINS UNDESIRABLE

| | | |
|------------------|---|-----|
| permittivity | μ -wave resonators | yes |
| pyroelectricity | IR detectors | yes |
| | IR-imaging | yes |
| electro-optics | lumped modulators | yes |
| | spatial light modulators | yes |
| | directional couplers | no |
| nonlinear optics | frequency multipliers based on phase matching | yes |
| | parametric oscillators | yes |
| | phase conjugators | yes |
| | optical memories | no |
| photorefractive | image processors | no |

C.A. - commercial availability

is based on the fact that in a two-beam coupling arrangement the sign of the energy transfer depends on the direction of polarization [5]. Analysis of scattered second harmonic light enables one to analyze sizes of 180° domains [6].

ment the sign of the energy transfer depends on the direction of polarization [5]. Analysis of scattered second harmonic light enables one to analyze sizes of 180° domains [6].

Electron holography provides a tool for imaging the distribution of electric potential in the vicinity of domain walls [7,8] and grain boundaries [9]. Analysis of interference pattern around a 90° wall in BaTiO_3 made it possible to map how polarization changes within the wall [7].

The *liquid crystal decoration* method [10-12] met with a remarkable success; it is one of the few techniques enabling direct observations of slower kinetic processes in real time, such as spontaneous development of domains after passing the Curie point.

Atomic force microscopy is an effective surface technique which can operate in several difference modes sensitive to electric fields above the sample or to its surface topography [13,14]. It has provided information on the thickness of 180° domain wall in triglycine sulphate (8 nm) at the crystal surface. It can even reach molecular resolution [15].

These and some other new methods for domain imaging are powerful but still rather limited in possible applications. Methods based on second harmonic generation demand samples transparent for both wavelengths, methods based on photorefractive call for photoconductive and transparent materials; in addition, the presence of complex patterns of ferroelastic domains make any optical method impractical. The price paid in using HRTEM or electron holography is the transformation of a real sample into an artificial thin object with profoundly changed boundary conditions. Both mentioned surface methods - liquid crystal decoration and AFM, require extremely high quality surfaces with no artefacts, which are available for only a few ferroelectric materials.

While X-ray topography can render information on inner domain patterns in single crystals, we have no method capable of providing sectional views of domains inside a ceramic grain. In particular, techniques distinguishing 180° nonferroelastic domain pairs do not have high enough resolution or are not able to penetrate into the bulk of samples with ferroelastic domain patterns. Thus our knowledge on domains in grains remains incomplete; at present we depend on surface observations, indirect data for thinned samples and indirect information relating X-ray diffraction data with polarization measurements. Simple questions like what is the density of 180° domain pairs in BaTiO_3 ceramics remain unanswered. A number of related problems concern ferroelectric thin films; in fact we have almost no data on domain structures in thin films and, in particular, on what kind of domain processes proceed in a thin film during switching. We might even ask the question - is this process in films really connected with classical domain kinetics at all? There is a lot of empty space here to be filled in - perhaps by new techniques to come.

B. Some Observations of Static Patterns

There is a wealth of recent data on the *orientations* of domain walls and all seem to agree well with expectations. Thus in large crystals of BaTiO_3 180° domains form cylinders prolonged along the polar axis (to avoid charge), with square cross-sections (to comply with the anisotropy of domain wall energy). Similarly, all data on ferroelastic walls are in agreement with predictions based on mechanical compatibility. Increasing number of materials show the presence of *S*-walls [16,17] which are characterized by general orientations with irrational crystallographic indices. It was predicted long ago that their orientation may be strongly

temperature dependent. This effect has now been observed [18] in crystals of sodium niobate where rotation of the wall occurs over an angle of 30° . In ceramic materials which allow for the existence of *S*-walls the effect may result in extremely very high stress levels. In addition, the presence of these walls is predicted to induce large anisotropy of effective piezoelectric coefficients [19].

While complex domain patterns in ferroelastic-ferroelectric single crystals have been investigated (see e.g. [20]), our knowledge on domains in *ceramic grains* is limited for reasons given above. Observations indicate that domains materialized in ceramics differ in some features from those in single crystals. While domain wall orientations follow the same compatibility rules, domain patterns in grains are to a large extent influenced by mechanical boundary conditions. This has two aspects; first, the grain is clamped and ferroelastic domains are responsible for preserving its shape at the phase transition. The requirement of stress relief leads to the relation $d \propto g^{1/2}$ between the width d of ferroelastic domains and the grain size g [21] and manifests itself in a large density of ferroelastic walls up to $2 \times 10^9 \text{ m}^{-1}$. Second, TEM observations [22] suggest that domain patterns in neighbouring grains are not independent of each other. In commercial ceramics close to morphotropic phase boundary the situation will be even more complicated because of coexistence of two phases.

C. New dynamic phenomena

We point only in passing to several exciting phenomena that have been recently investigated. By means of a modified atomic force microscope it has become possible to record information into the surface of a TGS crystal; the method represents a true writing process [23] by nanoscale domain nucleation.

Very stimulating new observations [24] showed that the degree of polarization reversal in BaTiO_3 crystals can be controlled by UV illumination together with an applied biasing field. The effects have been connected with domain walls providing traps for electronic charge.

It was found that photorefractive holograms in ferroelectrics can be strongly enhanced and their lifetime prolonged by a process in which partial polarization reversal is controlled by optically induced electric fields [25].

D. New application aspects

Starting with single crystals, devices attracting a lot of attention are optical frequency multipliers working in the quasi-matched mode. They are based on the fact that in many ferroelectrics 180° domains differ in sign of the non-linear optical coefficient. If a periodic domain pattern is produced whose spatial frequency equals the coherence

length, depending on the light wavelength and refractive index dispersion, the efficiency of energy conversion from the incident to the second harmonic light greatly increases. Typically, domain periodicity of several μm is required. Many successful techniques have been developed [26] to achieve this goal in crystals of LiNbO_3 , LiTaO_3 and KTiOPO_4 . Some of the methods which are based on applying electric field, electron bombardment, thermal pulsing or chemically driven movement of Li are still semi-empirical. Tailoring domain patterns to increase figures of merit envisaged long ago is thus becoming a reality.

Domain-based applications working with both ferroelectric single crystals and ceramics are based on the effect of electron emission [27,28]. When the charge equilibrium in a single-domain ferroelectric is disturbed by changing temperature or by polarization reversal in applied field, unscreened charges appear producing additional electric field of 10^6 to 10^8 V/m . This gives rise to the field-exoemission of electrons. Large current densities - up to 10^7 Am^{-2} have been observed and applications in form of ferroelectric cathodes developed.

Reversal of spontaneous polarization in ferroelectric thin films is perhaps the hottest subject concerning domains. The key issues here are the speed of polarization reversal (switching times of the order of ns have been reported) and undesired side-effects such as fatigue (loss of switchable polarization) or imprint (a tendency of remanent polarization to keep a preferential direction). All these phenomena are believed to be connected with the kinetic properties of domain walls and their pinning to various kinds of defects. To keep the length of this contribution within limits we do not cover the subject here; it has been discussed in detail in several review papers (see e.g. [29]) and is periodically covered in the Proceedings of Materials Research Society [30].

III. PRESSING PROBLEMS, OLD AND NEW

Let us briefly mention some of the problems which call for intensive research. One concerns thin film memories where direct information on polarization reversal mechanisms is urgently needed. In particular, the problem of nucleation is one which calls for both experimental and theoretical work. While nucleation mechanism may be considered responsible for thickness dependence of the coercive field [31], it has been known for a long time that switching in bulk samples often starts at so-called repeaters; surprisingly, models for defect-assisted nucleation are not available. The old puzzle of unrealistically high nucleation energies remains unresolved. Systematic studies of the influence of material purity on coercive field and on nucleation in particular are absent even for single crystals; yet one might think of governing these parameters by controlled doping.

The issue of spontaneous polarization screening is repeatedly addressed by theoreticians [32] but there seem to exist no clear experimental data on the degree of screening and charge distribution. Yet these are properties determining to a large extent any behaviour of ferroelectrics in practical devices. Similarly, the influence of metal-ferroelectric interfaces [33,34], which play a crucial role in ferroelectric memories as well as in high permittivity materials for DRAMS, on domain processes are unknown.

In ceramic ferroelectrics, extrinsic contributions to permittivity and piezoelectric coefficients play a major role [35]. Recent data showed [36] that lamellar domain structure in single crystals of ferroelectric RbH_2PO_4 are responsible for high piezoelectric coefficient d_{36} which exceeds 3000 pC/N in a temperature interval of 30 K. It appears possible that controlling crystal purity may lead to further enhancement of piezoelectric response by decreasing wall pinning. Another interesting issue is the thickness t_w of domain wall. Targeted crystal doping could lead to a decrease of the correlation coefficient and increase of t_w ; this again, with large wall densities, could considerably enhance the overall response of multidomain samples.

Also, one may think of ways to control domain wall density. A domain system which is close to ideal is one we encounter in incommensurate and lock-in phases of materials like Rb_2ZnCl_4 . Here a periodic system of 180° ferroelectric domain walls is formed [37] giving a large contribution to permittivity such that wall motion induced by applied field is determined by mutual interaction between walls [38]. Bias field provides a huge, almost nonhysteretic nonlinearity.

These few examples are meant to indicate two things: a number of basic problems concerning domain behaviour remain unanswered; at the same time, some domain-conditioned macroscopic properties of ferroelectrics offer interesting avenues, attractive from the practical point of view.

IV. CONCLUSIONS.

Since a question was asked in the title it seems appropriate to conclude with an answer. Perhaps it may sound like this: The destinations of domain research are not badly defined. Treasures to be found are very promising. Domains definitely move forwards: in recent years there has been a considerable progress in developing a basis for understanding perhaps all involved phenomena and there is a new wave of application efforts. It appears to the present author, however, that the field suffers from a lack of communication between those who (believe to) do basic research and those who (would like to) apply; that there is a lack of ability to present needs or results in a language accessible to the other party.

Domain phenomena in ferroic materials are periodically discussed at the International Symposia On Ferroic Domains And Mesoscopic Structures whose Proceedings are published as special issues of *Ferroelectrics*. After the meeting in Vienna, 1996, the fifth one will take place in State College, PA in 1998.

*) On leave from the Dept. of Physics, Technical University, CZ-46117 Liberec, Czech Republic.

REFERENCES

- [1] J. L. Peng and L. A. Bursill, "HREM investigation of ferroelectric and ferroelastic domains in bronze type tunnel structures," *Phase Transitions*, vol. 34, pp. 171-178, 1991.
- [2] J. L. Peng and L. A. Bursill, "On the width of charged $\{110\}$ ferroelectric domain walls in potassium niobate," *Phil. Mag. A*, vol. 48, pp. 251-263, 1983.
- [3] L. A. Bursill, "Atomic resolution imaging of ferroelectric domains," *Ferroelectrics*, vol. 191, pp. 129-134, 1997.
- [4] V. Grubsky, S. MacCormack, and J. Feinberg, "All-optical, three-dimensional mapping of 180° domains hidden in a BaTiO_3 crystal," *Optics Letters*, vol. 21, pp. 6-8, 1996.
- [5] R. Cudney, J. Fousek, M. Zgonik, P. Günter, M. H. Garrett, and D. Rytz, "Interaction between domain reversal processes and light in barium titanate," *Ferroelectrics*, vol. 157, pp. 45-50, 1994.
- [6] R. S. Cudney, V. Garces-Chavez, and P. Negrete-Regnaron, "Analysis of ferroelectric 180° -domain structures in BaTiO_3 by use of second harmonic scattering," *Optics Letters*, vol. 22, pp. 439-441, 1997.
- [7] X. Zhang, D. C. Joy, Y. Zhang, T. Hashimoto, L. Allard, and T. A. Nolan, "Electron holography techniques for study of ferroelectric domain walls," *Ultramicroscopy*, vol. 51, pp. 21-30, 1993.
- [8] W. Cao and C. Randall, "Theory of the fringe patterns in the study of ferroelectric domain walls using electron holography," *Solid State Commun.*, vol. 86, pp. 435-439, 1993.
- [9] V. Ravikumar, R. P. Rodriguez, and V. P. Dravid, "Space-charge distribution across internal interfaces in electroceramics using electron holography: I, Pristine grain boundaries," *J. Am. Ceram. Soc.*, vol. 80, pp. 1117-1130, 1997.
- [10] L. I. Dontsova, N. A. Tikhomirova, and L. A. Shuvalov, "Investigation of domain structure and switching processes in ferroelectrics by the liquid crystal method," *Ferroelectrics*, vol. 97, pp. 87-124, 1989.
- [11] N. Nakatani, "Ferroelectric domain structure in TGS just below the Curie point after heat treatment," *Jpn. J. Appl. Phys.*, vol. 24, pp. L528-L530, 1985.
- [12] M. Glogarová and G. Durand, "Anchoring strength of a nematic liquid crystal on a ferroelectric crystal interface," *J. Phys. France*, vol. 49, pp. 1575-1581, 1988.
- [13] F. Saurenbach and B. D. Terris, "Imaging of ferroelectric domain walls by force microscopy," *Appl. Phys. Lett.* vol. 56, pp. 1703-1705, 1990.
- [14] L. Eng, J. Fousek, and P. Günter, "Ferroelectric domains and domain boundaries observed by scanning force microscopy," *Ferroelectrics*, vol. 191, pp. 211-218, 1997.
- [15] M.-K. Bae, T. Horiuchi, K. Hara, Y. Ishibashi, and K. Matsushige, *Jpn. J. Appl. Phys.*, vol. 33, Part I, pp. 1390-1393, 1994.

- [16] L. E. Balyunis, V. Yu. Topolov, I. S. Bah, and A. V. Turik, "The S-type domain and twin boundaries in late-like PbZrO_3 crystals having complicated twinned structures," *J. Phys.: Condens. Matter*, vol. 5, pp. 1419-1426, 1993.
- [17] A. I. Otko, J. Dec, and S. Miga, "Domain structure evolution and crystalloptical peculiarities of incommensurate ferroelastic $\text{KSc}(\text{MoO}_4)_2$," *Ferroelectrics*, vol. 191, pp. 253-259, 1997.
- [18] S. Miga, J. Dec, and M. Pawelczyk, "Peculiarities of thermal switching in sodium niobate crystals," *J. Phys.: Condens. Matter*, vol. 8, pp. 8413-8420, 1996.
- [19] V. Yu. Topolov, "Anisotropy of electromechanical properties in KNbO_3 crystals with S-type domain boundaries," *J. Phys.: Condens. Matter*, vol. 7, pp. 7405-7408, 1995.
- [20] E. G. Fesenko, V. G. Gavrilachenko, and A. F. Semenchov, *Domain Structure of Multiaxial Ferroelectric Crystals* (in Russian), Rostov on Don: Publishing House of the Rostov University, 1990.
- [21] G. Arit, "Twinning in ferroelectric and ferroelastic ceramics: stress relief," *J. Mat. Sci.*, vol. 25, pp. 2655-2666, 1990.
- [22] W. Cao and C. A. Randall, "Grain size and domain size relation in bulk ceramic ferroelectric materials," *J. Phys. Chem. Solids*, vol. 57, pp. 1499-1505, 1996.
- [23] L. Eng, private communication.
- [24] W. L. Warren, D. Dimos, and B. A. Tuttle, "Electronic and ionic trapping at domain walls in BaTiO_3 ," *J. Am. Ceram. Soc.* vol. 77, pp. 2753-2757, 1994.
- [25] R. Cudney, J. Fousek, M. Zgonik, P. Günter, M. H. Garrett, and D. Rytz, "Enhancement of the amplitude and lifetime of photo-induced space charge fields in multi-domain ferroelectric crystals," *Phys. Rev. Letters*, vol. 72, pp. 3883-3886, 1994.
- [26] M. Houé and P. D. Townsend, "An introduction to methods of periodic poling for second harmonic-generation," *J. Phys. D: Appl. Phys.*, vol. 28, pp. 1747-1763, 1995.
- [27] G. Rosenman and I. Rez, "Electron emission from ferroelectric materials," *J. Appl. Phys.*, vol. 74, pp. 1904-1906, 1993.
- [28] L. Schachter, J. D. Ivers, J. A. Nation, and G. S. Kerslick, "Analysis of a diode with a ferroelectric cathode," *J. Appl. Phys.*, vol. 74, pp. 8097-8110, 1993.
- [29] P. K. Larsen, R. Cuppens, and G. A. C. M. Spierings, "Ferroelectric memories," *Ferroelectrics*, vol. 128, pp. 265-292, 1992.
- [30] *Ferroelectric Thin Films IV*, Eds. B. A. Tuttle, S. B. Desu, R. Ramesh, and T. Shiosaki, Materials Research Society Symposium Proceedings, vol. 361, Pittsburgh: Materials Research Society, 1995.
- [31] A. K. Tagantsev, "Mechanism of polarization switching in ferroelectric thin films," *Ferroelectrics*, vol. 184, pp. 79-88, 1996.
- [32] A. S. Sidorkin, B. M. Darinskii, and A. S. Sigov, "Evolution of domain structure in ferroelectrics in the presence of polarization screening by charges bound to surface states and by free charge carriers," *Phys. Solid State*, vol. 39, pp. 823-825, 1997.
- [33] O. G. Vendik and L. T. Ter-Martirosyan, "Size effect in layered structures: ferroelectric/normal metal and ferroelectric/high-TC superconductor," *Phys. Solid State*, vol. 36, pp. 1778-1781, 1994.
- [34] G. Teowee and D. R. Uhlmann, "A model of the metal-ferroelectric-metal capacitor," *Mat. Res. Symp. Proc.*, vol. 310, pp. 415-422, 1993.
- [35] Q. M. Zhang, H. Wang, N. Kim, and L. E. Cross, "Direct evaluation of domain wall and intrinsic contributions to the dielectric and piezoelectric response and their temperature dependence on lead zirconate-titanate ceramics," *J. Appl. Phys.*, vol. 75 pp. 454-459, 1994.
- [36] M. Štula, J. Fousek, H. Kabelka, M. Fally, and H. Warhanek, "Extrinsic contribution to piezoelectric properties of RbH_2PO_4 crystals in the ferroelectric phase", unpublished.
- [37] V. Novotná, H. Kabelka, J. Fousek, M. Havránková, and H. Warhanek, "Dielectric properties of Rb_2ZnCl_4 crystals in the commensurate phase," *Phys. Rev. B*, vol. 47, pp. 11019-11026, 1993.
- [38] T. Hauke, V. Müller, H. Beige, and J. Fousek, "Modelling of ferroelectric hysteresis loops in purified Rb_2ZnCl_4 ," *J. Appl. Phys.* vol. 79, pp. 7958-7964, 1996.

Domain Configuration and Ferroelectric Related Properties of Relaxor Based Single Crystals

S. Wada*, S.-E. Park, L.E. Cross, and T.R. Shrout

Materials Research Laboratory, The Pennsylvania State University,
University Park, PA 16802, U.S.A.

*Visiting Scholar, current address
Department of Applied Chemistry, Tokyo University of Agriculture & Technology
24-16 Nakamachi 2-chome, Koganei, Tokyo 184, JAPAN

Abstract- Domain configuration and ferroelectric related properties of rhombohedral $\text{Pb}(\text{Zn}_{1/3}\text{Nb}_{2/3})\text{O}_3$ and its solid solution with PbTiO_3 were investigated as a function of E-field and crystallographic orientation. Although a single domain state could be achieved by applying an E-field along the rhombohedral polar direction [111], a multidomain state was recovered with the removal of the E-field. This domain instability resulted in hysteresis of the strain vs. E-field behavior. In contrast, an engineered domain configuration of [001] oriented rhombohedral crystals was found to be stable with no domain motion detectable under DC-bias, resulting in hysteresis minimized strain vs. E-field behavior. Crystallographically, this domain stability could be ascribed to the macroscopically tetragonal symmetry (4mm), resulting from the engineering of domains with rhombohedral symmetry (3m).

I. INTRODUCTION

Recent crystallographic engineering of relaxor ferroelectric single crystals of $\text{Pb}(\text{Zn}_{1/3}\text{Nb}_{2/3})\text{O}_3$ (PZN), $\text{Pb}(\text{Mg}_{1/3}\text{Nb}_{2/3})\text{O}_3$ (PMN) and their solid solutions with the normal ferroelectric PbTiO_3 (PT) revealed piezoelectric properties much superior to morphotropic phase boundary (MPB) ceramics such as PZT [1-4]. Ultrahigh piezoelectric properties ($d_{33} \sim 2500$ pC/N) and large E-field induced strain values (1.7%) were achievable from rhombohedral (1-x)PZN-xPT ($x=0-0.09$), (1-y)PMN-yPT ($y=0.2-0.35$), and (1-z) $\text{Pb}(\text{Sc}_{1/3}\text{Nb}_{2/3})\text{O}_3$ (PSN)-zPT ($z=0.25-0.45$) crystals oriented along [001]. As [001] is not the polar direction, [001] poled crystals must be comprised of a multidomain state. However,

it should be noted that strain values as high as 0.6% were realized with minimized hysteresis, indicating little domain motion under bias, a phenomena not expected for multidomain ferroelectric crystals. In contrast, crystals oriented along [111], the polar direction of rhombohedral crystals, exhibited inferior properties such as $d_{33} \sim 82$ pC/N, significantly smaller than PZT's. Furthermore, the E-field induced strain was also accompanied by large hysteresis, which was believed to be originated from domain instability and subsequent domain motion under bias [2,3]. Fig. 1 presents the strain vs. E-field behavior for [111] and [001] oriented PZN crystals and apparent crystallographic anisotropy. To further evaluate the origin of the apparent anisotropy, in-situ domain observations were proposed to further substantiate the concept of domain instability. In this study, in-situ domain observations were carried out as a function of E-field and crystallographic orientation. Based on the commonalities inherent to relaxor-PT systems, [5-6], our research was limited to a rhombohedral PZN and PZN-8%PT crystals oriented along [111] and [001]. The concept of macroscopic symmetry, resulting from crystallographic domain engineering, will be discussed in conjunction with the observed hysteresis minimized strain behavior and associated static domain configuration in multidomain crystals.

II. EXPERIMENTAL

PZN and PZN-8%PT single crystals were grown by a

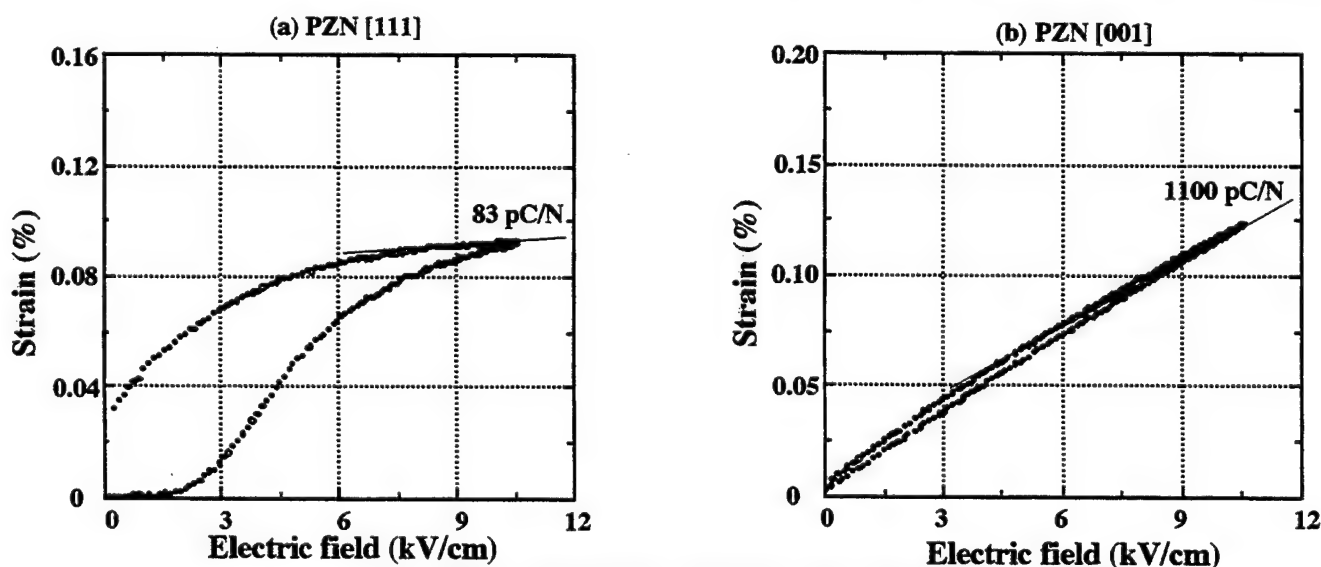


Fig. 1. Strain vs. E-field behavior for PZN single crystal oriented along [111] and [001].

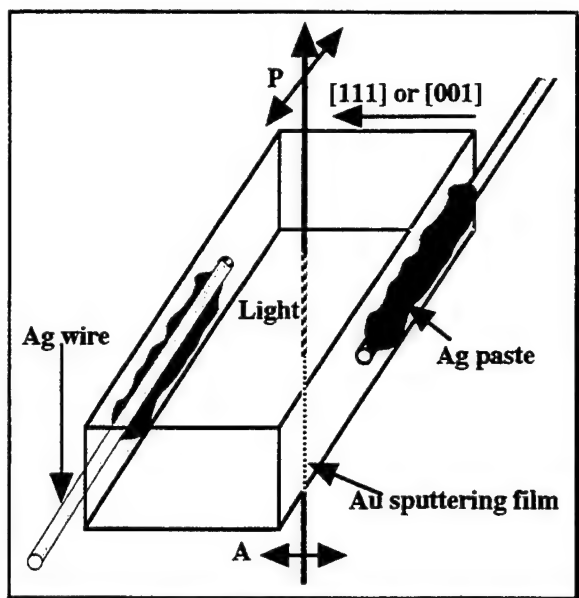


Fig. 2. Schematic diagram of in-situ domain observation.

flux method. Further details on the crystal growth were reported elsewhere [2,7]. Flux grown crystals were oriented along $[111]$ or $[001]$ direction using a back reflection Laue camera. Samples were heat-treated at 250°C for 16 hr in air before domain observations, in order to remove residual stress that might result in the formation of ferroelastic domains. For in-situ domain observation under DC-bias, the sample surface was mirror-polished with the sample thickness approximately $200\text{--}300\ \mu\text{m}$ along the transmittance direction of polarized light. Gold electrodes were sputtered on both sides parallel to the polarized light. Sample width between sputtered Au electrodes was approximately $500\text{--}600\ \mu\text{m}$. Thin samples ($\sim 50\ \mu\text{m}$) with mirror-finished (111) or (001) surfaces were also prepared to observe domain walls more clearly before and after E-field exposure under no bias, for crystallographic interpretation. The domain configuration, or state of the crystals, was observed under cross-nicol condition using a Polarized microscopy (Carl Zeiss, D-7082). The application of an E-

field was along the $[001]$ or $[111]$ direction, being normal to the polarized light, using a Trek 610A HV Amplifier. A schematic diagram of the experimental apparatus used to investigate the domain state is presented in Fig. 2.

III. RESULTS AND DISCUSSION

A. Domain configuration - no bias before and after E-field exposure

As grown PZN crystals were previously reported to be optically isotropic [8-9] with ferroelectric domains observed in PZN crystals only upon exposure with an applied E-field, resulting from the microdomain-macrodomain transition. As shown in Figs. 3(a) and 4(a), however, stripe-shaped domain patterns were observed for both $[111]$ and $[001]$ oriented PZN crystals upon heat treatment at 250°C for 16 hr. Surprisingly, this stripe pattern did not disappear even at temperatures above T_{mx} (145°C). Therefore, these stripe patterns may have resulted from another origin, such as residual stress associated with lattice defects.

Figs. 3(b) and 4(b) present the domain configurations of $[111]$ and $[001]$ oriented PZN crystals, respectively, after E-field ($\sim 40\ \text{kV/cm}$) exposure. As shown, macroscopic domain configuration was observed. The $[111]$ oriented PZN crystals (Fig. 3(b)) consisted of band-shaped domains with three equivalent polar vectors ($[\bar{1}11]$, $[1\bar{1}1]$ and $[\bar{1}\bar{1}1]$). All domain boundaries could be interpreted as 109° domain walls on $\{110\}$ planes, consistent with crystallographic domain wall relationships [10-11]. As shown in Fig. 4(b), fiber-like domains with sharp edges on both ends were observed for $[001]$ oriented PZN crystals. Although crystallographic interpretation was limited by the depth of focus of optical microscopy, each domain must have one of four possible polar vectors, $[111]$, $[\bar{1}11]$, $[1\bar{1}1]$ and $[\bar{1}\bar{1}1]$. This configuration is schematically presented in Fig. 5. Similar domain configuration and behavior was found for PZN-8%PT to that of PZN, except for the ferroelectric domains initially observed from as-grown crystals.

B. In-situ domain observations

Figs. 6(a), 6(b) and 6(c) exemplify the domain configuration for $[111]$ oriented PZN crystals as a function of

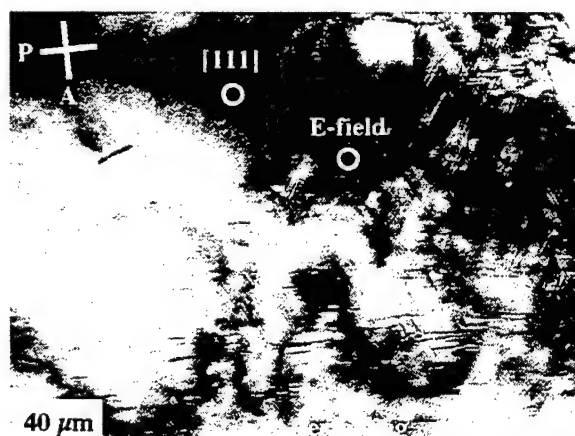
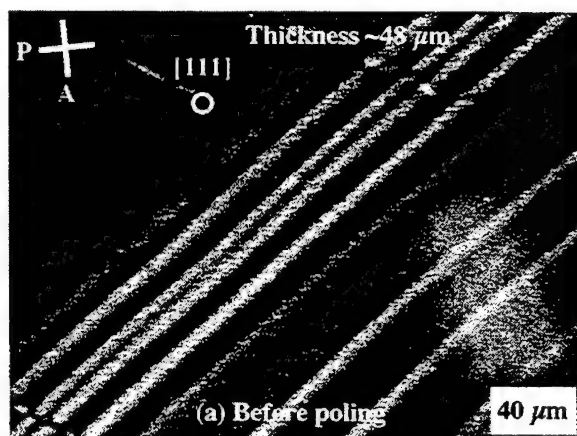


Fig. 3. Domain structure of pure PZN single crystal oriented along $[111]$ before and after poling at $42\ \text{kV/cm}$.

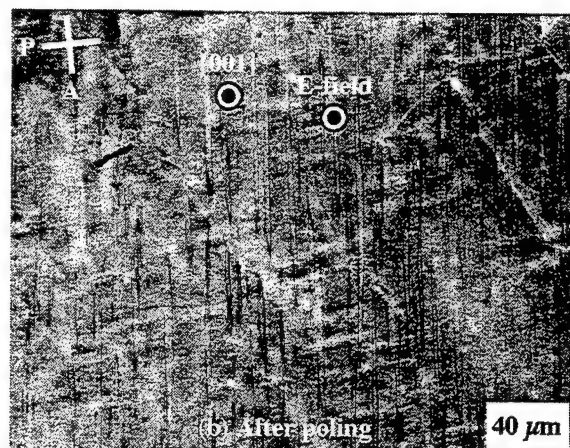
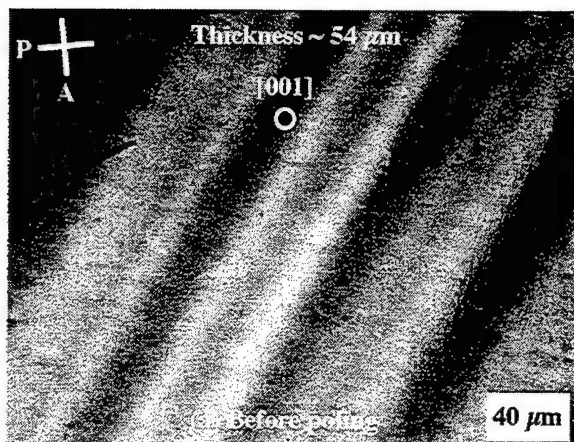


Fig. 4. Domain structure of pure PZN single crystal oriented along [001] before and after poling at 37 kV/cm.

E-field, increased incrementally to 30 kV/cm. The Domain wall density in the crystals was found to decrease with increased E-field, implying the increased domain size with domain reorientation. At approximately 30 kV/cm, the PZN crystals became almost single domain, with some domain walls observed near the electrode due to crystal-electrode interfacial stress. However, upon removal of the E-field, a multidomain state was observed as presented in Figs. 6(e) and 6(f). Domain reorientation was found to occur at 7.5 kV/cm (Fig. 6(d)), starting near the electrode. The initial multidomain state of Fig. 6(a) was completely recovered as shown in Fig. 6(f). However, it should be noted that the domain configuration exhibited hysteresis. The domain wall density was observed to be lower for an equivalent E-field upon removing the E-field, the origin of hysteresis in strain vs. E-field curve shown in Fig. 1(a). Hence, to achieve single domain PZN crystals at 0 E-field, the application of an elastic force, as used to fabricate single domain BaTiO₃ crystal, may be required [12]. In contrast to the domain instability observed with [111] oriented PZN crystals, [001] oriented crystals exhibited stable domain configurations as shown in Fig. 7. Domain configuration did not change under bias, being further evidenced by hysteresis minimized strain vs. E-field behavior in Fig. 1(b). Similar domain behavior was found in PZN-8%PT but at different E-fields, i.e., a single domain state was observed for PZN-8%PT at 13 kV/cm.

C. Domain engineering and macroscopic symmetry

Based on the domain observations presented in previous sections, the ability to engineer a macroscopic symmetry different from the local symmetry (lattice symmetry) is suggested, as can be found for the case of poled piezoelectric ceramics, i.e., the macroscopic symmetry being ∞m regardless of the lattice symmetry resulting from randomly orientated grains. For ferroelectric single crystals, only single domain crystals possess macroscopic symmetry identical to the lattice symmetry. For example, unpoled tetragonal ferroelectric crystals are macroscopically $m3m$, if the number of each domain is equivalently distributed. As shown in Fig. 5, each domain in [001] oriented crystals must have four

possible polarization directions, $[111]$, $[\bar{1}\bar{1}1]$, $[1\bar{1}\bar{1}]$ and $[\bar{1}1\bar{1}]$. For [001] oriented crystals to exhibit a static domain configuration under bias, each domain must be distributed equivalently. As a result, each domain experiences the same driving force for reorientation with respect to an applied E-field, otherwise domain reorientation under bias would occur resulting in hysteresis in strain vs. E-field behavior. Therefore, the coexistence of domains with four equivalent polar vectors results in a 4-fold axis along [001], consequently resulting in the macroscopic symmetry $4mm$ arising from the local $3m$ symmetry.

IV. SUMMARY

Domain configuration and ferroelectric related properties of rhombohedral PZN, and PZN-8%PT crystals were

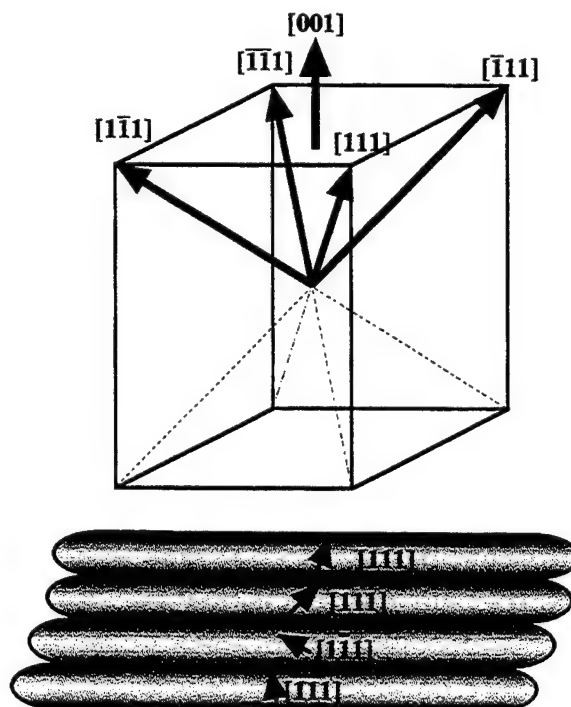


Fig. 5. Domain configuration of PZN single crystal applied along [001].

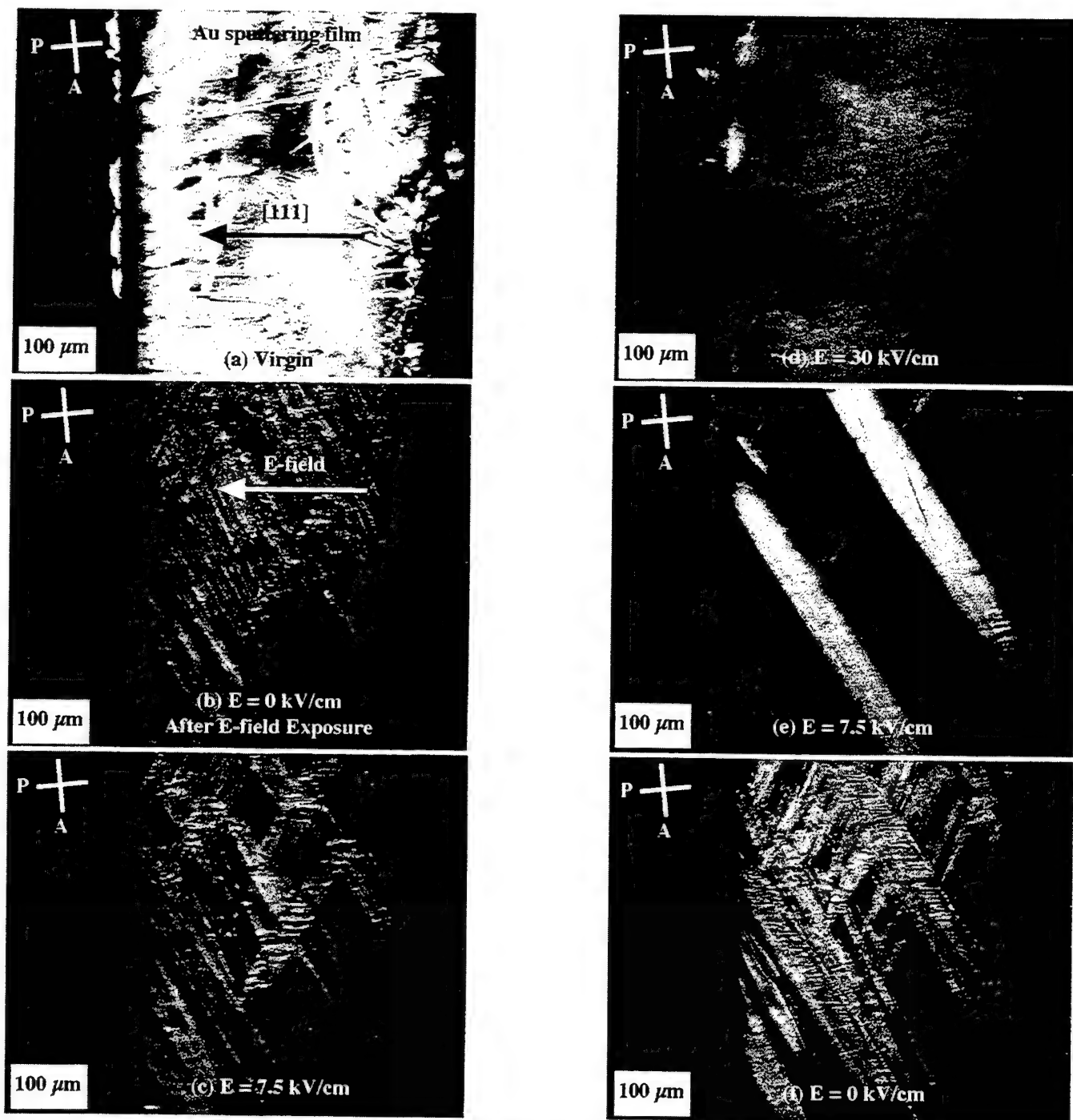


Fig. 6. Domain structure of pure PZN single crystal oriented along [111] under DC-bias.

investigated as a function of E-field and crystallographic orientation. In-situ domain observations revealed the domain instability for [111] oriented rhombohedral crystals, resulting in hysteresis of the strain vs. E-field behavior. In contrast, an engineered domain configuration of [001] oriented rhombohedral crystals was found to be stable. No domain motion was detectable under DC-bias, resulting in hysteresis minimized strain vs. E-field behavior. Crystallographically, the macroscopic tetragonal symmetry (4mm) arising from local rhombohedral 3m symmetry

resulting from the four equivalent domain state was suggested. Further studies such as TEM observations are required to understand the stripe patterns observed in as-grown PZN crystals.

ACKNOWLEDGMENT

Authors would like to thank Mrs. Lei for her help with sample preparation. We also thank Dr. Fousek, Dr. Newnham, Dr. Randall and Dr. Cao for their helpful suggestions.

REFERENCES

- [1] J. Kuwata, K. Uchino and S. Nomura, Jpn. J. Appl. Phys., 21 (1982)

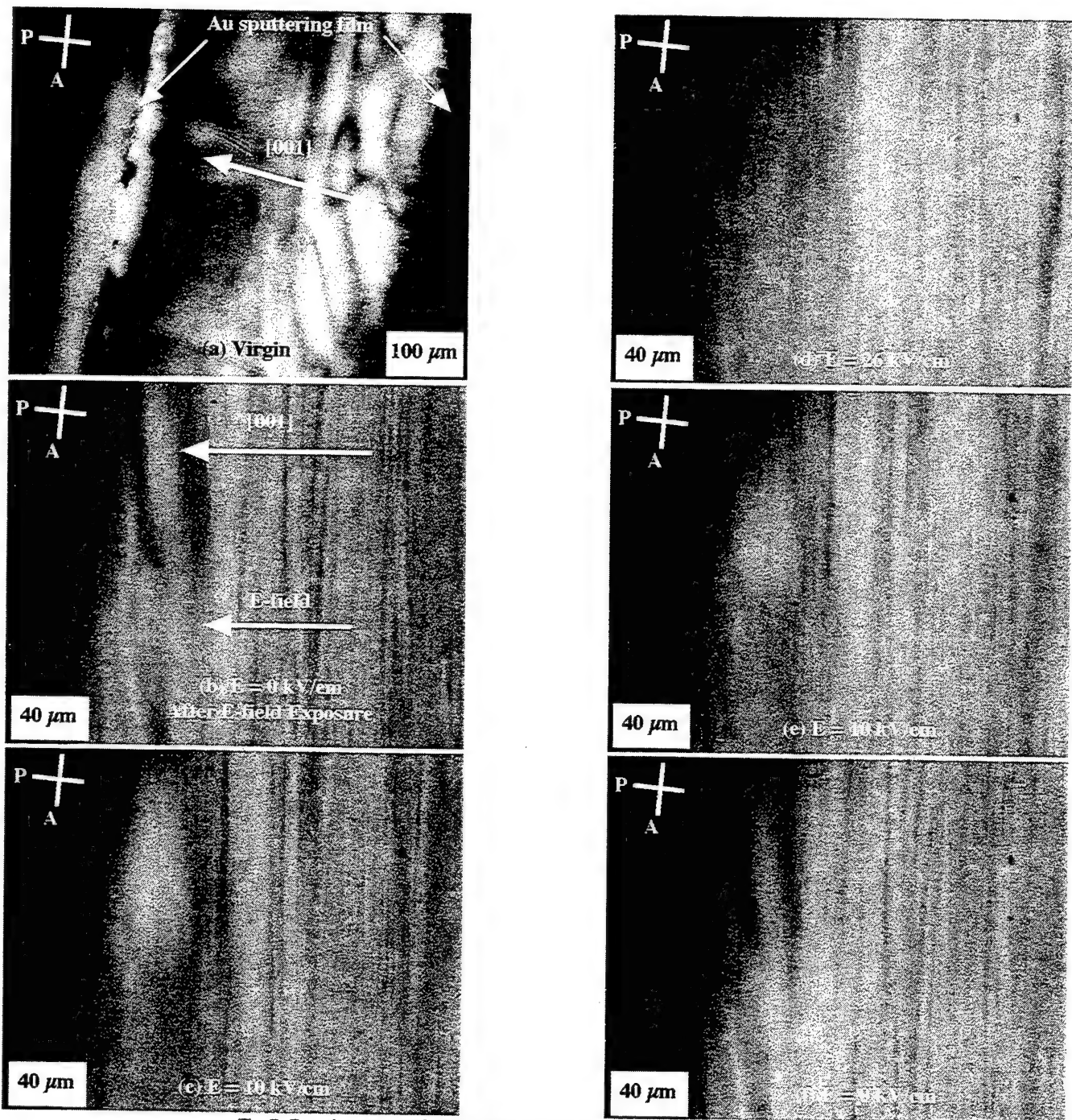


Fig. 7. Domain structure of pure PZN single crystal oriented along [001] under DC-bias.

- 1298-1302.
- [2] S.-E. Park, M.L. Mulvihill, P.D. Lopath, M. Zipparo and T.R. Shrout, Proceedings of the 10th IEEE International Symposium on Applications of Ferroelectrics, Vol. I (1996) 79-82.
 - [3] S.-E. Park and T.R. Shrout, J. Appl. Phys., in press.
 - [4] S.-E. Park and T.R. Shrout, submitted to Ferroelectrics.
 - [5] T.R. Shrout and J. Fielding, Jr., Proceedings of the 1990 IEEE Ultrasonics Symposium, (1990) 711-715.
 - [6] C.A. Randall, A.S. Bhalla, T.R. Shrout and L.E. Cross, J. Mater. Res., 5 (1990) 829-834.
 - [7] S.-E. Park, M.L. Mulvihill, G. Risch and T.R. Shrout, Jpn. J. Appl. Phys., 36 (1997) 1154-1158.
 - [8] S. Nomura, M. Endo and F. Kojima, Jpn. J. Appl. Phys., 13 (1974) 2004-2008.
 - [9] M.L. Mulvihill, Doctor thesis of Pennsylvania State University (1996).
 - [10] J. Fousek, Czech. J. Phys., B21 (1971) 955-968.
 - [11] E.I. Eknadiosiants, V.Z. Borodin, V.G. Smotrakov, V.V. Eremkin and A.N. Pinskaya, Ferroelectrics, 111 (1990) 283-289.
 - [12] A. Kurosaka, K. Tomomatsu, O. Nakao, S. Ajimura, H. Tominaga and H. Osanai, J. Soc. Mater. Eng. Res., 5 (1992) 74-82. (Japanese)

Domain Structure of PbTiO_3 and $\text{Pb}(\text{Zn}_{1/2}\text{Nb}_{1/2})_{0.91}\text{Ti}_{0.09}\text{O}_3$ Single Crystals by Atomic Force and Kelvin Force Microscopy

Takashi Yamamoto, Kenrou Kawano, Mitsuru Saito and Shinobu Omika
Dept. of Electrical Eng., National Defense Academy, Yokosuka 239 Japan

Abstract—Nanometer scale surface morphologies in pure PbTiO_3 , Mn-doped PbTiO_3 and $\text{Pb}(\text{Zn}_{1/2}\text{Nb}_{1/2})_{0.91}\text{Ti}_{0.09}\text{O}_3$ single crystals prepared by flux method have been investigated by atomic force microscopy and discussed in connection with 90° and 180° domain. Regular gradients with angles of 3.4° to 3.6° at the domain boundary were measured on (001) surface in as-grown crystal with so-called typical 90° a-c domain. The angle of the gradient is controlled by the crystal tetragonality (c/a) in the crystal and is 3.4° to 3.6° in pure PbTiO_3 and Mn-doped PbTiO_3 with a $c/a=1.063$, and 0.5° to 0.8° in $\text{Pb}(\text{Zn}_{1/2}\text{Nb}_{1/2})_{0.91}\text{Ti}_{0.09}\text{O}_3$ with a $c/a=1.004$. In pure PbTiO_3 and Mn-doped PbTiO_3 , the 180° c-c domain is constructed from the trapezoidal form with a step of 80 to 100 nm and confirmed by the electric potential measurement using Kelvin force microscopy.

I. INTRODUCTION

Recently, extensive research and development have focussed on ferroelectric thin films for non-volatile random access memory (FRAM). One of the main features is the fatigue of polarization, which closely relates to the reversal phenomena of domain by the electrical field. There still remained many unsolved matters even in the single crystal. Moreover, when the thickness of ferroelectric thin film in FRAM reduces to nanometer order, surface roughness, for example the convex-concave shape of film, becomes serious problems. Over the past years, numerous observation techniques have been developed to study the domain structure in ferroelectric materials from viewpoint of physical interest. For example, domains have been imaged by polarizing light microscopy,¹⁾ scanning electron microscopy (SEM) with etching²⁾ and decoration,³⁾ transmission electron microscopy (TEM).⁴⁾ Using these methods, four kinds of domain structure as drawn in Fig.1 have been reported in ferroelectric materials with tetragonal crystal structure, such as BaTiO_3 , PbTiO_3 and $\text{Pb}(\text{Zr}_{1-x}\text{Ti}_x)\text{O}_3$ ($x > 0.465$).⁵⁾ Compared with these traditional methods for domain structure observation, atomic force microscopy (AFM) has several merits; wide measurement range of X-Y direction, high measurement resolution of Z-direction and unnecessary surface treatment.

In this paper, pure PbTiO_3 , 1.0 mol% Mn-doped PbTiO_3 and $\text{Pb}(\text{Zn}_{1/2}\text{Nb}_{1/2})_{0.91}\text{Ti}_{0.09}\text{O}_3$ single crystals were prepared by flux method with excess PbO. Surface

structures on as-grown single crystal have been observed by the contact mode using atomic force microscopy (AFM) and the electric potential on surface have been measured using Kelvin force microscopy (KFM). Relations among 90° , 180° domain structures and surface morphologies have been discussed.

II. EXPERIMENTAL PROCEDURE

Pure PbTiO_3 (pure-PT), 1.0 mol% Mn-doped PbTiO_3 (Mn-doped PT) and $\text{Pb}(\text{Zn}_{1/2}\text{Nb}_{1/2})_{0.91}\text{Ti}_{0.09}\text{O}_3$ (PZNT) single crystals were grown by flux technique in air. A 99.99%-pure TiO_2 , a 99.99%-pure PbO and a 99.6%-pure MnCO_3 were mixed at a mol ratio of $0.3(\text{PbTiO}_3)-0.7\text{PbO}$ for pure-PT and $0.3(\text{PbTiO}_3+1.0\text{mol}\%\text{MnO})-0.7\text{PbO}$ for Mn-doped PT. Also, a 99.99%-pure TiO_2 , a 99.99%-pure PbO, a 99.99%-pure ZnO, and a 99.99%-pure Nb_2O_5 were mixed at a mol ratio of $0.3(\text{Pb}(\text{Zn}_{1/2}\text{Nb}_{1/2})_{0.91}\text{Ti}_{0.09}\text{O}_3)-0.7\text{PbO}$ for PZNT. The single crystal was synthesized in platinum (Pt) crucible. The rising rate of temperature is $200^\circ\text{C}/\text{h}$ up to 1200°C . The soaking time for melting the pure-PT, Mn-doped PT and PZNT was 3 h at 1200°C . It is then cooled slowly, at $2^\circ\text{C}/\text{h}$, to between 1200°C and 800°C where pure-PT, Mn-doped PT and PZNT single crystals were grown up into the excess PbO flux. The crystals are then cooled down to room temperature by $100^\circ\text{C}/\text{h}$. The plate-shape single crystals with (001) major surface have grown up in the center and sides of the crucible. After that, excess PbO was removed in hot HNO_3 water solution. Optical

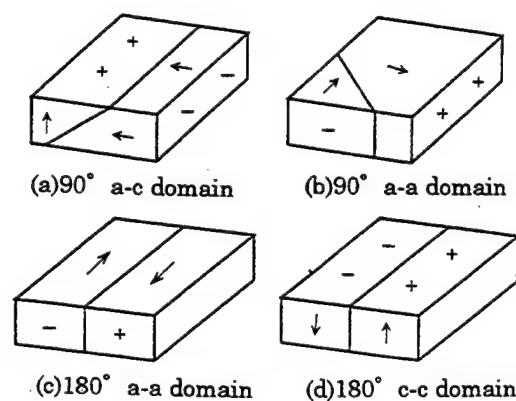


Fig.1 Domain structures formed in tetragonal crystal

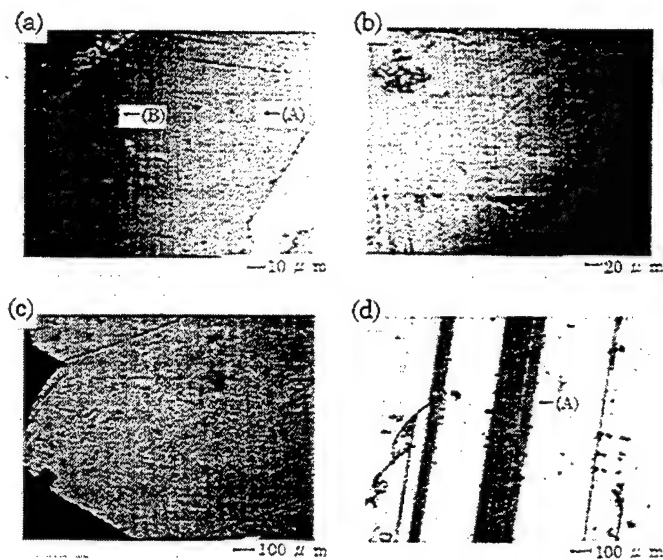


Fig.2 Optical micrographs of (001) surfaces in (a) and (b) pure-PT, (c) PZNT and (d) Mn-doped PT

microscopy using polarizing microscope (OP) was first used to observe the domain. The AFM measurements have then carried out with a commercially available apparatus (Seiko Electronics Co., SPI 3700) with a contact mode and also KFM measurement was used by the same instrument. Large scans were performed with a $30\text{-}\mu\text{m}$ -scanner in the constant force.

III. RESULTS AND DISCUSSIONS

Figure 2 shows the optical micrographs of as-grown surfaces in pure PT, Mn-doped PT and PZNT single crystals. Shown by the mark (A) in Fig. 2(a), regular bright and dark stripes on (001) surface in pure PT could be observed. Only bright stripes are reduced by light polarization and so these stripes might be assumed as the typical 90° a-c domain as depicted in Fig. 1(a). Moreover, as can be seen by mark (B), the widths of bright and dark stripes change by the measurement place. In Fig. 2(b), the areas, which bright strip does not change by light polarization and the width of dark stripes was extremely narrow, was observed in pure-PT and these are attributed to 180° c-c domain. Secondly, as-grown surface of PZNT is shown in Fig. 2(c). Although the widths of bright and dark stripes are not constant and changed by the measurement place, the 90° domain was clearly confirmed. Finally, optical micrograph of (001) surface in Mn-doped PT is shown in Fig. 2(d). The width of 90° a-c domain was drastically increased by Mn-doping and the bright area occupied the major surface on the (001) plate. Figure 3(a) shows the AFM bird-eye view image measured by contact mode with $30\text{ }\mu\text{m} \times 30\text{ }\mu\text{m}$ in area and 200 nm in height and drawn by the horizontal and elevation

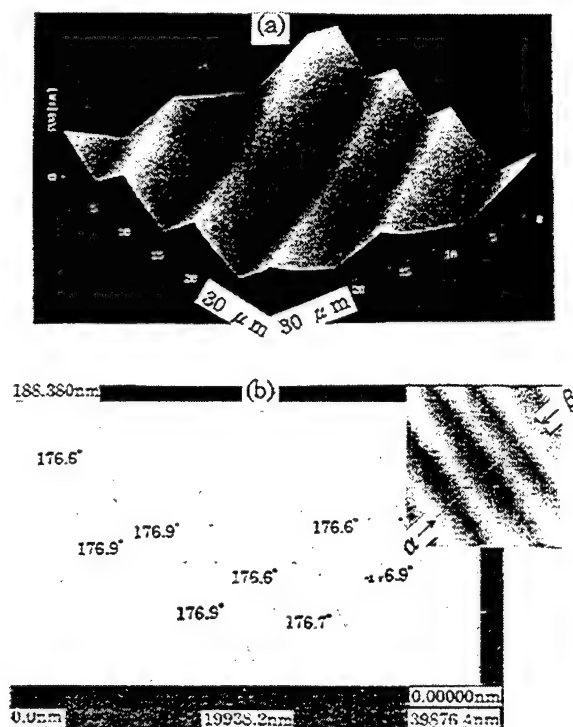


Fig.3 (a) AFM bird-eye view images of 90° a-c domain in Fig.2(a) of pure-PT and (b) cross section perpendicular to the stripes along α - β line

angles of $H\theta = 54^\circ$ and $E\theta = 30^\circ$, respectively on (001) surface in pure PT, which is the same area as shown by mark (A) in Fig. 2(a). It is revealed that the convex-concave shape on (001) surface was constructed with the regular gradient. Figure 3(b) shows the cross section of plane AFM image along α - β line on the right portion in Fig. 3. The angles of the gradients are 3.1° (the angle of crest is 176.9°) to 3.4° for convex shape, and were 3.1° (the angle of valley bottom is 176.9°) to 3.6° for concave shape, respectively. The flatness in gradient is less than 4 nm . Moreover, the height between crest and valley bottom in gradient is 96.3 nm to 146.5 nm . These exaggerated drawing are due to the high measurement sensitivity (200 nm) in the Z-direction compared with those in X-Y direction measurement ($30\text{ }\mu\text{m} \times 30\text{ }\mu\text{m}$). Also, as shown in Fig. 3(b), the gradient is changed at the crest of convex and valley bottom of concave, i.e., 90° a-c domain boundary. In the stripes shown by the mark (B) in Fig. 2(a), where the width ratio of bright and dark areas is not unit and nearly 2, the angles of gradient are 1.8° to 3.7° for the convex angles and 2.0° to 3.9° for the concave angles. The height between crest and valley bottom is 69.7 nm to 95.4 nm . Preliminary, it is pointed out by OP method that the dark stripes are areas with wide width and confirmed to the c-domain by light polarization. The schematic

figure of domain structure estimated by OP and AFM methods in (001) pure-PT single crystal is illustrated in Fig. 4. These domains are the same 90° a-c domain as shown in Fig. 1(a). The angle of gradient has been discussed from the viewpoints of theory⁶⁾ and experiment by AFM in previous paper.⁷⁾ The angle of gradient, θ shown in Fig. 6 is controlled by the crystal tetragonality (ratio of c and a-axis lattice constants in the crystal, c/a) and is calculated by following equation, θ (deg) = $2\tan^{-1}(c/a) - 90$. Theoretical value of θ in pure PT is 3.5° using the values of c-axis = 4.152 \AA and a-axis = 3.904 \AA . This value extremely coincides with the experimental values of 3.1° to 3.9° . In Fig. 3, although the angles (θ') of crest for convex and bottom for concave are drawn, the angle of gradient shown in Fig. 4 can be easily recalculated by Eq. of $\theta = 180^\circ - \theta'$. According to the former discussions, the angle of gradient might be varied by the ratio of c/a . Single crystals of $(1-x)\text{Pb}(\text{Zn}_{1/2}\text{Nb}_{2/3})\text{O}_3 - (x)\text{PbTiO}_3$ solid solution could be made by flux method for changing the c/a in the crystal and keeping the crystal structure tetragonal. Figure 5 shows the AFM plane image and its cross section of PZNT single crystals with the $c/a = 1.008$, where dark stripes are not straight but lied in a zigzag line as pointed out in Fig. 2(c). Similarly, the gradient varies at the domain boundary, and the angles of gradient were 0.5° to 0.8° for experiment and 0.5° for theory. Moreover, the height of a crest to

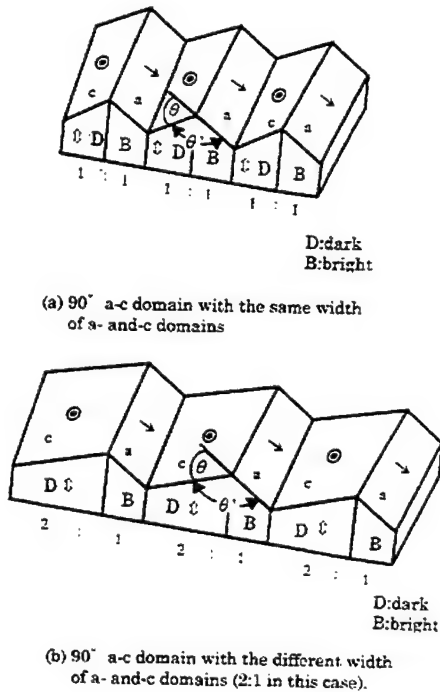


Fig.4 Schematic figures of 90° a-c domain structure estimated by OP and AFM method in pure-PT

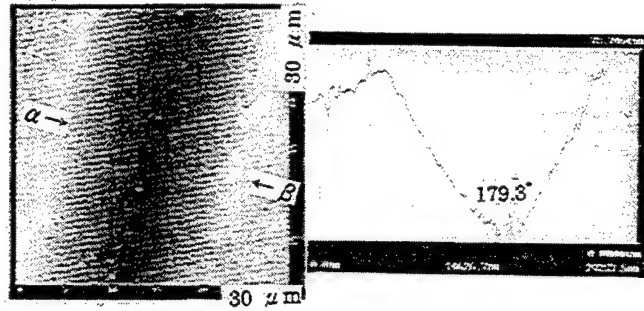


Fig.5 AFM plane image and cross section along α - β line of 90° a-c domain of PZNT

bottom is 66.4 nm , although the domain width is so large compared with those in pure PT and Mn-doped PT. In Mn-doped PT of areas marked by (A) in Fig. 2(d), the angle of gradient was 3.2° . Although the width of c and a-domains in 90° a-c domain, about $60 \mu\text{m}$ to $340 \mu\text{m}$, is so large compared with those of pure-PT, the angle of gradient was almost the same as that in pure PT. However, the height between crest and bottom is about $2.8 \mu\text{m}$ and so large compared with those in pure-PT, because the domain width in Mn-doped PT is 3 times larger than that in pure-PT. From these experimental results, it has been revealed that the 90° a-c domain is major on (001) surface in pure-PT, Mn-doped PT and PZNT and the angle of a-c domain boundary is strictly controlled by a c/a ratio. Figure 6 shows the AFM bird's-eye view in pure-PT shown in Fig. 2(b). The regular trapezoidal steps are constructed with a height of 80 nm to 100 nm and is different from the domain form in typical 90° a-c domain discussed in Figs. 3, 4 and 5. Such forms could not be made in 90° domain depicted in Fig. 1. If the 180° domain may be constructed in pure-PT and Mn-doped PT, the 180° c-c domain, in which polarization is aligned to antiparallel and

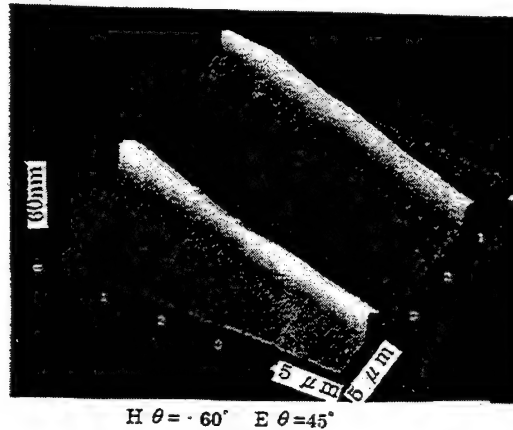


Fig.6 AFM bird's-eye view cross of 180° c-c domain shown in Fig. 2(a) of pure-PT

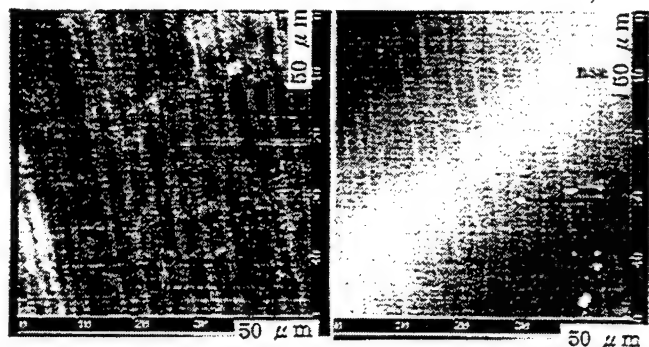


Fig. 7 (a) Electrical potential and (b) AFM image of 180° c-c domain with trapezoidal steps

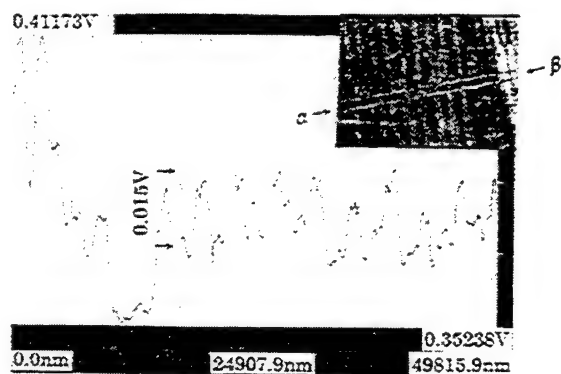


Fig.8 Distribution of electrical potential along α - β line in the trapezoidal steps

perpendicular to the surface on (001) surface in PT case as shown in Fig. 1(d), may be formed. Figure 7 shows the electric potential image of trapezoidal steps measured by Kelvin force microscope (KFM) and for comparison the AFM image is shown at the same time. The convex area has the high electric potential compared with that in the flat area, although the width of high voltage in KFM image is a little larger compared with that in AFM image, i.e., the edge becomes shaded. Figure 8 shows the distribution of the electric potential measured along the direction perpendicular to the trapezoidal steps as shown by the rectangular shape (α - β) on the right portion. The top area of trapezoidal steps have high voltage clearly and the difference of electric potential of 0.015 V was measured between the top and bottom of trapezoidal step. From consideration of shape and electric potential measurement, such trapezoidal steps may be concluded as the 180° c-c domain. Figure 9 illustrates 180° c-c domain obtained in pure PT. The height of 180° c-c domain boundary ought to be zero or a little as shown in Fig.1 (d), however the height was 80 to 100 nm in our study. During the

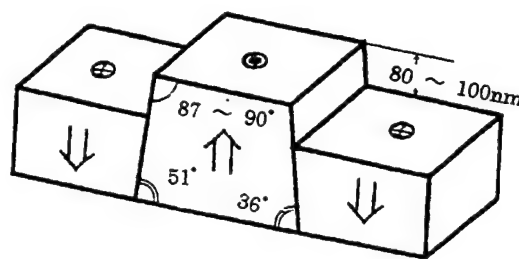


Figure 9 Schematic figure of 180° c-c domain in pure PT

sample procedure, these samples after crystallization were soaked for a long time in hot HNO_3 water solution for excess PbO removal. At that time, because the etching rate of plus and minus planes of c domain in 180° c-c domain was different, it may be concluded that the height of trapezoidal step was constructed.

IV. CONCLUSIONS

Relation between surface and domain structures has been investigated in pure-PT, 1.0 mol%Mn-doped PT and PZNT single crystal using AFM and KFM method. For 90° a-c domain, the regular gradient of the surface is strictly controlled by the crystal tetragonality (c/a). The angles of gradient are 3.4° to 3.6° in pure-PT, Mn-doped PT with a $c/a=1.063$, and 0.5° to 0.8° in PZNT with a $c/a=1.004$. For 180° c-c domain, trapezoidal steps are constructed with a height of 80 to 100 nm. The top of trapezoid has the plus charge of polarization.

REFERENCES

- 1)F. Gilletta : Phys. Status: Solidi 11 (1972) 721.
- 2)A. Sawada and R. Abe : Jpn. J. Appl. Phys. 6 (1967) 699.
- 3)V.P. Konstantinova, N.A. Tichomirova and M. Glogarova : Ferroelectrics 20 (1978) 259.
- 4)M. Tanaka and G. Honjo : J. Phys. Soc. Jpn. 19 (1964) 954.
- 5)T. Mitsui, T. Tatsuzaki and E. Nakamura : Ferroelectrics, Maki Book Co. Tokyo (1969) 307.
- 6)F. Jona and G. Shirane : Ferroelectric Crystals, Pergamon Press, London (1962) 162.
- 7)S. Hamazaki, F. Shimizu, S. Kojima and M. Takashige : J. Phys. Soc. Jpn. 64 (1995) 3660.

NANOSCALE IMAGING OF DOMAIN DYNAMICS AND RETENTION IN FERROELECTRIC THIN FILMS

A. Gruverman, A. S. Prakash*, S. Aggarwal*, B. Yang*, M. Wuttig*,
H. Tokumoto, O. Auciello* *, T. Venkatesan# and R. Ramesh#

Joint Research Center for Atom Technology (JRCAT), Higashi 1-1-4, Tsukuba, Japan

*Department of Materials and Nuclear Engineering, University of Maryland, College Park, USA

**Argonne National Laboratory, Materials Science Division, Argonne, IL, USA

#Department of Materials and Nuclear Engineering and Center for Superconductivity Research,
University of Maryland, College Park, MD, USA

ABSTRACT

We report results on direct observation of the microscopic origins of backswitching in ferroelectric thin films. The piezoelectric response generated in the film by a biased atomic force microscope was used to obtain static and dynamic piezoelectric images of individual grains in a polycrystalline material. We demonstrate for the first time that polarization reversal occurs under no external field (i.e., loss of remanent polarization) via a dispersive continuous-time random walk process, identified by a stretched exponential decay of the remanent polarization.

1. INTRODUCTION

High density memories require storage elements that approach sub-micron dimensions and exhibit high speed and unlimited endurance.¹ To achieve this goal, substantial improvement in understanding of films microstructure and switching behavior is necessary. Therefore, direct studies of the effects of granularity on polarization reversal dynamics and data retention characteristics are crucial. In this paper we describe first studies using scanning force microscopy (SFM) to directly investigate the nanoscale ferroelectric domain relaxation processes in $\text{Pb}(\text{Zr}_x\text{Ti}_{1-x})\text{O}_3$ thin films with particular emphasis on understanding the mechanism for loss of polarization (retention loss).

Fundamental issues in ferroelectric thin film capacitors are related to the exact nature of the complex domain structures and their interactions with defects, the domain dynamics under high speed switching conditions, and their evolution in the absence of an external field (polarization relaxation). In this respect, theoretical models and electrical measurements (e.g., hysteresis loops, switching currents), have provided significant insight into understanding polarization switching in thin films. Polarization switching from one state to another under the influence of an external field has been studied extensively and is conventionally understood using classical nucleation and growth concepts of phase transformation (e.g., the Avrami model), as modified by Ishibashi.² However, there have been very few experimental studies focused on the fundamental mechanisms that control the spontaneous reversal of polarization leading to a progressive loss of remanent polarization, a phenomenon referred to as retention loss. Application of high resolution techniques such as scanning force microscopy (SFM) in conjunction with conventional electrical measurements provides a unique opportunity to achieve a microscopic insight into the physical processes occurring in ferroelectric thin films. The recent progress in using SFM as an effective tool for high resolution visualization of domain structure in ferroelectric thin films provides the appropriate background for this report.³⁻⁵

In a typical retention experiment, a capacitor is written into a polarization state and left in that state for fixed periods of time, after which the polarization remaining in the capacitor is measured. In such a macroscopic measurement, one obtains an average of the retention characteristics of an

ensemble of grains. It is important to note that this reversal occurs in the absence of an external field and is driven primarily by internal depolarizing fields and elastic strain fields. In some cases, the retention loss fits a log-time dependence; however in most cases they seem to fit a stretched exponential (i.e., an equation of the form $y = I - \exp[-kt^n]$) better. In Fig. 1, the retention loss data from a PZT capacitor is plotted in a stretched exponential $[\ln(\partial P/\partial P_i) - \text{time}]$ form with a very good fit and a slope of 0.24. In a variety of systems, a stretched exponential behavior with $n < 1$ has been characterized as a dispersive transport or random walk-type process.⁶ Similarly, the good fit, in Fig. 1, of the retention data to a stretched exponential type behavior, suggests that this retention loss process occurs by a random walk process. However, these macroscopic studies do not provide information on the initial location of the reversal process and its progress as a function of time. In this respect, the SFM imaging method used in this study provides the capability for the direct observation of domain structure that is naturally linked to the polarization state of a ferroelectric film.

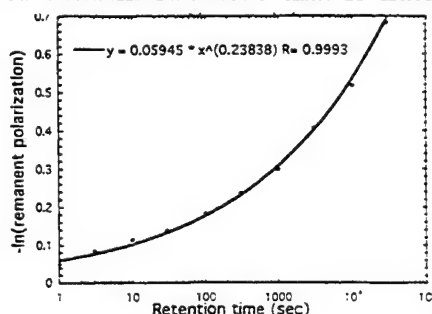


Figure 1. Logarithmic plot of a PZT film switched polarization as a function of time, showing the stretched exponential fit.

2. EXPERIMENTS AND DISCUSSION

Experiments were carried out using the SFM piezoresponse method, based on the detection of the piezoelectric vibration of the ferroelectric sample.⁵ Application of the external voltage to the ferroelectric film results in a change of the film thickness due to the inverse piezoelectric effect. Whether the film thickness will expand or compress locally depends on its polarization state. It means that under the action of an AC electric field regions with opposite orientation of polarization will vibrate out of phase. The amplitude of the vibration signal provides information about the magnitude of the piezoelectric coefficient, while the polarization direction can be determined from the phase of the signal.⁵ The key point in the SFM piezoresponse mode is that the imaging AC field is applied between the bottom electrode and the conductive SFM tip, which is used as a movable top electrode, thus generating piezoelectric vibration in a very small film area underneath the tip. Therefore a lateral resolution of the order of nanometers is achievable. Application of a DC voltage pulse to the probing tip generates a strong and sufficiently localized electric field, which makes possible nanoscale writing of ferroelectric domains and subsequent read-out.

A commercial force microscope (Seiko Instruments SPA 300) was employed in this study. In our experiments, piezoresponse images of the films were acquired in ambient air by applying a small AC voltage with an amplitude of 2.5 V (peak to peak) and a frequency of 10 kHz while scanning the film surface. The external voltage was applied through a standard gold coated Si_3N_4 cantilever with a spring constant of 0.09 N/m. The probing tip, with an apex radius of about 20 nm, was in mechanical contact with the uncoated film surface during the measurements. The cantilever vibration was detected using a conventional lock-in technique. A topographic image of the film surface was taken simultaneously with the domain imaging. Experiments were performed using tetragonal $\text{Pb}(\text{Zr}_{0.2}\text{Ti}_{0.8})\text{O}_3$ films deposited by laser ablation onto Si substrates with bottom metal oxide electrode layers. Specifically, a PZT composition that showed a strong loss of remanent polarization with retention time was chosen for this study. Details of the thin film deposition protocols are described in earlier papers.⁷

We investigated the retention loss and the role of grain boundaries in the process of spontaneous backward (reverse) switching in the PZT thin film described above. The experimental sequence consisted of preliminary piezoresponse and topographic characterization of the film. The tip was then positioned at specific locations in a grain (at the center of the grain or at the grain periphery) polarized normally to the film surface and a single voltage pulse was applied. By

varying the pulse width we could induce full or partial switching of the grain. Subsequently, piezoresponse images of the grain were recorded at various time intervals thus providing information about time evolution of the domain structure after the switching.

Figure 2(a) is a conventional topographic image of a single grain in the polycrystalline ensemble of the PZT film under study. For the sake of identification, the six grains (one central grain and five adjacent grains) are numbered from 1 to 6. The piezoresponse image in Fig. 2(b) shows uniform contrast across the central grain 1, indicating that it is uniformly polarized in the negative direction (polarization upwards). Upon application of a positive 6 V, 200 ms pulse to the center of the grain, it was fully switched into the opposite polarity, indicated by a change in grain contrast (Fig. 2(c)). Note that the adjacent grains are still in their original polarization states. The piezoresponse images in Fig. 2(d,e) show time-evolution snapshots of the change in the domain structure of the grain 1, occurring after the removal of the DC field. Fig. 2(d), is a piezoresponse image recorded 4 hours after the pulse switching; the first stages of backward switching, which started at the grain boundary, are discernible. This is direct evidence for the role played by grain boundaries in initiating spontaneous polarization reversal. In this case, the interesting point is that the reversal begins along the grain boundary that borders grain 2, suggesting that the electrostatic interaction across the grain boundary might influence the switching behavior. Once the reversal begins, it proceeds through the sidewise expansion of the reversed portion of the grain, as shown in Figs. 2(d,e). To summarize this backward switching process, in Fig. 2(f) the time dependence of the reversed polarization fraction of the grain is fitted to a stretched exponential dependence with an exponent of 0.68. The difference in the exponent in this case compared to that of the macroscopic electrical measurements (Fig 1(b)) is attributed to the different depolarizing fields and elastic fields in the microscopic measurements.

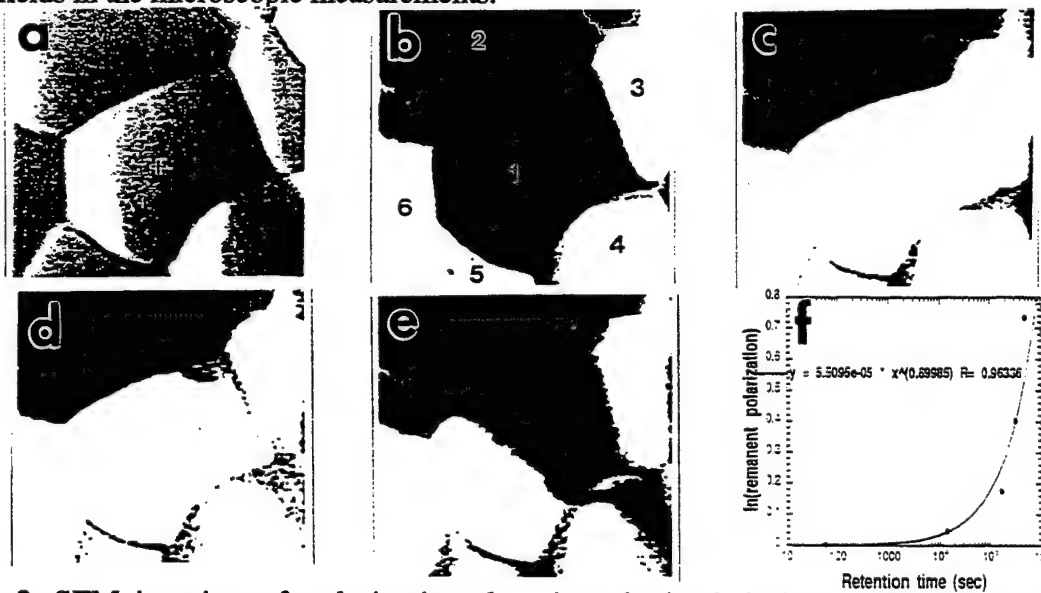


Figure 2. SFM imaging of polarization domains obtained during a retention experiment performed using a PZT (20/80) film grown on LSCO/TiN/Si. (a) Topographic image (200 x 200 nm²), (b) piezoresponse image of the as grown PZT film for an excitation AC pulse of 2.3 V, (c) piezoresponse image after poling grain 1 with a DC pulse of a 6 V, 200 ms applied in the center of the grain, (d) piezoresponse image after 4hrs of the DC pulse, without any external field, (e) piezoresponse image after 140 hrs, and (f) stretched exponential fit of the SFM data corresponding to remanent switched grain area vs. time.

The role of grain boundaries and other internal interfaces in stabilizing the switched state is another important factor that needs to be considered in determining the retention characteristics. To study these effects, partial switching was accomplished by using shorter 6 V pulses of 50 ms. The SFM images in Figs. 3(a,d) show, a grain (*in dark contrast*) where two locations marked by

crosses were identified; namely in the center of grain and near its edge. When partial switching is induced well within the grain by applying the pulse to the grain center, we notice that the reversed domain of less than 30 nm in size is unstable and reverts back within a time interval of 10 minutes (Figs. 3(b,c)). On the other hand, if partial switching is generated near the grain boundary, Fig. 4(d), the reversed domain is stabilized by the boundary (Fig 3(e,f)), such that it does not switch back to its original state for at least 40 minutes.

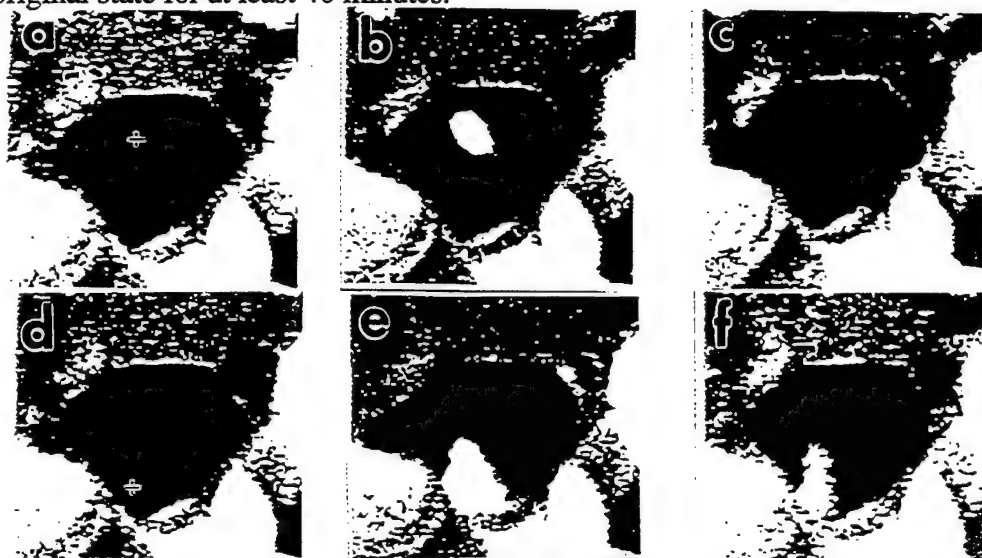


Figure 3. Retention experiments to study the role of grain boundaries on polarization reversal. Piezoresponse images were obtained at different time-intervals on different grain locations. Grain center: (a) before polarization, (b) immediately after DC poling (6 V, 50 ms), and (c) 9 min after poling. Grain edge: (d) before polarization, (e) immediately after DC poling (6 V, 50 ms), and (f) 40 minutes after poling.

From the studies discussed here, it appears that the spontaneous reversal nucleates at the grain boundary and reversed domain stabilization requires a grain boundary. The data suggests that the spontaneous reversal may proceed via a random walk type mechanism similar to that postulated for magnetization reversal in spin-glass.⁸ Our SFM studies fit a similar stretched exponential type behavior. The random walk-type mechanism for polarization reversal brings forth new interpretations of the ferroelectric phenomenon and further studies are imperative to assess the validity of our suggested mechanism of polarization reversal.

The work at JRCAT is supported by the NEDO Program, the work at the University of Maryland is supported by the NSF-MRSEC Program, and the work at Argonne National Laboratory is supported by the Department of Energy.

3. REFERENCES

1. J. F. Scott, C. A. Araujo, *Science*, **246** (1989) 1400.
2. Y. Ishibashi, in "Ferroelectric Thin Films : Synthesis and Basic Properties," Vol. **10** (Gordon and Breach Publishers, 1996) p. 135.
3. R. Luthi, H. Haefke, K. P. Meyer, E. Meyer, L. Howald, and H. J. Guntherodt, *J. Appl. Phys.* **74** (1993) 7461.
4. K. Franke, J. Besold, W. Haessler and C. Seegebarth, *Surf. Sci. Lett.* **302** (1994) 83.
5. A. L. Gruvannan, O. Auciello, and H. Tokumoto, *Appl. Phys. Lett.* **69**, 3191 (1996).
6. J. Kakalios, R. A. Street and W. B. Jackson, *Phys. Rev. Lett.* **59** (1987) 1037.
7. O. Auciello, R. Dat and R. Ramesh, in "Ferroelectric Thin Films : Synthesis and Basic Properties," Vol. **10** (Gordon and Breach Publishers, 1996) P. 525.
8. H. Scher and E.W. Montroll, *Phys. Rev.* **B12** (1975) 2455.

Domain Wall Mobility and Stress Effects in Piezoelectric Thin Films

S. Troler-McKinstry, F. Chu, J. L. Lacey, J. F. Shepard, Jr., T. Su, F. Xu

Materials Research Laboratory and Materials Science and Engineering Department

Pennsylvania State University

University Park, PA 16802

G. Zavala, J. Fendler

Department of Chemistry

Syracuse University

Abstract - Piezoelectric thin films for microelectromechanical systems (MEMS) typically show somewhat lower piezoelectric coefficients than do bulk ceramics of the same composition. To separate the relative importance of grain size and film stress state in influencing the properties, controlled stress levels were imposed on several types of ferroelectric thin films while the dielectric and electromechanical properties were measured. It was found that for thin undoped sol-gel lead zirconate titanate 52/48 films crystallized by rapid thermal annealing, the extrinsic contributions to the dielectric and electromechanical properties make very modest contributions to the film response. No significant enhancement in the properties was observed even when the film was brought through the zero global stress condition. Similarly, PZT films ablated from PZT-4 and PZT-5A targets showed very little difference in properties. Finally, measurements on PZT films made with atomic force microscopy demonstrated negligible mechanical depoling under high uniaxial loads.

I. INTRODUCTION

Although (001) ZnO is currently the most widely used thin film piezoelectric for MEMS, ferroelectric films such as lead zirconate titanate (PZT) have higher piezoelectric coefficients, higher electrically-induced strain levels, and convert electrical to mechanical energy more efficiently than ZnO. Consequently, many groups are pursuing the integration of PZT into MEMS [1-5]. For this application, it is helpful to understand which factors contribute to the observed electromechanical properties, as this will control the magnitude of the piezoelectric coefficients. Thus, this paper describes the role of intrinsic and extrinsic contributions to the piezoelectric properties of bulk and thin film PZT. It is suggested that in most PZT thin films $< 0.5\mu\text{m}$ in thickness, domain walls contribute little to the piezoelectric properties.

II. INTRINSIC AND EXTRINSIC RESPONSE IN PZT CERAMICS

In bulk polycrystalline $\text{Pb}(\text{Zr}_{1-x}\text{Ti}_x)\text{O}_3$ ceramics, the room temperature dielectric and piezoelectric properties result from a combination of the intrinsic response of the material (that which can be characterized by averaging the response expected from a single domain single crystal) and extrinsic, or domain

wall contributions. For the dielectric constant, ϵ_r , both ferroelectric and ferroelectric-ferroelastic domain wall motions enhance the measured permittivity. However, since there is no spontaneous strain difference between 180° domains in PZT, only non- 180° domain wall motion contributes to the piezoelectric coefficient. It is well known that extrinsic contributions to the piezoelectric properties are responsible for the difference between hard and soft PZTs. Most estimates suggest that at the morphotropic phase boundary, ~50 - 60% of the piezoelectric properties are extrinsic in origin [6,7].

Since many MEMS devices require high piezoelectric coefficients and large strains, extrinsic contributions to the film piezoelectric properties are desirable. Thin films are, however, appreciably different from bulk ceramics. Most thin film grain sizes are $< 1\mu\text{m}$, which is smaller than conventionally prepared ceramics. In addition, thin films are often non-stoichiometric, have high defect densities, and are constrained by large biaxial stresses. Each of these factors can influence domain wall mobilities and so it is useful to look at their relative roles in controlling film properties.

The role of grain size in PZT ceramics has been discussed by Kim [8]. He demonstrated that when Nb-doped PZT 52/48 ceramics are prepared with clean grain boundaries, the materials demonstrate sharp phase transitions, and negligible changes in properties for grain sizes above $1\mu\text{m}$. Below that size, ϵ_r and the piezoelectric coefficients begin to decrease. In contrast, fine powders with the same particle sizes showed grain size-independent spontaneous strains, implying that the three-dimensional stresses in the polycrystalline ceramic are responsible for the changes in the spontaneous strain in ceramics. Consequently, some of the observed change in properties was intrinsic.

More significant, however, were the concurrent changes in the domain structure. Via transmission electron microscopy, Cao and Randall [9] demonstrated that the size of twin domains in PZT ceramics drops with the square root of the grain size over the size range of 0.2 to $10\mu\text{m}$. For grains under $\sim 0.2\mu\text{m}$ in extent, the domain size drops even more quickly. Accompanying the smaller twin domain size was a decrease in the number of variants per grain. This point is particularly important, as twin walls have been observed to be related across grain boundaries in PZT ceramics [9,10]. Poling thus requires a cooperative motion of the walls in multiple grains. If there are few variants available per grain, this may inhibit efficient poling. Moreover, the domain wall mobility should decrease with increasing domain density [11].

The net result of these effects was a drop in both the saturation and the remanent polarizations as well as the piezoelectric coefficients as a function of decreasing grain size [8]. Thus, as the grain size was reduced from 1 μm to 0.2 μm , the room temperature remanent polarization decreased from 38 $\mu\text{C}/\text{cm}^2$ to 30 $\mu\text{C}/\text{cm}^2$, while the piezoelectric charge coefficient, d_{33} decreased from 460 pC/N to 350 pC/N. Measurements made at 10K showed less changes in the properties, suggesting that the grain size effects observed were primarily extrinsic in origin. Since most thin films have grain sizes under 0.5 μm , it becomes a significant question as to whether it will be possible to generate appreciable domain wall contributions to dielectric or piezoelectric properties in thin films.

A second significant difference between ceramics and thin films is the stress state of the materials. In bulk ceramics, the average stress on each particle is roughly hydrostatic, whereas in thin films, the stress is largely biaxial. Since PZT is ferroelastic as well as ferroelectric, stresses should strongly influence the properties. Consequently, size effects may differ for thin films relative to bulk ceramics.

Given these possible domain pinning mechanisms in films, it is not clear whether truly "soft" piezoelectric properties can be achieved in PZT films. To date, there is no convincing evidence for randomly oriented thin films with piezoelectric coefficients which surpass those of a hard bulk PZT. It is interesting, then, to determine whether non-180° domain walls can be made mobile in thin films. To investigate this question, this paper focuses on the interaction between the film dielectric properties and applied stresses for both undoped and doped PZT compositions.

III. DOMAIN WALL MOBILITY IN FERROELECTRIC THIN FILMS

Undoped sol-gel PZT films were prepared as described elsewhere [12] using a methoxyethanol solvent approach and a PbO top coat prior to crystallization to eliminate the formation of a lead-deficient pyrochlore surface layer [13]. Following rapid thermal annealing at 700°C for 60 seconds, the films were polycrystalline, with some (111) orientation. The PZT 52/48 films were in a residual stress state of ~100 MPa tension. To determine whether it was possible to stress-induce ferroelastic wall motion, the samples were placed in a state of uniform biaxial stress by clamping the wafer over a cavity which could be either evacuated or pressurized [14]. The stress state in the film could then be calculated using large deflection plate theory and published values of the elastic moduli of Si [15] and PZT [16]. This allows the properties of the films to be examined as a function of stress without changing the microstructure. Fig. 1 shows the changes in the low-field dielectric response of an undoped sol-gel PZT film ~250nm thick as a function of applied biaxial stress. Several points are evident from the data: first, ϵ_r drops as the film is placed in tension and shows a shallow maxima when stressed compressively. Secondly, the changes even for applied stresses on the order of 140 MPa relative to the unstressed state are small, typically under 5%. Third, ϵ_r recovers almost completely on unloading from either stress

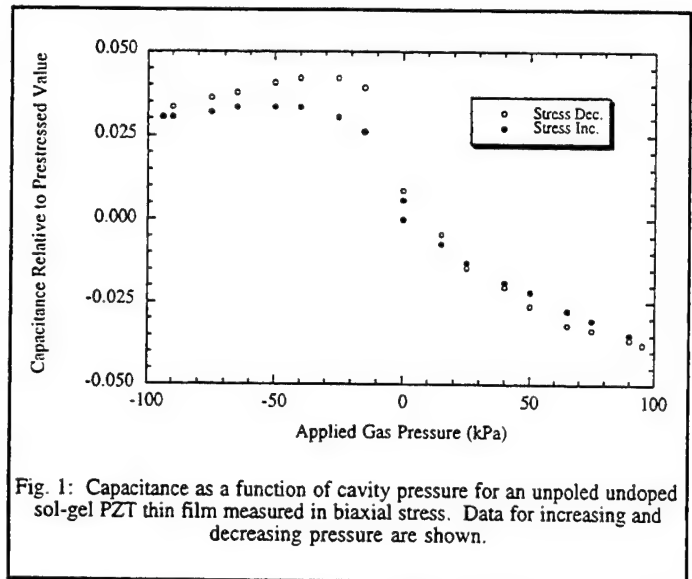


Fig. 1: Capacitance as a function of cavity pressure for an unpoled undoped sol-gel PZT thin film measured in biaxial stress. Data for increasing and decreasing pressure are shown.

state. The dielectric loss showed little change for the entire stress range. Similar behavior was observed for poled and unpoled samples.

These data are in strong contrast to biaxial stress measurements on poled bulk PZT ceramics. In particular, when measured along a direction perpendicular to the biaxial stress, both hard and soft PZT compositions showed a decrease in the capacitance of ~50% or more for compressively stressed material. These changes were attributed largely to changes in the domain structure [17]. That is, a compressive biaxial stress should force the polarization direction to orient perpendicular to the stressing plane, which, in turn, leads to changes in the dielectric properties measured. On unloading, the bulk soft PZT did not return to its original value due to mechanical depoling of the sample, while the hard PZT-4 recovered more fully. For the thin films, on the other hand, the reversibility of the stress-induced changes, coupled with their small magnitude, strongly suggests that it is not possible to force much ferroelastic reorientation of domains over the stress range investigated. Indeed, when the high field properties of the films were measured, there was no appreciable variation in the coercive field of the film for stress levels between -140 MPa and 140 MPa. A similar difficulty in inducing 90° domain reorientation was observed in x-ray measurements as a function of the poling field for a sol-gel PZT 40/60 film on Pt-coated Si by Tuttle et al. [18].

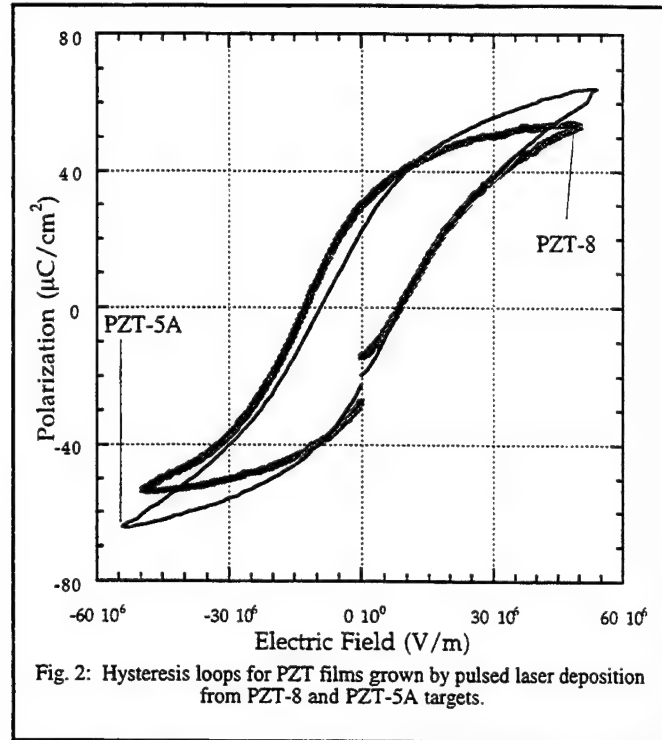
It is also interesting to note that the maximum in ϵ_r measured for the 52/48 film occurs approximately where the applied stress state counterbalances the residual stress state after processing. Similar maxima were seen in 40/60 and 60/40 films. The reason for the maxima is currently under investigation. However, it is clear from the relatively small increase in ϵ_r in each case, as well as the modest changes in the coercive field, that domain walls do not become appreciably more mobile at the maxima. Consequently, although the residual stress value in films may modulate the low and high field properties of PZT somewhat, if non-180° domains exist in the grains, the pinning sites which clamp

their motion must be on a local scale. Grain boundaries, point defects, crystal defects, and the film-substrate interface are all possible pinning sites.

Very similar behavior was observed in PZT thin films grown by pulsed laser deposition from commercial hard (PZT-8) and soft (PZT-5A) targets [19]. Films of these compositions were examined to determine whether domain wall mobility could be increased via donor doping, as is typically done in bulk ceramics. The films were grown at room temperature on Pt-coated Si substrates, and were subsequently crystallized by rapid thermal annealing. The films were polycrystalline, with some degree of (100) orientation. The grain size was $\sim 0.1 \mu\text{m}$. The observed behavior under biaxial loading is similar to that seen in the undoped sol-gel PZT films. That is, the changes in the low field properties are small (a few percent) for stresses up to $\sim 140 \text{ MPa}$, and largely reversible. There was no appreciable irreversible wall motion even in the film grown from the soft target. The low domain wall mobility even in the soft PZT film compositions is consistent with the observations that both types of films have similar dielectric constants (>1000) and nearly identical coercive fields ($\sim 120 \text{ kV/cm}$) [See Fig. 2]. Possible explanations for the low domain wall mobility in the soft composition films include the small grain size of the thin films, pinning at the film-substrate interface, high defect densities (especially lead vacancies), or segregation of the dopants to the grain boundaries. The incorporation of at least some of the dopants into the PZT-5A grains is strongly suggested by the fact that the dielectric loss in the soft compositions is consistently lower than that of either hard or undoped films. Given the relatively modest changes in properties as a function of applied biaxial stress, the macroscopic residual stress state is not believed to dominate the low domain wall mobilities.

A third demonstration of limited ferroelastic domain wall mobility was obtained in atomic force microscopy measurements of the piezoelectric coefficients of an undoped sol-gel PZT film on a platinized silicon substrate. Piezoelectric measurements were made by bringing the AFM tip into contact with the film, poling the film locally with a dc voltage, and then applying a small alternating field between the bottom electrode and the tip. The tip was then used to follow the electrically-induced displacement. Additional details on the experimental procedure are given elsewhere [20] Fig. 3 shows the normalized d_{33} as a function of the force holding the tip in contact with the sample. For reference the typical behavior of several PZT ceramics under uniaxial stress is also shown. For the film, the data decrease monotonically with increasing contact force. On decreasing the load, the piezoelectric coefficient recovers, demonstrating that mechanical depoling is negligible for these conditions. These data make an interesting contrast to data on bulk PZT under uniaxial load. As seen in the figure, when compressively loaded along the poling axis, soft PZTs show a small increase in d_{33} , followed by a reduction associated with ferroelastic switching.

On the other hand, hard PZTs show a maxima in the observed d_{33} with increasing stress, and on decreasing the



stress, d_{33} recovers to a higher value than the original number. This is attributed to the mechanical stress depinning the originally inactive non- 180° domain walls so that they can contribute to the macroscopic behavior. At higher stresses, it is believed that ferroelastic switching occurs, accounting for the decreased d_{33} at high stress levels. As the stress is released, the hard PZT re-poles due to the defect dipoles, so the piezoelectric coefficient rises. The increased zero stress values are then associated with the contribution from the de-pinned non- 180° domain walls. The harder the PZT, the higher the stress required to induce de-poling [21,22]. In contrast, the sol-gel PZT film shows no increase in d_{33} over the observed range attributable to de-pinning inactive walls, as well as no irreversible ferroelastic wall motion.

On the basis of these experiments it is not clear that extrinsic contributions to properties can be utilized to enhance the piezoelectric properties of thin films $<0.5 \mu\text{m}$ in thickness. This may ultimately limit the magnitude of the piezoelectric coefficients which can be achieved in PZT films.

IV. ALTERNATIVE MEANS TO HIGHER ELECTROMECHANICAL COEFFICIENTS

Although it may not be possible to prepare PZT films with soft piezoelectric properties, there are alternative routes to developing larger strains and/or higher piezoelectric coefficients for MEMS actuators, including using higher drive levels, oriented films, or different compositions. Indeed, one of the attractive aspects of many thin films is the high breakdown strengths ($\sim 1 \text{ MV/cm}$). Thus, even though the

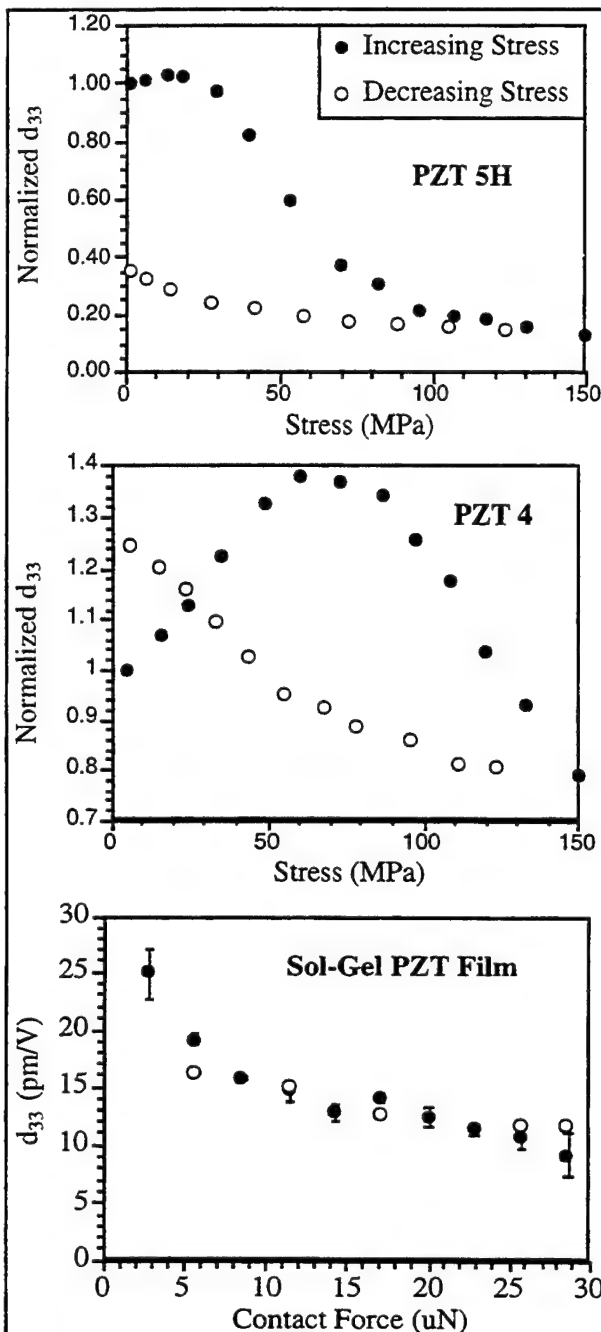


Fig. 3: d_{33} as a function of uniaxial stress for PZT films and ceramics. The data for ceramics is taken from Zhang et al.²³

piezoelectric coefficients are lower, it is possible to reach high strain values due to the field strengths which can be applied. A second alternative is oriented films. As has been demonstrated by Theis and Schlom [23], in epitaxial films, domain walls may be clamped at the substrate due to elastic considerations. However, discounting that contribution, oriented films clearly display higher remanent polarizations than randomly oriented films (i.e. (001) PZT films with remanent polarizations of $\sim 55 \mu\text{C}/\text{cm}^2$ have been prepared, whereas polycrystalline films generally show remanent

polarizations of $\sim 20 - 35 \mu\text{C}/\text{cm}^2$) [24]. It remains to be seen how much improvement this can offer the piezoelectric properties. A third approach would be to switch from PZT to single crystal relaxor ferroelectric - PbTiO_3 solid solution films or antiferroelectric-ferroelectric phase switching films. Both of these show higher strain levels than can be achieved in PZT. It is not clear yet what role film stresses have in affecting the properties of either family of materials.

V. CONCLUSIONS

PZT thin films can be integrated into MEMS for sensors and actuators. Excellent properties have been demonstrated by several groups throughout the world. Relative to bulk PZT, however, most PZT thin films show negligible extrinsic contributions to the dielectric and piezoelectric properties. This may provide an upper limit to the piezoelectric coefficients available unless an alternative contribution to the electromechanical properties can be tapped.

VI. ACKNOWLEDGMENTS

Work supported by NSF grants DMR-9223847 and DMR-9502431 and by DARPA through grant DABT63-95-C-0053

VII. REFERENCES

- [1] Ph. Luginbuhl, G. - A. Racine, Ph. Lerch, B. Romanowicz, K. G. Brooks, N. F. de Rooij, Ph. Renaud, and N. Setter, *Sensors and Actuators A54*, 530 (1996).
- [2] P. Muralt, M. Kohli, T. Maeder, A. Kholkin, K. Brooks, N. Setter, and R. Luthier, *Sensors and Actuators A48*, 157 (1995).
- [3] H. D. Chen, K. R. Udayakumar, C. J. Gaskey, and L. E. Cross, *Appl. Phys. Lett.* **67**, 3411 (1995).
- [4] K. R. Udayakumar et al., *Ferroelectrics* **160**, 347 (1994).
- [5] D. Polla and L. F. Francis, *MRS Bull.* **21**(7), 59 (1996).
- [6] X. L. Zhang, Z. X. Chen, L. E. Cross, and W. A. Schulze, *J. Mat. Sci.* **18**, 968 (1983).
- [7] Q. M. Zhang, H. Wang, N. Kim, and L. E. Cross, *J. Appl. Phys.* **75**, 454 (1994).
- [8] Namchul Kim, PhD Thesis, The Pennsylvania State University, 1994.
- [9] W. Cao and C. Randall, *J. Phys. Chem. Sol.* **57**, 1499 (1996).
- [10] B. G. Demczyk, R. S. Rai, and G. Thomas, *J. Am. Ceram. Soc.* **73**, 615 (1990).
- [11] G. Arlt and N. A. Pertsev, *J. Appl. Phys.* **70**, 2283 (1991).
- [12] M. Hendrickson, T. Su, S. Trolrier-McKinstry, B. J. Rod, and R. J. Zeto, *Proc. 10th Int. Symp. Appl. Ferro.*, 683 (1996).
- [13] T. Tani, C. D. E. Lakeman, J. F. Li, A. Xu, and D. A. Payne, *Ceram. Trans.* **43**, 89 (1994).
- [14] J. F. Shepard, S. Trolrier-McKinstry, M. A. Hendrickson, and R. Zeto, *Proc. 10th Int. Symp. Appl. Ferro.*, 161 (1996).
- [15] W. Brantley, *J. Appl. Phys.* **44**, 534 (1973).
- [16] T. Tsuchiya, T. Itoh, G. Sasaki, and T. Suga, *J. Ceram. Soc. Jpn.* **104**, 159 (1996).
- [17] R. F. Brown, *Can. J. Phys.* **39**, 741 (1961).
- [18] B. A. Tuttle, T. J. Garino, J. A. Voight, T. J. Headley, D. Dimos, and M. O. Eatough, in *Science and Technology of Electroceramic Thin Films*, O. Auciello and R. Waser (eds) (Kluwer Academic Publishers, The Netherlands 1995), pp. 117 - 132.
- [19] Piezokinetics, Inc.
- [20] G. Zavala, J. H. Fendler, and S. Trolrier-McKinstry, *J. Appl. Phys.* **81**, 7480 (1997).
- [21] S. W. Meeks and R. W. Timme, *J. Appl. Phys.* **46**, 4334 (1975).
- [22] Q. M. Zhang, J. Zhao, K. Uchino, and J. Zheng, *J. Mat. Res.* **12** 226 (1997).
- [23] C. D. Theis and D. G. Schlom *MRS Proc.* **401**, 171 (1996).
- [24] C. Foster et al., *MRS Proc.* **401**, 139 (1996).

THE APPLICATION OF ACOUSTIC EMISSION (AE) METHOD FOR FERROELECTRIC DEVICES AND MATERIALS

Hideaki Aburatani and Kenji Uchino
International Center for Actuators and Transducers (ICAT)
Materials Research Laboratory, The Pennsylvania State University
University Park, PA 16802 USA

Field induced acoustic emissions (AE) in the ferroelectric PZT ceramics have been studied. The field induced AE was not observed after the poling was completed. The domain related Kaiser effect in terms of the applied field was observed. However, in damaged sample the Kaiser effect would not take place anymore (Felicity Effect). It has been demonstrated that the AE method can be used for the determination of the damage of material and safe driving electric field.

I. INTRODUCTION

The contributions of domain structures for the field induced strain in the ferroelectrics have been studied by AE method. By eliminating the extrinsic AE signal caused by an electromechanical coupling between sample's piezoelectricity and feedback from power supply, it was confirmed that the field induced AE originated at the initiation of induced displacement and ended when the applied field was decreased during poling [1]. The AE was not observed after domain reorientation was completed at a given electric field except under bipolar field. Since new AE generation required larger electric fields than that applied during poling, the Kaiser effect[2] in terms of applied electric field was observed in the ferroelectric ceramics[1]. The damage of ferroelectric material at high electric field levels during the poling was also examined by AE method [3, 4]. However, intrinsic AE signals generated by domain reorientation as well as cracking and extrinsic AE signals caused by a coupling of piezoelectricity and feedback from power supply and bonding layer between sample and waveguide were not separated. AE generation in the damaged ceramics after poling has not been studied yet.

In stress induced AE, the Kaiser effect is not observed when any AE source can grow under a given condition (i.e. failure). The felicity effect is a breakdown of the Kaiser effect and is important for evaluating material damage[2]. In the stress induced AE, this effect

can be defined as a decrease of AE onset stress in the Kaiser effect. The decrease in the AE onset stress is caused by time-dependent effect controlled deformation (e.g. creep) in the material such as fiber-reinforced plastic composite (FRP) and a friction between free and damaged surfaces of crack. Therefore, the breakdown of the Kaiser effect is also expected in the damaged ferroelectrics ceramics under lower electric fields than poling electric field.

The paper deals with the AE generation in the damaged ferroelectric ceramics. The degree of damage of the thermally shocked single plate PZT ceramics was evaluated through the felicity effect with respect to electrically damaged and non-damaged sample. The feasibility of using the non-destructive AE method for the evaluation of damage in ferroelectric ceramics is demonstrated.

II. EXPERIMENTAL PROCEDURE

The PZT 5A ceramics with silver electrodes fired on both surfaces were employed for this study. Thus, the damage on the interface between electrode and ceramics was also measured as a damage of sample. The size of sample was 12.7 mm in diameter and 0.4 mm in thickness. Thermal shock was employed to introduce the damage in this study. The samples were placed in an oil bath at 200 °C for 30 seconds, then in an oil bath at room temperature for 30 seconds under short circuit condition. This process was repeated for 10 cycles.

The induced displacement, frequency response and AE measurement were employed to evaluate the damage of sample in this study. Figure 1 shows the AE and induced displacement measurement system. The total amplification of AE signal and signal threshold were 90 dB and 400 mV, respectively. The natural background level was about 10 dB lower than the threshold level. Thus, the measured AE results did not contain any noise from the environment. The AE generations at various electric fields were also measured to observe the electric field dependence.

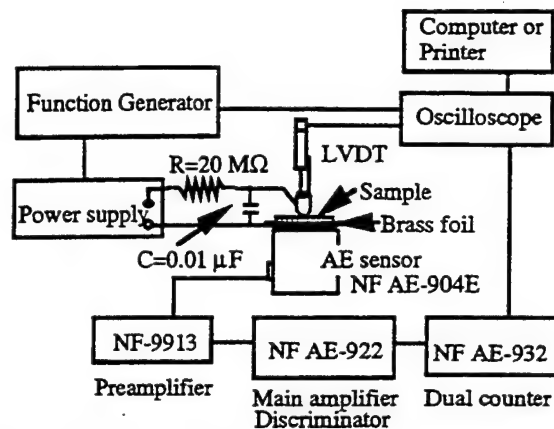


Figure 1. The AE and induced displacement measurement system.

III. RESULTS AND DISCUSSIONS

A. Induced Displacement Measurement

The field induced displacement at the center of the disk in both non-shocked and thermally shocked PZT ceramics as a function of the applied field is shown in Figure 2. The applied field had a triangular wave form with a peak value of 37.5 kV/cm at a frequency of 0.01 Hz. The damage effects could be measured as a decrease in the displacement, since they might decrease the effective electric field in the sample and clamp the displacement. The results were obtained after 10 cycles of the electric field application.

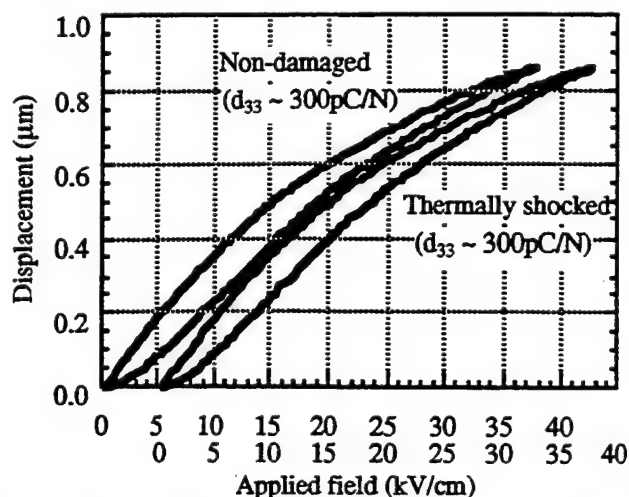


Figure 2. Induced displacement of non-shocked and thermally shocked PZT ceramics as a function of applied field.

There was no apparent difference in the induced displacement between non-shocked and thermally shocked samples. The obtained piezoelectric constants d_{33} were

almost identical. It seemed that even if the damage such as microcrack existed in the sample, it was too small to affect the displacement. The induced displacement also depends on the measuring point. To measure the effect of cracks, it is necessary to place the displacement sensor over or in the vicinity of the crack. From this measurement, only a local induced displacement property was obtained. It was not feasible to distinguish between the thermally shocked and non-shocked samples by this displacement measurement.

B. Frequency Response Measurement

When the piezoelectric sample is damaged, the properties of sample as a piezoelectric vibrator degrades and changes in the frequency response such as coupling factor and mechanical quality factor are expected[5]. The frequency response of both thermally shocked and non-shocked samples are plotted in Figures 3 (a) and (b).

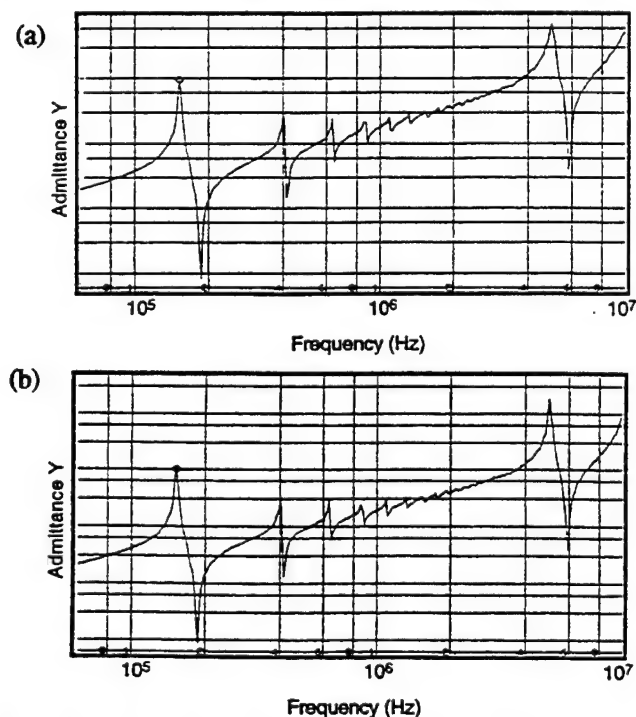


Figure 3. Admittance change as a function of frequency (a) non-shocked sample, and (b) thermally shocked sample.

Both the samples showed clear resonance and anti-resonance peaks. No spurious peaks were observed. The frequency at resonance and antiresonance were almost identical for all samples. The electromechanical coupling factor for the radial mode K_p and the mechanical quality factor Q_m of the non-shocked and thermally shocked samples were listed in table 1. The coupling factor K_p of 0.65 was obtained for both thermally shocked and

non-shocked samples. The mechanical quality factor Q_m of the thermally shocked sample was observed to be slightly lower than that of non-shocked sample.

Table 1. The coupling factor K_p and mechanical quality factor Q_m of non-shocked and thermally shocked PZT.

| | K_p | Q_m |
|-------------------|-------|-------|
| Non-shocked | 0.65 | 78 |
| Thermally shocked | 0.65 | 75 |

C. AE Measurements

The normalized total AE event count per cycle as a function of the number of field application cycle is shown in Figure 4. The AE event rate per cycle decreased markedly after poling with the electric field of 25 kV/cm. No AE was observed after the domain reorientation was completed. When an electric field of 37.5 kV/cm was applied to the non-shocked sample poled at 25 kV/cm, the AE event count simply decreased with the number of field application cycle. The observed AE event count after 10 cycles was higher than that of the sample exposed to an electric field of $E=25$ kV/cm. It seemed that the domain reorientation was not completed due to high internal stresses present at higher field, resulting in more AE generations.

In a thermally shocked sample, the AE event count per cycle decreased until the 4th cycle, and started to fluctuate. This fluctuation in the AE count were observed in all of the thermally shocked sample. It was supposed that AE events in the thermally shocked samples originated from two sources: domain reorientation and damage caused by thermal shock. The domain reorientation related AE simply decreased with number of field application cycle. However, the AE caused by the damage (i.e., microcrack) was present throughout due to the internal motion and started to dominate in measurement after the level of the domain related AE tapered off.

The AE event rate and induced displacement of the non-shocked sample as a function of time are shown in Figure 5 (a). The AE generations of the non-shocked sample falls into two categories. A small number for the AE events was observed at first (Type I). The AE event rate then reached a maximum at the maximum field (Type II). The AE onset field and the AE event count rate at the maximum field are shown in Figure 5 (b). The AE event count rate at the maximum field decreased with number of field application cycle. However, the AE onset field did not change. The AE at the maximum field (Type II) was identified as the domain reorientation related AE, because of decrease in

AE count with the number driving cycles. If the AE observed at lower field (Type I) was related to the domain reorientation, it should decrease similarly with the number of cycle. Therefore, the AE observed at lower field (Type I) was due to electrically induced damage, since it did not change with the number of field application cycle. It was also supposed that the AE event count near 0 kV/cm was due to the electrically induced damage.

For the thermally shocked sample, AE was observed at lower field than that of the non-shocked sample as shown in Figure 6 (a). The samples became "noisy" in terms of the AE generation. This AE was most probably caused by the friction at the crack surfaces. The AE generation was observed even when the applied electric field was decreased to 25 kV/cm (Figure 6 (b)). After the displacement was induced, the AE events were also observed even when the applied field reached 0 kV/cm. This was probably due to the time dependent motion (stress relaxation near cracks) in the material. Since this AE was not observed in non-shocked samples exposed to an electric field of 25 kV/cm after poling, these AE events were obviously caused by the thermally induced damage.

The damage related AE event count was much less than that associated with domain reorientation. This can be understood as follows. During the poling the entire sample contributed to the AE generation. However, the damage related AE originated from the individual cracking regions and friction at the crack surfaces. Therefore, the damaged volume was much less than volume generating AE during poling, resulting in a small number of AE events. It was shown that the thermally induced damage and electrically induced damage in the sample were observed from the AE measurements.

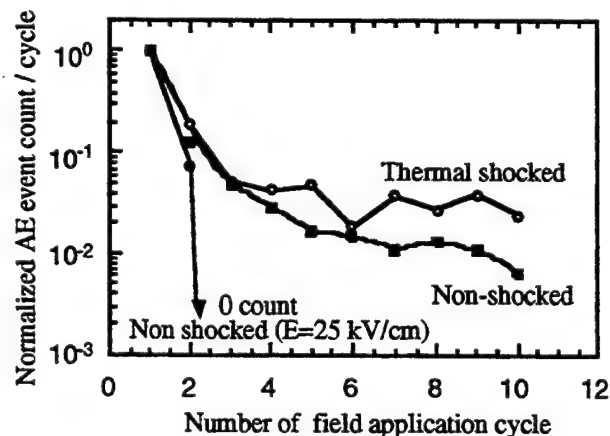


Figure 4. Normalized total AE event count per cycle as a function of the number of field application cycle.

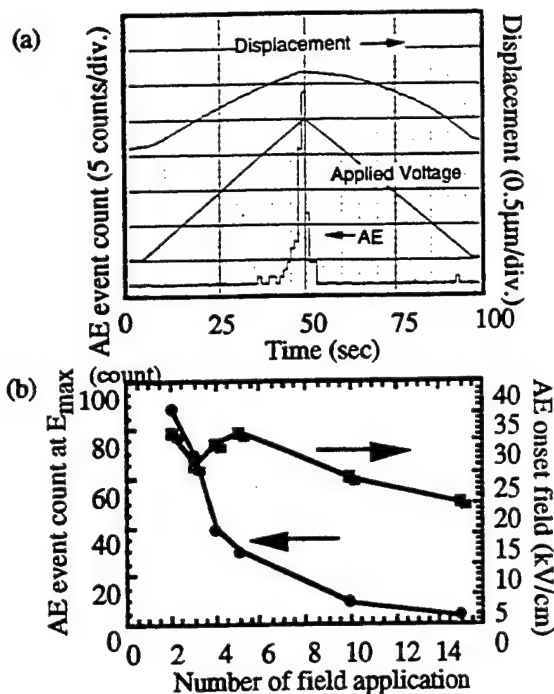


Figure 5. (a) AE event count rate and induced displacement of non-shocked sample as a function of time, and (b) AE onset field and AE event count at the maximum field of non-shocked sample as a function of the number of field application cycle.

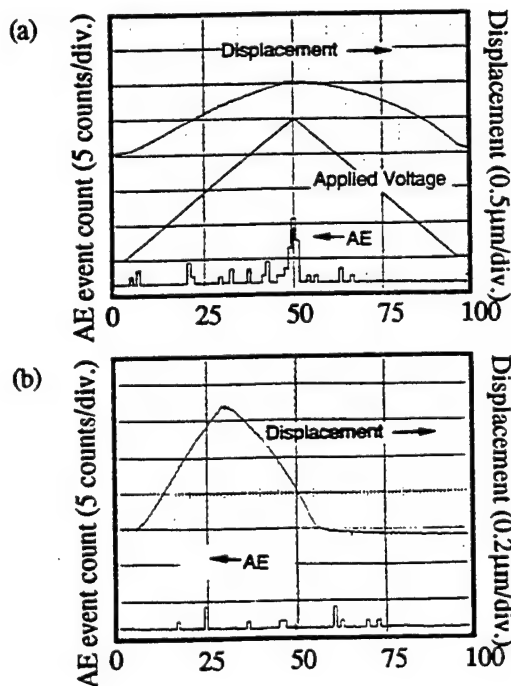


Figure 6. AE event count rate and induced displacement of thermally shocked sample as a function of time (a) $E=37.5$ kV/cm, and (b) $E=25$ kV/cm.

IV. Summary

The induced displacement, frequency response measurement and AE method were used for the damage evaluation of ferroelectric PZT ceramics under unipolar field. The thermally shocked and non-shocked sample exposed to an electric field of 37.5 kV/cm. Non-shocked samples were also examined at an electric field of 25 kV/cm. A small change in the mechanical quality factor Q_m was observed in the damaged sample. However, neither the induced displacement nor frequency response measurements obviously indicated damage in the samples.

On the contrary, the damage of the sample was clearly observed using the AE method in terms of breakdown of the Kaiser effect (felicity effect) and an AE generation at low electric field. The AE was observed even around 0 kV/cm in the thermally shocked sample. The friction generated through induced displacement and its relaxation at crack surface might be the source of AE. Moreover, it seemed that the electric field of 37.5 kV/cm was large enough to induce a damage even in the non-shocked samples. Damage related AE was also observed the non-shocked sample at this electric field level.

By measuring the AE, the damage in the samples was clarified. Damage occurring when a thermally shocked sample was at an electric field of 37.5 kV/cm was more than damage occurring when a non-shocked sample was subjected to an electric field of 37.5 kV alone. This in turn was more than the damage occurring at an electric field of 25 kV/cm.

These experiments show that the AE method can be extended to determine safe poling and driving field for piezoelectric ceramics and devices. This technique can be also used for evaluating the condition of the samples.

ACKNOWLEDGMENT

This work was supported by the Office of Naval Research through Contract No. N00014-92-J-1510.

REFERENCES

- [1] H. Aburatani and K. Uchino, "Acoustic Emission (AE) Measurement in piezoelectric ceramics," Proc. 10th IEEE Int. Symp. Appl. Ferroelectrics, pp. 871 (1996)
- [2] R. Halmshaw: *Non-Destructive Testing*, 2nd ed., (Edward Arnold, London, 1991) Chap 2 p.273
- [3] E. C. Subbarao, V. Srikanth, W. Cao and L. E. Cross "Domain Switching and Microcracking During Poling of Lead Zirconate Titanate Ceramics," *Ferroelectrics*, 145, pp. 271 (1993)
- [4] D. G. Choi and S. K. Choi, "Dynamic behavior of domains during poling by acoustic emission measurements in La-modified PbTiO_3 ferroelectric ceramics", *J. Mat. Sci.*, 32, 421 (1997)
- [5] T. Sakai, M. Ishikiriya and R. Shimazaki, "Durability of Piezoelectric Ceramics for Actuator," *Jpn. J. Appl. Phys.*, 31 (9B), pp. 3051 (1992)

The Influence of Mobile vs. Randomly Quenched Impurities on Ferroelectric Phase Transformations

Qi Tan, Jie-Fang Li and Dwight Viehland

Department of Materials Science and Engineering, University of Illinois at Urbana-Champaign, Urbana, IL 61801

Abstract - A comparative study of the influence of both mobile and randomly quenched impurities on ferroelectric phase transformations in lead zirconate titanate ceramics has been performed by dielectric spectroscopy and transmission electron microscopy. These investigations have shown a strong dependence of the structure-property relations on the mobility of impurities and/or defect complexes in the temperature range near and below the phase transformation.

I. Introduction

Aliovalent A-site modifications can be categorized on the basis of the compensation mechanism required to maintain charge neutrality: (i) A-site modifications which require associated A-site vacancies [1] such as La^{3+} , and (ii) A-site modifications which require B-site vacancies and suppresses A-site ones [2] such as K^{1+} . Previous studies of La^{3+} -modified PZT (PLZT) have shown dramatic changes in ferroelectric properties and domain stability with increasing La^{3+} impurity concentrations. [1,3,4] Systematic studies of the structure-property relationships have revealed a common sequence of domain-like states with increasing La^{3+} concentration [3], including: (i) normal micron-sized domains, (ii) tweed-like subdomain structures, and (iii) polar nanodomains. Recent studies of K^{1+} -modified PZT (PKZT) have shown significantly different changes in ferroelectric properties and phase stability with increasing K^{1+} impurity concentrations [5], relative to La^{3+} . These investigations have shown the development of "wavy" domains from

micron-sized domains with relatively small K^{1+} concentrations (~ 1 at.%). Further increments in K^{1+} concentration did not result in dramatic changes in domain stability. Comparisons of dielectric property data suggested that the "wavy" domains result from pinning effects.

The purpose of this work was to systematically investigate in a comparative manner the influence of both lower and higher aliovalent compositional modifications on the ferroelectric behavior of rhombohedral-structured PZT. It was anticipated that the difference between lower and higher valent modifications might be understood in terms of differences between mobile and randomly quenched impurities, respectively. In addition, it was hoped that a better understanding of ferroelectric phase transformations in impure systems might develop, in particular with respect to the importance of interactions between impurities (mobile and quenched) and domains.

II. Experimental design

Studies were made on $(\text{Pb}_{1-3/2x}\text{La}_x)(\text{Zr}_{0.65}\text{Ti}_{0.35})\text{O}_3$ (PLZT $x/65/35$) and $\text{Pb}_x\text{K}_{1-x}(\text{Zr}_{0.65}\text{Ti}_{0.35})_{1-x/4}\text{O}_3$ (PKZT $x/65/35$) ceramics fabricated by a conventional mixed oxide method. Dielectric constant measurements were made using a HP 4284A inductance-capacitance-resistance (LCR) meter which can cover a frequency range between 20 and 10^6 Hz. The P-E behavior was characterized with a computer-controlled, modified Sawyer-Tower circuit. Thin sections were prepared for TEM studies. Specimens were coated with carbon before examination. The TEM studies were

carried out on a Phillips EM-420 microscope at 120 kV.

III. Structure-property relationships

A. Dielectric studies

Figures 1(a) and (b) show the temperature dependent dielectric constant data for various compositions in the PLZT $x/65/35$ and PKZT $x/65/35$ sequences, respectively. Figure 1(a) exhibits a strong influence of La^{3+} concentration on the phase transformation and the dielectric response characteristics. For 0/65/35, a normal ferroelectric transformation can be seen to occur near 340°C . For PLZT 4/65/35, the ferroelectric transformation temperature was lowered to $\sim 250^\circ\text{C}$ and the temperature dependent response was significantly broadened, relative to the base composition. Upon increasing the La^{3+} concentration to 8 at.%, the dielectric constant maximum was shifted down to $\sim 100^\circ\text{C}$ and strong relaxor ferroelectric characteristics became evident, indicating significant disordering of the ferroelectric state which persists on cooling until temperatures far below that of the dielectric maximum.

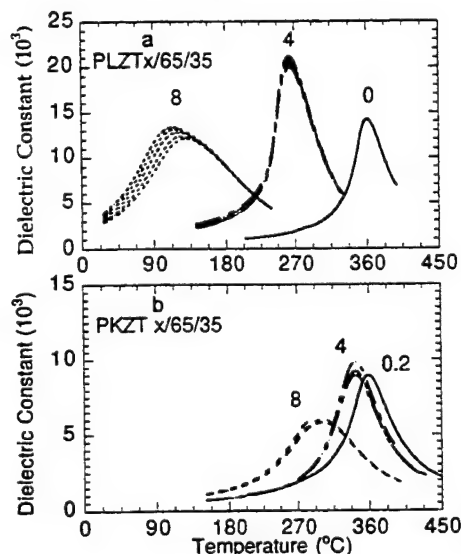


Fig. 1. Dielectric constant as a function of temperature for various PLZT and PKZT compositions. (a) PLZT 0/65/35, 4/65/35, and 8/65/35, and (b) PKZT 0.2/65/35, 4/65/35, and 8/65/35.

Figure 1(b) illustrates the dependence of K^{1+} concentration on the temperature dependent dielectric response. The changes with increasing K^{1+} can be seen to be significantly different than that with increasing La-content. For the composition 0.2/65/35, a ferroelectric phase transformation can be seen to occur near 350°C . For the PKZT 4/65/35, a small decrease of the temperature of the dielectric maximum (T_{max}) to $\sim 325^\circ\text{C}$, a slight decrease ($\sim 5\%$) in the maximum value of the dielectric constant (K_{max}), and a minor degree of broadening of the temperature dependent response characteristics were observed. On further increasing the K^{1+} concentration to 8 at.%, T_{max} was decreased to $\sim 290^\circ\text{C}$, K_{max} was decreased by $\sim 40\%$, and a strong broadening of the temperature dependent characteristics was observed. The comparisons of these results to those for PLZT clearly demonstrate a significant difference between the effects of lower and higher valent A-site compositional modifications on PZT.

III.2. TEM studies

Room temperature bright field images are shown in Figures 2(a)-(d) for PLZT 0/65/35, 5/65/35, 7/65/35 and 10/65/35. Distinct changes in the domain size and morphology are evident in Figure 2 with increasing La-content. For the composition 0/65/35 normal micron-sized domains are readily observed at room temperature (see Figure 2(a)). The dielectric response for 0/65/35 was typical of a normal long-range ferroelectric state. For the composition 5/65/35 (Figure 2(b)), a micron-sized domain structure was again observed. However, a finer-scale subdomain structure can be seen to coexist within the micron-sized domain patterns. These smaller domains were near-periodically spaced and had a striation-like morphology. The dielectric response for 5/65/35 had little relaxor-like character, however a broadening of the response was evident. For 7/65/35 (see Figure 2(c)), no normal micron-sized domains were observed at room temperature, rather tweedlike structures were evident. The corresponding

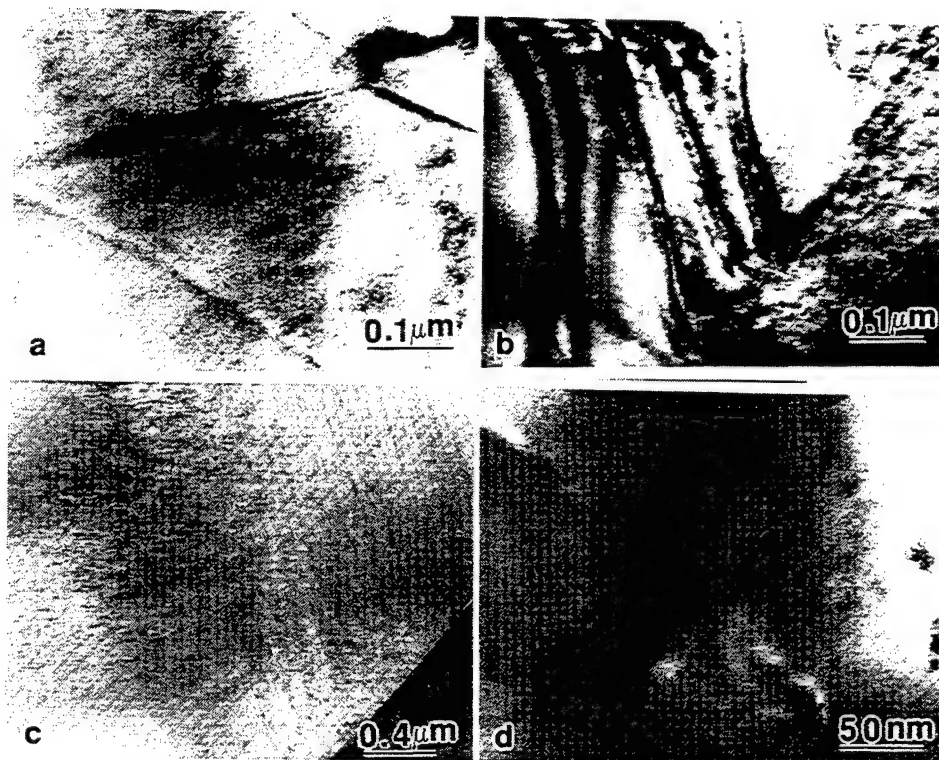


Fig. 2 Room-temperature bright-field TEM images for various PLZT compositions. (a) 0/65/35, (b) 1/65/35, (c) 4/65/35, and (d) 8/65/35.

dielectric response for 7/65/35 exhibited only weak relaxor characteristics. For the composition 10/65/35, polar nanodomains were observed as previously reported [4]. In addition, enhanced relaxor ferroelectric characteristics were evident in the dielectric response characteristics.

Figures 3(a)-(d) show the room temperature bright-field images for the PKZT compositions 0.2/65/35, 1/65/35, 4/65/35 and 8/65/35, respectively. Significant changes in the domain structure can be seen with increasing K-content. For 0.2/65/35 (Figure 3(a)), normal micron-sized 180° domains can readily be seen. However, with the addition of only 1 at.% K^{1+} , significant changes in the domain morphology were observed. In Figure 3(b), the size of the domain structures can be seen to be decreased dramatically for 1/65/35, relative to that for 0.2/65/35. In addition, the domain boundaries can be seen to be significantly more wavy, relative to the nearly straight

boundaries found for the lower K-content specimen. For 4/65/35, a further decrease in the domain size was observed, as can be seen in Figure 3(c). The lengths of the domains were less than $0.5 \mu\text{m}$ and their widths were approximately several hundred angstroms. In addition, the degree of wavy character in the domain patterns was significantly increased. The domains maintained a significant degree of preferred orientation along a family of crystallographically equivalent polar directions. The waviness in the morphology was due to continuous bending of the domain orientation between various equivalent directions on a length scale of $\sim 0.5 \mu\text{m}$. For 8/65/35, the trends of decreasing domain size and increasing irregularity in the domain patterns was observed to continue, as can be seen in Figure 3(d). For this composition, the presence of polar clusters or nanodomains was infrequently found. The characteristic feature for high K-content ferroelectrics in the x/65/35 sequence was the irregular wavy domain patterns.

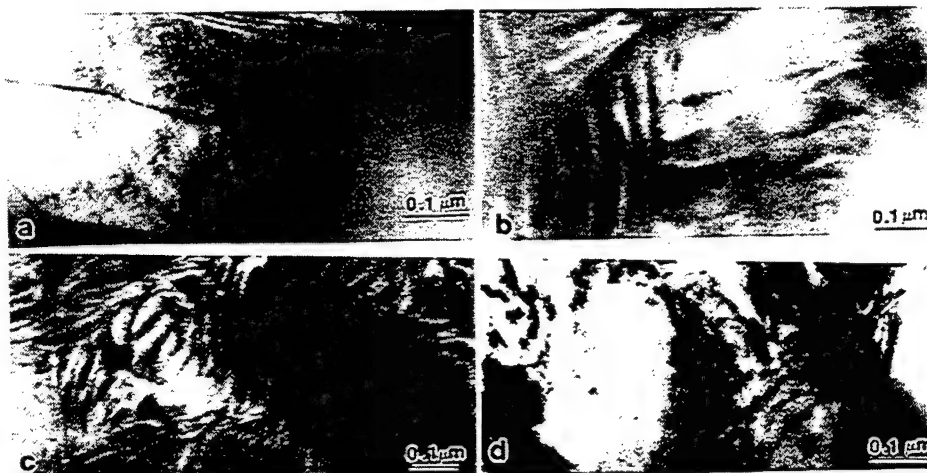


Fig. 3 Room-temperature bright-field TEM images for various PKZT compositions. (a) 0.2/65/35, (b) 1/65/35, (c) 4/65/35, and (d) 8/65/35.

Comparison of the results presented above for PKZT $x/65/35$ to those for PLZT $x/65/35$ will reveal distinct differences between the influence of lower valent A-site modifications, relative to higher valent ones. For PLZT, normal micron-sized domains were found to remain present with increasing La^{3+} , until concentrations between 4 and 6 at.%. However, for PKZT, a rapid decrease in the domain size was observed with the addition of only 1 at.% K^{1+} . Further increment in K^{1+} concentration to 4 at.% resulted in additional dramatic changes in domain size and morphology. Although, higher K^{1+} concentrations did not result in the evolution of polar nanodomains or clusters at room temperature, as La^{3+} modification did. These results clearly demonstrate that the effects of minor concentrations of K^{1+} impurities on the domain structures are much more pronounced than for La^{3+} . However, ferroelectric order is not destroyed by high K^{1+} concentrations as for La^{3+} , rather a strong degree of longer range ferroelectric order is maintained.

IV. Conclusions

A study of the influence of La^{3+} (randomly quenched) and K^{1+} (mobile) modifications on PZT has been performed. These investigations have revealed significant

differences in the structure property relations between these two modified PZT materials.

Acknowledgments

This work was supported by the Office of Naval Research (ONR) under contract No. N00014-95-1-0805 and by Naval UnderSea Warfare Center contract No. N66604-95-C-1536. The use of the facilities in the Center for Microanalysis in Materials Research Laboratory at the University of Illinois at Urbana-Champaign is gratefully acknowledged.

References

- [1] Haertling, G. and C.E.Land, J.Am.Ceram.Soc. 54, 1 (1971).
- [2] Ikeda, T. and T.Okano, Japan J. appl.Phys. 3, 63 (1963).
- [3] Dai, X., Z. Xu, and D. Viehland, Phil Mag. B 70, 33 (1994).H.
- [4] Li, J., X.H.Dai, A.Chow and D.Viehland, J.Mater. Res. 10, 926 (1995).
- [5] Tan, Q., Z. Xu, J.F.Li and D.Viehland, J. Appl. Phys. (accepted).

Thermochemical Interactions at Electrode Interfaces in Electroceramic Applications

David P. Cann and Clive A. Randall

The Center for Dielectric Studies
The Pennsylvania State University
University Park, PA 16802 USA

Abstract- Device properties such as contact resistance, high frequency conductor loss, fatigue, and mechanical strength are all known to be influenced by the electrode-ceramic interface. In this work, the electrical properties of electrode-ceramic interfaces will be related to the thermodynamic properties of the interface in order to establish a phenomenology for describing the fundamental interactions which determine the electrical properties of electrode-ceramic interfaces. The electrical characteristics of these interfaces were characterized by impedance spectroscopy, while the thermochemical properties were probed by sessile drop wetting experiments. With knowledge of the dominant thermochemical interactions, it will be shown that the composition of the electrode can be tailored to obtain optimum electrical properties.

I. INTRODUCTION

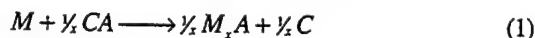
Recent accomplishments in semiconductor processing schemes has forced the dimensions of passive components, packaging, and associated surface mount devices to dimensions which are an order of magnitude smaller than the devices of the previous decade. The driving force for miniaturization has produced multilayer ceramic capacitors with dielectric layer thicknesses approaching 1 μm [1,2]. Evidence of the influence of the electrode-ceramic interface on overall device properties has been shown in the literature for many different systems [3,4]. As the dimensions of electroceramic devices continue to decrease, the role of the electrode-ceramic interface on device performance will become more and more important. In this work, a fundamental link between the electrical properties of electrode-ceramic interfaces and the thermochemical interactions present at the interface will be explored with the aim of establishing a scientific methodology to design the composition of electrodes in order to optimize the electrical properties of electroceramic devices.

II. BACKGROUND

The literature concerning metal-ceramic interfaces encompasses a wide variety of topic areas such as high resolution microscopy of interfaces [5], joining/brazing of metal/ceramic interfaces [6], interfacial thermodynamics, and electrical properties of metal-semiconductor interfaces [7]. Applications in which the study of interfaces is critical include electroceramics, heterogeneous catalysis, various

semiconductor devices, sensors, piezoelectrics, and metal/ceramic joining. All of the observed macroscopic phenomena are inherently linked to the thermochemical forces at the interface. Quantitatively, these can be expressed in terms of the thermodynamic parameters such as the heat of oxidation, ΔH^{ox} , and the partial enthalpy of mixing at infinite dilution, $\Delta \bar{H}^{\infty}$.

Brillson [7] showed that the variation in the Schottky barrier height (Φ_B) of different electrode metals on ZnO was a function of the chemical reactivity of the interface (Fig. 1). Specifically, electrode metals which had a strong affinity to react with ZnO tended to yield Ohmic contacts ($\Phi_B \sim 0$). In contrast, electrode metals with a only a weak affinity to react tended to yield large Φ_B . The driving force for reaction at the interface was quantified in terms of the following reaction:



Alternatively, the wetting and adhesion of liquid metals on ceramic substrates has also been observed to depend upon thermochemical driving forces at the interface. In a phenomenological model developed by Chatain [8], the thermodynamic work of adhesion can be fit to the empirical equation:

$$W_{ad} = -\frac{\alpha}{\Omega} \left(\Delta \bar{H}_{O(me)}^{\infty} + \frac{1}{4} \Delta \bar{H}_{Me(me)}^{\infty} \right) \quad (2)$$

where α is a constant, Ω is the interfacial molar area, $\Delta \bar{H}_{O(me)}^{\infty}$ and $\Delta \bar{H}_{Me(me)}^{\infty}$ are the partial enthalpies of mixing at

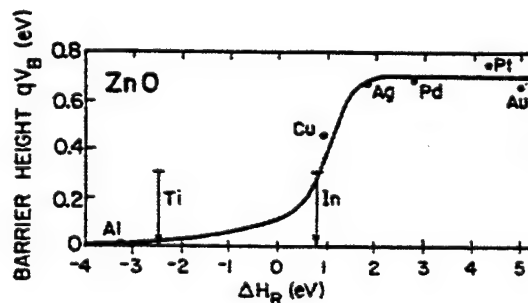


Figure 1. Schottky barrier height(eV) versus interface heat of reaction (oxidation) for various electrode metals on ZnO. (after Brillson [7])

infinite dilution of oxygen in the liquid metal (me) and the ceramic cation (Me) in the liquid metal, respectively.

Equation (2) illustrates the correlation between the macroscopic property of adhesion (W_{ad}) and the fundamental thermochemical forces at the interface as described by the thermodynamic parameters, $\Delta H_{O(me)}^{\circ}$ and $\Delta H_{Me(me)}^{\circ}$. As shown in Fig. 1, these same thermochemical interactions strongly influence the electrical properties of metal-ceramic interfaces as well. The summation of these facts suggests that both the energetic and electronic interfacial properties of metal-ceramic interfaces can be universally described in terms of the fundamental thermochemical forces at the interface. Thus with tabulated thermodynamic data [9,10], it is possible to predict the interfacial characteristics of a given metal on a ceramic substrate.

In this work, the role of thermochemical interactions at semiconducting PTCR BaTiO₃ interfaces were explored. The interfacial energetics were quantified via sessile drop wetting experiments. The electrical properties of the interfaces were characterized by complex plane impedance analysis. From the results of the experiments conducted on pure metal electrodes, the composition of bimetallic electrodes were designed in order to optimize the interfacial properties.

III. EXPERIMENTAL

For this study, ceramic BaTiO₃-based thermistors were supplied from a commercial vendor. The ceramics were in the form of discs with a diameter of approximately 12 mm and a resistivity of between 10-100 Ω -cm. Metal foils with a thickness of approximately 0.1 mm of Au, Ag, Cu, Ge, Sn, Ti, and Zr were used as the electrodes with a purity of at least 99.99%.

Sessile drop wetting experiments were conducted under vacuum in a furnace with SiC heating elements consisting of a mullite tube connected up to standard aluminum and stainless steel vacuum components. A maximum vacuum of 10⁻⁵ Torr was obtained through the use of a Balzers TSH-065D Turbomolecular Drag Pump Station. Photographs of the samples were taken through a quartz viewport with a 35 mm camera. Wetting angles were measured from enlargements of the photographs. Calculations of the liquid surface energy (necessary for calculation of W_{ad}) were approximated using the calculations of the surface energy of binary metal alloys of Li, Coudurier, and Eustathopoulos [11]. The thermodynamic W_{ad} was then calculated from the Young-Dupré equation [12].

Thin film bimetallic electrodes were synthesized by pulsed laser deposition (PLD) using an excimer laser pulsed at 25 Hz at an energy of approximately 350 mJ. Typically the film thicknesses were on the order of 1000 Å.

Electrical measurements were made at room temperature using the solidified metal drop in the wetting experiments as one electrode and a standard Ohmic In-Ga alloy as the back electrode. Impedance spectroscopy measurements were made on a Hewlett-Packard HP4194A Impedance Analyzer at frequencies ranging from 100 Hz up to 40 MHz. The oscillating voltage utilized was typically 10 mV.

IV. RESULTS AND DISCUSSION

Sessile drop wetting experiments conducted on pure Au, Ag, and Cu electrodes on PTCR BaTiO₃ revealed that the W_{ad} varied linearly with the heats of formation of their constituent oxide (Fig. 2). Table I lists some of the relevant thermodynamic data for the electrode metals in this study. Thus Cu, which has a relatively strong affinity for oxygen, yielded the strongest W_{ad} . In contrast, Au, which has a weak interaction with oxygen as evidenced from its positive heat of oxidation was observed to have the lowest W_{ad} .

The results of these experiments show that the dominant thermochemical interaction at the interface for these systems were *me-O* interactions as can be seen from the relationship:

$$W_{ad} \propto -\Delta H^{ox} \quad (3)$$

Based on these results, bimetallic alloys were synthesized in order to enhance the *me-O* interactions at the interface. Metals with a strong affinity for oxygen, e.g. Ti and Zr, were added to the noble metals Au and Ag at concentrations up to approximately 20 mole percent. Figure 3 below shows the change in contact angle with the addition of Ti to Au.

The addition of Ti decreased the contact angle from 114° for pure Au to as low as 64° for Au with 19.6 mole percent Ti

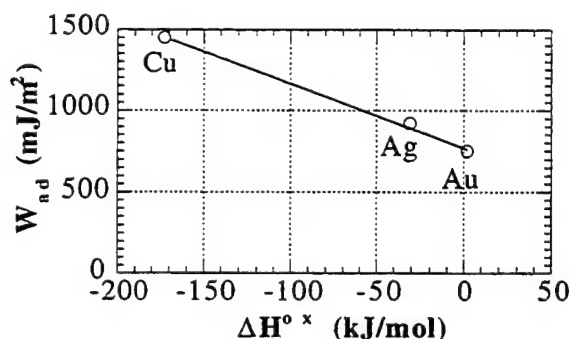


Figure 2. Thermodynamic W_{ad} derived from wetting experiments for pure Cu, Ag, and Au on PTCR BaTiO₃.

TABLE I
THERMODYNAMIC DATA FOR THE ELECTRODE METALS IN THIS STUDY.

| Metal | T _m (°C) | ΔH ^{ox} (kJ/mol) | γ _{lv} (mJ/m²) |
|-------|------------------------|------------------------------|----------------------------|
| Ag | 963 | -31 | 960 |
| Au | 1064 | +3 | 1185 |
| Cu | 1083 | -162 | 1360 |
| Ge | 937 | -580 | 590 |
| Sn | 232 | -578 | 550 |
| Ti | 1660 | -944 | 1410 |
| Zr | 1852 | -1101 | 1430 |

added. The decrease in wetting angle corresponds to an increase in the W_{ad} by a factor of 2.5.

Electron microprobe experiments confirmed the existence of a Ti-rich layer at the (Au,Ti)-BaTiO₃ interface [13]. This interfacial microstructural feature has been found in a number of systems in which the contact angle is strongly dependent upon the composition [12]. The strong affinity of Ti for oxygen drives the segregation and enhances the chemical interaction at the interface, which in turn results in a significant increase in W_{ad} . This same phenomena was observed for the bimetallic alloys of Ag-Ti, and Ag-Zr as listed in Table II.

The addition of Sn and Ge to Ag and Au-based alloys showed virtually no change in wetting behavior (Fig. 3). It is believed that the low surface energies of Sn and Ge ($\gamma_v < 600$ mJ/m²) enabled segregation of the solute atoms to the surface of the droplet during the sessile drop wetting experiments. Surface segregation in bimetallic alloys has been studied extensively by Miedema and others [14]. The semi-quantitative model expressed in [14] predicts segregation for the Sn and Ge-containing alloys consistent to the results in this work. In the case of the Ti and Zr-containing alloys discussed previously, no surface segregation was predicted nor was any observed.

Brillson [7] has shown that the electronic properties of interfaces are inherently related to the thermochemical characteristics of the interface. Therefore, the electrical properties of the bimetallic alloys in the previous wetting study were measured using impedance spectroscopy.

With impedance spectroscopy, the bulk and interfacial contributions to the complex impedance can be separated graphically by representing the data in the complex plane. An equivalent circuit can be derived from geometric parameters related to the graphical representation of the data. Barrier resistances introduced by the non-Ohmic character of an electrode can then be quantified by this technique.

Figure 4 displays the data for the Au-Ti bimetallic

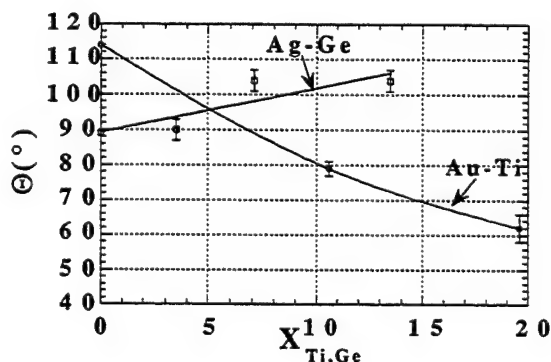


Figure 3. Contact angle (Θ) and W_{ad} for Au-Ti and Ag-Ge alloys on PTCR BaTiO₃.

TABLE II
CONTACT ANGLE AND W_{ad} FOR AG-TI AND AG-ZR ALLOYS ON PTCR BaTiO₃.

| Alloy | Θ (°) | W_{ad} (mJ/m ²) |
|----------|-----------------|----------------------------------|
| Ag | 90±2 | 950±30 |
| Ag-2.4Ti | 95±2 | 870±40 |
| Ag-5.0Ti | 69±11 | 1300±180 |
| Ag | 91±2 | 930±40 |
| Ag-1.2Zr | 91±1 | 940±20 |
| Ag-2.4Zr | 57±2 | 1480±30 |

electrodes. For the pure Au electrodes, a non-Ohmic contact was observed. The data can be represented by the equivalent circuit pictured in Figure 5 [15,16]. The series resistance R_{gr} is the resistance of the interiors of the grains and the parallel R_{gb} - C_{gb} element represents the resistance and capacitance of the internal grain boundaries of the ceramic PTCR. The second parallel R_{if} - C_{if} element represents the resistance and capacitance of the electrode interface. The impedance spectra for the Au-10.6Ti electrode showed no second semi-circle indicating an Ohmic contact. This is consistent with the trend observed in Fig. 1. The enhanced chemical interaction introduced by the addition of Ti to the relatively inert Au drove the contact behavior from non-Ohmic to Ohmic. The current-voltage curves for the (Au,Ti) electrodes as displayed in Fig. 6. These results corroborate the conclusions drawn from the impedance data. The pure Au electrode produced a non-Ohmic contact, while the Au-10.6Ti electrode produced an Ohmic contact.

This same behavior was observed in the Ag-Ti and Ag-Zr bimetallic alloys where the addition of a few mole percent (X~1-2 mol %) Ti and Zr was sufficient to develop an Ohmic contact. For the Sn and Ge containing alloys, concentrations greater than approximately 3-4 mole percent were necessary to observe the transition from non-Ohmic to Ohmic (e.g. Fig. 5).

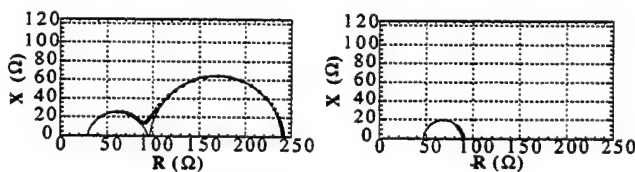


Fig. 4. Impedance spectra for Au (left) and Au-10.6Ti (right) electrodes on PTCR BaTiO₃.

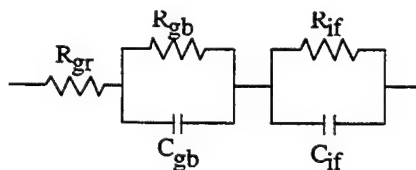


Figure 5. Equivalent circuit diagram for non-Ohmic electrode-PTCR BaTiO₃.

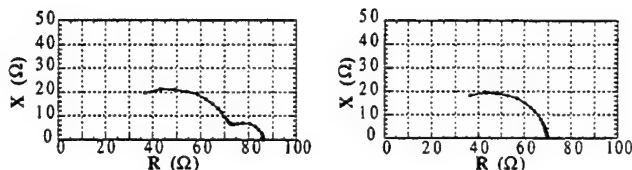


Fig. 6 Impedance spectra for Ag (left) and Ag-13.5Ge (right) electrodes on PTCR BaTiO₃.

Electrodes based on the alloys used in the sessile drop wetting experiments were deposited via PLD. Electrodes of four configurations were deposited: pure Au, pure Ti, a Au/Ti bilayer film, and a codeposited (Au,Ti) alloy film. The composition of the (Au,Ti) bimetallic films was nominally 5 weight percent Ti. The depositions were made at room temperature.

Impedance spectra of the pure Au electrode deposited by PLD was similar to the vacuum melted Au electrodes showing a double semi-circular form signifying an non-Ohmic contact. The pure Ti deposition showed an impedance spectra indicative of an Ohmic contact. Both configurations of (Au,Ti) alloy electrodes showed Ohmic contacts. This indicates that the strong affinity for oxygen by Ti is strong enough to create an Ohmic contact at room temperature and in concentrations as low as 5 weight percent.

The Ohmic contact behavior seen in the Ti containing samples was probably the result of the creation of a tunneling contact as described in Rhoderick and Williams [17].

V. CONCLUSIONS

The thermodynamic properties of electrode-PTCR BaTiO₃ interfaces, specifically the W_{ad} , was correlated to the contact resistance of the interface as determined from both impedance spectroscopy and current-voltage measurements. It was shown that the contact resistance was related to the strength of thermchemical interactions present at the interface. Interfaces with strong chemical interactions and hence a large W_{ad} tended to show Ohmic contacts, while weak interfaces, (those with low W_{ad}), tended to have large contact resistances. Furthermore, it was shown that the degree of chemical interaction at a given interface can be enhanced by

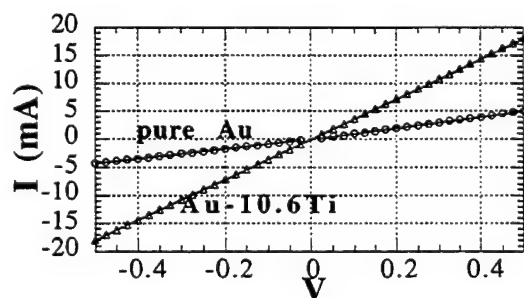


Figure 7. Current-Voltage data for Au and Au-10.6Ti electrodes on PTCR BaTiO₃.

modifying the composition of the electrode. The addition of a few mole percent of Sn, Ge, Ti, and Zr was found to transform the contact behavior from non-Ohmic to Ohmic. By identifying the underlying forces at the interface which determine the electrical properties, electrode compositions can be designed to achieve optimum properties.

ACKNOWLEDGMENT

The authors would like to acknowledge the assistance and insights of Mr. William R. Drawl with regards to the wetting experiments and Mr. Jon-Paul Maria with regards to the PLD experiments. The authors would also like to thank the Center for Dielectric Studies for their support on this project. The authors would also like to thank the International Microelectronics and Packaging Society Educational Foundation for their support as well.

REFERENCES

- [1] Y. Sakabe, "Trends in Integrated Electroceramic Device Manufacture," presented at the Electroceramic Device Manufacturing Workshop, April 1997.
- [2] S. Sato, "Tapecasting Thin Layers," presented at the Electroceramic Device Manufacturing Workshop, April 1997.
- [3] A. Kanda, S. Tashiro, and H. Igarashi, "Effect of firing temperature on electrical properties of multilayer semiconducting ceramics having positive temperature coefficient of resistivity and Ni-Pd internal electrodes," *Jap. J. Appl. Phys.*, vol. 33, pp. 5431-5434, September 1994.
- [4] S. Dey, J.J. Lee, P. Alluri, "Electrical properties of paraelectric (Pb_{0.72}La_{0.28})TiO₃ thin films with high dielectric permittivity: Schottky and Ohmic contacts," *Jpn. J. Appl. Phys. B* p. 3142, 1995.
- [5] W. Mader and G. Necker, "Electron Microscopy Studies on Naturally Grown Metal/Oxide Interfaces," *Metal-Ceramic Interfaces*, eds. Rühle, Evans, Ashby, and Hirsch, *Acta-Scripta Met. Proc. Ser.* vol. 4, p. 222, 1990.
- [6] M. Rühle and A.G. Evans, "Structure and Chemistry of Metal/Ceramic Interfaces" *Mat. Sci. and Engr.* vol. A107 p. 187, 1989.
- [7] L.J. Brillson, "Metal-Semiconductor Interfaces," *Surf. Sci.* vol. 299/300 p. 909, 1994.
- [8] D. Chatain, I. Rivollet, et N. Eustathopoulos, "Adhésion Thermodynamique Dans Les Systèmes Non-Réactifs Métal Liquide-Alumine," *J. de Chim. Phys.* vol. 83 p. 561, 1986.
- [9] A.R. Miedema, F.R. de Boer, R. Boom, and J.W.F. Dorleijn, "Tables for the heats of solution of liquid metals in liquid metal solvents," *CALPHAD*, vol. 1, pp. 353-359, 1977.
- [10] O. Kubaschewski, E. L. Evans, and C.B. Alcock, *Metallurgical Thermochemistry*, New York: Pergamon, 1974, pp. 303-448.
- [11] J.G. Li, L. Coudurier, and N. Eustathopoulos, "Work of adhesion and contact-angle isotherm of binary alloys on ionocovalent alloys," *J. Mat. Sci.*, vol. 24, pp. 1109-1116, 1989.
- [12] Ju. V. Naidich, "The wettability of solids by liquid metals," *Prog. in Surf. Memb. Sci.*, vol. 14, pp. 353-484, 1981.
- [13] D.P. Cann and C.A. Randall, "Thermochemistry and Electrical Contact Properties at the Interface Between Semiconducting BaTiO₃ and (Au-Ti) Electrodes," *J. Mater. Res.* vol. 12, 1997.
- [14] F.R. de Boer, R. Boom, W.C.M. Mattens, A.R. Miedema, and A.K. Niessen, *Cohesion in Metals*, New York: North Holland, 1988, pp. 103-637.
- [15] H.S. Maiti and R.N. Basu, "Complex-Plane Impedance Analysis for Semiconducting Barium Titanate," *Mater. Res. Bull.* vol. 21 p. 1107, 1986.
- [16] D.P. Cann and C.A. Randall, "Electrode effects in positive and negative temperature coefficient devices measured by complex-plane impedance analysis," *J. Appl. Phys.* vol. 80 p. 1628, 1996.
- [17] E.H. Rhoderick and R.H. Williams, *Metal-Semiconductor Contacts*, Oxford: Clarendon, 1988, pp. 1-49.

Resistivity Anomaly of (Ba,Ca,Sr,Pb)TiO₃ Semiconducting Ceramics Fired by Reduction-Reoxidation Method

Shinjiro Tashiro, Akihiro Osonoi and Hideji Igarashi

Department of Electronic Engineering,
The National Defense Academy,
Hashirimizu, Yokosuka 239, Japan

Abstract—The effects of A-site substitution on microstructure and electrical properties of BaTiO₃ semiconducting ceramics fired by the reduction-reoxidation method were experimentally investigated. Ba ions were substituted with Ca and (Sr_{0.5}Pb_{0.5}). This complex substitution attained small grain sizes of 5 to 8 μ m and high resistivity jumps above 5 orders. These materials were developed for a multilayer semiconducting ceramics with positive temperature coefficient of resistivity.

I. INTRODUCTION

The ultimate objective of this work is a multilayer PTCR ceramics with low resistance below the Curie point and several orders of resistivity jump above the Curie point. We have adopted the reduction-reoxidation firing to realize the ohmic contact between Pd-based internal electrodes and ceramics, and low resistivity of grains and high potential barrier at grain boundaries in BaTiO₃-based multilayer semiconducting ceramics with positive temperature coefficient of resistivity (PTCR) in the temperature region above the Curie point [1, 2].

A part of Ba ions in BaTiO₃ had been substituted with Ca ions, and the substitution quantity had been fixed at 15 atm% to prevent oxygen vacancies during firing in reducing atmosphere, according to the experimental results of (Ba_{0.85}Ca_{0.15})TiO₃-based multilayer ceramic capacitors with Ni internal electrodes developed by Sakabe and co-workers [3]. However, (Ba_{0.85}Ca_{0.15})TiO₃-based PTCR ceramics fired in reducing atmosphere accompanied with large grain sizes around 40 μ m and small resistivity jump less than 3 orders [1]. It is necessary to improve large grain size and small resistivity jump.

We investigated that the effect of A-site substitution and firing temperature on grain size and resistivity jump. In this substitution, Ba ions were substituted with only Ca or only (Sr_{0.5}Pb_{0.5}). From these experiments, We obtained the results as follows [4]: 1) Ca substitution prevents grain growth in BaTiO₃ semiconducting ceramics fired reduction-reoxidation firing. 2) The solubility limit of Ca to BaTiO₃ is 0.25. 3) The substitution of (Sr_{0.5}Pb_{0.5}) promotes the reoxidation at grain boundaries although exerts hardly effect on the suppression of grain growth. 4) The grain sizes above

5 μ m are necessary in order to reoxidize only grain boundaries.

The experimental results suggests that the simultaneous substitution of Ca and (Sr_{0.5}Pb_{0.5}) is effective to realize fine grains and large resistivity jump. In this paper, the effects of the simultaneous substitution and firing temperature on microstructure and electrical properties of samples obtained by the reduction-reoxidation firing were investigated.

II. EXPERIMENTAL

In the material compositions used in this study, the ratio of Ba and Ca was fixed at (Ba_{0.7}Ca_{0.3}), and (Ba_{0.7}Ca_{0.3}) was substituted with (Sr_{0.5}Pb_{0.5}) as follows;
(Ba_{0.7}Ca_{0.3})_{1-z}(Sr_{0.5}Pb_{0.5})_zTi_{1.01}O_{3.02}+0.1mol%Y₂O₃+0.25mol%SiO₂+0.06mol%MnO.

Furthermore, in order to investigate the effect of Mn concentration on PTCR characteristics, Mn concentration was changed from 0 to 0.06 atm% in the sample of $z=0.20$.

The pair substitution of Sr and Pb is for the fixation of the Curie point at around 120°C. The substitution quantities of (Sr_{0.5}Pb_{0.5}) are 0 to 0.30. The starting materials were extra-pure BaCO₃, CaCO₃, SrCO₃, Pb₃O₄, Y₂O₃, TiO₂, SiO₂ and Mn(NO₃)₂ · nH₂O.

These materials, except Mn(NO₃)₂ · nH₂O, were mixed by wet ball milling for 11 h and calcined at 1100°C for 2 h in air. Sufficient Mn(NO₃)₂ · nH₂O was added to the calcined

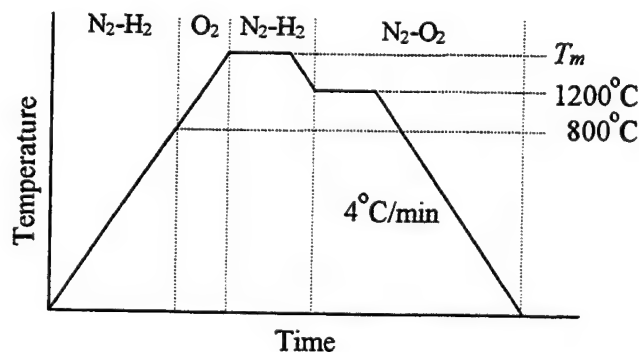


Fig. 1. Firing profile for reduction-reoxidizing firing.

powders so that Mn would be equal to desired concentrations. The calcined powders were ground and mixed with $\text{Mn}(\text{NO}_3)_2 \cdot n\text{H}_2\text{O}$ by wet ball milling for 11 h. After granulation using a solution of polyvinyl alcohol as binder, the powders were pressed into disks 15 mm in diameter and about 2.5 mm in thickness under 100 MPa. The binder was removed at 400 °C for 2 h in air.

The samples were fired according to the firing program shown in Fig. 1 which was already reported in detail [5]. In Fig. 1, an oxygen atmosphere introduced in the heating process from 800°C to firing temperatures T_m is for obtaining dense ceramic body. The samples were fired for 2 h at firing temperatures T_m of 1350, 1320 and 1290°C, and annealed at 1200°C for 2 h in oxygen atmosphere. A reducing atmosphere is necessary from room temperature to 800°C to avoid the oxidation of Pd-based internal electrodes of the multilayer samples which we aim to obtain as the final product, although the data for the multilayer samples are not reported in this paper.

Grain size was determined by the linear intercept method on the chemical or thermal etched surfaces. The Ag alloy electrodes (NAMICS Corporation, SR5083) with ohmic contact to PTCR ceramics were formed on the major surfaces of the disk samples ground to 1 mm in thickness, by firing at 560°C for 10 min in air. Resistance in temperature dependence was measured using a digital multimeter (IWATSU VOAC 7513).

III. RESULTS AND DISCUSSION

Table 1 shows lattice constant, theoretical and sintered density, porosity, average grain size, resistivity at room temperature and the magnitude of resistivity jump of PTCR, in the samples fired at 1350°C for 2 h. The magnitude of resistivity jump is shown with $\log(\rho_{\max}/\rho_{\min})$, where ρ_{\max} and ρ_{\min} are the maximum and minimum resistivity in temperature dependence of resistivity. The porosities were calculated using theoretical and sintered densities.

The porosities increased above $z=0.15$. This is for the

firing temperature of 1350°C which is too high to obtain dense ceramic body, for the samples with $(\text{Sr}_{0.5}\text{Pb}_{0.5})$ concentrations above $z=0.15$. The porosities decrease with decrease of firing temperature.

The change of grain size is not consistent with the substitution quantity of $(\text{Sr}_{0.5}\text{Pb}_{0.5})$ although changes between 5.3 to 10.4 μm . These grain sizes are smaller compared with the no substitution sample (BaTiO_3). This is probably due to Ca substitution from the results of only Ca substitution [4]. Resistivities at room temperature were greatly different among all the samples. These resistivity changes occur during the annealing at 1200°C in oxygen atmosphere since those samples were uniform semiconductors with 10 to 20 Ωcm unless annealed at 1200°C in Oxygen atmosphere.

The resistivities in the temperature region below the Curie point include not only the resistivity of grain interiors but also that due to the residual potential barrier at grain boundaries [6, 7]. In order to distinguish the two effects on the total resistivity, the frequency locus of impedance is usually measured from 5 Hz to 13 MHz (Cole-cole plot). The locus converges to the resistivity of grain interiors at high frequencies. We have demonstrated using the Cole-cole plot that the reoxidation during annealing at 1200°C occurs mainly at only grain boundaries [1, 5, 8].

However, in the samples with $(\text{Sr}_{0.5}\text{Pb}_{0.5})$ concentrations of $z=0.05$ and 0.10, the resistivities around room temperature increased to 2.0×10^6 and $1.5 \times 10^4 \Omega\text{cm}$. This is probably due to the reoxidation extended to inside of grains not only grain boundaries. The samples with $(\text{Sr}_{0.5}\text{Pb}_{0.5})$ concentrations above $z=0.15$ show resistivity jumps above 5 orders. In these samples, the reoxidation during annealing at 1200°C occurs mainly at only grain boundaries.

Since fine grains and high density are essential in multilayer structure, in addition to low resistivity at room temperature and high resistivity jump above the Curie point, we defined the figure of merit (F.M.) which estimates the

TABLE I
Lattice constant, density, porosity, average grain size, resistivity at room temperature and magnitude of resistivity jump of PTCR, in the samples fired at 1350°C

| Substitution quantity | Lattice constant | | Theoretical density | Sintered density | Porosity | Average grain size | Resistivity at room temp. | Resistivity jump |
|-----------------------|------------------|-------|----------------------|----------------------|----------|--------------------|------------------------------|---------------------------------|
| | a (Å) | c (Å) | (g/cm ³) | (g/cm ³) | (%) | (μm) | ($\Omega \cdot \text{cm}$) | $\log(\rho_{\max}/\rho_{\min})$ |
| no substitution | 3.994 | 4.037 | 6.01 | 5.76 | 4.20 | 35 | 13 | 2.75 |
| $z=0$ | 3.956 | 3.997 | 5.42 | 5.27 | 2.72 | 7.0 | 26 | 2.78 |
| $z=0.05$ | 3.952 | 3.990 | 5.49 | 5.31 | 3.32 | 10.4 | 2.0×10^6 | 2.36 |
| $z=0.10$ | 3.945 | 3.987 | 5.56 | 5.37 | 3.46 | 8.1 | 1.5×10^4 | 4.21 |
| $z=0.15$ | 3.945 | 3.987 | 5.62 | 5.44 | 3.24 | 7.9 | 202 | 5.66 |
| $z=0.20$ | 3.945 | 3.983 | 5.68 | 5.39 | 4.99 | 5.3 | 560 | 5.51 |
| $z=0.25$ | 3.942 | 3.987 | 5.73 | 5.36 | 6.43 | 7.7 | 290 | 5.53 |
| $z=0.30$ | 3.942 | 3.976 | 5.80 | 5.23 | 9.80 | 6.2 | 840 | 5.02 |

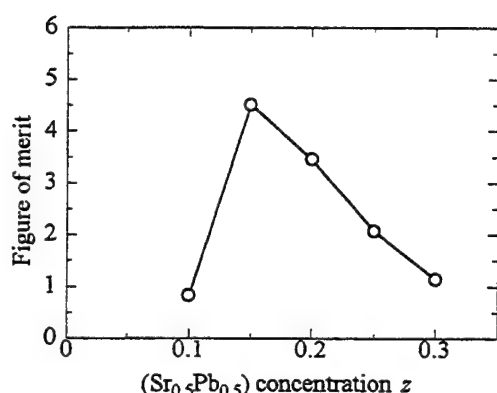


Fig. 2. Figure of merit of the samples fired at 1350°C as a function of $(\text{Sr}_{0.5}\text{Pb}_{0.5})$ concentration z .

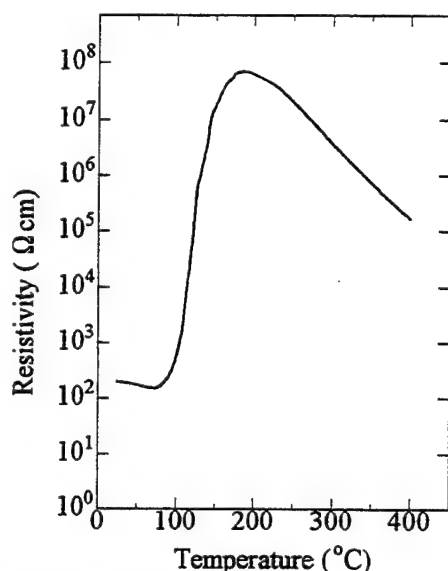


Fig. 3. Temperature dependence of resistivity of the sample with a $(\text{Sr}_{0.5}\text{Pb}_{0.5})$ concentration of 0.15, fired at 1350°C.

material for multilayer PTCR ceramics, as shown in

$$F.M. = \frac{\log(\rho_{\max} / \rho_{\min}) - 3}{(G_s / 1[\mu\text{m}]) \cdot p \cdot \log(\rho_{\min} / 1[\Omega\text{cm}])} \quad (1)$$

Where, PTCR jump is evaluated using the difference with 3 orders as the reference value, and G_s and p are average grain size and porosity. Average grain size is evaluated using the ratio to the unit length of 1 μm , e.g. expressed in μm . As well as grain size, resistivities are expressed in Ωcm .

Fig. 2. shows the figure of merits of the samples, having PTCR jumps above 3 orders, fired at 1350°C. The sample of $z=0.15$ shows the maximum value, and next is $z=0.20$. Thus, $(\text{Sr}_{0.5}\text{Pb}_{0.5})$ concentrations are 0.15 to 0.20 for high figure of merit, in the firing at 1350°C. Fig. 3. shows

TABLE II
Porosity, average grain size, resistivity at room temperature and magnitude of resistivity jump of PTCR, in the samples fired at 1320°C

| Substitution quantity | Porosity (%) | Average grain size (μm) | Resistivity at room temp. ($\Omega \cdot \text{cm}$) | Resistivity jump $\log(\rho_{\max} / \rho_{\min})$ |
|-----------------------|--------------|--------------------------------------|--|--|
| no substitution | 5.50 | 33 | 20 | 3.17 |
| $z=0$ | 1.78 | 16 and 1~2 | 3.4×10^2 | 2.36 |
| $z=0.05$ | 1.95 | 1.1 | 4.8×10^9 | - |
| $z=0.10$ | 2.10 | 1.1 | 3.6×10^9 | - |
| $z=0.15$ | 2.77 | 3.5 | 6.9×10^5 | 2.45 |
| $z=0.20$ | 3.53 | 3.3 | 4.8×10^4 | 3.80 |
| $z=0.25$ | 4.67 | 3.5 | 9.2×10^3 | 4.60 |
| $z=0.30$ | 5.73 | 3.5 | 2.1×10^3 | 5.13 |

TABLE III
Porosity, average grain size, resistivity at room temperature and magnitude of resistivity jump of PTCR, in the samples fired at 1290°C

| Substitution quantity | Porosity (%) | Average grain size (μm) | Resistivity at room temp. ($\Omega \cdot \text{cm}$) | Resistivity jump $\log(\rho_{\max} / \rho_{\min})$ |
|-----------------------|--------------|--------------------------------------|--|--|
| no substitution | 4.52 | 35 | 20 | 2.17 |
| $z=0$ | 1.43 | 1.5 | 4.1×10^9 | - |
| $z=0.05$ | 1.59 | 0.77 | 4.9×10^9 | - |
| $z=0.10$ | 1.7 | 0.80 | 4.0×10^9 | - |
| $z=0.15$ | 2.13 | 2.4 | 4.1×10^9 | - |
| $z=0.20$ | 1.01 | 2.9 | 2.5×10^9 | - |
| $z=0.25$ | 1.45 | 2.5 | 5.4×10^9 | - |
| $z=0.30$ | 3.96 | 2.3 | 4.5×10^9 | - |

temperature dependence of resistivity of the sample of $z=0.15$.

Table II shows porosity, average grain size, resistivity at room temperature and the magnitude of resistivity jump, in samples fired at 1320°C for 2 h, and table III shows those of samples fired at 1290°C for 2 h. The values of theoretical densities, using to calculate porosities, referred to table I.

Lowering firing temperature to 1320°C, the samples of above $z=0.05$ became dense and fine in grain size compared with the samples fired at 1350°C, however, the resistivities at room temperature increased. This is probably due to the reoxidation extended to inside of grains not only grain boundaries as well as the samples of $z=0.05$ and 0.10 fired at 1350°C. These changes became clear in the samples fired at 1290°C, as shown in table III.

All the samples of above $z=0$ in table III showed the resistivities at room temperature above $1 \times 10^9 \Omega\text{cm}$. This is probably due to the grain sizes, e.g. the grain sizes are too small to reoxidize only grain boundaries during annealing at

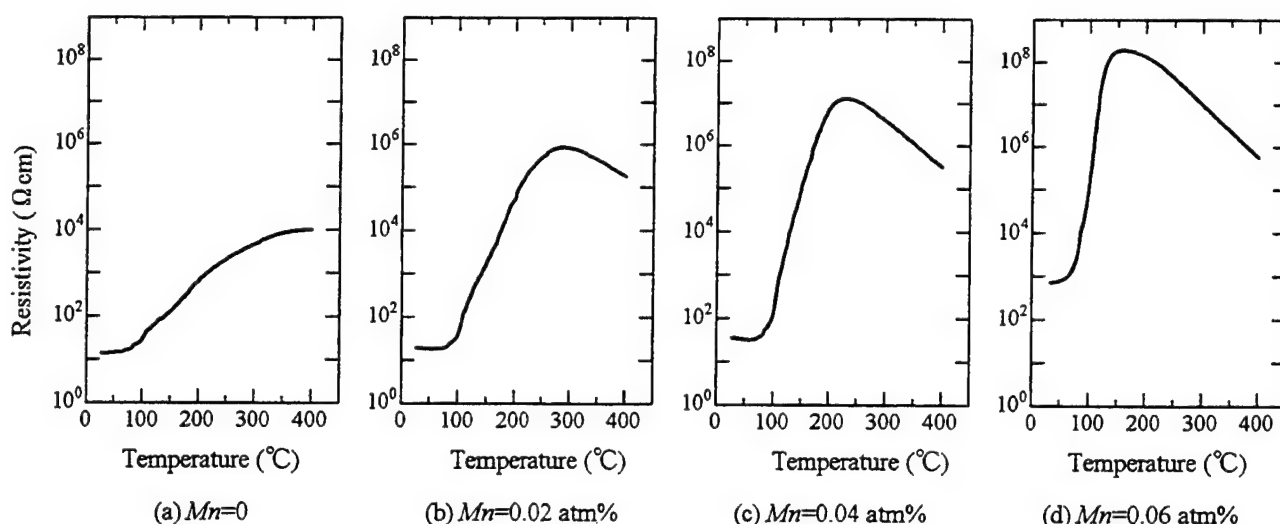


Fig. 4. Effect of Mn concentration on temperature dependence of resistivity in the sample of $z=0.20$.

1200°C. Since the reoxidation into inside of grains is probably dominated by grain size and Mn concentration, it is possible to lower the resistivity at room temperature by optimizing grain size and Mn concentration.

The effect of Mn concentration on temperature dependence of resistivity was investigated in the sample of $z=0.20$ since the sample showed the minimum grain size in the series fired at 1350°C as shown in table I. Figs. 4(a), (b), (c) and (d) show temperature dependence resistivity of those samples. Resistivity jump increases with increase of Mn concentration although the resistivity at room temperature also increases. The values of figure of merit calculated using (1) were 5.02 for Mn=0.02 atm%, 6.60 for Mn=0.40 atm% and 3.45 for Mn=0.60 atm%, respectively. The figure of merit for the sample without Mn can not be derived since the resistivity jump was lower than 3 orders. Thus, temperature dependence of resistivity is very sensitive to Mn concentration as well as conventional PTCR ceramics fired in air. From the values of figure of merit, the optimum Mn concentration is 0.04 atm% in the sample of $z=0.20$. In this sample, the resistivity at room temperature is 32 Ω cm, the resistivity jump is 5.61, the average grain size is 5.28 μm and the porosity is 0.050.

REFERENCES

[1] S. Tashiro, A. Kanda and H. Igarashi, "PTCR characteristics of

semiconducting (Ba,Ca)TiO₃ ceramics fired in reducing-reoxidizing atmosphere," *J. Ceram. Soc. Japan*, vol. 102, pp. 284-289, March 1994 [inJapanese] [*J. Ceram. Soc. Japan Int'l Edition*, vol. 102, in English.]

[2] A. Kanda, S. Tashiro and H. Igarashi, "Effect of firing temperature on electrical properties of multilayer semiconducting ceramics having positive temperature coefficient of resistivity and Ni-Pd internal electrodes," *Jpn. J. Appl. Phys.* vol. 33, No. 9B, pp. 5431-5434, September 1994.

[3] Y. Sakabe, K. Minai and K. Wakino, "High-dielectric constant ceramics for base metal monolithic capacitors," *Proc. 3rd Meeting on Ferroelectric Materials and Their Applications (FMA-3)*, Kyoto, 1981, *Jpn. J. Appl. Phys.* vol. 20, Supplement 20-4, pp.147-150, September 1981.

[4] A. Osonoi, S. Tashiro and H. Igarashi, "Effect of A-site substitution on microstructure and electrical properties of BaTiO₃ semiconducting ceramics fired by reduction-reoxidation method," *Jpn. J. Appl. Phys.* in press.

[5] S. Tashiro, T. Ishiya and H. Igarashi, "Effect of firing atmosphere on densification of semiconducting (Ba,Sr)TiO₃ ceramics and their dielectric properties and varistor characteristics," *Jpn. J. Appl. Phys.* vol. 35, pp. 5074-5079, September 1996.

[6] B. Kulwicki and A. Purdes, "Diffusion potentials in BaTiO₃ and the theory of PTC materials," *Ferroelectrics*, vol. 1, pp.253-263, 1970.

[7] H. B. Haanstra and h. Ilrig, "Transmission electron microscopy at grain boundaries of PTC-type BaTiO₃ ceramics," *J. Ceram. Am. Soc.* vol. 63, pp. 288-291, March 1980.

[8] T. Ishiya, S. Tashiro and H. Igarashi, "Varistor characteristics of (Ba,Sr)TiO₃ semiconducting ceramics fired reducing-reoxidizing atmosphere," *Jpn. J. Appl. Phys.* vol. 34, pp. 5309-5312, September 1995.

Hypothesis on Rare Earth Doping of BaTiO₃ Ceramic Capacitors

A. Hitomi*, X. Liu, T.R. Shrout and C.A. Randall

Materials Research Laboratory
The Pennsylvania State University
University Park, PA 16802 USA

Abstract- This paper discusses recent advances in the compositional development of BaTiO₃-based ceramics for base metal multilayer capacitors. We hypothesize on the significance of rare earth and yttrium doping on the degradation mechanism and the formation of microstructural loop dislocations found within the grain structure. It is proposed that rare earth doping substitutes in the octahedral perovskite site and acts as an acceptor ion during firing at reduced oxygen partial pressures. Through both electrostatic and strain interactions, the trivalent rare earths cation elements Ho, Dy and also the element Y, pin the mobility of the oxygen vacancies more effectively than smaller acceptors, e.g. Mn²⁺ and Fe²⁺, therefore enhancing the lifetime of the multilayer capacitors.

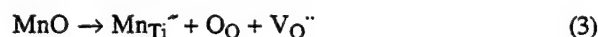
I. INTRODUCTION

For many years there has been a commercial interest in multilayer capacitors (MLCs) manufactured with base metal electrodes such as copper and nickel instead of the more expensive noble metals and alloys such as palladium or silver-palladium. In particular, nickel electrodes are usually selected for cofiring with BaTiO₃ dielectric materials. To avoid oxidation of the nickel electrodes during firing, a reducing atmosphere is necessary. There are two basic problems that must be overcome to successfully produce Ni-MLCs; (1) the increase in electronic conductivity (loss in insulation resistance) of the BaTiO₃ and (2) the increase in equilibrium concentration of oxygen vacancies that limit reliability.

To solve the first problem, various formulations of BaTiO₃ dielectrics compatible with cofiring Ni electrodes have been studied for a number of years. Sakabe et al. reported the significance of the dopants, MnO and CaO, on the resistivity of BaTiO₃ during reduced firing [1,2]. To understand the role of these dopants, let us recall some important aspects of the nonstoichiometry of metal oxides in reducing atmospheres. The full Kröger-Vink diagram for generalized MO is divided into distinct regions depending on the dominant defect compensation mechanism at specific oxygen partial pressures, see Fig. 1. In region I, the dominant defect is the oxygen vacancies, and in region II, the concentration of acceptors fixes the oxygen vacancy concentration as follows;

$$\begin{aligned} [A'] &= 2[V_O'] & (1) \\ \text{or } [A'] &= [V_O'] & (2) \end{aligned}$$

Considering the Kröger-Vink diagram, we can infer the importance of controlling the acceptor concentration at low partial pressures of oxygen. The higher the acceptor concentration, the lower PO₂ pressure region II dominant. This effectively reduces the electronic conductivity of the metal oxides at lower partial pressure of oxygen. A more comprehensive review can be found in Smyth [3]. It is understood that Mn is on the B-site and acts as an acceptor ion to reduce the electronic conductivity and render the BaTiO₃ insulating at room temperature.



In addition, Ca is also thought to act as an acceptor ion. In the A-site, Ca is isovalent but in the octahedral B-site Ca_{Ti}²⁺ is a doubly charged acceptor. The concentration of Ca²⁺ on the B-site can be influenced by the BaO content, as shown by Smyth et al. [4]. From this data, the conductivity minima shifts to lower partial pressures with higher BaO content, and the slope of the conductivity is approximately 1/4, which is consistent with acceptor doping.

The recent advances of Ni-MLC technologies can be represented by the reliability improvement which is the solution of the second problem mentioned above. A key microstructure property relationship was first reported by Nomura et al., who discovered loop dislocations are highly prevalent in degraded BaTiO₃ dielectrics [5]. First let us review the significance of the loop dislocations. The loop dislocations are found to accumulate in BaTiO₃ under an electric field near the cathodic electrode during degradation.

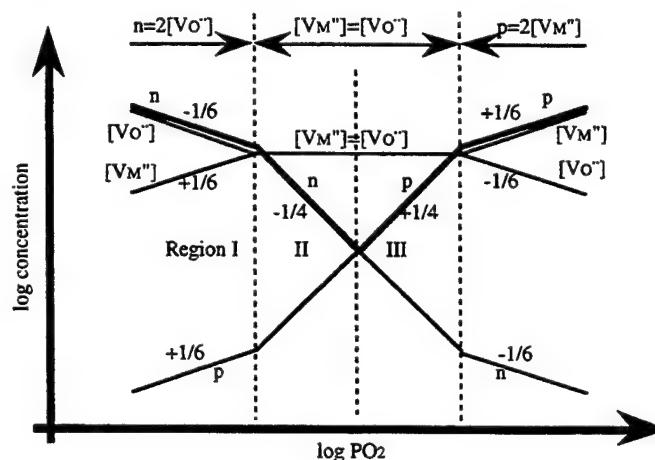


Fig. 1. Kröger-Vink diagram for a typical metal oxide MO (by Smyth [1]).

In poorly performing dielectric compositions i.e. poor reliability characteristics, loop dislocations also are found to occur dispersed throughout the grains when firing in a reducing atmosphere. Post oxygen annealing has been shown to dramatically reduce loop dislocation concentration, and annealed samples have shown lower degradation rates. The loop dislocations are inferred to be the result of clusters of oxygen vacancies [6]. Hence, the key to improving reliability has been found through limiting the mobility of oxygen vacancies which is structurally observed in the formation of dislocation clusters.

Recently there has been new approaches in the formulations of BaTiO₃ for Ni-MLCs for both Y5V and X7R characteristics based on rare earths and yttrium substitutions. Several compositional studies to improve reliability have been recently reported. According to Nomura's data, Table I, Y³⁺ was identified as a most significant additive to prolong the lifetime to failure among a selection of rare earth and transition metal elements [7]. The lifetimes were determined through changes in the insulation resistance after exposure to high voltages and temperatures (HALT: highly accelerated lifetime tests). Kishi et al. recently reported on the influence

Table I.
Effect of additives on the life time of Ni-MLCs (by Nomura et al.[7])

| Additive | Lifetime (Relative Values) |
|--------------------------------|-------------------------------|
| No Additive | 1.0 |
| Y ₂ O ₃ | 15.5 |
| CeO ₂ | 0 |
| V ₂ O ₅ | 6.7 |
| Nb ₂ O ₅ | 0.3 |
| MoO ₃ | 2.8 |
| Ta ₂ O ₅ | 0 |
| WO ₃ | 1.8 |

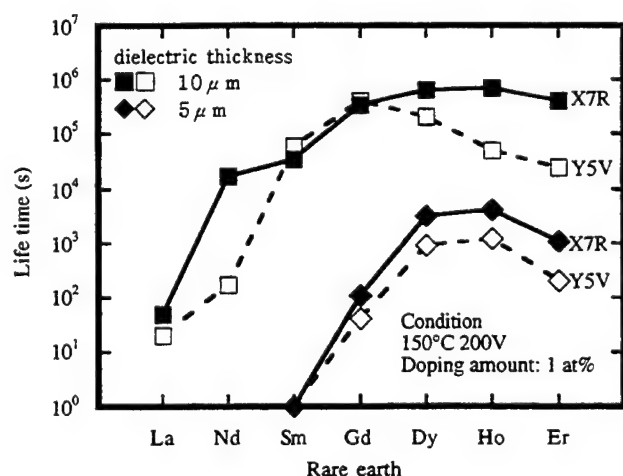


Fig. 2. Effect of rare-earth dopants on the lifetime of Ni-MLCs (by Kishi et al. [8]).

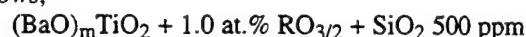
of various rare earth substitutions of 1 at.% in BaTiO₃ on the lifetimes measured on Y5V and X7R Ni-MLCs with dielectric thicknesses of 5 and 10 μm with the best additives being Dy³⁺ and Ho³⁺, see Fig. 2 [8]. Hamaji et al. also reported significance of rare earth doping such as Dy³⁺ and Y³⁺ on lifetime [9].

It is suggested that these dopants, Y³⁺, Dy³⁺ and Ho³⁺ have some role on limiting the mobility of oxygen vacancies, however the mechanism is still unclear. The objective of this paper is to share our rationalization of the role of the rare earth dopants, Y, Ho and Dy in dielectric formulations developed for base metal electrodes.

II. EXPERIMENTAL

A. Materials

The nominal composition prepared from raw materials was as follows;



$$(m = 0.99, 1.00, 1.01, R = \text{Y, Ho, Gd, Nd}).$$

Regent grade raw materials, BaCO₃ (Sakai Chemical), TiO₂ (Ishihara), SiO₂ (Junsei, as a sintering aid) and a rare earth oxide were mixed in a plastic jar using ZrO₂ media and de-ionized water for 16h and calcined at 1200°C for 2h. The calcined materials were milled in a plastic jar using ZrO₂ media and de-ionized water for 16h and then pan-dried.

B. Firing

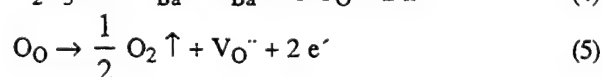
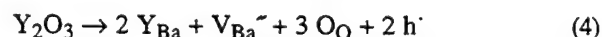
The materials which were mixed with an acrylic binder were pressed into pellets (diameter 6.35mm, thickness 2.0mm) and then fired at 1300°C for 2h in air or a reducing atmosphere. The reducing atmosphere PO₂ = 10⁻¹⁰ atm was prepared by a mixture of N₂-H₂-H₂O gases.

C. Electrical Measurements

Dielectric constant measurements as a function of temperature were determined from capacitance measurements using a Hewlett-Packard HP4274A LCR meter at 1 kHz with a thermostat chamber. Resistivity measurements were made with a digital multimeter. For these measurements, In-Ga alloy electrodes were used to provide ohmic contact.

III. RESULTS AND DISCUSSION

The question is raised to the functionality of the additives, Y³⁺, Dy³⁺ and Ho³⁺, in relation to better degradation properties. One possible explanation for the role of Y³⁺ limiting degradation was given by Nomura et al [7].



The V_{Ba} and V_O are proposed to interact through a coulombic force leading to a pinning of the mobility of the oxygen vacancies. They reported that the loop dislocations appearing with MnO additions, and disappearing with additional Y_2O_3 doping were assumed to be on the A-site [10]. The argument above describes the disappearance of loop dislocations for Y_2O_3 , but this is not true for all donors, according to their data, see Table I. In addition, Kishi et al. reported that there are differences in the relative performance of elements throughout the rare-earth series, the best additives being Dy^{+3} and Ho^{+3} [8]. Hamaji et al. also noted the different effects of the rare-earth dopants on the lifetime of Ni-MLCs [9]. They reported the Dy-doped and Y-doped dielectrics have longer lifetimes than that of the La-doped dielectric.

An alternative hypothesis is outlined below which explains universally the advantage of the key Y^{+3} , Ho^{+3} and Dy^{+3} elements when substituted into the $BaTiO_3$ structure. At this time there is some uncertainty on the location of the rare-earth elements and yttrium. Yttrium is used as an A-site donor dopant in $BaTiO_3$ for PTCR (positive temperature coefficient resistors). But yttrium cations can also occupy the B-site in perovskites, as indicated in the $Pb(Y_{1/2}Nb_{1/2})O_3$ compound. There are a number of elements soluble in perovskites that can occupy both the A- and B-sites. Ca^{+2} is an excellent example, as we have already discussed; a further example is the rare earth Ce^{+3} or Ce^{+4} [11]. To access the size limitations of B-site occupation, let us consider the Ca^{+2} ion. On the A-site, Ca^{+2} is twelve-fold coordinated and would have an ionic radius of 1.34Å, but with excess BaO and/or firing in a reducing atmosphere, the Ca can be forced to occupy the B-site with octahedral coordination where its ionic radius is 1.00Å [12].

We believe that many of the rare earth dopants are equally sensitive to site occupancy. The ability of a rare earth to occupy the B-site depends on the ionic radii, the Ba/Ti ratio, and the oxygen partial pressure. Smyth et al. demonstrated through equilibrium conductivity data [13] that larger ions such as Dy^{+3} , Sm^{+3} and Nd^{+3} act as donors. This would be consistent with A-site occupancy, whereas smaller ions such as Yb^{+3} and Er^{+3} act as acceptors, corresponding to B-site occupancy when Ba/Ti = 1.01. It was also noted that Er^{+3} changes the occupying site when Ba/Ti = 0.99, and acts as donors. These results suggest the occupying site dependence on the ionic radii and Ba/Ti ratio. All the rare earth-doped $BaTiO_3$ became semiconductive when fired in a reducing atmosphere, $PO_2 = 10^{-10}$ atm, see Fig. 3. However, the resistances of the samples being Ba/Ti = 1.01 were higher than those of Ba/Ti = 0.99 and 1.00. This was particularly evident for Y-doped samples which showed higher resistivity ($10^4 \Omega cm$) than that of Nd-doped samples ($10^1 \Omega cm$). These data suggest that Y acts more effective as an acceptor than Nd due to its smaller ionic radius; i.e. smaller ions have a larger solubility in the B-site, and also suggest that the B-site solubility is large when BaO is in excess. A typical PTCR composition doped with Y [14] is Ti-rich as follows;

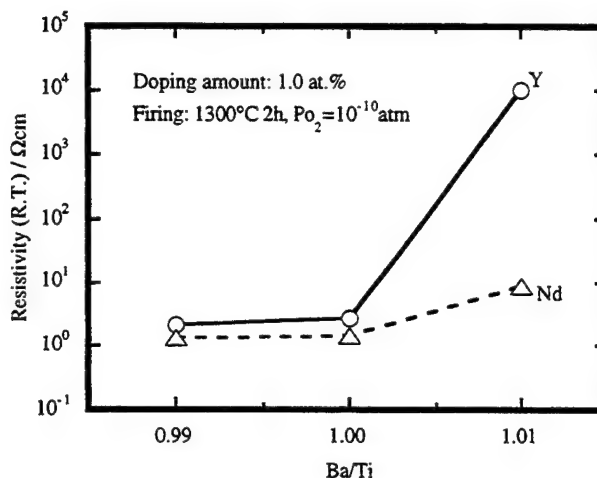
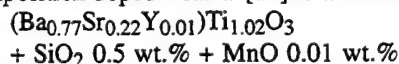


Fig. 3. Resistivity at room temperature of the Y- and Nd-doped $BaTiO_3$ fired in a reducing atmosphere (this work).

In this composition, Y is thought to occupy the A-site and act as a donor. On the other hand, it is reported that the Ba-richness is important to prolong the lifetime of Ni-MLC $BaTiO_3$ [7]. In this case, we believe that Y occupies the B-site and act as an acceptor when considered with the data above.

We also believe that the atomistic role of the dopants such as Y, Ho, or Dy in improving reliability is to more strongly attract oxygen vacancies by both electrostatic and strain interactions. Electrostatic interaction is simply the positive charged V_O and negative charged Y_{Ti} , Ho_{Ti} or Dy_{Ti} attraction to each other. The strain interaction, which is not typically considered, in the degradation mechanism is explained as follows: the octahedrally coordinated rare earth creates a compressive strain in the lattice owing to its large ionic radius compared to typical B-site ions. This local compressive strain field attracts oxygen vacancies which produce tensile strain. The more mobile oxygen vacancies will be attracted to the rare earths and locally pinned in the lattice. This interaction is sufficiently strong and retards the formulation of loop dislocations and reduces ionic migration to the cathode under bias. With rare earths occupying the B-site, there is a balance between the B-site solubility (= the acceptor concentration) and the lattice strain produced by specific dopants in the $BaTiO_3$ lattice. The larger rare earth ions would be expected to have higher strain fields but limited in concentration on the B-site. The smaller ionic rare earth atoms will have higher concentrations on the B-site but lower strain fields. We note that the best rare earth elements are Ho and Dy which have very similar ionic radii in octahedral coordination: Ho = 0.901Å and Dy = 0.912Å by replottting Kishi's data [8] against ionic radii, Fig. 4. In addition, the ionic radius of Y in octahedral coordination is 0.900Å, also being very similar. It is believed that the balance between the B-site solubility and the lattice strain produced, which depends on the ionic radii of the dopants, is the reason why there is an optimum effect at an ionic radius around 0.90Å.

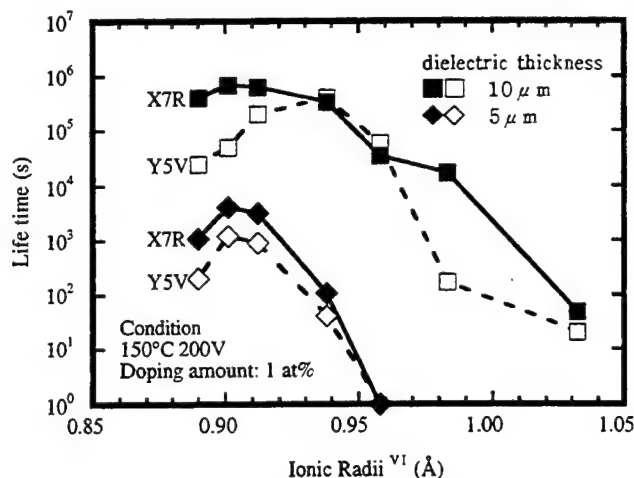


Fig. 4. Effect of rare-earth dopants on the lifetime of Ni-MLCs replotted from Fig. 2 [8].

IV. CONCLUSIONS

This paper identifies the key role of acceptor dopant strain fields in limiting oxygen vacancy migration in a perovskite crystal structure fired in a reducing atmosphere with excess Ba content. The hypothesis consistently rationalize the anomalous reliability performance of Dy, Ho and Y dopants, and the microstructural observations in base metal electrode MLC ceramics.

ACKNOWLEDGMENT

The authors gratefully acknowledge Dr. Nomura, TDK

Corporation, and Prof. Huebner, University of Missouri-Rolla, for helpful discussions.

REFERENCES

1. Y. Sakabe, K. Minai, and K. Wakino, "High-Dielectric Constant Ceramics for Base Metal Monolithic Capacitors," *Jpn. J. Appl. Phys.*, **20 Suppl. 20-4**, 147-150 (1981).
2. Y. Sakabe, "Dielectric Materials for Base-Metal Multilayer Ceramic Capacitors," *Ceram. Bull.*, **66**, 1338-1341 (1987).
3. D.M. Smyth, "The Role of Impurities in Insulating Transition Metal Oxides," *Prog. Solid State Chem.*, **15**, 145-171 (1984).
4. N.H. Chan, M.P. Harmer, M. Lai, and D.M. Smyth, "Calcium Site Occupancy in BaTiO₃," *Mat. Res. Soc. Symp. Proc.*, **31**, 345-350 (1984).
5. M. Shiojiri, T. Isshiki, H. Saijo, M. Tsujikura, A. Nakada, Y. Nakano, M. Ikeda, and T. Nomura, "High-Resolution Electron Microscopy Study of Domain Boundaries and Dislocation Loops in BaTiO₃ Crystals," *Phys. Stat. Sol. (a)*, **129**, 353-362 (1992).
6. Y. Nakano, A. Sato, A. Hitomi, and T. Nomura, "Microstructure and Related Phenomena of Multilayer Ceramic Capacitors with Ni-electrode," *Ceramic Transactions*, **32**, 119-128 (1993).
7. H. Kishi, Y. Okino, and N. Yamaoka, "Electrical Properties and Reliability Study of Multilayer Ceramic Capacitors with Nickel Electrodes," pp. 255-260 in Proceedings of The Seventh US-Japan Seminar on Dielectric and Piezoelectric Ceramics (Tsukuba, Japan, November 1995).
8. Y. Hamaji, H. Sano, H. Wada, and K. Tomono, "Effect of Rare Earth Oxides on X7R Dielectrics," pp. 273-276 in Proceedings of The Seventh US-Japan Seminar on Dielectric and Piezoelectric Ceramics (Tsukuba, Japan, November 1995).
9. Y. Nakano, A. Sato, A. Hitomi, and T. Nomura, "On the Microstructure of the Multilayer Ceramic Capacitor with Ni-electrode," *J. Soc. Mater. Eng. for Resources of Jpn.*, **7**, 21-27 (1994).
10. D. Makovec, Z. Samaridzija, and D. Kolar, "Solid Solubility of Cerium in BaTiO₃," *J. Solid State Chem.*, **123**, 30-38 (1996).
11. R.D. Shannon, "Revised Effective Ionic Radii and Systematic Studies of Interatomic Distances in Halides and Chalcogenides," *Acta Cryst.*, **A32**, 751-767 (1976).
12. K. Takada, E. Chang, and D.M. Smyth, "Rare Earth Addition to BaTiO₃," *Adv. Ceram.*, **19**, 147-152 (1987).
13. A. Hitomi, S. Sato, C. Takahashi, and T. Nomura, "Microstructure and Electrical Properties of BaTiO₃-based Semiconductive Ceramics," *J. Jpn. Soc. of Powder and Powder Metallurgy*, **43**, 1049-1054 (1996).

Grain Size Effects in Dielectric Barium Titanate

Steven P. Ostrander and Walter A. Schulze
New York State College of Ceramics
at Alfred University,
Alfred, NY 14802, USA

SCHULZE@BIGVAX.ALFRED.EDU

Introduction

Grain size effects in barium titanate's dielectric behavior were studied. Dense capacitors (96-98% of ρ_{th}) of various average grain size (~ 0.7 to ~ 18 μm) were fast-fired from one lot of near-stoichiometric (titania-excess) powder. Fine-grain samples exhibit a weak field K ~ 5500 with $\tan(\delta) \sim 0.02$ at room temperature, yet support distinct first-order discontinuity at the Curie-transition. With respect to the coarse-grain material, they show suppressed paraelectric and ferroelectric losses, slower dielectric-aging, and less dielectric dispersion. Increased grain-boundary contributions and diminished hysteretic domain-wall contributions are suggested to explain trends observed in respective paraelectric and ferroelectric phases of fine-grain barium titanate.

This study investigates the temperature, frequency, and aging dependencies of real and imaginary parts of weak-field permittivity in a set of fine- and coarse-grain barium titanate ceramics. Conclusions are based on interpretation of the subtle differences in the complex dielectric response between fine- and coarse-grain materials as functions of temperature and time.

Experimental Procedure

High-purity chemically prepared powder was fast-fired to produce a set of samples with grain sizes ranging from submicron to ~ 20 microns. In effort to minimize extrinsic influences on dielectric behavior, a single powder-lot was batch wet-processed and batch green-formed. Grain size was controlled by varying only sintering temperature.

Samples were stored at $120^\circ C$ in a convection oven prior to fast-firing. For sintering, they were heated at $100^\circ C/min$ to $600^\circ C$ then held 5 min. to equilibrate. Samples were then heated at a rate of $100^\circ C/min$, to the sintering temperature and held for 10 minutes. Samples were fired at 1200, 1250, 1300, 1350 and $1400^\circ C$ in air.

Aluminum electrodes were evaporated on the pellet faces. A layer of 'air-dry' silver electrode paste was added to protect the aluminum layer from oxidation and mechanical damage. Dynamic permittivity measurements were performed after de-aging the samples at $170^\circ C$ for 30 minutes, and data was collected with a logarithmic frequency sweep while cooling from $170^\circ C$ at $-1^\circ C/min$. For isothermal dielectric aging measurements, samples were de-aged in a separate $170^\circ C$ convection oven, while the empty test chamber was equilibrated at $50^\circ C$. After one hour, the samples were quenched from the de-aging oven into an ethanol bath, then loaded into the preheated test chamber. Dielectric-aging was measured over several days at near isothermal conditions (the 95 % confidence interval was $\pm 0.2^\circ C$).

Results and Discussion

Figure 1 shows the temperature-dependent dielectric response in capacitors of various average grain sizes. As expected, fine grain material shows a substantially greater room temperature permittivity than that of coarse grain material. This grain size induced permittivity enhancement (or "grain-size-effect") appears only in the orthorhombic and tetragonal phases. Yamaji, et al. have demonstrated that grain size has negligible influence on relative permittivity in the paraelectric phase, and that the grain-size-effect is thus tied to ferroelectricity. His evidence supported the existing internal stress model, suggesting that permittivity enhancement in fine grain material results from stresses developed with the inability to compensate for the normal 1% lattice distortion associated with cooling through the Curie transition. In addition, with later Doveshire-type phenomenological calculations, Bell demonstrated that the grain-size-effect is specifically related to normal-stresses, and that despite the presence of considerable shear, the permittivity of the rhombohedral phase would also be independent of grain size. The data in Figure 1 reinforce those published by Yamaji, et al., and confirm the theoretical work of Bell.

The Curie-transitions of the fine-grain materials demonstrate clear first order discontinuities. These samples exhibit little evidence of a distribution of transition temperatures. The diffuse-phase-transitions reported in many earlier investigations likely result from processing-related chemical-heterogeneities or -impurities, as indicated by Bell and Moulson, or possibly from low point-to-point temperature resolution. The fine grain materials show shifted transition temperatures. With respect to coarse grain material, their Curie transition temperatures decrease by $\sim 5^\circ C$, while the lower two ferroelectric-to-ferroelectric phase transition temperatures increase by $\sim 10^\circ C$. In addition, two distinct Curie transitions are observed by both DSC and dielectric property measurements in samples that suffer discontinuous microstructures.

This step-change in transition temperature could be attributed to relief of elastic stresses, as indicated by Bell, or possibly to an elimination of defects resulting from grain coarsening. That is, grain-coarsening might allow the formation of stress-relieving-twins, and/or possibly act as a zone-refinement cleansing process which substantially alters the defect-population within a grain. In chemically prepared powders, those formed with conservative heat treatments, the potential defects are likely to include solid-solubility of excess-titania (the most abundant impurity in this powder), the trace-impurities from reagent-grade raw materials, and possibly the lattice perturbations present in fine barium titanate powders and at grain boundaries in bulk ceramics. To the authors' knowledge, this zone-refinement process has

not previously been acknowledged as a potential cause for shifted transition temperatures. In addition, Frey, et al. have shown similar shifts in transition temperatures in near-stoichiometric capacitors fabricated with high pressure (8 GPa) compaction. Fully dense compacts coarsened from 0.6 to 1.7 mm average grain size show no apparent shift in Curie temperature. However, after significant coarsening (to ~20 mm grain size), these show a step increase of about ~3°C in the Curie temperature. Further, Frey et al. also observed two distinct Curie-transitions in samples with discontinuous microstructures. Relief of the elastic clamping effect (or internal stress) with grain coarsening was concluded responsible for these shifts, but note that these were also chemically prepared powders with slight Ti-excess.

As temperature is increased above ~50°C, hysteretic domain wall motion increasingly contributes to the lower-frequency (<10 Hz) ferroelectric losses of coarse-grain material. These coarse-grain materials also suffer the usual loss-anomalies that peak with impending crystal-structure degeneracy at temperatures near structural phase transitions. Both the thermally-activated- and phase-transition-losses are generally suppressed in fine-grain material.

The decrease in thermally activated domain-wall contributions suggest either a decreased concentration of -walls, or a suppression (pinning) of wall-motion in fine-grain material. The low concentration of 90° domain-walls reported by Buessem et al. and Yamaji et al. provides credible explanation for this observation. Alternatively, the simple-lamella 90° twinning reported by Arlt et al. might also account for diminished domain-wall mobility.

The typical loss anomalies of a coarse grain barium titanate ceramic are much smaller than that expected from a orientational average of those from a single-crystal. This has been indicated as evidence of grain boundary pinning of domain wall motion in polycrystalline material. It is suggested that this suppression is perhaps exaggerated in the fine grain material with the large number density of grain boundaries (~2 orders of magnitude more grain boundaries in fine grain material). This provides yet another possible explanation for the observed differences in domain-wall-motion contributions to the losses of fine- and coarse-grain barium titanate.

Above the Curie temperature the coarse grain material shows thermally activated and frequency dependent conductivity losses. These conductivity losses are suppressed in the fine grain material. Losses in the paraelectric phase are obviously not related to stresses or domain wall motion, and thus point-out another important distinction between these materials.

These samples all originate from one powder batch and near-identical processing. However, potential extrinsic influences on dielectric properties may include variation in oxygen stoichiometry, and the above mentioned differences in the redistribution of impurities or heterogeneities.

Natural occurring impurities in barium titanate are dominated by loss-damping acceptor impurities. However, the paraelectric conductivity losses indicate that atmospheric reduction has occurred while sintering the coarse grain samples. The absence of a conductivity loss in fine-grain material suggests that either the firing temperature was not sufficient to activate significant atmospheric reduction, the

larger density grain boundaries provides a better path for rapid re-oxidation, or perhaps that this larger relative portion of grain boundary perturbed material affects conductivity losses as well as ferroelectric domain wall motion.

The absence of dispersion in the fine grain material suggests that either the sub-eutectic fired material was not appreciably reduced (i.e. was never semiconducting), or that the fine grain material is more readily re-oxidized with the large number of grain boundaries serving as oxygen diffusion paths.

Typical intrinsic Schottky barrier layer thicknesses are on the order of 0.2-0.3 mm in boundary layer capacitors. It is interesting to note that the grain size (radius) of the fine-grain material is on the order of a typical barrier layer. This suggests that the Maxwell-Wagner effect, in fact, should not be expected in these fine-grain samples.

Domain wall motion dominated the losses in the ferroelectric phases of the coarse-grain material (Figure 2.). These are thermally activated, and relax at relatively low frequency. An anomaly is observed at temperatures slightly below the orthorhombic-tetragonal transition temperature; this bump is assumed to be a release of free charge carriers with the annihilation and reconstruction of domain systems. These charge carriers are soon swept to low-energy positions, and their contributions decrease over time (and with increased frequency). Their effect broadens the apparent $\tan(\delta)$ peak associated with the orthorhombic to tetragonal phase transition in the coarse-grain material.

Figure 2. shows the frequency dependence of dielectric losses at several temperatures. Essentially these are isothermal cross-sections. These samples were de-aged for one half hour, oven quenched (10~20 °C/min) to the measurement temperature, then equilibrated for a half hour before collecting data. Therefore, with the obvious differences in cumulative thermal history, some variations are to be expected between these and the data obtained during uniform cooling rate experiments. Nevertheless, the variations appear quite small in this case.

The differences between the frequency dependence of the fine and the coarse-grain materials are remarkable. From Figure 2., it is apparent that the dispersion in the coarse-grain material is dominated by a low frequency relaxation mechanism (off-scale). There also appears to be a minor relaxation event (shoulder) that varies from about 10^2 to 10^4 Hz with increasing temperature. In general, the loss spectra shift up to higher losses and to the right to higher frequency with increasing temperature, with an activation energy of ~0.5 eV. In the fine-grain material, the low frequency event is absent. There appears to be a smaller amplitude relaxation that sits near the above mentioned coarse-grain relaxation frequency, and another off-scale on the high frequency side. The characteristic frequencies for these relaxations also increase with temperature (0.5 eV).

As mentioned, the dielectric properties of ferroelectric barium titanate result from a sum of several polarization mechanisms. These include domain wall motion, defect dipole motion (rotation or translation), space-charge polarization, piezoelectric coupling of grains or domains, intrinsic contributions such as electronic and ionic polarizations, and possibly others. Assigning particular polarization mechanisms to the relaxation events in Figure

2. would be difficult, at best. The literature is contradictory in the assumed assignments of relaxation events.

It is possible, however, to eliminate several mechanisms. For example, the intrinsic contributions relax at very high frequencies (about 10^{13} and 10^{17} Hz). Space charge polarization (at electrodes and at grain boundaries) would be expected to relax at very low frequencies (between 10^0 and 10^3 Hz). These are likely to dominate the low frequency edge of the coarse-grain loss spectrum. The fine-grain material does not exhibit appreciable conductivity, and thus, the space charge contribution is quite low.

If the samples were poled, piezoelectric coupling would show resonances that depend on the bulk sample dimensions. In these *unpoled* samples, piezoelectric clamping might be expected to depend on grain and/or domain dimensions. Based on the upper limits of grain and domain dimension, however, these are expected to relax at frequencies in the gigahertz range. Reported relaxation frequencies for domain wall motion vary considerably. McQuarrie suggests that relaxation frequencies of domain wall motion covers a broad distribution of relaxation times,

extending from 1 to 10^6 Hz. Benguigui indicated that a superposition of four distinct relaxations could account for the 90° domain wall motion in the frequency range from $100 - 10^7$ Hz. He implied that the relaxations corresponded to the four usual configurations of 90° domains. He indicated also that interaction with 180° domains would affect the spectrum.

Arlt demonstrated that it is possible to estimate the domain wall contribution by plotting aging data as the real part of the complex dielectric constant (K') as a function of the imaginary part ($K'' \tan \delta$). He suggested that as the material ages, and domain wall contributions are eliminated, the extrapolated value at zero loss is characteristic of the intrinsic contribution. In Figure 3, it is apparent that the fine-grain material sees an internal stress contribution of ~ 2000 over the intrinsic dielectric constant of the coarse-grain material.

The contribution of the intrinsic and the domain wall portions of the dielectric response may be estimated with the concept postulated by Arlt. By plotting the real component of the complex permittivity as a function of the imaginary or loss component, over time, and by extrapolation to infinite time, the zero loss intercept indicates the intrinsic portion of the dielectric response (i.e. with hysteretic effects aged out). The dispersion in the short-term (high loss) dielectric response indicates the relative contribution of the extrinsic (lossy and hysteretic) domain wall and conductivity portions of the complex permittivity.

Extrapolation of the 50°C aging data in Figure 3 indicates an intrinsic contribution of ~ 2000 , a hysteretic domain-wall contribution of 500-600 in coarse grain material, and an internal stress contribution of an additional ~ 2000 in the fine grain material. The frequency dependencies of the fine and coarse grain material are also evident here. The coarse grain material demonstrates low frequency relaxation typical of space-charge polarization or hysteretic domain wall motions, while the fine grain material exhibits a high frequency relaxation typical of a larger restoring force event.

Summary

1. All specimens originated from one powder batch.
2. Grain size was controlled through firing temperature. Differences in potential extrinsic influences may include variation in oxygen stoichiometry and the redistribution of impurities or heterogeneities (e.g. porosity and excess titania).
3. Strong first order character was observed at the Curie-transition of all samples.
4. A small ($\sim 5^\circ\text{C}$) decrease in the Curie-temperature, and an increase ($\sim 10^\circ\text{C}$) in the rhombohedral-to-orthorhombic and orthorhombic-to-tetragonal phase transitions were observed in fine-grain samples.
5. Fine-grain samples show permittivity enhancement in the orthorhombic and tetragonal phases.
6. Hysteretic domain wall motion increasingly contributes to the lower-frequency ferroelectric losses of coarse-grain material as temperature is increased above $\sim 50^\circ\text{C}$. Losses also peak with the degeneracy of crystal structure near phase transitions. Both the thermally activated losses and the phase-transition losses are largely suppressed in the fine-grain material.
7. Above T_C , the coarse-grain material shows thermally activated, frequency dependent, conductivity losses. These are also suppressed in the fine-grain material.
8. Microstructural heterogeneities affect Curie-Weiss behavior. Porosity forms a low permittivity parallel mixture, and decreases the Curie-constant. Grain boundary phases form low permittivity serial mixtures, and decrease the Curie-Weiss temperature.
9. Permittivity of the coarse-grain material is slightly dispersive in the paraelectric phase. This is believed to be a weak Maxwell-Wagner effect caused by the incomplete, or graded re-oxidation of coarse-grain samples. No paraelectric dispersion was observed in the fine-grain material.
10. Permittivity and loss are dispersive in the three ferroelectric phases of both the fine- and coarse-grain materials. This is a not an instrumental artifact. The frequency dependance is different for the fine and coarse, grained ceramic and suggests the superposition of several mechanisms.

References

- G. Arlt, "Review: Twinning in Ferroelectric and Ferroelastic Ceramics: Stress Relief," *J. Mater. Sci.*, **25** [6] 2655-66 (1990).
- G. Arlt and N.A. Pertsev, "Force Constant and Effective Mass of 90° Degree Domain Walls in Ferroelectric Ceramics," *J. Appl. Phys.*, **70** [4] 2283-2289 (1991).
- A.J. Bell and A.J. Moulson, "The Effect of Grain Size on the Dielectric Properties of Barium Titanate Ceramic," *Br. Ceram. Proc.*, No. 36 57-66 (1985).
- A.J. Bell, "Calculations of Finite Size Effects in Barium Titanate," *Ferroelect., Lett. Sect.*, **15** 133-140 (1993).
- L. Benguigui, "Ferroelectric Losses in BaTiO_3 Produced by the Domain Walls," *Ferroelectrics*, **7** [2] 315-317 (1974).
- W.R. Buessem, L.E. Cross and A.K.

Goswami, "Phenomenological Theory of High Permittivity in Fine-Grained Barium Titanate," *J. Am. Ceram. Soc.*, **49** [1] 33-36 (1966).

M.H. Frey and D.A. Payne, "Grain Size Effect on Structure and Phase Transformation for Barium Titanate," *Accepted for Publication, Phys. Rev. B: Condens. Matter*, (1996).

M. McQuarrie, "Role of Domain Processes in

Polycrystalline Barium Titanate," *J. Am. Ceram. Soc.*, **39** [2] 54-59 (1956).

A. Yamaji, Y. Enomoto, K. Kinoshita and T. Murakami, "Preparation, Characterization, and Properties of Dy-Doped Small-Grained BaTiO₃ Ceramics," *J. Am. Ceram. Soc.*, **60** [3-4] 97-101 (1977).

Summary of Properties.

| Temp (°C) | Size (μm) | Density % | C (x10 ⁵ °C) | T ₀ (°C) | T _c (°C) | K _{Max} | K ₂₀ °C | T _{O-T} (°C) | T _{R-O} (°C) |
|--------------|--------------|--------------|----------------------------|------------------------|------------------------|------------------|-----------------------|--------------------------|--------------------------|
| 1200 | ~ 0.4 | 87 | 1.16 | 101 | 120 | 5500 | 3600 | 16 | - 73 |
| 1250 | 0.70 | 96 | 1.54 | 103 | 120 | 8400 | 5500 | 20 | - 72 |
| 1300 | 1.0 & 60 | 96 | 1.57 | 109 | 120 & 125 | 10600 | 4800 | 13 | - 81 |
| 1350 | 9.3 | 98 | 1.68 | 113 | 125 | 13900 | 3700 | 11 | - 85 |
| 1400 | 18 | 98 | 1.55 | 113 | 125 | 12600 | 3000 | 11 | - 84 |

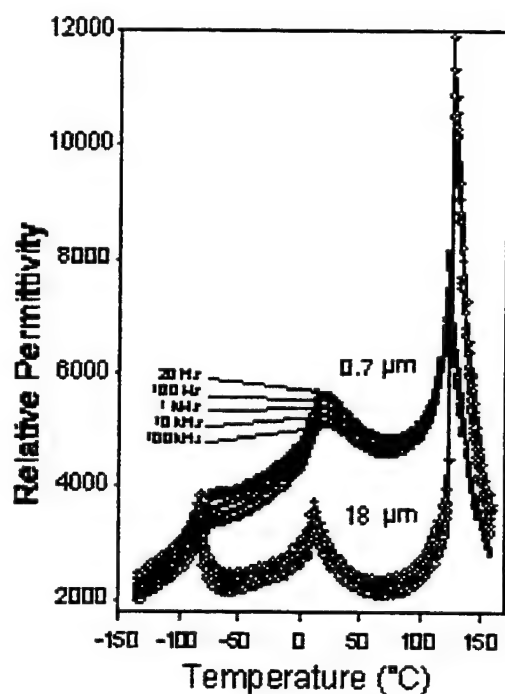


Figure 1

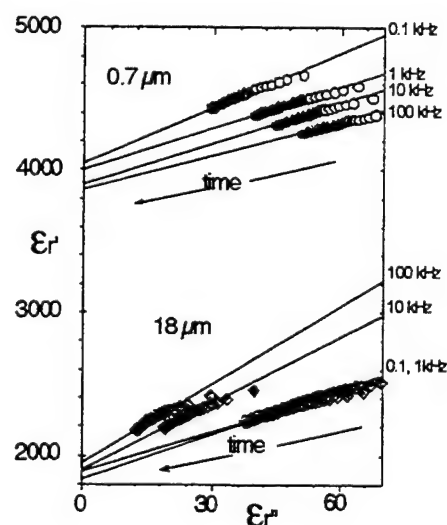


Figure 3

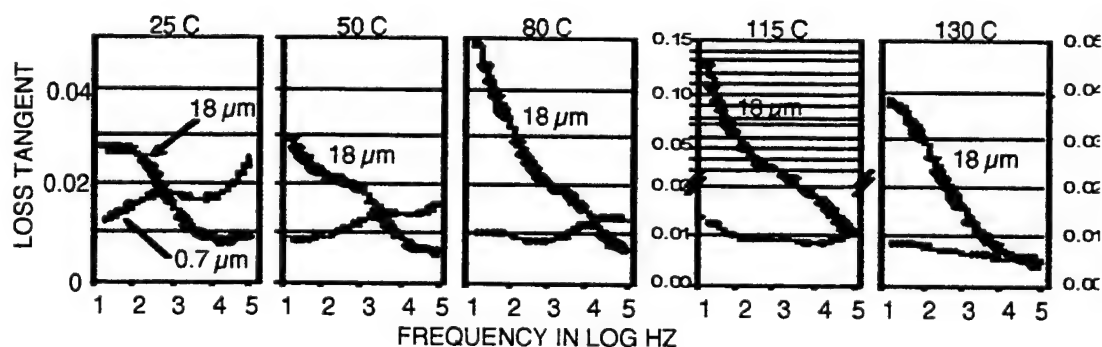


Figure 2

Processing, Characterization and Modeling of BaTiO₃ Glass Ceramics Showing Finite Size Effects.

C.A. Randall, D.L. McCauley, and X. Liu

Materials Research Laboratory
Pennsylvania State University
University Park, Pa 16802 USA

Abstract. BaTiO₃ glass ceramics were fabricated from mixed oxides BaO-Al₂O₃-TiO₂-B₂O₃-SiO₂. Compositions were determined that could nucleate a predominant BaTiO₃ phase and heat treatments found that grew the dispersed crystals from 20 to 80 nm. The size distributions were determined through electron microscopy and x-ray powder diffraction analysis. The phase transition temperature was determined through the dielectric constant temperature dependences. The transition temperature shifts systematically with the mean of the particle size distributions. The shift was compared to the empirical transition temperature relation suggested by Ishikawa et al. to predict a critical size of 17 nm. The data was also analyzed with the Zeks-Tilley phenomenological model where the data showed excellent agreement over the size range and predicts a critical size 12.6 nm for BaTiO₃.

I. INTRODUCTION

The academic question of the stability of ferroelectricity in finite ferroelectric crystals has long been of interest to the community [1-3]. In recent years there has been an enhanced effort to better understand the effect of size with the development of superior processing of powders and thin films. In many of the reports on these materials there are drastic disparities in the data, with critical sizes ranging from 10 nm to 100 nm in BaTiO₃. To avoid experimental problems such as powder agglomeration and difficulties in determining the phase transition temperature a novel glass ceramic study was conducted. A glass-ceramic material is a composite created through controlled crystallization of an appropriate glass composition. The synthesis process involves glass formation through the melting of the initial batch composition, then nucleation and subsequent growth of the crystalline phase is controlled through thermal treatments. Extremely fine crystallites (~10 nm) can be developed with a high nucleation efficiency and limited primary grain growth. It was the objective of this work to use the heat treatments to control nucleation and growth of the BaTiO₃ in a

residual glass matrix and then to study fundamental aspects of the size effect phenomena.

II. EXPERIMENTAL PROCEDURE

The compositional selection for forming BaTiO₃ glass-ceramics was based on the pioneering work of Herczog and his collaborators[4]. Compositions were selected based on the formation of a single BaTiO₃ crystalline phase, small crystallite sizes, crystal morphology and bulk nucleation. Table I summarizes the constituent batch formulations of the glasses. The raw materials were BaCO₃ (99+% purity); SiO₂ (99.5%), Al₂O₃ (99+%), and TiO₂ (99+%), all obtained from Johnson Matthey. The components were mixed with de-ionized water in a 250 ml nalgene bottle and ball milled with zirconia grinding media for 24 hours. After milling, excess water was evaporated in a drying oven at 70°C for 24 hours. The powder was transferred to a 400 cm³ platinum crucible. Using a bottom loaded Deltac furnace preheated to 1550°C and held at temperature for two hours, a homogeneous melt was obtained. The melt was subsequently quenched between two aluminum slabs and immediately placed in an annealing oven at 650°C. Once in the anneal oven, the furnace was turned off and allowed to cool slowly for twelve hours.

All glasses were subjected to differential thermal analysis (DTA) Perkin-Elmer thermal analysis system 1700) to determine annealing ranges and crystallization temperatures. The heating schedule involved ramps up to 1100°C at rates of 5, 10, 15, and 20°C/min. Various temperature and time schedules were tested to establish systematic variations in crystallite sizes. Isothermal heat treatments were made over a temperature range of 700°C to 1000°C and a time range of 5 minutes to 2 weeks. The physical characterization of the glass-ceramic was performed in terms of density variations and phase development. Phases were identified from x-ray diffraction patterns using a Scintag DMC 105 and a Philips APD 3600 diffractometer. Prior to analysis, samples were ground and polished with 400 grit silicon carbide powder slurries to eliminate surface nucleation effects. Scans were recorded from 2θ of 20° to 110° at a scan rate of 2°/min. to determine primary and secondary phases. A detailed analysis of the x-ray diffraction

TABLE I
GLASS BATCHING FORMULATIONS AND SOME GENERAL
OBSERVATIONS OF THE GLASS CERAMIC.

| Oxide | Batch 1. | Batch 2 | Batch 3 | Batch 4 | Batch 5 |
|--------------------------------|----------|----------|-----------|---------|---------|
| BaO | 42.9 | 42.9 | 42.9 | 38.2 | 40.6 |
| TiO ₂ | 35.8 | 35.8 | 35.8 | 31.8 | 33.9 |
| SiO ₂ | 14.2 | 12.2 | 10.2 | 20 | 17 |
| Al ₂ O ₃ | 7.1 | 7.1 | 5.1 | 10 | 8. |
| B ₂ O ₃ | — | 2.0 | 6.0 | — | — |
| Formability | Poor | Moderate | Very poor | Good | Good |
| Second Phase | None | One | One | One | One |
| Surface/Bulk Nucleation | Bulk | Bulk | — | Surface | Surface |

patterns was used to determine variations in lattice strains and coherent crystallite size. Given the pseudocubic nature of submicron BaTiO₃, the Williamson-Hall method was applied to the h00 family. This method permits a separation of line broadening due to both microstrain and crystallite size and is readily applicable to submicron BaTiO₃ ferroelectrics as shown by Leonard and Safari[5].

Microstructural analysis of the crystallite sizes was also determined by imaging etched surfaces. Polished surfaces were etched in a 2.5% hydrofluoric-5% nitric acid mixture for 30 seconds to 2 minutes, depending on the glass content. Field Emission Scanning Electron Microscopy was performed with a JEOL 6300F. Direct measurements of 50-100 crystallites were made from various regions of the sample to establish a statistical description of the size variations. This was necessary to obtain a mean crystallite size and standard deviation. Transmission electron microscopy investigations were performed on ion beam thinned samples on a Philips EM430 TEM.

A Hewlett Packard 4274A multifrequency LCR meter recorded capacitance at three frequencies (1, 10 and 100 kHz) over a temperature range of -150°C to 200°C using a Delta Design 2300 furnace and a liquid nitrogen cooling system. The low capacitance of the BaTiO₃ glass-ceramic samples required a 100x measuring voltage amplifier.

III. RESULTS

Phase Development

It is observed that there exists one crystallization exotherm at a temperature of 730°C in the presented

temperature range. This result is consistent with the evolution of the x-ray diffraction data observed for different isothermal heat treatments over the temperature range 700°C to 1000°C. The major phase is consistent with BaTiO₃, no other phases are detectable with x-ray diffraction. Minor phases of rutile and hexagonal Feldspar were detected in the TEM studies. Batch 1 was used for the detailed study reported here.

Crystallite Sizes

The sizes of the crystals were determined through two methods; 1) Hall-Williamson Analysis and 2) Stereological analysis. Leonard and Safari demonstrated the use of the Hall-Williamson method to separate line broadening contributions from microstrain and coherent crystallite size in submicron BaTiO₃ powders. This approach was also adopted here for the glass ceramics to establish the BaTiO₃ crystal size and an error of the data through the least squares method. A second method was used to obtain histograms of the crystallite sizes. This method measured the dimensions of the particles from SEM images of etched surfaces. The data from these two methods is listed in Table II. Extremely good agreement is found between the two methods in relation to the experimental errors.

Dielectric Properties

Room temperature dielectric properties are dependent on the annealing conditions. The dielectric losses are typically low for all the annealing conditions ranging from $\tan \delta$ 0.004 to 0.006 at kHz. Figure 1 compares the dielectric constant temperature dependences for various annealing conditions. The pure glass has a positive temperature coefficient of capacitance typical for a glass material with low losses in this temperature

TABLE II
CRYSTALLITE SIZE DATA FROM X-RAY AND MICROSCOPY TECHNIQUES

| Sample Processing | Average Size Via X-Ray | Average Size Via SEM |
|-------------------|------------------------|----------------------|
| 1 hrs. 950°C | 20 nm ± 3 nm | 25 nm ± 12 nm |
| 3 hrs. 950°C | 22nm ± 5 nm | 32 nm ± 17nm |
| 10 hrs. 950°C | 40 nm ± 9 nm | 38 nm ± 12 nm |
| 47hrs. 950°C | 51 nm ± 20 nm | 45 nm ± 9 nm |
| 2 weeks. 950°C | 83nm ± 43 nm | 78 nm ± 19 nm |

range. The annealed glasses have a maximum in the dielectric temperature dependence. There is a systematic increase in the magnitude of the temperature maximum and its corresponding dielectric constant with longer annealing times. The maximum temperature profile is associated with the superposition of all the crystals undergoing a phase transition from the paraelectric phase to the ferroelectric phase, the maximum being associated with the median of the crystal size distributions.

IV. MODELING AND DISCUSSION

The electrical and mechanical boundary conditions can have a strong influence on the nature of the paraelectric ferroelectric phase transitions and need to be first considered in relation to this investigation[6-7]. In the case of BaTiO₃ a compressive hydrostatic pressure could lower the transition temperature. A typical derivative change of transition temperature with pressure is quoted as -5.2°C/kilobar for BaTiO₃ crystals. The large shifts in the transition temperature observed here over 100°C cannot be related to a stress phenomena, as the stress levels would exceed typical rupture strengths of glass. The transition of the ferroelectric could be considered to be elastically clamped by the residual glass matrix, and the consequence for this would be a change from a first order to a second order phase transition.

A further consideration in ferroelectric materials is the electric boundary conditions. The spontaneous polarization within the crystal creates a depolarization field that requires compensation at the crystal surface. The boundary condition of the individual ferroelectric crystals is a low loss dielectric glass which cannot supply sufficient charge densities. Therefore depolarization fields have to be compensated from mechanisms other than surface charge. Depolarization fields could be reduced via domain formation or polarization gradients within these crystals. From the TEM data we observe no evidence of a domain structure; therefore, surface polarization gradients are assumed to be required for the onset of the ferroelectric transition.

There have been a number of theoretical studies that have considered the ferroelectric state in finite sized crystals [8]. In this study we compared our data to the one-dimensional phenomenological model of Zeks and

Tilley. Although the geometry of the crystals observed in this study are different from those modeled, the basic physics is applicable. The data from this glass ceramic study is compared to the phenomenological modeling in Figure 2. The locus of the theoretical plot is described through the relation given in equation (1).

$$\tan \left(\frac{L\tau^{1/2}}{2\xi(o)} \right) = \frac{\xi(o)}{\delta\tau^{1/2}} \quad (1)$$

where: L is the crystal diameter,
 τ is the reduced temperature,
 δ is a measure of the gradient,
 and $\xi(o)$ is coherence length at absolute zero.

$$\tau = \left(1 - \frac{T_c}{T_{\infty}} \right) \quad (1a)$$

where: T_c is transition temperature of a finite crystal
 and T_{∞} is transition temperature of infinite (bulk) crystal.

$$\xi^2(T) = \frac{-K}{\alpha_0 (T - T_{\infty})} \quad (1b)$$

where: $\xi(T)$ is Coherence length at any temperature
 K is gradient coefficient
 α_0 = Phenomenological Curie Constant

The critical size is determined with the reduced temperature $T = 1$, equation (2).

$$L_{\text{critical}} = 2\xi(o) \tan^{-1} \left(\frac{\xi(o)}{\delta} \right) \quad (2)$$

The critical size for the BaTiO₃ was determined to be 12.6 nm from this fitting to the Tilley-Zeks model. It is also of importance since the ratio of the gradient coefficient K and the α_0 term in the coherence length relation, equation (3) remains constant for all the crystal sizes of the BaTiO₃ measured in this study. This implies these fundamental constants for BaTiO₃ are independent of size.

$$T_c = T_{\infty} + \frac{\text{constant}}{L - L_{\text{critical}}} \quad (3)$$

An empirical analysis of this data using the scaling relationship developed by Ishikawa et al, equation (4), is shown in Figure 3 [2]. Here our data is contrasted to other data dedicated to size effect studies. The extrapolated critical size for our BaTiO₃ data, 17 nm, is in excellent agreement with the work of Ishikawa

V. SUMMARY AND CONCLUSIONS

A series of glass ceramics were synthesized to produce bulk materials with nanometer BaTiO₃ crystals grown in the residual glass matrix. Structure property relations were made to determine the size distribution of the crystals and the dielectric temperature dependence of the ceramics. The data reveals a systematic variation of the transition temperature with the median crystal sizes. Analysis of this trend with the Tilley-Zeks model predicts a critical size for BaTiO₃ to be 12.6 nm.

VI. ACKNOWLEDGMENTS

We wish to thank Professors R.E. Newnham, L.E. Cross, W. Cao, and T.R. Shroud for many interesting discussions throughout this work. We wish to also thank the National Science Foundation for sponsoring some of this work.

VII. REFERENCES

- (1) M. Anliker, H.R. Brugger, and T. Kanzig, "Behavior of Colloidal Seignette-Electrics: III," *Helv. Phys. Acta* Vol. 27, pp. 99-124 1954.

- (2) K. Ishikawa, K. Yoshikawa, and N. Okada, "Size Effect on the Ferroelectric Phase Transition in PbTiO₃ Ultrafine Particles," *Phys. Rev. B* vol. 37, No. 10, pp. 5852-5855 (1988).
- (3) K. Uchino, E. Sadanaga, and T. Hirose, "Dependence of the Crystal Structure on Particle Size in Barium Titanate," *J. Am. Ceram. Soc.* Vol. 72 [8], pp. 1555-58 (1989).
- (4) A. Herczog, "Microcrystalline BaTiO₃ by Crystallization from Glass," *J. Am. Ceram. Soc.* Vol. 47, No. 3, pp. 107-115 (1964).
- (5) M.R. Leonard and A. Safari, "Crystallite Size Effects on BaTiO₃'s Cubic-Tetragonal Transition Temperature," *Proceedings of the 7th US-Japan Seminar on Dielectric and Piezoelectric Ceramics, Lahaina, Hawaii, 1993*, pp. 235-240, Edited by A.Safari.
- (6) R. Kretschmer and K. Binder, "Surface Effects on Phase Transitions in Ferroelectrics and Dipolar Magnets," *Phys. Rev. B*, Vol. 20, No. 3, pp. 1065-75 (1979).
- (7) K. Binder, "Finite Size Effects on Phase Transitions," *Ferroelectrics*, Vol. 73, pp. 43-67 (1987).
- (8) D.R. Tilley and B. Zeks, *Solid State Communications* Vol. 49, p. 823 (1984).

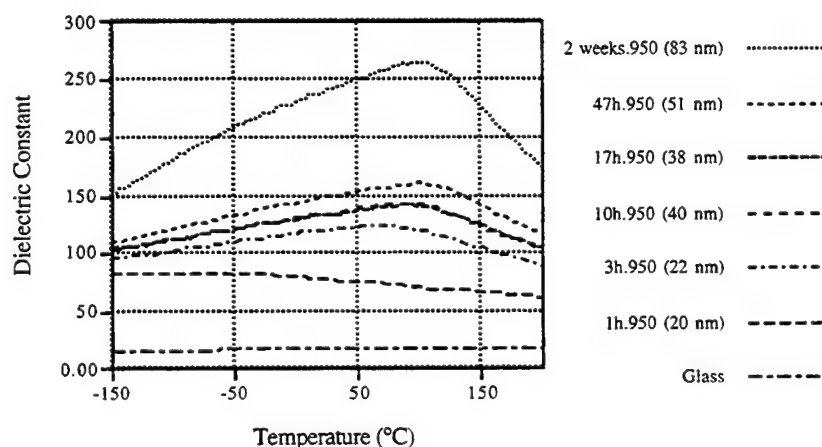


Figure 1: Variation of dielectric response as a function of annealing condition at 1 kHz for a series of glass-ceramics annealed from 1 hour to two weeks.

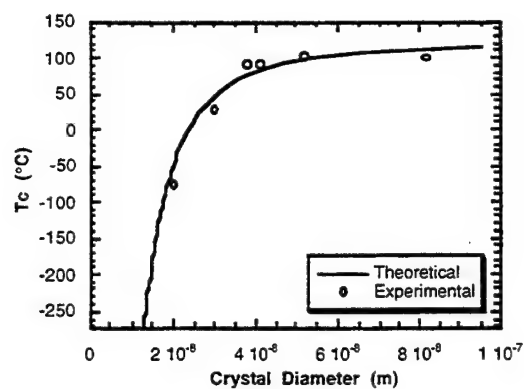


Figure 2: Comparison of T_c shift in BaTiO_3 glass-ceramic system to 1-dimensional phenomenological model

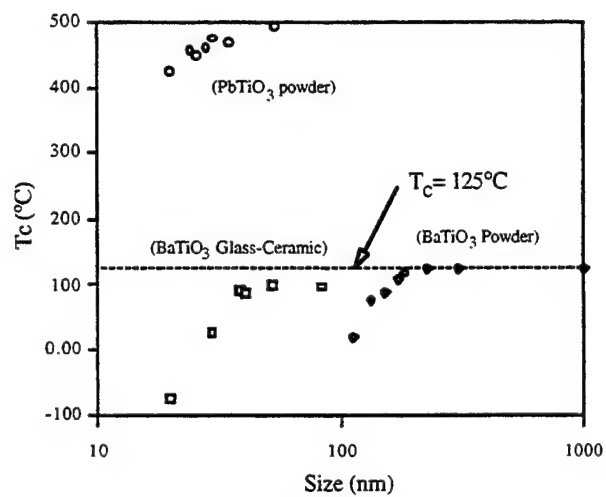


Figure 3: Comparison of T_c shift in BaTiO_3 glass-ceramic system to BaTiO_3 powder³ and PbTiO_3 powder²

Crystal Growth and Characterization of New Piezoelectric Materials: Langasite and its Related Compounds

Tsuguo FUKUDA, Kiyoshi SHIMAMURA, Hiroaki TAKEDA
Institute for Materials Research, Tohoku University, 980-77, Japan

We have successfully grown new piezoelectric single crystals, $\text{La}_3\text{Nb}_{0.5}\text{Ga}_{5.5}\text{O}_{14}$ and $\text{La}_3\text{Ta}_{0.5}\text{Ga}_{5.5}\text{O}_{14}$ comparable to $\text{La}_3\text{Ga}_5\text{SiO}_{14}$, by the Czochralski technique. The piezoelectric and device properties of grown crystals were investigated. New langasite-type materials search was also performed.

1. Introduction

Recent progress of electronic technology requires new piezoelectric crystals with high thermal stability of frequency and large electromechanical coupling factors. For designing devices such as filters with a wide pass band while maintaining high stabilities and small insertion attenuation, the necessity has arisen in discovering new piezoelectric crystals having intermediate properties between those of quartz and LiTaO_3 (LT). $\text{La}_3\text{Ga}_5\text{SiO}_{14}$ (langasite, LGS) has been reported as a leading candidate to satisfy those requirements [1]. Recently, we have developed $\text{La}_3\text{Nb}_{0.5}\text{Ga}_{5.5}\text{O}_{14}$ (LNG) and $\text{La}_3\text{Ta}_{0.5}\text{Ga}_{5.5}\text{O}_{14}$ (LTG) single crystals, which showed superior piezoelectric properties than those of LGS.

In this paper, the growth of LNG and LTG single crystals by the Czochralski (Cz) method was demonstrated, as compared with that of LGS. The uniformity and congruency of these crystals were investigated. Piezoelectric and device properties were also reported. A series of new langasite-type crystals were developed by equivalent or aliovalent substitutions.

2. Experimental Procedure

Single crystals were grown by a conventional RF-heating Cz technique with a Pt crucible (50mm in diameter and height) or an Ir crucible (100mm in diameter and height). Starting materials were prepared by mixing 99.99% pure oxide powders. The growth atmosphere was either air or a mixture of Ar plus 1 or 2 vol% O_2 gasses, in order to avoid the evaporation of gallium suboxide from melt during growth. The phase identification of grown crystals was performed by the X-ray powder diffraction method. Chemical composition of the grown crystals was measured by the quantitative X-ray fluorescent analysis.

For characterization of piezoelectric properties, we actually made resonators and filters. Wafer-like samples ($9 \times 9 \times 1$ mm) were cut from grown crystals perpendicular to X axis, which corresponds to [100] crystallographic direction. Cut samples were polished, and thereafter the aluminum electrodes were deposited by the vacuum evaporation technique. Using filters and resonators, electromechanical coupling factors were measured by the resonance method. Other piezoelectric characteristics such as

piezoelectric strain constants and elastic stiffness moduli, were also determined. The distribution of LSAW velocity was examined in order to investigate the homogeneity of grown crystals.

The langasite phase formation was studied in various mixtures by the solid state reaction technique. Single phase polycrystals prepared were used as starting materials for the growth of fiber form micro crystals by the micro-pulling-down (μ -PD) method [2], which is convenient to know whether single crystals of the material can be grown by the Cz technique or not. Growth of micro crystals was performed at the pulling down rate of 1.2-6 mm/h in air, by the use of Pt or Pt/Rh crucibles with a nozzle (0.8-1.0 mm in diameter).

3. Results and Discussion

3.1. Crystal growth

High quality LNG and LTG single crystals with 1 or 2 inches in diameter comparable to LGS [1], were grown by the Cz technique. Fig. 1 shows a typical as-grown LTG single crystal with approximately 50mm in diameter and 130mm in length. These crystals were pulled at the rate of 1mm/h with crystal rotation rate of 10 rpm by using an Ir crucible under Ar plus 1 vol% O₂ gas

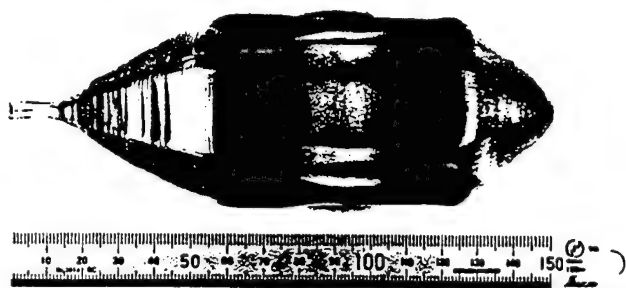


Fig.1 2-inch size as-grown LGS single crystal.

mixture atmosphere. No cracks and no inclusions

were observed inside a crystal under microscopic observation. Grown crystals had an orange color,

and were transparent and optically homogeneous. Results of the phase identification showed that grown crystals consisted of the only langasite-type single phase. No distinct differences were observed on the growth results when Pt crucible was used. Compared with crystals grown in air and those under Ar plus 1 vol% O₂ gas mixture atmosphere (Fig. 1), the former had a deeper orange color than the latter. This shading of color was supposed to be caused by the vacancy concentration dependent on the amount of oxygen in the growth atmosphere.

Lattice parameters of grown crystals were found to keep almost constant values of $a=8.234\pm0.001\text{\AA}$ and $c=5.129\pm0.001\text{\AA}$ (LNG), $a=8.235\pm0.001\text{\AA}$ and $c=5.128\pm0.001\text{\AA}$ (LTG) from shoulder to tail part of boules.

This fact was the same as that of the case of LGS; $a = 8.172\pm0.001\text{\AA}$ and $c=5.102\pm0.001\text{\AA}$. Concentrations of

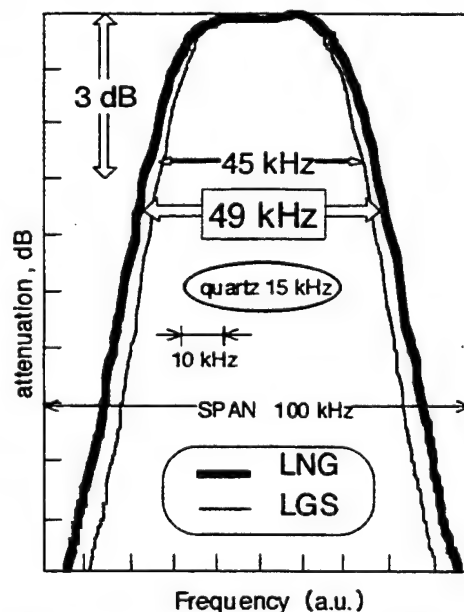


Fig.2 The pass band characteristics of LNG and LGS filters, compared with that of quartz.

each oxide such as La_2O_3 , Ga_2O_3 , Nb_2O_5 and Ta_2O_5 , were almost constant within the estimated errors through the crystallizing process. The uniformity of lattice parameter and chemical composition suggest that the stoichiometric composition is close to the congruently melting composition of LNG and LTG. This well agrees with results that many cracks and inclusions were involved in grown crystals when starting melt composition varied from stoichiometric one.

3.2. Piezoelectric properties

Fig. 2 shows the pass band characteristic of LNG and LGS filters, compared with that of quartz. The pass band widths of LNG and LGS filters were three times wider than that of quartz, and LNG showed slightly wider one than that of LGS. This indicates that the value of electromechanical coupling factors of LNG and LGS is three times as large as that of quartz, and that of LNG is slightly larger than that of LGS.

Physical constants of LNG, LTG and LGS are listed in Table. 1. It shows that elastic constants of these crystals are almost same but dielectric constants, ϵ_{33} , of LNG and LTG are considerably larger than those of LGS, and piezoelectric constants, d_{ij} , of LTG are relatively larger than the other ones. This indicates that piezoelectric

Table.1 Full sets of LNG and LTG physical constants c_{ij} , d_{ij} and ϵ_{ij} in comparison with those of LGS.

| | LGS | LNG | LTG |
|---|-------|-------|-------|
| Elastic constants [$\times 10^{10}$ N/m ²] | | | |
| c_{11} | 19.09 | 18.87 | 19.2 |
| c_{12} | 10.63 | 10.86 | 10.8 |
| c_{13} | 10.42 | 10.23 | 9.87 |
| c_{14} | 1.52 | 1.099 | -1.3 |
| c_{33} | 26.19 | 25.9 | 26.4 |
| c_{44} | 5.24 | 4.857 | 5.1 |
| Piezoelectric d -constants [$\times 10^{-12}$ C/N] | | | |
| d_{11} | -6.16 | -6.63 | -9.49 |
| d_{14} | 5.36 | 5.55 | 5.35 |
| Dielectric constants | | | |
| ϵ_{11} | 18.99 | 20.3 | 19.97 |
| ϵ_{33} | 49.3 | 79.3 | 78.42 |

Table.2 Characteristics of LNG, LTG and LGS compared with those of LT and quartz.

| | LiTaO ₃ | LGS | LNG | LTG | quartz |
|---|--------------------|---------------|---------------|---------------|---------------|
| phase transition | exist | none | none | none | exist |
| melting point (°C) | 1650 | 1490 | 1470 | 1500 | — |
| hardness | 5.5 | 6~7 | 6~7 | 6~7 | 7 |
| electromechanical coupling factor k (%) | 43 | 15~25 | ~30 | ~30 | 7 |
| Q-factor | 5000 | 30,000~40,000 | 40,000~60,000 | 40,000~60,000 | 60,000~80,000 |
| equivalent series resistance (Ω) | — | 5~10 | 2~5 | 2~5 | 10~20 |
| thermal stability (ppm) (20~70 °C) | 200~400 | ~150 | ~150 | ~150 | 10~20 |

properties of LTG crystal are better than those of LNG and LGS.

In Table.2, characteristics of LNG, LTG and LGS are given as compared with those of LT and quartz. Since LNG, LTG and LGS have no phase transitions from melting temperature to room temperature and they have lower melting temperature and higher hardness than those of LT and quartz, their possibility of growing high quality and of easy processing is expected to be high. The additional characters that they are not ferroelectric, that is, poling procedure is not required, and not easily soluble in any acids and bases, also help above possibility. Their electromechanical coupling factors k and thermal stability of frequency locate between those of LT and quartz. Mentioned above characteristics show that LGS family crystals are promising materials for piezoelectric devices than lithium tetraborate ($\text{Li}_2\text{B}_4\text{O}_7$) and berlinite ($\alpha\text{-AlPO}_4$) single crystals, which have similar piezoelectric properties[3]. $\text{Li}_2\text{B}_4\text{O}_7$ single crystal is easily soluble in all acids and bases, and easily deliquescent in air. The large size of $\alpha\text{-AlPO}_4$ single crystal is difficult to grow.

When the distribution of LSAW velocity of LNG was measured along the growth axis, the deviation of it was small (± 0.18 m/s). This result also well agrees with the congruency of crystals mentioned above.

3.3. New materials search

New materials search with langasite-type structure, has been carried out by solid state reaction. Materials which showed langasite-type single phase, were crystallized in fiber form by the μ -PD method, subsequently their single crystals were also grown by the Cz technique. $\text{Sr}_3\text{Ga}_2\text{Ge}_4\text{O}_{14}$, $\text{Na}_2\text{CaGe}_6\text{O}_{14}$, $\text{Na}_2\text{SrGe}_6\text{O}_{14}$ and $\text{La}_3\text{Al}_x\text{Ga}_{5-x}\text{SiO}_{14}$ were found to be new candidates for piezoelectric applications. Fig.3 shows a typical grown $\text{La}_3\text{Al}_x\text{Ga}_{5-x}\text{SiO}_{14}$ single crystal. $\text{Sr}_3\text{Ga}_2\text{Ge}_4\text{O}_{14}$ showed three times larger electromechanical coupling factor than that of LGS.

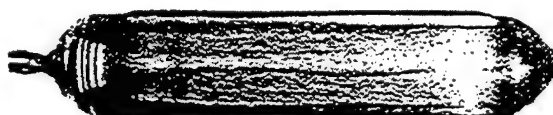


Fig.3 As grown $\text{La}_3\text{Al}_{0.9}\text{Ga}_{4.1}\text{SiO}_{14}$ single crystal.

4. Summary

LNG and LTG single crystals comparable to LGS, with the maximum size of 2 inches in diameter, were successfully grown by the Cz technique. LNG and LTG single crystals as well as LGS were shown to be superior materials than the other compounds such as $\text{Li}_2\text{B}_4\text{O}_7$ or $\alpha\text{-AlPO}_4$. A series of new promising langasite-type materials was also found.

References

- [1] K.Shimamura, H.Takeda, T.Kohno and T.Fukuda, J. Crystal Growth 163(1996)388.
- [2] D-H.Yoon, I.Yonenaga, T.Fukuda and N.Ohnishi, J. Crystal Growth 142(1994)339.
- [3] J.Détaint, J.Schwartzel, A.Zarka, B.Capelle, J.P.Denis and E.Philippot, 1994 IEEE International frequency control symposium, p.58.

Growth and Properties of Tungsten-Bronze Ferroelectric Potassium Lithium Niobate (KLN) Single Crystals

Zhiming Chen, Kenya Miyashita, Masatoshi Adachi and Akira Kawabata
Department of Electronics and Informatics,
Faculty of Engineering, Toyama Prefectural University
Kosugi-machi, Toyama 939-03, Japan

Abstract—Potassium lithium niobate (KLN) single crystals were grown using the rf-heating Czochralski technique from a melt with potassium and lithium enriched composition. A crystal with composition of $0.315\text{K}_2\text{O}-0.15\text{Li}_2\text{O}-0.535\text{Nb}_2\text{O}_5$ was grown from melt of $0.348\text{K}_2\text{O}-0.178\text{Li}_2\text{O}-0.465\text{Nb}_2\text{O}_5$. The transparent crystal is pale-yellow with the absorption edge at 376nm and very small optical absorption (1cm^{-1} at 400nm, 0.5cm^{-1} at 410nm, and less than 0.3cm^{-1} in 420-800nm region). The sample shows the Curie temperature $T_c=436^\circ\text{C}$, and electrooptic coefficients $r_{33}=66 \pm 5\text{pm/V}$, $r_{13}=8 \pm 2\text{pm/V}$, $r_{42}=87 \pm 5\text{pm/V}$ at a wavelength of 632.8nm.

I. INTRODUCTION

Among various ferroelectric materials, many ferroelectric niobates having tungsten-bronze structure with the general chemical formula $(A_1)_4(A_2)_2C_4(B_1)_2(B_2)_8O_{30}$, have attracted much attention due to their potential applications in electrooptic, nonlinear optic and piezoelectric devices.[1-8] $\text{K}_3\text{Li}_2\text{Nb}_5\text{O}_{15}$ (KLN) single crystals belonging the tungsten-bronze type are recently expected to be a superior material for blue second harmonic generation (SHG), because of their advantages in high damage resistance, low losses, and wide phase matching characteristics at room temperature.

The phase equilibrium study of the $\text{K}_2\text{O}-\text{Li}_2\text{O}-\text{Nb}_2\text{O}_5$ ternary system has been carried out by Scott *et al.* and Ikeda *et al.*[9,10] Crystal growth of the KLN has been successfully attempted by various methods.[3-13] However, the KLN crystals were pale yellow with large optical absorption in the region of 400-500 nm, which limits the usability of these crystals for high power blue SHG applications.

TABLE I Properties of KLN crystals grown in this work.

| | Sample A | Sample B |
|-----------------------|---|---|
| Melt composition | 0.342/0.175/0.483 | 0.348/0.178/0.465 |
| Crystal composition | 0.310/0.140/0.550 | 0.315/0.150/0.535 |
| Curie temperature | 370°C | 436°C |
| Lattice constant | a=12.5Å c=3.97Å | |
| Dielectric constant | $\epsilon_{33}=145$ | $\epsilon_{33}=86$ |
| Electrooptic constant | $r_{13}<2\text{pm/V}$ $r_{33}=35 \pm 5\text{pm/V}$ | $r_{13}=8 \pm 2\text{pm/V}$ $r_{33}=66 \pm 5\text{pm/V}$ $r_{42}=87 \pm 5\text{pm/V}$ |
| Absorption edge | 376nm | 376nm |
| Absorption at 400nm | 2.4cm^{-1} | 1.0cm^{-1} |
| at 420nm | 0.8cm^{-1} | 0.3cm^{-1} |
| at 450nm | 0.4cm^{-1} | 0.3cm^{-1} |

In this paper, the growth of the KLN crystals using the Czochralski method from different composition melt, and the optical properties the crystals are reported.

II. CRYSTAL GROWTH

The starting materials used in this work were K_2CO_3 of 99% purity, Li_2CO_3 of 99.99% purity, and Nb_2O_5 of 99.99%. The oxide mixture, weighing about 340 g (about 300 g of KLN) with the composition listed in Table I, was charged into a $\phi 50 \times 50\text{mm}$ Zr-reinforced platinum crucible and was melted by a rf-heating equipment. A platinum after-heater was employed to reduce thermal gradient above the melt surface. Seeding temperature was about 1050°C . The growth along the $\langle 001 \rangle$ direction always induced

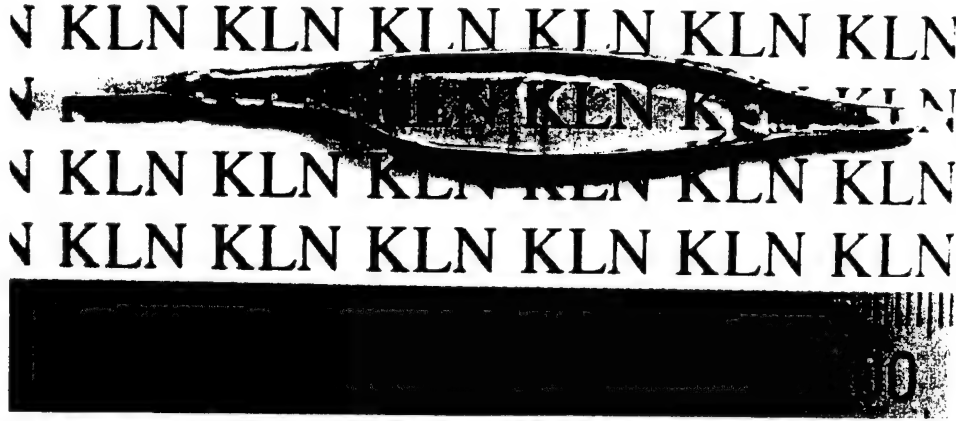


Fig. 1. Photograph of crystal B.

macrocrack formation, the faces of which crack were vertical to the $\langle 001 \rangle$ axis. It could be explained that the crystal is grown from incongruent melt, and the temperature changes a little when the auto-diameter-control system works. Therefore, the growth direction was chosen in the $\langle 110 \rangle$ direction in our work to minimize the cracking. The growth rate was 3mm/h.

For the growth of crystal A, a $\text{K}_2\text{BiNb}_5\text{O}_{15}$ (KBN) crystal was used as seed material. The KBN has the tungsten-bronze structure and its melting point is higher by about 250°C than that of KLN. Because of a little mismatching in the crystal lattice, it should be careful to grow slowly after necking down in order to prevent the crack formed from the seed.

The crystal B was grown using a KLN seed. A well-grown crystal is shown in Fig. 1. One of other key points in the growth is to whittle down the crystal end before moving the boule from the melt (see Fig. 1). Otherwise, a drop of the melt remains on the bottom face, and crack forms from the interface during cooling down.

Since the crystal is grown from potassium and lithium enriched incongruent melt, wide temperature change and fast growth would cause anomalous solidification leading to a loose polycrystalline lump.

The crystals grown along $\langle 110 \rangle$ are generally prismatic with clearly defined faces such as (001) and (110). The longer lateral direction presents the $\langle 001 \rangle$ axis. To prepare samples for measurement, the crystal was X-ray-oriented and cut off. The samples were poled the field cooling method under a DC current of about $1\text{-}2\text{mA}/\text{cm}^2$ from temperature of 500°C to 300°C along the $\langle 001 \rangle$ axis.

III. RESULTS AND DISCUSSION

The Fresnel reflectivity and optical transmittance were measured using a c -cut plate. The transmittance of the crystal B is shown in Fig. 2. The transparent crystal is pale-yellow with the absorption edge at 376nm and has very small optical absorption. The crystal A has the optical absorption coefficient of 2.4cm^{-1} at 400nm , 1.2cm^{-1} at 410nm , 0.78cm^{-1} at 420nm , 0.6cm^{-1} at 430nm , 0.47cm^{-1} at 440nm , 0.4cm^{-1} at 450nm , and less than 0.3cm^{-1} in $480\text{-}800\text{nm}$ region. The crystal B shows the optical absorption coefficient of 1cm^{-1} at 400nm , 0.5cm^{-1} at 410nm , and less than 0.3cm^{-1} in $420\text{-}800\text{nm}$ region. The low absorption make the crystal B possible to the use of blue SHG.

Electrooptic constants of the KLN crystal were measured using a Mach-Zehnder interferometer. The KLN has tetragonal $4mm$ symmetry, and there are three independent coefficients r_{33} , $r_{13}=r_{23}$ and $r_{42}=r_{51}$. By introducing light propagating in the x_2 direction with polarization along the x_3 and x_1 directions, we can easily measure r_{33} and r_{13} when an external electrical field is applied in the x_3 direction of the sample. Changes in the field-induced indices are

$$\Delta n_3 = -\frac{1}{2}n_e^3 \left[r_{33} - \frac{2(n_e - 1)}{n_e^3} d_{31} \right] E_3,$$

$$\Delta n_1 = -\frac{1}{2}n_o^3 \left[r_{13} - \frac{2(n_o - 1)}{n_o^3} d_{31} \right] E_3,$$

where n_e and n_o are respectively extraordinary and

ordinary refractive indices, and d_{31} the piezoelectric strain coefficient. For measurement of r_{42} , because the index ellipsoid in this case is rotated by a small angle, the conventional method involves applying a field along the x_2 direction and propagating light in the x_2x_3 plane at 45° to the x_2 axis, as shown in Fig. 3(a). The disadvantage of this method is that two corners of the sample must be cut off. In our experiment, an extraordinary polarized light was introduced through a cuboid sample at the Brewster incident angle α_B , as shown in Fig. 3(b). Thus sample preparation is facilitated. When E_2 field is applied in the x_2 direction, the change in field-induced index becomes

$$\Delta n = -\frac{\sin \alpha \cos \alpha r_{42} E_2}{(\cos^2 \alpha / n_o^2 + \sin^2 \alpha / n_e^2)^{3/2}},$$

where α is equal to $90^\circ - \alpha_B$. Another obvious advantage is that the Brewster angle α_B can be determined by rotating the θ -stage on which the sample is fixed, because Fresnel reflection is lowest in this direction. The crystal A has values of $r_{33} = (35 \pm 5)$ pm/V and $r_{13} < 2$ pm/V, and the crystal B shows values of $r_{42} = (87 \pm 5)$ pm/V, $r_{33} = (66 \pm 5)$ pm/V and $r_{13} = (8 \pm 2)$ pm/V, respectively, at a wavelength of 632.8 nm.

The SHG measurement is now carried out. The results will be reported in the seminar.

REFERENCES

- [1] W. W. Ho, W. F. Hall, and R. R. Neurgaonkar, *Ferroelectrics*, vol. 50, p.325, 1983.
- [2] T. Yamada, *J. Appl. Phys.*, vol. 46, p.2894, 1975.
- [3] L. G. Van Uitert, S. Singh, H. J. Levinstein, J. E. Geusic, and W. A. Bonner, *Appl. Phys. Letters*, vol. 11, p.161, 1967.
- [4] M. Adachi and A. Kawabata, *Jpn. J. Appl. Phys.*, vol. 17, p.1969, 1978.
- [5] R. R. Neurgaonkar, W. K. Cory, J. R. Oliver, and L. E. Cross, *Mat. Res. Bull.*, vol. 24, p.1025, 1989.
- [6] J. J. E. Reid, *Appl. Phys. Letters*, vol. 62, p.19, 1993.
- [7] Y. Furukawa, S. Makio, T. Miyai, and M. Sato, *Appl. Phys. Letters*, vol. 68, p.744, 1996.
- [8] Z. Chen, M. Tago, M. Adachi, and A. Kawabata, *Ferroelectrics*, vol. 196, p.265, 1997.
- [9] A. Scott, E. A. Giess, B. L. Olson, G. Burns, A. W. Smith, and D. F. O'Kane, *Mat. Res. Bull.*, vol. 5, p.47, 1970.
- [10] T. Nagai and T. Ikeda, *Jpn. J. Appl. Phys.*, vol. 12, p.199, 1973.
- [11] T. Fukuda, H. Hirano, and S. Koida, *J. Crystal Growth*, vol. 6, p.293, 1970.
- [12] S. C. Abrahams, P. B. Jamieson, and J. L. Bernstein, *J. Chem. Phys.*, vol. 54, p.2355, 1971.

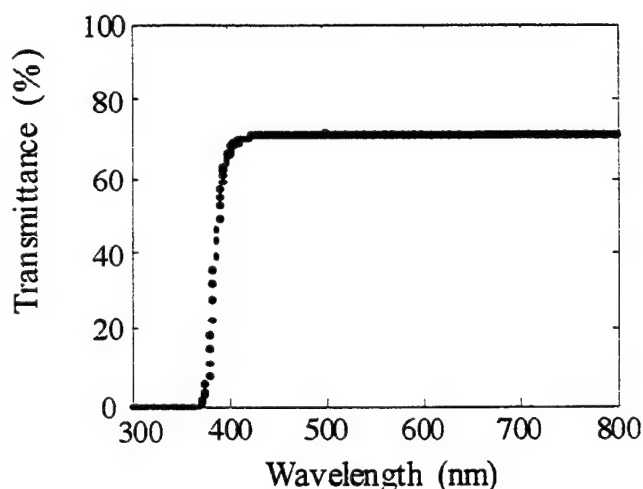


Fig. 2. Transmittance of KLN crystal B for 0.71mm-thickness sample.

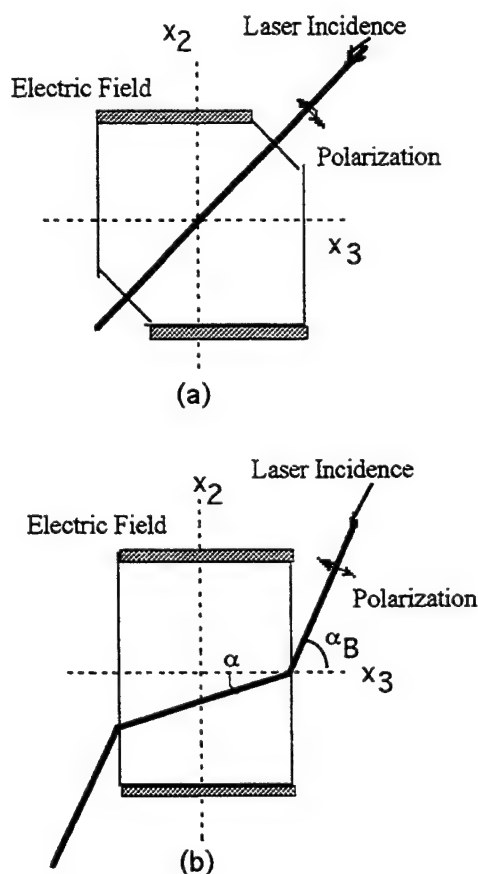


Fig. 3. Schematic arrangement for measuring r_{42} . (a)conventional method; (b) method used in this work.

- [13] D. H. Yoon, M. Hashimoto, and T. Fukuda, *Jpn. J. Appl. Phys.*, vol. 33, p.3510, 1994.

Growth and Characterization of KLN fiber Crystals by μ -PD method

Masakuni Takahashi, Ryuichi Komatsu and Satoshi Uda
Central Research Institute, Mitsubishi Materials Corporation
1-297 Kitabukuro-cho, Omiya, Saitama 330, Japan

Abstract

Potassium lithium niobate $K_{6-x-y}Li_{4+x}Nb_{10+y}O_{30}$ (KLN) is attractive as a nonlinear optical material. We have studied the growth of KLN crystal by μ -PD (micro-Pulling Down) method[1]. We examined the local change of chemical composition of KLN fiber single crystal by using KLN bulk single crystal as a standard sample for EPMA (Electron Probe Micro Analysis). As-grown KLN fiber crystal was light yellow color and was the diameter of 200-1000 μ m and length of 150mm. Cross section showed rectangular crystal habit. The results of EPMA were that the constitutional dispersion in growth direction of KLN fiber single crystal was about 2% by point-by-point and did not detect localization of the element by mapping.

1. Introduction

Potassium lithium niobate that belongs to the point group 4mm is a ferroelectric material with the tungsten bronze structure[2]. This crystal is attractive as a nonlinear optical material because KLN has large damage threshold as compared with $KNbO_3$ and the non-critical phase matching wavelength at room temperature also can change according to its composition. However it is difficult to grow the high quality KLN single crystal from the melt because of the incongruent melting, the wide solid solution range and more cleavage. In particular to use it as an optical material, it needs to suppress the composition change in grown KLN single crystal. The μ -PD method which pulls fiber crystal down through μ -nozzle from the melt is possible to solve these problems. We have been studying to produce high quality KLN fiber crystals by μ -PD method.

In this paper, we try to grow the KLN fiber crystal by μ -PD method and examine the local composition change of grown KLN fiber crystal.

2. Experimental Procedure

2-1. Crystal growth by μ -PD method

KLN crystal was grown by μ -PD (Pulling Down) method (Fig.1). The raw materials were reagent grade K_2CO_3 , Li_2CO_3 and Nb_2O_5 with 99.99% purity, and

calcined after mixing. The chemical composition of the starting materials is 33mole%K₂O-23mole%Li₂O-44mole%Nb₂O₅[5]. The growth direction is parallel to [110] and growth rate is 2.4mm/hour (Table.1). SHG wavelength conversion range of growth KLN crystal is measured by using OPO and Ti : sapphire pulse laser.

2-2. Composition change in KLN fiber crystal

The content of the element in KLN fiber single crystal was examined by EPMA point-by-point and mapping. It is difficult to examine local chemical composition of KLN fiber crystal by EPMA because KLN includes K and Li elements. To reveal accurately the change of composition, we grew large KLN bulk single crystal and used it as a standard sample for EPMA. KLN bulk crystal was grown by TSSG method. The chemical composition of starting materials was 35mole%K₂O-17.3mole%Li₂O-47.7mole%Nb₂O₅ [6]. Grown KLN bulk crystal was 20×15×40mm and included cracking parallel to (001) and (110) plane due to cleavage. Crack-free part in this crystal (3×3×3mm) was examined by ICP-MS and was used as a standard sample for EPMA. The result of ICP-MS was about K, Li, Nb, O respectively 13.2, 1.25, 55.9, 29.65wt%. The longitudinal plane of KLN fiber crystals (about 700×500 μm, 22mm) for EPMA were polished. The content of K, Nb, O in growth direction was measured by point-by-point and distribution of element in narrow area was also examined by mapping. Measurement conditions of EPMA were as following ; for point-by-point analysis measurement interval was every 500 μm from 0mm to 22mm and impressed voltage was 15KV (5×10⁻⁸A) and probe diameter was φ 30 μm, for mapping analysis examination area was 700×700 μm and measurement scanning interval was every 20 μm and impressed voltage was 15KV (5×10⁻⁸A) and probe diameter was φ 30 μm (Table.2).

3. Result and Discussion

As-grown KLN fiber crystal was light yellow color and was the diameter of 200-1000 μm and length of 150mm. Cross section showed rectangular crystal habit (Fig.2). The result of EPMA point-by-point of KLN fiber crystal was shown in Fig.3. The content change (standard deviation) of K, Nb and O in growth direction were respectively 0.19wt%, 0.42wt% and 1.02wt% and fluctuation ratio (standard deviation / average percentage) were respectively 1.68%, 2.07% and 1.59%. Assuming that the rest of measured elements is the content of Li, calculated fluctuation ratio of Li is 39.97%. This result largely differed with fluctuation ratio of others because Li is light metal and sensitive to fluctuation of others. The result of EPMA mapping of KLN fiber crystal was shown in Fig.4. In those mapping image localization of the element was not detected in the area of 700×700 μm. Fluctuation ratio of K, Nb and O was regarded as about 2%.

But the calculated fluctuation ratio of Li on point-by-point is not reliable because fluctuation ratio of Li is too much large as compared with fluctuation ratio of others. Using point-by-point and mapping of EPMA in this examination, fluctuation ratio of Li could not be detected.

SHG wavelength conversion range of growth KLN fiber crystal was measured by using OPO and Ti : sapphire pulse laser and its SHG wave conversion range could be 750~1100nm.

4. Conclusions

Fluctuation ratio of K, Nb and O in KLN fiber crystal with 22mm length by EPMA point-by-point was regarded as about 2% and on EPMA mapping image localization of the element was not detected in the area of $700 \times 700 \mu\text{m}$. In spite of the use of standard sample for EPMA, fluctuation ratio of Li could not be estimated. SHG wavelength conversion range of growth KLN fiber crystal was 750 to 1100nm.

References

- [1] N. Ohnishi : ETL News Issue. MITI Japan 552 (1993)
- [2] S.C. Abrahams, P.B. Jamieson and J.L. Bernstein :
J.Chem.Phys. Vol.54, 2355-2364 (1971)
- [3] J.J.E. Reid, M. Ouwerkerk and L.J.A.M. Beckers : Philips J.Res, 46, 199-213 (1992)
- [4] B.A. Scott, E.A. Giess, B.L. Olson, G. Burns, A.W. Smith, D.F. O'Kane :
Mat.Res.Bull. Vol.5, 47-56 (1970)
- [5] N. Ohnishi, M. Yoshimura, T. Obana, Y. Mori, T. Sasaki : Extended Abstracts (The 55th Autumn Meeting 1994 J.S.A.P and Related Societies) 1, 217
- [6] R.R. Neurgaonkar, W.K. Cory, J.R. Oliver, L. Eric Cross :
Mat.Res.Bull., Vol.24, 1025-1030 (1989)

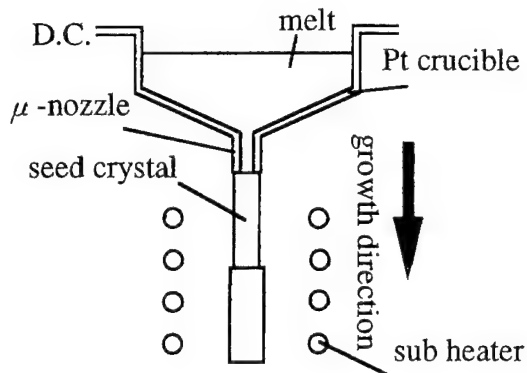


Fig.1 μ -PD crystal growth method

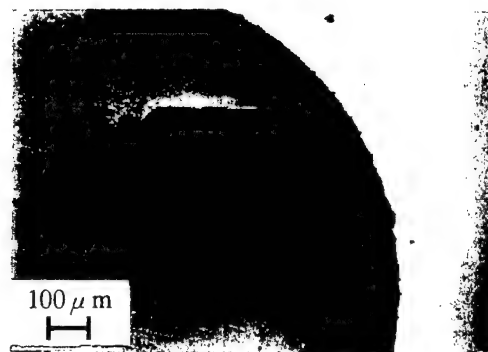


Fig.2 Cross section of KLN fiber crystal

Table .1 Growth condition with μ -PD method of fiber like crystal

| | |
|--------------------|--|
| melt composition; | 33mole%K 2O-23mole% Li 2O-44mole%Nb 2O5 |
| atmosphere; | nomal air |
| growth direction; | <110> |
| pulling down rate; | 2.4mm/hour |

Table .2 Measurement condition of EPMA

| | point-by-point | mapping |
|---|------------------------------------|------------------------------|
| standard sample ; (KLN bulk crystal) | wt% K:Li:Nb:O=13.2:1.25:55.9:29.65 | |
| voltage ; | 15.0KV (5×10^{-8} A) | |
| probe diameter ; | $\phi 30 \mu\text{m}$ | $\phi 20 \mu\text{m}$ |
| measurement dimension ; | 22mm | $700 \times 700 \mu\text{m}$ |

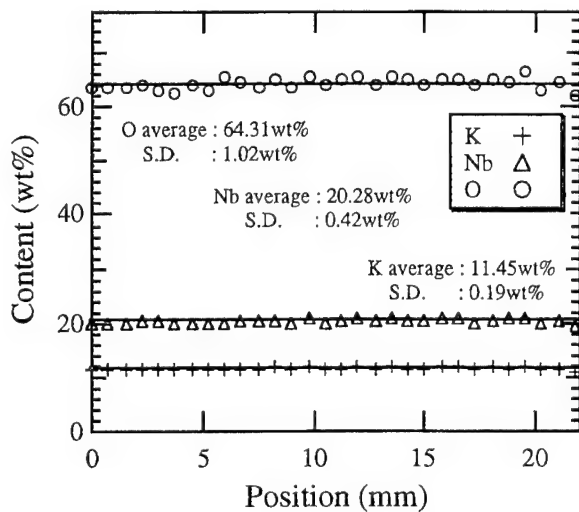


Fig.3 Constitutional dispersion along growth direction in KLN fiber crystal

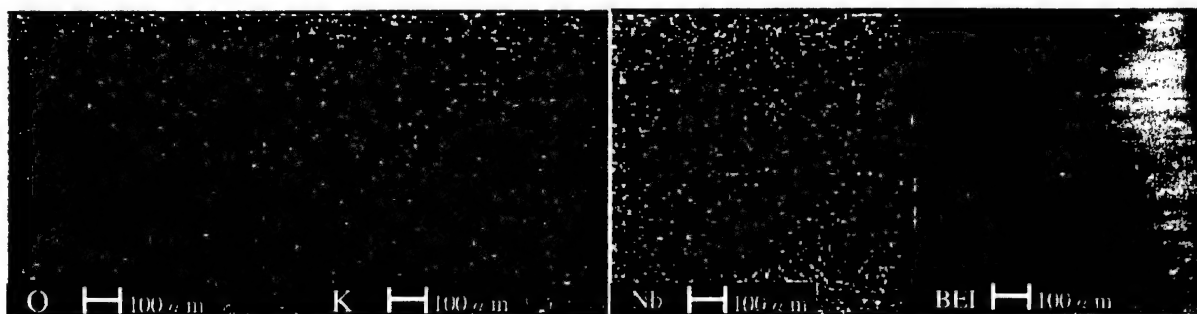


Fig.4 EPMA mapping image in narrow area of longitudinal section of KLN fiber crystal

Effect of Calcium Zirconate Addition to Ca Doped LaMnO_3 Ceramics

Kazunobu Abe and Jiaan Ren Zen
Research Center
Sakai Chemical Industry Co. Ltd.
5-1 Ebisujima, Sakai, Osaka 590, Japan

Abstract: Effect of calcium zirconate (CZ) addition to Ca doped LaMnO_3 (LCM) ceramics was investigated in order to improve its thermal stability at high temperature. As the result, shrinkage of the LCM modified by 5-10 mol% of calcium zirconate was decreased to 1/2-1/3. But 10-20% reduction of electro-conductivity took place.

I. Introduction

Solid oxide fuel cell (SOFC) is an attractive electric power source generator for high energy conversion efficiency, low pollutant emission and variety of fuel. LCM is one of the strong candidates for cathode material of the SOFC for the reason that heat expansion coefficient of them is same as Y stabilized zirconia which is solid state electrolyte. LCM works as a O^{2-} ion conductor. SOFC is usually operated at around 1000 °C. Much better stability at high temperature, therefore, is necessary. A method of improving heat stability of LCM and LSM is described in this paper.

II. Experimental Procedure

Experiments were carried out as follows;

1) Preparation of LCM:

20 % of La in lanthanum manganite was substituted by Ca. High pure grade of La_2O_3 , CaCO_3 , and MnCO_3 were stoichiometrically weighed and mixed in a ball mill for one night. After milling, the slurry was dried by spray-dryer and calcined in the MgO crucible at 1500 °C for 2 hrs. Calcined materials was milled with wet disk mill into 10 microns.

2) Preparation of CZ:

CaCO_3 and ZrO_2 were mixed as same as the method described above. Then, the mixture was calcined at 1200 °C for 2 hrs. and wet-milled into around 1 micron.

3) Fabrication of ceramics:

LCM powder was mixed with zirconate in a wet ball mill for one hour and dried. 100 weight parts of the mixture and 10 part of 8% PVA solution were mixed in a mortar and sieved to under 35 mesh. The obtained granular was pressed in a die under 1000 kg/cm^2 into $5 \times 5 \times 50$ (mm). Then, they were fired at 1500-1600 °C for 2 hours in the air to be about 30 % of open pore.

4) Thermal stability test:

Each sintered samples were treated in a furnace at 1400 °C for 2 hours.

5) Measurement of shrinkage:

Shrinkage was calculated by the ratio of their length before and after heat treatment.

6) Measurement of porosity:

Open porosity was measured by Archimedes method.

7) Measurement of electro-conductivity:

Electro-conductivity was measured by 4 terminal pair configuration method at 1000 °C in the air using platinum wire.

8) X-ray diffraction measurement:

X-ray diffraction measurements were carried out by RIGAKU RAD IIC under the condition of 40 kV-20 mA.

III. Results and discussion

The results are shown in Table-1 and Figure-1. Addition of CZ to LCM can be expressed that Mn in LCM is substituted by Zr. It seems that the existence of the Zr ions in B site restrict the diffusion of Mn ions at high temperature. Shrinkage of LCM was decreased to about 1/3 by the addition of 5-10% of zirconate. On the other hand, the electro-conductivity decreased 20% by the addition of 5 % of CZ. The decrease of electro-conductivity is pro-

portional to the amount of CZ added between 1-20 mol%.

SEM image of the fracture cross section of LCM ceramics added 5% CZ is shown in Figure-2. LCM ceramics as cathode have to be porous as shown in this figure. In general, porous ceramics more easily shrinks than non-porous ceramics. This is the reason why better thermal stability is necessary in the case of FOFC cathode.

X-ray diffraction diagram of the LCM added 5% CZ is illustrated in Figure 3. The added zirconate was completely dissolved in LCM. A slight peak shift to lower angle took place.

Same phenomena mentioned above were observed in the cases of titanate stannates as additives to LCM and in the case of strontium substituted lanthanum manganite (LSM) ceramics.

LCM and LSM is also useful for oxidation catalyst in which high thermal stability is necessary. It is a matter of course that this technique can be applied in this field.

IV. Conclusions

The addition of calcium zirconate to LCM improved its thermal stability. Shrinkage of LCM decreased to 1/3 by the addition of 5-10 % of CZ.

V. References

- 1) K. Abe, J. R. Zen : Japan Kokai Tokkyo Koho 7-14584
- 2) K. Fueki, M. Takahashi : "Designing of Fuel Cell" Science Forum, (1987, in Japanese)



Fig.-2 SEM Image of Fracture Cross Section of LCM

Table-1 Experimental Results in LCM

| Amount of CZ (%) | Porosity (%) | Shrinkage (%) | Conductivity ($\times 10^3$ S/cm) |
|------------------|--------------|---------------|------------------------------------|
| 0 | 30.1 | 0.33 | 112 |
| 1 | 30.0 | 0.22 | 103 |
| 5 | 30.3 | 0.12 | 92 |
| 10 | 30.0 | 0.10 | 79 |
| 20 | 29.9 | 0.10 | 54 |

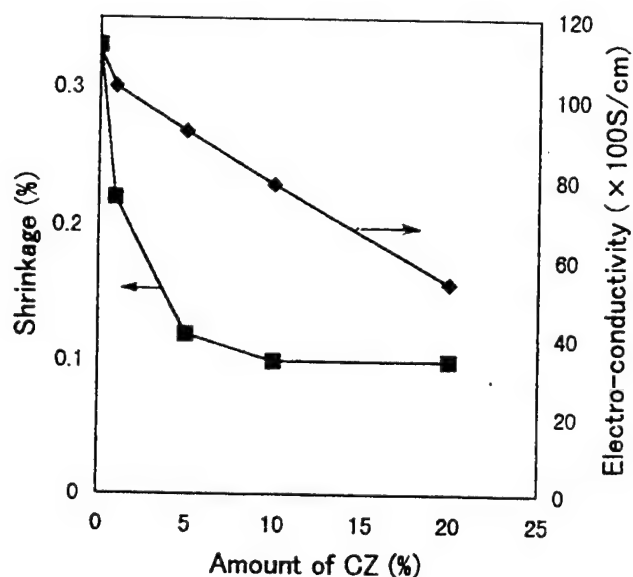


Fig.-1 Experimental Results in LCM

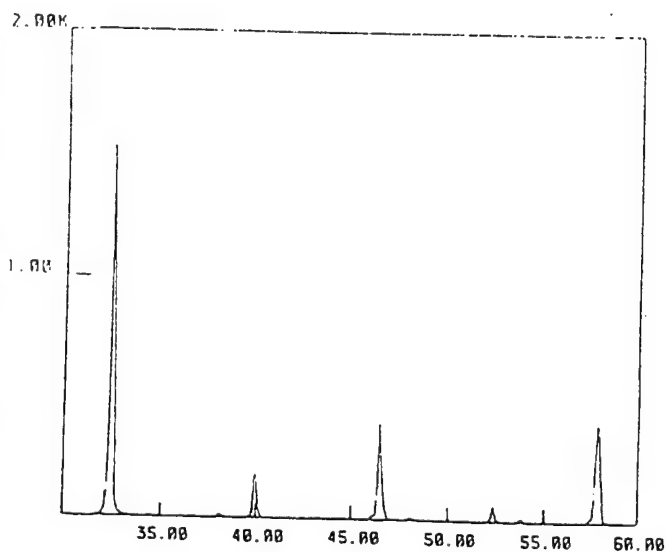


Fig.-3 X-ray Diffraction Diagram of LCM

PROCESSING AND INDUCED-PHASE TRANSFORMATION IN SR-DOPED PZT CERAMICS

Yongjian Yu and Raj N. Singh

Department of Materials Science and Engineering

University of Cincinnati, Cincinnati, P.O. Box 210012, Ohio 45221-0012

Abstract: Lead strontium zirconate titanate [$\text{Pb}_{1-x}\text{Sr}_x(\text{Zr}_{1-y}\text{Ti}_y)\text{O}_3$] ceramics with compositions near the phase boundary between the antiferroelectric tetragonal (A_T) and the ferroelectric rhombohedral (F_R) phases are prepared by powder processing and tape casting techniques. The antiferroelectric compositions near the A_T - F_R boundary showed higher dielectric constants than the compositions further away from this boundary. The coercive field and remnant polarization decreased with increasing Sr content. A large field-induced longitudinal strain is also observed near the phase boundary.

I. INTRODUCTION

Lead zirconate titanate (PZT) ceramics are extensively used as sensors and actuators in a variety of applications because of their electromechanical response [1]. Some of these ceramics also exhibit electric field-induced antiferroelectric (A) to ferroelectric (F) phase transformation which can lead to unusual electrical and electromechanical properties. Recent studies on the La and Sn modified PZT compositions have shown high dielectric constants and large displacements for compositions close to the A-F phase boundary [2,3]. In this active area, we noticed that little work was reported on $(\text{PbSr})(\text{ZrTi})\text{O}_3$. In fact, Sr as a divalent dopant replaces Pb in the structure and enlarges the antiferroelectric phase area as La and Sn do.

In this paper, $(\text{PbSr})(\text{ZrTi})\text{O}_3$ samples close to A_T - F_R boundary were prepared by tape casting and were studied for the polarization behavior, dielectric properties, x-ray diffraction, and longitudinal strain.

II. EXPERIMENTAL PROCEDURE

(A) Composition Selection and Sample Preparation

The phase diagram of $\text{PbSr}(\text{ZrTi})\text{O}_3$ [4] was used as a reference for the composition selection, as shown in Fig. 1. The function of Sr is obvious as can be observed from the phase diagram. As the Sr increases, A_T phase expands greatly. One can also find from Fig. 1 that there is a long phase boundary between the A_T and F_R phases. The compositions chosen for this study and their formula are listed in Table I. The compositions are represented by the formula $\text{Pb}_{1-x}\text{Sr}_x(\text{Zr}_{1-y}\text{Ti}_y)\text{O}_3$, where x and y are the mole percent of Sr and Ti, respectively. It is simplified to a form $100x/100(1-y)/100y$.

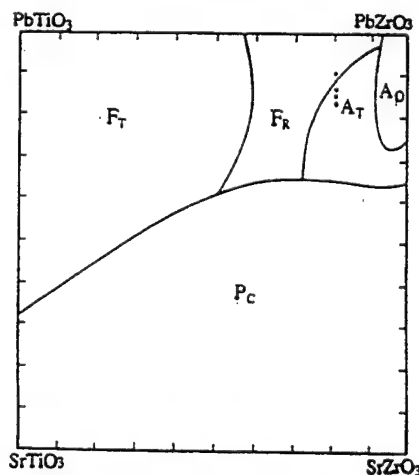


Fig. 1. The phase diagram of $\text{PbSr}(\text{ZrTi})\text{O}_3$ (after T. Ikeda [4])

Polycrystalline PZT ceramics investigated in this study were prepared by using the appropriate amount of reagent grade powder of PbO , ZrO_2 , $\text{Sr}(\text{NO}_3)_2$ and TiO_2 with a purity greater than 99%. The raw materials were wet-mixed with distilled water and ball-milled in polyethylene bottle containing zirconia media for 2 hours. An amount of 1% Darvan C was added as a dispersant. After drying at 100°C , the powders were calcinated in air at 850°C for 1.5 hours. During the calcination, $\text{Sr}(\text{NO}_3)_2$ decomposed to SrO_2 at about 700°C . After calcination, the powders were ball-milled for 12 hours. The polyvinyl butyral was selected as a binder in developing the slip. The solvents were a mixture of toluene and methyl isobutyl ketone. The powders were ball-milled for 2 hours with proper ratio of the binder, solvent, dispersant, and plasticizer. Before tape casting, the slurry was de-aired in a vacuum container for 5 minutes. The tape casting was carried out on a fixed bed laboratory tape caster. The gap for the doctor-blade was set at 0.015 inch. The dried tapes were cut into 25 x 25 mm. They were laminated at 115°C for 30 minutes. After binder was burned out, the sample was sintered at closed Al_2O_3 crucibles, in the temperature range of 1250 - 1350°C in an excess PbO atmosphere. The density of the fired samples was in the range of 7.5 - 7.7 g/cm^3 . Silver electrodes were applied to the polished surfaces of the samples and then fired at 550°C for 1 hour.

(B) CHARACTERIZATION

Structural properties were analyzed by a Siemens Model D-500 X-ray Diffractometer at room temperature using $\text{Cu K}\alpha$ radiation. The polarization hysteresis loops were measured at room temperature using a modified Sawyer-Tower circuit. The longitudinal field-induced strain was measured by a MTI-2000 Fonic Sensor. The sample was mounted in a manner shown in Fig. 2.

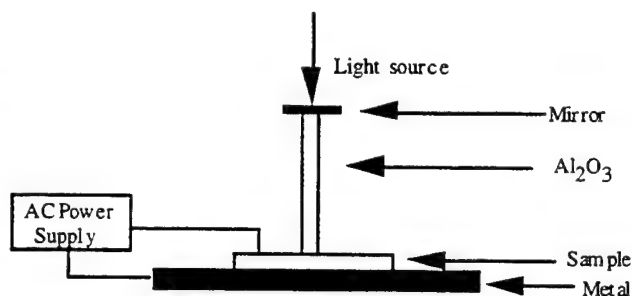


Fig. 2 Schematic drawing of sample holder and sample mounting for longitudinal strain measurement

The light beam was reflected off a mirror attached at one end of the rod of which another end was in contact with the sample. The sample displacement was measured by measuring the displacement of the upper mirror.

III. RESULTS and DISCUSSION

(A) X-ray Investigation

The x-ray diffraction patterns of the fired PSZT are shown in Fig. 3. In this figure, samples had a fixed Zr/Ti ratio but different Sr content. It can be observed that a complete reaction of the oxides occurred and that a single perovskite phase was obtained for every composition.

In a material with the composition $x=0.10$, there is no splitting on any peak. This means that the composition #4 is fully rhombohedral phase. As the Sr content increases in the sequence from #4 to #9, note the peaks near $2\theta=45^\circ$. In the samples of composition $x=0.175$ and $x=0.20$, two peaks appear. They are 002 (lower angle side) and 200 (higher angle side) diffraction peaks of the tetragonal system. Splitting is also evident for the $\{211\}$ and $\{220\}$ peaks as the Sr content is increased. This splitting indicates the transition from the rhombohedral phase to the tetragonal phase and associated distortion of the lattice [5]. Similar behavior was observed as the ratio of Zr/Ti was increased in which the sample compositions shifted from the F_R to A_T area.

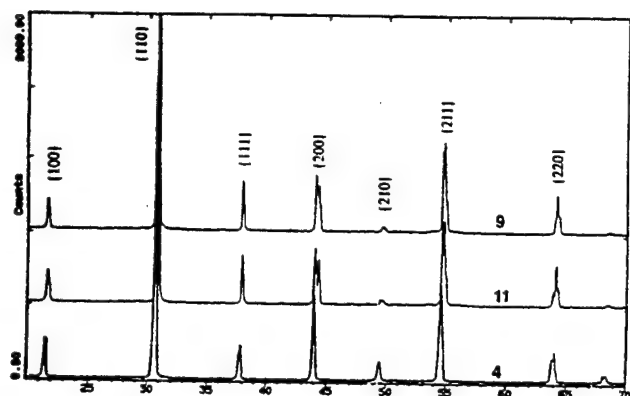


Fig. 3 XRD spectra for different samples with fixed Zr/Ti ratio

(B) Dielectric Properties

Table I lists the relative dielectric constant and loss tangent for a set of samples at room temperature. With increasing Sr content, the dielectric constant increases and reaches a maximum near the A_T - F_R boundary for composition #11 (17.5/80/20) at two different frequencies. And then it decreases with further increase of the Sr content. It should also be noted that the composition #11 has the lowest dielectric loss tangent.

Table I. Dielectric constant and loss tangent at room temperature of PSZT ceramics.

| Composition Number | | K (1 k Hz) | K (10 k Hz) | $\tan \delta$ (%) (1 k Hz) |
|--------------------|--------------|------------|-------------|----------------------------|
| 4 | (10/80/20) | 757 | 744 | 1.22 |
| 11 | (17.5/80/20) | 1156 | 1142 | 0.800 |
| 9 | (20/80/20) | 855 | 844 | 1.02 |

C) POLARIZATION and STRAIN BEHAVIOR

Figure 4 shows the hysteresis loops of a set of samples as a function of the Sr content with a fixed Zr/Ti ratio (100x/80/20). Composition #4 has a square hysteresis loop typical of a ferroelectric phase, while composition #5 and #11 show the classic antiferroelectric double hysteresis loops. The

coercive field and remnant polarization decreases with the increase of Sr content, accompanied with the phase changes from the ferroelectric to the antiferroelectric phase.

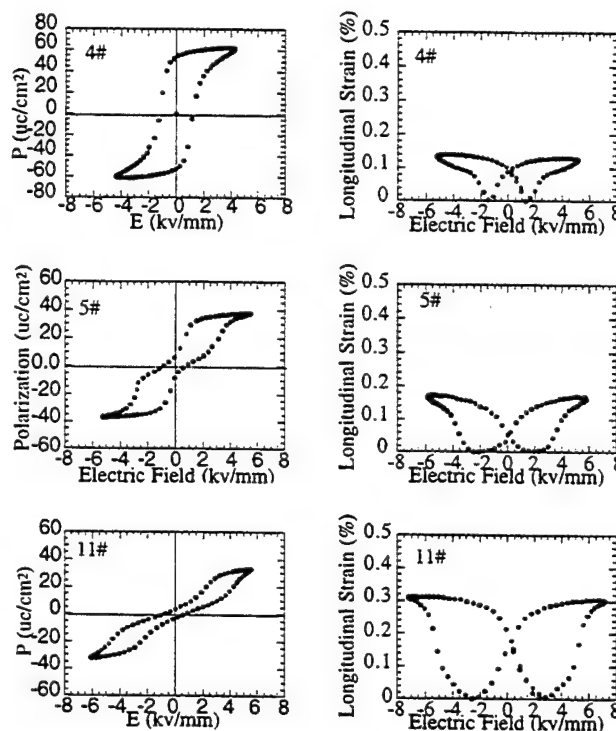


Fig. 4 Polarization hysteresis loops and electrically induced strain for composition #4 (10/80/20) #5 (15/80/20) and #11 (17.5/80/20).

The longitudinal strains were measured at 0.1HZ for all the samples. The strain for composition #4 is only 0.14% due to domain switching in pure ferroelectric PSZT ceramics. The field induced strain is 0.18% for composition #5 when Sr content is increased from $x=0.10$ to $x=0.15$. When the composition is close to the phase boundary for composition #11, the longitudinal strain we measured is 0.31%, and this induced strain is produced when ferroelectric phase is induced from the antiferroelectric phase. It is seen that above the electric field required to induce an antiferroelectric to ferroelectric phase transition, the strain produced due to the piezoelectric effect of the ferroelectric phase is less than the strain due to the phase transition.

IV. CONCLUSIONS

Samples of various compositions across the A_T - F_R phase boundary were prepared by tape casting and their ferroelectric and dielectric properties were studied. The following conclusions are drawn:

1. High density Sr-doped PZT can be made using tape casting. The XRD results show an evidence of the phase transition from the ferroelectric to the antiferroelectric phase.
2. Near the F_R - A_T phase boundary, the dielectric constant reaches a maximum value.
3. Near the F_R - A_T phase boundary, as the Sr content is increased for sample with a fixed Zr/Ti ratio, the coercive field and remnant polarization are both decreased. The field-induced longitudinal strain reaches a maximum near the phase boundary.

Acknowledgment

This research is supported by National Science Foundation through a grant # DMR-9522504.

References

- ¹L. E. Cross, "Dielectric, Piezoelectric and Ferroelectric Components," *Am. Ceram. Soc. Bull.*, 63[4] 586-590 (1984).
- ²W. Y. Pan, C. Q. Dam, Q. M. Zhang, and L. E. Cross, "Large Displacement Transducers Based on Electric Field Forced Phase Transitions in the Tetragonal $(Pb_{0.97}La_{0.02})(TiZrSn)$ Family of Ceramics," *J. Appl. Phys.*, 66[12] 6014-23 (1989).
- ³Wuyi Pan, Qiming Zhang, Amar Bhalla, and Leslie E. Cross, "Field Forced Antiferroelectric-to-Ferroelectric Switching in Modified Lead Zirconate Titanate Based Antiferroelectrics," *J. Am. Ceram. Soc.*, 72 [4] 571-78 (1989).
- ⁴T. Ikeda, "A Few Quaternary Systems of Perovskite Type $A^{2+}B^{4+}O_3$ Solid Solutions," *J. Phys. Soc. Jpn.*, 14[10] 1286-94 (1959).
- ⁵Hongxue Zhang, Antti Uusimäki, Seppo Leppavuori, Pentti Karjalainen, "Phase Transition Revealed by Raman Spectroscopy in Screen-printed Lead Zirconate Thick Film," *J. Appl. Phys.*, 76[7] 4294-98 (1994).

Session II—Thin Films

PAGE

Invited Papers

- | | |
|--|----|
| Fatigue Mechanism of PZT Thin-Film Capacitors, <u>K. Aoki</u> , Y. Fukuda, K. Numata, and A. Nishimura, Texas Instruments, Japan | 74 |
| CVD of Thin Perovskite Films, <u>P.C. Van Buskirk</u> , M.W. Russell, S.T. Johnston, and S.M. Bilodeau, Advanced Technology Materials, Inc., USA | 80 |

Contributed Papers

Review

- | | |
|---|----|
| II-1 Comparative Assessment of Electronic Ceramics R&D in the U.S. and Japan, <u>S. Swartz</u> , NexTech Materials, USA; T.R. Shrout, Penn State University, USA; and Tadashi Takenaka, Science University of Tokyo, Japan. | 84 |
|---|----|

BaTiO₃ & Ba,SrTiO₃

- | | |
|---|-----|
| II-2 Dielectric Behavior of (Ba,Sr)TiO ₃ Thin Films and its Correlation with Oxygen Defect Density, <u>Y. Fukuda</u> and K. Aoki, Texas Instruments Tsukuba R&D Center; H. Haneda and I. Sakaguchi, National Institute for Research in Inorganic Materials, Japan; K. Numata and A. Nishimura, Texas Instruments Memory R&D Center, USA. | 88 |
| II-3 Preparation of BaTiO ₃ and SrTiO ₃ Thin Films for Communications Applications, <u>R. W. Schwartz</u> , Clemson University; and P.G. Clem and D. Dimos, Sandia National Laboratories, USA | 92 |
| II-4 Phase Transition and Ferroelectric Properties of BaTi _{0.91} (Hf _{0.5} Zr _{0.5}) _{0.09} O ₃ by a Laser Ablation Method Using the Fourth-harmonic Wave of a YAG Laser, <u>Y. Masuda</u> , S. Fujita, and A. Baba, Hachinohe Institute of Technology; H. Matsumoto and T. Hirai, Tohoku University; and K. Nagata, National Defense Academy, Japan | 96 |
| II-5 The Effect of Oxygen on the Barium Titanate Film Capacitor, B.H. Tsao and R.L.C. Wu, K Systems Corp.; and <u>S. Fries Carr</u> and J.A. Weimer, Wright Laboratory, Wright-Patterson Air Force Base, USA | 100 |

PbTiO₃

- | | |
|--|-----|
| II-6 Electrical Properties of (Pb,Ca)TiO ₃ Thin Films by Multiple-Cathode Sputtering, <u>H. Maiwa</u> , Shonan Institute of Technology; and N. Ichinose, Waseda University, Japan | 104 |
| II-7 Effect of Niobium on Some Electrical Properties of Nb-doped PbTiO ₃ Thin Films, <u>T. Shiosaki</u> , R.C. Ibrahim, T. Horiuchi, and K. Matsushige, Kyoto University, Japan | 108 |

| | PAGE |
|---|-------------|
| II-8 Electrical and Structural Analysis of Epitaxial Lanthanum Modified PbTiO ₃ Thin Films Exhibiting a-Oriented Domains, <u>J.P. Maria</u> and <u>S. Troler-McKinstry</u> , <i>Penn State University, USA</i> | 112 |
| <u>PZT/Devices</u> | |
| II-9 Bioanalytical MEMS Based on Piezoelectric Materials, <u>D.L. Polla</u> , <u>R.C. McGlennen</u> , and <u>L.T. Furcht</u> , <i>University of Minnesota, USA</i> | 116 |
| II-10 Effect of Thickness and Texture on the Ferroelectric Properties of Lead Zirconate Titanate Thin Films by Sol-Gel Processing, <u>F. Chu</u> , <u>T. Su</u> , and <u>S. Troler-McKinstry</u> , <i>Penn State University, USA</i> | 120 |
| II-11 Properties of Sputtered Ir and IrO ₂ Electrodes for PZT Capacitors, <u>M. Shimizu</u> , <u>S. Hyodo</u> , <u>S. Nakashima</u> , <u>H. Fujisawa</u> , and <u>H. Niu</u> , <i>Himeji Institute of Technology</i> ; and <u>H. Okino</u> and <u>T. Shiosaki</u> , <i>Kyoto University, Japan</i> | 124 |
| II-12 The Low-Field Biaxial Stress Response and Transverse Piezoelectric Coefficients of Sol-Gel PZT Thin Films, <u>J.F. Shepard, Jr.</u> and <u>S. Troler-McKinstry</u> , <i>Penn State University, USA</i> | 128 |
| <u>Optical/SAW/Miscellaneous</u> | |
| II-13 Theoretical Study on SAW Characteristics of LiNbO ₃ /Sapphire Structures, <u>T. Shiosaki</u> , <u>T. Nishida</u> , <u>T. Horiuchi</u> , and <u>K. Matsushige</u> , <i>Kyoto University, Japan</i> | 132 |
| II-14 Fabrication and Electrical Properties of LiTaO ₃ /ZnO/Al ₂ O ₃ Hexagonal Heterostructure, <u>T. Tsurumi</u> , <u>Y. Ma</u> , <u>H. Kimura</u> , and <u>N. Ohashi</u> , <i>Tokyo Institute of Technology, Japan</i> | 136 |
| II-15 Synthesis and Properties of K(Sr _{0.5} Ba _{0.5}) ₂ Nb ₅ O ₁₅ Thin Films by Chemical Solution Deposition Method, <u>W. Sakamoto</u> , <u>A. Kawase</u> , <u>T. Yogo</u> , and <u>S. Hirano</u> , <i>Nagoya University, Japan</i> | 140 |
| II-16 Crystal Orientation and Dielectric Properties of Sol-Gel Derived SrBi ₂ Ta ₂ O ₉ Thin Films, <u>T. Hayashi</u> and <u>T. Hara</u> , <i>Shonan Institute of Technology, Japan</i> | 144 |

Fatigue Mechanism of PZT Thin-Film Capacitors

Katsuhiro Aoki, Yukio Fukuda, Ken Numata* & Akitoshi Nishimura*

Texas Instruments Tsukuba R&D Center, Ltd.

**Texas Instruments Inc., Memory R&D Center*

E-mail : kaok@dlep1.itg.ti.com

Abstract Recently, fatigue-free PZT thin film capacitors were demonstrated by application of oxidizable metal and oxide electrodes. However, the reason for drastic improvement in fatigue property was not clear. This paper described fatigue mechanism, and discusses reasons for improvement from the standpoints of microstructure, and of interaction between PZT and electrode materials. It is clearly identified that unexpected formation of surface transition layer of PZT, which is strongly dependent on crystallization process, and decrease in the interfacial capacitances by oxygen vacancy accumulation between PZT and non-oxidizable metal electrode with high work function are the causes of fatigue. Oxidizable metal and oxide electrode suppress oxygen vacancy accumulation by oxidation-reduction reaction. Fatigue-free capacitor can be formed while oxidizable metal or conductive oxide electrodes are applied to columnar-grain-structured PZT thin film.

1 Introduction

Polarization fatigue of PZT thin film capacitor is one of the most serious issues for application to the semiconductor devices¹⁾. "Fatigue" makes a ceiling of read/write operation specification of the ferroelectric memory modules. This phenomenon has been studied from the standpoints of the intrinsic property of PZT²⁻⁵⁾.

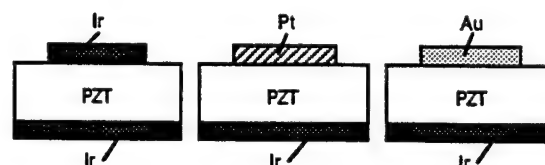
However, fatigue-free PZT capacitors were demonstrated successfully by use of oxide and oxidizable metal electrodes⁶⁻⁹⁾. Such successful reports clearly indicate that the selection of electrode material enables us to fabricate the fatigue-free PZT capacitors, and "fatigue" is not an intrinsic property of PZT. In another approach of avoiding fatigue, SBT⁹⁾ has been introduced as new candidate of ferroelectric material which never exhibits polarization fatigue.

In the present study, we discuss "fatigue of

sol-gel derived PZT thin film capacitor" from the standpoints of the PZT film structure and of the interactions between PZT and electrodes. Finally, we identify fatigue mechanism, and established the method to make fatigue-free PZT capacitor.

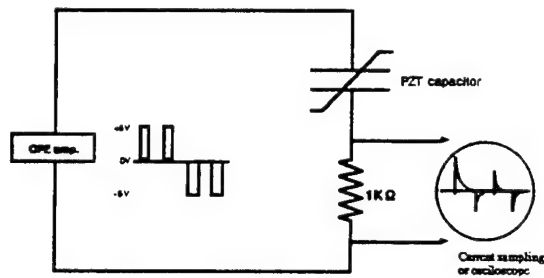
2 Experimental

The e-beam deposited Ir/SiO₂/Si substrates were prepared for deposition of sol-gel PZT thin-films with thicknesses of 300nm. The excess-Pb concentration in the precursor solution varies from 0% to 20%. The Zr/Ti ratio was fixed at 0.5/0.5. PZT thin-films were crystallized at 600 °C, 650°C and 700°C in air. Ir, Pt and Au top electrodes with areas of 8x10⁻⁴cm² were formed on the PZT layers by e-beam evaporation. The capacitor structures are shown in figure 1. The cross-sections of the capacitors were carefully observed by TEM. Fatigue properties were evaluated by the pulse switching characterization technique. For evaluation of the effects of the La and Nb modifications, the PLZT and PNZT thin film capacitors were fabricated from the precursor solutions containing 1atm%-La and 1atm%-Nb by the same capacitor formation process.



PZT capacitor structures

Fig.1 Experimental Tool & Samples



Pulse Switching circuit

Fig.1 Experimental Tool & Samples

3 Results and Discussion

3.1 Structure Dependences

PZT film structure dependences of fatigue are discussed here. Figure 2 shows final annealing temperature dependences of polarization fatigue properties of Ir/PZT/Ir capacitors. It is clear that the 2Pr-value for switching cycles is strongly dependent on the annealing temperature. Only the capacitor formed at 600°C exhibits drastic decrease of 2Pr-value. In contrast, the 2Pr-values of the capacitors formed at 650°C and 700°C are not reduced up to the switching cycles of 1×10^8 . It is suggested that there could be some structural difference between those PZT layers because the basic capacitor structures (Ir/PZT/Ir) are entirely same.

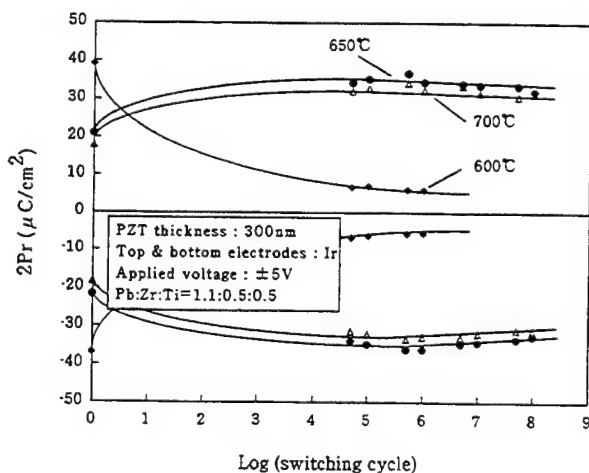
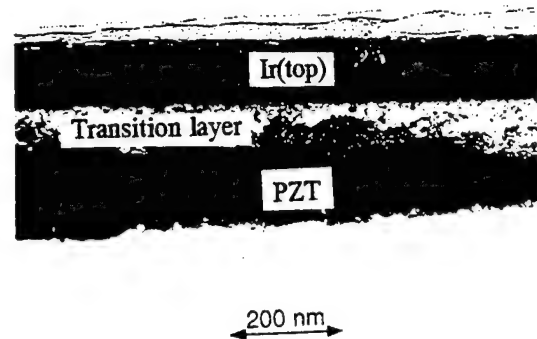


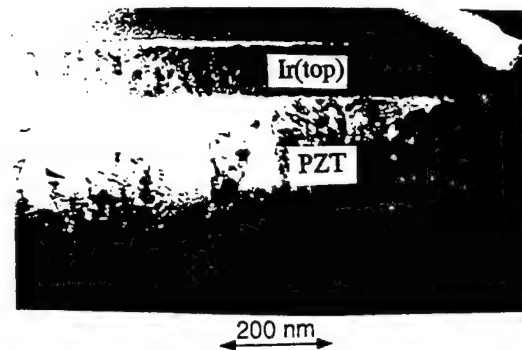
Fig.2 Final Annealing Temperature Dependences of Fatigue Properties

Figure 3 shows the cross-sectional TEM images

of Ir/PZT/Ir capacitors exhibiting fatigue (formed at 600°C) and non-fatigue (formed at 650°C). In (a), the structural transition layer is clearly observed between PZT layer and top electrode. This PZT capacitor showed significant fatigue. In contrast, in the PZT capacitor with good fatigue property, such transition layer is not observed at the PZT surface. The columnar grains of the PZT contact top electrode directly.



(a) Formed at 600°C

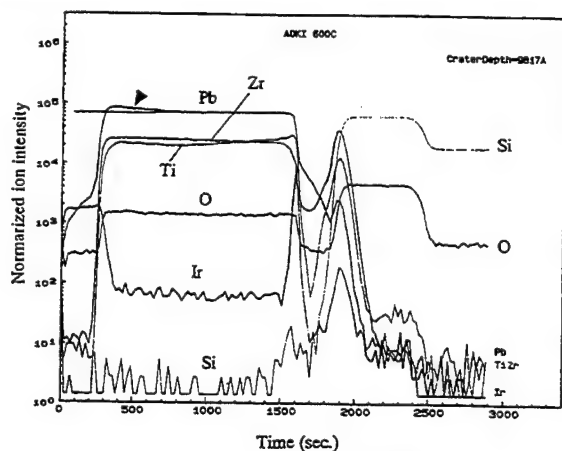


(b) Formed at 650°C

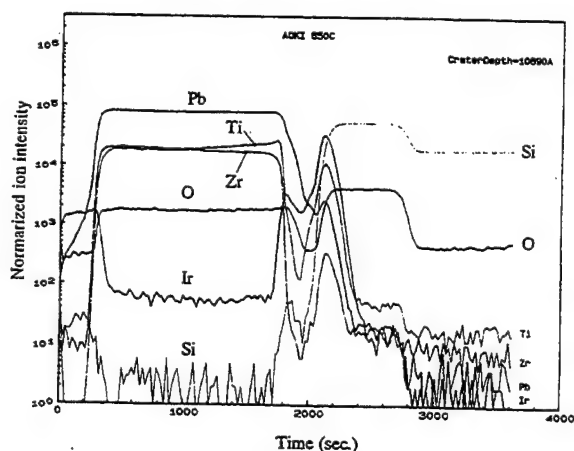
Fig.3 Cross-Sectional TEM Images of Ir/PZT/Ir Capacitors Exhibiting (a) Fatigue and (b) Non-Fatigue

These observations suggest that formation of structural transition layer at the PZT surface is a one of the reasons of polarization fatigue. Furthermore, the transition layer formed at 600°C is fully removed by the annealing at 650°C. Here, we examined the transition layer by use of SIMS. Figure 4 shows the SIMS depth profiles of two PZT capacitors shown in Fig.3. In (a), while we observe the secondary ion intensity of Pb

carefully, it is found that the Pb intensity increases at the PZT surface. On the other hand, in (b), Pb intensity is not changed from the top to the bottom of PZT layer. The SIMS analysis results clearly indicate that the transition layer is formed by segregation of excess-Pb in precursor solution, and is removed by annealing at 650°C. PbO in transition layer is considered to be vaporized. Therefore, one of the reasons of "fatigue" is said to be due to formation of the structural transition layer, which is strongly dependent on the fabrication process conditions.



(a) Formed at 600°C



(b) Formed at 650°C

Fig.4 SIMS Depth Profiles of Ir/PZT/Ir Thin Film Capacitors

3.2 Electrode Dependences

Thus, the grain structures of PZT should be optimized to form the fatigue-free capacitors. Desirable PZT thin film is columnar grain structure. The SEM image of the columnar grains

of the sol-gel PZT thin film on the Ir is shown in Figure 5. Electrode dependences of fatigue was discussed based the results obtained from such PZT thin films.

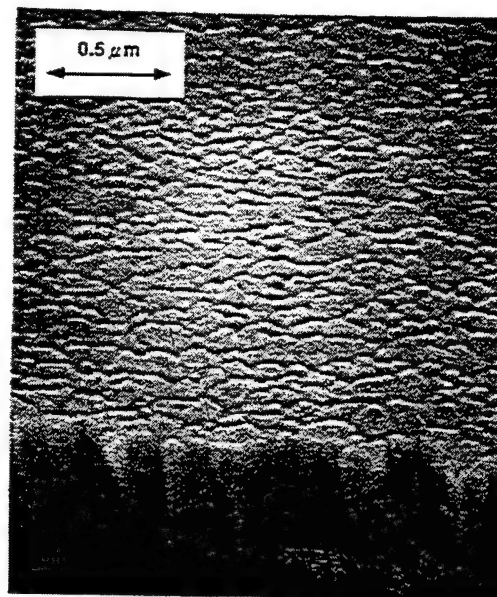


Fig.5 SEM Images of Sol-Gel PZT Film on Ir

Figure 6 shows the electrode dependences of fatigue properties. The capacitor structures are Ir/PZT/Ir, Pt/PZT/Ir and Au/PZT/Ir. The PZT/Ir multilayers were fabricated under the same conditions. Drastic decreases of $2P_r$ -values by switching are observed in the Pt/PZT/Ir and Au/PZT/Ir capacitors. However, The Ir/PZT/Ir capacitor does not exhibit such a phenomenon. Because the PZT/bottom electrode structures of those capacitors are fabricated through same process, it is believed that there could be the cause of fatigue at the interfaces between Pt and PZT, and between Au and PZT. We could expect to obtain the knowledge by comparing the nonswitched charges reflecting the interfacial capacitance.

Figure 7 shows the changes in polarization properties of the Pt/PZT/Ir capacitor such as the switched charges and remanent polarizations at positive and negative biases. When we observed the relations between the switched charges [$\Delta P(+)$, $\Delta P(-)$] and the $2P_r$ -values carefully, it is

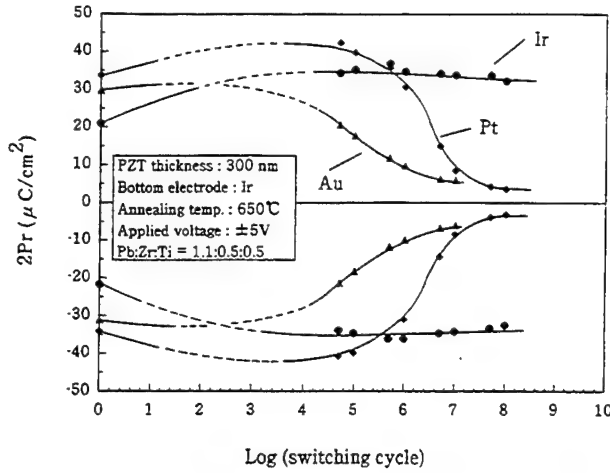


Fig.6 Electrode Dependences of Fatigue.

found that the decrease of the $2Pr$ -values are accompanied by the $\Delta P(-)$. The $\Delta P(-)$ reflects the interfacial capacitance between PZT and Pt top electrode. Therefore, the decrease of the $2Pr$ -value is induced by the reduction of such interfacial capacitance at the Pt interface.

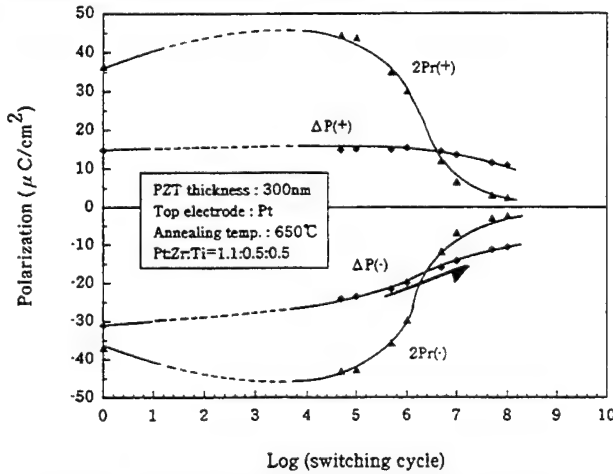


Fig.7 Polarization Properties of Pt/PZT/Ir Capacitor for Switching Cycles.

Figure 8 shows the stability of polarization properties for negative unipolar pulse application onto the top electrode. When negative bias is applied to the top electrode, the $\Delta P(-)$ is gradually decreased with increasing the pulse application number. This changes in the polarization properties for pulse application suggest the electric field response of charged species contained in the PZT thin film.

3.3 Fatigue Mechanism

In the perovskite crystals, oxygen vacancies are considered to be mobile ions. The oxygen vacancy is positively charged relative to the regular perovskite crystals. The activation energy of its motion is reported as 1eV^{12} . Figure 9 Show the oxygen vacancy accumulation model in the case of negative bias application onto the top electrode. When the top electrode is negatively biased, oxygen vacancies are drifted toward the top electrode, and accumulate at the interface. The oxygen accumulation layer is believed to provide small interfacial capacitances according to the results shown in Fig.8. Because the interfacial capacitance are connected with ferroelectric region of PZT in series, the reduced interfacial capacitance controls the properties of the capacitor. Namely, fatigue is caused by the small interface capacitance induced by oxygen vacancies.

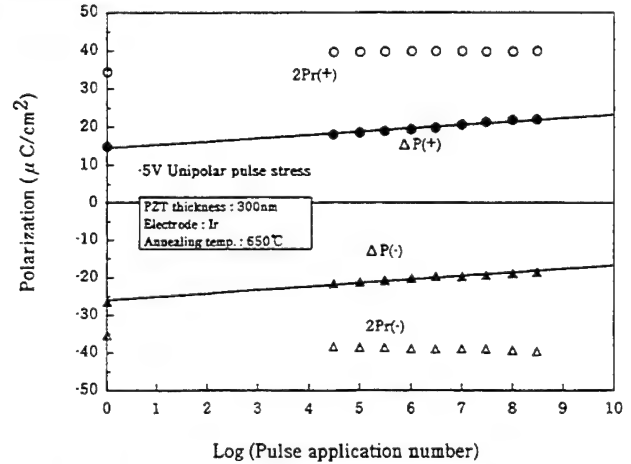


Fig.8 Stability of Polarization for Negative Unipolar Pulse Application.

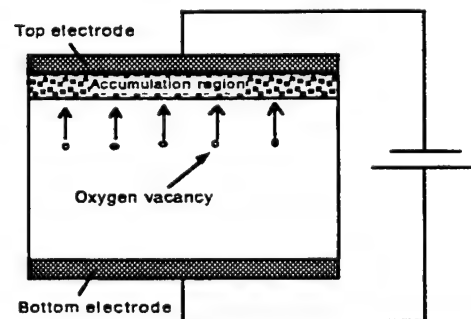


Fig.9 Oxygen Vacancy Model

According to the above discussions, it was clarified that there are at least two reasons in polarization fatigue. One is "formation of structural transition layer". The other is "reduction of interfacial capacitance at the Pt interface. Here, we would like to discuss the fatigue mechanism and why Ir electrodes drastically improve fatigue property. Figure 10 show the band models of PZT/Pt and PZT/Ir interfaces. High built-in potential V_{bi} is believed to be established at the PZT/Pt interface since Pt has large work function of 5.6eV. Oxygen vacancies in PZT region might be drifted toward the Pt electrode in high internal electric field around the interface, and accumulate there. Since the accumulation layer works as small interfacial capacitance, oxygen accumulation is accelerated by the localized electric field of the switching pulse application.

On the other hand, it is believed that V_{bi} established at the PZT/Ir interface is lower than that of PZT/Pt interface because the work function of IrO_2 (Ir at interface is considered to be oxidized) might be much lower than that of Pt. Therefore, the oxygen vacancies have smaller coulomb forces from the V_{bi} . Furthermore, the oxidation-reduction reactions between PZT and Ir electrode might suppress the oxygen vacancy accumulation. Consequently, fatigue property is improved markedly by Ir electrode since the interfacial capacitance at the PZT/Ir interfaces are not reduced.

It is concluded that fatigue of the PZT thin film capacitor is not an intrinsic property of PZT but the phenomenon caused by motion of the oxygen vacancies.

3.4 The Effect of La and Nb Modification

La and Nb modifications are widely studies for improvement of fatigue properties. In the present study, 1atm%-La and Nb modified PZT capacitors were evaluated from the standpoints of "fatigue" and "retention". Figure 11 shows the fatigue properties of the PZT, PLZT and PNZT

thin film capacitors which were post-annealed at 600 for 3min. Those capacitors exhibits relatively good fatigue properties. The 2Pr-value of the PLZT capacitor is lower than those of other capacitors.

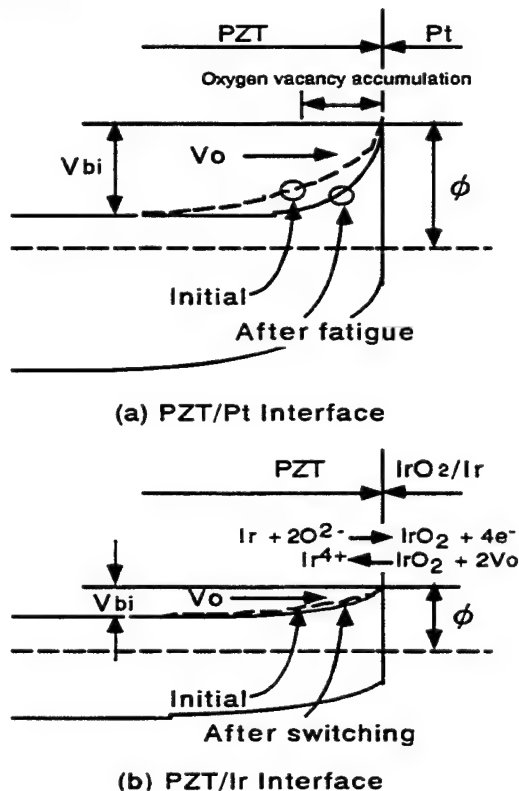


Fig.10 Band Models of PZT/Pt and PZT/Ir Interfaces

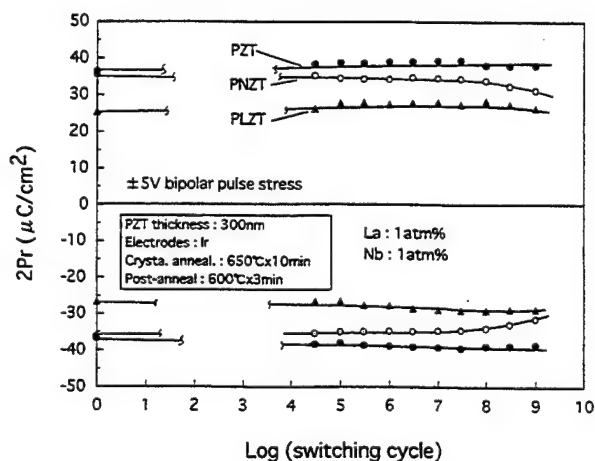


Fig.11 Fatigue Properties of PZT, PNZT and PLZT thin film capacitors.

Figure 12 shows the polarization properties of PZT, PNZT and PLZT thin film capacitors. The property of a Pt/PZT/Pt capacitor is also shown

for reference. Table 1 summarizes the retention properties. Here, the initial loss and the secondary loss are defined as follows. (1) "Initial loss" is the reduction rate of 2Pr-values in the first second, (2)"Secondary loss" is the reduction rate of 2Pr-values between 1s and 1000s. It is clear that La and Nb modification strongly affect the retention properties of the PZT capacitors. The initial loss is increased markedly by modification of La and Nb. These values are 37.8% for Nb and 39.0% for La although those for nonmodified PZT capacitors with Pt and Ir electrodes are 11.1% and 11.4%, respectively. Furthermore, the secondary loss(7.9%) of the PNZT capacitor is larger than the loss(3.9%) of the PZT capacitor.

Thus, a nonmodified PZT capacitor with Ir electrodes shows better retention property than La and Nb modified capacitors.

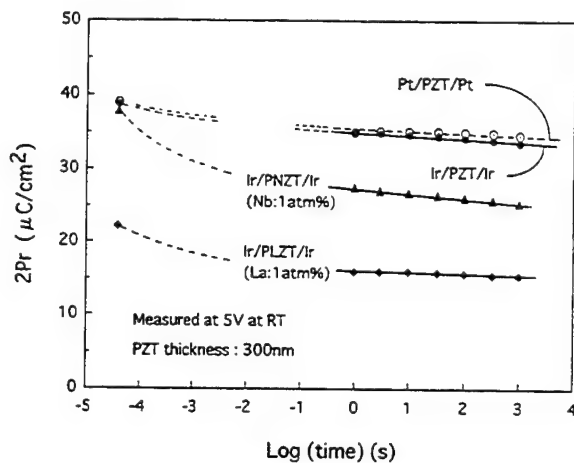


Fig.12 Retention Properties of Various PZT-Based Thin-Film Capacitors.

Table 1 Remanent Polarization Losses of Various Capacitors.

| Electrode | Pt | Ir | Ir | Ir |
|---|------|------|------|------|
| Dielectric | PZT | PZT | PLZT | PNZT |
| Initial 2Pr ($\mu\text{C}/\text{cm}^2$) | 38.7 | 38.9 | 22.1 | 37.8 |
| Initial loss(%) | 11.1 | 11.4 | 39.0 | 37.5 |
| Secondary loss(%) | 1.1 | 3.9 | 3.5 | 7.9 |

4 Conclusions

Fatigue mechanism of sol-gel derived PZT thin film capacitor was discussed. It was identified

that there are at least two reason for fatigue. One is formation of the structural transition layer, which is strongly dependent on the formation conditions. The other is the interaction between electrode and PZT. Oxygen vacancies are believed to play important roles in fatigue mechanism. When oxidizable metal and oxide electrodes are applied to the PZT thin film capacitor, those electrodes provide fatigue-free capacitors by suppressing the oxygen vacancy accumulation. La and Nb modifications rather degrade the retention property.

References

- 1) J.F.Scott et al.: Science **246**(1989)1400.
- 2) T.Mihara et al.:Peoc.4th Int.Symp.Integrated Ferroelectrics, Monterey (1992)137.
- 3) K.Amanuma et al.: Jpa.J.Appl.Phys.**33**(1994) 5211.
- 4) S.K.Dey et al.: Ferroelectrics **108**(1990)37.
- 5) T.Shiosaki : Oyobutsuri, **62**(1993)1212.
- 6) T.Nakamura et al.:Jpn.J.Appl.Phys.**33**(1994) 5207.
- 7) J.J.Lee et al.:J.Appl.Phys.**78**(1995)5073.
- 8) H.N.Al-Shareef et al.:Appl.Phys.Lett.**66** (1995)239.
- 9) K.Aoki et al.: Jpn.J.Appl.Phys.**35**(1996) 2210.
- 10) T.Mihara et al.: NIKKEI Electronics **584** (1993)77.
- 11) P.K.Larsen et al.: Sci.& Technol. of Electroceram.Thin Films **284**(1995)201.
- 12) R.Waser : J.Am.Ceram.Soc.**74**(1991)1934.

CVD of Thin Perovskite Films

Peter C. Van Buskirk, Michael W. Russell, Stephen T. Johnston, Steven M. Bilodeau

Advanced Technology Materials, Inc.
7 Commerce Drive, Danbury, CT 06810

Abstract--While the unique properties of ferroelectric ceramics have been known for over 40 years, the application of thin film ferroelectrics to advanced IC memories has only recently become commercially significant. Numerous semiconductor companies are actively pursuing both high permittivity BST, and ferroelectric SBT and PZT thin films. To meet the demand for thin film materials, processing methods are continuing to evolve and chemical vapor deposition (CVD) is viewed by many to be the method of choice for fabricating perovskite thin films. Several advantages of CVD, including flexible control of composition and excellent spatial uniformity in both thickness and composition will address the sub-micron geometry, 100 nm thickness and low-voltage operation requirements of future-generation dielectrics. This paper will discuss CVD of PZT, and focus on PZT film properties in the "self-correcting" composition regime where film composition is largely insensitive to the ratio of gas-phase reactants. Film properties in this regime, however, may vary significantly due to PbO volatility and its effects on microstructure.

I. INTRODUCTION

The recent past has witnessed a revolution in thin film processing of multicomponent oxides due in large part to the discovery of high temperature superconductors in 1987. The realization of superior properties in thin film HTSC materials was primarily due to the control of crystalline orientation via epitaxial growth on lattice matched substrates and buffer layers. In addition to requiring microstructural control, these materials demanded deposition techniques that could provide both precise compositional control of the cation species and high deposition temperatures (500-800°C) in oxidizing environments to form the desired crystalline phase. The discovery of YBaCaO, TlCaBaCuO and BiSrCaCuO spurred researchers to refine thin film deposition methods to address the unique attributes of these layered-structure perovskite materials. Despite scientific interest and numerous applications for the HTSC oxides, there was no direct experience base for these new materials to build upon, in contrast to the perovskite ferroelectrics which had been intensively studied and commercially exploited (in bulk forms) since the 1940's.

Due in part to the confluence of the discovery of HTSC materials and the continued rapid progress in integrated circuit technology, thin film ferroelectrics have recently overtaken their HTSC brethren, and several applications for semiconductor memories have spurred great interest in thin

film perovskites. Two principal memory applications, high permittivity films for ultra high density DRAMs [1, 2] and ferroelectrics for a new class of non-volatile memories (FeRAMs) [3] are being developed in parallel. The DRAM application for high permittivity perovskites (typically BaSrTiO₃) has a sizable commodity market, and the demand is presumably well known. FeRAMs offer the promise of entirely new applications because of the possibility of exceptionally low power and high-speed non-volatile data storage. Despite their different stages of commercial maturity, the two memory applications share remarkably similar device processing, circuit design, and materials integration challenges.

For FeRAMs, most research groups are working on either ferroelectric SrBi₂Ta₂O₉ (SBT) or Pb(Zr,Ti)O₃ (PZT) thin films. Each material has advantages and disadvantages for this application. Pt/SBT/Pt capacitors, for example, have been shown to have excellent fatigue and retention characteristics, although processing temperatures in excess of 750°C pose integration issues. For PZT, phase pure thin films can be deposited at temperatures in the 550-650°C range, although Pt/PZT/Pt capacitors are known to suffer from poor fatigue and retention. For PZT the use of doping and/or oxide electrodes may be needed to produce satisfactory capacitor electrical properties.

CVD processes for PZT have been reported by numerous groups [4, 5, 6, 7] and demand for a production worthy process is expected to emerge as high density (> 1 Mb) memories are developed. A particularly intriguing phenomenon, first reported by De Keijser et al., concerns regimes for CVD process parameters where the film Pb composition is insensitive to changes in precursor concentrations [8, 9]. Since such a characteristic may be highly desirable for a manufacturing process and we have investigated film properties for films deposited over a range of precursor concentrations within this self-correcting regime. We have found that although the composition remains nearly independent of precursor concentration, the film microstructure and properties can vary significantly.

II. EXPERIMENTAL

Film depositions were carried out in a Varian Associates High K research CVD tool that was described previously [10]. It is configured for 6" wafers and uses an ATMI LDS-

300B liquid delivery system to introduce metalorganic precursors to the reactor. The use of liquid delivery for vaporization of metalorganics facilitates precise adjustment of solution concentrations, and therefore simple control of precursor gas-phase concentrations in the CVD reactor. Deposition conditions for the present experiments are given in Table 1.

Solutions with a range of different Pb/(Zr+Ti) ratios were used over a series of deposition runs. This ratio is hereafter defined as $(A/B)_g$, denoting the conventional assignment of Pb to the "A" site, and Zr and Ti each to the "B" site in the perovskite cell, ABO_3 . The subscript g denotes the gas-phase concentration in the reaction chamber, while $(A/B)_f$ denotes the equivalent ratio in the film.

The gas phase ratio of Zr/(Zr+Ti) was held constant at 0.612. Under the conditions given above and for our reactor, that ratio resulted in films with Zr/Ti ~ 40/60, which for bulk materials results in a tetragonal crystal structure and ferroelectric properties. It is a common composition chosen for FeRAM applications because of its high P_r and the relative ease in forming the perovskite phase for lower Zr/Ti ratios.

The effect of Pb gas phase concentration on film composition, crystallinity and electrical properties was explored using by x-ray fluorescence (XRF), x-ray diffraction (XRD), and atomic force microscopy (AFM). Capacitors were defined by shadow mask deposition of Pt top electrodes and subsequently annealed at 550°C in air for 60 min. Capacitance and loss were measured at 1 kHz, no bias, and a 0.1 V amplitude using a HP-4192A Impedance Analyzer. Hysteresis loops and pulse testing were performed using a Radiant RT6000 ferroelectric test system.

III. RESULTS AND DISCUSSION

A series of PZT films were deposited with fixed deposition time; the effect on $(A/B)_f$ of $(A/B)_g$ is shown in Fig. 1. Nominal film thickness was 100 nm. For low $(A/B)_g$, $(A/B)_f$ increased monotonically with mole fraction of lead in the gas phase. Over the range $0.93 < (A/B)_g < 1.53$ a plateau was observed in $(A/B)_f$ in the range of 1.10 to 1.15. For those films the perovskite phase was the only crystalline phase present.

The appearance of this processing window, where film composition is insensitive to changes in the composition of Pb in the gas-phase, is rationalized in term of two competing processes: the formation of perovskite PZT via decomposition of Pb, Zr and Ti precursors, and the desorption of excess PbO from the growth surface. We believe that the vapor pressure of PbO over PZT is significantly lower than it is for solid PbO, as is known for

Table 1. CVD deposition conditions

| | |
|--------------------------|--|
| Precursors | Pb(thd) ₂ , Zr(thd) ₄ , Ti(OPr) ₂ (thd) ₂ |
| Solution molarity (typ.) | 0.5 M |
| Liquid flow rate | 0.14 ml/min |
| Substrate temperature | 550°C |
| Pressure | 1.2 torr |
| Deposition rate | 3.5 nm/min |
| Substrate | Ir/MgO/SiO ₂ /Si |

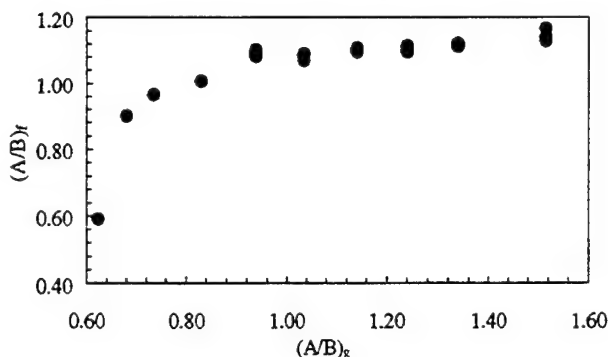


Fig. 1. Film composition vs. gas-phase composition.

bulk PZT [11]. Under process conditions where the kinetics of PZT formation are fast, and PbO volatility is high, single phase, stoichiometric PZT can be formed.

The presence of the plateau at $(A/B)_f$ values exceeding 1.00 may be due to inaccuracy in the XRF measurement or excess Pb diffused into the bottom electrode. Analysis of incorporation efficiencies for the metallic constituents revealed a decrease in Pb efficiency for $(A/B)_g > 0.83$, while Zr and Ti efficiencies remained nearly constant over the same range (Fig. 2). This is consistent with the appearance of the plateau, and the absence of PbO from XRD analysis of the films.

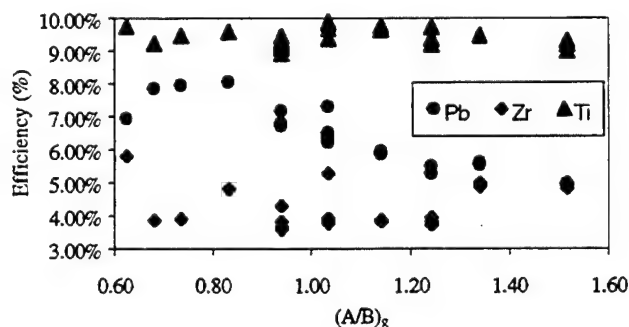


Fig. 2. Film incorporation efficiency versus gas phase composition for Pb, Zr and Ti. Zr and Ti efficiencies are relatively insensitive to gas phase composition. Pb efficiency is reduced for high gas-phase Pb compositions.

Film thickness decreased slightly with increased $(A/B)_g$, as shown in Fig. 3, where an increase in relative lead concentration from 38 to 60% resulted in a 20 nm decrease in average film thickness. This corresponded to an approximate growth rate decrease from 3.8 to 3.2 nm/min.

The as-deposited films were all smooth, dense, and fine-grained. The surface morphologies of PZT layers grown at selected values of $(A/B)_g$ are shown in Figs. 4 through 6. The roughness and grain size values calculated from these images are given in Table 2. The measured film roughness was insensitive to gas phase composition and was approximately double the starting surface roughness of the Ir films used as substrates.

With increasing $(A/B)_g$, the grain size increased as did the extent of faceting, suggesting an enhanced surface mobility. We believe that this was a consequence of the higher PbO surface coverage that must be present during growth at higher gas-phase Pb concentrations if the growth model described earlier is to be valid. The faceting in the high-Pb sample (Fig. 4) revealed predominately square features that suggested the presence of (001)-type orientations. This is supported further by the x-ray diffraction results.

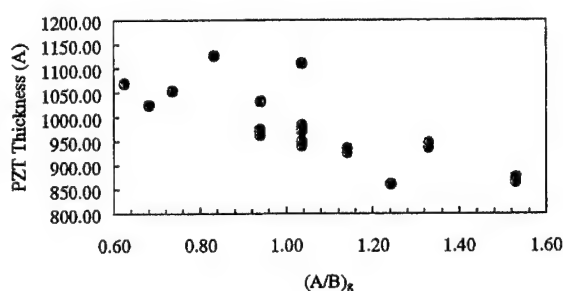


Fig. 3 PZT film thickness as a function of gas-phase Pb

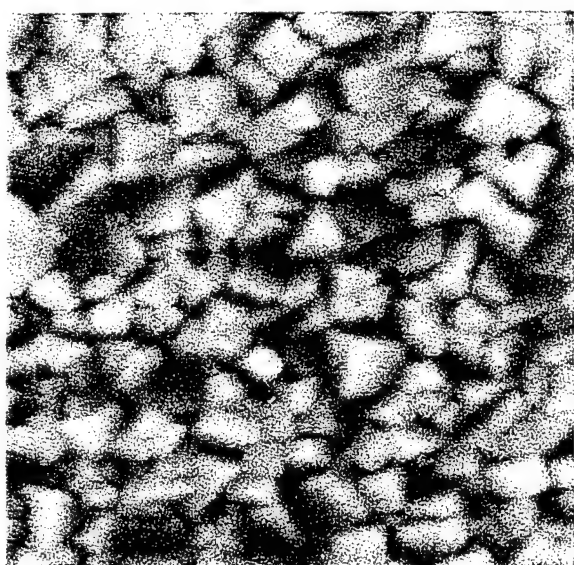


Fig. 4. $1 \times 1 \mu\text{m}^2$ tapping mode AFM image of a 100nm PZT film deposited with an $(A/B)_g = 1.03$.

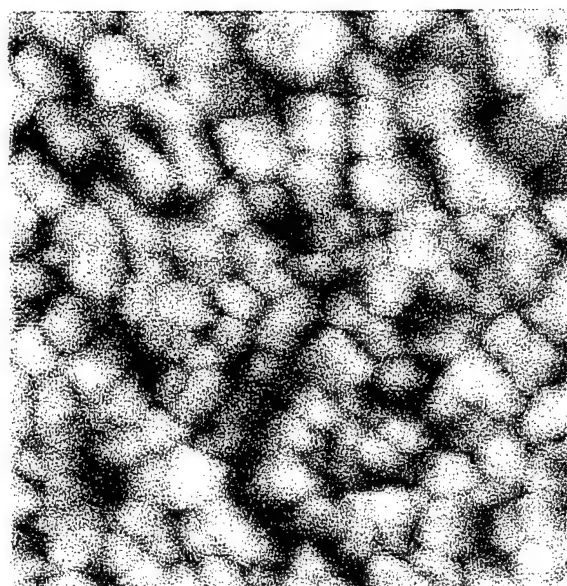


Fig. 5. $1 \times 1 \mu\text{m}^2$ tapping mode AFM image of a 100nm PZT film deposited with an $(A/B)_g = 0.83$.

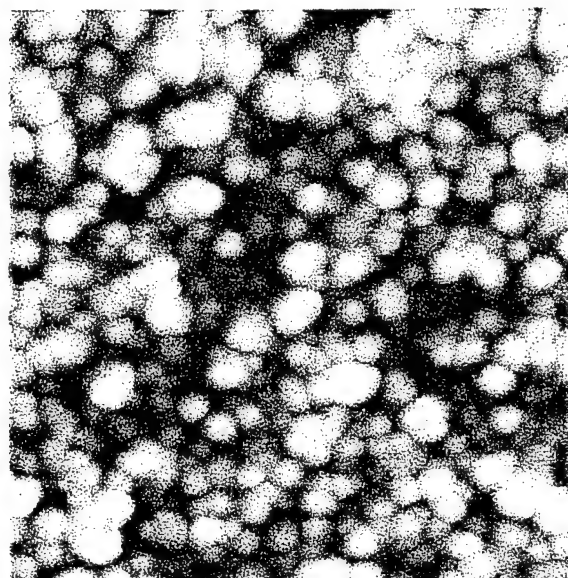


Fig. 6. $1 \times 1 \mu\text{m}^2$ tapping mode AFM image of a 100nm PZT film deposited with an $(A/B)_g = 0.63$.

Table 2. Summary of AFM data for PZT/Ir/MgO layers. Film thickness is nominally 100 nm.

| $(A/B)_g$ | $(A/B)_I$ | RMS roughness (nm) | Grain size (nm) |
|-----------|-----------|--------------------|-----------------|
| 0.631 | 0.59 | 6.6 | 67 |
| 0.731 | 0.97 | 8.4 | 72 |
| 0.831 | 1.01 | 7.8 | 86 |
| 1.031 | 1.08 | 7.7 | 91 |

X-ray diffraction analysis revealed single perovskite phase for films deposited with $(A/B)_g \geq 0.83$. For $(A/B)_g < 0.83$, an additional peak was observed at $2\theta = 29.9^\circ$. The intensity of this peak decreased with increasing $(A/B)_g$ and was attributed to formation of the pyrochlore phase under lead-deficient deposition conditions.

PZT films on Ir/MgO displayed dominant (001) and (101) PZT orientations; furthermore, the (001)/(101) ratio of PZT peak intensities increased with increased $(A/B)_g$, i.e. oriented toward the tetragonal c-axis with a c-axis lattice constant of 0.406 nm. No appreciable (111) PZT texture was observed on Ir/MgO. X-ray diffraction of the as-received substrates revealed principally (111) oriented Ir; however, a considerable (200) Ir peak was present.

The best electrical properties were found for films with $(A/B)_g$ just above the knee in the curve shown in Fig. 1. Films with much higher or much lower $(A/B)_g$ were electrically shorted. Fig. 7 shows a hysteresis curve for a 150 nm thick film deposited at $(A/B)_g = 0.93$. For 3V operation, the remanent polarization ($2P_r$) and coercive voltage (V_c) were measured to be $85 \mu\text{C}/\text{cm}^2$ and 0.77 V, respectively. This high value of remanent polarization was likely due to the strong preferred (001) orientation and the high degree of crystallization obtained on the Ir substrate.

IV. SUMMARY

Crystalline perovskite PZT thin films were deposited on Ir/MgO substrates by low pressure MOCVD at 550°C using variable gas-phase lead concentrations. The as-deposited films were dense, smooth, and exhibited increased faceting and larger grain size with higher $(A/B)_g$. For gas-phase

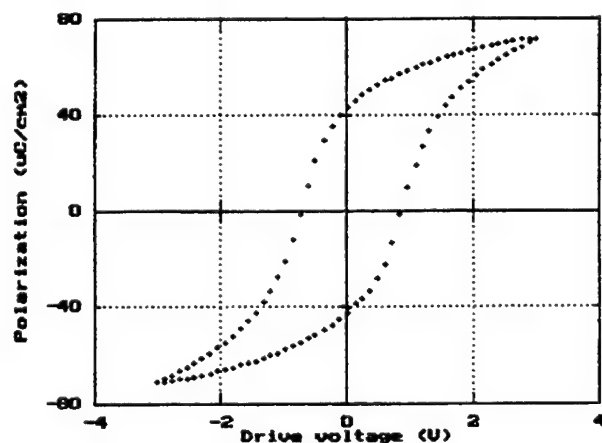


Fig. 7. Hysteresis loop from a 150 nm film deposited at $(A/B)_g = 0.93$. Remanent polarization ($2P_r$) is $85 \mu\text{C}/\text{cm}^2$ and coercive voltage (V_c) is 0.77 V.

compositions in the range $0.93 < (A/B)_g < 1.53$, film composition was controlled by a self-regulating mechanism wherein the formation of PZT and the desorption of PbO competed to produce films with a composition in the range $1.10 < (A/B)_t < 1.15$. Pt/PZT/Ir capacitors possessed $2P_r$ of $85 \mu\text{C}/\text{cm}^2$ and a coercive voltage of 0.77 V for 3V operation. Further optimization of process conditions is necessary to determine the utility and other considerations regarding the self-correcting composition regime.

ACKNOWLEDGEMENTS

We would like to acknowledge extremely helpful discussions with Jeff Roeder, as well as the efforts of Norman James and Scott Summerfelt at Texas Instruments, who deposited the bottom electrodes used in this study.

REFERENCES

- [1] K. Koyama, T. Sakuma, S. Yamamichi, H. Watanabe, H. Aoki, S. Ohya, Y. Miyasaka, T., Kikkawa, "A stacked capacitor with $(\text{Ba,Sr})\text{TiO}_3$ for 256Mb DRAM," 1991 IEDM Proceedings, 823-826.
- [2] L.H. Parker, A.F. Tasch, "Ferroelectric materials for 64 Mb and 256 Mb DRAMs," IEEE Circuits and Devices Magazine, Vol. 17 (1990).
- [3] J. Evans, R. Womack, "An experimental 512-bit nonvolatile memory with ferroelectric storage cell," J. of Solid State Circuits, Vol. 23, No. 5 (1988) 1171-1175.
- [4] M. Shimizu, M. Sugiyama, H. Fujisawa, T. Hamano, T. Shiosaki, and K. Matsushige, J. Cryst. Growth 145, 226 (1994).
- [5] H. Miki, Y. Ohji, "Uniform ultra-thin $\text{Pb}(\text{Zr,Ti})\text{O}_3$ films formed by metal-organic chemical vapor deposition and their ferroelectric characteristics" Jap. J. Appl. Phys., Vol 33 (1994) 5143-5146.
- [6] G.J.M. Dormans, M. DeKeijser, and P.J. vanVeldhoven, "Ferroelectric PbZrTiO_3 thin films grown by organometallic chemical vapor deposition", in Ferroelectric Thin Films, edited by E.R. Myers and A.I. Kingon, Mater. Res. Soc. Proc. Vol. 243, Pittsburgh, PA, 1992) pp. 203-211.
- [7] Y. Sakashita, T. Ono, H. Segawa, K. Tominaga, M. Okada, "Preparation and properties of MOCVD-deposited PZT thin films", J. Appl. Phys., Vol. 69, No. 12, (1991) 8352-8357.
- [8] M. De Keijser, P. Van Veldhoven and G. Dormans, Mat. Res. Symp. Proc., Vol. 310 (1993) p223-234.
- [9] J. Roeder, B.A. Vaartstra, P.C. Van Buskirk, H.R. Beratan, "Liquid delivery MOCVD of ferroelectric PZT," Mat. Res. Symp. Proc., Vol. 415 (1996) p123-128.
- [10] S. Bilodeau, P. Van Buskirk, R. Carl, P. Kirilin, S. Streiffer, C. Basceri, A. Kingon, "Dielectric properties of very thin films of $\text{Ba}_{0.70}\text{Sr}_{0.30}\text{TiO}_3$," Proc. of the 1996 Int. Conf. On Solid State Devices and Materials, 797-799.
- [11] K.H. Hartl and H. Rau, Solid State Comm., 7, 41 (1969).

Comparative Assessment of Electronic Ceramics R&D in the U.S. and Japan

Scott L. Swartz

NexTech Materials, Ltd.
720-I Lakeview Plaza Blvd.
Worthington, OH 43085

Thomas R. Shrout

Materials Research Laboratory
Pennsylvania State University
University Park, PA 16802

Tadashi Takenaka

Science University of Tokyo
Noda, Chiba-ken
278 JAPAN

Abstract - An assessment of ongoing research and development in the U.S. and Japan was conducted to identify and characterize future development areas in the field of electronic ceramics. The three topics covered by this study included: dielectric ceramics for capacitors and microwave filters; piezoelectric ceramics for transducers and actuators; and ferroelectric thin films for semiconductor memories and microactuators. Information was obtained by an analysis of the U.S. patent literature from January of 1990 through August of 1996, and by fax and e-mail responses to questionnaires sent to Japanese technologists. The results of this assessment recently were published in the American Ceramic Society Bulletin [1-2]. In this paper, the results of the patent search on the topic of ferroelectric thin films are presented, with information obtained from the survey of Japanese technologists used to supplement the discussion.

I. INTRODUCTION

The field of electronic ceramics encompasses a broad range of existing device markets and future applications currently under development. For the most part, electronic ceramic markets are dominated by U.S. and Japanese companies, with a small but significant European market presence and a growing presence by Far Eastern companies (e.g., Korea, Singapore, China). This study was conducted to obtain a current perspective and to assess future directions of U.S. and Japanese research and development in the field of electronic ceramics. This paper summarizes the results of this study, with a focus on the topic of ferroelectric thin films. Information for this survey was obtained as follows:

- A keyword search of the U.S. patent literature was performed, covering the time period of January 1990 through August 1996. Abstracts of identified patents were obtained and reviewed. Patents on ferroelectric films were classified by the nature of the invention (e.g., material or process), by the application type (e.g., semiconductor memory or microactuator), and by the assignee organization (e.g., large or small company, government, university, etc.). Trends in patent activities were identified based on these classifications.

- Questionnaires were sent distributed by fax to over 400 Japanese technologists active in electronic ceramics research, development, and manufacturing, and 61 responses were obtained via fax and e-mail. The questionnaires addressed the following topics: most significant developments during the previous five years; important developments and applications anticipated to occur within the next five years; development activities expected to have decreasing importance in the next five years; economic and environmental factors that will impact future developments; and key requirements for commercializing new products. Analysis of the questionnaire responses provided an important perspective on how Japanese technologists view the past and look toward the future.

Information obtained above was supplemented by recent review articles, by information presented at several workshops and technical symposia dedicated to the field of electronic ceramics, and by discussions with leading U.S. technologists in the field.

For the purposes of this survey, ferroelectric thin films were defined as *inorganic* ferroelectric films with thicknesses less than 10 microns. Liquid-crystalline and other polymeric thin-film ferroelectric materials for displays and other applications are subjects of intense R&D activity, but these materials were not included in this assessment. The topic of ferroelectric thin films is in its relative infancy, when compared to other electronic ceramic topics. Large-scale research and development efforts were initiated in the late 1980's, when improved thin-film deposition techniques became available and ferroelectric films were recognized as an enabling technology for developing high-capacity nonvolatile memories (NVMs) and dynamic random-access memories (DRAMs). Although most of the current development focuses on semiconductor memories, a variety of other applications are being pursued, including microactuators, pyroelectric detectors, and optical waveguide devices.

II. REVIEW OF U.S. PATENTS (1990-1996)

A total of 255 U.S. patents were found within the topic of ferroelectric thin films, and a breakdown of these patents by calendar year is provided in Figure 1. U.S. organizations received about 54 percent, and Japanese organizations received 40 percent of the total number. Patent activity increased steadily from 1992 through 1996, which is consistent with the explosion of research activity in ferroelectric thin films that began in the late 1980's. Results of the patent review are summarized by the following identified trends:

- (1) About 98 percent of Japanese-assigned patents were assigned to large Japanese companies. However, only 44 percent of U.S.-assigned patents were assigned to large U.S. manufacturing firms, and 33 percent were assigned to small businesses. The remaining patents were distributed among universities, the U.S. government, and contract research organizations.
- (2) The pre-competitive nature of ferroelectric thin-film technology has fostered several alliances between U.S. and Japanese organizations. Virginia Tech has assigned many of their patents to Sharp; and Symetrix and Olympus Optical are jointly developing and patenting ferroelectric thin-film technology. Other examples of active U.S.-Japanese alliances include Ramtron International, Fuji-Xerox, and Texas Instruments-Japan.

- (3) The semiconductor industry is clearly the market-driving force behind development of ferroelectric thin-film technology. About 80 percent of the patents were directly related to semiconductor memories (NVMs and DRAMs), or to semiconductor fabrication processes for integrating ferroelectric films on silicon. Most of the remaining patents were specific to thin-film deposition processes for semiconductor substrates, or to applications involving ferroelectric films deposited onto semiconductors. The ten most prolific Japanese developers of ferroelectric thin-film technology, accounting for 78 percent of Japanese-assigned patents, are manufacturers of semiconductor components and/or electronic systems.
- (4) It is difficult to make precise conclusions on deposition methods, because most of the identified patents were non-specific with respect to the thin-film deposition processes. However, out of the 25 process-specific patents assigned to U.S. organizations, nine were assigned to universities, eight to small businesses, three to contract research organizations, and only five were assigned to large companies. Relatively new thin-film deposition processes (e.g., sol-gel, MOCVD, and laser-deposition) were first patented by U.S. organizations, before any process patents were received by Japanese firms.

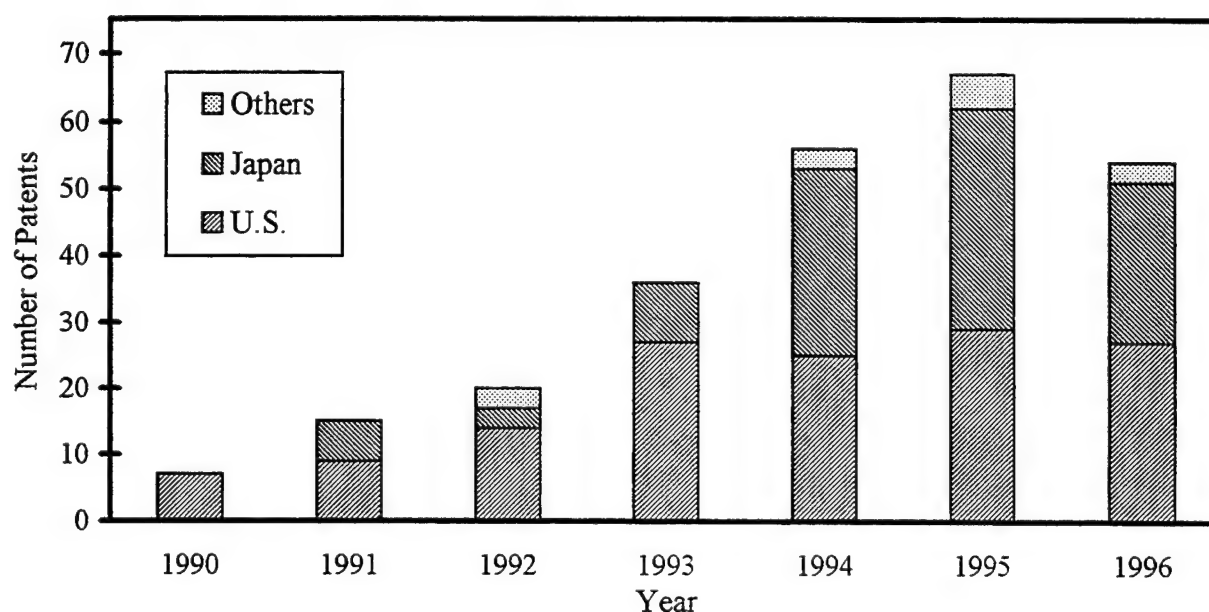


Fig. 1. Total number of U.S. patents on ferroelectric films assigned to organizations in the United States, Japan, and other countries, from January of 1990 through August of 1996.

- (5) Several patents, assigned both to U.S. and Japanese organizations, addressed issues related to integrating ferroelectric thin films on semiconductor substrates. Many of these patents described interlayers of various materials to prevent diffusion of film constituents into the semiconductor. In some patents, interlayer films were described that served as templates for improving crystallinity and/or promoting epitaxial growth of subsequently deposited ferroelectric films. Several other patents described novel electrode materials that resulted in reduced fatigue or lower leakage currents in semiconductor memories.

III. DISCUSSION OF RESULTS

Information obtained during this assessment provided a definite contrast between development trends identified by the patent review and the expectations of Japanese scientists on future R&D directions. Of course, there is a significant lag time between the conception of an invention and publication of a patent, so that the patent review process, by its nature, tends to monitor development activities that are at least two years old. However, there usually is a significant amount of development time (typically 3-5 years or longer) before a patented invention reaches commercial implementation. For this reason, one may have expected that the two assessment approaches would provide complementary information. Within this context, the assessment results are discussed below.

The topic of ferroelectric thin films has created considerable excitement within the electronic ceramics community, with R&D beginning in earnest during the late 1980's and continuing throughout the present decade. The potential advantages of using ferroelectric films in semiconductor memories have been known for some time, but suitable deposition techniques for multi-component oxide ferroelectrics have only recently become available. Many of these deposition methods were developed for high-temperature superconductors, and then applied to ferroelectric materials as government funding for thin-film superconductors diminished and increased funding for thin-film ferroelectrics became available.

In the U.S., a considerable amount of the initial ferroelectric thin-film R&D has been supported by government funding and conducted at universities, small businesses, and government laboratories. In the late 1980's, U.S. government support was provided for the development of nonvolatile memories, with programs led by Raytheon and McDonnell Douglas. However, these heavily funded development programs failed to produce a commercial memory product. Current U.S. developers of nonvolatile memories include two small companies,

Ramtron and Symetrix, both of which are collaborating with several Japanese companies. Motorola and National Semiconductor appear to be funding their own NVM development work, based on patent search and their contributions to recent technical symposia. Beginning in 1992, the U.S. government shifted its priorities to the development of DRAMs, and work continues under a DoD-supported consortium of U.S. DRAM manufacturers (Micron, IBM, and Texas Instruments), with support provided by North Carolina State University, Advanced Technology Materials, and Varian. Motorola is funding its own DRAM development work. In recent years, the financial responsibility for much of the memory development work has been transferred from the U.S. government to semiconductor manufacturers, with a corresponding reduction in government support of R&D at universities and small businesses.

In Japan, industry has funded essentially all of the ferroelectric thin-film R&D to date, and this support has increased substantially in recent years. Japan's ferroelectric thin-film technology development work has received little direct support from the Japanese government, and there has been only limited Japanese university involvement in ferroelectric thin-film research (probably due to the high capital costs for semiconductor processing equipment). Similar to the U.S., there is a strong interest in ferroelectric thin-film research by large industrial companies in Japan. Japanese companies involved with NVM development include Rohm, Toshiba, Hitachi, Fujitsu, Matsushita Electronics, and Olympus Optical. Japanese DRAM developers include Mitsubishi Electric, NEC, Toshiba, and Hitachi. With the considerable investment that will be required by both U.S. and Japanese industry to sustain the development of semiconductor memories and other ferroelectric thin-film devices, the future growth of this R&D topic will be contingent on steady technical progress toward commercial applications.

The survey indicated Japanese confidence that nonvolatile semiconductor memories will be successfully developed within the next decade, and that development of other thin-film applications, such as microactuators, will follow thereafter. Many of the technical hurdles to commercialization of ferroelectric memories have been addressed, including deposition methods for high quality thin films, interlayer and electrode materials, and integration onto semiconductors. However, a significant amount of development is still required to assure success.

A current issue with PZT-based nonvolatile memories is fatigue after numerous polarization reversal cycles. However, recent reports indicate successful fabrication of PZT films that withstand up to 10^{13} cycles, which is sufficient for most memory applications. An important

development, achieved at Symetrix, was the identification of bismuth-layer-structured $\text{SrBi}_2\text{Ta}_2\text{O}_9$ (SBT) as a ferroelectric thin-film material with fatigueless polarization reversal properties. This patent alone led to subsequent development and several additional patents on deposition methods and semiconductor integration methods for SBT. However, SBT still requires very high deposition temperatures ($T \geq 750^\circ\text{C}$), which are incompatible with successful integration into high capacity memories. Development work to be conducted over the next few years will determine which ferroelectric material (PZT or SBT) will be successfully incorporated into commercial memories.

The ongoing development of deposition processes and integration methods for NVMs and DRAMs is synergistic with the future development of other semiconductor-based devices, including microactuators, surface acoustic wave filters, frequency-agile microwave filters, and optical waveguides. For example, semiconductor integration methods being developed for PZT may eventually be applied to microactuators and surface acoustic wave devices. Also, deposition technology being developed for $(\text{Ba,Sr})\text{TiO}_3$ may be applied to frequency agile microwave filters. The key issue to be addressed with these newer applications is that relatively thick PZT and $(\text{Ba,Sr})\text{TiO}_3$ films will be needed. Currently, there are no inexpensive thick-film fabrication methods available that provide the required quality, although this is an area of considerable ongoing R&D.

IV. SUMMARY AND CONCLUSIONS

This study was conducted to obtain a future perspective of electronic ceramics R&D in the U.S. and Japan. The recent patent literature was reviewed, and a questionnaire survey of Japanese technologists in the field of electronic ceramics was conducted. Based on the results of this assessment, as presented and discussed above, the following conclusions are offered:

- (1) Based on the patent review, there are substantial differences in the structure of research and development of electronic ceramics between the U.S. and Japan. In the U.S., a large share of the R&D is funded by the U.S. government and is focused on specific needs of the U.S. military. In Japan, electronic ceramics research is almost entirely supported by large industrial companies and targeted toward specific products. In the U.S., universities, small businesses, and government laboratories all are active patenters of electronic ceramic materials technology. In Japan, patents are assigned almost exclusively to industrial companies.
- (2) Successful development of high capacity (>4 Mbyte) semiconductor memories is expected within the next several years. The key technical issue is integration, because the relatively high processing temperatures of ferroelectric films ($T \geq 650^\circ\text{C}$) must not adversely affect underlying semiconductor circuitry. Current ferroelectric nonvolatile memory materials include $\text{Pb}(\text{Zr,Ti})\text{O}_3$ and $\text{SrBi}_2\text{Ta}_2\text{O}_9$, each having their own development hurdles. The primary ferroelectric thin-film material for DRAMs is $(\text{Ba,Sr})\text{TiO}_3$. For this application, near-term success is critical, so that the technology can be implemented before competing high-capacity DRAM designs are selected.
- (3) The successful commercialization of semiconductor memories is expected to be followed by the development and commercialization of ferroelectric films for microactuators and related micro-electro-mechanical systems. The key development issue is the development of fabrication processes for relatively thick ($t > 5\mu\text{m}$) ferroelectric films with high piezoelectric activity (e.g., PZT), and semiconductor integration processes for these thick films.
- (4) The development time for electronic ceramic products is expected to become shorter, and the resources available for electronic ceramics R&D are expected to be reduced. This will require substantial focusing of R&D resources toward specific product targets. An increased emphasis on marketing and market research will be required, so that limited R&D resources can be matched to market needs.

ACKNOWLEDGMENTS

Funding for this study was provided by the Air Force Office of Scientific Research (Asian Office of Aerospace R&D). The authors are grateful to Dr. Shiro Fujishiro of AFOSR for his encouragement throughout the project. The authors also thank all of the Japanese scientists that responded to the questionnaire. Useful insights also were provided by Raj Gururaja of Hewlett Packard, Angus Kingon of North Carolina State University, and Clive Randall of Penn State University.

REFERENCES

- [1] S.L. Swartz, T.R. Shrout, and T. Takenaka, "Electronic Ceramics R&D in the U.S., Japan, Part I: Patent History", *Am. Ceram. Soc. Bull.*, vol. 76, no. 7, pp. 59-65, July 1997.
- [2] S.L. Swartz, T.R. Shrout, and T. Takenaka, "Electronic Ceramics R&D in the U.S., Japan, Part II: Questionnaire", *Am. Ceram. Soc. Bull.*, vol. 76, pp. 51-55, August 1997.

Dielectric Behavior of (Ba,Sr)TiO₃ Thin Films and its Correlation with Oxygen Defect Density

Yukio Fukuda and Katsuhiro Aoki

Texas Instruments Tsukuba R & D Center, 17 Miyukigaoka, Tsukuba, Ibaraki 305, Japan

Hajime Haneda and Isao Sakaguchi

National Institute for Research in Inorganic Materials, 1-1 Namiki, Tsukuba, Ibaraki 305, Japan

Ken Numata and Akitoshi Nishimura

Texas Instruments Memory R & D Center, 13588 New Central Expressway, Dallas, Texas 75243

ABSTRACT

This paper describes the dielectric properties of (Ba,Sr)TiO₃ (BST) thin films deposited by rf magnetron sputtering, focusing on their correlation with the oxygen defect density in the films. The dielectric behavior specific to the BST films can be explained by considering the influence of the dielectric relaxation phenomenon following a power law dependence on time in the time-domain measurement and on frequency in the frequency-domain measurement. From electrical comparison of the films with and without post-annealing in oxygen ambient, it is derived that charging/discharging electrons at oxygen vacancies in the interfacial Schottky depletion layers, whose widths are modulated by applied voltage, are responsible for the observed dielectric behavior. Preliminary results of the oxygen vacancy density measurement using a gas-solid oxygen isotopic exchange reaction showed that the higher the post-annealing temperature is, the lower the oxygen vacancy concentration is.

INTRODUCTION

(Ba,Sr)TiO₃ (BST) thin films are very promising high dielectric constant materials for use in advanced dynamic random access memories and integrated decoupling capacitors. Regarding their device applications, the electrical properties such as low leakage current, fast dielectric response, low dielectric loss and long life time are especially important from the

quality and reliability standpoints.

BST thin films show remarkable dielectric relaxation phenomenon which greatly affects the dielectric properties of the films[1]. This paper describes the dielectric behavior of BST thin films deposited by rf magnetron sputtering and its correlation with the oxygen defect density in the films.

EXPERIMENT

BST films with various thickness were deposited at a substrate temperature of 530°C by sputtering ceramic BST target with Ba/Sr=50/50. The sputtering ambient was 82%Ar + 18%O₂ mixture with a total pressure of 0.55 Pa. The substrates used were Pt(100 nm)/SiO₂(100 nm)/Si(100) and SrTiO₃(100). For electrical characterizations, Pt top electrodes were deposited through a metal shadow mask with an area of 8×10^{-4} cm² by electron-beam evaporation without substrate heating. Some capacitors were then post-annealed in oxygen ambient at various temperatures. The electrical properties of the as-deposited and post-annealed capacitors were closely compared using HP-4284A LCR meter and HP-4142B semiconductor parameter analyzer. Electrical measurements were performed at 25°C.

The oxygen self-diffusion was investigated by a gas-solid isotopic exchange technique using ¹⁸O as a tracer[2]. As-deposited and post-annealed BST films were diffusion-annealed in ¹⁸O₂ at 1.3×10^4 Pa in a high-frequency induction furnace.

The depth profiles were measured by a secondary ion mass-spectroscopy (SIMS, CAMECA, IMS4f). The cesium positive ions were used as primary ions with an acceleration voltage of 10 kV and an ion current of 6 nA. To maintain a constant electric field at the sample surface, gold thin films were sputter-deposited on the sample surfaces. A normal incident electron gun was used to eliminate excess electric charge. The depth calibration was performed using a Dektak-3030 surface profiler.

RESULTS AND DISCUSSION

Figure 1 shows current density versus time (J-t) characteristics of the as-deposited and post-annealed Pt/BST/Pt capacitors with a dielectric thickness of 25 nm when a step-function voltage of 1 V is applied to the top Pt electrode. The post-annealing condition was at 500°C for 30 min. The result indicates that both characteristics can be expressed by a power-law relationship of $J \propto t^{-n}$. The index values of the as-deposited and post-annealed capacitors are 0.89 and 0.94, respectively. Note that the current density of the post-annealed capacitor is about one order of magnitude lower than that of the as-deposited capacitor.

Figure 2 shows frequency dependence of the capacitance of the capacitors shown in Fig.1 for the frequency range from 20 Hz to 400 kHz measured with an oscillation voltage of 30 mV. It is shown that the capacitance of the as-deposited capacitor decreases drastically with increase in the frequency. On the other hand, the capacitance of the post-annealed capacitor is almost constant independent of the frequency for the measured frequency range. Supposing that the observed frequency dependence of the capacitance were attributed to the dielectric relaxation [3], the frequency dependence of the capacitance $C(f)$ could be expressed by $C(\infty) + C(0) \times f^{-n-1}$, where

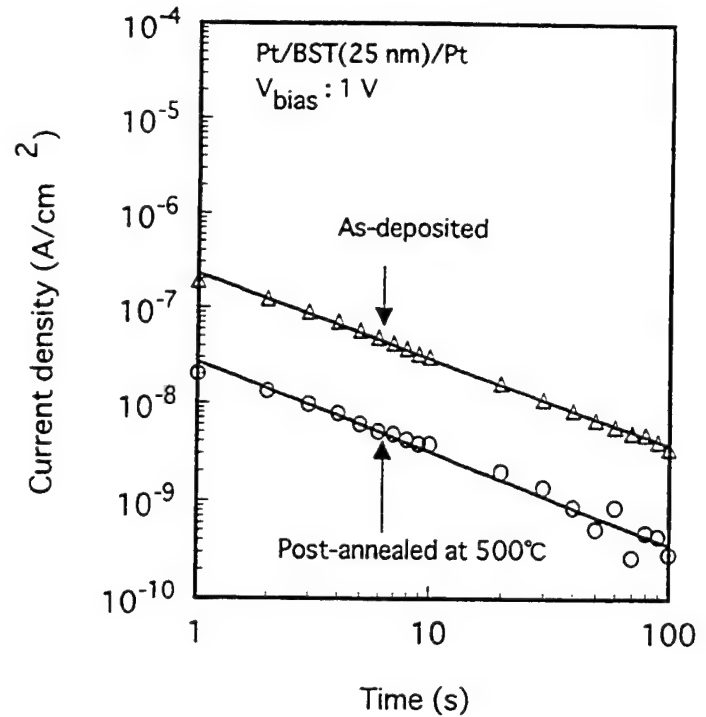


Fig.1 J-t characteristics of as-deposited and post-annealed Pt/BST(25 nm)/Pt capacitors.

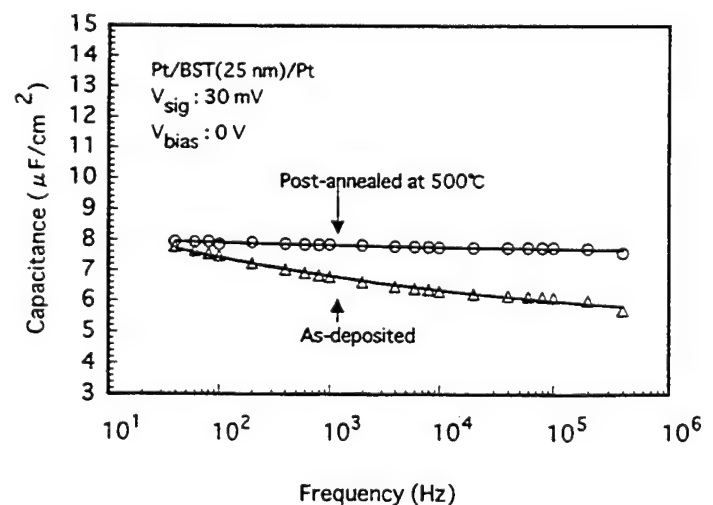


Fig.2 C-f characteristics of as-deposited and post-annealed Pt/BST(25 nm)/Pt capacitors.

$C(\infty)$ denotes the capacitance which can respond to very high frequency, $C(0)$ the capacitance due to the dielectric relaxation and f the frequency. By fitting this equation to the experimental results, using the index values obtained in Fig. 1, we obtained that $C(f)$ of the as-deposited capacitor is $4.5 + 4.7 \times f^{0.11}$ ($\mu\text{F}/\text{cm}^2$) and that of the post-annealed capacitor $7.3 + 0.87 \times f^{0.06}$ ($\mu\text{F}/\text{cm}^2$). $C(0)$ of the as-deposited capacitor is 5.4 times larger than that of the post-annealed capacitor. Therefore, we can point out that the remarkable frequency dependence of the capacitance observed for the as-deposited capacitor is attributed to the dielectric relaxation and the influence of this phenomenon is dramatically suppressed by the post-annealing. On the other hand, the value of $C(\infty)$ of the post-annealed capacitor is 1.6 times larger than that of the as-deposited capacitor. Since the post-annealing temperature (500°C) is lower than the deposition temperature (530°C), this increase in $C(\infty)$ by the post-annealing cannot be attributed to the increase in the grain size of BST film.

Figure 3 shows the thickness dependence of $C(0)$ and $C(\infty)$ obtained from the capacitors post-annealed at 500°C for 30 min. The result shows that $C(\infty)$ increases with decrease in the BST thickness. On the other hand, $C(0)$ is almost constant independent of the thickness. Therefore, we can say that the observed dielectric relaxation is not a bulk-related phenomenon but a two-dimensional one. This result is very important to investigate a physical origin of the dielectric relaxation.

Recently, we studied temperature dependence of the dielectric relaxation current of the BST capacitor and found that its thermal activation energy is 0.3 eV[4]. This relatively small activation energy suggests that the electron is the most likely to be responsible for the observed dielectric relaxation. Therefore, the result

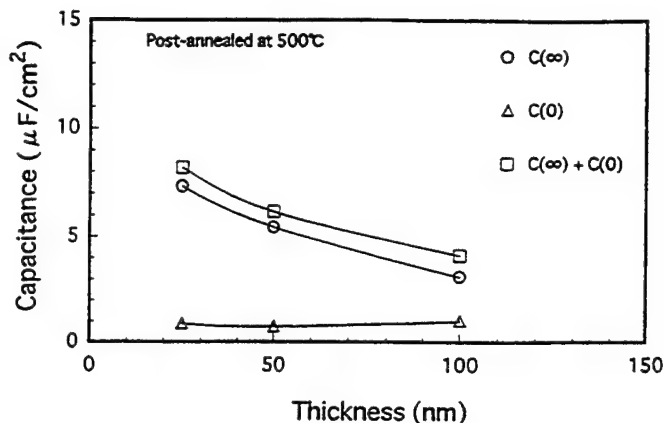


Fig.3 Thickness dependence of $C(0)$ and $C(\infty)$.

shown in Fig.1 can be simply interpreted as that the density of electron responsible for the dielectric relaxation is reduced by the post-annealing. Furthermore, considering that an oxygen vacancy is an electron donor in perovskite-oxide [5,6], the effect of the post-annealing is supposed to compensate such vacancies by introduction of oxygen atoms. To confirm this, we measured the diffusion coefficient of oxygen atom in the BST films which were post-annealed at various temperatures. Since the oxygen vacancy concentration is thought to be proportional to the oxygen diffusion coefficient[7], the difference in the diffusion coefficients results in the relative difference in the oxygen vacancy concentrations. Figure 4 shows the relations between the diffusion coefficient and the post-annealing temperature obtained from the BST films deposited on Pt(100 nm)/SiO₂(100 nm)/Si(100) and SrTiO₃(100) substrates. The result clearly shows that the higher the post-annealing temperature is, the smaller the diffusion coefficient is. The oxygen vacancy concentration of the BST film post-annealed at 500°C is over two orders of magnitude lower than that of the as-deposited film.

As well as the other perovskite-type oxides, the Pt/BST contact forms Schottky

junction at the interfaces [8]. If we apply a step-function voltage in the current-time measurement or an oscillation voltage in the capacitance measurement to the capacitor, the applied voltage mainly drops at a one-sided reversely biased Schottky junction, and as a result, its depletion-layer width is modulated with electrons charging or discharging at oxygen vacancies in the depletion layer. We proposed that these electrons in the voltage-modulated Schottky depletion layer are the origin of the dielectric relaxation[9].

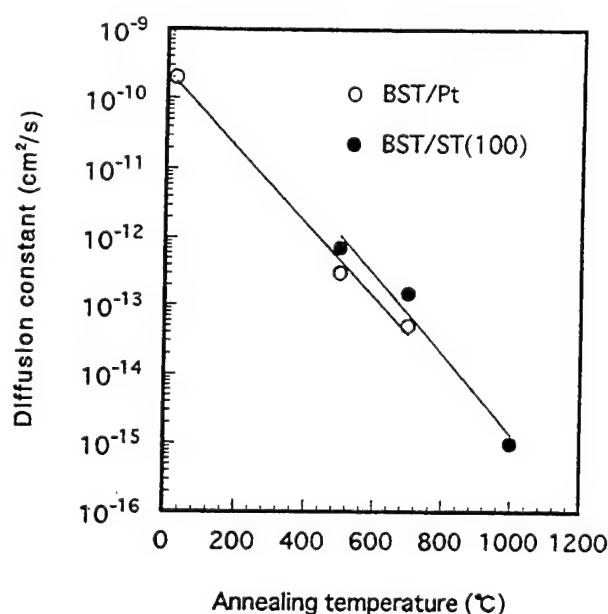


Fig.4 Post-annealing temperature dependence of ^{18}O diffusion coefficient in BST films.

CONCLUSION

We investigated the dielectric properties of $(\text{Ba,Sr})\text{TiO}_3$ (BST) thin films deposited by rf magnetron sputtering. The di-

electric behavior specific to the BST films can be explained by considering the influence of the dielectric relaxation phenomenon. From electrical comparison of the films with and without post-annealing in oxygen ambient, we concluded that charging/discharging electrons at oxygen vacancies in the interfacial Schottky depletion layers are responsible for the observed dielectric behavior. The oxygen vacancy density measurements using an oxygen isotopic exchange reaction showed that the oxygen vacancy concentration in the films is actually reduced by the post-annealing.

REFERENCES

- [1] T. Horikawa, T. Makita, T. Kuroiwa and N. Mikami: *Jpn. J. Appl. Phys.* 34 (1995) 5478.
- [2] T. Izaki, H. Haneda, A. Watanabe, J. Tanaka, S. Shirasaki and K. Tsuji: *J. Ceram. Soc. Jpn.* 101 (1993) 133.
- [3] Y. Inuishi, T. Nakajima, K. Kawabe and M. Ieda, *Yudentai Gensyoron (Dielectric Phenomenology)*, Denki-Gakkai, Ed. Tokyo: Ohmsya, 1973, p. 349.
- [4] Y. Fukuda, K. Numata, K. Aoki and A. Nishimura: *Ext. Abstr. 56th Autumn Meet. Japan Society of Applied Physics*, Kanazawa, 26aZG9.
- [5] D. M. Smyth, M. P. Harmer and P. Peng: *J. Am. Ceram. Soc.* 72 (1989) 2276.
- [6] R. Waser: *J. Am. Ceram. Soc.* 72 (1989) 2234.
- [7] D. Mapother, H. Crooks and R. Mauer: *J. Chem. Phys.* 18 (1950) 1231.
- [8] S. O. Park, C. S. Hwang, H. J. Cho, C. S. Kang, H. K. Kang, S. I. Lee and M. Y. Lee: *Jpn. J. Appl. Phys.* 35 (1996) 1548.
- [9] Y. Fukuda, K. Numata, K. Aoki and A. Nishimura: *Jpn. J. Appl. Physics*, 35 (1996) 5178.

Preparation of BaTiO₃ and SrTiO₃ Thin Films for Communications Applications

Robert W. Schwartz

Clemson University

Department of Ceramic and Materials Engineering

Olin Hall

Clemson, SC 29634

Paul G. Clem and Duane Dimos

Sandia National Laboratories

Materials and Process Sciences Center

Albuquerque, NM 87185-1349

Abstract – Ferroelectric thin films are currently under investigation for a number of electronic applications. In particular, because their dielectric constant is voltage-dependent, barium titanate, strontium titanate, and barium strontium titanate thin films are of interest for communication applications such as resonators, filters, and phase shifters. However, for optimum device performance, the films must display maximum tunability (i.e., the change in capacitance with field) and minimum dielectric loss.

In this paper, the fabrication of BaTiO₃ and SrTiO₃ films by a solution deposition route will be considered. Processing strategies that allow for tailoring of thin film microstructure and orientation, as well as optimization of dielectric and tuning properties will be discussed. BaTiO₃ films with dielectric constants of 1200 and losses as low as 0.005 have been prepared. The best tunabilities thus far obtained have exceeded 40%. The tuning performance of the solution-derived films is comparable to sputter-deposited films.

I. INTRODUCTION

Perovskite thin films are currently under development for a number of electronic applications. Uses being considered include capacitors [1], DRAMs (Dynamic Random Access Memories), pyroelectric imaging arrays [2], microsensors [3], smart cards [4], and microwave devices [5]. Due to the rapid growth of the telecommunications industry, the development of microwave components, in particular, voltage tunable devices such as resonators, filters, and phase shifters has received considerable attention. For these components, it is important to fabricate devices that demonstrate maximum tunability (i.e., the change in capacitance with applied dc bias) and minimum dielectric loss [5]. Tunability (tuning) is defined by the change in capacitance with field according to:

$$\% \text{tunability} = \frac{(C_{\max} - C_{\min})}{C_{\max}} \quad (1)$$

where C_{\max} is the maximum capacitance and C_{\min} is the minimum capacitance for the voltage range under investigation. Consideration of tuning and loss tangent lead to the definition of a useful figure of merit (FOM) for film performance in voltage-tunable dielectrics, which is given by:

$$\text{FOM} = \frac{\% \text{tunability}}{\tan \delta} \quad (2)$$

where $\tan \delta$ is the dielectric loss in percent.

For the manufacture of miniaturized telecommunication devices, thin film dielectrics offer an attractive possibility. A variety of deposition techniques, including sputtering, pulsed laser deposition (PLD), chemical vapor deposition (CVD), and chemical solution deposition (CSD) have been studied for the fabrication of BaTiO₃ and SrTiO₃ films. However, it has frequently been observed that in the preparation of films of these materials, the dielectric properties of the films do not compare favorably to the reported properties of the bulk materials of the same composition [6-8]. For example, lower room temperature dielectric constants (200-300) and higher dielectric losses (2-14%) have been reported. One reason typically cited for the comparatively poor properties of the films is the small grain sizes that are obtained, which tend to suppress the ferroelectric response of the films. These losses are significant in decreasing the FOM of the films, making them less attractive for device development. For device-quality materials, films with lower losses and higher dielectric constants are required.

To improve the voltage-tunability of the films we have developed a number of film processing strategies for our solution-derived films. The methodologies we have investigated are based on consideration of the kinetics and thermodynamics of the processes which govern the phase transformation of the as-deposited film into the crystalline perovskite structure. In the present study, we report on a number of film fabrication and heat treatment strategies to improve the dielectric and voltage-tunability properties of solution derived thin films.

II. EXPERIMENTAL PROCEDURE

A. Solution synthesis and film fabrication

The barium and strontium titanate thin films of the present study were prepared by a chelate solution deposition approach based on a method previously used for the fabrication of lead zirconate titanate (PZT) thin films [9]. Barium or strontium acetate (Aldrich Chemical Company, Inc.; Milwaukee, WI) was dissolved in purified acetic acid (Aldrich Chemical Company, Inc.; Milwaukee, WI) at room temperature with stirring. The concentration of barium or strontium in this solution was 0.6 M. Following dissolution, titanium butoxide was added, and solution preparation was completed by dilution to 0.3 M with purified methanol (Aldrich Chemical Company, Inc.; Milwaukee, WI). For selected films, slight excesses of Ti were employed to promote grain growth. Barium titanate solutions were, in general, stable for 1 to 2 days following preparation, after which BaTi_2O_5 and TiO_2 (trace) were observed to precipitate [10]. The precipitate was identified by x-ray diffraction following filtration.

Films were fabricated onto three types of substrates: platinum-coated silicon wafers (Pt/Ti/SiO₂/Si) obtained from Silicon Quest International, Santa Clara, CA; polished (100) lanthanum aluminate (LaAlO_3) single crystal substrates from Lucent Technologies; and (100) Pt/(100) LaAlO_3 fabricated in-house. The Si substrates were cleaned by rinsing with filtered methanol and drying at 140°C for 10 minutes prior to deposition. The single crystal substrates were cleaned by rinsing successively in acetone, trichloroethane, and isopropanol, followed by drying in an oven at 140°C for 10 minutes. The "standard" film deposition process was to flood the wafer with the 0.3 M solution and spin off the excess solution at 3000 rpm for 30 seconds. In general, films that were 3 layers thick were deposited. Each layer was pyrolyzed at ~ 300°C for 5 minutes prior to the crystallization anneal and was approximately 90 to 100 nm thick. Although other pyrolysis conditions (250-450°C) were evaluated, no significant variations in film microstructure were observed.

For the preparation of the thinner deposits, which were investigated as "seed" layers and for the preparation of novel microstructures, the BaTiO_3 and SrTiO_3 precursor solutions were diluted to 0.05 - 0.10 M and deposition speeds as high as 6000 rpm were employed.

B. Crystallization heat treatment

As-deposited films were transformed into the perovskite structure by heat treatment in a Lindberg tube furnace; nitrogen, air and oxygen were investigated as heat treatment atmospheres. Films were either inserted directly into the furnace at temperature, or were heated at rates ranging from

20°C/min. to 50°C/min. Heat treatment temperatures from 750 to 1100°C were employed and heat treatment times ranged from 60 to 120 minutes.

C. Film Characterization

The films were characterized by scanning electron microscopy, x-ray diffraction, and measurements of film capacitance, loss and voltage-tunability. Dielectric properties and voltage-tunability were measured in both parallel plate geometry and using an interdigitated electrode structure deposited onto the surface of the film. While dielectric properties were measured at 10 kHz, previous reports have indicated that there is minimal dispersion in the capacitance of these materials up to 10 GHz [11], and thus, capacitance and tunability measured at 10 kHz provide a reasonably good indication of film performance at microwave frequencies.

III. RESULTS AND DISCUSSION

A typical thin film microstructure for BaTiO_3 prepared by the standard solution deposition process described above and heat treated to 750°C is shown in Fig. 1. It may be seen that the film consists of equiaxed grains, approximately 30-50 nm in size. This microstructure is representative of those obtained most frequently by solution deposition and is similar to the results obtained by other investigators [8,12,13].

The dielectric properties for this film are shown in Table I; dielectric constants ranged from 180 to 300 and loss tangents varied from 0.015 to 0.065. These properties are

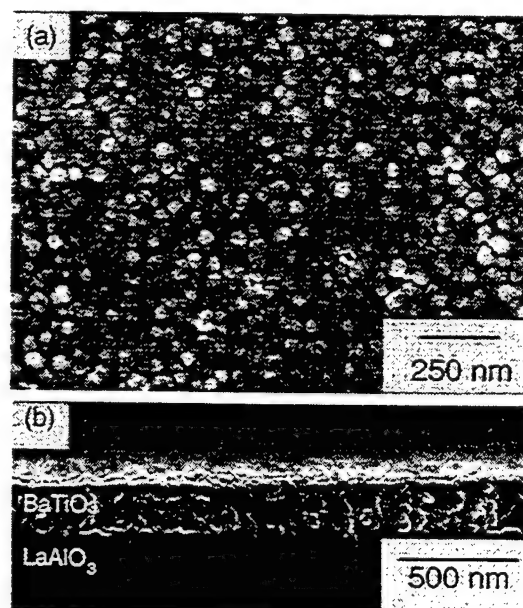


Fig. 1. (a) Surface and (b) cross-sectional SEM photomicrographs of a BaTiO_3 thin film prepared by the standard process and heated to 750°C.

TABLE I
DIELECTRIC PROPERTIES OF BaTiO_3 AND SrTiO_3 THIN FILMS

| Film | k' | $\tan\delta$ | Tuning (%) | FOM |
|---|--------------|------------------|-----------------|-----------------|
| ST/Pt/Si Standard process (750°C) | 210 - 250 | 0.025 - 0.060 | Not measured | Not measured |
| BT/Pt/Si ^a Standard process (750°C) | 180 - 300 | 0.015 - 0.065 | Not measured | Not measured |
| BT/LAO ^a Standard process (750°C) | 280 | 0.038 | 6 | < 2 |
| BT/LAO ^a Standard process (1100°C) | 1200 | 0.005 | 21 | 42 |
| BT/PT/Pt-Si ^b BT on PT seed layer (750°C) | 530 | 0.015 | 40 | 27 |
| BT/Pt-Si ^b 12-layer Columnar microstructure (750°C) | 380 | 0.011 | 37 | 33 |
| BT/BT/Pt/LAO ^b BT on BT seed layer (900°C) | 495 | 0.007 | 47 | 67 |

^a Tuning and dielectric properties measured with interdigitated electrodes on film surface.

^b Tuning and dielectric properties measured with parallel plate geometry; 5 volts applied.

similar to those reported previously by other investigators [6-8]. For strontium titanate films prepared by the same process, dielectric constants from 210 to 250 and loss tangents from 0.025 to 0.060 were measured. These results were obtained in a parallel plate geometry.

The tunability of the equiaxed polycrystalline BaTiO_3 film prepared on LaAlO_3 by the standard process and heated to 750°C is also reported in Table I. Tuning (and loss) characteristics of the film were measured with an interdigitated electrode architecture that has been described previously [5]. The film exhibited only a 6% capacitance tunability at an applied field of 83 kV/cm. The loss factor for the film measured with the interdigitated electrode architecture was 0.04. The comparatively poor properties of the film are believed to be related to the fine (~ 30-50 nm) grain size of the film.

Crystallization of a similar film at 1100°C rather than 750°C significantly improved the tuning behavior and decreased the loss, as shown in Fig. 2 and Table I. A dielectric constant of 900 to 1100 (depending on field) was measured and the loss was ~0.005. The improvement in dielectric and tuning properties may be related to the increase in grain size that results from the higher heat treatment temperature, as shown in Fig. 3.

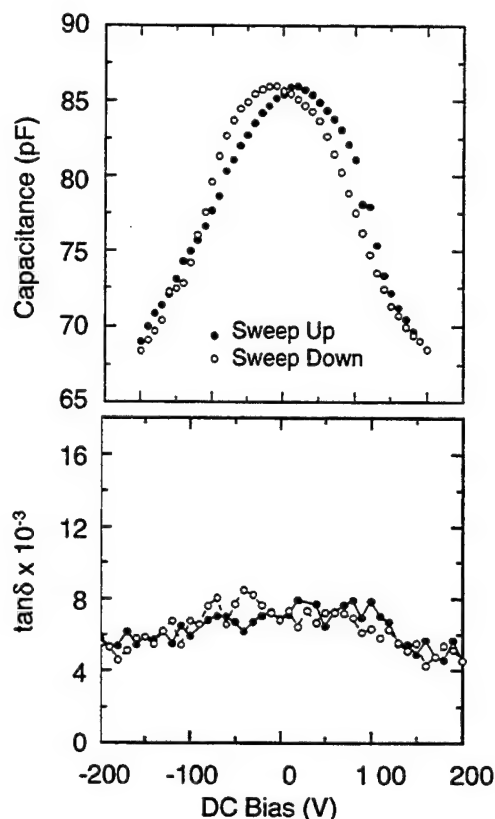


Fig. 2. Capacitance and dielectric loss as a function of field for a BaTiO_3 film on LaAlO_3 prepared by the standard process and heated to 1100°C

While simple film heat treatments at higher temperatures improved the tuning response of the films, alternate film processing strategies were also investigated in an attempt to further improvement in dielectric and tuning performance. One technique evaluated involved the deposition of a thin, 15 - 20 nm "seed" layer prior to the deposition of the 200-300 nm film. For both BaTiO_3 and SrTiO_3 , using this approach, it was possible to fabricate highly (100) oriented films on LaAlO_3 substrates, as shown in Fig. 4. The use of lead titanate as a seed layer for growth of oriented BaTiO_3 was also evaluated. While the degree of orientation of these BaTiO_3 films was typically less than BaTiO_3 prepared on BaTiO_3 seed layers, it was also possible to significantly reduce the film processing temperature to 750°C using this methodology.

The properties of the films prepared using these two approaches are illustrated in Table I. For these films, dielectric and tuning properties were measured with a standard parallel plate geometry with an applied field of 5 volts. While the properties of the films were not quite as good as the 1100°C BT/LAO sample, reasonable dielectric constants, dielectric losses, and capacitance tuning were obtained at these lower processing temperatures.

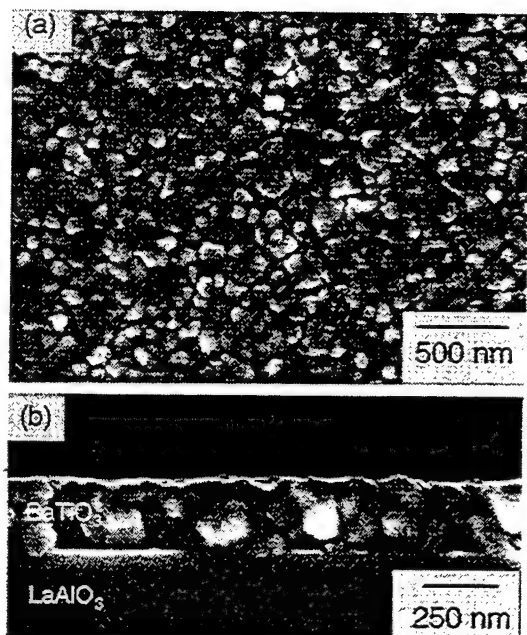


Fig. 3. (a) Surface and (b) cross-sectional SEM photomicrographs of a BaTiO₃ film prepared by the standard process and heated to 1100°C.

The concept of restricting perovskite nucleation to the interface, as in the seeded growth process, was also used to prepare columnar BaTiO₃ on Pt/Si. By reducing the thickness of each layer and using a multilayering approach, it was possible to prepare a film in which each layer that was deposited "templated" off of the underlying layer, resulting in a film with a columnar microstructure. A typical result is shown in Fig. 5 for a 12 layer BaTiO₃ film. The dielectric and tuning properties are shown in Table I. With the applied field varying from 0 to ~330 kV/cm, a capacitance tuning of 37% and a FOM of 67 were observed.

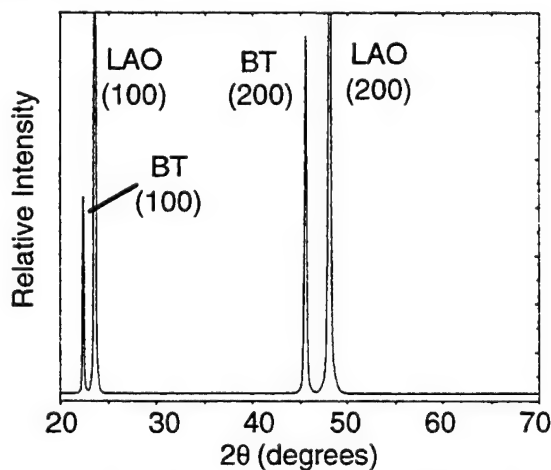


Fig. 4. X-ray diffraction pattern of a BaTiO₃ film on LaAlO₃ prepared by a seeded growth process at 1100°C.

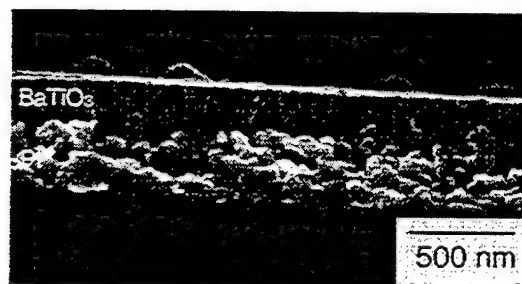


Fig. 5. Cross-sectional SEM photomicrograph of a columnar BaTiO₃ thin film on Pt/Si; 750°C heat treatment.

IV. CONCLUSIONS

By using a solution deposition approach and novel processing strategies (i.e., single crystal oxide substrates and high firing temperatures, seed layers, or multilayering of thin layers), BaTiO₃ thin films with dielectric and tuning properties that are attractive for communication applications were obtained.

ACKNOWLEDGMENT

The portion of this work carried out at Sandia National Laboratories was supported by the US Department of Energy under Contract DE-AC04-94AL85000. Sandia is a multi-program laboratory operated by Sandia Corporation, a Lockheed Martin Company for the US Department of Energy.

REFERENCES

- [1] D. Liu and J. Mevissen, "Thick layer deposition of lead-based dielectrics using diol-based chemical solution approach," *Int. Ferro.* (1997) in press.
- [2] J. A. Ruffner, "Uncooled thin film pyroelectric IR detector with aerogel thermal isolation," U.S. Pat. Appl. (1997).
- [3] D. L. Polla, et al., "Applications of PZT and related thin films in piezoelectric microsensors," *Mat. Res. Soc. Symp. Proc.*, **243**, 55 (1992).
- [4] H. Takasu, "Integrated ferroelectrics as a strategic device," *Int. Ferro.*, **14**, 1 (1997).
- [5] H. N. Al-Shareef, D. Dimos, M. V. Raymond, R. W. Schwartz, and C. H. Mueller, "Tunability and calculation of the dielectric constant of capacitor structures with interdigitated electrodes," *J. Electroceramics*, (1997) in press.
- [6] M. N. Kamalasanan, N. D. Kumar, and S. Chandra, "Structural, Optical, and Dielectric Properties of Sol-Gel Derived SrTiO₃ Thin Films," *J. Appl. Phys.*, **74** (1), 679 (1993).
- [7] T. Hayashi, M. Ohji, K. Hirohara, T. Fukunaga, and H. Miawa, "Preparation and Properties of Ferroelectric BaTiO₃ Thin Films by Sol-Gel Process," *Jpn. J. Appl. Phys.*, **32**, 4092 (1993).
- [8] M. Kuwubara, T. Kuroda, S. Takahashi, and T. Azuma, "Preparation of BaTiO₃ and PbTiO₃ Thin Films on BaPbO₃ Substrates by the Sol-Gel Method and Their Properties," *Mat. Res. Soc. Symp. Proc.*, **271**, 365 (1992).
- [9] R. A. Assink and R. W. Schwartz, "¹H and ¹³C NMR investigations of PZT thin-film precursors solutions," *Chem. Mat.*, **5**, 511 (1993).
- [10] R. W. Schwartz and M. Van Stry, unpublished.
- [11] V. Chivukula, et al., "Dielectric properties of ferroelectric thin films in the frequency range of mHz-GHz," *Int. Ferro.*, **10**, 247 (1995).
- [12] T. Hayashi, N. Ohji, and H. Miawa, "Film Thickness Dependence of Dielectric Properties of BaTiO₃ Thin Films Prepared by a Sol-Gel Method," *Jpn. J. Appl. Phys.*, **33**, 5277 (1994).
- [13] W. Ousi-Benommar, et al., "Structural and Optical Characterization of BaTiO₃ Thin Films Prepared by Metal-organic Deposition from Barium 2-Ethylhexanoate and Titanium Dimethoxy Dineodecanoate," *J. Mater. Res.*, **9** (4), 970 (1994).

**Phase Transition and Ferroelectric Properties of $\text{BaTi}_{0.91}(\text{Hf}_{0.5}\text{Zr}_{0.5})_{0.09}\text{O}_3$ by
a Laser Ablation Method Using the Fourth-harmonic Wave of a YAG Laser**

Yoichiro Masuda, Sigetaka Fujita, Akira Baba, Hiroshi Masumoto¹,
Kunihiro Nagata² and Toshio Hirai¹

Department of Electrical Engineering, Faculty of Engineering,
Hachinohe Institute of Technology,
88-1 Ohbiraki, Myo, Hachinohe, Aomori 031, Japan.

¹Institute for Materials Research,
Tohoku University,
2-2-1 Katahira, Aoba-ku, Sendai, Miyagi 980, Japan.

²Department of Electronic Engineering,
The National Defense Academy,
10-20 Hashirimizu, Yokosuka, 239 Japan.

Abstract

$\text{BaTi}(\text{Hf}_{0.5}\text{Zr}_{0.5})\text{O}_3$ (BTHZ) thin films are successfully synthesized using a laser ablation technique, which employs the fourth harmonic wave of a pulsed YAG (FHG-YAG) laser, for the first time to our knowledge. The BTHZ thin film with a preferred orientation in c-axis can be attained under an oxygen gas pressure of 3 Pa at 800°C. Chemical bonds of the BTHZ compounds can easily be decomposed by an irradiation with an optical energy of 7.47×10^{-19} J and an optical power density of 300 mJ/cm². Crystallinity of the deposited films is found to be dominated by a mean free path of each element.

Introduction

A significant amount of research on ferroelectric materials and ferroelectric thin films have been made due to their ferroelectric, piezoelectric and pyroelectric properties. In particular, with increasing density of memory devices, ferroelectric thin films, which possess high dielectric constants to maintain sufficient storage capacitance, have recently attracted great interest as new dielectric materials for Gbit-scale integrated dynamic random access memories (DRAMs)¹⁾ and nonvolatile ferroelectric random access memories (FRAMs)²⁾. So far, some FRAMs, which utilize $(\text{BaSr})\text{TiO}_3$ ³⁻⁵⁾, $\text{Pb}(\text{TiZr})\text{O}_3$ ⁶⁻⁸⁾, $\text{Bi}_4\text{Ti}_3\text{O}_{12}$ ⁹⁻¹³⁾ and $\text{SrBi}_2\text{Ta}_2\text{O}_9$ ¹⁴⁻¹⁸⁾ thin films, have been proposed and investigated since they have attractive features such as nonvolatile property, fast storage time, high density and so on. The fabrication of ferroelectric thin films involves various techniques

such as radio frequency (RF) magnetron sputtering, electron cyclotron resonance (ECR) sputtering, sol-gel, metal-organic chemical vapor deposition (MOCVD) and laser ablation (LA). Among these fabrication techniques of ferroelectric thin films, the laser ablation technique has received much attention as a novel processing method of ferroelectric thin films. Since an incident laser beam can be irradiated on a target from outside a reacting vacuum chamber, we can change deposition conditions arbitrarily, such as a deposition rate, substrate temperature and oxygen gas pressure. Therefore, we can easily obtain the ferroelectric thin films with high crystallinity.

Besides, Payne et al.¹⁹⁾ investigated dielectric and structural properties of BaTiO_3 - BaHfO_3 systems. They reported that the Curie temperature in BaTiO_3 - BaHfO_3 systems shifted in lower temperature and the second and third phase transition points increased with increasing Hf ions. This phenomenon is called "pinch effect" and is corresponding to the morphotropic phase boundary (MPB) in the PZT systems. The electrical and physical properties of these films abruptly change as getting close to MPB; that is, the D-E hysteresis loop of the BaTiO_3 - BaHfO_3 systems tends to be a square loop characteristics with increased Hf additions. Substitution of Hf ions for Ti ions in BaTiO_3 resulted in the formation of softer ferroelectrics, i.e., polarization was more easily reversed and saturation polarization was attained with an application of small applied fields. Nagata *et al.*²⁰⁾ also reported the same results in $\text{BaTi}(\text{Hf}_{0.5}\text{Zr}_{0.5})\text{O}_3$ systems.

Although a considerable number of the studies on synthesis of ferroelectric thin films by laser ablation

have so far been made using an excimer laser which utilizes KF or ArF gas as a active media, few attempts have been performed using a YAG laser as a light source of laser ablation to our knowledge. In this study, we describe synthesis of $\text{BaTi}_{0.91}(\text{Hf}_{0.5}\text{Zr}_{0.5})_{0.09}\text{O}_3$ (BTHZ) thin films by means of laser ablation using the fourth harmonic wave of a YAG laser ($\lambda=266$ nm). The structural and dielectric properties of BTHZ thin films are investigated and the mechanism by which the BTHZ thin films with good crystallinity are formed is discussed.

Experimental

Ceramic $\text{BaTi}_{0.91}(\text{Hf}_{0.5}\text{Zr}_{0.5})_{0.09}\text{O}_3$ (BTHZ) targets were prepared from BaCO_3 (Shin Nihon Chemical Kogyo, Co., 99.97%), TiO_2 (Tohou Titanium Co., 99.94%), HfO_2 (Kanto Chemical Co., 99.5%) and ZrO_2 (Daiichi Rare Metal Co., 99.9%). They were mixed and pressed into disks (20 mm in diameter and 2 mm thickness) and then sintered for 3 hours at 1360°C . Figure 1 shows an experimental setup we use to prepare the specimens. The target and substrates set in the vacuum chamber (Anelva Co.) and a distance between the target and substrate was 50 mm. Temperature of substrates on a sample holder was controlled by a heater (from 780°C to 840°C). We used a pulsed YAG laser ($\lambda=1064$ nm, SL805: Spectron Laser System) as a light source and the fourth harmonic wave ($\lambda=266$ nm) was generated using a nonlinear optical crystal (KDP: KH_2PO_4). A repetitional frequency was 10 Hz. The fourth harmonic generation (FHG) wave of the YAG laser beam was focused and irradiated on the BTHZ target, which was rotated by motor, through a fused quartz window. The target was ablated at a focal point and a prume was formed.

Results and Discussion

The XRD (X-ray diffraction) patterns of BTHZ films, deposited on fused-quartz substrates are shown in Fig.1 with substrate temperature as parameter. An oxygen pressure was 3 Pa and a temperature of the substrate was varied in the range of 780°C to 830°C . As it can be seen in Fig.1. The X-ray diffraction intensities of the BTHZ film deposited at 780°C are weak and crystallization of the BTHZ film could not proceed at this temperature. The X-ray diffraction intensities of (001) and (002) planes begin to appear, when the substrate temperature is 800°C , and the

BTHZ film with a preferred orientation in c-axis is attained. As increasing the substrate temperature from 820°C to 840°C during deposition, many diffraction peaks, which indicate the diffraction patterns of the perovskite structure, can be observed and the BTHZ films are found to be polycrystalline structures at this temperature range.

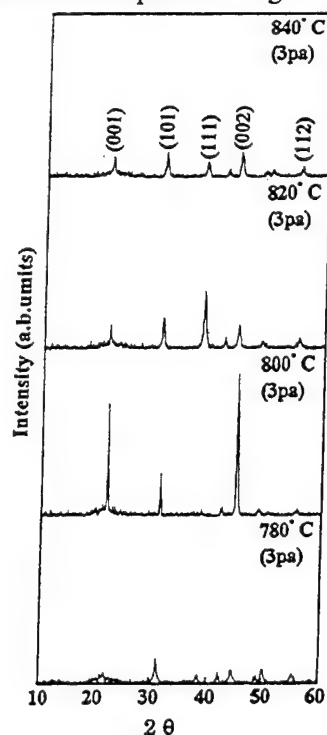


Fig.1 The XRD patterns of BTHZ films with substrate temperature as parameter.

On the other hand, The BTHZ films were deposited on fused-quartz substrates with temperature of 800°C with varying the oxygen pressure in the range of 2 Pa to 5 Pa. When the oxygen gas pressure is 2 Pa, a BTHZ film is not crystallized because the intensities of diffraction peaks are weak. Then the X-ray diffraction intensities of (001) and (002) planes increase, when the oxygen gas pressure of 3 Pa was applied, and the BTHZ film with a preferred orientation in c-axis can be obtained. Furthermore, as increasing the oxygen gas pressure from 4 Pa to 5 Pa, the BTHZ film begins to grow in the direction of a (111) plane and many diffraction peaks which represent the perovskite structure can be observed and the BTHZ film with a polycrystalline structure is grown in this oxygen gas pressure range. From these results, it is found that the BTHZ films of good crystallinity can be synthesized under deposition conditions with substrate temperature of 800°C and the oxygen gas pressure of 3 Pa. Crystallinity of the deposited films seems to be affected by the mean free path of the atoms, since it

strongly depends on oxygen gas pressure during deposition. As a gas pressure dependence of the composition ratio of the BTHZ films deposited at 800°C. A composition ratio of Ba ion of deposited films is 6-11 mole% lower and that of the Ti ion is 2-4 mole% higher compared to that of the target. While the composition ratio of Hf and Zr ions in the deposited films are 0.5-1.98, 3-7.5mole % higher compared to that of the target in the range of 2Pa to 5Pa at oxygen gas pressure.

These results also suggests that the mean free path of each element affect on the composition ratio of the deposited films. The reasons for differences in the EPMA results mentioned above, when each ion is evaporated, it seems necessarily that the mean free path of each ion is different as the specific gravity of each ion differs from oxygen gas pressure. From these results, it is found that use of the target with Ba rich and Ti poor is necessary to grow the BTHZ films with a desired composition ratio. Next, when the optical power density of the irradiated FHG-YAG laser beam (P) was 506 mJ/cm², 900 mJ/cm², 1199 mJ/cm² and 2025 mJ/cm², the deposition rate of the films increases linearly with increasing irradiation times. In this case, the deposition rates are estimated to be 0.10128 Å/shot ($P=506$ mJ/cm²), 0.16605 Å/shot ($P=900$ mJ/cm²), 0.30047 Å/shot ($P=1199$ mJ/cm²) and 0.37396 Å/shot ($P=2025$ mJ/cm²), respectively.

The relation between an optical power density of the FHG-YAG laser and a thickness of the BTHZ film after 36,000 shots. The thickness of the BTHZ films increases linearly with increasing optical power density of the irradiated FHG-YAG laser beam. An extrapolated line through the measured points crosses the horizontal axis at 300 mJ/cm². This value represents the threshold of the laser ablation; that is, chemical bonding of the BTHZ compounds can easily be decomposed by this irradiation condition with the optical energy $E (=hc/\lambda)$, where h and c denote the Planck constant and optical velocity in the vacuum, and the optical power density of 300 mJ/cm². The irradiated optical energy E of the FHG-YAG laser beam correspond to an activation energy to decompose the ceramic BTHZ target and is estimated to be 7.47×10^{-19} J. To examine surface morphologies of the deposited BTHZ films, we performed the observations of the surface morphologies of the BTHZ films by means of AFM(Atomic Force Microscopy).

Each surface morphologies of the specimens present different morphological aspects and it can be seen that the surface of the deposited films tends to be flat and uniform with increase the oxygen gas

pressure. To investigate the electrical properties, the BTHZ film was deposited on a Pt substrate at 800°C under oxygen gas pressure of 3 Pa. The thickness of the deposited film was 2 μm.

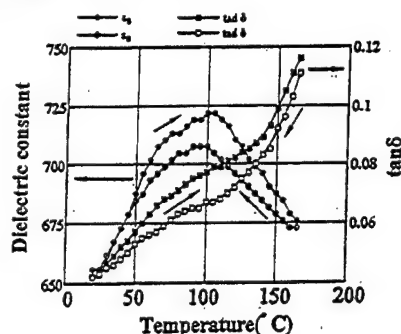


Fig.2 Change in dielectric constants and the dielectric loss tangent of BTHZ films as a function of temperature.

The dielectric constant, dielectric loss tangent at 1kHz was measured using an impedance-gain-phase analyzer(HP-4194A). Figure 2 shows the changes in dielectric constant (ϵ') and dielectric loss tangent of the BTHZ film with temperature. From this result, it is found that the Curie temperature (cubic-tetragonal phase transition) exists at 100°C and the second phase transition point; that is, the orthorhombic-tetragonal phase transition point appears at 72°C. Then the dielectric constants at room temperature, the Curie point and the second phase transition points are estimated to be 670, 720 and 710, respectively. The dielectric loss tangent is varied from 0.035 to 0.15 in this experiment. Nagata *et al.*²⁰ reported that the Curie temperature of the BTHZ ceramic was 91°C with the dielectric constant of 27000 and the second phase transition point existed at 72°C, where the dielectric constant was 10000. The dielectric constant at room temperature was 2500. The difference in electrical properties between the BTHZ ceramic and BTHZ thin film does not only result from deviation of the composition ratio but also the size effected in ferroelectricity, since the ferroelectricity of the bulk and thin film material is strongly affected by the grain size of the material. Another reason for this deviation can be explained by difference in the measurement conditions; that is, the measurement of the electrical properties in this experiment was performed in the (001) direction of the BTHZ film, while the spontaneous polarization direction of the BTHZ film exists in (111) direction. The reasons for the difference in the electrical properties mentioned above are under investigation and will be communicated in next paper.

Figure3 shows a D-E hysteresis loop of the BTHZ film by means of the Sawyer-Tower circuit, where an AC voltage with a triangle wave of 1kHz was applied

to the specimen.

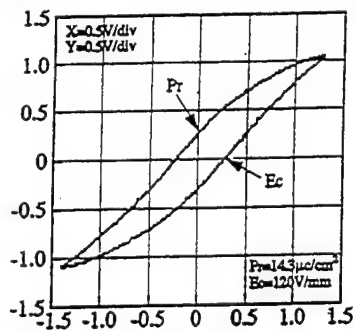


Fig.3 The hysteresis loop of the BTHZ film.

From this figure, the remanent polarization (P_r) and coercive field (E_c) of the BTHZ film are determined to be $14.3 \mu\text{C}/\text{cm}^2$ and $120 \text{ V}/\text{mm}$, respectively, and P_r is about two times larger and E_c is one-third that compared to the BaTiO_3 ceramic. The structure of the BTHZ thin film shows a rhombohedral phase at room temperature and a spontaneous polarization direction appears in a $\langle 111 \rangle$ direction. Provided that the spontaneous polarization direction of the BTHZ film exits in the $\langle 111 \rangle$ direction, the remanent polarization is determined to be $24.4 \mu\text{C}/\text{cm}^2$, since the remanent polarization of the BTHZ thin film which orients in a $\langle 001 \rangle$ direction is $14.3 \mu\text{C}/\text{cm}^2$. This value is 1.6 times larger than that of the BaTiO_3 ceramic. The remanent polarization and coercive field of the BaTiO_3 ceramic are $7 \mu\text{C}/\text{cm}^2$ and $350 \text{ V}/\text{mm}$, respectively. These results can be explained by change in soft ferroelectric due to the substitution of $(\text{Hf}_{0.5}\text{Zr}_{0.15})$ ions.

Conclusions

In this study, we have successfully synthesized the $\text{BaTi}(\text{Hf}_{0.5}\text{Zr}_{0.15})\text{O}_3$ films using a laser ablation technique, which employs a fourth harmonic wave of a YAG laser for the first time to our knowledge. The BTHZ film with a preferred orientation in c-axis can be attained under the oxygen gas pressure of 3 Pa at 800°C . The deposition rate found to be increased linearly as increasing the irradiating laser power density and is $0.37396 \text{ \AA}/\text{shot}$ at an optical power density of $2025 \text{ mJ}/\text{cm}^2$. Decomposition of the chemical bonds of the BTHZ compounds begins to occur under the irradiation conditions of the FHG-YAG laser with an optical energy of $7.47 \times 10^{-19} \text{ J}$ and an optical power density of more than $300 \text{ mJ}/\text{cm}^2$. It is found that crystallinity of the deposited film and deviation of the composition ratio between the BTHZ

film and target seems to be governed by the mean free path of each element.

Acknowledgements

The authors would like to thank emeritus professor Koichiro Sakata, professor Takeyo Tsukamoto for their helpful discussions. We also wish to express our thanks to Dr. Shizutoshi Andoh of Tokyo Science University for chemical analysis (EPMA) and Mr. Toshiya Shimotsubo of Hachinohe Institute of Technology for his technical assistance.

A part of this work was supported by High Performance Multi-Functional Transducers of Dielectric Composite Films, Research on Artificial Materials for Next Generation, Research for The Future, Japan Society for the Promotion of Science (JSPS-RFTF 96P00105) and the Visiting Research Program of the Laboratory for Development Research of Advanced Materials, Institute for Materials Research, Tohoku University.

References

- 1) A. I. Kingon, S. K. Strelffer, B. Baseri and S. R. Summerfeet: MRS Bulletin, 7, 21 (1996) 46.
- 2) J. F. Scott, F. M. Ross, C. A. Paz de Araujo, M. C. Scott and M. Huffman: MRS Bulletin, 7, 21 (1996) 33.
- 3) J. Tanimura, M. Kataoka, K. Sato and M. Nunoshita: Jpn. J. Appl. Phys. 32(1993) 4126.
- 4) K. Abe and S. Komatsu: J. Appl. Phys., 77(12) (1995) 6461.
- 5) T. Kawahara, M. Yamamura, A. Yuuki and K. Ono: Jpn. J. Appl. Phys., 35 (1996) 4880.
- 6) K. Hirata, N. Hosokawa, T. Hase, T. Sakuma and Y. Miyasaka: Jpn. J. Appl. Phys., 31 (1992) 3021.
- 7) M. Shimizu, T. Katayama, M. Sugiyama and T. Shiosaki: Jpn. J. Appl. Phys., 32 (1993) 4074.
- 8) K. Aoki, Y. Fukuda and A. Nishimura: Jpn. J. Appl. Phys., 32 (1993) 4147.
- 9) A. Kakimi, S. Okamura, Y. Yagi, K. Mori and T. Tsukamoto: Jpn. J. Appl. Phys., 33 (1994) 5301.
- 10) H. Masumoto, T. Goto, Y. Masuda, A. Baba and T. Hirai: Appl. Phys. Lett., 58(3) 21 (1991) 243.
- 11) M. Yamashita, T. Nagatomo and O. Omoto: Jpn. J. Appl. Phys., 34 (1995) 5116.
- 12) H. Tabata, H. Tanaka and T. Kawai: Jpn. J. Appl. Phys., 34 (1995) 5146.
- 13) W. Wu, Y. Oishi, M. Okuyama and Y. Hamakawa: J. Korean Phys. Soc., (Proc. Supp.) 29 (1996) s660.
- 14) D. Dimons, H. N. Al-Shareef, W. L. Warren and B. A. Tuttle: J. Appl. Phys. 80 (3) (1996) 1682.
- 15) D. J. Taylor, R. E. Jones, P. Zurcher, P. Chu, Y. T. Lii, B. Jiang and S. J. Gillespie: Appl. Phys. Lett. 68 (16) (1996) 2300.
- 16) T. Hayashi, H. Takahashi and T. Hara: Jpn. J. Appl. Phys. 35 (1996) 4952.
- 17) J. J. Lee, C. L. Thio and S. B. Desu: J. Appl. Phys. 78 (8) (1995) 5073.
- 18) T. S. Song, J. K. Lee and H. J. Jung: Appl. Phys. Lett. 69 (25) (1996) 3839.
- 19) W. H. Payne and V. J. Tennery: J. Am. Ceram. Soc., 48 (8) (1965) 413.
- 20) K. Nagata and T. Kiyota: Jpn. J. Appl. Phys., 28 (Suppl.28-2) 98.

THE EFFECT OF OXYGEN ON THE BARIUM TITANATE FILM CAPACITOR

Bang-Hung Tsao, Richard L.C. Wu

K Systems Corporation
1522 Marsetta Drive
Dayton OH 45432
Tel: (937) 429-5151
Fax: (937) 255-3211

Sandra Fries Carr, Joseph A. Weimer

U.S. Air Force, WL/POOC
Wright-Patterson AFB OH 45433
Tel: (937) 255-6016
Fax: (937) 255-3211

ABSTRACT

Thin BaTiO_3 film (5000 Angstroms) capacitor devices were fabricated by using rf sputtering techniques and applying various levels of oxygen-rich environments (0% to 20 %). In this study, the gas compositions were specifically 100% Ar and the variations of oxygen content were 1%, 3%, 5%, 10%, 15% and 20%. The dielectric constant was measured in the range of 13 to 19 for the as-deposited samples. For the samples annealed at 750°C in argon for half an hour, the dielectric constant of BaTiO_3 films increased as much as a 2 to 3X. It was also observed that the higher the total pressure, the lower the deposition rate was. The addition of the 5% oxygen apparently decreases the deposition rate.

INTRODUCTION

Thin film ceramics (0.5 to 2 μm) are being developed for use in integrated passive capacitor components. The search for electrically and thermally superior ceramic dielectric materials is an on-going task for many organizations. Current day materials lack many attributes (miniaturization, high capacitance, high reliability, etc.) desired by application engineers. The materials typically are thick (about 25-35 μm), porous, and temperature limited. The dielectric properties of BaTiO_3 films were studied because of their potential application as a high dielectric constant material in micro-electronic components of high volumetric efficiency (McClure, 1979). Films of BaTiO_3 have been produced with various vacuum techniques of which radio-frequency (rf) sputtering appears to be the most reproducible approach. Both amorphous and

tetragonal BaTiO_3 films can be produced by rf sputtering depending on the substrate temperature, ratio of oxygen to argon, deposition rate, and post-deposition heat treatment.

EXPERIMENTAL PROCEDURES

BaTiO_3 films were produced under several conditions. These parameters include gas environments (0 to 20 % oxygen/ balance argon), and heat treatments (without annealing and annealing at 750°C for 30 minutes). Some conditions were held constant. These constant parameters included pressure (7mtorr), the dielectric material (BaTiO_3), power (150 watts), and electrical contacts (Palladium) deposited by rf sputtering. Although the electrical contacts were palladium for this study, some aluminum and titanium data are also presented for comparison (Tsao, 1996 a, b). The deposition system used to produce the barium titanate films is a rf sputtering system, model DV502-A, manufactured by Denton Vacuum with an RFX generator from Advanced Energy Industries.

EXPERIMENTAL RESULTS

Films prepared with various sputtered conditions were examined by optical microscopy and SEM. No signs of cracking or peeling were observed. The adhesion of the films to the substrate was good. The morphology of as-deposited BaTiO_3 films was smooth and featureless. The X-ray diffraction indicated that these films were amorphous. These films were annealed at 750°C in an argon atmosphere to obtain the crystallized microstructure. Figure 1 shows a typical microstructure of BaTiO_3 film annealed at 750°C for half an hour at a magnification of 1000. Under these

conditions, the previously smooth, continuous BaTiO_3 film broke down into small grain particles. Figure 2(a) is a TEM micrograph of the BaTiO_3 film as deposited at a magnification of 50K. Figure 2(b) is a corresponding electron diffraction pattern of Figure 2(a) at a camera length of 52 cm. The diffraction pattern indicated that the BaTiO_3 film is amorphous. Figure 3(a) is a TEM micrograph of the film annealed at 650°C at a magnification of 50K. Figure 3(b) is an electron diffraction pattern of Figure 3(a) at a camera length of 52 centimeters. Figure 3(b) showed that the BaTiO_3 film is in the onset of the crystallization. Figure 4 is a SEM micrograph of the actual device. The thickness of the electrode is about 2000 \AA and the dielectric film is about 5000 \AA .

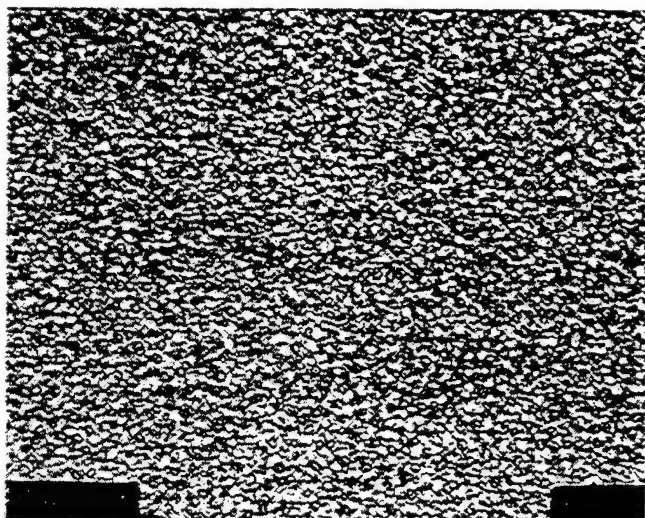


Figure 1 shows a typical microstructure of BaTiO_3 film annealed at 750°C for half an hour.

The following measurements were made on several samples under the various conditions:

| | Average Dielectric Constant Before Annealing | Average Dielectric Constant After Annealing |
|-------------------|--|---|
| 100 % Ar | 16.15 | 31.90 |
| 1 % O_2 | 15.22 | 32.79 |
| 3% O_2 | 11.79 | 35.34 |
| 5% O_2 | 13.09 | 45.03 |
| 10 % O_2 | 33.64 | 30.90 |
| 15% O_2 | 12.64 | 21.46 |
| 20% O_2 | 13.68 | 32.39 |

The dielectric constant for those samples grown under a 100% argon environment displayed a slightly higher dielectric constant than those grown in 1%, 3% or 5% oxygen. A previous study (Tsao, 1996b) showed an even higher dielectric constant in a 100% argon environment

compared to a 5% oxygen environment when power levels were increased to 300W. The samples grown in a 10% oxygen environment had an unusually high dielectric constant (pre-annealed). The dielectric constant of the samples grown in a 15% and 20% oxygen environment dropped to the average level of all the samples produced. The general trend observed here was the annealing process increased the dielectric constant about 2 to 3 times regardless of the deposition conditions. As a whole, the samples grown in a pure argon environment did not demonstrate as low leakage current as those in the oxygen/argon environment.

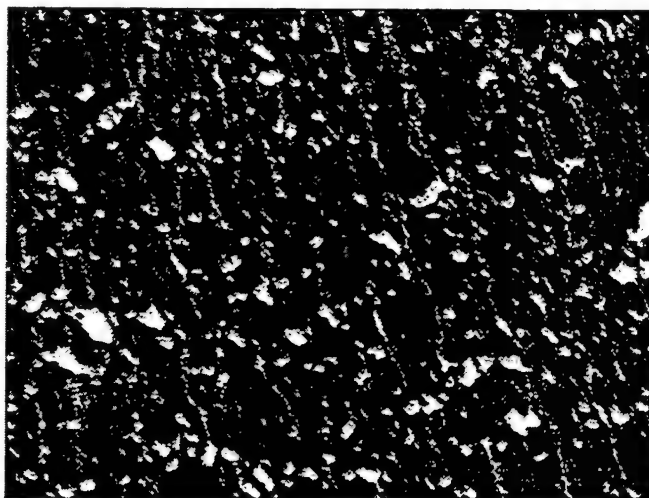


Figure 2(a) is a TEM micrograph of the BaTiO_3 film as deposited at a magnification of 50K.



Figure 2(b) is a corresponding electron diffraction pattern of Figure 2(a) at a camera length of 52 cm.

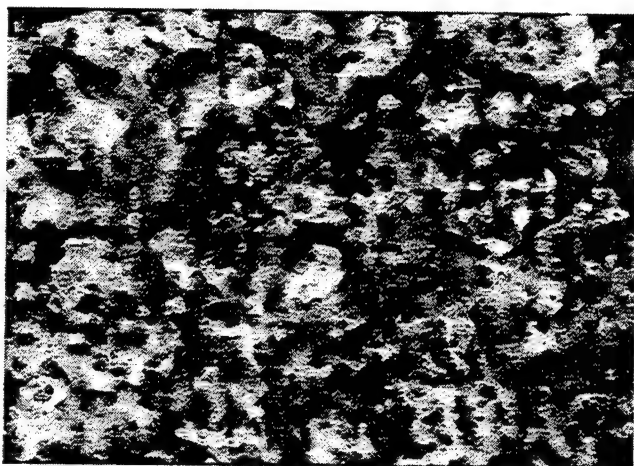


Figure 3(a) is a TEM micrograph of the film annealed at 650°C at a magnification of 50K.



Figure 3(b) is an electron diffraction pattern of Figure 3(a) at a camera length of 52 centimeters.



Figure 4 is a SEM micrograph of the actual device.

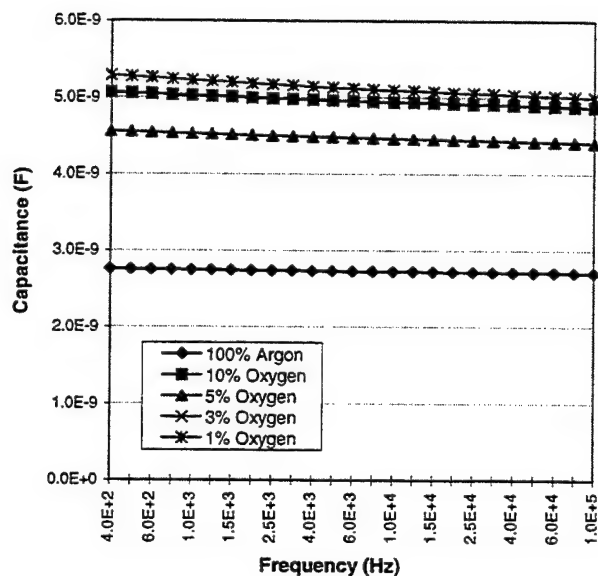


Figure 5 Capacitance versus frequency for several BaTiO₃ capacitor samples.

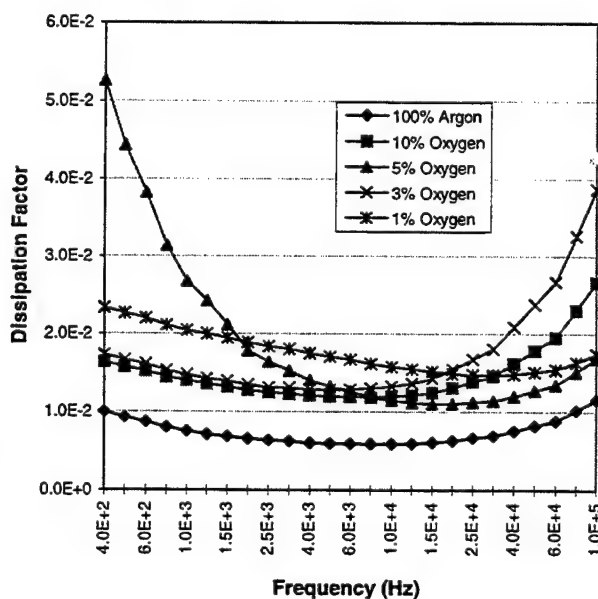


Figure 6 Dissipation factor versus frequency for BaTiO₃ samples at different oxygen concentrations.

Figure 5 shows the frequency response versus capacitance from 400 Hz to 100 KHz at various oxygen concentrations for several BaTiO₃ capacitor samples. The capacitance changed very little with increasing frequency. The frequency characterizations from 400 Hz to 100 KHz for dissipation factor, depicting the same BaTiO₃ samples are shown in Figure 6.

DISCUSSION

The deposition rate of BaTiO₃ increased with increased rf power. The addition of oxygen decreased the deposition rate of BaTiO₃. Such a decrease of the deposition rate was expected due to the capturing of the secondary electron by oxygen. However, at higher oxygen concentrations (10% or more) the deposition rate was not significantly reduced. The major difference was between the pure argon and 5% oxygen. No quantitative measurements of decreasing deposition rate were performed at this stage. It is also observed that additions of oxygen to the sputtering gas at levels of 10% and 20% degraded the properties of the films by producing a higher defect density. The sputtering rate for films prepared in 20% O₂ was about 60% of that for films prepared in pure argon. It is also reported (Tsao, 1996 a, b) that a mixture of 5% O₂/95% Ar also reduced the growth rate and without the presence of the oxygen it was difficult to obtain the stoichiometric BaTiO₃. It is noted (Tsao, 1996 a, b) that the pressure change from 7 millitorr to 15 millitorr reduced the deposition rate for pure argon from 0.78 to 0.74 Å/sec, and for 5% O₂/95% Ar from 0.50 to 0.44 Å/sec. The influence of the total pressure was not as significant as the addition of the oxygen.

The electrode materials used in this study, such as Au, Ti, and Ni, encountered the problem of low parallel resistance (R_p) of the capacitor. Evaporated and sputtered Al showed evidence of a reaction with BaTiO₃ film at a temperature of 500°C. This effect may be caused by back sputtering of the film by the negative oxygen ions. The bombardment by these ions caused pin holes in the BaTiO₃ films. Therefore, the BaTiO₃ film thickness was slightly increased and the quality of the electrical response did improve. In the study of BaTiO₃ film-Au contacts, the composite lifted from the substrate after deposition.

The voltage breakdown strength depends on the substrate surface roughness, electrode material, thickness, and area. We only reported typical breakdown values determined under chosen specific conditions (Tsao, 1996 a, b). For a 0.4 µm film on 19 mm² Pyrex substrate, with a 0.2 µm thick aluminum electrode, the breakdown strength was about 5 MV/m (130V/mil). The breakdown strength for a BaTiO₃ sample with a Ti electrode prepared in a 5% O₂/95% Ar environment was 26MV/m (660V/mil) which is approximately three times higher than those prepared in a pure Ar atmosphere. It appears that the 5% oxygen compensates the oxygen deficiency of BaTiO₃ films and stabilizes the microstructure.

SUMMARY

Capacitors using BaTiO₃ film as the dielectric were processed and tested. The capacitance of these BaTiO₃ film capacitors was stable with frequency from 400 Hz to 100 KHz. The average dielectric constant of these films was

approximately 16 before annealing and 33 after annealing. The resistivity of the BaTiO₃ films was consistently in the 10¹² ohm-cm range. The high oxygen concentration (10%, 15%, 20%) reduced the resistivity to the 10⁷ ohm-cm range. The breakdown strength approached 30 MV/m. The dissipation factor of the BaTiO₃ films were in the range of 0.004 to 0.009, which is satisfactory. In order to obtain the high dielectric constant of BaTiO₃ film, the modification of the microstructure will be necessary. High temperature annealing (750°C and higher) would convert the BaTiO₃ film from an amorphous to a dense crystalline structure. For the same reason, the high temperature electrodes need to be improved to achieve the required high temperature, high volumetric efficient capacitor devices for future applications.

ACKNOWLEDGMENT

Research activities were performed by K Systems Corporation through Air Force contract F33615-94-C-2423. The authors would like to thank Mr. Victor McNier, K Systems Corporation, and Mr. Jeff Fox, University of Dayton Research Institute for their assistance in the electrical characterization and data acquisition.

REFERENCES

- McClure D. J. and J.R. Crowe, "Characterization of Amorphous Barium Titanate Films Prepared by RF Sputtering," J. Vac. Sci. Technol, Vol. 16, 1979, pp. 331-314.
- Tsao B.H., S. J. Fries Carr, J. A. Weimer, "Sputtered Barium Titanate Films for Capacitor Applications," IECEC 96, Vol.1, p.560-565
- Tsao B.H., S. J. Fries Carr, J. A. Weimer, "Sputtered Barium Titanate Films for Capacitor Applications," MRS Fall 1996, session K30.3.

Electrical Properties of (Pb,Ca)TiO₃ Thin Films by Multiple-Cathode Sputtering

Hiroshi Maiwa and Noboru Ichinose¹

Department of Materials Science and Ceramic Technology, Faculty of Engineering, Shonan Institute of Technology, 1-1-25
Tsuji-dou-Nishikaigan, Fujisawa, Kanagawa 251, Japan

¹ Department of Materials Science and Engineering, School of Science and Engineering, Waseda University, 3-4-1 Ohkubo,
Shinjuku, Tokyo 169, Japan

Abstract - (Pb,Ca)TiO₃ (PCT) thin films were fabricated by multiple-cathode RF-magnetron sputtering, using PbO, CaTiO₃ and Ti metal targets. PCT films deposited on Pt/Ti/SiO₂/Si and Pt/MgO at the substrate temperature from 460°C to 540°C had perovskite structures. The relation between substrate temperature and film properties were investigated. The remanent polarization, dielectric constant and leakage current of the 200-nm-thick PCT(Ca/Ti=0.30) thin films deposited on Pt/Ti/SiO₂/Si at 460°C and on Pt/MgO at 500°C were 22.5 μ C/cm², 225 and on the order of 10⁻⁷ A/cm² (at a field of 250 kV/cm), 41 μ C/cm², 174 and on the order of 10⁻⁷ A/cm² (at a field of 250 kV/cm), respectively.

I. INTRODUCTION

Recently, ferroelectric thin films have been attracting great attention because of their potential applications to microelectronic and micromechanical applications [1][2]. Among various ferroelectrics, PZT thin films were intensively investigated [3][4], while PbTiO₃ thin films were paid less attention, due to their high coercive field and large tetragonal distortion *c/a* of 1.064. The addition of La, Ca is used for to decrease the coercive field and tetragonality [5]. In the PbTiO₃-CaTiO₃ system, 40% Ca replacement of Pb site induces tetragonal-cubic phase transition at room temperature [6]. In addition, it was reported that Ca modified PbTiO₃ exhibited large piezoelectric anisotropy [7]. PCT thin films has been investigated by several groups and they exhibited relatively large remanent polarization. Yamaka *et al.* showed that sputter-deposited epitaxial Pb_{0.7}Ca_{0.3}TiO₃ films showed spontaneous polarization of over 40 μ C/cm² [8]. And recently, Kholkin *et al.* reported that sol-gel deposited Pb_{0.76}Ca_{0.24}TiO₃ thin films had a remanent polarization of 38 μ C/cm² and the remanent piezoelectric coefficient of 70 pm/V which is comparable bulk ceramics, and they insisted that the high piezoelectric constant was due to the piezoelectric anisotropy [9]. However, the electrical properties of PCT films which are thinner than 500nm have not been sufficiently studied.

In this work, PCT thin films with Ca content, Ca/Ti=0.30, were fabricated by multiple cathode RF magnetron sputtering. This method offers a highly controllable deposition process because the sputtering rate of each target can be changed individually [10][11]. This paper describes the relation

between sputtering conditions and the fundamental electrical properties of the deposited PCT thin films.

II. EXPERIMENTAL

Multiple-cathode RF magnetron sputtering was used to deposit (Pb,Ca)TiO₃ (PCT) thin films. The apparatus employed in this experiment is shown in our previous papers [10][11]. The sputtering targets used were 3-inch disks of PbO (99.99%), CaTiO₃ (99.9%) and Ti (99.99%) metals, and each target was individually controlled by the RF power supply.

The substrates were Pt(180nm)/Ti(20nm)/SiO₂(1000nm)/Si and Pt/MgO. The Pt films showed (111) and *a*-axis orientation on the SiO₂ (1000nm)/Si and MgO substrate, respectively. The substrates were fixed to the rotary-type substrate holder through a load-lock chamber. The substrate holder was rotated at a speed of 11.25 rpm. Input RF power for CaTiO₃ and Ti were kept at 200W and 450 W, respectively and that for PbO was 50 W-70 W. Reactive sputtering was carried out in a mixed gas of argon and oxygen.

The chemical composition of the films was determined by inductively coupled plasma spectroscopy (ICP). Thin film crystallinity was characterized by X-ray diffraction (monochromated CuK α radiation). A typical deposition rate was 1.2-1.4 nm/min.

Au thin films were evaporated at room temperature as the top electrode with a diameter of 0.2 mm. Capacitances were measured using an impedance analyzer (HP 4192A) at room temperature. The dielectric constant of the films was calculated from the capacitance measured without a bias voltage at a frequency of 100 kHz. The current versus voltage was measured using an electrometer (Advantest TR8652). Ferroelectric properties were measured using the Radiant Technology RT66A tester operating in the virtual ground mode.

III. RESULTS AND DISCUSSION

PCT thin films with Ca content from Ca/Ti=0.30 could be fabricated. X-ray diffraction patterns revealed that PCT thin films deposited on Pt/Ti/SiO₂/Si and Pt/MgO at the substrate temperature between 460°C and 540°C had perovskite

structure. This result suggests that multiple cathode sputtering using a metal target is effective in lowering the substrate temperature compared to sputtering using a compound target [8] and to sol-gel method [9]. PCT thin films on Pt/Ti/SiO₂/Si had a preferred orientation in the (111) plane. While the films on Pt/MgO had a preferred a- and c-axis orientation, the degree of the preferred orientation increased with increasing substrate temperature. Peak splitting due to tetragonal distortion was clearly seen in the sample deposited on Pt/MgO, however, the splitting was narrower compared to pure PbTiO₃ thin films, suggesting that Ca is incorporated into the perovskite lattice.

Fig. 1 shows FE-SEM micrographs of the PCT thin films deposited at 460 °C on Pt/Ti/SiO₂/Si and Pt/MgO. The both films have smooth surface and free of crack. The film surface on Pt/Ti/SiO₂/Si is consist of the grains 50-200nm. While, the film surface on Pt/MgO is closely packed, compared to the one on Pt/Ti/SiO₂/Si, and is consist of the grains of 30-150nm.

P-E hysteresis loops of the 200-nm-thick PCT films deposited on Pt/Ti/SiO₂/Si at 460 °C, 500 °C, 540 °C are shown in Figs.2(a) and 2(b), respectively. In the case of the films on Pt/Ti/SiO₂/Si, the film deposited at 460 °C exhibited symmetric loop and lower coercive field (Ec), the film deposited at 500 °C showed higher remanent polarization (Pr) and Ec, compared to the one deposited at 460 °C. The films deposited at 540 °C had a narrow loop and lower polarization, indicating poor ferroelectricity. While, in the case of the films on Pt/MgO, the film deposited at 460 °C exhibited the lowest Pr, the film deposited at 500 °C showed the highest Pr of 41 $\mu\text{C}/\text{cm}^2$, and the degree of degradation of Pr value and the loop shape by heating up to 540 °C was not severe, compared to the case of the films on Pt/Ti/SiO₂/Si. With increasing of substrate temperature, Ec and the shift of loop along E-axis increased.

These results are explained as follows. With increasing substrate temperature, film crystallinity increased, leading to improve the electrical properties. While, the loss of Pb due to re-evaporation from substrate also increased. From our previous study concerning (Pb,Li)TiO₃ film deposition, Pb loss was accelerated by higher temperature heating, leading to degradation of electrical properties of the films [11]. The properties of PCT films in this study seem to be determined by trade-off between the increase of the film crystallinity and the number of defects in the films by heating. Due to the better lattice matching, Pb re-evaporation on Pt/MgO was more gentle, compared to the one on Pt/Ti/SiO₂/Si, consequently, electrical properties of the films deposited on Pt/MgO at 540 °C showed better electrical properties than the one on Pt/Ti/SiO₂/Si. The increase of Ec and the shift of loop along E-axis seems to be explained by the increase of the number of defect and/or the lattice clamping by the substrate. Both the number of defect and the lattice clamping by the substrate

seem to increase by heating, therefore, Ec and the loop shift increased in any case.

Pr value of 41 $\mu\text{C}/\text{cm}^2$ obtained in the PCT films deposited on Pt/MgO at 500 °C is comparable with previous reports [8][9]. Considering thickness of 200nm in this study, film quality is estimated to be even better than the previous reported one.

Thickness dependence of P-E hysteresis loops of PCT thin films deposited on Pt/Ti/SiO₂/Si at 460 °C is shown in fig.3. 100nm-thick films exhibited worse loops than 200nm-thick films. The loop shape was round, suggesting leaky aspect of the capacitor. Furthermore, Ec increase offset the decrease the film thickness, as a result, switching voltage was almost equivalent to the 200nm-thick, about 3V is required to switch polarization in both films. These results indicate that the PCT films obtained in this study is not suitable for non-volatile memory applications.

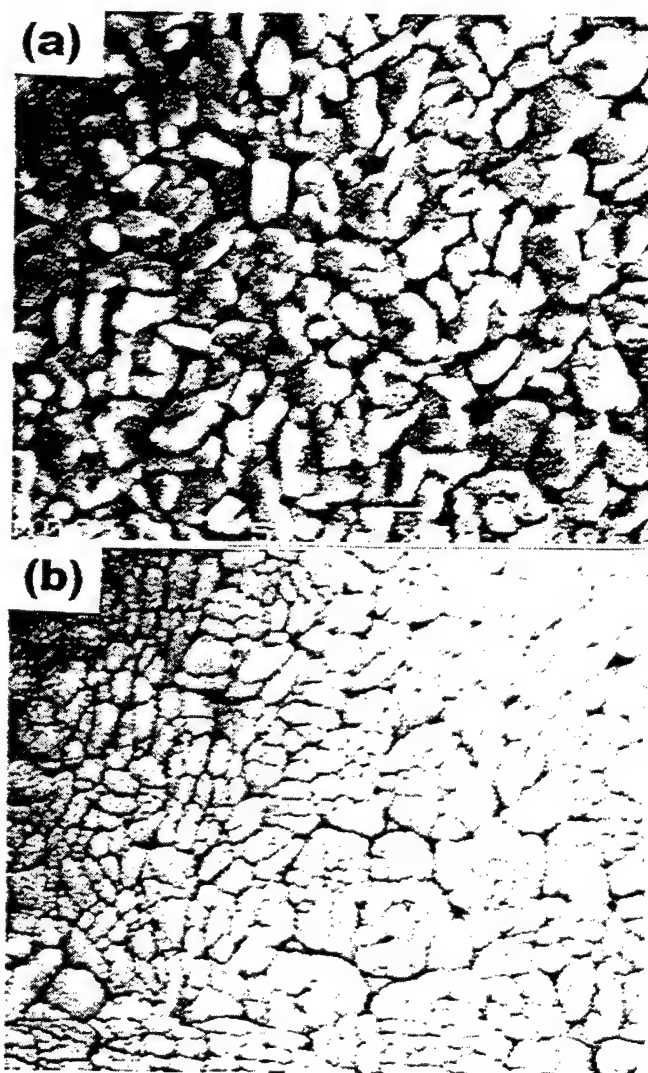


Fig. 1. SEM micrographs of (Pb,Ca)TiO₃ thin films on (a)Pt/Ti/SiO₂/Si and (b)Pt/MgO substrates.

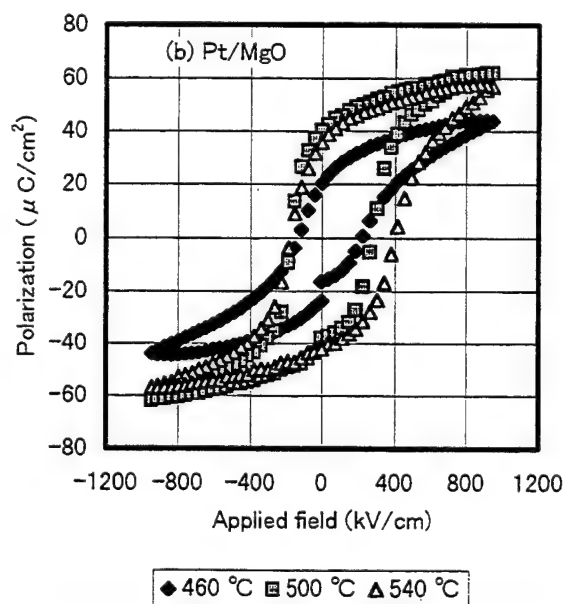
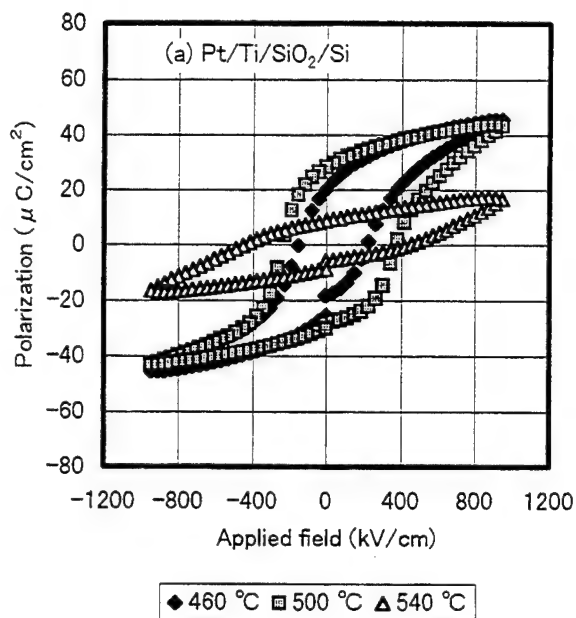


Fig.2. P-E hysteresis loops of (Pb,Ca)TiO₃ thin films on (a)Pt/Ti/SiO₂/Si and (b)Pt/MgO.

The dielectric constant and loss tangent of the 200nm-thick PCT films deposited at 460°C on Pt/Ti/SiO₂/Si and Pt/MgO were 225, 0.05 and 230, 0.07, respectively. Those of the 200nm-thick PCT films deposited at 500°C on Pt/MgO were 179 and 0.04, respectively. Thickness dependence of the

dielectric constant of the PCT thin films deposited on Pt/Ti/SiO₂/Si at 460°C is shown in fig.4. With decreasing film thickness, dielectric constant decreased. In comparison with PZT [3][4], low dielectric constant and high Pr are attractive properties for application to pyroelectric sensor and microactuators.

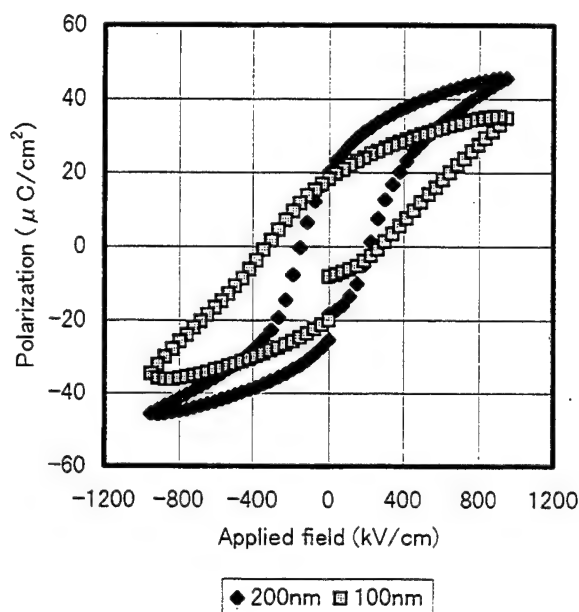


Fig.3. Thickness dependence of P-E hysteresis loops of (Pb,Ca)TiO₃ thin films on Pt/Ti/SiO₂/Si.

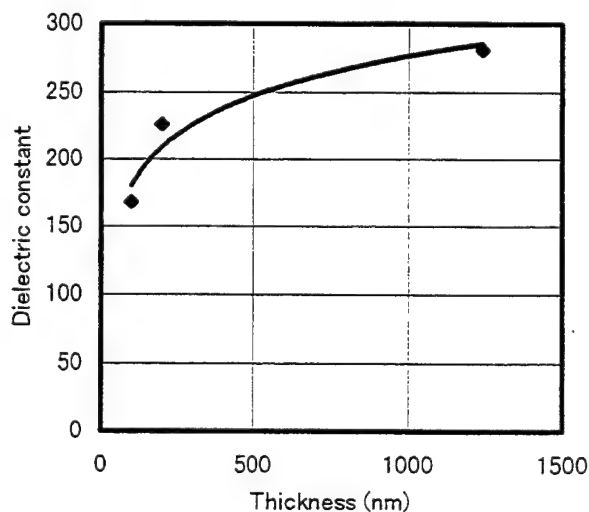


Fig.4. Thickness dependence of the dielectric constant of the (Pb,Ca)TiO₃ thin films on Pt/Ti/SiO₂/Si.

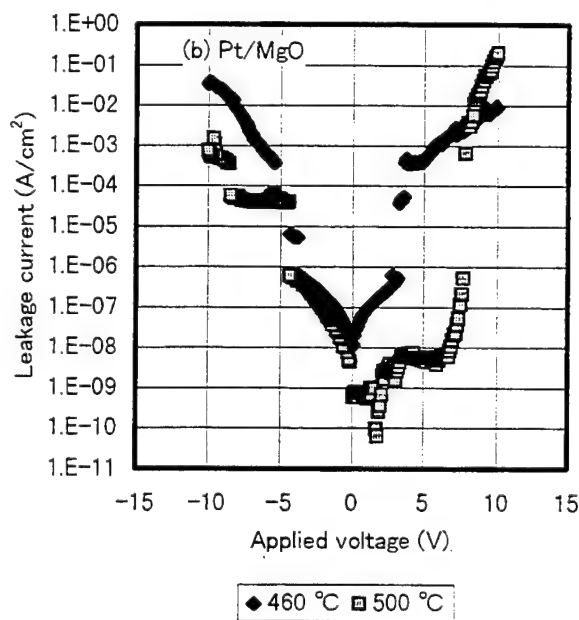
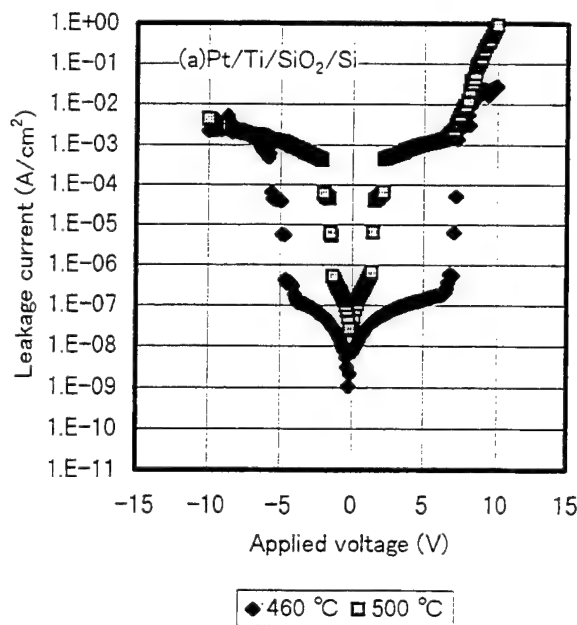


Fig.5. Current-voltage characteristics of the 200-nm-thick (Pb,Ca)TiO₃ films on (a)Pt/Ti/SiO₂/Si and (b)Pt/MgO.

Leakage currents of the 200-nm-thick PCT films are shown in Figs.5(a) and 5(b). In the case of the films on

Pt/Ti/SiO₂/Si. With increasing substrate temperature, the breakdown voltage decreased. This is probably due to the grain growth of the samples. The films on Pt/MgO deposited at 500 °C exhibited asymmetrical curve, which reflects asymmetrical P-E hysteresis loop, as shown in fig.2(b). The better insulating properties of the films on Pt/MgO, compared to the one on Pt/Ti/SiO₂/Si, is probably due to the more densely packed morphology of the sample, as shown in Fig.1. The leakage currents of the 200-nm-thick PCT films deposited on Pt/Ti/SiO₂/Si at 460 °C and on Pt/MgO at 500 °C were on the order of 10⁻⁷ A/cm² up to 5 V (250 kV/cm).

IV. CONCLUSION

(Pb,Ca)TiO₃ (PCT) (Ca/Ti=0.30) thin films were fabricated by multiple cathode RF magnetron sputtering. Films having a perovskite structure could be obtained at deposition temperature of 460 °C. Maximum Pr value of 41 μC/cm² were obtained in the PCT films deposited on Pt/MgO at 500 °C. With increasing substrate temperature, Ec and loop shift along E-axis increased, generally. The dielectric constant and loss tangent of the 200nm-thick PCT films deposited at 460 °C on Pt/Ti/SiO₂/Si and Pt/MgO were 225, 0.05 and 230, 0.07, respectively. The leakage current of the 200-nm-thick PCT films deposited on Pt/Ti/SiO₂/Si at 460 °C were on the order of 10⁻⁷ A/cm² up to 5 V (250 kV/cm). From the results of this work, PCT thin films fabricated by multiple-cathode sputtering are concluded to be promising candidates for various device applications.

ACKNOWLEDGMENT

This work was supported in part by a Grant-in-Aid for Encouragement of Young Scientists from the Ministry of Education, Science, Sports and Culture.

REFERENCES

- [1] J.F.Scott and C.A.Paz de Araujo: *Science* 246(1989) 1400.
- [2] P.Muralt, M.Kohli, T.Maeder, A.Kholkin, K.Brooks, N.Setter and R.Luthier: *Sens. Actuators A* 48 (1995) 157.
- [3] M.Shimizu, M.Fujimoto, T.Katayama, T.Shiosaki, K.Nakaya, M.Fukagawa and E.Tanikawa: *Mater.Soc.Symp.Proc.* 310 (1993) 255.
- [4] T.Asakusa, K.Ishikawa, A.Sato and M.Okada: *Jpn.J.Appl.Phys.* 35 (1996) 4886.
- [5] E.Sawaguchi: *J.Phys.Soc.Jpn.* 11 (1956) 1998.
- [6] K.Okazaki: *Ferroelectrics* 41 (1982) 77.
- [7] Y.Yamashita, K.Yokoyama, H.Honda, T.Takahashi: *Jpn.J.Appl.Phys.* Suppl. 20 (1981) 183.
- [8] E.Yamaka, H.Watanabe, H.Kimura and H.Oikuma: *J.Vac.Sci.Technol.* A6 (1988) 2921.
- [9] A.L.Kholkin, M.L.Calzada, P.Ramos, J.Mendiola and N.Setter: *Appl.Phys.Lett.* 69 (1996) 3602.
- [10] H.Maiwa, N.Ichinose and K.Okazaki: *Jpn.J.Appl.Phys.* 31 (1992) 3029.
- [11] H.Maiwa, N.Ichinose and K.Okazaki: *Jpn.J.Appl.Phys.* 33 (1994) 6227.
- [12] H.Maiwa and N.Ichinose: submitted to *Jpn.J.Appl.Phys.*

Effect of Niobium on Some Electrical Properties of Nb-Doped PbTiO₃ Thin Films

Tadashi Shiosaki¹, Ricardo Cury Ibrahim, Toshihisa Horiuchi and Kazumi Matsushige
Dep. of Electronic Science and Engineering, Faculty of Engineering, Kyoto University
Yoshida Honmachi, Sakyo-ku, Kyoto-shi 606, Japan

1. Introduction

Doping of ferroelectric bulk ceramic materials has been a common practice since long ago.^{1,2)} In general, several types of dopants are used in order to enhance some properties of the material.

Recently, it has been verified that by doping PZT or PbTiO₃ films with certain donor-type dopants (lanthanum³⁾ and niobium^{4,5)} some dielectric properties can be considerably improved/modified. In particular, niobium doping has been verified to enhance the resistivity, the dielectric loss, the breakdown voltage and the leakage current characteristics of lead titanate. Therefore, doping seems to be a very convenient technique to obtain good quality PbTiO₃ films.

On the other hand, it has been commonly observed that the D-E hysteresis curves of lead-based perovskite-type ferroelectric thin films deposited at low pressure exhibit noticeable voltage (field) offsets. Such characteristics have been associated with internal defect dipoles due to vacancies induced during the film deposition.⁶⁾ In addition, the leakage current characteristics have a sharp dependency on material composition, substrate type, fabrication conditions etc. These are very important aspects that should be solved before such films can be reliably used in devices. This is specially important for sensitive applications like memory devices and microactuators.

In our study it has been found that the reactive sputtering process is very convenient to deposit Nb-doped PbTiO₃ films. In that process, niobium is co-sputtered resulting in a uniformly doped film. Leakage is considerably reduced in doped films.

Experimental results concerning the D-E hysteresis characteristics, leakage characteristics and dielectric permittivity of Nb-doped PbTiO₃ thin films epitaxially grown on (100)Pt/(100)MgO substrates are presented.

2. Experimental

2.1. Film Deposition

In this work (100)-cut MgO single crystals were used as substrates for deposition of PbTiO₃ films. The MgO substrates were always kept in a desiccator to prevent reaction with moisture. Their dimensions were 10 mm × 10 mm × 1 mm. A layer of platinum (~100 nm thick) was epitaxially deposited by using an rf planar magnetron sputtering system and keeping the MgO substrates heated to 500°C.

PbTiO₃ thin films were deposited by reactive sputtering using an rf planar magnetron sputtering system. The substrates were heated (~530°C) during the deposition. The target consisted of a disk of metallic titanium on top of which small PbO pellets were disposed symmetrically. Doping was carried out by placing several small pieces of metallic niobium symmetrically on the titanium target. This proved to be a very convenient technique for doping the PbTiO₃ films. The deposition conditions are listed in Table I. The thickness of the samples, measured using a profilometer, varied from 350 to 400 nm. Gold top electrodes were evaporated at room temperature over the films covered with a metallic mask of the desired pattern. The diameters of the top electrodes were 0.25 μm or 0.30 μm.

| | |
|---------------------------|--|
| Substrate temperature | ~530°C |
| Input power | 40–60 W (0.51–0.76 W/cm ²) |
| Deposition pressure | 70–90 mTorr |
| Target | metallic Ti disk, PbO pellets, metallic Nb chips Purity 99.9% |
| Sputtering gas | Ar(50%) + O ₂ (50%) |
| Target-substrate distance | ~50 mm |
| Deposition rate | 2–4 nm/min |
| Cooling rate | 7–8°C/min |

Table I: Range of conditions for deposition of PbTiO₃ films on Pt/MgO substrates by reactive sputtering.

¹E-mail: tshiosak@kuee.kyoto-u.ac.jp

2.2. Measurement of Electrical Properties

The dielectric permittivity, ϵ_r , and the dielectric loss, $\tan\delta$, characteristics of the capacitor-type samples have been evaluated using an HP4192A LF impedance analyzer. All measurements have been performed using a sinusoidal signal of 300 mV in amplitude and at a frequency of 1 kHz.

D-E hysteresis curves were obtained using an RT 66 system from Radiant Technologies connected to a PC computer.

For each sample, the D-E hysteresis was first measured for the as-grown film (without any treatment) applying the drive signal to the top electrode. Later, using the same top electrode, a high DC voltage (top electrode positive) was applied for a few seconds (~ 20 – 30 sec). Such applied bias was of the order of 250 kV/cm, and, then, the hysteresis was observed again.

I-V (leakage) characteristics were obtained using an HP4140B pA meter connected to a microcomputer. The measurements were performed only for as-grown samples, without subsequent treatment.

3. Results and Discussion

Samples were doped at a niobium concentration of approximately 1, 2, 3 or 4 mol% varying the number of Nb chips in the target.

All samples used in the present study were analyzed by conventional θ - 2θ X-ray diffractometry and only perovskite phase was observed, Fig. 1. All PbTiO_3 films were highly (001)-oriented. Epitaxy in relation to the (100)Pt/(100)MgO substrates was evaluated using the energy-dispersive total-reflection X-ray diffractometry, EDTXRD (to be reported elsewhere). Films were epitaxially grown. Two types of domain regions were observed, a and c types. The c -type domains were predominant, while the minor a -type domains account for the low intensity (100) peaks in the conventional X-ray patterns. The main surface of the samples was observed using an atomic force microscope (AFM) and only a single crystal-type structure was seen.

The dielectric permittivity and the dielectric loss characteristics at 1 kHz of the (001) highly-oriented PbTiO_3 films are shown in Fig. 2. Permittivity varied from 180 to 210. It can be seen that a minimum value occurs for a niobium concentration of 1 mol%. This is likely to be related to a corresponding variation of the lattice parameters promoted by niobium doping. The dielectric loss, on the other hand, was substantially decreased with doping.

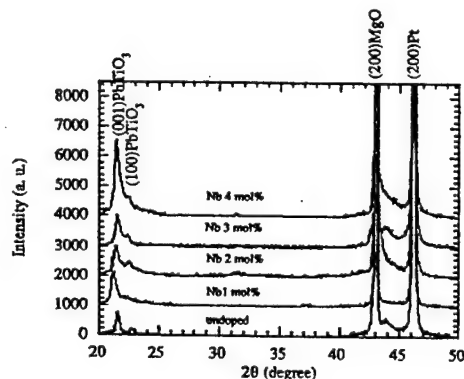


Fig.1. Variation of the structure of PbTiO_3 films deposited on Pt/MgO substrates due to niobium doping by conventional θ - 2θ XRD.

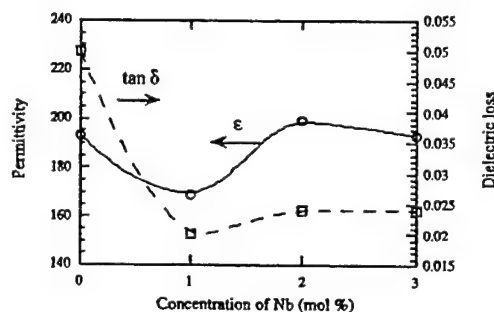


Fig.2. Variation of dielectric permittivity and dielectric loss with niobium doping of (001) highly-oriented PbTiO_3 /Pt/MgO films at 1 kHz.

D-E hysteresis patterns of PbTiO_3 /Pt/MgO thin films for as grown and after applying a DC bias conditions are shown in Figs. 3, 4 and 5. The undoped sample exhibited very slim hysteresis behavior, with low remanent polarization, Fig. 3. After applying a DC bias, the remanent polarization increased a little. Doped samples exhibited much higher remanent polarizations, Figs. 4 and 5.

The hysteresis curves of all samples at the condition of as-grown exhibit voltage offsets. Such phenomenon is commonly observed in lead-based perovskite-type ferroelectric thin films deposited in a reducing atmosphere. This has been recently associated with the creation of vacancies throughout the volume of the thin film and specially near the interfaces with the electrodes which induce the formation of internal defect dipoles.⁶⁾ Pike et al's model includes the formation of defect-dipoles due to lead and oxygen vacancies existing throughout the volume of the film. In addition, electrons and oxygen vacancies may be trapped near the electrode-film interface.

In our case, such voltage offsets could be minimized in doped samples after applying a DC bias (poling). In fact, for a niobium concentration of 3 mol% the voltage offset could be practically eliminated after applying a DC bias. On the other hand, a negative DC bias had the inverse effect of increasing the voltage offset.

We can suggest a compensation model to explain our results based on Pike et al's model. Since niobium in our films probably occupies the *B* site of the perovskite ABO_3 structure, and since niobium is likely to be pentavalent (Nb^{5+}), a valence electron may be free from the niobium atom and compensate for oxygen vacancies existing throughout the volume of the film when a high DC bias is applied. In addition, since niobium is uniformly distributed throughout the film due to the co-sputtering deposition technique employed, this compensation can easily occur. A niobium concentration of 3 mol% seems to offer an almost complete compensation.

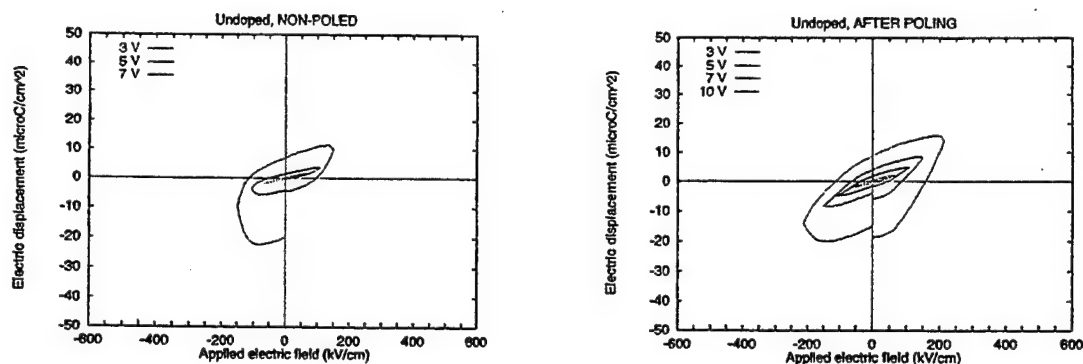


Fig.3. D-E hysteresis curves of undoped (001)-highly-oriented $PbTiO_3$.

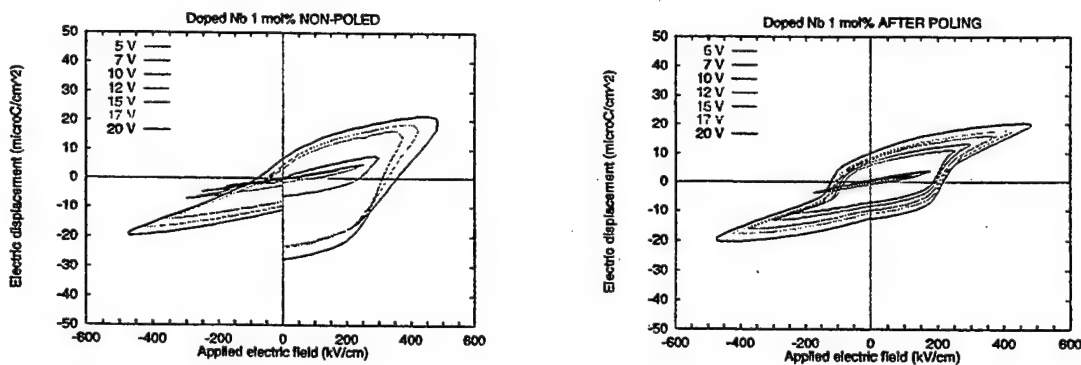


Fig.4. D-E hysteresis curves of Nb 1 mol% doped (001)-highly-oriented $PbTiO_3$.

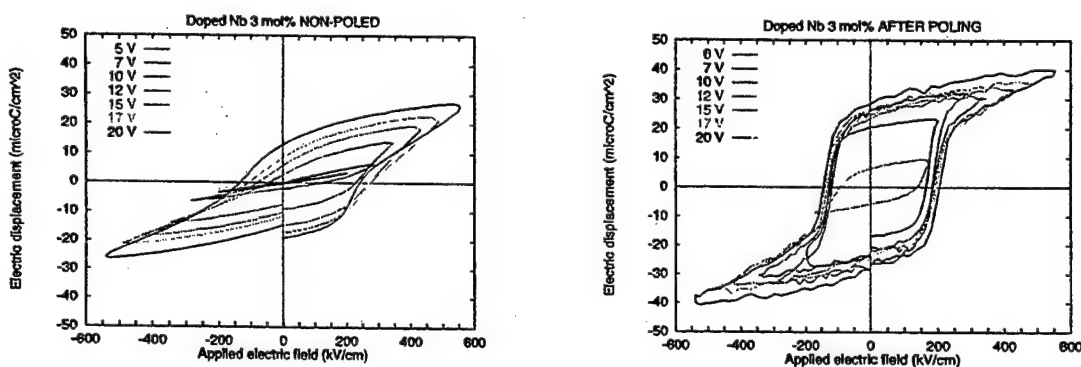


Fig.5. D-E hysteresis curves of Nb 3 mol% doped (001)-highly-oriented $PbTiO_3$.

The I-V leakage characteristics of (001) highly-oriented PbTiO_3 thin films are shown in Fig. 6. It is clear the advantage of doping PbTiO_3 films with niobium: both the leakage current and the voltage for breakdown are greatly enhanced.

A similar behavior was observed ⁵⁾ for PbTiO_3 films deposited on $\text{Pt/SiO}_2/\text{Si}$. The reason is likely to be a decrease in the p-type conductivity, commonly found in lead-base perovskites, by a charge compensation mechanism. The p-type conductivity is associated with holes generated due to lead vacancies (lead evaporates easily). Such charge carriers can eventually be annihilated by combination with the electrons from the pentavalent niobium (Nb^{+5}) substituting for the tetravalent titanium (Ti^{+4}) in the *B* site of the perovskite ABO_3 . However, these are only suppositions and have not been confirmed yet.

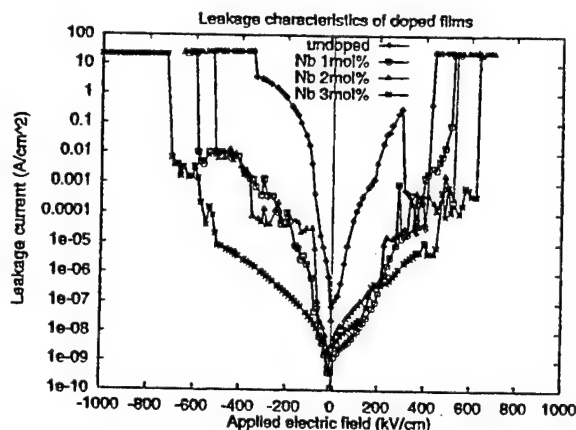


Fig.6. Leakage characteristics of Nb doped (001) highly-oriented PbTiO_3 .

References

- [1] R. Gerson and H. Jaffe: J. Phys. Chem. Solids 24 (1963) 979.
- [2] B. Jaffe, W. R. Cook and H. Jaffe, *Piezoelectric Ceramics*, (Academic Press, London, 1971).
- [3] I. Kanno, S. Hayashi, T. Kamada, M. Kitagawa and T. Hirao: Jpn. J. Appl. Phys. 32 (1993) 4057.
- [4] R. D. Klissurska, K. G. Brooks, I. M. Reney, C. Pawlaczyk, M. Kosec and N. Setter: J. Am. Ceram. Soc. 78 (1995) 1513.
- [5] R. C. Ibrahim, T. Sakai, T. Nishida, T. Horiuchi, T. Shiosaki and K. Matsushige: Jpn. J. Appl. Phys. 35 (1996) 4995.
- [6] G. E. Pike, W. L. Warren, D. Dimos, B. A. Tuttle, R. Ramesh, J. Lee, V. G. Keramidas and J. T. Evans Jr.: Appl. Phys. Lett. 66 (1995) 484.

Electrical and Structural Analysis of Epitaxial Lanthanum Modified PbTiO₃ Thin Films Exhibiting a-oriented Domains

Jon-Paul Maria and Susan Trolier-McKinstry
The Pennsylvania State University Materials Research Laboratory
State College, PA 16802

Abstract — Epitaxial lanthanum modified PbTiO₃ thin films with the composition Pb_{0.88}La_{0.10}Mn_{0.02}Ti_{0.96}O₃ (PLT) were deposited by pulsed laser deposition (PLD) on LaAlO₃ substrates using epitaxial SrRuO₃ bottom electrodes. In combination with a partial ozone ambient, ceramic targets including excess PbO were used to control lead stoichiometry. A strong dependence of the lattice constants and the film morphology on Pb-content was observed. Temperature and deposition rate were optimized for the production of stoichiometric films. Structural characterization revealed that a-oriented domains exist and are tilted ~1° with respect to the substrate normal. Electrical measurements of the heterostructures determined dielectric constants between 250-300 and tan δ values of 0.5% at 10 kHz. Remanent polarizations as large as 46 $\mu\text{C}/\text{cm}^2$ were recorded.

I. INTRODUCTION

Because materials such as PbTiO₃ have strongly anisotropic structures and properties, the ability to process single crystals with specific orientations is necessary for optimization in many applications. Provided that the appropriate substrate is available, epitaxial deposition of thin films is an efficient way of achieving this goal. However, in materials exhibiting phase transitions accompanied by large strains, such as PbTiO₃, upon cooling through the ferroelectric transition, coherent domains can emerge¹. The domains orient in such a manner as to minimize the strain imposed by rigid clamping to the substrate². The resulting domain structures are manifested as regions in the film with an a-axis orientation (i.e., the a-axis and the substrate normal are approximately collinear), surrounded by c-axis oriented material: the interfaces between them are 90° domain walls which run along the <101>-type directions^{1,2}. Formation of domains is accompanied by a puckering of the film where a and c-oriented regions tilt with respect to the substrate in opposite directions - again acting as a strain relief mechanism³. Though the film has a puckered surface profile, the interface with the substrate must maintain its integrity. To do so, appropriate populations of edge dislocations with Burger's vectors parallel and perpendicular to the interface nucleate³. In PbTiO₃, as $P_{r1} = P_{r2} = 0$, it is clear why such microstructures may be undesirable. Previous researchers

have reported this behavior for pure PbTiO₃ films, finding that below a critical thickness a-oriented material does not occur⁴. However, electrical property measurements indicating the presence or absence of a-domains have not been reported: this is likely a function of the extreme difficulty in preparing highly resistive PbTiO₃ films.

In this work, the behavior of a-oriented domains in the lead lanthanum titanate system was investigated. Even though the film may not be perfectly stoichiometric the flexible defect chemistry in the PLT composition allows high resistivity material to be synthesized⁵. For La contents ~10%, the tetragonality and spontaneous strain are large enough to permit x-ray observation of domain structures

II. EXPERIMENTAL

PLT epitaxial films on LaAlO₃ substrates with SrRuO₃ epitaxial electrodes were prepared by on-axis pulsed laser deposition. Films were deposited at temperatures ranging from 600 to 680°C. These temperatures were achieved by adhering the substrates to a block heater with silver paint. The reported measurements refer to the temperature of the stainless steel block into which a k-type thermocouple was embedded. The deposition atmosphere was a mixture of 10% ozone / 90% oxygen (i.e., the output of a PCI 1 ozone generator). Deposition pressures ranged from 100 to 300 mTorr of the O₃/O₂ mix. A 248 nm KrF excimer laser operating between 10 and 15 Hz and a target to substrate distance of 6-7 cm were used. The typical beam energy was 200 mJ/pulse and was focused with a plano-convex lens to an energy density of 2.0 J/cm². Ceramic targets incorporating excess PbO were fabricated. Several compositions were investigated, the most useful containing a PbO excess of 25 weight %. Targets were prepared by ball milling stoichiometric PLT powder with PbO for 1 hr in ethanol, then pulverizing the dried powder in an alumina mortar and pestle. 1" pellets were pressed then sintered in air at 1050°C for 1 hr. To conserve as much PbO as possible, the pellets were buried in PbO-PbZrO₃ powder - less than a 1% change in the mass was observed during sintering.

The films were characterized structurally using a Picker 4-circle diffractometer with a graphite monochromator. Electrical characterization of the polarization hysteresis and permittivity was performed using a Radiant Technologies RT66A Test System and an HP 47240 bridge respectively.

III. RESULTS AND DISCUSSION

Initially, x-ray analysis was used to approach the conditions necessary for stoichiometric film growth. Both the lattice constants and the presence of extra phases could be used to approximate the composition of the film. Excessive Pb was indicated by broad PbO reflections while Pb deficiency was marked by pyrochlore and anatase peaks. Once phase pure material was produced, the lattice constant of the PLT, in comparison to that of the bulk material, was indicative of the stoichiometry. Lead deficient films exhibited a reduced c-axis, while films with a stoichiometric quantity, or excess lead had a bulk lattice constant; Fig. 1 illustrates.

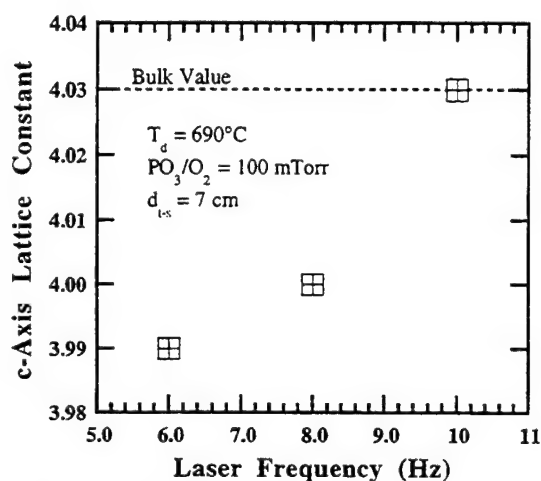


Fig. 1. Variation of lattice constant with deposition rate

Because the deposition is dynamic, where Pb and PbO are continuously and simultaneously condensing and evaporating, the deposition parameters were changed in order to adjust the equilibrium film composition. Since the volatility of Pb and PbO is exponential with temperature, small adjustments result in considerable stoichiometric variations making reproducibility difficult. Since wafer temperature measurement even in the case of a conductive block heater is non-trivial, a constant temperature for deposition was chosen. Reproducible temperatures were achieved by monitoring both the thermocouple reading and the power consumed by the stage. Changes in the emissivity of the block during deposition, the age of the thermocouple, and variable deposition pressures could affect the block temperature as much as 5 °C, which is sufficient to affect the film composition. Oxygen pressure was also effective in controlling the Pb stoichiometry. Since the volatility of Pb is greater than PbO, raising the pressure during deposition oxidizes more of the free Pb species and reduces the evaporation rate. In addition, the PbO volatility is a function of oxygen pressure with higher pressures favoring reduced

volatility. Unfortunately, in PLD oxygen pressure is coupled with deposition rate, which has a dramatic effect on Pb loss. To minimize this complication, a constant pressure of 100 mTorr was chosen. The simplest way to control the Pb content was by modulating the laser frequency. Since PLD is a discontinuous growth process, with the time between pulses being much longer than the plasma lifetime, increasing or decreasing the frequency only changes the time between plasma exposures during which Pb and PbO will evaporate. The laser frequency can be adjusted very accurately and reproducibly, making it an ideal variable with which the growth can be optimized. Figs. 2 and 3 give x-ray patterns for a typical PLT film.

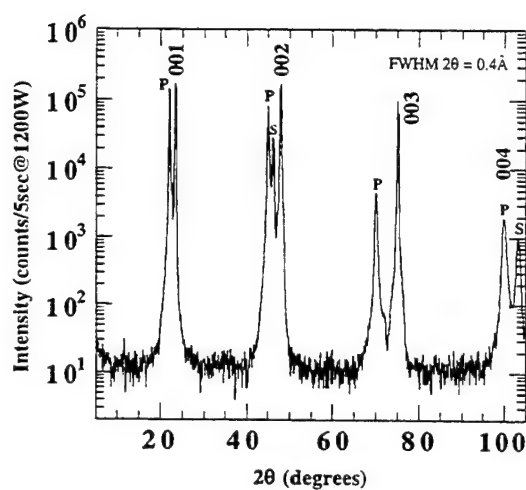


Fig. 2. θ - 2θ diffraction pattern
FWHM = full width half maximum
P = PLT, S = SrRuO₃, * = LaAlO₃

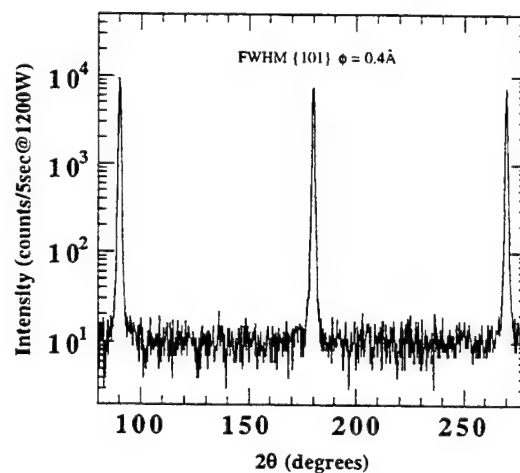


Fig. 3. ϕ -scan of PLT film showing 4-fold in-plane symmetry corresponding to in-plane epitaxial alignment

The peak widths in 2θ and ϕ are 0.4° and 0.8° , a rocking curve for this PLT film is not shown, but typical widths are measured at 0.5° .

In order to detect the a-oriented grains in the PLT films, the θ - 2θ conditions which satisfy the Bragg conditions for a 200 reflection are established. The diffractometer is then scanned in ω . The ω angle at which the maximum intensity is found corresponds to the angular tilt of the a-grains with respect to the substrate normal. Fig. 4 illustrates the microstructure.

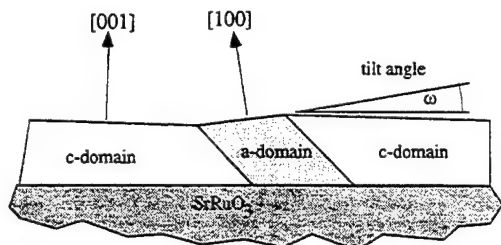


Fig. 4. Schematic of film microstructure

Rocking curve measurements of a-oriented PLT domains reveal a tilt angle of $\sim 1^\circ$. Fig. 5 shows an x-ray rocking curve about the θ - 2θ values which satisfy the Bragg conditions for both the 200 PLT and SrRuO₃ reflections. The central peak corresponds to the SrRuO₃ diffraction centered at $\omega=0$, while the two shoulders correspond to the tilted a-oriented PLT regions. It should be noted that when the scan represented in Fig. 5 is taken at a ϕ value greater by 90° a similar profile is recorded.

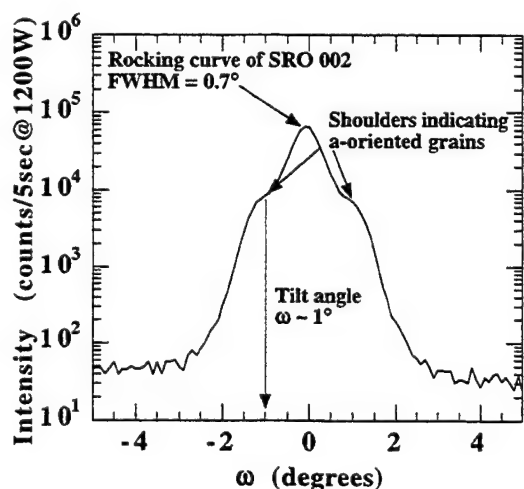


Fig. 5. ω -scan of SrRuO₃ and a-oriented PLT grains

Similar a-oriented domains have been observed by Theis

et al. in pure PbTiO₃ thin films on SrTiO₃, however, the tilt angle was considerably larger; about 3.1° . In addition, the relative distribution of the a-grains about $\omega=0$ was found to depend strongly upon the miscut of the substrate⁶. Typically, the population of the tilted grains would be skewed along the direction of miscut with the domains favoring the "uphill" side. Foster et al.³ reported a-domain tilt angles for PbTiO₃ films deposited on SrRuO₃, finding a smaller angle of 2.2° . In similar fashion, the c-domains were found to be tilted away from the substrate normal by a much smaller angle of 0.4° . It is suspected that there is a small but finite tilt in the c-oriented PLT which is beyond the resolution of our diffractometer. In these PLT thin films, the smaller tilt angle is expected as the tetragonality, or spontaneous strain, is approximately a factor of two smaller than that of pure PbTiO₃; less distortion should be required to accommodate the strain associated with the transition. The PLT a-oriented grains are distributed equally about $\omega=0$, this again is consistent with previous work as the LaAlO₃ substrates are miscut $\leq 0.1^\circ$.

The formation of domains in PbTiO₃ epitaxial ferroelectric films on SrTiO₃ is subject to a critical thickness which has been reported between 100 and 1400 Å^{3,4}. The PLT film from which Fig. 5 was taken had a thickness of about 2000 Å, well above this critical value. Given the smaller spontaneous strain, it is likely that thin films of this PLT composition will have a larger critical thickness than PbTiO₃.

Polarization hysteresis and capacitance measurements were recorded for the PLT thin films. The electrical property measurements were used to fine tune the composition of the PLT. Fig. 6 is a hysteresis loop for a highly resistive ($10^{10} \Omega\text{-cm}$) PLT film deposited very rapidly ($\sim 600 \text{Å/min}$).

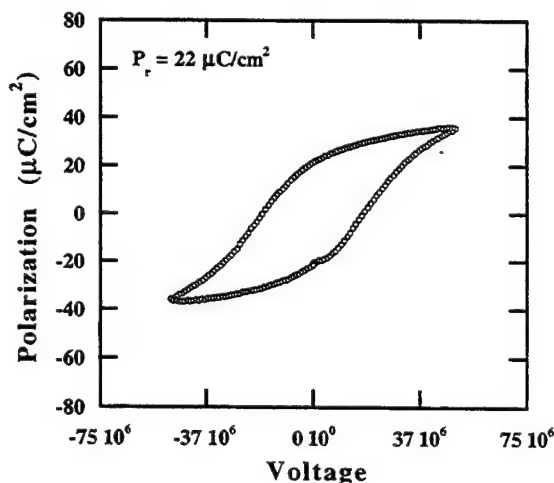


Fig. 6. Polarization hysteresis in rapidly deposited PLT

Since the ability of the films to support large fields was very sensitive to the stoichiometry, the shape of the hysteresis loops was used as feedback to determine the optimized deposition parameters. The very rapid deposition of the film in Fig. 6 was required for maintenance of Pb stoichiometry with a target containing 12% excess PbO. X-ray line widths for this sample were greater by a factor of two in all circles than those given in Figs. 2 and 3. The broad line widths and the low value of remanent polarization are indicative of higher defect concentrations and the strong mosaic structure in samples prepared in these conditions. A target with 25% excess PbO allowed the deposition rate to be reduced, the results are shown in Fig. 7.

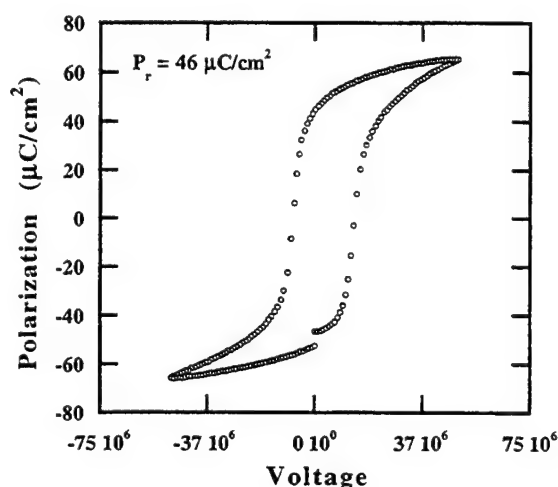


Fig. 8. Polarization hysteresis in optimized PLT

Reduction of the deposition rate allowed the growth of a more perfect structure with a hysteresis loop more similar to that of a single crystal. Additionally, the surface morphology - as measured by Nomarski phase contrast microscopy - improved for the more slowly deposited sample. At 3000x, no surface microstructure is visible in the slowly grown film, while on the rapidly grown sample under the same imaging conditions considerable roughness can be detected. The dielectric constants for both films ranged between 250 and 300. It is likely that a thin surface layer of Pb deficient material is present on both sample surfaces which reduces the measured capacitance. It is suspected that during cooldown the PLT film loses Pb from the surface, as it requires about 2 minutes to cool below 500°C.

IV. SUMMARY AND CONCLUSIONS

Epitaxial thin films of $\text{Pb}_{0.88}\text{La}_{0.1}\text{Mn}_{0.02}\text{Ti}_{0.96}\text{O}_3$ were deposited on SrRuO_3 coated LaAlO_3 by pulsed laser deposition. PLT targets with 12% and 25% excess PbO were

fabricated and used as the source material. In order to deposit near stoichiometric films, the PLD process was optimized using the laser repetition rate as the control variable.

As has been observed in pure PbTiO_3 films, a-oriented domains existed in the epitaxial PLT layers. In the case of PLT on SrRuO_3 , the a-domains were tilted 1° with respect to the substrate normal. If c-domain tilting occurred, it was beyond the resolution of our diffractometer. Samples as thin as 100 nm exhibited a-domain populations; thinner samples were not investigated.

Using a PLT target with 12% excess PbO, high resistivity films were grown, however, growth rates which provided poor morphology and microstructure were necessary to conserve lead. Remanent polarization values as large as $22 \mu\text{C}/\text{cm}^2$ were measured. A target composition including 25% PbO allowed the deposition rate to be reduced to a value which rendered smooth films with good crystallinity. In these films remanent polarizations of $46 \mu\text{C}/\text{cm}^2$ were recorded.

V. REFERENCES

- 1 B. Jaffe, W. R. Cook, and H. Jaffe, *Piezoelectric Ceramics* (R. A. N. Publishers, Marietta, OH, 1971).
- 2 C. M. Foster, Z. Li, M. Buckett, D. Miller, P. M. Baldo, L. E. Rehn, G. R. Bai, D. Guo, H. You, and K. L. Merkle, *J. Appl. Phys.* **78**(4), 2607-2622 (1995).
- 3 C. M. Foster, W. Pompe, A. C. Daykin, and J. S. Speck, *J. Appl. Phys.* **79**(3), 1405-1415 (1996).
- 4 J. S. Speck and W. Pompe, *J. Appl. Phys.* **47**(10), 6012 (1993).
- 5 D. Hennings and K. H. Härdtl, *Phys. Stat. Sol. (a)* **3**, 465-74 (1970).
- 6 C. D. Theis and D. G. Schlom, *J. Mat. Res.* **12**(5), 1297-1305 (1997).

Bioanalytical MEMS Based on Piezoelectric Materials

Dennis L. Polla, Ronald C. McGlennen, and Leo T. Furcht

Microtechnology Laboratory
and
Department of Laboratory Medicine and Pathology
University of Minnesota
200 Union Street S.E. (1-165)
Minneapolis, Minnesota USA 55455

Correspondence: TEL: 612-624-8005; FAX: 612-625-5012; polla@ee.umn.edu

Abstract

Abstract - Biomedical Micro-electromechanical Systems (Bio-MEMS) represent an exciting new extension of commonly used thin film deposition, lithography, etching, and packaging techniques. This work has incorporated piezoelectric materials in the realization of two important classes of bioanalytical microinstruments. Examples of applying piezoelectric-based BioMEMS include molecular recognition piezoelectric cantilevers and microfluidic pumps and valves for reagent control in genetic microchips. These applications are directly derived from previous work in physical microsensors and micro-actuators based on piezoelectric MEMS.

I. Introduction

Piezoelectric MEMS¹⁻³ are usually operated in one of two modes: sensor or actuator. When used as a sensor one usually detects a change in internal dipole moment within the piezoelectric crystal induced through either a stress. This change in internal dipole moment is usually detected in the form of a charge or voltage developed across a set of appropriately located electrodes surrounding the piezoelectric crystal. When used as an actuator, a voltage is

applied across a set of electrodes thereby inducing a strain or deformation of the crystal. This controlled deformation is used to do work. This paper combines microfabrication with the above device principles.

II. Piezoelectric Materials and Fabrication

Several applications of piezoelectric microsensors and microactuators are presented in this paper. All applications are based on thin films of lead zirconate titanate, or PZT. These films are deposited in thicknesses between 3000 Å to 1.5 µm using sol-gel processing methods⁴ (see Fig. 1).

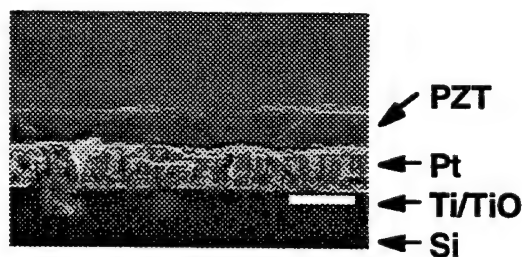


Fig. 1. SEM of a PZT microsensor capacitor (Ref. 4).

Materials and processing of PZT thin films and their integration with on-chip signal processing electronics are described elsewhere¹⁻². A representative fabrication sequence used in the construction of a molecular recognition cantilever biosensor to be described is shown in Fig. 2.

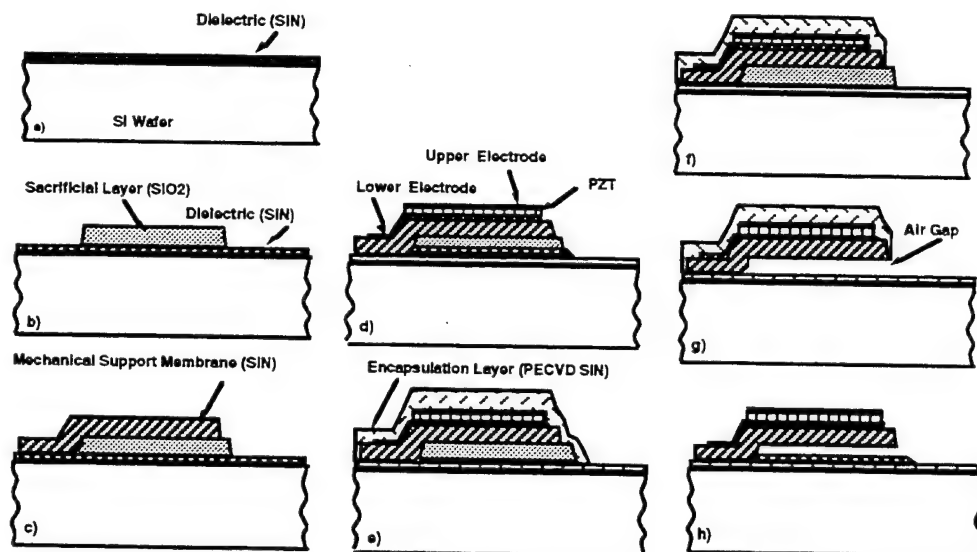


Fig. 1. Main steps in the formation of piezoelectric microcantilevers with a biomolecular recognition coating on the top surface. See also structure in Fig. 2.

III. Molecular Recognition Biosensor

A piezoelectric microcantilever beam has been fabricated for the detection of viruses. This device is based the detection of specific biochemical binding which takes place on the top surface of the cantilever as shown in Fig. 2. A finished device is shown in Fig. 3.

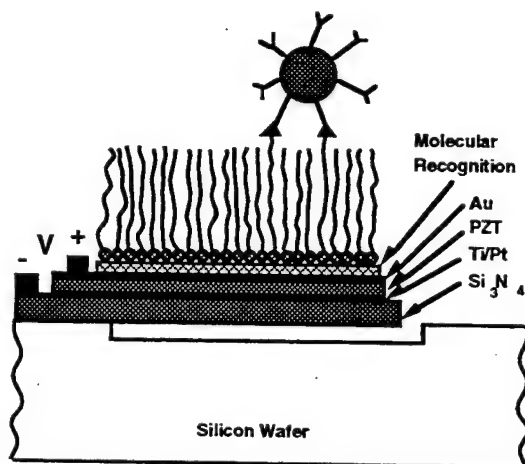


Fig. 2. Molecular recognition biosensor.

The specific binding induces a stress in a polydiacetylene polymer overlying the microcantilever. This stress is transduced

to a piezoelectric sensor structure and a corresponding charge (or voltage) is produced. An amplifier detects the piezoelectric response and a characteristic biochemical binding signature is produced. The response time (~ 1 ms) depends on the biochemical reaction kinetics and the electrical characteristics of the piezoelectric microsensor. After all binding sites have reacted, charge leakage of the piezoelectric capacitor is observed as shown in Fig. 4.

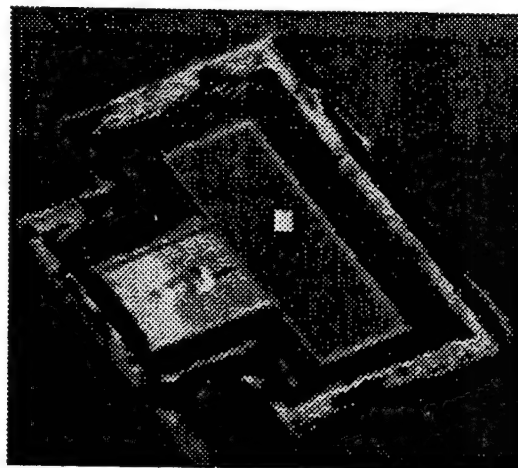


Fig. 3. SEM of a microfabricated biomolecular recognition sensor as described in Fig. 1.

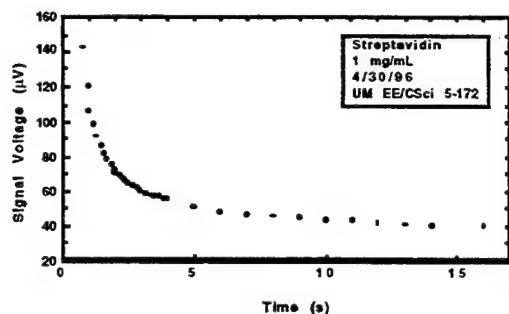


Fig. 4. Piezoelectric microsensor response to the binding of streptavidin on a biotin coated cantilever surface.

The piezoelectric device is capable of ultra high sensitivity detection of several human viral pathogens including influenza and rhinovirus. Testing of this device has revealed its remarkable characteristic to function is air, atomized aerosol, and submerged in a liquid. Application of this device to patient care include environmental monitoring of filtered air and possibly the measurement of potential pathogens in administered blood products and drugs.

III. DNA Microchips

Piezoelectric thin films are also being developed in our laboratory for controlling fluids on a microchip in common molecular diagnostic tests. The goal of this research is to apply MEMS-based IC processing in the realization of batch-fabricated genetic microchips. Such chips require the ability to 1) extract nucleic acid from a tissue sample (most commonly blood), 2) amplify segments of DNA for a pre-selected genetic test commonly carried out through the polymerase chain reaction (PCR), and 3) detect the amplified DNA. A common detection method is capillary electrophoresis (CE). All of these processes rely on the controlled manipulation of sample fluids, reagents, and other solutions. Our approach is to use piezoelectric MEMS for the active

control of fluids. Fig. 5 shows a schematic of a genetic microchip.

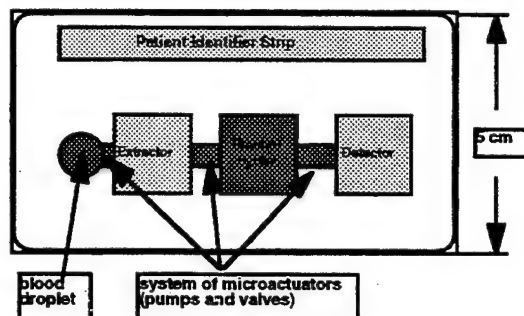


Fig. 5. Microchip-based strategy of genetic testing. Micropumps and fluid control valves are used to move both sample and reagents in a controlled manner through microcapillaries interconnecting the main functional locations on the microchip.

This requires the ability to both pump and restrict (valve) fluid flow. Piezoelectric thin films deposited on silicon nitride membranes are connected in the form of a three-stage peristaltic micropump. A device cross section is shown in Fig. 6.

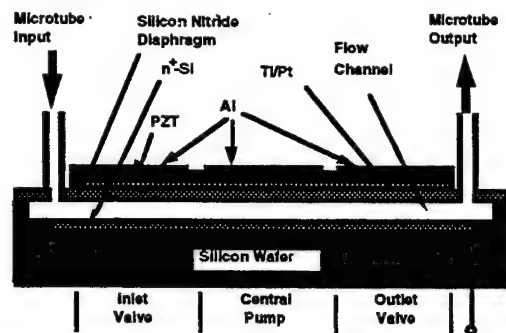


Fig. 6. Piezoelectric micro-diaphragm for fluid control micropumps and microvalves.

Independent actuation of the three-stages is used to move a reagent or sample in a controlled direction. Membranes of 400 μm -dia. have been connected in parallel to increase the pumping volume. Synchronous timing at 800 Hz is used to

deliver fluid volumes on the order of 0.5 to 1.0 $\mu\text{L/s}$ with a controlled dispense volume of approximately 10 nL. Prototype micropumps are shown in Fig. 7.

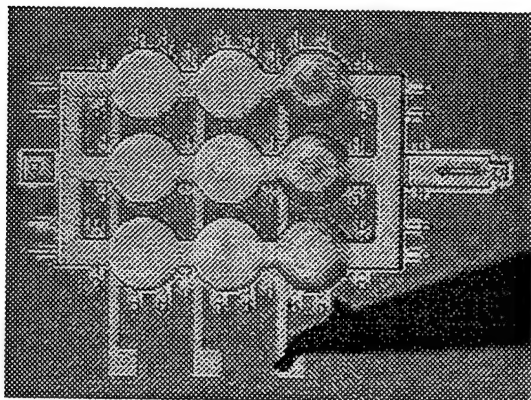


Fig. 7. Microfluidic control system. Three membranes forming output control valves are actuated at 52 V.

At the time of this writing, the full genetic microchip shown in Fig. 6 has not been realized on a single chip. Compatible microfabrication methods have been designed however to use the microfluidic controls of Fig. 7 to interface with the DNA extractor, PCR reactor, and DNA detector (CE). These other components have been functionally realized and are shown in Figs. 8. It is our goal to use the microfluidic control shown in Fig. 7 to interconnect these other building blocks to form an inexpensive DNA processor.

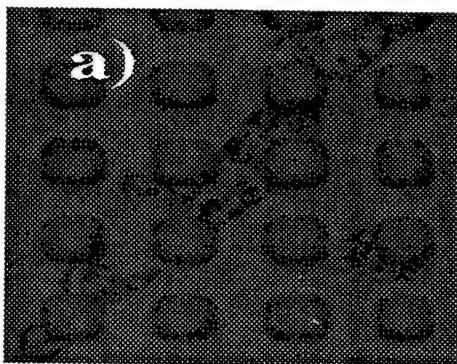


Fig. 8a. Nucleic acid extractor based on a size discrimination of white- and red-

blood cells. Shown is immobilized nucleic acid.

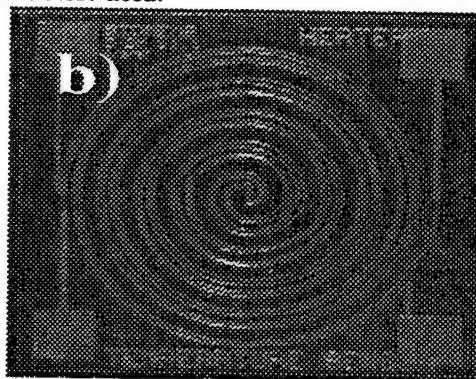


Fig. 8b. PCR thermocycler.

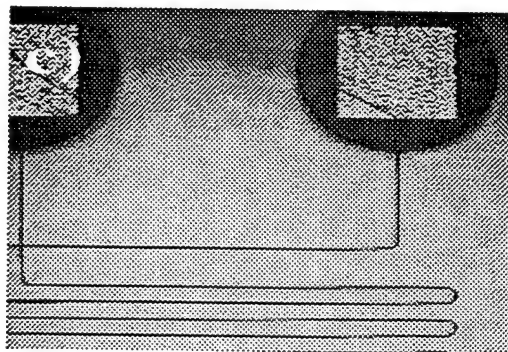


Fig. 8c. Microcapillary electrophoresis column.

V. Conclusions

Piezoelectric materials have been integrated with MEMS structures in the formation of components for bioanalytical instruments. Device feasibility has been demonstrated in biomolecular recognition cantilevers and microfluidic controls for genetic testing. System integration of these building blocks is underway.

References

1. D. L. Polla, *Microelectronic Engineering* 29, 51-58, 1995.
2. D. L. Polla and P. J. Schiller, *Int. Ferroelectrics* 7, 359-370, 1995.
3. D. L. Polla and L. F. Francis, *Materials Research Society Bulletin*, V. 21, No. 7, July 1996, pp. 59-65.
4. L. Francis, J. Wright, and D. Drinkwater, to be published.

Effect of Thickness and Texture on the Ferroelectric Properties of Lead Zirconate Titanate Thin Films by Sol-Gel Processing

Fan Chu, Tao Su, and Susan Trolier-McKinstry

Intercollege Materials Research Laboratory
The Pennsylvania State University
University Park, PA16802 USA

Abstract — The thickness dependence of the texture development and ferroelectric properties of sol-gel PZT films deposited on platinum-based electrodes were investigated. Crack-free PZT films with (111) orientation were obtained by using multiple-spin-coating and rapid thermal annealing techniques. The (111) preferred orientation became weaker with increasing film thickness. The remanent polarization (P_r) increases and the coercive field (E_c) decreases with increasing thickness. It was found that, for films prepared using multiple crystallization steps, a higher pyrolysis temperature such as 445 °C did not result in a strong (100) orientation. However, thermally annealing the substrate prior to depositing the ferroelectric film favors the formation of (100) oriented perovskite film and reduces the coercive field of the PZT film about 30% without sacrificing much P_r .

I. INTRODUCTION

Micro-Electro-Mechanical Systems (MEMS) have attracted great attention for miniaturized sensors, analytical equipment and optical components etc.. In MEMS, micro-actuators play an important role in converting electrical energy to mechanical energy. Because of their strong piezoelectric behavior, lead zirconate titanate (PZT) ceramic compositions near the morphotropic phase boundary have been widely utilized in bulk actuator and transducer applications. Therefore, PZT thin films are a promising candidate for MEMS micro-actuators. Many approaches such as sol-gel spinning, MOCVD, sputtering, and laser ablation etc. have been used to prepare PZT thin films. Among them, sol-gel derived PZT thin films are of particular interest because of the low crystallization temperature, easy control of composition and thickness of the films as well as the simplicity of the sol-gel processing. The crystallization and the texture development of sol-gel PZT thin films as a function of pyrolysis and crystallization temperatures have been reported in detail [1,2]. It was concluded that the preferred orientation of PZT thin films can be controlled by varying the pyrolysis temperature, heating rate and composition. However, this conclusion was drawn based on films crystallized in a single crystallization step. In MEMS applications, where large amplitude displacements are required, relatively thick films, which cannot be crystallized easily in a single step without cracking are needed. Less is

known about the development of preferred orientation in this case. One of the few exceptions pertains to the thickness dependence of the dielectric and piezoelectric properties of PZT films prepared using acetic acid-based solutions [3]. Strong (100) orientation was observed in those PZT films crystallized in a conventional box furnace.

In the present paper, sol-gel derived PZT thin films with the morphotropic boundary composition (PZT 52/48) were prepared on Pt/Ti/SiO₂/Si substrates using a methoxyethanol-based precursor solution and rapid thermal annealing (RTA). Multiple spin-coatings and multiple RTA treatments were used in order to prepare PZT films with thicknesses greater than 1 μ m. The texture change of the multi-layer PZT thin films were studied as a function of various processing parameters. The electrical properties of PZT thin films with (111) and (100) orientations were characterized. The correlation between texture development and electrical properties will be discussed.

II. PROCEDURE

A. PZT 52/48 thin film preparation.

The sol-gel solutions were prepared following the methoxyethanol process, which was proposed by Budd [4] and modified by Brooks [5]. First, lead acetate trihydrate was dissolved in 2-methoxyethanol and the water of hydration was distilled at 120 °C under vacuum of 130mbar. Appropriate quantities of Zr propoxide, Ti isopropoxide and the lead acetate were mixed in 2-methoxyethanol, and then refluxed at 110 °C for 2.5 hours. A 0.4 Molar working solution containing 12% excess Pb was prepared for thin film fabrication. PZT films were produced by spin coating the precursor solution on substrates at 3000 rpm for 30 seconds. Each PZT layer was pyrolyzed at 340 °C for 60 second unless otherwise noted. After four cycles of the spin coating and pyrolysis, the deposited film was crystallized at 700 °C for 30 sec using rapid thermal annealing (RTA), and a PZT film of approximately 0.2 μ m thickness was obtained. Thicker PZT films were fabricated by repeating this procedure.

The substrates used for this work were Pt/Ti/SiO₂/Si wafers commercially produced by Nova Electronics. The thickness of the SiO₂, Ti and Pt layers were 0.2 μ m, 200 Å and

1200 Å respectively. The Pt layer is strongly (111) oriented. The diameter of the sputtered Pt top electrode was 1.6 mm.

B. Characterizations

The structure of the PZT films was investigated at room temperature using a Scintag X-ray diffractometer with Cu K α radiation. The relative intensity in this work is defined as

$$(I/I^*)/[(I/I^*)_{111} + (I/I^*)_{110} + (I/I^*)_{100}]$$

Where I and I^* represent the integrated intensity of the (111), (110) or (100) XRD peaks of the PZT film and of the PZT bulk ceramic powder.

The ferroelectric hysteresis loops were tested using an RT-66A standardized ferroelectric test system produced by Radiant Technologies.

III. RESULTS AND DISCUSSION

PZT 52/48 films with thicknesses between 0.4 and 5.0 μm were prepared. Fig. 1 shows the XRD patterns of PZT films with different thicknesses. It can be seen that the PZT films were strongly (111) oriented, probably due to the (111) orientation of the Pt layer on the Si substrate. PZT films may grow with a local epitaxial relation to individual Pt grains, forming a (111) textured film, which is random in plane. The XRD pattern of a crystallized PZT film with a pyrolysis temperature of 445 °C showed no change in film texture (Fig. 1), indicating a different mechanism for the texture evolution in the PZT films prepared using a multiple crystallization approach compared to previous reports. For the PZT thin films (thickness=0.2 μm) prepared using single crystallization step, a strong (111) XRD peak was observed in the film pyrolyzed at 235 °C whereas the (100) peak was largely enhanced when the film was pyrolyzed at 445 °C. This is consistent with the results reported in [1] and [2]. Fig. 2 shows the ferroelectric hysteresis loops of PZT 52/48 films with different thicknesses. It is evident that the thicker film

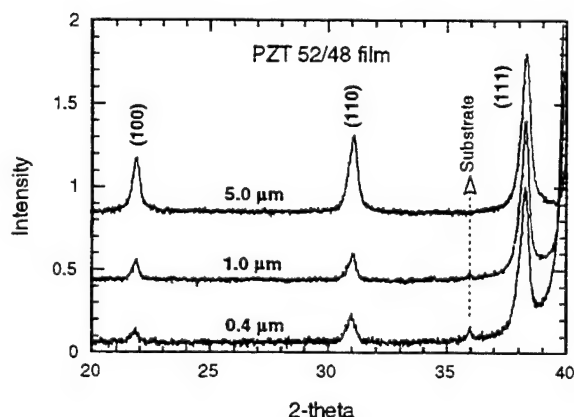


Fig. 1 X-ray diffraction patterns of the PZT 52/48 films with thickness of 0.4 and 5 μm (pyrolyzed at 340°C) and 1 μm (pyrolyzed at 445 °C). The reflection peaks at 36 ° are from the substrate.

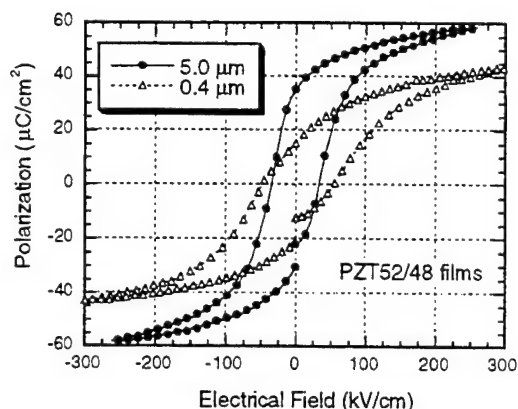


Fig. 2 Polarization as a function of electric field for PZT 52/48 films .

exhibits a higher remanent polarization and a lower coercive field. In order to compare the orientations of the films quantitatively, the relative XRD peak intensities of the (111), (100) and (110) peaks are shown in Fig. 3 as a function of the thickness of the PZT films. With increasing thickness, the (111) orientation of the film decreases whereas the (110) and (100) orientations increase. Below 2 μm , the orientation was approximately constant.

The remanent polarization of the PZT films increases and the coercive field decreases with increasing thickness (Fig. 4). It is noted that the thickness dependence is much stronger for the films with thicknesses under 2 μm .

As shown in Fig. 1 and Fig. 3, samples prepared with a higher pyrolysis temperature (445 °C) showed the same film texture as the films fabricated at a lower pyrolysis temperature (340 °C). Even a change of the heating rate and annealing time during crystallization did not change the texture of the PZT films. For example, a PZT 52/48 film was thermally annealed at 700°C for 1 hour with a heating rate of 20°C/min. The crystallized film was still strongly (111) oriented.

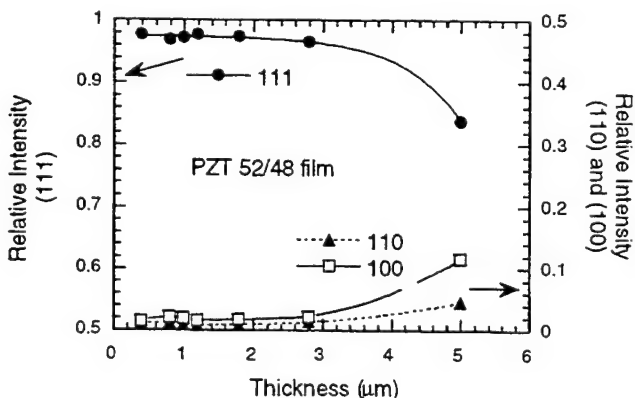


Fig. 3 The relative intensities of the XRD (111), (100) and (110) peaks as a function of thickness for PZT 52/48 films. The 1 μm film was pyrolyzed at 445°C and the rest of the films were pyrolyzed at 340 °C.

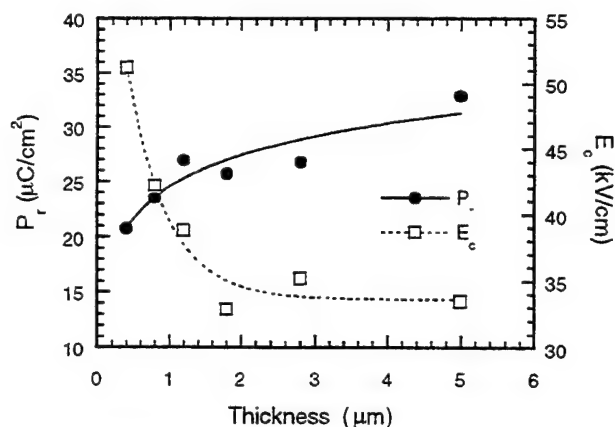


Fig. 4 The remanent polarization and the coercive field as function of thickness for PZT 52/48 films. P_r and E_c were determined from hysteresis loops. The applied maximum electric field was 300kV/cm and the frequency was 50 Hz.

Therefore, it is difficult to manipulate the preferred orientation of the PZT films prepared using multiple crystallization treatment by varying the pyrolysis temperature. However, it is found that the texture of the PZT films can be varied by thermally annealing the substrates before the deposition of the PZT film. Fig. 5 shows the relative XRD peak intensities of PZT 52/48 thin films (thickness = 1 μm) as a function of the pre-annealing temperature of the substrates. The relative intensity of the (111) peak decreases to 25% if the substrate is annealed at 850 $^{\circ}\text{C}$ before depositing the PZT film, whereas the relative intensity of the (100) peak increases to 70%. The strong influence of substrate pre-annealing on the texture of PZT films suggests that the preferred orientation of the multiply annealed PZT films is governed by the texture of the bottom electrode or substrate. The origin of the texture change due to substrate pre-annealing is still not completely understood. One possible mechanism relates to the diffusion of Ti to the Pt surface. At high temperatures, Ti diffuses

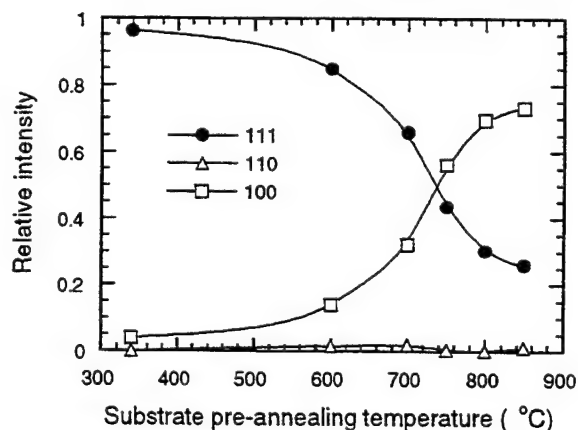


Fig. 5 Relative intensities of the (111), (100) and (110) XRD reflection peaks as a function of the substrate pre-annealing temperature for PZT 52/48 films. The thickness of the films is 1 μm .

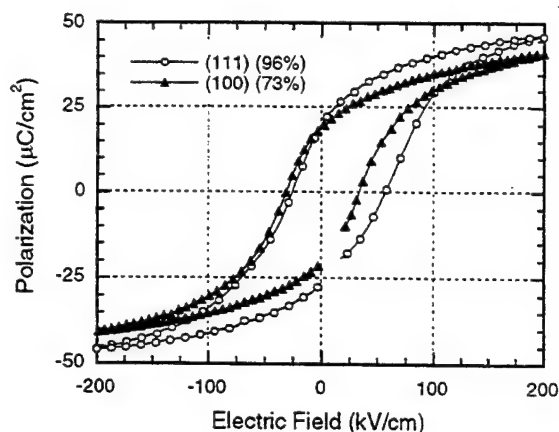


Fig. 6 Ferroelectric hysteresis loops of (111) and partially (100) textured films measured at 50 Hz showing the difference in E_c . Thickness of the films = 1 μm .

through the Pt layer forming a thin layer of TiO_2 or Ti-Pt alloy [6, 7, 8], so that the effect of the (111) orientation of Pt is inhibited and the nucleation of (111) oriented PZT grains is less strongly favored. This is evidenced by the fact that an additional TiO_2 thin layer between Pt and PZT film has been reported to favor the formation of a partially (001) textured PZT film [9]. The ferroelectric hysteresis loops of the (111) textured and the (100) dominated films are shown in Fig. 6. The coercive field of the (100)-oriented film is lower than that of the (111) textured film. Fig. 6 shows P_r and E_c for the PZT 52/48 films as a function of substrate pre-annealing temperature. When pre-annealing temperatures are lower than 700 $^{\circ}\text{C}$, P_r increases slightly and E_c decreases with increasing temperature. However, if the pre-annealing temperatures are higher than 700 $^{\circ}\text{C}$, both P_r and E_c decrease with increasing temperature. The decreased E_c with increasing pre-annealing temperature might be due to the fact that (100) is the neutral crystal face in perovskite and possesses the lowest energy

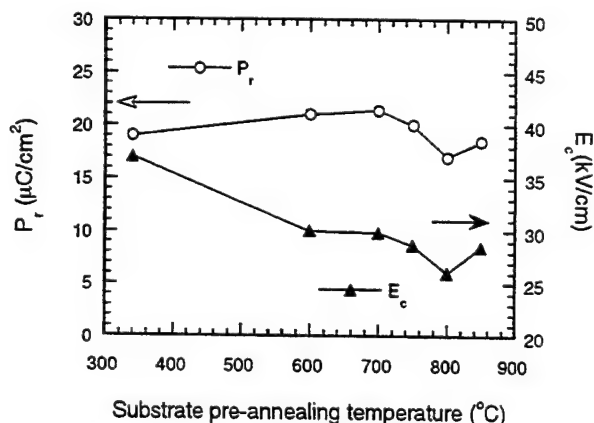


Fig. 7 Remanent polarization and coercive field of PZT 52/48 films (thickness = 1 μm) as a function of the substrate pre-annealing temperature.

[10], so that the film is self-textured [11]. Since there is no epitaxy involved, the built-in stress during the formation of the PZT film should be lower, which may give rise to a lower E_c .

IV. SUMMARY

Sol-gel derived PZT 52/48 films with various thicknesses were prepared on (111) textured Pt/Ti/SiO₂/Si substrates using a 2-methoxyethanol-based precursor solution and rapid thermal annealing. It was found that the film texture was not strongly related to the pyrolysis temperature for the PZT films prepared by multiple crystallization. Instead, pre-annealing the substrate (bottom electrode) changes the orientation of the PZT films. The substrate thermal annealing can also reduce the coercive field of the PZT films while the remanent polarization is not strongly affected.

ACKNOWLEDGMENT

This work is sponsored by the National Science Foundation IUCRC Program (EEC-95 2808).

REFERENCES

- [1] S.Y. Chen and I.W. Chen, "Temperature-time texture transition of Pb (Zr_{1-x}Ti_x)O₃ thin films: I. Role of Pb rich intermediate phases. II, heat treatment and compositional effects," *J. Am. Ceram. Soc.* Vol. 77 (9), pp. 2332-2344, 1994
- [2] K.G. Brooks, "Ferroelectric thin film processing," *Growth and Applications of Thin Films*, edited by L. Eckertova and T. Ruzicka. Proc. Int. Summer School, June 20-25, 1994, Chlum u Trebone, Czech Republic (Prometheus Publishing, Prague, 1994).
- [3] H. D. Chen, K.R. Udayakumar, C. J. Gaskey and L.E. Cross, "Fabrication and electrical properties of lead zirconate titanate thick films," *J. Am. Ceram. Soc.* Vol. 79 (8), pp. 2189-22192, 1994
- [4] K.D. Budd, S.K. Dey, and D.A. Payne, "Sol-gel processing of PT, PZ, PZT and PLZT thin films," *Brit. Ceram. Proc.* Vol 36, pp. 107-121, 1985.
- [5] K. Brooks, I.M. Reaney, R. Klissurska, Y. Huang, L. Bursill and N. Setter, "Orientation of rapid thermally annealed lead zirconate titanate thin films on (111) Pt substrates," *J. Mater. Res.*, vol. 9, pp. 10, 1994
- [6] C. J. Kim, D. S. Yoon, J. S. Lee, C. G. Choi and K. No, "Effect of substrate and bottom electrodes on the phase formation of lead zirconate titanate thin films prepared by the Sol-Gel method," *Jpn. J. Appl. Phys.* Vol 33, pp.2675-2678, 1994
- [7] J.G.E. Gardeniers, A. Smith and C. Cobianu, "Characterization of sol-gel PZT films on P₁-coated substrates," *J. Micromech. Microeng.* Vol. 5 pp. 153-155, 1995
- [8] C. S. Hwang, M. D. Vaudin and P. K. Schenck, "Influence of the microstructure of P₁ / S₁ substrates on textured growth of barium titanate thin films prepared by pulsed laser deposition," *J. Mater. Res.*, in press
- [9] K. G. Brooks, M. Kohli, D.V. Taylor, T. Maeder, I.M. Reaney, A. Kholkin, P. Muralt and N. Setter, "Sol-gel deposition of PZT thin films on ceramic ZrO₂ substrates," *Proceedings of the Tenth IEEE International Symposium on Applications of Ferroelectrics*, East Brunswick, NJ. U.S.A., Aug. 18-21, 1996, Vol. II, pp. 611-614
- [10] T. Tani, Z. Xu and D. Payne, *Ferroelectric thin films III*, *Mat. Res. Soc. Symp. Proc.* Vol 310, pp.269, 1993
- [11] S. Goto, N. Fujimura, et al., *J. Crystal Growth*, Vol. 115, pp. 816, 1991

Properties of Sputtered Ir and IrO₂ Electrodes for PZT Capacitors

M. Shimizu, S. Hyodo, S. Nakashima, H. Fujisawa and H. Niu

Department of Electronics, Faculty of Engineering, Himeji Institute of Technology

2167 Shosha, Himeji, Hyogo 671-22, Japan

and

H. Okino and T. Shiosaki

Department of Electronic Science and Engineering, Graduate School of Engineering, Kyoto University

Yoshida Honmachi, Sakyo-ku, Kyoto 606-01, Japan

Abstract - Ir and IrO₂ thin films for electrodes of PZT capacitors were prepared by rf magnetron sputtering using an Ir metal target and an IrO₂ ceramic target. Polycrystalline PZT films were grown on Ir/SiO₂/Si, IrO₂/SiO₂/Si and Ir/IrO₂/SiO₂/Si substrates by MOCVD. The barrier properties of these electrode materials were investigated by SIMS analysis. From the SIMS analysis, it was found that interdiffusion at the interface between PZT and the electrode was influenced by the thickness of the bottom electrode.

I. INTRODUCTION

A variety of electrode materials, such as Pt, Ru, Ir, RuO₂, IrO₂, PtRhO_x, YBCO, LSCO and SrRuO₃, have been reported for memory device applications using ferroelectric thin film and high-dielectric-constant thin film. Among these electrode materials, Ir and IrO₂ are very promising materials for PZT capacitors because of the fact that sol-gel PZT capacitors using these electrodes showed no polarization fatigue [1-3]. In our previous report, MOCVD-PZT capacitors using Ir and IrO₂ electrodes (Ir/IrO₂/PZT/Ir/IrO₂/SiO₂/Si) showed no fatigue up to a switching cycle of 10¹¹ and small current density of 10⁻⁷ A/cm² at 3V, and we confirmed the effectiveness of the use of Ir and IrO₂ electrodes [4-7]. At this stage, it seems that the effectiveness of the use of Ir and IrO₂ can be attributed to their high diffusion barrier properties. In order to understand this effectiveness, however, further investigation of the interface between PZT and Ir/IrO₂ electrode are required.

In this study, we optimized the growth conditions of Ir and IrO₂ thin films and investigated the interface between PZT and electrodes using Secondary Ion Mass Spectrometry (SIMS).

II. EXPERIMENTAL PROCEDURE

Ir and IrO₂ thin films were prepared by an rf magnetron sputtering system (ANELVA : L-100S) using a pure Ir metal target (Furuya Metal Co., purity : 99.9%). IrO₂ films were also prepared by rf magnetron sputtering using a ceramic IrO₂ target. PZT films were grown on these electrode materials by the MOCVD method using Pb(C₂H₅)₄, Zr(O-tC₄H₉)₄ and Ti(O-iC₃H₇)₄ as precursors [4,6]. SiO₂/Si was used as a substrate. The interface conditions between the PZT films and electrode materials were mainly analyzed using SIMS. The electrical properties of PZT capacitors, including I-V and fatigue characteristics, were measured using an electrometer (Keithley : 6517), an LF impedance analyzer (HP : 4192A), and an RT-66 test system (Radiant Technology).

III. RESULTS AND DISCUSSIONS

Ir thin films were prepared by sputtering at deposition temperatures ranging from 350 to 530°C, rf input powers of 10-50W and sputtering pressures of 1.0-8.0×10⁻²Torr. The orientation and degree of the orientation were strongly influenced by the growth parameters [7]. Highly (111)-oriented Ir films were grown on SiO₂/Si at 530°C, 30W and 2×10⁻²Torr.

IrO₂ films were also prepared by reactive sputtering using an Ir metal target at the same sputtering conditions as those of the Ir films. In these experiments, a sputtering gas mixture ratio of Ar/O₂ was one of the most important growth parameters, evidenced by the fact that the orientation and

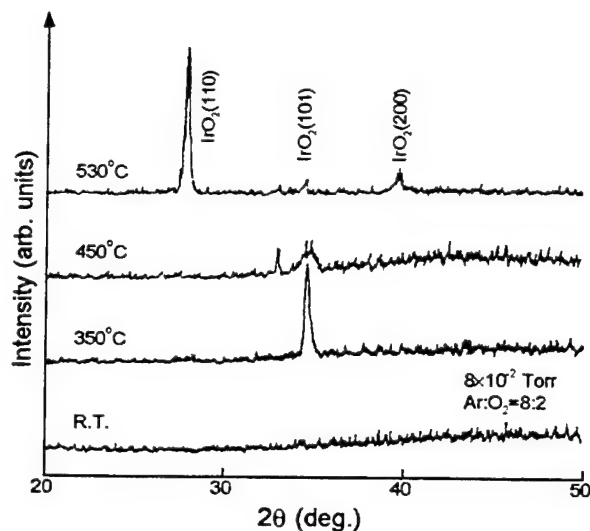


Fig. 1. X-ray diffraction patterns of IrO₂ thin films deposited at various growth temperatures.

resistivity were strongly influenced by the Ar/O₂ gas ratio [7]. (110), (101) and (200) mixed-oriented IrO₂ films with a minimum resistivity of about 52.5 μΩ·cm were successfully grown at a deposition temperature of 530°C.

When IrO₂ films were prepared by reactive sputtering, control of such film characteristics as orientation and stoichiometry was quite difficult because of a complex reaction on the target surface. For this reason IrO₂ films were also prepared by sputtering using an IrO₂ ceramic target for the first time. The film orientation was influenced by the deposition temperature. Highly (110)-oriented IrO₂ films were grown at 530°C and (101)-oriented films were also grown at 350°C as shown in Fig.1. The resistivities of the IrO₂ films decreased as the deposition temperature increased and a minimum value of 170 μΩ·cm was obtained. Fig.2 shows the dependence of the resistivity of IrO₂ grown using an IrO₂ ceramic target and an Ir metal target on the deposition temperature. IrO₂ films obtained using a ceramic target showed higher resistivities than those of IrO₂ films obtained using a metal target. The deposition rate of IrO₂ films prepared using an IrO₂ ceramic target was lower than that of films prepared using a metal target.

Polycrystalline PZT thin films were grown on Ir, IrO₂ and Ir/IrO₂ bottom electrodes at 600°C by MOCVD. Fig.3 shows X-ray diffraction patterns of PZT grown on Ir, IrO₂ and Ir/IrO₂ bottom electrodes. This figure shows that perovskite PZT films were successfully obtained on these electrodes.

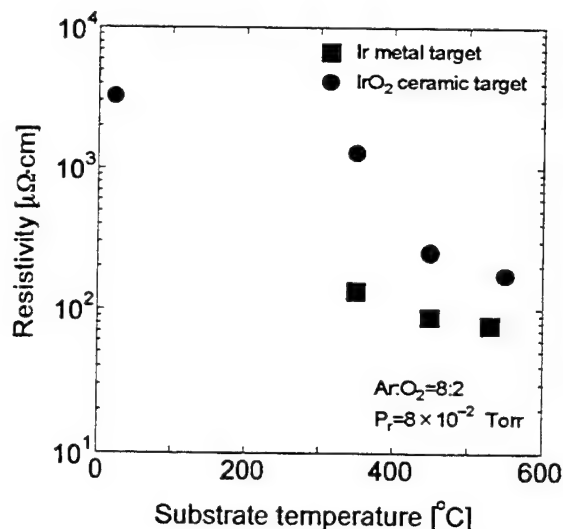


Fig. 2. Dependence of resistivities of IrO₂ films obtained by sputtering using an Ir metal target and an IrO₂ ceramic target on the growth temperature.

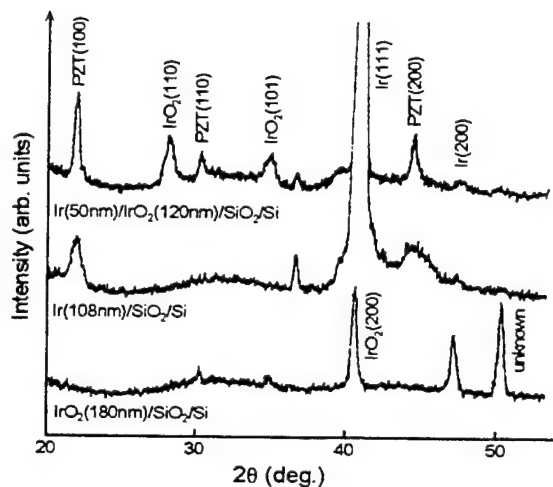


Fig. 3. X-ray diffraction patterns of PZT thin films grown on Ir, IrO₂ and Ir/IrO₂ bottom electrodes.

In order to investigate the interface conditions between PZT films and electrode materials, SIMS analysis was performed. Fig.4 shows the SIMS depth profile of PZT/Ir/SiO₂/Si, PZT/IrO₂/SiO₂/Si and PZT/Ir/IrO₂/SiO₂/Si. In this figure, IrO₂ films were grown by sputtering using a metal target. From Fig.4, it was found that elements of PZT, Pb, Zr and Ti did not diffuse into SiO₂, and Ir, IrO₂ and Ir/IrO₂ bottom electrodes act as a good barrier for the elements of PZT. Among these electrodes, the Ir/IrO₂ electrode showed a good barrier property, as shown in Fig.4. When the thickness of the Ir and IrO₂ bottom electrodes were much thinner than those in Fig.4, their electrodes did not

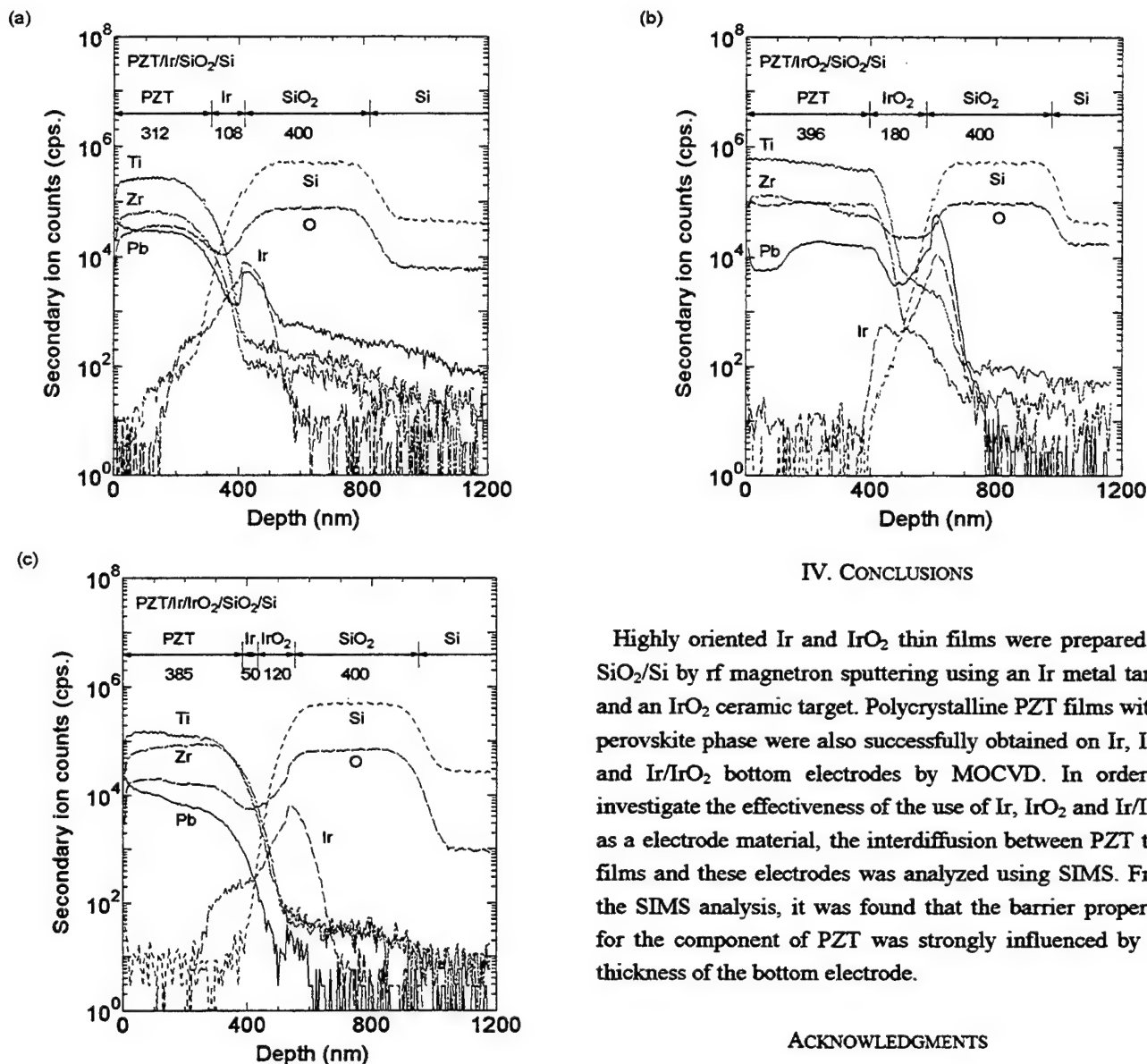


Fig. 4. SIMS depth profiles of (a) PZT/Ir/SiO₂/Si, (b) PZT/IrO₂/SiO₂/Si and (c) PZT/Ir/IrO₂/SiO₂/Si.

play as a barrier layer. In particular, the Pb component diffused into the Si side when the thickness of the bottom electrode was small. This dependence of the diffusion barrier properties on the electrode thickness is very important to the electrical properties of PZT capacitors.

IV. CONCLUSIONS

Highly oriented Ir and IrO₂ thin films were prepared on SiO₂/Si by rf magnetron sputtering using an Ir metal target and an IrO₂ ceramic target. Polycrystalline PZT films with a perovskite phase were also successfully obtained on Ir, IrO₂ and Ir/IrO₂ bottom electrodes by MOCVD. In order to investigate the effectiveness of the use of Ir, IrO₂ and Ir/IrO₂ as a electrode material, the interdiffusion between PZT thin films and these electrodes was analyzed using SIMS. From the SIMS analysis, it was found that the barrier properties for the component of PZT was strongly influenced by the thickness of the bottom electrode.

ACKNOWLEDGMENTS

This work was partly supported by Grant-in-Aid for Scientific Research (B)(2)(08455150) and (C)(2)(09650366) from the Ministry of Education, Science and Culture, and by Japan Society for the Promotion of Science (JSPS-RFTF96P00105), and by research grants from the Murata Science Foundation and from Foundation for Promotion of Material Science and Technology.

REFERENCES

- [1] T.Nakamura, Y.Nakao, A.Kamisawa and H.Takasu, "Preparation of

- Pb(Zr,Ti)O₃ thin films on electrodes including IrO₂," *Appl. Phys. Lett.*, Vol.65, pp.1522-1524, September 1994.
- [2] T.Nakamura, Y.Nakao, A.Kamisawa and H.Takasu, "Preparation of Pb(Zr,Ti)O₃ thin films on Ir and IrO₂ electrodes," *Jpn. J. Appl. Phys.*, Vol.33, pp.5207-5210, September 1994.
- [3] K.Aoki, Y.Fukuda, K.Numata and A.Nishimura, "Improvement of fatigue of PZT capacitors by optimizing electrode materials and PZT crystallinity," *Ext. Abs. The third Pacific Rim Conference on Ferroelectric Applications* (May 27-29, Kyoto, Japan, 1996)pp.87-90.
- [4] M.Shimizu and T.Shiosaki, "MOCVD of ferroelectric Pb(Zr,Ti)O₃ and (Pb,Lu)(Zr,Ti)O₃ thin films for memory device applications," *Mat. Res. Soc. Symp. Proc.*, Vol.361., pp.295-305, 1995.
- [5] M.Shimizu, K.Nakao, H.Okino, H.Fujisawa and T.Shiosaki, "Electrical properties of PZT thin films on Ir and IrO₂ by MOCVD," *Ext. Abs. The seventh US-Japan Seminar on Dielectric and Piezoelectric Ceramics* (Nov.14-17, Tsukuba, Japan, 1995)pp.40-43.
- [6] M.Shimizu and T.Shiosaki, "Growth and characterization of Pb-based ferroelectric oxide thin films by MOCVD," *Mat. Res. Soc. Symp. Proc.*, Vol.401, pp.129-138, 1996.
- [7] M.Shimizu, H.Okino, H.Fujisawa and T.Shiosaki, "Electrical properties of Pb(Zr,Ti)O₃ thin films on Ir and IrO₂ Electrodes by MOCVD," *Proc. the tenth IEEE Int. Symp. on Applications of Ferroelectrics* (Aug.18-21, East Brunswick, NJ, U.S.A., 1996)pp.471-474.

The Low-Field Biaxial Stress Response and Transverse Piezoelectric Coefficients of Sol-Gel PZT Thin Films

Joseph F. Shepard Jr. and Susan Trolier-McKinstry
Intercollege Materials Research Laboratory
The Pennsylvania State University, University Park, PA 16802

Abstract—The low-field stress response of unpoled lead zirconate titanate (PZT) thin films was measured as a function of applied biaxial stress. Sol-gel films of 40/60, 60/40, and 52/48 compositions were investigated over an applied stress range of ± 140 MPa. The normalized capacitance was found to change by less than 5% with applied stress (regardless of sign). Comparison of the magnitudes of the changes with earlier work on bulk PZT ceramics showed obvious discrepancies which indicate a limited twin wall contribution to the low-field stress response of PZT thin films.

The wafer flexure technique has been developed to characterize the transverse piezoelectric coefficient (d_{31}) of PZT thin films. The technique is based upon the controlled bending of a PZT coated silicon wafer which changes the biaxial stress on the film. The biaxial load results in the production of a piezoelectric charge which is measured electronically and used together with the calculated mechanical stress to determine the film's d_{31} coefficient. Results from experiments using the technique show the d_{31} coefficient to range from -3 pC/N in the as-deposited condition to -68 pC/N after extended poling.

I. INTRODUCTION

The continued investigation of PZT thin films has in recent years revealed that the piezoelectric coefficients (d_{33} and d_{31}) of the material are generally lower than those of bulk PZT ceramics [1, 2]. Because films are subjected to large residual stresses [3], it would be expected that clamping effects might restrict twin wall motion, thus limiting the film's piezoelectric coefficients. The investigation reported here is aimed at evaluating the effects of residual film stress by measuring the dielectric and piezoelectric properties *in-situ* while biaxial stress is applied to the film via mechanical deformation of the silicon substrate.

II. EXPERIMENTAL PROCEDURE

A. Sol-Gel PZT Thin Films

Sol-gel films were deposited using previously described sol-gel techniques [4]. Solutions were synthesized in 0.5M concentrations and spin coated at 3000 rpm onto 3" platinumized silicon substrates (Pt/Ti/SiO₂/Si). Amorphous films were pyrolyzed at 300°C for 30 sec. and fired at 700°C for 60 sec. Three compositions, 40/60, 60/40, and 52/48 (zirconium to titanium ratio) were used for the experiments conducted. Final film thicknesses were measured using surface profilometry and were found to lie between 0.3 and 0.6 μ m.

B. Low-Field Biaxial Stress Experiments

Biaxial stress was applied to unpoled PZT films using the uniform pressure rig described elsewhere [5]. For low-field dielectric measurements, coated 3" silicon wafers were clamped between two 2.5" Viton o-rings and the pressure in the cavity behind the wafer was changed using a gas bottle and regulator or a 1 micron roughing pump. Capacitance and $\tan \delta$ were then measured *in-situ* with 10mV at 10 kHz and correlated to gas pressure within the rig. Large deflection plate analysis [6] was used to determine the range of applied stress for the center of the wafer. For the maximum and minimum applied pressures (+100 and -90 kPa) the principal stresses at the center of the substrate were on the order of ± 140 MPa.

C. Transverse Piezoelectric Characterization

The transverse piezoelectric coefficient (d_{31}) of the PZT thin films was measured with the wafer flexure method [7]. PZT coated substrates are clamped in the uniform pressure rig and deformed with a change of air pressure in the cavity located behind the wafer. Flexure of the substrate stresses the film and results in the production of an electric charge. The charge produced is measured and used together with the calculated biaxial stress to determine the film's d_{31} coefficient.

Piezoelectric data presented here are effective values (the film is clamped to the substrate) and are reported as an average d_{31} coefficient. The numerical analyses used assume isotropic materials and because the substrate is a single crystal, maximum and minimum values were calculated based on the known elastic anisotropy of silicon [8]. The elastic properties of the 52/48 film are also required and were assumed to be 101 GPa and 0.3, respectively [9]. The relation between the upper and lower limits is a constant (ratio of 1.2), and for the sake of clarity therefore, d_{31} data reported are given as an average of the two extremes.

Figure 2 is an illustration of the d_{31} measurement apparatus. Pressure in the cavity is changed either manually with a 60cc syringe or continuously via the oscillation of a 10" audio speaker. For the speaker configuration, excitation is induced with a reference signal from an EG&G 7260 lock-in amplifier and the piezoelectric signal produced is then monitored with the lock-in amp locked onto the frequency of the pressure oscillation (i.e. that of the reference signal).

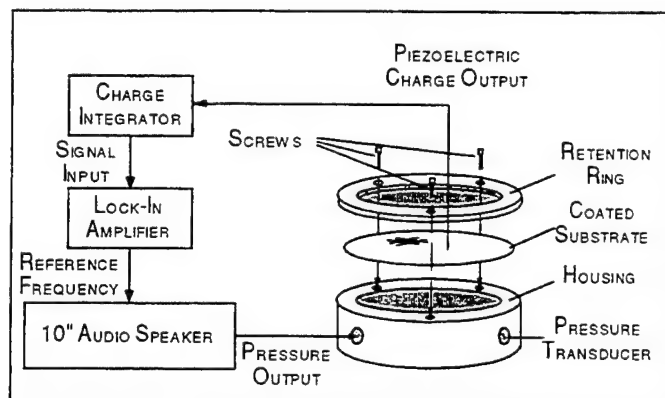


Figure 1. d_{31} characterization setup.

III. RESULTS

A. Low-Field Tension Experiments

The low-field stress response is shown in Figures 2 and 3 for the applied tension experiments (note that the x-axis of the plots is applied gas pressure and not applied stress). Figure 2 indicates that with the application of a tensile stress to the 40/60 and 60/40 films the capacitance decreases less than 3%. With release of the applied pressure the capacitance increased, retracing the original path back to some value comparable with, or slightly greater than, the original. For comparison Figure 3 shows the response of a 52/48 film. Over the same pressure range, similar behavior was observed with a 4.5% reduction of capacitance resulting. The results indicate that for all compositions tested; (1) the film capacitance decreases less than 5% in response to 140 MPa of biaxial tension and (2) the reduction of capacitance is reversible with final values comparable to those in the unstressed condition.

B. Low Field Compression Experiments

Results from the applied compression experiments are given in Figures 4 and 5. The data show that upon application of a compressive stress capacitance first increases, reaches some maximum, and then decreases. Upon release of the applied stress the film's capacitance approximates the initial path, although at smaller values, and returns to a magnitude on the order of the original. Relative changes at the endpoint pressure of -90 kPa (pressure in the cavity) were found to be less than 3% for all compositions tested.

The low-field stress response of PZT films show changes of capacitance which are much smaller than, and in directions opposite to, those of PZT ceramics [10]. The bulk ceramic behavior is attributed to non-180° domain wall motion which changes the material's dielectric constant in response to an applied biaxial stress. The discrepancies between the thin film and ceramic behavior suggest only

limited mobility of non-180° domain walls in the PZT films tested and forces the consideration of alternative mechanisms for an explanation of the observed stress response. This is important because it suggests that domain wall contributions to the piezoelectric properties will also be limited.

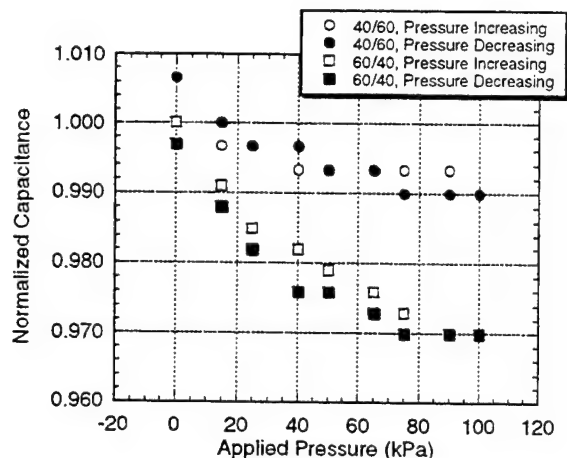


Figure 2. Normalized capacitance for unpoled 40/60 and 60/40 films as a function of applied tensile pressure.

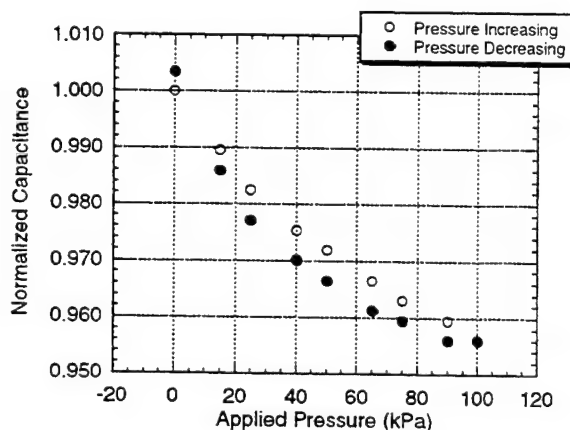


Figure 3. Normalized capacitance for an unpoled 52/48 film as a function of applied tensile pressure.

The consistency of the low-field behavior of the different PZT films suggests that the mechanism responsible is not governed by the composition of the material. In particular, films on both sides of the morphotropic phase boundary show similar stress dependence. Consideration of the applied compression results have suggested however, that the peak of the capacitance curve occurs with the alleviation of residual film stress [5]. The differences in the location of the capacitance maximum for the films shown here may be due to a combination of; (1) changes in the capacitor location on the wafer (for a given pressure applied stress is a function of radial location), (2) differences in the film's residual stress,

and (3) experimental error. Additional work is underway to verify which of these effects predominates.

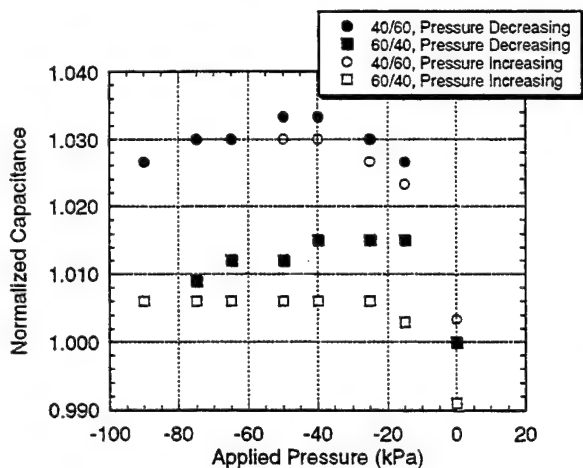


Figure 4. Normalized capacitance for 40/60 and 60/40 films as a function of applied compressive pressure.

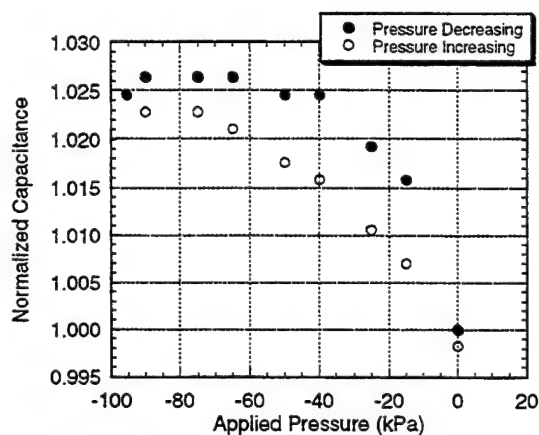


Figure 5. Normalized capacitance for a 52/48 film as a function of applied compressive pressure.

C. The Transverse Piezoelectric Coefficient of 52/48 PZT Thin Films

The transverse piezoelectric coefficients (d_{31}) of a number of 52/48 films were measured using the wafer flexure method [11, 12]. Experiments were conducted as a function of poling field (considered positive if the top electrode was the anode) and poling time with applied fields both comparable to and greater than the coercive field of the material.

The plot in Figure 6 illustrates the sensitivity of the measurement technique and shows that with a poling field of +25 kV/cm (E_c was on the order of 40 kV/cm) the d_{31} of the material decreases from the as-deposited value of -3 pC/N to zero after 17 minutes. With continued poling time

the magnitude of the piezoelectric coefficient moved through zero and increased to -2 pC/N after 145 min. Variations in d_{31} of ± 1 pC/N were easily detected.

Data from Figure 6 provide information on the direction of the remanent polarization of the as-deposited sample. Because the d_{31} value first decreases with poling the material's polarization vector must be oriented with its positive end towards the surface of the film. The initial decrease observed corresponds to depoling this weak original orientation.

Figure 7 illustrates the behavior of the d_{31} coefficient in response to a poling field of +333 kV/cm. The data show a rapid increase of d_{31} with initial exposure to the electric field with a maximum of -68 pC/N achieved after poling the sample at room temperature for 23 hours.

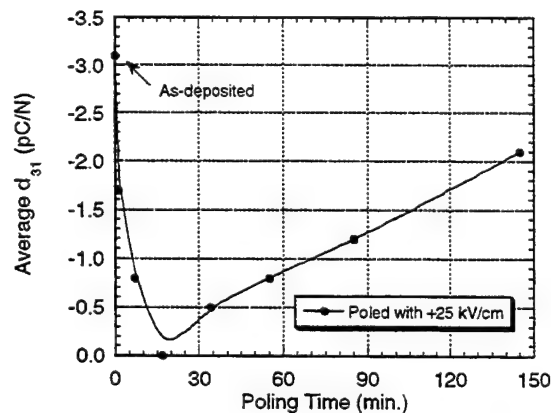


Figure 6. The average d_{31} coefficient as a function of poling time at +25 kV/cm.

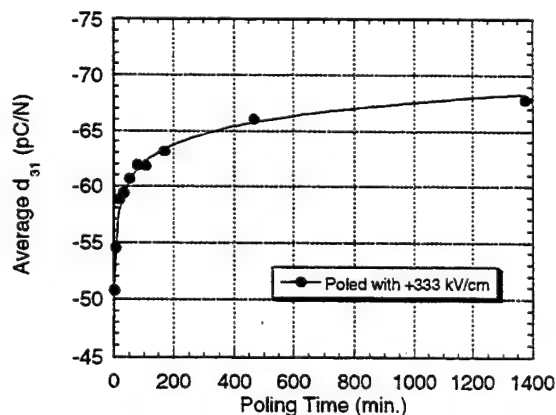


Figure 7. The average d_{31} coefficient as a function of poling time at +333 kV/cm.

The increase of the d_{31} coefficient with time is most likely related to an increase of poling efficiency with

continued exposure to the poling field. The rapid increase of d_{31} shown in Figure 7 over the course of the first 16 min. of poling is likely the result of 180° domain reorientation. With continued exposure to the poling field the number of domains permanently switched continues to increase but the rate at which reorientation occurs slows and thus d_{31} begins to saturate.

IV. CONCLUSIONS

Comparison of the low-field stress data with earlier experiments on bulk PZT ceramics show that the magnitudes of the changes are more than an order of magnitude less than would be expected for a bulk ceramic material. In addition, the stress-induced changes are opposite to those shown by bulk ceramics. The discrepancies between the two behaviors indicate that non- 180° domain reorientation is limited in the PZT films tested. Experiments showed that the manner in which the capacitance changed was independent of composition i.e. trends were the same for 40/60, 60/40, and 52/48 films under $0.6\ \mu\text{m}$ thick.

Experiments were conducted on the d_{31} characterization of PZT thin films. Low-field poling experiments showed as-deposited films to have d_{31} coefficients on the order of $-3\ \text{pC/N}$ and illustrated the sensitivity of the wafer flexure method in measuring changes as small as $\pm 1\ \text{pC/N}$. It was shown that with proper orientation of the applied electric field the net polarization and thus the piezoelectric coefficient of the material can be moved through zero. For poling with fields exceeding E_c , d_{31} increases in an approximately logarithmic fashion to a maximum of about $-68\ \text{pC/N}$ after poling for 23 hours. With increased poling time the permanent reorientation of 180° domains enhances the net polarization of the material and thus the film's transverse piezoelectric coefficient.

ACKNOWLEDGEMENT

The authors would like to acknowledge the assistance of Paul Moses with construction of the piezoelectricity monitor and Tao Su and Pavadee Aungkavattana for deposition of the films used in this investigation. This work is funded under DARPA contract DABT63-95-C-0053.

REFERENCES

- [1] A. L. Kholkin, E. L. Colla, A. K. Tagantsev, D. V. Taylor, and N. Setter, "Fatigue of Piezoelectric Properties of $\text{Pb}(\text{Zr,Ti})\text{O}_3$ Films," *Appl. Phys. Lett.*, vol. 68, pp. 2577-2579, 1996.
- [2] P. Muralt, A. Kholkin, M. Kohli, T. Maeder, and N. Setter, "Characterization of PZT Thin Films for Micromotors," *Microelectronic Engineering*, vol. 29, pp. 67-70, 1995.
- [3] G. A. C. M. Spierings, G. J. M. Dormans, W. G. J. Moors, M. J. E. Ulenaers, and P. K. Larsen, "Stress in $\text{Pt/Pb}(\text{Zr,Ti})\text{O}_3/\text{Pt}$ Capacitors for Integrated Ferroelectric Devices," *International Symposium on Applications of Ferroelectrics*, pp. 29-32, 1994.
- [4] M. Hendrickson, T. Su, S. Trolier-McKinstry, and R. Zeto, "Processing of PZT Piezoelectric Thin Films for Microelectromechanical Systems," *International Symposium on Applications of Ferroelectrics*, vol. II, pp. 683-686, 1996.
- [5] J. F. Shepard Jr., S. Trolier-McKinstry, and J. P. Maria, "The Effects of Applied Biaxial Stress on the Low and High-Field Characteristics of Thin Film PZT," submitted to *J. Mat. Research*, 1997.
- [6] R. J. Roark and W. C. Young, *Formulas for Stress and Strain*, 6th ed. New York: McGraw-Hill, 1989.
- [7] J. F. Shepard Jr., P. J. Moses, and S. Trolier-McKinstry, "The Wafer Flexure Technique for the Determination of the Transverse Piezoelectric Coefficient (d_{31}) of PZT Thin Films," submitted to *Sensors and Actuators*, 1997.
- [8] W. A. Brantley, "Calculated Elastic Constants for Stress Problems Associated with Semiconductor Devices," *J. Appl. Phys.*, vol. 44, pp. 534-535, 1973.
- [9] T. Tsuchiya, T. Itoh, G. Sasaki, and T. Suga, "Preparation and Properties of Piezoelectric Lead Zirconate Titanate Thin Films for Microsensors and Microactuators by Sol-Gel Processing," *J. Ceram. Soc. Japan*, vol. 104, pp. 159-163, 1996.
- [10] R. F. Brown, "Effect of Two-Dimensional Mechanical Stress on the Dielectric Properties of Poled Ceramic Barium Titanate and Lead Zirconate Titanate," *Can. J. Phys.*, vol. 39, pp. 741-753, 1961.
- [11] J. F. Shepard Jr., P. J. Moses, and S. Trolier-McKinstry, "A Technique for the Measurement of d_{31} Coefficient of Piezoelectric Thin Films," *Materials for Smart Systems II*, vol. 459, pp. 225-230, 1996.
- [12] J. F. Shepard Jr. and S. Trolier-McKinstry, "The Effects of Poling Field and Poling Time on the d_{31} Coefficient of PZT Thin Films," submitted to *Sensors and Actuators*, 1997.

Theoretical Study on SAW Characteristics of LiNbO₃/sapphire structures

Tadashi Shiosaki, Takashi Nishida, Toshihisa Horiuchi and Kazumi Matsusige.
Dept. of Elec. Sci. and Eng., Kyoto Univ. Yoshida Honmachi, Sakyo-ku, Kyoto 606, JAPAN.

1 Introduction

LiNbO₃ bulk crystal with high surface acoustic wave (SAW) velocity and high SAW coupling material has been used for SAW devices. High performance SAW devices and their materials have been widely desired in order to account for the rapid progress of mobile communications, satellite communications, etc. Therefore, LiNbO₃ films fabricated on high velocity material, sapphire (α -Al₂O₃), have been investigated. LiNbO₃ films can be epitaxially grown on α -Al₂O₃(001), (012) and (110) with several deposition methods.[1, 2] Although in order to fabricate and realize SAW devices with the LiNbO₃/ α -Al₂O₃ structures the minute analyses of the SAW characteristics in the structures and the optimal conditions of thickness of LiNbO₃ layer and azimuthal angle of SAW propagation are necessary, yet few investigations have been presented.

In this report, the SAW properties are calculated for each LiNbO₃(001)/ α -Al₂O₃(001), LiNbO₃(012)/ α -Al₂O₃(012) and LiNbO₃(110)/ α -Al₂O₃(110) structure with IDT on the top surface and without conduction layer at the interface between LiNbO₃ and α -Al₂O₃. The optimal conditions for devices and the SAW properties for the studied ranges are revealed.

2 Calculations

SAW properties in the LiNbO₃/ α -Al₂O₃ structures were calculated using Campbell's method[3] and material constants of LiNbO₃ crystal[4, 5] and α -Al₂O₃ crystal.[6, 7, 8] The dependencies on LiNbO₃ thickness and propagation azimuthal angle (ψ) of SAW velocity (v), SAW coupling (k^2) and Temperature coefficients of delay (TCD) were presented. The thickness was expressed in hK instead of the thickness of LiNbO₃ layer: h . The hK is a value normalized by the wavenumber of SAW (K).

3 Results and Discussion

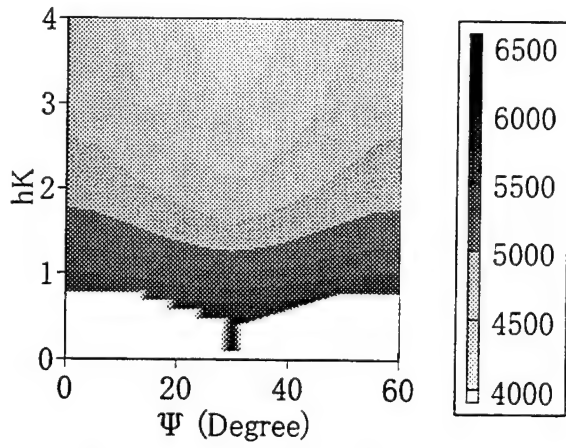
Results calculated for LiNbO₃/ α -Al₂O₃ structures displayed that there are many propagation modes of SAW in the double-layered structures, and only the 0th mode, whose SAW velocity is the lowest, and the 1st mode could be propagated in case of thin LiNbO₃ layer. Therefore, the modes of not less than 2nd, whose velocities are faster than the 0th and 1st modes, are not presented.

3.1 LiNbO₃(001)/ α -Al₂O₃(001) structure

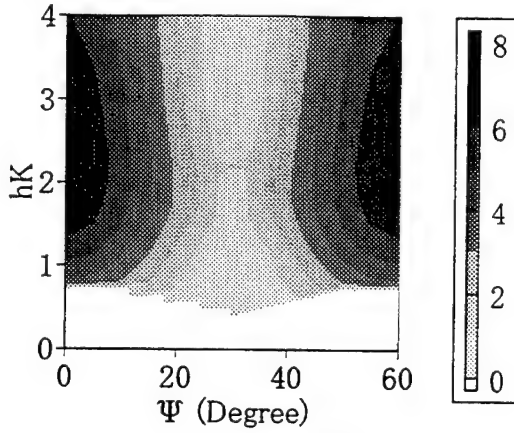
SAW properties in the 0th mode and the 1st mode of LiNbO₃(001)/ α -Al₂O₃(001) structures were theoretically calculated and were compared to those of LiNbO₃ bulk crystal. There was little improvement in the properties calculated for the 0th mode. However, high velocity, high coupling and low TCD , that is, desirable properties were obtained for the 1st mode, as shown in Fig. 1, since the velocity of the substrate α -Al₂O₃ crystal is higher than that of LiNbO₃ and the temperature coefficients of α -Al₂O₃ are lower than the coefficients of LiNbO₃. It was also indicated that both the highest velocity and the highest coupling can be obtained at $\psi = 30^\circ$ (α -Al₂O₃[100]).

3.2 LiNbO₃(012)/ α -Al₂O₃(012) structure

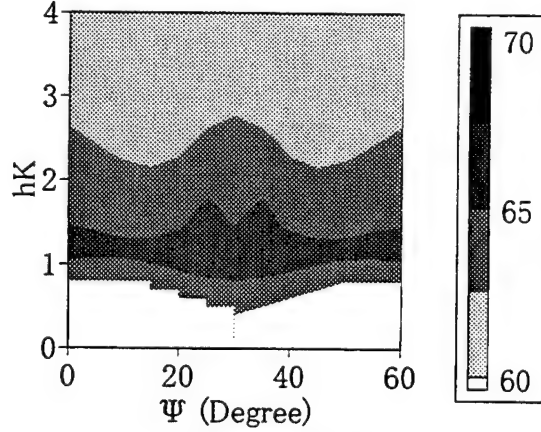
In the case of LiNbO₃(012)/ α -Al₂O₃(012) structure, it was indicated that there was also no noticeable improvement in the properties calculated for the 0th mode. The results calculated for the 1st mode are shown in Fig. 2, revealing that a very high coupling coefficient could be obtained at the 1st mode. The maximum value of the SAW coupling coefficient $k^2 = 24.1\%$ was displayed at $hK = 2.2$ and $\psi = 0^\circ$ (α -Al₂O₃[110]). The value was more than four times the value of LiNbO₃ bulk crystal because the k^2 of LiNbO₃ bulk is lower than 5.7%. Since the high velocity $v = 5140\text{m/s}$ and the low temperature coefficient $TCD = 53.1\text{ppm/K}$ were also obtained at the same hK and ψ , it was indicated that these conditions of the propagation direction of α -Al₂O₃[110] and the thickness $hK = 2.2$ of LiNbO₃ layer in the LiNbO₃(012)/ α -Al₂O₃(012) structure are very suitable for high performance SAW devices.



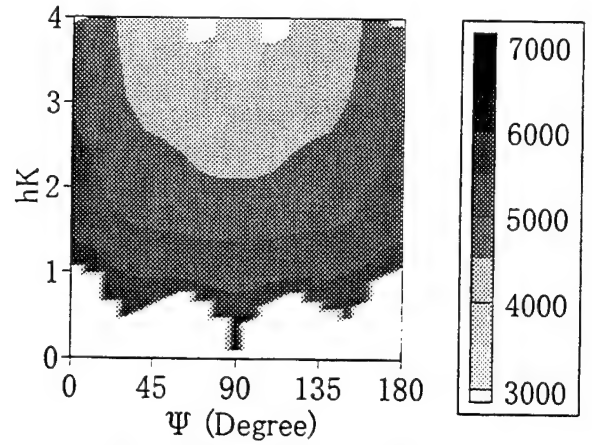
(a) velocity $v(\text{m/s})$



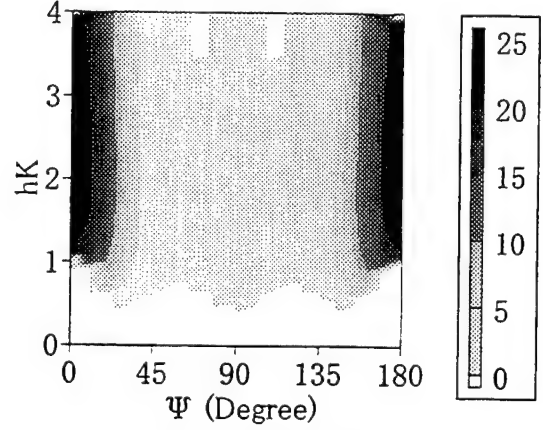
(b) coupling $k^2(\%)$



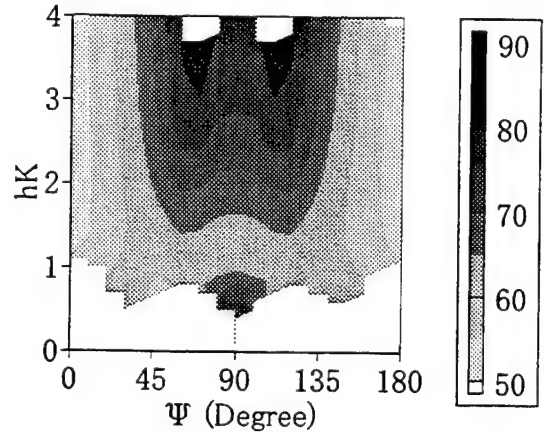
(c) $TCD(\text{ppm/K})$



(a) velocity $v(\text{m/s})$



(b) coupling $k^2(\%)$



(c) $TCD(\text{ppm/K})$

Figure 1: Dependence of the thickness hK and propagation angle ψ on SAW properties in the 1th mode of $\text{LiNbO}_3(001)\alpha\text{-Al}_2\text{O}_3(001)$ structure. ($\psi = 0$: $\alpha\text{-Al}_2\text{O}_3[2\bar{1}0]$)

Figure 2: Dependence of the thickness hK and propagation angle ψ on SAW properties in the 1th mode of $\text{LiNbO}_3(012)\alpha\text{-Al}_2\text{O}_3(012)$ structure. ($\psi = 0$: $\alpha\text{-Al}_2\text{O}_3[2\bar{1}0]$)

Table 1 SAW properties for maximum of k^2 .

| structure | $\psi(^{\circ})$ | hK | mode | $v(\text{m/s})$ | $k^2(\%)$ | $TCD(\text{ppm/K})$ |
|--|------------------|------|------|-----------------|-----------|---------------------|
| LiNbO ₃ (001)/ α -Al ₂ O ₃ (001) | 30 | 4.0 | 0 | 4023 | 2.28 | 65.2 |
| | 0 | 2.2 | 1 | 4854 | 6.97 | 63 |
| LiNbO ₃ (012)/ α -Al ₂ O ₃ (012) | 30 | 0.8 | 0 | 5184 | 2.40 | 64.3 |
| | 0 | 2.2 | 1 | 5139 | 24.1 | 53.1 |
| | 30 | 0.5 | 0 | 5355 | 1.83 | 63.8 |
| | 30 | 0.7 | 0 | 5410 | 0.590 | 59.3 |
| LiNbO ₃ (110)/ α -Al ₂ O ₃ (110) | 10 | 1.6 | 0 | 4804 | 9.28 | 64.2 |
| | 150 | 0.7 | 0 | 5166 | 2.43 | 65.1 |
| | 10 | 2.9 | 1 | 4823 | 18.8 | 59.8 |
| | 80 | 2.8 | 1 | 4258 | 3.09 | 83.3 |

3.3 LiNbO₃(110)/ α -Al₂O₃(110) structure

Since the spontaneous polarization axis of LiNbO₃ is parallel to the surface of LiNbO₃(110)/ α -Al₂O₃(110) structure, high efficiency excitation of SAW with Inter-digital Transducer and high coupling may be expected in the structure. However, the polarization in the LiNbO₃ layer deposited may be made into multipolarization domains, therefore poling for the LiNbO₃ layer may be required. The calculated results for the 0th mode and the 1st mode are shown in Fig. 3 and 4, respectively, revealing that high coupling can be obtained in both modes.

Because the velocities ranged from 4000m/s to 6000m/s as shown in Fig. 1-4, and that of LiNbO₃ bulk is lower than 4000m/s, the velocity in the LiNbO₃/ α -Al₂O₃, that is, operating frequency of devices may be one-and-a-half times higher than that of LiNbO₃ bulk. The range of TCD of LiNbO₃ bulk is 70-90ppm/K, while that of the LiNbO₃/ α -Al₂O₃ was 60-80ppm/K. Consequently, the temperature coefficient in the LiNbO₃ films may be reduced by about 10ppm/K.

The values of thickness hK of LiNbO₃ layer and the propagation direction ψ in which maximum coupling could be obtained and the SAW properties for each LiNbO₃/ α -Al₂O₃ structures were summarized in Table. 1. Since maximum values of SAW velocity and coupling and minimum TCD in LiNbO₃ bulk crystals are $\sim 4000\text{m/s}$, 5.7% and 70ppm/K, respectively, it was displayed that more desirable properties, that is, higher velocity and coupling and lower TCD could be obtained in the LiNbO₃/ α -Al₂O₃ structures.

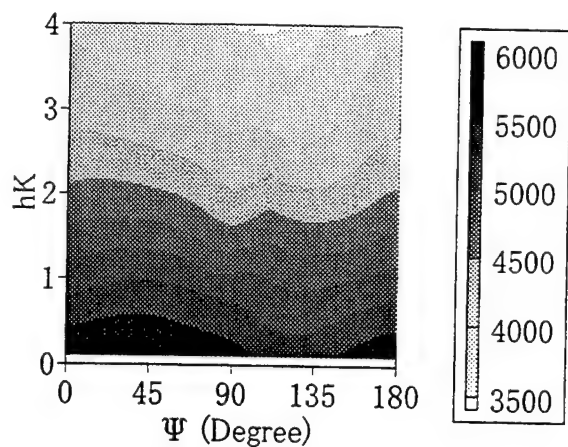
4 Conclusions

The SAW characteristics of LiNbO₃/sapphire structures were theoretically calculated in detail, and thickness and azimuthal angular dependences of SAW velocity, SAW coupling and Temperature coefficients were displayed, revealing that high velocity and high coupling could be obtained in the 1th propagation mode of the structures. Moreover, it was found that the lower TCD in the structures may be also obtained compared to the TCD of LiNbO₃ bulk. Consequently, the LiNbO₃/sapphire structures may have enhanced efficiency, thermal stability and operational frequency, which may make them very suitable for high performance SAW devices.

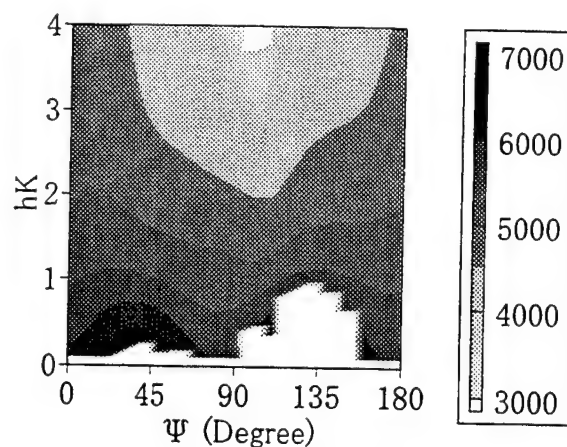
References

- [1] M. Shimizu, Y. Furushima, T. Nishida and T. Shiosaki: Jpn. J. Appl. Phys. **32** (1993) 4111.
- [2] Y. Shibata, K. Kaya, K. Akashi, M. Kanai, T. Kawai and S. Kawai: Jpn. J. Appl. Phys. **32** (1993) L745.
- [3] J J. Campbell and W. R. Jones: IEEE Trans. Son. Ultrason. **15** (1968) 209.
- [4] A. W. Warner, M. Onoe and G.A.Coquin: J. Acoust Soc. Am. **42** (1967) 6.
- [5] R. T. Smith and F. S. Welsh: J. Appl. Phys. **42** (1971) 6.
- [6] A. J. Slobodnik, Conway E. D. and R. T. Delmonico: Microwave Acoustic Handbook, Vol 1A (1973) 672.
- [7] Landort-Bornstein Numerical Data and Functional Relationships in Science and Technology III/2 (1969) 13.

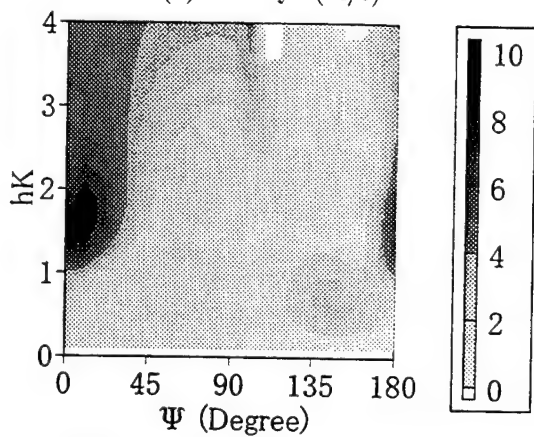
[8] W. M. Yim and R. J. Paff: J. Appl. Phys. **45** (1974) 1456.



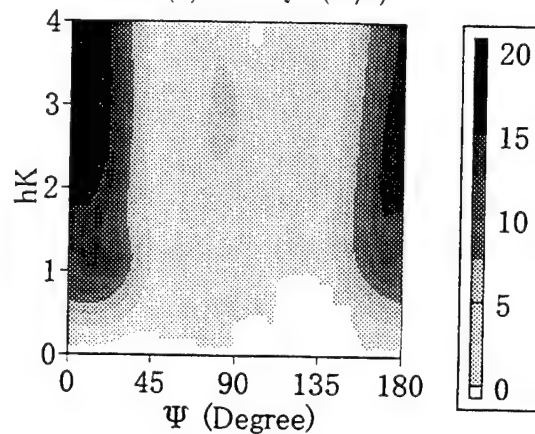
(a) velocity v (m/s)



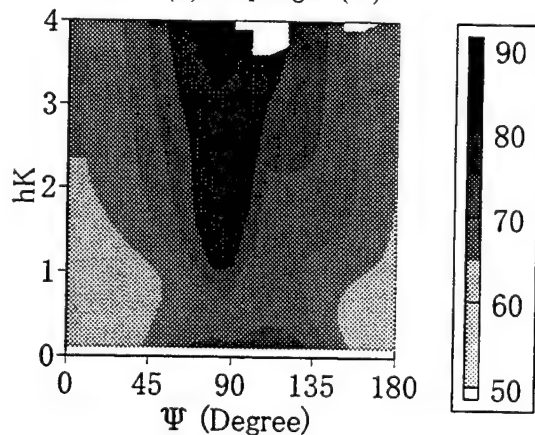
(a) velocity v (m/s)



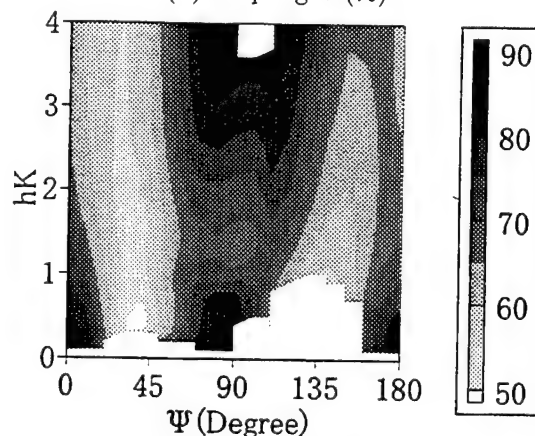
(b) coupling k^2 (%)



(b) coupling k^2 (%)



(c) TCD(ppm/K)



(c) TCD(ppm/K)

Figure 3: Dependence of the thickness hK and propagation angle ψ on SAW properties in the 1th mode of $\text{LiNbO}_3(110)\alpha\text{-Al}_2\text{O}_3(110)$ structure. ($\psi = 0$: $\alpha\text{-Al}_2\text{O}_3[\bar{1}10]$)

Figure 4: Dependence of the thickness hK and propagation angle ψ on SAW properties in the 1th mode of $\text{LiNbO}_3(110)\alpha\text{-Al}_2\text{O}_3(110)$ structure. ($\psi = 0$: $\alpha\text{-Al}_2\text{O}_3[\bar{1}10]$)

Fabrication and Electrical Properties of $\text{LiTaO}_3/\text{ZnO}/\text{Al}_2\text{O}_3$ Hexagonal Heterostructure

T.Tsurumi, Y.Ma, H.Kimura and N.Ohashi

Department of Inorganic Materials, Tokyo Institute of Technology,
Ookayama, Meguro-ku, Tokyo 152, Japan.

Abstract

A heterostructure of $\text{LiTaO}_3/\text{ZnO}/\text{Al}_2\text{O}_3$, where three compounds have hexagonal close packing of oxide ion in their crystal structures, was formed as a first step to make an all oxide electric device or optoelectronic device. Ion beam sputtering method was used to make the heterostructure. A fairly good epitaxial relationship was observed between ZnO and $\alpha\text{-Al}_2\text{O}_3$. The resistivity of ZnO films increased by doping with Al. The lowest resistivity was obtained when 2wt% of Al_2O_3 was doped to the ZnO ceramic target. An epitaxial relationship was also observed between LiTaO_3 and ZnO, indicating the formation of the heterostructure. The capacitance of the heterostructure was measured as a function of bias voltage using a C-V plotter. The capacitance changed with bias voltage and the C-V curve showed a hysteresis due to the polarization switching of LiTaO_3 .

Introduction

Electronic application of oxide materials ranges from capacitors, ferroelectric devices, superconductors and transparent conductors as well as to magnets and optical devices. Oxide electronics is a new innovative field to utilize these properties by fabricating artificially designed crystal lattices and heterostructures.¹⁾

In the present study, we have made a heterostructure of $\text{LiTaO}_3/\text{ZnO}/\text{Al}_2\text{O}_3$, where LiTaO_3 is a ferroelectric material with the ilmenite structure, ZnO is an oxide semiconductor with the wurtzite structure and Al_2O_3 is an insulator with the corundum structure.²⁾ The wurtzite structure belongs to the hexagonal system, while ilmenite and corundum structures belong to the trigonal system. These structures are commonly composed of the hexagonal close packing of oxide ions, therefore, the heterostructure was tentatively termed as "hexagonal" heterostructure. The spontaneous polarization of LiTaO_3 was estimated to be $50\mu\text{C}/\text{cm}^2$ at room temperature and its Curie temperature is 938K.³⁾ ZnO shows one of the highest electron mobility in oxide ($\sim 200\text{cm}^2/\text{Vs}$).⁴⁾ They are transparent in visible range because of wide band gaps. We have made the heterostructure as a first step to make an all oxide electric or optoelectronic device.

Experimental

The $\text{LiTaO}_3/\text{ZnO}/\text{Al}_2\text{O}_3$ hexagonal heterostructure was made by ion beam sputtering (IBS) method. The IBS system developed in this study is shown in Fig.1⁵⁾. We used a rotary pump and a turbo molecular pump to evacuate the deposition chamber under 10^{-6} Pa. An infrared lamp was set at the upper side of the substrate holder to increase the substrate temperature up to 800°C . Targets

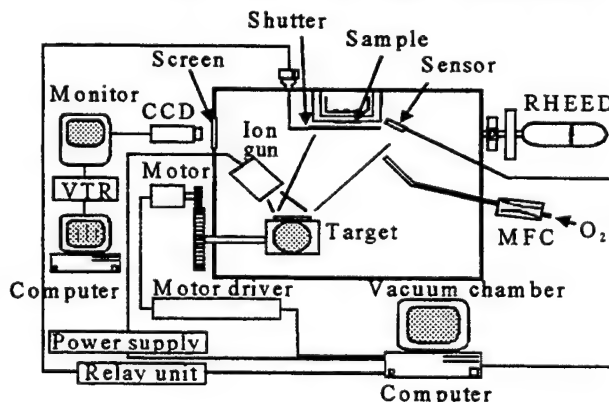


Fig.1 Schematic diagram of IBS system

of ZnO doped with 0-3wt% Al₂O₃ and Li₂O-Ta₂O₅ ceramics with the size of about 50mmφ were prepared by an ordinal ceramics process. They were fixed about 100mm below a substrate and faced to a Kaufman-type ion beam gun (Ion Tech Inc.) with 45 degrees. The outlet of a stainless nozzle of oxygen gas was set near by the substrate in order to obtain a high oxygen partial pressure around the substrate. During depositions, the thickness of thin films was continuously monitored with a quartz oscillating sensor. An *in-situ* RHEED observation of diffraction pattern including intensity monitoring on a specular spot was also carried out. The intensity of a specular spot was measured by a CCD camera as a function of time. A shutter operation, selection of target and control of ion beam gun were performed with a personal computer according to the information from the quartz oscillating sensor. The thickness of ZnO films and that of LiTaO₃ films deposited in this study were about 50nm and 60nm, respectively.

A rotating-analyzer type spectroscopic ellipsometer (Mizojiri Optical) was used to measure optical properties of films. In the schematic diagram shown in Fig.2, P,C,S and A represent a polarizer, a compensator, an optical system under measurements and a rotating-analyzer, respectively. An ellipsometer measures so-called ellipsometric parameters, Ψ and Δ , which are amplitude and project phase of the complex reflectance ratio ρ_s , that is,

$$\rho_s = r_p / r_s = \tan \Psi_s \exp(i \Delta_s)$$

where r_p and r_s are complex reflectance of p-polarized and s-polarized lights.⁶⁾

Electric resistivity of ZnO films on Al₂O₃ substrate was measured by Van der Pauw method at room temperature. The change in capacitance with bias voltage of LiTaO₃/ZnO/Al₂O₃ heterostructure was measured using a C-V plotter (hp4280A) at 1MHz as shown in Fig.3.

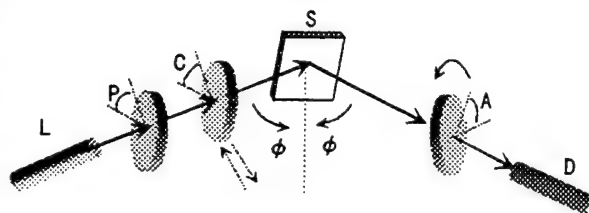


Fig.2 Schematic representation of ellipsometer
L:light, P:polarizer, C:compensator,
S:sample, A:analyzer and D:detector

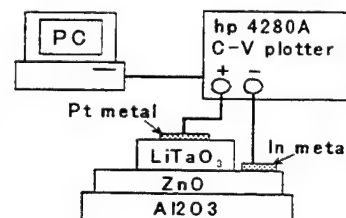


Fig.3 Capacitance measurement of the heterostructure

Results and Discussion

An RHEED pattern observed during the deposition of ZnO thin film is shown in Fig.4(A). The pattern is an assemblage of streaks, which indicated the surface of the film was good crystalline quality with no three dimensional islands. The RHEED pattern also indicated that the ZnO film was a single crystal and epitaxially grown with [001] direction on α -Al₂O₃ (001) substrate. RHEED intensity oscillation on a specular spot was also observed during the deposition as shown in Fig.5. From these results, it is obvious that the 2-dimensional layer-by-layer growth was achieved. The period in the oscillation corresponded to the half length of c-axis of ZnO, in other words, one layer of ZnO. An RHEED pattern of LiTaO₃ formed on ZnO/Al₂O₃ was shown in Fig.4(B). Some diffraction spots are observed on streaks, indicating that the surface of film was not flat in an atomic level. However, the epitaxial relation where [001] of ZnO is parallel to [001] of hexagonal cell of LiTaO₃ was maintained during the deposition.

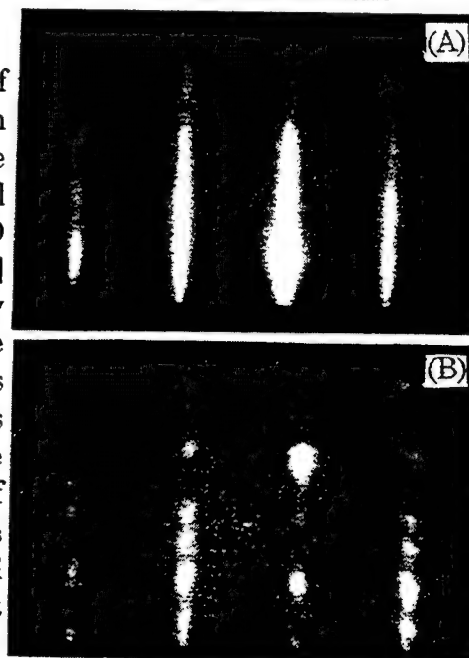


Fig.4 RHEED patterns of (A)ZnO/Al₂O₃ and (B)LiTaO₃/ZnO/Al₂O₃

XRD patterns of ZnO/Al₂O₃ and LiTaO₃/ZnO/Al₂O₃ are shown in Fig.6. The pattern of a ZnO/Al₂O₃ film shows only 002 peak of ZnO at $2\theta=34.2^\circ$ besides the diffraction peak of Al₂O₃ substrate. On the other hand, that of LiTaO₃/ZnO/Al₂O₃ film shows 006 peak of LiTaO₃ ($2\theta=38.5^\circ$) besides the diffraction peaks in Fig.6(A). These results of XRD analyses and the RHEED patterns in Fig.4 show that ZnO and LiTaO₃ have the epitaxial relation between Al₂O₃ substrate and the heterostructure was formed. These epitaxial relations were explained by the continuity of close packing layer of oxide ions.

Figure 7 shows results of ellipsometric analyses of Al₂O₃ substrate, ZnO/Al₂O₃ and LiTaO₃/ZnO/Al₂O₃. The complex refractive indices of Al₂O₃ and ZnO were calculated to explain experimentally obtained Ψ and Δ using least-squares fitting method. The refractive index of Al₂O₃ was consistent with reported value. The dotted lines in Fig.7(B) are the results of polycrystalline ZnO bulk specimen⁷⁾. Although the both results were slightly different in absolute values, the wavelength at which the peak of refractive index was observed and shape of whole curves were consistent with each other. The photon energy of the peak is about 3.4eV which was near the band cap of bulk ZnO.⁸⁾ In Fig.7(C), an additional peak was observed in the Δ curve at around 430nm. The Ψ and Δ curves were changed by the deposition LiTaO₃ on ZnO/LiTaO₃, but we have not get complex refractive indices of LiTaO₃ to explain the behaviors of Ψ and Δ in Fig.7(C).

Figure 8 shows the change in electric resistivity of Al-doped ZnO thin films as a function of Al₂O₃ content in the ceramics target. The electric resistivity decreases with increasing Al₂O₃ content, has minimum value at 2wt%, and increases with the Al₂O₃ content. This behavior is consistent with those in reports.⁹⁾ ZnO is an n-type semiconductor and Al is a donor dopant. The increase in electric resistivity at a high content of Al is attributable to the decrease in electron mobility.

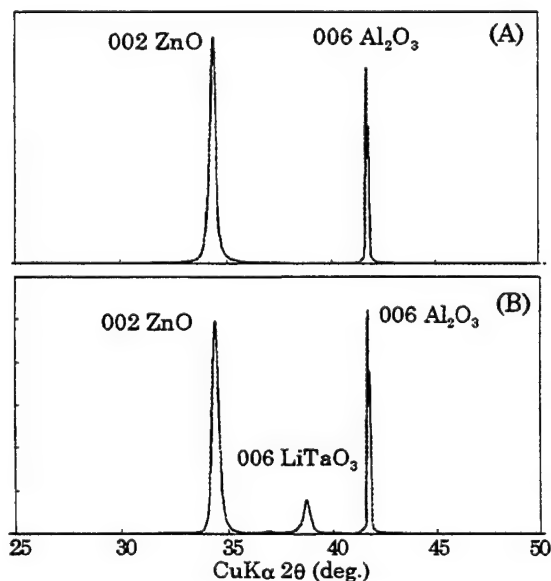


Fig.6 XRD patterns of (A) ZnO/Al₂O₃ and (B) LiTaO₃/ZnO/Al₂O₃.

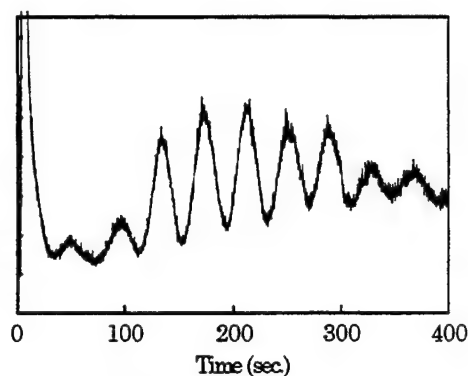


Fig.5 RHEED intensity oscillation on a specular spot observed during the deposition of ZnO

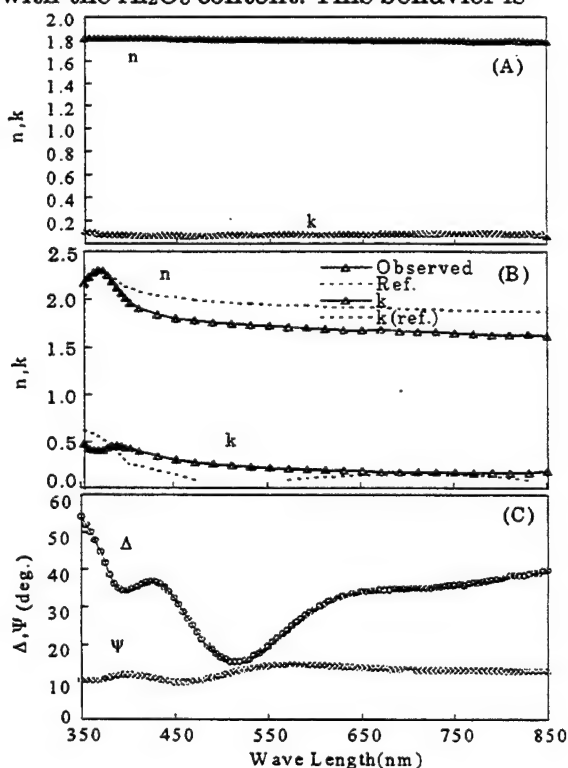


Fig.7 (A) complex refractive index ($n+ik$) of Al₂O₃ substrate, (B) those of ZnO in ZnO/Al₂O₃ and (C) Ψ and Δ of LiTaO₃/ZnO/Al₂O₃ as a function of wave length.

The ZnO target with 2wt% of Al_2O_3 was used in the formation of $\text{LiTaO}_3/\text{ZnO}/\text{Al}_2\text{O}_3$ heterostructure. Figure 8 shows the change of capacitance of the heterostructure measured as shown in Fig.3 as a function of bias voltage. Clear hysteresis curves were observed on the positive side of bias voltage. The width of the hysteresis curve increased with maximum bias voltage applied on the specimen (Fig.10). These hysteresis curves seem to be caused by the change in capacitance at the $\text{LiTaO}_3/\text{ZnO}$ interface due to the polarization switching in LiTaO_3 .

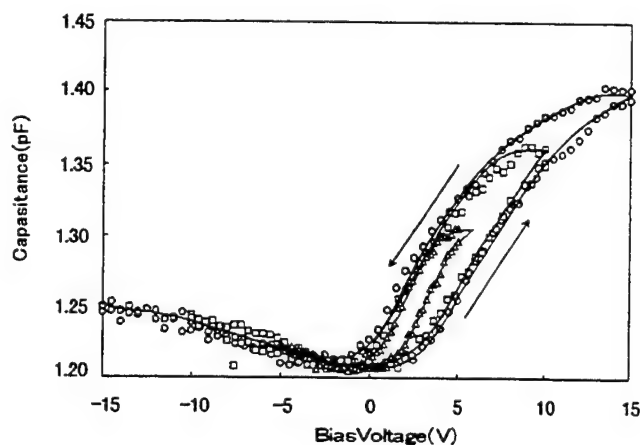


Fig.9 Capacitance of heterostructure as a function of bias voltage

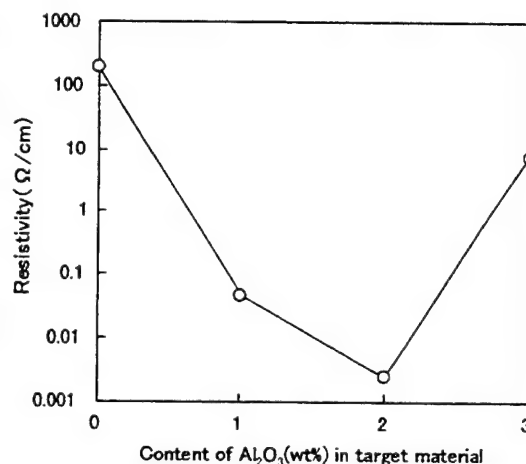


Fig.8 Change in electric resistivity of ZnO film as a function of Al_2O_3 content in ceramic target

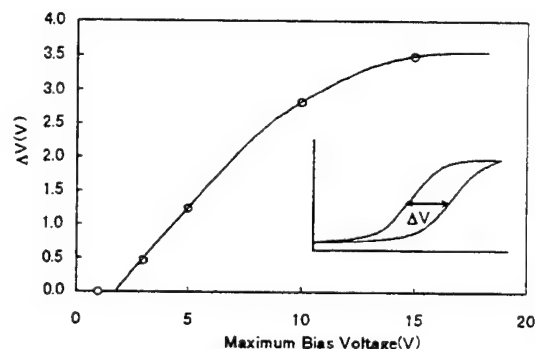


Fig.10 Change of the width of hysteresis curve as a function of maximum bias voltage

Acknowledgments

A part of this work was supported by a Grant-in-Aid for Scientific Research from the Ministry of Education, Science and Culture of Japan and Matsuda foundation.

References

- 1) H.Koinuma, Bull.Mater.Sci., 18 (1995) 435.
- 2) R.C.Evans, "Crystal Chemistry", (Cambridge Univ. Press, 1964)
- 3) S.Miyazawa, "Kougaku Keshou, Advanced Electronic Series", (Baifukan, 1995) in Japanese.
- 4) S.M.Sze, "Physics of Semiconductor Devices", (John Wiley & Sons, 1981).
- 5) S.Nishizawa, T.Tsurumi, H.Hyodo, Y.Ishibashi, N.Ohashi, M.Yamane and O.Fukunaga, Thin Solid Films, in press.
- 6) R.M.A.Azzam and N.M.Bashara, "Ellipsometry and Polarized Light", (Elsevier Sci. Pub. 1977).
- 7) T.Tanaka, Jap.J.Appl.Phys., 18 (1979) 1043.
- 8) W.Hirschwald et al., "Zinc Oxide---Properties and Behaviour of the Bulk, the Solid/Vacuum and Solid/Gas Interface", Current Topics in Materials Science, (North-Holland Publish Company, 1981).
- 9) T.Minami, H.Nanto and S.Takata, Jap.J.Appl.Phys., 23(1984) 280.

SYNTHESIS AND PROPERTIES OF $K(\text{Sr}_{0.5}\text{Ba}_{0.5})_2\text{Nb}_5\text{O}_{15}$ THIN FILMS BY CHEMICAL SOLUTION DEPOSITION METHOD

Wataru Sakamoto, Akihiro Kawase, Toshinobu Yogo and Shin-ichi Hirano

Department of Applied Chemistry, Graduate School of Engineering,

Nagoya University, Furo-cho, Chikusa-ku, Nagoya 464-01, Japan

Abstract

A homogeneous and stable $K(\text{Sr}_{0.5}\text{Ba}_{0.5})_2\text{Nb}_5\text{O}_{15}$ (KSBN50) precursor solution was prepared by the reaction control of metal alkoxides in ethanol with a key additive of 2-ethoxyethanol. Crack-free tungsten bronze KSBN50 thin films were successfully synthesized from the precursor solution on fused silica, $\text{MgO}(100)$ and $\text{Pt}(100)/\text{MgO}(100)$ substrates from 600°C to 700°C . KSBN50 thin films with c-axis preferred orientation were obtained on $\text{MgO}(100)$ and $\text{Pt}(100)/\text{MgO}(100)$. KSBN50 thin films on $\text{Pt}(100)/\text{MgO}(100)$ exhibited the typical P-E hysteresis.

1. Introduction

Strontium barium niobate ($\text{Sr}_{1-x}\text{Ba}_x\text{Nb}_2\text{O}_6$, SBN) has a large pyroelectric coefficient, excellent piezoelectric and electro-optic properties.^{1,2} Therefore, SBN has been expected for applications in pyroelectric sensors, SAW filters and several electro-optic devices. Alkali or rare-earth ion modified SBN also has been investigated to improve its properties.³⁻⁴ Recently, the demand for thin film processing has increased for the integrated-device development.⁵ Highly c-axis oriented tungsten bronze SBN thin films are expected for pyroelectric and electro-optic applications. A chemical solution deposition process has been developed for the ferroelectric film fabrication providing several advantages, such as high purity, good homogeneity, lower processing temperature, ease of composition control and versatile shaping.⁶⁻⁹ The crystallization of ferroelectric tungsten bronze phase on substrates encounters the problem of the formation of low temperature phase, which has poor dielectric properties.^{8,9} Tungsten bronze structure can be stabilized by the formation of filled-tungsten bronze.⁴ Neither BaNb_2O_6 (BN) nor SrNb_2O_6 (SN) is ferroelectric material and has tungsten bronze structure. However, BN and SN constitute the solid solution with alkali ions, yielding ferroelectric tungsten bronzes, such as $\text{Ba}_2\text{NaNb}_5\text{O}_{15}$ (BNN) and $\text{Sr}_2\text{KNb}_5\text{O}_{15}$ (SKN). Strontium barium niobate (SBN) also could be stabilized as a ferroelectric tungsten bronze phase by the substitution with alkali ion.

This paper describes the synthesis and characterization of highly oriented potassium-substituted SBN (KSBN) thin films through metal alkoxides. The crystallization process and dielectric properties of $K(\text{Sr}_{0.5}\text{Ba}_{0.5})_2\text{Nb}_5\text{O}_{15}$ (KSBN50) thin films were investigated.

2. Experimental Procedure

Strontium metal, barium metal, KOEt and $\text{Nb}(\text{OEt})_5$ were selected as starting materials. All procedures were conducted in a dry N_2 atmosphere. Metallic strontium, barium

and KOEt corresponding to $\text{K}(\text{Sr}_{0.5}\text{Ba}_{0.5})_2\text{Nb}_5\text{O}_{15}$ (KSBN50) composition were dissolved in absolute ethanol. 2-Ethoxyethanol (EGMEE) was added to the solution as a stabilizing agent. The molar ratio of EGMEE to KSBN50 precursor was set to be 30. The solution was mixed with $\text{Nb}(\text{OEt})_5$ solution. The mixed solution was reacted again at a reflux temperature for 18h. Then, the solution was condensed to about 0.1 mol/l. Films were fabricated using the precursor solution by dip-coating on fused silica, $\text{MgO}(100)$ and $\text{Pt}(100)/\text{MgO}(100)$ substrates. After the precursor film was calcined at 350°C for 1h, the film was heated to a crystallization temperature for 2h, and then cooled down in an O_2 flow at a rate of $5^\circ\text{C}/\text{min}$. The coating-crystallization process was repeated several times in order to increase the film thickness. Powders were also prepared from the precursor solution in order to investigate the crystallization behavior.

The prepared powders and films were characterized by X-ray diffraction (XRD) analysis. The crystallographic phases of KSBN powders and films were characterized by Raman microprobe spectroscopy. The surfaces of films were observed by atomic force microscopy (AFM). The dielectric measurement of films was conducted using a LCR meter. The P-E hysteresis loops of films were evaluated by a Radiant RT66A test system.

3. Results and Discussion

A homogeneous KSBN50, $\text{K}(\text{Sr}_{0.5}\text{Ba}_{0.5})_2\text{Nb}_5\text{O}_{15}$, precursor solution was prepared by the reaction of Ba metal, Sr metal, KOEt and $\text{Nb}(\text{OEt})_5$ in ethanol added with 30 equiv. EGMEE (EGMEE/KSBN precursor=30). The KSBN50 powders were prepared by the hydrolysis of the KSBN50 precursor solution. Figure 1 shows XRD profiles of KSBN50 powders heat-treated at 550°C and 600°C . The KSBN50 powders were X-ray amorphous below 550°C and directly crystallized to the tetragonal tungsten bronze phase at 600°C . In the case of $\text{Sr}_{0.5}\text{Ba}_{0.5}\text{Nb}_2\text{O}_6$ (SBN50) synthesis, SBN50 orthorhombic low temperature phase was formed at 700°C prior to the formation of tetragonal tungsten bronze SBN, then the orthorhombic SBN powder was transformed to the tetragonal phase at 1200°C .⁷ It turns out from Fig.1 that the formation of solid solution with potassium was very effective to form the tungsten bronze phase at lower temperatures without formation of the orthorhombic low temperature phase.

Figure 2 shows XRD profiles of KSBN50 thin films crystallized at 600°C on fused silica and $\text{MgO}(100)$ substrates. The KSBN50 films on fused silica substrate directly crystallized to the tetragonal tungsten bronze phase (Fig.2(a)). The KSBN50 films on $\text{MgO}(100)$ show strong 001 and 002 reflections as shown in Fig.2(b). KSBN50 thin films on $\text{Pt}(100)/\text{MgO}(100)$ also showed a prominent c-axis preferred orientation. Figure 3 shows the Raman spectra of KSBN50

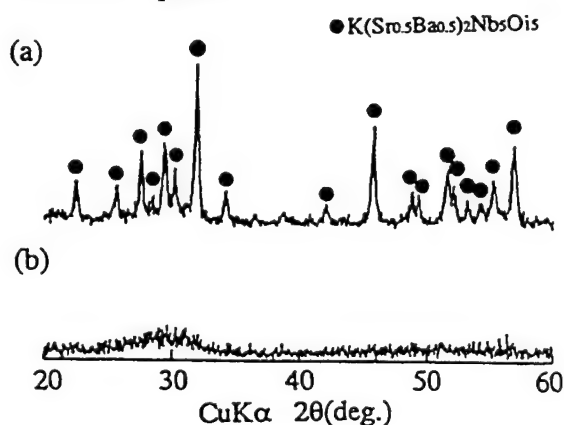


Fig.1 XRD profiles of $\text{K}(\text{Sr}_{0.5}\text{Ba}_{0.5})_2\text{Nb}_5\text{O}_{15}$ powders heat-treated at (a) 550°C and (b) 600°C .

powder and thin film on MgO(100) crystallized at 700°C. The spectrum pattern of the KSBN50 powder shown in Fig.3(a) is in good agreement with that of the tetragonal tungsten bronze SBN50 powder⁹, although the scattering positions are slightly shifted to each other. The KSBN50 thin films crystallized at 700°C are judged to be tungsten bronze single-phase (Fig.3(b)), since the profile is consistent with that of KSBN50 powder shown in Fig.3(a). Furthermore, the orientation of the KSBN50 thin films on MgO(100) and Pt(100)/MgO(100) was investigated by X-ray pole figure measurement. From the results, it was found that two crystal lattice planes of KSBN were intergrown at an orientation of 18.5° on MgO(100) and Pt(100)/MgO(100) substrates.

Figure 4 shows the AFM image of KSBN50 thin film on a Pt(100)/MgO(100) substrate heat-treated at 700°C. The surface of film appears smooth (surface roughness; about 10 nm), and the grain size of crystallized film was about 50-100 nm.

Figure 5 shows the temperature dependence of dielectric constant and loss tangent at 10 kHz for the KSBN50 film crystallized at 700°C on a Pt(100)/MgO(100) substrate. The dielectric maximum of the KSBN50 film was observed at around 140°C at 10 kHz. The Curie point of the KSBN50 thin film is higher than that of SBN50 single crystal. However, the ϵ -T curve was broadened compared with SBN single crystals.

Figure 6 shows a typical P-E hysteresis loop for a 0.7 μm -thick KSBN50 thin film crystallized at 700°C on a Pt(100)/MgO(100) substrate.

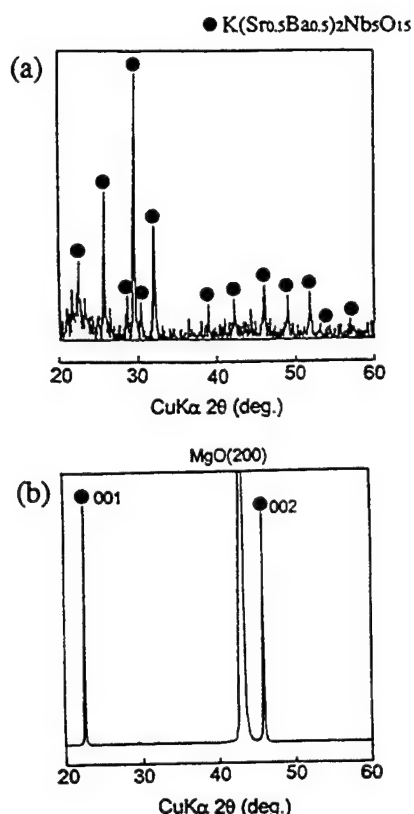


Fig.2 XRD profiles of $\text{K}(\text{Sr}_{0.5}\text{Ba}_{0.5})_2\text{Nb}_5\text{O}_{15}$ thin films heat-treated at 600°C on (a) fused silica and (b) MgO(100) substrates.

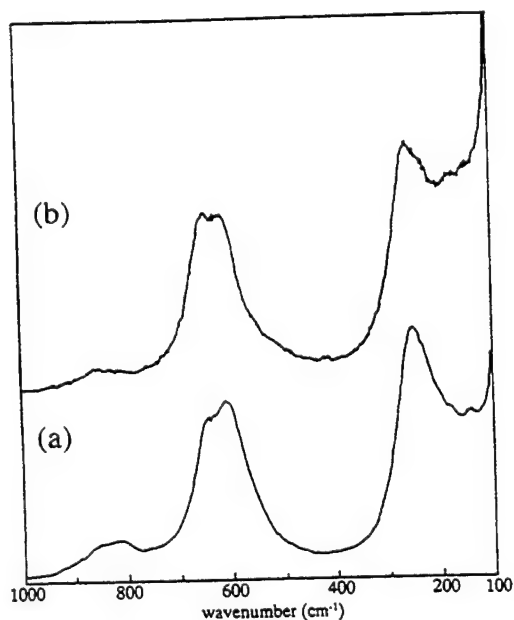


Fig.3 Raman spectra of (a) $\text{K}(\text{Sr}_{0.5}\text{Ba}_{0.5})_2\text{Nb}_5\text{O}_{15}$ powder and (b) $\text{K}(\text{Sr}_{0.5}\text{Ba}_{0.5})_2\text{Nb}_5\text{O}_{15}$ thin film on MgO(100) heat-treated at 700°C.

The hysteresis was measured at -190°C . The remnant polarization (P_r) was $22\ \mu\text{C}/\text{cm}^2$, and the coercive field (E_c) was $99\ \text{kV}/\text{cm}$. The value of remnant polarization was decreased with raising the measurement temperature. The shape of hysteresis loop changed from typical ferroelectric one to paraelectric one. Also, the remnant polarization of KSBN50 thin film showed a lower value than that of SBN single crystal ($32\ \mu\text{C}/\text{cm}^2$). The effect of the substitution with potassium, the Sr/Ba ratio and the lattice mismatch with substrates on the properties of KSBN films are now under investigation.

References

1. A.M.Glass,
J. Appl. Phys., **40** 4699 (1969).
2. R.R.Neurgaonkar and W.K.Cory,
J. Opt. Soc. Am. B, **3** 274 (1986)
3. R.R.Neurgaonkar, W.K.Cory,
J.R.Oliver, M.D.Ewbank and
W.F.Hall,
Optical Engineering, **26** 392 (1987).
4. K.Umakantham, S.N.Murty, K.S.Rao
and A.Bhanumathi,
J. Mat. Sci. Lett., **6** 565 (1987).
5. L.M.Sheppard,
Am. Ceram. Soc. Bull., **71** 85 (1992).
6. S.Hirano, T.Yogo, K.Kikuta and
K.Ogiso,
J. Am. Ceram. Soc., **75** 1697(1992).
7. C.J.Chen, Y.Xu, R.Xu and
J.D.Mackenzie,
J. Appl. Phys., **69** 1763 (1991).
8. W.Sakamoto, T.Yogo, K.Kikuta,
T.Arimoto and S.Hirano,
J. Am. Ceram. Soc., **79** 889 (1996).
9. W.Sakamoto, T.Yogo, K.Kikuta,
K.Ogiso, A.Kawase and S.Hirano,
J. Am. Ceram. Soc., **79** 2283 (1996).

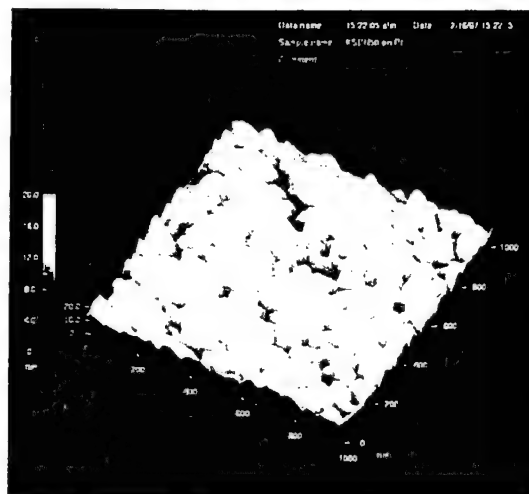


Fig.4 AFM image of $\text{K}(\text{Sr}_{0.5}\text{Ba}_{0.5})_2\text{Nb}_5\text{O}_{15}$ thin film on a $\text{Pt}(100)/\text{MgO}(100)$ substrate crystallized at 700°C .

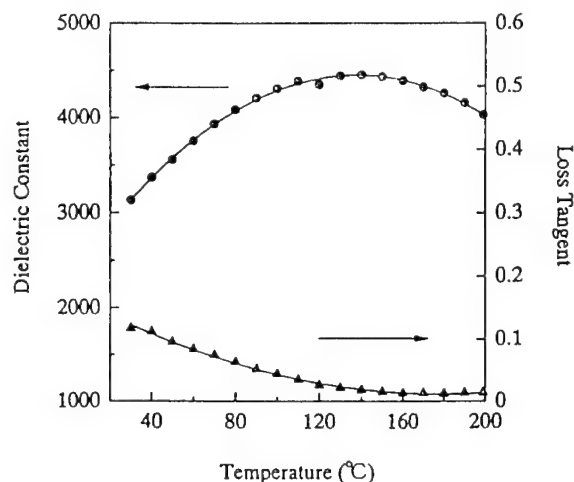


Fig.5 Temperature dependence of dielectric constant and loss tangent of $\text{K}(\text{Sr}_{0.5}\text{Ba}_{0.5})_2\text{Nb}_5\text{O}_{15}$ thin film on $\text{Pt}(100)/\text{MgO}(100)$ substrate heat-treated at 700°C . [measured at 10 kHz]

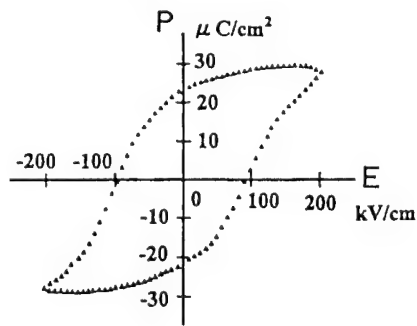


Fig.6 P-E hysteresis loop of $\text{K}(\text{Sr}_{0.5}\text{Ba}_{0.5})_2\text{Nb}_5\text{O}_{15}$ thin film on a $\text{Pt}(100)/\text{MgO}(100)$ substrate crystallized at 700°C .

Crystal Orientation and Dielectric Properties of Sol-Gel Derived $\text{SrBi}_2\text{Ta}_2\text{O}_9$ Thin Films

Takashi Hayashi and Takuya Hara

Department of Materials Science and Ceramic Technology,
Shonan Institute of Technology, 1-1-25 Tujido-Nishikaigan, Fujisawa,
Kanagawa 251, Japan

Ferroelectric $\text{SrBi}_2\text{Ta}_2\text{O}_9$ (SBT) thin films were prepared on Pt/Ti/SiO₂/Si substrates at 800 °C by sol-gel method using metal alkoxide solution. The preparation conditions of SBT precursor solution and an addition of acetylacetone or diethanolamine to alkoxide solutions affected the crystal orientation and/or the morphologies of SBT thin films. SBT thin films with a highly (00 ℓ) preferred orientation consisted of the grain structure resembling a stone wall, while randomly-oriented those with a high (105) diffraction intensity consisted of rod-like grain structure. SBT thin films with a random orientation exhibited ϵ_r of about 90, Pr of about 6.5 $\mu\text{C}/\text{cm}^2$ and Ec of 80 kV/cm, while those with (00 ℓ) orientation degree of 80% exhibited ϵ_r of about 78, Pr of about 1.6 $\mu\text{C}/\text{cm}^2$ and Ec of 110 kV/cm. The (00 ℓ) preferred orientation and an addition of diethanolamine tended to involve the deterioration of ferroelectric properties.

1. Introduction

Recently, Bi-layered perovskite thin films such as $\text{Bi}_4\text{Ti}_3\text{O}_{12}$, $\text{SrBi}_2\text{Ta}_2\text{O}_9$ or $\text{SrBi}_2\text{Nb}_2\text{O}_9$ have become candidates for use in nonvolatile random access memory (NvRAM) applications. Among them, $\text{SrBi}_2\text{Ta}_2\text{O}_9$ (SBT) thin films have especially a high potential for NvRAM device application, because SBT has superior fatigue-free properties and small Ec. Koiwa et al.¹⁾ have prepared SBT thin films by sol-gel method using alkoxides of strontium, bismuth and tantalum, and reported that the kind of strontium source is very important factor to control crystal orientation of SBT thin films. We reported that sol-gel derived SBT thin films showed a higher (00 ℓ) preferred orientation^{2),3)}, compared to MOD-derived SBT thin films. However, as c-axis-oriented SBT thin films have no or little

polarization along c-axis, it is very critical to suppress (00 ℓ) preferred orientation of the films by improving the preparation process of alkoxides solution.

In this paper, SBT thin films were synthesized by sol-gel method using mixed metal alkoxides which were prepared by two mixing processes. Their differences in crystal orientation, surface morphology and dielectric properties were investigated.

II. Experimental

SBT precursor solutions were prepared by two mixing processes with metal alkoxides. Strontium di-n-butoxide, bismuth tri-i-propoxide and tantalum pentaethoxide were used as starting materials and 2-methoxyethanol was used as a solvent.

In process A, firstly, strontium di-n-butoxide and tantalum pentaethoxide were mixed together and refluxed in 2-methoxyethanol, and then, the solution was added to bismuth alkoxide solution which was dissolved in 2-methoxyethanol at 60 °C. On the other hand, in process B, strontium di-n-butoxide was initially dissolved in 2-methoxyethanol and refluxed at 130 °C for 1h, and then, bismuth tri-i-propoxide was added to the solution and heated at 60 °C for 1h. Finally, tantalum pentaethoxide dissolved at 130 °C in 2-methoxyethanol was added to strontium-bismuth mixed alkoxide solution. Bismuth tri-i-propoxide, which is poorly soluble in common organic solvents, could be easily dissolved in 2-methoxyethanol containing strontium di-n-butoxide. Acetylacetone or diethanolamine was added to precursor solution to improve the stability of the precursor solution toward hydrolysis.

The final concentration of SBT in the solutions

was about 10, mass%. The nominal composition of SBT thin films used in this work was $\text{Sr}_{0.7}\text{Bi}_{0.2}\text{Ta}_{0.9}\text{O}_9$.

SBT gel thin films were prepared on Pt(200nm)/Ti(50nm)/SiO₂/Si substrates by spin-coating technique from SBT precursor solutions. The gel thin films were crystallized by conventional furnace annealing or rapid thermal annealing (RTA) at 800 °C for 1 h after repeating the process of spin-coating/preheating at 500 or 800 °C for 5 min in O₂ atmosphere. Film thickness of SBT was controlled by adjusting the number of repetitions of the coating/heating cycles. The speed of spin-coating was 2500 rpm.

The crystalline phases of thin films were identified by X-ray diffraction (XRD). The microstructure of the thin films was observed with a field-emission scanning electron microscope (FE-SEM). Gold electrodes of 0.2 mm diameter were vacuum-deposited through a mask onto the surface of SBT thin films. The dielectric constant (ϵ_r) of SBT thin films was measured using an impedance analyzer (YHP - 4192A) at 1 kHz with a micro manipulator. P-E hysteresis loops were also obtained for SBT thin films using RT-66A (RADIANT TECHNOLOGIES, Inc.) at 1 kHz. Applied voltage was 10 V.

III. Results and Discussion

Figure 1 shows XRD patterns of SBT thin films prepared on Pt/Ti/SiO₂/Si substrates at 800 °C for 1 h by furnace annealing with two processes. SBT thin films with perovskite structure could be prepared as a single phase. The crystal orientation of SBT thin films was affected by mixing processes of metal alkoxides to prepare SBT precursor solutions. SBT thin films prepared by process A showed a (00 ℓ) preferred orientation along with a high (105) diffraction intensity, whereas those prepared by process B showed random orientation. Figure 2 shows XRD patterns of SBT thin films prepared by process B with an addition of acetylacetone or diethanolamine. In this work, (00 ℓ) orientation degree of SBT thin films varied from 0 to 43%, depending upon the amount of added acetylacetone. But, XRD patterns of SBT thin films did not changed with an addition of diethanolamine.

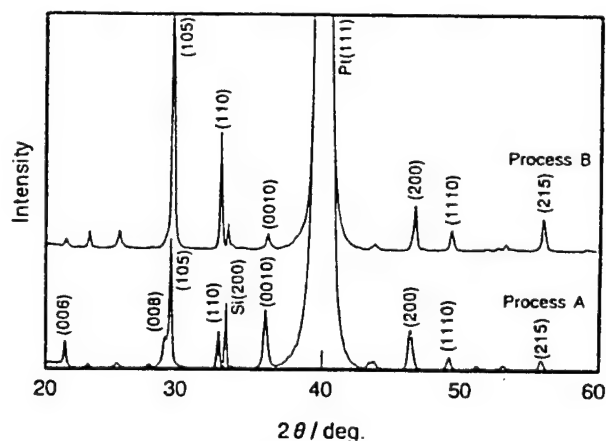


Fig.1. XRD patterns of SBT thin films prepared on Pt/Ti/SiO₂/Si substrates at 800 °C for 1 h by furnace annealing with two processes.

In process B, the values of orientation degree of SBT thin films increased as mole ratio of acetylacetone to Bismuth tri-*i*-propoxide increases to 0.3, above which it decreased to 40%.

Figure 4 shows FE-SEM micrographs of surfaces of SBT thin films prepared on Pt/Ti/SiO₂/Si at 800 °C for 1 h in process B. The surface morphologies of SBT thin films changed with (00 ℓ) preferred orientation degrees. The surface morphology of SBT thin films with a higher (00 ℓ) preferred orientation exhibited the grain microstructure resembling a stone wall with grain sizes of 100 ~ 300 nm, while those with a low (00 ℓ) orientation factor exhibited somewhat porous bimodal grain

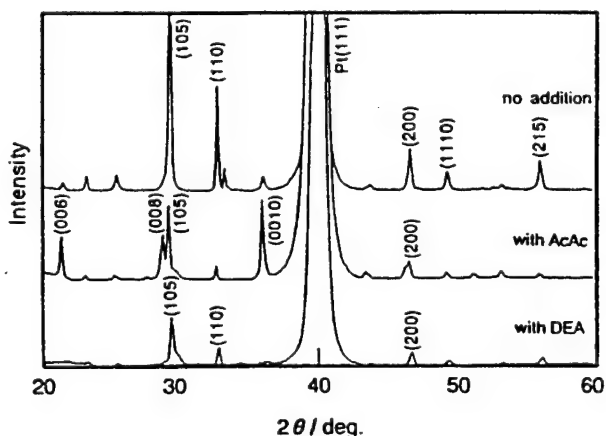


Fig.2. XRD patterns of SBT thin films prepared by process B with an addition of acetylacetone and diethanolamine.

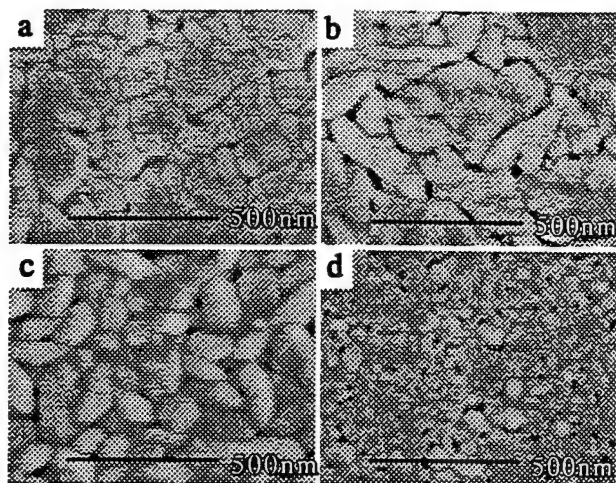


Fig.3. FE-SEM micrographs of surfaces of SBT thin films prepared on Pt/Ti/SiO₂/Si at 800 °C for 1 h in process B.

a) F=80% b) F=46% c) F=0%
d) F=0% with DEA

microstructure consisting of a mixture of stone wall-like grains and rod-like grains of about 300nm length and about 100nm width. Furthermore, SBT thin films with a random orientation showed grain microstructure consisting of only rod-like grains. The stone wall like grains are considered to have c-axis orientation from the results of XRD. On the other hand, when diethanolamine was added, the surface morphology of SBT thin films showed granular grain with 50-100nm.

Figure 4 shows P-E hysteresis loops of SBT thin films prepared by furnace annealing with different preferred orientations. The well-saturated hysteresis loops were obtained for SBT thin films with a low degree of (00 ℓ) preferred orientation. SBT thin films with the (00 ℓ) orientation degree of 43% showed the dielectric constant, ϵ_r , of about 220, the remanent polarization, P_r , of about 4.8 $\mu\text{C}/\text{cm}^2$, and the coercive field, E_c , of 60 kV/cm. On the other hand, SBT thin films with the (00 ℓ) orientation factor of 80% showed ϵ_r of about 78, P_r of about 1.6 $\mu\text{C}/\text{cm}^2$ and E_c of 110 kV/cm.

Figure 5 shows current density of SBT thin films prepared by furnace annealing with different preferred orientation degrees.

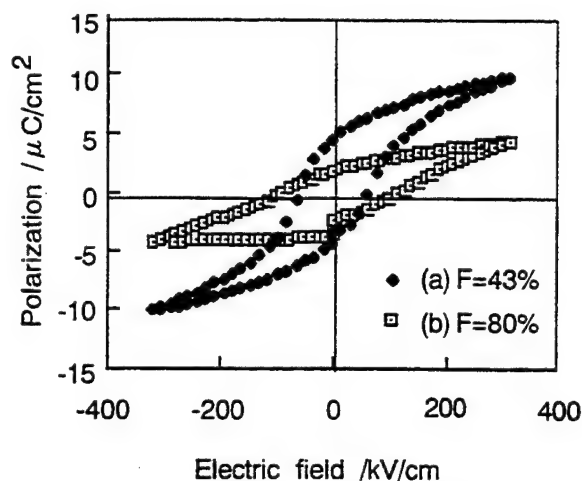


Fig.4. P-E hysteresis loops of SBT thin films prepared by furnace annealing with different preferred orientations.

Randomly-orientated films showed a higher leakage current related to porous morphologies. Therefore, the ferroelectric properties of randomly-orientated SBT thin films, which were prepared by furnace annealing without acetylacetone and with diethanolamine, could not be measured. Therefore, RTA annealing was used for the preparation of thin films with random orientation. RTA-treated thin films showed a dense microstructure with smaller grain sizes.

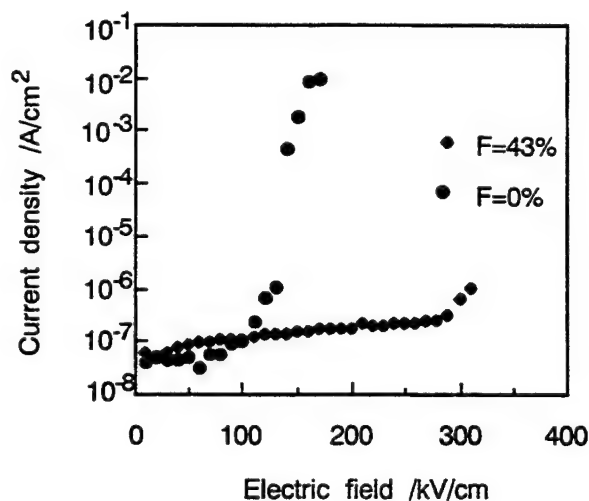


Fig.5. Current density of SBT thin films prepared by furnace annealing with different preferred orientations.

Figure 6 showed P-E hysteresis loops of randomly-oriented SBT thin films prepared with and without an addition of diethanolamine by RTA. The randomly-oriented SBT thin films prepared with no addition of diethanolamine showed ϵ_r of about 90, and exhibited the saturated hysteresis loop with Pr of $6.5 \mu\text{C}/\text{cm}^2$, and Ec of 80 kV/cm, while those prepared with an addition of diethanolamine showed Pr of about $3.0 \mu\text{C}/\text{cm}^2$ and Ec of 80 kV/cm.

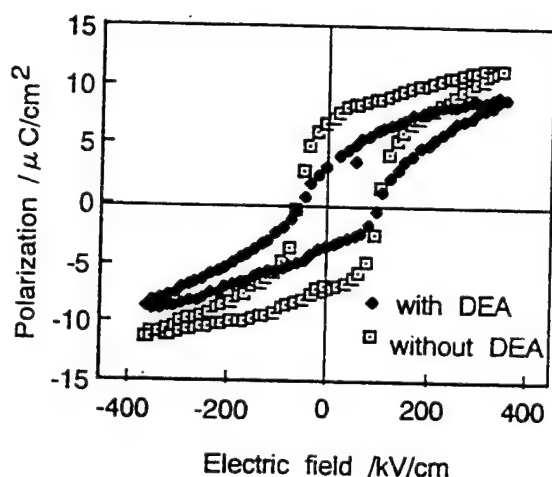


Fig.6. P-E hysteresis loops of randomly-oriented SBT thin films prepared with and without an addition of diethanolamine by RTA annealing.

IV. Conclusions

$\text{Sr}_{0.7}\text{Bi}_{2.2}\text{Ta}_2\text{O}_9$ thin films were prepared at 800 °C for 1h using SBT precursor solutions of alkoxides. The crystal orientation and the microstructure of SBT thin films formed by sol-gel method was influenced by a coordination state, depending upon the mixing conditions of metal alkoxides and an addition of acetylacetone or diethanolamine to the alkoxide solutions. SBT thin films with c-axis preferred orientation showed stone wall-like grains microstructure, while those with random orientation showed rod-like grain microstructure. But, SBT thin films prepared by an addition of diethanolamine showed granular grain with random orientation. The randomly oriented SBT thin films exhibited ϵ_r of about 90, Pr of about $6.5 \mu\text{C}/\text{cm}^2$ and Ec of 80 kV/cm. However, the (001) preferred orientation and an addition of diethanolamine tended to deteriorate ferroelectric properties of SBT thin films.

References

- 1) I. Koiwa, T. Kanehara, T. Iwabuchi and T. Osaka : Extended Abstracts of International Conference on Solid State Devices and Materials, Yokohama, 1996, p.628 (J. Soc. Appl. Phys.)
- 2) T. Hayashi, H. Takahashi and T. Hara : Jpn. J. Appl. Phys. 35 (1996) 4952.
- 3) T. Hayashi, H. Takahashi and T. Hara : submitted to Jpn. J. Appl. Phys.

Recent Topics in Multilayer Ceramic Capacitor Technology

Takeshi NOMURA, Tomohiro ARASHI, Akira SATO,
Yukie NAKANO, and Shigeki SATO

Materials Research Center, TDK Corporation, Narita-shi, Chiba 286, Japan

Abstract—Recently, reduction of production costs with maintaining high reliability is required for wider applications of capacitors. The demand for high capacitance multilayer ceramic capacitors (MLCCs) are rapidly increasing for noise reduction of electronic facilities, such as cellular phone and personal computer. Ni-electrode MLCCs of BaTiO_3 -based dielectrics were developed to meet the requirements. Thinner dielectric layers, miniaturization, and high capacitance are also major requirements for MLCCs. In these circumstances, much effort has been paid in order to achieve higher reliability. Ni-electrode MLCCs are promising way to satisfy the requirements of high capacitance, low cost, and high reliability. High capacitance Ni-electrode MLCCs are partially substituting electrolytic capacitors, because of their advantages of high reliability, low ESR, no directionality, and so on, and they are expanding their field to that of film capacitors. Self-restoring function, COG characteristics, and high voltage-use Ni-electrode MLCCs are now developing. These capacitors are expected to enlarge the application of Ni-electrode MLCCs.

1. INTRODUCTION

In recent years, electronic components have been rapidly developed with the production of new electronic devices. Multilayer ceramic capacitors (MLCCs) are particularly important electronic components that are used in almost all areas of electronics. Recently, required are reduction of production cost, miniaturization, high capacitance, and high reliability, in order to increase the range of applications of capacitors. Among these requirements, low cost is of prime importance from the view point of industrial product. The cost of the electrode materials occupies a large part of the total cost. So far, palladium or silver-palladium has been the majority of the internal electrode material. In order to lower the production cost, much effort has been devoted to develop the base-metal electrode system. Ni-electrode multilayer ceramic capacitors are a promising means of reducing the cost. Currently, an increasing number of Ni-electrode MLCCs are

being produced. Dielectric layers are made thinner and the number of these layers has been increased in order to meet the requirements for MLCCs being smaller in size but providing large capacitance. An Ni internal electrode is, however, easily oxidized during firing under ambient conditions. Firing should be therefore carried out in a reducing atmosphere using a reduction-resistive dielectric material. When a reduction-resistive material is used and fired in a reducing atmosphere, the capacitors with internal Ni electrodes can provide initial characteristics similar to those provided by capacitors that use Pd as the internal electrode. Major problems involved regarding the reliability of such capacitors are as follows: a short lifetime of insulation resistance under a highly accelerated life test and aging of the capacitance. These problems are, however, solved by the means of rare earth oxide doping to the dielectric composition and the microstructure control. The increase of digital electronic equipment such as personal computer, cellular phone and so on, and raising of their driving frequency, result in a great demand for noise suppression component. In general, MLCCs have so large capacitance that they reduce the noise with fast response, while they would easily break down irreversibly when surge current or static electricity intrude. Under these circumstances, MLCCs of high voltage use or self-restoring function are required. Multilayer ceramic capacitors have a large share in the capacitor market, as shown in Fig. 1.

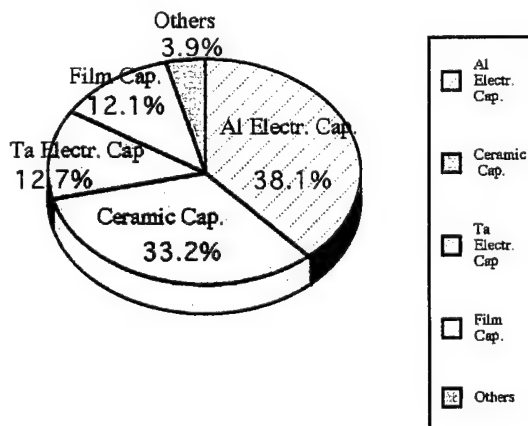


Fig.1 Share in the capacitors market

Aluminum electrolytic capacitors also have a large share because of its feature as low cost and high capacitance despite the short lifetime of insulation resistance. Tantalum electrolytic capacitors have a larger capacitance and excellent temperature stability but they have not good cost performance. Recently, much effort has been paid to achieve higher capacitance for MLCCs with smaller size. High capacitance MLCCs are expected to extend the application field in which electrolytic capacitors or plastic film capacitors are much used. Many capacitors are used in switched-mode power converter, but tantalum electrolytic capacitors can be substituted by MLCCs. Much designers of switched-mode power converter want to employ MLCCs because of the high reliability. The major theme of ceramic capacitors is to extend their region to those of electrolytic and film capacitors.

The aim of this paper is to present recent topics about R&D in the field of materials technology of multilayer ceramic capacitors, especially Ni-electrode MLCCs.

II. COG CHARACTERISTICS

Film capacitors have some features of very small temperature coefficient of capacitance, self-restoring characteristics. In order to replace film capacitors by MLCCs, high capacitance Ni-electrode MLCCs with COG characteristics are required. Many dielectric materials of reduction-resistive ceramics have been reported as is shown in Fig. 2. Major constituent are CaO, SrO, and ZrO₂ in any case. Dielectric constant, however, are not enough to achieve high capacitance. The authors have widely investigated high K materials with COG characteristics, such as La-Ti-O system. Dielectric relaxation, however, were observed at thinner dielectric layer and at lower frequencies.

Frequency dependence of temperature coefficient of dielectric constant of film capacitors are shown in Fig. 3. Capacitance is not stable for frequency, especially for lower frequencies. In order to obtain high K dielectric materials of COG characteristics, rare earth oxide compounds were widely investigated. As an example, effect of donor doping on temperature dependence of dielectric constant for La-Ti-O system is shown in Fig. 4. Dielectric constant is as high as 1.5 times of that of Ca(ZrTi)O₃ system. At higher frequencies, dielectric constant is very stable for temperature. On the other hand, dielectric dispersion at higher temperature were observed at lower frequencies. This is similar to film capacitors, and is remarkably suppressed by V₂O₅ doping. However, V₂O₅ doping is not perfect, unfortunately. Dielectric relaxation at low frequencies in the (CaSr)(TiZr)O₃

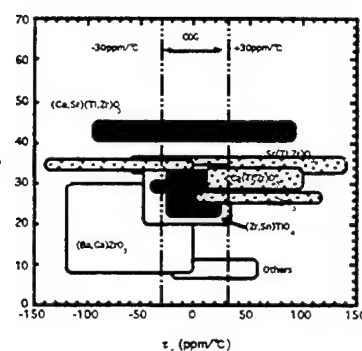


Fig. 2 Patent view of low K dielectric materials for Cu- or Ni- electrode MLCCs.

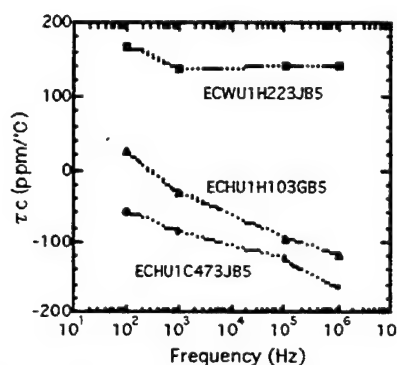


Fig. 3 Frequency dependence of temperature coefficient of dielectric constant of film capacitors.

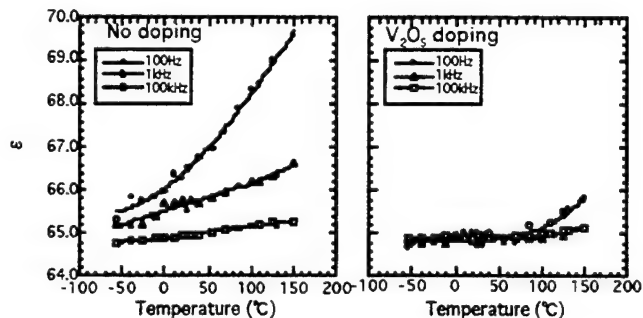


Fig. 4 Effect of donor doping on temperature dependence of dielectric constant for COG characteristic materials.

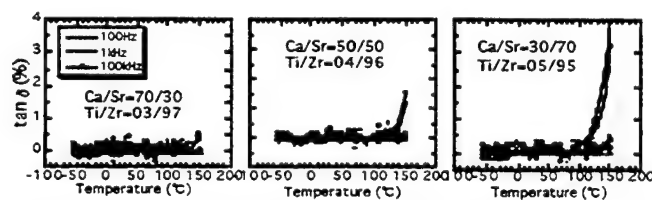


Fig. 5 Effect of chemical composition on the dielectric loss at low frequencies.

Session III—Capacitors and Dielectrics

PAGE

Invited Papers

- | | |
|--|-----|
| Recent Topics in Multilayer Ceramic Capacitor Technology, <u>T. Nomura</u> , <i>T. Arashi, A. Sato, Y. Nakano, and S. Sato, TDK Corp. Japan</i> | 148 |
| Changing the Equilibrium in MLCC Manufacturing, <u>A. Rae</u> , <i>J. Bultitude</i> , <i>S. Butcher, M. Chu, and V. Ganine, TAM Ceramics, USA</i> | 155 |

Contributed Papers

Base Metal Systems

- | | |
|--|-----|
| III-1 Mechanism of Improvement in Resistance Degradation in Y-doped BaTiO ₃ Based Multilayer Ceramic Capacitors with Ni Electrodes Under Highly Accelerated Life Testing, <u>S. Sato</u> , <i>Y. Nakano, A. Sato, and T. Nomura</i> , <i>TDK Corp., Japan</i> | 161 |
| III-2 Microstructure and Reliability Study of MLCs with Ni Electrodes, <u>M. Chu</u> , <i>J. Bultitude, V. Ganine, and A. Rae, TAM Ceramics Inc., USA</i> | 165 |
| III-3 Electron Microscopy Study of Dislocation Loops in Stoichiometric BaTiO ₃ and Nonstoichiometric (Ba,Ca)TiO ₃ , <u>T. Suzuki</u> , <i>M. Ueno, Y. Nishi</i> , <i>K. Arai, and M. Fujimoto, Taiyo Yuden Co. Ltd., Japan</i> | 168 |
| III-4 Ca Ion Selective Site Occupation at Ruddlesden-Popper-Type Faults and the Resultant Dielectric Properties of A-site-excess (Sr,Ca) TiO ₃ Ceramics, <u>M. Fujimoto</u> , <i>T. Suzuki, Y. Nishi, and K. Arai, Taiyo Yuden Co. Ltd.; and</i> <i>J. Tanaka, National Institute for Research in Inorganic Materials, Japan</i> | 172 |
| III-5 Effects of Heat Treatment on Dielectric Properties of X7R Designated MLCs with Ni Internal Electrodes, <u>H. Shoji</u> , <i>H. Matsushita, Y. Nakano, H. Ogawa</i> , <i>and A. Onoe, Nippon Chemi-con Corp.; and Y. Yamashita and H. Kanai</i> , <i>Toshiba Corp., Japan</i> | 176 |

Thin Layers/X7R

- | | |
|---|-----|
| III-6 Electrical and Physical Characteristics of Low-Fire X7R MLCCs with $\leq 3 \mu\text{m}$ Active Layers and 70 Ag-30 Pd Electrodes, <u>J.J. Beeson</u> and <i>L. A. Mann</i> , <i>Kemet Electronics Corp.; S. Venigalla and S.A. Costantino, Cabot Performance</i> <i>Materials; USA</i> | 180 |
| III-7 Effect of AC Signal Field on the Electrical Properties of Thin Layer MLC's with X7R Characteristics, <u>G.H. Maher</u> , <i>V. Bheemineni, and</i> <i>T.I. Prokopowicz, MRA Laboratories Inc., USA</i> | 184 |
| III-8 High Energy Storage X7R Dielectrics, <u>W. Huebner</u> , <i>S.C. Zhang, M. Pennell</i> , <i>X.M. Ding, University of Missouri -Rolla, USA</i> | 188 |

Synthesis and Manufacturing

- III-9 Dielectric Properties of PMN Based Ceramic Under D.C. and A.C. Fields, U. Kumar, J. Hock, B. Rawal and M. Randall, *AVX Corporation, USA* 193
- III-10 Manufacturing of Barium Titanium Powder by Oxalate Process, M. Nishido and K. Harada, *Fuji Titanium Ind. Co. Ltd., Japan* 197
- III-11 Use of Low Fire BaTiO₃ Dielectrics in the Manufacture of MLCCs, S.P. Gupta and L.A. Mann, *Kemet Electronics Corp., USA* 201
- III-12 Preparation of Barium Strontium Titanates by Vapor Phase Hydrolysis of Precursors Via Modified Alkoxide Route, T. Hayashi, K. Sunaga, S. Satoh, and H. Satoh, *Shonan Institute of Technology,;* and K. Sasaki, *former Research Associate, DuPont, Japan* 205

Microwave/Miscellaneous

- III-13 The Effect of Calcining Sequence and Dopant Addition on the Densification and Microwave Properties of Zirconium Tin Titanate, J. Wilson, P. Pruna, and M. Megherhi, *Ferro Transelco Division, USA* 209
- III-14 Dielectric Properties of Ba(Zn_{1/3}Ta_{2/3})O₃ - KTaO₃ Ceramics, H. Yokoi, A. Tosa, and K. Ohbayashi, *NGK Spark Plug Co., Ltd., Japan* 212
- III-15 Development of the Varistor/Capacitor Co-fired Multilayer Device, T. Sogabe, *TDK Corp., Japan* 216
- III-16 Dielectric Properties of Ta₂O₅ Based Ceramics, N. Ichinose and T. Ukai, *Waseda University;* and Y. Yamashita, *Toshiba R&D Center, Japan* 220
- III-17 Effect of Poling on Conducting Barium Titanate, R.D. Roseman, *University of Cincinnati, USA* 223
- III-18 Effect of pH and Cation Concentration on PMN Powders Prepared by a Coprecipitation Method, D.-Y. Jeng, C.J. Chen, and S.R. Chaudhuri, *YTC America, Inc., USA* 227

system was investigated. Effect of chemical composition on the dielectric loss at low frequencies is shown in Fig. 5. In any composition, loss is very low and stable for temperature at higher frequencies. On the contrary, dielectric dispersion at high temperature and low frequencies strongly depends on the chemical composition. Dielectric dispersion is pronounced in Sr and/or Ti rich compositions. This might be related with defect chemistry, and is strongly affected by dielectric layer thickness. Effect of dielectric thickness on the temperature coefficient of dielectric constant is shown in Fig. 6. Gradual deterioration in temperature coefficient of dielectric constant can be observed with thinner dielectric layers. This might be caused by the electric field strength and NiO diffusion into dielectrics from internal Ni-electrode.

In order to analyze the relaxation, temperature dependence of dielectric loss at low frequencies was investigated as is shown in Fig. 7. At higher temperature, the peak of loss tangent shifts to higher frequency, with both Ca-rich and Sr-rich compositions. Relaxation time can be calculated from the peak of loss tangent, according to equation (1).

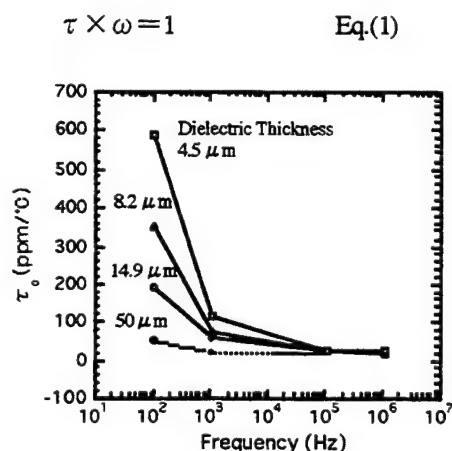


Fig. 6 Effect of dielectric thickness on the temperature coefficient of dielectric constant.

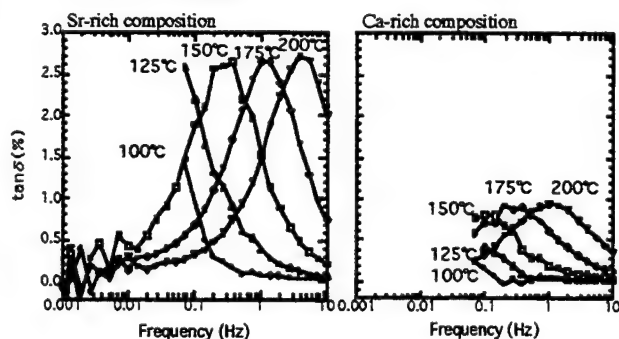


Fig. 7 Frequency dependence of $\tan \delta$ for COG characteristic materials.

Arrhenius plot of relaxation time for dielectric relaxation at low frequencies is shown in Fig. 8. Activation energies are about 0.9 eV at any composition of $(\text{CaSr})(\text{TiZr})\text{O}_3$ system. Figures 9 and 10 show the Arrhenius plots of thermally stimulated current and conductivity, respectively. In both case, activation energies are about 0.9 eV. Activation energies from the different viewpoints show the same value. Effect of annealing condition on the dielectric loss at low frequencies is shown in Fig. 11. Dielectric dispersion at 100 kHz is significantly suppressed by the annealing under relatively high partial pressure of oxygen for reoxidation of dielectric ceramics. This suggests that oxygen vacancies are the cause of the dielectric dispersion at low frequencies. Thermally stimulated current was also remarkably suppressed by the annealing. Acceptor doping such as Mg and Zn emphasized the dielectric dispersion. On the contrary, donor doping suppressed the dielectric dispersion and thermally stimulated current. Adopting these techniques mentioned above, highly reliable and high capacitance MLCCs with COG characteristics are obtained, as is shown in Fig. 12.

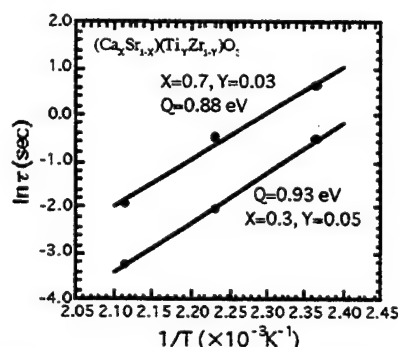


Fig. 8 Arrhenius plot of relaxation time for dielectric dispersion at low frequencies.

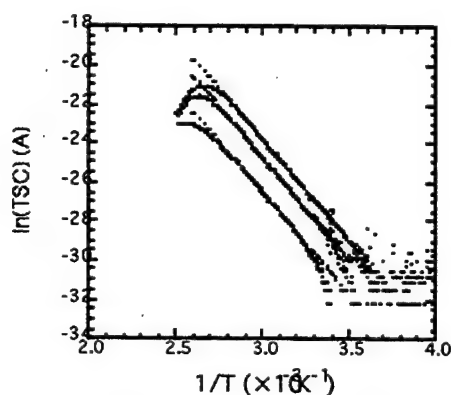


Fig. 9 Arrhenius plot of thermally stimulated current for $(\text{Ca}_x\text{Sr}_{1-x})(\text{Ti}_y\text{Zr}_{1-y})\text{O}_3$ system.

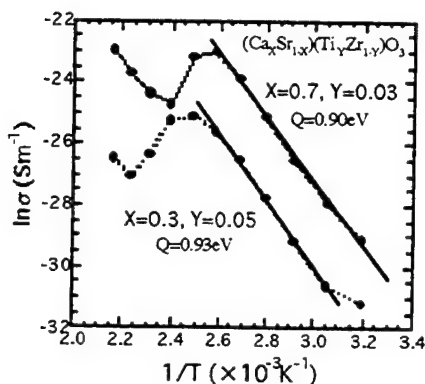


Fig. 10 Arrhenius plot of conductivity for COG characteristic materials.

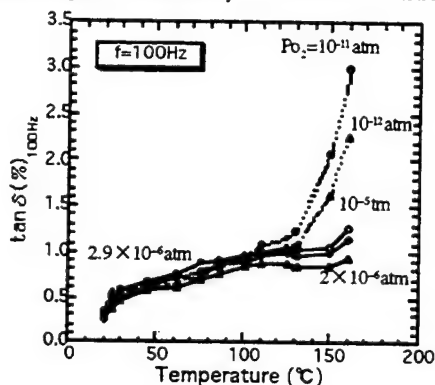


Fig. 11 Effect of annealing condition on the dielectric loss at 100Hz.

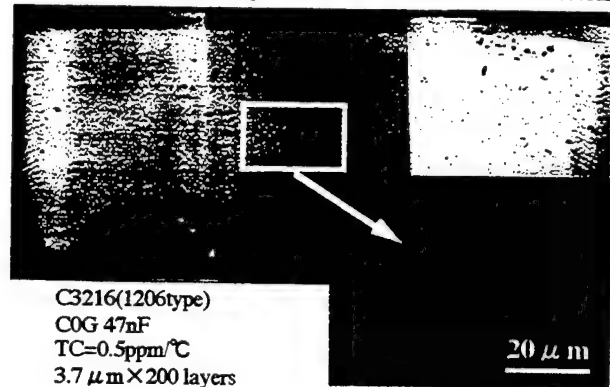


Fig. 12 Cross section of newly developed MLCC.

III. VARISTIC CAPACITOR

In general, MLCCs have so large capacitance that they reduce the noise with fast response, while they would easily break down irreversibly when surge current or static electricity intrude. From these circumstances, reoxidized capacitor in the SrTiO_3 system has been reported as a varistor-capacitor, because it has both varistor functions, such as noise suppression and transient surge protection and capacitor function. However, few study of BaTiO_3 varistor has been reported so far. The

authors have developed varistic MLCCs with X7R characteristics and they have features that they would not break down.

Typical voltage-current characteristics shown in Fig. 13 has two regions : ohmic low voltage region and nonlinear high voltage region. In this case, nonlinearity coefficient, α was 7.1. In order to control the varistor characteristics, important factors are as follows: (1)The dielectric composition and the grain size of BaTiO_3 -based ferroelectric phase, (2)firing and annealing condition, i.e. temperature, soak time and oxygen partial pressure, (3)the construction of MLCCs, i.e. thickness and the number of dielectric layers.

First, the effect of additive content in dielectric material on the varistor voltage were studied on the composition of BaTiO_3 - MgO - $\text{Ba}_{0.4}\text{Ca}_{0.6}\text{SiO}_3$ - MnO - Y_2O_3 - V_2O_5 . Content of MgO and MnO , and annealing conditions are the major factors of varistor characteristics. Figure 14 shows the relationship between Mn content and varistor voltage. It is apparent, however, that non-annealed MLCCs do not practically exhibit a varistor characteristics, varistor voltage is proportional to Mn content when annealing was carried out. Moreover, Mn

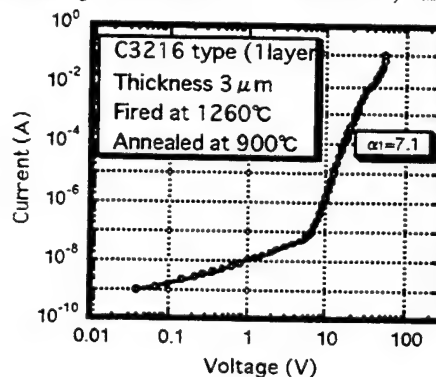


Fig. 13 Typical V-I characteristics of varistic MLCC.

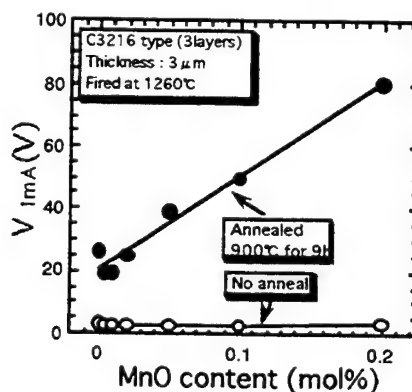


Fig. 14 Effect of Mn content on the varistor voltage.

content does not affect the capacitor characteristics, such as permittivity and dissipation factor at all as shown in Fig. 15. Figure 16 shows the relationship between Mg content and varistor voltage. When no Mg was added to dielectric material, BaTiO₃ ceramics was not reoxidized so that MLCCs remained low IR. On the other hand, excess Mg addition caused worse sinterability, resulting in the low varistor voltage. Thus annealing step is essential for MLCCs to attain varistor characteristics, indicating varistor voltage may strongly depend on the annealing condition, such as temperature, soak time and oxygen partial pressure. The effect of annealing condition on the varistor voltage shown in Fig. 17 indicated that both the higher annealing temperature and the longer soak time led to the rise of varistor voltage. Since grain boundary layer might be preferably reoxidized while annealing, it is suggested that the appearance of varistor characteristics is closely related to potential barrier formed at grain boundary and the properties along the grain boundary layer. Figure 18 shows that the maximum peak current of newly developed MLCCs with 140 layers was over 130A and is ten times as large as that of typical MLCCs. Static electricity resistance test in Fig. 19 indicates that newly developed MLCCs shows no breakdown, while rate of breakdown in typical MLCCs was 100% after 20 times discharge, respectively. From the viewpoint of chip construction and composition of dielectrics, not only reduction of layer thickness but also less Mn content provide the MLCCs with more superior varistor characteristics mentioned above.

Though these MLCCs consist of BaTiO₃-based ceramics in essence, it shows superior varistor characteristics. Then, dc bias voltage dependence of capacitance, so-called C-V characteristics, was carried out in order to examine the varistor mechanism of the MLCCs. Because of C-V plot in Fig. 20 shows nonlinear relationship, the conduction mechanism could not be explained by double schottky barrier model which is proposed in ZnO or SrTiO₃ varistor, suggesting the existence of other conduction mechanisms.

Ni-electrode MLCCs with superior varistor characteristics were obtained employing BaTiO₃-based dielectrics, and they are expected to replace plastic film capacitors.

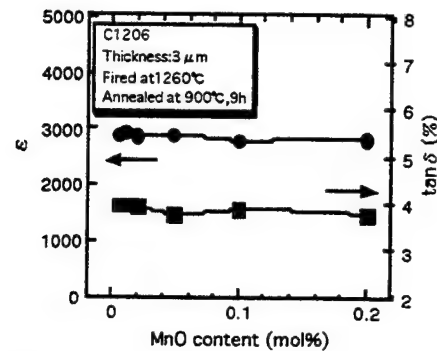


Fig. 15 Effect of Mn content on the capacitor characteristics.

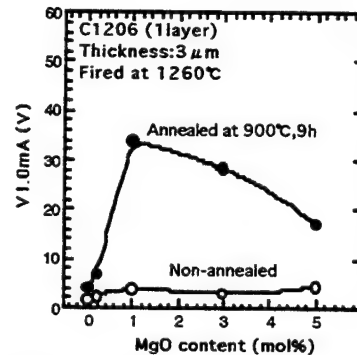


Fig. 16 Effect of Mg content on the varistor voltage.

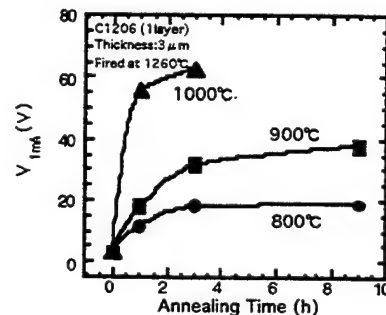


Fig. 17 Effect of annealing condition on the varistor voltage.

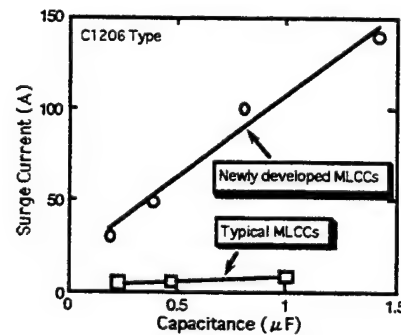


Fig. 18 Maximum peak current of the varistic capacitor.

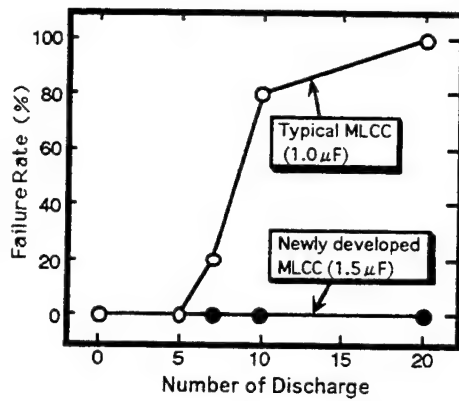


Fig. 19 Results of static electricity resistance test.

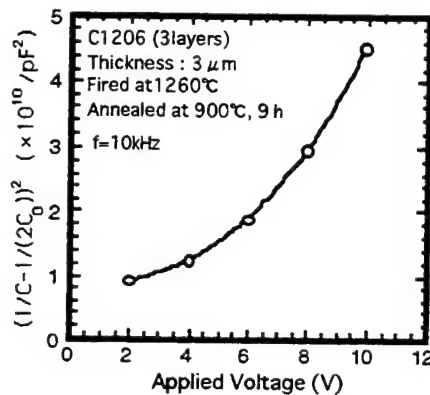


Fig. 20 C-V characteristics of the varistic MLCC.

IV. X7R CHARACTERISTICS

The authors had already reported that the capacitance aging behavior might be fitted to Richter model, and that the capacitance aging behavior under dc field might be fitted to a new model. Moreover, highly reliable Ni-electrode MLCCs with X7R characteristics had been developed, which had capacitance as high as 10 μ F for 1206-type capacitors (3.2mm \times 1.6mm \times 1.4mm). When the dc field is applied to ceramic capacitors, capacitance aging is pronouncedly accelerated. It has been previously reported that microstructure, crystal structure, and defect chemistry are the factors of capacitance aging of BaTiO₃-based ferroelectric dielectrics. It is pointed out that the capacitance aging under dc field is caused by the residual electric field. New model explaining the capacitance aging behavior under dc field is shown in Fig. 21. Moreover, it is proposed that the relaxation time and the capacitance change could be expressed by Boltzmann's factor with the acceleration factor of dc electric field, as shown in eqs.(2) and (3), respectively.

$$\tau = \tau_0 \exp(Q/kT) = aV^n \exp(Q/kT) \quad \text{Eq.(2)}$$

Where Q is the activation energy, k is the Boltzmann's constant, T is the aging temperature in absolute temperature, V is a dc electric field, n is an acceleration factor, and a is a constant.

$$\Delta C = d_0 V n \exp(vK/kT) \quad \text{Eq.(3)}$$

Where v is volume of grains and K is crystallographic anisotropy.

In order to suppress the capacitance aging in the case of thin dielectric layers, in which electric field is much stressed, finer grain size is preferable as is shown in Fig. 22. This is because of its low tetragonality. Figure 23 shows the effect of tetragonality on long-term aging. These data well support eq.(3).

Many studies had been reported about the capacitance aging of ferroelectric material. Internal stress of dielectrics is reported as one of the cause of the capacitance aging. The authors investigated the capacitance aging from the viewpoint of internal stress, but clear relationship between internal stress and capacitance aging was not obtained. Side margin of

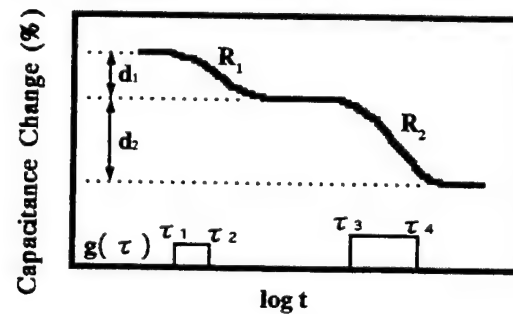


Fig. 21 New model for the capacitance aging under dc field.

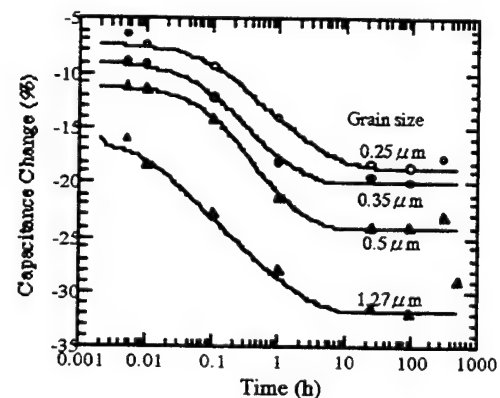


Fig. 22 Effect of grain size on capacitance aging under dc field.

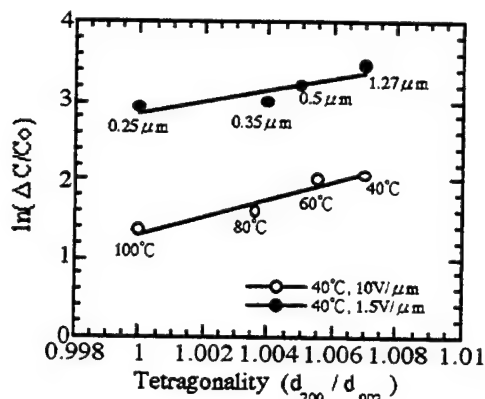


Fig. 23 Effect of tetragonality on long-term aging of Ni-electrode MLCCs of X7R characteristics.

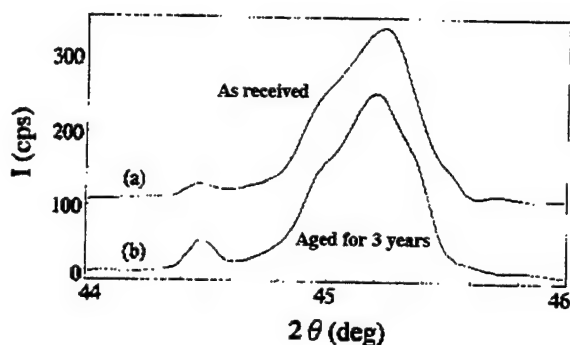


Fig. 24 Change in XRD profile by aging.

MLCCs, however, had an effect of stressing capacitance aging. Moreover, XRD profile changed by the aging, as is shown in Fig.24. These facts suggest that the mechanical stress is concerned in the capacitance aging. More detailed studies should be done for clarify the dielectric aging. In the case of dielectric composition, $\text{BaTiO}_3\text{-MgO-Ba}_{0.4}\text{Ca}_{0.6}\text{SiO}_3\text{-MnO-Y}_2\text{O}_3\text{-V}_2\text{O}_5$, grains scarcely grow during sintering, so that the particle size of raw BaTiO_3 particles should be small enough to minimize the capacitance aging. Smaller particle size, however, lead low permittivity. As a conclusion, appropriate particle size is about $0.3\text{-}0.4\text{ }\mu\text{m}$ for the dielectric thickness of $2\text{ }\mu\text{m}$. This dielectric material has a feature of high breakdown voltage. In general, commercial

X7R characteristics MLCCs show $60\text{-}70\text{ V}/\mu\text{m}$ of breakdown voltage. On the contrary, new material shows superior high breakdown voltage as $120\text{ V}/\mu\text{m}$. This is available for MLCCs for high voltage use.

V. CONCLUDING REMARKS

This paper focused on the recent topics of R&D about multilayer ceramic capacitors with special reference to the Ni-electrode MLCCs. Ni-electrode MLCCs are now the majority of high capacitance MLCCs, because of their cost merit and high reliability. Materials and process technologies of MLCCs had greatly advanced in last 10 years. Trends of MLCCs as miniaturization, high capacitance which is achieved by thinning dielectric layers, low cost, and high reliability are considerably progressed.

So far, Ni-electrode MLCCs is the key to achieve them at the same time. However, there is a limit for them. New technology is required to be developed in order to overcome this barrier. On the other hand, new application of Ni-electrode MLCCs to the field of plastic film and electrolytic capacitors is expected to progress more rapidly.

REFERENCES

- 1) J.M.Herbert, Trans.Br.Ceram.Soc., 62 (1963)645.
- 2) I.Bur, and G.H.Maher, J.Mater.Sci., 10 (1975) 633.
- 3) Y.Sakabe, K.Minai and K.Wakino, Jpn.J.Appl.Phys., 20 (1981) Suppl. 20-4 147.
- 4) T.Nomura, A.Sato and Y.Nakano, J.Soc.Mater.Eng.Resour.Jpn., 5 (1992) 44.
- 5) T.Nomura, S.Sumita, Y.Nakano and K.Nishiyama, Proc.5th US-Jpn. Seminar Dielectric Piezoelectric Ceramics,Kyoto,Japan, (1990) 29.
- 6) S.Sumita, M.Ikeda, Y.Nakano, K.Nishiyama and T.Nomura, J.Am.Ceram.Soc., 74 (1991) 2739.
- 7) T.Nomura and Y.Nakano, Denshi Tokyo, 31 (1993) 168.
- 8) Y.Nakano, A.Sato, J.Hitomi and T.Nomura, Ceram.Trans., 32 (1993) 119.
- 9) J.Yamamatsu, N.Kawano, T.Arashi, A.Sato, Y.Nakano and T.Nomura, J.Power Sources, 60 (1996) 1996.
- 10) T.Nomura, N.Kawano, J.Yamamatsu, T.Arashi, Y.Nakano, and A.Sato, Jpn.J.Appl.Phys., 34 (1-9B) (1995) 5389.
- 11) G.Arlt, D.Hennings and G. de With, J.Appl.Phys., 58 (4) (1985) 1619.
- 12) K.Uchino, E.Sadanaga and T.Hirose, J.Am.Ceram.Soc., 72 (8) (1989) 1555.
- 13) L.Neel, Ann.Geophys., 599-136 (1949).
- 14) S.Minomura, T.Kawakubo and T.Nakagawa, Jpn.J.Appl.Phys., 3 (1964) 562.
- 15) A.K.Goswami, J.Phys.Soc.Jpn., 21 (6) (1966) 1037.
- 16) G.Arlt and H.Neumann, Ferroelectrics, 87 (1988) 109.

Changing the Equilibrium in MLCC Manufacturing

Alan Rae, John Bultitude, Steve Butcher, Mike Chu and Vladimir Ganine

TAM Ceramics Inc.
4511 Hyde Park Blvd.
Niagara Falls
NY14305-0067, USA
Phone 716 278 9400
Fax 706 285 3026
[http:// tamceramics.com](http://tamceramics.com)
e-mail Arac@tamceramics.com

Abstract

The MLCC industry is changing dramatically, driven by the electronics creed that the next generation of products must be better-smaller-faster-cheaper. Because of constraints on the extraction of basic raw materials such as Ba, Nd, Nb, Pd, Ag, or Ti, the response to demands for reduced cost, reduced size and improved performance must be from a total technology package that delivers high reliability, thin layers, high dielectric constant, reduced metal cost and all the other physical, chemical and electrical attributes in a form MLCC makers can use.

This paper reviews the alternative technologies including precious metal high fire, low fire, ultra low fire and base metal in relation to the materials systems used. It also tackles the issue of fitness for use in combination of ceramic, metal, binder, dispersant, termination and processing equipment and attempts to draw conclusions on the applicability of these technologies for particular types of MLCC manufacture for different markets.

Electrode Metal Constraints

In order to be compatible with traditional barium titanate based systems with acceptable electrical and physical properties, co-fired electrodes in the 1300°C range were developed. Typically in Japan these were 100% Pd, elsewhere in the world they were 70%Pd-30%Ag. Because of the concern in Japan about premature failure due to Ag, precious metal inks have stayed predominantly 100% Pd there. In the rest of the world, however most "high-fire" (1300°C) capacitors have used 70% Pd. Another class, "low-fire" dielectrics are similar to high fire dielectrics but have frits and fluxes added to make a compromise between the 1100°C firing

temperature and dielectric properties. Lead relaxor dielectrics fire at around 1000°C but typically also use 30% Pd.

The real problem with Pd is that it is a commodity metal with only two sources of supply, South Africa and Russia. There are competing applications such as auto catalysis and even dentistry and as a result the price can fluctuate. Although it has hovered in the mid \$100s per Troy Ounce for the past couple of years, recent supply issues in Russia have pushed spot prices over \$240. Even in the mid \$100s the value of precious metals in capacitor electrodes was 150% of the cost of the functional ceramic in a MLCC. As of the time of writing the price had dropped to the \$180 range on the news that Russian shipments would restart in August. The minerals press cautioned at the same time that no spot material would be available for some time and that any industrial dispute in South Africa could have a dramatic effect.

While this price fluctuation has gone on, the price of a given MLCC has been dropping at between 15% and 30% per annum. This means that MLC makers find themselves in a rather unpleasant squeeze. The only way out is to either reduce the cost of existing parts by reducing the cost or number of electrode layers or to develop new higher-margin products with either smaller case sizes or larger capacitance values to allow competition with Aluminum or Tantalum capacitors

Ni electrode systems have a particular edge in that. Base metal parts made with this technology have lower impedance and higher reliability than traditional Tantalum capacitors.

Traditional Dielectric Powder Constraints

Conventional wisdom says that COG dielectrics are produced by solid state routes from materials such as neodymium titanate and that X7R and Z5U dielectrics are based on high-purity precipitated or solid state barium titanates. The powders are partially reacted and react further during MLC sintering. Reaction is normally not fully complete, either to restrict grain size or deliberately develop an inhomogeneous structure such as the X7R core-shell.

Powders are typically 1 to 1.5 microns in size, with fired grain sizes ranging from less than a micron in COG to more than 3 microns in Y5V.

New Approaches

Many MLCC manufacturers use a combination of the tactics listed below to achieve their goals:

Using less Pd

Thinner electrode layers

Especially in the case of 100% Pd, ink laydowns have been reduced dramatically. This is limited in the extreme by the surface tension effects of the metal during sintering, the fineness of grind of the ink, the ink application method and the surface roughness of the green ceramic substrate. "Lacy" electrodes have an advantage in that they allow ceramic layer to ceramic layer contact to optimize physical properties but unfortunately the more holes in the lace, the less efficient is the electrode coverage and the lower is the measured capacitance

More dilute Pd alloys

Outside Japan, the approach has been to reduce the Pd cost by dilution with Ag and very sophisticated metal alloys have been developed in order to do this. Initially the major compositions were almost exclusively 70% Pd or 30% Pd but a new development has been to stretch the performance of ceramics to sinter at slightly lower temperatures allowing 70% Pd to relax to 60% and 30% Pd to relax to 25%. A major reduction in firing temperature to allow the use of 10% Pd is only possible with the latest generation lead relaxors which fire well below 1000C.

In COG systems the 70% Pd 30% Ag alloy has a particular conductance advantage.

Much of MLCC technology is a balance of compromises however. The above schematic shows how cost rises with increasing capacitance (read – increasing number of layers).

Although the variable electrode cost of Ni base metal systems (Ni paste cost) is lower than that of high Pd systems, the fixed cost of operating a base metal system is much higher due to the need for reducing atmosphere furnaces. As a result it is more expensive in layer counts less than about 100 or for small volumes of MLCCs.

Cutting the Pd has other effects: virtually all other electrode metals have a higher reactivity than Pd and can dissolve in the ceramic or form an interface layer which can be beneficial by improving conduction or detrimental by cloaking the electrode in a low-dielectric constant layer.

Ceramic additives to the ink have both chemical and physical effects but if used in excess can contribute to excess "laciness" as described above.

Using no Pd

Pb alloy injection

Lead alloy injection has been successfully used for many years to produce high reliability parts. The technology, originally patented by TAM in the 1970's, involves making MLCCs with a fugitive ink which is burned out during the firing cycle. The ceramic firing is thus independent of the electrode formation, which occurs after sintering when parts cool and low-melting alloy is injected in such a way as to fill the electrode patterns by capillary action.

Ni base metal

Ni systems have been used in the USA and Japan for many years. The real breakthroughs however have occurred in the last 5 years when new high quality Ni powders became available, the powder technology developed to form extremely thin layers and X7R formulations were developed and reliability was dramatically increased. Coupled with the new ability to make very high layer count parts, the Ni base metal parts have taken significant market share from precious metal electrode parts.

The barriers to entry for a new base metal MLCC manufacturer have been dramatic. Until recently all the formulation technology has been

proprietary to a very few in-house makers, the technology has been heavily patented worldwide, and processing equipment was unavailable. Furthermore, high quality Ni powder was very scarce. Now however, formulations and processing technology, materials and equipment are all becoming available but it still will require a major monetary and technical effort for any MLCC maker to begin to compete in this field.

A variant of the Ni base metal system is the NiO system developed at TAM. Although Ni powders are less expensive than Pd they are by no means cheap. With the right formulations and processing, NiO pre-electrodes can be co-fired with the ceramic in the MLCC and then subsequently reduced. Although originally proposed as a low-cost start-up route (existing sintering furnaces can be used) the technology was too novel to be applied as a first step. Instead the technology is showing real promise as a way for customers already in the base metal business to make a dramatic reduction in their electrode costs and an increase in their throughput.

Cu base metal

The real benefit of Cu is in its electrical properties, especially for high frequencies. Although Cu end terminations are applicable to Ni base metal parts, Cu electrodes now seem to have a market niche developing for high frequency COG parts.

Thinner layer opportunities

Market extension

It used to be so simple! If you looked at capacitance, the pecking order was quite simple.

Ceramic <Tantalum <Aluminum.

Because of the dramatic increase in ceramic volumetric efficiency and the constant electronics pressure for better-smaller-faster-cheaper parts, the market dynamics are changing. First of all, Aluminum capacitors are not well suited to high frequencies and Tantalums and lead relaxor MLCCs are taking share from them. In turn, base metal MLCCs are nibbling at the lower end of the Tantalum market and in response Tantalums are being downsized and made more surface mount friendly as their volumetric efficiency increases!

Metal implications

The fastest growing area is Ni base metal. Other technologies such as lead relaxors, composites and regular low fires are not standing still though; a year ago the magic layer count was 100 with base metal owning the territory above 100 layers. Now processing details have been worked out, advanced low fire parts with up to 500 layers have been produced.

Powder implications

Thin layers, different metal systems, different processing conditions. Particle size control, surface condition and interactions with additives need to be tightly controlled. And that is before we consider compatibility with inks, binders, terminations, plating systems or build design!

Powder formulation

The right distribution of additives is critical. This can be achieved by co-precipitation, super-precipitation, pre-calcination as well as more traditional co-milling and mixing.

The choice of raw material now runs much more to finer particle sizes much less than 1 micron, finer additive systems and an overall package which is resistant to dissolution, unmixing or undesirable mixing in the next step, slip preparation.

Base metal system formulation is highly complex and involves a careful preparation of reduction-resistant phases.

Slip processing

Slips for ultra thin layers must be uniformly dispersed, stable and appropriate for the casting technology chosen. Cooperation between the slip technologist and the ceramist is vital here to ensure that additives do not selectively settle or become chemically changed to the extent that either the slip or ceramic properties are affected.

The jury at this stage is evenly divided on water-based or solvent-based systems, and tape or wet lay-up systems. Each permutation has its champions. Each process has its unique challenges as MLCC makers "push the envelope".

Firing

This is key to base metal production success. Carefully controlled burn-out, firing and annealing brings a large capital cost penalty.

Termination

Termination is also a critical issue especially with base metal systems. Interactions with electrodes and ceramic that never used to be a problem with simpler parts has become more complex.

Although Ag terminations suitably plated are the most common types, Cu and/ or Ni for base metal and in some cases Ag-Pd terminations are used.

The aggressiveness of plating solutions can cause problems with low fire materials if porosity is present or grain boundary etching takes place.

Electrical properties

The game is changing here all the time. The EIA is changing DF and other specifications to allow thinner lower-voltage parts. One of the key issues is the standardization of HALT (Highly Accelerated Life Testing). There isn't any standardization and each MLCC maker seems to have their own set of conditions, sometimes to score a competitive point.

Composite dielectrics

The composite approach involves tuning the electrical properties by superposing layers of different electrical properties but similar processing characteristics. This allows a very high apparent dielectric constant (over 8000 for X7R composites) and allows manufacturers the opportunity to

- A) fine tune electrical properties to a customer's needs e.g. X8R
- B) Reduce the number of electrode layers needed by half in a given part to give thicker layers and a higher voltage rating; or
- C) Reduce the part size dramatically.

This new technology is just starting to become commercialized and shows great promise especially for difficult-to-build parts.

Powder responses

Overall requirements

As discussed above, small but processable powders with the correct level of homogeneity. These are based on high-purity rather than solid state systems although it is surprising and gratifying to the author just how far "conventional" powders can be pushed in performance.

System interactions

"Fitness for use" is the term used to describe the interaction between materials and processes. It becomes much more sensitive to change as performance demands on MLCCs become greater. Differences in part build or caster mean that formulation changes may be necessary to optimize performance.

Binder system

Generally, powers with low surface energy and with components that are insoluble do well. Traditional high-fire ceramics are the easiest, low-fire ceramics the toughest.

Electrode ink

Interactions are critical with all systems. Ink dissolution into the bulk or the formation of diffusion layers can dramatically degrade or improve performance.

Termination

Glass diffusion from termination systems is an issue more usually found with low fire systems.

Plating

Low fire systems generally are more prone to plating attack

Choosing the most appropriate system

This really depends on the MLCC house and their customers' preferences.

Performance

High volumetric efficiency – relaxor, base metal, composite.

High strength, toughness and thermal shock – any BaTiO₃ based system.

Cost and Flexibility

In high volumes – base metal

In moderate volumes – low fire, relaxor, composite.

Overall Conclusion

The attached table tries to summarize the strengths and weaknesses of the different systems. Is there one clear winner? We think not. It depends on the properties desired and also the number of parts desired. For example, to get lowest cost in very high volumes base metal looks obvious – but only if the layer count is high, the voltage is low and the parts volume is high. For extremely high capacitance, relaxors are the clear choice if MLCC makers are comfortable handling lead. To get maximum flexibility most mid size and large companies embrace several technologies. For a smaller and more specialized company a combination of low-fire, relaxor and composite systems covers the entire range.

Will any one technology dominate in the future – no, we don't think so. Some may be curtailed by outside circumstances – high fire manufacturers are severely stretched by the Pd price, relaxor manufacturers may face environmental challenges in the future. But we think that in ten years' time we'll still be using a mix of the above technologies to fight our new competitors, on-chip integration and embedded capacitors.

Acknowledgements

The authors thank their colleagues for support and encouragement and TAM Ceramics Inc. for permission to publish this paper.

Dielectric Technology Spreadsheet

| Technology | Strength | Capacitor Type | Electrode Cost | S=Strength | | | W=Weakness | | | Thin Layer Capable | Volumetric Efficiency | Cost/Performance |
|--------------------------|--------------------------------|--------------------|----------------|--------------|--------------|--------------|-------------|------------|----------|--------------------|-----------------------|------------------|
| | | | | Ceramic Cost | Capital Cost | Process Cost | Flexibility | Electrical | Physical | Chemical | Reliability | |
| BaTiO3/100% Pd | Electricals, physical strength | COG, X7R, Y5V, Z5U | W | | | | S | S | | S | S | SS |
| BaTiO3/70% Pd | Electricals, physical strength | COG, X7R, Y5V, Z5U | W | S | | | S | S | | S | S | SS |
| BaTiO3/30% Pd | Toughness | COG, X7R, Y5V, Z5U | S | S | | | S | S | | S | S | S |
| Relaxor/30% Pd | Electricals | Y5V,Z5U | S | | | | | S | | | S | S |
| Relaxor/10% Pd | Electricals, cost | Y5V,Z5U | SS | | | | | S | | | S | SS |
| BaTiO3 / Ni | Thin layers | X7R, Y5V, Z5U | SS | W | W | W | | S | | S | SS | SS |
| BaTiO3 / Pb | Reliability | X7R, Y5V, Z5U | SS | W | W | W | | S | | S | S | S |
| Nd-TiO3 / Cu | High frequencies | COG | SS | W | W | W | SS | S | W | | S | SS |
| Relaxor Composite/30% Pd | High temp, custom TC, cost | Custom | SS | | | | | | | | | |

Mechanism of Improvement in Resistance Degradation in Y-doped BaTiO₃ Based Multilayer Ceramic Capacitors with Ni Electrodes under Highly Accelerated Life Testing

Shigeki Sato, Yukie Nakano, Akira Sato, and Takeshi Nomura

Materials Research Center, TDK Corporation, 570-2 Aza-Matsugashita, Minamihatori, Narita-shi, Chiba-ken, 286 Japan.

Abstract The mechanism of improvement of resistance degradation in Y³⁺-doped BaTiO₃-based materials has been studied using electrical measurement techniques such as admittance spectroscopy, thermally stimulated current (TSC). TSC measurements show three relaxations which have long relaxation times and are considered to be due to Mn²⁺, V_{Ba}²⁺, and V_O defects. Admittance spectroscopy also indicated three types of relaxation, with activation energies of 0.4, 0.8, and 0.8-1.0eV. The intensity of the 0.4 eV relaxation peak increased with Y³⁺ doping and disappeared at low P_{O2} annealing. The 0.4 eV relaxation is considered to be due to the transition of electrons from the valence band to barium vacancy states. These results suggest that Y³⁺ acts a donor and creates barium vacancies, which compensate for the oxygen vacancies and thereby improve the resistance to degradation.

1. Introduction

The requirement for higher capacitance and further miniaturization in multilayer ceramic capacitors (MLCCs) is driven by the down-sizing trend in electronics. Structurally this has meant reduced layer thickness and an increase in the number of layers. The internal electrode of choice has shifted from Pd to Ni in order to realize low cost production. We previously reported that the degradation of insulation resistance observed during highly accelerated life testing (HALT) is due to the migration of oxygen vacancies⁽¹⁾⁻⁽⁸⁾. Y³⁺ doping in BaTiO₃-based ceramics is an excellent method for improving resistance degradation under HALT for Ni electrode MLCCs.

In this paper we investigate the effect of Y³⁺ doping on resistance degradation for BaTiO₃-based materials using admittance spectroscopy⁽⁹⁾ and thermally stimulated current (TSC)⁽¹⁰⁾⁽¹¹⁾.

2 Specimen preparation and evaluation of electrical properties.

The dielectric compositions employed here were (Ba_{1-x}Ca_xO)_m(Ti_{1-y}Zr_yO₂)₂+aMnO+bSiO₂+cY₂O₃ (BCTZ system) with x=0-0.07, y=0.18, m=1.004, a=0.2 wt%, b=0.2 wt%, c=0.32wt%. These compositions show the Y5V characteristics for temperature dependence of capacitance.

MLCCs were prepared by the so-called sheet method. Green sheets were formed by doctor blade casting, and thickness was controlled between 15 and 30 microns. After casting the sheet was dried and the Ni electrode printed using a screen printing system. Next, 4 to 280 layers of the sheets were stacked, laminated, and cut into green chips. Binder burn-out was followed by sintering between 1300 and 1340°C. During sintering, the oxygen partial pressure was controlled to between 10⁻⁸ and 10⁻¹³ MPa by adjusting the amounts of H₂ and H₂O in the N₂-H₂-H₂O gas mixture. The chips were then annealed between 700 and 1100°C in a N₂-H₂O gas mixture in order to reoxidize the dielectrics. After sintering, samples were painted with In-Ga electrodes to evaluate their electrical properties.

The TSC measurement system is shown in Fig.1. The specimen was first poled at temperature *T_b* by applying dc voltage *V_b* for a period *t_b*. In this procedure, the MLCCs insulation resistance degraded, as typically occurs during HALT. After poling, the specimen was cooled down to 77K while keeping the applied voltage constant. Then the electrodes were short-circuited and the MLCCs were heated at a fixed rate. The TSC spectra from the MLCCs were measured and recorded using a computer.

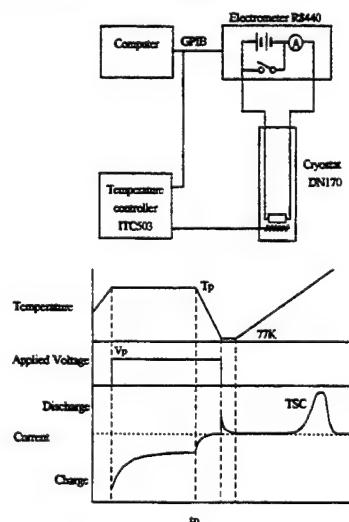


Fig.1 Thermally stimulated current measurement system.

3 Results and Discussion

3.1 Previous work.

The effect of double addition of MnO and $1/2\text{Y}_2\text{O}_3$ on the mean time to failure (MTTF) is shown in Fig.2. This suggests that the oxygen vacancies formed by acceptor doping are compensated for by donor doping. The MTTF obtained here is more than 10^3 times that for a conventional composition.

The microstructure of the dielectrics was then investigated using TEM, as shown in Fig.3. A lot of dislocation loops can be observed in the non- Y^{3+} doped material. On the other hand, in the Y^{3+} doped material, dislocation loops could not be found. These dislocation loops are aggregates of oxygen vacancies, as reported by Shiojiri, et.al.⁽¹²⁾ These results support the concept that the degradation of IR is caused by electrolytic migration of oxygen vacancies, and that Y_2O_3 compensates for the oxygen vacancies.

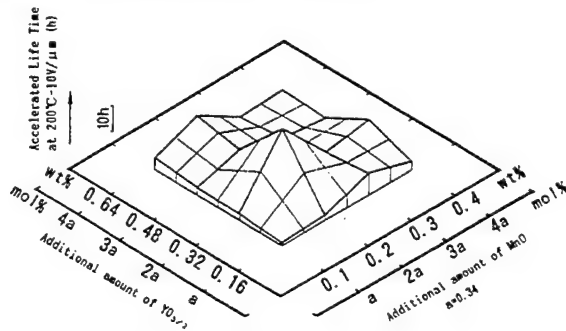


Fig.2 Effect of addition of MnO and $1/2\text{Y}_2\text{O}_3$ on the MTTF under HALT.

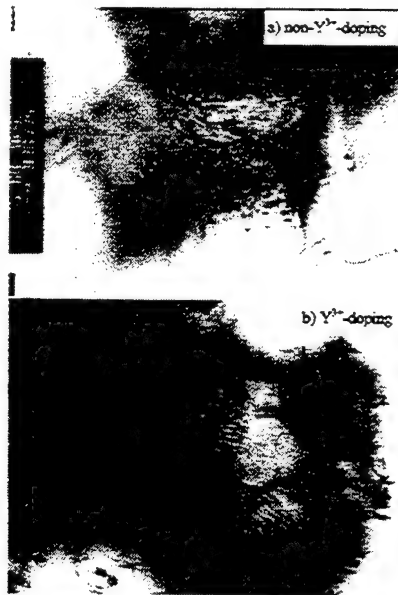


Fig.3 Effect of Y^{3+} doping on the microstructure using TEM : (a) non- Y^{3+} -doped and (b) Y^{3+} -doped.

3.2 Thermally Stimulated Current Analysis

Figure 4 shows the TSC in the Y^{3+} -doped and non- Y^{3+} -doped BCTZ systems. Six peaks were observed in the TSC measurement for both compositions. The peaks at 170 and 270 K are due to the crystalline phase transitions, and the peaks at 345, 415, and 490 K labelled α , β and γ , respectively, originate from poling. The relaxation at peak β was not found in the non- Y^{3+} -doped BCTZ system and was therefore considered to originate from Y^{3+} doping. Table I indicates the results of relaxation analysis of the TSC data for the BCTZ system with and without Y^{3+} -doping. The relaxation parameters for the peak β could not be calculated because it could not be separated from peaks α and γ . The activation energy observed were about 0.6 eV at peak α and 0.7 eV at peak γ for both compositions. The relaxation time at 25°C (τ_{25}) in the Y^{3+} -doped BCTZ system was 5×10^3 seconds at peak α and 4×10^7 seconds at peak γ . τ_{25} for Y^{3+} -doped BCTZ system was longer than that of the non- Y^{3+} -doped system. These values of activation energies in TSC are in disagreement with those from HALT ($E_s = 1.4\text{eV}$) because the activation energy in the latter was the sum of V_O creation and migration energies, whereas possibly only the migration energies are measured by the former technique. However, these results suggest that these long relaxation time are due to deep trap levels or low mobility carriers.

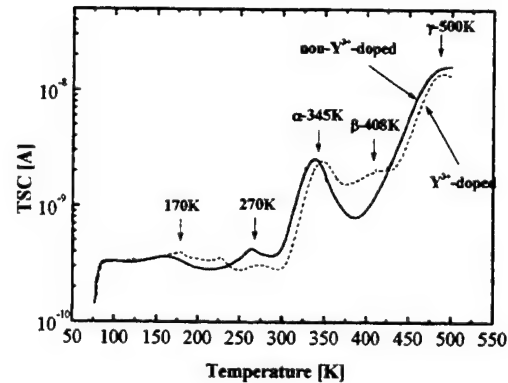


Fig.4

TSC in Y^{3+} -doped and non- Y^{3+} -doped BCTZ system.

Table I Results of relaxation analysis of TSC data.

| | Non- Y^{3+} -doping | | Y^{3+} -doping | |
|-------------------|------------------------------|---------------------|-------------------------|---------------------|
| Peak | α | γ | α | γ |
| E_s (eV) | 0.713 | 0.524 | 0.775 | 0.567 |
| τ_{25} (sec) | 2.719×10^7 | 4.488×10^3 | 4.395×10^7 | 5.277×10^3 |

3.3 Admittance spectroscopy

Figure 5 shows the admittance spectroscopy for the Y^{3+} -doped and non- Y^{3+} -doped BCTZ systems. Three relaxations were observed in the low frequency range, with activation energies of 0.4, 0.8, and 0.8-0.9 eV labelled δ , ζ and η , respectively. The values of activation energy at δ and ζ are close to those measured at α and γ in the TSC data. It may therefore be assumed that these relaxations are caused by the same mechanism. These relaxations were not influenced by Y^{3+} -doping, and rather may be related to the Mn_{Ti}'' and V_o states. On the other hand, the intensity at the peak δ increased with Y^{3+} -doping which indicated that the latter increased defect density, because the peak intensity relates to the density of states in admittance spectroscopy. Furthermore, the peak δ disappeared under low P_{O_2} annealing. Thus the reason for the relaxation at δ is assumed to be either the defects in BCTZ, which originated from Y^{3+} doping or high P_{O_2} annealing.

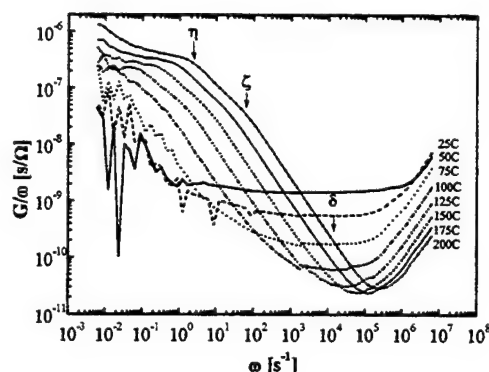


Fig.5(a) Admittance spectroscopy in non- Y^{3+} -doped BCTZ system annealed under 4×10^{-7} MPa partial pressure of oxygen.

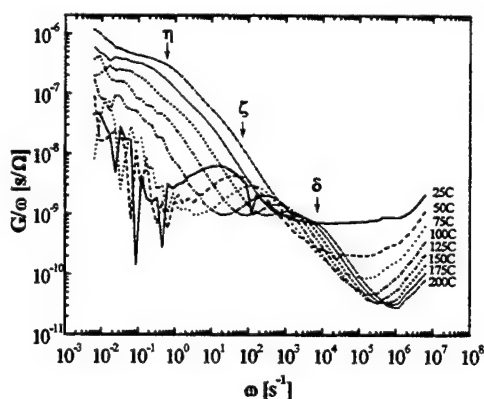
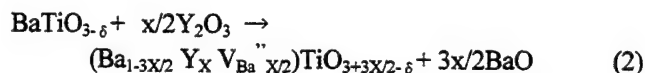


Fig.5(b) Admittance spectroscopy in Y^{3+} -doped BCTZ system annealed under 4×10^{-7} MPa partial pressure of oxygen.

3.4 Effect of donor doping

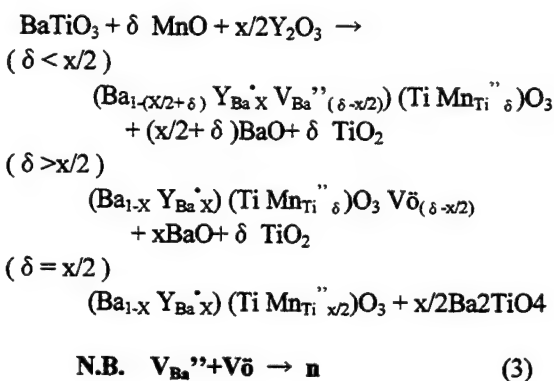
When Y^{3+} substitutes at the perovskite A-sites, Ba^{2+} vacancies (V_{Ba}'') are created. Therefore, V_{Ba}'' should increase with Y^{3+} doping as shown in equation(2)



This equation is in agreement with the relaxation at peak δ in the admittance spectroscopy. The peak δ was influenced strongly by Y^{3+} -doping and the annealing atmosphere, according to the TSC analysis and admittance spectroscopy.

An activation energy of 0.4 eV is assumed for the transition of an electron from the valence band to a V_{Ba}'' site. Thus, holes should also be formed with V_{Ba}'' creation. The temperature dependence of insulation resistance for the BCTZ system, shown in Fig.7, indicated that resistance increased again between 70 and 120°C. The magnitude of this increase for Y^{3+} -doping was larger than for non- Y^{3+} -doping. This increase of resistance is believed to originate from the hole creation. Therefore, these results support the proposition that Y^{3+} acts as a donor in $BaTiO_3$.

The effects of Y_2O_3 and MnO addition in the $BaTiO_3$ system support our previous hypothesis shown in the following equations.



The insulation resistance was degraded by migration of oxygen vacancies from anode to cathode. $BaTiO_3$ -based dielectrics for MLCCs often contains MnO in order to prevent reduction during low P_{O_2} sintering. The Mn^{2+} ion is considered to act as an acceptor which induces oxygen vacancies during sintering. On the other hand, the addition of a donor such as Y^{3+} to $BaTiO_3$ based materials is thought to create Ba vacancies which compensate for the oxygen vacancies generated by acceptor doping, and are considered to create holes in the valence band. Thus the decrease in oxygen vacancy concentration resulting from the donor doping is

believed to be the reason for the improved life time in HALT.

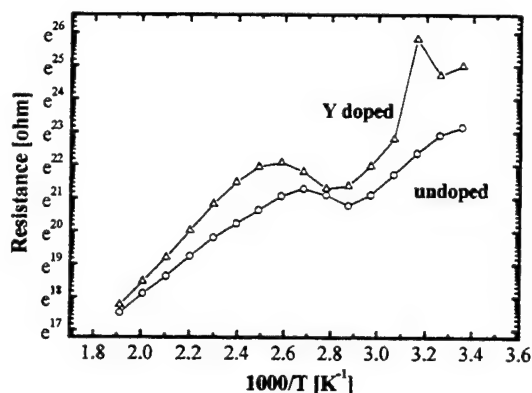


Fig.7 Arrhenius plots of insulation resistance of MLCCs for Y^{3+} -doped and non- Y^{3+} -doped BCTZ system.

4. Conclusions

The effect of Y-doping on resistance degradation of MLCCs with Ni electrodes under a Highly Accelerated Life Test was studied and the following conclusions were obtained.

- (1) Three types of relaxation in BCTZ system were observed from TSC and admittance spectroscopy. The relaxation at 0.4 eV is expected from the transition of an electron from the valance band to the V_{Ba} site due to the Y^{3+} doping. The relaxations at 0.8 and at 0.8-0.9 eV are considered to originate from the transition between the Mn_{Ti} site and the V_O site or between Mn_{Ti} site and conduction band.
- (2) The results mentioned that Y^{3+} doped into $BaTiO_3$ -based materials acts as a donor and creates the V_{Ba}'' , and then compensates for the oxygen vacancies generated by acceptor doping, such as MnO. Y^{3+} doping and the creation of V_{Ba} is considered to improve the life time in HALT.

References

- 1) T. Nomura, A. Sato, and Y. Nakano: J. Soc. Mater. Eng. Resour. Jpn. **5** (1992) 44 [Japanese].
- 2) T. Nomura, S. Sumita, Y. Nakano, and K. Nishiyama: Proc. 5th US-Jpn. Seminar Dielectric Piezoelectric Ceramiss, 1990 (Kyoto, 1990) p.20.
- 3) S. Sumita, M. Ikeda, Y. Nakano, K. Nishiyama and T. Nomura: J. Am. Ceram. Soc. **74** (1991) 2739.
- 4) T. Nomura, A. Sato, A. Hitomi and Y. Nakano: J. Jpn. Soc. Powder & Powder Metall. **39** (1992) 590 [in Japanese].

- 5) T. Nomura and Y. Nakano: Denshi Tokyo **31** (1993) 168.
- 6) Y. Nakano, A. Sato, A. Hitomi and T. Nomura: Ceram. Trans. **32** (1993) 119.
- 7) Private Communications.
- 8) T. Nomura, A. Hitomi, A. Sato and Y. Nakano: J. Jpn. Soc. Powder & Powder Metall. **40** (1993) 677 [in Japanese].
- 9) D.L. Losee: J. Appl. Phys., **21** (1972) 54.
- 10) H. Shimizu: Rigaku Denki Journal **24** (1993) 2.
- 11) T. Fukami and J. Karasawa: J. Ceram. Soc. Jpn. **101** (1993) 4.
- 12) M. Shiojiri, T. Isshiki, H. Saijo, M. Tsujikura, A. Nakada, Y. Nakano, M. Ikeda, T. Nomura: Phys. Stat. Sol. (a) **129** (1992) 353.

Microstructure and Reliability Study of MLCs with Ni Electrodes

M. Chu, J. Bultitude, V. Ganine, and A. Rae

TAM Ceramics, Inc.
Niagara Falls, NY 14305, USA

Abstract — The production volume of ceramic multilayer capacitors (MLCs) using Ni as internal electrode has increased rapidly over the last several years due to the technical and economical advantages. In this paper, microstructure development and reliability behavior of MLCs made with Ni electrodes is investigated and reported. The investigation has been focused particularly on (1) the degradation of insulation resistance (IR) as a function of time, (2) the ceramic/electrode interface, (3) the BaTiO₃ and additive solid state reaction, and (4) the grain growth mechanism.

I. Introduction

The ceramic multilayer capacitors (MLCs) have become a dominant passive capacitor component in electronic circuitry for the past 20 years. Typical MLCs are composed of a ceramic dielectric, inner electrodes and terminations. MLCs are used in circuits for decoupling, bypassing, filtering, resonating and timing.

The typical manufacturing processes require the co-sintering of ceramic dielectric powder and the metal to consolidate these materials into a working device. The co-sintering process is generally carried out in an air atmosphere and thus the inner electrodes of the devices generally comprise a precious metal such as platinum, silver, gold, palladium, or alloys thereof, to avoid oxidation during the sintering process. In most of the commercial MLCs, especially for those high capacitance components that require a large number of dielectric layers, precious metals (Pd, Ag) account for a large proportion of material costs.

However, there has recently been a constant increase of palladium price due to several factors such as new applications in auto catalyst to replace platinum, limited supply, and strong electronic component demand.

To reduce the metal cost, MLCs made with Ni as inner electrode have been around for some time for Y5V/Z5U category. But only recently units in X7R category becomes commercially available. However, there has been concerns about the reliability level of MLCs made with Ni as inner electrodes. Reasons of these concerns mainly come from the fact that MLCs made with Ni electrodes have to be sintered in a reducing atmosphere at low oxygen partial pressure, PO₂, of less than 10⁻⁷ to prevent Ni from oxidizing to NiO. At such a low PO₂, oxygen vacancies are usually generated. They are mobile at high temperatures under an applied electric field. The accumulation of these vacancies near the electrode regions causes even higher local voltage stress and therefore insulation resistance (IR) failures.

In the case of high K, Z5U/Y5V type capacitors, it is also critical to control solid state reaction and grain growth mechanism when ceramics are sintered in reduced atmosphere. This area, however, had not been studied extensively.

In the present work, microstructure development and reliability behavior of MLCs made with Ni electrodes is investigated and reported. The investigation has been focused particularly on (1) the degradation of insulation resistance (IR) as a function of time, (2) the ceramic/electrode interface, (3) the BaTiO₃ and additive solid state reaction, and (4) the grain growth mechanism.

II. Experimental

1) Ceramic powders — X7R and Y5V powders were made by blending TAM high purity BaTiO₃ (HPB), together with small amounts of additives such as BaZrO₃, CaZrO₃, BaCO₃, MgCO₃, CaCO₃, CoO, MnO₂ to adjust the Curie temperature and total A/B ratio, and a silica based glass composition to enhance its sintering.

2) Disc capacitors – green disc capacitors were prepared via. procedure well known in the industry. Powders were mixed with corn syrup binder, sieved, and pressed into discs. They were then sintered at 1250-1360°C for 2 hours at PO_2 of 10^{-8} to 10^{-12} . $N_2/CO/CO_2$ gas mixture was used to achieve low partial oxygen pressure. In some cases, discs were sintered in air at 1250-1360°C for 2 hours. Sintered discs were then painted with glass containing silver electrode paste and fired in air at about 815°C for 15 minutes to form a capacitor.

3) MLCs – green MLCs with Ni electrodes were prepared via. procedure well known in the industry. Powder was milled together with PVB binder to form a uniformly mixed slurry. It was then followed by casting tape, printing Ni electrodes, stacking, laminating, and cutting into green chips. They were then debindered at about 260°C in air and sintered at 1250-1360°C for 2 hours at PO_2 of 10^{-8} to 10^{-12} . $N_2/CO/CO_2$ or $N_2/H_2/H_2O$ gas mixtures were used to achieve low oxygen partial pressure. Sintered MLC blocks were then annealed in air at 200-900°C for 4 hours, terminated at the ends with Cu paste, and then fired at 900°C for 15 minutes at PO_2 of 10^{-8} . $N_2/CO_2/H_2$ gas mixture was used to achieve the desired PO_2 .

5) Measurement – capacitance, DF, IR at 25°C, IR at 125°C (or 85°C), and TC, of the chips were then measured to evaluate basic properties of the BME chips. IR vs. time of the chips at 150°C and at 100-300 V/mil DC applied voltage were measured to evaluate their reliability level. Grain size, porosity, and composition were analyzed by SEM or TEM.

III. Results and Discussion

1) Insulation Resistance (IR) as a function of time – It was observed that for most of the MLCs tested, $\log(IR)$ vs. $\log(\text{time})$ curve can be divided into three regions. It starts out as a region I, where IR remains quite constant followed by a region II where IR has a slow and steady decay, and then followed by a region III where IR decays at a very fast rate until failure. The duration of region I and region II become shortened rapidly when test voltage is increased. It was also observed that MLCs would not have any significant life time unless samples are annealed in air at 500°C or above. MLCs

sintered at lower PO_2 have shorter life time even if they are annealed.

The IR decay is believed to be caused by oxygen vacancy migration. Oxygen vacancy could be generated when ceramic is fired under low oxygen partial pressure. Or, it could be generated when Ni electrode removes oxygen from the ceramic to form a NiO film during the process of annealing or during the accelerated test conditions. Current work did not generate enough evidence to distinguish one over the other. It must await further study.

2) The ceramic/electrode interface – The ceramic/electrode interface were analyzed by SEM backscattered images, X-ray microprobes, and TEM. After sintering in low PO_2 and before annealing, several samples showed a thin reaction layer but several samples showed only a gap where the ceramic and electrode are separated. However, after annealing, samples always showed such ceramic/electrode reaction layer. The thickness of the this reaction layer is estimated to be less than 0.1 micron. It was not possible to determine exact composition of the interface layer due to resolution limit of the X-ray microprobe. TEM analysis indicates, however, that the oxygen to barium ratio is 2 to 5 times higher than that in the bulk. Segregation of several additives into the reaction layer was also found.

One possible model to explain the above observation is that the gap is resulted from shrinkage mismatch between nickel electrode and ceramic during the sintering. During annealing, nickel partially oxidizes to nickel oxide and fills the gap. It is not clear at this time if the oxygen rich interface layer has positive or negative impact on reliability.

3) $BaTiO_3$ and additive solid state reaction – It was observed that, when sintered in air, addition of $BaZrO_3$, $CaZrO_3$, MgO downshifts Curie temperature of the $BaTiO_3$ and addition of MnO_2 (or $MnCO_3$) has no effect. However, when sintered in low PO_2 , all the above additives downshift Curie temperature of the $BaTiO_3$.

4) Grain growth – It was observed that ceramic sintered in lower PO_2 have overall smaller grain size than those sintered in air. The phenomena

holds true for both BaTiO_3 - BaZrO_3 - CaZrO_3 (BT-BZ-CZ) precursors or BT-BZ-CZ-Additive compositions.

IV. Conclusions

When BME chips were tested under highly accelerated condition, such as 150°C and 100 V/mil or higher applied DC voltage, the IR vs. time shows the following three regions of decay.

Region I : Fast decay,

Region II : Steady and slow decay, and

Region III : Very rapid decay.

Annealing conditions is critical to life time.

There is a reaction layer between ceramic and Ni electrode. Such reaction layer is high in oxygen content. Its impact to reliability is not clear

Addition of BaZrO_3 , CaZrO_3 , MgO (MgCO_3) downshifts BaTiO_3 Curie temperature regardless of firing PO_2 . Addition of MnO_2 (MnCO_3) downshifts BaTiO_3 Curie temperature only when sintered in low PO_2 .

Grain size is smaller when BT-BZ-CZ precursor and BT-BZ-CZ-Additive compositions are sintered in low PO_2 .

Reference

- (1) "Materials and processes for MLCs with base metal electrode", A. Rae, M. Chu, and J. Bultitude, CARTS-EUROPE, Amsterdam, October 1995
- (2) "Reliability study of MLCs made with Ni electrode", M. Chu, J. Bultitude, J. Carminati, I. Thompson, M. Rand, and C. Hood, ACS-96, Indianapolis, May 1996
- (3) "Microstructure analysis of MLCs with Ni electrode", M. Chu, J. Bultitude, V. Ganine, A. Rae, J. Dougherty, M. Angelone, and S.C. Cheng, ACS-97, Cincinnati, May 1997

Acknowledgments

The authors would like to acknowledge the efforts of many colleagues at TAM towards developing base metal dielectrics.

The authors would also like to acknowledge the permission granted by TAM Ceramics, Inc. for publishing this work.

The authors would also like to acknowledge Dr. J. Dougherty, Mr. M. Angelone, and Dr. S. C. Cheng of Penn. State University in performing SEM and TEM analysis.

Electron Microscopy Study of Dislocation Loops in Stoichiometric BaTiO₃ and Nonstoichiometric (Ba,Ca)TiO₃

Toshimasa Suzuki, Mituo Ueno, Yuuji Nishi, Katsuhiko Arai, and Masayuki Fujimoto
Taiyo Yuden Co., Ltd.

562 Hongo-Tsukanaka, Haruna-machi, Gunma 370-33, Japan

Abstract - Dislocation loops observed in stoichiometric BaTiO₃ and nonstoichiometric (Ba,Ca)TiO₃ were characterized using transmission electron microscopy (TEM) contrast analysis under two beam conditions and stereomicroscopy. Almost all dislocation loops had the same crystallographic nature, lying on {100} planes with Burgers vector $\langle 100 \rangle$, irrespective of nonstoichiometry and Ca substitution. Dynamic behavior of dislocation loops during the electron-beam-irradiation, however, was considerably different between the two. That is, in (Ba,Ca)TiO₃, the contrasts of dislocation loops faded completely away but, in BaTiO₃, fine line-contrasts remained. Crystallographic structure models of dislocation loops were determined using TEM with obtained images indicating these dislocation loops were unstable and consisted of double-layers TiO₂ or BaO.

I. INTRODUCTION

Multilayer ceramic capacitors (MLCs) are viewed as vital to the circuitry of consumer-electronic goods, such as notebook computers, video cameras, and cellular phones. The high volumetric capacitance and strong heat cycle shock of MLCs outperform those of electrolytic capacitors. Much research is being done to determine how to manufacture MLCs with higher volumetric capacitance to replace electrolytic capacitors. Large-capacitance MLCs with Ni internal electrodes have the advantage of lower manufacturing cost despite technological difficulties such as firing in a low-oxygen atmosphere to prevent oxidation of the Ni internal electrode, whose low-cost Ni replaces the noble metal Pd. Starting powders for MLCs with Ni inner electrodes usually have an A-site excess nonstoichiometric chemical composition, such as $(\text{Ba}_{1-x}\text{Ca}_x)_m(\text{Ti}_{1-y}\text{Zr}_y)\text{O}_3$ ($1.000 < m < 1.005$) [1]. The nonstoichiometric chemical composition is the key to preventing produce oxygen vacancies during reducing-atmosphere sintering, which should increase MLCs electron conductivity.

Previously we reported the presence of numerous dislocation loops in BaTiO₃-based perovskite ceramics sintered under reducing atmosphere with TEM [2]. The formation of such dislocation loops may be attributable to the accumulation of oxygen vacancies. Assuming the defect structure model mentioned above, such as oxygen-vacancy dislocation loops, the (110) plane in the perovskite structure would be the most likely defect plane [3]. However, the extraction of the oxygen plane results in repulsion among adjacent cations and charge-balance breakdown. Thus, the defect structure model appears to be energetically unstable, so such simple model of dislocation loops should be reconsidered.

Here, we report the relationship between nonstoichiometry and dislocation loop formation in BaTiO₃ and (Ba,Ca)TiO₃

ceramics, and discuss the appropriate crystallographic structure of dislocation loops.

II. EXPERIMENTAL PROCEDURE

Starting powders of precisely determined chemical composition $[(\text{Ba}_{0.85}\text{Ca}_{0.15})_x\text{TiO}_3]$ for $x=0.98, 1.00$ and 1.02 were prepared by conventional powder processing techniques. This compositional formula assumes that Ca occupies the A-site in perovskite structure ABO₃. Powders were wet-milled for 16 hours and then were sintered at 1,350°C in an air or a reducing atmosphere. The same process applied to the synthesis of stoichiometric BaTiO₃ except for sintering at 1,400°C.

For TEM observation, these samples were mechanically ground and then further thinned by ion milling. The thinned specimens were examined by high-resolution scanning transmission electron microscopy (HR-STEM) (EM-002B, Topcon) with the use of energy-dispersive X-ray detector (VOYAGER and PIONEER, Noran Instruments, Inc.) and a digital imaging system (Megascan, Gatan Inc.).

III. RESULTS

Dislocation loops were observed in almost all samples, stoichiometric BaTiO₃ (BT), B-site-excess $(\text{Ba}_{0.85}\text{Ca}_{0.15})_{0.98}\text{TiO}_3$ (B-BCT), A-site-excess $(\text{Ba}_{0.85}\text{Ca}_{0.15})_{1.02}\text{TiO}_3$ (A-BCT), and stoichiometric $(\text{Ba}_{0.85}\text{Ca}_{0.15})_{1.00}\text{TiO}_3$ (S-BCT), except for B-BCT sintered in an air.

The contrast of these dislocation loops readily shrinks during TEM observation, — that is, under electron beam (EB) irradiation — probably due to their unstable structure. Fig. 1(a) shows the shrinking of dislocation loops in A-BCT sintered in a reducing atmosphere under EB irradiation. In this observation, dislocation loops lay almost parallel in the EB direction (edge-on). With increased exposure to EB irradiation, the diffuse contrast of dislocation loops decreased and then we observed fine single lines without such diffuse contrast, but this line contrast eventually disappeared. Similar behavior was observed in each of the B-BCT and S-BCT samples. The behavior of the dislocation loops in BT sample sintered in a reducing atmosphere during EB irradiation is showed in Fig. 1(b). In BT, a diffuse contrast shrunk with exposure as in the case of A-BCT, but a fine line contrast finally remained. The resultant fine line image remained even after long time and strong exposure to EB irradiation. Fig. 2 shows the high-resolution image of a remaining dislocation loop in BT. This image was taken in the [100] direction. This indicates that the remaining dislocation loop had a complicated crystallographic structure and cannot be described as a simple vacancy or interstitial dislocation loop. We inferred that

remaining dislocation loops would be a mixed dislocation loop consisting of several defect structures. These results are important to the discussion on the origin of the dislocation loops and the crystallographic structure.

As mentioned above, dislocation loops are unstable against EB irradiation. The Burgers vector of the dislocation loop was determined under lower-dose operation using a digital imaging system. Contrast analysis of the two beam conditions was conducted to identify the crystallographic nature of dislocation loops in samples. In a low magnified bright field TEM image of B-BCT sample sintered in a reducing atmosphere with $g=(110)$ (Fig 3), two types of dislocation loops can be seen, which have orthogonal contrasts denoted as A and B. The dislocation loops denoted as A, were out of contrast with $g=(100)$ and (010) operating conditions. The other dislocation loops denoted as B were out of contrast with $g=(010)$ and (011) operating conditions. This indicates that A and B dislocation loops have Burgers vectors $[010]$ and $[100]$. Stereomicroscopy showed that dislocation loop A lay on the (100) plane and B on the (010) plane. Thus, both dislocation loops have the same crystallographic nature and are pure-edge dislocation loops lying on a $\{001\}$ plane with Burgers vector $\langle 001 \rangle$ normal to their habit planes. We could not distinguish the type of dislocation loop (interstitial or vacancy), however, because of the change of the contrast during operation. The same analysis was applied to other samples exhibiting dislocation loops. Results indicated that dislocation loops in these specimens had similar size and contrast, and were all the same pure-edge dislocation loops lying on the $\{001\}$ plane with Burgers vector $\langle 100 \rangle$ perpendicular to its habit

plane, as in B-BCT sample sintered in a reducing atmosphere. In such perovskite structures, it has been reported that the glide direction would be $\langle 110 \rangle$ and the glide plane would be $\{100\}$, $\{110\}$, and $\{112\}$. Thus dislocation loops observed in this study are presumed to be so-called sessile dislocation loops.[4]

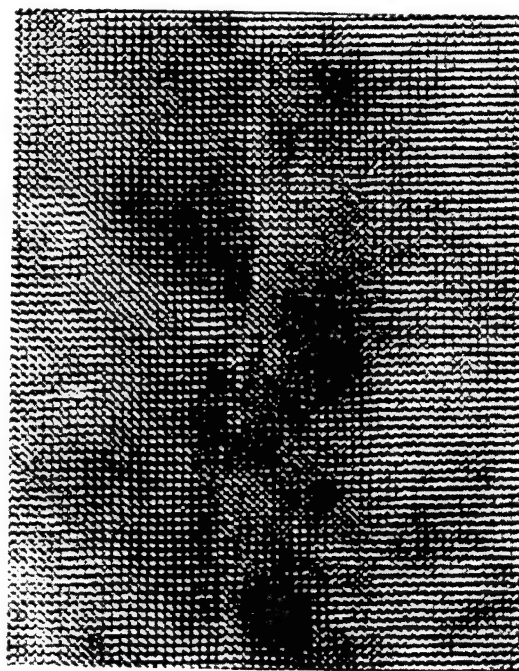


Fig. 2 High resolution image of dislocation loop in BaTiO_3 .

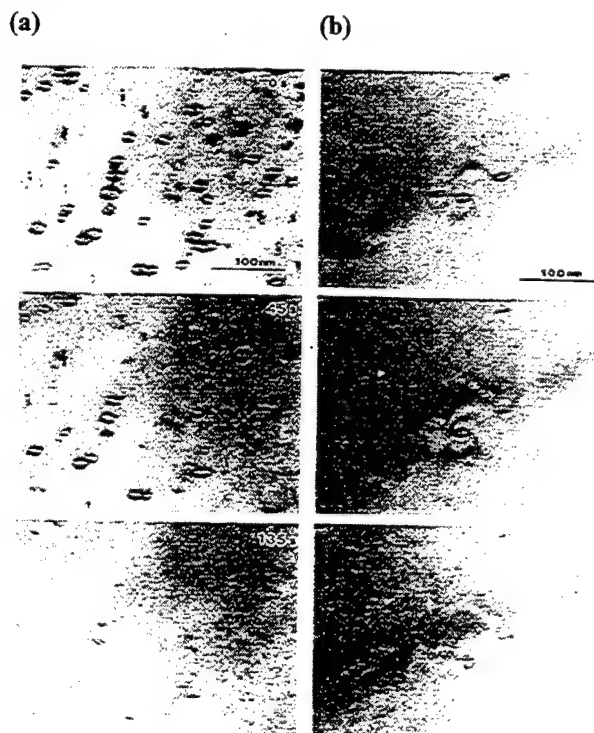


Fig.1 Dynamic behavior of EB-irradiated dislocation loops in A-site-excess $(\text{Ba,Ca})\text{TiO}_3$ sintered in a reducing atmosphere(a) and stoichiometric BaTiO_3 sintered in a reducing atmosphere(b).

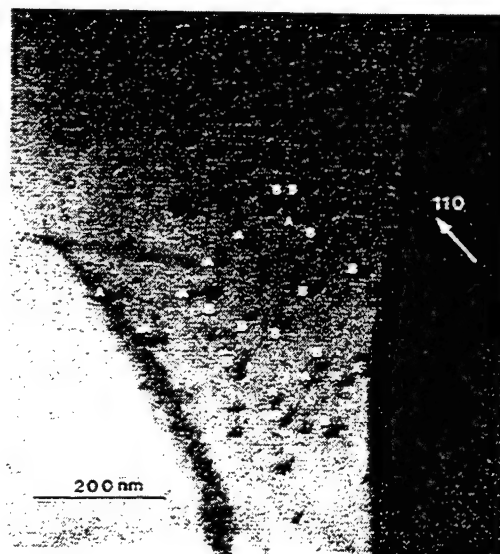


Fig.3 Bright-field TEM image of dislocation loops in B-site-excess $(\text{Ba,Ca})\text{TiO}_3$ with $g=(110)$ two beam operating condition.

IV. DISCUSSION

We could not distinguish vacancy or interstitial defects in the observed dislocation loops, but found that they were sessile dislocation loops lying on the (001) plane with Burgers vector $\langle 001 \rangle$. Formation of the interstitial dislocation loop is considered unlikely, however, due to the closely packed perovskite structure. Therefore, the reasonable structure model of this dislocation loop would appear to be a vacancy. In general, the perovskite structure is a stacking structure consisting of alternating BaO and TiO₂ layers, each preserving an electrostatically neutral condition. Therefore, as the structural model for this dislocation loop, four structural configurations are assumed, each of which is formed by removing a single BaO layer, a single TiO₂ layer, a single BaTiO₃ layer or various combinations thereof from the normal perovskite structure. All satisfy a electrostatically neutral condition due to the elimination of the equivalent cations and anions. However, the elimination of the last one is obviously considered unlikely, since the formation of such structures causes serious lattice strain. The elimination of a single BaTiO₃ layer seems to be energetically more attractive due to the relatively small strain and the absence of the repulsion of neighboring ions in contrast to elimination of a BaO and TiO₂ layer. The elimination of a single BaTiO₃ layer results in the formation of a dislocation loop composed of a perfect edge dislocation with Burgers vector $\langle 100 \rangle$. The presence of a straight dislocation with the same defect nature in BaTiO₃ is highly stable toward EB irradiation. Therefore, this structural model cannot account for the dynamic behavior of the dislocation loop, since experimental findings suggest instability in contrast to this model.

Accordingly, two sets of structural models are proposed, formed by the elimination of a single BaO or TiO₂ layer. Note that these models have two significant features.

The first feature concerns structural instability resulting from the electrostatic repulsion. Although the elimination of a single BaO or TiO₂ layer preserves an electrostatically neutral condition in BaTiO₃, it leads to local repulsion among adjacent ions with opposite charges. Therefore, this structure seems to be energetically unstable. The ordered planer defect as referred to as crystallographic shear (CS) plane analogous to this structure is well known [4][5]. Interestingly, this CS structure can be readily produced by the translation of each perovskite block in the preceding structural model parallel to the habit plane. This transformation would decrease electrostatic repulsion in this stacking and, as a result, stabilize the dislocation loop. In a magnified image of a dislocation loop in BaTiO₃, rearranged by EB irradiation, the presence of displacement is obvious at the defect plane and suggests a disordered CS-like structure. (Fig. 4) The translation vector value is assumed to be either $1/2\langle 100 \rangle$ or $1/2\langle 110 \rangle$. In $1/2\langle 100 \rangle$, a double layer of TiO₂ will be stabilized by sharing the edge of the TiO₆ octahedron, while a double layer of BaO will be less stable compared to $1/2\langle 110 \rangle$, where a double layer of BaO adopts a rock salt structure, found in A-site-excess SrTiO₃ and referred to as the Ruddlesden-Popper layer [6] (Fig. 5). In our study, it was unclear whether this contrast would be attributed to the presence of either a double-layer BaO or TiO₂, and the translation vector $1/2[100]$ or $1/2[110]$.

The second feature concerns nonstoichiometry created by

dislocation formation. Dislocation loops in BaTiO₃ are presumably produced by the elimination of a single BaO or TiO₂ layer, as indicated above, and configurations are rearranged under EB irradiation to minimize electrostatic repulsion in this stacking. Note that, assuming the alternative formation of a double layer of BaO or TiO₂, BaTiO₃ ceramics containing many dislocation loops should virtually accommodate nonstoichiometry to a considerable extent. As previously shown by many investigators, BaTiO₃ actually accommodates no nonstoichiometry[7][8], and therefore it is difficult to presume that either a double layer of TiO₂ or BaO would be preferentially generated. In other respects, all dislocation loops appear to adopt a similar crystallographic structure from the fact that they have similar size, defect nature, and dynamic behavior under irradiation. Consequently, these dislocation loops are speculated to exist as complex dislocation loops consisting of both the region of double BaO layers and of double TiO₂ layers, not as a

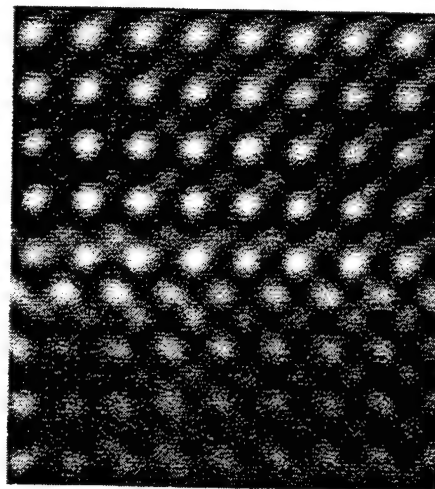


Fig. 4 Enlarged HRTEM image of the dislocation loop in BaTiO₃.

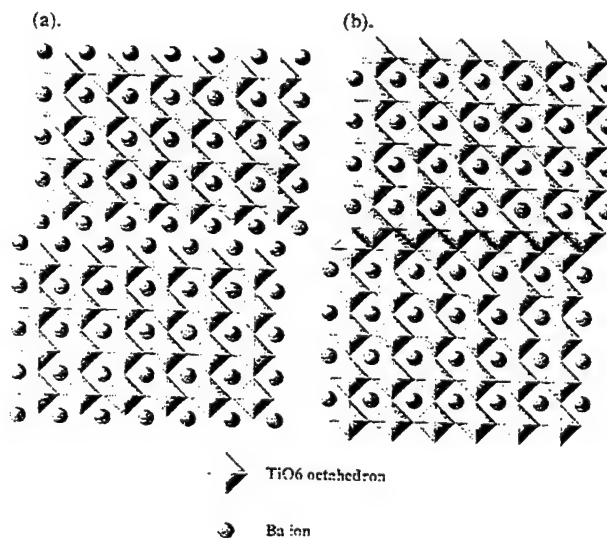


Fig. 5 Models of rearranged dislocation loop in BaTiO₃
(a) Double-layer BaO, (b) Double-layer TiO₂.

mixture of two kinds of dislocation loops, each of which consists solely of a double layer of BaO or a double layer of TiO₂. The complicated form supports this speculation.

In (Ba,Ca)TiO₃, no information on the atomic configuration of the dislocation loop has been obtained except for that of a fundamental crystallographic nature, such as the Burgers vector and habit plane. This is why high-resolution TEM observations could not be applied, given the loop's unstable structure. Given the analogy of their fundamental crystallographic nature, we concluded that a dislocation loop in (Ba,Ca)TiO₃ would adopt the same defect structure as in BaTiO₃. Therefore, different behavior under irradiation is probably attributable to a compositional factor, not a structural one. Judging from the structural feature of the dislocation loop models proposed above, the disappearance of these defects would require the diffusion of cations and anions. Consequently, the difference in behavior under irradiation seems ascribable to that in cation diffusivity caused by the substitution of Ca for Ba.

In our reports[9], the nonstoichiometric (Sr_{0.85},Ca_{0.15})_xTiO₃ system has been investigated, and we clarified that excess AO is accommodated by forming a Ruddlesden-Popper structure, in which constituent Ca ions preferentially occupy cation sites of double layers of SrO. This selective occupation of Ca ions at the fault plane is readily interpreted as the geometric effect of ionic radii. That is, the coordination number of cation sites in a double layer of SrO is smaller than that in perovskite and therefore cation sites are stabilized by the occupation of Ca ions with a smaller ionic radius. Given the above analogy, the preferential occupation of Ca ions would take place at dislocation loops in (Ba,Ca)TiO₃. In addition, the possibility of the substitution of Ca on Ti sites is found to be very high in A-site-excess (Ba,Ca)TiO₃, leading to the enhancement of cation diffusivity. This peculiar behavior of Ca ions, such as the substitution of Ca on Ti sites and the concentration of Ca at the defect plane, enhance the cation diffusivity around dislocation loops. From these speculations, the annihilation process observed in our work would be attributable to this peculiarity of Ca ions in perovskite structure.

In addition, it should be noted that oxygen vacancies accelerate diffusivity in relation to a reducing sintering atmosphere.

V. CONCLUSION

Dislocation loops observed in stoichiometric BaTiO₃ and nonstoichiometric (Ba,Ca)TiO₃ samples were identified as pure-edge dislocation loops lying on the {001} plane with Burgers vector <100> perpendicular to its habit plane. These dislocations were sessile, considering their glide planes. The diffuse contrast of the dislocation loop decreased with electron beam irradiation. The dislocation loops in (Ba,Ca)TiO₃ samples completely disappeared, while the dislocation loops in BaTiO₃ remained as complex defect structures which could be considered complexes of double-layer TiO₂ and BaO. In (Ba,Ca)TiO₃, the diffusivity of Ca ions stemmed from nonstoichiometry strongly influencing the phenomena.

ACKNOWLEDGMENT

This study was supported by Special Coordination Funds for Promoting Science and Technology from the Japanese Science

and Technology Agency, to whom we are indebted.

REFERENCES

- [1] S. Sumita, M. Ikeda, Y. Nakano, K. Nishiyama, and T. Nomura, "Degradation of multilayer ceramic capacitors with Nickel electrodes." *J. Am. Ceram. Soc.*, 74 [11], 1991, 2739-46
- [2] M. Fujimoto, *Seramikkusu*, 25, 1044 (1990)
- [3] M. Shiojiri, T. Isshiki, H. Saijo, M. Tsujikura, A. Nakada, Y. Nakano, M. Ikeda, and T. Nomura, "High-resolution electron microscopy study on domain boundaries and dislocation loops in BaTiO₃ crystals.", *Phys. Stat. Sol.(a)*, 129, (1992), 353-362
- [4] V. V. Prisedsky, G. F. Pan'ko and V. V. Klimov, "Linear and planar faults in electron microscopic structures of PZT crystals.", *Ferroelectrics*, Vol. 64, (1985), 257-273
- [5] O. Eibl, P. Pongratz, P. Skalicky, and H. Schmelz, "Dislocation in BaTiO₃ ceramics", *Phys. Stat. Sol. (a)*, 108, (1988), 495-502
- [6] S. N. Ruddlesden and P. Popper, "The compound Sr₃Ti₂O₇ and its structure.", *Acta Cryst.*, 11, (1958) 54-55
- [7] R.K. Sharma, N. H. Chan, and D. M. Smyth, "Solubility of TiO₂ in BaTiO₃", *J. Am. Ceram. Soc.*, Vol. 64, 8, (1981), 448-451
- [8] Y. H. Hu, M. P. Harmer, and D.M. Smyth, "Solubility of BaO in BaTiO₃", *J. Am. Ceram. Soc.*, 68, 7, (1985) 372-76
- [9] M. Fujimoto, T. Suzuki, Y. Nishi, and K. Arai, "Ca ion selective occupation at Ruddlesden-Popper-type faults and the resultant dielectric properties of A-site-excess (Sr,Ca)TiO₃ ceramics.", *J. Am. Soc.*, in press.

Ca Ion Selective Site Occupation at Ruddlesden-Popper-type Faults and the Resultant Dielectric Properties of A-Site-Excess (Sr,Ca)TiO₃ Ceramics

Masayuki Fujimoto, Toshimasa Suzuki, Yuji Nishi and Katsuhiko Arai

Taiyo Yuden Co., Ltd.

562 Hongo-Tsukanaka, Haruna-machi, Gunma-gun, Gunma 370-33, Japan

Junzo Tanaka

National Institute for Research In Inorganic Materials
1-1 Namiki, Tsukuba, Ibaraki 305, Japan

Abstract - The microstructure and dielectric properties of A-site-excess and stoichiometric composition (Sr,Ca)TiO₃ ceramics were investigated in the present study. Ruddlesden-Popper-type planar faults in A-site-excess specimen were observed using high-resolution scanning transmission electron microscopy (HR-STEM). STEM microchemical analysis, calculation of the high-resolution image using a multislice method, and structural energy calculation furthermore revealed Ca ions selectively occupied the cation sites of the faults. An observed peak dielectric-constant shift to low temperature and the lattice parameter expansion of the A-site-excess specimen were attributed to the selective occupation of the cation sites of the planar faults by Ca ions.

I. INTRODUCTION

The defect structure of SrTiO₃-based ceramics has been studied extensively.[2-8] It has been especially pointed out that a large excess of SrO remarkably influences the crystallographic structure.[5-7] A large excess of SrO can be accommodated by the insertion of individual layers of SrO between blocks of perovskite structure, the so-called Ruddlesden-Popper-type faults. Three oxides - Sr₂TiO₄, Sr₃Ti₂O₇, and Sr₄Ti₃O₁₀, - have been reported. [9,10] These ordered structures correspond to a homologous general formula, Sr_{n+1}Ti_nO_{3n+1}, in which SrTiO₃ corresponds to the composition equivalent to $n=\infty$ and SrO corresponds to that equivalent to $n=0$. Intermediate oxides thus can be regarded as intergrowths between an almost complete sheet of SrO rock-salt structure and lamellae of the SrTiO₃ perovskite structure, n unit cells thick, united along planes rich in Sr. Using TEM, Tilley^[15] observed such a structure in Sr_{n+1}Ti_nO_{3n+1} oxides with $n=1,2,3,4,5$ and $n=\infty$ as a [100] one-dimensional lattice fringe. For the $n=\infty$ sample, especially, with a composition slightly more rich in SrO than that in stoichiometric SrTiO₃, Tilley found planar faults and assumed them to be SrO interfacial layers present between the perovskite slabs. He was, however, unable to determine the actual structure of those interfaces. [11]

Udayakumar and Cormack[12] also introduced the ordering of the crystallographic structure by calculating the formation energies of Sr₂TiO₄ as a K₂NiF₄ structure based on Ruddlesden-Popper-type faults -- that is, a composite of the perovskite and rock-salt structure -- and as a K₂SO₄ structure with special titanium and oxygen coordination (each titanium atom tetrahedrally coordinated by four oxygen atoms). These results indicated that much less energy was required for K₂NiF₄-structure Sr₂TiO₄ (-0.11eV) than for the K₂SO₄ structure (0.36eV). Further calculations of the formation energy for Ruddlesden-Popper-type faults in the system of Sr_{n+1}Ti_nO_{3n+1} were

made by the same authors. [12] In those studies, the authors examined the energetics of Ruddlesden-Popper layer formation. Their calculation results for the formation enthalpy of a homologous series of Ruddlesden-Popper compounds showed that the reaction enthalpy drops from a value of -0.11eV for Sr₂TiO₄ formation to -0.14eV for Sr₃Ti₂O₇ formation. Moreover, the energies of the homologous series with higher n values were almost equal to that of Sr₃Ti₂O₇. The authors thus concluded that only a limited number of superstructures can form a single phase, with smaller amounts of excess SrO resulting in disordered intergrowth in a matrix of stoichiometry Sr₃Ti₂O₇.

In this paper, we report selective Ca ion occupation at the rock-salt structure cation site of Ruddlesden-Popper type faults and the resultant dielectric property changes in A-site-excess (Sr,Ca)TiO₃ ceramics as revealed through STEM chemical analysis, calculation of high resolution images, plane wave structural energy calculation, and so on. In addition, the observed structural details of Ruddlesden-Popper type faults in A-site-excess (Sr,Ca)TiO₃ ceramics are compared with hypotheses from the previous paper. [12]

II. EXPERIMENTAL PROCEDURE

Starting powders of precisely determined chemical composition [(Sr_{0.85}Ca_{0.15}O) _{m} TiO₂: $m=1.00, 1.02, 1.05, \text{ and } 1.10$] were mixed by wet milling for 20h, using high-purity (99.9%) SrCO₃, CaCO₃, and TiO₂. The lattice parameters of the specimens were obtained by X-ray diffraction. The dielectric were measured with an LCR meter at 10kHz in the temperature region from near 0 to 300K using a liquid-helium cooling cryostat. The thin foil specimens were examined by high-resolution scanning transmission electron microscopy (HR-STEM) with the use of an ultra-high-resolution polepiece (Cs=0.4mm, Cc=0.8mm), an ultra-thin window (UTW) energy-dispersive X-ray detector. High-resolution images were simulated by a standard procedure based on the multislice method. The simulated images were computed using the same electron microscopic parameter (the semiangle of incident beam convergence = 1.5mrad, objective aperture radius = 8.6nm⁻¹, the half width of a Gaussian spread of focus due to chromatic aberration = 6nm, acceleration voltage = 200keV, foil thickness = 5.9nm) under two different conditions: (1) with the Ca ions randomly occupying the cation sites of the perovskite and rock-salt structure and (2) with the Ca ions selectively occupying the cation site of the rock-salt structure.

The structural stability of the Ca selective site occupation at

Ruddlesden-Popper type faults were substantiated through plane wave calculation (using a plane wave from Biosym Technologies, Inc., San Diego, CA) of the band structure and total energy of the materials made by generating first-principle norm-conserving pseudopotentials. [13] The internal coordinates of $\text{Sr}_3\text{Ti}_2\text{O}_7$ obtained by optimizing the calculation were checked to confirm the suitability of the calculation method and parameters for verifying Ca site occupation and its structural stability in comparison with X-ray data on $\text{Sr}_3\text{Ti}_2\text{O}_7$. The total formation energies of Ca-ion rock-salt structure site occupation and Ca ion perovskite A-site occupation were then calculated in a $2 \times 2 \times 1$ supercell based on a $\text{Sr}_3\text{Ti}_2\text{O}_{12}$ unit cell using the certified parameters.

III. RESULTS AND DISCUSSION

Fig.1 summarizes the lattice parameters of stoichiometric ($\text{Sr}_{1-x}\text{Ca}_x$) TiO_3 and A-site-excess ($\text{Sr}_{0.85}\text{Ca}_{0.15}\text{O}_m$) TiO_2 specimens. The lattice parameters of the stoichiometric specimens are quoted from Mitsui and Westphal. [1] The lattice parameters obtained for the stoichiometric and A-site-excess specimens in the present study were plotted onto their fitting curve with the a value. The lattice parameters of the stoichiometric specimens coincided with the fitting curve of Mitsui and Westphal. The values of the A-site-excess specimens, on the other hand, tended to coincide with those for the smaller x value stoichiometric specimens, i.e., the a value increased with increasing m values, and further increases in m value resulted in a decreasing of the value.

These results can be explained as phenomena of A-site - excess dependence caused by a combination of factors, that is, Ruddlesden-Popper fault formation and Ca occupation at the A-site of the perovskite structure. Ruddlesden-Popper faults shrink the a -axis and expand the c -axis in the SrO-SrTiO_3 system. Comparing the rates of expansion and contraction show that c -axis expansion is larger than a -axis contraction; in the compositional region of $x > 0.09$, occupation of Ca at the A-site of the perovskite structure shrinks the a -axis and expands the c -axis slightly.

Given a combination of these effects, in a nonstoichiometric sample with $m=1.02$ and $m=1.05$, the effect of Ca occupation at the A-site of the perovskite structure predominates over the effect of Ruddlesden-Popper fault formation, while in a nonstoichiometric sample with $m=1.10$ and $m=1.15$, the effect of Ruddlesden-Popper fault formation predominates over the effect of Ca occupation at the A-site of the perovskite structure.

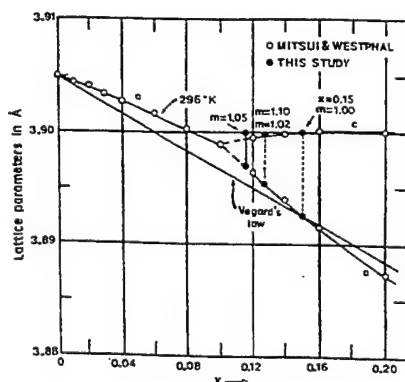


Fig.1. Lattice parameters of stoichiometric and A-site-excess($\text{Sr}_{1-x}\text{Ca}_x\text{O}$) $m\text{TiO}_2$ ceramics.

The dielectric constants of the stoichiometric and A-site-excess specimens as a function of temperature are shown in Fig. 2. Values for the stoichiometric specimens are taken from Mitsui and Westphal. [1] The dielectric constants of the stoichiometric and A-site-excess specimens as a function of temperature are indicated by the broken lines. The peak dielectric constant of the stoichiometric specimen agrees well with the data of Mitsui and Westphal. On the other hand, the value for the A-site-excess-specimen clearly is shifted to the lower temperature region and higher than that of the stoichiometric specimen with the same x value. The observed lattice parameters and dielectric constants thus suggest that the actual content of Ca ions occupying the Sr site of the perovskite structure in the A-site-excess specimen was lower than that in the stoichiometric specimen.

A higher-magnification image of A-site-excess specimen ($m=1.10$) is shown in Fig. 3(a). Both planar-fault-free region A and fault-concentrated region B are indicated in the image. The microdiffraction patterns were obtained from regions A and B, respectively (Fig. 4(a) and (b)). The electron beam spot size for diffraction was 20nm in diameter, as small as the alphabetical indexes shown in Fig. 3(a). The microdiffraction pattern from A

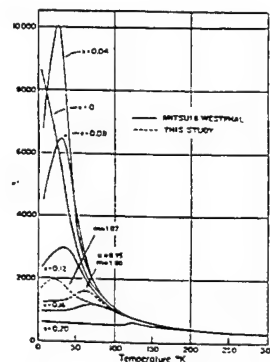


Fig.2. Dielectric constant of stoichiometric and A-site-excess($\text{Sr}_{1-x}\text{Ca}_x\text{O}$) $m\text{TiO}_2$ ceramics as functions of temperature.

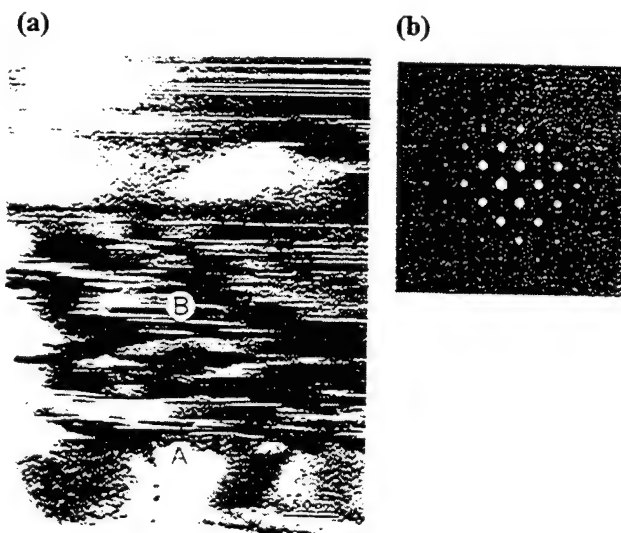
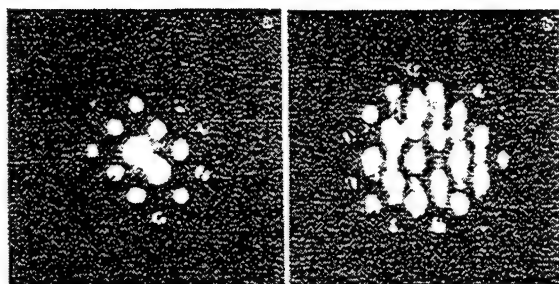


Fig.3 (a). A higher magnification image of planar faults in A-site-excess($\text{Sr}_{0.85}\text{Ca}_{0.15}\text{O}$) 1.05TiO_2 specimen. (b). SAD pattern from the area including region "A" and "B".



(a) (b)
Fig.4. (a) Microdiffraction pattern from defect-free region A and (b) from the defect concentrated region.

Table 1. X-ray count and atom% calculated from the count and K factor.

| | Element | Counts | $K_{M,Ti}$ | atom% |
|---------------------|---------|--------|------------|-------|
| Defect-free Region | Sr | 5907 | 1.864 | 45.15 |
| | Ca | 462 | 0.920 | 3.81 |
| | Ti | 6806 | 1.000 | 51.04 |
| Defect-concentrated | Sr | 6639 | 1.864 | 46.58 |
| | Ca | 984 | 0.920 | 7.45 |
| | Ti | 6679 | 1.000 | 45.98 |

showed no satellite spots, as expected, whereas the pattern from region B clearly revealed more and stronger satellite spots, including spots derived from the $Sr_3Ti_2O_7$ -type structure.

The obtained EDX spectra indicate that the fault-concentrated region had a higher Ca concentration than the fault free-region (Fig. 5). The X-ray count of each element at the two points and the calculated atom% of each element are shown in Table 1.

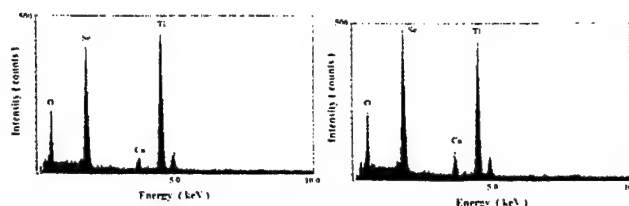
Such results imply that Ca ions had concentrated onto the planar faults or the region adjacent to the planar faults.

Fig.6 shows a high-resolution image of the faults from Fig. 3. The electron beam is parallel to the [100] axis. The arrangement of the black points in the image visually identifies the individual layers of the rock-salt structure between blocks of the perovskite structure as Ruddlesden-Popper-type faults. The inset of Fig. 6 represents a plausible structural model. High-resolution image simulation using the multislice method next was achieved under various conditions for Ca-ion site occupation. From the previously derived experimental results, two different Ca-ion site occupation models were established: one a model of 100% Ca ions predominantly occupying the sites of the rock-salt structure (model I) and the other of Ca ions randomly occupying sites in both the rock-salt and verifying the validity of image matching are shown in Fig. 7. (a) shows a series of high-resolution images, and (b) and (c) show series of simulated images based on models I and II. The image simulated based on model II clearly cannot accurately interpret the perovskite structures (model II). High-resolution micrographs and corresponding simulated images at different defocus settings high-resolution image, whereas the image based on model I can. The Ca-ion selective site occupation in the rock-salt structure of the Ruddlesden-Popper type fault thus clearly was confirmed from the high-resolution image and its computer simulation using the multislice method.

The presently obtained results also are important for another reason. The investigated SrO excess $SrTiO_3$ system is not simple, even though the precise periodicity of the insertion layer of rock-salt structure between the perovskite structure blocks can be recognized clearly from the interpreted high-resolution image accompanied by the simulated image. In addition, the electron diffraction patterns,

especially the microdiffraction pattern from region B, suggest a strong periodicity from the $Sr_3Ti_2O_7$ type of structure. The results thus argue persuasively for adopting the structural model of an SrO-excess $SrTiO_3$ system predicted from the shell model, based on calculations of the formation energy of the homologous series of $Sr_{n+1}Ti_nO_{3n+1}$. [12] In other words, the structure of the homologous series can be deduced as blocks of perovskite structure unit cells of $SrTiO_3$ with randomly accommodated insertion layers of $Sr_3Ti_2O_7$.

The total lattice formation energy in a $2 \times 2 \times 1$ supercell of $Sr_3Ti_2O_7$ was calculated for two different cases: first, with one Ca ion replacing the rock-salt structure cation site and then, with one Ca ion replacing the perovskite A-site. The obtained results are shown in Table 2. The total lattice formation energy of the Ca ion replacing



(a) (b)
Fig.5. (a) STEM EDX spectrum from the defect free region and (b) from the defect concentrated region

Table 2. Plane wave calculation results.

| $(Sr_{23}, Ca)_1 Ti_{16} O_{56}$ | $(Sr_3 Ti_2 O_7 \times 2 \times 1 \text{ super cell})$ |
|----------------------------------|--|
| Replaced Site | Formation total energy (hartree) |
| NaCl | -1428.7998937122 |
| Perovskite A site | -1428.7671210373 |

Difference 0.03277 hartree

0.89eV



Fig.6. A high resolution image of planar faults shown in fig.4.

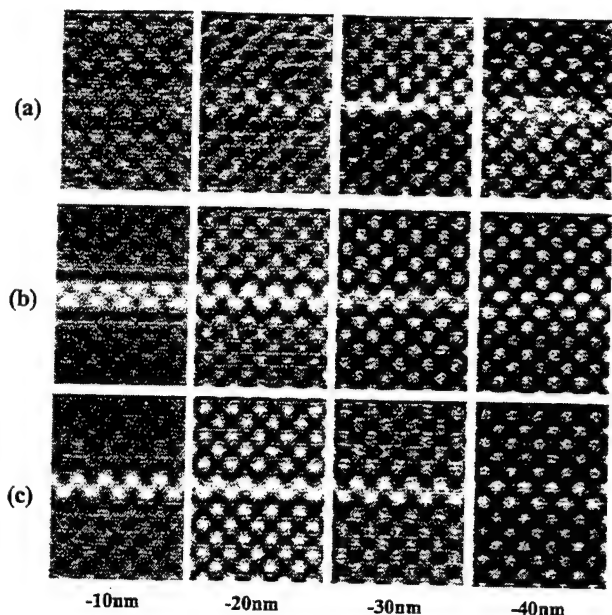


Fig. 7. (a) Through-focal series of high-resolution images, (b) corresponding to the computer simulation image based on model I (Ca ions predominantly occupy the cation site of the rock-salt structure), (b) and (c) based on model II (Ca ions randomly occupy both the rock-salt cation site and perovskite structure). Foil is 5.9nm thick.

the rock-salt site was smaller than that of the Ca ion replacing the perovskite A-site. The 0.89eV difference between the two cases can be regarded as significant. That Ca ions selectively occupy the cation sites of the Ruddlesden-Popper-type faults therefore is reasonable from a structural-energy-stability point of view.

IV. CONCLUSIONS

The microstructure and resultant dielectric properties of A-site-excess $(\text{Sr}_{0.85}\text{Ca}_{0.15}\text{O})_m \text{TiO}_2$ ceramics were investigated in the present study. The results show that the lattice parameters of the a value increased with increases in the m value. The peak dielectric constant of the A-site-excess specimen shifted to the lower temperature region and was higher than that of the stoichiometric specimen. STEM chemical microanalysis, high-resolution image calculation, and structural energy calculation revealed that these specific results were driven by Ca-ion selective site occupation at the rock-salt structure of Ruddlesden-Popper type faults.

Furthermore, the previously predicted SrTiO_3 intergrowth structure model of SrO-excess SrTiO_3 — that is, in a matrix of stoichiometric $\text{Sr}_3\text{Ti}_2\text{O}_7$ — was substantiated by the presently obtained results.

ACKNOWLEDGMENTS

This study was supported by Special Coordination Funds for Promoting Science and Technology from the Japanese Science and Technology Agency, to whom we are indebted.

REFERENCES

[1] T. Mitsui and W. B. Westphal, "Dielectric and X-ray Studies of CaXBal-XTiO_3 and CaXSrI-X TiO_3 ," *Phys. Rev.*, 124 [5] 1354-1359 (1961).

[2] H. Yamada and G.R. Miller, "Point Defects in Reduced Strontium Titanate," *J. Solid State Chem.*, 6 169-77 (1973).
 [3] N.H. Chan, R.K. Sharma, and D.M. Smyth, "Nonstoichiometry in SrTiO_3 ," *J. Electrochem. Soc.*, 128 [8] 1762-1769 (1981).
 [4] N.G. Eror and U. Balachandran, "High-Temperature Defect Structure of Acceptor-Doped Strontium Titanate," *J. Am. Ceram. Soc.*, 65 [9] 426-431 (1982).
 [5] U. Balachandran and N.G. Eror, "Electrical Conductivity in Lanthanum-Doped Strontium Titanate," *J. Electrochem. Soc.*, 129 [5] 1021-26 (1982).
 [6] U. Balachandran and N.G. Eror, "On the Defect Structure of Strontium Titanate with Excess SrO ," *J. Solid State Chem.*, 17 2133-40 (1982).
 [7] S. Witek, D.M. Smyth, and H. Pickup, "Variability of the Sr/Ti Ratio in SrTiO_3 ," *J. Am. Ceram.*, 67[5] 372-75 (1984).
 [8] Y. H. Han, M. P. Harmer, Y. H. Hu, and D. M. Smyth, "A2+/Ti Nonstoichiometry in Alkaline-Earth Titanates, ATiO_3 ," pp. 73-85 in *Transport in Nonstoichiometric Compounds*. Edited by G. Simkovich and V. S. Stubican. Plenum Press, New York, 1981.
 [9] S.N. Ruddlesden and Popper, "New Compound of the K_2NiF_4 Type," *Acta Crystallogr.*, 10 538-39 (1957).
 [10] S.N. Ruddlesden and Popper, "The Compound $\text{Sr}_3\text{Ti}_2\text{O}_7$ and Its Structure," *Acta Crystallogr.*, 11 54-55 (1958).
 [11] R. J. D. Tilley, "An Electroscopic Study of Perovskite-Related Oxides in the Sr-Ti-O System," *J. Solid State Chem.*, 21 (1977) 293-301.
 [12] K.R. Udayakumar and A.N. Cormack, "Structural Aspects of Phase Equilibria in the Strontium-Titanium-Oxygen System," *J. Am. Ceram. Soc.*, 71 [11] C469-471 (1988).
 [13] N. Troullier and Jose Luis Martins, "A Straightforward Method for Generating Soft Transferable Pseudopotentials," *Solid State Commun.*, 74 [7] 613-616 (1990).

Effects of Heat Treatment on Dielectric Properties of X7R Designated MLC's with Ni Internal Electrodes.

Hironari Shoji, H. Matsushita, Y. Nakano, H. Ogawa, A. Onoe,
Y. Yamashita*, and H. Kanai*

R&D Department II, Nippon Chemi-con Corp.

1-167-1, Higashioume, Oume, Tokyo, 198, Japan

*Materials and Devices Research Laboratories, Toshiba Corp.

Abstract:

Heat treatment after reduction of BaTiO₃ base X7R characteristics multilayer ceramic capacitor(MLC) with Ni internal electrode recovers insulation resistance of the MLC. Heat treatment is oxygen diffusion, which is controlled by oxygen partial pressure and temperature. Usually, heat treatment atmosphere is controlled N₂-H₂-H₂O, but this method is expensive. Heat treatment in air is inexpensive, so it will be useful for industry.

Heat treatment in air for base metal electrode MLC was investigated, and we found out that the heat treatment in air recovers the insulation resistance, as same as high oxygen partial pressure atmosphere does. Heat treatment in air at higher than 800°C showed cracks, which came from volume expansion of Ni through oxidation. It became clear by TG-DTA analysis that the oxidation behavior for Ni electrode in MLC differs from Ni plate or Ni powder. The capacitance of the tested MLC is 1.2 μ F for EIA1206 size.

I. Introduction:

With the trend of miniaturization of MLC, the thickness of dielectric layer is decreasing and the number of dielectric layer is increasing. The increase in the number of the stacked layers leads to the rise of the production cost of the MLC. As a result, the development of MLC

with inexpensive internal electrode such as Ni has been accelerated.

Oxidation and reduction behavior of Ni electrode in MLC has a great influence on the reliability of MLC.

A lot of anti reduction dielectric materials were investigated, but only a few papers report about Ni electrode performance.

In this paper, we report on the Ni oxidation behavior through the recovery heat treatment.

II. Experimental Procedure:

The BaTiO₃ base X7R dielectric material powder was prepared. The powder was mixed with binder, and tape-cast. Ni paste was printed by screen printing method. One hundred sheets were stacked and pressed. The binder in the green chips were burnt out at 300°C in air. These chips were fired at 1300°C for 2 hours in low oxygen atmosphere(PO₂=10-11atm) which was controlled by N₂, H₂, and H₂O. The oxygen partial pressure was measured by Zr sensor.

In order to investigate the effect of the heat treatment after firing, the atmosphere was scanned through 900°C~1200°C for PO₂=10-6atm and 600°C~900°C for air.

Dielectric properties of the chips were measured by LCR meter(4284A) and the insulation resistance was measured by 4339B.

Microstructure of the Ni electrode was observed

by SEM. Oxidation of the edge of the Ni electrode was analyzed by XPS.

Oxidation behaviors of Ni as internal electrode, as powder and as Ni plate were analyzed by TG-DTA.

III. Results and Discussions:

Fig.1 shows the oxidation behavior difference for Ni electrode in MLC, Ni plate and Ni powder through TG-DTA analysis. The oxidation of Ni powder starts at 300°C, and ends at 600°C. We may say that the Ni powder is oxidized easily. Ni plate oxidation in air starts slowly at 600°C, and continues until 1200°C. The oxidation of Ni electrode in MLC shows more moderate curve. The reason is that the Ni internal electrodes are laminated between ceramics and the oxidation occurs very slowly.

Fig.2 shows XPS analysis results for after fired (reduction only) sample and recovery heat treated samples. Heat treatment conditions are A: 100°C, PO₂=10⁻⁶ and B: 700°C, in air. XPS depth profile analysis shows that the oxidation of the Ni electrode occurs at the surface of the exposed edge of the electrode.

Fig.3 shows insulation resistance versus temperature. The heat treatment in air at higher than 800°C reveals cracks due to oxidation expansion. (photo 1). But 700°C in air shows good insulation resistance value, without any cracks.

Table 1 shows electrical and mechanical characteristics of the MLC. Electrical characteristics for air anneal samples are as good as for the samples annealed under controlled atmosphere. Breakdown voltage is 66V/ μ m in air and 68V in controlled atmosphere.

Photo 2 shows SEM images of 6 micron dielectric layers. Comparing the results of the two types heat treatments (A to B), it becomes clear that the heat treatment in air is possible.

IV. Conclusion:

Heat treatment for base metal electrode MLC was investigated.

- ① Heat treatment in air recovers insulation resistance, as same as the heat treatment under high oxygen partial pressure atmosphere.
- ② Heat treatment at higher than 800°C in air shows cracks, which come from the volume expansion by Ni oxidation.
- ③ Oxidation behavior of Ni electrode in MLC differs from the behavior of Ni plate or Ni powder.
- ④ Recovery anneal in air is feasible.
- ⑤ The capacitance of X7R designated MLCs is 1.2 μ F in EIA1206 size.

References

- 1) J. Yamamatsu and T. Nomura "Ni powder for multilayer ceramic capacitor powder properties and fired properties" *hunta* oyobi *hunmatsuyakin* 41(1994)1042-1047
- 2) K. Ozeki et al. "Microstructure-property relationships in the BaTiO₃-SrTiO₃-CaTiO₃ system ceramics. *Sozabuseigai* 7-1(1994)42-49

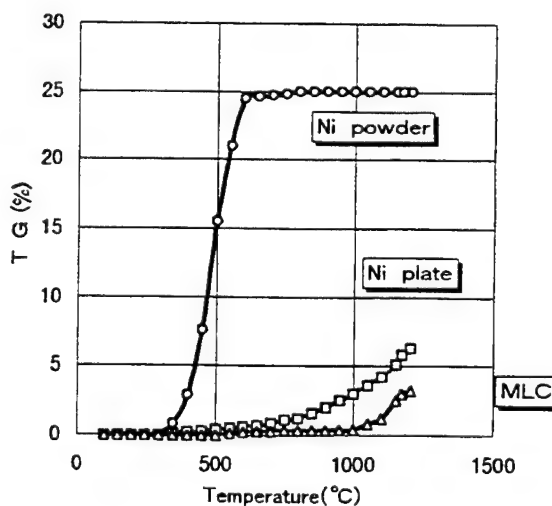


Fig.1 TG-DTA analysis results for different forms of Ni.

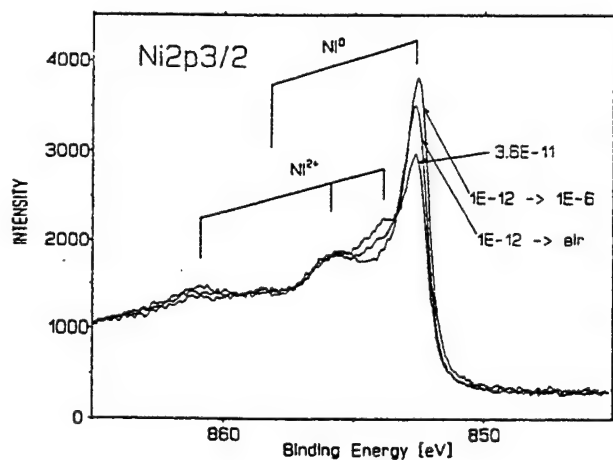


Fig.2 XPS analysis results of heat treatment for three different types of heat treatment..

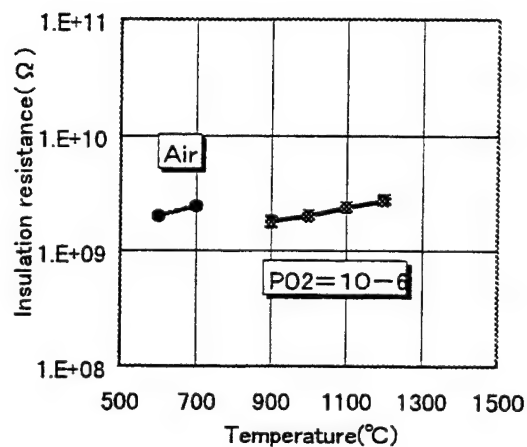


Fig.3 Insulation resistance for various heat treatment conditions.

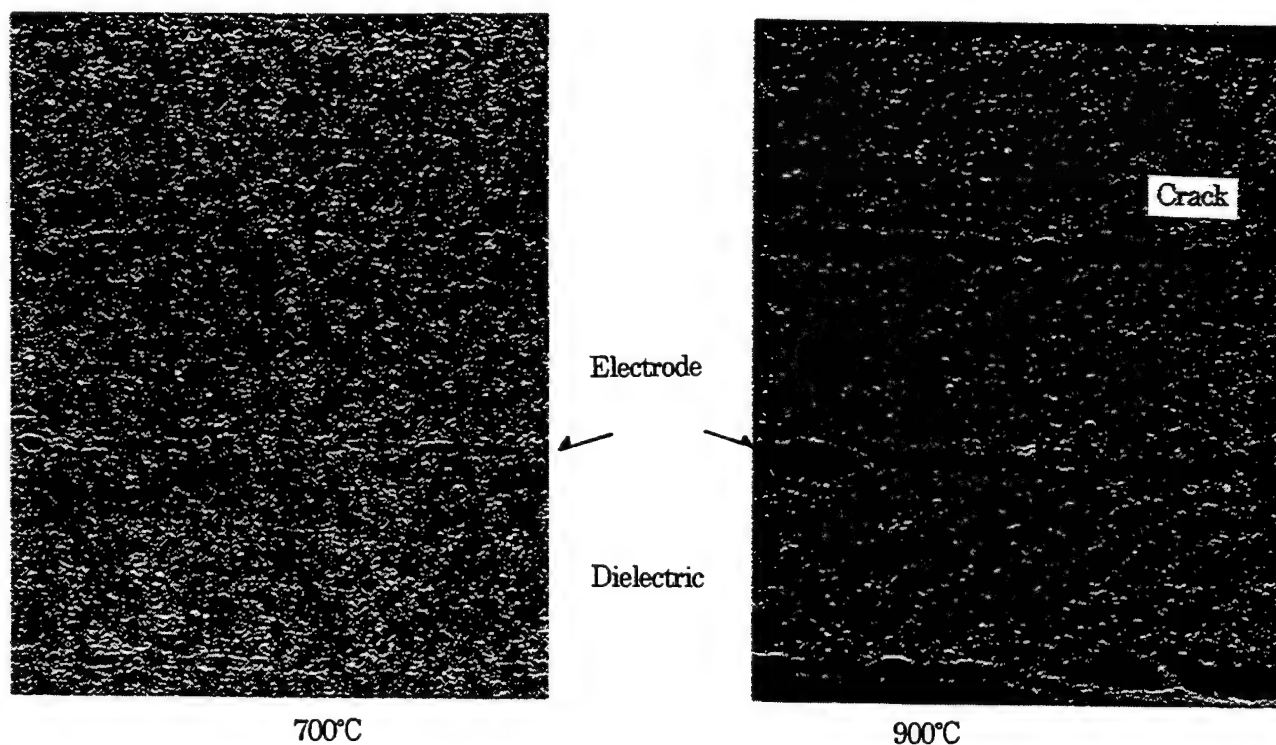


Photo.1 SEM microphotographs of two samples with the heat treatment conditions in air at 700°C and 900°C.

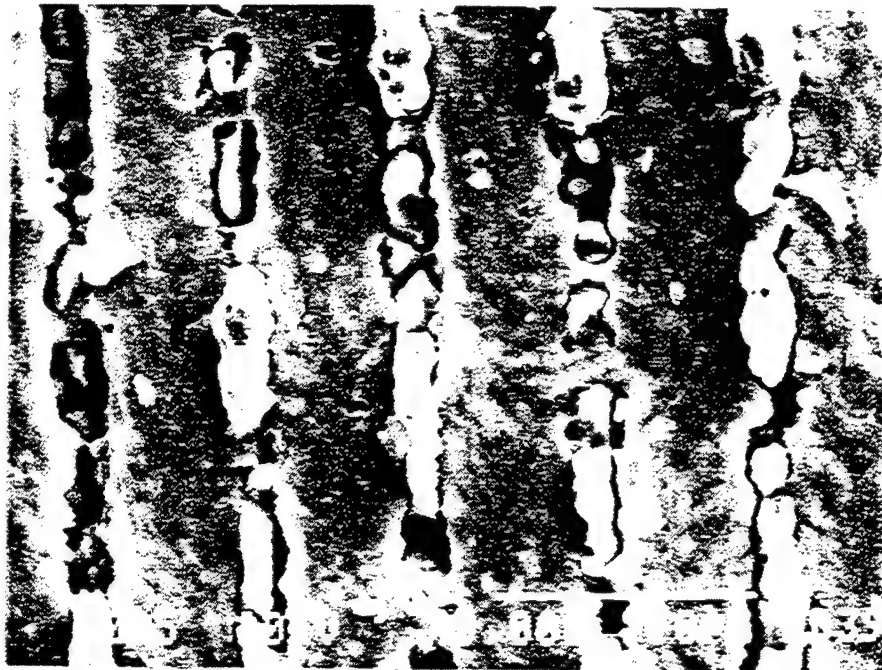


Photo.2 SEM microphotograph of $6\mu\text{m}$ dielectric layers.

Table.1 Electrical and mechanical properties of the MLC's for two different conditions of heat treatment.

| Atmosphere | Air | $\text{P O}_2 = 10^{-6}$ |
|--|-------------------|--------------------------|
| Temperature ($^{\circ}\text{C}$) | 700 | 1100 |
| EIA size | 1206 | 1206 |
| Number of layer | 100 | 100 |
| Thickness (μm) | 6 | 6 |
| Capacitance (μF) | 1.24 | 1.24 |
| Dissipation factor (%) | 4.2 | 4.3 |
| Insulation resistance (Ω) | 2.5×10^9 | 2.4×10^9 |
| Breakdown voltage ($\text{V}/\mu\text{m}$) | 66 | 68 |

Electrical and Physical Characteristics of Low-Fire X7R MLCCs with $\leq 3 \mu\text{m}$ Active Layers and 70Ag-30Pd Electrodes

James J. Beeson and Larry A. Mann
Kemet Electronics Corporation, Ft. Inn, SC 29644

Sridhar Venigalla and Stephen A. Costantino
Cabot Performance Materials, Boyertown, PA 19512

Abstract - Multilayer ceramic capacitors having X7R characteristics were fabricated from sub-micron hydrothermal barium titanate materials, suitably formulated for use with 70Ag-30Pd electrodes. Using novel aqueous-based dispersions, green sheets were fabricated to yield active dielectric thickness in the 2-4 μm range after sintering between 1100 - 1140°C. High volumetric efficiencies were achieved by stacking 100-500 active layers, in various styles ranging from 0603 - 1206 case sizes. Uniform sheet thickness combined with a high green density and defect-free microstructure results in good product yields even at high layer counts. As a result of the high density dielectric with very fine grain structure (0.2 μm - 0.3 μm), these capacitors also exhibited good insulation resistance ($\sim 7500 \Omega \cdot \text{F}$ @25°C and $\sim 3000 \Omega \cdot \text{F}$ at 125°C) and high breakdown strength ($\sim 75 \text{ V}/\mu\text{m}$).

I. INTRODUCTION

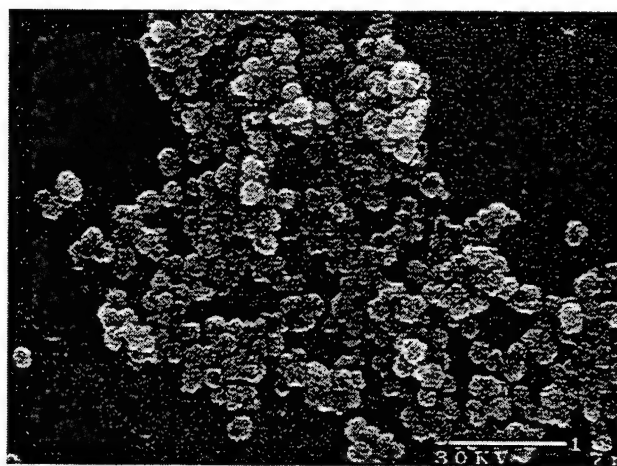
The microelectronic industry's continued push towards miniaturization and high performance (high frequency), has created an immediate need for higher volumetric efficiencies in X7R type multilayer ceramic capacitors (MLCC). This translates to the necessity for manufacturing very thin (≤ 3 micron) ceramic layers, with acceptable physical and electrical characteristics, especially, breakdown strength and reliability. The general understanding among the capacitor industry is that the fired ceramic grain size should not exceed 1/3 to 1/5 of the active layer thickness to achieve these characteristics. Therefore, the use of conventional barium titanate (prepared via calcination and milling route) is typically limited to the sheet thickness above 5 microns, due to its larger, non-uniform particle size. Another aspect of conventional barium titanate materials is that the X7R dopants and sintering fluxes are mechanically mixed together, contributing to further non-uniformity in grain size.

The current work evaluates the suitability of hydrothermally prepared, sub-micron barium titanate with uniform particle size for fabrication of high capacitance X7R value MLCCs with ≤ 3 micron thick active layers. In order to achieve a fine, uniform grain size, all dopants were introduced in the form of a surface coating on barium titanate particles. Another underlying philosophy of this work is to exploit the aqueous nature of hydrothermal process and preserve the environmental and economical benefits of an aqueous-based MLCC manufacturing process.

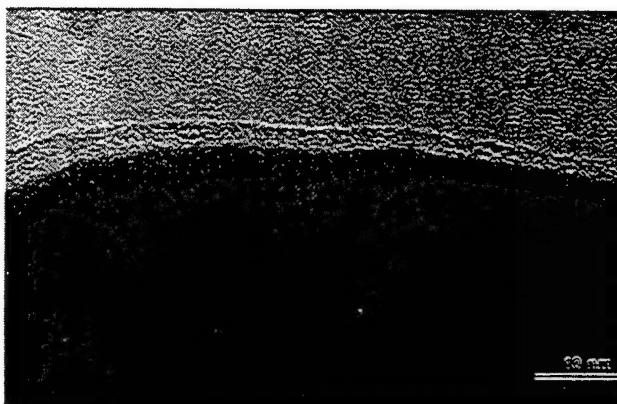
II. MATERIALS AND METHODS

A. Dielectric Formulation and Dispersion

Uniform, sub-micron (0.12 μm average particle size) spherical barium titanate (Fig. 1. (a)) made via a hydrothermal process was used to prepare a low-fire (compatible with 70%Ag-30%Pd electrode) X7R formulation, which can be sintered to full density at $\leq 1140^\circ\text{C}$. Since the hydrothermal process can directly produce fine,



(a)



(b)

Fig. 1. (a) SEM micrograph of sub-micron hydrothermal BaTiO_3 particles and (b) TEM micrograph of a dopant coated particle surface

crystalline barium titanate, there is no need to dry or calcine this material prior to formulation. Using an aqueous precipitation process, various dopants were introduced in the form of a surface coating (Fig. 1. (b)), thereby eliminating the need for drying or milling to achieve a uniform dopant distribution. The formulated particles are then directly dispersed into sub-micron aqueous suspensions (Fig. 2) through simple blending and deagglomeration techniques. Slurries made from this "total aqueous" process were reproducibly dispersed, agglomerate-free and highly stable over a long period of time. This enables the coating of very thin sheets with a good surface quality and microstructure.

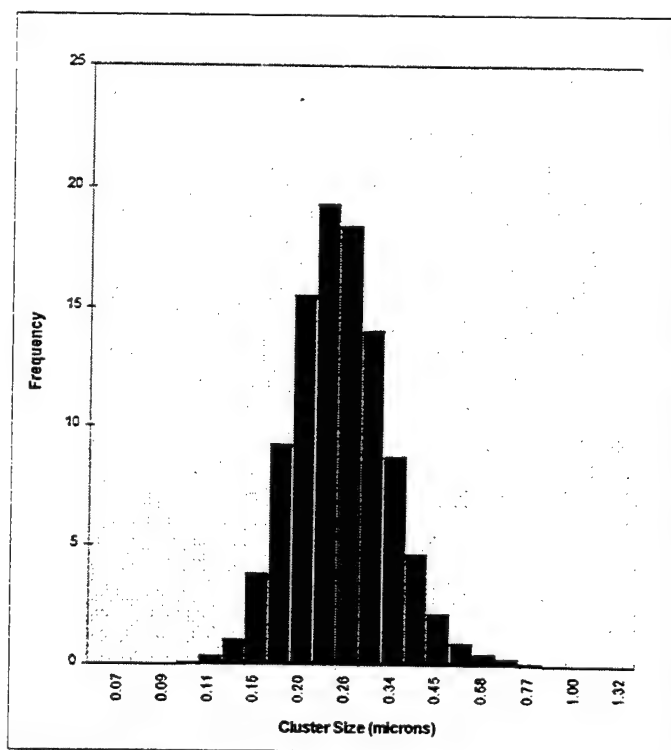


Fig. 2. Size distribution analysis of a typical dispersion of coated sub-micron low-fire X7R barium titanate particles.

B. Green Sheet Preparation

Good quality, thin green sheets are fabricated on a carrier film, in the 4-5 μm range using aqueous-based slips. Uniform, defect-free microstructure (Fig. 3) are obtained by controlling particle dispersion and the organic components in the slip. Uniformity of sheet thickness is controlled very precisely ($\pm 3\%$) using contact-free coating devices together with in-line thickness measurement.

C. Multilayer Fabrication

Green ceramic sheet is subsequently printed with 70%Ag-30%Pd electrode ink, in patterns suitable for 0603, 0805 and 1206 case sizes. The printed sheet is then laminated to build green pads containing 120 - 750 active layers. Lamination

parameters, such as load, die/platen temperatures, sheet strength and plasticity were carefully controlled to achieve good quality stacking. Green pads were mechanically diced to yield individual chips of various sizes.

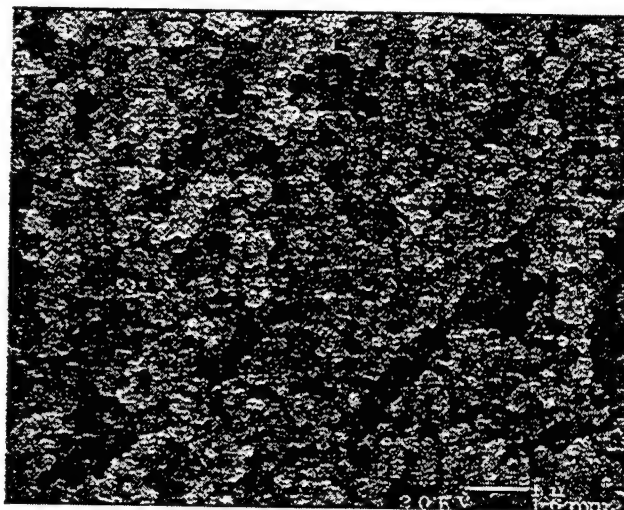


Fig. 3. SEM micrograph of the top surface of a typical 5 μm thick green sheet.

D. Burnout/Firing/Finishing

Green chips are processed in two separate stages: a slow, binder removal (burnout) at low temperature, and a final sintering at $\leq 1140^\circ\text{C}$. Sintered chips are then polished (corner rounding) and terminated with Ag, followed by Ni/Sn plating. Representative samples are mounted and polished for cross-sectional examination of stacking, electrode overlap and physical defects. Electrical analysis includes % yield, capacitance and dissipation factor (both measured at 1 Vrms), insulation resistance (at RT and 125°C), ultimate breakdown strength, capacitance variation with temperature (TCC), board mount reliability and highly accelerated life test (HALT).

III. RESULTS AND DISCUSSION

A. Physical Characteristics

Optical microscopy analysis of polished cross sections from various samples with 3.0 μm and 2.2 μm thick active dielectric layers revealed no physical defects (delaminations, excessive porosity, bowing, etc.) even with as many as 750 active layers (in the 1206 case size). Stack quality and electrode overlap have also been extremely good. A representative cross-sectional image is shown in Fig. 4, where uniform, 3 micron thick dielectric layers with minimal porosity and fine pore size are evident. Good physical characteristics are partly attributed to the thin ($\leq 1\mu\text{m}$), uniform electrodes, as shown in Fig.4.

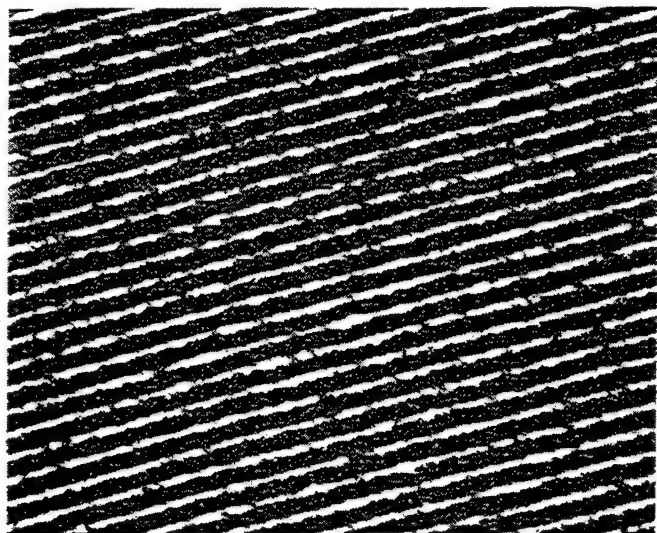


Fig. 4. Cross sectional view of a 0.47 μ F/0603 with 3.0 μ m thick active dielectric layers.

B. Capacitance(C) and Dissipation Factor(DF)

MLC samples possessing high volumetric efficiency have been fabricated from 3 micron active layers (Table I), with capacitance ranging from 0.47 μ F (0603) to 10.0 μ F (1206). Dissipation factors (measured at 1.0 Vrms) typically range between 4 -5%.

C. X7R Characteristics

As shown in Fig. 5, X7R type temperature characteristics (max. $\pm 15\%$ change in capacitance between -55°C and 125°C) were obtained in all case sizes. It has been found that control over sintering temperature, soak time, chemistry and concentrations of dopants is critical to achieve the core-shell microstructure (Fig. 6) needed for X7R type behavior in these sub-micron dielectrics.

D. Insulation Resistance (IR)

Room temperature as well as hot (125°C) IR values (Table I) are excellent. Readings were taken at 16V applied voltage

TABLE I
ELECTRICAL DATA FOR VARIOUS CASE SIZE MLCCs WITH 3.0 μ m THICK
ACTIVE DIELECTRIC LAYERS

| Case Size | Active Layers | C (μ F) | DF (%) @1.0V | IR (G Ω) 25°C/ 125°C | BDV (V) |
|-----------|---------------|--------------|--------------|------------------------------|---------|
| 0603 | 120 | 0.49 | 4.3 | 11.0 / 7.0 | 281 |
| 0805 | 255 | 2.27 | 3.9 | 4.0 / 1.0 | 252 |
| 1206 | 205 | 4.66 | 4.6 | 1.8 / 0.5 | 280 |

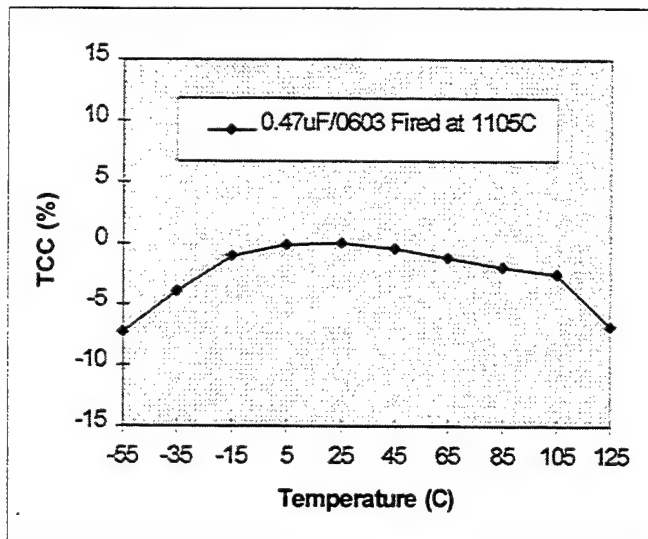


Fig. 5. Temperature coefficient of capacitance (TCC) curve for a 0.47 μ F /0603 MLCC with 3 micron active layers.

E. Breakdown Voltage (BDV)

As also listed in Table I, breakdown strengths for MLCCs with 3 micron active dielectric layers are significantly high, in the range 75-100 V/ μ . High breakdown strength and insulation resistance are attributed to the relatively dense microstructure with fine, uniform ($\sim 0.2\mu$) grain size, as shown in Fig. 7.

F. Equivalent Series Resistance (ESR)

As expected, these high capacitance X7R capacitors exhibit very low ESR at high frequencies, making them attractive for applications in high performance digital circuits. A typical impedance vs frequency curve is shown in Fig. 8, for a 10 μ F / 1206 MLCC, with a minimum ESR between 3-4 m Ω at frequencies above 1 MHz.



Fig. 6. TEM micrograph showing core-shell microstructure.

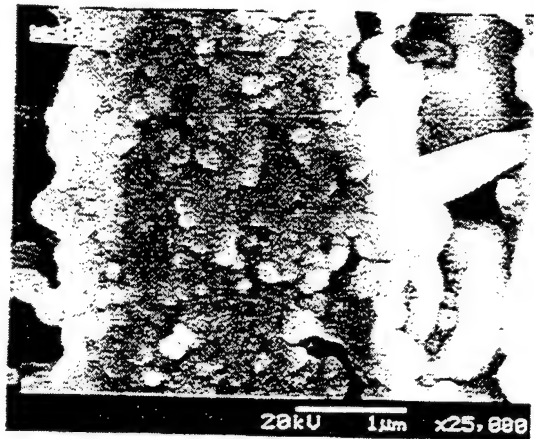


Fig. 7. SEM micrograph of the thermally etched cross section of an MLCC, showing the fine grain structure in a 3 μm thick dielectric layer.

G. Reliability / HALT Testing

Board mount test (25V, 85% R.H., 85°C, 32 h) on 0.47 μF /0603 chips revealed no failures among 2400 specimens, as determined by IR measurements. This suggests that fine grain, dense microstructure is also beneficial to the mechanical integrity of these components. Highly accelerated life test (HALT) was also conducted on 0.47 μF /0603 chips with 40, 64 and 80V bias at 125°C. A residual RC factor of 100 is set as the failure criterion, which translates to an IR value of 212 M Ω for these parts. The time to failure at all voltages has been remarkably good (samples did not fail at 40V, even at 62 h when the test ended), with only few specimens showing premature failure, mainly owing to the physical defects. IR analysis of the failed specimens showed very stable values until the failure: indicating good inherent capability of the dielectric to withstand degradation and an "electronic avalanche" type failure caused by the physical defects. This leads to an understanding that voltage gradient (V/ μ) is the critical parameter in the accelerated life test rather than the bias voltage. Future life tests will be

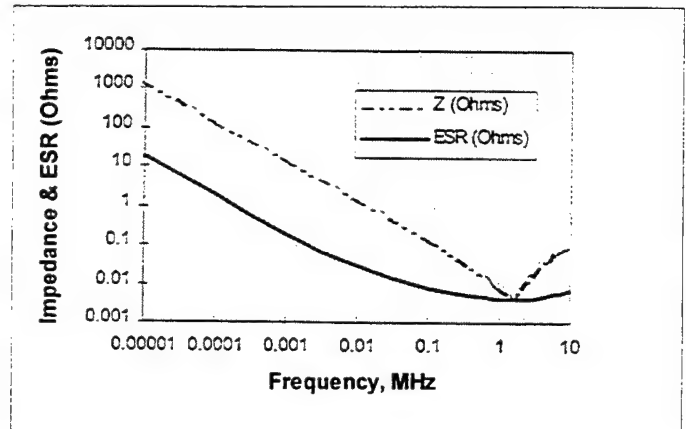


Fig. 8. Impedance (Z) and equivalent series resistance (ESR) data at various frequencies for a 10 μF /1206 MLCC.

conducted at higher temperatures (140-200°C) and voltage gradients in the range 15-20 V/ μ .

IV. SUMMARY

High volumetric efficiency (0.47-10.0 μF) X7R-type MLC capacitors comprising 3 micron thick active dielectric layers and 70Ag-30Pd electrodes are fabricated in various case sizes, utilizing aqueous processing. Characterization for physical and electrical properties is in progress. These capacitors possess excellent microstructural features such as high fired density; fine, uniform grain size (0.2 μ); and uniform dielectric and electrode layers. Electrical characteristics such as high breakdown strength (~ 75 V/ μ), high insulation resistance (RC $\sim 7500\Omega\cdot\text{F}$ @25°C and 3000 $\Omega\cdot\text{F}$ @125°C) and low equivalent series resistance (3-4 m Ω at >1 MHz) make them attractive for high performance applications. Preliminary reliability data shows promise for commercial viability of these high capacitance X7R capacitors.

Effect of AC Signal Field on the Electrical Properties of Thin Layer MLC's with X7R Characteristics

Galeb H. Maher
V. Bheemineni
Thomas I. Prokopowicz
MRA Laboratories
96 Marshall St.
North Adams, MA 01247

Abstract --Multilayer capacitors made with X7R formulations belonging to high fired and low fired categories are investigated to determine the effect of test signal strength on Capacitance and %DF. Both capacitance and %DF increase with signal strength. However, the rate of increase depends strongly on the temperature. Because of this the TCC of the MLCs change and tend to go out of X7R specification for high K formulations.

INTRODUCTION

The increasing demand for high volumetric efficiency multilayer ceramic capacitors has placed new demands on dielectric formulations^{1,2,3,4} and manufacturing methods. Advancement in manufacturing technologies, where the dielectric thickness was reduced to less than 8μ , and the number of layers increased to over 100, made it possible to produce 0805 $1\mu\text{F}$ chip capacitors.

As the active layer thickness decreases and the dielectric is put under more stress and (test) signal strength exerts strong influence on the properties of the MLCs. The objective of this paper is to examine the influence of ac signal field on the electrical characteristics (K, %DF, TCC) of various types of X7R barium titanate based dielectrics. This will include high fired, low fired and Ni electrode base compositions.

EXPERIMENTS

MLC samples of different formulations are obtained from various sources. The active dielectric layer thickness in these samples is between 4μ and 8μ . Capacitance and %DF are measured as a function of V_{rms} in the temperature range -55°C to $+125^\circ\text{C}$. Figures 1 & 2 show capacitance and %DF as a function of V_{rms}/μ . Figure 3 shows TCC curves at different signal strengths.

RESULTS & DISCUSSION

For all the MLCs tested, capacitance and %DF increased with signal strength. The rate of increase is highest at -55°C and smallest at 125°C . Due to the differences in the rate of increase, TCC curve rotates clockwise. The transition temperatures appear to shift to higher temperatures as signal strength increases. It is believed that these changes are related to the spontaneous polarization, P_s , of BaTiO_3 at the three transition temperatures (i.e. -80°C , $+25^\circ\text{C}$, and $+130^\circ\text{C}$). Due to these effects BaTiO_3 based dielectrics with high K will not meet the X7R requirements at $1 V_{\text{rms}}$ for thin active layers.

CONCLUSIONS

The influence of ac signal strength on dielectric properties of barium titanate based dielectric are examined between -55°C and $+125^\circ\text{C}$. Both the dielectric constant and dissipation factor increase more rapidly with signal strength at -55°C than at $+25^\circ\text{C}$ and $+125^\circ\text{C}$. As a result MLCs containing high K formulations and thin active layers ($<5\mu$) will not meet TCC requirement of X7R specification.

REFERENCES

- ¹G. H. Maher, "Capacitor With Fine Grained BaTiO_3 Body and Method of Making," U. S. Patent # 5010443, 1991.
- ²J. Wilson, "X7R Dielectric Ceramic Composition and Capacitor Made Therefrom," U. S. Patent # 5128289, 1992
- ³T. Dean, "Process for Producing Dielectric Ceramic Composition with High Dielectric Constant, Low Dissipation Factor, and Flat TC Characteristics," U. S. Patent # 4939108, 1990
- ⁴G.H. Maher, V. Bheemineni and T.I. Prokopowicz, "Comparison of Physical and Electrical Properties of low fire X7R dielectric with K between 4000 and 5000, in MLC with Layer thickness between 5 and 15 microns", pp. 35-46 in *17th Capacitor and Resistor Technology Symposium '97*

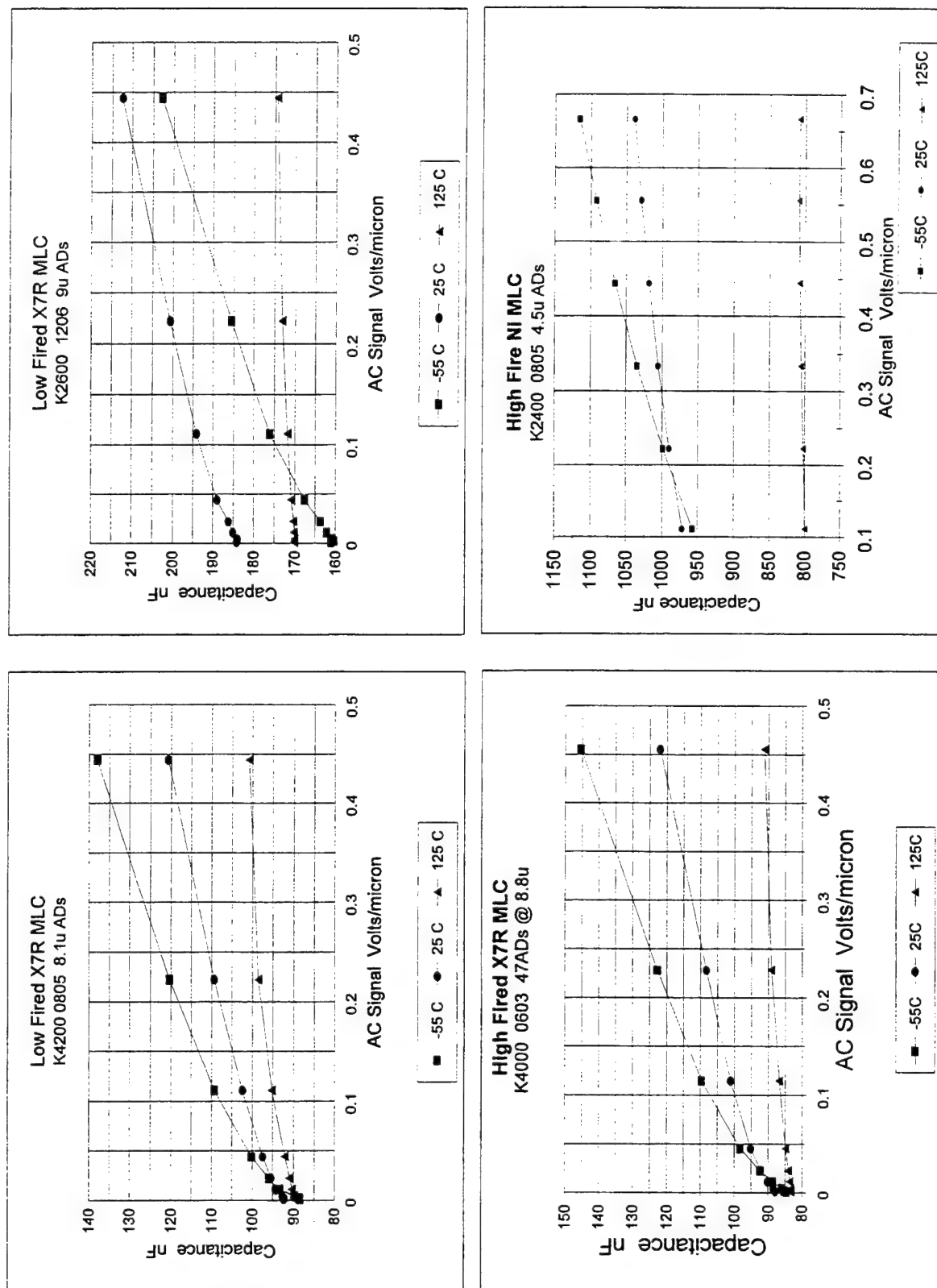


Figure 1. Effect of Signal Strength on Capacitance at different Temperatures.

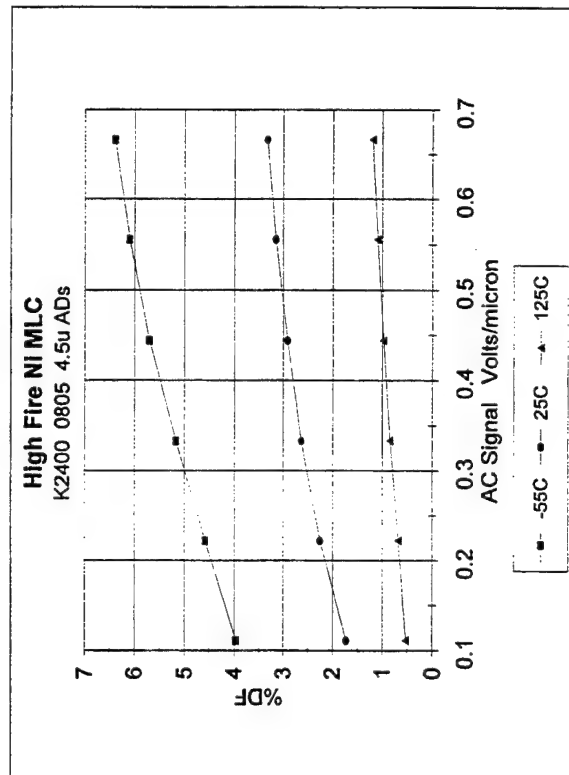
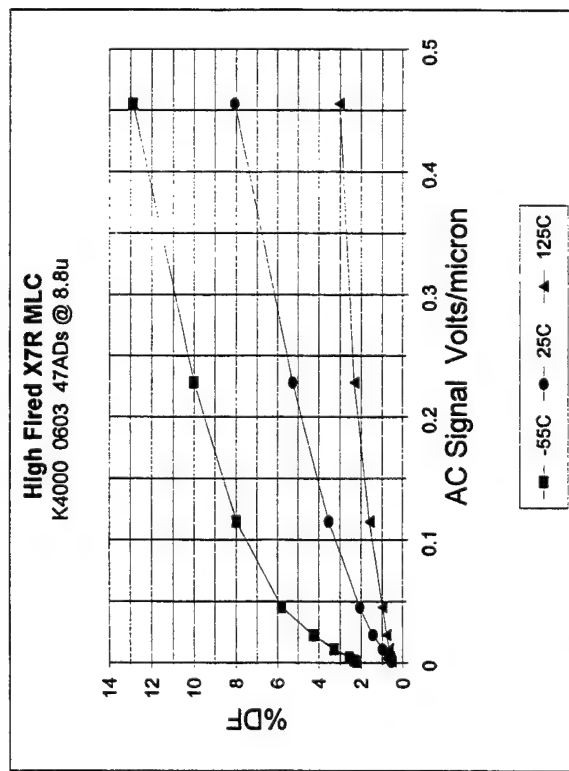
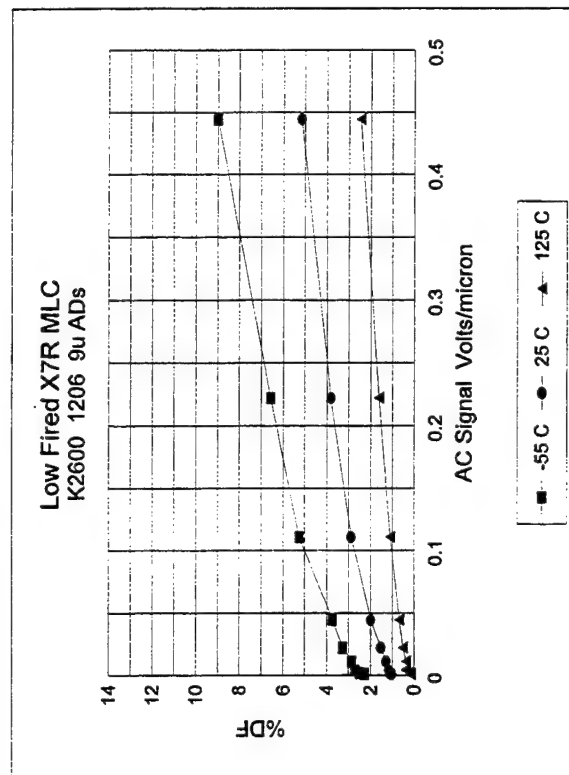
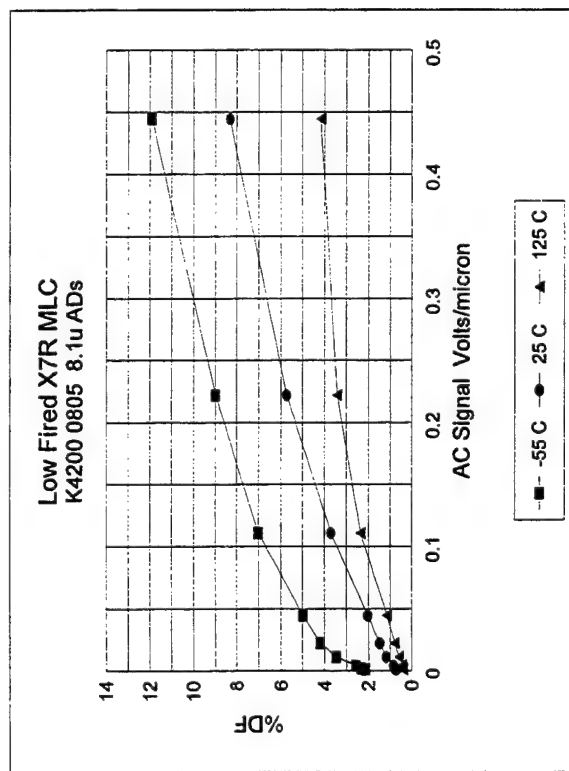


Figure 2. Effect of Signal Strength on %DF at different Temperatures.

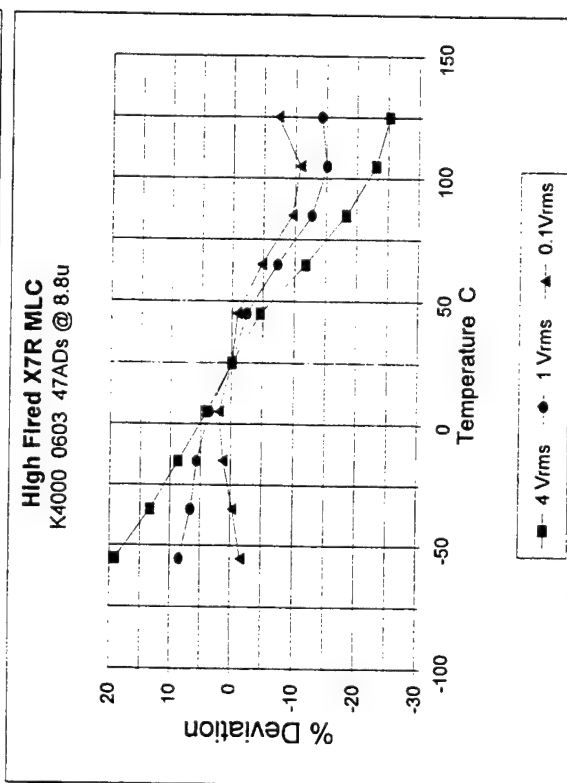
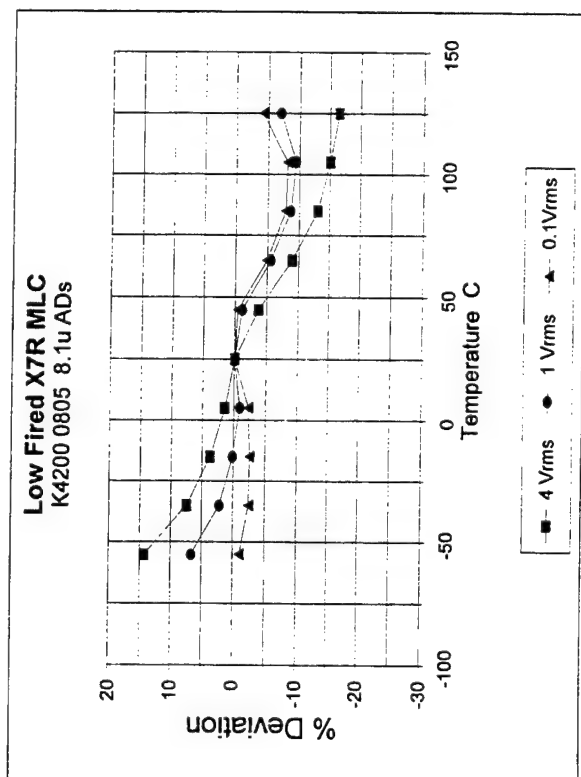
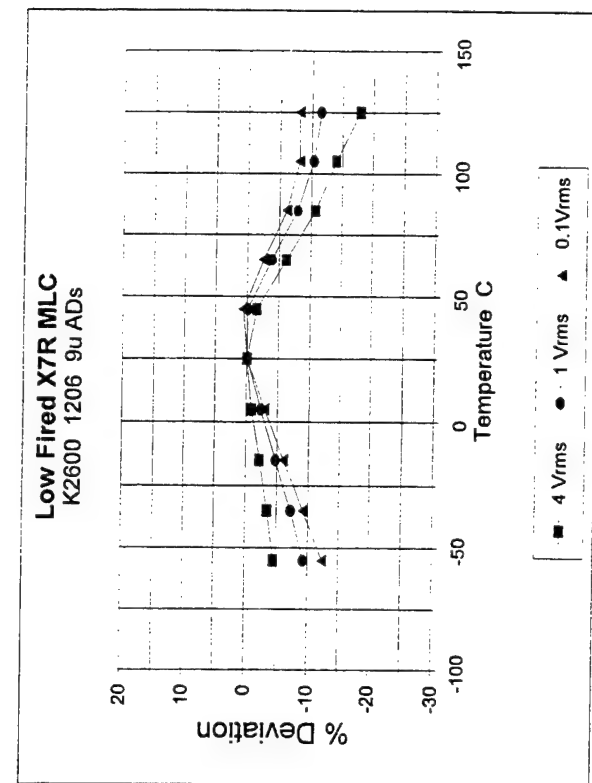


Figure 3. Effect of Signal Strength on TCC.

High Energy Storage X7R Dielectrics

Wayne Huebner, Shi C. Zhang, Marvin Pennell and Xiao M. Ding
Department of Ceramic Engineering
222 McNutt Hall
Rolla, MO 65401

Abstract - This paper summarizes the results of a project dedicated towards the development of dielectrics for high energy density discharge capacitors. The primary goal was to produce capacitors with the following specifications:

- Geometry:** ♦ Must fit within a space which is 1x1x0.020"
- Electrical:** ♦ Minimum 0.10 μF over -55 to 125°C, for $V_a=1000\text{ V}$
- ♦ Able to withstand voltage surges to 2000 V without failure
 - ♦ Charge/discharge cycle: 200 ms to 1000 V; hold at voltage for 2 min; discharge through a 150 m Ω resistor \rightarrow peak 2000 A in 200 ns.

Key to this project were the magnitude of the dielectric constant (K) at high field levels, and the breakdown strength (BDS). Studies on a commercially-available X7R composition yielded a dielectric with a $K=920$, and an average $\text{BDS}=250\text{ kV/cm}$. Processing studies showed the dielectric could be lapped down to a thickness of 4 mils; thermal annealing was necessary to retain the mechanical and electrical integrity. These boundary conditions forced the development of a multilayer capacitor instead of the originally-conceived single layer capacitor.

1.0 INTRODUCTION

High energy-density, high voltage capacitors are the key components in many existing and future technologies, including aerospace and avionics, cardiac defibrillators, pulse forming networks for radar, radio and TV transmitters, military communications equipment /electronics, ignition systems etc. The operating voltages, energy requirements, and duty cycles vary greatly between these applications, but in each case, the achievement of higher energy density, both volumetric and specific, is a discriminator that is needed to enable future developments.

The volumetric energy density, E_D , of a linear dielectric is given by:

$$E_D = \frac{1}{2} CV^2 = \frac{1}{2} \epsilon_0 K \left[\frac{V}{t} \right]^2 \quad (1)$$

where ϵ_0 is the permittivity of free space ($8.85 \times 10^{-12}\text{ F/m}$), K is the dielectric constant, C is the capacitance (F), V is the applied potential (V), and t is the dielectric thickness (m).

Clearly then, optimization of the energy density can be achieved by increasing the dielectric constant of the material (at high fields), decreasing the dielectric thickness, or both.

SOA high voltage (10-20 kV) energy storage capacitors are currently based on polymeric dielectrics with a $K \approx 2-3$, a thickness of $\approx 25\text{ }\mu\text{m}$, and hence operating fields up to several MV/cm .¹⁻³ This corresponds to an $E_D \approx 1-2\text{ J/cm}^3$. Of course the primary advantage of a polymeric dielectric is the high intrinsic breakdown strength. However, because of the very high fields already being used, and the low K of polymers, improvements in this technology have only been incremental.

Another technology developed to increase E_D is the electrolytic capacitor. Electrolytic capacitors also exhibit E_D 's of $\approx 1\text{ J/cm}^3$, however the operating voltage is fairly low, $\leq 500\text{ V}$. In addition, electrolytic capacitors commonly use sulfuric acid as an electrolyte.

The primary advantage of using a ceramic for the dielectric is its potentially high dielectric constant.⁵⁻⁷ This is illustrated in Fig. 1, which exhibits the energy density of a ceramic dielectric as a function of thickness, and a dielectric constant between 500 and 2000. The SOA breakdown strength (BDS) is also plotted. Hence for $V=1000\text{ V}$, a ceramic dielectric can yield between $\approx 3-10\text{ J/cm}^3$, for a minimum dielectric thickness of $\approx 25\text{ }\mu\text{m}$. This increase in E_D translates directly into volumetric savings.

This paper summarizes the results of a project sponsored by AlliedSignal dedicated towards the development of dielectrics for high energy density discharge capacitors with

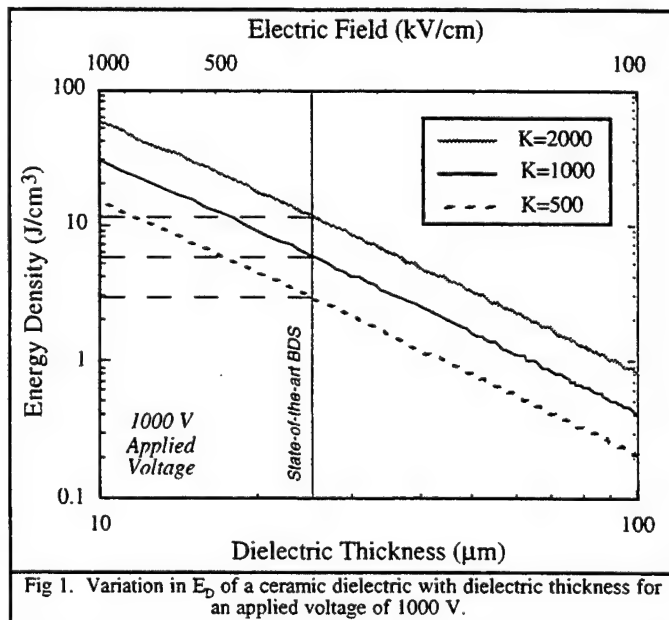


Fig 1. Variation in E_D of a ceramic dielectric with dielectric thickness for an applied voltage of 1000 V.

the specifications described in the abstract. These represented formidable requirements, pushing available technology right to the edge. Of particular importance were the magnitude of the dielectric constant at high field levels, and the breakdown strength. The simplest solution to this problem would be to manufacture a disk capacitor with full face electrodes. Table I exhibits the requisite dielectric constant as a function of dielectric thickness for a 1" diameter disk capacitor. Simple pressed dielectrics can be reliably fabricated down to ≈ 5 mils, corresponding to a dielectric with $K \approx 2230$. The choice of which dielectric formulation to use was critical; no high field dielectric data were available for temperature-stable dielectrics. Making the dielectric thinner diminishes the needed dielectric constant, but of course the associated field is higher. Hence this project focused on characterizing the dielectric formulation thoroughly, then evaluating the processing conditions necessary to achieve the needed dimensions.

TABLE I

Dielectric Constant Needed to Fabricate a 0.1 μ F Disk Capacitor as a Function of the Dielectric Thickness

| Dielectric Thickness mils | Needed Dielectric Constant | Field @ 2000 (kV/cm) |
|---------------------------|----------------------------|----------------------|
| 4 | 2230 | 200 |
| 6 | 3350 | 133 |
| 8 | 4460 | 100 |
| 10 | 5580 | 80 |
| 12 | 6690 | 67 |
| 14 | 7810 | 57 |
| 16 | 8920 | 50 |
| 18 | 10,040 | 44 |
| 20 | 11,160 | 40 |

2.0 RESULTS AND DISCUSSION

A. Dielectric Composition

The designated temperature requirements dictated use of an X7R dielectric based on BaTiO_3 , although the high field properties were unknown. An X7R dielectric was utilized from TAM Ceramics in Niagara Falls, NY (TAMTRON X7R412H). Discussions with TAM personnel indicated this X7R dielectric is being incorporated into multilayer, tape cast structures in which the active dielectric layer thickness is $\leq 10 \mu\text{m}$, with a corresponding BDS on the order of 800 V/mil (315 kV/cm). The room temperature (1 kHz) dielectric constant is 3746, with a $\tan \delta = 0.0075$. The K falls off $\approx 30\%$ for an applied field of 40 V/mil, but was unknown for higher field levels. Answering this question was a high priority in the initial stage of this project in order to design the requisite dielectric thickness.

B. Microstructural Development

Figure 2 overviews the processing steps necessary to complete the desired capacitors. Initial experiments focused on developing the optimum processing conditions necessary to achieve high density dielectrics with a minimum grain size. The particle size distribution of the TAMTRON

X7R412H powder shows that 40% of the powder is $\leq 1 \mu\text{m}$ in size, with 100 % $\leq \approx 4 \mu\text{m}$. A finer powder would be desirable, but this powder proved to be more than adequate to achieve full density. After a series of processing studies on the influence of compaction pressure on the green density, uniaxial pressing at 10,000 psi, followed by cold isostatic pressing at 40,000 psi was utilized. Green densities were on the order of 60% theoretical (using a T.D. of 5.83 g/cm^3 - TAM literature). A series of 12 firing runs yielded the best combination of microstructure and dielectric properties (X7R temperature stability) for the sintering conditions shown in Figure 3.

Figure 4 contains a representative microstructure of a fracture surface. Some porosity still remains; the density measurements indicated $\approx 2 \text{ vol}\%$. The size of the porosity indicates the source may be powder agglomeration / aggregation; indeed the size distribution results on the powder indicate the presence of relatively large ($\approx 4 \mu\text{m}$) structures. While the presence of any porosity is not good for the mechanical or electrical breakdown strength, in this study the measured electrical breakdown was more than sufficient.

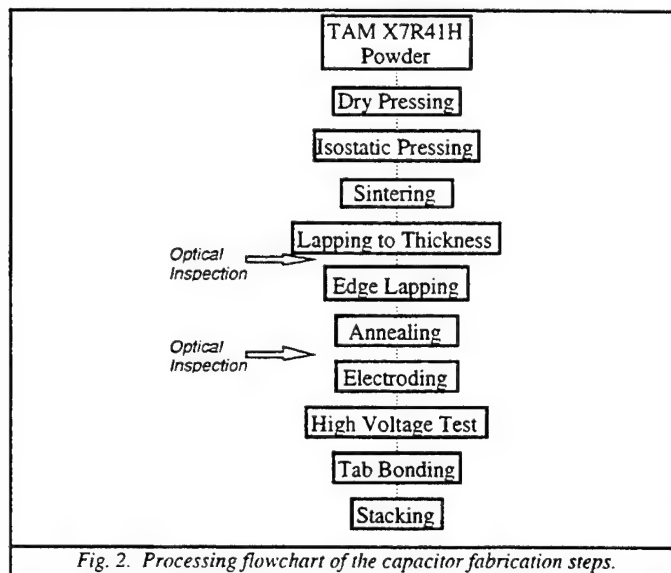


Fig. 2. Processing flowchart of the capacitor fabrication steps.

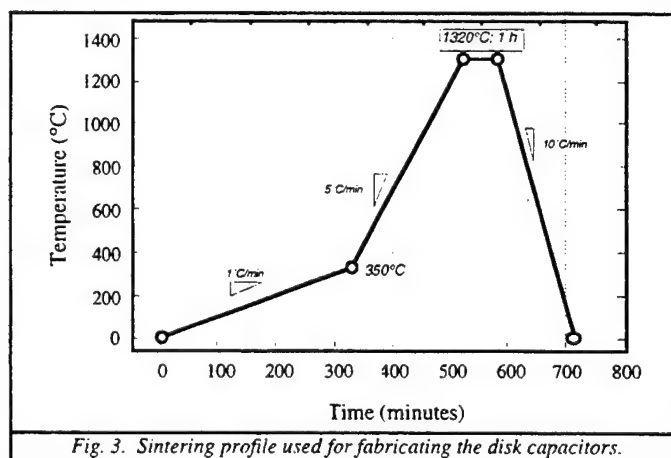


Fig. 3. Sintering profile used for fabricating the disk capacitors.

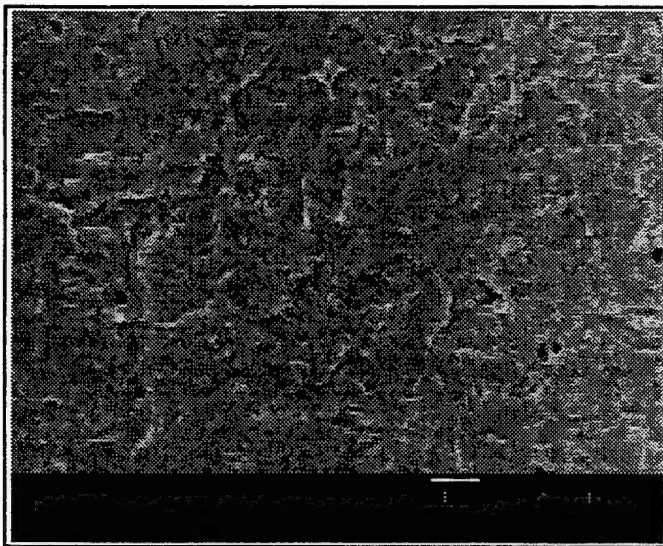


Figure 4. Fracture surface of the TAM X7R412H powder sintered using the profile of figure 2.

C. Electrical Characterization

The low field dielectric properties of a the TAM X7R412H dielectric processed as above are shown in Figure 5. At room temperature the K is ≈ 4250 (1 kHz), decreasing to 3750 at 95°C. The corresponding losses are all $\leq 5\%$. These properties fall well within X7R characteristics. This dielectric is clearly doped such that the maximum K falls right at room temperature, yet retains a BaTiO_3 core structure as evidenced by the steep rise in K as 125°C is approached. The dispersion is related to the domain wall contributions and their frequency dependence.

Of course the low field characteristics are not important for high energy density capacitors; the high field K was needed to determine the dimensions of the capacitor. Initially the high field K was initially measured via a Sawyer Tower hysteresis system. Later the high field capacitance was measured by applying a small 1 V AC ripple on top of a DC bias. A circuit was built to protect the HP 4194 bridge in the event of breakdown. On the basis of the K vs. T results shown in Fig. 5, the high field K was measured at room temperature, 95°C, and -15°C. The P vs. E behavior at these temperatures is shown in Figure 6, along with the corresponding K vs. E results shown in Figure 7. At ≈ 50 kV/cm the K is stabilized at a value of ≈ 920 . Higher field levels do reduce the K further; clearly the linear ionic & electronic polarization mechanisms are dominant. These results compare well with those of Love⁶ on a different X7R system.

Understanding why the dielectric constant is nearly independent of temperature at high fields is important. The low field K of a polycrystalline, normal ferroelectric is attributable to both intrinsic and extrinsic contributions. Intrinsic contributions are those properties exhibited by a single domain, single crystal, i.e. the polarizability associated with the predominant polarization mechanisms. Extrinsic contributions are related to the presence of domains and

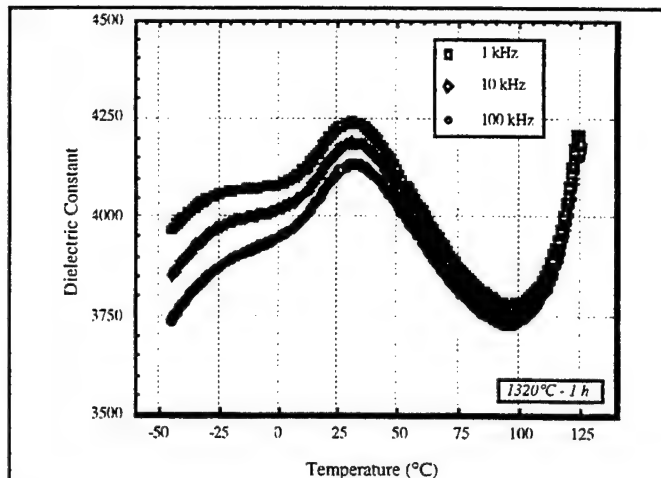


Fig. 5. Low field dielectric properties of the TAM X7R412H dielectric.

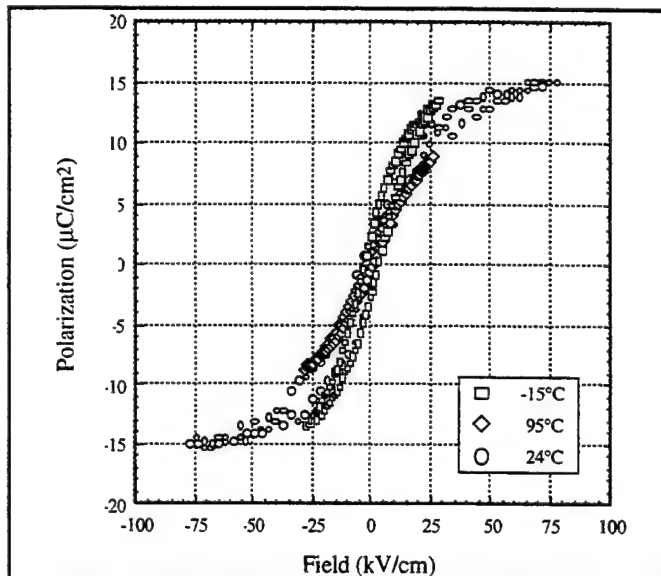


Fig. 6. Hysteretic properties of the TAM X7R412H dielectric.

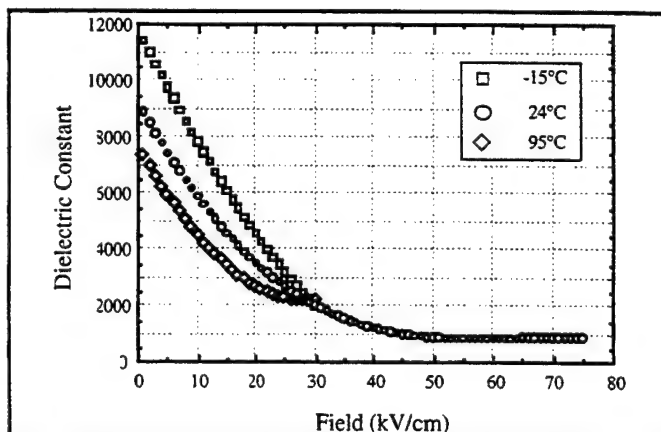


Fig 7. K vs. E properties of the TAM X7R412H dielectric.

domain walls. Keep in mind that the K of a single crystal is very anisotropic; it is a second rank tensor. For instance, in the tetragonal state BaTiO_3 exhibits a $K \approx 2000$ along the a -axis, and only ≈ 200 along the c -axis. On first inspection, this might seem backwards, particularly since the Ti -ion is displaced along the c -axis. However, this is a dramatic example of understanding the difference between low field and high field behavior. At low fields, the Ti^{4+} ion in a single crystal is locked in place along the c -axis in its oxygen octahedra. Small fields applied in an orthogonal direction, the a -axis, can move it significantly further. Hence the K along the a -axis is much higher.

At high fields, i.e. AC electric fields greater than the coercive field, E_c , this situation changes. When we switch the Ti^{4+} ion back and forth, a huge polarization is switched, and the dielectric constant is higher. The effective K as we sweep through E_c is very large along the c -axis.

Note that for a high DC bias, the dielectric constant is significantly lower, but for an AC bias it exhibits a maxima. This behavior might be best understood by considering the hysteresis loop for a single crystal of BaTiO_3 . For a monodomain, single crystal, a remanent polarization equal to the saturation polarization is present. By definition, a depoled, zero polarization state is not possible. The slope at this point is very low, and essentially constant \rightarrow the high field linear behavior extrapolates back to the polarization axis. Only when the polarization direction is switched will K be higher.

The situation is significantly different for a polycrystalline ceramic. In the absence of any anisotropy due to grain morphology, after sintering a ferroelectric ceramic exhibits no net polarization. In this state the low field dielectric constant is a strong function of the extrinsic contributions related to the domain wall configuration. In general, both 90° and 180° domain walls will be present, and oriented along crystallographic directions dictated by the lattice structure of an individual grain. In turn, grains are randomly oriented in the ceramic.

Upon application of a field, domains present in a normal ferroelectric do not totally follow the electric field; only slight motions (several unit cells) of the domain walls occurs. Even though the domain wall motion is slight, it can lead to significant extrinsic contributions to the dielectric constant. Importantly, the dielectric constant will increase with increasing field as long as the ceramic is not saturated (compared to the single crystal). The polarization which is achieved at a given field strength is a complex function of the ability of domains to reorient, in particular 90° domains which also switch a large 1% strain. It is not surprising then that the high field dielectric constant saturates to the same level even though the temperature is significantly different.

From Table I it is clearly impossible to fabricate a single layer capacitor which could meet the geometric and capacitance requirements. A multilayer approach was deemed necessary; 4 layers of dielectric would yield the necessary capacitance for thicknesses ranging from 4-6 mils.

At this stage of the program it was apparent that the dielectric formulation would work well; the remaining issue was the dielectric strength. Note the field level; for a 4 mil dielectric the field at 2000 V is 197 kV/cm. Electrical breakdown strength measurements were performed (per ASTM D-149) on disks which were planar lapped, followed by thermal annealing at 1320°C for 10 mins to removed lapping defects. The average BDS was 250 kV/cm, well below the needed BDS. Post-mortem evaluation showed that the low BDS's were attributable to either macroscopic defects (grain pullouts & hence a thinner active dielectric), or edge breakdown. Optical inspection procedures helped cull these samples out prior to the electroding step.

D. Capacitor Fabrication

After optimizing the sintering conditions and obtaining the design boundary conditions associated with the dielectric properties, two capacitor stacks were targeted for fabrication. The first stack consisted of 7 mil thick active dielectrics, and the second was comprised of 4 mil dielectrics.

Referring back to Fig. 2, after pressing and sintering 1" dielectrics, the remaining steps to create a single layer dielectric were to planar lap down to thickness, edge lap, planar lap to final thickness, thermally anneal, screen print an electrode, and then fire it on. Over 100 disks were prepared in this manner.

The fact that we needed to make a stack of dielectrics to make a single capacitor greatly complicated matters. Issues related to connecting the individual electrodes within layers, bonding the layers together uniformly, and encapsulating the unit all needed to be systematically addressed. The following components were successfully utilized:

- Tab ♦ 8 μm Cu foil
Bonding ♦ epo-tek® H31" Ag epoxy

*Epoxy Technology Inc.
 14 Fortune Dr.
 Billerica, MA 01821*

- Stacking ♦ Ciba Geigy Epoxy System
 Resin: CY179 (10 parts)
 Hardener: HY 906 (13 parts)
 Accelerator: DY 062 (0.1 parts)
 ♦ vacuum immersion
 ♦ removal & suspended in air
 ♦ 125°C - 8 h cure

Ultimately these stacks satisfied the needed criteria, exhibiting a value of $0.119 \mu\text{F}$ at voltage. This corresponded to an energy density of $\approx 3 \text{ J/cm}^3$.

4.0 SUMMARY AND CONCLUSIONS

The results of this research can be summarized as follows:

- ◆ The TAMTRON X7R412 dielectric chosen for study was suitable in terms of its electrical characteristics:
 - high field $K \approx 920$; independent of temperature
 - Average BDS $\approx 250 \text{ kV/cm}$
 - Energy density of $\approx 3 \text{ J/cm}^3$
- ◆ The dielectric constant at high field levels dictated that a multiple layer approach be implemented. Several stack designs were implemented and successfully used to fabricate the needed capacitors. Including the packaging materials, these capacitors exhibited an energy density of $\approx 3 \text{ J/cm}^3$.

REFERENCES

1. D.K. Gupta and Z. Shuren, *Ferroelectrics*, **134**, 71 (1992).
2. J.L. Suthar and J.R. Laghari, *J. Mater. Sci.*, **3**, 77 (1992).
3. R.J. Mammone and M. Binder, *IEEE Intl. Power Sources Symp.*, cat #90CH2863-9, p. 395 (1990).
4. G.A. Shirn and I. Burn, Proceedings of a Symposium on High Energy Density Capacitors and Dielectric Materials, National Academy Press (1981).
5. I. Burn and D.M. Smyth, *J. Mater. Sci.*, **7**, 339-43 (1972).
6. G.R. Love, *J. Amer. Cer. Soc.*, **73**[2], 323 (1990).
7. K. Bridger, A. Sutherland, E. Fiore, A. Bailey, J. Christdoulou and S. Winzer, *IEEE*, 35th Intl. Power Sources Symp., p 387, June 22-25, 1992.

DIELECTRIC PROPERTIES OF PMN BASED CERAMIC UNDER D.C. AND A.C. FIELDS

Umesh Kumar, Joseph Hock, Bharat Rawal, Mike Randall

Advanced Products and Technology Center
AVX Corporation
Myrtle Beach, SC 29577
(803)946-0660 (p)
(803)626-9632 (f)

ABSTRACT

Multilayer ceramic capacitors with high volumetric efficiency are prepared by reducing the layer thickness. When the thickness is reduced below 10 μm , the dielectric properties of capacitors with Y5V characteristics become sensitive to electrical test conditions. In this paper, the effect of d.c. and a.c. electric fields on the temperature dependent dielectric properties of a PMN-based material are discussed. These properties are compared with those of BaTiO₃ (BT) based dielectric material. The advantages of the PMN-based system over BT-based system for thin layer devices are identified by comparing the temperature - electric field - thickness relationships.

INTRODUCTION

Miniaturization of consumer electronic products drives the demand for surface mountable multilayer ceramic chip capacitors with high specific capacitance. The capacitance value of a capacitor with predetermined size is increased primarily by decreasing the layer thickness and by increasing the number of actives.

In this paper, the effects of electric field conditions on the dielectric properties of lead magnesium niobate (PMN) and Barium Titanate (BT) based ceramics with Y5V characteristics are discussed. For this study, capacitors with dielectric thickness of 7 and 9 μm were used. The capacitors were made by standard production procedure. The average grain size of the PMN and BT ceramics were 2.0 and 1.5 μm , respectively.

Experimental Conditions

Capacitance and dielectric loss of the devices were measured using an HP 4284 unit (Hewlett-Packard, Rockville, MD), after soaking the test specimens in an environmental chamber (4220A, Saunders & Associates Inc., Scottsdale, AZ) at pre selected temperatures for 10 min. The measurements were recorded while the test samples were heated from -55°C to 85°C. The capacitance and d.f. were measured in parallel mode with varying a.c. signal @ 1 KHz.

D.C. Bias Effects

In Fig. 1 and 2, the effect of temperature and d.c. bias on the dielectric constant and dielectric loss of the PMN and BT based materials are shown. The dielectric constant (K) was calculated from the capacitance values measured with 1V a.c. signal. In both systems, increasing d.c. field increases T_{max} (temperature corresponding to peak K) and reduces the dielectric constant and the dielectric loss. In the BT system, higher peak broadening in K is observed.

In Fig. 3, the effect of d.c. bias on the dielectric constant of the two materials at 25°C is compared. As noted by several earlier researchers (Ref. 1-4), PMN-based compositions show markedly reduced field dependence as compared to the BT-based compositions.

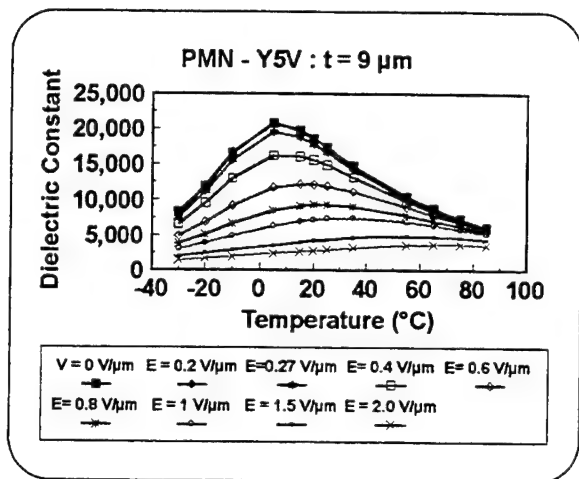


Fig. 1a. Dielectric constant of PMN based capacitor as a function of temperature and d.c. bias.

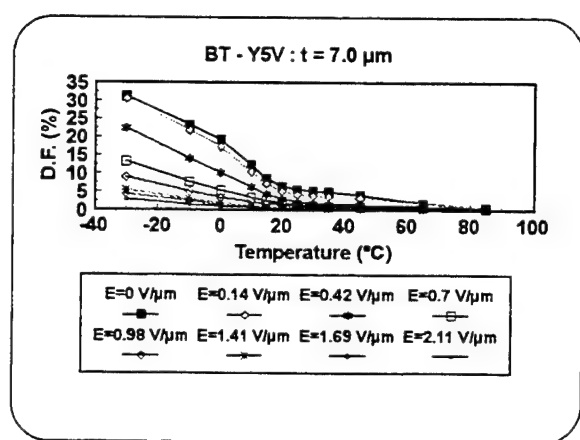


Fig. 2b. D.F. (%) of BT based capacitors as a function of temperature and d.c. bias.

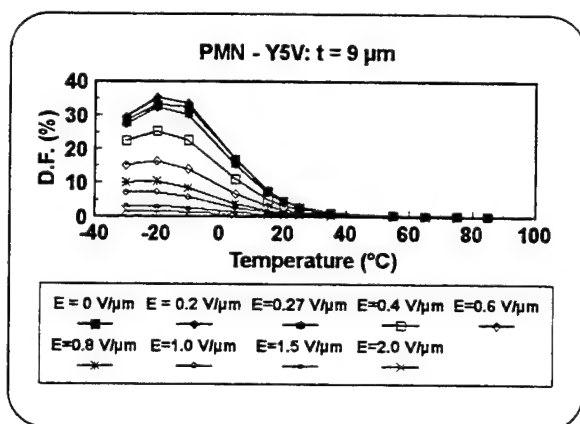


Fig. 1b. D.F. (%) of PMN based capacitors as a function of temperature and d.c. bias.

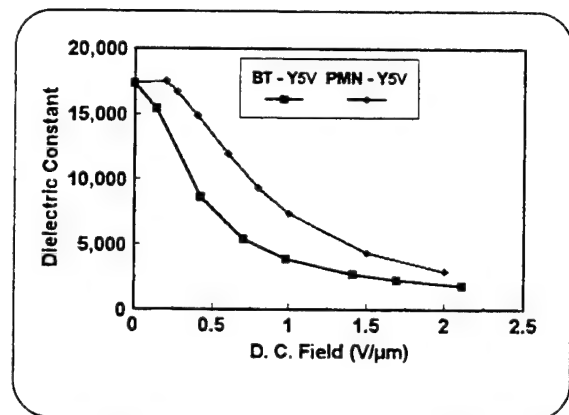


Fig. 3. Effect of d.c. field on room temperature dielectric constant of PMN & BT-based Y5V capacitors

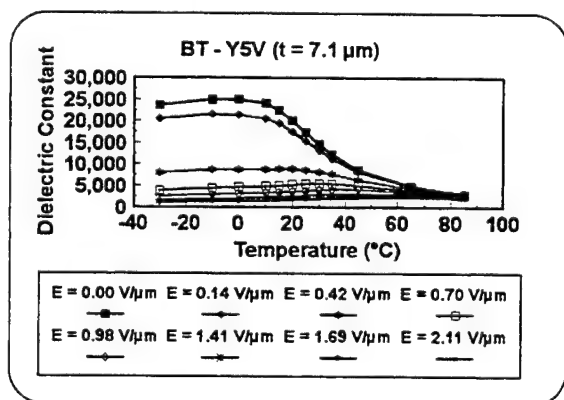


Fig. 2a. Dielectric Constant of BT based capacitor as a function of d.c. bias.

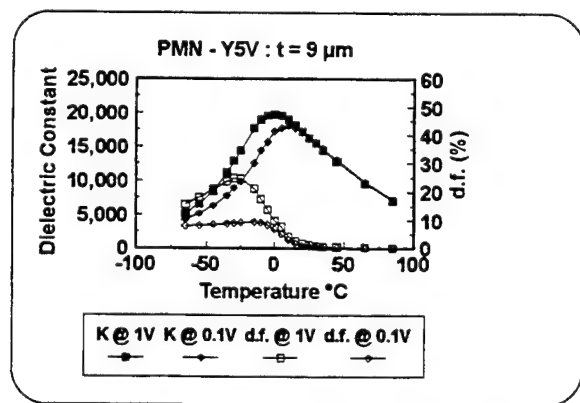


Fig. 4. Effect of a.c. signal on dielectric behavior of PMN capacitors.

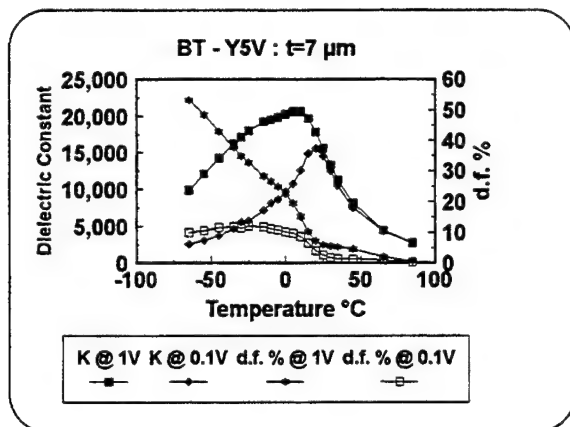


Fig. 5. Effect a.c. measurement voltage on the dielectric behavior of BT based capacitors.

A.C. Field Effect

In Fig. 4 and Fig. 5., the effect of temperature and the a.c. measuring signal on K and D.F. are plotted.

In both systems, increasing a.c. field shifts T_{max} to lower temperature. The peak temperature observed with $V_{a.c.} < 100$ mV is defined as small signal T_{max} . Below this temperature, higher a.c. signal increases both K and D.F., significantly. But these properties are relatively unaffected above T_{max} . To extend the understanding of a.c. field effect, to thinner layer devices, additional measurements were performed near small signal T_{max} with $V_{a.c.} = 10$ mV to 3V and the results are plotted in Fig. 6 and 7. In both systems, higher a.c. field shifts T_{max} to lower temperatures.

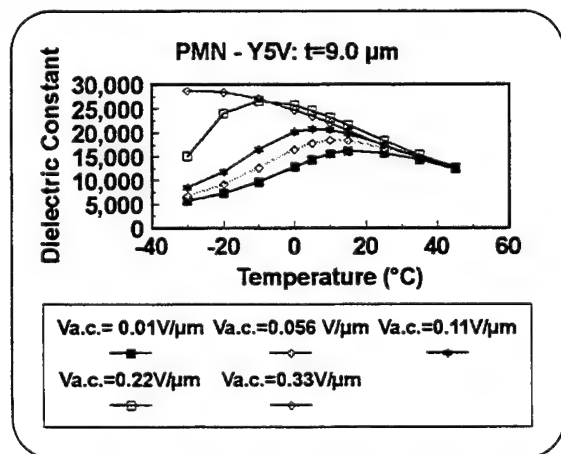


Fig. 6. Effect of a.c. field on the dielectric constant of PMN capacitors.

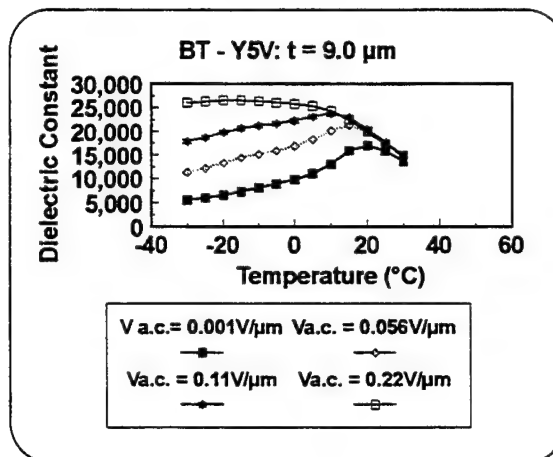


Fig. 7. Effect of a.c. field on the dielectric constant of BT based capacitors.

Discussion

The electronic industry association (EIA), categorizes capacitors into different classes based upon electrical properties. In Y5V capacitors, the capacitance can vary from +22% to -82% between temperatures from -30°C to +85°C. The variations are measured with reference to 25°C at a d.c. bias of 0V and an a.c. signal of 1V (Ref. 5). At present, d.f. < 5 % at 25°C is widely used as industry standard.

Figures 1 to 7 can be used to predict the properties of PMN and BT based capacitors as a function of dielectric thickness. For example, capacitors with $t = 5 \mu m$ will be subjected to an electric field of 0.2 V/ μm when tested at $V_{a.c.} = 1V$. At this test condition, the capacitance will increase by approximately 40% when measured below 25°C. The dielectric loss (Fig. 4 and 5) of PMN and BT capacitors at 25°C will be ~ 2% and ~ 5%, respectively. It is possible to alter the chemistry of the PMN system to shift T_{max} by ~ +8°C (Fig. 4), while keeping the D.F. below 5%. Thus, using 17°C as reference, the change in capacitance of a PMN capacitor is expected to be ~ +18%, which is well within the EIA specification.

Fig. 3., can be used to calculate the effect of the device operating d.c. voltage on the specific capacitance of thin devices. For the calculation, a 1210 style capacitor with a total thickness of 1.27 mm (50 mil) and a cover layer thickness of approximately 0.2 mm (8 mil) is considered. Excluding the electrode thickness, it is possible to produce capacitors with 188 and

130 active layers when the dielectric thickness is reduced to 3 and 5 μm , respectively. At 25° C and Vd.c.=0V, the specific capacitance of these devices will be 58 μF and 22 μF , respectively. In Fig. 8., the effect of d.c. operating voltage on the capacitance of the PMN and BT based capacitors is plotted. As the first order calculation, the effect of a.c. measurement voltage was ignored.

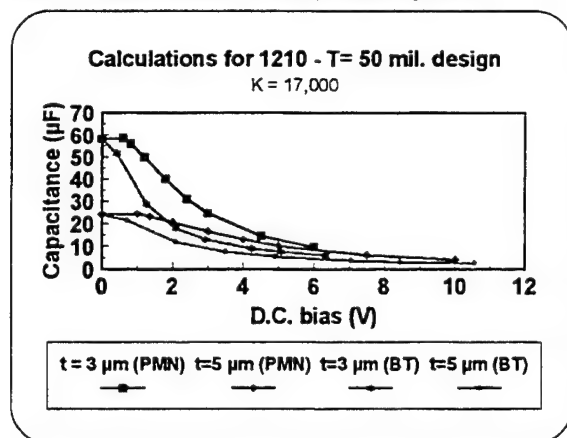


Fig. 8. Effect of d.c. field on room temperature capacitance (calculated)

As seen, at an operating voltage of 3.3V (which is becoming a standard for many digital electronic circuits), a 22 μF PMN-based capacitor will provide higher capacitance than a 58 μF BT-based capacitor.

CONCLUSIONS

A PMN-based composition with Y5V characteristics shows a reduced electric field sensitivity as compared to BT-based compositions. This effect can be utilized to prepare volumetrically efficient thin layer capacitors meeting EIA specifications.

REFERENCES

1. M. Yonezawa et al., " Properties of $\text{Pb}(\text{Fe}_{1/2}\text{W}_{1/2})\text{O}_3\text{-Pb}(\text{Fe}_{1/3}\text{Nb}_{2/3})\text{O}_3$ Ceramics," Proc. of 1st meeting on ferroelectrics and applications, p. 297 (1977).
2. J. P. Dougherty and T. R. Shrout, " Lead based $\text{Pb}(\text{B}_2\text{O}_3)\text{O}_3$ Relaxors vs. BaTiO_3 Dielectrics for Multilayer Capacitors," Proc. Symp. on Ceramic Dielectrics, Ed. H. C. Ling, Am. Ceram. Soc. (1989). (and the cited references)

3. H. Kanai, K. Harada, Y. Yamashita, and K. Handa, " Development of Large Capacitance Multilayer Ceramic Capacitors with Thin Dielectric Layers" CARTS 95: p. 9-14 (1995).

4. U. Kumar, H. Pak, B. Rawal, and M. Randall, "High Capacitance Value Multilayer Ceramic Capacitors from PMN based Dielectrics" CARTS 97: p. 286-291 (1997).

5. Electronic Industry Association (EIA) publication no. RS-198.

Manufacturing of Barium Titanium Powder by Oxalate Process

Morihito Nishido and Kenzo Harada

Research and Development Department, Electronic Material Division, Fuji Titanium Ind. Co., LTD
12-8 Sengen-cho, Hiratsuka-city, Kangawa-Prf., Japan

Abstracts

High purity stoichiometric barium titanate powders with fine and uniform particle size distribution to be used for multilayer ceramic capacitors (MLCs) have been manufactured commercially by an oxalate process under controlled process conditions, such as precipitation of oxalate and its calcination as well as milling of the calcination products.

Introduction

Barium titanates are widely used as a basic raw materials for ceramic capacitors. Recent trend of MLCs towards miniaturization with thinner dielectric layers and higher layer count requires high purity barium titanate with fine particles. To meet such requirements, wet chemical processes, such as oxalate process, sol-gel process, hydrothermal process, and alkoxide process, etc. have been developed. Among these, the oxalate process has several advantages in view of process economy, chemical purity and stoichiometry of the product.

In this process, barium titanyl oxalate, which is the intermediate product of the process, must be calcined carefully to achieve barium titanate of good crystallinity and appropriate particle size. Since the calcination tends to cause agglomerated particles, it is also necessary to disintegrate such agglomerates by pulverization.

This paper presents the overview of our oxalate process, and effects of process conditions on the product properties are discussed.

Manufacturing process

Barium chloride ($\text{BaCl}_2 \cdot 2\text{H}_2\text{O}$), aqueous solution of Titanium tetrachloride ($\text{TiCl}_4/\text{H}_2\text{O}$) and Oxalic acid dihydrate ($\text{H}_2\text{C}_2\text{O}_4 \cdot 2\text{H}_2\text{O}$) are used as starting raw material. $\text{BaCl}_2 \cdot 2\text{H}_2\text{O}$ and $\text{TiCl}_4/\text{H}_2\text{O}$ are dissolved in deionized water and mixed. Then the mixed solution is added to aqueous solution of oxalic acid to form precipitates of barium titanyl oxalate tetrahydrate (BTO). The precipitate (BTO) is washed and filtered. The BTO is calcined and then pulverized to obtain barium titanate powder.

Fig.1 shows our oxalate process, which is basically the same as that reported by Clabaugh et al³⁾.

Barium Titanyl Oxalate

By adjusting process conditions, such as concentrations of aqueous solutions of Ba^{2+} - Ti^{4+} and oxalic acid, mixing ratio of Ba:Ti : Oxalic acid, temperature of the solution and rate of mixing (reaction time), the coprecipitate BTO with particle size of $5\text{--}200\ \mu\text{m}$ can be obtained. Stoichiometric BTO can be precipitated by mixing each solutions at Ba:Ti:Oxalic Acid=1.05:1:2.2 by mole⁴⁾. The crystallinity (tetragonality) and agglomeration of barium titanate formed after calcination depend, to some extent, upon the aging of the precipitated

BTO and degree of its washing.

We applied technique of experimental design, to find optimal combination of process conditions to manufacture barium titanates of required properties consistently.

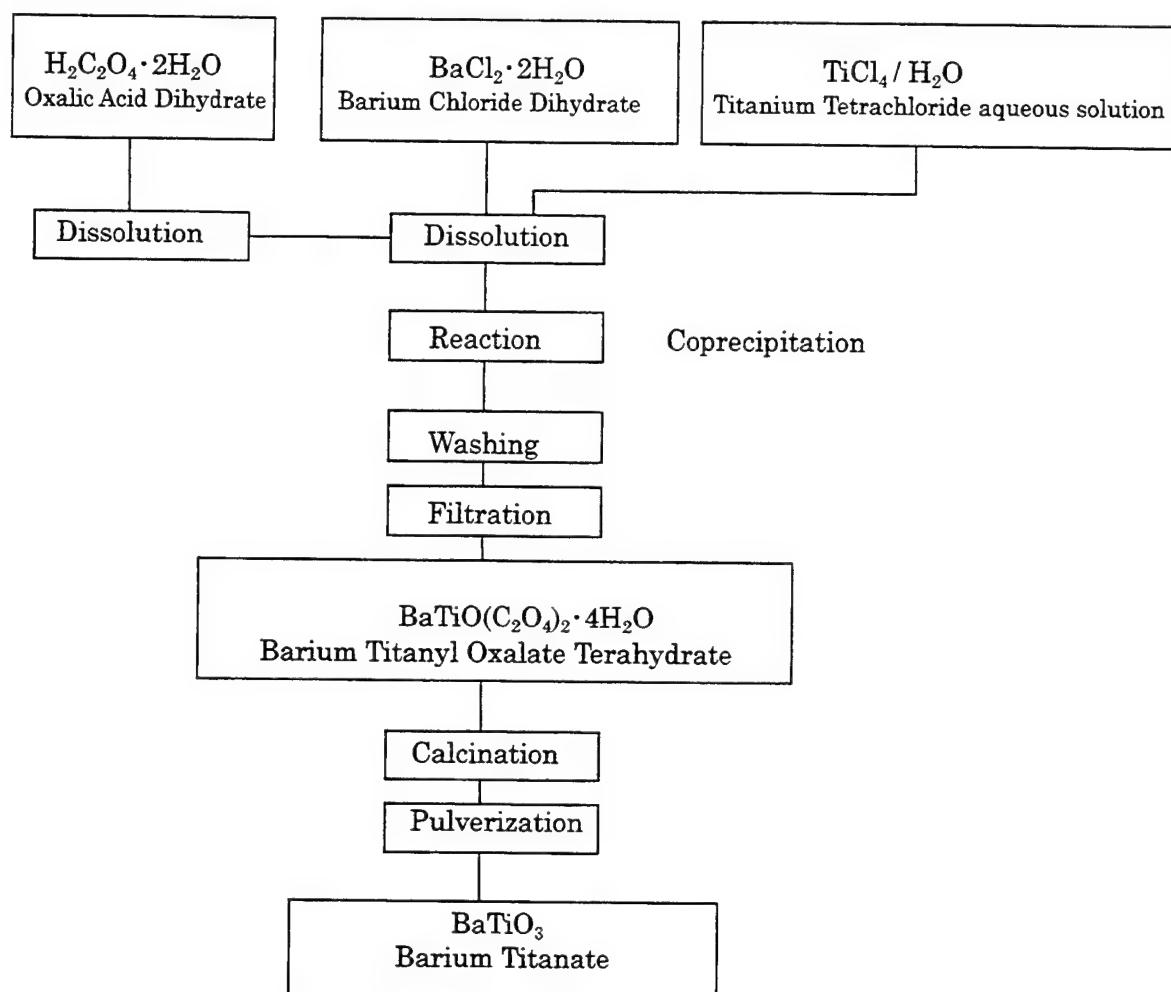
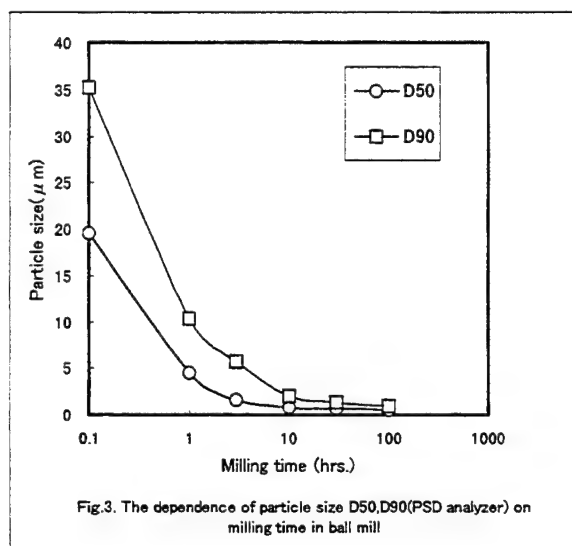
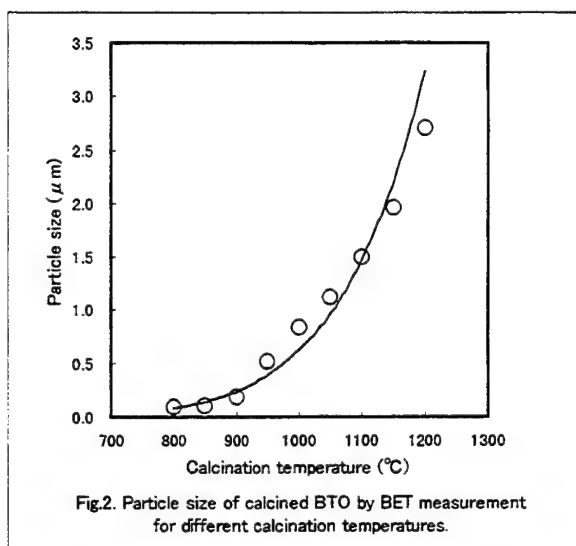


Fig.1 Flow chart for manufacturing process of barium titanate by oxalate process

Calcination

The formation of barium titanate is assumed to start at a temperature above 720°C by the reaction between amorphous BaCO₃ and TiO₂, which are formed by decomposition of BTO. The formation reaction is completed above 800°C⁶. The particle size of formed barium titanate increases with increasing calcination temperature and Fig.2 shows the dependence of the particle size, measured by BET method, on the calcination temperature. Barium titanates of various particle sizes can be produced by controlling the calcination conditions.

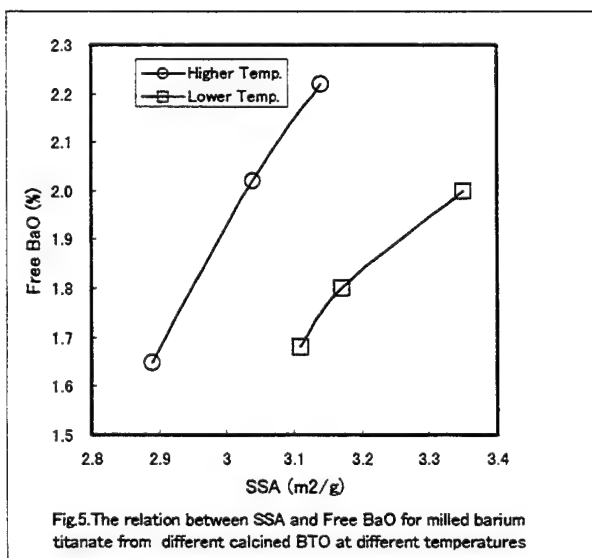
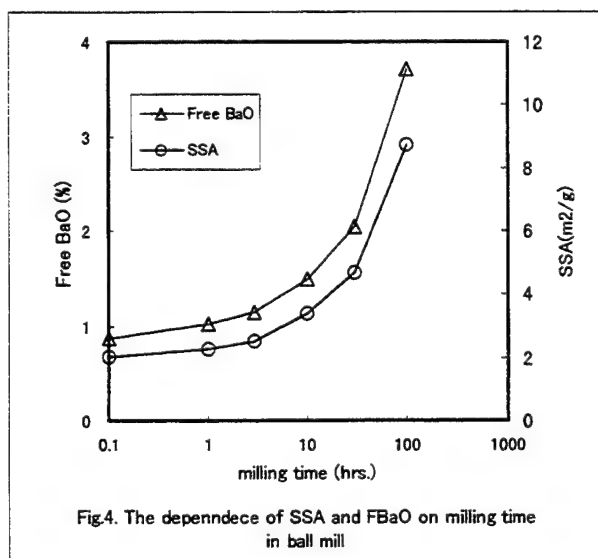
Since the barium titanates obtained by calcination of BTO contains agglomerated particles, the calcined barium titanates need to be pulverized to eliminate such agglomerates.



Pulverization

Fig.3 shows the dependence of particle size, expressed by D50 and D90(Microtrac PSD Analyzer), on milling time by ball mill. Both D50 and D90 decrease with increasing milling time and especially D90, which reflects the presence of agglomerates, becomes very close to D50 at 10 hrs of milling time, indicating the elimination of agglomerates.

Fig 4 shows that specific surface area (SSA, measured by BET method) and Free BaO(Acetic acid soluble BaO) also increase with the milling time. These facts suggest that the barium titanate becomes under severe mechanochemical reaction by extensive milling over 10 hrs.



Summary

Commercial process of manufacturing high purity and stoichiometric barium titanate with controlled particle size via oxalate route has been established.

1. Barium titanyl oxalate, precursor of barium titanate, with consistent chemistry and physics can be prepared under optimized process conditions.
2. Barium titanate of fine particle size without agglomerates can be prepared under controlled calcination and subsequent milling.

Table 1. Typical Barium Titanate Powder HPBT-1 by Oxalate Process

Chemical Analysis

| | |
|--------------------------------|---------|
| Ba/Ti Mol Ratio | 0.997 |
| SrO | 0.04 % |
| SiO ₂ | 0.004 % |
| Al ₂ O ₃ | 0.003 % |
| Na ₂ O | 0.002 % |
| Fe ₂ O ₃ | 0.002 % |

Physical Analysis

| | | |
|---------|------|-------------------|
| SSA | 3.07 | m ² /g |
| PS(BET) | 0.33 | μm |
| PSD D10 | 0.35 | μm |
| D50 | 0.62 | μm |
| D90 | 1.21 | μm |

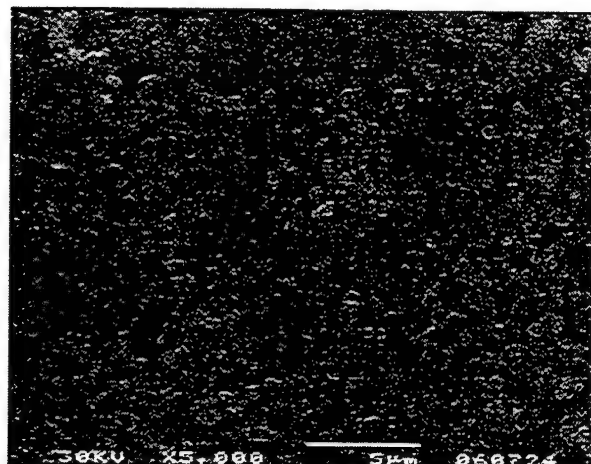


Fig.6 SEM Photomicrograph of HPBT-1

Acknowledgments

The authors are grateful to K.Sasaki for helpful discussions and supports.

References

- 1) A.D. Hilton , et al, "Recent Developments in the Manufacture of Barium Titanate Powders", Key Engineering Materials Vols. 66 & 67(1992) pp.145-184
- 2) Katuya Kudaka , et al "Some Observation on the Aggregate Particles Produced during Pyrolysis of PTC Barium Titanate Precursor Synthesized by the Oxalate Method", Journal of the Ceramic Society of Japan 102 [5] 449-501 1994
- 3) W.Stanley Clabaugh , et al "Preparation of Barium Titanyl Oxalate Tetrahydrate for Conversion to Barium Titanate of High Purity.", Journal of Research of the National Bureau of Standards, vol.56, No.5, May 1956
- 4) K.Kudaka, et al, "Preparation of Stoichiometric Barium Titanyl Oxalate Tetrahydrate", J.Am.Ceram.Soc., 61,1236(No.11,1982)
- 5) Tsang-Tse Fang, et al, "Factor affecting the Preparation of Barium Titanyl Oxalate Tetrahydrate", J.Am.Ceram.Soc., 72[10] 1899(1989)
- 6) K.Kudaka, et al, "Thermal Decomposition of Barium Titanium Oxalate and the Formation of Barium Titanate" Journal of the Ceramic Society of Japan, 92[1] 1984

Use Of Low Fire BaTiO₃ Dielectrics In The Manufacture Of MLCCs

S.P.Gupta and Larry Mann

Kemet Electronics Corporation
P.O.Box 847
201 Fairview Street Extension
Ft.Inn, S.C. 29644-0847 USA

ABSTRACT

Y5V multilayer ceramic capacitors (MLCC) with high capacitance values for surface mount applications have been developed using low fire BaTiO₃ base dielectric materials. The compositions are formulated by the addition of shifters and depressors. Reactive sintering aids are selected and added to the dielectric formulation to sinter the dielectric at lower temperature in order to utilize low cost silver/palladium electrodes. The reactive sintering aid also increases the mechanical strength which makes surface mount capacitors less susceptible to damage due to mechanical or thermal stresses during the assembly process. The electrical and mechanical properties of different sizes of MLCC made with a Y5V dielectric formulation are discussed.

INTRODUCTION

The demand for miniaturized surface mount multilayer ceramic capacitors (MLCC) has impelled manufacturers to develop ceramic materials that offer both volumetric efficiency and thermal/mechanical robustness. In the US, the 0603 (0.060 x 0.030 inches) chip size is rapidly replacing the 0805 chip (0.080 x 0.050) and 1206 chip (0.12 x 0.060) as the most popular in the industry. The smaller chip size 0402 (0.040 x 0.020) is now available. This transformation has been made possible by the development of materials that possess both high dielectric constant and sufficient mechanical strength to withstand the various mechanically and thermally induced stresses associated with the manufacture of surface mount circuit assemblies. The development of a family of low-fire barium titanate materials that meet the Electronics Industries Association (EIA) specifications for Y5V dielectrics is discussed below.

BACKGROUND

A key characteristic of an MLCC is the interleaving of the dielectric and electrode materials, which are cofired into a monolithic structure as shown in Figure 1.

Barium titanate continues to be the backbone of most ceramic dielectrics used in the manufacture of ceramic capacitors. By itself barium titanate sinters at 1400 °C, which would require expensive, pure palladium electrodes to successfully manufacture MLCC. It also has its highest K at 130 °C and has much lower K at room temperature (see figure 2).

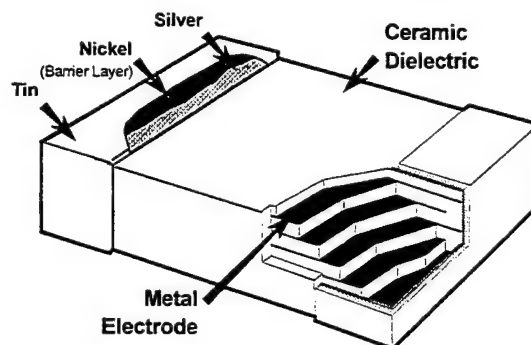


Fig. 1 Typical Multilayer Ceramic Chip Construction

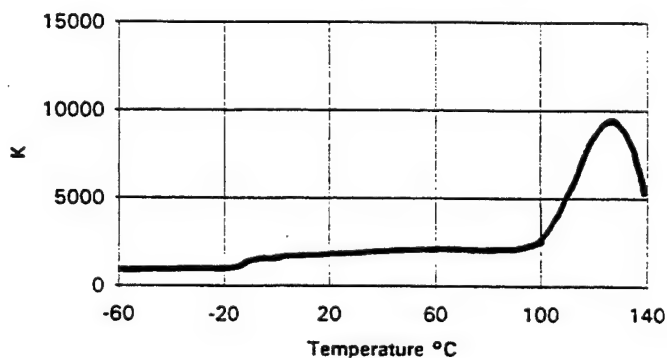


Fig. 2 K vs Temperature for Barium Titanate

The barium titanate crystal structure can be modified with small amounts of other cations which replace the barium and titanium cations in the crystal lattice to modify the temperature coefficient of capacitance into a more usable shape. Several specifications have been defined. In general the less temperature stable the capacitance, the higher the capacitance that can be achieved. Figure 3 shows the relationship between K and temperature and figure 4 shows the percentage change in capacitance vs temperature for the most important types of capacitors that are manufactured today.

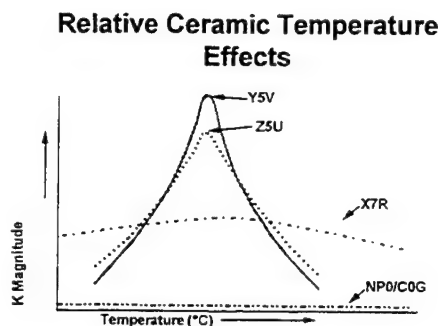


Fig. 3 K vs Temperature for Major Capacitance Types

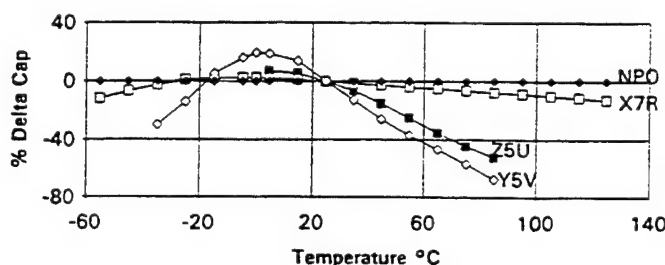


Fig. 4. Temperature Coefficient Of Capacitance For Major Capacitor Types

A high purity, fine particle size barium titanate was used, as the basis for an improved Y5V dielectric. Several types of shifters such as CaZrO_3 , BaZrO_3 , SrZrO_3 , CaSnO_3 , and BaSnO_3 were added to shift its Curie point from 130°C to around 10°C . The composition was further enhanced with MgZrO_3 , CaTiO_3 to flatten the TCC curve. Modifiers such as CeZrO_3 , MnO_2 , Nb_2O_5 were added to minimize dissipation factor and maximize insulation resistance. In order to sinter the dielectric formulation at less than 1150°C , two types of reactive sintering aids were added to the dielectric formulation. This allowed the use of 30% Pd/ 70% Ag electrodes, reducing the cost very significantly compared to using 100% palladium electrodes. Using the right type of sintering aids also enhanced the mechanical strength of the ceramic. This is an important consideration in developing low fire dielectrics for use in surface mount ceramic capacitors.

EXPERIMENTAL

The dielectric formulation consisting of BaTiO_3 and various additives was wet milled with a dispersing agent in a Sweco vibratory mill for 15 to 20 hours to reduce the particle size to < 0.7 microns. The milled slurry was mixed with an

aqueous binder system and coated 13 to 14 microns thick on a polymer carrier. Green chips were manufactured in a clean room (class 10,000) environment in order to ensure high reliability. The process involved screen printing electrode patterns using 30% Pd/70% Ag ink. The printed layers were stacked, laminated, and then diced into individual chips. The green chips then went through a binder bake-out process with a max temperature of 600°C and a duration of 50 hours. The chips were fired using a batch kiln in a crucible with a layer of Zirconia sand at temperatures from 1130°C to 1140°C for 3 to 4 hours soak time. The fired parts were corner rounded, silver terminated and then plated with nickel and tin. Figure 5 summarizes the processing steps. The capacitance, DF, TC, and IR of the fired chips were measured. Modulus of rupture was measured using a three-point bend test with a sample size of 30 chips. The reliability of the chips was assessed using several standard tests, including load life, load humidity, and HALT.

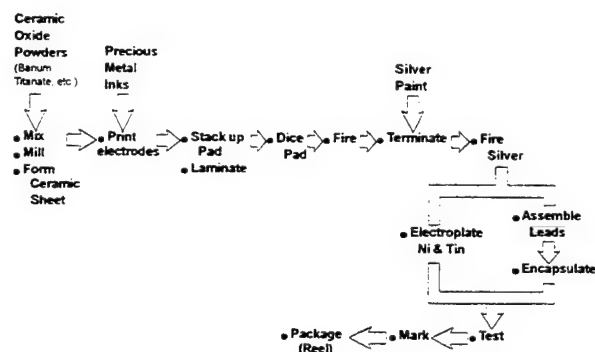


Fig. 5 Ceramic Capacitor Manufacturing Process

RESULTS AND DISCUSSIONS

The electrical properties of the typical Y5V MLCC are summarized in Table I.

TABLE I

Typical electrical properties of Y5V MLCC

| | |
|--------------------|----------------------|
| K | 11,000 to 12,000 |
| DF (1v) | < 5% |
| -30 °C TCC | - 15% |
| 10 °C TCC | 20% |
| 85 °C TCC | -66% |
| IR @ 25 °C | > 30,000 ohm -F |
| IR @ 85 °C | > 3,000 ohm -F |
| Aging Rate | 2.4% per decade |
| Breakdown Voltage | 20,000 volts per mm. |
| Modulus of rupture | > 400 MPa |

From the Table I it can be seen that the chips had K's of 11,000 and DFs of < 5% (1 volt). The TCC was well within the Y5V specification. The IRs were > 30,000 ohm -F at 25 ° C and > 3000 ohm -F at 85 ° C. The aging rate was quite low (2.4% per decade) for a high K dielectric.

A photomicrograph of the fractured surface, which has been thermally etched, and also the cross-sections of 0603 chips are shown in figures 6 and 7.

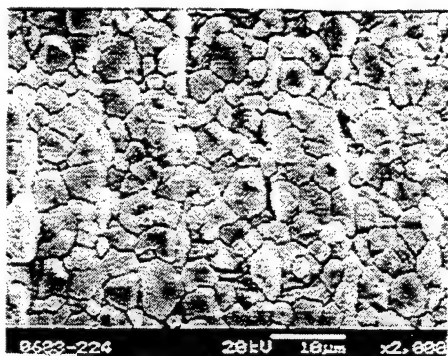


Fig. 6. Microstructure of Thermally etched Y5V 0603 Chips

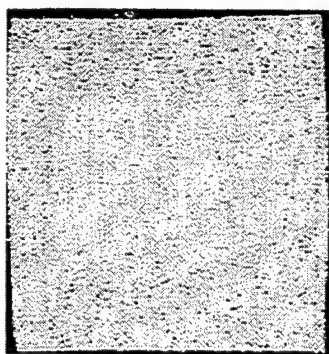
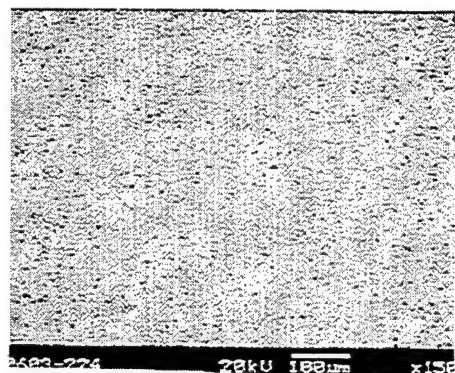


Fig. 7. Cross - sections of Y5V 0603 chips

Figure 7 show the photomicrographs of cross sections of the typical 0603 chips, demonstrating uniform electrode stacking and precision dicing.

The typical TCC curve of the Y5V MLCC is shown in figure 8.

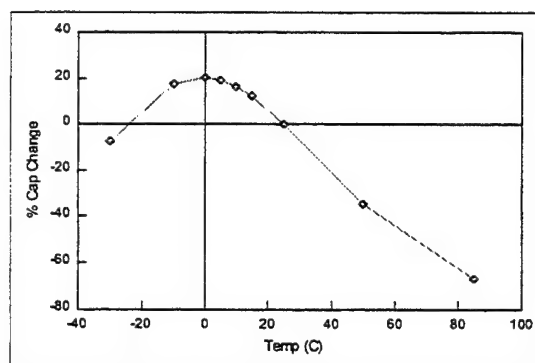


Fig. 8. Temperature Coefficient of Y5V Chips

Figure 9 shows impedance and ESR vs frequency and figure 10 shows % capacitance change and DF vs AC and DC bias.

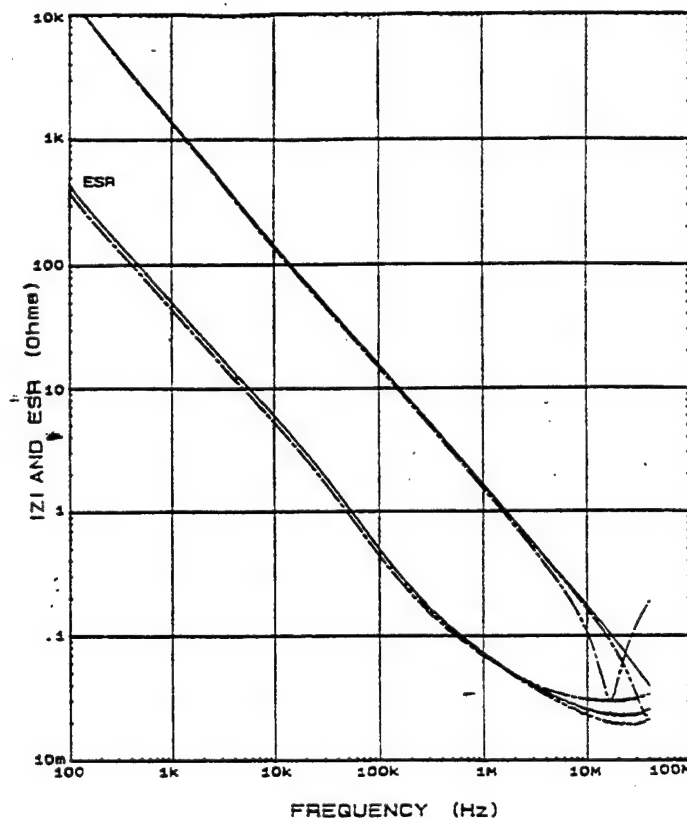


Fig. 9. Impedance and ESR vs Frequency for Y5V Chips

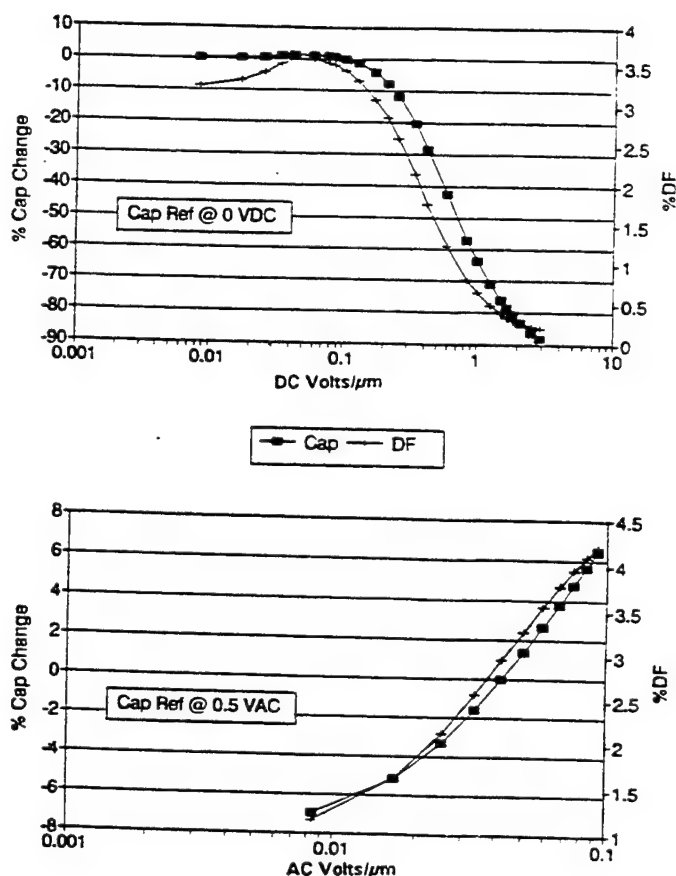


Fig. 10. Cap and DF vs DC and AC Bias

Figure 11 shows a typical distribution of breakdown voltages of the 1206 2.2 uF chips, demonstrating consistent dielectric thickness and uniformity. The low porosity and the mixed grain size (2 to 5 microns) as shown in figures 6 and 7 were responsible for the high breakdown voltage and high mechanical strength. These two properties led to good mechanical reliability.

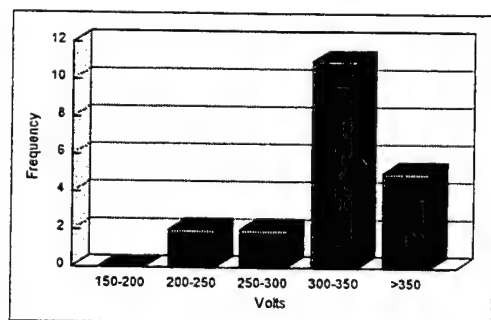


Fig. 11. UVBD of Y5V Chips

Table II summarizes important properties and characteristics of the 0603 0.22 uF, 0805 1.0 uF, and 1206 2.2 uF chips. The 0603 was rated at 25 volts and the 0805 and 1206 products were rated at 16 volts because of the life test and HALT test performance. The DF measured at 1 volt was < 5%. All chips exhibited the Y5V TCC characteristics. The IRs at 25 °C and 85 °C were very good. The aging rate was 2.4% per decade. The chips performed very well in life test, load humidity, and HALT. The actual fired dielectric thickness for these products was 9 microns. Overall the chips had outstanding electrical characteristics, high mechanical strength, and high breakdown voltage. These properties are especially significant in light of its relatively large grains size (2 to 5 microns). The modulus of rupture is higher than that of most X7R dielectrics. These characteristics make it an ideal material for manufacturing high capacitance surface mount capacitors.

TABLE II

| Typical Electrical Properties Of Y5V Chips | | | |
|--|-----------------|-----------------|-----------------|
| | 0603-224 | 0805-105 | 1206-225 |
| Chips Dim. (mm) | 1.6 x 0.8 x 0.8 | 2.0 x 1.2 x 1.2 | 3.2 x 1.6 x 1.1 |
| Cap (uF) | 0.22 +/- 20% | 1.0 +/- 20% | 2.2 +/- 20% |
| DF (1 volt) | < 5% | < 5% | < 5% |
| Voltage Rating | 25V | 25V | 25V |
| TCC | Y5V | Y5V | Y5V |
| Fired dielectric thickness | 9 micron | 9 micron | 9 micron |
| Firing Temperature | 1135°C | 1135°C | 1135°C |
| Electrode Ink | 30Pd/ 70Ag | 30Pd/ 70Ag | 30Pd/ 70Ag |
| Aging rate | 2.4% decade | 2.4% decade | 2.4% decade |
| Life Test @ 2xVr, (85°C, 2000hrs) | 0/50 | 0/50 | 0/50 |
| Load Humidity @ Vr (85% RH, 1000hrs) | 0/50 | 0/50 | 0/50 |
| HALT @ 8xVr, (125°C, 8 hrs) | 0/50 | 0/50 | 0/50 |

CONCLUSIONS

A high K, low fire Y5V barium titanate based dielectric with excellent mechanical properties has been developed that is compatible with 30% Pd/ 70% Ag electrodes. Using this dielectric formulation, it is now possible to manufacture 0603 0.22 uF, 0805 1.0 uF, and 1206 2.2 uF chips with Y5V characteristics. The reliability is excellent and the breakdown voltage is very high. With all these excellent properties this dielectric makes an ideal material for the manufacture of surface mount multilayer ceramic capacitors.

Preparation of Barium Strontium Titanates by Vapor Phase Hydrolysis of Precursors Via Modified Alkoxide Route

T.Hayashi, K.Sunaga, S.Satoh, H.Satoh, Department of Materials Science and Ceramic Technology, Shonan Institute of Technology, Fujisawa, Japan; K.Sasaki, former Research Associate at DuPont

Abstract

Methanol solutions of Ba and Sr hydroxides are reacted with Ti-isopropoxide at room temperature, and then dried under reduced pressure at $\leq 40^\circ\text{C}$ to form powder precursors. The resulting precursors are hydrolyzed by introducing nitrogen gas containing water vapor at $\geq 100^\circ\text{C}$. The hydrolyzed product are highly crystalline nano size powders of $(\text{Ba}_{1-x}\text{Sr}_x)\text{TiO}_3$ solid solution with specific surface areas of 40-70 m^2/g .

I. Introduction

BaTiO_3 and its related ceramics are of interest owing to their ferroelectric and dielectric properties. These ceramics are widely used in the main electroceramic components such as multilayer capacitors, PTC resistor and piezo electric transducers.

BaTiO_3 powders have been prepared by various methods such as coprecipitation¹⁾, oxalate²⁾, sol-gel^{3,4)} and hydrothermal synthesis⁵⁾.

Preparation of BaTiO_3 by sol-gel with alkoxides has been studied over more than two decades. However, the process has rarely been used to prepare titanates even for research purpose, because of the instability of alkoxides and complexity of the processing.

It is very useful to use BaO and $\text{Ba}(\text{OH})_2$, which are soluble in methanol, as a barium source instead of expensive and unstable Ba or Sr alkoxide. We reported the preparation of BaTiO_3 powders by the hydrolysis of a Ba-Ti solution, which was obtained by mixing titanium isopropoxide and a methanol suspension of barium hydroxide⁶⁾.

Our objective is to develop a simple and economical preparation method of $(\text{Ba}_{1-x}\text{Sr}_x)\text{TiO}_3$ powders by

utilizing the reaction of methanol solution of Ba and/or Sr hydroxides with Ti-alkoxide.

II. Experimental

$\text{Ba}(\text{OH})_2 \cdot 8\text{H}_2\text{O}$ and $\text{Sr}(\text{OH})_2 \cdot 8\text{H}_2\text{O}$ were dehydrated by heating at 300°C for 3h. Then, the anhydrous hydroxides were dissolved in methanol, and filtered with an Ultra filter to remove undissolved hydroxides and other impurities. After the filtration, the concentrations of hydroxides were determined by titration. The concentrations of $\text{Ba}(\text{OH})_2$ and $\text{Sr}(\text{OH})_2$ were adjusted to 0.5mol/L and 0.25mol/L, respectively.

The methanol solutions of barium and strontium hydroxides were mixed at a desired ratio, and then mixed with stoichiometric amount of Ti isopropoxide and stirred overnight at room temperature. After the reaction at room temperature, methanol was evaporated under reduced pressure at $\leq 40^\circ\text{C}$ using a rotary evaporator. Thus the precursors were obtained as free flowing white powders.

The precursor was hydrolyzed by introducing N_2 gas containing water vapor into the rotary evaporator at $\geq 100^\circ\text{C}$. This was done by bubbling the N_2 gas through DI water. The precursors and hydrolyzed products were examined by TG/DTA and XRD. The whole process is shown in Fig.1.

In this work, $(\text{Ba}_{1-x}\text{Sr}_x)\text{TiO}_3$ powders with $x=0\sim 1.0$ were prepared. Some hydrolyzed powders were calcined at 900°C . After grinding the calcined powders overnight in alcohol, these were pressed into disks and sintered at 1250, 1300 and 1350 $^\circ\text{C}$ for 2h. Electrical properties were measured for the sintered disks.

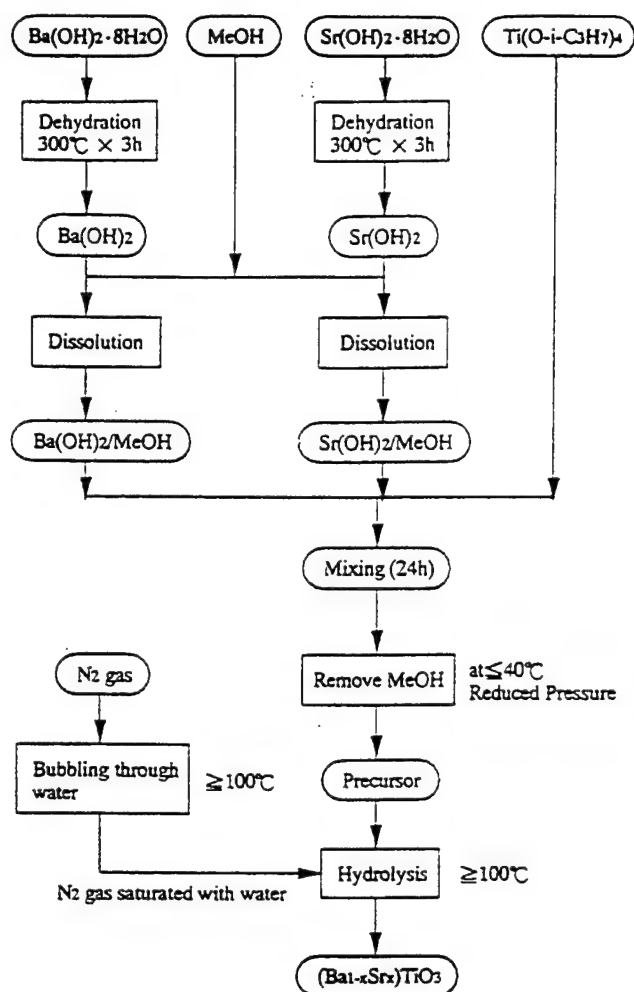


Fig.1 Flow Diagram of Preparation of $(\text{Ba}_{1-x}\text{Sr}_x)\text{TiO}_3$ Powders by Vapor Phase Hydrolysis.

III. Results and Discussion

1. $(\text{Ba}_{1-x}\text{Sr}_x)\text{TiO}_3$ Precursor Powders

The precursor powders were amorphous and showed weight loss of about $30 \pm 2\%$ at $\sim 1000^\circ\text{C}$ by TG. The hydrolysis of the precursor in water did not result in the formation of BaTiO_3 . The resulting product recovered by filtration was almost amorphous and gave Ba:Ti mole ratio close to 1:2 by ICP, indicating dissolution of Ba ion into water. On the other hand, by vapor phase hydrolysis of the precursor, crystalline barium titanate could be obtained. Figure 2 shows TG/DTA of the precursor and the hydrolyzed product.

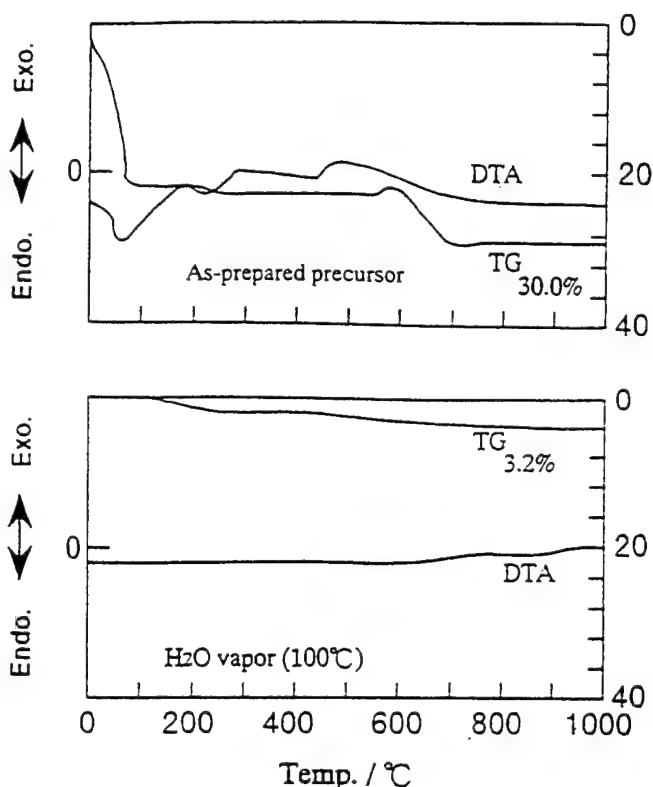


Fig.2 TG/DTA Curves of Precursor and Hydrolysis Products.

By calcining at 400°C , the precursor became black in color due to charring of the organics in it, resulting in the formation of barium carbonate confirmed by XRD. The precursor became pseudo cubic barium titanate by calcining at 600°C and transformed to tetragonal phase at 1000°C or higher.

2. Hydrolyzed $(\text{Ba}_{1-x}\text{Sr}_x)\text{TiO}_3$ Products

$(\text{Ba}_{1-x}\text{Sr}_x)\text{TiO}_3$ powders prepared by hydrolysis of the precursor were dried at 120°C for several hours to remove absorbed water. SEM micrographs of as-hydrolyzed $(\text{Ba}_{1-x}\text{Sr}_x)\text{TiO}_3$ powders are shown in Fig.3. The particle sizes are very small and less than 100nm.

Specific surface areas of as-hydrolyzed $(\text{Ba}_{1-x}\text{Sr}_x)\text{TiO}_3$ powder are summarized in Table 1. The values varied from about $40\text{m}^2/\text{g}$ to over $70\text{m}^2/\text{g}$, probably depending upon hydrolysis conditions, such

as temperature and partial pressure of water vapor. The values are in good coincidence with the particle sizes shown in the SEM pictures.

The as-hydrolyzed $(\text{Ba}_{1-x}\text{Sr}_x)\text{TiO}_3$ powders showed high crystallinity with cubic phase and the XRD peak angles shifted to higher angles with increasing Sr content in the $(\text{Ba}_{1-x}\text{Sr}_x)\text{TiO}_3$.

By calcination, the peaks became more sharp. But, at 900°C , the calcined BaTiO_3 powders were still cubic. Lattice constants were calculated for both as-hydrolyzed $(\text{Ba}_{1-x}\text{Sr}_x)\text{TiO}_3$ powders and those calcined at 900°C after hydrolysis. Both of them were plotted against Ba content (mole ratio) of $(\text{Ba}_{1-x}\text{Sr}_x)\text{TiO}_3$ powders as shown in Fig.4. The values calculated from JCPDS cards are also shown as black dots in Fig.4.

Both lattice constants decreased with increasing Sr content and those for calcined products showed good coincidence with the data from JCPDS, indicating the products are homogeneous solid solution of Ba and Sr titanates. The lattice constants of hydrolyzed products were larger than those for calcined products, suggesting expanded structures probably due to the presence of OH group. The Curie temperature of the sintered $(\text{Ba}_{1-x}\text{Sr}_x)\text{TiO}_3$ are also plotted in Figure 4.

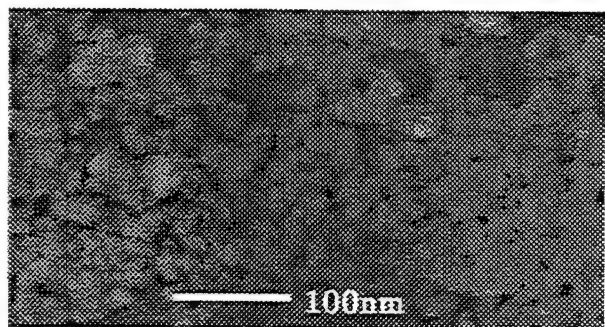
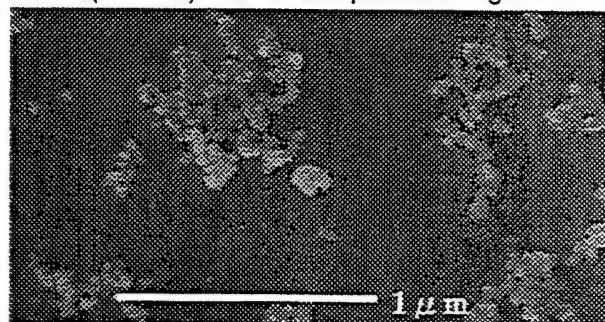


Fig.3 SEM Micrographs of As-hydrolyzed BaTiO_3 Powders.

Table 1 Specific Surface Areas of As-prepared $(\text{Ba}_{1-x}\text{Sr}_x)\text{TiO}_3$ Powders.

| | SSA(m^2/g) |
|--|------------------------------|
| BaTiO_3 | 58.7 |
| $\text{Ba}_{0.8}\text{Sr}_{0.2}\text{TiO}_3$ | 67.1 |
| $\text{Ba}_{0.7}\text{Sr}_{0.3}\text{TiO}_3$ | 75.7 |
| $\text{Ba}_{0.6}\text{Sr}_{0.4}\text{TiO}_3$ | 44.4 |
| $\text{Ba}_{0.5}\text{Sr}_{0.5}\text{TiO}_3$ | 41.4 |
| $\text{Ba}_{0.3}\text{Sr}_{0.7}\text{TiO}_3$ | 54.3 |
| $\text{Ba}_{0.2}\text{Sr}_{0.8}\text{TiO}_3$ | 53.4 |
| SrTiO_3 | 63.7 |

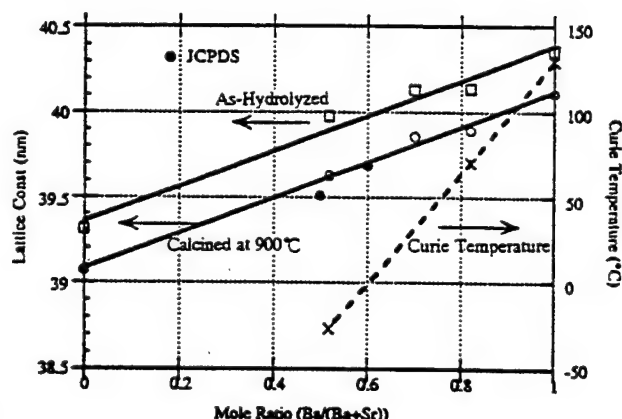


Fig.4 Lattice Constant & Curie Temperature vs Mole Ratio $\{\text{Ba}/(\text{Ba}+\text{Sr})\}$.

3. Microstructure and Dielectric Constant

SEM micrographs of the BaTiO_3 and $(\text{Ba}_{0.5}\text{Sr}_{0.4})\text{TiO}_3$ bodies sintered at 1250°C are shown in Fig.5. BaTiO_3 sintered bodies exhibited relatively homogeneous microstructure with grain sizes of $300\sim 400\text{nm}$. On the other hand, $(\text{Ba}_{0.5}\text{Sr}_{0.4})\text{TiO}_3$ sintered bodies exhibited the heterogeneous microstructure with abnormally grown grains.

Figure 6 shows the temperature dependence of dielectric constants of $(\text{Ba}_{1-x}\text{Sr}_x)\text{TiO}_3$ ceramics. The dielectric constants of sintered bodies increased with increase of sintering temperature. The Curie temperatures shifted to lower temperature with increasing Sr content.

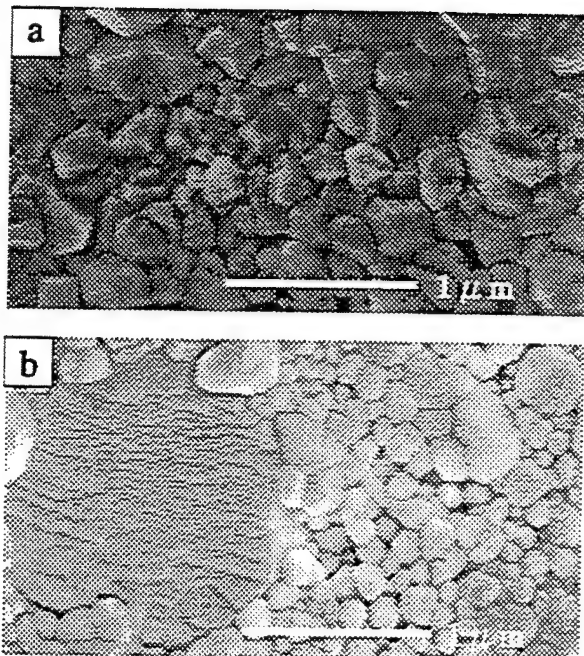


Fig.5 SEM Micrographs of Bodies Sintered at 1250°C for 2h.
(a) BaTiO₃ (b) (Ba_{0.6}Sr_{0.4})TiO₃

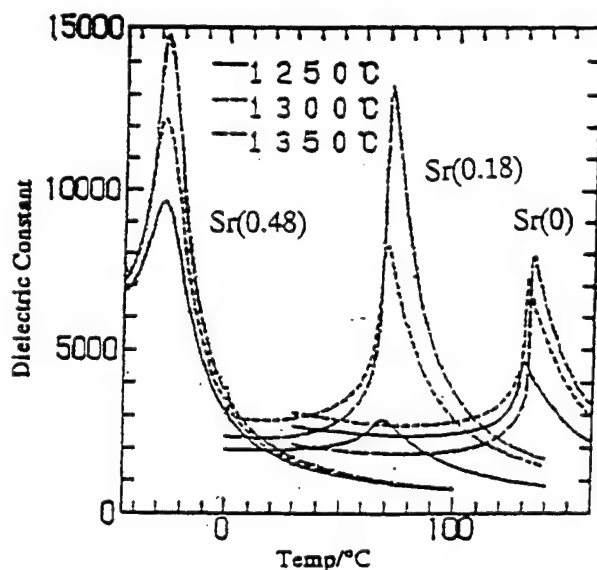


Fig.6 Temperature Dependence of Dielectric Constants of (Ba_{1-x}Sr_x)TiO₃ Sintered Bodies.

IV. Conclusions

Precursors for (Ba_{1-x}Sr_x)TiO₃ have been prepared by reacting the mixture of methanol solutions of Ba and Sr hydroxides with Ti-isopropoxide.

By vapor phase hydrolysis of the precursors, highly crystalline nano size (Ba_{1-x}Sr_x)TiO₃ powders have been prepared successfully.

The calculated lattice constants of (Ba_{1-x}Sr_x)TiO₃ were in good coincidence with those calculated from JCPDS data.

The Curie temperatures of (Ba_{1-x}Sr_x)TiO₃ sintered bodies shifted to lower temperature with increasing Sr content.

References

1. A. I. Savos'kina, et al, "Formation of BaTiO₃ from Coprecipitation Products", *Izv. Akad. Nauk. SSSR, Neorg. Mater.*, 11 [12] 2245 (1975).
2. T. T. Fang, H. B. Lin, "Factors Affecting the Preparation of Barium Titanate Tetrahydrate", *J. Am. Ceram. Soc.*, 72 [10] 1899-906 (1989).
3. K. S. Mazdiyashi, et al, "Preparation of High-Purity Submicron Barium Titanate Powders", *J. Am. Ceram. Soc.*, 52 [10] 523-26 (1969).
4. F. Chaput, J. P. Boilot, "Alkoxide-Hydroxide Route to Synthesize BaTiO₃-Based Powders", *J. Am. Ceram. Soc.*, 73 [4] 942-48 (1990).
5. D. Hennings, S. Schreinemacher, "Characterization of Hydrothermal Barium Titanate", *J. Europ. Ceram. Soc.*, 9, 41-46 (1992).
6. Takashi Hayashi, et al, "Chemical Processing and Dielectric Properties of BaTiO₃ Ceramics", *J. Am. Ceram. Soc.*, Vol.51, 733, 1995.

The Effect of Calcining Sequence and Dopant Addition on the Densification and Microwave Properties of Zirconium Tin Titanate

James Wilson, Phil Pruna and Mohammed Megherhi
Ferro Transelco Division
1789 Transelco Drive
Penn Yan, NY 14527 USA

I. INTRODUCTION

Ceramic microwave dielectrics are playing an increasingly significant role in the wireless communications industry where they are used in a wide variety of filtering applications. These materials exhibit a range of permittivity from approximately 6 to 120 (ϵ'), very low dielectric losses ($\tan \delta = 1/Q$) and excellent stability of coefficient of resonant frequency (τ_f) in the microwave region. Current industrial research efforts are focused on increasing ϵ' to reduce the physical dimensions of filtering devices and improve material Q values to allow greater channel-carrying capability while attempting to maintain near zero temperature stability.

One material of significant interest is Zirconium-Tin-Titanate ($(\text{Zr}_{1-x}\text{Sn}_x)\text{TiO}_4$) which has been widely utilized for base station ring resonator applications. The dielectric properties of ZrTiO_4 were first reported by Rath in 1941 [1]. Wakino and others studied the use of $(\text{Zr}_{1-x}\text{Sn}_x)\text{TiO}_4$ in microwave filtering applications during the 1970's [2-4]. Wolfram and Göbel identified a useful solid solution range in the ZrO_2 - SnO_2 - TiO_2 system in a 1981 publication [5]. Wakino, Minai and Tamura investigated the effects of transition doping of Zirconium-Tin-Titanate on microwave dielectric properties in the mid-1980's [6]. They reported an ϵ' of 38, Q of 13,000 at 3 GHz and τ_f near 0 ppm/ $^\circ\text{C}$. Other researchers have studied the effects of donor/acceptor ion doping of this system throughout the late 1980's and into 1990's [7-9].

While there has been a great deal published on the acceptable solid solutions range and dopant effects on the dielectric properties of Zirconium-Tin-Titanate, little has been reported on the effect of processing/property relationships in this system. The present work is focused on studying the effects of calcination sequence and order of dopant additions on the densification and microwave dielectric properties of $(\text{Zr}_{0.8}\text{Sn}_{0.2})\text{TiO}_4$. Specifically, alternate calcination routes (e.g. pre-calcination of $\text{ZrO}_2\cdot\text{TiO}_2$ and $\text{SnO}_2\cdot\text{TiO}_2$ end members), the effects of adding dopants before and after ZST phase formation, and the use of partial dopant additions to enhance ZT end member formation were investigated.

II. EXPERIMENTAL PROCEDURES

High purity (>99%) ZrO_2 , SnO_2 , TiO_2 , NiO and ZnO raw materials were weighed in the appropriate amounts. The materials were milled in isopropyl alcohol for 3 hours and dried. The dried powders were calcined at various time/temperature

profiles and X-rayed to evaluate phase formation. The calcined powders were then milled in distilled water and appropriate amounts of PVA binder and a polyelectrolyte dispersant were added. The slurries were spray dried. Discs were pressed and sintered over a range of temperatures. The fired parts were X-rayed, machined to the desired geometry for high frequency measurements, and characterized for physical and electrical properties. The Courtney method was used to evaluate sample permittivity and the Cavity method was used for both Q and τ_f determinations. Table 1 details the various calcination/firing conditions utilized in this experiment.

III. RESULTS AND DISCUSSION

This extended abstract only contains XRD, fired density and microwave property results for the first three processing routes described in Table 1. It is expected that a complete characterization for all seven processing routes will be presented at the U.S. - Japan Seminar.

Table 1
Processing Routes

| | |
|----------------------|---|
| Process → Route 1 | $\text{ZrO}_2 + \text{SnO}_2 + \text{TiO}_2 + 0.5 \text{ wt } \% \text{ ZnO} + 0.5 \text{ wt } \% \text{ NiO}$ Calcined at $1100^\circ\text{C} / 3 \text{ hrs.}$ Sintered at $1350^\circ\text{C} - 1425^\circ\text{C}$ for 1.5 hrs. |
| Process → Route 2 | $\text{ZrO}_2 + \text{TiO}_2$ calcined at $1250^\circ\text{C} / 2 \text{ hrs.}$ Then recalcined at $1350^\circ\text{C} / 4 \text{ hrs.}$ $\text{SnO}_2\cdot\text{TiO}_2$ calcined at $1325^\circ\text{C} / 3 \text{ hrs.}$ $+ 0.5 \text{ wt } \% \text{ ZnO} + 0.5 \text{ wt } \% \text{ NiO}$ Sintered at $1350^\circ\text{C} - 1450^\circ\text{C}$ for 1.5 hrs. |
| Process → Route 3 | $\text{ZrO}_2 + \text{SnO}_2 + \text{TiO}_2$ calcined at $1350^\circ\text{C} / 4 \text{ hrs.}$ $+ 0.5 \text{ wt } \% \text{ ZnO} + 0.5 \text{ wt } \% \text{ NiO}$ Sintered at $1325^\circ\text{C} - 1400^\circ\text{C}$ for 1.5 hrs. |
| Process → Route 4 | $\text{ZrO}_2\cdot\text{TiO}_2 + 0.25 \text{ wt } \% \text{ ZnO}$ calcined at $1200^\circ\text{C} / 4 \text{ hrs.}$ $+ 0.25 \text{ wt } \% \text{ ZnO} + 0.5 \text{ wt } \% \text{ NiO} + \text{SnO}_2 + \text{TiO}_2$ Sintered at $1350^\circ\text{C} - 1425^\circ\text{C}$ for 1.5 hrs. |
| Process → Route 5 | $\text{ZrO}_2 + \text{TiO}_2$ calcined at $1250^\circ\text{C} / 2 \text{ hrs.}$ Then recalcined at $1350^\circ\text{C} / 4 \text{ hrs.}$ $+ 0.5 \text{ wt } \% \text{ ZnO} + 0.5 \text{ wt } \% \text{ NiO} + \text{SnO}_2 + \text{TiO}_2$ Sintered at $1350^\circ\text{C} - 1425^\circ\text{C}$ for 1.5 hrs. |
| Process → Route 6 | $\text{ZrO}_2 + \text{SnO}_2 + \text{TiO}_2$ calcined at $1100^\circ\text{C} / 3 \text{ hrs.}$ $+ 0.5 \text{ wt } \% \text{ ZnO} + 0.5 \text{ wt } \% \text{ NiO}$ Sintered at $1350^\circ\text{C} - 1425^\circ\text{C}$ for 1.5 hrs. |
| Process → Route 7 | $\text{ZrO}_2 + \text{SnO}_2 + \text{TiO}_2 + 0.25 \text{ wt } \% \text{ ZnO}$ calcined at $1100^\circ\text{C} / 3 \text{ hrs.}$ $+ 0.25 \text{ ZnO} + 0.50 \text{ NiO}$ Sintered at $1350^\circ\text{C} - 1400^\circ\text{C}$ for 1.5 hrs. |

A. XRD Results:

X-ray analysis of the calcined material of Route 1 did not show a complete Zirconium-Titanate phase formation. Peaks corresponding to ZrO_2 , SnO_2 and TiO_2 were observed. However, after sintering phase pure ZST was obtained.

X-ray analysis of the calcined ZT utilized in Route 2 revealed minor phase formation at 1250°C and mostly phase pure ZT formed at 1350°C , with small amounts of free ZrO_2 and TiO_2 observed. Due to refractory nature of $\text{SnO}_2\cdot\text{TiO}_2$ mixtures, no evidence of phase formation was observed after calcination at temperatures as high as 1400°C . On sintering of these precalcined powders, complete phase transformation to ZST was achieved. We have observed that the addition of 0.25 wt % ZnO to $\text{ZrO}_2 + \text{TiO}_2$ (Route 4) allowed for the formation of ZrTiO_4 at temperatures as low as 1200°C with minor TiO_2 and ZrO_2 phases.

The ZST calcined at 1100°C for three hours without the addition of dopants did not show phase formation which is consistent with results obtained with Route 1. The higher calcination temperature of 1350°C was required to produce ZST major phase with minor TiO_2 and minor ZrO_2 . Upon adding the 0.5 wt % ZnO and 0.5 wt % NiO and sintering at 1350°C - 1400°C , phase pure ZST was achieved.

B. Physical and Microwave Property Results

Figure 1 shows density vs temperature for the three processing routes. High sintered densities of 5.05 g/cm^3 - 5.17 g/cm^3 were obtained for both routes 1 and 3 samples fired at 1350°C - 1400°C . However, lower densities were observed from samples made via Route 2. A monotonic increase in sintered density was obtained with increasing firing temperature. The low densification rate is attributed to the high calcination temperature required to achieve a phase pure ZST which may have resulted in coarsening of the precursor material.

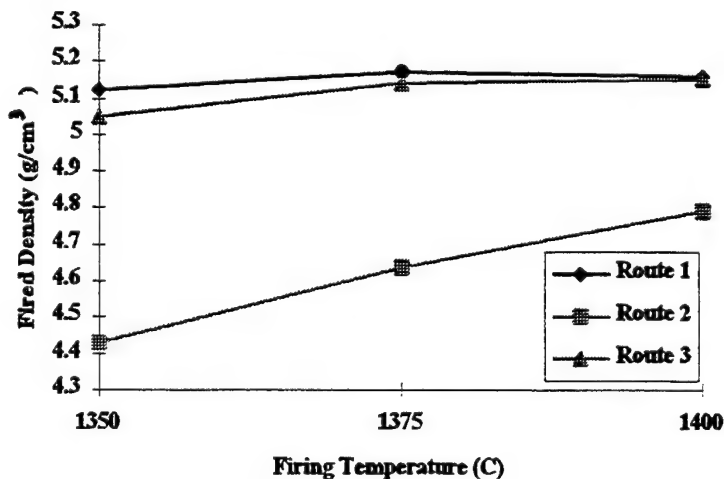


Fig. 1. Fired density as a function of firing temperature.

The dielectric permittivity measurements were conducted at frequencies of 6.1 - 6.4 GHz. (see Table 2). Samples prepared via Route 1 resulted in permittivities of 38.24 - 39.01 with the highest ϵ' observed at 1375°C .

Processing Route 2 samples showed a similar trend in dielectric permittivity to that of the sintered density. ϵ' was observed to increase from 30.55 at 1350°C to 34.33 at 1400°C .

Samples made using Route 3 exhibited a similar trend, on increasing permittivity, with increasing sintering temperature as those prepared via Route 2. However, higher ϵ' values (37.29 - 38.58) were observed for Route 3 samples at all firing conditions.

Q and τ_f measurements were conducted on all samples in the frequency range of 4.1 - 4.5 GHz. and are expressed in terms of Q^*f . Samples prepared via Route 1 exhibited Q^*f s which ranged from 37910 to 42523 and τ_f s of -1.69 ppm/ $^\circ\text{C}$ to -2.00 ppm/ $^\circ\text{C}$. Q maxima was obtained at 1375°C . τ_f was observed to be consistent over the firing range. Route 1 appears to offer the widest processing window of those characterized thus-far. Acceptable dielectric properties were obtained throughout the firing range. However, Q^*f began to drop rather significantly at the higher firing temperature.

No resonance frequency peaks were found for the Route 2 samples sintered at 1350°C . Q^*f ranged from 8847 to 36557 at 1375°C and 1400°C , respectively. τ_f values of -2.25 and -2.97 were measured, respectively. Again, this trend in the data can be attributed to the densification kinetics of this processing route.

Processing Route 3 exhibited similar behavior to Route 1. Q^*f ranged from 38910 at 1400°C to 41039 at 1350°C . τ_f ranged from -1.41 ppm/ $^\circ\text{C}$ at the higher sintering temperature to -2.08 ppm/ $^\circ\text{C}$ at the lower sintering temperature. Of particular note of interest to these researchers was the observation of a wide processing window with this route. This is despite the fact that the ZST phase was formed at the relatively high temperature of 1350°C . This suggests that the ZnO and NiO dopants are very effective sintering aids.

Table 2
Microwave Property Results

| Process Route | Firing Temp ($^\circ\text{C}$) | ϵ' | Q^*f | τ_f (ppm/ $^\circ\text{C}$) |
|---------------|----------------------------------|-------------|--------|-----------------------------------|
| Route 1 | 1350 | 38.24 | 40,794 | -2.00 |
| | 1375 | 39.01 | 42,523 | -1.83 |
| | 1400 | 38.63 | 37,910 | -1.69 |
| Route 2 | 1350 | 30.55 | none | |
| | 1375 | 33.06 | 8,847 | -2.25 |
| | 1400 | 34.43 | 36,557 | -2.97 |
| Route 3 | 1350 | 37.29 | 41,039 | -2.08 |
| | 1375 | 38.44 | 40,858 | -1.52 |
| | 1400 | 38.58 | 38,910 | -1.41 |

IV. CONCLUSION

Processing Route 1 appears to be the most economically advantageous method for processing low loss doped ZST materials for microwave application based on results obtained to date. This one step calcination appears to yield a powder with a wide processing window and high sinterability.

High temperature precalcination required to produce the ZT phase. In turn, a lower densification rate was observed for samples processed via Route 2.

The addition of 0.25 wt % ZnO to $\text{ZrO}_2 \cdot \text{TiO}_2$ prior to calcination allowed the formation of ZrTiO_4 at temperatures as low as 1200°C.

Despite the high calcination temperature required to produce pure phase ZST in Route 3, the addition of the dopants after calcining resulted in comparable densities and electrical properties to those obtained via Route 1. This is in spite of the fact that no particle size reduction was performed on the ZST and suggest the very effective role of ZnO and NiO as sintering aid in this system.

Results to date, indicate that a Q maxima is reached in the ZST system and subsequently a high sintering temperature which comparable or increased densities actually results in lower Q values.

V. FUTURE WORK

Complete the characterization of all seven processing routes outlined in Table 1. This will include detailed SEM/EDS studies of the resulted microstructure in which we will attempt to further define the role of the dopants in developing optimized electrical performance in this system.

REFERENCES

- [1] W. Rath, *Keram. Rdsch.* 49 (1941), 137.
- [2] K. Wakino, T. Nishikawa, S. Tamura, and Y. Ishikawa, *Proc. IEEE MTT Symposium*, 1975 p.63.
- [3] K. Wakino, T. Nishikawa, H. Matsumoto, and Y. Ishikawa, "Miniaturized band pass filters using half wavelength dielectric resonator with improved spurious response," *IEEE MTT Symposium*, 1978 pp. 230-232.
- [4] K. Wakino, T. Nishikawa, H. Matsumoto and Y. Ishikawa *Proc. IEEE MTT Symposium*, 1979, p278.
- [5] G. Wolfram and Göbel, "Existence range, structural and dielectric properties of $\text{Zr}_x\text{Ti}_y\text{Sn}_z\text{O}_4$ ceramics ($x+y+z=2$)," *Mater. Res. Bull.*, vol16, No.11, 1981 pp 1455-1463.
- [6] K. Wakino, K. Minai and H. Tamura, "Microwave characteristics of (Zr, Sn)TiO₄ and BaO-PbO-Nd₂O₃-TiO₄ dielectric resonators," *J. Am. Ceram. Soc.*, vol.67, No.4, 1984, pp 278-281.
- [7] Y. C. Heiao, L. Wu, and C. C. Wei, "Microwave dielectric properties of (ZrSn)TiO₄ ceramic," *Mat. Res. Bull.*, vol. 23, 1988 pp. 1687-1692.
- [8] N. Michiura, T. Tatekawa, Y. Higuchi and H. Tamura, "Role of donor and acceptor ions in the dielectric loss tangent of $(\text{Zr}_{0.8}\text{Sn}_{0.2})\text{TiO}_4$ dielectric resonator material," *J. Am. Ceram. Soc.*, vol 78, No. 3, 1995, pp793-796.
- [9] R. Christofferson, P. K. Davies and X. Wei, "Effect of Sn substitution on cation ordering in $(\text{Zr}_{1-x}\text{Sn}_x)\text{TiO}_4$ microwave dielectric ceramics," *J. Am. Ceram. Soc.*, vol 77, No. 6, 1994, pp 1441-1445.

Dielectric Properties of $\text{Ba}(\text{Zn}_{1/3}\text{Ta}_{2/3})\text{O}_3$ - KTaO_3 Ceramics

Hitoshi Yokoi*, Akifumi Tosa, and Kazushige Ohbayashi

R & D Center, NGK Spark Plug Co., Ltd.

2808, Iwasaki, Komaki, Aichi 485, JAPAN

Abstract—Dielectric properties of $\text{Ba}(\text{Zn}_{1/3}\text{Ta}_{2/3})\text{O}_3$ - KTaO_3 ceramics have been studied from the stoichiometrical point of view on each component. The addition of KTaO_3 facilitated the sintering of $\text{Ba}(\text{Zn}_{1/3}\text{Ta}_{2/3})\text{O}_3$. The quality factor, Q was very sensitive to the stoichiometry of each component although dielectric constant, ϵ , and temperature coefficient of resonant frequency, τ_f were not much. The addition of potassium tantalate containing excess potassium with respect to the stoichiometric composition, KTaO_3 increased the Q value of the $\text{Ba}(\text{Zn}_{1/3}\text{Ta}_{2/3})\text{O}_3$ ceramics. On the other hand, the compositional deviations of barium and zinc from stoichiometric $\text{Ba}(\text{Zn}_{1/3}\text{Ta}_{2/3})\text{O}_3$ deteriorated it. The highest $Q \times f$ value, 103,000 GHz was obtained when 2.5 mol% of non-stoichiometric potassium tantalate, $\text{K}_{1.25}\text{TaO}_{3+\delta}$ was added to stoichiometric $\text{Ba}(\text{Zn}_{1/3}\text{Ta}_{2/3})\text{O}_3$. As an annealing time to improve the Q value, 24 hours were long enough for this composition.

I. INTRODUCTION

The family of 1:2 stoichiometric complex perovskites $\text{A}(\text{B}'_{1/3}\text{B}''_{2/3})\text{O}_3$ having ordered and disordered structures [1] has been widely studied [2] because of its attractive dielectric properties and application to microwave resonators which are necessary for communication systems at high frequencies. The ceramic of one of the family, $\text{Ba}(\text{Zn}_{1/3}\text{Ta}_{2/3})\text{O}_3$ (BZT) is known as a material having a small temperature coefficient of resonant frequency, $|\tau_f|$ and a high quality factor, Q at microwave frequencies.

It has been reported that the Q value of BZT can be improved by extending the sintering time [3, 4]. This phenomenon has been attributed to the formation of a superstructure arising from hexagonal ordering of the B-site ions by annealing at high temperatures; 120-hour annealing is required for completing the ordering of the B-site ions. These experimental observations on the monolithic BZT ceramic have agreed with the theoretical calculations [5, 6].

Various solid solutions of BZT and other simple or complex perovskites as end members have been tested to control the dielectric properties, in particular, to improve the Q value [7-9]. In some solid solutions, e.g. BZT- BaZrO_3

[8] and BZT-(Sr,Ba)($\text{Ga}_{1/2}\text{Ta}_{1/2}$) O_3 [9], the Q values have been reported to be improved without the lattice distortion resulting from the formation of hexagonal superstructures. This suggests that the ordering of the B-site ions by long time sintering, which is not favorable from the practical point of view, is not only the approach to improve the Q value of the BZT ceramics.

The purpose of the present study is to develop a novel solid solution system with BZT having the high Q value without long time sintering from the practical point of view. Potassium tantalate (KT) was selected as an end member of the solid solution with BZT from the group of simple perovskites containing an alkali ion because the prior experiments showed that other perovskites of the group such as lithium tantalate and sodium tantalate were not effective for the Q value improvement of BZT [10]. The perovskites containing alkali ions were expected to work as a sintering additive of BZT. The focal point of the present study is not only the B-site ion ordering but also the stoichiometry of each component. Very few studies have been performed regarding the influence of the deviation from the stoichiometric composition of BZT or its solid solutions on their Q values.

II. EXPERIMENTAL PROCEDURE

A. Sample Preparation

The commercially available powders of BaCO_3 , ZnO , Ta_2O_5 , and K_2CO_3 (purity > 99%) were weighed and ball milled in ethanol for 15 h. The ball milled slurry then was dried and calcined at 1100°C for 2 h. The calcined powder was re-milled with organic binder and dispersant in ethanol for 15 h. The resulting dried powder was pressed into pellets with dimensions of 20 mm in diameter and 12 mm in thickness under a compaction pressure of 1 GPa and CIPed under a pressure of 15 GPa. These pellets were sintered in air at 1450 ~ 1650°C for 2 h and subsequently annealed at 1450°C for 0 ~ 48 h. The both end surfaces of the specimens were ground using a #200 diamond wheel.

Bulk densities were determined by Archimedes' method. The specimens were examined by X-ray diffraction analysis (XRD) with Cu radiation. A least square method was used for lattice parameters calculations. The microstructures were observed and analyzed by scanning electron microscopy (SEM) attached with a analytical capability, energy dispersive X-ray spectroscopy (EDS). To confirm the volatilized amount of ZnO and K₂O, the chemical compositions of the specimens were determined with an inductive coupled plasma analyzer (ICP).

C. Dielectric Properties

The dielectric properties were measured at ~ 4 GHz by resonant cavity method in the TE₀₁₁ mode. For the unloaded Q value, Q_u measurement, the specimen was placed on the support made of forsterite. The Q_u value was calculated using the following equation:

$$Q_u = (f_0 / \Delta f) / (1 - 10^{-1/L/20}) \quad (1)$$

where f_0 is the center frequency of resonance and Δf is the frequency between 3 dB points.

A dielectric constant, ϵ_r and $\tan \delta$ were obtained from f_0 and Q_u for the TE₀₁₁ resonant mode. The τ_f value was evaluated from the measurement at 25°C and 80°C:

$$\tau_f = \Delta f_0 / f_0 (80 - 25) \quad (2)$$

where Δf_0 is the shift in the center frequency led from the temperature difference, 55°C.

A. Addition of the Stoichiometric KTaO₃

Fig. 1 shows the results of addition of stoichiometric KT to BZT sintered at 1550°C for 2 h and annealed at 1450°C for 24 h. The density of the monolithic BZT sintered and annealed under the conditions adopted in this experiment was well below the theoretical density, 7.920 g/cm³ [3]. Although it has been reported that the effect of pores on the Q value is negligible [3] and the effect of grain boundary is small, this result indicated that at least, $\sim 96\%$ relative density is required to obtain the high Q value. As can be seen in this figure, the addition of the small amount of KT clearly improved the sinterability of BZT. When 2.5 mol% of KT was added, the density reached maximum. Further addition resulted in a decrease of density. This is because the density of KT is smaller than that of BZT. After the sinterability was improved, the Q value gradually increased with an increase of the amount of KT while the influence of the KT addition on ϵ_r and τ_f was negligible.

B. Relations between Stoichiometry and the Q Value

From the results of the previous section, the amount of KT to add to BZT was determined as 2.5 mol%. Next, the relationships between the stoichiometry of potassium in KT and barium and zinc in BZT and the Q value were examined. These results are summarized in Fig. 2 and Fig. 3.

The stoichiometry of potassium in KT had a large effect on the improvement of the Q value. The addition of the

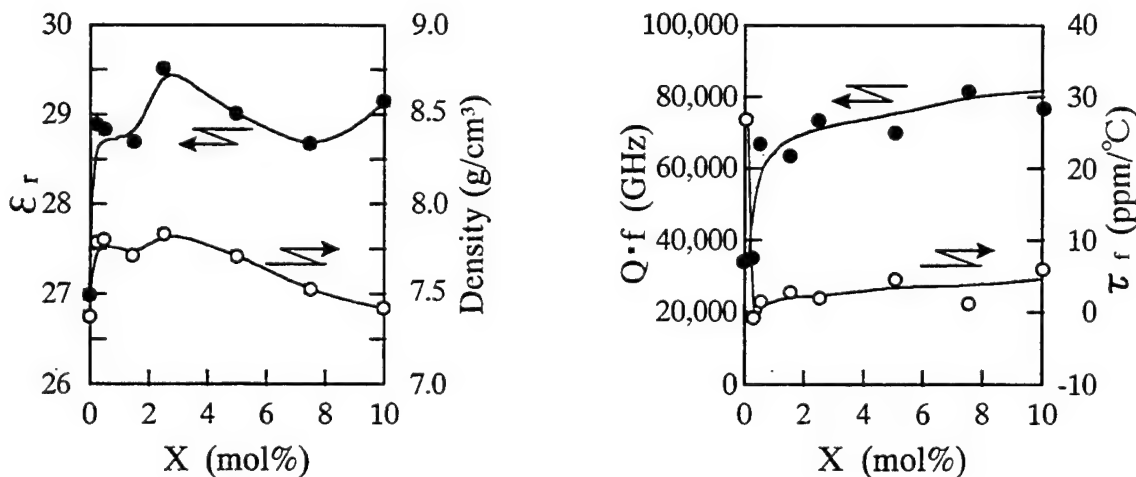


Fig. 1. Effect of addition (X mol%) of the stoichiometric KTaO₃ on the properties of BZT.

non-stoichiometric composition, $K_{1.25}TaO_{3+\delta}$ gave the best Q value. Further excess of the potassium led to a decrease of the Q value. The ICP analysis on this specimen revealed that potassium volatilized during sintering and annealing. That is, when the excess potassium volatilizes during sintering and annealing and the amount of the remained potassium reaches to the stoichiometric composition after sintering and annealing, the high Q value can be obtained.

On the other hand, for both barium and zinc, the stoichiometric composition gave the best Q value. The Q value was very sensitive; only 1% deviation from the stoichiometric composition resulted in the drastic deterioration. The ICP analysis showed the volatilization of zinc also occurred as reported by Desu and O'Bryan [4] but its amount was much smaller than that of potassium.

C. Effects of annealing on the Q value

For the composition, $97.5BZT-2.5K_{1.25}TaO_{3+\delta}$, the sintering and annealing conditions were optimized. The Q value of the specimen sintered at $1600^{\circ}C$ was slightly higher than that sintered at $1550^{\circ}C$. The sintering above $1600^{\circ}C$ resulted in the formation of the porous layer due to the volatilization of potassium and zinc and the generation of the hair cracks due to the grain growth.

Effect of the annealing time on the Q value is depicted in Fig. 4. After the sintering at $1600^{\circ}C$ for 2 h, the temperature was lowered from $1600^{\circ}C$ to $1450^{\circ}C$ and kept for 18~48 h. The 24-hour annealing was long enough to

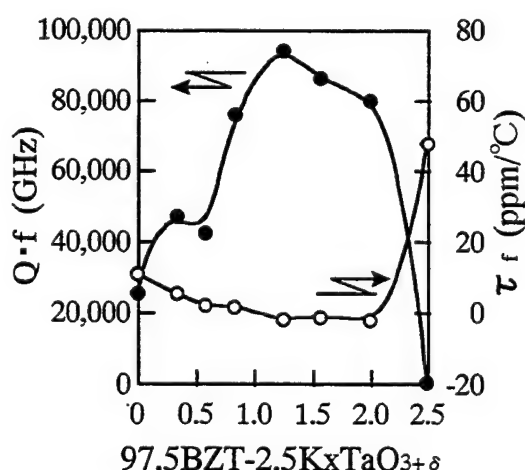


Fig. 2. Relationship between the stoichiometry of potassium in potassium tantalate and the $Q \times f$ value.

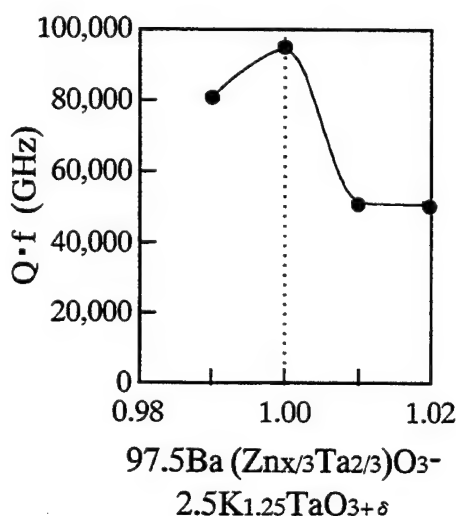
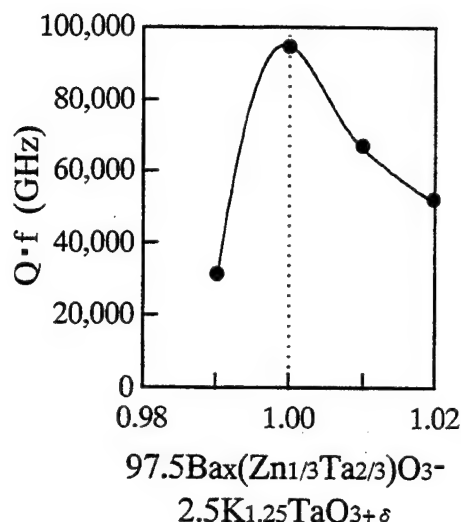


Fig. 3. Relationships between the stoichiometry of barium (above) and zinc (below) in BZT and the $Q \times f$ value.

obtain the dielectric resonators of which the $Q \times f$ value was $>100,000GHz$.

D. XRD analysis

Only the single phase of perovskite was detected in the XRD analysis although Desu and O'Bryan [4] observed barium tantalate phases in their BZT ceramics resulting from the ZnO volatilization. Since the ionic radius of K^+ (1.38 \AA) is close to that of Ba^{2+} (1.36 \AA), potassium is thought to go into the A site of the perovskite structure.

The deflections from the hexagonal superstructure were

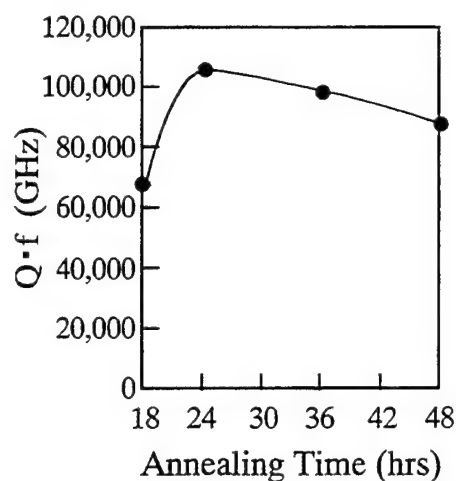


Fig. 4. Effect of the annealing time on the $Q \times f$ value of 97.5BZT-2.5K_{1.25}TaO_{3+δ} sintered at 1600°C for 2 h.

observed in the 24-hour annealed specimen whereas not in the specimen without annealing. That is, the ordering of the B-site ions in this composition is effective for the Q value improvement as observed in BZT and the solid solutions with BZT [3,4,9]. From XRD analysis, the evidence of the lattice distortion for which the peak split of (422) and (226) was confirmed was not obtained. Thus, it was concluded that the Q value was improved without the lattice distortion in the system of BZT-KT, similar to the systems of BZT-BaZrO₃ [8] and BZT-(Sr,Ba)(Ga_{1/2}Ta_{1/2})O₃ [9].

The ceramic microwave resonators of the 97.5BZT-2.5K_{1.25}TaO_{3+δ} composition developed in the present study have been successfully manufactured. Various properties of this ceramic are summarized in Table I.

TABLE I
VARIOUS PROPERTIES OF THE 97.5BZT-2.5K_{1.25}TaO_{3+δ} CERAMIC

| Properties | |
|--|----------------------|
| Density (g/cm ³) | 7.77 |
| Water Absorption (%) | < 0.01 |
| Dielectric Constant | 29.3 |
| $Q \times f$ (GHz) | 103,000 |
| Temperature coefficient of resonant frequency (ppm/°C) | -1.1 |
| $\tan \delta$ | 4.1×10^{-5} |
| Volume Resistivity (Ω m) | 3.2×10^{15} |
| Linear Expansion Coefficient (ppm/°C) | 9.52 |
| Thermal Conductivity (W/m°C) | 5.23 |
| Bending Strength (MPa) | 90 |

IV. CONCLUSIONS

The solid solutions of Ba(Zn_{1/3}Ta_{2/3})O₃ and KTaO₃ were investigated from the viewpoint of the practical use as microwave resonators. The addition of KTaO₃ improved the sinterability of the Ba(Zn_{1/3}Ta_{2/3})O₃ ceramics. The Q value was very sensitive to stoichiometry of each composition; when 2.5 mol% of the potassium tantalate containing 25 at% of excess potassium was added to the stoichiometric Ba(Zn_{1/3}Ta_{2/3})O₃, the highest $Q \times f$ value, 103,000 GHz was obtained. The resonant frequency of this ceramic against the temperature change was very stable ($\tau_f = -1.1$ ppm/°C). The 24-hour annealing at 1450°C after sintering was long enough to improve the Q value. The lattice distortion was not observed in this ceramic.

REFERENCES

- [1] A. F. Wells; Structural Inorganic Chemistry. 4th Edition. Clarendon Press, Oxford, 1975.
- [2] S. Nomura, "Ceramics for microwave dielectric resonator," *Ferroelectrics*, **49**, 61-70 (1983).
- [3] S. Kawashima, M. Nishida, I. Ueda, and H. Ouchi, "Ba(Zn_{1/3}Ta_{2/3})O₃ ceramics with low dielectric loss at microwave frequencies," *J. Am. Ceram. Soc.*, **66**[6] 421-23 (1983).
- [4] S. B. Desu and H. M. O'Bryan, "Microwave loss quality of Ba(Zn_{1/3}Ta_{2/3})O₃ ceramics," *J. Am. Ceram. Soc.*, **68**[10] 546-51 (1985).
- [5] D. A. Sagala and S. Nambu, "Microscopic calculation of dielectric loss at microwave frequencies for complex perovskite Ba(Zn_{1/3}Ta_{2/3})O₃," *J. Am. Ceram. Soc.*, **75**[9] 2573-75 (1992).
- [6] D. A. Sagala and S. Nambu, "Lattice energy calculations for ordered and disordered Ba(Zn_{1/3}Ta_{2/3})O₃," *J. Phys. Soc. Jpn.*, **61**[5] 1791-97 (1992).
- [7] S. Kawashima, M. Nishida, I. Ueda, and H. Ouchi, "Dielectric properties of Ba(Zn_{1/3}Nb_{2/3})O₃ - Ba(Zn_{1/3}Ta_{2/3})O₃ ceramics at microwave frequency," pp.293-96 in *Proceedings of the first meeting on Ferroelectric Materials and Their Applications*. Keihin Printing Co., Kyoto, Japan, 1977.
- [8] H. Tamura, T. Konoike, Y. Sakabe, and K. Wakino, "Improved high- Q dielectric resonator with complex perovskite structure" *J. Am. Ceram. Soc.*, **67**[4] C-59-C61 (1984).
- [9] K. Kageyama, "Crystal structure and microwave dielectric properties of Ba(Zn_{1/3}Nb_{2/3})O₃ - (Sr,Ba)(Ga_{1/2}Ta_{1/2})O₃ ceramics" *J. Am. Ceram. Soc.*, **75**[7] 1767-71 (1992).
- [10] H. Yokoi, A. Tosa, and K. Ohbayashi, unpublished.

Development of the Varistor/Capacitor Co-Fired Multilayer Device

Tomohiro Sogabe

TDK Corporation, Material Research Center

570-2 Matsugashita Minamihatori Narita City Chiba pref. Japan

Abstract -Varistor/Capacitor co-fired Multilayer Devices (VCMD) were obtained without the curvature which usually results from differential shrinkage. The varistor was Pr-doped ZnO and the capacitor was a $\text{La}_2\text{Ti}_2\text{O}_7$ dielectric with 1wt% borosilicate glass.

Varistor voltage was 18V with a non-linearity coefficient (α) of 20, while the overall device capacitance was 1500pF (C3216 size). The VCMDs were able to absorb a 1-2kV pulse of less than 10ns in which time range the varistor alone could not. It was found that near the interface between the capacitor and varistor, Pr, Co and Mn diffused forming a reaction layer in which the electrical resistance of the varistor was very low. The depth of the reaction layer increased with increasing firing temperature. This resulted in a large decrease in α and a large increase in $\tan \delta$. By using HRTEM, lattice defects were shown to exist at the varistor/dielectric interfaces.

I . Introduction

Recently, the markets for personal computers, electric appliances and portable telephones have grown tremendously. Each has experienced rapidly increasing performance and miniaturization, a result of which has been the increase in demand for ZnO varistors, which find use as surge absorbers. However, ZnO varistors alone are inadequate as anti static-electricity devices. For example, ZnO cannot absorb EM noise in less than 10ns as an intrinsic limitation.^{1,2} Hitherto RC combinations were used to eliminate noise at such short wavelengths, though there were problems with overvoltage and capacitor breakdown because these devices lacked the voltage limiting ability and almost completely lacked surge absorption ability too.

This paper reports on TDK's efforts to solve this problem by combining both the advantages of ZnO varistors and capacitors in varistor/capacitor co-fired multilayer devices developed using sheet lamination of co-firing technique.

II . Experimental Procedure

(1) Materials and Sample Preparation

High purity raw materials for preparing ZnO varistor samples were mixed in the follow proportions: 97.89 mol% ZnO, 0.98 mol% Pr_2O_3 , 0.78 mol% Co_3O_4 , 0.25 mol% Cr_2O_3 , 0.089 mol% SrCO_3 and 0.005 mol% Al_2O_3 . Those for the preparation of the dielectric were mixed as follows: 66.3 mol% La_2O_3 , 33.5 mol% TiO_2 and 0.20 mol% MnCO_3 .³ The raw materials for the dielectric alone were mixed by conventional wet milling for 16h after which they were dried at 130°C followed by calcination at 1100°C for 2h. The calcined powder was ground, 1wt% borosilicate glass added and milled for 16h again. After drying, both powders were ground, made into a slip and cast into sheets us-

ing the doctor blade method. Pd electrodes were printed the on both green sheets and laminated in alternate varistor and dielectric layers. Laminated sheets were cut into the C3216 shape after being warm pressed. The green chips were co-fired at 1100°C-1300°C in oxygen atmosphere for 4h. The co-fired bodies were barreled, and Ag terminal electrodes were printed and then fired at 600°C.

(2) Properties Measurements

Varistor and dielectric characteristics were measured using a DC power supply (KEITHLEY 237) and LCR meter (HEWLETT PACKRD 4284A). Noise absorption ability was measured using an impulse noise simulator (NOISE LABOR. INS-4310) and digitizing oscilloscope (Tektronix TDS520). The resistance distribution of co-fired bodies were measured using a microprobe⁴ (Alessi REL-4800).

(3) Microstructural Observations

The fine structure near the interface of varistor and dielectric was observed with EPMA (JEOL JCMA-733) and HRTEM⁵ (JEOL JEM-2010F).

III . Results and Discussion

(1) Co-firing Process

The shrinkage curves during firing are shown in Fig.1 for each material. The starting temperature for shrinkage is very high in the $\text{La}_2\text{Ti}_2\text{O}_7$ single phase, though appropriate borosilicate glass additions yield a very similar shrinkage curve to that of the ZnO varistor.

The resistance near the interface between the ZnO varistor

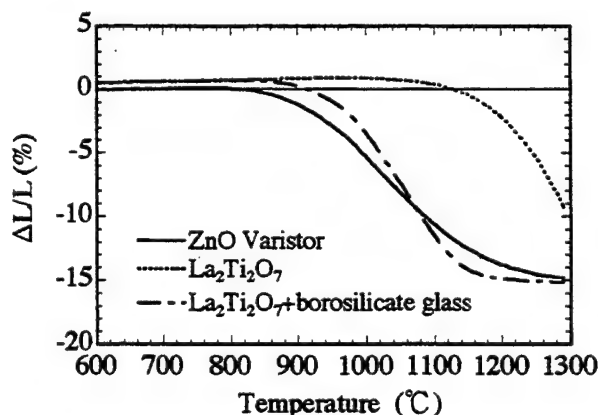


Fig.1. Thermal analysis of ZnO varistor, $\text{La}_2\text{Ti}_2\text{O}_7$ and 1wt% borosilicate glass added $\text{La}_2\text{Ti}_2\text{O}_7$

and $\text{La}_2\text{Ti}_2\text{O}_7$ was measured with a microprobe as shown in Fig.2. It was found that a region of low resistance exists near the interface on the varistor side at 1150°C , and that at 1300°C resistance deteriorates further and the size of the region of low resistance increases. It is thought that additives which are indispensable to varistor characteristics diffuse into the $\text{La}_2\text{Ti}_2\text{O}_7$ in this way.

The elemental distribution near the interface measured by

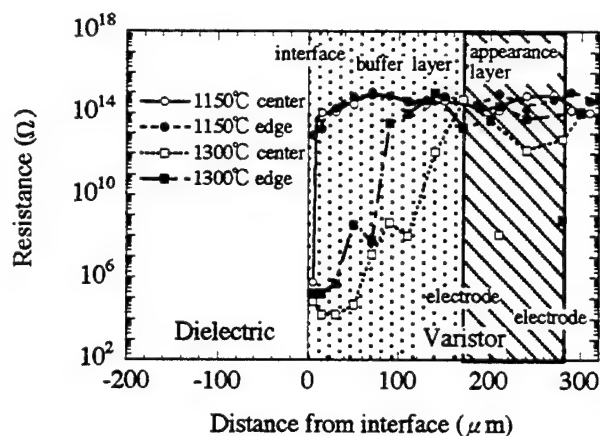


Fig.2. Resistance distribution of the polished cross section of co-fired body by microprobe.

EPMA is shown in Fig.3. It was found that Pr and Co diffused from varistor side into $\text{La}_2\text{Ti}_2\text{O}_7$ side at higher than 1200°C and conversely Mn diffused from the $\text{La}_2\text{Ti}_2\text{O}_7$ side into the ZnO varistor.

The low resistance region created near the interface in this way caused varistor characteristics to deteriorate remarkably. The varistor and dielectric characteristics after having increased the quantity of additives in the varistor in order to increase resistance near the interface are shown in Fig.4 and Fig.5. It was found that increasing the quantities of additives increased the α value and decreased $\tan \delta$, and that the V-I characteristic

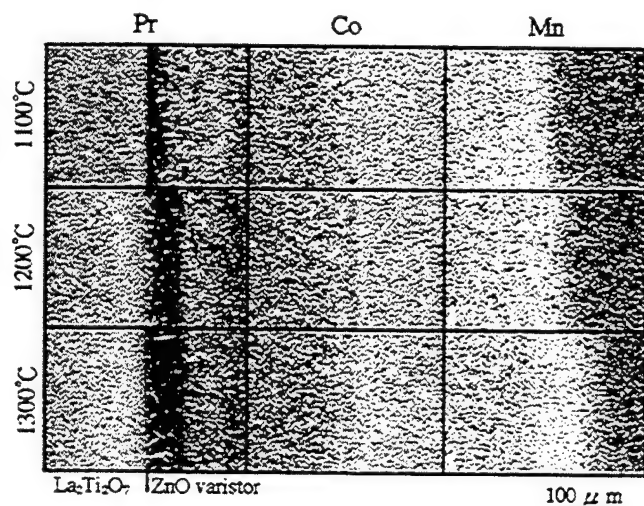


Fig.3. EPMA images of polished cross section of co-fired body.

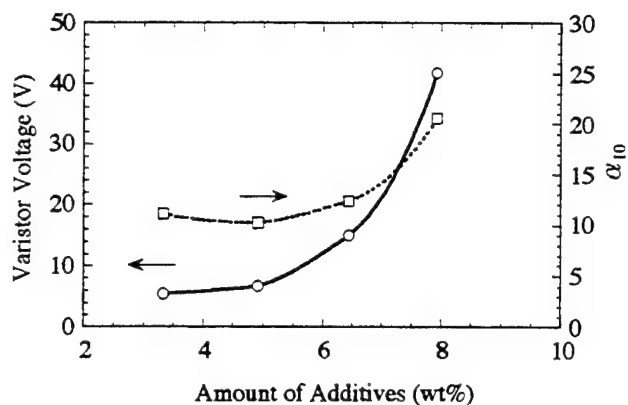


Fig.4. Varistor voltage and non linearity dependence on the amount of additives.

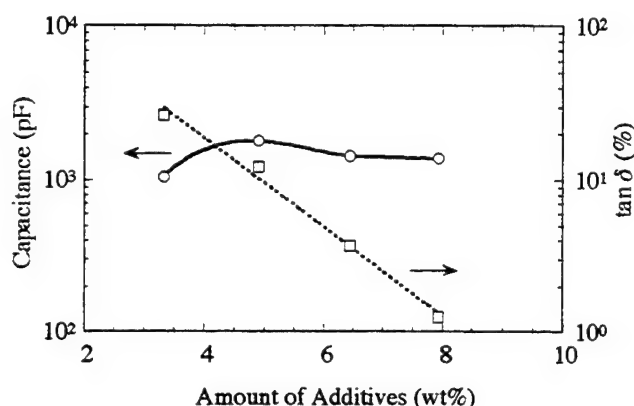


Fig.5. Capacitance and $\tan \delta$ dependence on the amount of additives.

improved.

(2) Noise absorption

The noise absorption characteristic of the VCMD is shown in Fig.6. The ZnO varistor cannot absorb noise pulses at less than 10ns, while the VCMD can.

(3) Microstructural Studies

A HRTEM image of the interface of the ZnO varistor and $\text{La}_2\text{Ti}_2\text{O}_7$ dielectric is shown in Fig.7. On the ZnO varistor side near the interface, many lattice defects of the edge-or screw-dislocation type were observed. On the other hand, lattice defects are far fewer in the region remote from the interface.

It seems likely that an amorphous layer of several nanometers existed at the interface.

(4) The Inverse Thickness-Gradient Lamination (ITGL) Structure

A schematic of the ITGL structure and a cross-sectional photograph of the same are shown in Fig.8 and Fig.9. Use of the ITGL structure causes reduced and dispersed residual stress near the interface and, as a result, cracks are largely reduced in

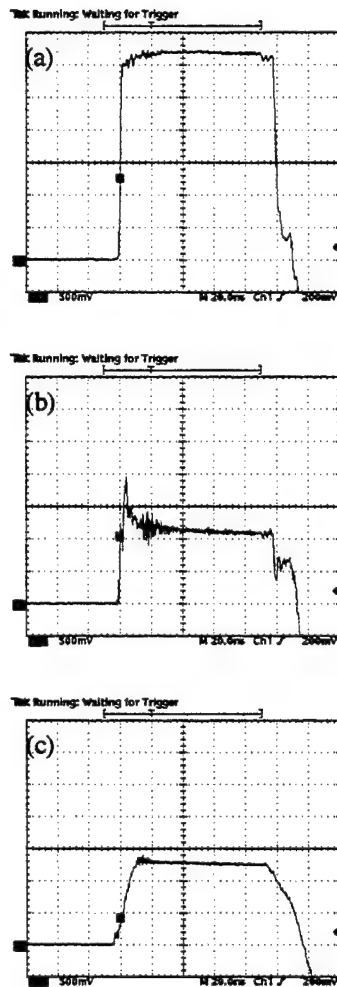


Fig.6. Noise absorption characteristics. (a) Applied pulse (b) ZnO varistor (c) VCMD.

number.

The shear stress of the laminate structure at the interface is given as follows.⁵

$$\tau \approx \frac{\left(\frac{V_v E_v}{1-\mu_v} \right) \left(\frac{V_d E_d}{1-\mu_d} \right)}{\left(\frac{V_v E_v}{1-\mu_v} \right) + \left(\frac{V_d E_d}{1-\mu_d} \right)} \Delta \alpha \Delta T \frac{d}{l} \quad (1)$$

V : Volume
E : Young's modulus
 μ : Shear modulus
 α : Linear thermal expansion coefficient
T : Temperature
d : Thickness
l : Length

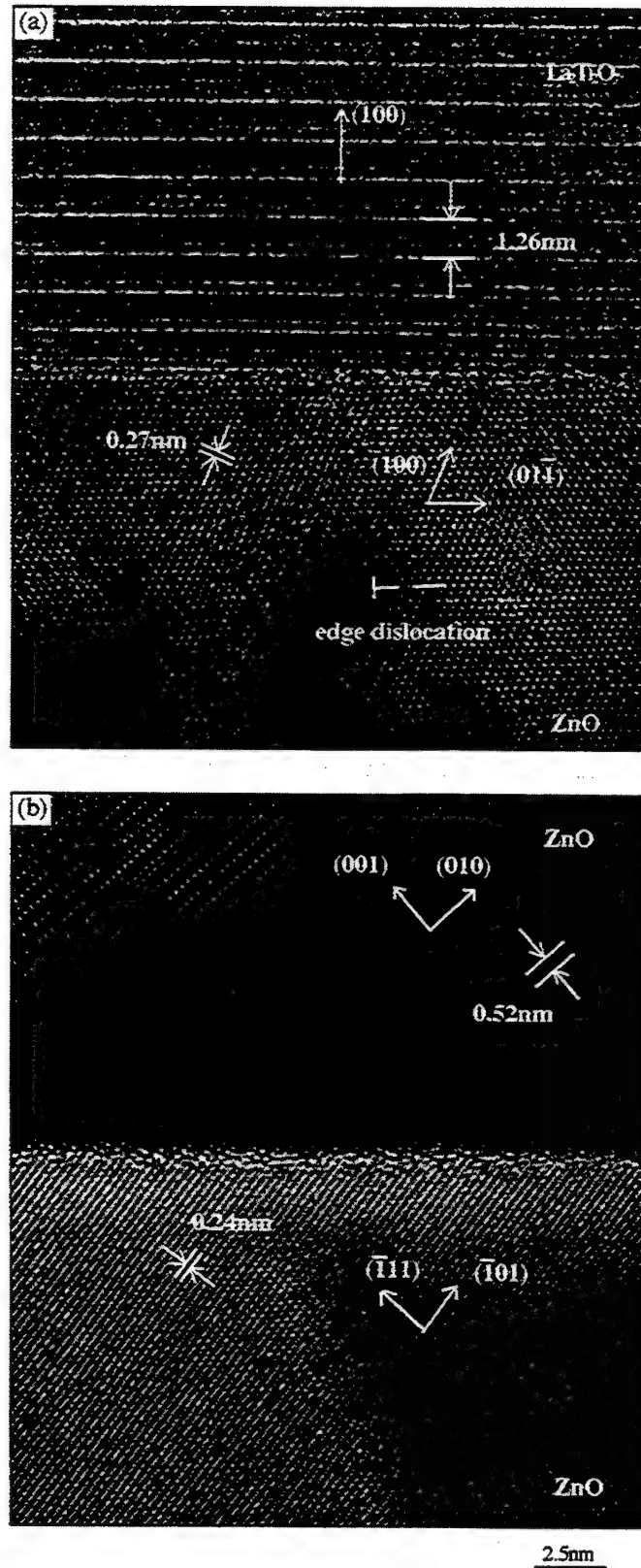


Fig.7. HRTEM image of the interface. (a) Interface of ZnO varistor and $\text{La}_2\text{Ti}_2\text{O}_7$ (b) ZnO at a distance from interface.

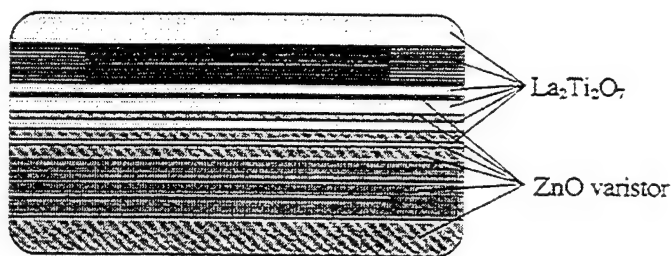


Fig.8. Typical figure of the ITGL structure.

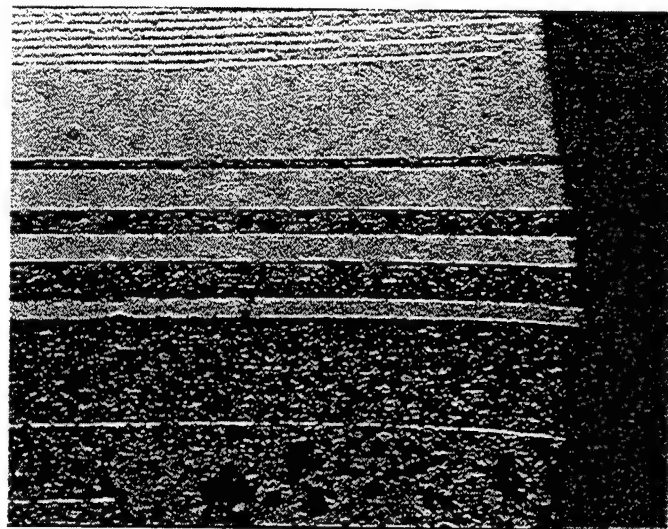


Fig.9. Optical micrographs of polished cross section of the ITGL structure.

The tension at alternate varistor/dielectric interfaces is opposite and thus cancels out, resulting in no overall shape change. Equation 1 indicates that as layer thickness decreases, shear stress is reduced. In addition, the gradual decrease in layer thickness in opposite directions for each component yields an over-

all decrease in inter-layer tension and compression, and therefore reduces cracking.

IV. Conclusions

(1) Varistor/capacitor co-fired multilayer devices (VCMD) were obtained without the curvature which usually results from differential shrinkage. The varistor was Pr-doped ZnO and the capacitor was a $\text{La}_2\text{Ti}_2\text{O}_7$ dielectric with 1wt% borosilicate glass.

(2) In the co-firing process Pr and Co diffuse from the varistor side to the dielectric across the varistor/dielectric interface, while Mn diffuses from the dielectric side. It was thought these elements contributed to the bonding between the ZnO varistor and $\text{La}_2\text{Ti}_2\text{O}_7$ dielectric.

(3) Increasing additives (Pr, Co, Cr and Sr) at the interface boundary and omitting Al as a donor dopant in the buffer layer proved effective in improving α and $\tan \delta$.

(4) The varistor/capacitor co-fired multilayer devices can absorb noise pulses of less than 10ns.

(5) It was found by using HRTEM that an amorphous layer of about 1nm existed at the interface of the ZnO varistor and dielectric, along with many lattice defects.

(6) The ITGL structure is effective in reducing the residual stress. This is supported by the decrease in lattice defects, such as dislocations, observed near the interface using ERTEM.

Acknowledgments

The author would like to thank T. Yoshioka, JEOL HIGHTECH CO., Ltd, for performing the HRTEM analyses.

References

- [1] F.J.Toal, T.R.Shroud, P.J.Moses, J.P.Dougherty, C.A.Randall, "Processing and Electrical Characterization of a Varistor/Capacitor Co-fired Multilayer Device", 16th *Capa. and Resis. Techno.Symp.* (1996) 245-255
- [2] H.Yamamoto, "Improvement of surge and response by varistor to improve immunity", *Electric Techno.*, 5 (1991) 61-67
- [3] T.Sogabe, S.Sato, M.Furukawa, T.Nomura, M.Ogasawara "Effect of Sintering Atmosphere on Maximum-Energy Capability of Pr-doped ZnO Varistor", *J.J.Sci.Powder and Powder Metal.*, 42 (1995) 592
- [4] J.D.Russell, D.C.Halls, C.Leach, "Direct observation of grain boundary Schottky barrier behavior in zinc oxide varistor material", *J.Mater.Sci.*, 14 (1995) 676-678
- [5] G.Y.Sung, S.McKernan, C.B.Carter, "Flat interfaces in zinc oxide-based varistor ceramics", *J.Mater.Res.*, Vol.7, No.2 (1992) 474-481
- [6] W.D.Kingery, H.K.Bowen, D.R.Uhlmann, "Introduction to Ceramics",

Dielectric Properties of Ta₂O₅ Based Ceramics

N. Ichinose, T. Ukai and Y. Yamashita*

Waseda University, Dept. of Materials Science and Engineering

3 - 4 - 1 Ohkubo Shinjuku-ku Tokyo 169, Japan

*Toshiba R&D Center, Materials and Devices Res. Lab.

1 Toshiba-cho, Saiwaiku, Kawasaki 210, Japan

Abstract—This paper describes the crystal structure and dielectric properties of Ta₂O₅ based ceramics such as Ta₂O₅—SiO₂ and Ta₂O₅—TiO₂ system. The maximum dielectric constant is 47 in the composition of 97mol% Ta₂O₅—3 mol% SiO₂. From the X-ray diffraction analysis, enhanced dielectric constant ($\epsilon_r \sim 130$) observed in the Ta₂O₅—TiO₂ system may be due to a formation of the H'-monoclinic phase (Ta_{1.92}Ti_{0.08}O_{5.6}).

I. INTRODUCTION

For the demand of smaller capacitive components, exotic compounds with high dielectric constants, such as (Ba, Sr)TiO₃ and (Ba, Pb) (Zr, Ti)O₃ are widely investigated. But such materials invariably incorporate chemical elements foreign to current microelectronics fabrication procedures and must pass extensive commercially compatibility test before they can be used. From a compatibility point of view, tantalum oxide (Ta₂O₅) is considered more promising, although its dielectric properties are modest.¹⁾

In this paper, crystal structure and dielectric properties of Ta₂O₅ based ceramics such as Ta₂O₅—SiO₂ and Ta₂O₅—TiO₂ system have been investigated.

II. EXPERIMENTAL

Ta₂O₅ based ceramics were prepared by the conventional method as shown in Fig. 1. Raw materials Ta₂O₅, SiO₂ and

TiO₂ were mixed and calcined at 1200°C for 4 hours. The calcined powder was supplemented with 0.4 mg / g PVA (Polyvinyl alcohol) binder. After that, the powder was granulated and cold pressed into disks of 18mm in diameter under a pressure of 1ton / cm². These disks were sintered at 1420°C for 4 hours in air. Then, they were ground and electroded with Ag paste.

Densities were measured by the Archimedes method. The final products were examined by X-ray diffraction using CuK α radiation. The microstructure was checked by SEM method. The dielectric constant ϵ_r was measured by a LCR meter (YHP - 4261A) at several frequencies. Loss tangent ($\tan \delta$) was also measured.

III. RESULTS AND DISCUSSION

A. Densities of samples and crystal structure

Densities in the Ta₂O₅—SiO₂ system are depending on the composition as shown in Fig. 2. Higher dense samples over 95% of theoretical density are obtained. Figure 3 shows X-ray diffraction patterns for the Ta₂O₅—SiO₂ system. It is found in these figures that the solid solution exists in this system. On the other hand, the (Ta₂O₅)_{1-x}(TiO₂)_x system has different phase from that of Ta₂O₅ at x = 0.06 as found in Fig. 4.

This is ascertained to be the metastable H'-monoclinic phase as reported.²⁾

B. Dielectric properties

The dielectric constant ϵ_r and loss tangent in the Ta₂O₅—SiO₂ system are shown for the 100kHz and 1MHz in Figs 5 and 6, respectively. The maximum dielectric constant is 47 in the composition of 97mol% Ta₂O₅—3mol% SiO₂. Figure 7 represents the frequency dependence of ϵ_r and $\tan \delta$ for the sample of 0.97 Ta₂O₅—0.03 SiO₂. It is almost not

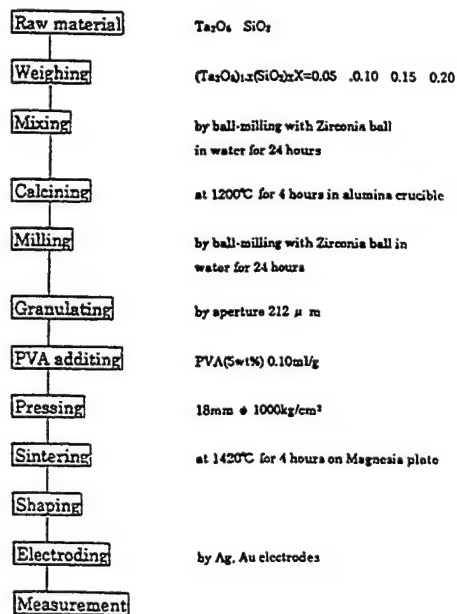


Fig. 1 Simplified flow diagram for the fabrication of samples

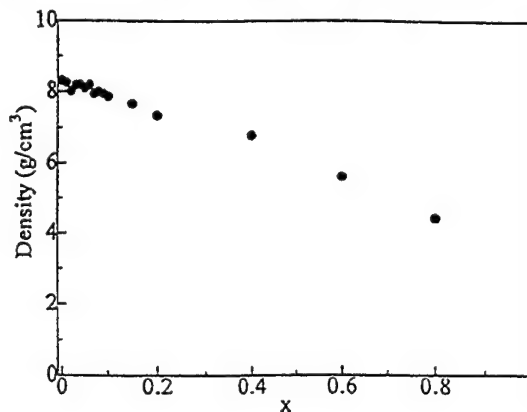


Fig. 2 Density vs. composition in the (Ta₂O₅)_{1-x}(SiO₂)_x system

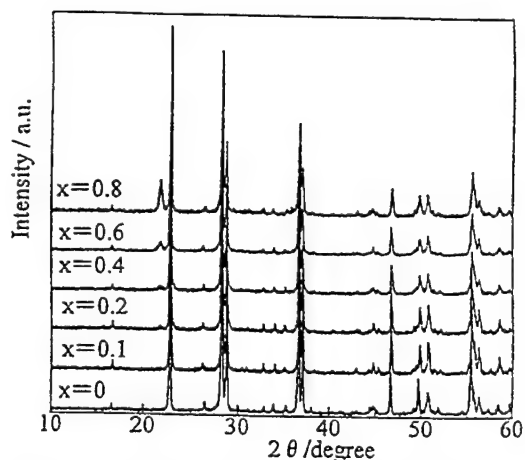


Fig. 3 X-ray diffraction patterns of the $(\text{Ta}_2\text{O}_5)_{1-x}(\text{SiO}_2)_x$ system

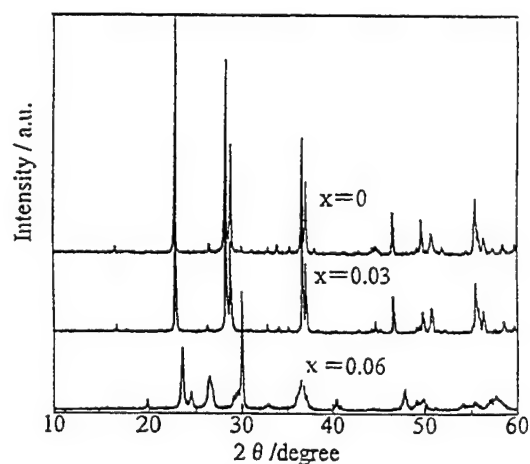


Fig. 4 X-ray diffraction patterns of the $(\text{Ta}_2\text{O}_5)_{1-x}(\text{TiO}_2)_x$ system

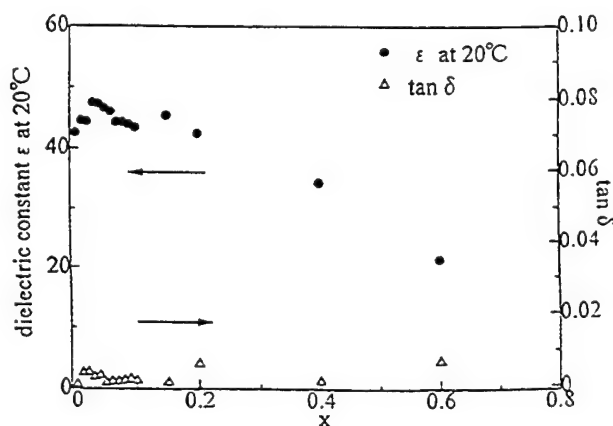


Fig. 5 ϵ_r and $\tan \delta$ as a function of x in the $(\text{Ta}_2\text{O}_5)_{1-x}(\text{SiO}_2)_x$ system at 100 kHz

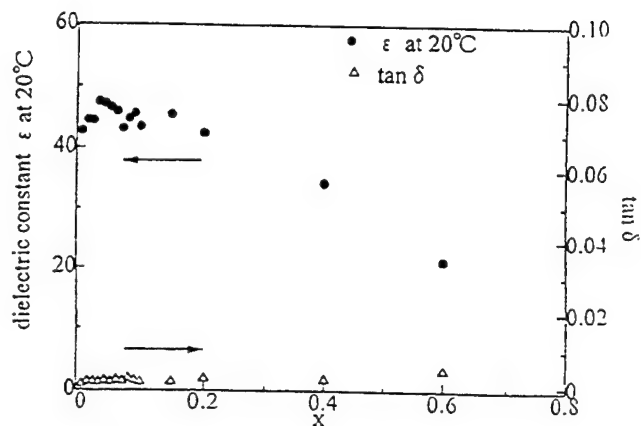


Fig. 6 ϵ_r and $\tan \delta$ as a function of x in the $(\text{Ta}_2\text{O}_5)_{1-x}(\text{SiO}_2)_x$ system at 1 MHz

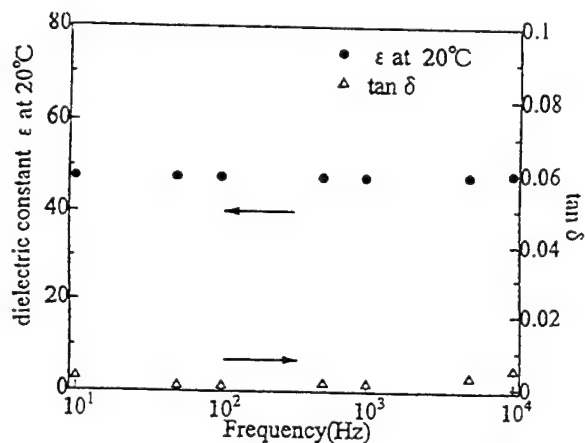


Fig. 7 Frequency dependence of ϵ_r and $\tan \delta$ for the composition 97mol% Ta_2O_5 –3mol% SiO_2

dependent on the frequency. The dielectric constant, ϵ_r and $\tan \delta$ in the Ta_2O_5 – TiO_2 system are shown for the 100 kHz and 1 MHz in Figs. 8 and 9, respectively. The frequency dependence of ϵ_r and $\tan \delta$ for the 94mol% Ta_2O_5 –6mol% TiO_2 is also shown in Fig. 10.

Characterization of the $(\text{Ta}_2\text{O}_5)_{1-x}(\text{TiO}_2)_x$ materials by conventional powder X-ray diffraction in Fig. 4 showed that the enhanced dielectric constant for the sample of 6mol% TiO_2 content may be associated with the appearance of the H'-monoclinic Ta_2O_5 solid solution phase, in agreement with the published phase-equilibria diagram.²⁾ The crystal structure of Ta_2O_5 itself is complex, involving highly distorted TaO_7 and TaO_6 coordination polyhedra, in a structure whose periodicity is known to be sensitive to small quantities of additives.³⁾ Dielectric properties for these system are listed in Table 1.

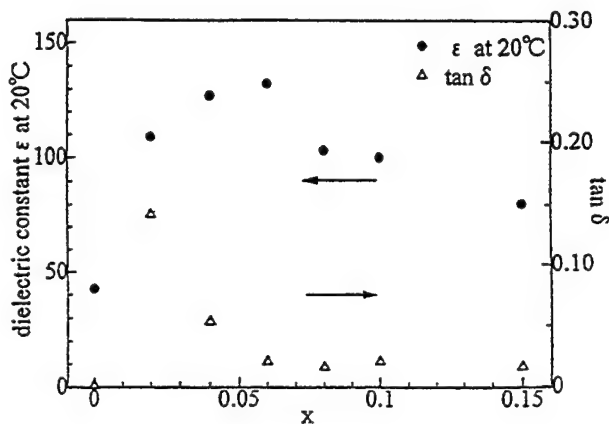


Fig. 8 ϵ_r and $\tan \delta$ as a function of x in the $(\text{Ta}_2\text{O}_5)_{1-x}(\text{TiO}_2)_x$ system at 100kHz

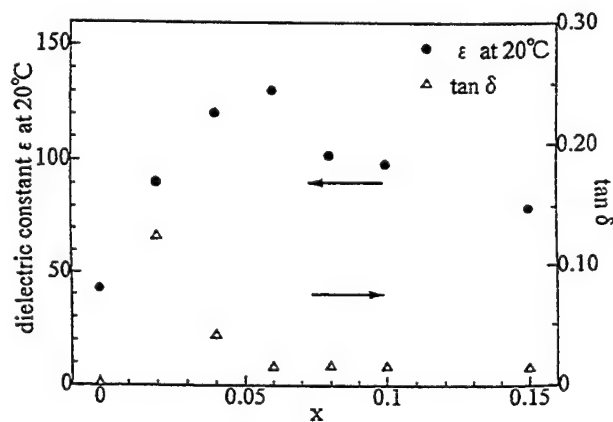


Fig. 9 ϵ_r and $\tan \delta$ as a function of x in the $(\text{Ta}_2\text{O}_5)_{1-x}(\text{TiO}_2)_x$ system at 1MHz

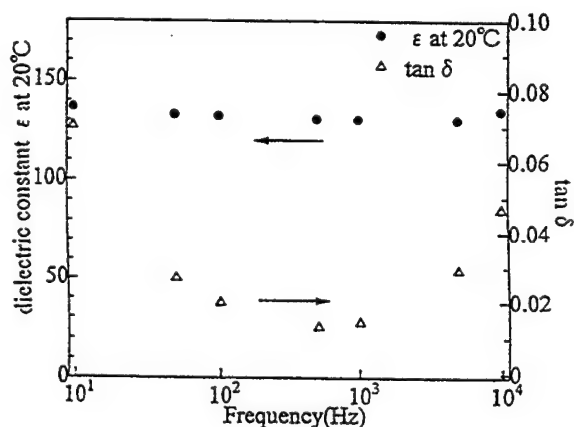


Fig. 10 Frequency dependence of ϵ_r and $\tan \delta$ for the composition 94mol% Ta_2O_5 -6mol% TiO_2

Table 1. Dielectric properties for the Ta_2O_5 based ceramics (at 100kHz)

| composition | Ta_2O_5 | $\text{Ta}_2\text{O}_5-\text{SiO}_2$ 97/3 | $\text{Ta}_2\text{O}_5-\text{TiO}_2$ 96/4 |
|--|-------------------------|--|--|
| Dielectric constant (ϵ_r) | 42.6 | 47.5 | 132.4 |
| Loss tangent ($\tan \delta$) $\times 10^{-3}$ | 0.3 | 2.4 | 20 |
| Resistivity ($\Omega \cdot \text{cm}$) $\times 10^{11}$ | 20 | 0.59 | 1.5 |

IV. CONCLUSIONS

In conclusion, we have shown that modification of Ta_2O_5 through substitution with small amount of SiO_2 or TiO_2 enhances the dielectric constant. In the $(\text{Ta}_2\text{O}_5)_{1-x}(\text{SiO}_2)_x$ system, the maximum dielectric constant is 47 in the composition of $x = 0.03$. On the other hand, the dielectric constant of Ta_2O_5 can be increased by nearly a factor of three—from 42 to 132—through the addition of 6mol% TiO_2 due to appearance of the H'-monoclinic phase.

REFERENCES

- [1] R. F. Cava, W. F. Peck Jr. and J. J. Krajewski : Nature **377** · 21 Sept. (1995) 215
- [2] J. L. Waring and R. S. Roth : J. Res. Nat. Bur. Stds. **72A** (1968) 177
- [3] H. Fujikawa and T. Taga : J. Appl. Phys. **75** (1994) 2538

Effect of Poling on Conducting Barium Titanate

R.D. Roseman

Department of Materials Science and Engineering
University of Cincinnati, Cincinnati, OH 45221-0012

Abstract

Poling of donor-modified BaTiO₃ was carried out by cooling from (650°- 750°C) under an electric field. Poling of non-annealed PTCR samples results in a highly suppressed resistivity transition in direction of the applied field. This state is stable with cycling and the phase transition has effectually no influence on the resistivity response. The low cubic state resistivity ($\rho_{200} < 30 \Omega\text{-cm}$) is due to alignment of the domain structure (>70%) in a coherent nature in direction of the applied field. The perpendicular direction remains in a PTCR state ($\rho_{\text{max}}/\rho_{\text{min}} \sim 2$ orders of magnitude). Annealed samples are unaffected by poling and do not show enhanced domain alignment due to inhomogeneous grain boundaries which pin the domain structure. Conversion from typical PTCR behavior to one which exhibits minimal dependence on the phase transition and results in a highly conductive cubic state is described in terms of grain boundary / domain alignment.

I. INTRODUCTION

In unmodified BaTiO₃ there is a typical randomness to the domain sets and structure within each grain [1-3]. Poling significantly affects domain alignment, creating an increase in polarization within direction of the applied field. In donor modified, semiconducting BaTiO₃ there is a directionality to the domain structure throughout the interior of individual grains [4-8]. In these materials it has been shown [5], through TEM analyses as a function of temperature, that upon cooling through T_c the domain structure always transformed back into the same position and orientation as it was before heating. The directionality to the domain structure has also been related to being built-in from a high temperature, thereby creating a memory to the domain orientation and being a function of the whole sample and not a regional effect [4,5].

Differences between grain boundary and grain interior regions in PTCR materials as a function of heat treatment have been related to segregation effects [9-11]. Microstructure studies [4-7] of the near grain boundary in annealed materials have shown dopant / defect segregation, high strains and a different domain structure than the interior. This is compared to non-annealed samples which show limited segregation effects, low boundary strain and a uniform domain structure throughout the grain.

The objective of this study is to address the influence of grain/domain orientation and alignment on the resistivity-temperature behavior of semiconducting BaTiO₃. The goal is to align the domains within a

direction parallel to the thickness of the sample. In this manner domain and grain boundary structural effects can be better understood.

II. EXPERIMENTAL

BaTiO₃ was doped with Y₂O₃ and ZrO₂ added as nitrate solutions. Samples were prepared by standard ball milling and spray drying techniques. Pellets were pressed and sintered at 1350°C / 2hr in air with half of the samples annealed at 1220°C / 6hr. Average grain size was 15 μm and the density was 93%. Al or Au electrodes were applied for resistivity characterization (Al: $T < 350^\circ\text{C}$; Au: $T < 1000^\circ\text{C}$). Resistance measurements were made using a constant voltage source at 0.015 volts in series with the sample and ammeter at a heating rate of 5°C / min., up to 350°C or by using an electrometer in series with the sample at a heating rate of 10°C / min., up to 800°C.

Poling consisted of re-heating the sintered samples to 600°- 1000°C and applying a field across the samples with mica used as the insulating layers. A Pt wire and baseplate was used for applying voltage. After poling Al electrodes were evaporated onto the surfaces and the resistivity-temperature behavior characterized. Samples for microstructural analyses were prepared by polishing and chemically etching with a HCl- HNO₃-HF solution.

III. RESULTS

The resistivity-temperature (ρ -T) characteristics of the Y₂O₃-modified, PTCR BaTiO₃ samples over a wide temperature range (25°- 800°C) are given in Figure 1. Non-annealed materials exhibit a smaller and more diffuse resistivity transition near T_c (~125°C) along with a lower room temperature resistivity (ρ_{RT}). Common to each ρ -T profile is a second transition near 650°C. This transition is characterized by a change in slope in which the resistivity rapidly decreases to values lower than ρ_{RT} . The profiles are not affected by heating to 800°C.

Non-Annealed Materials

The ρ -T behavior as a function of poling is given in Figure 2. The response for the non-poled / non-annealed samples is given by curve (NA1). After characterization, these larger discs were cut into smaller, equal size sections, with the ρ_{RT} and ρ -T behavior of each being similar to the virgin response. After poling the cut sections, Figure 2 shows that a significant suppression of the resistivity transition (NA2) was obtained using a

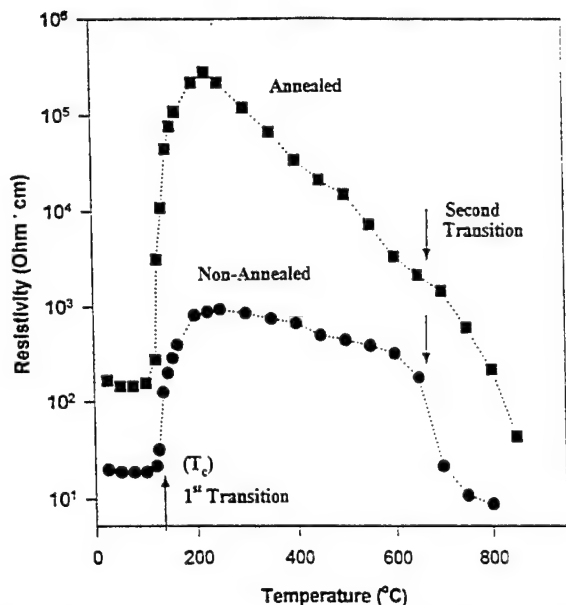


Fig. 1. Resistivity behavior as a function of temperature for annealed and non-annealed PTCR BaTiO₃.

technique of steadily increasing the voltage during cooling (15°C/min) from 700°C. Under these conditions the phase transformation is discerned by a slight change in slope, where at 200°C the resistivity is nearly 2 orders of magnitude lower than that of the virgin curve (NA1). It is also shown that the ρ_{RT} noticeably drops after poling. The ρ -T profiles were found to be stable with cycling. If reheated to temperatures above the 2nd critical transition temperature (T_{c2}), as described by Figure 1, the ρ -T behavior reverts to the original state. T_{c2} was found to be a critical parameter for poling. Application of a field did not significantly affect the ρ -T profile when applied at temperatures less than 600°C.

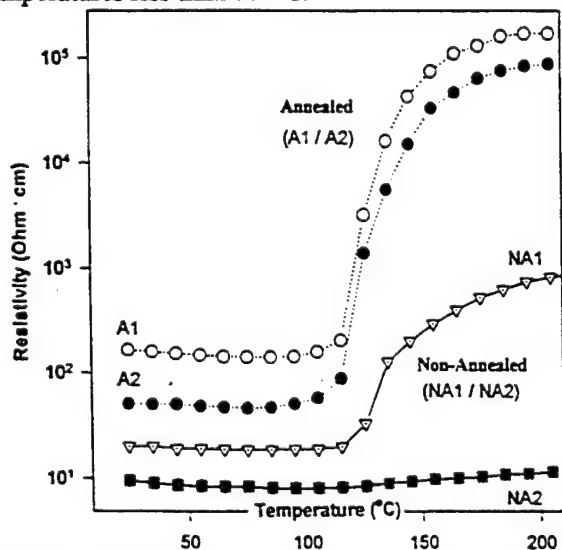


Fig. 2. Resistivity behavior as a function of temperature for poled samples.

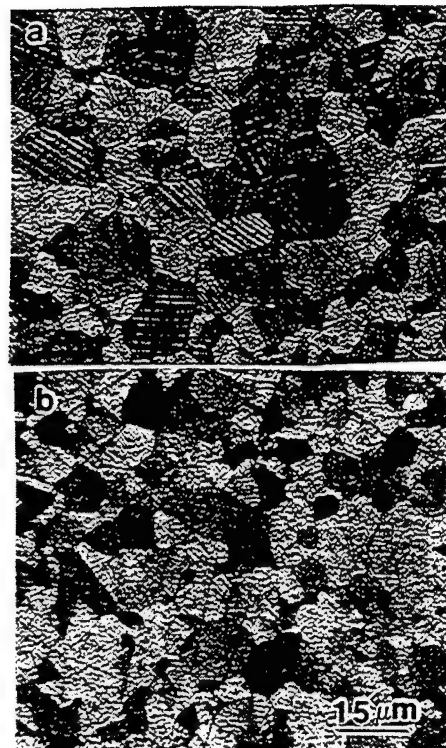


Fig. 3. SEM micrographs of polished and etched sections of surfaces: a) perpendicular and b) parallel, to the applied field for non-annealed / poled samples.

SEM studies of polished and etched sections were used to examine domain structure as a function of poling and direction to applied field. Non-poled materials result in a general randomness to the grain / domain alignment. Optimally poled samples exhibit significant bulk alignment of the grain / domain structure within direction of the applied field, as shown by the micrographs of Figures 3A and 3B. Figure 3A shows the induced microstructural response of a surface perpendicular to the applied field. Grain / domain alignment in direction of the applied field is shown by the banded domain structures in which alternating fine and coarse, columnar (a-c) type domains are obtained. More than 70 % of the grains show this orientation. Figure 3B shows the induced microstructural response of a surface parallel to the applied field. In this case (a-a) type domain structures are dominant, showing a reversal of the orientation.

Figure 4 shows the ρ -T response as a function of poling direction. The poled samples were tested by: a) electrodes deposited on faces perpendicular to the applied field; and b) electrodes removed and re-deposited on faces parallel to the applied field. All cut sections for this study had a square geometry. Figure 4 shows that the ρ -T response of the direction perpendicular to the applied field results in an increase in resistivity of over an order of magnitude. The poled direction exhibits the suppressed transition state ($\rho_{RT} \sim 10$ to $\rho_{200} \sim 25 \Omega\text{-cm}$).

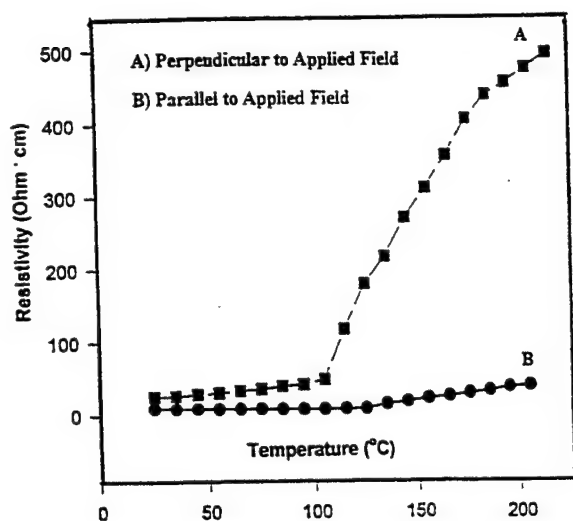


Fig. 4. Resistivity behavior as a function of temperature and poling direction for non-annealed / poled samples.

Annealed Materials

In comparison to the non-annealed samples discussed above, poled / annealed materials do not exhibit the same resistivity suppression tendencies. Similar to the non-annealed material studies, many variations on the poling conditions were used, yet none significantly affected the annealed materials, as shown in Fig. 2. The ρ_{RT} was slightly lowered, yet the magnitude of the rise in resistivity (ρ_{max}/ρ_{min}) is not significantly affected.

The parallel and perpendicular to applied field ρ - T characteristics were also investigated. Poling was found to not have a significant effect on the resistivity transition or ρ_{RT} as a function of poling direction. It was also found through microstructural analysis that there is no high degree of grain / domain alignment.

IV. DISCUSSION

Non-poled / Non-annealed State: Depolarization and mechanical strain affect the domain character of the grain boundaries in ferroelectric BaTiO₃ [15,16]. Due to these effects and the domain / grain directionality in donor-modified, PTCR BaTiO₃, there is a general randomness to the grain-to-grain domain orientation in the non-poled state. It has been found [4,5] that in the non-poled state that a portion of at least two grain boundaries per grain have preferential orientation or coherency to the domain structure across the boundary. This has been found to occur in an irregular or tortuous fashion through the bulk and not directly through each grain on one plane.

In this respect, the conduction mechanism in these materials can be described as either electron flow along the tortuous pathways or as a percolation of conducting electrons through coherent grain boundaries. This infers that all other grain boundaries play a minor

role and have a limited contribution to bulk conduction of electrons through the material.

Poled / Non-annealed State: As shown in Figure 3, poling of non-annealed samples results in a field induced crystallographic arrangement in which a high degree of grain / domain orientation is in direction of the applied field. TEM analyses were performed on grain boundaries as that in the cross sectional view of figure 3B. These type coincident or coherent grain boundaries are described by domains which cross the boundary with a strong preference for certain crystallographic relationships. It has been demonstrated [4,17] that these type boundaries consist of 90° a-a type domains with a head-to-tail, c-axis relationship across the boundary. These boundaries are limited to crystallographic rotations which result in nominal strain and vacancies, significantly decreasing distortions produced by depolarization and mechanical effects. This results in a large portion of the grain boundaries in the poled direction being interconnected in a coherent nature through the material bulk. This high degree of structural orientation is the basis for the high cubic state conductivity and suppressed PTCR behavior.

To obtain the highly oriented state it is necessary to pole at temperatures near the second transition. At this temperature, polarization orientation and ion movement easily occurs. In non-annealed materials a more homogeneous distribution of the dopant occurs with limited segregation [4,5]. In this case, under an applied field near T_{c2} , both the localized polarization and strain fields associated with donor defect states mutually interact and create a preferentially oriented and stabilized alignment of the local polarization and strain fields. It is the high temperature poling which creates a "memory" to domain formation and allows the bulk preferential alignment and stable domain structure to develop.

Above T_c , because of the anisotropy in resistivity in the cubic state, the conversion of domain orientations results in a change in resistivity. This change is calculated to be small and the grain interior resistivity is affected by a factor of 2 to 3. The change in bulk resistivity or mobility across the grain boundary is dependent on the change in grain boundary potential. It is the concentration of coherent grain boundaries, percent of each boundary which is of coherent character, and the directional nature of these boundaries which determines the resistivity-temperature characteristics.

The ρ - T response of the direction perpendicular to the applied field in the poled material results in the PTCR behavior being similar to the non-poled material response. The resistivity behavior of the field-aligned direction of the optimally poled materials exhibit a highly suppressed transition in which the resistivity differs by a

factor of 2-3. This is the same order of magnitude change predicted for crystals with no grain boundaries. The difference in grain boundary potential, above and below T_c , for coherent grain boundaries is, therefore, analogous to the change in grain interior resistivity (ρ_n), and the differences are directly associated with microstructure.

The high cubic or paraelectric state conductivity in non-annealed, poled samples is associated with not only the high coherency of many grain boundaries but with the oriented polarization and strain fields which behave as a channel to electron flow even without the domains, domain walls and spontaneous polarization being present. In these materials the conductivity is high both above and below T_c , with the ferroelectric transition having effectually no influence on electrical behavior. The poled materials can, therefore, be associated with single-crystal-like behavior within direction of the applied field.

The similarity in electrical behavior of the virgin-non-poled material and the poled samples examined in direction perpendicular to the poling field is revealed through the relationship in connectivity of coherent grain boundaries. Grains oriented in the anti-poled direction do not exhibit connectivity across the viewing surface. This is similar to the non-poled state where only limited domain coherency across a grain boundary is found. The resistivity behavior obtained can be described as a percolation of electrons along tortuous pathways. The similarity in ρ -T behavior is, thus, associated with a limited number of conducting grain boundaries, approaching that of the connectivity threshold. Upon disappearance of the spontaneous polarization, the increase in resistance, as shown by the field-aligned data, is largely due to the structural character and a decrease in mobility along the tortuous electron pathways.

Annealed Materials

Direct observation of induced microstructure changes as a function of annealing reveals inhomogeneity in structure due to enhanced grain boundary segregation [4-7, 17]. The near grain boundary shows regions which are highly defected and structurally incoherent. In other areas grain boundary structural coherency results, exhibited by 90° a-a domain morphology with head-to-tail, c-axis orientation. These regions reflect low mechanical and electrical boundary potentials and dominate charge transport.

The ρ -T response and bulk grain / domain orientation of annealed samples is essentially unaffected by poling, although the ρ_{RT} is slightly lowered. Therefore, the bulk microstructure was found to be similar to the random alignment found in non-poled materials. These results indicate that: a) the non-uniform and more highly stressed grain boundaries pin the domain structure during

the annealing schedule; and, b) high temperature poling does not relieve boundary strain or redistribute segregated ions or defects in order to allow the bulk domain structure to align within the field. Conduction in the ferroelectric state can, thus, be modeled as a percolation of conducting electrons along mutually interacting domains. This is analogous to that described for non-annealed materials, except that there is a large reduction in grain boundary area in which a low potential electrical barrier exists.

The small regions of domain coherency across the grain boundaries, therefore, behave as electrical gates and controlling the breadth and number of these leads to changes in electron mobility and differences in ρ -T characteristics. The extent of the coherent grain boundary regions directly relate to either suppressed (non-annealed, poled), diffuse (non-annealed) or sharp (annealed) resistivity transitions.

V. CONCLUSION

Poling of non-annealed PTCR samples results in a highly suppressed resistivity transition in direction of the applied field. This state is stable with cycling. The phase transition and disappearance of the spontaneous polarization has effectually no influence on the resistivity response. The high cubic state conductivity is due to alignment of the domain structure in a coherent nature in direction of the applied field. The perpendicular direction, though, remains in a PTCR state. The diffuse nature of this PTCR effect in the non-aligned direction is associated with a limited number of coherent grain boundaries and a decrease in mobility along tortuous electron pathways. Annealed samples are unaffected by poling and do not show enhanced domain alignment due to inhomogeneous grain boundaries which pin the domain structure.

REFERENCES

- [1] R.C. DeVries and J.E. Burke, *J. Am. Cer. Soc.*, **40**, [6] 200 (1956)
- [2] V.J. Tennery and F.R. Anderson, *J. Appl. Phys.*, **29**, [5] 755 (1958)
- [3] Y. Hu, H. Chan, Z. Wen, M. Harmer, *J. Am. Cer. Soc.*, **69**, [8] 594 (1986)
- [4] R. Roseman, J. Kim and R. Buchanan, *Ferroelectrics*, **177**, 273 (1996)
- [5] R. Roseman, J. Kim and R. Buchanan, *Ferroelectrics*, **177**, 255 (1996)
- [6] R. Roseman, J. Kim and R. Buchanan, *Cer. Trans.*, **41**, 153 (1994)
- [7] R. Buchanan, R. Roseman and T. Armstrong, *Ferroelectrics*, **135**, 343 (1992)
- [8] G. Goodman, *J. Am. Ceram. Soc.*, **46**, [1] 48-54, 1963
- [9] Y. Chiang and T. Takagi, *J. Am. Ceram. Soc.*, **73**, [11] 3278 (1990)
- [10] S. Desu and D. Payne, *J. Am. Ceram. Soc.*, **73**, [11] 3407 (1990)
- [11] D. Wang and K. Uneya, *J. Am. Ceram. Soc.*, **73**, [6] 1574-81 (1990)
- [12] T. Malis and H. Gleiter, *J. Appl. Phys.*, **50**, [7] 4920 (1979)
- [13] T. Malis and H. Gleiter, *J. Appl. Phys.*, **50**, [7] 4924 (1979)
- [14] B. Kulwicki and A. Purdes, *Ferroelectrics*, **1**, [4] 253-263 (1970)
- [15] J. Weertman and J. Weertman, *Elementary Dislocation Theory*, Ox. Univ. Press, New York (1992)
- [16] I. Bunget and M. Popescu, *Physics of Solid Dielectrics*, C. Laird, ed., in *Mat. Sci. and Mono.*, **19**, Elsevier, Amsterdam (1978)
- [17] J. Kim, Submitted, unpublished (1997)

Effect of pH and Cation Concentration on PMN Powders Prepared by a Coprecipitation Method

De-Yin Jeng, Chorng-Jeou Chen, S.Ray Chaudhuri
YTC America, Inc.

Abstract- Stoichiometric $\text{PbMg}_{2/3}\text{Nb}_{1/3}\text{O}_3$ powders were prepared by coprecipitation from mixed solutions of niobium oxalate, magnesium nitrate and lead nitrate. Processing parameters such as pH and cation concentration play an important role in determining the characteristics of coprecipitated PMN powders. The effect of pH in the solution on the crystal structure of calcined powders was studied by varying the pH values of the precipitation between 6.0 to 11.0. High purity (>99.0 %) perovskite phase can be obtained by proper control of pH values in the solution. Increasing the cation concentration, however, led to the formation of pyrochlore phase in the calcined powders. The microstructures of sintered PMN pellets revealed an average grain size of 2 - 4 μm after sintering at 900°C for 2 hrs. The dielectric permittivity of PMN pellets was measured using an LCR meter.

I. Introduction

Lead magnesium niobate (PMN) is a perovskite relaxor ferroelectric having unusually high dielectric constant, relatively low sintering temperature and high electrostrictive strains. This unique combination of properties offers numerous applications of PMN as multilayer capacitors, actuators and tunable transducers. These advantages, however, are offset by the processing difficulties encountered in fabricating single-phase PMN. The appearance of a minor pyrochlore phase in addition to the perovskite phase leads to drastic reduction in its dielectric properties. Various synthesis techniques have been reported to produce single-phase PMN [1,2], including conventional mixed oxide method, the columbite precursor method, the wet chemical route and salt-based method. Of special interest is the wet chemical route which is capable of producing high purity submicron size powders with controlled morphology, particle size distribution and stoichiometry. Submicron size PMN powders possess high sinterability which allows densification of ceramic compacts at lower temperatures, resulting in smaller grain size and the use of low cost Ag-Pd as electrode materials. By controlling the preparation parameters, and hence the solution chemistry, a synthesis process with good reproducibility can be established.

Watanabe et al [3-8] prepared a salt solution of lead, magnesium and niobium which are precipitated simultaneously by adding a precipitant. The niobium oxalate solution was prepared by dissolving $\text{Nb}_2\text{O}_5 \cdot x\text{H}_2\text{O}$ in a hot oxalic solution. Tetramethylammonium hydroxide was found

to be effective for the formation of single phase PMN among various precipitants used. Suyama et al reported a modified oxalate method in ethanol solution to produce high purity perovskite PMN powders. This process utilizes the high solubility of niobium oxalate in ethanol as the niobium ion source which was precipitated as hydroxides by adding ammonium hydroxide. Although it has been demonstrated that coprecipitation method is an effective way of preparing pyrochlore free PMN, the effect of pH value and cation ion concentrations on the formation of perovskite phase remains unclear. Due to the extremely complex solution chemistry involved, the purpose of this paper was to empirically find out the powder characteristics and crystal structure of calcined PMN powders prepared under different pH values and cation concentrations. The dielectric properties and microstructure of sintered PMN pellets will be discussed.

II. Experimental

Modified oxalate method in ethanol solution was used to prepare $\text{PbMg}_{2/3}\text{Nb}_{1/3}\text{O}_3$. The flow diagram for powders preparation is shown in Fig.1. Stoichiometric amount of niobium oxalate ($\text{Nb}_2\text{O}_5 \cdot 5\text{C}_2\text{O}_4 \cdot 2\text{NH}_4\text{OH}$), ACS grade lead nitrate ($\text{Pb}(\text{NO}_3)_2$) and magnesium nitrate ($\text{Mg}(\text{NO}_3)_2 \cdot 6\text{H}_2\text{O}$) were used as starting materials. Niobium oxalate was first dissolved into de-ionized water and ethanol was added to form a clear solution which is further mixed with another ethanol solution containing oxalic acid. Aqueous solution of lead nitrate and magnesium nitrate was then added to the mixture solution. The pH of the resulting solution was adjusted with ammonium hydroxide and allowed to stir for three hrs at room temperature. The concentration of the cations was varied by changing the amount of water and ethanol used in the solution. Centrifugation method was used to separate the precipitated powders from the solvent. The wet powders were dried at 100°C for 12 hrs before further calcination.

Thermal analysis of the as-dried powders was carried out with DTA/TGA. Based on the thermal analysis results, the dried powders were calcined by firing in static air at 500°C for 6 hr with a heating rate of 4°C/min. The calcined powders were mixed with 5% polyvinylbutyral (PVB) binder in acetone before pressing into a 1/4" diameter pellet under 1.5 tons of pressure. The green compacts were then sintered in air at 900°C for 2 hrs. Crystal structure of the sintered

powders was performed using Philips X'pert X-ray diffractometer (CuK α). Dielectric constants were measured using a LCP meter (HP4263A).

III. Results and Discussion

A. Thermal analysis of as-dried powders

Fig.2 shows the DTA analysis of the as-dried powders. The two major endothermic peaks and one exothermic peaks below 400°C can be attributed to the organic burn-off process, as evidenced from the TGA curve from Fig.3. The broad bump between 500°C and 900°C is, however, a result of the crystallization process giving rise to pyrochlore and perovskite phase. A close-up view of the curve between 600 and 900°C, revealing two distinct humps. The lower temperature hump, peaking around 650°C, corresponds to the metastable pyrochlore phase formation. The higher temperature hump, peaking at around 775°C, is associated with the transformation to perovskite phase. The weight loss above 900°C is a result of PbO evaporation.

B. Effect of pH on the crystal structure of calcined Powders

Table 1 shows the crystalline phase of the calcined powders (900°C/2 hrs) prepared under different pH values. A wide spectrum of perovskite content can be produced using the same processing procedures but under different pH values. It can be seen that for pH values between 9.40 to 9.50, more than 99.0% of the perovskite phase can be obtained with good reproducibility, as indicated by the XRD pattern shown in Fig. 4. The perovskite phase decrease precipitously as the pH value drops below 9.0, indicating a drastic change in solubility of the cations in the solution. At pH= 5.92, only 1% of perovskite is detectable. Pyrochlore phase also begins to appear as the pH value crossed the "window" and increased to above 9.50. The perovskite phase becomes essentially negligible as the pH increased to 10.40.

Table 1:
Effect of pH values on perovskite phase formation

| pH | % Perovskite | pH | Perovskite |
|------|--------------|-------|------------|
| 5.92 | 1 | 9.45 | 99.89 |
| 6.47 | 22.07 | 9.50 | 99.02 |
| 7.52 | 26.33 | 9.50 | 99.57 |
| 8.45 | 17.62 | 9.51 | 98.00 |
| 9.04 | 21.01 | 9.86 | 92.01 |
| 9.41 | 99.71 | 9.97 | 84.71 |
| 9.45 | 99.99 | 10.02 | 80.66 |
| | | 10.40 | 2.27 |

Compositional analysis of the sintered samples from powders prepared at pH =9.45 showed stoichiometric ratio of the constituent cations. Further titration of the filtrate with either

ammonium hydroxide or oxalic acid showed no evidence of precipitation. This result indicates that all the cations were precipitated as solid powders when the pH values fall between 9.40 and 9.50. For pH values outside this range, the solubility of the cation species varies resulting in loss of ions from the solid precipitate powders to the solvent phase. The details of this solubility change was not studied in this work.

C. Effect of cation concentrations on perovskite phase

The effect of cation concentration on perovskite formation is shown in Table 2. All the batches were prepared with pH values between 9.40 and 9.50 and the mixing time was kept the same. The results showed that higher cation concentrations led to the appearance of pyrochlore phase. This may have arisen due to incomplete mixing of the precipitates as the concentration increases. It is noted that there is a threshold concentration value beyond which homogeneous mixing of the precipitated becomes difficult and a secondary pyrochlore phase starts to appear. To improve the compositional homogeneity, three batches of the powders prepared at various cation concentrations were calcined a second time at 900°C for 2 hrs after careful regrinding in a mortar and pestle. The crystal structure of powders showed basically the same crystalline phase before and after regrinding and recalcination. This shows that the compositional homogeneity of the precipitated powders is best achieved in the liquid state. It is speculated that, with pH values properly controlled to within the "window" value, prolonging the mixing time or using sonication technique during the precipitation stage will help in improving the homogeneity of the powders. Further work is required to verify this point.

Table 2
Effect of Pb²⁺ ions concentration on perovskite phase formation

| Pb ²⁺ (M) | 0.038 | 0.047 | 0.058 | 0.061 | 0.077 | 0.090 | 0.110 |
|----------------------|-------|-------|-------|-------|-------|-------|-------|
| % Perovskite | 100 | 100 | 100 | 85.78 | 87.97 | 85.78 | 75.14 |

D. Dielectric Constants and Microstructure

Fig.5 shows the dielectric constants of pellets sintered at 900°C for 2 hrs. Sintered specimens were polished and sputtered with gold as the electrode materials for dielectric measurement. Although the exact temperature of the low temperature specimen was not measured, the dielectric constant showed a frequency dispersion characteristic which is typical of relaxor materials. The maximum dielectric constant measured at low temperature was 18,000. At room temperature, the dielectric constant of the materials was independent of the frequencies and showed a value around 11,000.

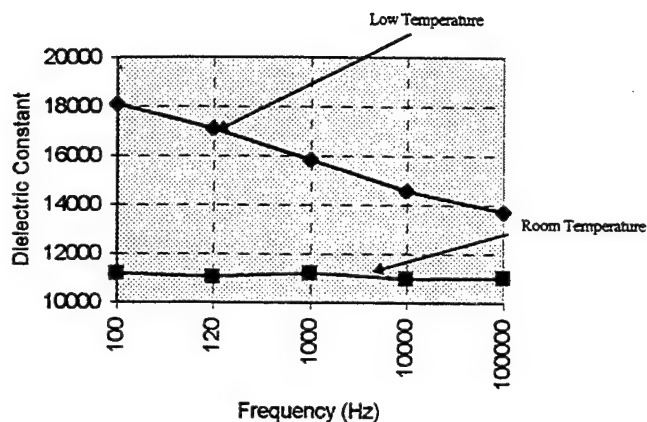


Fig. 5: Dielectric constants of samples sintered at 900C for 2 hrs.

Fig.6 shows the SEM micrograph of the fracture surface of the sintered pellets. It reveals a high density, pore free microstructure with uniform average grain size $\sim 2-4 \mu\text{m}$. Notice the absence of inter granular phases such as PbO .

IV Conclusions

High purity, stoichiometric PMN powders were synthesized via coprecipitation method by controlling the pH value of the solution. Compositional homogeneity of the precipitated powders is affected by the cation concentrations in the liquid phase. Below a threshold value of $\text{Pb}^{+2}=0.058\text{M}$, 100% pure perovskite phase can be obtained reproducibly. Above this threshold value, pyrochlore phase starts to appear even though the pH value is controlled properly. The maximum dielectric constant measured was 18,000 and the average grain size after sintering at 900°C for 2 hrs was $2-4 \mu\text{m}$.

REFERENCES

1. S.L. Swartz and T.R. Shrout, Mat. Res. Bull., Vol.17, pp. 1245-1250, 1982
2. S.M. Gupta, A.R. Kularni, Materials Chemistry and Phys., 39(1994)98 - 109
3. A. Watanabe, H. Haneda, Y. Moiyoshi, S. Shirasaki, S. Kuramoto and A. Yamamura, J. Mater. Sci., 72 (1992)1245 - 1249
4. T.R. Shrout, J. Fielding, Jr., Ultrasonics Symposium, 1990, pp. 711 - 720
5. S.M. Guha, H.U. Anderson, Advances in Ceramics, Vol.21: Ceramic Powder Science, 1987, pp. 91-98

6. Jin-Ho Choy, Yang-Su Han, Seung-Wan Song, and Soon-Ho Chang, J. Amter. Chem., 1994, 4(8), 1271-1274
7. P. Ravindranathan, S. Komarneni, S.C. Choi, A.S. Bahlla, and R. Roy, Ferroelectrics, 1988, Vol.87, pp.133-140
8. H. Yamamura et al, Ceramic International, 11, 23(1985)

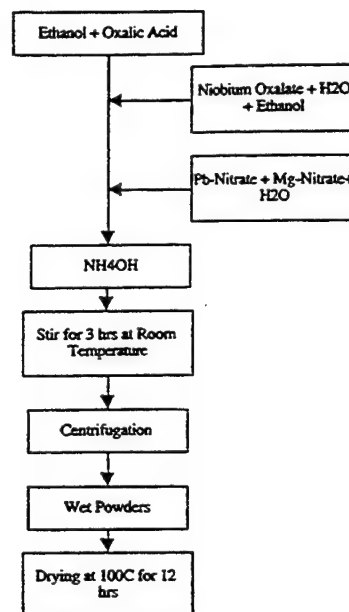


Fig.1 Process flow chart for the synthesis of PMN powders by coprecipitation method

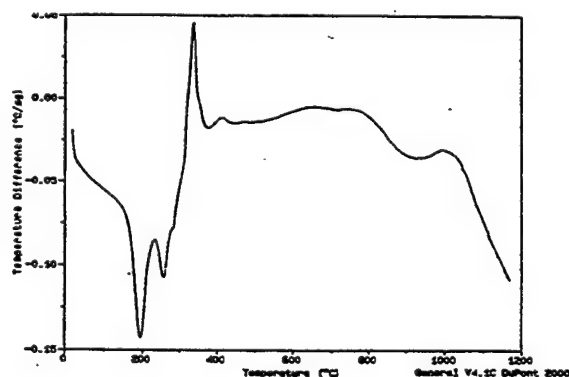


Fig.2 DTA analysis of as-dried PMN powders.

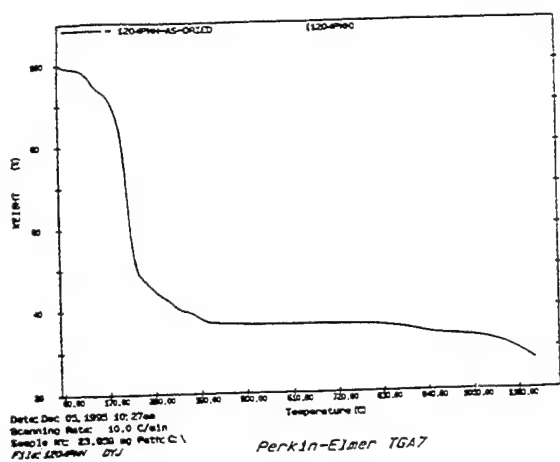


Fig.3 TGA curve of as-dried PMN powders

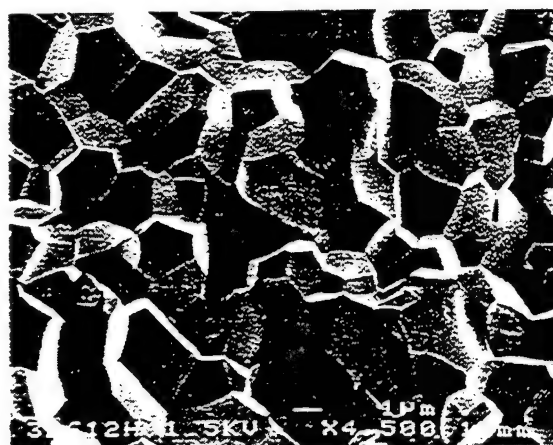


Fig.6 SEM micrograph of PMN pellets sintered at 900°C for 2 hrs.

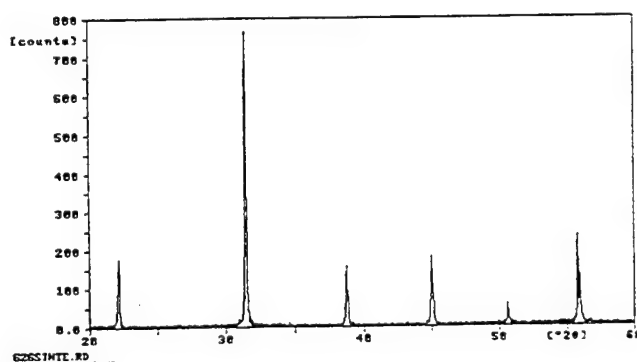


Fig.4 XRD pattern showing perovskite phase of the PMN powders calcined at 900°C for 2 hours

Session IV—Piezoelectrics, Actuators, and Sensors

PAGE

Invited Papers

- | | |
|--|-----|
| Mechanical Loss in Piezoceramics Under High Vibration Level, <u>S. Takahashi</u> and Y. Sasaki, NEC Corp.; and S. Hirose, Yamagata University; Japan | 231 |
| Relaxor Based Ferroelectric Single Crystals with High Piezoelectric Performance, <u>S.-E. Park</u> and Thomas R. Shrout, Penn State University, USA | 235 |

Contributed Papers

Single Crystals

- | | |
|---|-----|
| IV-1 Growth of Single Crystal PMN-PT, <u>P. Bridenbaugh</u> , J. Rottenberg, and G.M. Loiacono, Crystal Associates Inc., USA | 242 |
| IV-2 Relaxor Single Crystals from Polycrystalline Precursors, <u>M.P. Harmer</u> , H.M. Chan, T. Li, F. Meschke, and A.M. Scotch, Lehigh University, USA | 244 |
| IV-3 Templated Grain Growth of Ferroelectric Materials, B. Brahmaroutu, P. Rehrig, S.H. Hong, <u>S. Trolier-McKinstry</u> , and G.L. Messing, Penn State University, USA | 248 |
| IV-4 Effect of Electrode Material on the Physical and Electrical Properties of a PZN Relaxor-PT Single Crystal, <u>J.Y. Yamashita</u> , K. Harada, T. Kobayashi, S. Shimanuki, and S. Saito, Toshiba Corp., Japan | 252 |
| IV-5 Intelligent Engineering of Hydrothermal Reactions, <u>R.E. Riman</u> , B.L. Gersten and S.B. Cho, Rutgers University; M.M. Lencka and A. Anderko, OLI Systems Inc.; and L.E. McCandlish, Ceramaré Corp., USA | 256 |

Polycrystalline Ceramics

- | | |
|--|-----|
| IV-6 Dielectric and Piezoelectric Properties of Ceramics in the Lead Indium Niobate-Lead Titanate Solid Solution, E.F. Alberta and <u>A.S. Bhalla</u> , Penn State University, USA | 260 |
| IV-7 Preparation and Electric Properties of $\text{Pb}(\text{Yb}_{1/2}\text{Nb}_{1/2})\text{O}_3\text{-PbTiO}_3\text{-PbZrO}_3$ Ceramics, <u>H. Ohuchi</u> , T. Sanada, M. Ueda, and T. Hashimoto, Shonan Institute of Technology, Japan | 264 |
| IV-8 Ferroelectric Properties and Crystal Orientation in Rhombohedral PZT Ceramics, <u>T. Ogawa</u> and A. Yamada, Shizuoka Institute of Science and Technology, Japan | 268 |
| IV-9 High Power Ceramic Materials for Piezoelectric Transformer, <u>Y. Fuda</u> , M. Katsuno, and M. Tamura, Tokin Corp., Japan | 272 |
| IV-10 Temperature Stable Piezoelectric Ceramics for Cylindrical Vibrators of Vibratory Gyroscopes, <u>M. Tamura</u> , K. Satoh, O. Ise, and E. Otsuki, Tokin Corp., Japan | 276 |

| | PAGE |
|---|------|
| IV-11 The Influence of the Heat Treatment Conditions on the Temperature Stability of the Piezoelectric Properties and Absolute Values of the Lead Titanate Ceramics, <u>K. Miyabe</u> , <u>K. Tachimoto</u> , <u>K. Horino</u> , <u>T. Tsukada</u> , and <u>M. Takada</u> , <i>TDK Corp., Japan</i> | 280 |
| IV-12 Non-Lead Piezoelectric Ceramics Based on $(\text{Bi}_{1/2}\text{Na}_{1/2})\text{TiO}_3$, <u>T. Takenaka</u> and <u>H. Nagata</u> , <i>Science University of Tokyo, Japan</i> | 284 |
| <u>Electromechanical Properties</u> | |
| IV-13 Effect of Grain Size on the Electromechanical Properties of Antiferroelectric-to-Ferroelectric Phase Switching PLSnZT Ceramics, <u>M.-J. Pan</u> and <u>S. Yoshikawa</u> , <i>Penn State University, USA</i> | 288 |
| IV-14 Technique for Measuring Electromechanical Coupling in Electrostrictors and Piezoelectrics, <u>S.P. Leary</u> and <u>S.M. Pilgrim</u> , <i>Alfred University, USA</i> | 292 |
| IV-15 Flexural Failure in Navy Type III PZT, <u>L. Ewart</u> , <i>Naval Undersea Warfare Center, USA</i> | 295 |
| IV-16 Electromechanical Fatigue of Lead Zirconate Titanate Ceramics, <u>H. Makino</u> and <u>N. Kamiya</u> , <i>Toyota Central R&D Lab. Inc., Japan</i> | 299 |
| IV-17 Electromechanical Properties of High Temperature Piezoelectric Materials, <u>Y. Sakabe</u> , <u>M. Kimura</u> , <u>K. Ogiso</u> , and <u>A. Ando</u> , <i>Murata Manufacturing Co. Ltd., Japan</i> | 303 |
| <u>Composite Fabrication</u> | |
| IV-18 Solid Freeform Fabrication (SFF) of Novel PZT Ceramic/Polymer Composites, <u>A. Safari</u> , <u>S.C. Danforth</u> , <u>R.K. Panda</u> , <u>T.F. McNulty</u> , and <u>A. Bandyopadhyay</u> , <i>Rutgers University, USA</i> | 307 |
| IV-19 PZT MicroRod Composite Ultrasonic Transducers, <u>M.T. Strauss</u> and <u>M.V. Parish</u> , <i>CeraNova Corp., USA</i> | 311 |
| IV-20 Preparation of Fine Scale PZT Fibers and Their 1-3 Composite Properties, <u>R.J. Meyer, Jr.</u> , <u>T.R. Shrout</u> , and <u>S. Yoshikawa</u> , <i>Penn State University, USA</i> | 313 |
| IV-21 Anisotropic Piezoceramic (3-3) Composites, <u>V.S. Venkataramani</u> , <u>P.C. Schaefer</u> , and <u>L.S. Smith</u> , <i>GE Corporate R&D, USA</i> | 317 |
| <u>Actuators/Transducers</u> | |
| IV-22 Fine Grain Piezoelectric Ceramics for Transducer and Actuator Applications, <u>W. Hackenberger</u> and <u>J. Helgeland</u> , <i>TRS Ceramics Inc.</i> ; <u>M. Zipparo</u> , <u>C. A. Randall</u> , and <u>T.R. Shrout</u> , <i>Penn State University; USA</i> | 323 |
| IV-23 Piezocomposite Materials for Ultrasonic Imaging Applications, <u>B. Pazol</u> , <u>H. Pham-Nguyen</u> , <u>J. Hollenbeck</u> , <u>M. Callahan</u> , <u>K. Gabriel</u> , and <u>G. Schmidt</u> , <i>Materials Systems Inc., USA</i> | 326 |

| | PAGE |
|---|-------------|
| IV-24 Computer Simulation of Piezocomposite Transducers, <u>W. Cao</u> , <i>Penn State University, USA</i> | 329 |
| IV-25 Medical Ultrasonic Transducers with Switchable Frequency Bands Centered About f_0 and $2f_0$, <u>T.R. Gururaja</u> and <i>J. Chen, Hewlett Packard Co.; and A. Shurland, University of Pennsylvania; USA</i> | 333 |
| IV-26 Bimorph and Pseudo Shear Mode Actuation, <u>L.E. Cross</u> , <i>Penn State University, USA</i> | 337 |
| IV-27 Capped Ceramic Underwater Sound Projector, <u>J.F. Tressler</u> , <i>W. J. Hughes, W. Cao, K. Uchino, and R.E. Newnham, Penn State University, USA</i> | 340 |
| IV-28 Piezocomposite SmartPanels™ for Active Surface Control Applications, <u>D. Fiore</u> , <i>R. Torri, and R. Gentilman, Materials Systems Inc., USA</i> | 344 |

Mechanical Loss in Piezoceramics under High Vibration Level

Sadayuki Takahashi, Yasuhiro Sasaki and Seiji Hirose*

Research and Development Group, NEC Corporation

4-1-1, Miyazaki, Miyamae-ku, Kawasaki-shi 216, Japan

*Department of Engineering, Yamagata University

4-3-16, Jyonan, Yonezawa-shi 992, Japan

Abstract—Mechanical loss in lead-zirconate-titanate (PZT) based piezoelectric ceramics was studied by introducing three complex physical constants: a complex elastic, a dielectric, and a piezoelectric constant. The elastic and dielectric losses had finite values, while the piezoelectric loss was negligibly small. More than 60% of the mechanical loss at resonance under a relatively low vibration-velocity was the elastic-origin component, and the rest was the dielectric-origin component. The dielectric-origin component rose sharply, however, as the vibration-velocity increased and became dominant at high vibration-velocity. The mechanical loss was reduced by doping Fe_2O_3 into the PZT, which was apparently caused by pinning of the ferroelectric domain wall.

I. INTRODUCTION

New piezoelectric power devices, such as ultrasonic motors, piezoelectric actuators, and piezoelectric transformers, have been watched with keen interest in recent years. These devices require piezoelectric ceramics capable of generating high level vibration-velocity, because the output power of these devices generally increases as the vibration-velocity increases. We have been studying electromechanical properties in lead-zirconate-titanate (PZT) based piezoelectric ceramics from the vibration-velocity viewpoint, aiming to develop high-power-usage piezoelectric ceramics. [1-8]

The vibration-velocity linearly increases as the driving electrical field-level increases when the field-level is low. When the field-level exceeds a certain value, the vibration-velocity converges toward its saturation point accompanied by a great amount of heat generation. This vibration-velocity saturation accompanied by heat generation was found to be caused by an increase in the mechanical loss, which is the reciprocal of the mechanical quality factor. Accordingly, to develop high-power-usage piezoelectric ceramics, the relationship between the mechanical loss and the physical constants must be clarified.

The mechanical loss can be taken into account by using complex elastic, dielectric, and piezoelectric constants. We

will first clarify the relationship between the mechanical loss and the phases of these physical constants by using the theory established by Dr. Takuro Ikeda. [9,10] Next, we will measure the phases of the physical constants and separate the mechanical loss into components relevant to the phases. Finally, we will discuss the cause of vibration-velocity saturation from the phases of the physical constants viewpoint.

II. RELATIONSHIP BETWEEN MECHANICAL LOSS AND PHASES

In this study we consider the transverse-effect longitudinal vibration mode. We introduce mechanical loss by using three complex physical constants:

$$s_{11}^{D*} = s_{11}^D (1 - j \phi), \quad (1)$$

$$\epsilon_{33}^{LS*} = \epsilon_{33}^{LS} (1 - j \phi), \quad (2)$$

$$h_{31}^* = h_{31} (1 + j \eta), \quad (3)$$

where s_{11}^D , ϵ_{33}^{LS} , and h_{31} are the elastic compliance, the dielectric constant, and the piezoelectric constant, respectively. The values of ϕ , ϕ , and η represent the phase of each constant. Since s^D and h are the most fundamental constants for elastic and piezoelectric properties, respectively, ϕ and η are considered to be the intrinsic elastic and intrinsic piezoelectric losses. Phase ϕ is not intrinsic dielectric loss in the true sense because as it still includes ϕ and η components in addition to the intrinsic dielectric loss of ϵ_{33}^S , ϕ (ϵ_{33}^S):

$$\phi = [\phi (\epsilon_{33}^S) + f(\phi - 2\eta)] / (1 - f), \quad (4)$$

where f is the type of coupling, such as $\epsilon_{33}^{LS} = \epsilon_{33}^S / (1 - f)$. However, $\phi \doteq \phi (\epsilon_{33}^S) / (1 - f)$ because $\phi (\epsilon_{33}^S) \gg f(\phi - 2\eta)$. [9] Consequently, ϕ can be regarded as a quasi-intrinsic dielectric loss.

For your information, the phases of elastic compliance s^E , dielectric constant ϵ^T , and piezoelectric constant d are not

intrinsic losses because all these phases include ψ , ϕ , and η components.

The mechanical losses at resonance Q_{mr}^{-1} and at antiresonance Q_{ma}^{-1} are expressed as functions of ψ , ϕ , and η : [10]

$$Q_{mr}^{-1} = [\psi + k_{31}^2 (\phi - 2\eta)] / (1 - k_{31}^2), \quad (5)$$

$$Q_{ma}^{-1} = [\psi + (1 - 8/\pi^2) k_{31}^2 (\phi - 2\eta)] / [1 - (1 - 8/\pi^2) k_{31}^2]. \quad (6)$$

If L_{er} , L_{ea} , L_{dr} , and L_{da} are defined as

$$L_{er} = \psi / (1 - k_{31}^2), \quad (7)$$

$$L_{ea} = \psi / [1 - (1 - 8/\pi^2) k_{31}^2], \quad (8)$$

$$L_{dr} = k_{31}^2 (\phi - 2\eta) / (1 - k_{31}^2), \quad (9)$$

$$L_{da} = (1 - 8/\pi^2) k_{31}^2 (\phi - 2\eta) / [1 - (1 - 8/\pi^2) k_{31}^2], \quad (10)$$

then L_{er} and L_{ea} can be considered the elastic-origin components of Q_{mr}^{-1} and Q_{ma}^{-1} , respectively. Because $\eta \ll \phi$, as will be discussed in IV. A, L_{dr} and L_{da} can be considered the dielectric-origin components of Q_{mr}^{-1} and of Q_{ma}^{-1} as well.

III. EXPERIMENTAL

We used rectangular-plate piezoelectric transducers with length L of 43 mm, width W of 7 mm, and thickness T of 1 mm, polarized in the thickness direction, for most of our measurements.

The value of ϕ was determined by measuring ϵ_{33}^{LS*} for a transducer with length $2L$. The Measurement frequency was the resonant frequency of a transducer with length L . This frequency corresponds to the 2nd-mode resonant frequency in a transducer with length $2L$. The values of ψ and $\chi (= \phi - 2\eta)$ were derived from eqs. (5) and (6).

We measured Q_{mr}^{-1} , Q_{ma}^{-1} , k_{31} , and ϕ under a low vibration-velocity by using a Hewlett Packard 4194A impedance analyzer. The vibration-velocity characteristics were measured using a constant-current control method.

[11]

Four different PZT compositions were used in the transducers:

- (#1) $Pb(Zr_{0.54}Ti_{0.46})O_3$ + Dopant (0.54PZ-0.46PT + Dopant, Dopant: none, 0.5wt% Nb_2O_5 or 0.5wt% Fe_2O_3),
- (#2) $Pb(Zr_{0.52}Ti_{0.48})O_3$ + α wt% Fe_2O_3 (0.52PZ-0.48PT + α wt% Fe_2O_3 , $0 \leq \alpha \leq 1.0$),
- (#3) $Pb(Zr_xTi_{1-x})O_3$ + 0.5wt% Fe_2O_3 (x PZ-(1- x)PT + 0.5wt% Fe_2O_3 , $0.48 \leq x \leq 0.58$),

(#4) N-61 (Tokin Corporation).

IV. RESULTS AND DISCUSSIONS

A. Dielectric Loss

Figure 1 shows the relationship between ϕ determined from the measured ϵ_{33}^{LS*} and $\chi (= \phi - 2\eta)$ derived from measured Q_{mr}^{-1} and Q_{ma}^{-1} for specimens #1, #2, and #3. It can be seen that $\phi \approx \chi$, suggesting $\eta \ll \phi$. This is consistent with the proposed assumption [9] that h is a real number. Consequently, we regard the χ derived from the Q_{mr}^{-1} and Q_{ma}^{-1} measurements as ϕ hereafter.

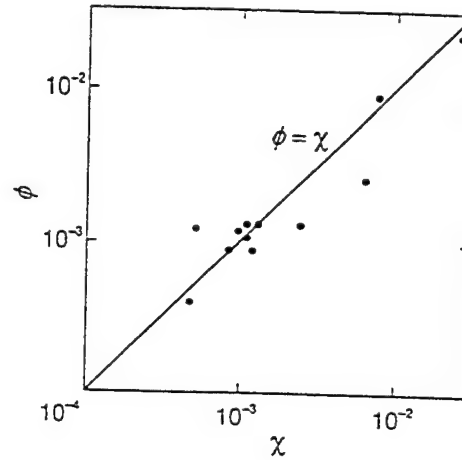


Fig. 1 Relationship between ϕ and $\chi (= \phi - 2\eta)$ for specimens #1, #2 and #3.

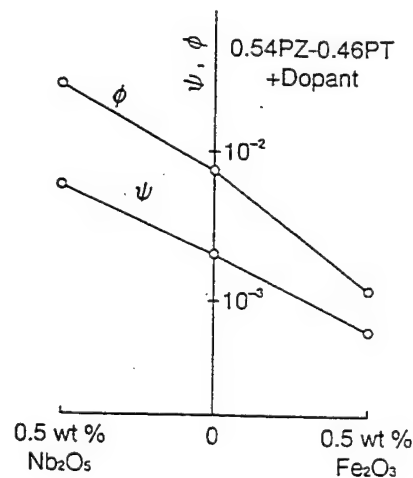


Fig. 2 Values of ψ and ϕ for specimen #1.

B. Mechanical Loss under a Low Vibration-Velocity

The values of ϕ and ϕ for specimen #1 are shown in Fig. 2. They increase with Nb_2O_5 doping and decrease with Fe_2O_3 doping. The Nb_2O_5 doping apparently facilitates ferroelectric non-180° domain wall motion, and the Fe_2O_3 doping apparently has a pinning effect on the domain wall. [12] These doping effects might be reflected in both the ϕ and ϕ values.

As shown in Fig. 3,

(a) Q_{mr}^{-1} decreases with Fe_2O_3 doping and increases with Nb_2O_5 doping,

(b) $Q_{mr}^{-1} > Q_{ma}^{-1}$,

(c) $(0.6-0.9) \times Q_{mr}^{-1} = L_{er}$,

(d) $Q_{ma}^{-1} \approx L_{er}$, and

(e) $L_{er} > L_{dr}$ (though $\phi > \phi$).

The Q_{mr}^{-1} , Q_{ma}^{-1} , L_{er} , and L_{dr} for specimen #2 are shown in Fig. 4 as a function of the Fe_2O_3 doping concentration (α wt%). When $\alpha \leq 0.5$, both Q_{mr}^{-1} and Q_{ma}^{-1} decrease as α increases, and relations (b), (c), (d), and (e) hold true. When $\alpha > 0.5$, however, Q_{mr}^{-1} and Q_{ma}^{-1} increase as α increases. As a matter of interest, $Q_{mr}^{-1} < Q_{ma}^{-1}$ at $\alpha \geq 0.8$. This means that $\phi + \phi < 0$ in eqs. (5) and (6), which is quite impossible. Therefore, eqs. (5) and (6) cannot be applied to these materials as is because the Fe ions would exceed their solubility limit in PZT. This would likely cause the non-ferroelectric crystal phase to segregate around the grain boundaries, generating additional elastic and dielectric losses, which are not electromechanically coupled to each other.

C. Vibration-Velocity Characteristics of Mechanical Loss

The Q_{mr}^{-1} , L_{er} , and L_{dr} for specimen #4 are shown in Fig. 5 as a function of effective vibration velocity v_o at the transducer end. [13] The mechanical loss at resonance, Q_{mr}^{-1} , increases as v_o increases. The value of L_{dr} is negligibly small at low vibration-velocity. However, it rises sharply as v_o increases. The L_{er} is approximately constant, so it is unaffected by v_o . The increase in Q_{mr}^{-1} with v_o is clearly caused by the increase in dielectric-origin component L_{er} . Because the ferroelectric domain wall motion affects both ϕ and ϕ (Fig. 2), the factor affecting only ϕ , as seen here, is different from the domain wall motion.

The Q_{ma}^{-1} , L_{er} , and L_{da} for specimen #4 are shown in Fig. 6 as a function of v_o . Similarly to Q_{mr}^{-1} , the increase in mechanical loss at antiresonance Q_{ma}^{-1} is due to the increase in the dielectric-origin component, L_{da} , with v_o .

V. CONCLUSION

The mechanical loss in PZT-based piezoelectric ceramics was studied by introducing three complex physical constants:

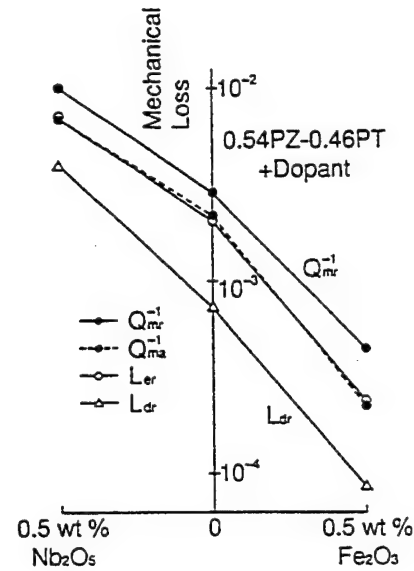


Fig. 3 Values of Q_{mr}^{-1} , Q_{ma}^{-1} , L_{er} and L_{dr} for specimen #1.

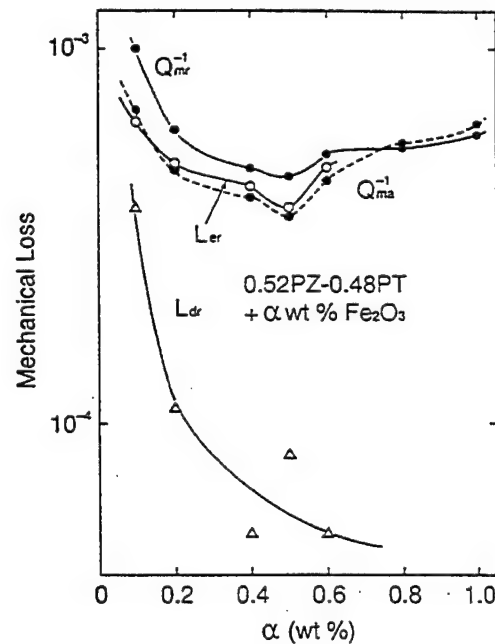


Fig. 4 Values of Q_{mr}^{-1} , Q_{ma}^{-1} , L_{er} and L_{dr} as a function of α for specimen #2.

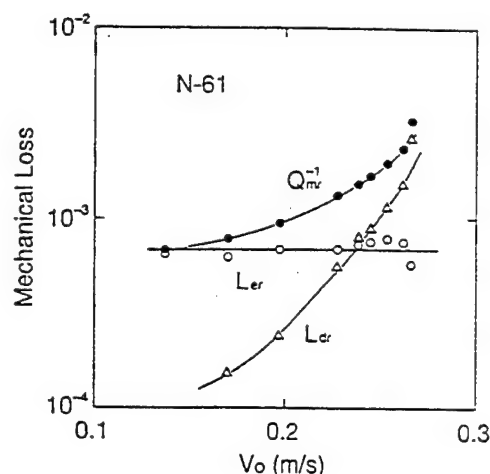


Fig. 5 Vibration velocity v_0 dependence of Q_m^{-1} , L_{er} and L_d for specimen #4.

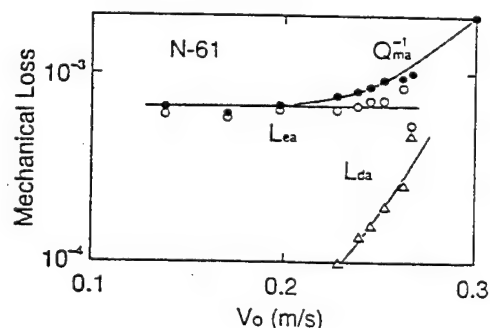


Fig. 6 Vibration velocity v_0 dependence of Q_{ma}^{-1} , L_{ea} and L_{da} for specimen #4.

elastic, dielectric and piezoelectric. The elastic, dielectric, and piezoelectric losses were determined from the measured mechanical losses at resonance and at antiresonance, and from the measured complex dielectric constant. Both the elastic and dielectric losses have finite values, while the piezoelectric loss is negligibly small in comparison.

When the vibration-velocity is low, the elastic-origin component accounts for more than 60% of the mechanical loss at resonance, and the mechanical loss at antiresonance approximately equals the elastic-origin component. When the vibration-velocity is high, however, the dielectric-origin component dominates the mechanical losses at both resonance and antiresonance. Therefore, the saturation in the vibration-velocity is apparently caused by an unusual increase in the dielectric loss, although the origin has not been clarified yet.

The mechanical loss in PZT-based ceramics is reduced by

Fe_2O_3 doping, which decreases the elastic- and dielectric-origin components, due to its pinning effect on ferroelectric non- 180° domain walls.

We are indebted to Dr. Takuro Ikeda for his useful suggestions. [10]

REFERENCES

- [1] S. Takahashi and S. Hirose, "Vibration level characteristics of lead-zirconate-titanate piezoelectric ceramics," *Jpn. J. Appl. Phys.*, vol. 31, Pt. 1, no. 9B, pp. 3055-3057, 1992.
- [2] S. Takahashi and S. Hirose, "Vibration level characteristics for iron doped lead-zirconate-titanate piezoelectric ceramics," *Jpn. J. Appl. Phys.*, vol. 32, Pt. 1, no. 5B, pp. 2422-2425, 1993.
- [3] S. Takahashi, S. Hirose and K. Uchino, "Stability of PZT piezoelectric ceramics under vibration level change," *J. Am. Ceram. Soc.*, vol. 77, no. 9, pp. 2429-2432, 1994.
- [4] S. Takahashi, S. Hirose, K. Uchino and K. Y. Oh, "Electro-mechanical characteristics of lead-zirconate-titanate ceramics under vibration-level change," *Proc. 9-th IEEE Int. Symp. Appl. Ferroelectrics*, pp. 377-382, 1994.
- [5] S. Takahashi, Y. Sasaki, S. Hirose and K. Uchino, "Electro-mechanical properties of $\text{PbZrO}_3\text{-PbTiO}_3\text{-Pb(Mn}_{1/3}\text{Sb}_{2/3})\text{O}_3$ ceramics under vibration-level change," *Mat. Res. Symp. Proc.*, vol. 360, pp. 305-310, 1995.
- [6] S. Takahashi, Y. Sasaki, S. Hirose and K. Uchino, "Stability of $\text{PbZrO}_3\text{-PbTiO}_3\text{-Pb(Mn}_{1/3}\text{Sb}_{2/3})\text{O}_3$ piezoelectric ceramics under vibration-level change," *Jpn. J. Appl. Phys.*, vol. 34, Pt. 1, no. 9B, pp. 5328-5331, 1995.
- [7] S. Takahashi, Y. Sasaki, H. Kawai and S. Hirose, "High-power piezoelectric characteristics in $\text{Pb(Mn}_{1/3}\text{Sb}_{2/3})\text{O}_3\text{-Pb(Mg}_{1/3}\text{Nb}_{2/3})\text{O}_3\text{-PbTiO}_3$ solid solution system," *Proc. 10-th IEEE Int. Symp. Appl. Ferroelectrics*, pp. 309-312, 1996.
- [8] S. Takahashi, Y. Sasaki and S. Hirose, "Driving electric field effects on piezoelectric transducers," *Jpn. J. Appl. Phys.* vol. 36, Pt. 1, no. 5B, pp. 3010-3015, 1997.
- [9] T. Ikeda, *Fundamentals of Piezoelectricity*, 1st ed., Oxford: Tokyo, 1996.
- [10] T. Ikeda, private communication.
- [11] S. Hirose, "Measurement method of high-power characteristics in piezoelectric ceramics," in *New Actuators Handbook for Precision Control*, K. Uchino, S. Takahashi, I. Hayashi and H. Fujita, Eds. Fuji Technosystems: Tokyo, 1994, pp. 336-346. [in Japanese]
- [12] K. Uchino, *Introduction to Electric Solid State Physics for Ceramists* Uchida Rokakuho: Tokyo, 1990. [in Japanese]
- [13] S. Hirose, Y. Yamayoshi, M. Taga and H. Shimizu, "A method of measuring the vibration level dependence of impedance-type equivalent circuit constants," *Jpn. J. Appl. Phys.* vol. 30, Suppl. 30-1, pp. 117-119, 1991.

RELAXOR BASED FERROELECTRIC SINGLE CRYSTALS WITH HIGH PIEZOELECTRIC PERFORMANCE

Seung-Eek Park and Thomas R. Shrout

Materials Research Laboratory, The Pennsylvania State University, University Park, PA 16802, U.S.A.

Abstract- Relaxor ferroelectric single crystals of $\text{Pb}(\text{Zn}_{1/3}\text{Nb}_{2/3})\text{O}_3$ (PZN), $\text{Pb}(\text{Mg}_{1/3}\text{Nb}_{2/3})\text{O}_3$ (PMN) and their solid solutions with the normal ferroelectric PbTiO_3 (PT) were investigated for actuator and transducer applications. Crystals offer adjustable properties, not only by compositional tailoring but also by domain state engineering associated with crystallographic orientations, not achievable in polycrystalline materials. Longitudinal coupling coefficients (k_{33}) as high as 94 % and dielectric constants (K_3^T) in the range of 3500-6000 were achieved with low dielectric loss (<1%) using <001> oriented rhombohedral crystals of (1-x)PZN-xPT and (1-y)PMN-yPT, where $x < 0.09$ and $y < 0.35$. Piezoelectric coefficients (d_{33} 's) > 2500 pC/N and subsequent strain levels up to >0.6% with minimized hysteresis were observed. Ultrahigh strain levels up to 1.7%, an order of magnitude larger than those available from conventional piezoelectric and electrostrictive ceramics could be achieved, being related to an E-field induced phase transformation.

1. INTRODUCTION

Piezoelectric ceramics are currently the material of choice for transducer and actuator applications, offering relatively high electromechanical coupling (k_{ij}), piezoelectric coefficients (d_{ij}), and a wide range of dielectric constants (K) with low dielectric loss. For transducer applications, these key merits of piezoelectric ceramics translate into enhanced performance in the form of high sensitivity, broad bandwidth, electrical impedance matching and minimal thermal heating. For actuators the piezoelectric coefficient (d_{ij}), determining the level of induced strain at a given electric field, and actual induced strain levels are the most widely used parameters describing actuator performance.

A. Morphotropic Phase Boundary and Compositional Engineering

$\text{Pb}(\text{Zr}_{1-x}\text{Ti}_x)\text{O}_3$ (PZT) ceramics have been the mainstay for transducer and actuator applications. Compositionally, PZT ceramics lie near the morphotropic phase boundary (MPB) between the tetragonal and rhombohedral phases as shown in figure 1. MPB compositions exhibit anomalously high dielectric and piezoelectric properties as a result of enhanced polarizability arising from the coupling between two equivalent energy states, i.e. the tetragonal and rhombohedral phases, allowing optimum domain reorientation during the poling process. Alternate MPB systems can be found in Relaxor- PbTiO_3 , also as shown in figure 1. Lead based relaxor materials are complex perovskites with the general

formula $\text{Pb}(\text{B}_1\text{B}_2)\text{O}_3$, ($\text{B}_1 = \text{Mg}^{2+}, \text{Zn}^{2+}, \text{Ni}^{2+}, \text{Sc}^{3+} \dots$, $\text{B}_2 = \text{Nb}^{5+}, \text{Ta}^{5+}, \text{W}^{6+} \dots$). Characteristic of relaxors is a broad and frequency dispersive dielectric maxima [1].

To achieve a high piezoelectric coefficient, MPB-based ceramics are further engineered by compositionally adjusting the Curie temperature (T_C) downward relative to room temperature. The effect of transition temperature (T_C) on the piezoelectric properties is clearly evident in figures 2 and 3. As shown, the room temperature values of dielectric constant (K) and piezoelectric coefficient (d_{33}) are plotted as a function of T_C for a variety of modified PZT ceramics, including Relaxor-PT systems. Enhanced piezoelectric activity of MPB-based ceramics, achieved by compositionally adjusting T_C downward relative to room temperature, results in 'soft' piezoelectric ceramics. This enhanced piezoelectric effect, therefore, comes with the expense of more temperature dependent properties, and less polarization stability, i.e. aging and loss of piezoelectric activity. For electromechanical coupling, such as k_{33} , no relationship with T_C is evident as shown in figure 4. Further details on the relationship between dielectric/piezoelectric properties and Curie temperature (T_C) can be found in the article by S. -E. Park et al. [2].

As a general rule of thumb, piezoelectric materials can be safely used to approximately $1/2 T_C$, without significant reduction in piezoelectric activity. This can restrict the working range of the device or limit fabrication techniques. During the fabrication process of transducers, the piezoelectric material may experience excessive temperature due to cutting/dicing, polymer curing, or the attachment of

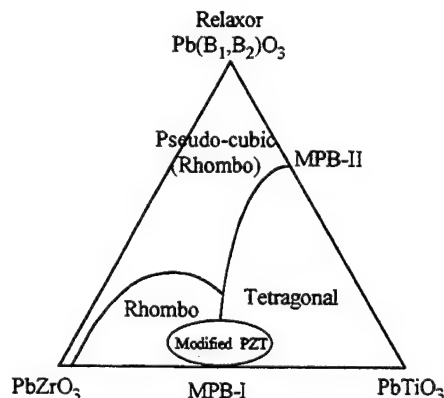


Fig. 1 Ternary diagram depicting MPBs in PZT and Relaxor-PT systems for piezoelectric ceramics. [3]

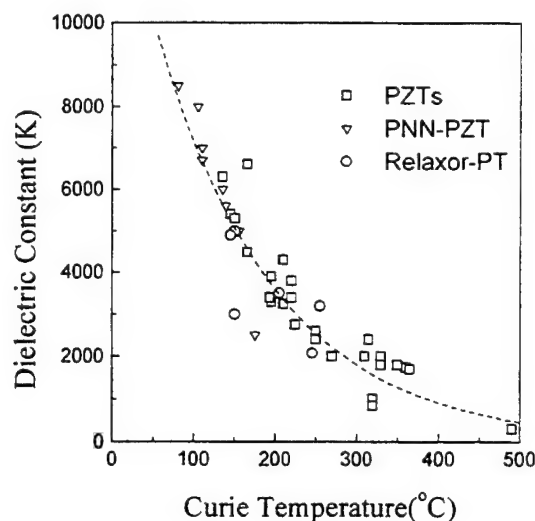


Fig. 2 Dielectric constant as a function transition temperature (T_c) for piezoelectric ceramics, including PZT, modified PZTs, and Relaxor-PT systems. Data were compiled from references, commercial brochures and internal investigations.

acoustic matching/backing materials. It is noted that the most widely used material in the ultrasonic imaging industry has a $T_c \sim 210^\circ\text{C}$ owing to the materials relatively high dielectric constant and coupling coefficient while providing good temperature stability.

Furthermore, regarding actuator applications, a consequence of increased piezoelectric activity for these "soft" ceramics is large hysteresis in the strain vs. E-field behavior as a result of domain motion. Strain vs. E-field

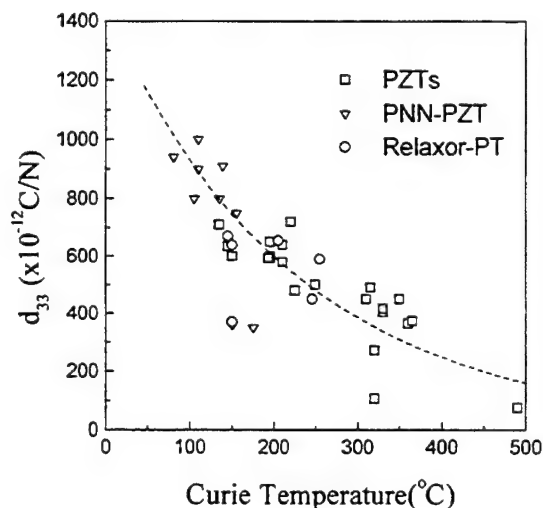


Fig. 3 Piezoelectric Coefficient (d_{33}) as a function transition temperature (T_c) for piezoelectric ceramics, including PZT, modified PZTs, and Relaxor-PT systems. Data were compiled from references, commercial brochures and internal investigations.

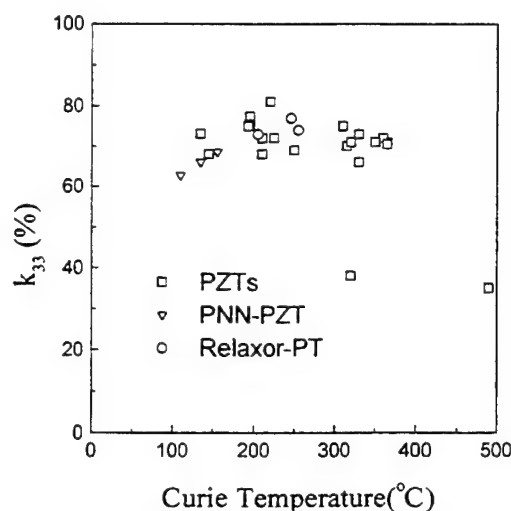


Fig. 4 Electromechanical coupling (k_{33}) as a function transition temperature (T_c) for piezoelectric ceramics, including PZT, modified PZTs, and Relaxor-PT systems. Data were compiled from references, commercial brochures and internal investigations.

behavior for PZT-5H (Navy type -VI) is shown in figure 5 as an example. Though the piezoelectric coefficient (d_{33}) of PZT-5H ceramics is in the range of ~ 600 to 700 pC/N [4] (implying ~ 0.06 to 0.07% strain at 10 kV/cm), with strain levels as high as 0.1% observed at 10 kV/cm. This enhanced nonlinear strain is the result of domain motion, and therefore, accompanied by significant hysteresis, resulting in poor positioning accuracy. The area within the strain vs. E-field curve also results in significant heat generation during operation. Heat generation combined with a decreased

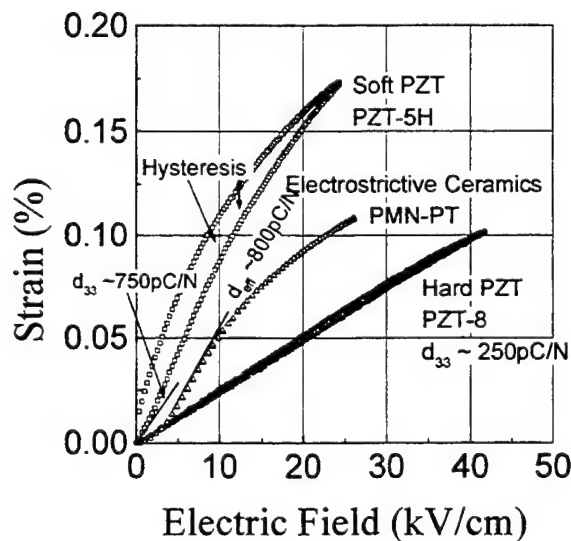


Fig. 5 Strain vs. E-field behavior for various electromechanical Actuators.

temperature usage range, results in poor temperature stability and limits these ceramics to low frequency applications.

Polarization instability and strain vs. E-field hysteresis can be minimized with the use of the "hard" piezoelectric ceramics. Hard piezoelectric ceramics such as PZT-8 (Navy type III) offer very low hysteresis as shown in figure 5. However, the reduction in hysteresis and loss comes at the expense of k_{33} (~60% vs. ~75%) and d_{33} (~200 vs. ~700 pC/N) for PZT-8 and PZT-5H, respectively.

Among electrostrictors, another category of electromechanical ceramics, a few materials such as PMN and its solid solution with PT exhibit significant electrostrictive strain (> 0.1%) with virtually no hysteresis as shown in figure 5. Effective d_{33} 's > ~800 pC/N calculated directly from the strain vs. E-field curve can be achieved, but only over a very narrow range of E-field and temperature.

In summarizing the observations presented above, the dielectric and piezoelectric properties of piezoelectric ceramics are strongly related to the transition temperature T_c . Upon direct comparison, *no one type of material*, whether PZT-based or Relaxor-PT, offer significant advantages in overall performance. Especially for actuators, Soft PZT's, exhibiting piezoelectric coefficients (d_{33}) as high as 750 pC/N, are inherently limited due to hysteresis caused by domain motion. Hysteresis can be minimized with the use of hard piezoelectric ceramics, but d_{33} values of only ~200 to 300 pC/N are available. Even though electrostrictive ceramics offer effective d_{33} 's ~ 800 pC/N, maximum strain level is limited by its dielectric breakdown strength and polarization saturation. *The question arises, are there opportunities for new piezoelectric materials with enhanced properties?*

To answer the question above, one must look to the single crystal form of piezoelectric materials, the topic of the following section.

B. Single crystal Piezoelectrics

Single crystal piezoelectrics such as quartz (SiO_2), lithium niobate (LiNbO_3), and the analogue lithium tantalate (LiTaO_3) are widely employed in specific applications that include oscillators, surface acoustic wave (SAW) devices, and in optics. In contrast to PZT ceramics, however, these single crystals offer inferior piezoelectric properties, with d_{33} 's < 50 pC/N.

Attempts to grow single crystals of MPB PZTs have been made by numerous researchers, resulting in crystallites too small to allow adequate property measurements [5,6,7,8,9]. In contrast to PZT crystal growth, relaxor-PT materials can be readily grown in single crystal form. This key distinction was first realized by Soviet researchers [10,11], later by Nomura and co-workers for the PZN and PZN-PT systems [12,13] and by Shrout [14] for PMN-PT system. In general, most $\text{Pb}(\text{B}_1\text{B}_2)\text{O}_3$ -PT crystals can be grown by high temperature solution growth using Pb-based fluxes [15,16].

Table 1 Dielectric and Piezoelectric Properties of $\text{Pb}(\text{A}_{1/3}\text{B}_{2/3})\text{O}_3$ - PbTiO_3 single crystals ($\text{A}=\text{Zn}^{2+}, \text{Mg}^{2+}$)

| Composition | Orient- -ation. | K_{33} | s_{33}^E (10^{-12} m^2/N) | K_3^T | Loss | d_{33} (pC/N) |
|-------------|--------------------|----------|---|---------|-------|--------------------|
| PZN | 111 | 0.38 | 7.4 | 900 | 0.012 | 83 |
| | 001 | 0.85 | 48 | 3600 | 0.008 | 1100 |
| PZN-4.5%PT | 111 | 0.35 | 9.0 | 1500 | 0.004 | 110 |
| | 001 | 0.91 | 102 | 4000 | 0.004 | 2000 |
| PZN-6%PT | 111 | 0.33 | 7.3 | 720 | 0.004 | 74 |
| | 001 | 0.93 | 133 | 4800 | 0.012 | 2400 |
| PZN-8%PT | 111 | 0.39 | 7.4 | 2150 | 0.012 | 82 |
| | 001 | 0.95 | 152 | 5500 | 0.010 | 2600 |
| PZN-9.5%PT | 111 | 0.64 | 10.4 | 4300 | 0.007 | 600 |
| | 001 | 0.89 | 77 | 1600 | 0.004 | 1600 |
| PZN-12%PT | 001 | 0.86 | | 900 | 0.004 | 500 |
| PMN-24%PT | 001 | | | 3700 | 0.009 | 900 |
| PMN-33%PT | 001 | 0.94 | 79 | 4500 | 0.012 | 1700 |
| PMN-35%PT | 001 | 0.92 | 67 | 3100 | 0.014 | 1240 |

Although ultra high coupling and piezoelectric properties of the PZN-PT and PMN-PT systems, with d_{33} and k_{33} values greater than 1500 pC/N and 90%, respectively, have been known for several years, their potential for high performance ultrasound transducer, actuator, and related devices has only been recognized recently. Serious efforts on the development of $\text{Pb}(\text{B}_1\text{B}_2)\text{O}_3$ -PT crystals for high performance transducers includes investigations at Toshiba Co. and at the Pennsylvania State University. Though the Curie temperature (T_c) of these materials are relatively low < 200°C, the significance of these values becomes evident by directly comparing their values in relation to T_c in Figures 2-4. Although clearly evident, few systematic studies on the crystallographic aspects of these crystals have yet to be made.

In the following section, the results based on the author's ongoing investigation are presented, reporting electromechanical, dielectric/piezoelectric properties.

II. RESULTS AND DISCUSSION

A. Dielectric and Piezoelectric Properties - Low Field Measurements

Commonalities inherent to Relaxor-PT systems have been discussed in reviews by Shrout [17] and Randall [18]. Based on these commonalities, our research was limited to two representative systems, PZN-PT and PMN-PT. Though PMN-PT MPB crystals exhibit piezoelectric properties comparable with PZN-PT, more focus was given to the PZN system owing to its relatively lower PT content for MPB, allowing more uniform crystal growth of these solid solution materials. Figure 6 shows an example of oriented, cut, and polished crystals for transducer and actuator fabrication. Dielectric, piezoelectric, and electromechanical coupling coefficients for the various crystals are reported in table 1. As reported in table 1, large coupling coefficients (k_{33}) and large piezoelectric coefficients (d_{33}) were found for PZN-PT

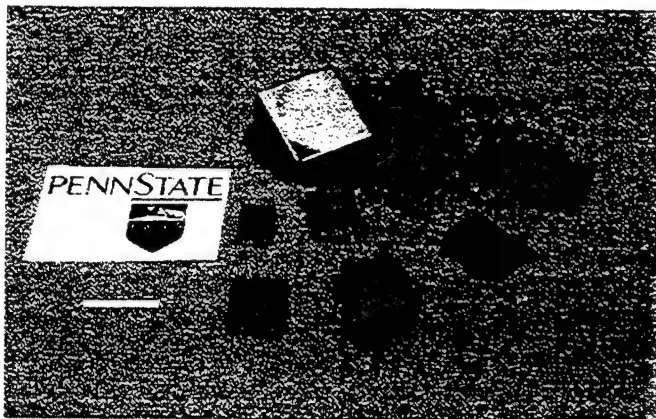


Fig. 6 Oriented, cut and polished crystals of PZN-PT.

crystals with MPB compositions (PZN-9.5%PT), as previously reported by Kuwata [13]. Electromechanical coupling (k_{33}) equal to and larger than MPB crystal compositions were found for domain engineered rhombohedral crystals[#] as shown in Figure 7. Pure PZN, and PZN-8%PT crystals were found to possess high k_{33} values of ~85% and 94%, respectively, for (001) crystal cuts. Low values of dielectric loss < 1%, significantly less than their polycrystalline counterparts, should also be noted. Figure 8 presents the piezoelectric coefficient (d_{33}) as a function of composition, calculated based on IEEE standards. Maximum d_{33} values of ~2500 pC/N were determined with domain engineered rhombohedral PZN-8%PT crystals. In contrast to PZT's, d_{33} dramatically decreases at MPB to levels ~500pC/N for tetragonal compositions. Though <111> is the polar direction for rhombohedral crystals, such cuts exhibited low values in both electromechanical coupling factor and piezoelectric coefficient as shown in figures 7 and 8.

It should be noted that direct observation of the strain vs. E-field behavior is essential in order to investigate hysteresis and maximum levels of strain, key experiments to directly confirm actuator performance, the topic of the next section.

C. Direct Observation of Strain vs. E-field Behavior

As presented in the previous section, piezoelectric coefficients (d_{33}) as high as 2500 pC/N were determined from <001> oriented rhombohedral crystals. In relation to actuators, several questions arise, 1) How do the high d_{33} values determined using low field techniques correlate to direct measurements? 2) As for piezoelectric and electrostrictive ceramics, will the strain level saturate with increased E-field? 3) How much hysteresis accompanies the strain?

[#] Rhombohedral crystals oriented and poled along pseudocubic <001> direction. Crystallographically, polarization direction of rhombohedral crystal is pseudocubic <111> direction. The role of domains and their stability on the dielectric and piezoelectric properties of single crystals are investigated and reported in the article by Wada et. al.[19]

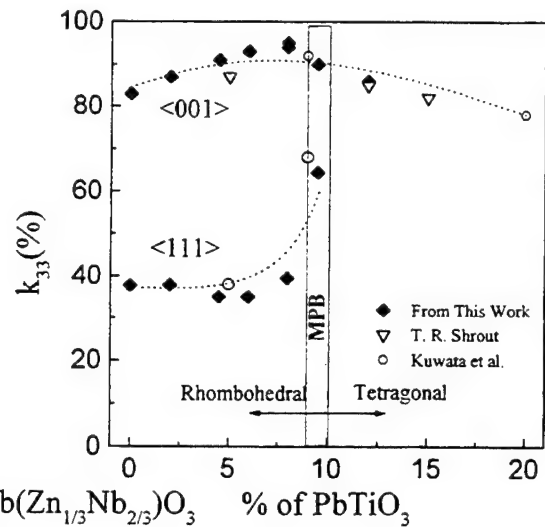


Fig. 7 k_{33} as a function of composition and orientation for PZN-PT crystal.

Strain as a function of electric field for various <001> oriented rhombohedral crystals (pure PZN, PZN-4.5%PT, PZN-8%PT, and PMN-24%PT) are presented in figure 9. Also, E-field induced strains of various electromechanical ceramics such as soft PZT (PZT-5H), hard PZT (PZT-8) and electrostrictive ceramics (PMN-PT) are compared. Piezoelectric coefficients (d_{33}) directly calculated from the slope of strain vs. electric field curves confirmed the piezoelectric coefficients determined by the low-field resonance method. Strains as high as 0.6% were observed with low hysteresis for these crystals, significantly larger than that for polycrystalline ceramics. Figure 10 presents the E-field required to achieve 0.5% strain for various <001> oriented relaxor-PT crystals including $\text{Pb}(\text{Sc}_{1/2}\text{Nb}_{1/2})\text{O}_3$ (PSN) -PT. As shown, the E-field required to obtain a certain strain level was a

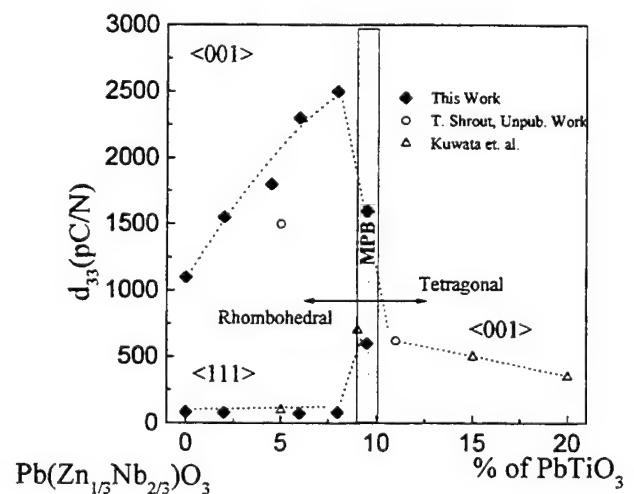


Fig. 8 d_{33} as a function of composition and orientation for PZN-PT crystal.

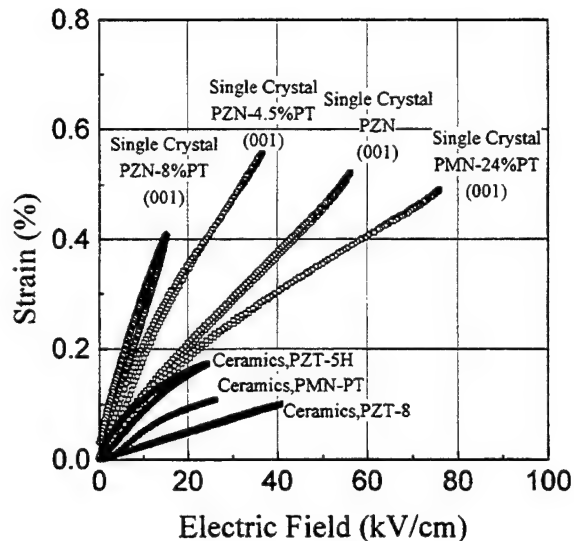


Fig. 9 Strain vs. E-field behavior for <001> oriented rhombohedral crystals of PZN-PT and PMN-PT and for various electromechanical ceramics

function of PT content away from MPB, confirming the commonality of relaxor ferroelectrics.

Figure 11 schematically presents the engineered domain state and their piezoelectric response under bias for rhombohedral crystals oriented and poled along <001>. When actuation is induced by an E-field along <001>, the polar direction is expected to incline close to the E-field direction in each domain (A in figure 11), possibly resulting in the lattice symmetry lower than its original symmetry, such as monoclinic. Domain reorientation is not necessary during this step because neighboring domains must involve an equal amount of induced distortion, nullifying all strains in

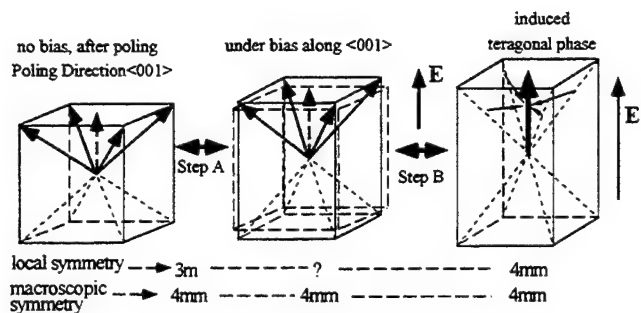


Fig. 11 Schematic diagram of domain configuration in <001> oriented rhombohedral crystals

individual domains, resulting in macroscopic symmetry of 4mm. The macroscopic symmetry and its relationship with hysteresis minimized strain behavior for <001> oriented rhombohedral crystals are presented in the paper by Wada et al. [19].

D. E-field Induced Phase Transition

Strain saturation for <001> oriented rhombohedral crystals was investigated until dielectric breakdown, as presented in figure 12. Far from saturation, the strain abruptly increased with strain levels as high as 0.8% being achieved for all crystals tested. Strain levels >1.7% for the PZN-8%PT crystals were the result of higher breakdown voltage. The observed strain behavior is believed to be associated with an E-field induced rhombohedral-tetragonal phase transition. Increased E-field will result in collapse of all polarization's into <001> direction, step B in figure 12, resulting in an induced tetragonal phase. The piezoelectric coefficient (d_{33})

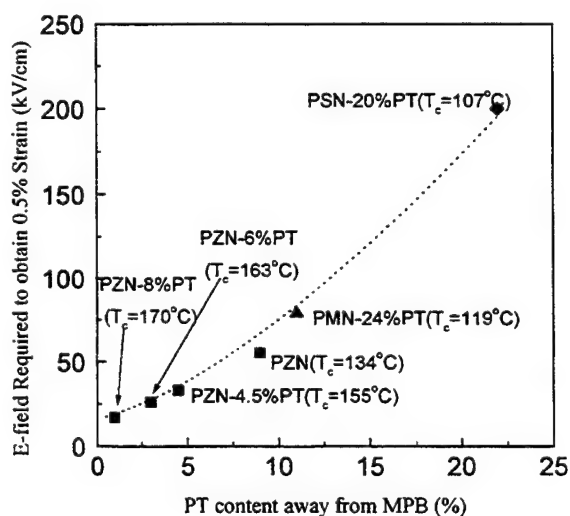


Fig. 10 E-field required to obtain 0.5% strain as a function of PT content away from MPB for <001> oriented rhombohedral crystals

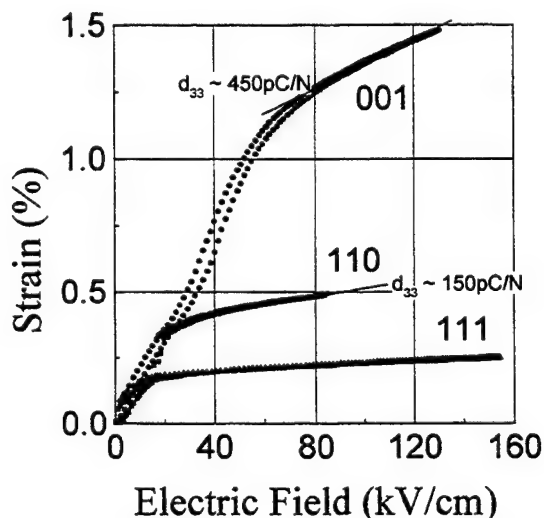


Fig. 12 Strain vs. E-field behaviors for crystals of PZN-PT and PMN-PT, and for various electromechanical ceramics. Maximum field was limited either by dielectric breakdown or by voltage limit of the apparatus.

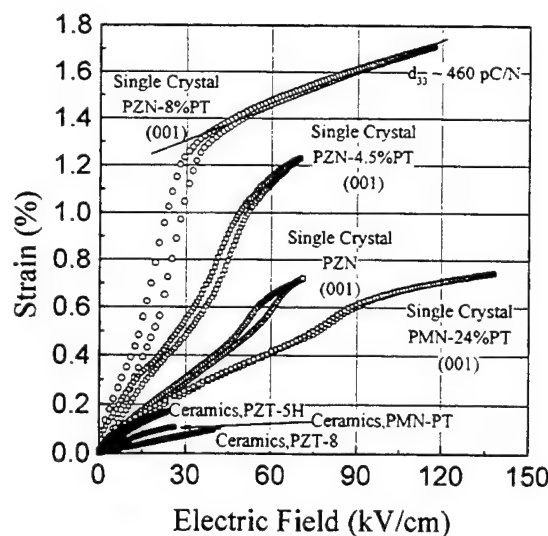


Fig. 13 Strain vs. E-field behavior as a function of crystallographic orientation for PZN-4.5%PT crystals

~ 480 pC/N calculated directly from the slope of strain vs. E-field in the high field region corresponded to values determined for tetragonal phase with a d_{33} value (~500 pC/N, in table 1).

Strain behavior as a function of crystallographic orientation are presented in figure 13, for rhombohedral PZN-4.5%PT crystals. In contrast to the strain behavior of <001> oriented crystals, strain saturation was observed with crystals oriented along the polar <111> direction. The E-field induced phase transition is more apparent for <110> oriented PZN-4.5%PT crystals, possibly resulting in E-field induced orthorhombic crystal with 2mm symmetry. Piezoelectric coefficients (d_{33}) directly calculated from the strain vs. E-field curve were 150 pC/N for the E-field induced orthorhombic phase. The E-field required for the induced phase transition was found to

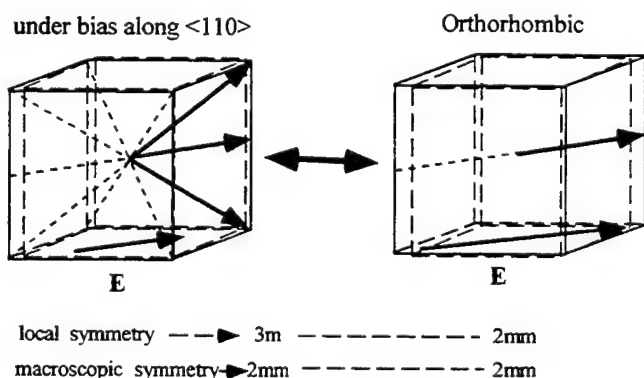


Fig. 14 Schematic diagram of <110> oriented rhombohedral crystals.

be smaller than the case of <001> oriented crystals, suggesting a simpler engineered domain structure as shown in figure 14.

III. SUMMARY

The single crystal form of Relaxor-PT materials offers the possibility of dramatic improvements in transducer performance. Electromechanical coupling coefficients greater than 90% with non-MPB compositions as well as MPB compositions enables a degree of freedom in designing transducers with broad bandwidth and/or improved sensitivity. A range of dielectric constants from ~1000 to 6000 in the PZN-PT system offers designers dielectrics for optimum electrical impedance matching.

Pseudocubic <001> oriented relaxor based rhombohedral crystals such as (1-x)PZN-xPT ($x < 0.09$) and (1-x) PMN- xPT ($x < 0.35$) exhibited actuation levels not available with current piezoelectric ceramics. Ultrahigh piezoelectric coefficients (d_{33}) > ~2500 pC/N and strain levels up to 0.6% with minimized hysteresis were observed. In contrast to strain saturation observed from <111> oriented rhombohedral crystals, ultrahigh strain levels up to 1.7% could be achieved for <001> oriented rhombohedral single crystals as a result of an E-field induced rhombohedral-tetragonal phase transition. Similar induced transition behavior was observed from the <110> oriented rhombohedral crystals at lower E-field. Other relaxor based rhombohedral crystals are expected to exhibit similar strain vs. E-field behavior. E-field required to achieve a certain strain level (such as 0.5%) was a function of PT content away from MPB composition. Though clearly promising candidates for high performance transducers and actuators, further investigations in crystal growth and pre-stress testing are required for single crystal piezoelectrics to become the next generation of ultrasound and actuator materials.

ACKNOWLEDGMENT

This research has been supported by Office of Naval Research and Whitaker Center for Ultrasonic Imaging. The authors would like to thank L. E. Cross and C. Randall for their helpful suggestions, and Wesley Hackenberger, Patrick D. Lopath, Michael J. Zipparo for their helps with the property measurements, and Shi-Fang Liu and Hua Lei for their helps with crystal growing and sample preparation, respectively.

REFERENCES

- [1] L. E. Cross, "Relaxor Ferroelectrics," *Ferroelectrics*, vol. 76, pp. 241-267, 1987.
- [2] Seung-Eek Park, and Thomas R. Shrout, "Characteristics of Relaxor-Based Piezoelectric Single Crystals for Ultrasonic Transducers," in press *IEEE Trans. on UFFC*, Vol. 44, No. 5, pp. 1-8, 1997.

- [3] Y. Yamashita, "Large Electromechanical Coupling Factors in Perovskite Binary Material System," *Japanese Journal of Applied Physics*, vol. 33, Pt. 1[9B], pp. 5328-5331, 1994.
- [4] H. Jaffe and D. A. Berlincourt, "Piezoelectric Transducer Materials," *Proceedings of IEEE*, vol. 53 no. 10, pp. 1372-1386, 1965.
- [5] S. Fushimi and T. Ikeda, "Phase Equilibrium in the System $\text{PbO-TiO}_2\text{-ZrO}_2$," *Journal of the American Ceramic Society*, vol. 50, no. 3, pp. 129-132, March 1967.
- [6] V. A. Kuznetsov, "Crystallization of Titanium, Zirconium and Hafnium Oxides and Some Titanate and Zirconate Compounds under Hydrothermal Conditions," *Journal of Crystal Growth*, vol. 34, pp. 405-410, 1968.
- [7] R. Clarke and R. W. Whatmore, "The Growth and Characterization of $\text{PbZr}_{1-x}\text{Ti}_x\text{O}_3$ Single Crystals," *Journal of Crystal Growth*, vol. 33, pp. 29-38, 1976.
- [8] T. Hatanaka and H. Hasegawa, "Dielectric Properties of $\text{Pb}(\text{Zr}_{1-x}\text{Ti}_x)\text{O}_3$ Single Crystals Including Monoclinic Zirconia," *Japanese Journal of Applied Physics*, vol. 34, pp. 5446-5448, Sept. 1995.
- [9] K. Yanagisawa, H. Kanai, and Y. Yamashita, "Hydrothermal Crystal Growth of Lanthanum-Modified Lead Zirconate Titanate," *Japanese Journal of Applied Physics*, vol. 34, pp. 536-538 Sept. 1995.
- [10] V. A. Bokov and I. E. Myl'nikova, *Soviet Physics-Solid State*, Vol. 2, No. 11, pp 2428-2432, 1961
- [11] G. A. Smolenskii, V. A. Isuov, A. I. Agranovskaya, and S. N. Popov, "Ferroelectric with diffuse Phase Transitions," *Soviet Physics-Solid State*, Vol. 2, No. 11, pp 2584-2594, 1961.
- [12] J. Kuwata, K. Uchino, and S. Nomura, "Phase Transitions in the $\text{Pb}(\text{Zn}_{1/3}\text{Nb}_{2/3})\text{O}_3\text{-PbTiO}_3$ System," *Ferroelectrics*, vol. 37, pp. 579-582, 1981.
- [13] J. Kuwata, K. Uchino, and S. Nomura, "Dielectric and Piezoelectric Properties of $0.91\text{Pb}(\text{Zn}_{1/3}\text{Nb}_{2/3})\text{O}_3\text{-}0.09\text{PbTiO}_3$ Single Crystals," *Japanese Journal of Applied Physics*, vol. 21, no. 9, pp. 1298-1302, Sept. 1982.
- [14] T. R. Shrout, Z. P. Chang, N. Kim, and S. Markgraf, "Dielectric Behavior of Single Crystals near the $(1-x)\text{Pb}(\text{Mg}_{1/3}\text{Nb}_{2/3})\text{O}_3\text{-}(x)\text{PbTiO}_3$ Morphotropic Phase Boundary," *Ferroelectric Letters*, vol. 12, pp. 63-69, 1990.
- [15] M. L. Mulvihill, S.-E. Park, G. Risch, Z. Li, K. Uchino, T. R. Shrout, "The Role of Processing Variables in the Flux Growth of Lead Zinc Niobate-Lead Titanate Relaxor Ferroelectric Single Crystals," *Japanese Journal of Applied Physics*, vol. 35, no. 7, pp. 51-57, July 1996.
- [16] S.-E. Park, M. L. Mulvihill, G. Risch, and T. R. Shrout, "The Effect of Growth Condition on Dielectric Properties of $\text{Pb}(\text{Zn}_{1/3}\text{Nb}_{2/3})\text{O}_3$ Crystal," *Japanese Journal of Applied Physics*, Pt. 1, vol. 36, no. 3, March 1997.
- [17] T. R. Shrout and J. Fielding, Jr., "Relaxor Ferroelectric Materials," in *Proceedings of the 1990 IEEE Ultrasonics Symposium*, 1990, pp. 711-715.
- [18] C. A. Randall, A. S. Bhalla, T. R. Shrout, and L. E. Cross, "Classification and Consequences of Complex Lead Perovskite Ferroelectrics with regard to B-site Cation Order," *Journal of Materials Research*, vol. 5, no. 4, pp. 829-834, 1990.
- [19] S. Wada, S.-E. Park, L. E. Cross, and T. R. Shrout, "Domain Configuration and Ferroelectric Related Properties of Relaxor Based Single Crystals," *Proceedings of 8th US-Japan Seminar on Dielectric and Piezoelectric Ceramics*, in press.

Growth of Single Crystal PMN-PT

Paul Bridenbaugh, Jason Rottenberg, and G.M. Loiacono
Crystal Associates Inc.
31 Farinella Drive
East Hanover, NJ 07936

Single crystals of PMN were first grown in 1959¹. Growth took place from a pure PbO flux or a PbO flux with some source of B₂O₃ such as B₂O₃ itself or Na₂B₂O₇ used as a flux modifier. Growth solutions were contained in platinum crucibles with either a tightly fitted lid or a welded lid to suppress volatilization of the flux. Typically, solutions were concentrated having 0.5 to 1.0 moles solute per mole of flux. These concentrations required high soak temperatures (1200°C) for homogenization at which PbO volatility becomes a problem. After some arbitrary soak time, the solutions were slow cooled to a temperature of about 900°C to grow crystals of PMN. Crystals were recovered either by pouring off the flux or by soaking in dilute nitric acid. Crystals grown by this procedure are about 3 mm on a side or occasionally larger. The method of growth of PMN and PMN-PT has remained basically the same for the last thirty years. Lead zinc niobate was first prepared in single crystal form in 1960². Again, PbO with 3% Na₂B₂O₇ was used as a flux and dielectric and electrooptical properties were studied. Worth mentioning are several important studies of crystal growth and dielectric and piezoelectric properties of both PMN-PT and PZN-PT. The solid solution PZN-PT was grown by Nomura et al.³ in 1969. From this study, the composition of the MPB in this system was

determined. The dielectric and piezoelectric properties of PZN-PT were studied by Kuwata et al.⁴ and later more completely by Mulvihill et al.⁵ Growth and properties of PMN-PT single crystals at the MPB were studied by Shrout et al.⁶.

All the studies mentioned above have been made with crystals that were grown by random nucleation and slow cooling the solution. The result is that many crystals are nucleated, compete with one another for available nutrients, and never reach large sizes. Also, crystals from adjacent nuclei often grow into one another with neither growing large. There is clearly a need for seeded growth where nucleation is controlled and growth limited to one crystal. In the past, only seeded growth has produced large crystals by any growth technique.

Because in the past growth took place from concentrated solutions of PMN in PbO fluxes, the temperatures required for homogenization of the solutions was such that volatilization of the flux precluded growing in open systems. This study investigates growth from more dilute solutions where volatilization of the flux is not a problem. The first flux considered was PbO-B₂O₃. Dilute solutions of (PbO-0.132B₂O₃)_x-(0.65PbMg_{1/3}Nb_{2/3}O₃-

$0.35\text{PbTiO}_3)_1$ where $x=6$ to 14 were employed. The flux has a melting temperature of $< 840^\circ\text{C}$, and homogenization of these solutions is complete at 1050°C . By observing the onset of spontaneous nucleation, we have obtained an approximate measure of solubility over this range of dilution. Saturation temperatures were found to vary from 900°C for 14:1 to 970°C for 6:1 flux to solute concentrations. The slope of the solubility was 0.0009 moles/mole/ $^\circ\text{C}$. This change in solubility with temperature is reasonable for high temperature solution growth. Using this data we have grown single crystals of PMN-PT larger than 1 cm^3 .

The second flux we studied was lead pyrophosphate, $\text{Pb}_2\text{P}_2\text{O}_7$. $\text{Pb}_2\text{P}_2\text{O}_7$ has a melting point of 824°C , lower than lead oxide and even lower than the melting point of the $\text{PbO}-0.13\text{B}_2\text{O}_3$ flux. $\text{Pb}_2\text{P}_2\text{O}_7$ has a higher viscosity than PbO but about the same as $\text{PbO}-0.13\text{B}_2\text{O}_3$. Initial attempts to crystallize PMN-PT out of this flux resulted in the formation of the pyrochlore phase. It was found, however, that the addition of MgO to the flux allowed the perovskite phase to be formed over a wide range of temperatures. A flux of the composition $\text{Pb}_2\text{P}_2\text{O}_7-1.25\text{ MgO}$ was determined to be suitable. Solubility of PMN-

PT in $\text{Pb}_2\text{P}_2\text{O}_7-1.25\text{ MgO}$ was greater than in pure $\text{Pb}_2\text{P}_2\text{O}_7$, but the difference was not measured. The most important property of $\text{Pb}_2\text{P}_2\text{O}_7$ for crystal growth in open systems is its low volatility. Vaporization losses were minimal even at 1050°C , and at 1020°C , a typical growth temperature, they were less than 1% over a 20 day run. Saturation temperatures ranged from 1070°C for a 3:1 to 1000°C for a 6:1 flux to solute concentrations. The slope of the solubility was 0.0024 moles/mole/ $^\circ\text{C}$. Again, we were able to grow seeded crystals larger than 1 cm^3 .

References

1. E. Myl'nikova and V.A. Bokov, *Kristallografiya*, **4**, 433 (1959).
2. V.A. Bokov and I.E. Myl'nikova, *Soviet Phys. - Solid State*, **2**, 2428 (1961).
3. S. Nomura, T. Takahashi, and Y. Yokomizo, *J. Phys. Soc. Japan*, **27**, 262 (1969).
4. J. Kuwata, K. Uchino, and S. Nomura, *Jpn. J. Appl. Phys.*, **21**, 1298 (1982).
5. M.L. Mulvihill, S.-E. Park, G. Risch, Z. Li, K. Uchino, T.R. Shrout, *Jpn. J. Appl. Phys.*, **35**, 51 (1996).
6. T.R. Shrout, Z.P. Chang, N. Kim, S. Markgraf, *Ferroelectric Letters*, **12**, 63 (1990).

Relaxor Single Crystals from Polycrystalline Precursors

Martin P. Harmer, Helen M. Chan, Tao Li, Frank Meschke, and Adam M. Scotch
Materials Research Center
Lehigh University
Bethlehem, Pennsylvania 18015
(610) 758-3850

Recent developments have established that relaxor-based single crystal ferroelectrics possess enhanced performance characteristics compared to the alternative polycrystalline materials. Single crystals of $\text{Pb}(\text{Mg}_{1/3}\text{Nb}_{2/3})\text{O}_3$ (PMN), $\text{Pb}(\text{Zn}_{1/3}\text{Nb}_{2/3})\text{O}_3$ (PZN), and their solid solutions with PbTiO_3 (PT) have been shown to exhibit E-field induced strains $>1\%$,¹ longitudinal coupling coefficients (k_{33}) $>90\%$, piezoelectric coefficients (d_{33}) $>2000\text{pC/N}$, and dielectric constants from 1000-5000 with low dielectric loss $<1\%$.²

Conventional flux techniques for growing ceramic single crystals are relatively slow and not well suited for mass production. In addition, such processes are unsuitable for systems which melt incongruently, or contain volatile elements, such as lead. A potentially more economical method of fabricating single crystal relaxor-based ferroelectric materials has been investigated. The procedure entails bonding a seed single crystal to a dense polycrystalline precursor and allowing the boundary to migrate through the polycrystal under the influence of grain boundary curvature. This process has been used by NGK in Japan for producing single crystal ferrites,³⁻⁵ and has been proven feasible for the BaTiO_3 system.⁶ A similar procedure has also been used to convert polycrystalline alumina into sapphire single crystals.⁷ The present work has established the feasibility of growing relaxor-based PMN-35mol%PT single crystals from polycrystalline precursors.

Seed single crystals (Pennsylvania State University) were embedded in PMN-35mol%PT powder (TRS Ceramics, State College, PA) and cold isostatically pressed at 340 MPa into 13 mm diameter compacts. The compacts were sintered and annealed at temperatures from 900°C to 1200°C for dwell times up to 140 hours under pressureless conditions. A double crucible arrangement was used with PbZrO_3 packing powder as a sacrificial material to suppress the volatilization of lead in the compacts.

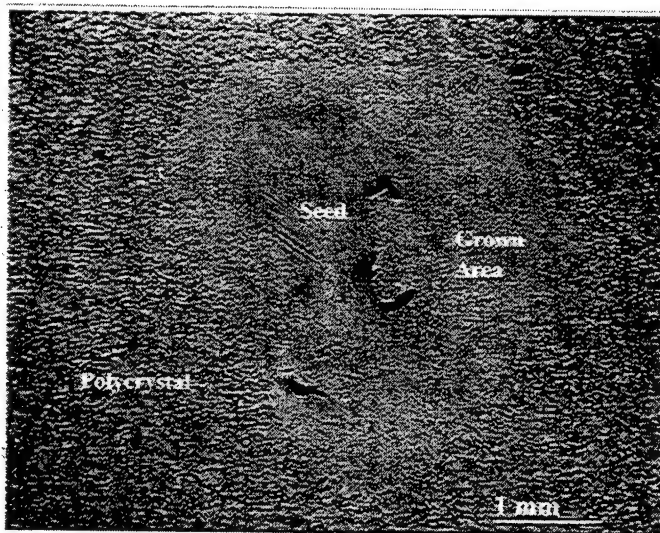


Fig. 1 – Optical micrograph of grown single crystal of PMN-35mol%PT embedded in a polycrystalline matrix for 140 hours at 1150°C.

In order to get a fully dense matrix prior to crystal growth, seeded polycrystalline compacts of PMN-35%PT were hot-pressed from 900-1000°C for 1-12 hours at 40 MPa. The samples were subsequently annealed under pressureless conditions to allow for crystal growth. A top-seeded growth technique was also employed by bonding a seed single crystal to a dense compact and annealing. Mating surfaces of the compacts and seed single crystals were polished to a 1 μ m finish.

Figure 1 shows the cross-section of a seed single crystal that has grown several millimeters into the polycrystalline matrix after annealing for 140 hours at 1150°C in air under pressureless conditions. This micrograph confirms that the polycrystalline precursor technique is feasible for growing single crystals of PMN-35mol%PT.

Figure 2(a) shows a cross-section of a seeded PMN-35mol%PT compact after annealing for 16 hours at 1200°C under pressureless conditions. The grown single crystal exhibited a cubic morphology, as outlined with solid white in Figure 2(a). Figure 2(b) displays a second cross-section taken perpendicular to the polished surface at the dashed line in Figure 2(a).

The crystallographic orientations of the grown PMN-35mol%PT single crystal were determined using an electron backscatter diffraction technique in an SEM.⁸ Figure 2(c) presents

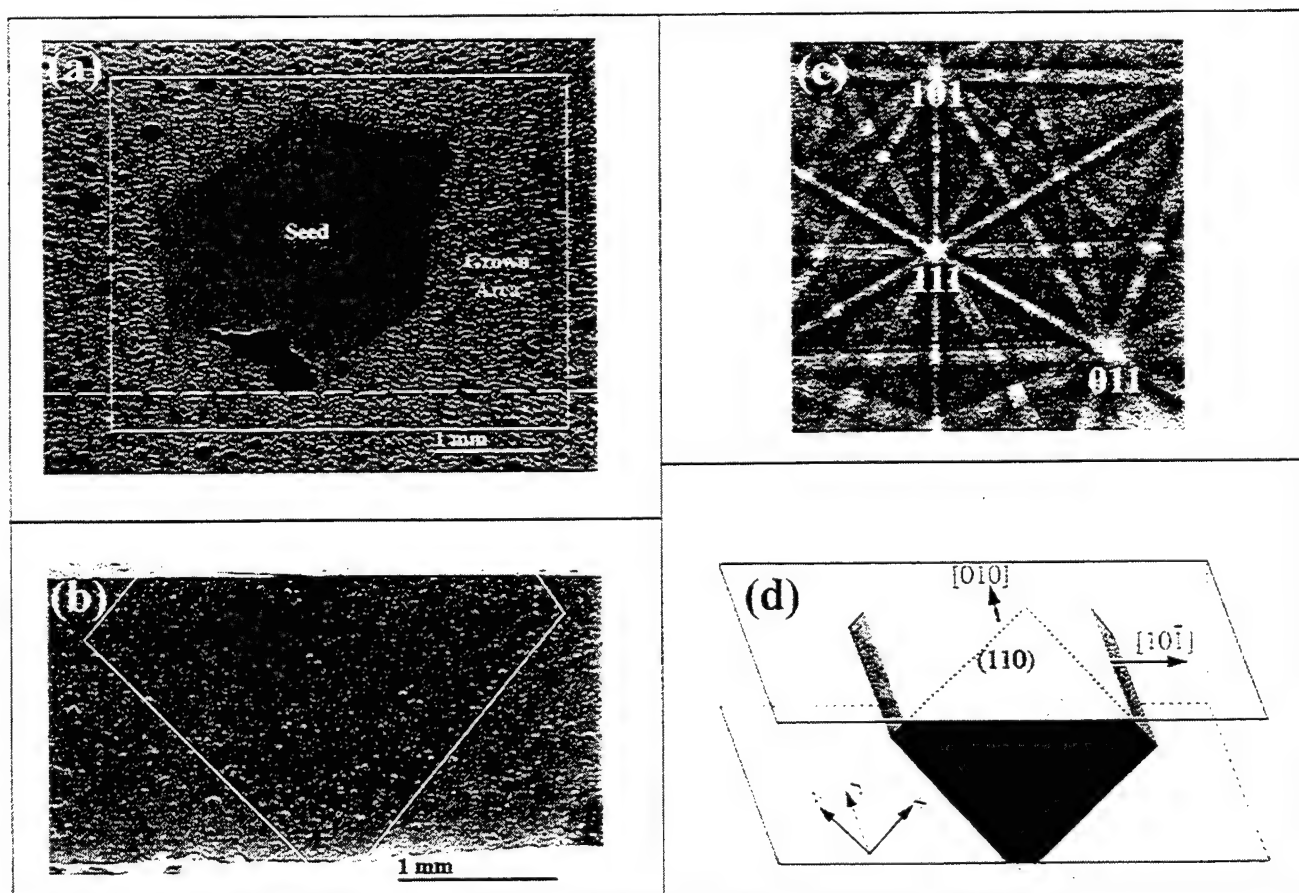


Fig. 2 – Orientation study of PMN-35mol%PT grown single crystal.

a Kikuchi pattern taken from the polished surface of the single crystal shown in Figure 2(a). The primary poles were indexed and are consistent with a pseudo-cubic crystal structure. Applying the information from the Kikuchi pattern to the single crystal morphologies seen in Figures 2(a) and 2(b), a schematic diagram was constructed to illustrate the crystal directions (Figure 2(d)). It is observed that PMN-35mol%PT single crystals grown from polycrystalline precursors exhibit cubic growth morphologies with (100) faces. Thus, it is concluded that $\langle 100 \rangle$ is the slowest macroscopic growth direction. The relationship of single crystal orientation and growth in PMN-35mol%PT is currently being examined in a systematic study.

In an effort to reduce the pore drag effect and facilitate the grain boundary migration of the single crystal, fully dense PMN-35mol%PT powder compacts were produced by hot-pressing. During the subsequent anneal, the single crystals were grown into the matrix with a significant reduction in porosity compared to crystals grown under pressureless conditions. Figure 3 depicts the interface of a single crystal grown after hot-pressing for 1 hour at 950°C and 40 MPa, followed by an anneal for 16 hours at 1100°C. More emphasis will be placed on the effect of porosity on crystal growth velocity in future work.

In general, the velocity of a grain boundary is directly proportional to both the boundary mobility, and the driving force for migration. An increase in either of these would thus enhance the growth rate of the crystal. Rödel and Glaeser reported that the mobility of an alumina single crystal boundary depends on the orientation of the single crystal.⁹ The structure and chemistry of the boundary,¹⁰ and the processing temperature¹¹ have been also reported to affect mobility. These factors will be evaluated in future work that will consider grain boundary chemistry, graded matrix compositions, and thermal gradients.



Fig. 3 – SEM micrograph showing the interface of a polycrystal matrix and grown single crystal after hot-pressing and annealing.

Acknowledgments: The authors would like to thank Dr. J. R. Michael at Sandia National Laboratory for his electron backscatter diffraction work on the SEM. The authors also thank Dr. T. R. Shrout and Dr. S. E. Park at Pennsylvania State University for graciously supplying the PMN-35mol%PT seed single crystals and powders. This research is supported by Office of Naval Research, Contract No. N00014-96-I-0627.

References

- ¹T. R. Shrout and S. E. Park; "Relaxor Ferroelectric Single Crystals for High Strain Actuators", presented at Piezoelectric Crystal Planning Workshop, Washington, D. C., May 14-16, 1997.
- ²S. E. Park and T. R. Shrout, "Characteristics of Relaxor-based Piezoelectric Materials for Ultrasonic Transducers", Proceedings of the 1996 IEEE International Ultrasonics Symposium.
- ³N. Yamamoto and S. Matsuzawa, "The Solid-Phase Epitaxial Growth Method", Fine Ceramics, edited by S. Saito, Elsevier Pub., New York, 39-44, (1988).
- ⁴S. Matsuzawa and S. Mase, "Method for Producing a Single Crystal Ferrite", U.S. Patent # 4,339,301 (1982).
- ⁵K. Kugimiya, K. Hirota, and K. Matsuyama, "Process for Producing Single Crystal Ceramics", U.S. Patent # 4,900,393 (1990).
- ⁶T. Yamamoto and T. Sakuma, "Fabrication of Barium Titanate Single Crystals by Solid-State Grain Growth", *J. Am. Ceram. Soc.*, **77**[4], 1107-109 (1994).
- ⁷C. Scott, J. Strook, and L. Levinson, "Solid State Thermal Conversion of Polycrystalline Alumina to Sapphire Using a Seed Crystal", U.S. Patent # 5,549,746 (1996).
- ⁸D. Dingley and V. Randle, "Microtexture Determination by Electron Backscatter Diffraction", *J. Mat. Sci.*, **27**[17], 4545, (1992).
- ⁹J. Rödel and A. Glaeser, "Anisotropy of Grain Growth in Alumina", *J. Am. Ceram. Soc.*, **73**[11], 3292-301, (1990).
- ¹⁰C. Simpson and K. Aust, "Grain Boundary Migration", *Surf. Sci.*, **31**, 479-97, (1972).
- ¹¹M. Yan, R. Cannon, and K. Bowen, "Grain Boundary Migration in Ceramics", Ceramic Microstructures '76, Ed. By R. Fulrath and J. Pask, Westview Press, Boulder CO, 276-307, (1977).

Templated Grain Growth of Ferroelectric Materials

B. Brahmaroutu, P. W. Rehrig, S. H. Hong, S. Trolrier-McKinstry, and G. L. Messing

Intercollege Materials Research Laboratory
The Pennsylvania State University
University Park, Pennsylvania 16802 USA

Abstract - *In situ* and surface templated grain growth (TGG) of polycrystalline ceramics were used to prepare oriented ferroelectric single crystals and ceramics. *In situ* TGG relies on the texturing effect of anisotropic grain growth which occurs when oriented single-crystal template particles are dispersed in a dense, fine-grained matrix. It does not require a high temperature-high pressure processing step. This process was used to prepare highly oriented (>90%) $\text{Sr}_2\text{Nb}_2\text{O}_7$ and $\text{Bi}_4\text{Ti}_3\text{O}_{12}$ polycrystalline ceramics for high temperature piezoelectric applications. By donor doping, the dielectric loss can be kept low up to 400°C. In Nb-doped $\text{Bi}_4\text{Ti}_3\text{O}_{12}$, piezoelectric coefficients >30 pC/N were obtained in oriented ceramics. Large anisotropy was also achieved in the polarization-electric field hysteresis loops. In addition, single crystals of BaTiO_3 were fabricated using surface TGG. This process involves contacting a polycrystalline matrix with a single crystal seed and then heating the assemblage to a temperature which promotes the migration of the single crystal boundary through the matrix. In this investigation mm-sized single crystals of BaTiO_3 were produced by heating a 99% dense polycrystalline matrix with a Ba/Ti ratio < 1.00 for 8 hours at 1350°C. The resulting crystals obey the Curie - Weiss law and show very low dielectric loss.

I. INTRODUCTION

For a variety of optical and electromechanical applications, the high angle grain boundaries and random arrangement of grains in polycrystalline ceramics are problematic. For example, many of the high temperature piezoelectrics, including the layered perovskites, are low symmetry structures, with few possible orientations for the polarization direction. As a result, it is difficult to pole a randomly oriented ceramic efficiently, and the resulting piezoelectric coefficients are well below the single crystal values. Poling the ceramic would be made easier by strong texture, since the axes of the crystals are already aligned. Similarly, BaTiO_3 single crystals are being exploited for their electrooptic effects in switches and photorefractive storage among other applications. Extensive utilization of such devices is hampered by the expense of the crystals. In each of these cases, it would be extremely interesting to develop an alternative, lower-cost production method for highly textured or single crystal materials which uses polycrystalline ceramics as a starting point.

This paper describes templated grain growth (TGG) as one means of achieving strong texture in several types of

electroceramics. In *in situ* TGG, orientation in a polycrystalline ceramic is achieved by aligning a small percentage of anisometric grains in a matrix of fine grains (e.g. by tape casting). Subsequent grain growth during sintering extends the texture through the matrix. The TGG method has previously been demonstrated for Al_2O_3 [1,2], mullite [3], SiC [4,5], and Si_3N_4 [6]. Surface TGG is done by mounting a single crystal seed on a fine-grained ceramic and heating the assembly to propagate the single crystal boundary into the polycrystalline matrix. This process has been used to prepare single crystal ferrites [7], alumina, and BaTiO_3 [8], among others. These two processes are described in the following for the preparation of oriented $\text{Bi}_4\text{Ti}_3\text{O}_{12}$ ceramics as well as BaTiO_3 single crystals.

II. *IN SITU* TEMPLATED GRAIN GROWTH OF ORIENTED CERAMICS

A coprecipitation method was developed for making ultrafine $\text{Bi}_4\text{Ti}_3\text{O}_{12}$ and $\text{Bi}_4\text{Ti}_{2.96}\text{Nb}_{0.04}\text{O}_{12}$ particles. Bi_2O_3 and $\text{TiO}(\text{OH})\text{Cl}$ were dissolved in the stoichiometric ratio in a nitric acid solution at pH < 3. Nb was added as Nb oxalate. The solution was slowly dripped into concentrated NH_4OH , producing a gel-like coprecipitate at pH > 10. This coprecipitate was washed in dilute NH_4OH , dried, and ground with a mortar and pestle. The resultant powder was x-ray amorphous, transforming to phase pure $\text{Bi}_4\text{Ti}_3\text{O}_{12}$ when calcined above 550°C in air. Powder calcined at 700°C was comprised of equiaxed particles, having an average diameter of about 200 nm and specific surface area of $8 \text{ m}^2\text{g}^{-1}$. The SSA corresponds to an equivalent spherical diameter of 93 nm, indicating that the particles are aggregates of a few primary particles.

Platelike particles were prepared by a molten salt technique. The platelets were approximately 5 - 20 μm in diameter and 0.5 μm thick.

Slurries for tape casting were prepared with 15 - 30 vol% powder in a commercial organic binder solution (B73305, FERRO). Calcined powder was dispersed in toluene with a polymeric dispersant (KD3, ICI Specialty Chemicals) using an ultrasonic horn. The dispersion was added to the binder solution in a Nalgene bottle containing a small amount of ZrO_2 media and mixed on a roller mill for 24 h. The slurry was then poured into a beaker and covered. Platelets (5 or 10% of the fine powder volume) were dispersed in toluene with KD3 using an ultrasonic bath, then stirred into the powder-binder mixture with a magnetic bar.

Tapes were cast at ~ 7 cm/s with a blade opening of 200–300 μm on a glass surface and dried under ambient conditions. The tapes were cut, stacked, heated to 70°C , and pressed uniaxially at 50 MPa. The binder was burned out by heating at $1^\circ\text{C}/\text{min}$ to 450°C , and the laminates were sintered in air.

Texture was calculated from x-ray diffraction data by the Lotgering method. Samples were scanned from $2\theta = 10^\circ$ to 80° on the surface parallel to the casting plane. The degree of orientation, f , is defined as $f = (p - p_0)/(1 - p_0)$, where $p = \sum I\{00\ell\} / \sum I\{hkl\}$ for intensities, I , between $2\theta = 10^\circ$ and 80° . The calcined powder was used as a randomly oriented standard to determine p_0 .

Figure 1 shows the as-sintered edge of a $\text{Bi}_4\text{Ti}_3\text{O}_{12}$ TGG specimen, sintered at 900°C for 10 minutes. The matrix is $\sim 90\%$ dense and no appreciable grain growth is apparent. The seed particles and their orientation is clearly evident. Orientation of the matrix develops quickly for sintering at 1000°C and higher. The microstructures then consist primarily of plate-like grains, approximately 10–50 μm long and 1–2 μm thick, aligned in the casting plane. Little change in the average grain size or orientation was observed between 10 minutes and 2 hours at 1000°C . It was found that grains misaligned with the casting plane did not grow as large as the oriented grains. Sintering at 1050°C for 1 hour led to ceramics which were better than 90% oriented throughout the thickness of the part as measured by the Lotgering factor. The lower sintering temperature relative to conventionally prepared $\text{Bi}_4\text{Ti}_3\text{O}_{12}$ should also reduce problems associated with Bi volatilization.

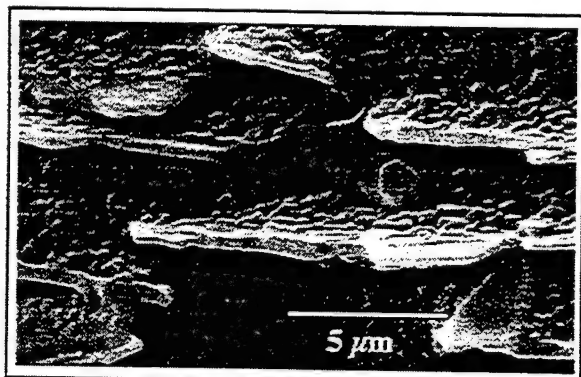


Fig. 1: $\text{Bi}_4\text{Ti}_3\text{O}_{12}$ template particles in a fine-grained matrix. Side view

Randomly oriented pure bismuth titanate ceramics (sintered at 1050°C for 2h) exhibit a room temperature dielectric constant of ~ 145 , and Nb-doping slightly increases the room temperature dielectric constant for the same conditions. With increasing sintering temperature, the room temperature dielectric constant decreases for all the pellets, which is probably due to a decrease in the density. The dielectric constant and loss tangent in pure samples rapidly increase above 200°C because of high electrical conductivity. However, Nb-doping clearly reduced the dielectric loss; the loss tangent is below 0.1 up to 450°C , which make poling possible at higher electric fields and higher temperatures. The sintered TGG tapes have anisotropic dielectric constants: ~ 160

perpendicular to and ~ 120 parallel direction to the casting plane. These values are close to the earlier results on oriented ceramics, although they are smaller than single crystal room temperature values ($K_a=120$, $K_b=205$, $K_c=140$ at 5 MHz) [9].

As can be seen in Figure 2, the remanent polarization (P_r) and coercive field (E_c) for the TGG samples are also anisotropic: $P_r=24.5 \mu\text{C}/\text{cm}^2$, $E_c=30 \text{ kV}/\text{cm}$ parallel to and $P_r=1.4 \mu\text{C}/\text{cm}^2$, $E_c=10 \text{ kV}/\text{cm}$ perpendicular to the casting plane. These are close to previous reports for hot-forged $\text{Bi}_4\text{Ti}_3\text{O}_{12}$ [10]. In $\text{Bi}_4\text{Ti}_3\text{O}_{12}$, the spontaneous polarization lies in the monoclinic *a-c* plane at a small angle ($\sim 4.5^\circ$) to the *a*-axis and exhibits two independently reversible components: $50 \mu\text{C}/\text{cm}^2$ along the *a*-axis and $4 \mu\text{C}/\text{cm}^2$ along the *c*-axis. The observed remanent polarization of the tape in each direction is about half of the spontaneous polarization of single crystal $\text{Bi}_4\text{Ti}_3\text{O}_{12}$.

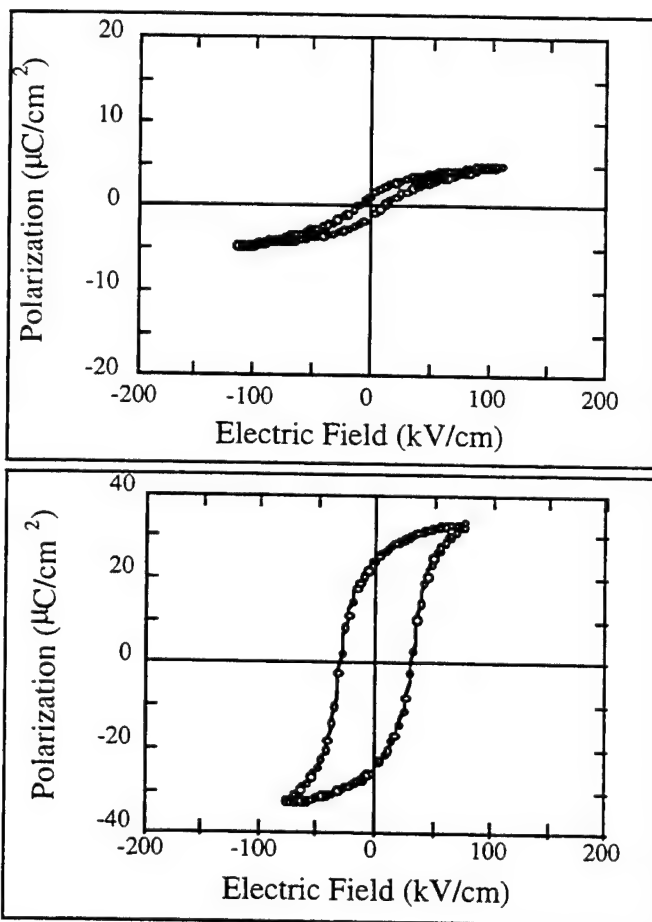


Fig. 2: Polarization-electric field hysteresis loops for an oriented $\text{Bi}_4\text{Ti}_3\text{O}_{12}$ sample measured (a) parallel and (b) perpendicular to the casting plane.

Variations in the piezoelectric constant of the Nb-doped sample with respect to poling time and applied electric field were studied. It was found that the piezoelectric constant increases monotonically with applied field up to 80 kV/cm and is quickly saturated within 10 min. The measured piezoelectric constants for randomly oriented pellets and for

TGG samples are shown in Fig. 3. For the randomly oriented ceramics, the Nb-doped samples have d_{33} values ~ 20 pC/N which is comparable to earlier reports [11]. The TGG sample again exhibited anisotropic piezoelectric behavior, with d_{33} parallel to the casting plane ~ 30 pC/N. The reported piezoelectric constants for a single domain single crystal are as follows: $d_{11}=39$ pC/N, $d_{22}=0$, and $d_{33}=9$ pC/N [12]. The observed piezoelectric constants parallel to the casting plane are comparable to the single crystal values of d_{11} .

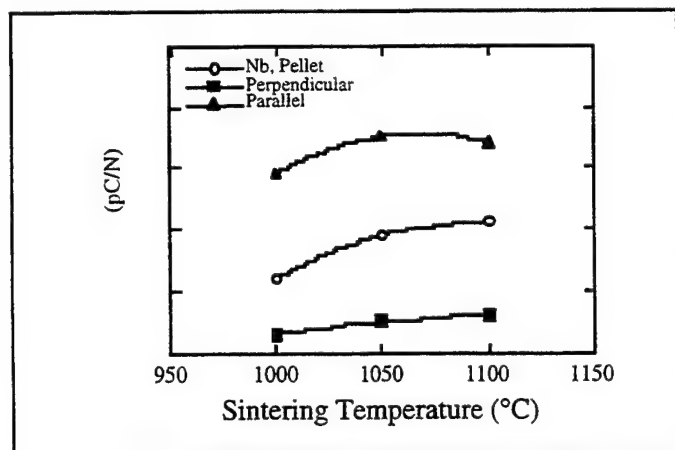


Fig. 3: d_{33} for $\text{Bi}_4\text{Ti}_3\text{O}_{12}$ ceramics sintered at different temperatures showing the effect of orientation.

Samples were also heat-treated at various temperatures to determine where thermal depoling occurred. Both randomly oriented and TGG Nb-doped samples retain 90% of their room temperature values up to 600°C for a 10 minutes exposure to the annealing temperature. Also Nb-doped samples retained more than 90% of their initial value after annealing for 100 h at 450°C . These studies clearly demonstrate that doped BIT can be used for high temperature piezoelectric applications operating $>300^\circ\text{C}$.

Work is on-going for the preparation of templated $\text{Sr}_2\text{Nb}_2\text{O}_7$ for higher temperature piezoelectric applications. To date, good orientation has been achieved in pure samples via the TGG approach.

III. SURFACE TEMPLATED GRAIN GROWTH OF BaTiO_3 SINGLE CRYSTALS

Surface templated grain growth entails using a single seed crystal, rather than multiple oriented seed particles to produce a single crystal specimen from a polycrystalline matrix. This next portion of this paper focuses on using this technique for the preparation of single crystal BaTiO_3 . As seed crystals, Lockheed Sanders Inc. (Nashua, NH) (001) BaTiO_3 single crystal cutoffs were oriented via 4-circle or Laue X-ray diffraction, and polished to a $1\text{ }\mu\text{m}$ finish using diamond paste. The polycrystalline ceramic part was prepared from Sakai Chemical Industry Co. Ltd. hydrothermal BaTiO_3 with an average grain size of 90 nm. The as-received powder had a

$\text{Ba/Ti} = 1.00$. The powder was acid-washed in dilute HNO_3 at a pH ~ 4.0 to develop a Ti-rich surface. Pellets were then uniaxially dry pressed into 2.5 cm diameter pellets at ~ 9 MPa, followed by a cold isostatic pressing at ~ 280 MPa. To increase the density, the samples were then hot pressed at 61 MPa and 1200°C for 30 min. in argon. The resulting ceramic was 99% of theoretical density and had an average grain size of $\sim 0.2\text{ }\mu\text{m}$.

The seed was then placed on the ceramic surface and the two were heated together at 1350°C for 1 - 20 hours. Fig. 4 shows a cross-sectional micrograph of the sandwich following an eight hour hold at 1350°C . It can be seen there that the single crystal surface propagated ~ 1.4 mm into the polycrystalline matrix. Exaggerated grains in the remaining ceramic can also be distinguished. The wedge-shaped region is clearly a single crystal as measured by Laue x-ray diffraction, and has a well-defined boundary with the matrix ceramic as seen by electron microscopy.

For samples heat-treated at 1350°C , the growth rate was nearly linear for annealing times up to eight hours. Beyond that point, the rate decreased somewhat. Growth was appreciably slower when samples were heated to 1300°C , rather than 1350°C . It is believed that a small amount of liquid phase associated with the eutectic on the Ti-rich side of BaTiO_3 of the phase diagram is important.

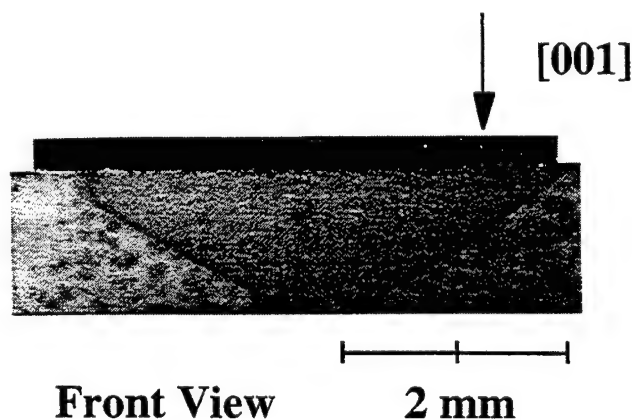


Fig. 4: Surface templated grain growth of (001) BaTiO_3 . The dark slab at the surface is the seed crystal. The wedge-shaped area is the grown crystal.

A section was cut from a grown crystal, electroded, and the dielectric properties were measured. The crystal shows a well-defined maximum in the dielectric constant versus temperature at 128°C , and no dispersion. The data fit the Curie-Weiss law, and the slope of the line is quite close to accepted values for BaTiO_3 . The dielectric loss is also low. To date, the polarization - electric field hysteresis loops show low P_r values, probably due to difficulties in completely re-orienting the domains associated with the residual porosity in the grown crystal. Work is on-going to eliminate the remaining porosity in the crystal.

IV. CONCLUSIONS

Both surface and *in situ* templated grain growth have been demonstrated in ferroelectric materials. For the case of $\text{Bi}_4\text{Ti}_3\text{O}_{12}$, it is clear that the TGG process enables the production of strongly oriented samples. The resulting piezoelectric properties are superior to those observed in randomly oriented samples. In addition, the fact that this processing does not require a high pressure - high temperature step should make it attractive in production relative to techniques like hot forging. The processing route described here also utilizes a lower sintering temperature than does standard bulk ceramic processing. As a result, bismuth loss during sintering should be less problematic.

Surface templated grain growth of BaTiO_3 enables the production of mm-sized single crystals during an eight hour annealing step. As the crystal quality is improved by elimination of residual porosity, this approach should be extremely interesting as a low-cost alternative to conventional single crystal growth processes.

V. ACKNOWLEDGMENTS

The authors gratefully acknowledge the support of DARPA and AFOSR through contracts F49620-94-1-0428 and DAAH04-95-1-0484

VII. REFERENCES

- 1 M. M. Seabaugh, I. H. Kerscht, and G. L. Messing, "Texture Development by Templated Grain Growth in Liquid-Phase-Sintered α -Alumina," *J. Am. Cer. Soc.*, 80 [5] 1181-88 (1997).
- 2 T. Carisey, I. Levin, and D. G. Brandon, "Microstructure and Mechanical Properties of Textured Al_2O_3 ," *J. Eur. Cer. Soc.*, 15 283-289 (1995).
- 3 S.-H. Hong, W. Cermignani, and G. L. Messing, "Anisotropic Grain Growth in Seeded and B_2O_3 -Doped Biphasic Mullite Gels," *J. Eur. Cer. Soc.*, 16, 133-41 (1996).
- 4 N. P. Padture, "In-Situ-Toughened Silicon Carbide," *J. Am. Cer. Soc.*, 77 [2] 519-23 (1994).
- 5 M. J. Sacks, G. W. Scheiffele, and G. A. Staab, "Fabrication of Textured Silicon Carbide via Seeded Anisotropic Grain Growth," *J. Am. Cer. Soc.*, 79 [6] 1611-16 (1996).
- 6 K. Hirao, M. Ohashi, M. Brito, and S. Kanzaki, "Processing Strategy for Producing Highly Anisotropic Silicon Nitride," *J. Am. Cer. Soc.*, 78 [6], 1687-90 (1995).
- 7 S. Matsuzawa and S. Mase, "Method for Producing a Single Crystal of Ferrite", US Patent 4,339,301 (1982).
- 8 T. Yamamoto and T. Sakuma, "Fabrication of BaTiO_3 Single Crystals by Solid State Grain Growth", *J. Am. Ceram. Soc.*, 77 1107 - 1109 (1994).
- 9 A. Fouskova and L. E. Cross, "Dielectric Properties of Bismuth Titanate," *J. Appl. Phys.*, 41[7] 2834-38 (1970).
- 10 T. Takenaka and K. Sakada, "Grain Orientation and Electrical Properties of Hot-Forged $\text{Bi}_4\text{Ti}_3\text{O}_{12}$ Ceramics," *Jpn. J. Appl. Phys.*, 19[1] 31-39 (1980).
- 11 H. S. Shulman, M. Testorf, D. Damjanovic, and N. Setter, "Microstructure, Electrical Conductivity, and Piezoelectrical Properties of Bismuth Titanate," *J. Am. Ceram. Soc.*, 79[12] 3124-28 (1996).
- 12 A. Saneto and L. E. Cross, "Electro-mechanical Behavior of Single Domain Single Crystals of Bismuth Titanate ($\text{Bi}_4\text{Ti}_3\text{O}_{12}$)," *J. Mater. Sci.*, 17, 1409-12 (1982).

Effect of Electrode Material on the Physical and Electrical Properties of a PZN Relaxor -PT Single Crystals

John Y. Yamashita, K. Harada, T. Kobayashi, S. Shimanuki and S. Saito

Materials and Devices Research Laboratories,
Toshiba Research & Development Center, Toshiba Corporation.
70 Yanagi-cho, Saiwai-ku, Kawasaki 210, JAPAN
(e-mail/yohachi.yamashita@toshiba.co.jp)

Abstract- The microstructure, dielectric constants and electromechanical coupling coefficients of $\text{Pb}[(\text{Zn}_{1/3}\text{Nb}_{2/3})_{0.91}\text{Ti}_{0.09}]\text{O}_3$ (PZNT 91/9) single crystals with different electrode materials have been investigated. Various electrodes, consisting of sputtered Au and certain kinds of fired Ag, were applied to PZNT 91/9 single crystals. The dielectric constant K_{max} at the Curie temperature was 55,000 for specimens with Au electrodes. However, specimens with various fired Ag electrodes had a lower K_{max} value of 8,000. The reason for this difference is pyrochlore phase formation between the PZNT 91/9 single crystal and the fired Ag electrodes. A suitable Ag electrode paste choice for PZNT 91/9 single crystals is introduced.

I. INTRODUCTION

Lead-based ferroelectric perovskite compounds with the general formula $\text{Pb}(\text{B}'\text{B}'')\text{O}_3$ have found application in capacitors, electrostrictive actuators, and generators. The solid solutions of lead zinc niobate, $\text{Pb}(\text{Zn}_{1/3}\text{Nb}_{2/3})\text{O}_3$ (PZN), and lead titanate, PbTiO_3 (PT), have a morphotropic phase boundary (MPB) near 9 mol% PT. The electrical properties of PZNT91/9 single crystals were reported by Kuwata et al. in 1982[1]. The (001) plane crystal has an exceptionally large piezoelectric constant ($d_{33} > 1,500$ pC/N) and electromechanical coupling coefficient ($k_{33} > 92\%$). Thus, these single crystals are expected to find application in high-quality ultrasonic transducers as replacements for conventional $\text{Pb}(\text{Zr,Ti})\text{O}_3$ (PZT) ceramics. Fired Ag electrodes are used for PZT ceramics due to their excellent soldering properties, reasonable cost, and high reliability. However, the effects of fired Ag electrodes on the physical and electrical properties of PZNT 91/9 single crystals have not been studied so far. The purpose of this study is to investigate the dielectric and electromechanical properties of PZNT91/9 single crystals with various types of fired Ag electrodes.

II. EXPERIMENTAL DETAILS

The PZNT 91/9 single crystal was prepared by the PbO flux method. Raw powders of PbO , ZnO , Nb_2O_5 , and TiO_2 were mixed in a pestle and mortar, and the mixture was

calcined at 800°C for two hours in an Al_2O_3 sagger. A 55 mol% PZNT91/9 and 45 mol% PbO flux were placed in a 100 cm^3 Pt crucible. The Pt crucible was heated to $1,250^\circ\text{C}$ for 4 hours and then cooled to 900°C at $0.5^\circ\text{C}/\text{hour}$. The crucible was then air-quenched to room temperature for about 24 hours. The resulting PZNT 91/9 single crystal was cut along the (100) plane after its orientation was determined from its Laue X-ray diffraction pattern. The obtained wafer size was about $15\text{ mm} \times 15\text{ mm}$. Thin films of Au of 200 nm were formed by sputtering. The wafer was cut into specimens $4\text{ mm} \times 4\text{ mm} \times 0.4\text{ mm}$ with a dicing saw (DISCO DAD-2H/6T). After measuring dielectric properties as a function of temperature, the specimens were immersed in silicone oil and poled in a 1 kV/mm electric field. The field was applied at a temperature of 200°C for 15 minutes, and the specimens were afterwards cooled to 30°C in the field for about 3 hours. The electromechanical coupling coefficient thickness mode k_t was measured using an impedance analyzer (HP-4195A; network mode) by the resonance anti-resonance frequency method. The Au electrodes were then removed by lapping with #4,000 sand paper. Commercially available Ag electrode pastes (Type I, and Type II in Table I) were formed on the specimens by a screen printing method and then fired in an air atmosphere at 700°C for 5 minutes. The thickness of the Ag electrodes was about 13 microns. After applying these Ag electrodes, the same process of dielectric measurement, poling, and piezoelectric measurement was carried out. The microstructure of the cross section and surface of the fired Ag specimens was observed using an SEM (JEOL JSM-T20).

III. RESULTS AND DISCUSSION

Figure 1 shows the temperature dependence of dielectric constants and dissipation factors of specimens with two types of Ag electrodes and Au sputtered electrodes after removal of the Ag electrodes. The dielectric constant of the specimen with Ag electrodes decreases rapidly below the Curie temperature, T_c . At the same time, the temperature dependence of dissipation factor increases. These phenomena are reported as mechanical poling[3].

Mechanical poling is caused by shrinkage of the fired Ag electrodes[4]. Mechanical poling decreases the dielectric constant, K , below T_c and increases it at T_c . The dielectric constant, K_{max} , of specimens with Type I fired Ag electrodes is higher at T_c . However, the K_{max} of specimens with Type II Ag electrodes is lower at T_c .

Figure 2 shows a cross section through a PZNT 91/9 specimen with a) Type I, b) Type II, and Au/Ti electrodes. No additional phase[2] (such as pyrochlore or glass) is observed at the boundary between the electrode and the single crystal with the Type I and Au electrodes. However, an additional phase is observed in the single crystal with Type II electrodes.

The lower dielectric constant at T_c is caused by an additional phase in the PZNT 91/9 with Ag electrodes. Figure 3 shows a cross section through a PZNT 91/9 specimen with Type II electrodes fired for 1 hour at 800°C. The pyrochlore phase forms in the surface of the PZNT 91/9 with Type II electrodes. Figure 4 shows X-ray diffraction patterns of PZNT 91/9 wafer surfaces after polishing the electrodes. Surfaces with Type II and Type I electrodes, indicate coexisting pyrochlore and perovskite phases. However, no pyrochlore phase is seen in the specimen with no electrodes. The additional pyrochlore phase forms between the electrodes and PZNT 91/9. As a result, the dielectric constant decreases. In other words, the dielectric constants of specimens decrease as a result of the ferroelectric phase.

Table I shows the components of glass flit in the Ag electrode paste. Type I paste does not include B_2O_3 , while Type II does. Type II includes more than 10 times the amount of Bi_2O_3 in Type I. Type I includes more glass components than Type II. Imoto[6] et al. Reported that a perovskite phase transforms into a pyrochlore phase with B_2O_3 , Bi_2O_3 , and SiO_2 . They reported also that MgO , PbO , and ZnO have no effect on the perovskite phase. Glass flits play an important role in forming contacts with specimens thorough chemical reaction; however, they may destroy the perovskite phase. It is therefore very important to select a suitable glass flit for a PZN T91/9 single crystal.

Figure 4 shows how the perovskite phase transforms into the pyrochlore phase in specimens with Ag electrodes. According to this, specimens might be expected to have a small k_t . For PZNT 91/9 with Ag electrodes, however, electrical poling is easier than with the Au sputtered electrode specimen because of mechanical poling[5]. Accordingly, a large k_t might be expected. Table I and Fig.5 show k_t values for specimens with Ag electrodes. The specimens with fired Ag electrodes have a much larger k_t value (= 61.4% and 61.5%) than the specimen with sputtered Au electrodes (=52.7%). These k_t values are large in spite of the pyrochlore phase because of mechanical poling. However, the pyrochlore phase can be expected to pose problems with the PZNT 91/9 single crystals used in some new devices, since

boundaries between pyrochlore and perovskite seem to be fragile. Reliability problems may arise in some devices as a result of this fragility. Type II electrodes attack to perovskite more than Type I because the amount of glass flits in Type II electrode paste is greater. Type I includes Bi_2O_3 and B_2O_3 , which have extremely detrimental effects on the reliability of certain devices using PZNT91/9. Type I electrodes are more suitable than Type II for PZNT 91/9 single crystals.

IV. CONCLUSION

Two types of fired Ag were applied as electrodes to $Pb[(Zn_{1/3}Nb_{2/3})_{0.91}Ti_{0.09}]O_3$ (PZNT 91/9) single crystals with the results given below.

- (1) The dielectric constant K_{max} at the Curie temperature is lower when electrode pastes including Bi_2O_3 and B_2O_3 are used. The lass flits are thought to attack the perovskite phase.
- (2) After electrical poling, Au specimens indicate an electromechanical coupling coefficient k_t of 52.7%, while specimens with fired Ag have relatively high k_t values of 61.4% and 61.5%.
- (3) Type I electrodes are more suitable than Type II for PZNT 91/9 single crystals. More suitable Ag electrodes may be found if we will research into the effects of glass flits on PZNT 91/9 is promoted.

References

- [1] J. Kuwata, K. Uchino, and S Nomura, "Dielectric and Piezoelectric Properties of $0.91Pb(Zn_{1/3}Nb_{2/3})O_3-0.09PbTiO_3$ Single Crystals," Jpn. J. Appl. Phys., 21, pp.1298-1302 (1982).
- [2] H. M. Jang, S. Hoon Oh, and Jong H. Moon, "Thermodynamic Stability and Mechanisms of Formation and Decomposition of Perovskite $Pb(Zn_{1/3}Nb_{2/3})O_3$ Prepared by the PbO Flux Method," J. Am. Ceram. Soc., 75, pp.82-88(1992).
- [3] K. Kakuta, T. Tsurumi, and T. Fukunaga, "Dielectric property of flux-grown $PbTiO_3$ single crystal," Jpn. J. Appl. Phys., 34, 9B, pp.5341-5345(1995).
- [4] K. Harada, S. Shimanuki, and Y. Yamashita, "Effect of Sintered Ag Electrode on Electrical Properties of $Pb[(Zn_{1/3}Nb_{2/3})_{0.91}Ti_{0.09}]O_3$ Single Crystal," Proceedings of 16th Electronics Division Meeting of The Ceramic Society of Japan, Tokyo, September 27, pp95-96 (1991) (in Japanese).
- [5] Y. Matsuo, "Growth of Single Crystals of $Pb(Zn_{1/3}Nb_{2/3})O_3$ and Its Properties," 78(7), pp.213-220(1970) (in Japanese).
- [6] F. Imoto and H. Takase, "Preparation and Several Properties of Ferroelectric Powder $Pb[(Mg,Zn)_{1/3}Nb_{2/3}]O_3$ (Part II)," Yogyo-Kyokai-Shi, 94(9), pp.213-220(1986)(in Japanese).

TABLE I Comparison of PZNT 91/9 with Fired Ag Electrodes and Sputtered Au Electrodes

| | Fired Ag electrodes, Type I | Fired Ag electrodes, Type II | Evaporated Au electrodes |
|---|--|--|-----------------------------|
| Glass type | PbO, ZnO, SiO ₂ , and Bi ₂ O ₃ | PbO, ZnO, SiO ₂ , Bi ₂ O ₃ , and B ₂ O ₃ | — |
| Flit quantity(wt%) | 1.0 | 10.0 | 0 |
| Thickness(μ m) | 10 | 13 | 0.25 |
| Dielectric constant @20°C | 1,000 | 500 | 8,000 |
| Dielectric constant @Curie Temp. | 59,000 | 5,000 | 40,000 |
| Dissipation factor @20°C (%) | 3.0 | 3.0 | 4.0 |
| Dissipation factor @ Curie Temp. (%) | 8.3 | 3.0 | 2.2 |
| E/M coupling kt(%) | 61.5 | 61.4 | 52.7 |

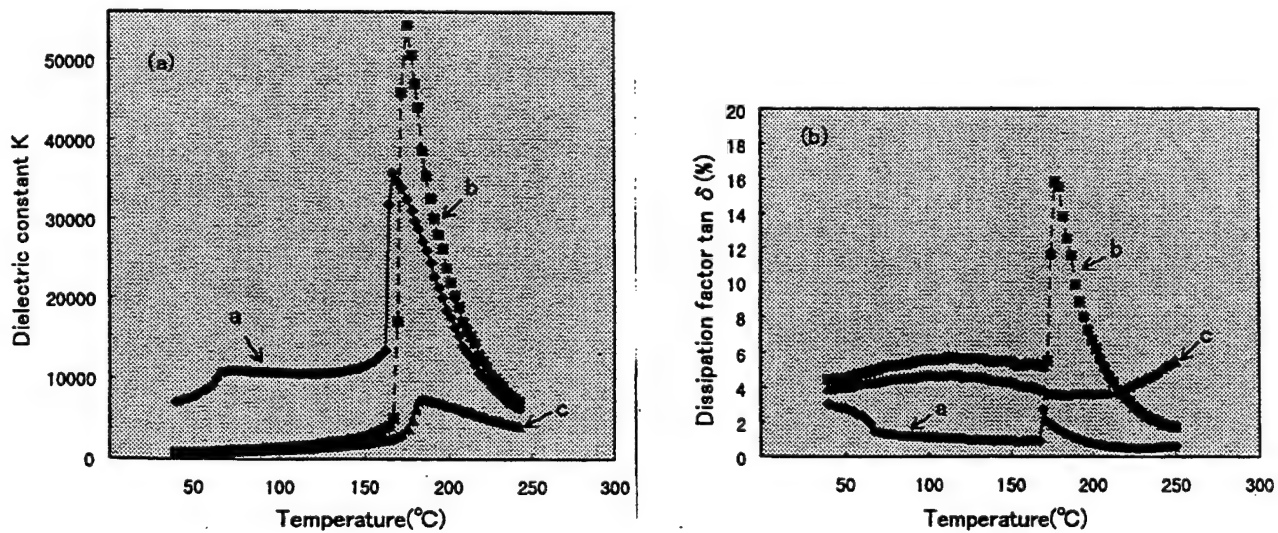


Fig.1 Temperature dependence of dielectric constant and dissipation factor of PZNT 91/9 single crystal. a) with sputtered Au electrodes; b) with Type I and c) Type II fired Ag electrodes

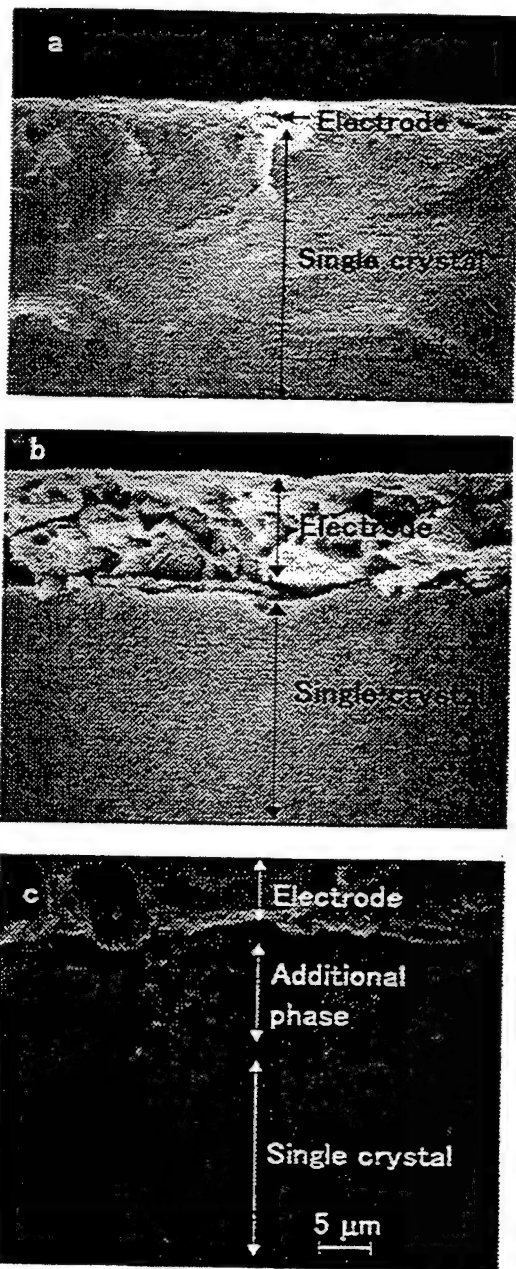


Fig.2 Cross section of boundary between PZNT91/9 single crystal and a) Au electrode; b) Type I Ag electrode; and c) Type II Ag electrode

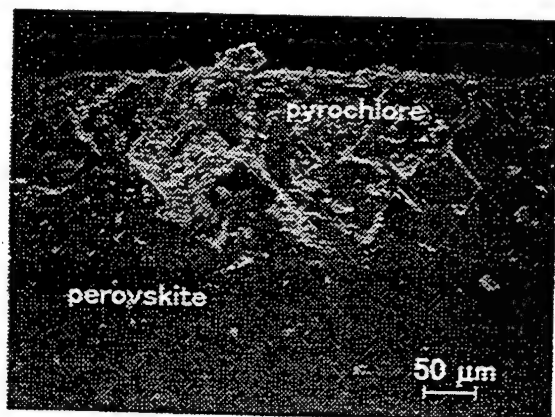


Fig.3 Cross section of boundary between PZNT91/9 single crystal and Type II Ag electrode fired at 800°C

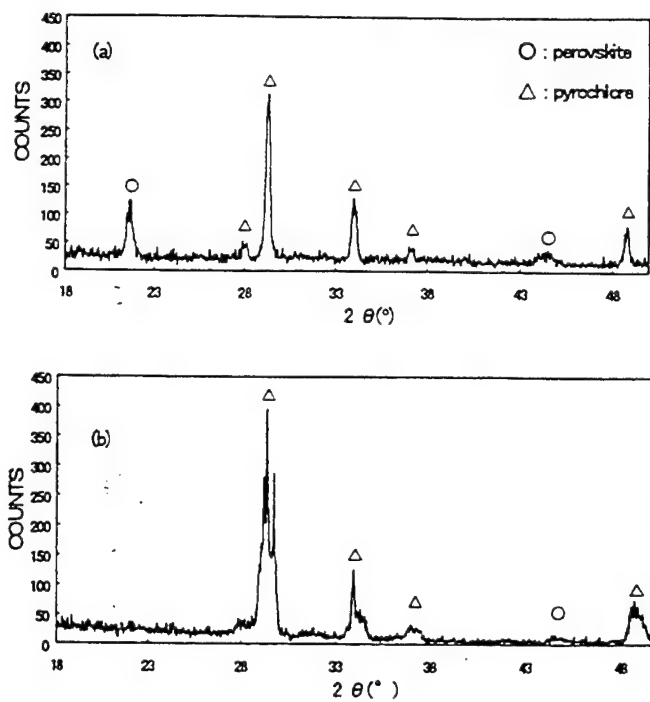


Fig.4 X-ray diffraction patterns of surface of PZNT91/9 wafer after polishing. a) Type I and b) Type II Ag electrodes

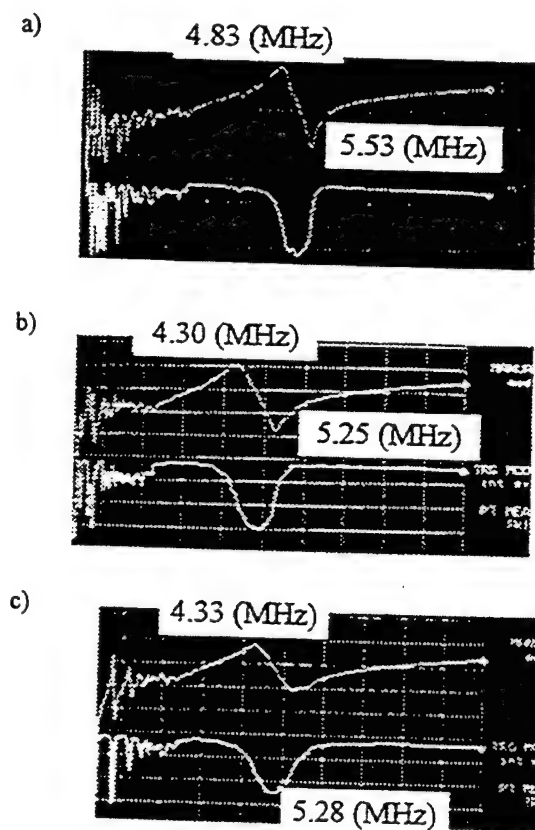


Fig.5 Impedance properties of PZNT91/9 with a) sputtered Au electrodes and b) fired Type I and type II Ag electrodes

Intelligent Engineering of Hydrothermal Reactions

R.E. Riman, B.L. Gersten, and S.B. Cho

Rutgers University, Department of Ceramics, P.O. Box 909, Piscataway, NJ 08855-0909

M.M. Lencka and A. Anderko

OLI Systems, Inc., 108 American Road, Morris Plains, NJ 07950

L.E. McCandlish

Ceramare Corporation, 262 Lincoln Avenue, Highland Park, NJ 08904

Abstract. Hydrothermal research at the Rutgers University is focused on the preparation of multicomponent perovskite oxide compounds. Engineering principles are being developed by examining process thermodynamics and kinetics.

I. INTRODUCTION

This paper shall briefly review our hydrothermal research focusing on the synthesis of multicomponent perovskite oxide compounds. Hydrothermal methods are of interest since they facilitate the preparation of anhydrous oxides in a single process step. Many ceramic synthesis processes require high-temperature process steps such as calcination or solid-state reaction. Practically all of these processes require a comminution step. The additional processing steps, impurity phases and foreign contamination imparted from conventional processes are incentives for developing hydrothermal technology.

The objective of our research is to develop a fundamental approach that will enable us to transform hydrothermal synthesis from an empirically-based technology to one that revolves around engineering principles. Another key objective of our program is to develop technology that is amenable to inexpensive large scale materials production and agile enough to rapidly evolve to a wide spectrum of materials chemistries. In order to accomplish this goal, we are approaching this problem from a multidisciplinary perspective of chemistry, chemical engineering and physical chemistry, which all embrace principles of thermodynamics and kinetics.

II. THERMODYNAMICS

Thermodynamic principles enable one to determine how to design a reaction to yield phase-pure materials. Without knowledge of how to do this, it is impossible to distinguish a process that is being controlled by thermodynamics versus kinetics.

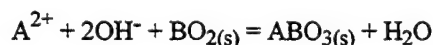
Hydrothermal reaction equilibria for multicomponent perovskite oxides involve a large number of independent reactions. A substantial thermodynamic database is required to examine these equilibria. Furthermore, real hydrothermal

solutions are nonideal and require excess thermodynamic properties to account for interactions between all species in solution. Both the ideal and excess thermodynamic properties, must be calculated as functions of temperature and pressure. At this level of complexity, a computer is essential for thermodynamic modeling of hydrothermal reactions. Currently, our process simulation capabilities [1] extend up to temperatures of 300°C, pressures of 1 kbar and ionic strengths as high as 30 m, which is relevant for many industrial hydrothermal processes.

Computations performed in the composition-temperature-pressure space facilitate the construction of stability [2] and yield diagrams [3]. For the hydrothermal synthesis of phase-pure ceramics, the yield diagram is the most important. This diagram specifies the concentrations of precursors required to achieve an intended final state. For the purposes of making phase-pure materials, regions of the diagram having 99 mol% or greater yield of reaction product are of interest (cf. shaded areas in Figs. 1 and 2).

To construct a yield diagram, computations must be performed in a systematic but time-consuming fashion. Recently, we have developed a computer program that autogenerates these diagrams [4]. Furthermore, the program specifies experimental conditions that can be utilized to validate the thermodynamic model as well as other conditions required to prepare phase-pure materials. Thus, availability of this computer program enables an engineer unfamiliar with the details of aqueous electrolyte thermodynamics to have a design tool for engineering hydrothermal processes.

Our simulation approach has been validated for numerous multicomponent perovskite oxide systems, which include alkaline-earth titanates [5], alkaline-earth zirconates [4,6], lead titanate [3], lead zirconate and various solid solutions of lead zirconate titanate [7]. The general reaction chemistry is as follows:



Our computations examining numerous systems have uncovered a series of thermodynamic trends. First, the

stability of alkaline-earth titanates and zirconates is limited by lower boundaries of pH. The presence of excess A-site ions (e.g., $A/B > 1$) expands the width of the yield region for alkaline-earth perovskites. However, if the pH becomes too high, alkaline-earth hydroxides precipitate as an impurity phase [2, 4-6]. In contrast to the alkaline-earth perovskites, lead zirconate and lead titanate are amphoteric, and their stabilities are bounded by lower and upper pH limits (cf. Fig. 2). The presence of excess lead can narrow the yield region for reactions employing conventional lead acetate or nitrate because of the precipitation of lead oxide. However, with the aid of complexing agents and our simulation-based approach, we have been able to solve this problem [8]. Our computations have revealed the conditions suitable for suppressing lead oxide precipitation yet facilitate lead titanate formation over a range of reaction conditions. Fig. 2 shows how excess lead species can expand the yield region for lead titanate.

Recently, we have focused on identifying new chemistries that are important to the electroceramics community. In particular, many hydrothermal systems incorporate intolerable amounts of alkaline metals [9,10], which is introduced in the form of mineralizers. Our work has examined the possibility of utilizing organic mineralizers. In particular, we have found that tetramethylammonium hydroxide ($N(CH_3)_4OH$) is a favorable substitute for alkaline metal hydroxide mineralizers in producing phase-pure PZT [10] (cf. Fig.1). This form of precursor engineering allows one to make criteria-based choices of chemical precursors as opposed to the commonly employed time-consuming empirical selection process.

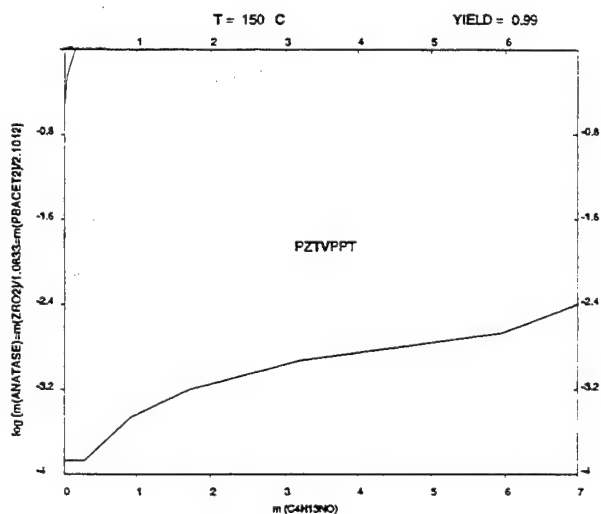


Fig. 1. Calculated yield diagram for the precipitation of $PbZr_{0.52}Ti_{0.48}O_3$ (PZT) in the Pb-Zr-Ti- H_2O system.

The complexity of the thermodynamic system depends on the scale of mixing of the various components. For instance, reaction of hydrous zirconium titanium oxide coprecipitate with a lead acetate-potassium hydroxide solutions form a product that is entirely consistent with our model for lead zirconate titanate solid solution formation. On the other hand, if a physical mixture of hydrous titania and zirconia are reacted with lead acetate-potassium hydroxide solutions, no solid solution products form. Instead, the reaction system behaves as if it were a superposition of two independent equilibrium subsystems: lead titanate and lead zirconate. These results suggest that the gains in chemical homogeneity offered by coprecipitation facilitates the reaction between lead, zirconium and titanium species while the physically mixed system only facilitates localized reactions between lead and titanium species or lead and zirconium species.

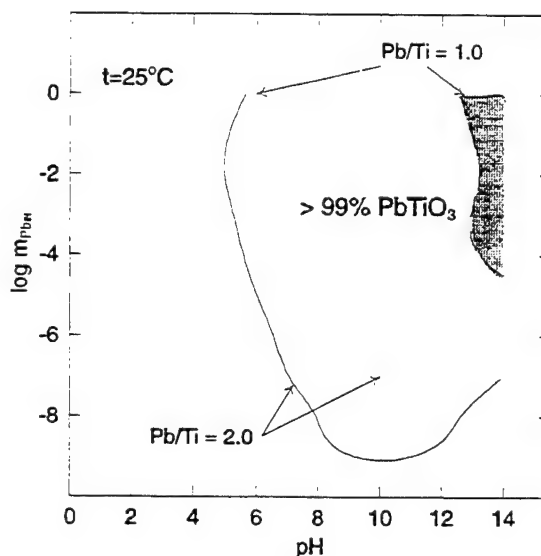


Fig. 2. Calculated yield of $PbTiO_3$ in the Pb-Ti- H_2O -complexing agent system for various Pb/Ti ratios.

Contamination of the hydrothermal reaction product is always a concern in that it can upset the A/B ratio in the perovskite phase. Both hydroxide and carbonate formation can occur during the synthesis of barium titanate [2] and strontium zirconate [4]. While these impurities can be eliminated with washing, the leaching of A-site ions from the perovskite lattice is also an important concern [11]. In the synthesis of strontium zirconate, carbonate formation due to precursors and/or atmospheric sources were compared via simulation and experimental approaches. Table 1 reveals that there is excellent agreement between simulated and experimental data. Most important, computations show that contamination of the zirconium,

strontium or potassium cation precursors with carbon dioxide is the most significant source of carbonate contamination while other sources such as atmospheric carbon dioxide are not significant contributors.

TABLE I
CALCULATED AND EXPERIMENTAL AMOUNTS OF CARBON DIOXIDE IN
STRONTIUM ZIRCONATE

| Precursors: *-CO ₂ -containing | CO ₂ wt% calc. | CO ₂ wt% TGA | CO ₂ wt% Anal. |
|---|---------------------------------|-------------------------------|---------------------------------|
| Sr(NO ₃) ₂ +ZrO ₂ *+0.8m KOH* | 1.0 | 1.1 | 1.0 |
| Sr(NO ₃) ₂ +ZrO ₂ *+3.5m KOH* | 1.9 | 1.7 | 2.0 |
| Sr(NO ₃) ₂ +ZrO ₂ *+3.3m KOH* | 1.0 | 0.8 | 0.6 |
| Sr(OH) ₂ *+ZrO ₂ * | 2.1 | 2.2 | 2.1 |
| Sr(OH) ₂ +ZrO ₂ * | 0.7 | 0.8 | 0.7 |

III. KINETICS

There are numerous methods for making single crystals, thin films and powders. Practically all of this technology was developed with empirical investigation methods. Our fundamental understanding of hydrothermal crystallization kinetics is at an early stage. For instance, in the preparation of perovskite powders, our work [12] as well as others [13,14] has revealed that the crystallization of hydrothermal powders is not well described by classical nucleation and growth theory. In order to apply our understanding to engineering practice, predictive models must be developed. Ultimately, we would like to engineer a process to a level where powders can be grown to a specific size distribution. This goal may be more feasible as our ability to model crystallization processes advances.

In order to advance our knowledge in the absence of predictive models, we must empirically define the fundamental role of temperature, pressure, precursor, and time on crystallization kinetics of perovskite oxides. Early work by Battelle Laboratories [15] set the stage for development of hydrothermal processes that provide excellent morphological control for a variety of ceramic chemistries. A great deal of patent activity followed in both Japan and the U.S. Recent efforts in universities throughout the world are also focusing on this issue. More specifically, in our case, we are focusing on the morphological control of lead zirconate titanate and lead titanate precipitated from organic mineralizer solutions [16]. Morphologies obtained for these perovskites are very similar to what can be achieved with alkaline metal hydroxides (cf. Fig. 3). Collectively, industrial and academic sources will provide us with a rich data base for model building.

Crystallization is only one of the areas where our fundamental understanding of hydrothermal kinetics is lacking. For example, we have little knowledge of the reactive intermediates that form in solution. Insight into this

would enable us to understand how to control the formation of solution species, solid phases

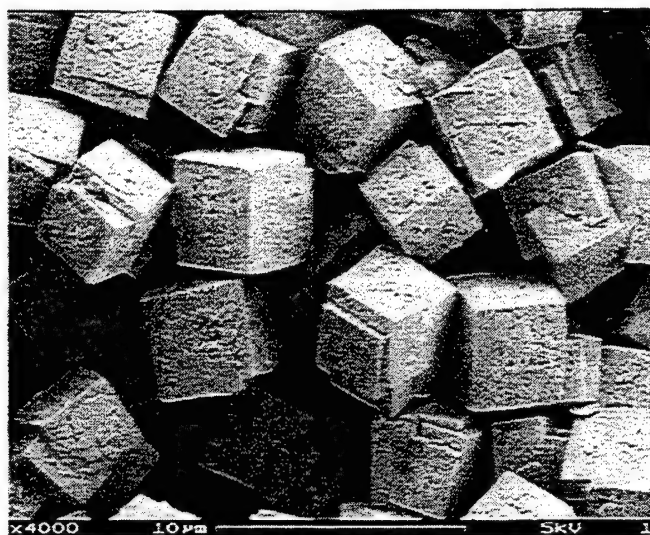


Fig. 3. The morphology of Sr-doped PZT obtained hydrothermally at 150°C.

and the rate of their formation. For instance, in our work with barium titanate, we have noted that higher pH leads to a tetragonal lattice with increasing c/a ratios and progressively less lattice water (cf. Fig. 4). We have speculated that a reaction mechanism involving a competition between octahedral and tetrahedral titanium solution species could explain this dependence [17].

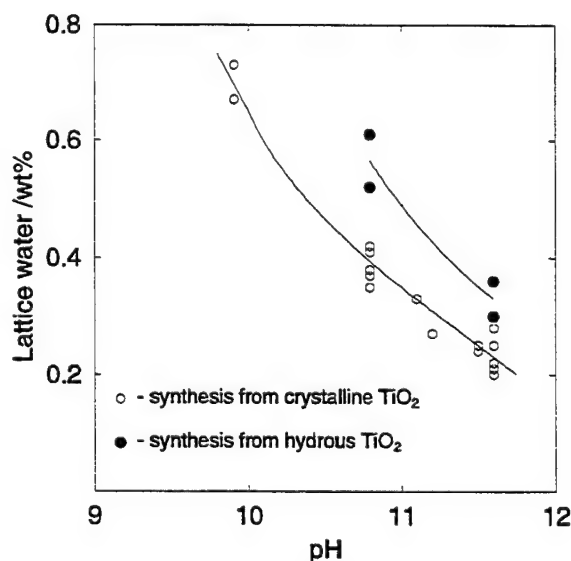


Fig. 4. Lattice water content in BaTiO₃ powders as a function of solution pH.

It would be useful to test the plausibility of this mechanism well as others. If we could conclusively determine the reactive intermediates that rate-control hydrothermal reactions, we could then develop strategies for accelerating reaction rate and inducing phase selectivity. Until we get to this point, we will need to empirically identify process variables that perform this function. For instance, in our research on lead titanate synthesis, lead precursor choice and increased Pb/Ti ratios reduces the synthesis temperature from 140 to 90°C [8]. In addition, the processing employed for the precursors is extremely important [18]. In the synthesis of lead zirconate titanate, dispersion of a zirconium-titanium hydrous oxide in a lead acetate solution yields nearly-pure lead zirconate titanate in 3 h at 200°C. On the other hand, if the zirconium-titanium hydrous oxide is precipitated in a solution of lead acetate, full conversion to PZT is accomplished in 0.5 h.

IV. CONCLUSIONS

Our thermodynamic model of hydrothermal processes for the preparation of perovskite oxides is a valid tool for engineering reactions that yield a phase-pure product. On the other hand, the principles for engineering facile hydrothermal processes that yield products with controlled size and morphology are not mature. To achieve this goal, much experimental and theoretical work will be required. With renewed interest in hydrothermal technology, the future looks bright for developing the appropriate fundamental principles.

ACKNOWLEDGEMENTS

The authors wish to acknowledge the generous support of the Office of Naval Research under the auspices of the Young Investigator Programs (N00014-91-J-4074, N00014-95-1-4072), and the Small Business Technology Transfer program (N000014-95-C-0260).

REFERENCES

- [1] M. Rafal, J.W. Berthold, N.C. Scrivner, S.L. Grise, "Models for electrolyte solutions," in *Models for Thermodynamics and Phase Equilibria Calculations*. S.I. Sandler, Ed. Marcel Dekker, Inc., New York, 1994, pp. 601-670.
- [2] M.M. Lencka and R.E. Riman, "Thermodynamic modeling of hydrothermal synthesis of ceramic powders," *Chem. Mater.*, vol. 5, pp. 61-70, January 1993.
- [3] M.M. Lencka and R.E. Riman, "Synthesis of lead titanate: thermodynamic modeling and experimental verification," *J. Am. Ceram. Soc.*, vol. 76, pp. 2649-2659, October 1993.
- [4] M.M. Lencka, E. Nielsen, A. Anderko and R.E. Riman, "Hydrothermal synthesis of carbonate-free strontium zirconate: thermodynamic modeling and experimental verification," *Chem. Mater.*, vol. 9, pp. 1116-1125, May 1997.
- [5] M.M. Lencka and R.E. Riman, "Thermodynamics of the hydrothermal synthesis of calcium titanate with reference to others alkaline-earth titanates," *Chem. Mater.*, vol. 7, pp. 18-25, January 1995.
- [6] M.M. Lencka, L. Renomeron and R.E. Riman, "Hydrothermal synthesis of barium zirconate," unpublished.
- [7] M.M. Lencka, A. Anderko and R.E. Riman, "Hydrothermal precipitation of Lead zirconate titanate solid solutions: thermodynamic modeling and experimental verification," *J. Am. Ceram. Soc.*, vol. 78, pp. 2609-2618, October 1995.
- [8] B. Gersten, M.M. Lencka, and R.E. Riman, "Hydrothermal synthesis of lead titanate powders using chelate ligands as a kinetic enhancing agent," in ISAF 96, vol. 2. B.M. Kulwicki, A. Amin and A. Safari, Eds. IEEE, Piscataway, NJ, 1996, pp. 723-726.
- [9] K.C. Beal, "Precipitation of Lead zirconate titanate solid solutions under hydrothermal conditions," in *Advances in Ceramics*, vol. 21: *Ceramic Powder Science*. ACS, Westerville, OH, 1987, pp. 33-41.
- [10] I. Petrovic, M.M. Lencka, A. Anderko and R.E. Riman, "Hydrothermal synthesis of lead zirconate titanate ($\text{PbZr}_{0.52}\text{Ti}_{0.48}\text{O}_3$) using organic mineralizers," in ISAF 96, vol. 2. B.M. Kulwicki, A. Amin and A. Safari, Eds. IEEE, Piscataway, NJ, 1996, pp. 735-738.
- [11] C. C. Hung, "Hydrothermal BaTiO_3 Synthesis: The Effect of Aqueous Rinsing on Surface Chemistry," M.Sc. Thesis, Rutgers University, New Brunswick, NJ, October 1990.
- [12] J.O. Eckert, C.C. Hung-Houston, B.L. Gersten, M.M. Lencka and R.E. Riman, "Kinetics and Mechanisms of hydrothermal synthesis of barium titanate," *J. Am. Ceram. Soc.*, vol. 79, pp. 2929-2939, November 1996.
- [13] G.A. Rossetti, Jr., D.J. Watson, R.E. Newnham and J.H. Adair, "Kinetics of the hydrothermal crystallization of the perovskite lead titanate," *J. Cryst. Growth*, vol. 116, pp. 251-259, 1992.
- [14] D.J. Watson, C.A. Randall, R.E. Newnham and J.H. Adair, "Hydrothermal formation diagram in the lead titanate system," in *Ceramic Transation*, vol. 1: *Ceramic Powder Science II*, ACS, Westerville, OH, 1988, pp. 154-161.
- [15] E.P. Staumbagh and J.F. Miller, Proc. of the First Int. Symp. on Hydrothermal Reactions. S. Somiya, Ed. Gakujutsu Bunken Fukyu-Kai, Tokyo, Japan, 1982, pp. 858-871.
- [16] S-B. Cho, Rutgers University, unpublished.
- [17] M.M. Lencka, B.-K. Park and R.E. Riman, "Hydrothermal synthesis of tetragonal barium titanate," in preparation.
- [18] L.E. McCandlish, unpublished.

Dielectric and Piezoelectric Properties of Ceramics in the Lead Indium Niobate - Lead Titanate Solid Solution.

Edward F. Alberta and Amar S. Bhalla

Materials Research Laboratory, The Pennsylvania State University, University Park, PA 16802, USA

ABSTRACT

Piezoelectric and electrical properties of ceramics in the $(x) \text{Pb}(\text{InNb})_{1/2}\text{O}_3 : (1-x) \text{PbTiO}_3$ [PIN:PT (x)] system are described. A high dielectric constant and remanent polarization were obtained for compositions near the morphotropic phase boundary. In this system, the morphotropic phase boundary is found to be located at the composition $x = 62$ mol % PIN. For this composition, the dielectric constant is 2600 at room temperature and increases to 22400 at its transition temperature of 280 °C. The remanent polarization is approximately 35 $\mu\text{C}/\text{cm}^2$ and corresponds to a coercive field of 16 kV/cm. Finally, poled ceramics of the morphotropic phase boundary composition possess a d_{33} value of 395 pC/N, a d_{31} of -175 pC/N and a k_{31} of 30 %.

INTRODUCTION

Lead titanate based solid solutions, such as lead zirconate titanate [PZT], have been the focus of extensive research for many years. Recently, studies have shown both the $\text{Pb}(\text{ScTa})_{1/2}\text{O}_3 : \text{PbTiO}_3$ [PST:PT] and the $\text{Pb}(\text{ScNb})_{1/2}\text{O}_3 : \text{PbTiO}_3$ [PSN:PT] systems to be highly promising piezoelectric materials.^{1,2,3,4} Similar behavior has also been found in the indium based systems $\text{Pb}(\text{InTa})_{1/2}\text{O}_3 : \text{PbTiO}_3$ [PIT:PT] and $\text{Pb}(\text{InNb})_{1/2}\text{O}_3 : \text{PbTiO}_3$ [PIN:PT]⁵. In this paper, the piezoelectric and dielectric properties of the morphotropic phase boundary composition, PIN:PT (62:38), are reported.

EXPERIMENTAL PROCEDURES

(a) Sample Preparation.

Ceramic samples of various PIN:PT compositions near the morphotropic phase boundary were prepared. The compositions were batched and calcined as described

elsewhere⁷. After adding a binder, the calcined powder was pressed into disks and sintered in closed Al_2O_3 crucibles for 3 hours at 1250 °C. The atmosphere within the crucible was maintained using In_2O_3 and PbO source powders. The sintered samples were then polished and sputtered-platinum electrodes were applied.

(b) Dielectric Measurements.

The temperature dependence of the dielectric constant was measured using a computer controlled measurement system consisting of a multifrequency LCR meter (HP4274A, Hewlett Packard Co.), a desktop computer (HP9816) and a nitrogen-fed furnace (Delta Design Inc.).

Dielectric hysteresis measurements were made using a modified Sawyer-Tower circuit. Simultaneous strain measurements were made using an LVDT and lock-in amplifier (SR860, Stanford Research Inc.).

(c) Piezoelectric Measurements.

In preparation for the piezoelectric measurements, the samples were immersed in a silicone oil to prevent electrical breakdown and poled at 40 kV/cm for 10 min. The piezoelectric resonance measurements were made using a HP 4194A impedance analyzer.

RESULTS

The temperature dependence of the dielectric constant was determined for several compositions across the PIN:PT solid solution. Figure 1 illustrates the loss of the characteristic relaxor ferroelectric behavior of PIN with increasing lead titanate concentration as well as the increase in the transition temperature. The morphotropic phase boundary composition ($x = 62$ mol % PIN) is also clearly shown. From figure 2 the frequency dependence of the dielectric constant for this composition can be observed. The room temperature dielectric constant,

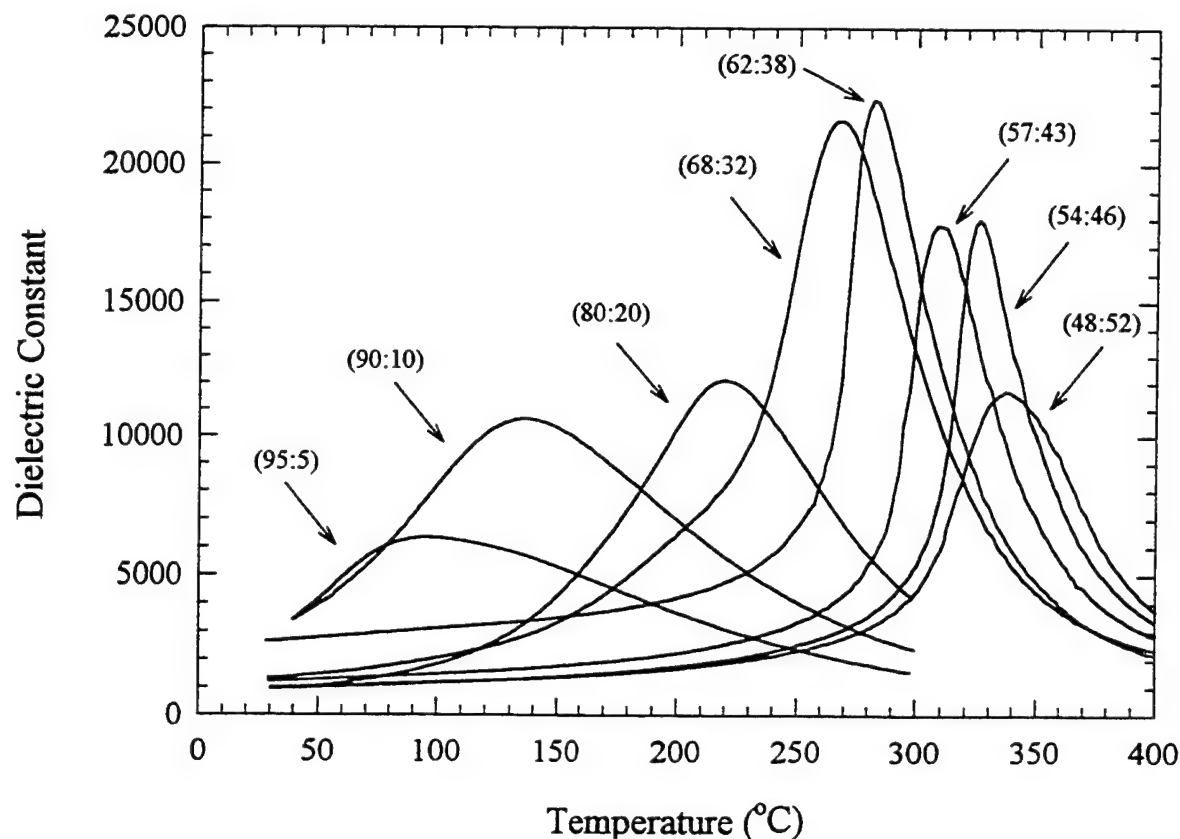


Figure 1. Temperature dependence of the dielectric constant for various compositions in the PIN:PT (x:1-x) system.

measured at 1 kHz, for this composition was found to be 2600. The transition temperature was found to be 280 °C and corresponded to a maximum dielectric constant of 22400. Figure 3 shows the P-E hysteresis loop for PIN:PT(62:38). The remanent polarization, P_r , was 34.5 $\mu\text{C}/\text{cm}^2$ and the coercive field was found to be 16 kV/cm. The maximum strain, measured with an applied field of 46 kV/cm, was determined to be 0.37 %. A summary of the hysteresis data for samples near the phase boundary is shown in figure 5. The addition of lead titanate increases the remanent polarization from nearly zero for pure PIN to a maximum value of 34.5 $\mu\text{C}/\text{cm}^2$ at the morphotropic phase boundary⁷. In addition, the coercive field also increases with increasing lead titanate concentration.

Ceramics in the PIN:PT system were found to be easily poled with a field of 40 kV/cm applied at room temperature. After poling, the piezoelectric coefficient, d_{33} , was measured using a Berlincourt d_{33} -meter. The optimum poling time was determined to be approximately 10 minutes. The piezoelectric coefficient was found to reach a maximum value of 395 pC/N in the composition (62:38). The piezoelectric coupling coefficient, k_{33} ,

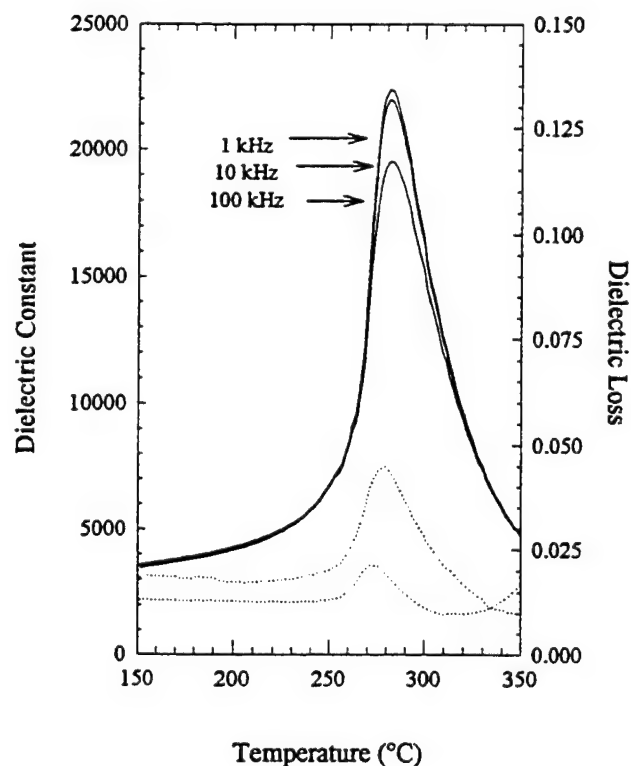


Figure 2. Variation of the dielectric constant and loss for PIN:PT(62:38) ceramics.

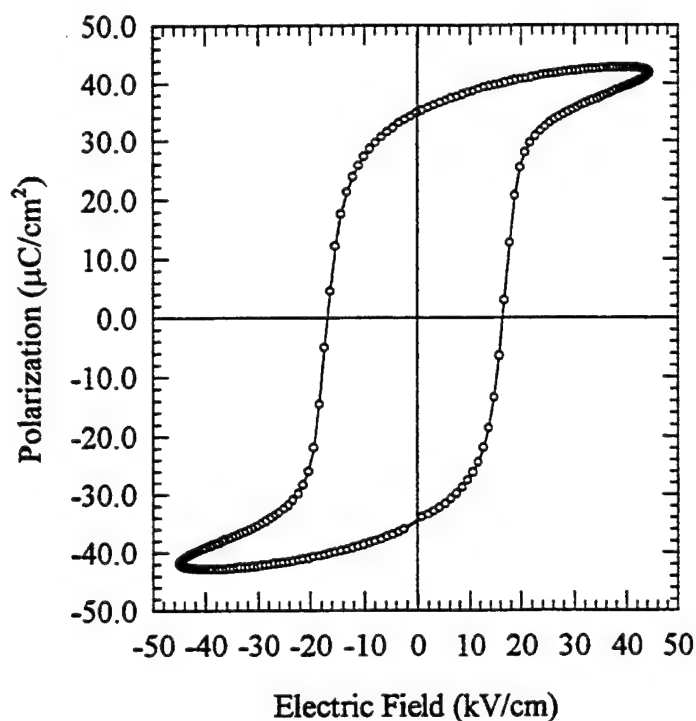


Figure 3. Dielectric hysteresis loop for PIN:PT (62:38).

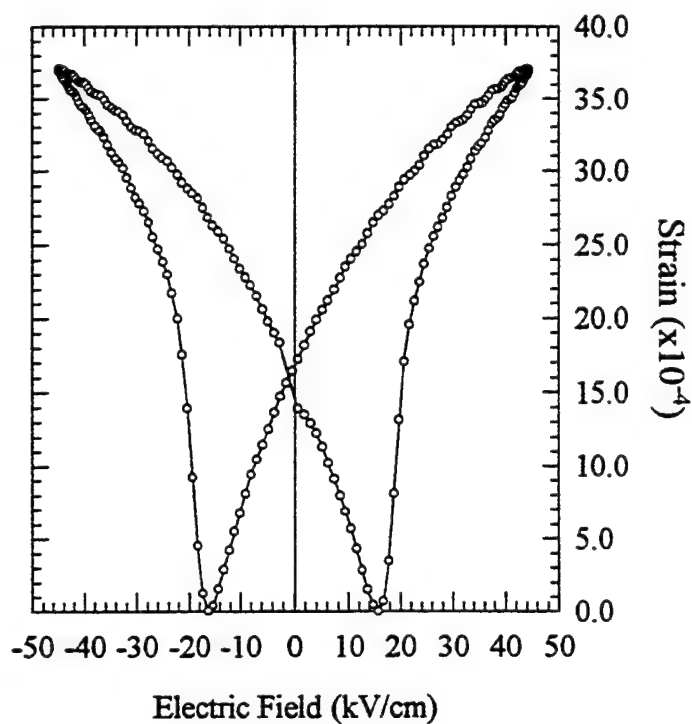


Figure 4. Strain behavior for PIN:PT (62:38).

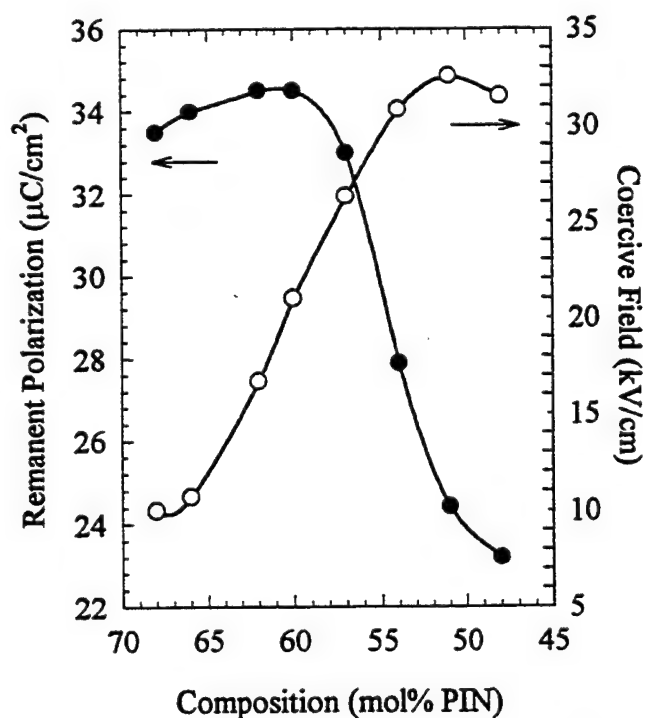


Figure 5. Compositional dependence of the remanent polarization and coercive field for PIN:PT ceramics.

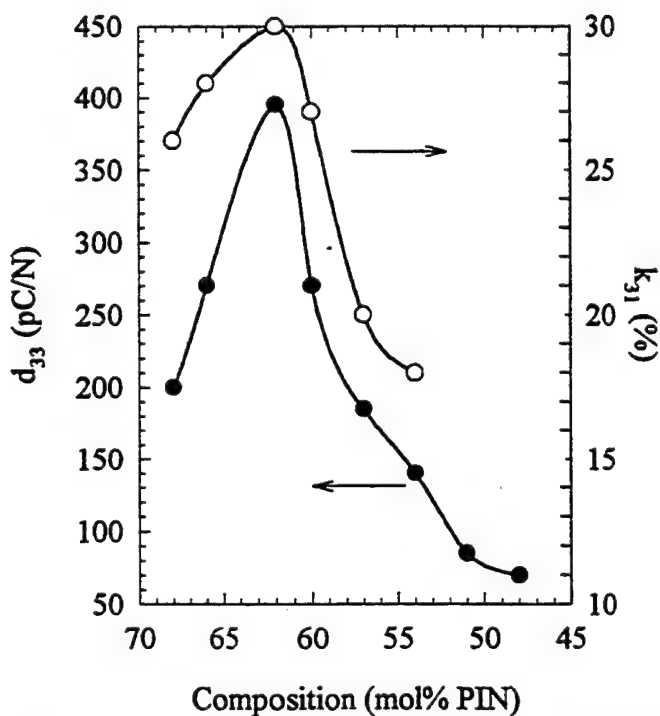


Figure 6. Compositional dependence of the piezoelectric coefficient d_{33} and piezoelectric coupling coefficient, k_{31} , for PIN:PT ceramics.

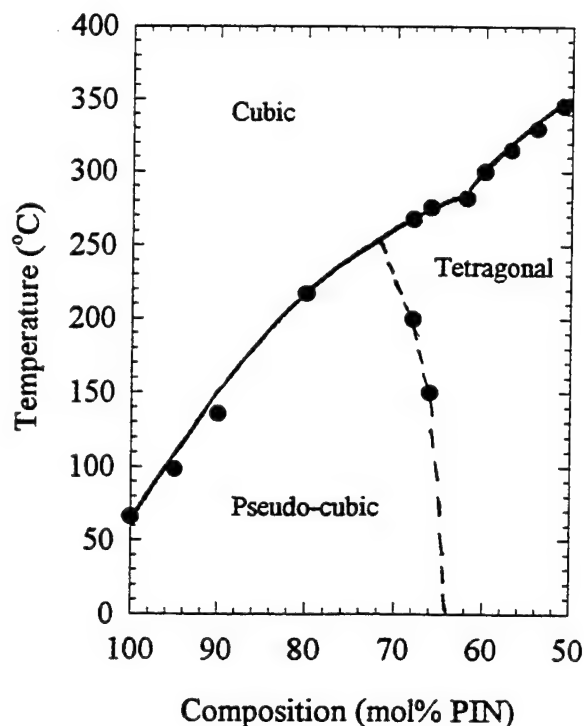


Figure 7. PIN:PT phase diagram.

followed a similar trend, reaching a maximum of 30 % at the morphotropic phase boundary.

SUMMARY

Piezoelectric and electrical properties of ceramics in the PIN:PT solid solution have been investigated. A high dielectric constant and remanent polarization were obtained for compositions near the morphotropic phase boundary, which is located at a composition with $x = 62$ mol % PIN. The dielectric constant for this composition is 2600 at room temperature and increases to 22400 at its transition temperature of 280 °C. The remanent polarization is approximately 35 $\mu\text{C}/\text{cm}^2$ and corresponds to a coercive field of 16 kV/cm. Finally, piezoelectric properties of ceramics poled with a field of 40 kV/cm for 10 minutes at room temperature were measured. The poled ceramics were found to have a d_{33} value of 395 pC/N, a d_{31} of -175 pC/N and a k_{31} of 30 %.

References:

- [1] Giniewicz, J.R., "An Investigation of the Lead Scandium Tantalate-Lead Titanate Solid Solution System," *Ph.D. Thesis, The Pennsylvania State University*, University Park, PA (1991).
- [2] Wang, J.F., J.R. Giniewicz, and A.S. Bhalla, "Soft Piezoelectric $(1-x)\text{Pb}(\text{Sc}_{1/2}\text{Ta}_{1/2})\text{O}_3 - (x)\text{PbTiO}_3$ Ceramics with High Coupling Factors and Low Q_m ," *Ferroelectrics Letters*, **16**, 113 (1993).
- [3] Tennery, V.J., K.W. Hang, and R.E. Novak, "Ferroelectric and Structural Properties of the $\text{Pb}(\text{Sc}_{1/2}\text{Nb}_{1/2})_{1-x}\text{Ti}_x\text{O}_3$ System," *J. Am. Ceram. Soc.*, **51** 671 (1968).
- [4] Alberta, E.F. and A.S. Bhalla, "Dielectric and Piezoelectric Properties of Niobium-Doped PSN:PT Ceramics," Submitted for publication 1997.
- [5] Kodama, U., M. Osada, O. Kumon, and T. Nishimoto, "Piezoelectric Properties and Phase Transition of $\text{PbIn}_{1/2}\text{Nb}_{1/2}\text{O}_3 - \text{PbTiO}_3$ Solid Solution Ceramics," *Ceramic Bulletin*, **48** [12] 1123 (1969).
- [6] Alberta, E.F. and A.S. Bhalla, "Piezoelectric Properties of The Lead Indium Tantalate - Lead Titanate Ceramics," Submitted for publication 1997.
- [7] Alberta, E.F. and A.S. Bhalla, "Preparation of phase-pure perovskite lead indium niobate ceramics," *Materials Letters* **29** 127 (1996).

Hiromu Ohuchi, Tarou Sanada, Masaharu Ueda and
Tsuneo Hashimoto
Department of Material Science and Ceramic Technology,
Shonan Institute of Technology
Tsuji-dou-nishikaigan Fujisawa Kanagawa, 251 Japan

Abstract--Solid solution ceramics of the system $x\text{Pb}(\text{Yb}_{1/2}\text{Nb}_{1/2})\text{O}_3\text{-yPbTiO}_3\text{-zPbZrO}_3$, where $x=0.1\text{-}0.7$, $y=0.2\text{-}0.7$, $z=0.1\text{-}0.7$, and $x+y+z=1$, were prepared by the solid state reaction of powder materials. Ceramic, dielectric and piezoelectric properties and crystal structures of the system were studied. The system is composed of three crystal phases at room temperature: the monoclinic, tetragonal and rhombohedral. Sintering of the system $x\text{Pb}(\text{Yb}_{1/2}\text{Nb}_{1/2})\text{O}_3\text{-yPbTiO}_3\text{-zPbZrO}_3$ is much easier than that of each end compositions and a well sintered high density ceramics was obtained for the compositions near the morphotropic transformation. Piezoelectric ceramics with high relative dielectric constants and high radial coupling coefficient, k_r , and low mechanical quality factor were obtained for the composition near the morphotropic transformation. The composition $\text{Pb}(\text{Yb}_{1/2}\text{Nb}_{1/2})_{0.1}\text{Ti}_{0.5}\text{Zr}_{0.4}\text{O}_3$ showed the highest k_r of 0.46.

I. INTRODUCTION

It is known that piezoelectric ceramics are generally ferroelectric materials with perovskite-type structure. To make a piezoelectric ceramics, it is necessary that the crystal unit cells of the material have no center of symmetry. Furthermore, it should also be possible to orient the spontaneous polarization in the crystallographic directions by an externally applied field.

B. Jaffe, R. S. Roth and S. Marzullo succeeded in obtaining lead zirconate titanate ceramics from the solid solution of PbTiO_3 (ferroelectric, tetragonal) and PbZrO_3 (antiferroelectric, orthorhombic) [1]. After discovery of piezoelectric properties in the binary system lead zirconate titanate, studies on piezoelectric ceramics were expanded to develop more solid solution ceramics composed of multicomponent system such as the ternary rather than those of the binary [2].

G. A. Smolenskii and A. I. Agranovskaya showed a possible method of preparing complex compounds with perovskite structure [3], much attention has focused on the piezoelectric properties of ternary system consisting of complex compounds for example $\text{Pb}(\text{Mg}_{1/3}\text{Nb}_{2/3})\text{TiZrO}_3$ [4] and $\text{Pb}(\text{Mg}_{1/3}\text{Ta}_{2/3})\text{TiZrO}_3$ [5].

T. Yamamoto and S. Ohashi developed solid solution ceramics of the binary system $\text{PbTiO}_3\text{-Pb}(\text{Yb}_{1/2}\text{Nb}_{1/2})\text{O}_3$ (antiferroelectric, monoclinic) [6]. However, there is no information on the electric properties in the ternary system $\text{Pb}(\text{Yb}_{1/2}\text{Nb}_{1/2})\text{O}_3\text{-PbTiO}_3\text{-PbZrO}_3$.

The main purpose of the present work is to describe the ceramic and electric properties of the $\text{Pb}(\text{Yb}_{1/2}\text{Nb}_{1/2})\text{O}_3\text{-PbTiO}_3\text{-PbZrO}_3$ system. Another purpose of this work is to show a morphotropic transformation in the ternary system, a phenomenon expected from the difference in the crystal structures of each end compound at room temperature.

II. EXPERIMENTAL PROCEDURE

1) Sample preparation

The ceramic samples of the system $x\text{Pb}(\text{Yb}_{1/2}\text{Nb}_{1/2})\text{O}_3\text{-yPbTiO}_3\text{-zPbZrO}_3$, where $x=0.1\text{-}0.7$, $y=0.2\text{-}0.7$, $z=0.1\text{-}0.7$ and $x+y+z=1$, were prepared from chemical reagent grade PbO (99.99%), Yb_2O_3 (99.9%), Nb_2O_5 (99.9%), TiO_2 (98.65%), and ZrO_2 (99.9%) by solid state reaction of powder materials. Weighed raw material (1 batch = 35g) of a given composition was wet-milled in a plastic mill with partially stabilized zirconia balls (about 5mm in diameter; total weight 100g) and water (50ml) for 17h, dried and pressed into tablets at 40MPa. The tablets were calcined at 850°C (a uniform heating rate of 5°C/min) for 2h in a covered alumina crucible, cooled wet-ground for 17h in the plastic mill and then dried. The ground material was thoroughly mixed with polyvinyl alcohol (5wt%) in a mortar and was pressed into disks 10mm in diameter by about 2mm in thickness at a pressure of 100MPa. Five stacked disks were fired at 1000-1150°C (heating rate of 5°C/min) in an electric furnace on a platinum sheet covered with a magnesia crucible to minimize evaporation of PbO . The fired disks were ground to a thickness of about 0.5 mm, and silver paste was fired on the disk surfaces at 700°C as electrodes. Poling was carried out in silicone oil at 100°C by applying a DC field of 4kV/mm for 1h, and samples were field cooled to room temperature in 30 min.

2) Measurement

2.1 Density and water absorption

The density of fired samples was computed from the sample weight in air, in water, with absorbed water in air, and from the density of the water used (Archimedes method).

2.2 Linear shrinkage

The linear shrinkage was obtained by comparing the diameter of the disk-shaped samples before and after heat treatment.

2.3 X-ray analyses

X-ray powder diffraction examinations were made with

a recording diffractometer (Rigaku Denki, RAD-RC) using Cu K α radiation through a nickel filter at room temperature. From these diffraction patterns, the morphotropic boundary of the crystal phase was determined.

2.4 Electrical resistance measurements

The resistance was measured with an HP4329A high-resistance meter. The electrical resistivity was calculated from the resistance, thickness and diameter of samples.

2.5 Dielectric measurements

Capacitance and dissipation factor, $\tan \delta$, were measured at room temperature with an HP4192A impedance analyzer using a frequency of 1kHz. The dielectric constant was calculated from the capacitance, diameter and thickness of samples.

2.6 Piezoelectric measurements

Twenty-four hours after poling, the piezoelectric property was measured with an HP4192A impedance analyzer by a method similar to that of the Institute of Radio Engineers Standards [7].

The resonant frequency f_r , antiresonant frequency f_a and resonant resistance R of the radial fundamental mode were measured at room temperature. Mechanical quality factor Q_M was calculated from f_r , f_a , R and capacitance (at 1kHz).

III RESULTS AND DISCUSSION

III-1 Sintered density

It was difficult to obtain a well sintered body from each end composition of the ternary system, because PbTiO_3 has a large anisotropic crystallographic transformation at the Curie temperature of 490°C. PbZrO_3 shows intense evaporation of PbO , and $\text{Pb}(\text{Yb}_{1/2}\text{Nb}_{1/2})\text{O}_3$ exhibits low sinterability. For example, $\text{Pb}(\text{Yb}_{1/2}\text{Nb}_{1/2})\text{O}_3$ ceramics fired at 1000°C for 45min show density of 8.45g/cm³, shrinkage of 8.7% and water absorption of 2.3%. As the $\text{Pb}(\text{Yb}_{1/2}\text{Nb}_{1/2})\text{O}_3$ - PbTiO_3 - PbZrO_3 compositions are free of these difficulties, however, their water absorption is less than 0.95% and the near morphotropic phase boundary composition becomes nearly zero % at optimum firing temperature from 1000 to 1100 °C which is lower than that of PbTiO_3 - PbZrO_3 binary compositions of 1220°C. Therefore, sintering of the ternary composition becomes easier.

Fig. 1 shows the effect of compositional dependence on the sintered density for $\text{Pb}(\text{Yb}_{1/2}\text{Nb}_{1/2})\text{O}_3$ - PbTiO_3 - PbZrO_3 solid solution ceramics. Shrinkage(s), sintered density(d) and water absorption(w) for $\text{Pb}(\text{Yb}_{1/2}\text{Nb}_{1/2})\text{O}_3$ - PbTiO_3 - PbZrO_3 ceramics were obtained as $s=13.4$ - 2.7% , $d=8.52$ - 7.40g/cm^3 and $w=0.00$ - 0.95% , respectively. Thus, well sintered and highdensity ceramics were obtained for compositions near the morphotropic phase boundary.

Grain structure of $\text{Pb}(\text{Yb}_{1/2}\text{Nb}_{1/2})_{0.1}\text{Ti}_{0.5}\text{Zr}_{0.4}\text{O}_3$ ceramics with the near morphotropic phaseboundary composition is fine and grain growth is inhibited and grain size of 2-3 μm was obtained as shown in Fig. 2.

III-2 Phase relations

Fig. 3(a) shows the relation between the composition studied in the ternary system $x\text{Pb}(\text{Yb}_{1/2}\text{Nb}_{1/2})\text{O}_3$ - $y\text{PbTiO}_3$ - $z\text{PbZrO}_3$ and the crystal phase at roomtemperature. The solid solution of ternary system $\text{Pb}(\text{Yb}_{1/2}\text{Nb}_{1/2})\text{O}_3$ - PbTiO_3 - PbZrO_3 is composed of monoclinic, tetragonal and rhombohedral crystal phases. A morphotropic transformation between a tetragonal phase (PbTiO_3) and a monoclinic phase ($\text{Pb}(\text{Yb}_{1/2}\text{Nb}_{1/2})\text{O}_3$) occurred at $y=0.5$ to 0.475 mole fraction of PbTiO_3 [6] and another transformation between a tetragonal and a rhombohedral phase (PbZrO_3) occurred at $y=0.45$ to 0.475 mole fraction of PbTiO_3 [2]. In the ternary system, a morphotropic transformation from a tetragonal phase to a rhombohedral or a monoclinic phase is found in the vicinity of $y=0.5$ mole fraction of PbTiO_3 for $x=0.1$, 0.2, 0.3 and 0.4 mole fraction of $\text{Pb}(\text{Yb}_{1/2}\text{Nb}_{1/2})\text{O}_3$. The tetragonal phase area is bounded by a convex curve to PbTiO_3 .

Fig. 3(b) shows the relation of crystal phase versus 2θ at the near morphotropic phase boundary by X-ray analysis; in particular, when 2θ is within the range of 40 to 60 degree, a morphotropic transformation is found from change of (002) and (200) peak. A morphotropic transformation between the rhombohedral and the monoclinic phase is still uncertain but may be drawn as shown in Fig. 3(a) within the accuracy of the present experiment.

III-3 Electric properties

The electrical resistivity for the ternary system $x\text{Pb}(\text{Yb}_{1/2}\text{Nb}_{1/2})\text{O}_3$ - $y\text{PbTiO}_3$ - $z\text{PbZrO}_3$ ceramics change with composition from 6.25×10^8 to 0.66×10^8 ($\Omega \cdot \text{m}$) and for most ceramics show electrical resistivity higher than 1×10^8 ($\Omega \cdot \text{m}$) and there was no break down during the poling treatment.

Fig. 4 shows the relative dielectric constants ($\epsilon_{33}^T/\epsilon_0$) after poling for the ternary system $x\text{Pb}(\text{Yb}_{1/2}\text{Nb}_{1/2})\text{O}_3$ - $y\text{PbTiO}_3$ - $z\text{PbZrO}_3$ with $x\text{Pb}(\text{Yb}_{1/2}\text{Nb}_{1/2})\text{O}_3$ as a parameter. The relative dielectric constants and dissipation factor for the ternary system change with the addition of $\text{Pb}(\text{Yb}_{1/2}\text{Nb}_{1/2})\text{O}_3$ from 190 to 1150 and from 0.015 to 0.112, respectively. In each series of Fig. 4, the composition with maximum relative dielectric constant also coincides with the morphotropic transformation. This result is in agreement with the behavior described in the ternary system $\text{Pb}(\text{Mg}_{1/3}\text{Nb}_{2/3})\text{O}_3$ - PbTiO_3 - PbZrO_3 [4]. The relative dielectric constant of $x\text{Pb}(\text{Yb}_{1/2}\text{Nb}_{1/2})\text{O}_3$ - $y\text{PbTiO}_3$ - $z\text{PbZrO}_3$ at the morphotropic transformation increases with increasing $\text{Pb}(\text{Yb}_{1/2}\text{Nb}_{1/2})\text{O}_3$ content up to $x=0.2$ and decreases with increasing $\text{Pb}(\text{Yb}_{1/2}\text{Nb}_{1/2})\text{O}_3$ content up to $x=0.4$.

Fig. 5 shows the radial coupling coefficient for the ternary system $x\text{Pb}(\text{Yb}_{1/2}\text{Nb}_{1/2})\text{O}_3$ - $y\text{PbTiO}_3$ - $z\text{PbZrO}_3$ with $x\text{Pb}(\text{Yb}_{1/2}\text{Nb}_{1/2})\text{O}_3$ as a parameter. The radial coupling coefficient change with composition from 0.13 to 0.46 for the composition $x \leq 0.6$. A high radial coupling coefficient over 0.35 was obtained in the region of $x=0.1$ to 0.3 and $z=0.2$ to 0.5 (mole fraction). The highest radial coupling coefficients of each series in Fig. 5 are for the compositions (mole fractions) $z=0.4$

for $x=0.1$, $z=0.3$ for $x=0.2$, $z=0.2$ for $x=0.3$, and $z=0.1$ for $x=0.4$. The foregoing compositions are in good agreement with those exhibiting maxima in dielectric constants. The high radial coupling coefficient thus was obtained near the morphotropic transformation for each compositional series up to $x=0.4$.

The mechanical quality factor (Q_M) and frequency constant (N_p) for the ternary system $x\text{Pb}(\text{Yb}_{1/2}\text{Nb}_{1/2})\text{O}_3$ - $y\text{PbTiO}_3$ - $z\text{PbZrO}_3$ change with the composition from 24 to 317 and from 1654 to 2774 [$\text{Hz} \cdot \text{m}$], respectively. Q_M and N_p values are low for the composition at which the high radial coupling coefficient and high relative dielectric constant were obtained as shown in Figs. 6 and 7, respectively.

The composition $\text{Pb}(\text{Yb}_{1/2}\text{Nb}_{1/2})_{0.1}\text{Ti}_{0.5}\text{Zr}_{0.4}\text{O}_3$ showed the high relative dielectric constant, $\epsilon_{33}^T/\epsilon_0 = 1010$, high radial coupling coefficient, $kr = 0.46$, low $Q_M = 45$, $N_p = 1909$ [$\text{Hz} \cdot \text{m}$] and Curie point $T_c = 244^\circ\text{C}$.

IV CONCLUSION

The present study led to the following conclusions:

(1) Sintering of the ternary system $x\text{Pb}(\text{Yb}_{1/2}\text{Nb}_{1/2})\text{O}_3$ - $y\text{PbTiO}_3$ - $z\text{PbZrO}_3$, where $x=0.1$ - 0.7 , $y=0.2$ - 0.7 , $z=0.1$ - 0.7 and $x+y+z=1$, is much easier than sintering each end composition, and well sintered, high density ceramics were easily obtained for compositions near the morphotropic transformations.

(2) Phase relation of the ternary system $x\text{Pb}(\text{Yb}_{1/2}\text{Nb}_{1/2})\text{O}_3$ - $y\text{PbTiO}_3$ - $z\text{PbZrO}_3$ is composed of monoclinic, tetragonal and rhombohedral crystal phases. A morphotropic transformation from a tetragonal phase to a rhombohedral or a monoclinic phase is found in the vicinity of $y = 0.5$ mole fraction of PbTiO_3 for $x=0.1$, 0.2 , 0.3 and 0.4 mole fraction of $\text{Pb}(\text{Yb}_{1/2}\text{Nb}_{1/2})\text{O}_3$.

(3) Piezoelectric ceramics with new ternary composition, high relative dielectric constant, high radial coupling coefficient, low mechanical quality factor and low frequency constant were obtained at compositions near the morphotropic transformation.

The composition $\text{Pb}(\text{Yb}_{1/2}\text{Nb}_{1/2})_{0.1}\text{Ti}_{0.5}\text{Zr}_{0.4}\text{O}_3$ showed the high $\epsilon_{33}^T/\epsilon_0 = 1010$, high $kr = 0.46$, low $Q_M = 45$, low $N_p = 1909$ [$\text{Hz} \cdot \text{m}$] and Curie point $T_c = 244^\circ\text{C}$.

ACKNOWLEDGMENT

The authors would like to thank Mr. S. Tsukamoto for his technical assistance.

REFERENCES

- [1] B. Jaffe, R.S. Roth and S. Marzullo, "Piezoelectric Properties of Lead Zirconate-Lead Titanate Solid-Solution Ceramics", J. Appl. Phys., vol. 25 pp. 809-810, June 1954.
- [2] B. Jaffe, R.S. Roth and S. Marzullo, "Properties of Piezoelectric Ceramics in the Solid-Solution Series Lead Titanate-Lead Zirconate-Lead Oxide: Tin Oxide and Lead Titanate-Lead Hafnate", J. Res.

- Natl. Bur. Standards, vol. 55 pp. 239-254, Nov. 1955.
- [3] G.A. Smolenskii and A.I. Agranovskaya, "Dielectric Polarization of A Number of Complex Compounds", Soviet Phys. Solid State, vol. 1 pp. 1429-1437, 1960.
- [4] H. Ouchi, K. Nagano, and S. Hayakawa, "Piezoelectric Properties of $\text{Pb}(\text{Mg}_{1/3}\text{Nb}_{2/3})\text{O}_3$ - PbTiO_3 - PbZrO_3 Solid Solution Ceramics", J. Am. Ceram. Soc., vol. 48 pp. 630-635, Dec. 1965.
- [5] H. Ouchi and M. Nishida, "Phase Relation and Electric Properties of $\text{Pb}(\text{Mg}_{1/3}\text{Ta}_{2/3})\text{O}_3$ - PbTiO_3 - PbZrO_3 Ceramics", J. Japan Soc. Powder and Metallurgy, vol. 40 pp. 687-692, July 1993.
- [6] T. Yamamoto and S. Ohashi, "Dielectric and Piezoelectric Properties of $\text{Pb}(\text{Yb}_{1/2}\text{Nb}_{1/2})\text{O}_3$ - PbTiO_3 Solid Solution System", Jpn. J. Appl. Phys., vol. 34 pp. 5349-5353 Part 1 No. 9B, Sept. 1995.
- [7] H. Jaffe et al., "IRE Standards on Piezoelectric Crystals: Measurement of Piezoelectric Ceramics", Proc. IRE, vol. 49 p1161, No. 7 1961.

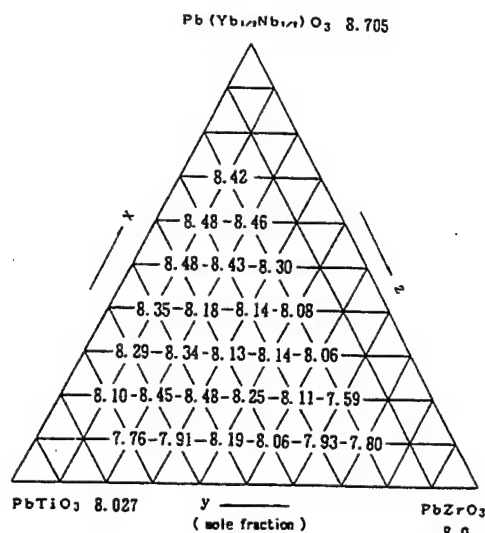


Fig. 1. Density for $x\text{Pb}(\text{Yb}_{1/2}\text{Nb}_{1/2})\text{O}_3$ - $y\text{PbTiO}_3$ - $z\text{PbZrO}_3$ ceramics sintered at 1050°C for 45 min. (g/cm^3)

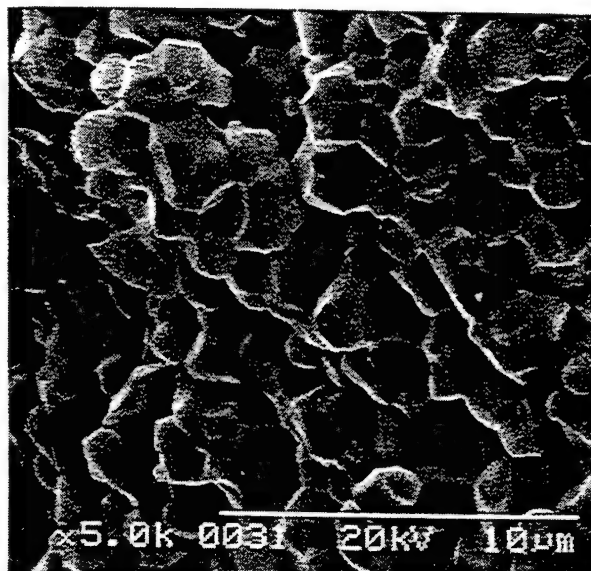


Fig. 2. Microstructure of $\text{Pb}(\text{Yb}_{1/2}\text{Nb}_{1/2})_{0.1}\text{Ti}_{0.5}\text{Zr}_{0.4}\text{O}_3$ ceramics sintered at 1000°C for 45 min.

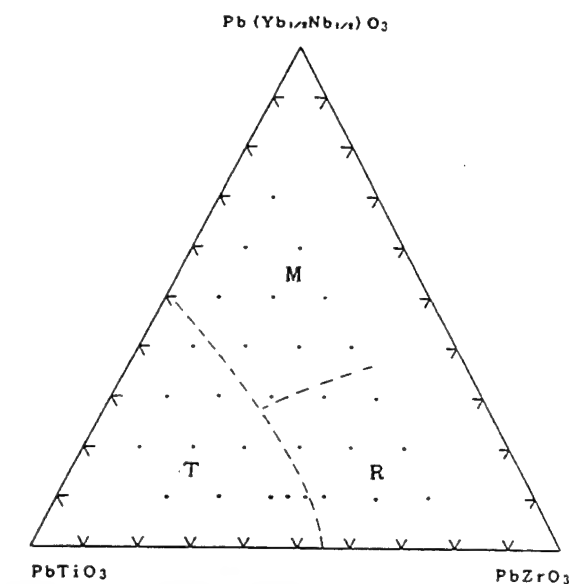


Fig. 3(a). Phase diagram of ternary system $x\text{Pb}(\text{Yb}_{1/2}\text{Nb}_{1/2})\text{O}_3 - y\text{PbTiO}_3 - z\text{PbZrO}_3$ ($x+y+z=1$). M = Monoclinic, T = tetragonal, R = Rhombohedral.

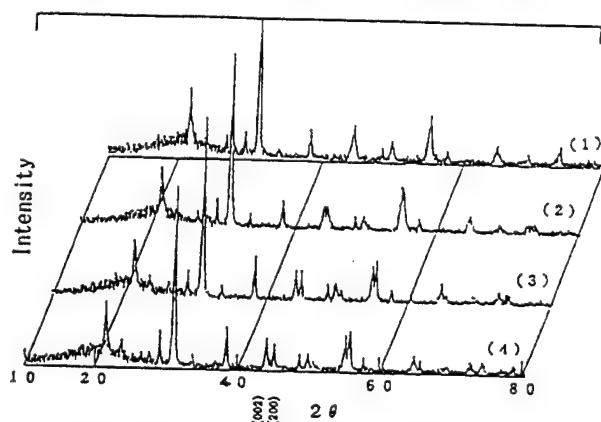


Fig. 3(b). X-ray diffraction pattern for $x\text{Pb}(\text{Yb}_{1/2}\text{Nb}_{1/2})\text{O}_3 - y\text{PbTiO}_3 - z\text{PbZrO}_3$, where (1) $x=0.1, y=0.4$ (2) $x=0.1, y=0.425$, (3) $x=0.1, y=0.45$, (4) $x=0.1, y=0.5$.

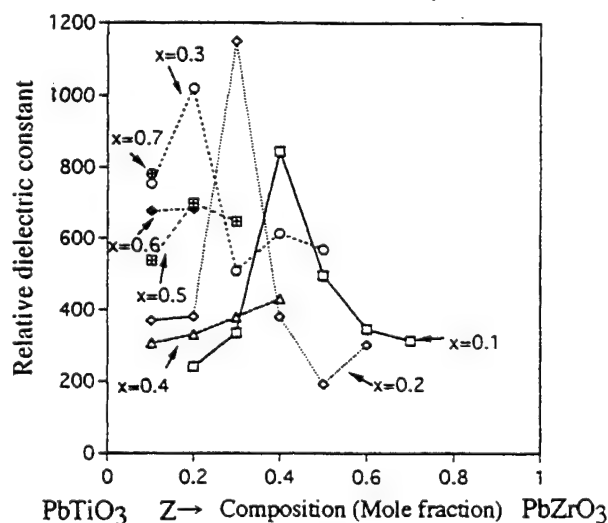


Fig. 4. Dielectric constant, $\epsilon_{33}^T/\epsilon_0$ for the system $x\text{Pb}(\text{Yb}_{1/2}\text{Nb}_{1/2})\text{O}_3 - (1-x-z)\text{PbTiO}_3 - z\text{PbZrO}_3$ with $\text{Pb}(\text{Yb}_{1/2}\text{Nb}_{1/2})\text{O}_3$ as a parameter.

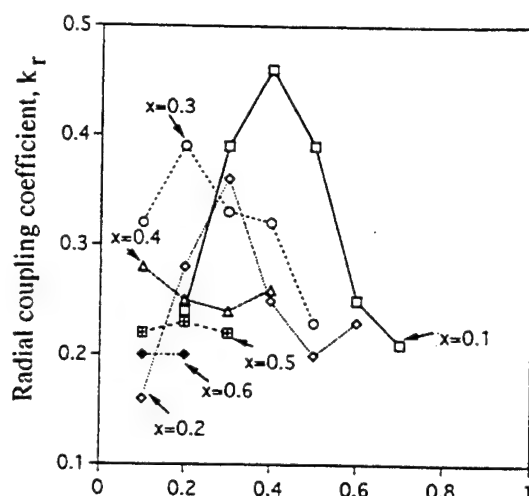


Fig. 5. Radial coupling coefficient for the system $x\text{Pb}(\text{Yb}_{1/2}\text{Nb}_{1/2})\text{O}_3 - (1-x-z)\text{PbTiO}_3 - z\text{PbZrO}_3$ with $\text{Pb}(\text{Yb}_{1/2}\text{Nb}_{1/2})\text{O}_3$ as a parameter.

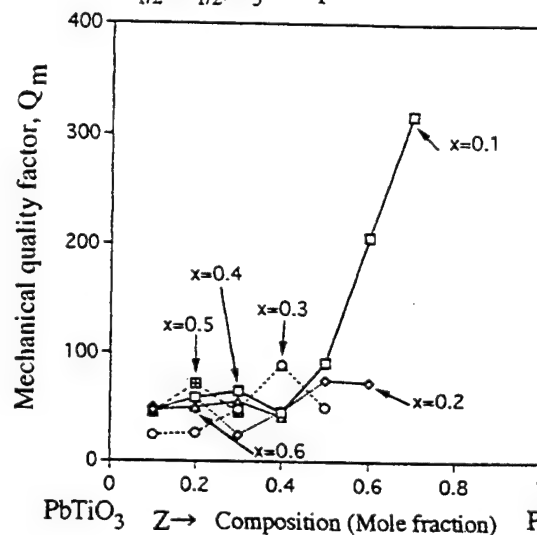


Fig. 6. Mechanical quality factor, Q_m for the system $x\text{Pb}(\text{Yb}_{1/2}\text{Nb}_{1/2})\text{O}_3 - (1-x-z)\text{PbTiO}_3 - z\text{PbZrO}_3$ with $\text{Pb}(\text{Yb}_{1/2}\text{Nb}_{1/2})\text{O}_3$ as a parameter.

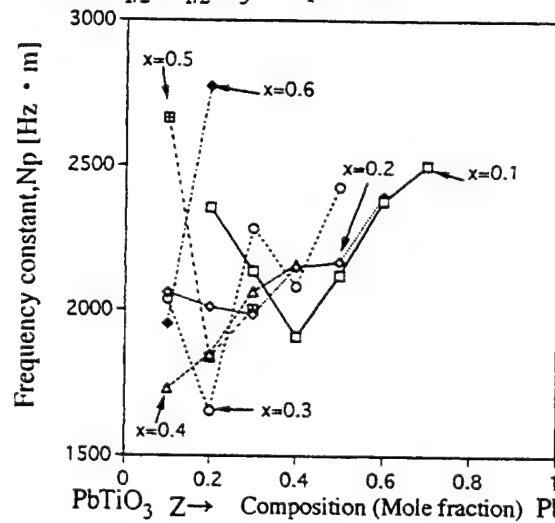


Fig. 7. Frequency constant, N_p for the system $x\text{Pb}(\text{Yb}_{1/2}\text{Nb}_{1/2})\text{O}_3 - (1-x-z)\text{PbTiO}_3 - z\text{PbZrO}_3$ with $\text{Pb}(\text{Yb}_{1/2}\text{Nb}_{1/2})\text{O}_3$ as a parameter.

Ferroelectric Properties and Crystal Orientation in Rhombohedral PZT Ceramics

Toshio Ogawa and Ayako Yamada

Department of Electronic Engineering

Shizuoka Institute of Science and Technology

2200-2, Toyosawa, Fukuroi, Shizuoka 437, Japan

e-mail: ogawa@ee.sist.ac.jp, Fax: +81-538-450154, Tel: +81-538-450149

INTRODUCTION

We investigated the relation between ferroelectric properties and crystal orientation of rhombohedral PZT ceramics to clarify the ferroelectric domain structures in the ceramics. We believe this research may introduce one of the best way to approach "fatigue free PZT materials"¹ as well as well-understanding domain structure controlled PZT ceramics.^{2,3}

EXPERIMENTAL

The ceramic compositions of rhombohedral phase were $0.05\text{Pb}(\text{Sn}_{1/2}\text{Sb}_{1/2})\text{O}_3-0.20\text{PbTiO}_3-0.75\text{PbZrO}_3$ with 0.4wt% MnO_2 .⁴ PZT ceramic disks with 14mm in diameter and 1mm thickness were produced by a conventional ceramic processing. After the PZT ceramic disks were fully polarized at a poling field(E) of 3.0kV/mm, a poling temperature(T_p) of 80 °C and a poling time(t_p) of 30minutes, reverse poling fields were applied to the disks on the same poling conditions. The poling field dependence of relative dielectric constant(ϵ_r), electromechanical coupling factor(k_p) and frequency constant(f_{cp}) was measured by a LCR meter(HP4263A) and an impedance/ gain-phase analyzer(HP4194A), respectively. Crystal orientation in the ceramics as-fired, ground and polished was evaluated by X-ray diffraction (XRD) of {222} peaks. Furthermore, the poling field dependence of crystal orientation was investigated by XRD for as-fired ceramics.

RESULTS AND DISCUSSIONS

Ferroelectric Properties

Figure 1 shows the poling field dependence of ϵ_r (a), k_p (b) and f_{cp} (c), respectively. Although the ϵ_r decreased with increasing E at the initial poling process($E=0 \rightarrow 3.0\text{kV/mm}$), the maximum ϵ_r was obtained at $E=\pm 0.5 \sim \pm 0.75\text{kV/mm}$ by the reverse poling. The k_p , however, was saturated over E of $\pm 1.75\text{kV/mm}$ and it took the minimum at $E=\pm 1.0\text{kV/mm}$. Furthermore, the f_{cp} increased with increasing E from 0 to 3.0kV/mm, and the f_{cp} became minimum at $E=\pm 0.5\text{kV/mm}$ by the reverse poling. It was confirmed that the poling field dependence of ϵ_r had a inverse tendency of that of f_{cp} .

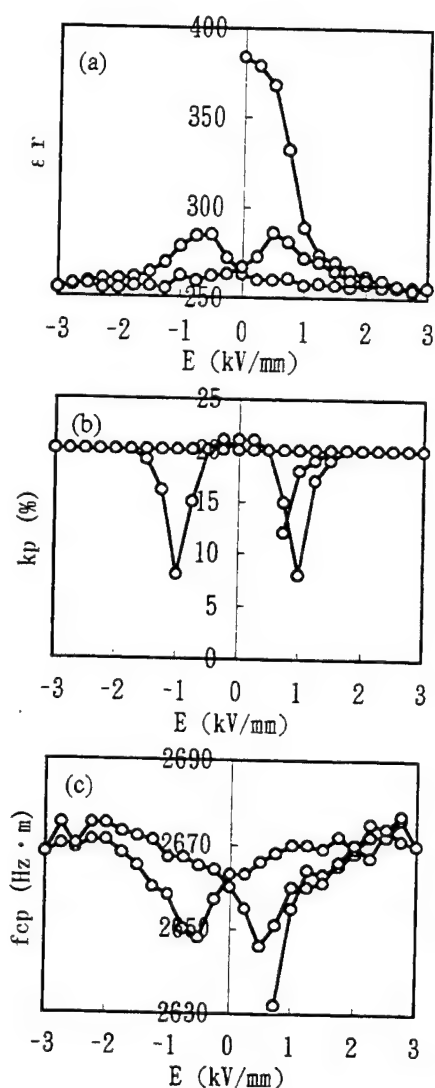


Fig. 1 Poling field(E) dependence of (a): dielectric constant(ϵ_r), (b): electro-mechanical coupling factor(k_p) and (c): frequency constant(f_{cp}).

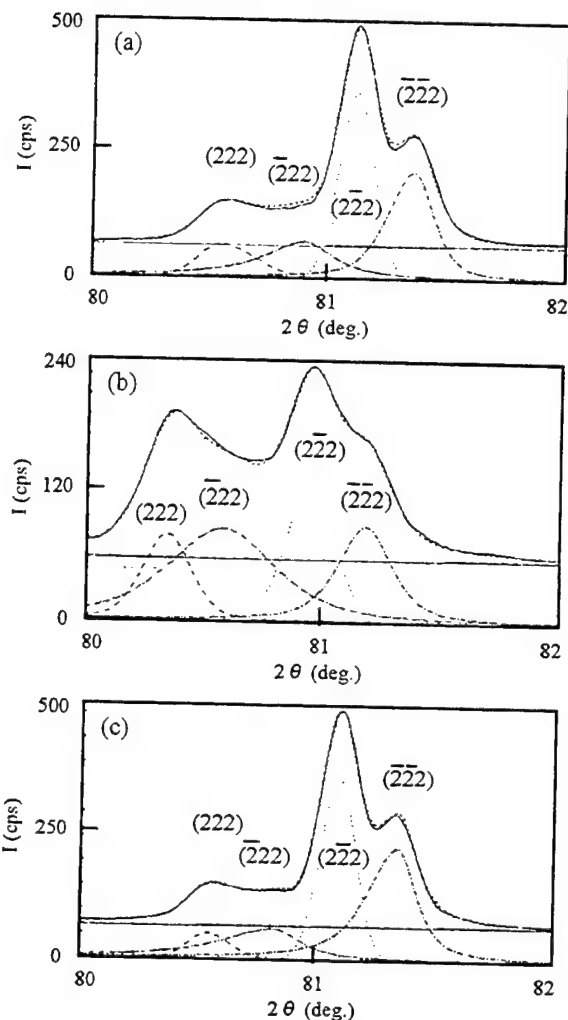


Fig. 2 XRD $\{222\}$ peaks of as-fired(a), ground(b) and polished(c) surfaces.

Crystal Orientation at Various Surfaces

In rhombohedral phase three XRD peaks were expected from the equivalent of $(\bar{2}22)$ and $(2\bar{2}2)$ peaks. The $\{222\}$ XRD pattern of as-fired(1240 °C for 2h) ceramics consisted of four peaks of (222) , $(\bar{2}22)$, $(2\bar{2}2)$ and $(\bar{2}\bar{2}2)$ as shown in Fig. 2(a). The reason the four peaks appeared was thought that the stress generated by passing through the Curie point after firing affected the crystal axes and their angles. The XRD patterns of the ceramics ground by a SiC sand paper(#1200) and the ceramics polished by SiO₂ polishing slurry(Glanzox 3700, Fujimi Co., Japan) were shown in Fig. 2(b) and (c), respectively. The (222) peak intensity increased and the $(\bar{2}22)$ and $(2\bar{2}2)$ peak intensity decreased after grinding in comparison with the ones of the as-fired ceramics. The additional surface alignment⁵⁻⁸ in the direction of $[111]$ occurred by the stress while grinding.

In the following process, the ground surface was polished with SiO₂ particles (0.01 μ m), the size of which is extremely smaller than the grain size (2 – 3 μ m). The XRD pattern of the polished surface, however, was almost the same as that of the as-fired surface. We confirmed the damaged depth of ground surface was about 5 – 10 μ m.⁹

Poling Field Dependence of Crystal Orientation

The XRD patterns of the as-fired ceramics fully poled at $E=3.0\text{kV/mm}$ and reversely poled at $E=-1.0\text{kV/mm}$, at the E of which the k_p became minimum, were shown in Fig. 3(a) and (b), respectively. The (222) and $(\bar{2}\bar{2}\bar{2})$ peak intensities increased and the $(2\bar{2}\bar{2})$ and $(\bar{2}22)$ peak intensities decreased after full poling in comparison with the ones before poling (Fig. 2(a)). It was found that the polarization of the rhombohedral PZT ceramics was oriented in the direction of $[111]$ and $[\bar{1}\bar{1}\bar{1}]$. When the E varied from +3.0 to -1.0 kV/mm, there was no remarkable change in the crystal orientation such as the poling field dependence of k_p (Fig. 1(b)). We believe that the 180° switching in the direction of $[111]$, $[\bar{1}\bar{1}\bar{1}]$ mainly occurred at the E of $\pm 1.0\text{kV/mm}$, as are result the k_p became minimum.

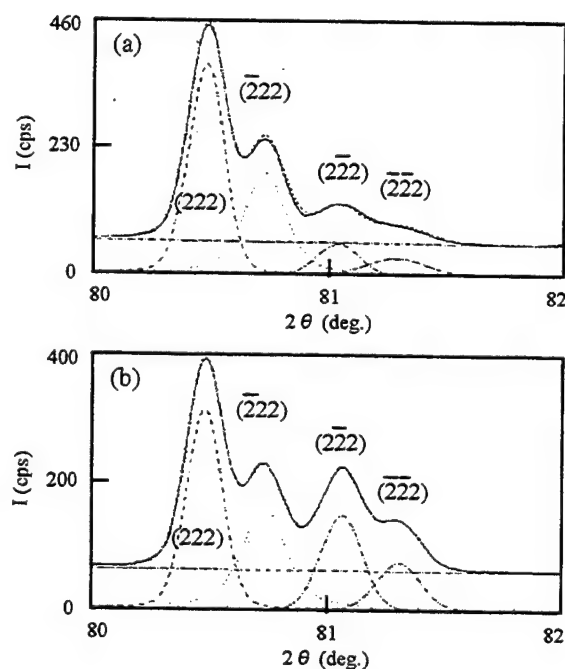


Fig. 3 Poling field(E) dependence of XRD {222} peaks of (a): after poling($E=3.0\text{kV/mm}$) and (b): after reverse poling($E=3.0\text{kV/mm} \rightarrow -1.0\text{kV/mm}$).

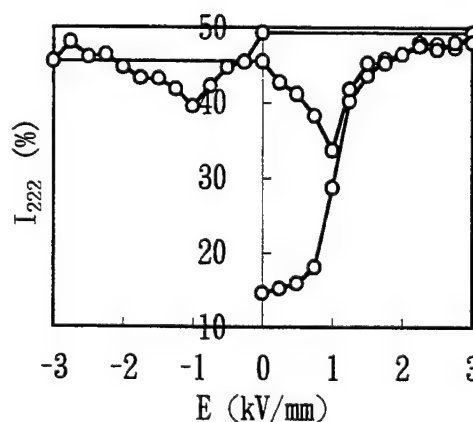


Fig. 4 Poling field(E) dependence of I_{222} peak intensity for as-fired ceramics.

The poling field ($T_p=80^\circ\text{C}$, $t_p=30\text{minutes}$) dependence of the I_{222} [$I_{(222)} / \{I_{(222)} + I_{(\bar{2}\bar{2}\bar{2})} + I_{(2\bar{2}\bar{2})} + I_{(\bar{2}22)}\}$] peak intensity was shown in Fig. 4.

There was a threshold field of $E=1.0\text{kV/mm}$ to begin orienting ferroelectric domains. Since the I_{222} was in proportion to the E from 1.0 to 1.75kV/mm , the increase in ferroelectric domain orientation due to 71° and 109° rotations directly corresponded with the increase in the k_p as well as the increase in the intensity. We believe the k_p mainly depended on these rotations at the initial poling process. After reverse poling, the I_{222} became minimum at $E=\pm 1.0\text{kV/mm}$. Since the decrease in I_{222} was small, the 71° and 109° domains changed into 180° domains. As a result, the 180° switching was the dominant factor affecting k_p .¹⁰ This result was also supported by the E dependence of ϵ_r as shown in Fig. 1(a).

CONCLUSIONS

The poling field dependence of the ferroelectric properties and crystal orientation in rhombohedral PZT ceramics were investigated when the alternating poling field were applied. There were four peaks of $\{222\}$, in the peaks of which the polarization axes were $[111]$ and $[\bar{1}\bar{1}\bar{1}]$ directions. When an alternating poling field was applied to the ceramics, 71° and 109° domains changed into 180° domains. Furthermore, the 180° domain switching occurred at the E of $\pm 1.0\text{kV/mm}$ with a maximum ϵ_r and a minimum k_p .

ACKNOWLEDGEMENTS

This work was partly supported by Grants-in-Aid for Scientific Research (C) (No. 06650375) from the Ministry of Education, Science and Culture; and Tong Yang Central Laboratories in Korea.

REFERENCES

1. T.Ogawa, Proc. of the 6th US-Japan Seminar on Dielectric and Piezoelectric Ceramics, 348 (1993).
2. T.Ogawa, Ferroelectrics, 169, 55 (1995).
3. T.Ogawa, Y.Takesita, T.Miyamoto and D.I.Chun, Ferroelectrics, 186, 119 (1996).
4. T.Ogawa, Ceramic Bulletin, 70, 1042 (1991).
5. T.Ogawa, A.Yamada, M.Takahashi and Y.K.Chung, Proc. of the 7th US-Japan Seminar on Dielectrics and Piezoelectrics Ceramics, 141 (1995).
6. Y.K.Chung, T.Ogawa, M.Takahashi and A.Yamada, Proc. of the 12th Japan-Korea Seminar on Ceramics, 96 (1995).
7. A.Yamada, T.Ogawa, M.Takahashi and Y.K.Chung, Transaction of the MRS Japan, 20, 603 (1996).
8. T.Ogawa, A.Yamada, M.Takahashi and Y.K.Chung, Proc. of ELECTRO-CERAMICS, 1, 177 (1996).
9. A.Yamada, T.Ogawa and Y.K.Chung, To be published in Jpn. J. Appl. Phys.
10. A.Yamada, Y.K.Chung, M.Takahashi and T.Ogawa, Jpn. J. Appl. Phys., 35, 5232 (1996).

High Power Ceramic Materials for Piezoelectric Transformer

Yoshiaki FUDA, Masafumi KATSUNO, Mitsuo TAMURA

Tokin Corporation

6-7-1 Kooriyama Taihakku-ku Sendai 982 Japan

Abstract Maximum vibration velocity v_{\max} is introduced to express maximum output power of piezoelectric transformer as product of square of v_{\max} and square of force factor A_2 and load resistance, while A_2 is proportioned to the product of the square root of electromechanical coupling factor k and ϵ_{33}^T and the square root of Young's modulus Y^E . These were inspected for two different inverter transformer (Rosen and Transverse). As a result, it was confirmed that material characteristics contribute differently for each transformer or load condition, and that v_{\max} is more important for Rosen type.

V_0, V_2 : input and output voltages
 I_3 : output current
 C_{d1}, C_{d2} : damping capacitances of Input and output part
 A_1, A_2 : force factors of input and output
 m : equivalent mass
 s : elastic compliance
 r : equivalent resistance
 v : vibration velocity
 R_L : loading resistance

Output current is represented to the product of force factor A_2 and v , and output current of loading resistance I_3 and output power P are expressed as (1) and (2).

I. INTRODUCTION

Piezoelectric transformers have been developed for Back Light Inverter of Liquid Crystal Displays and partially it is beginning to be practical used. The power transmission of the piezoelectric transformer is proportional to the product of square of vibration velocity v , mass of the transformer and driving frequency. Increasing v is necessary to minimize the size of the transformer, but the mechanical quality factor Q_m is decreased and heat generation rapidly occurs. As a result, the efficiency of the transformer declines. In recent, the improvements of v were reported by $\text{Pb}(\text{Mn}_{1/3}\text{Sb}_{2/3})\text{O}_3$ doped material and fine powder process [1] [2]. In this paper, the relations between P_{\max} , v_{\max} material constants and structures of transformer were investigated theoretically and this theory was verified in practice by two type of transformers.

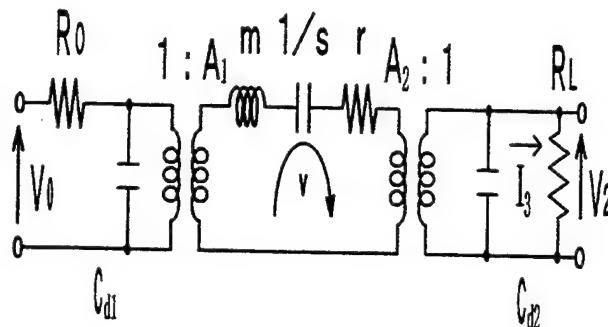


Fig.1 Equivalent circuit of piezoelectric transformer.

$$I_3 = \frac{A_2 v}{\sqrt{1 + \omega^2 C_{d2}^2 R_L^2}} \quad (1)$$

$$P = I_3^2 R_L = \left(\frac{A_2 v}{\sqrt{1 + \omega^2 C_{d2}^2 R_L^2}} \right)^2 R_L \quad (2)$$

Here, maximum output power P_{\max} is expressed by (3) when maximum vibration

II. ANALYSIS OF OUTPUT POWER

2-1. Equivalent circuit analysis

Output power of the transformer was calculated from equivalent circuit shown in Fig. 1. The symbols showed as follows;

R_0 : Impedance of power supply

velocity v_{\max} is velocity at 25 °C raising temperature, under the impedance matching is expressed as follows.

$$R'_L = 1 / \omega C d_2.$$

$$P_{\max} = \frac{A_2^2 v_{\max}^2}{2} R'_L \quad (3)$$

2-2. Influences of material constants and transformer structure

Rosen type transformer is shown in Fig. 2 as a typical piezoelectric transformer. Here w , t and l are width, thickness and length of the transformer, and k_{33} , ϵ_{33}^T and Y_3^E are electromechanical coupling factor, dielectric constant and Young's modulus of ceramic materials respectively. For a another piezoelectric transformer, Fig. 3 shows the construction of output power of piezoelectric transverse effect (after express as transverse type) .

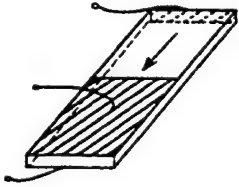


Fig.2 Rosen type transformer.

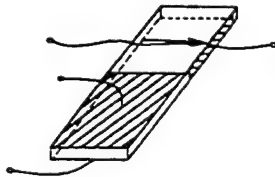


Fig.3 Piezoelectric transformer using transverse effect.

Force factors A_2 of Rosen type and transverse type transformer can be expressed as (4) and (5). Moreover, when loading resistance of the transformer is about 10 Ω as converter, it is necessary that damping capacitance C_{d2} is increased. Therefore, multilayer structure of internal electrodes is considered as shown in Fig.4. In this case, force factors A_2 can be expressed as (6).

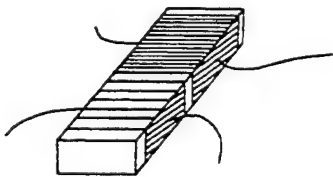


Fig.4 Piezoelectric transformer for converter.

$$\begin{aligned} A_2 &= (4Wtd_{33}Y_3^E) / l \\ &= (4Wtk_{33}\sqrt{\epsilon_{33}^T Y_3^E}) / l \end{aligned} \quad (4)$$

$$\begin{aligned} A_2 &= 2tk_{31}Y_1^E \\ &= 2tk_{31}\sqrt{\epsilon_{33}^T Y_1^E} \end{aligned} \quad (5)$$

$$\begin{aligned} A_2 &= 2tk_{31}Y_1^E \\ &= 2tk_{31}\sqrt{\epsilon_{33}^T Y_1^E} \end{aligned} \quad (6)$$

Equations (4), (5) and (6) are similar with each other. Equation (4) using piezoelectric longitudinal effect is different to (5) using piezoelectric transverse effect about electromechanical coupling factor and (6) includes the multilayer number. Differences of A_2 values mean differences of v values at equal output power, as a result, heat generations of transformers are different with each other. Consequently, the transformer structure relates to P_{\max} and heat generation of transformer. Then, (7) is obtained by substituting (4), (5) and (6) in place of A_2 of (3) . Equation (7) shows the relationship P_{\max} and material constants if v can be considered to be material constant.

$$P_{\max}' = \xi^2 k^2 Y^E v_{\max}^2 \quad (7)$$

From (7), it seems that requirement for ceramic material constants is the large value of $k^2 Y^E v_{\max}^2$ in order to obtain the large P_{\max} . Further, the large ϵ_{33}^T is required for converter transformer. It is distinct that requirements for ceramic material differ according to the application of the transformer.

III. EXPERIMENTAL RESULT AND CONSIDERATION

Table 1 shows two types of material constant for the transformer. Table 2 shows calculation values of $k^2 v_{\max}^2$ in (7). It is found that in table 1, k_{31} and $\epsilon_{33}^T / \epsilon_0$ of material A are large value than that of material B, and in table 2, maximum output power P_{\max} using k_{33} are large value than that using k_{31} regardless materials, and in case of using k_{33} , the P_{\max} of material A is large than that of material B.

Table 1 Typical characteristics of ceramic materials in this experiment.

| | k_{31} (%) | k_{33} (%) | $\epsilon_{33}^T / \epsilon_0$ | Q_m | v_{\max} (m/s) |
|---|-----------------|-----------------|--------------------------------|-------|---------------------|
| A | 25 | 61 | 600 | 2200 | 0.45 |
| B | 36 | 64 | 1100 | 1800 | 0.35 |

Table 2 Comparison of $k^2 v_{\max}^2$ value for each materials.

| | $k^2 v_{\max}^2$ for material A | $k^2 v_{\max}^2$ for material B |
|----------|---------------------------------|---------------------------------|
| K_{31} | 1.26E-3 | 1.58E-3 |
| K_{33} | 7.54E-3 | 5.02E-3 |

Rosen and transverse type transformers were made using these materials. The relation between vibration velocity and output power were measured and compared with calculated values. These transformers were 42 mm long, 12 mm wide and 1.5 mm thick. Vibrator characteristics of these transformers under small electric field were shown in Table 3. It is found from Table 3 that the capacitance ratio of material B is small than that of material A and the damping capacitance of material B is large than that of material A due to differences from material constants. And the output part capacitance ratio of transverse transformer γ_2 is large value than that of Rosen type due to differences from transformer structures.

Table 3 Typical electric characteristics of piezoelectric transformers.

| | γ_1 | γ_2 | Cd_1 (nF) | Cd_2 (nF) | Q_m |
|---------|------------|------------|-------------|-------------|-------|
| Transv. | 27 | 17 | 1.26 | 28 | 2200 |
| Transv. | 50 | 29 | 0.77 | 14.4 | 1800 |
| Rosen B | 25 | 5 | 1.3 | 5.0 | 2000 |
| Rosen A | 44 | 5.5 | 0.71 | 2.9 | 1800 |

Output characteristics of the transformer were measured after connecting the load resistance for impedance matching. Relationships between vibration velocity and output power of Rosen type and transverse type transformer were shown in Fig.5 and Fig.6, respectively. It is recognized that the vibration velocity of Rosen type is lower than that of transverse type at the same output power, and the measurement value coincides with calculated one. But, the measurement value of transverse type transformer differs slightly from calculated one. It is considered that values of material constants used in calculation differed from that of actual transformer. The relation between output power and heat generation was shown in Fig.7. It seems that the heat generation of transverse type transformer is more than that of

Rosen type and the heat generation of transformers of material B which maximum vibration velocity is lower, is large than that of material A.

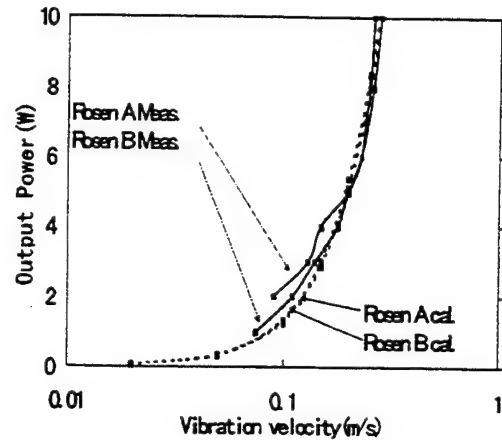


Fig.5 Output power versus vibration velocity (Rosen type).

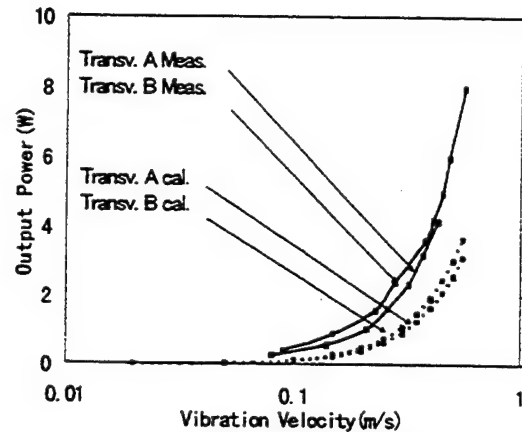


Fig.6 Output power versus vibration velocity (transv. type).

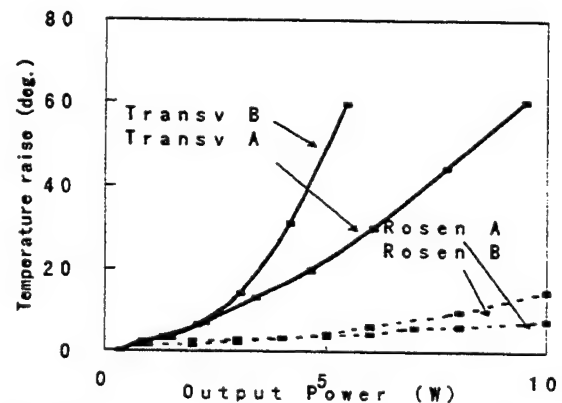


Fig.7 Temperature raise versus output Power.

These indicate that heat generations of transformers are sufficiently influenced by its structure. At 10 W output power of Rosen type transformer, the heat generation of material B is 20 °C and one of material A is 10 °C. It is confirmed that large value of $k^2 v_{\max}^2$ is profitable in point of the heat generation as before mentioned

IV. CONCLUSIONS

Using ceramic materials with different maximum vibration velocities, theoretical analysis and the evaluation of articles were executed.

- (1) Heat generations between Rosen and transverse type differed at same output power due to the differences of transformer structure and vibration velocity.
- (2) Square of output force factor A_2 is proportional to the output power of transformer. The large value of A_2 is profitable for obtaining high power of the transformer.
- (3) Product of square of electromechanical coupling factor k , Young's modulus Y and square of maximum vibration velocity v_{\max} is proportional to the maximum output power. It is considered that the requirement for material constants is large $k^2 Y v_{\max}^2$.

ACKNOWLEDGMENTS

The authors would like to thank Dr. Sadayuki Takahashi NEC corporation for his useful advises.

References

- [1] S.Takahashi and S.Hirose:Jpn.J.Appl.Phy Vol.31(1992) pp.3055-3057
- [2] S.Takahashi,Y.Sasaki,S.Hirose and K,Uchino:Jpn.J.Appl.Phy.Vol.34(1995) pp.5328-5331

Temperature Stable Piezoelectric Ceramics for Cylindrical Vibrators of Vibratory Gyroscopes

Mitsuo TAMURA, Kaoru SATOH, Osamu ISE and Etsuo OTSUKI

Materials Development Laboratory, Tokin Corporation, 6-7-1 Koriyama Taihakuku, Sendai 982, Japan

Abstract

The relationships between piezoelectric characteristics of a ceramic cylindrical vibrator and the performance characteristics of vibratory gyroscope such as in terms of sensitivity and zero offset were assessed by means of an equivalent circuit model. It was confirmed that the temperature stability of the gyroscope depends on temperature variations of the mechanical quality factor (Q_m), the damped capacitance (C_d) and the resonant frequency (f_r). The piezoelectric characteristics were investigated in the ternary system of $\text{PbTiO}_3 - \text{PbZrO}_3 - \text{Pb}(\text{Mn}_{1/3}\text{Sb}_{2/3})\text{O}_3$. It was noticed that reduction of the $\text{Pb}(\text{Mn}_{1/3}\text{Sb}_{2/3})\text{O}_3$ proportion to less than 5 mol% and addition of MnO , Fe_2O_3 and Sm_2O_3 enhances the temperature stabilities of Q_m , C_d and f_r . Consequently, a material having ranges of temperature variations of Q_m , C_d and f_r of within +12 %~-29 %, +16 %~-9 % and +0.2 %~-1.1 % respectively in the temperature range of -30 °C ~+80 °C was developed. Finally a gyroscope having a range of temperature variation of sensitivity of within ± 10 % and one of zero offset of within ± 10 %/s was obtained, which is applicable to direction sensors of car navigation systems.

1. Introduction

Recently, small and inexpensive vibratory gyroscopes have been used as vibration sensors in image stabilizing systems of camcorders, direction sensors of car navigation systems and so forth.¹⁾ Several different types of vibratory gyroscopes have been proposed, and Tokin Corp. has developed and produces vibratory gyroscopes which have a piezoelectric-ceramic cylinder with interdigital electrodes on its surface as a vibrator. These gyroscopes are referred to as Piezoelectric-ceramic Cylinder Vibratory Gyroscopes. Compared with other types which have an elinvar-vibrator, this type has the advantage of a simple structure, but its stability is sensitive to the properties of the piezoelectric material.

In this work, we examined the relationship between the characteristics of a piezoelectric material and the performance characteristics of a piezoelectric-ceramic cylinder vibratory gyroscope by means of an equivalent circuit model, and clarified the requirements of the piezoelectric material for piezoelectric-ceramic cylinder vibratory gyroscopes. Subsequently we investigated the piezoelectric characteristics in the ternary system of

$\text{PbTiO}_3 - \text{PbZrO}_3 - \text{Pb}(\text{Mn}_{1/3}\text{Sb}_{2/3})\text{O}_3$, and developed a temperature stable material. Using this material, we fabricated a piezoelectric-ceramic cylinder vibratory gyroscope which satisfies the specifications required for car navigation systems.

2. Requirements of piezoelectric material

Figure 1 shows an equivalent circuit for a piezoelectric-ceramic cylinder vibratory gyroscope proposed by Shuta *et al.*²⁾ Sensitivity and zero offset can be simulated by equations for the equivalent circuit. Output of the gyroscope is obtained by synchronous detection of the difference between the two output voltages V_z and V_s . The sensitivity of the gyroscope is defined as the output at the angular velocity of 1 %/s. The zero offset is the output at the angular velocity of 0 %/s. In this simulation, the zero offset was assumed to depend only on δ which is the deviation angle of the vibration direction from the driving direction,³⁾ and determined at $\delta = 1^\circ$. The simulation was performed for the piezoelectric material in $\text{PbTiO}_3 - \text{PbZrO}_3 - \text{Pb}(\text{Mn}_{1/3}\text{Sb}_{2/3})\text{O}_3$ system denoted A which is the current material of piezoelectric-ceramic cylinder vibratory gyroscopes. The vibrator characteristics of A are given in Table I. The contributions of the

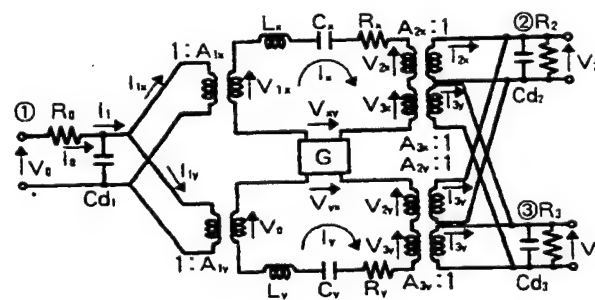


Fig. 1. An equivalent circuit of the vibratory gyroscope with a piezoelectric cylindrical vibrator.

Table I. Characteristics of the cylindrical vibrator consisting of material A. (Vibrator size : $\phi 2 \times L 25$ mm)

| Characteristic | at 25 °C | Temperature variation (-30 °C ~+80 °C) |
|----------------|----------|---|
| Q_m | 496 | 365% |
| f_r | 9850 Hz | 0.6% |
| C_d | 167 pF | 30.9% |
| γ | 57.4 | 10.0% |

temperature dependences of the vibrator constants to the variations of the sensitivity and the zero offset were determined by the simulation. As a result, the temperature variations of Q_m , Cd and f_r are the main factors to be reduced for developing high-performance piezoelectric-ceramic cylinder vibratory gyroscopes.

As concerns Q_m , it is well known that the frequency response deteriorates and sensitivity increases as Q_m increases, and S/N decreases as Q_m decreases.⁴⁾ Hence, the target Q_m value is set to be in the range of 300 ~ 1200, according to the results of previous studies with various materials and the present simulation.

3. Experimental Results and Discussion

3.1 Relationship between temperature characteristic of Q_m and material composition

Many materials based on the ternary system of $\text{PbTiO}_3 - \text{PbZrO}_3 - \text{Pb}(\text{Mn}_{1/3}\text{Sb}_{2/3})\text{O}_3$ have been developed and used widely in various applications, because superior piezoelectric characteristics are

obtained in the wide compositional range of this system. Tsubouchi *et al.* reported on the radial electromechanical coupling coefficient (K_p) and Q_m in $\text{PbTiO}_3 - \text{PbZrO}_3 - \text{Pb}(\text{Mn}_{1/3}\text{Sb}_{2/3})\text{O}_3$ system.⁵⁾

However, the relationship between the temperature characteristic of Q_m and composition has not been investigated. Therefore the temperature variation of Q_m in the range of $-40^\circ\text{C} \sim +80^\circ\text{C}$ was studied in the area near the morphotropic phase boundary. The results are shown in Fig. 2. As seen in Fig. 2,

① The temperature characteristic of Q_m peaks at a certain temperature, and the peak shifts to higher temperature with reduction of the $\text{Pb}(\text{Mn}_{1/3}\text{Sb}_{2/3})\text{O}_3$ content.

② The temperature at which Q_m is maximum depends weakly on the ratio of Zr to Ti, and decreases with decreasing Zr/Ti.

③ Reduction of the $\text{Pb}(\text{Mn}_{1/3}\text{Sb}_{2/3})\text{O}_3$ content results in a decrease in the peak Q_m and the temperature variation of Q_m .

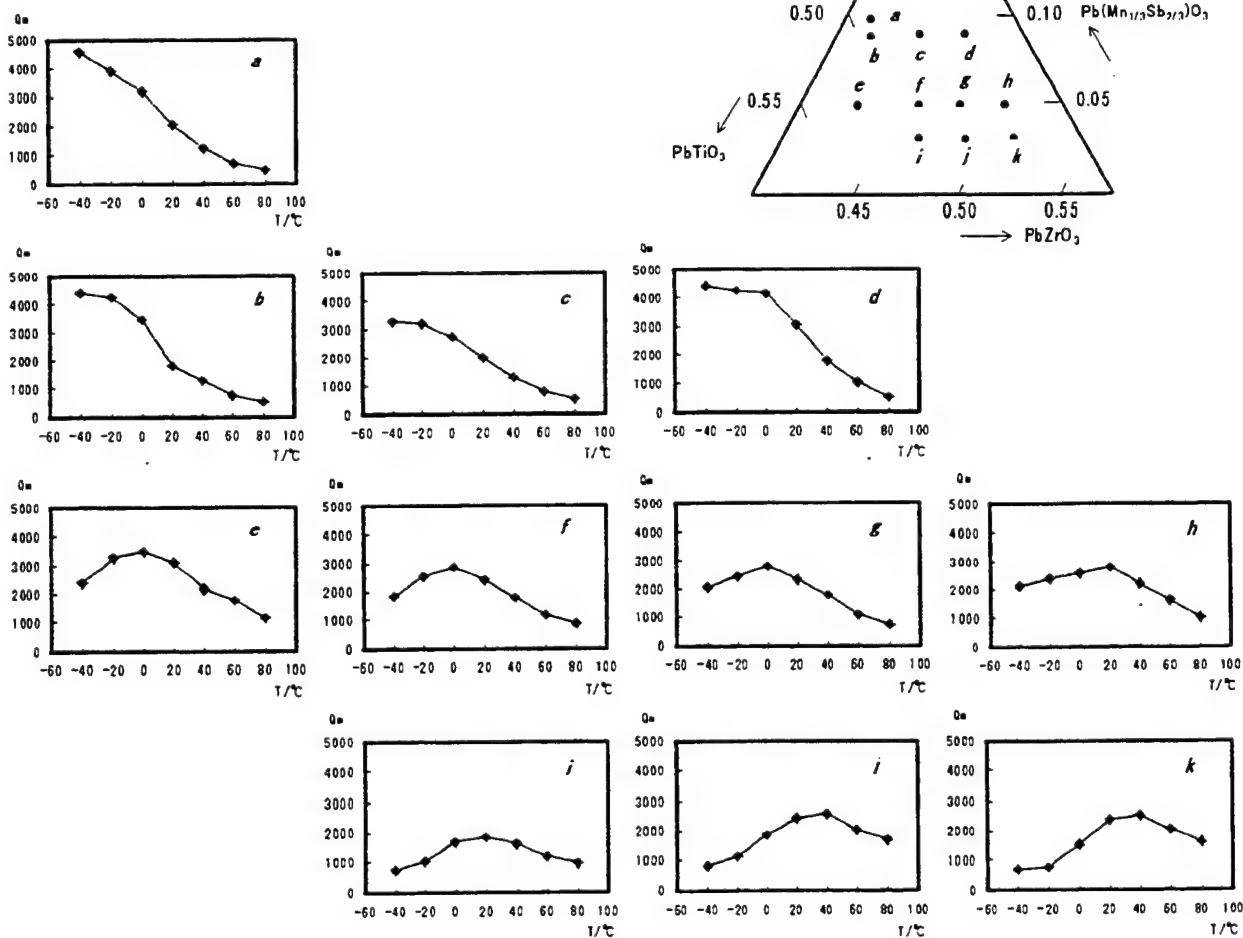


Fig. 2. Relationship between temperature dependence of Q_m and composition of $\text{PbTiO}_3 - \text{PbZrO}_3 - \text{Pb}(\text{Mn}_{1/3}\text{Sb}_{2/3})\text{O}_3$ ceramics.

In addition, T_c tends to increase with decreasing the $\text{Pb}(\text{Mn}_{1/3}\text{Sb}_{2/3})\text{O}_3$ content,⁵⁾ hence the compositional range of PbTiO_3 — PbZrO_3 — $\text{Pb}(\text{Mn}_{1/3}\text{Sb}_{2/3})\text{O}_3$ in which the temperature variation of Q_m is relatively small is also suitable for reducing the temperature variation of C_d . On the other hand, the temperature coefficient of f_r becomes more than 100 ppm/°C at less than 5 mol% $\text{Pb}(\text{Mn}_{1/3}\text{Sb}_{2/3})\text{O}_3$, while it is minimum at 25 ppm/°C at around point *b* in Fig. 2. Accordingly, if the temperature characteristic of f_r at less than 5 mol% $\text{Pb}(\text{Mn}_{1/3}\text{Sb}_{2/3})\text{O}_3$ can be improved, it will be possible to obtain a material suitable for piezoelectric-ceramic cylinder vibratory gyroscopes. Still, the $\text{Pb}(\text{Mn}_{1/3}\text{Sb}_{2/3})\text{O}_3$ content must be adjusted for the Q_m value, which is required to be in the range of 300 ~ 1200 as stated above.

3.2 Improvement of temperature characteristic of f_r

As mentioned in §3.1, the compositional range of the ternary system in which the temperature variation of Q_m is relatively small is limited. However, the temperature variation of f_r tends to be large in this range. Thus, we investigated the effect of additives on the temperature characteristic of f_r , and found addition of MnO , Fe_2O_3 and Sm_2O_3 to PbTiO_3 — PbZrO_3 — $\text{Pb}(\text{Mn}_{1/3}\text{Sb}_{2/3})\text{O}_3$ system to be effective for improvement of the temperature characteristic of f_r . By the addition, the Q_m values are lowered throughout the measured temperature range, and the Q_m curves are flattened. Accordingly, the temperature variation of Q_m is also improved by the additives. Consequently, the addition of MnO , Fe_2O_3 and Sm_2O_3 at less than 5 mol% $\text{Pb}(\text{Mn}_{1/3}\text{Sb}_{2/3})\text{O}_3$ reduces the temperature variations of f_r and Q_m simultaneously.

3.3 Characteristics of developed material

Finally, material *B* which seems to be suitable for the gyroscopes was developed on the basis of the composition near *g* in Fig. 2. The vibrator constants for materials *A* and *B* are shown in Table II. The temperature characteristics of Q_m for materials *A* and *B* in the range of -30°C ~ $+80^\circ\text{C}$ are shown in Fig. 3. The temperature characteristics of Q_m and C_d are improved by use of material *B*. Concerning material *B*,

the range of Q_m is approximately from 700 to 1100, which means that Q_m varies from +12 % to -29 % relative to the value at room temperature. Similarly, the range of C_d variation of material *B* is +16 % ~ -9 %, whereas that of material *A* is +16 % ~ -15 %.

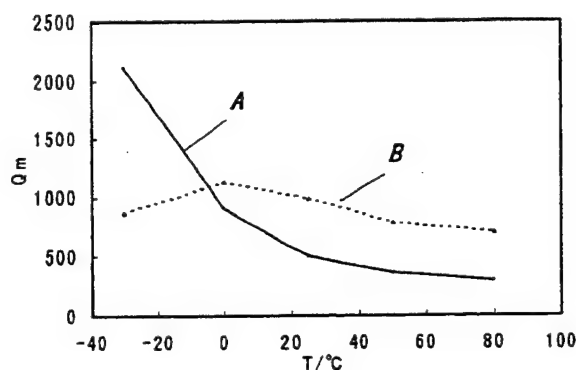


Fig. 3. Q_m vs temperature of cylindrical vibrators consisting of material *A* and *B*.

3.4 Performance characteristics of the piezoelectric-ceramic cylinder vibratory gyroscope

The piezoelectric-ceramic cylinder vibratory gyroscope shown in Fig. 4 was made using material *B*, and its performance was evaluated. The temperature characteristics of the sensitivity for material *A* and *B* are shown in Fig. 5. The temperature characteristics of the zero offset for material *A* and *B* are shown in Fig. 6. By use of material *B*, the temperature characteristic of the sensitivity is improved, and its range is from -10 % to +4 % which is approximately a third of that for material *A*. The temperature variation of the zero offset is also reduced, and its range is half of that for material *A*. A temperature variation of the sensitivity of within ± 10 % and one of the zero offset within 10

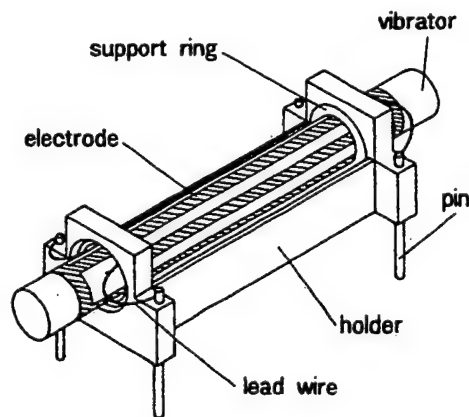


Fig. 4. Perspective structural diagram of the vibratory gyroscope with a cylindrical vibrator.

Table II. Characteristics of the cylindrical vibrators consisting of material *A* and *B*. (vibrator size : $\phi 2 \times L 25$ mm)

| Characteristic | at 25 °C | |
|----------------|----------|----------|
| | <i>A</i> | <i>B</i> |
| Q_m | 496 | 989 |
| f_r | 9850 Hz | 9540 Hz |
| C_d | 167 pF | 146 pF |
| γ | 57.4 | 65.7 |

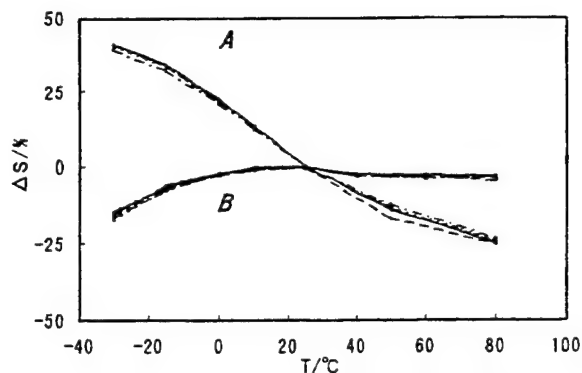


Fig. 5. Sensitivity vs temperature of the gyroscope.

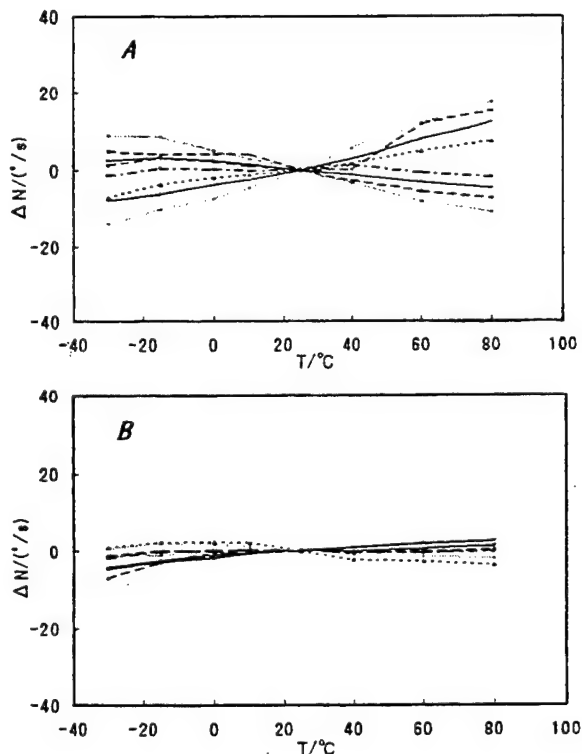


Fig. 6. Zero offset vs temperature of the gyroscope.

%/s are required for car navigation systems. This gyroscope meets these specifications. As a consequence, it was confirmed that a gyroscope applicable to car navigation systems can be fabricated using material *B*. However, the zero offset shows inconsistent temperature dependences, which might be due to the influence of the silicon resin and the holder which support the vibrator. Therefore, examination and improvement of structure of the support are subjects for further study.

4. Conclusions

The materials used for a piezoelectric-ceramic cylinder vibratory gyroscope have been investigated for the improvement of the performance characteristics of the gyroscope such as the temperature characteristics of sensitivity and zero offset.

The material characteristics required were estimated by use of an equivalent circuit, and it was found that stability of Qm is most important.

In the ternary system of $PbTiO_3 - PbZrO_3 - Pb(Mn_{1/3}Sb_{2/3})O_3$, the temperature variation of Qm is relatively small at less than 5 mol% $Pb(Mn_{1/3}Sb_{2/3})O_3$, and the temperature characteristic of fr is improved by the addition of MnO , Fe_2O_3 and Sm_2O_3 .

A material suitable for the gyroscope was developed, and the performance of a gyroscope made of this material was evaluated. It was confirmed that this gyroscope is applicable to car navigation systems.

Acknowledgments

The authors would like to thank Dr. Tetsuo Yoshida for his valuable advice, and Mr. Yukihiro Takahashi for his help with the experiments.

References

- 1) Y. Koga, T. Minobe, M. Naka and Y. Watanabe: *Nikkei Electronics* **11.25** (1991) No. 541, 217 [in Japanese].
- 2) K. Shuta and H. Abe: *Jpn. J. Appl. Phys.* **36** (1997) 3041.
- 3) H. Abe, T. Yoshida and K. Nakamura: *IEICE J78-C- I* (1995) 567 [in Japanese].
- 4) S. Kudoh: *J. Acoust. Soc. Jpn.* **52** (1996) 311 [in Japanese].
- 5) N. Tsubouchi, M. Takahashi, T. Akashi, "Piezoelectric ceramic material," U.S. Patent 3699 045 (1972).

The influence of the heat treatment conditions on the temperature stability of the piezoelectric properties and absolute values of the Lead Titanate ceramics.

Kazuo Miyabe, Kazushi Tachimoto, Kenji Horino, Takeo Tsukada, Mahoko Takada

TDK Corporation, Materials Research Center

570-2, Aza-Matsugashita, Minami-Hatori, Narita-shi, 286, Japan

Abstract-We have performed the heat treatment of the PT-based substrates in several atmospheres (air/O₂/N₂), and measured their piezoelectric properties. The frequency shift and degradation of the *k_t* were then evaluated after the heat resistance test. As a result, *Q_m* and heat resistant properties were highly improved the specimens heat treated in the N₂ atmosphere (at 750-900°C, before poling) as compared to those treated in other environments. It can be concluded from the above results that the improvement in modified P T occurred after the heat-treatment in the N₂ atmosphere, which resulted in the balance of the defects such as oxygen vacancies and cation vacancies in the substrate. Consequently, a stable domain structure, high *Q_m* and superior heat resistant properties were obtained.

Introduction

A couple of decades ago, Quartz resonators were widely in use, but have now been replaced by ceramic ones in a variety of applications. Ceramic resonators have dominated the field in the frequencies ranging from 400KHz to 40MHz.

In particular, the shapes required by appliance manufacturers have changed from discrete-type to chip-type products. It is important for the chip-type components to maintain high level of temperature stability. Frequency shift due to soldering and heat-shock test cycles are undesirable. In case of resonators, It is required that the piezoelectric properties remain unchanged in a wide temperature range.

Trend has been growing towards high frequency applications. Until recently PZT resonators were in use but these resonators have frequency limit as they resonate on their natural (first harmonic) frequency. PT (PbTiO₃) resonators have overcome this problem as they utilize the 3rd harmonic over-tone mode, which, in turn, makes them useful for high frequency applications. We have been studying on the

relationship between the ceramic fabrication process and the piezoelectric properties in the modified PT. We have recognized the importance of the heat treatment process on the piezoelectric properties.

Experimental Procedure

The composition of the specimens used in this study was 0.69PbTiO₃+0.3SrTiO₃+0.01Bi_{2/3}TiO₃ with Mn 0.1atm% and Nb 0.1atm%. The starting materials were PbO, TiO₂, Bi₂O₃, SrCO₃, MnCO₃ and Nb₂O₅. The powders were mixed, calcined at 900°C for 2hours and then milled. The calcined powder was then pressed into the blocks and sintered at 1200°C for 4hours. The sintered body was cut into square pieces of 7mm x 7.5mm and having a thickness of 0.23mm. The pieces were then heat treated at 700~1000°C in a tubular furnace, having 150mm diameter, in either air (PO₂: 20%), PO₂ 0.10% or N₂(PO₂:10⁻³%) or O₂. The flow rate was maintained at constant of 2 l/min for one hour in all the cases. After heat treatment in various environments, the poling was carried out by applying DC field of 5kV/mm for 30min in a silicon oil bath at a temperature of 120°C. Ag electrodes of 1mm in diameter were formed on both sides of the specimens by evaporation. Resonance and anti resonance frequency, impedance at resonance frequency and capacitance were measured by 4194A impedance analyzer. Mechanical Q factor, coupling factor and frequency constant were then calculated. Especially the calculation of coupling factor was made by the values of the 3rd overtone resonance and anti resonance frequency at the thickness extensional trapped energy mode. Heat test was carried out at 240°C for 30seconds. Insulating resistance of the samples was measured during the various heat treatment atmospheres at the temperatures ranging 700°C to 1100°C using a digital electro-meter (TR8652). The coercive field of all the samples was then measured as function of aging. O₂ partial pressure during N₂ heat treatment process in the

furnace was also observed. The specimens were then chemically etched by 0.1%HF solution for 15seconds and the microstructures were observed by scanning electron microscopy (SEM) at the room temperature.

Result and Discussion

Figure 1 shows the piezoelectric properties of the test samples as a function of heat treatment. N_2 heat treated specimens have higher frequency constant, high mechanical Q factor and low impedance at the resonance, which are different from the those of other specimens. There was a little difference between the piezoelectric properties of O_2 or air heat treated specimens.[1] Figure 2 shows the mechanical Q factor as a function of the temperature of various heat treated samples. N_2 ($PO_2:10^{-3}\%$) heat treated specimens have high mechanical Q factor, which are different from those of other specimens at the temperatures ranging from 700°C to 900°C. Figure 3 shows the insulating resistance as a function of temperature of several heat treated samples. As shown in fig 2, N_2 heat treated specimens have high insulating resistance as compared to the specimens treated at 700°C to 900°C. It is supposed that above 900°C the PbO starts to evaporate and shows a sharp reduction in the substrate.

Figure 4 shows the mechanical Q factor's dependence on the poling field. The saturation point of mechanical Q factor of N_2 heat treated specimens is about 1000 higher than that of the non heat treated specimens. Figure 5 shows the coercive field as a function of the aging time. N_2

heat treated specimens have larger coercive field than those of the non heat treated specimens. Figure 6 shows the improvement in the piezoelectric properties and mechanical Q factor of the samples shown in figure 1, after a heat test of 240 °C for 30seconds. N_2 heat treated specimens show better heat resisting properties than the other specimens.

Figure 7 shows the chemically etched surface of N_2 heat treated and the non heat treated specimens after poling. Distinct domain structures were observed only in the case of N_2 heat treated specimens. It shows that the domain structures of N_2 heat treated specimens are more stable. It was also reported in a previous paper that heat resisting properties of the PZT ceramics improves with high temperature poling.[2] Figure 8 shows the change in O_2 partial pressure during the N_2 heat treatment process. O_2 partial pressure in the furnace was considerably higher in the presence of the samples than without the samples. This means that the oxygen discharge from the specimen takes place during N_2 heat treatment process and creates oxygen vacancies in the PT ceramics. Considering this result, it may be that with high insulating resistance, as shown figure 3, oxygen vacancies compensate for the cation vacancies caused by the composition of the specimens.

Conclusions

The relationship between heat treatment process and piezoelectric properties in the PT ceramics were investigated. As a result, N_2 heat treated specimens were found to have higher mechanical Q factor and superior heat resisting properties as compared to those of the non heat treated, air or O_2 heat treated ones.

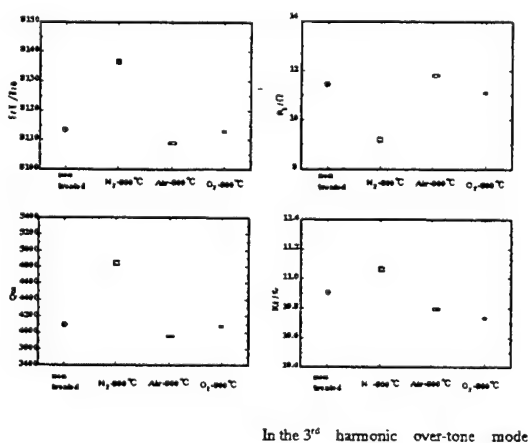


Fig.1 Piezoelectric properties as the function of heat treatment process

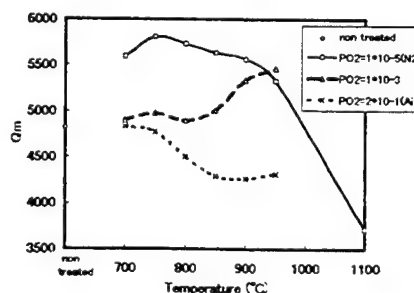


Fig.2 Q_m as the function of heat treatment temperature

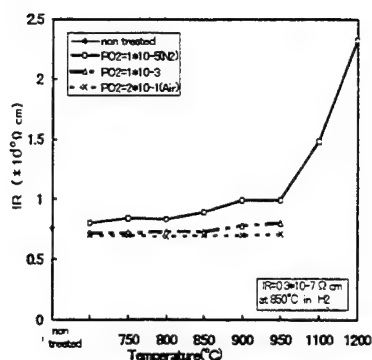


Fig.3 Insulation resistance as the function of heat treatment process

Higher E_c explains high mechanical Q factor of N_2 heat treated specimens. And superior heat resisting properties can be attributed to the distinct domain structures, which were observed by the SEM. It can be concluded that the oxygen defects which were made during N_2 heat treatment process would compensate for cation vacancies caused by the composition of the specimens. Thus the resulting specimens had higher insulating resistance and stable domain structures.

Acknowledgments

The authors would like extend their gratitude to Dr. Takeshi Nomura, Mr. Hitoshi Oka, Mr. masakazu Hirose and Mr. Amer Rathore for many helpful discussion and suggestions during the course of this study.

References

- [1] M. Hirose, M. Takada, H. Oka, K. Miyabe:
"Relationship between Poling Condition and Heat Resisting Properties in Lead Zirconate Titanate"
Jpn. J. Appl. Phys. 33 (1994) 5345.
- [2] K. Tachimoto, K. Horino, M. Takada, K. Miyabe:
"Relationship between Heat-treatment Process and Piezoelectric Properties in Lead Titanate Ceramics"
14th Ferroelectric Materials Application Meeting Japan (1997) 125

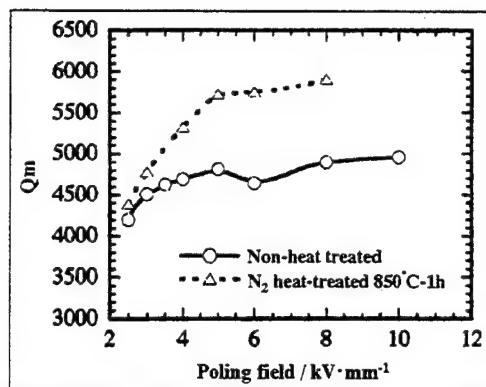


Fig.4 Q_m as the function of poling field

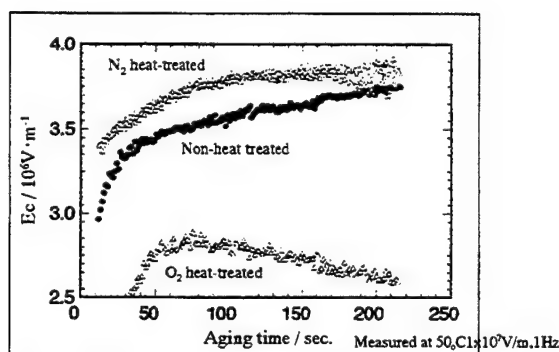


Fig.5 Coercive field as the function of aging time

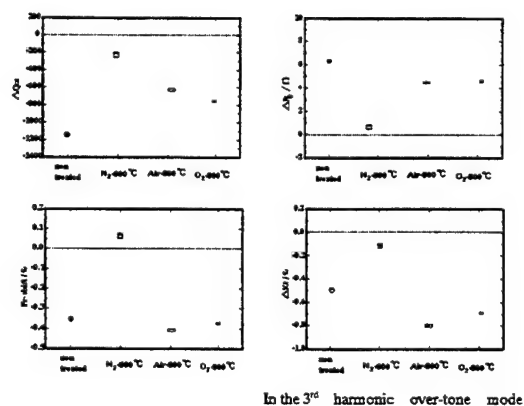


Fig.6 Change in piezoelectric properties due to temperature of heat treatment process

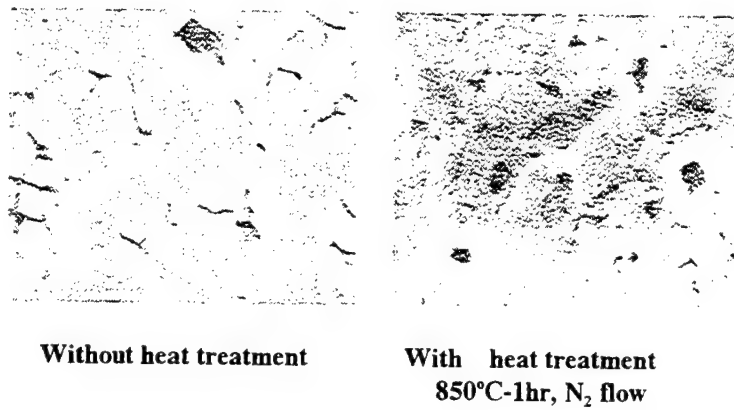


Fig.7 SEM micrographs of polished and chemically etched surface of PT ceramics (after poling)

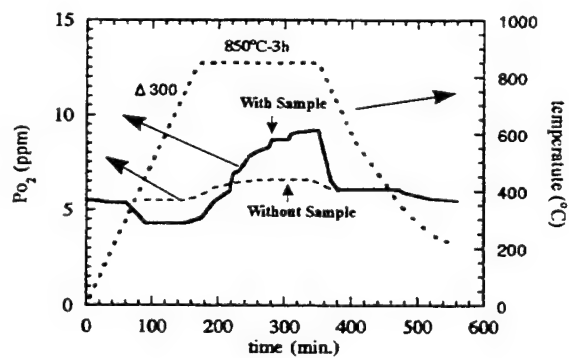


Fig.8 Change in the PO₂ during the N₂ heat treatment process in the furnace

Non-lead Piezoelectric Ceramics Based on $(\text{Bi}_{1/2}\text{Na}_{1/2})\text{TiO}_3$

Tadashi TAKENAKA and Hajime NAGATA

Faculty of Science and Technology, Science University of Tokyo,

Noda, Chiba-ken 278, Japan

[TEL] +81-471-24-1501 (+3716)

[FAX] +81-471-23-0856

E-mail: tadashi@takenaka.ee.noda.sut.ac.jp

Abstract --- Dielectric, ferroelectric and piezoelectric properties of bismuth sodium titanate, $(\text{Bi}_{1/2}\text{Na}_{1/2})\text{TiO}_3$ (BNT)-based three component solid solution, $a\cdot(\text{Bi}_{1/2}\text{Na}_{1/2})\text{TiO}_3$ - $b\cdot 1/2(\text{Bi}_2\text{O}_3\cdot\text{Sc}_2\text{O}_3)$ - $c\cdot\text{KNbO}_3$ [KTSN (100a/100b/100c)] are studied for a candidate as a lead-free piezoelectric ceramic family. The electromechanical coupling factor, k_{33} in the longitudinal mode is about 0.44 for KTSN(99/0.5/0.5). KTSN ceramics seem to be efficacious for non-lead based piezoelectric ceramics for clean environment.

1. INTRODUCTION

Most piezoelectric ceramic materials, which have been widely used, are $\text{Pb}(\text{ZrTi})\text{O}_3$ -based three-component ceramics (PZT system). They include a large quantity of lead oxide (PbO) as main compositions. However, it is very important for avoidance PbO -pollution of the earth to use the lead-free materials as electronic functional materials etc. Non-lead based materials such as lead-free or low-lead-content piezoelectric and/or pyroelectric ceramics have been recently taken an interest in clean environment. Consequently, it is necessary to search the lead-free piezoelectric materials with excellent properties such as those of PZT system.

Bismuth sodium titanate, $(\text{Bi}_{1/2}\text{Na}_{1/2})\text{TiO}_3$ [BNT] [1, 2], is considered to be an excellent candidate as a key material of lead-free piezoelectric ceramics because BNT is strongly ferroelectric and has the Curie temperature

$T_c=320^\circ\text{C}$, relatively large remanent polarization $P_r=38\text{ }\mu\text{C}/\text{cm}^2$, and coercive field $E_c=73\text{ kV}/\text{cm}$ at room temperature. However, data on the piezoelectric properties of BNT ceramics are scarce because it is difficult to pole fully this ceramics due to the large E_c . Recently some BNT-based solid solutions which can be poled easily were reported [3-9]. These reports suppose that a strong ferroelectricity of the BNT-based solid solutions is attributed to $(\text{Bi}_{1/2}\text{Na}_{1/2})^{2+}$ ions, especially Bi^{3+} ions, of A-site on ABO_3 perovskite structure. As a BNT-based solid solution without decreasing the amount of Bi^{3+} ions, $(\text{Bi}_{1/2}\text{Na}_{1/2})\text{TiO}_3$ - $1/2(\text{Bi}_2\text{O}_3\cdot\text{Sc}_2\text{O}_3)$ system was studied on their electrical properties [10]. A reason for expressing the $1/2(\text{Bi}_2\text{O}_3\cdot\text{Sc}_2\text{O}_3)$ is that any compounds between Bi^{3+} and Sc^{3+} ions have been found except a liquid phase. The solid solution has a relatively high electromechanical coupling factor, k_{33} ($=0.42$), and has no phase transition from ferroelectric to antiferroelectric phases around 200°C from the results of measuring the temperature dependence of dielectric, ϵ_s , and loss tangent, $\tan\delta$.

In this paper, dielectric, piezoelectric and ferroelectric properties of a BNT-based solid solution, $a\cdot(\text{Bi}_{1/2}\text{Na}_{1/2})\text{TiO}_3$ - $b\cdot 1/2(\text{Bi}_2\text{O}_3\cdot\text{Sc}_2\text{O}_3)$ - $c\cdot\text{KNbO}_3$ [KTSN (100a/100b/100c)] ($a+b+c=1$), especially with the compositions of BNT-side ($a \gg b$ and c), are studied from the viewpoint of a new group of lead-free piezoelectric ceramics. KNbO_3 is well known as a typical lead-free piezoelectric material with high electromechanical coupling factors [11].

$(\text{Bi}_{1/2}\text{Na}_{1/2})\text{TiO}_3$ - KNbO_3 solid solution was also studied and the piezoelectric properties show the relatively high electromechanical coupling factor, k_{33} (≈ 0.47) [12]. Figure 1 shows the phase relation between $(\text{Bi}_{1/2}\text{Na}_{1/2})\text{TiO}_3$, $1/2(\text{Bi}_2\text{O}_3\cdot\text{Sc}_2\text{O}_3)$ and KNbO_3 on the three component system.

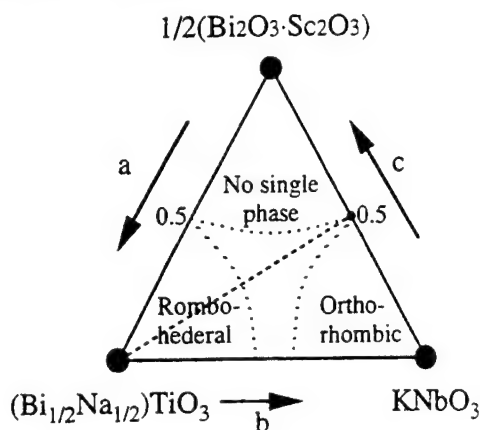


Fig. 1. Phase relation between $(\text{Bi}_{1/2}\text{Na}_{1/2})\text{TiO}_3$, $1/2(\text{Bi}_2\text{O}_3\cdot\text{Sc}_2\text{O}_3)$ and KNbO_3 .

2. EXPERIMENTAL

The conventional ceramic fabrication technique was used to prepare KTSN ceramics. Reagent-grade metal oxide or carbonate powders of Bi_2O_3 , TiO_2 , Na_2CO_3 , Sc_2O_3 , K_2CO_3 and Nb_2O_5 were used as the starting raw materials. The powders were mixed in acetone with zirconium balls by ball-milling for 10 h. After calcining, the ground and ball-milled ceramic powders were pressed into discs for samples and were sintered at $1150\sim 1250^\circ\text{C}$ for 2 h in an air atmosphere. The crystal phase of the sintered ceramics was checked using an X-ray diffractometer. Fire-on silver paste was used as the electrode for the electrical measurements such as dielectric, ferroelectric and piezoelectric measurements. Temperature dependence of the dielectric constant, ϵ_s , and the loss tangent, $\tan\delta$, were measured for the determination of the Curie temperature, T_c , at 1 MHz by means of an automated dielectric measurement system with a multifrequency LCR meter (YHP 4275A). D-E hysteresis loops were observed by a standard Sawyer-Tower circuit at 50 Hz.

Specimens for piezoelectric measurements were poled in a stirred silicone oil. Piezoelectric properties were measured by means of the resonance-antiresonance method on the basis of IEEE standards using an impedance analyzer (YHP 4192A). The electromechanical coupling factors, k_p , k_t , k_{31} , and k_{33} , in the planar, the thickness, the transverse and the longitudinal modes were calculated from the resonance and antiresonance frequencies using Onoe's formula.

3. RESULTS AND DISCUSSION

Figure 2 shows X-ray powder diffraction patterns of KTSN(99/0.5/0.5, 98/1/1, 97/1.5/1.5, 96/2/2, 92/4/4) as an example of this solid solution. All patterns of Fig. 2 (a)~(d) show a single phase of perovskite structure with a rhombohedral symmetry at room temperature. These ceramics were very easy to sinter the ceramics with a high measured density ratio than 93 % to the theoretical density.

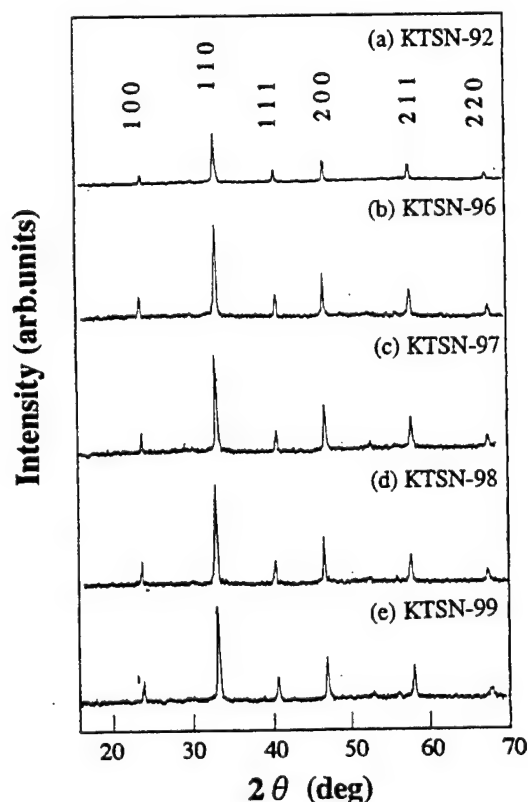


Fig. 2. X-ray diffraction patterns of KTSN ceramics, (a) 92/4/4, (b) 96/2/2, (c) 97/1.5/1.5, (d) 98/1/1, and (e) 99/0.5/0.5.

Figure 3 shows the temperature dependence of dielectric constant, ϵ_s , and loss tangent, $\tan\delta$, in KTSN ceramics at 1 MHz. The ϵ_s ($\approx 530 \sim 700$ at R.T.) are smaller than those of conventional PZT or PZT-based ceramics. The ϵ_s - T curves of KTSN display broad shapes near the Curie point, T_c . The T_c ($\approx 290 \sim 330$ °C) becomes lower with increasing the amount of modified $1/2(\text{Bi}_2\text{O}_3\text{-Sc}_2\text{O}_3)\text{-KNbO}_3$. The $\tan\delta$ - T curves also show broad near 200 °C except the KTSN(100/0/0) [BNT]. BNT in $\tan\delta$ - T curves has a peak at 195 °C. This result indicates that second phase transition from ferroelectric to antiferroelectric exists at near 195 °C. On the other hand, another KTSN ceramics seem to have no second phase transition from ferroelectric to antiferroelectric resulting in the good temperature dependence of piezoelectric properties in the working temperature range.

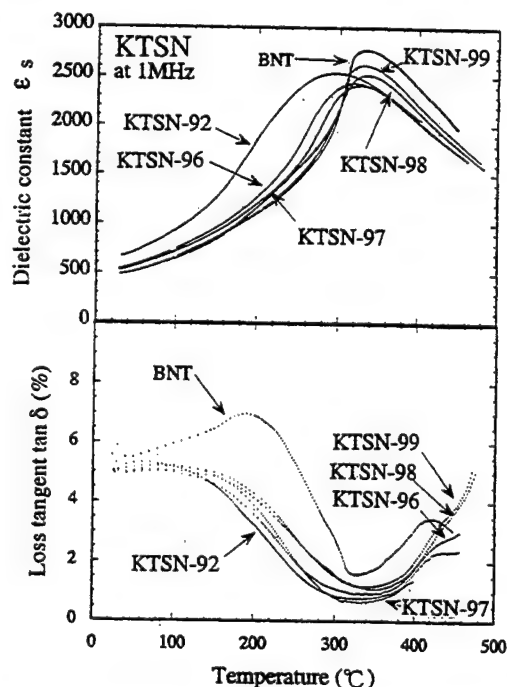


Fig. 3. Temperature dependence of dielectric constant, ϵ_s , and loss tangent, $\tan\delta$, in KTSN(100/0/0, 99/0.5/0.5, 98/1/1, 97/1.5/1.5, 96/2/2 and 92/4/4) at 1 MHz.

Figure 4 shows the electromechanical coupling factors, k_{33} and k_p , of KTSN as a function of modified $1/2(\text{Bi}_2\text{O}_3\text{-Sc}_2\text{O}_3)\text{-KNbO}_3$. The optimum poling condition of the KTSN

system is achieved to the poling field, $E_p \approx 8 \sim 9$ kV/mm, the poling temperature, $T_p = \text{R.T.}$ and the poling time, $t_p = 15$ min. The coupling factor, k_{33} , for KTSN(99/0.5/0.5) displays a maximum value of 0.44. Figure 5 shows piezoelectric strain constants, d_{33} , and free permittivity, $\epsilon_{33}^T/\epsilon_0$, as a function of modified $1/2(\text{Bi}_2\text{O}_3\text{-Sc}_2\text{O}_3)\text{-KNbO}_3$. The maximum d_{33} is 92×10^{-12} C/N for KTSN(96/2/2). The $\epsilon_{33}^T/\epsilon_0$ becomes larger with increasing the amount of $1/2(\text{Bi}_2\text{O}_3\text{-Sc}_2\text{O}_3)\text{-KNbO}_3$.

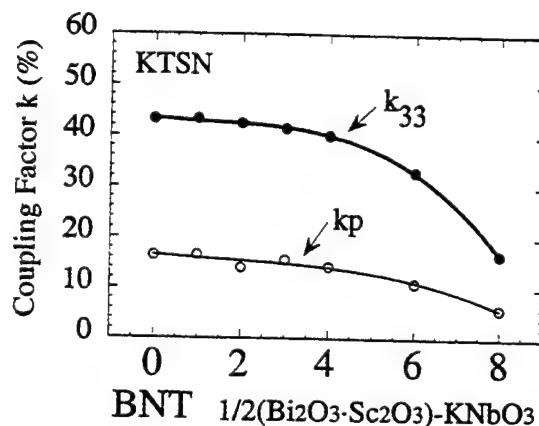


Fig. 4. Electromechanical coupling factors, k_{33} and k_p , of KTSN ceramics as a function of the amount of modified $1/2(\text{Bi}_2\text{O}_3\text{-Sc}_2\text{O}_3)\text{-KNbO}_3$.

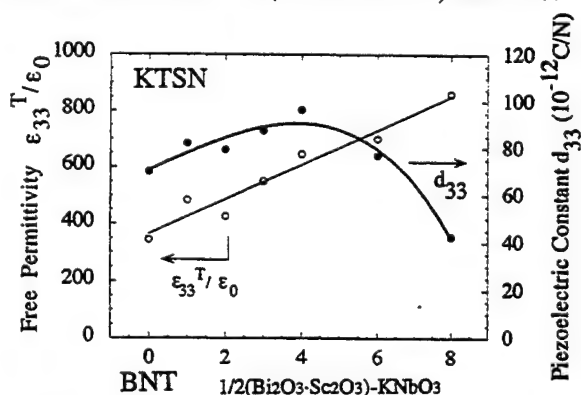


Fig. 5. Free permittivity, $\epsilon_{33}^T/\epsilon_0$, and piezoelectric constant, d_{33} , of KTSN ceramics as a function of the amount of modified $1/2(\text{Bi}_2\text{O}_3\text{-Sc}_2\text{O}_3)\text{-KNbO}_3$.

Table I summarizes the dielectric, piezoelectric and elastic properties of KTSN(99/0.5/0.5). KTSN ceramics seem to be superior as lead-free piezoelectric ceramics having a relatively low free permittivity, $\epsilon_{33}^T/\epsilon_0$ (~ 480), a high electromechanical coupling factor,

k_{33} (>0.4), and a high frequency constant, N_p (~ 3200 Hz·m). These data are comparable to those of other BNT-based lead-free system [13].

Table I Piezoelectric properties of KTSN (99/0.5/0.5) ceramic.

| | | |
|------------------------|---|---------------|
| Dielectric constant | $\epsilon_{33}^T/\epsilon_0$ | 483 |
| Loss tangent | $\tan\delta$ (%) | 5.12 |
| Curie temperature | T_c (°C) | 328 |
| Coupling factor | k_{33} | 0.434 |
| | k_p | 0.166 |
| Frequency constant | N_{33} (Hz·m) | 2521 |
| | N_p (Hz·m) | 3199 |
| Piezoelectric constant | d_{33} (pC/N) | 82.1 |
| Elastic constant | s_{33} ($\times 10^{-12}$ m ² /N) | 8.37 |
| Density (ratio) | ρ_0 | 5.78 (95.9 %) |

4. CONCLUSIONS

Dielectric, ferroelectric and piezoelectric properties of a -(Bi_{1/2}Na_{1/2})TiO₃- b -1/2(Bi₂O₃-Sc₂O₃)- c -KNbO₃ [KTSN (100a/100b/100c)] solid solution were studied. X-ray diffraction data show that KTSN ceramics are rhombohedral phase at room temperature. Well-sintered ceramics, with measured density ratios over than 93 %, were obtained in an uncontrolled atmosphere. The KTSN ceramics with a relatively low free permittivity, $\epsilon_{33}^T/\epsilon_0$, and a high electromechanical coupling factor, k_{33} , are a candidate for lead-free piezoelectric ceramics.

REFERENCES

- [1] G. A. Smolensky, V. A. Isupov, A. I. Agranovskaya and N. N. Krainik, "New Ferroelectrics of Complex Composition. IV", *Soviet Physics- Solid State*, vol. 2, pp.2651-2654, May, 1961.
- [2] C. F. Buhrer, "Some Properties of Bismuth Perovskites", *J. Chem. Phys.*, vol. 36, pp.798-803, February, 1962.
- [3] K. Sakata and Y. Masuda, "Ferroelectric

and Antiferroelectric Properties of (Na_{0.5}Bi_{0.5})TiO₃-SrTiO₃ Solid Solution Ceramics", *Ferroelectrics*, vol. 7, pp.347-349, 1974.

[4] T. Takenaka and K. Sakata, "New Piezo- and Pyroelectric Sensor Materials of (BiNa)_{1/2}TiO₃-based Ceramics", *Sensors and Materials*, vol. 1, pp.123-131, 1988.

[5] T. Takenaka and K. Sakata, "Dielectric, Piezoelectric and Pyroelectric Properties of (BiNa)_{1/2}TiO₃-Based Ceramics", *Ferroelectrics*, vol. 95, pp.153-156, 1989.

[6] T. Takenaka, K. Sakata and K. Toda, "Acoustic Wave Characteristics of Lead-Free (Bi_{1/2}Na_{1/2})_{0.99}Ca_{0.01}TiO₃ Piezoelectric Ceramic", *Jpn. J. Appl. Phys.*, vol. 28, Suppl. 28-2, pp.59-62, 1989.

[7] T. Takenaka, K. Sakata and K. Toda, "Piezoelectric Properties of (Bi_{1/2}Na_{1/2})TiO₃-Based Ceramics", *Ferroelectrics*, vol. 106, pp.375-380, 1990.

[8] T. Takenaka, K. Maruyama and K. Sakata: *Jpn. J. Appl. Phys.* vol. 30, No. 9B, pp.2236-2239, 1991.

[9] T. Takenaka, Y. Naitou, N. Takahashi and K. Sakata, "(Bi_{1/2}Na_{1/2})TiO₃-PbTiO₃-BaTiO₃ Solid Solution for Piezoelectric Ceramics", *Proc. 1990 IEEE 7th International Symposium on Applications of Ferroelectrics* (IEEE, 1991) pp.313-316.

[10] H. Nagata and T. Takenaka: "Piezoelectric Ceramics of (Bi_{1/2}Na_{1/2})TiO₃-1/2(Bi₂O₃-Sc₂O₃) System", *Jpn. J. Appl. Phys.* vol. 36 (1997) (to be published).

[11] L. Egerton and D. M. Dillon: "Piezoelectric and Dielectric Properties of Ceramics in the System Potassium-Sodium Niobate", *J. Am. Ceram. Soc.*, vol. 42, No. 9, pp.438-442, 1959.

[12] T. Takenaka, A. Hozumi, T. Hata and K. Sakata: "Mechanical Properties of (Bi_{1/2}Na_{1/2})TiO₃-based Piezoelectric Ceramics", *Silicates Industries - Ceramic Science and Technology*, vol. 58, No.7-8, pp.136-142, 1993.

[13] T. Takenaka, T. Okuda and K. Takegahara: "Lead-Free Piezoelectric Ceramics based on (Bi_{1/2}Na_{1/2})TiO₃-NaNbO₃", *Ferroelectrics*, vol. 196, pp.175-178, 1997.

Effect of Grain Size on the Electromechanical Properties of Antiferroelectric-to-Ferroelectric Phase Switching PLSnZT Ceramics

Ming-Jen Pan and Shoko Yoshikawa

Materials Research Laboratory
The Pennsylvania State University
University Park, PA 16802 USA

Abstract—In this study, the effect of processing on the phase transformation behavior of antiferroelectric lead lanthanum stannate zirconate titanate (PLSnZT) ceramics was investigated. Specifically, the effects of sintering condition, and consequently grain size, were examined in order to address some practical issues. Sub-micron PLSnZT powder was made by using conventional solid state reaction and additional attrition milling. Samples were sintered at different temperature and dwell time to produce different grain sizes ranging from approximately 15 to 0.5 μm . It was found that the sintering temperature for producing fully dense samples can be as low as 950°C with attrition-milled powder. The electrical properties of the samples were the same when the sintering temperature is higher than 1000°C. Below 1000°C, sample performance begins to deteriorate, possibly because of either excess lead remaining in the samples or the lack of domain formation in sub-micron grains. It was also found that decreased grain size can increase mechanical strength by 30%.

I. INTRODUCTION

The high electric field-induced strain in lead lanthanum stannate zirconate titanate (PLSnZT) family of ceramics has been of interest for high performance actuators and transducers. It was established by Berlincourt [1] that the antiferroelectric tetragonal (AFE_{tet}) phase can be readily switched to ferroelectric rhombohedral (FE_{rh}) phase with the application of an electric field. This antiferroelectric-to-ferroelectric (AFE-FE) phase transition is accompanied by a large volume strain, which is a result of the larger FE_{rh} cell as compared to the AFE_{tet} . Previous studies reported strain as high as 0.85% [2,3], although other crystallographic analyses based on X-ray diffraction have shown that 0.5% is the maximum strain possible for an ideal single crystal in this system [4,5]. For polycrystalline samples, strain of 0.2% should be readily achievable at the AFE-FE switching field [6,7].

Because of their high tin content, PLSnZT ceramics are usually sintered at temperatures higher than 1300°C, where lead volatility can cause serious quality control problems. In order to alleviate such problems, attempts were made to improve the material production process, especially the

possibility of using sub-micron powder to improve the reactivity during sintering. In this way, the sintering temperature can be lowered, thus improving consistency during production. More importantly, the ability to alter the sintering condition, and consequently grain size, provided an effective means to optimize material properties. As PLSnZT ceramics have been extensively studied in previous reports [6,7], the composition $\text{Pb}_{0.98}\text{La}_{0.02}(\text{Sn}_{0.33}\text{Zr}_{0.55}\text{Ti}_{0.12})_{0.995}\text{O}_3$ which offers reasonable strain and hysteresis was chosen for this study.

II. EXPERIMENTAL PROCEDURE

A. Sample Preparation

The composition (B1) used in this study is shown in Fig. 1. Stoichiometric ceramic powder was prepared by solid state reaction, using the appropriate amounts of reagent grade raw materials. Calcined powders were examined by X-ray diffraction (XRD) to insure phase purity. Typically, the samples showed a tetragonal structure within the detection limit of XRD. Calcined powder was then attrition-milled for 8 hours to reduce the particle size. The milled powder was

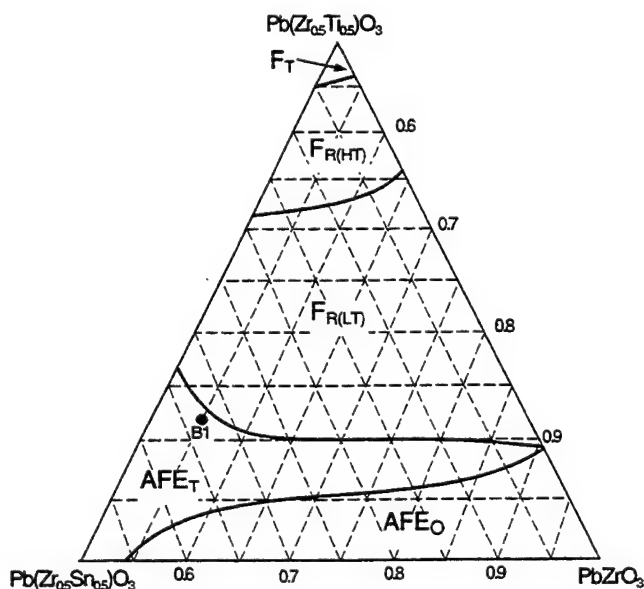


Fig. 1 PLSnZT ternary phase diagram

dried and then re-calcined at a lower temperature to improve its homogeneity. Finally, the powder was attrition-milled again and dried. The finished particle surface area was 9.1 m²/gram.

The sintering process was carried out in a lead rich environment in order to minimize lead volatilization. Samples were sintered at different temperatures and dwell times to produce different grain sizes. Table I shows a list of conditions and the resulted density and grain size. The samples were pale yellow after sintering and remained this color throughout processing.

For electrical measurements, disk samples (with diameter 11 mm and thickness 0.3 mm) were then prepared by polishing to achieve flat and parallel surfaces onto which gold was sputtered. For mechanical strength, bar samples (30 mm x 2 mm x 2 mm) were prepared and the edges were slightly chamfered to eliminate machining defects.

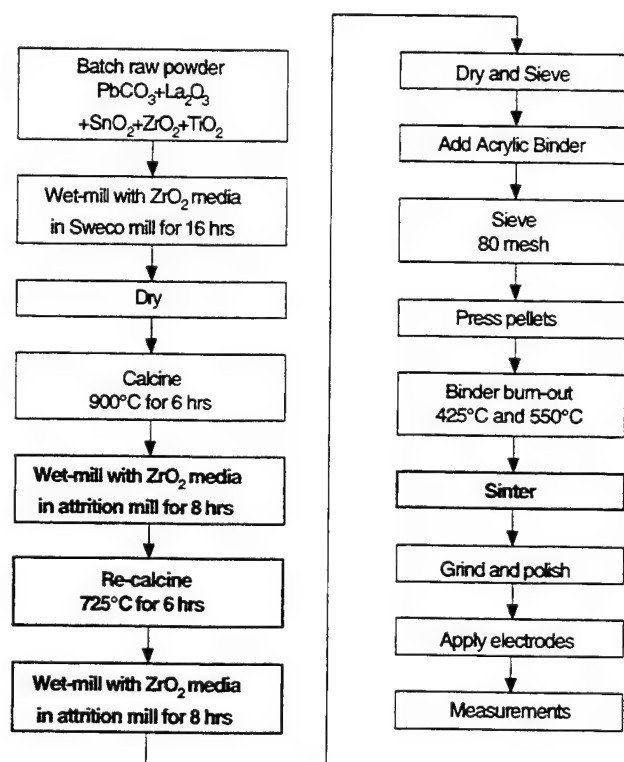


Fig. 2 Processing flow chart

B. Characterization

High-field measurements included polarization and strain hysteresis using a computer-controlled modified Sawyer Tower circuit and a linear variable displacement transformer (LVDT) driven by a lock-in amplifier (Stanford Research Systems, Model SR830). The voltage was supplied using a Trek 609C-6 high voltage DC amplifier. Through the LVDT, the strain of the samples can be measured with the application of an applied field. Electric fields as high as 70

TABLE I
LIST OF SINTERING CONDITIONS AND RESULTS

| Sintering Condition | Density (g/cm ³) | Weight Loss (%) | Grain Size (μm) |
|---------------------|------------------------------|-----------------|-----------------|
| A. 1300°C/10hrs | 8.12 | 1.72 | 10-20 |
| B. 1300°C/2hrs | 8.15 | 1.42 | 5-10 |
| C. 1200°C/2hrs | 8.22 | 1.32 | 3-5 |
| D. 1150°C/2hrs | 8.23 | 1.33 | 1.5-3 |
| E. 1100°C/2hrs | 8.28 | 1.20 | 1-2 |
| F. 1000°C/2hrs | 8.20 | 0.78 | 0.8-1.5 |
| G. 975°C/4hrs | 8.04 | 0.69 | 0.5-1 |
| H. 950°C/6hrs | 8.18 | 0.78 | 0.5-1 |
| J. 975°C/2hrs | 7.76 | 0.51 | 0.5-1 |

kV/cm were applied using an amplified sine waveform at 0.2 Hz. During testing the samples were submerged in Fluorinert (FC-40, 3M, St. Paul, MN), an insulating liquid, to prevent arcing. For mechanical strength, the samples were subjected to three-point bend test on an Instron machine (Model 4212, Instron Corp., Canton, MA).

III. RESULTS AND DISCUSSION

A. Microstructure

As shown in Table I, fully dense ceramics can be achieved at temperature as low as 950°C, with the exception of condition J. The weight loss due to lead volatilization decreases with decreasing sintering temperature. Depending on sintering conditions, the grain size varies from 15 μm to 0.5 μm. Some of the microstructures obtained under different conditions are shown in figure 3. Fully dense, well-defined microstructures are clearly visible.

B. Electrical Properties

The polarization and strain behaviors of these samples are shown in Figure 4. There is no difference in their properties when sintered at temperatures higher than 1000°C. Nevertheless, below 1000°C (conditions F, G, and H) the properties begin to deteriorate. The AFE-FE phase switching becomes more diffuse and both the polarization and strain level decrease. In particular, condition J (Figure 5a) shows only lossy hysteresis loops and no antiferroelectric characteristics.

This observation is attributed to two possible reasons. First is the existence of excess lead oxide along grain boundaries. This is partially evidenced by the decreasing weight loss with decreasing sintering temperature. Because of the low sintering temperatures, excess lead oxide did not have enough vapor pressure to escape completely. The excess lead residing along grain boundaries contributes to space charge and thus reduces the electric field that the grains actually

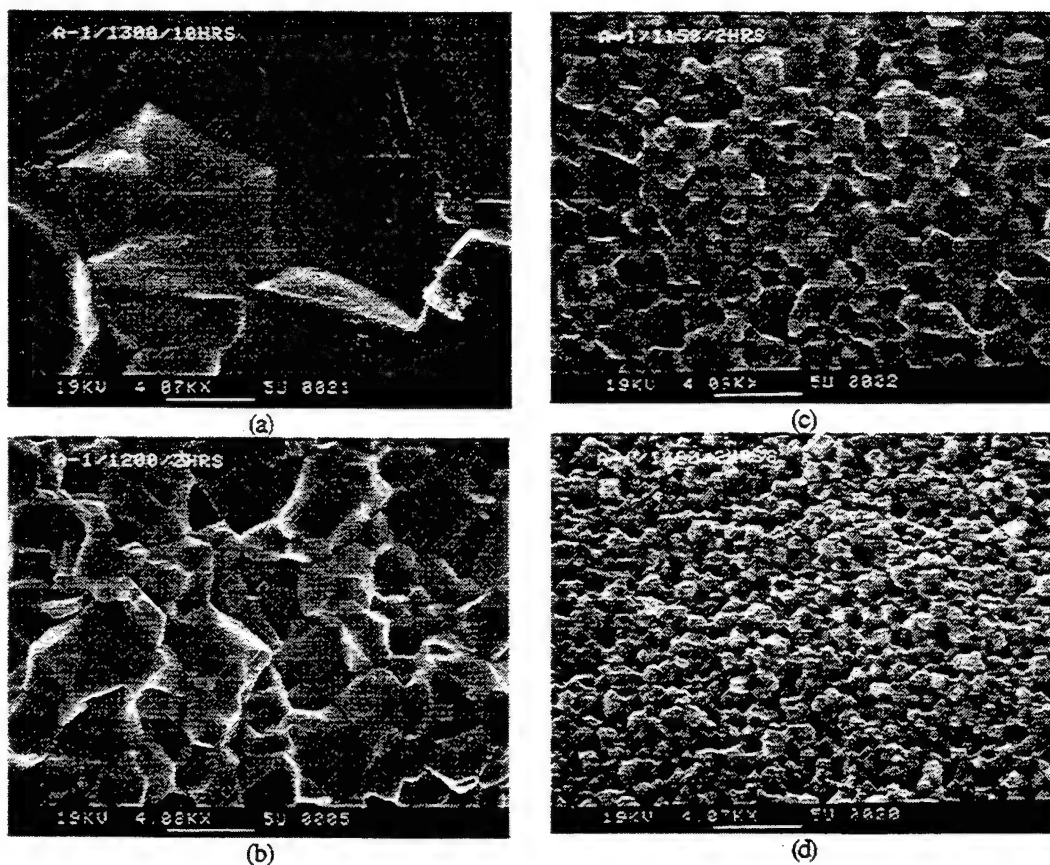


Fig. 3 Microstructures of some sintered samples: (a) 1300°C/10hrs, (b) 1200°C/2hrs, (c) 1150°C/2hrs, and (d) 1000°C/2hrs.

experience. If one takes a sample sintered under condition J and anneal it at 850°C for 12 hours in oxygen to remove excess lead, the hysteresis loops will shift towards those of the high-fired samples (Figure 5b).

Second possibility is the reduced tetragonality/crystallinity, which could be the result of the lack of domain formation or the low sintering temperature and thus low energy state. As shown in Figure 6, the X-ray diffraction patterns of {002} peaks clearly shows the trend of shifting tetragonality.

C. Flexural Strength

As shown in Table II, the flexural strengths of these materials are comparable to those of conventional PZTs. But more importantly, the samples sintered at 1100°C/2hrs show remarkable improvement in strength compared to other conditions. The 30% higher strength is very favorable for actuator applications as most actuators are meant to carry some form of mechanical load.

IV. CONCLUSIONS

Sub-micron ceramic powder can be produced by adding attrition-milling, re-calcining, and a second attrition-milling

to a normal solid state reaction process. Powder surface area can reach 9 m²/gram. Using this powder, samples of different grain sizes were made by adjusting sintering temperature and dwell time. It was found that fully dense ceramics with good electrical properties and superior mechanical properties can be sintered at temperatures as low as 1000°C. More importantly, this low sintering temperature implies that silver:palladium electrodes, instead of platinum, can be used for co-fired multilayer actuators to reduce production cost.

TABLE I
MECHANICAL STRENGTHS OF SAMPLES SINTERED UNDER VARIOUS CONDITIONS

| Sintering Condition | Mechanical Strength (MPa) | Standard Deviation (MPa) |
|---------------------|---------------------------|--------------------------|
| A. 1300°C/10hrs | 101 | 5 |
| B. 1300°C/2hrs | 103 | 5 |
| C. 1200°C/2hrs | 113 | 4 |
| D. 1150°C/2hrs | 120 | 5 |
| E. 1100°C/2hrs | 131 | 8 |
| F. 1000°C/2hrs | 103 | 9 |
| G. 975°C/4hrs | 98 | 7 |
| H. 950°C/6hrs | 89 | 8 |

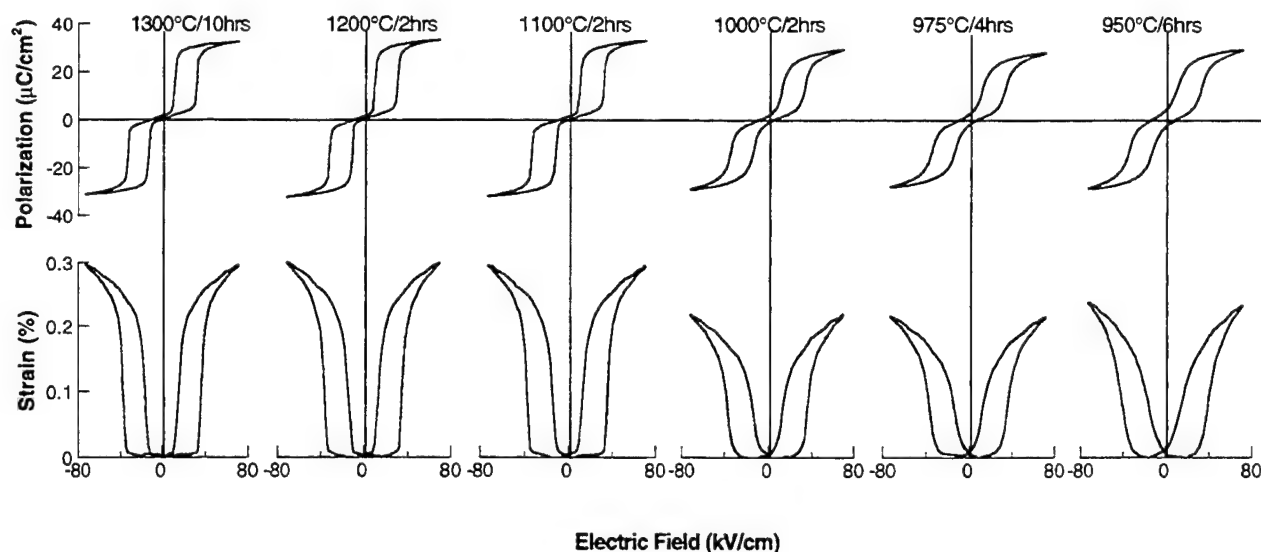


Fig. 4 The polarization and strain behaviors of samples sintered under various conditions

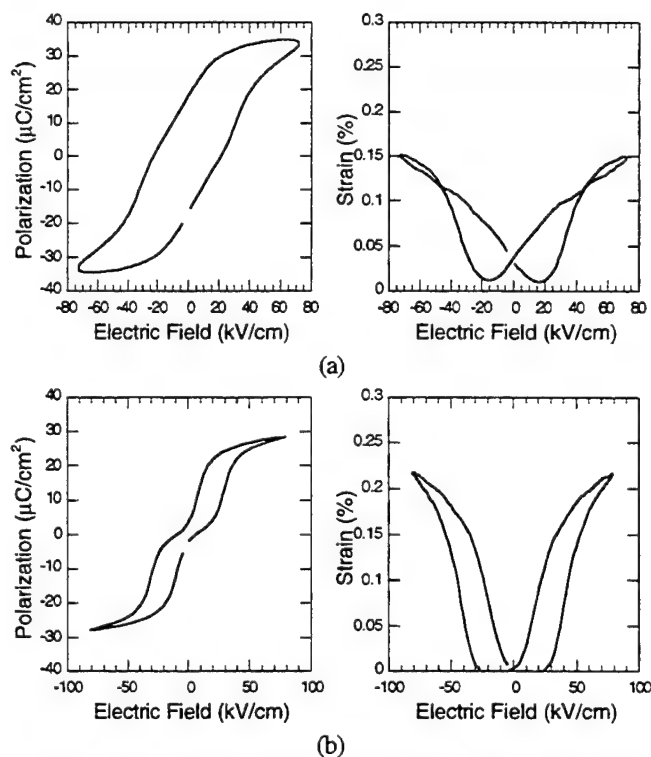


Fig. 5 (a) Lossy polarization and strain loops of samples sintered at 975°C/2hrs and (b) after being annealed at 850°C/12hrs in oxygen.

REFERENCES

- [1] D. Berlincourt, "Transducers Using Forced Transitions between Ferroelectric and Antiferroelectric States," *IEEE Transactions on Sonics and Ultrasonics*, Vol. SU-13 [4] 116-125 (1966).
- [2] W. Pan, Q. Zhang, A. Bhalla, and L.E. Cross, "Field-Forced Antiferroelectric-to-Ferroelectric Switching in Modified Lead

Zirconate Titanate Stannate Ceramics," *J. Am. Ceram. Soc.*, **72** [4] 571-78 (1989).

- [3] W.Y. Pan, C.Q. Dam, Q.M. Zhang, and L.E. Cross, "Large Displacement Transducers Based on Electric Field Forced Phase Transition in the Tetragonal $(\text{Pb}_{0.97}\text{La}_{0.02})(\text{Ti,Zr,Sn})\text{O}_3$ Family of Ceramics," *J. Appl. Phys.*, **66** [12] 6014-23 (1989).
- [4] C.T. Blue, J.C. Hicks, S.-E. Park, S. Yoshikawa, and L.E. Cross, "In situ X-Ray Diffraction Study of the Antiferroelectric-ferroelectric Phase Transition in PLSnZT ," *Appl. Phys. Lett.*, **68** [21] 2942-44 (1996).
- [5] L. Shebanov, M. Kusnetsov, and A. Sternberg, "Electric Field-Induced Antiferroelectric-to-Ferroelectric Phase Transition in Lead Zirconate Titanate Stannate Ceramics Modified with Lanthanum," *J. Appl. Phys.*, **76** [7] 4301-4 (1994).
- [6] K.A. Markowski, S.-E. Park, S. Yoshikawa, and L.E. Cross, "Effect of Compositional Variations in the Lead Lanthanum Zirconate Stannate Titanate System on Electrical Properties," *J. Am. Ceram. Soc.*, **79** [12] 3297-304 (1996).
- [7] S.-E. Park, K.A. Markowski, S. Yoshikawa, and L.E. Cross, "Effect on Electrical Properties of Barium and Strontium Additions in the Lead Lanthanum Zirconate Stannate Titanate System," *J. Am. Ceram. Soc.*, **80** [2] 407-12 (1997).

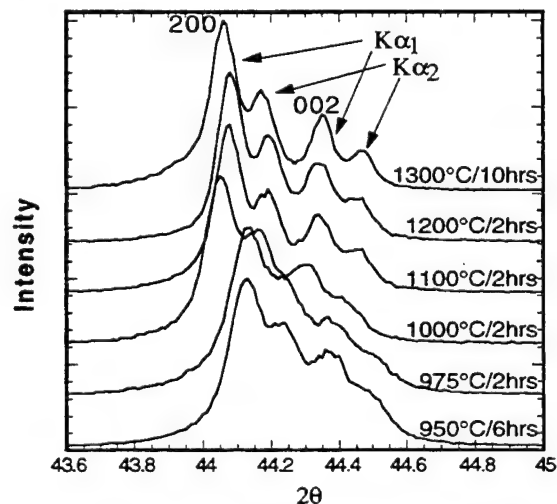


Fig. 6 XRD patterns show decreased crystallinity with decreasing sintering temperature

Technique for Measuring Electromechanical Coupling in Electrostrictors and Piezoelectrics

Sean P. Leary and Steven M. Pilgrim
New York State College of Ceramics at Alfred University
120 McMahon Building
Alfred, NY 14802

Abstract—The nonlinear and frequency-dependent response of electrostrictors, such as lead magnesium niobate (PMN), prohibits the determination of electromechanical coupling by standard methods used for piezoelectrics. A technique based on measuring the maximum input electrical energy and the maximum mechanical energy stored was developed; which is applicable to both piezoelectrics and electrostrictors.

I. INTRODUCTION

Modified lead magnesium niobate (PMN) exhibits large electrically induced nonlinear strains ($>0.07\%$) at moderate drive fields (~ 1.0 kV/mm) and low frequencies. Coupling a large dc bias with a small ac field induces a (mostly) linear response. PMN is also a relaxor ferroelectric and therefore the dielectric properties are strongly dependent on frequency [1].

Measurement of electromechanical coupling of traditional piezoelectrics is usually performed by applying a small electric field and measuring the frequencies at series and parallel resonance (or maximum and minimum admittance) [2]. This is known as the dynamic method. Unfortunately, materials with strain responses having no linear dependence on applied field do not possess a resonance response, therefore the coupling can not be determined in an unbiased state [3]. Harmonic distortion in the response of nearly linear materials can also affect the results obtained by the dynamic method [4]. The field and frequency dependence of linear loss angle is another source of error [5].

A different procedure for calculating electromechanical coupling, k , has been developed based on the ratio of the maximum mechanical energy, W_m , stored to the maximum input electrical energy, W_e , from the power source [6]:

$$k = \sqrt{\frac{W_m}{W_e}} \quad (1)$$

The total instantaneous power delivered to the electroactive sample is given by the product of the voltage applied and the resulting current. This power

can be expressed per unit volume in terms of the electric field, E , and polarization, P :

$$(\text{power})_{\text{elec}} = E \cdot \frac{dP}{dt} \quad (2)$$

The average value of this power signal represents energy dissipated as heat. The power per unit volume associated with the coupled mechanical motion can be expressed as:

$$(\text{power})_{\text{mech}} = YS \cdot \frac{dS}{dt} \quad (3)$$

In general, the strain, S , and the elastic modulus, Y , are functions of the applied field.

II. EXPERIMENTAL PROCEDURE

Commercial-grade PMN-based samples of composition: $0.8375\text{Pb}(\text{Mg}_{1/3}\text{Nb}_{2/3})\text{O}_3 - 0.1375\text{PbTiO}_3 - 0.025\text{SrTiO}_3$ (Lockheed Martin) and lead zirconate titanate PZT-8 (Navy III; Lockheed Martin) were used in this study. Polarization was measured using a Sawyer-Tower circuit: consisting of the sample in series with a low-impedance capacitor. A 1 Hz ac signal was generated by a Hewlett Packard 8904 waveform synthesizer and amplified by a Trek 610C high voltage amplifier. Longitudinal and transverse strains were determined using an MTI 2000 ftonic™ sensor and strain gauges (Micro-Measurements) respectively. The field dependence of the elastic stiffness was determined using the pulse-echo method at 10 MHz; while simultaneously applying a low frequency quasi-static voltage of high amplitude. A Tektronix TDS420 oscilloscope and Iotech ADC488/8SA were used for analog-to-digital conversion. The maximum input electrical, W_e , and the maximum mechanical energy, W_m , stored were calculated as the time-integral of a quarter cycle of the respective power signals. The average power dissipated as heat was evaluated from the dc-component of the discrete Fourier transform of (3) over one complete period.

III. RESULTS AND DISCUSSION

Fig. 1 shows the polarization and strain response of a PMN-PT-ST sample for an ac field of amplitude 1.0 kV/mm and frequency of 1.0 Hz. The resulting induced strains are shown in Fig. 2 for both the longitudinal and transverse cases. A significant decrease of the elastic stiffness with applied field was observed in PMN (Fig. 3); while the modulus of PZT was only weakly dependent on field (Fig. 4). The electrical and mechanical power signals used to calculate coupling are displayed in Figs. 5-6. Longitudinal and transverse coupling coefficients were calculated as a function of ac drive field (Fig. 7). For electric fields with amplitudes near 1.0 kV/mm, nominal values of coupling exceeded 0.5.

IV. CONCLUSIONS

Electromechanical coupling can be calculated for nonlinear electroactive materials based on energy considerations. The proposed method is also valid for linear materials and can be used for situations involving high drive fields and a wide range of frequencies below resonance.

ACKNOWLEDGMENT

Funding provided by NUWC contract #66604-96-C-1416.

REFERENCES

- [1] L.E. Cross, "Relaxor ferroelectrics", *Ferroelec.*, vol. 76, pp.24-67, 1987.
- [2] "IEEE Standard on Piezoelectricity," *ANSI-IEEE Std. 176*, 1987. (IEEE: New York, 1987).
- [3] W. P. Mason, "Electrostrictive effect in barium titanate ceramics," *Phys. Rev.*, vol. 74, no. 9, pp. 1134-47, Nov. 1948.
- [4] R. Holland and E. P. Eer Nisse, "Accurate measurement of coefficients in a ferroelectric ceramic," *IEEE Trans. Sonics and Ultrasonics*, vol. 16, pp.173-181, 1969.
- [5] K. H. Hardtl, "Electrical and mechanical losses in ferroelectric ceramics," *Ceram. Inter.*, vol. 8, no. 4, pp.121-7, 1982.
- [6] D. A. Berlincourt, "Piezoelectric and ferroelectric energy conversion," *IEEE Trans. Sonics and Ultrasonics*, vol. 15, no. 2, pp. 89-97, April 1968.

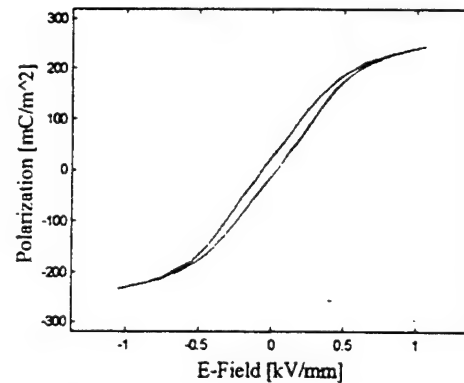


Fig. 1. Polarization hysteresis loop for PMN-PT-ST sample.

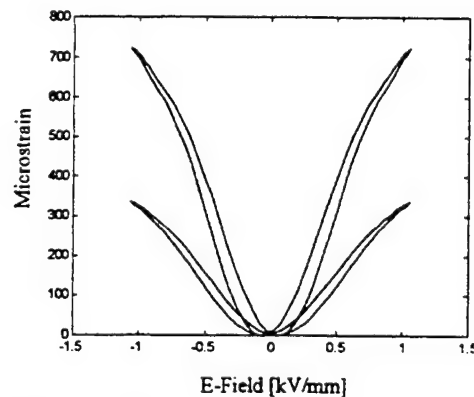


Fig. 2. Longitudinal and transverse strain as a function of applied electric field for PMN-PT-ST.

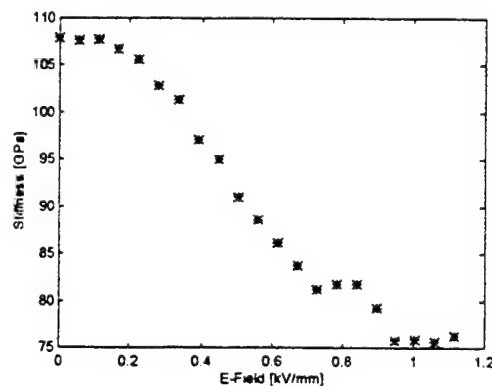


Fig. 3. Elastic modulus as a function of applied field for PMN-PT-ST.

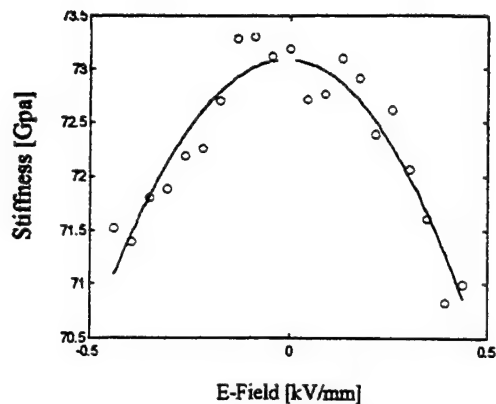


Fig. 4. Elastic modulus as a function of field for PZT-8 sample.

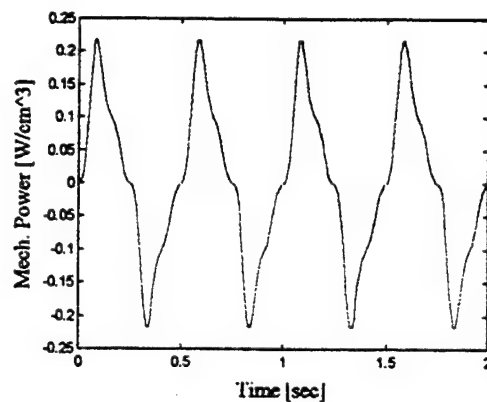


Fig. 6. Mechanical power stored by PMN-PT-ST sample.

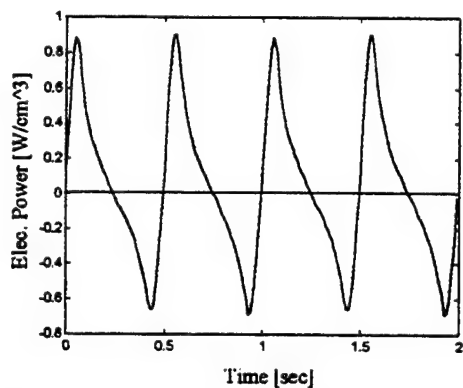


Fig. 5. Electrical power absorbed by PMN-PT-ST specimen. Solid line indicates average power.

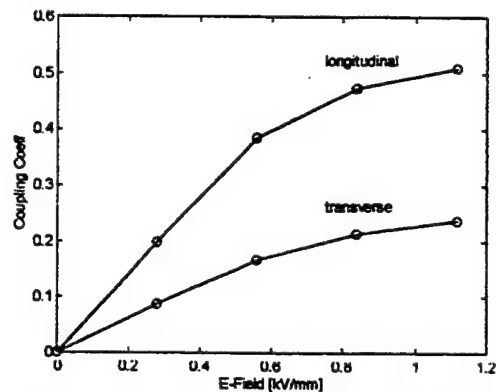


Fig. 7. Electromechanical coupling in PMN-PT-ST as a function of ac drive field amplitude.

Flexural Failure of Navy Type III PZT

Lynn Ewart

Naval Undersea Warfare Center
Code 2131, Building 1170
1176 Howell Street
Newport, RI 02841-1708

Abstract – In this study Navy Type III lead zirconium titanate (PZT) is stressed to failure in bending to examine its flexural behavior and strength limiting defects. Flexural strengths and Weibull moduli are reported for both unpoled and poled PZTs. Scanning electron microscopy reveals that aggregates and pores are the dominant critical flaw types. Strength differences between ceramics are attributed, in some cases, to flaw size and location and, in other cases, to differences in fracture toughness. Fracture toughness values are calculated and are discussed with respect to the trends reported in the literature. Comparison is made between the strength, Weibull modulus and fracture toughness values of the PZTs and of several doped lead magnesium niobates in solid solution with lead titanate (PMN-PT).

I. INTRODUCTION

PZT is commonly used as the active element in sonar transducers. For deep water use and high drive conditions it is typically subject to a compressive prestress. And, during active use PZT experiences considerable mechanical stress. Yet, the mechanical properties of PZT are not well characterized. Research measuring strength and fracture toughness (K_{IC}) and examining the microstructural mechanisms of failure of lead zirconium titanate based ceramics has been performed in tension as well as compression [1-5]. However, conflicting trends have been reported for the K_{IC} values of unpoled relative to poled piezoelectric ceramics [1,2].

Misalignment of a compressive load can create bending stresses. Yet, the examination of flexural behavior has been largely neglected. In this study flexural testing is employed to measure flexural strengths and Weibull moduli, to identify native strength limiting defects and to calculate the K_{IC} values of both unpoled and poled Navy Type III PZTs. Comparison of the measured mechanical properties of PZT to those of doped PMN-PT are made. The current results demonstrate that both unpoled and poled PZT performs better mechanically than PMN-PT.

II. EXPERIMENTAL PROCEDURE

The flexural failure of three Navy Type III PZTs was examined. The poled PZTs were manufactured by Lockheed Martin and EDO Corporations. The unpoled PZT was manufactured by EDO Corporation. For comparison, three

doped PMN-PTs with 10 mol% lead titanate were tested; two 3 wt% barium doped PMN-PTs manufactured by Lockheed Martin and TRS Ceramics, and one 1 wt% lanthanum doped PMN-PT manufactured by TRS Ceramics.

All six of the ceramics were machined into bend bars measuring 3 mm x 4 mm x 45 mm. Poling was across the 3 mm dimension in the case of the two poled PZTs. Specimens were tested under short circuit conditions in 4-point flexure according to ASTM Standard C 1161-90. Poled specimens were oriented so that crack propagation and failure would occur parallel to the poling direction. Thirty specimens of each of the PZTs were tested. The number of PMN-PT specimens varied between 25 and 30 per material.

After failure, microstructural examination of the fracture surfaces was performed on an Amray 1820 scanning electron microscope. Dimensions of the critical flaws were measured off of photomicrographs. For surface located flaws the flaw dimension along the tensile surface is designated "2c", and the flaw dimension perpendicular to the tensile surface is designated "a". For volume located flaws the flaw dimension parallel to the tensile surface is designated "2c", and the flaw dimension perpendicular to the tensile surface is designated "2a". The calculated flaw depths are an average of the depths of all the identifiable fracture origins. Surface fracture origins have a depth of zero.

Fracture toughness values were calculated using specimens which failed from flaws located on the tensile surface. The measured flaw dimensions and the peak failure stress were substituted in the stress intensity factor equation for a surface flaw in bending derived by Newman and Raju [6]:

$$K = \sigma \sqrt{\pi a} \cdot (MSH_1) / \Phi \quad (1)$$

where:

$$M = (1.13 - 0.09\alpha) + (-0.54 + (0.89/(0.2 + \alpha)))\beta^2 + \{0.5 - (1/(0.65 + \alpha)) + 14.0(1 - \alpha)^{2.5}\}\beta^4 \quad (2)$$

$$\Phi^2 = 1 + 1.464\alpha^{1.65} \quad (3)$$

$$S = (1.1 + 0.35\beta^2) \sqrt{\alpha} \quad (4)$$

$$H_1 = 1 - (0.34 + 0.11\alpha)\beta \quad (5)$$

and σ is the stress at failure, a is the flaw dimension perpendicular to the tensile surface, $\alpha=a/c$, $\beta=a/t$ and t is the specimen thickness (≈ 3 mm in this study).

III. RESULTS

The average flexural strengths and the Weibull moduli for the unpoled and poled PZTs are reported in Table I. The EDO unpoled PZT has both a lower strength and a lower Weibull modulus than either of the poled materials. The strength of 82 MPa for the EDO unpoled PZT is 24% less than the strength of 108 MPa for the EDO poled PZT. The Lockheed Martin poled PZT has a flexural strength of 113 MPa making it comparable in strength to the EDO poled PZT. The two poled PZTs have approximately the same Weibull modulus as well. The load versus crosshead displacement curves revealed some difference between the manufacturers. The curves for the Lockheed Martin poled PZT are slightly nonlinear, whereas the curves for both EDO PZTs are linear.

The flexural strengths and Weibull moduli of the PMN-PT ceramics are also given in Table I. On average, these ceramics are weaker than any of the PZTs tested. The Lockheed Martin barium doped PMN-PT has the lowest Weibull modulus of all six ceramics. However, while the PMN-PTs produced by TRS Ceramics are the weakest of the tested ceramics, they have the highest Weibull moduli of 24 and 23 for the barium and lanthanum doped materials, respectively.

Fractography on the PZTs revealed that the critical flaws are pores and aggregates. In the poled PZTs failure was caused predominately by pores. Pores comprised 63% and 57% of the fracture origins in the EDO and Lockheed Martin materials, respectively. Aggregates were found at 27% of both the EDO and the Lockheed Martin fracture origins. The remaining fracture origin flaws were unidentifiable. In the EDO unpoled PZT the majority of the failures, 53%, were caused by aggregates, whereas only 37% failed from pores. The remaining 10% of the specimens had unidentifiable flaws at the fracture origins.

The average size of the fracture origin flaws and their depth from the tensile surface varied among the PZTs, as seen in Table I. The EDO unpoled PZT has flaws which are,

on average, at least 2.5 times larger than those in the Lockheed Martin poled PZT. However, while the EDO unpoled PZT has the largest critical flaws, these flaws are typically located much deeper in the specimens compared to flaw depths in the other two PZTs.

Table I shows that the three PMN-PTs have fracture origin flaws which are all roughly the same size. The PMN-PT flaws are considerable larger than those found in the PZTs with the exception of the volume flaws in the EDO unpoled PZT which have an average size approximately the same as the PMN-PT flaws. Using the flaw dimensions and flexural strength for specimens failing from surface located fracture origins K_{Ic} values were calculated using (1) and their averages are reported in Table I.

IV. DISCUSSION

All three PZTs have flaw sizes at least ten times larger than the average grain size, which is about 5 μm , for these materials. With the K_{Ic} values given in Table I, a reduction in the flaw size down to 10 μm would double the flexural strength of the two poled PZTs and triple the strength of the EDO unpoled PZT. Among the identifiable flaws only two flaw types, pores and aggregates, were found. This should simplify the identification of the processing steps which need improvement.

The difference between the K_{Ic} values of the Lockheed Martin and the EDO poled PZTs, indicates that there is variability in the properties of nominally the same material when produced by different manufacturers. Even material from the same manufacturer has noticeable batch to batch differences. The EDO unpoled and poled PZTs come from different batches. The difference in average flaw size and depth between these two materials demonstrates the batch variability which occurs between processing runs at the same manufacturer. The two EDO PZTs have ostensibly the same K_{Ic} values. Thus, the effect of the difference in flaw size is clearly visible in their difference in strength. If the average flaw depth were the same for the two materials the strength difference would be even greater, as discussed below.

TABLE I
AVERAGE MECHANICAL PROPERTY AND FLAW DATA FOR PZT AND PMN-PT

| Material | Manufacturer | Flexural Stress (MPa) | Weibull Modulus | Average Flaw Size (μm) | | Critical Flaw Depth (μm) | Fracture Toughness K_{Ic} (MPa $\sqrt{\text{m}}$) |
|----------------|-----------------|--------------------------|-----------------|-------------------------------------|--------------------------------|---|--|
| | | | | Surface Flaws $2c \times a$ | Volume Flaws $2c \times 2a$ | | |
| Unpoled PZT | EDO | 82 ± 14 | 7 | 160×131 | 221×205 | 99 | 1.00 ± 0.08 |
| Poled PZT | EDO | 108 ± 10 | 13 | 88×61 | 129×85 | 49 | 0.98 ± 0.09 |
| Poled PZT | Lockheed Martin | 113 ± 11 | 11 | 64×37 | 49×40 | 12 | 0.80 ± 0.09 |
| PMN-PT w/3% Ba | Lockheed Martin | 60 ± 14 | 5 | 286×127 | 212×113 | 96 | 0.64 ± 0.09 |
| PMN-PT w/3% Ba | TRS Ceramics | 44 ± 2 | 24 | 225×124 | 219×131 | 14 | 0.58 ± 0.07 |
| PMN-PT w/1% La | TRS Ceramics | 48 ± 4 | 23 | 248×143 | 223×119 | 3 | 0.67 ± 0.07 |

Aggregates and pores are inherently volume distributed flaws. Consequently, the average critical flaw depth gives an indication of the relative population density of the flaws. An increasing average critical flaw depth indicates a decreasing flaw population density. Decreasing the population density of the flaws will improve the flexural strength. This is due to the fact that peak tensile stress is used to calculate flexural strength, but because of the stress gradient produced by bending the local stress at a volume distributed flaw decreases with the flaw's distance from the tensile surface.

While most researchers studying the fracture processes of piezoelectric ceramics have focused on the differences which occur between fracture parallel to and fracture perpendicular to the direction of poling, a few researchers have included the unpoled ceramic in their investigations. Okazaki [1] calculated the K_{Ic} of PLZT and found that the value of the unpoled material lies between the parallel K_{Ic} value (fracture parallel to the poling direction) and the perpendicular K_{Ic} value (fracture perpendicular to the poling direction). Specifically, the parallel K_{Ic} was highest. In contrast, research by Mehta and Virkar [2] calculated the highest K_{Ic} values in the unpoled PZT. However, they did calculate a higher value for the parallel K_{Ic} than for the perpendicular K_{Ic} , similar to Okazaki's results. Tanimoto, Yamamoto and Morii [3] recorded tensile strength behavior in PZT which is qualitatively similar to the PLZT behavior reported by Okazaki. The PZT was strongest when fractured parallel to the poling direction and weakest when fractured perpendicular to the poling direction. The strength of the unpoled material fell in between these two cases. If the assumption is made that the size of the native flaw population is the same for all three materials that Tanimoto, Yamamoto and Morii tested, then K_{Ic} values would show the same trend as reported by Okazaki.

In the current study, the EDO unpoled K_{Ic} value and the EDO parallel K_{Ic} value are effectively the same. Thus, it is instructive to examine the current results with respect to the microstructural mechanisms which are known to affect K_{Ic} in these ceramics. Okazaki [1] proposed that internal residual stresses created by poling cause directional differences in the value of K_{Ic} . There is not complete agreement in the literature as to the validity of this mechanism [2,4]. Further, calculations by Pohanka, Freiman and Bender [7] have indicated that the effect of internal stresses on strength (and consequently toughness) decreases as the flaw size increases relative to the grain size. In this study the flaw sizes are at least ten times larger than the grain size. Consequently, internal stresses are not expected to play a significant role in the fracture process.

Mehta and Virkar [2] explained their observed K_{Ic} differences in terms of domain realignment. Domain realignment occurs in both the poled and unpoled PZT as their x-ray

results indicate. Thus, in order to observe differences in K_{Ic} , domain realignment must occur more readily in one case than in the other. However, Mehta and Virkar could not explain why domain realignment was apparently most prevalent in the unpoled PZT.

The realignment of domains due to mechanical stress is affected by several factors. First, domain realignment occurs more readily in "soft" piezoelectric materials than in "hard" ones [5]. The PZT under investigation in this study is "hard". Second, domain realignment by 90° can typically be observed as a nonlinearity in the stress-strain curve. However, the EDO poled and unpoled PZT load versus crosshead displacement curves are all linear. Third, domain realignment is a time dependent process [2,5,8]. The speed at which fracture occurs has been shown to influence domain realignment. Mehta and Virkar [2] did not detect any domain realignment in specimens that failed from fast fracture. In the current study, fast fracture during flexural failure may inhibit domain realignment. Given these three factors domain realignment is not expected to contribute significantly to K_{Ic} in the current experiments.

Microcracking [7] and crack tip interactions with domains, seen as cleavage fracture, [9] have been suggested as toughening mechanisms in piezoelectric materials. Fig. 1 shows representative fracture surfaces from the EDO unpoled and poled PZTs. There is little evidence to support any contributions from these two toughening mechanisms. Qualitatively it appears that the poled PZT has slightly more intergranular fracture than the unpoled PZT, however, there are no striking differences in the fracture surfaces that would lead to an expectation that the K_{Ic} should be higher for one material compared to the other.

There is one factor which is expected to affect the K_{Ic} value of the poled PZT but not the unpoled PZT and which is not accounted for in the data in Table I. Pisarenko, Chushko and Kovalev [4] have pointed out the need to account for elastic anisotropy when calculating the K_{Ic} of poled piezoelectrics. They used both double-torsion and indentation tests to calculate K_{Ic} for different PZT and barium titanate compositions. In all cases the parallel K_{Ic} is higher than the perpendicular K_{Ic} . Pisarenko, Chushko and Kovalev did not include unpoled materials in the analysis. However, when elastic modulus is included in the derivation of the stress intensity factor, the resulting fracture toughness values are proportional to an effective elastic modulus. The effective modulus for the parallel K_{Ic} case, calculated from the relevant elastic constants, is larger than the estimated unpoled modulus for the PZTs Pisarenko, Chushko and Kovalev studied. Thus, including the effects of elastic anisotropy increases the calculated value of the parallel K_{Ic} relative to the unpoled K_{Ic} . Since the unpoled K_{Ic} and the parallel K_{Ic} values are ostensibly the same in the current

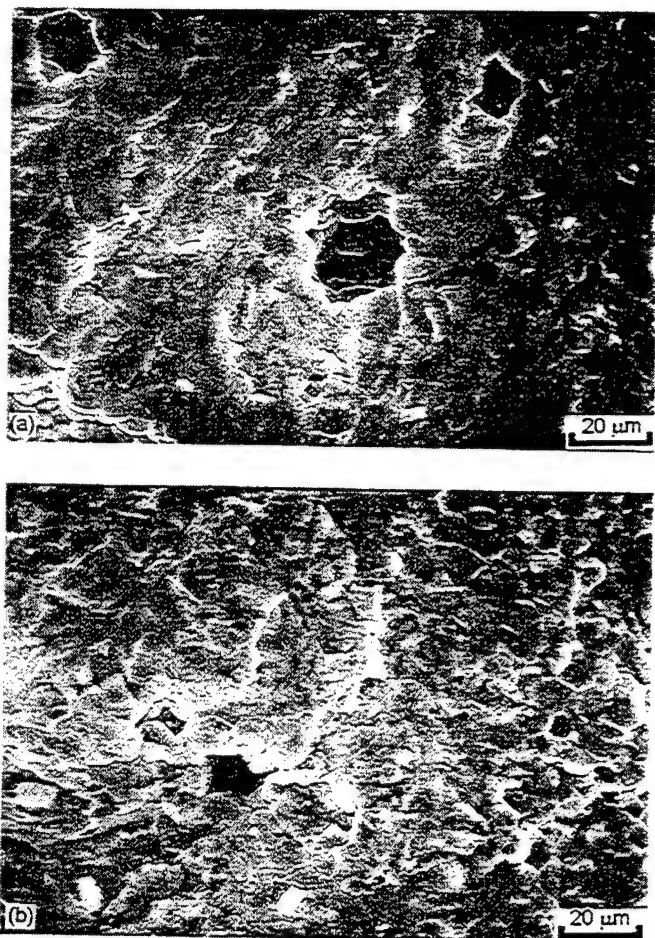


Fig. 1. Fracture surface of (a) EDO unpoled PZT, (b) EDO poled PZT

study, taking elastic anisotropy into account should increase the parallel K_{Ic} making the results of this study qualitatively the same as the results presented by Okazaki and Tanimoto, Yamamoto and Morii.

The research by Mehta and Virkar [2], which reports the highest K_{Ic} values for the unpoled material, it is not stated whether elastic anisotropy is taken into account in the K_{Ic} calculations. If it has not been taken into account, then recalculating the parallel K_{Ic} using an appropriate effective elastic modulus should increase the parallel K_{Ic} value. Depending upon the relative magnitudes of the relevant elastic constants for the material they tested it is possible that accounting for elastic anisotropy will lead to the parallel K_{Ic} having a higher value than the unpoled material, consistent with Okazaki, Tanimoto, Yamamoto and Morii, and the current study.

The Navy Type III PZTs in this study are all mechanically superior to the PMN-PTs. The K_{Ic} values and the strengths of the PZTs are higher than the respective values of the PMN-PTs. However, the PMN-PT flaw sizes are extremely large. Based upon the K_{Ic} values reported in Table I, reductions in these flaw sizes down to approximately 20 μm will

increase the strength of the PMN-PTs to approximately 115 MPa thus making them competitive with current Navy Type III PZTs.

V. CONCLUSIONS

The fracture origin flaws in the tested PZTs were predominately pores and aggregates. The flaw sizes varied considerably from batch to batch and from manufacturer to manufacturer. The average flaw size is at least 10 times larger than the average 5 μm grain size.

For nominally the same material K_{Ic} values also varied between manufacturers. Interestingly, unpoled and poled PZT from the same manufacturer had the same K_{Ic} values. It is believed that accounting for elastic anisotropies in the calculation of K_{Ic} for the poled PZT should increase its K_{Ic} value.

The PZTs studied have higher K_{Ic} values and smaller flaw sizes than the PMN-PTs tested. Consequently, the PZTs also have a higher strength than the PMN-PTs. Thus, Navy Type III PZT performs better mechanically than the current generation of PMN-PTs.

ACKNOWLEDGMENT

This work was sponsored by SPAWAR and the Office of Naval Research. The author wishes to thank Mr. Chris Bull for assistance with the mechanical testing.

REFERENCES

- [1] K. Okazaki, Mechanical behavior of ferroelectric ceramics, *Ceramic Bulletin*, vol. 63, pp. 1150-1157, 1984.
- [2] K. Mehta and A. V. Virkar, Fracture mechanisms in ferroelectric-ferroelastic lead zirconate titanate (Zr:Ti=0.54:0.46) ceramics, *J. Am. Ceram. Soc.*, vol. 73, pp. 567-574, 1990.
- [3] T. Tanimoto, K. Yamamoto, and T. Morii, Nonlinear stress-strain behavior of piezoelectric ceramics under tensile loading, *Proceedings of the 9th International Symposium on Application of Ferroelectrics*, pp. 394-397, 1994.
- [4] G. G. Pisarenko, V. M. Chushko, and S. P. Kovalev, Anisotropy of fracture toughness of piezoelectric ceramics, *J. Am. Ceram. Soc.*, vol. 68, pp. 259-265, 1985.
- [5] L. N. Syrkin and A. M. El'gard, Influence of the domain structure of ceramic ferroelectrics on their mechanical properties, *Soviet Physics-Solid State*, vol. 7, pp. 967-971, 1965.
- [6] Y. Murakami ed., *Stress intensity factors handbook* vol. 2, Pergamon Press, New York, pp. 42-45.
- [7] R. C. Pohanka, S. W. Freiman, and B. A. Bended, Effect of the phase transformation on the fracture behavior of BaTiO₃, *J. Am. Ceram. Soc.*, vol. 61, pp. 72-75, 1978.
- [8] E. C. Subbarao, M. C. McQuarrie and W. R. Buessem, Domain effects in polycrystalline barium titanate, *J. Appl. Phys.*, vol. 28, pp. 1194-1200, 1957.
- [9] T. L. Baker, K. T. Faber and D. W. Readey, Ferroelastic toughening in bismuth vanadate, *J. Am. Ceram. Soc.*, vol. 74, pp. 1619-1623, 1991.

Electromechanical Fatigue of Lead Zirconate Titanate Ceramics

Hiroaki Makino and Nobuo Kamiya

Ceramics Lab., Toyota Central Research and Development Laboratories Inc., 41-1 Yokomichi, Nagakute, Aichi, 480-11, JAPAN

Abstract- Electromechanical fatigue of lead zirconate titanate ceramics was investigated. During fatigue test, the electric field synchronized with the stress was applied to the specimen. Fatigue was not so accelerated by applying monopolar electric field. On the other hand, fatigue strengths remarkably degraded by applying bipolar electric fields. The cause of the degradation of the fatigue strengths was estimated to be the partial 180° domain switching which was induced by bipolar fields.

1. Introduction

Piezoelectric ceramics are currently used in high-power applications such as ultrasonic motors, a piezoelectric transformer and stack type actuators. For further high power applications, not only the improvement of the material properties but also the reliability such as fatigue of the piezoelectric ceramics is important.

A key to understand the reliability of the piezoelectric ceramics is to clarify how the electric field which is applied to the material influences the mechanical properties, especially fatigue. For the first step to understand it, we investigated the fatigue properties of lead zirconate titanate ceramic under dc electric fields.¹⁾ The fatigue strengths degraded in accordance with the magnitude of the applied dc electric fields.

In this paper, the electromechanical fatigue properties of the lead zirconate titanate ceramics under cyclic stress and electric field synchronized with the stress were investigated. Especially the effects of the offset field of the applied electric field on fatigue properties were studied.

2. Experimental

Rectangular sintered specimens (5x1x19mm) were prepared from commercially available lead zirconate titanate powder (Fuji Titan Industries Co., Ltd.; PE510). Piezoelectric properties of the material were shown in table 1. Electrodes of silver paste were painted on the surfaces (5x19mm). Then all the specimens were poled by applying the electric field of 3kV/mm at 100 °C in silicon oil.

The schematic figure of the experiment for measuring 4-point flexural fatigue strengths under electric field was shown in Fig.1. A cyclic fatigue testing machine (NGK Spark Plug Co., Ltd, model CFT-340-1) was used for the fatigue test. The upper and lower jigs were insulated from the fatigue testing machine. The electric field which was synchronized with the applied stress wave was applied to the specimens through the upper and lower jigs. Then the fatigue strengths were measured in the presence of the electric field. A span of the lower and upper fulcrums of 4-point flexural test was 13 and 3mm, respectively. Maximum electric field was applied when the maximum tensile stress was applied to the specimens. Waveform of the stress and the electric field, stress ratio (= minimum stress / maximum stress) and frequency during the fatigue test were sine wave, 0.1 and 350Hz, respectively.

In this paper, the amplitude of the electric field was fixed to 1kV/mm and the offset voltage was set to 0V or 500V in order to investigate the influence of the field polarity, that is, monopolar or bipolar. For comparison, the fatigue strengths under electrically short condition and applying dc voltage of 1kV/mm were measured.

Table 1 Piezoelectric properties of the specimen

| ϵ / ϵ_0 | Kp | d_{31} | Qm | Tc |
|-------------------------|------|-----------------------------------|----|-------|
| 5000 | 0.57 | $250 \times 10^{-12} \text{ m/V}$ | 60 | 170°C |

3. Results and Discussion

3.1 4-point flexural fatigue strengths under electrically short conditions, dc electric field and monopolar cyclic electric field.

4-point flexural fatigue strengths under electrically short conditions, dc electric field and monopolar cyclic electric field synchronized with the stress wave were shown in Fig.2. Under electrically short condition, the relationship between maximum stress σ_{max} and number to failure, i.e., S-N curves, exhibited good linearity. The reciprocal of the slope of the linear approximation of the S-N curve, n , is known as the crack propagation parameter which is related to the fatigue crack propagation rate ($V=A \cdot K_I^n$, V :crack propagation velocity, K_I :stress intensity factor). For example, in the case that the material has large number of n , the crack propagation rate is small, and thus the material is thought to be resistant against the fatigue. In case of short condition, the fatigue parameter n was calculated to be 57 by linear approximation using least square method.

Under dc electric field of 1kV/mm, it was impossible to calculate the fatigue parameter n , because the scattering of the data became rather large. Comparing with the data under short condition, the data had tendency to scatter lower side of the S-N line of the short condition. The scattering of the sizes of the fracture origins was small judging from the observation of the fracture origins which would be mentioned in the next section. The reason of large scattering data under dc electric field was not understood up to now.

Under monopolar cyclic electric field of 1kV/mm synchronized with the stress wave, the scattering of the data was small and linear approximation could be applied to the S-N curve. Comparing with the data under short condition, the slope of the approximated line was almost same and the S-N curve shifted to the lower side from the S-N curve under short condition. We reported that the strengths under dc electric field degraded with the applied dc electric fields.¹⁾ Accordingly, the reason of the shift of the fatigue strength was thought to be the degradation of the initial strengths under the electric field. Comparing with the data under dc electric field of 1kV/mm, the S-N curve of monopolar electric field was within the scattering of the data under dc electric field. Thus, it is possible that the influence of the monopolar electric field on the fatigue strength was not cycle-dependent but time-dependent.

3.2 4-point flexural fatigue strengths under monopolar and bipolar electric field

4-point flexural fatigue strengths under cyclic monopolar and cyclic bipolar electric field synchronized with the stress were shown in Fig.3. The electric

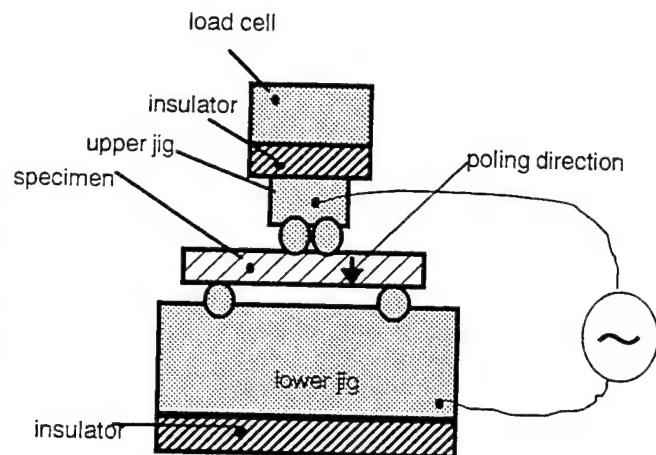


Fig.1 The schematic figure of measuring 4-point flexural fatigue strengths under electric field

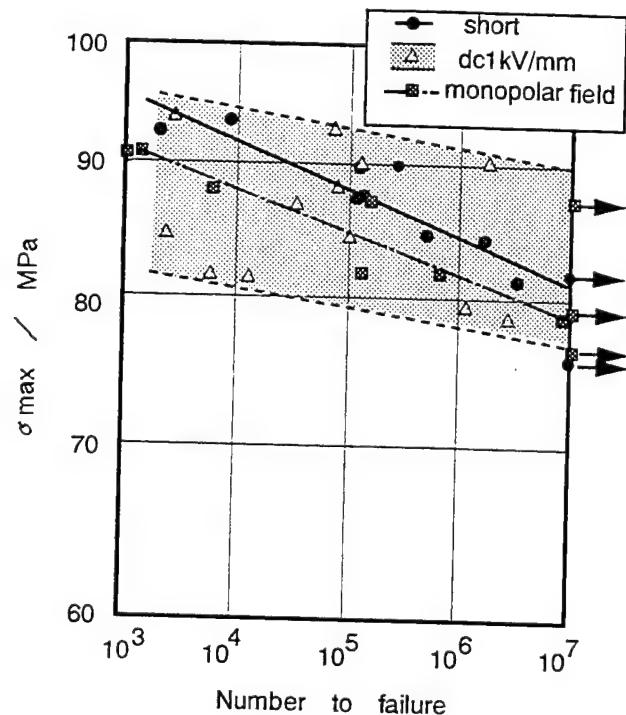


Fig.2 4-point flexural fatigue strengths under electrically short conditions, dc electric field and monopolar cyclic electric field synchronized with the stress wave

field strength was 1kV/mm for both cases. Under bipolar electric field, the slope of the S-N line was almost same as the S-N line under monopolar field. On the other hand, the degradation of the fatigue strength from monopolar field was almost 10 MPa and was remarkably larger than the degradation under monopolar field from short condition.

3.3 Fracture origins

Observing with the scanning electron microscope, the fracture surfaces of the specimens fractured in fatigue tests showed an almost intergranular morphology which were same as the fracture surfaces of the initial strength measurements. Although fracture origins were not found on almost half of the fracture surfaces, three kinds of fracture origins were detected such as a pore on the surfaces and inside the specimens which size was about 5 to 50 micrometer, a group of the grains and a place on which the electrode was not be painted. The group of grains was the fracture origin that tens of grains seemed to be the fracture origin because the group of grains fractured intragranularly at the initial fracture region and the example was shown in Fig.4. It is known that there are some grains that ferroelectric domains continue across the grain boundary. So, it was estimated that the microscopic internal stress which was concentrated at the boundary between the group of grains and the matrix caused the fracture. Group of the grains was thought to be one of the typical origins for the piezoelectric polycrystalline.

3.4 Effect of monopolar and bipolar electric field on the fatigue properties

Two mechanisms which affect the mechanical strength of piezoelectric material have been reported.^{2,3,4} One is the energy absorption at the crack tip due to the 90° domain switching of the domains which are parallel to the crack plane by the tensile stress at the crack tip,² which will increase the fatigue strength. Another mechanism is the microscopic tensile internal stress at the grain boundaries,^{3,4} which degrades the fatigue strength.

To consider the former mechanism, X-ray diffraction patterns of (002) and (200) of the specimen which survived after 10⁷ cycles fatigue tests under the bipolar and the monopolar electric field were measured. The results were shown in Fig.5. Although the intensities of (002) of both bipolar and monopolar fatigue tests remarkably decreased from poled specimen, the decrease ratios from the poled specimen were almost same for both cases. Therefore, the change of the amount of the 90° domains which could absorb the

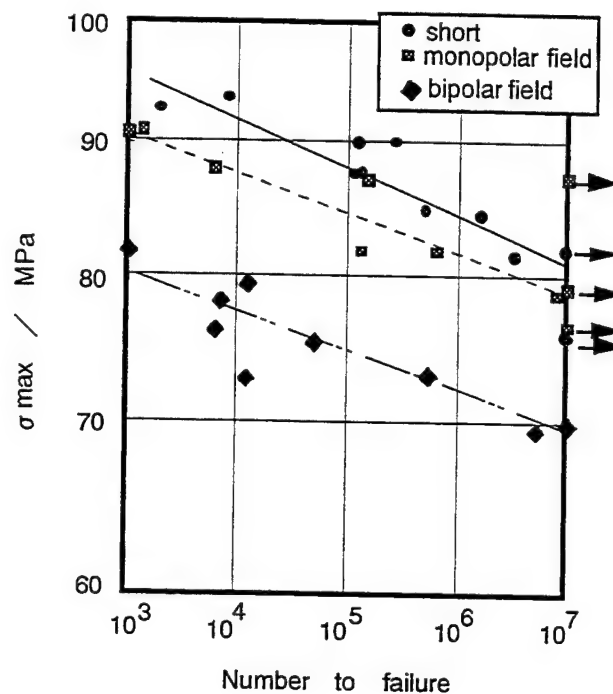


Fig.3 4-point flexural fatigue strengths under monopolar and bipolar electric field

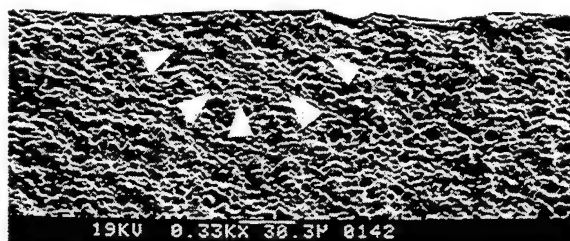


Fig.4 Scanning electron micrograph of the fracture origin of a group of grains

energy was not the main reason of the difference between bipolar and monopolar fatigue.

The internal stress was estimated to increase with the applied dc electric field¹⁾. Considering the fracture occurred when the maximum stress was applied, the maximum electric field determined the critical internal stress because the electric field synchronized with the stress. The voltage at the maximum stress was 1000V and 500V for monopolar and bipolar fatigue test, respectively. The internal stress under monopolar electric field was estimated to be larger than that under bipolar electric field, which did not coincide with the experimental results obtained. Accordingly, the internal stress induced from the maximum electric field was not thought to be the reason of the difference.

There must be other reason for the difference between the bipolar and monopolar fatigue strengths. Although it is not examined, partial 180° domain switching is thought to affect the mechanical property. As we reported previously, fatigue strengths extremely degraded by applying dc electric field which direction was opposite to the poling direction¹⁾. The reason was considered that the large internal stress would generate around partial 180° domain switching because the region where 180° domain switching occurred deformed opposite direction against the surroundings. Under the bipolar electric field, it was estimated that the partial 180° domain switching occurred and degraded the fatigue strengths because the minimum applied electric field was close with the coercive field. To investigate the partial 180° switching is the key to understand the fatigue phenomena and is the theme for future work.

4. Summaries

- (1) S-N curve of 4-point flexural fatigue strength under electrically short condition exhibited good linearity and the crack propagation parameter n was calculated to be 57.
- (2) Fatigue strengths under monopolar cyclic electric field synchronized with the stress degraded comparing with the fatigue strengths under short condition while the slope of the S-N line was same as the short condition.
- (3) Fatigue strengths under bipolar cyclic electric field notably degraded comparing with the fatigue strengths under monopolar condition.
- (4) The difference between the fatigue strengths under bipolar and monopolar electric field was thought to relate with the internal stress induced by the domain switching.

References

1. H.Makino, N.Kamiya, Jpn.J.Appl.Phys.,33(1994)5323
- 2.K. Mehta and A. V. Virker: J. Am. Ceram. Soc.,73(1990) 567
- 3.R. C. Pohanka, R. W. Rice and B. E. Walker,Jr: J. Am. Ceram. Soc. 59(1976)71.
- 4.R. C. Pohanka, S. W. Freiman and B. A. Bender: J. Am. Ceram. Soc. 61(1978)72.

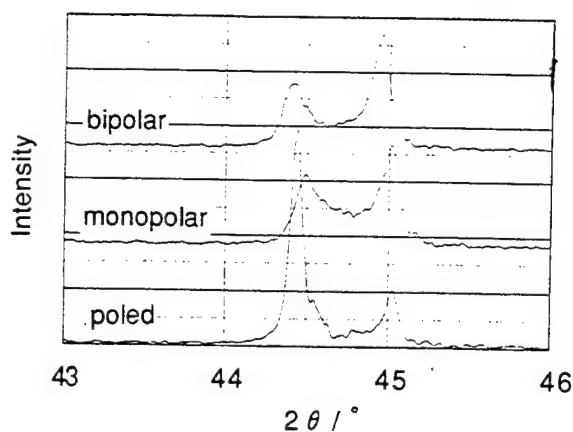


Fig.5 X-ray diffraction patterns of (002) and (200) of fatigue specimen under bipolar and monopolar field

Electromechanical Properties of High Temperature Piezoelectric Materials

Yukio Sakabe Masahiko Kimura Koji Ogiso Akira ANDO

Murata Mfg. Co. Ltd. Material R&D

2288 Oshinohara Yasu-cho Shiga 520-23 JAPAN

abstract --- Electromechanical Properties of high temperature piezoelectric ceramic materials are studied. lead titanate family materials, lead niobates family materials, and bismuth layer structured compound are chosen as high temperature piezoelectric materials. Their electrical and mechanical properties are governed by their 90° domain rotating behavior.

I. INTRODUCTION

Piezoelectric ceramic materials have been widely used in communication devices, actuators, transducers, and sensors. Especially in the sensor application, various kind of devices have been proposed and practicalised [1]. Recent development of smart control systems for the combustion in automobile engines requires high-temperature-stable shock and pressure sensors and piezoelectric materials used in them [2]. The piezoelectric materials need to have ferroelectric transition temperatures (T_c) higher than typical piezoelectric material $\text{Pb}(\text{Ti},\text{Zr})\text{O}_3$ (PZT).

Lead titanate(PbTiO_3), lead niobate(PbNb_2O_6), and bismuth layer structured compounds are well known as the materials which has high T_c 's than PZT [3],[4]. However there are few reports on temperature dependencies of piezoelectric properties and high temperature stability of these materials.

In this study, electromechanical properties of these high temperature piezoelectric materials are clarified, and the correlation between the high temperature electromechanical stability and 90° domain wall motion is discussed.

II. SAMPLE PREPARATION

Lead titanate(PbTiO_3), lead niobate(PbNb_2O_6), and bismuth layer structured compound($\text{Na}_{0.5}\text{Bi}_{4.5}\text{Ti}_4\text{O}_{15}$) are chosen as high temperature piezoelectric materials. These ceramic samples were fabricated by the conventional ceramic powder process. The starting materials were commercially available metal oxides or carbonates, of which purities are 99.9% or more. These starting materials were batched and mixed in 2-propanol and ball-milled with partially stabilized zirconia media. The mixed powder was calcined and the disc shaped green body was formed by the die press and fired in the ordinary furnace in the air. The ceramic disc was elctroded and polarized. These process conditions were shown in Table 1.

The compositions of the high temperature piezoelectric materials chosen in this study are as follows.

PT1: $(\text{Pb}_{0.94}\text{La}_{0.04})\text{TiO}_3 + 1.0^{\text{mol}\%}\text{MnO}_2$

PT2: $0.9\text{PbTiO}_3 + 0.1\text{BiFeO}_3 + 1.0^{\text{mol}\%}\text{MnO}_2$

PN1: $\text{Pb}_{0.94}\text{La}_{0.04}\text{Nb}_2\text{O}_6 + 1.0^{\text{mol}\%}\text{MnO}_2$

PN2: $\text{Pb}_{0.94}\text{La}_{0.04}\text{Nb}_2\text{O}_6 + 1.0^{\text{mol}\%}\text{MnO}_2 + 1.0^{\text{mol}\%}\text{ZrO}_2$

BLS: $\text{Na}_{0.5}\text{Bi}_{4.5}\text{Ti}_4\text{O}_{15} + 2.0^{\text{mol}\%}\text{MnO}_2$

High temperature characteristics of PZT was also studied for the comparison. The composition is as follows.

PZT: $(\text{Pb}_{0.9}\text{Sr}_{0.1})(\text{Zr}_{0.53}\text{Ti}_{0.47})\text{O}_3 + 1.0^{\text{mol}\%}\text{Cr}_2\text{O}_3$

TABLE 1
PROCESS CONDITIONS

| | calcining | firing | poling |
|-----|-----------------|------------------|-------------------------------|
| PZT | 900 °C for 2 hr | 1200 °C for 2 hr | 3 kV/mm for 30 min at 50 °C |
| PT1 | 800 °C for 2 hr | 1200 °C for 2 hr | 10 kV/mm for 30 min at 150 °C |
| PT2 | 800 °C for 2 hr | 1200 °C for 2 hr | 10 kV/mm for 30 min at 200 °C |
| PN1 | 900 °C for 2 hr | 1250 °C for 2 hr | 10 kV/mm for 30 min at 200 °C |
| PN2 | 900 °C for 2 hr | 1250 °C for 2 hr | 10 kV/mm for 30 min at 200 °C |
| BLS | 800 °C for 2 hr | 1100 °C for 2 hr | 10 kV/mm for 30 min at 200 °C |

III. RESULTS

A. Electrical Properties

Piezoelectric properties of the high temperature materials are shown in Table 2. The electromechanical coupling coefficient of the thickness vibration mode for disc is represented by k_t in Table 2.

TABLE 2
Electromechanical PROPERTIES AT ROOM TEMPERATURE

| | T_c (°C) | d_{33} (pC/N) | k_t (%) | ϵ_r | Q_m | bending strength (kg/mm ²) |
|-----|---------------|--------------------|--------------|--------------|-------|---|
| PZT | 270 | 250 | 58 | 1400 | 200 | 12.0 |
| PT1 | 420 | 64 | 48 | 200 | 280 | 15.0 |
| PT2 | 510 | 40 | 34 | 170 | 400 | 16.0 |
| PN1 | 510 | 80 | 47 | 370 | 15 | 7.5 |
| PN2 | 510 | 85 | 50 | 450 | 15 | 7.5 |
| BLS | 660 | 25 | 24 | 130 | 800 | 18.0 |

PT2 has the highest T_c reported ever as the well-sintered PbTiO_3 family piezoelectric ceramics. PT1 has La substitution for Pb, and its T_c is lowered from that of pure PbTiO_3 (490°C). PN1 and PN2 are PbNb_2O_6 family materials, of which Pb is substituted by La, and their T_c 's are lower than PbNb_2O_6 (560°C). Discrepancy between piezoelectric properties of PN1 and PN2 is not clear at room temperature. BLS also exhibits the highest kt as $\text{Na}_0.5\text{Bi}_{4.5}\text{Ti}_4\text{O}_{15}$ piezoelectric ceramics reported ever. Mn addition enhances its piezoelectric activity, however it needs further investigation to understand the effect of Mn additive on piezoelectric properties.

Dielectric permittivities of high temperature materials were shown in Figure 1(Fig.1). BLS does not exhibit clear dielectric anomaly, because of the increase in electric conductivity at high temperatures. However the transition temperature could be defined as the temperature which gives us the maximum of dielectric permittivity as those of other materials.

Fig.2 shows temperature dependencies of electromechanical coupling coefficients (kt) of those materials. The gradual decreases with increasing temperature are observed for PZT, PT1, and BLS, while the gradual increase is observed for PT2. The differences between PZT, PT1, and PT2 are discussed in following section. However kt of BLS is not discussed further more because its decrease tendency changes around 500°C , which seem to be some kind of phase transition point, and it is difficult to compare BLS with PZT or PT1, PT2. PN1 and PN2 have more complicated changes. PN1 has local maximum around 350°C , and PN2 has local minimum around 400°C . Zr additive of PN1 is considered to enhance the high temperature stability of kt by some effect such as the domain wall pinning. However more detailed study is necessary on this difference.

Fig.3 shows the change in piezoelectric constant d_{33} after retention at high temperature which is 10°C lower than T_c for each material. PT2 is the most stable material in this study. PN1 and PN2 seem to have been aged in 1h. PZT, PT2, and BLS de-aged more slowly.

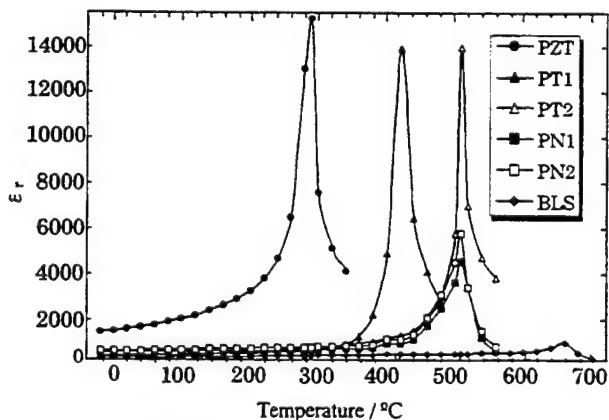


Fig.1 Relative dielectric permittivities ϵ_r as a function of temperature.

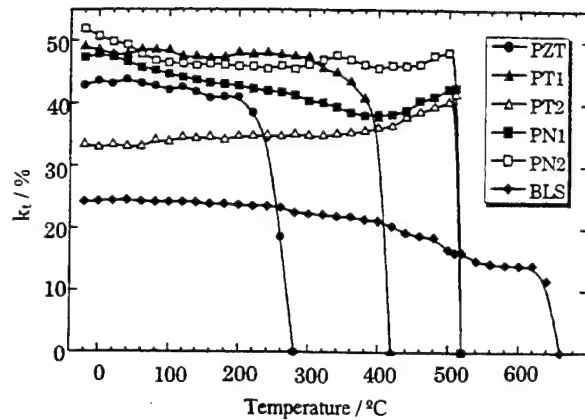


Fig.2 Electromechanical coupling coefficients k_t as a function of temperature.

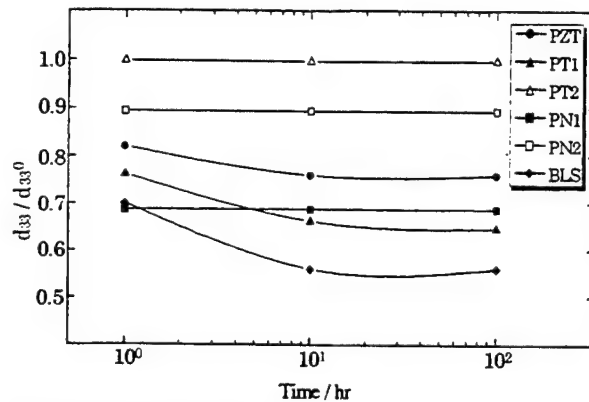


Fig.3 The decrement in piezoelectric constant as a function of holding time at temperatures 10°C lower than Curie temperatures ; 260, 410, 500, 500, 500 and 650°C for PZT, PT1, PT2, PN1, PN2 and BLS, respectively. d_{33}^0 indicate piezoelectric constant measured at room temperature just after polling.

B. Mechanical Properties

Mechanical properties of PZT, PT1, and PT2 at high temperatures were evaluated. Mechanical stress-strain characteristics was measured at various temperatures to clarify the behaviors of 90° domains of those materials. Bending stress was applied to the ceramic beam, and the displacement was measured. The Automatic mechanical strength measuring machine was used for this measurement. Stress was applied until 70% of the fracture strength, and measured strain was divided to the linear strain and the nonlinear strain. The linear strain(S_1) is elastic strain based on ionic polarization, and the nonlinear strain is the contribution of 90° domain rotation.

Fig.4 shows the stress-strain characteristics of PZT. The strain is divided to two parts which are linear and nonlinear parts, by drawing tangent at stress = 0. The temperature dependence of the nonlinear parts of PZT is shown in Fig.5 with those of PT1 and PT2. The nonlinear component of the strain for PZT decreases with increasing temperature. On the other hand, it

increases until the temperature goes up to the T_c for PT2, and it has a maximum around 200 °C for PT2. The low non-linear components for PT1 and PT2 mean low contribution of 90° domain rotation to electromechanical coupling at room temperature.

The contribution of 90° domain rotation to the total strain is divided to the restorable part (S_2) and the nonrestorable part (S_3). S_3 is the remanent strain of the stress-strain hysteresis. These divided strain components are schematically shown in Fig.6.

The stress-strain hysteresis were measured for PZT, PT1, and PT2 at room temperature and high temperature which is 50° C lower than each T_c . They are shown in Figs. 7-12.

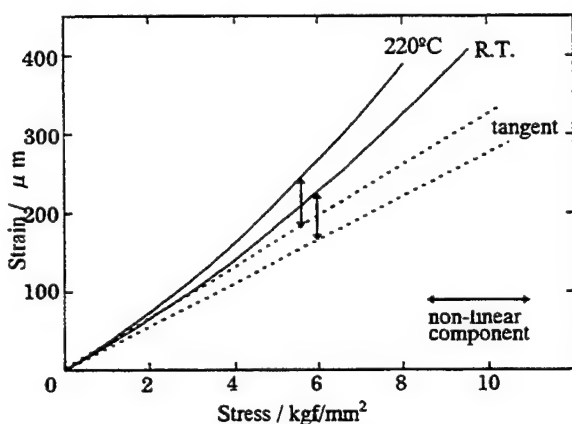


Fig.4 Stress-strain curves in three point bending test at room temperature and 220 °C for PZT. The broken lines are tangents of the curves at the starting points. The arrow lines indicate non-linear components of the strains.

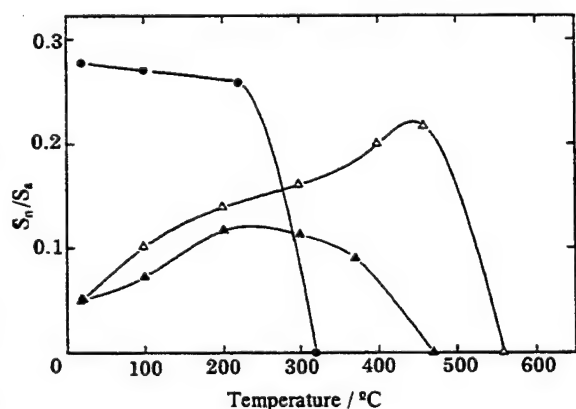


Fig.5 The ratios of non-elastic components of the strains applying loads of 6, 10 and 10 kgf/mm² for PZT, PT1 and PT2, respectively, in three point bending test as a function of temperature. S_t indicate total strains and S_n show non-elastic components of the strains.

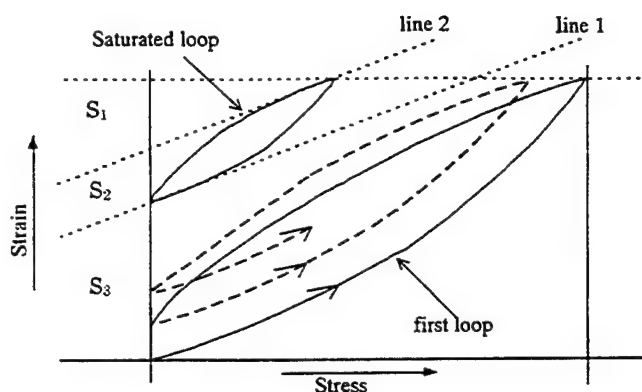


Fig.6 Schema of stress-strain hysteresis in cyclic three point bending test. The line 1 and line 2 are tangents at the ends of the saturated loop. It is considered that the area S_1 , S_2 and S_3 indicate a elastic component, a restorable component induced by domain rotations and a unrestorable component induced by domain rotations of the strains.

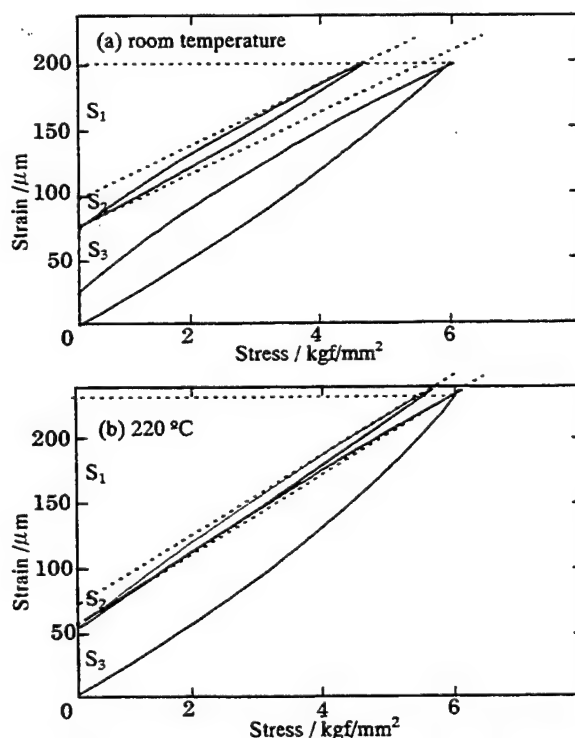


Fig.7 Stress-strain curve in cyclic three point bending tests fixed maximum strains for PZT. The maximum strains were regulated a strain applying a load of 6 kgf/mm² in single bending test.

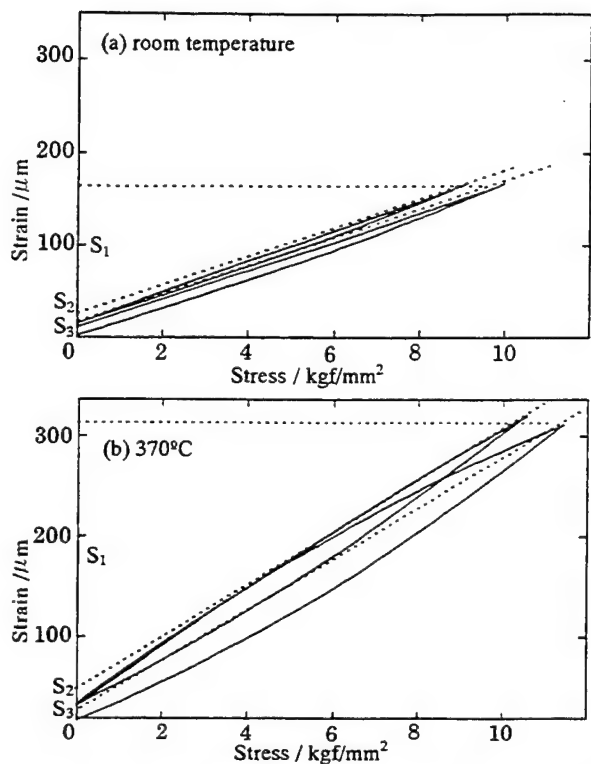


Fig.8 Stress-strain curve in cyclic three point bending tests fixed maximum strains for PT1. The maximum strains were regulated a strain applying a load of 10 kgf/mm² in single bending test.

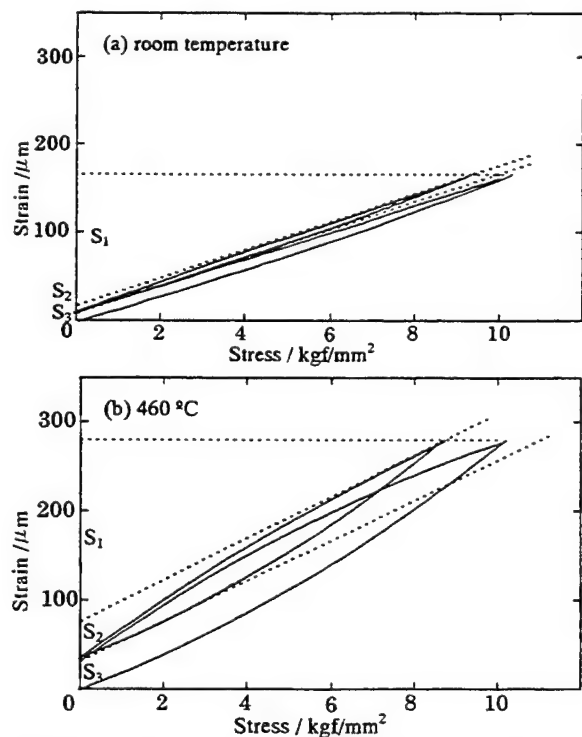


Fig.9 Stress-strain curve in cyclic three point bending tests fixed maximum strains for PT2. The maximum strains were regulated a strain applying a load of 10 kgf/mm² in single bending test.

IV. DISCUSSION

Temperature dependence of elastic compliance is similar as that of dielectric permittivity in general. Then the electromechanical coupling coefficient strongly correspond to the remanent polarization, because piezoelectric d-constant is represented by

$$d_{ij} = k_{ij} \sqrt{\epsilon_{ii} s_{jj}} \quad \text{and} \quad d_{ij} = 2 \cdot Q_{ij} \cdot P_3 \cdot \chi_{ij}$$

in the tetragonal systems, where k_{ij} , ϵ_{ii} , s_{jj} , Q_{ij} , P_3 , χ_{ij} are electromechanical coupling coefficient, dielectric permittivity, elastic compliance, electrostriction constant, dielectric susceptibility, respectively [5]. The electrostriction constant is independent from temperature change in the phenomenological theory by Devonshire [6]. Therefore the stability of the remanent polarization corresponds to the stability's of the piezoelectric properties.

Large value of the nonrestorable part of 90° domain rotation (S_3) means high stability of the domain structure, and it is considered to correspond to the high temperature stability means that piezoelectric property is not stable at high temperatures, such as for PZT or PT1.

The restorable part of 90° domain rotation means electromechanical coupling. Their correspondence seem to be typically shown in high temperature characteristics of PT2 in Figs.2, 5, and 7(a)-9(b).

V. CONCLUSION

High temperature piezoelectric ceramic materials were prepared and their piezoelectric properties were measured in the temperature ranges from room temperature to Tc's. High temperature stability of piezoelectricity well correspond to stability of domain structure estimated from the measurements of the mechanical properties.

The large contribution of nonrestorable 90° domain rotation to total strain at high temperatures means the high temperature stability of the piezoelectric material, while the restorable 90° domain rotation is strongly connected to the electromechanical coupling.

These relations are ascertained in the high temperature properties of PZT and PbTiO₃ family materials.

REFERENCES

- [1] J. M. Herbert Ferroelectric Transducers and Sensors : Gordon and Breach Science Publishers, 1982, pp.178-265
- [2] K. Takeuchi, "Properties of modified lead titanate ceramics for an ignition plug washer sensor" Jpn. J. Appl. Phys, vol.28, 1989, suppl. 28-2, pp.105-107
- [3] E.C.Subbarao, "Ferroelectric and antiferroelectric materials" Ferroelectrics, vol.5, 1973, pp.267-280
- [4] B.Jaffe Piezoelectric Ceramics : Academic Press 1971, p224
- [5] N.Setter Ferroelectric Ceramics : Birkhauser Verlag, 1993, pp.48-71
- [6] A.F.Devonshire, Phil. Mag., vol. 40, 1949, p.1040

Solid Freeform Fabrication (SFF) of Novel PZT Ceramic/Polymer Composites

A. Safari, S. C. Danforth, R. K. Panda, T. F. McNulty, and A. Bandyopadhyay

Department of Ceramic and Materials Engineering
Rutgers University, Piscataway, NJ 08855-0909, USA

Abstract – Solid freeform fabrication techniques, including Fused Deposition of Ceramics (FDC) and Sanders Prototyping (SP) were used to form a variety of novel piezoelectric ceramic/polymer composites. Many novel structures, including 1-3 rods and 3-3 oriented piezocomposites were made using these processes. The angular orientation of the rods was varied to get the optimum properties for the oriented structures. The composites were fabricated either by an indirect, direct, or soft tooling route. In the indirect route a sacrificial polymer mold which was a negative of the actual structure was infiltrated with lead zirconate titanate (PZT) slurry to form the green part. In the direct technique the green structures were made by the fused deposition of PZT loaded binder filaments. In soft tooling, flexible molds were made by encasing a prototype in a suitable polymer material. After the prototype was removed from the mold, the mold was then used to cast many samples in a fashion similar to injection molding. The different novel structures and their electromechanical properties have been discussed in this paper.

I. INTRODUCTION

The piezoelectric effect is observed in a variety of ceramics, single crystal and polymeric materials. Lead zirconate titanate (PZT) ceramics have been widely used for transducer applications because of their good electromechanical properties. However they have many disadvantages, including a high acoustic impedance mismatch with water or human tissue, and low values for the piezoelectric voltage coefficients. Instead of looking for an entirely new class of piezoelectric materials without the above limitations, researchers have successfully made composites of piezoelectric ceramics with inactive polymers. These piezocomposites show excellent electromechanical properties while limiting the various detrimental properties of the bulk ceramic. The properties of the ceramic/polymer composites can be tailored by changing the connectivity of the phases, volume fraction of the ceramic in the composite, and the spatial distribution of the active ceramic phase.

A variety of techniques including, dice and fill, tape casting, lost mold, ceramic injection molding, and solid freeform fabrication (SFF) have been used for making piezocomposites[1-5]. In this work, solid freeform fabrication methods were used to develop novel piezoelectric composite structures. Over the last decade, several SFF methods have been developed as techniques to fabricate polymer, metal, or ceramic structures on a fixtureless platform directly from a Computer Aided Design

(CAD) file. Structures are made without using any hard tooling, dies or molds. Among the different SFF or rapid prototyping methods which have found commercial success are stereolithography (SLA), fused deposition modeling (FDMTM), selective laser sintering (SLS), laminated object manufacturing (LOM), 3-D printing and SandersTM prototype (SP)[6]. Most of these techniques are designed to manufacture net shape polymer parts for form/fit applications and design verification, though some are also capable of manufacturing metal or ceramic parts. All SFF techniques begin with a common approach, namely, a CAD data description of the desired component. A surface file (also known as a .stl file) is created from the CAD file, which the manufacturing system takes as the input. This file is converted into cross sectional slices or slice file, where each slice can be uniquely defined about its build strategy by varying the tool path. The final part then built by layer by layer deposition of the material on a fixtureless platform moving along the Z- axis.

II. PROCESSING AND CHARACTERIZATION

The piezocomposites developed in this study were made by either an indirect, direct or soft tooling route. The indirect fabrication route utilizes a modified lost mold technique. In this process, sacrificial molds having a negative of the desired structures were manufactured using the Sanders Prototype Model-Maker system MM-6PRO (SPI Inc., Wilton, NH). The MM-6PRO is a liquid to solid inkjet plotter, which deposits the polymer on a movable Z-platform. The main advantages of SP technique include a very high resolution (a mold wall thickness of ~50 μm can be easily obtained), and a good surface finish. For the indirect process, a high solids loading of PZT ceramic slurry was specially developed to infiltrate the polymer molds and to avoid cracking in the sample during drying and binder burn out.

In the direct technique, the piezoelectric ceramic structures were fabricated via Fused Deposition of Ceramics (FDC). Ceramic loaded filaments with a diameter of 1750 μm were first extruded from a compounded mixture containing 52 vol. % PZT in a thermoplastic binder system containing elastomer, tackifier, wax, and plasticizer. These filaments formed the input material for the StratasysTM 3D-Modeler (Stratasys Inc., Eden Prairie, MN). The ceramic loaded filaments are fed into a liquifier heated to ~190°C.

The liquifier extrudes a road of material through a 250 μ m nozzle, depositing it on a foam substrate attached to a fixtureless platform capable of moving in the Z direction. The liquifier moves in the X - Y plane based on the shape of the part to be built. After depositing the first layer the fixtureless platform moves down the height of one layer, and the next layer is built on top of it. These steps are repeated until the whole structure is made. The final dimensions of the green ceramic part were about 25.4mm x 25.4mm x 10mm. The parts were then removed from the foam substrate for processing by conventional methods.

Soft tooling is a process in which flexible polymer molds are made by encasing a concept model in a suitable polymer material. After the model is removed from the mold, the mold is then used to cast duplicates in a fashion similar to injection molding (IM), using IM ceramic/thermoplastic compounds. Although not a new process, it has yet to find usage in the transducer community because of the difficulty in producing suitable models used for the creation of new molds. With the advent of SFF processes, a new technique has been created which will facilitate the quick and easy production of silicone molds.

Before any molds were made in the soft tooling technique, suitable prototypes were designed using Pro EngineerTM CAD software. Designs were optimized to facilitate easy release after casting. Various room temperature vulcanized (RTV) silicone rubbers were sampled in order to gain some insight into which material or materials work best in the production of flexible polymer molds. Several different silicone rubbers were used to make molds based on design requirements, ranging from low to high viscosity and flexibility. Experiments on binder development were performed concurrently. Several important factors governed material selection. Since operating at temperatures below 200 °C was one of the principal requirements, it is important that the developmental PZT / thermoplastic compound exhibits a low viscosity at temperatures at or below 200 °C. The compound must exhibit sufficient strength to allow for easy part removal once molded. The binder formulation must gradually decompose at temperatures up to about 500 °C to facilitate easy binder removal. Finally, the binder formulation must be hydrophobic to avoid complications in casting due to humidity changes. Materials were thus gauged on these criteria.

A developmental binder was formulated which meets each of the existing criteria. The formulation consists of a major and minor binder, fluidizer, tackifier, and plasticizer in the appropriate proportions. For this work, PZT-5H powder was coated with a surfactant, and compounded with the binder formulation loaded with 60 vol.% PZT. This formulation was used to cast multiple 12.5 x 12.5 mm. green preforms using a silicone rubber mold.

The green parts made either by direct, indirect, or soft tooling techniques were slowly heated to 550 °C and held for 1 hour to allow the organic components to evaporate. The temperature was then increased to 780 °C, with a dwell of 1 hour at that temperature, to provide enough bisque strength to the parts for mechanical handlability. They were then heated at 3.5°C/min to 1285°C, and held at that temperature for 1.5 hours to sinter the PZT ceramic. The sintered samples were then embedded in a standard Spurr Epoxy (Ernest F. Fullam Inc., Latham, NY) and cured in an oven at 70°C for 12 hours.

The top and bottom of the composite were electroded with an air dried silver paint and poled in a corona poling apparatus at 65°C[7]. Electromechanical properties of composites including capacitance (C_p), d_{33} coefficient, and k_p and k_t were evaluated and are discussed in the next section. Various architectures of the ceramic structures were also examined using a scanning electron microscope (Model 1400, Amray Corporation).

III. RESULTS AND DISCUSSION

Sacrificial molds having a negative of the 1-3 ceramic structure were made via an indirect technique. A CAD program was used to create a mesh structure which was then used to create molds with a road width of 100 μ m and hole sizes varying from 150-350 μ m. Fig. 1 shows a sintered 1-3 PZT ceramic structure obtained using this process. The ceramic rods with a width of 180 μ m are separated from each other with an edge to edge spacing of ~70 μ m. Large 1 in. x 1 in. samples with an aspect ratio of more than 10 could be easily produced by this technique. As shown in Table 1, these specimens had good electromechanical properties with a thickness coupling coefficient k_t about 70%.

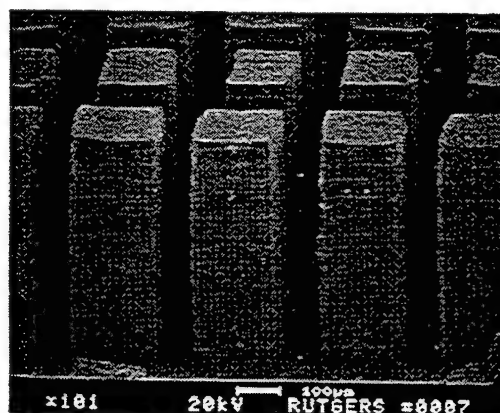


Fig. 1 : Scanning Electron Micrograph (SEM) of a 1-3 sintered PZT-5H ceramic structure obtained using the indirect technique.

Using the direct technique, a variety of composites were made, where the ceramic rods were oriented at different angles to the poling direction. The specimens were fabricated to give a ladder type structure (*Type A*) as shown in Fig 2. This structure could be poled along many directions to give different architectures and electromechanical properties. The *type A* structure was poled along the Z-direction [001]. This structure can be poled in another way if it is rotated such that either the [100] or [010] direction of Fig. 2 coincides with the [001] Z-poling axis. *Type A* structures were poled perpendicular to the fiber orientation, and the ceramic connectivity was through the joints of the rods in the specimen. In *type B* composites, half the rods are continuous along the poling axis while second half of the rods are continuous along the axes perpendicular to it. Yet another type of 3-3 connectivity structure (*Type C*) can be obtained when the [110] direction in Fig 2 is rotated to coincide with the [001] Z-poling axis. In this structure the rods will be oriented at $\pm \theta^\circ$ to the poling direction. Fig. 3 shows a SEM micrograph of a 3-3 composite where the rods are oriented $\pm 15^\circ$ to the poling direction.

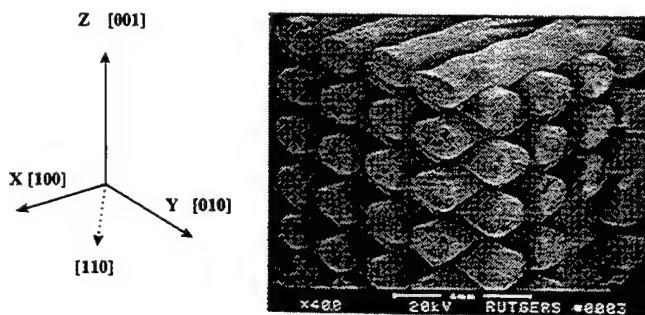


Fig 2 : SEM of sintered PZT-5H ladder type structure (*Type A*) obtained by direct deposition technique.

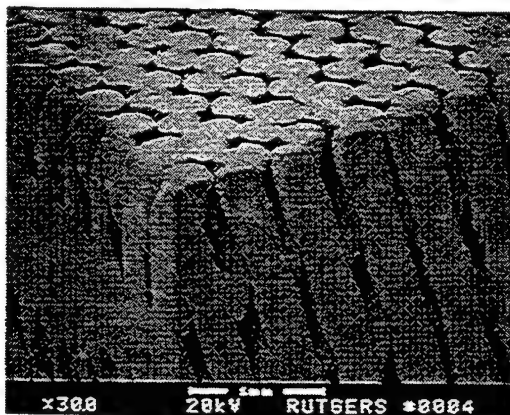


Fig 3 : SEM of the an oriented structure (*Type C*) where the PZT rods are aligned at $\pm 15^\circ$ to the poling axis.

A comparison of the properties of *Type A*, *Type B* and *Type C* structures is shown in Table 1. It can be seen that the observed d_{33} of most of the oriented composites (*Type C*) is higher than the ladder structure (*Type A*). The d_{33} rises as the angle of orientation to the vertical poling axis increases. A maximum value of 510 pC/N is observed for an orientation angle of $\pm 30^\circ$ to the vertical. The value decreases on further increasing the orientation angle. A value of 175 pC/N was obtained for an oriented composite where the rods were angled at $\pm 75^\circ$ to the vertical. The coupling coefficient k_t remained nearly constant for the different orientation angles for which k_t could be determined. The high values of d_{33} for these 3-3 composites could be because an effective d_{33} is observed on the face perpendicular to the Z direction. When a unit stress is applied to the oriented PZT composites along the Z direction, the polarization on the face perpendicular to it have contributions from the d_{33} , d_{31} and d_{15} components.

$$P_3 = d_{33(\text{effective})} \cdot \sigma_3 = (a \cdot d_{33} + b \cdot d_{31} + c \cdot d_{15}) \cdot \sigma_3 \quad (1)$$

The total polarization observed would depend on the values of a , b , and c which vary from $-1 < a, b, c < 1$. They quantify the contribution of the different d coefficients of the ceramic material, whether negative or positive, to the $d_{33(\text{effective})}$ coefficient. The actual values of a , b and c would depend on the orientation of the rods to the applied stress direction (Z axis).

Standard composites with 1-3 connectivity were made by the soft tooling technique. As shown in Fig. 4 and Fig. 5, the final PZT/polymer composites consisted of 800 μm . poles with a pitch of 2.0 mm. and an aspect ratio of approximately ten. Based on these dimensions, it corresponds to a composite of approximately 15 vol.% PZT. Composites made using this technique have exhibited high d_{33} values, with some reaching 450 pC/N. In addition,

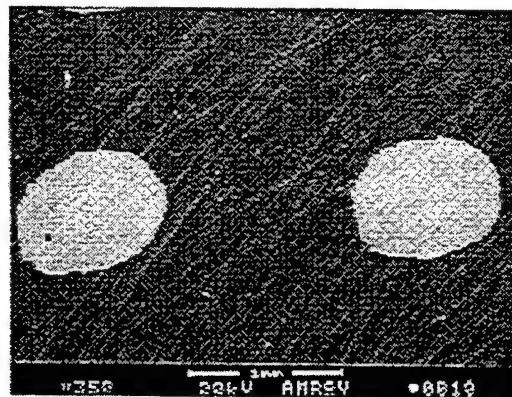


Fig. 4 : Top view of a 1-3 PZT/ polymer composite obtained via soft tooling.



Fig. 5 : SEM of a single sintered rod of PZT in a 1-3 structure made via soft tooling.

coupling factors as high as 70% have been measured. Table 1 lists some of the electromechanical properties of the resultant composites.

IV. CONCLUSIONS AND FUTURE WORK

In this work, Solid Freeform Fabrication (SFF) techniques, such as Fused Deposition (FD) and Sanders Prototype (SP) were used to form a variety of novel piezoelectric ceramic/polymer composites. The indirect, direct, and soft tooling methods were presented. The 1-3 composites made via lost mold technique gave good electromechanical properties. Using the direct technique, many novel oriented composites were fabricated. The properties of these oriented composites were found to greatly depend on the angular orientation of the rods. Theoretical modeling of the oriented composite structures is in progress to determine the structure with the best

electromechanical properties. Finally, soft tooling shows promise for faster and cheaper production of a large number of piezoelectric ceramics samples using a single mold.

ACKNOWLEDGMENTS

The authors would like to thank the Office of Naval Research (ONR) for the financial support which made this work possible. The authors would also like to thank Mr. Y. Rozov, Ms. N. Spratford and Mr. D. Patel for their help in processing and characterization of piezocomposites.

REFERENCES

- 1) V. F. Janas and A. Safari, "Overview of Fine-Scale Piezoelectric Ceramic/Polymer Composite Processing," *J. Am. Ceramic Soc.*, 78 [11] 2945-55 (1995)
- 2) H. P. Savakus, K. A. Klicker, and R. E. Newnham, "PZT-Epoxy Piezoelectric Transducers: A Simplified Fabrication Procedure," *Mater. Res. Bull.*, 16, 677-80 (1981)
- 3) L. J. Bowen, and K. W. French, "Fabrication of Piezoelectric Ceramic/Polymer Composites by Injection Molding," pp. 160-63 in *Proceedings of the IEEE International Symposium on the Applications of Ferroelectrics*, 1992
- 4) U. Bast, D. Cramer, and A. Wolff, "A new Technique for Production of Piezoelectric Composites with 1-3 Connectivity," pp. 2005-15 in *Ceramics Today-Tomorrow's Ceramics*, Vol 66C. Edited by P. Vincenzini, Elsevier Science Publishers, Amsterdam, Netherlands, 1991
- 5) A. Bandyopadhyay, R. K. Panda, V. F. Janas, M. K. Agrawala, S. C. Danforth and A. Safari, "Processing of Piezocomposites by Fused Deposition Technique," *J. Am. Ceram. Soc.*, 80 [6] 1366-72 (1997)
- 6) H. L. Marcus, and D. L. Bourell, "Solid Freeform Fabrication Finds New Applications," *Advanced Materials & Processing*, 9, 28-35 (1993).
- 7) D. J. Waller, and A. Safari, "Piezoelectric Lead Zirconate Titanate Ceramic Fiber/Polymer Composites," *J. Am. Ceram. Soc.*, 75 [6] 1648-55 (1992)

TABLE I
ELECTROMECHANICAL PROPERTIES OF PIEZOELECTRIC COMPOSITES MADE BY INDIRECT, DIRECT AND SOFT TOOLING ROUTES.

| Technique | Composite Type | Vol % PZT-5H | Dielectric Const. K | d_{33} (pC/N) | k_t (%) |
|--------------|---------------------------|--------------|---------------------|-----------------|-----------|
| Indirect | 1-3 composite | 35 | 680 | 390 | 68 |
| Direct | Ladder (Type A) | 70 | 1300 | 290 | 50 |
| | Oriented (0-90°) (Type B) | 65 | 1545 | 300 | 51 |
| | Oriented (±15°) (Type C) | 60 | 1560 | 350 | 62 |
| | Oriented (±30°) (Type C) | 60 | 1580 | 510 | 59 |
| | Oriented (±45°) (Type C) | 65 | 1350 | 390 | — |
| | Oriented (±60°) (Type C) | 66 | 1200 | 225 | — |
| | Oriented (±75°) (Type C) | 58 | 620 | 175 | — |
| Soft Tooling | 1-3 composite | 15 | 320 | 315 | 63 |

PZT MicroRod Composite Ultrasonic Transducers

Michael T. Strauss and Mark V. Parish

CeraNova Corporation
101 Constitution Blvd. Suite D
Franklin, MA 02038

Abstract—*CeraNova* is using its MicroRod technology to develop an alternative to the dice and fill method of producing composite ultrasonic transducers. MicroRods, 125 μ m in diameter, are packed into a cylindrical form. Epoxy is infiltrated into the compact and cured. The composite is sliced perpendicular to the axis of the cylinder. Each slice becomes an individual transducer after electroding and poling.

This technique adds increased flexibility to the design of ultrasonic transducers. Transducers have been made using this method with PZT volume fractions between 25 and 80%. Packing can take geometries unattainable by slice and dice techniques such as hexagonal or random. Random packing of the MicroRods can reduce interpost resonances in these transducers. In addition, MicroRods of different sizes can be combined in a single composite. The size and shape of these composites can be varied greatly and is determined by a suitable choice of container for the MicroRod compact.

I. INTRODUCTION

Ultrasonic transducers are used in many applications including nondestructive evaluation (NDE) and medical ultrasound. Currently, composite transducers are made by cutting a grid (called dicing) into a wafer of PZT with a diamond saw. The grooves are back-filled with epoxy and the backing is ground off. The resonance frequency of a composite, and therefore the operating frequency of a transducer is determined by the thickness of the wafer, not the post size. Typically, composites are 250 to 1250 microns thick for medical ultrasound. The advantage of using composites is that the small posts reduce lateral clamping, therefore allowing greater sensitivity. To reduce lateral clamping the post width should be smaller than the thickness of the wafer. In some applications, individual posts are electroded and accessed, allowing the use of phased array techniques to supply an input and analyze the signal, producing higher resolution.

Diced composites have their limitations. The size of the posts and grooves are limited by the diamond saw. Typically, 125 micron square

posts are used with 125 micron grooves. This gives a PZT volume fraction of 25%. The geometry of the array is also a limitation. Dicing produces arrays of posts with uniform spacings. Resonances related to the interpost spacing (Lam waves) can reduce the performance of the transducers.

Composites of PZT MicroRods and epoxy allow many more options in the design of transducers. The volume fraction of PZT in the composite can be increased significantly. Round MicroRods can pack to volume fractions of up to 79% in a square array and up to 91% in a hexagonal array. Mixtures of different size MicroRods could be packed to even higher densities. *CeraNova* has produced composites with PZT volume fractions over 70%. High volume fractions of active materials are appropriate for applications where the material being scanned has a high acoustic impedance - such as nondestructive testing of metal components. Lower volume fraction composites are more appropriate for medical ultrasound applications where body tissue has a low acoustic impedance.

Packed MicroRods allow many more geometry's than can be achieved by dicing. Hexagonal, random, and arrays of mixtures of MicroRods can be fabricated. Random arrays of MicroRods can reduce or eliminate extraneous resonances. The most important feature of this technology is the ability to tailor the volume fraction and arrangement of the active material.

The individual transducers are made by slicing the composite. Many transducers can be cut from an individual MicroRod composite, reducing manufacturing costs. The MicroRod composite also allows more flexibility in the shape and size of the transducer. The size is only limited by the number of MicroRods and the size and shape of the container.

CeraNova's technology can produce MicroRods of uniform diameter with long lengths that are straight. Straightness is important in producing composites. Each slice of the composite becomes a transducer. If the initial MicroRods are not

The support of the Office of Naval Research, contract number N0014-94-C0281, is greatly acknowledged.

straight they will not pack evenly along the composite. Each slice will be different from the other slices, making property measurements unpredictable. Also non-uniform fibers in a composite will not have their axes parallel to the axis of the composite, causing variations in properties.

II. FABRICATION

Composites were fabricated using 125 micron MicroRods. The composites were sliced into wafers 500 microns thick. This is a size representative of medical ultrasound transducers and is significantly thicker than the MicroRod diameter to reduce lateral clamping.

The polymer matrix chosen is a high temperature epoxy made by Epotek. The high temperature stability allows the epoxy to withstand elevated temperatures the composite experiences during poling. Several fabrication problems had to be overcome to produce high quality composite.

Air bubbles were initially trapped in the epoxy matrix. This problem was resolved by heating

the epoxy to lower its viscosity and injecting the epoxy into the composite under vacuum.

Shrinkage of the epoxy during curing caused the composites to crack. This was found to be caused by the epoxy adhering to the mold. This problem was solved by using a flexible material for the mold and a release agent on the surface.

Each slice must have a conductive coating put on both surfaces for electrical contacts. The choice of material greatly affects the performance of the composite. It was found that conductive paints, such as silver, were unreliable, causing a high variation in electrical measurements. Gold sputtered directly onto the surface did not adhere well. Electroless nickel was found to give the most reliable results for electrical measurements.

The PZT volume fraction in each wafer was measured separately. An Archimedes balance was used to measure the density of the composites, MicroRods, and epoxy. The epoxy has a density of 1.26. The MicroRods have a density of 7.2. Composite have been made with PZT volume fractions between 25% and 70%. Fig. 1 shows a representative MicroRod composite slice.

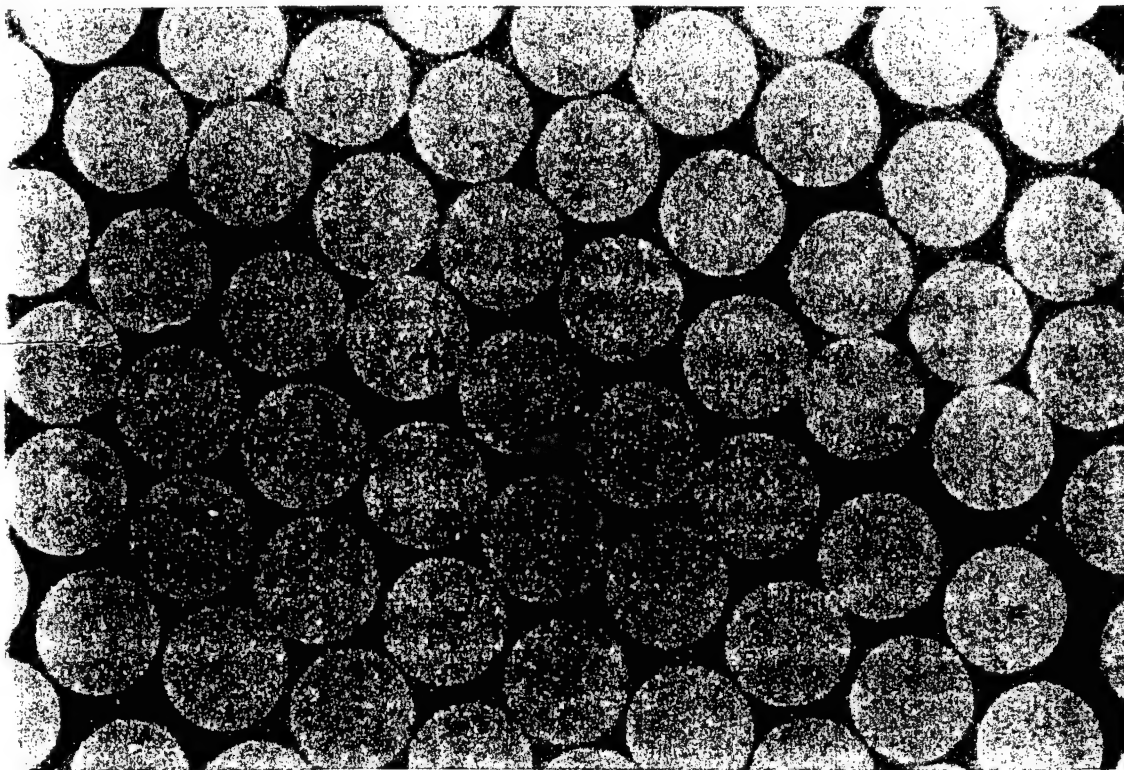


Fig. 1. A representative slice of a MicroRod composite transducer using 125 micron MicroRods at 65% volume fraction.

Preparation of Fine Scale PZT Fibers and Their 1-3 Composite Properties

Richard J. Meyer, Jr., Thomas R. Shrout, and Shoko Yoshikawa

Materials Research Laboratory
The Pennsylvania State University
University Park, PA 16802 USA

Abstract--Preparation of fine scale ($< 40 \mu\text{m}$ in diameter) PZT and modified PZT fibers has been established by spinning high viscosity metal alkoxide based solutions. Sharp exothermic reactions during conventional pyrolysis of lanthanum doped PZT (PLZT) resulted in cracking of the fiber. Fiber cracking problems were eliminated using careful atmosphere control during organic burnout. This study showed that the use of a reducing atmosphere followed by water vapor and air gave fibers with the highest dielectric constant. Dielectric and polarization/coercive field characteristics for single fibers were obtained using a specially designed fixture. Ceramic-polymer 1-3 composites were prepared for high frequency transducer applications. These composites, with randomly distributed ceramic fibers, contained ceramic volume fractions tailored from 15% to 45%. Thickness resonances from 15 to 35 MHz were achieved with coupling factors (k_t) of 65-70%.

I. INTRODUCTION

Recent trends toward high frequency medical ultrasonic imaging have focused on improved performance of high frequency transducers. Piezoelectric/polymer 1-3 composites, previously limited to frequencies up to 15 MHz, have good acoustic matching to the body and improved sensitivity over most high frequency materials [1]. By improving 1-3 composite design, resonance frequencies can potentially be pushed as high as 50 MHz. Obtaining these high frequency devices requires control of the composites spatial scale. Reducing the pillar diameter in 1-3 composites to 50% of the transducer thickness along with random pillar arrangement eliminates transverse coupling modes resulting in pure thickness mode vibrations [2]. Thus, a $65 \mu\text{m}$ thickness PZT based element resonating at 30 MHz requires roughly a $30 \mu\text{m}$ diameter pillar. Conventional methods for fabricating pillars for 1-3 type composites, such as dice and fill, injection molding, and powder based extrusion are limited typically to $> 80 \mu\text{m}$ in diameter [3]. Fine scale fiber development based on sol-gel [4,5] or viscous suspension spinning methodology [6] offers ceramic fibers with diameters between 10 and $80 \mu\text{m}$.

Metal alkoxide sol-gel technology was chosen in this paper to develop ceramic piezoelectric fibers with the desired diameters. Alkoxide based sol-gel processing allows for the continuous production of the

gel fibers and has the advantages of good chemical homogeneity and purity plus ease of compositional adjustments [5]. One disadvantage to this type of processing is the large organic content (15 weight%) in the gel fibers. Removal of the organics during the gel to ceramic conversion results in large shrinkage and cracking within the fiber diameter and along the fiber length.

Methods for controlling organic removal during pyrolysis include atmosphere and heating rate control. Atmosphere control has been utilized widely in the production of ceramic parts with large binder contents such as those made by extrusion and injection molding. Under these same principles, controlling the rates and temperatures of organic removal results in the ability to fabricate dense crack free fibers. In this study, a variety of atmospheres in conjunction with water vapor allow for the production of PLZT and PNZT fibers.

Characterization of the PLZT and PNZT fibers as well as the 1-3 fiber/polymer composites was the objective of this work. Issues concerning the use of these composites as high frequency transducers were also investigated.

II. EXPERIMENTAL PROCEDURES

A. Fiber Preparation

Gel fibers of PZT doped with La [$\text{PbLa}_{0.055}(\text{Zr}_{0.57}\text{Ti}_{0.43})\text{O}_3$] or Nb [$\text{PbNb}_{0.025}(\text{Zr}_{0.525}\text{Ti}_{0.475})\text{O}_3$] were fabricated using metal alkoxide precursors according to the flow diagram in figure 1. Stock solutions were produced using lead acetate tri-hydrate, (Aldrich, 99.999% pure) zirconium n-propoxide, (Aldrich, 70% in propanol), niobium ethoxide (Chemat technology, 99% in ethanol) lanthanum isopropoxide (Aldrich, 40% assay) and titanium isopropoxide (Aldrich, 97% in isopropanol) as starting precursors with 2-methoxyethanol (Aldrich, HPLC reagent grade) as a common solvent. Initially, the water groups associated with the lead precursor are distilled off, with the Zr, Ti, and La (Nb) precursors added and refluxed for a minimum of 4 hours. The resulting solutions are then modified for fiber spinning.

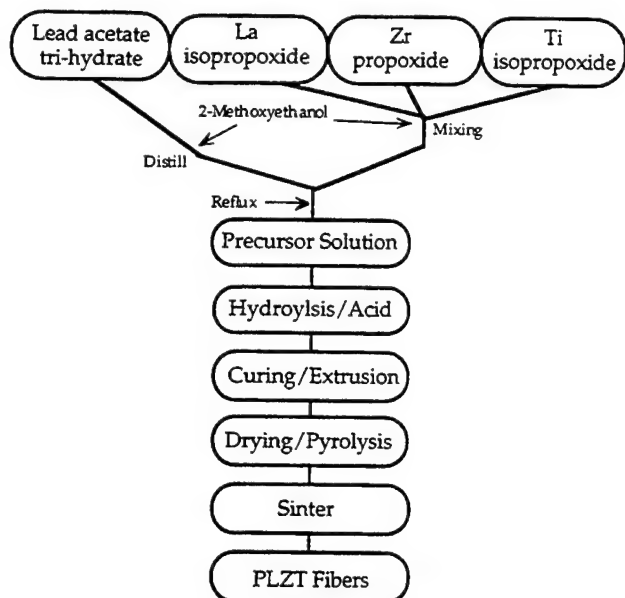


Fig. 1 Flow diagram for the production of PLZT fibers.

Fiber drawing was done during the high viscosity region near the gel point of the solution. The sol to gel transition was controlled with hydrolysis and acetic acid additions as well as curing temperature. Typical curing temperatures of 80°C were used. The high viscosity sol was extruded through a die or spinnerette containing four 100 μm diameter holes. Details of this continuous gel fiber production are reported elsewhere [5]. Subsequent drying and pyrolysis of the gel fibers were carried out using specific atmosphere control to prevent fiber cracking.

B. Pyrolysis and Sintering

Pyrolysis of the gel fibers was performed using various types of atmospheres to control organic burnout. A slow heating rate of 1°C/min was used for each stage. Atmospheres consisted of air, CO, N₂, and H₂O. Carbon monoxide and nitrogen atmospheres were used during the early stages of pyrolysis up to 300°C. Samples were exposed to water vapor during heating from 300° to 400°C. Air was used during the latter stages of pyrolysis up to 600°C. Dwell times varied from 0 to 30 minutes between stages. Fibers were allowed to cool and then transferred to a sealed vessel where they are sintered under a lead atmosphere. Typical sintering temperatures of 1200°C were used to obtain 1 - 1.5 μm grain sizes. Microstructural evolution, determination of fiber diameters and relative density were monitored using an environmental scanning electron microscope (ESEM; ElectroScan).

C. Composite Fabrication

Sintered fibers were prepared for composite fabrication by aligning and bundling several hundred 2.5 cm long fibers. Fiber bundles were immersed in low viscosity epoxy (Epo-Thin or Epo-Tec 2 part Epoxy, Buehler). The composite was degassed under vacuum. The composite was then diced to 125 μm wafers with the fibers aligned perpendicular to the face. Samples were then polished to the desired thickness. Gold sputtering was used to electrode the faces of the composite. Fiber volume fractions were obtained by counting the number of fibers under the electrode using photos taken at 15x magnification with an optical microscope.

D. Fiber/Composite Characterization

Dielectric constant (k), remanent polarization (P_r) and coercive field (E_c) were measured using a parallel plate fixture developed at The Pennsylvania State University. Details concerning the design of the fixture have been previously reported [5]. Ten and three millimeter fiber lengths were used to measure capacitance and polarization, respectively. Up to 10 fibers were measured to obtain average values. Comparisons were then made to bulk properties. Bulk properties were determined by pressing and sintering pellets made from sol-gel powder obtained after the spinning process.

Composite dielectric constant (k) was measured using an LCR meter (HP 4274), remanent polarization (P_r) and coercive field (E_c) were measured using a modified sawyer-tower circuit and composite displacement was obtained with a specially designed fixture incorporating an LVDT. The composites were poled at room temperature for 10 minutes under flourinert at 50 kV/cm. Resonance characteristics were measured using an Impedance/Gain Phase analyzer (HP 4194). Composite thickness mode coupling was calculated using frequencies at both maximum resistance and conductance. Mechanical Q was estimated using the bandwidth approximation.

III. RESULTS AND DISCUSSION

A. Gel to Ceramic Conversion

As spun fibers, examined under the SEM after drying in air at 25°C for 2 days, showed a glass like solid morphology with pristine surfaces and uniform cross-section. Gel fiber diameter can be controlled during fiber collection. For this study, both PLZT and PNZT gel fiber diameters averaged 80 μm .

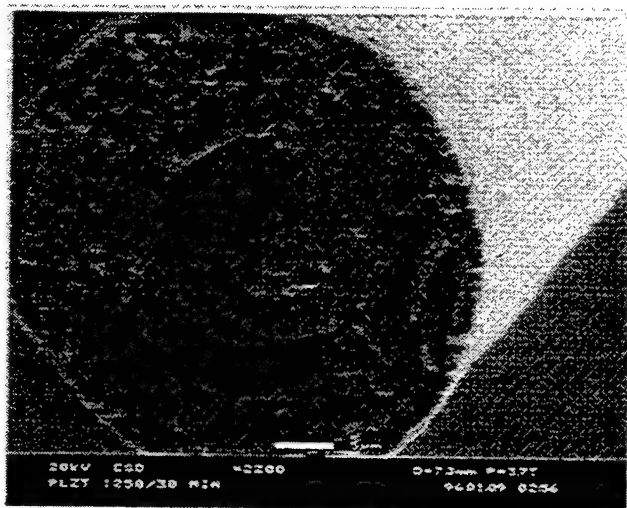


Fig 2: SEM micrograph of a cracked fiber obtained using air atmosphere during pyrolysis. Bar = 5 μ m.

Pyrolysis in air at heating rates as low as 1°C/min resulted in fiber cracking, shown in figure 2. This cracking, described as onion skin cracking, stems from the large shrinkage caused by organic removal. Improvements in pyrolysis step was achieved using atmosphere control.

By regulating atmospheric conditions within the furnace during pyrolysis, control of not only the rate of reaction but reacting species was obtained. This creates more uniform weight loss rates and reduces stress generated during shrinkage. Initially, reducing or inert atmospheres were used to suppress the large weight loss rates, shown in figure 3, occurring around 300°C.

Water vapor was then used to help remove residual carbon. Fibers fired using this stage were found to be crack free, although, final sintered samples, shown in

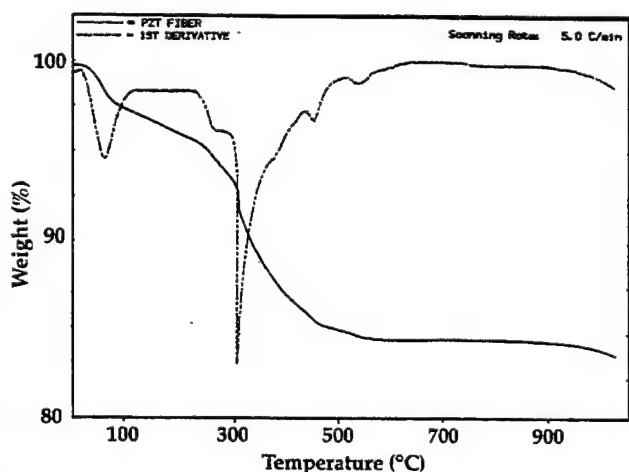


Fig 3: TGA weight loss curve and derivative of PZT fibers under air atmosphere,

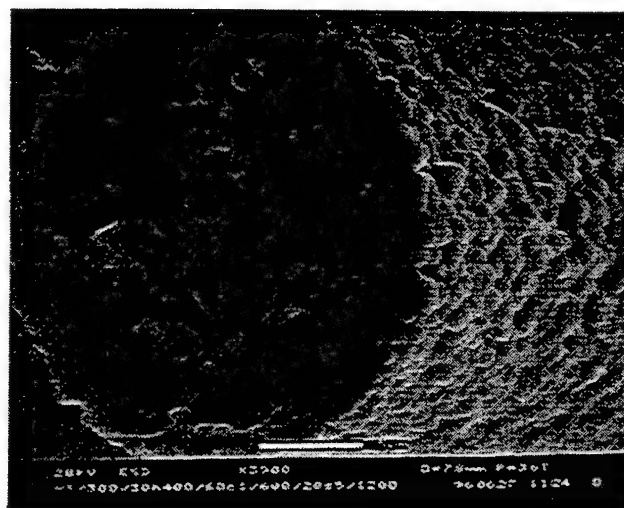


Fig 4: SEM micrographs of the fiber cross-section of CO-H₂O-Air pyrolyzed samples. Bar = 5 μ m.

figure 4, appear to be less dense. Also, the "shell" type structure was not as apparent compared to the air treated samples. It is believed that the water vapor may alter the pore structure of the fiber reducing the skin effect that is possibly hindering the removal of volatiles during calcination. Further experiments are being conducted to model the gel to ceramic conversion and to verify the effects of the various atmospheres on pyrolysis.

B. Single Fiber electrical characterization

Fibers pyrolyzed under various conditions were characterized using the special fixture for dielectric constant and polarization measurements. The results of the study reveal the highest dielectric constant and polarization for CO-H₂O-Air treated samples. These fibers had a dielectric constant of 1200, remanent polarization of 38 μ C/cm², and coercive field of 8.0 kV/cm compared to the bulk of 1400, 38 μ C/cm², and 8.5 kV/cm. Nitrogen treated samples with a similar grain size of 1.5 μ m had dielectric constants of 830 and below. Differences between carbon monoxide and nitrogen atmospheres are not yet clear. Prolonged treatments in water vapor resulted in breakdown below the coercive field, further implying the coarsening behavior of the water vapor.

C. Fiber/Epoxy 1-3 type composite properties

Fibers pyrolyzed using atmosphere controlled burnout were used for 1-3 composite property measurements. The average fiber diameter was 30 μ m. Composites, pictured in figure 5, could be fabricated with volume fractions between 15% and

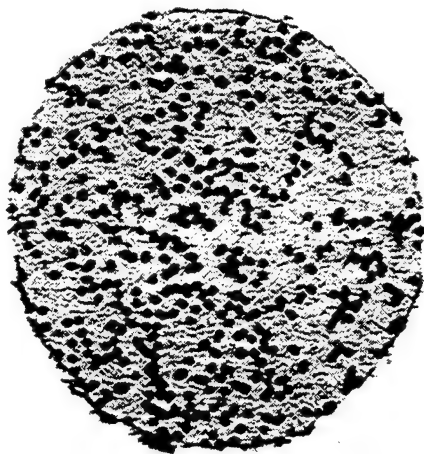


Fig 5: Optical micrograph of a 20% ceramic loaded 1-3 fiber/epoxy composite.

45% with diameters up to 3 mm. Varying the volume fraction allows tailoring of the composite dielectric constant and acoustic impedance. Dielectric constant of the ceramic phase could be obtained using composite dielectric constant, ceramic volume fraction and the parallel mixing rule and agrees quite well to single filament measurements. Polarization and coercive field measurements also agree with single fiber measurements. Effective d_{33} was calculated from the slope of the strain/field curve and had typical values of 250 pC/N. It was assumed that the low values of the d_{33} were a result of clamping from the epoxy matrix.

Composite transducer properties were evaluated with various transducer thicknesses. Thickness from 130 μm to 60 μm gave resonance frequencies from 15 MHz to 35 MHz, respectively. From the resonance data, thickness mode coupling, mechanical Q, and frequency constants were obtained. High thickness coupling from 65% to 70% was found for PLZT and

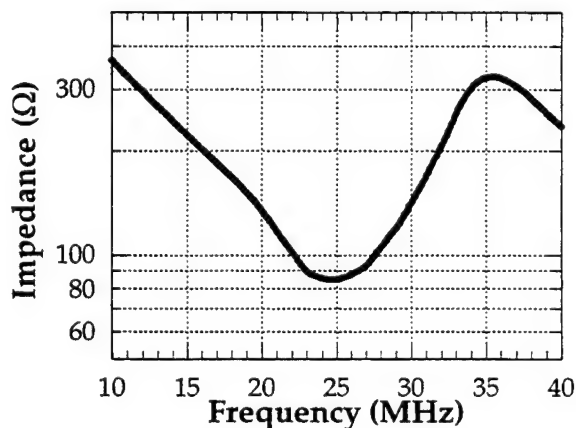


Fig 6: Impedance plotted as a function of frequency for a PNZT fiber/epoxy 1-3 composite.

PNZT samples resonating over the 15-35 MHz range, approaching the k_{33} value of 70% for these compositions [7]. The impedance of a PNZT 1-3 composite is shown in figure 6. Frequency constants averaged 1950 Hz•m for the 1-3 composites which compares to the bulk value of 1980 Hz•m. The mechanical Q ranged from 4 to 8.

IV. CONCLUSIONS

PZT fibers were successfully fabricated using metal alkoxide sol-gel chemistry. The conversion from gel to ceramic was investigated to determine the pyrolysis techniques needed to produce crack free high quality fibers. A method for making 1-3 fiber/epoxy composites was established.

Single fiber and composite properties agree well with each other and are comparable with bulk properties. Composite properties can be tailored for volume fraction and resonance frequency with high coupling making them viable candidates for 15 to 35 MHz medical imaging.

ACKNOWLEDGMENTS

The authors wish to thank AASERT ONR Grant #N00014-93-1-1054, Army Research Grant No. DAAH04-95-1-0465, Defense Advanced Research Agency, SSRC Consortium, plus Patrick Lopath of the Whitaker Center and Dr. Gary Messing for helpful discussions.

REFERENCES

- [1] T.R. Gururaja, W.A. Schulze, L.E. Cross, and R.E. Newnham, "Piezoelectric Composite Materials for Ultrasonic Transducer Applications. Part II: Evaluation of Ultrasonic Medical Applications," *IEEE Transactions on Sonics and Ultrasonics*, Vol. SU-32, [4] 499-513 (1985).
- [2] W.A. Smith, "New Opportunities in Ultrasonic Transducers Emerging From Innovations in Piezoelectric Materials," pp 3-26 in *New Developments in Ultrasonic Transducers and Transducer Systems*, SPIE Proceedings, Vol. 1733, San Diego, CA July (1992).
- [3] V. F. Janas and A. Safari, "Overview of Fine-Scale Piezoelectric Ceramic/Polymer Composite Processing," *J. Am. Ceram. Soc.* 78 [11], 2945-55 (1995).
- [4] W. Glaubitt, D. Sporn, and J. Rainer, "Sol-Gel Processing of PZT Long Fibers," in *Advances in Science and Technology 10: Intelligent Materials and Systems*, ed. by P. Vincenzini, Techna Srl, pp 45-54 (1995).
- [5] R.J. Meyer, Jr., T. ShROUT, and S. Yoshikawa, "Ultrafine Lead Zirconate Titanate Fibers Derived From Sol-Gel Technology," Accepted to *J. Am. Ceram. Soc.* July 1997.
- [6] R.B. Cass, "Fabrication of Continuous Ceramic Fiber by the Viscous Suspension Spinning Process," *Am. Ceram. Soc. Bull.*, 70 [3] 424-29 (1991).
- [7] B. Jaffe, W. Cook, and H. Jaffe, *Piezoelectric Ceramics*, Academic Press Limited, R.A.N. Publishers, Marietta, OH (1971).

ANISOTROPIC PIEZOCERAMIC (3 -3) COMPOSITES

Venkat S. Venkataramani and Peter C. Schaefer, Ceramics Laboratory,
Lowell S. Smith, Electronics Systems Laboratory,
General Electric Co, Corporate Research & Development, Schenectady, NY

Abstract

Novel piezoceramic polymer composites with anisotropic connectivity have been fabricated. The unique method of forming the ceramic precursor results in an anisotropic structure in which the ceramic phase as interconnected lamellae is more continuous in the thickness direction than in the other two planes. These composites have a predominance of 1-3 connectivity. The resulting better figures of merit such as high coupling coefficient (k_t), low acoustic impedance (Z_s), high dielectric constant (K_{33}) values make these promising candidates for sonar and medical ultrasound transducer applications.

1. Introduction

Piezoelectric ceramic-polymer composites, hereinafter referred to as piezocomposite, are finding increasing use in both low to mid frequency sonar and hydrophone and in the high frequency (~1-20 MHz) medical diagnostic transducer applications. There is an increasing need to improve the imaging range and resolution, as determined by the sensitivity and bandwidth of the transducer. There is also a move toward high frequency transducer use for endoscopy surgical procedures and intravascular imaging.

The piezocomposites offer three major advantages over the conventional piezoceramics - (1) Reduced specific acoustic impedance (Z_s), [2] increased thickness coupling (k_t), and (3) reduced planar coupling (k_p). However, tradeoffs in the design must often be made, as these three parameters cannot be optimized simultaneously. The designs are based on optimizing the "connectivities" of the phases of the composite, usually that of the ceramic and the compliant polymer. The evolution and development of this concept is described in Ref. 1. Most common of the various designs are the 0-3, 1-3, 3-3 and 2-2 connectivities. In the first three the ceramic is interconnected in 0, 1 and 3 orthogonal directions (dimensions) and the polymer is a continuous matrix. In the 2-2 composite both the ceramic and polymeric phases are self connected in two dimensions, specifically the x or y and the z directions. These designs enhance the figures of merit such as the hydrostatic d_{hg} , k_t or k_t/k_p and acoustic impedance Z , by either minimizing or negating the effects of the transverse modes and by averaging certain elastic and dielectric constants. Details of modeling calculations for some of these designs are explained in [2] and [3]. The 1-3 and 2-2 connectivity designs are the most

widely used for the hydrophone and ultrasound applications.

Over the past two decades several methods for fabrication of these composites have been developed. These include incorporating shaped particles such as granules [4], spheres [5], and rods [6] in a compliant matrix, fabrication from replication and impregnation methods [7,8], dicing a ceramic in one or two directions into strips or pillars and filling the kerfs with a suitable material [9], net shape fabrication of the precursor by injection molding or casting into sacrificeable molds [10-18], and fabrication from reticulated porous ceramics [19-23]. More than an order of magnitude reduction in feature sizes has been achieved with novel processes such as injection molding, fine fiber fabrication, fabrication of molds via high energy etching and photolithographic methods. However, most of these methods still remain as laboratory curiosities. Feature sizes of 50-100 micron ceramic rods with 25 micron spacing is available from the dice and fill method. The reduction of the feature sizes is limited by the processing technology, e.g. dicing blade thickness or mold design and robustness in injection molding. The simplest method of achieving a porous precursor is the reticulated ceramic fabrication. However, this method results in a rather isotropic 3-3 connected composite having larger than required feature sizes for the high frequency applications. Recently, there has been some breakthroughs in pore shape modification in this process [21-23]. In this paper we report a novel method of forming a piezoceramic precursor with most porosity oriented in the thickness direction having sub hundred micron interconnected features. This results in a composite with anisotropic connectivity. The enhanced performance characteristics of a composite made from such precursor are also discussed.

2. Composite Fabrication and Measurements

The overview of the process is shown in Fig. 1.

1.

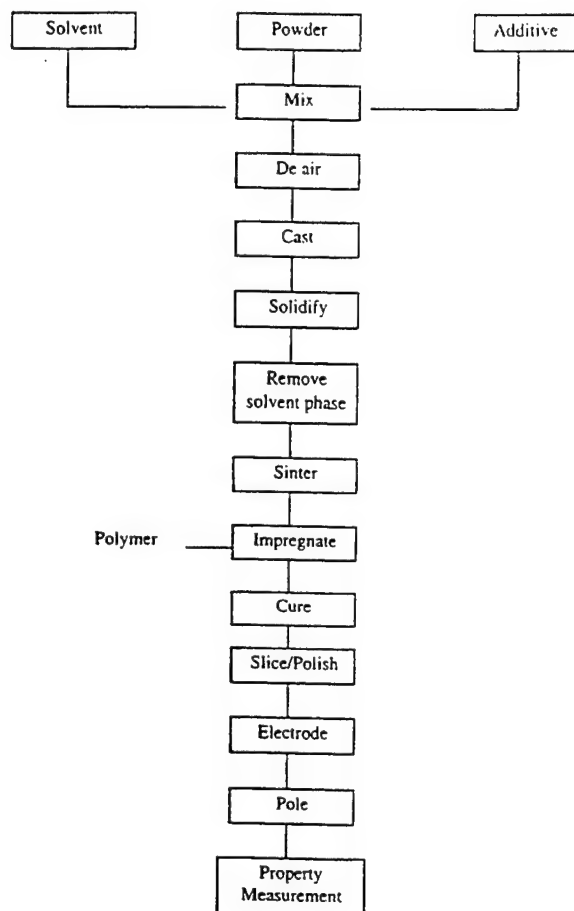


Figure 1: Fabrication Process Flow Chart

The fabrication is done in two steps. The first step is the preparation of the ceramic precursor. The desired slurry, containing the piezoelectric ceramic powder, the appropriate solvent and the additives for control of rheology, was poured into a suitable mold and directionally solidified by freezing in a controlled manner. This imparted the columnar alignment of the ceramic rich phase separated by the solvent phase with an interpenetrating lamellar structure oriented in the thickness direction. The frozen slurry was then subjected to a heat cycle under low pressure to sublime the solvent phase, resulting in a cellular ceramic with anisotropic structure containing the ceramic lamellae oriented along the thickness. The ceramic was then carefully sintered under controlled atmosphere to densify the ceramic regions to the required density.

The porous ceramic precursor thus obtained was then impregnated with the desired compliant polymeric material and cured as needed. Wafer sections were sliced off this block, shaped, ground, and lapped to the desired dimensions. The top and bottom surfaces were electroded with sputtered gold and the samples poled by the application of a DC electric field of 30 KV/cm at 80°C for 15 minutes in a Fluorinert bath.

Preliminary measurements of low frequency dielectric constant (10 KHz) and d_{33} coefficient were taken 24 hours after poling. The acoustic and electromechanical characteristics of the samples were then obtained through the measurement of resonance characteristics and calculating the required parameters such as k_t , Z_s , K_{33}^s , V_L etc. by fitting into the KLM model..

3. Results and Discussion

The solidified "green" ceramic precursor underwent a 30-45 vol% shrinkage on sintering, depending on the initial volume fraction of the ceramic powder in the slurry, which ranged between 10-50 vol%. At low volume fractions (<20 vol%) the structure was rather inhomogenous. The ceramic regions of the sintered samples however were densified to >95% of the theoretical density with average grain size of 3-6 μm .

3.1 Microstructure

The artist's rendition of a typical microstructure of the composite is shown in Fig. 2.

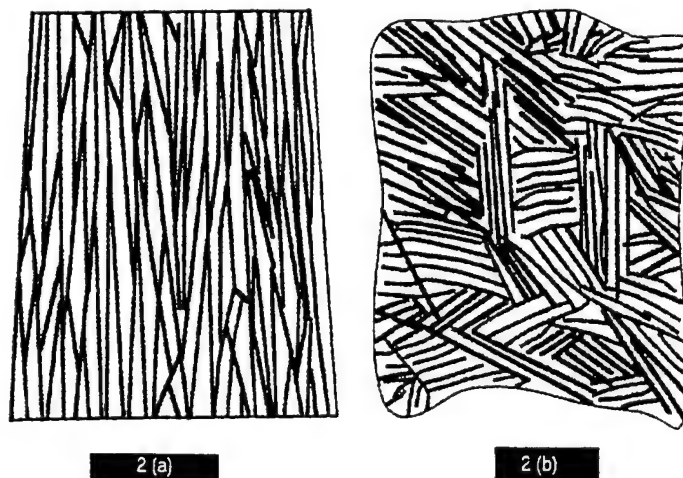


FIG 2. Artist rendition of the microstructure of the piezocomposite
2 (a) - Cross Sectional view : 2 (b) - top planar view.

represent the ceramic regions separated by the polymer phase indicated by the white areas. The optical micrograph of a typical sample is given in Fig. 3. Fig. 3A is the top planar section and Figs. 3B is the cross-sectional view.

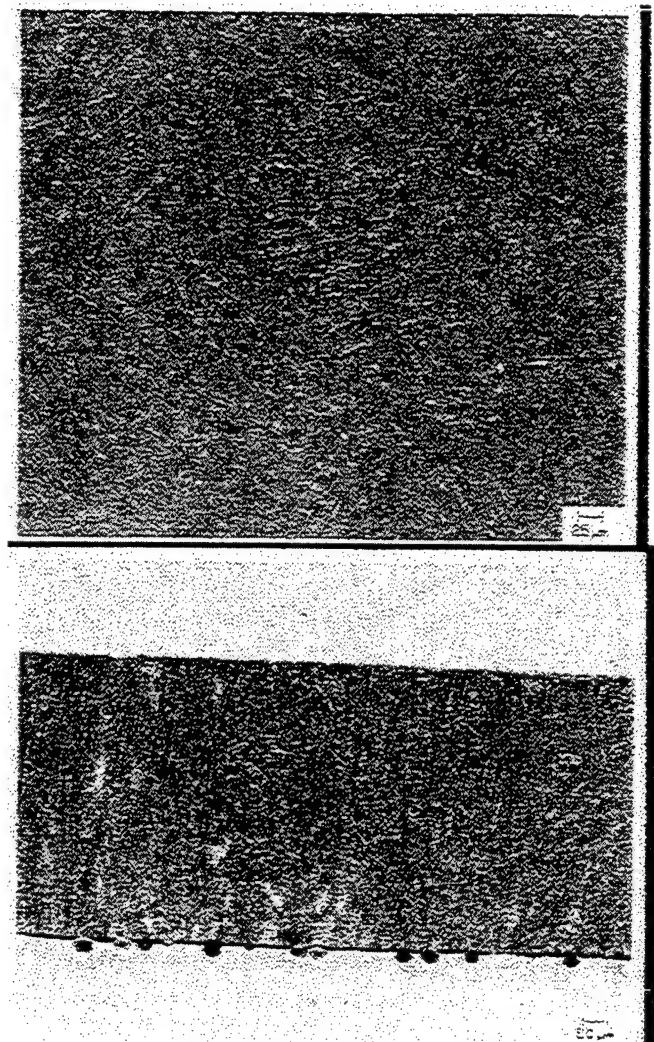


Fig 3. Optical micrographs of the composite surfaces.
Top: 3a - top view ; Bottom ; 3b - cross section.

The role of directional solidification resulting in the phase separation of the solute (ceramic) and the solvent phases and their formation of oriented interconnected lamellae is evident from these microstructures. The ceramic phase solidifies in columnar structures almost vertically from bottom to top across the thickness, and is weakly connected in the lateral directions. The wall thickness was around 50-100 μm and the pore channels were around 10-30 μm . The spacing between the walls and the thickness of the walls also varied as a function of the volume percent of the ceramic as shown in the top and bottom..

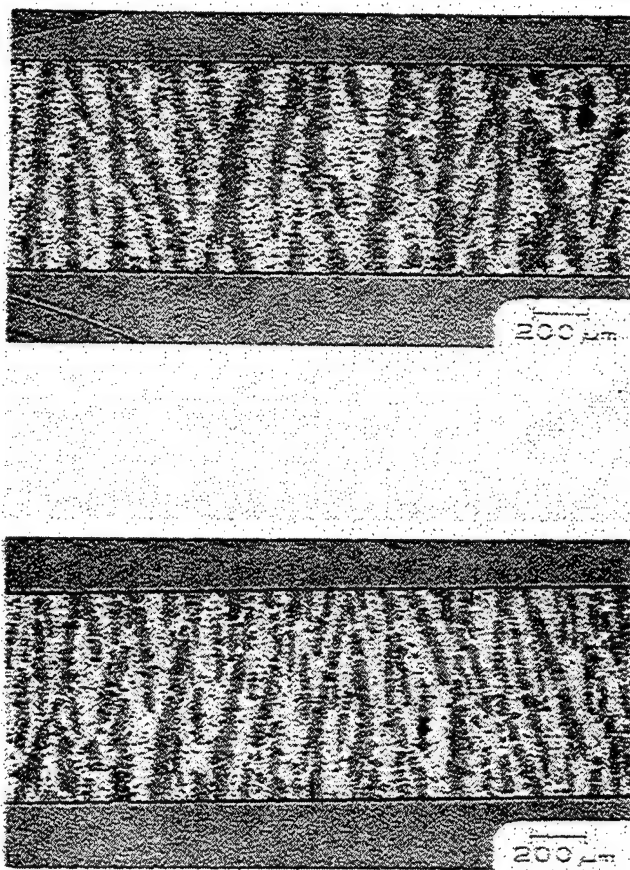


Fig . 4. Scanning electron Micrographs of cross sections of two composites. (Top -45 vol% : Bottom - 60 vol %)

The inter-lamellar spacing gets smaller with increasing volume fraction of ceramic and the size distribution of the wall thickness gets wider. At very low initial volume fraction of the ceramic (<15%), the structural homogeneity was inconsistent with non-uniform distribution of sizes and microstructure resulting in variations in the electromechanical characteristics within regions in a sample as well as between samples from different runs.

3.2 Acoustic and Electromechanical Characteristics.

The electromechanical characteristics of a typical anisotropic piezocomposite (~50 vol% ceramic) in comparison with a sintered PZT 5H ceramic is shown in Fig.5.

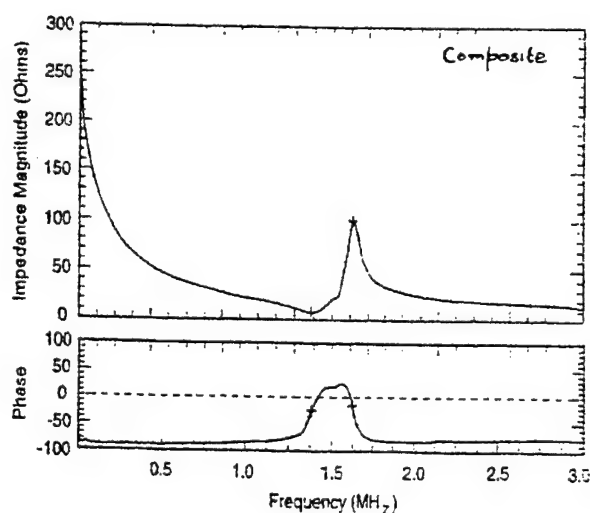
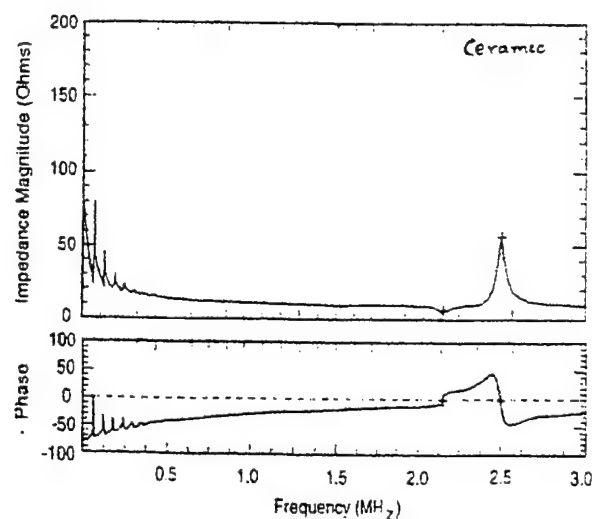


Fig 5. Impedance (magnitude) and Phase as a function of frequency. Top - Ceramic ; Bottom - Composite.

The lamellar structure results in the suppression of the planar resonance modes (low frequency) through the reduction of the planar coupling (k_{31}) as noted in (2,3). This anisotropic connectivity also results in the lower acoustic impedance, higher thickness and lower planar coupling coefficients as shown in Table below:

| | PZT -5H CERAMIC | PZT-5H - EPOXY COMPOSITE |
|---|--------------------|-----------------------------|
| CERAMIC VOLUME FRACTION - % | >97 | 55 |
| THICKNESS COUPLING CONST. (k_t) - % | 53 | 63 |
| PLANAR COUPLING CONST. (k_p) - % | 58 | 22 |
| SPEC. ACOUSTIC IMPEDANCE (Z_s) - M Rayls. | 33 | 18.9 |
| DIELECTRIC . CONST (K_{33}) | 1630 | 850 |

The values of the thickness mode coupling coefficient (k_t), specific acoustic impedance (Z_s) and the average longitudinal sound velocity for some of the specimen (v_l) are plotted on to the calculated values from the model [2] in Fig 6.

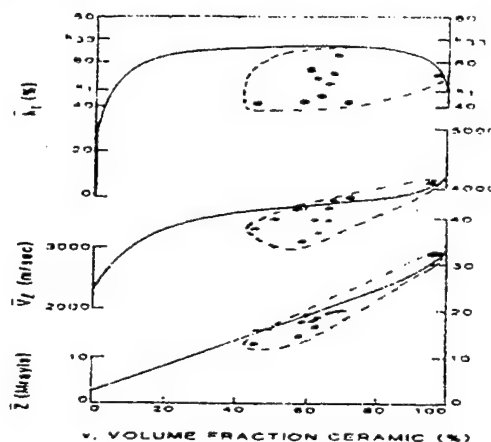


Fig. 6. Comparison of the calculated values (from [2]) with the actual values of the composites

From Fig. 6 it can be seen that there is general agreement of the obtained values with that predicted by the model for Z_s and v_l . However, the k_t values are lower than predicted by the model. The model described in [2] and [3] is based on an ideal 1-3 connectivity of the ceramic and the polymer phases.. While the acoustic properties , Z_s and v_l are averaged out over the whole structure, the electromechanical coupling depends more critically on the long range order of the microstructure of the phases. So for the composite samples measured , which do have some lateral connectivity of the phases, as described in [2] and [3], the lower k_t values can be attributed to one or more of the following reasons:

1.Lack of orientation of the lamellae in the thickness direction

2. Transverse bonding of the lamellae causing interference of the transverse coupling modes
3. Effects of the fine scales of the ceramic and polymer regions causing clamping of the desired vibration modes.
4. Stiffness of the polymer which has not yet been optimized for this application.

4. Summary and Conclusion

A novel and cost effective method of forming piezoceramic-polymer composites has been developed. Piezoceramic composites with thickness coupling coefficients of about 60% , low planar coupling coefficient of 22% and low acoustic impedance of 12 - 18 Mrayls have been demonstrated. The process is amenable to large cross sectional areas and thicknesses to cover the useful sonic and ultrasonic frequency ranges for a wide variety of applications such as hydrophones , medical ultrasound transducers etc. Fine spatial scales required for the ultrasound applications (of the order of 50 microns) can be achieved.

The fabrication process starts with the preparation of piezoelectric ceramic precursor structure consisting of lamellar walls of ceramic regions weakly bonded in the planar direction. The preferential orientation of the walls along the thickness of ceramic is accomplished by a novel process of directional solidification of the slurry causing a phase separation of the solute and solvent phases. On the removal of the solvent phase by evaporation the anisotropic ceramic structure is obtained. After densification of the ceramic, suitable compliant polymeric material can be infiltrated into the free space of the ceramic forming the functional composite. The resulting structure is predominantly "1-3" connected composite. The process is easily scalable for large area structures.

Optimization of the key process and material parameters such as solidification rate, control of the solidification front, particle size of the powder, volume fraction of the ceramic in the slurry and the use of optimized polymeric materials are in progress.

References

1. R.E. Newnham, D.O. Skinner and L.E. Cross, *Materials Research Bulletin*, 13, 525, (1978).
2. W.A. Smith and B.A. Auld, *IEEE Transactions on Ultrasonics, Ferroelectrics and Frequency Control*, 38(1), 40, (1991).
3. C. Oakley and P. Marsh, *SPIE Vol 1733*, 274, (1992).
4. W.B. Harrison, *Proceedings on the Workshop on Sonar transducers*, Naval Research Labs, 1978.
5. A. Safari, PhD thesis, Pennsylvania State University, 1983.
6. K.A. Klicker, PhD thesis, Pennsylvania State University, 1981.
7. M.T. Strauss, *ONR Review*, 1996.
8. D.P. Skinner, R.E. Newnham and L.E. Cross, *Materials Research Bulletin*, 13, 599 (1978).
9. H.P. Savakus, K.A. Klicker and R.E. Newnham, *Material Research Bulletin*, 16, 677,(1981).
10. N.M. Shorrocks, M.E. Brown, R.W. Whatmore and F.W. Ainger, *Ferroelectrics*, 54,215(84).
11. M. Baker and I. Bedwell, presented at the Amer. Cer. Soc. 86th Mtg., 1984.
12. L.J. Bowen and K.W. French, *Proc. 8th IEEE Internationa Symposium on Applications of Ferroelectrics*, pp.160-164, (1992).
13. L.J. Bowen, R.J. Crentilman, H.T. Pham, D.F. Fiore and K.W. French, *Proceedings IEEE Ultrasonics Transactions*, 191-196, (1995).
14. V. Bast, D. Cramer and A. Wolff, *Proceedings of the 7th CIMTEC*, 2005-2015, 1990.
15. K. Lubitz, A. Wolff and G. Preu, *Ferroelectrics*, 133, 21-26, (1992).
16. T.F. McNulty, V.F. Janas and A. Safari, presented at the 97th Annual Mtg. of the American Ceramic Society, 1995.
17. Y. Hirata, et al, *IEEE Ultrasonics Transactions*, 191-16 (1995).
18. K. Rittenmeyer, T.R. Shrout, W.A. Schulze and R.E. Newnham, *Ferroelectrics*, 49,265 (1983).

19. K.Hikita, K.M. Nishioka and M. Ono,
Ferroelectrics, 49, 265 (1983).
20. S.Pilgrim and R.E. Newnham, presented at
Electronics Div. 86th Annual Mtg., American Ceramic
Society, 1985.
21. M.J. Creedon, S. Gopalakrishnan and W.A.
Schulze, "3-3 Composite Hydrophones from
Reticulated Ceramics", pp. 299-302, Proceedings of
IEEE 9th Internal Symposium on the Application of
Ferroelectrics, 1994.
22. Mathew J. Creedon and Walter A. Schulze,
Ferroelectrics, 153, 333-39 (1994).
23. M.J. Creedon and W.A. Schulze, submitted to
Ferroelectrics.

Fine Grain Piezoelectric Ceramics for Transducer and Actuator Applications

Wesley Hackenberger and Jon Helgaland

TRS Ceramics, Inc.
2820 E. College Ave.
State College, PA 16801

M. Zipparo, C. A. Randall, and T. R. Shrout

Intercollege Materials Research Laboratory
The Pennsylvania State University
University Park, PA 16802

Abstract -- Navy Type II, III, and VI piezoelectric ceramics with grain sizes less than 1 μm have been produced using conventional ceramic processing techniques. The reduction in properties that normally occurs in piezoelectrics with grain sizes less than 1 μm were compensated in this work using new dopant strategies designed to increase domain wall mobility. The fine grain ceramics show promise for high frequency ultrasound arrays and high strength actuators.

I. Introduction

Submicron grain sized piezoelectric ceramics (0.5 μm) offer many advantages for both ultrasonic transducers and high driving field actuators. Reduced grain sizes lead to improved machinability for finer feature sizes in high frequency arrays (> 10 MHz), reduced yield loss for array fabrication, increased mechanical strength for high reliability actuators, and reduced layer thicknesses in tape cast multilayers for low driving voltage actuators [1]. A major problem with reducing grain sizes in piezoelectric ceramics has been a corresponding reduction in properties (see Fig. 1). TEM studies and cryogenic property measurements have revealed that reducing grain sizes effects the extrinsic contributions to piezoelectricity in PZT ceramics [2]. Domain observations indicate that in grains less than 1 μm in size, there is a reduction in the number of domain orientation variants [3]. This effectively results in a reduction of poling efficiency for fine grain ceramics compared to conventional materials (grain size ~ 3 to 5 μm).

At TRS Ceramics we have been able to compensate the effect of grain size by modifying traditional doping strategies to promote domain wall mobility [4]. This increases the extrinsic piezoelectric effect in fine grain ceramic to the extent that properties are equivalent to conventional materials (see Table 1). Currently all fine grain processing is done with the conventional mixed oxide route and sintering at atmospheric pressure. The material is, therefore, cost competitive with conventional ceramics. To date the materials that have been made in fine grain form are DOD Types II, III, and VI. A grain size comparison of conventional and fine grain Type II material is shown in Fig. 2.

A number of studies have been conducted using the fine grain Type II ceramic to demonstrate its potential benefit for a variety of applications. Dicing studies have been performed to compare the composite fabrication behavior of fine grain ceramic directly to conventional material. Very fine scale arrays have been fabricated to test the benefits of submicron ceramic for high frequency ultrasonic arrays. And finally, the benefits of fine grain ceramic for actuators has been investigated.

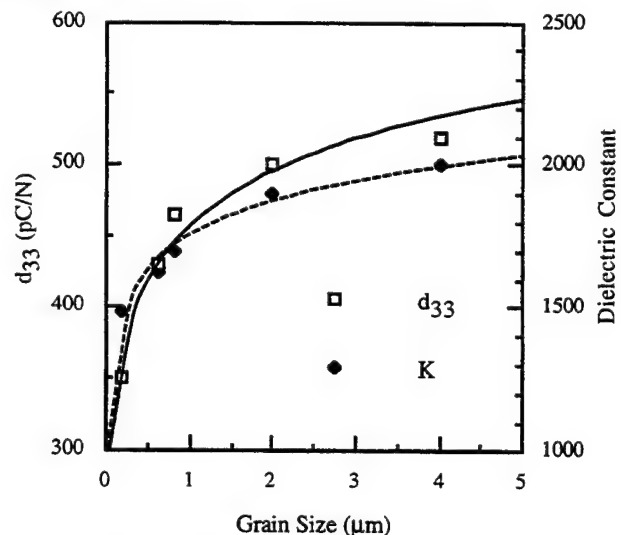


Fig. 1. Piezoelectric coefficient and dielectric constant as a function of grain size for a DOD Type II ceramic [2].

Table 1: Comparison of Fine Grain and Conventional Ceramic Properties.

| Property | Type II | Type II FG | Type III | Type III FG | Type VI | Type VI FG |
|----------|---------|------------|----------|-------------|---------|------------|
| K | 1900 | 1900 | 1150 | 1125 | 4500 | 4400 |
| Loss | 0.018 | 0.017 | 0.002 | 0.003 | 0.02 | 0.025 |
| d_{33} | 425 | 415 | 260 | 260 | 785 | 730 |
| k_p | 0.65 | 0.62 | 0.51 | 0.49 | 0.70 | 0.68 |
| T_c | 350 | 325 | --- | --- | 185 | 185 |

II. Dicing and 1-3 Composite Studies

A dicing study was performed for a side by side comparison of machinability for Type II fine grain ceramic (TRS200FG), and two conventional materials (Edo EC65 and Motorola 3195HD). Dicing conditions (blade rpm, travel speed, coolant flow and direction, dressing conditions, etc.) were the same for all samples. The dicing was done on all samples with the same blade. Multiple dicing trials were done using different sample testing sequences to account for blade wear. Results were characterized by the maximum post aspect ratio (height to width) that could be achieved. Results of the dicing experiments are summarized in Table 2. A 10 MHz 1-3 composite was constructed from the fine grain material and the effective k_t was 0.6, identical to composites made from the conventional ceramics. The results of this study indicate that fine grain ceramic should lead to significant improvements in dicing yields without a decrease in properties.

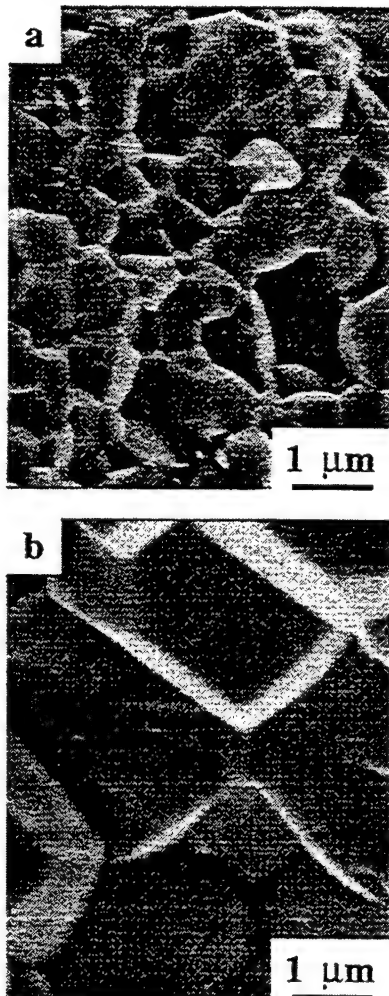


Fig. 2. Microstructure comparisons for a) TRS200FG (grain size ~ 0.5 μm) and b) 3195HD (grain size ~ 3 μm).

Table 2. Summary of Dicing Study; Smallest Post Sizes

| Material | Cut Depth (μm) | Kerf (μm) | Width (μm) | Aspect Ratio |
|----------|-----------------------------|------------------------|-------------------------|--------------|
| TRS200FG | 380 | 23 | 18 | 21:1 |
| 3195HD | 380 | 23 | 28 | 15:1 |
| EC65 | 380 | 23 | 38 | 10:1 |

III. Very High Frequency Transducers

The ultimate benefits of fine grain ceramic were determined by constructing Very High Frequency (VHF) transducers. A 2-2 composite with a resonant frequency of 50 MHz was diced using the TRS200FG material. The result is shown in Fig. 3. This composite had ceramic posts approximately 15 μm wide [5]. Arrays with these dimensions could not be diced from conventional ceramics. Single element transducer plates were also made by polishing fine grain ceramic. The thinnest samples achieved were 10 μm for a resonant frequency > 150 MHz. Such devices have potential for ultrasound backscatter microscopy. A 65 MHz single element transducer was constructed from TRS200FG ceramic and used for imaging tests. Fig. 4. shows the image of a mouse embryo made with this transducer [5].

IV. Actuators

Fine grain piezoelectrics offer several potential benefits for actuator applications. PZT ceramics with grain sizes less than 1 μm are about 30% stronger (bending strength) than conventional materials. Thus, stacked or cofired actuators made with fine grain ceramics should be more able to withstand tensile stresses during electric field driving. This will result in higher reliability actuators, and higher strain from a higher maximum driving field (see Fig. 5). Another advantage of fine grain ceramic is thinner layers in both stacked and cofired devices for lower driving voltages. Finally, the improved machinability of fine grain ceramics offers potential for constructing micro-electromechanical systems (MEMS) using mechanically thinned bulk ceramic. Bulk ceramic polished to 10 μm (already demonstrated in the transducer studies) could be bonded to silicon substrates with mounting structures and integrated control circuitry. The properties of machined, bulk ceramic are far superior to current thin film piezoelectrics, and the 10 μm thickness would allow the mN range forces needed for practical MEM devices.

V. Summary

Fine grain PZT's (< 0.5 μm) have been developed with properties comparable to conventional ceramics. Fabrication studies of ultrasonic arrays have shown that submicron grain sized PZT have superior machining characteristics to conventional ceramics. Diced or polished dimensions less than 15 μm have been achieved. Improved machinability is expected to increase array manufacturing yields and allow for the fabrication of very high frequency transducers (> 50 MHz). For actuators the improved strength of fine grain ceramics is expected to lead to increased reliability and larger

strains through high driving fields. Thinner layers in stacked and cofired actuators can also be produced with a corresponding decrease in drive voltage.

References

- [1] W. A. Smith, "New opportunities in ultrasonic transducers emerging from innovations in piezoelectric materials", *1992 SPIE International Symposium*, pp. 1-24, July 1992.
- [2] N. Kim, Ph.D. Thesis, "Grain size effect on the dielectric and piezoelectric properties in compositions which are near the morphotropic phase boundary of lead zirconate-titanate based ceramics," The Pennsylvania State University, May 1994.
- [3] W. Cao and C. A. Randall, "The grain size and domain size relations in bulk ceramic ferroelectric materials," *J. Phys. Chem. Solids*, in press.
- [4] W. S. Hackenberger, N. Kim, C. A. Randall, T. R. Shrout, and D. J. Pickrell, "Processing and Structure-Property Relationships for Fine Grained PZT Ceramics," *Proc. 10th Internl. Symp. Appl. Ferroelectrics*, IEEE, East Brunswick, NJ, Aug. 18-21, pp. 903-906 (1996).
- [5] M. Zipparo, Ph. D. Thesis, "Very High Frequency (50 to 100 MHz) Ultrasonic Transducers for Medical Imaging," The Pennsylvania State University, Dec. 1996.

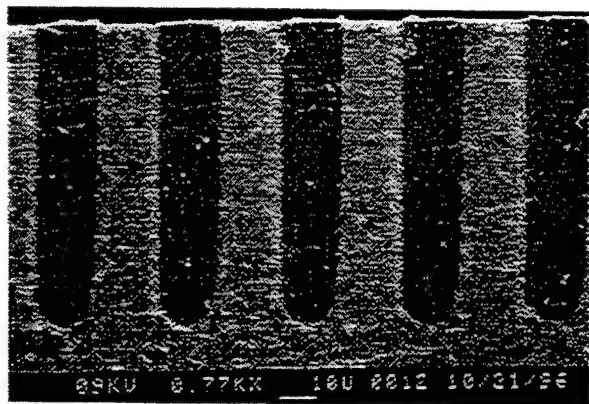


Fig. 3. 50 MHz 2-2 composite fabricated from TRS200FG ceramic (grain size $\sim 0.5 \mu\text{m}$).

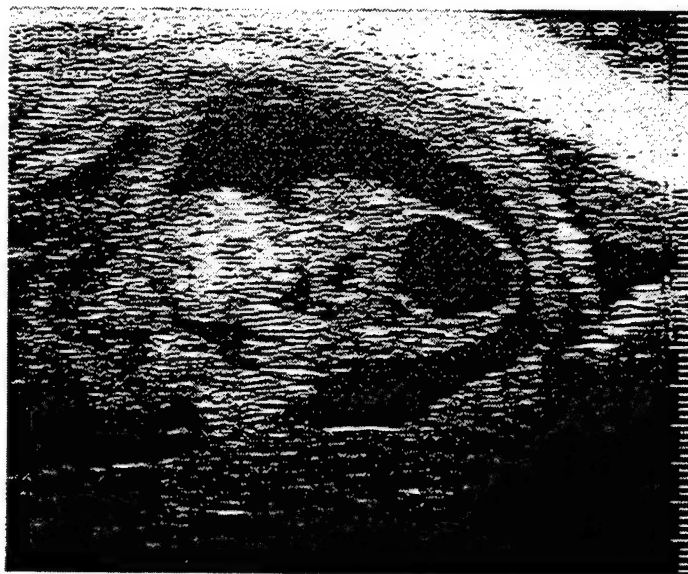


Fig. 4. Image of a mouse embryo made with a 65 MHz single element transducer constructed from TRS200FG ceramic.

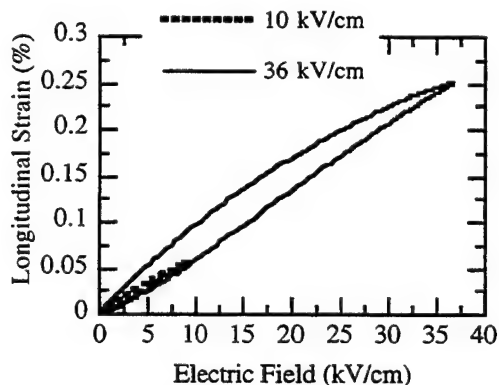


Fig. 5. Increased strain available from fine grain ceramic driven at a high electric field.

Piezocomposite Materials for Ultrasonic Imaging Applications

B. Pazol, H. Pham-Nguyen, J. Hollenbeck, M. Callahan,
K. Gabriel, and G. Schmidt

Materials Systems Inc.
521 Great Road
Littleton, MA 01460

Abstract - Materials Systems Inc. (MSI) has developed net shape processes for molding piezoelectric ceramics in complex shapes. These processes were originally developed to produce coarse ceramic structures for undersea applications in the range of 0.1 to 1 MHz. MSI has now demonstrated that these techniques are viable for producing extremely fine structures for medical ultrasonic imaging applications (typically above 2.5 MHz). Above this frequency, the ceramic dimensions become so fine that transducers cannot be fabricated cost-effectively by conventional techniques. MSI has demonstrated fine scale 1-3 structures with PZT rod diameters as small as $70\mu\text{m}$ and 2-2 piezocomposites with ceramic strips less than $25\mu\text{m}$ wide. The molding process was recently scaled to produce large area ($45\text{ mm} \times 130\text{ mm}$) sheets of fine scale 2-2 piezocomposite with pitches of $230\mu\text{m}$ and less. Currently, MSI is adapting the technology to produce 2D arrays for advanced acoustic imaging. This paper reviews recent advances in the capabilities of the molding process for fabricating 2-2 and 1-3 composites.

I. INTRODUCTION

Piezoelectric composite materials have many advantages over monolithic ceramic for ultrasonic imaging applications. Complex ceramic element geometry is possible, allowing greater design flexibility for improved acoustic impedance matching, increased electromechanical coupling, and lateral mode cancellation. In the past, the difficulty of forming and handling fine structures has been managed by dicing the desired configuration from a solid block of PZT and then back filling with a polymer. This approach has limitations in terms of cost, yield, dimensions, and design flexibility.

MSI has developed a net shape molding technique for manufacturing fine scale 2-2 and 1-3 piezocomposite [1]. Multielement arrays of PZT rods or strips are net-shape formed on an integral PZT baseplate. Thus, the difficulty of handling and aligning hundreds or thousands of fine elements during composite manufacturing was eliminated by directly forming the ceramic into the required 1-3 or 2-2 configuration, ready for assembly into finished piezocomposite.

Using these techniques, MSI has produced molded ultrafine scale 1-3 structures with PZT rod diameters as small as $70\mu\text{m}$ and 2-2 piezocomposites with ceramic strips less than $25\mu\text{m}$ wide [2]. The performance of these piezocomposites compared favorably to conventionally diced and filled materials.

Recent advances in MSI's molding technology have provided cost-effective techniques for producing large areas of fine piezocomposite. Large sheets ($45\text{ mm} \times 130\text{ mm}$) of fine scale 2-2 piezocomposite with pitches of $230\mu\text{m}$ and less have been produced. A new 1-3 tooling technology was also developed which extended the original injection molding process to mold finer, higher volume fraction PZT preforms. These preforms were recently used to fabricate piezocomposite for a high frequency curved mine hunting receive array demonstrated as part of an ONR funded Technical Collaboration Program (TTCP) [3].

II. DISCUSSION

Piezocomposites offer greater design flexibility than monolithic ceramic by allowing the designer to adjust the material properties for a specific application. Composite optimization is achieved by carefully selecting the appropriate ceramic dimensions, element spacing, and volume fraction as well as choosing suitable polymer fillers. The PZT molding process facilitates these options by allowing variations in PZT element width, volume fraction, and pitch.

A. 2-2 Composite Fabrication

MSI has adapted its fine scale 2-2 molding fabrication process to produce large area fine scale sheet 2-2 composite. Figure 1 is a photograph of a $45\text{ mm} \times 130\text{ mm}$ PZT-5H ceramic preform. Removable inserts with the required strip width, element pitch, and volume fraction were fitted into a universal tool body and used to mold the preforms. The preforms were burned out and sintered with standard processes [1]. Using removable inserts with a common tool body allowed a variety of configurations to be molded without incurring high retooling costs. Preforms with pitches from $125\mu\text{m}$ to $230\mu\text{m}$ have been molded with PZT-5H and PZT-5A. Other pitches, up to $400\mu\text{m}$, are possible with existing tooling.

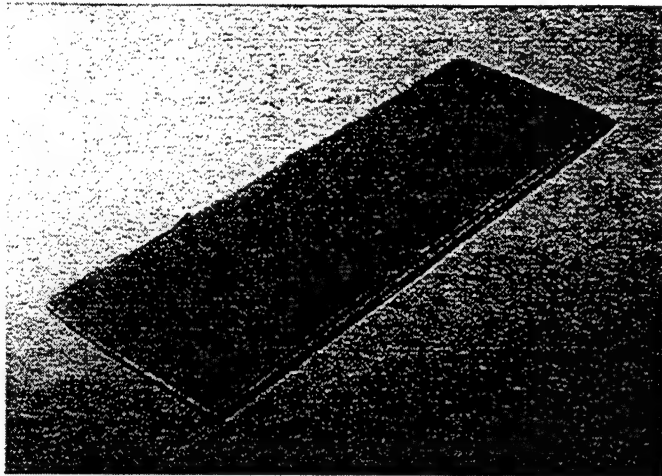


Fig. 1. Photograph of a 45 mm x 130 mm, 60 volume percent PZT-5H ceramic preform with 230 μ m pitch elements. Ceramic strips running in the long direction of the preform are molded on a common baseplate to facilitate the handling and aligning of the large number of elements.

Figure 2 shows a photomicrograph of a 60 volume percent, 230 μ m pitch preform and Figure 3 of a 50 volume percent, 125 μ m pitch preform. Notice that the strips have uniform spacing and width.

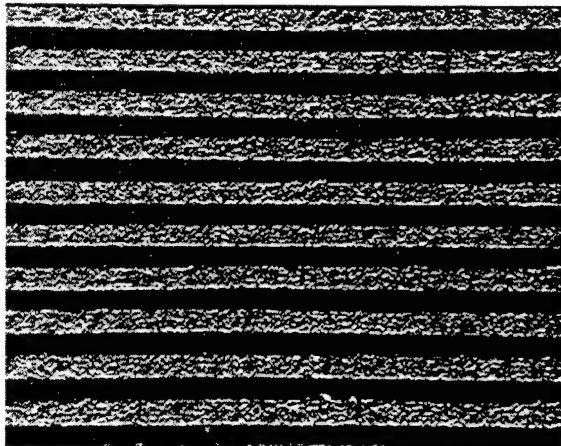


Fig. 2. Photomicrograph of a 60 volume percent PZT-5H molded preform with 230 μ m pitch.

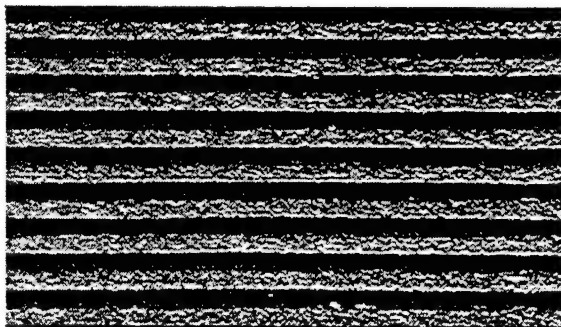


Fig. 3. Photomicrograph of a 50 volume percent PZT-5A molded preform with 125 μ m pitch.

B. 1-3 Composite Fabrication

Various configurations of 1-3 materials are needed to meet a variety of applications and requirements. Volume fraction, rod diameter, and rod spacing can all be tailored to meet specific design criteria. MSI has recently established the capability to fabricate tooling to manufacture a variety of configurations quickly and inexpensively. Figure 4 shows a 40 volume percent piezocomposite material made by injection molding. It consists of square ceramic elements, 624 μ m wide and spaced 992 μ m apart. Fine elements are necessary to operate at high frequencies without introducing unwanted lateral modes. Similar 1-3 structures with 474 μ m wide elements and 750 μ m pitch have also been molded.

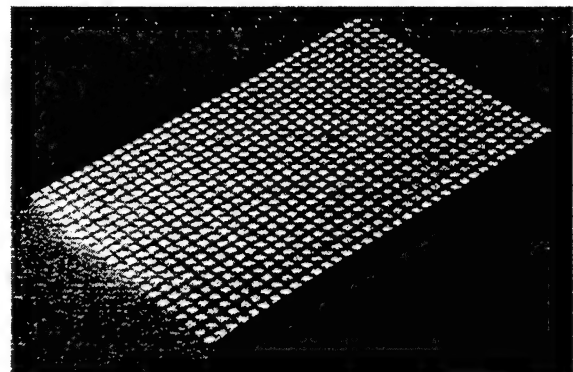


Fig. 4. Photograph of a 40 volume percent 1-3 composite. Elements are 624 μ m wide and spaced 992 μ m apart.

III. RESULTS

The 2-2 preforms shown in Figures 2 and 3 were filled with stiff epoxy. The baseplate was removed and the composite was ground to the final thickness. Gold electrodes were applied to both surfaces and the composite was poled under high electric fields. Figures 5 and 6 show impedance curves for these composites.

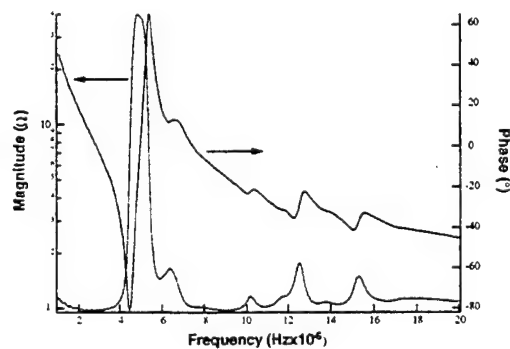


Fig. 5. Impedance curve of 60 volume percent PZT-5H composite with 230 μ m pitch.

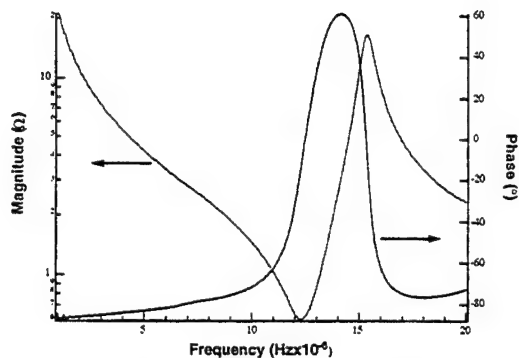


Fig. 6. Impedance curve of 50 volume percent PZT-5A composite with 125 μ m pitch.

Both had good resonance characteristics. The 230 μ m pitch composite (Figure 5) had a thickness resonance at 4.5 MHz with a coupling coefficient of 60%. The 125 μ m composite had a slightly higher coupling of 64% with a thickness resonance at ~12 MHz. Lateral modes, clearly visible in Figure 5, were shifted above the thickness resonance by properly choosing the ceramic element width and spacing.

Figure 7 shows the resonance characteristics and derived piezoelectric parameters for a 40 volume percent 1-3 composite. In this case the composite thickness mode coupling coefficient was 68%, which is almost as high as the length mode coupling coefficient for the ceramic alone (75%), and much higher than the ceramic thickness coupling coefficient (52%).

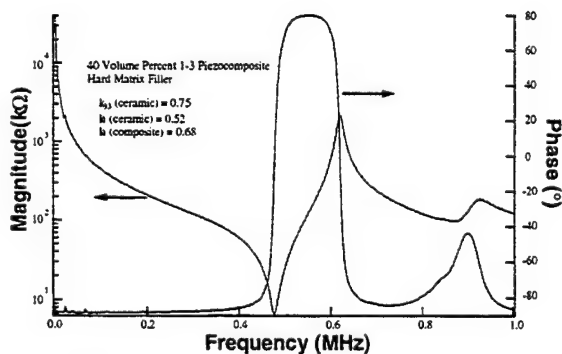


Fig. 7. Impedance curve of 40 volume percent PZT-5H composite.

IV. SUMMARY AND CONCLUSION

Net shape molding processes were used to mold large areas of fine scale piezocomposite at reduced cost. 2-2 composites with pitches from 125 μ m to 230 μ m and 50 to 60 volume percent PZT were produced. Similarly, 1-3 composites with 750 μ m pitch and 474 μ m wide elements were also fabricated. Composites displayed good resonance properties and had high coupling coefficients.

ACKNOWLEDGMENTS

This work was funded by the Office of Naval Research.

REFERENCES

- [1] L. Bowen, R. Gentilman, H. Pham, D. Fiore, and K. French, "Injection Molded Fine-scale Piezoelectric Composite Transducers", Proc. IEEE Ultrasonics Symposium, pp. 499-503, 1993.
- [2] B. G. Pazol, L. J. Bowen, R. L. Gentilman, H. T. Pham, W. J. Serwatka, C. G. Oakley, and D. R. Dietz, "Ultrafine Scale Piezoelectric Composite Materials for High Frequency Ultrasonic Imaging Arrays", Proc. IEEE Ultrasonics Symposium, pp. 1263-1268, 1995.
- [3] C. Desilets, B. Mukherjee, S. Sherrit, B. Pazol, M. Callahan, C. Maclean, V. Murray, G. Hayward, L. Kikodym, and G. Wojcik, "Composite Curved Linear Array for Sonar Imaging: Construction, Testing, and Comparison to FEM Simulations", presented at 1997 ONR Materials and Transducers Workshop, State College, PA, April 1997.

COMPUTER SIMULATION OF PIEZOCOMPOSITE TRANSDUCERS

Wenwu Cao

Department of Mathematics and Materials Research Laboratory
The Pennsylvania State University, University Park, Pennsylvania 16802

Abstract--Piezocomposites are widely used to make for medical ultrasonic transducers. With the increasing demand on higher frequency transducers for better resolution, more advanced design tools are required to optimize the complex composite structures. A simulation procedure is presented in this paper which illustrates a process of design-fabrication-testing on a virtual basis. It can duplicate quantitatively all aspects of transducer design and testing, including nonuniform vibration characteristics, beam forming, cross talk, and impulse response. Such simulation procedure not only saves time and money but also gives us much more insight into the complex vibration characteristics of a composite transducer and provides an efficient optimization tool.

I. INTRODUCTION

Piezoelectric composites have become the primary material for medical ultrasound transducers due to their superior coupling constant, relatively low acoustic impedance and relatively high piezoelectric constant in the thickness mode [1,2]. Design criteria for medical ultrasonic composite transducers have been established, both theoretically and experimentally [3], for transducers up to 7 MHz. The key to design a good composite transducer is to maintain an aspect ratio of the ceramic element large than three, which could decouple the lateral modes from the thickness modes and also relax the constraints from lateral dimensions to utilize the larger k_{33} values of the piezoceramic in the thickness resonance of the composite.

All material properties degrade when the aspect ratio is reduced. This degradation is true for both the non-resonance and resonance cases [4-6]. In reality, there are manufacture difficulties of maintaining the high aspect ratio when the transducer operating frequency is greater than 20 MHz, which is the reason why all high frequency transducers used today are still made of single phase materials which either have poor sensitivity (such as piezoelectric polymer) or poor resolution due to acoustic impedance mismatch (such as ceramics or single crystals). In order to extend the use of piezocomposites to higher frequencies, one needs to make some exploration on new designs to overcome this aspect ratio limitation. This paper provides a simulation design procedure which can be used for such a purpose, or other complex transducer design tasks. The simulation is based on realistic scales in three dimensions. There are little or none approximations besides numerical limitations. Examples of simulation using different softwares are given in the following section. Softwares used include ANSYS, PZ-Flex and a code developed in house. We found that if the input material parameters are accurate enough, the simulation results can be accurate to within a few percents of the experimental values.

II. SIMULATION PROCEDURE

In this section, the simulation modeling will be discussed and an example is given in each case.

A. Model Construction

The first step to perform a simulation on composite transducer is to construct a simplified finite element model which can reflect the realistic situation of a transducer, and at the same time, limits the amount of computation so that the simulation task can be accomplished in a reasonable time scale with minimum accumulated numerical errors. One must note, however, that over simplification often can lead to inaccurate results. For example, the unite cell scheme for modeling a composite transducer can differ substantially from the measured results for a composite transducer of a finite dimensions as shown in Ref. [6]. On the other hand, it is found that the reduction of dimensions, such as from 3-D to 2-D, is often acceptable for the situation of a 2-2 composite transducer [7]. The build in symmetry of composite structures can also help to reduce the computation task. Shown in Fig. 1. is an example of a transducer made of 1-3 piezocomposite. The system consists of 36 ceramic pillars in a polymer matrix. There are two symmetry planes parallel to the poling

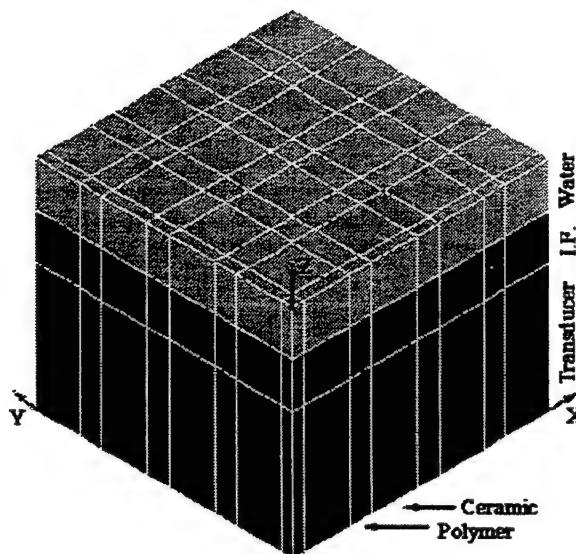


Fig. 1. Finite element model of a 1-3 composite transducer with 36 piezoceramics pillars.

direction (the z-direction). In addition, the plane at the middle of the structure in the poling direction will have no z-component displacement due to the mechanical symmetry (Note: the polarization is not symmetric!), we can therefore model the upper (lower) half of the composite transducer with the lower (upper) boundary fixed in the z-direction. With the above considerations, we can model 1/8th of the composite transducer structure without losing any physical significance. Water loading can also be added to the model via Fluid-Solid Interface elements which can convert the vector displacement variable in solids into scalar pressure variable in fluid. The volume of the water loading should be sufficiently large so that the outer boundary, which was set to be reflectionless, will not interfere the near-field computation. The reflectionless boundary is often called absorbing boundary condition which is used to mimic an infinite water medium. The 1-3 composite system shown in Fig. 1 is finite and the surfaces in the directions perpendicular to the poling direction are set to be stress free. With such a simplified model, one can simulate realistically the real performance of a 1-3 composite transducer [8].

B. Electrical Impedance Calculation

The first thing in the design of a composite transducer is to find out its operating frequency. Similar to the experimental procedure, we can simulate the variation of the electrical impedance versus frequency to get such information. The impedance calculation can show us the resonance characteristic of a composite transducer, i.e., the resonance frequency with and without loading, the coupling constant, the separation of the thickness mode from other modes, and the damping level that must be given to different materials in the finite element model. The damping level is very difficult to measure in reality for high frequencies, we therefore try to adjust the damping level in the finite element calculation to match the measured electrical impedance which can be obtained easily. One thing needs to be mentioned is that the damping considered in the finite element model is the mechanical loss only, the loss occurred in electrical circuits can not be included in the model. The calculation of the electrical impedance curve is based on the surface charge variation for a steady state in a forced harmonic vibration with damping. The transducer is treated as a pure capacitance system without electrical loss. An example of the calculated impedance curve for a 2-2 composite transducer is given in Fig. 2 together with the experimentally measured results [9].

C. Modal Shape

Although the impedance curve can give the resonance and antiresonance frequencies, it only reflects the collective effect, similar to any other effective 1-D models. In order to understand the nonuniform nature of the composite transducers, one needs to know the 3-D vibrational characteristics for each of the constituents in each mode, both in terms of the vibrational amplitude and phase distribution.

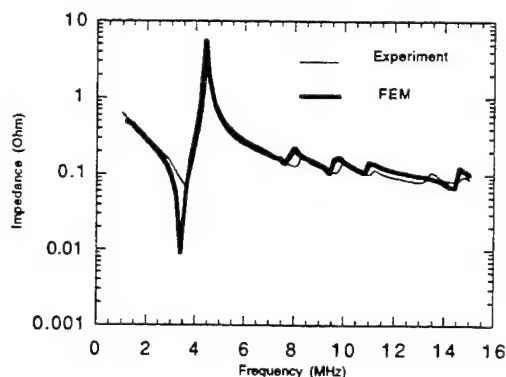


Fig. 2. Calculated and measured electrical impedance of a 2-2 composite transducer.

Such a task can also be accomplished by harmonic analysis using finite element method (FEM). In addition, the FEM results also show the displacement and stress distributions inside the composite associated with each mode. Showing in Fig. 3 is an analysis for a 2-2 type of composite structure where one can clearly see the difference between the thickness resonance and the first lateral mode of the composite transducer [7]. The system is air loaded in this case. One can see that both the ceramic and the polymer are vibrating in phase in the thickness mode [Fig. 3 (b)], while in the first lateral shear mode (pitch resonance), the polymer vibrates at a higher amplitude than the active ceramic phase [Fig. 3(c)], which is just the reverse of the quasi-static case [4,5] and there is a 180° phase lagging between the two constituents.

D. Beam Pattern Analysis

One of the most important characteristics of a transducer is its beam focusing capability. The beam size reflects the lateral resolution of a transducer. Theoretical analysis on the beam forming are abundant, but most of them are for single phase vibrators, such as a piston transducer. The surface vibration profile of a piezocomposite transducer is very complex due to the two phase nature, it is not possible to

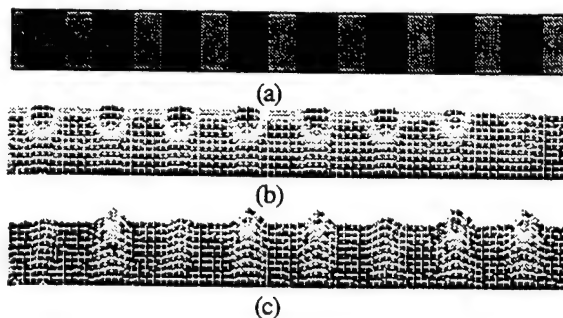


Fig. 3 (a) One half of a 2-2 composite model, larger phase is polymer. (b) The thickness resonance mode at 1.25MHz. (c) The lateral mode at 1.75MHz.

estimate the near field characteristics with assumed uniform surface vibration profile. With computer simulation, one can easily calculate the nonuniform surface displacement and velocity distributions, and use them to accurately predict the near-filed and far-filed pressure distributions produced by the composite transducer.

There are two ways to compute of the transducer beam pattern. The first is to construct a large FEM model which includes a sufficiently large piece of the medium so that the pressure distribution in the medium can be directly calculated together with the transducer assembly. Although this one step process is easy to do conceptually, there are two major difficulties associated with it: 1) the model can be really large if the focal point is far way from the transducer and 2) the error propagation can render the far-field calculation incorrect. We found that such a method fails in most of the cases, particularly in the far filed calculations. The second method is to do a two step process by feeding the FEM surface vibration profile and velocity distribution into a boundary element code to compute the Helmholtz Integral. This method can save computation time and also provides much accurate results both for the far field and for the near field. We have developed an in-house program and the format conversion code to perform this task. A typical example is shown in Fig. 4, where both the near-field and the far-field are correctly calculated. In addition, one could calculate the field distribution at a particular region of interest rather than having to calculate the entire field in the FEM technique. We found that the near field of a composite transducer can be quite different from that of a single phase transducer, while the far-field are very much the same. Since the near-filed is very

important in medical imaging, one need to find more dependable and powerful tool, such as the simulation procedure described in this paper, to help the design of composite transducers for medical imaging.

E. Impulse Response

Impulse response has been the main indicator in transducer industry for designing a broad band transducer. Such impulse response can also be simulated using FEM. With this impulse response simulation we can study the effect of different types of polymer fillers in the composites and to modify the damping characteristics of the backing as well as to study the thickness of the matching layers [10]. The frequency response can be simply obtained by performing FFT to the impulse response. An example of the impulse response of a 2-2 composite transducer is shown in Fig. 5. The simulation is performed by using a time domain FEM package, PZ-Flex, product of the Weidlinger Associates, Inc. Although such impulse response may also be modeled using equivalent circuit models, such as the KLM model, FEM provides the flexibility of pin point to the response of each individual elements, so that it could be used to study the element cross talk.

III. EFFECTS OF ASPECT RATIO AND MODELING SCHEMES

One of the crucial design parameters for a composite transducer is the element aspect ratio. Because the fundamental principle of having a large effective piezoelectric constant and coupling constant in the thickness direction of the composite transducer is to convert the longitudinal coupling coefficient k_{33} of each element into an effective thickness coupling coefficient k_t of the composite through geometric manipulations. The lateral dimension relative to the thickness dimension for a piezoelectric element is a measure of the lateral clamping for the thickness vibration. In order to achieve high efficiency in a composite



Fig. 4 Beam pattern of a 1-3 composite transducer calculated by the combination of FEM and in house boundary element method code.

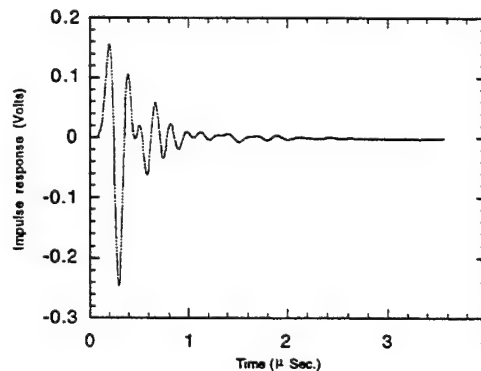


Fig. 5 Impulse response of a 2-2 composite transducer calculated by PZ Flex, a time domain FEM package.

structure and to decouple the thickness mode from the lateral modes, high aspect ratio for the ceramic element is required. However, for very high frequency transducers (> 20 MHz), such high aspect ratio is very difficult to manufacture, we therefore must understand the effects of changing aspect ratio in more details and try to find a way to overcome this limitation in composite designs. Such study can be easily carried out using FEM computer simulation[6]. There is a dilemma for FEM model construction between unit cell [11] and full model [6]. The former is faster but less accurate, particularly when the aspect ratio is approaching one or less. While the latter may take much more computation time but could give much dependable results. Shown in Fig. 6 is the comparison of different modeling results and experimental observations for a 2-2 composite with 40% ceramics. It is shown that when the aspect ratio is larger than 2.5 ($a/L < 0.4$), all theoretical models, including the effective medium model [3] agree well with experiments. However, when the aspect ratio becomes less than 2 ($a/L > 0.5$), one can see clearly the difference between different models. Generally speaking, the resonance frequency calculated from the effective medium model is too high while the one from the unit cell FEM model is too low. Only the full size FEM gives accurate results for the whole range of the aspect ratio[6]. We found that some of the inaccuracy in the FEM models were mostly from either the inaccurate input parameters or from over simplification of the real problem. After all, it is more important to obtain reliable modeling results than to speed up the simulation process.

V. SUMMARY AND CONCLUSIONS

A computer simulation design procedure for piezocomposite transducer is outlined in this paper. In principle, the simulation can duplicate virtually anything that can be measured experimentally. Some details of the procedure and necessary precautions are given through an example for each

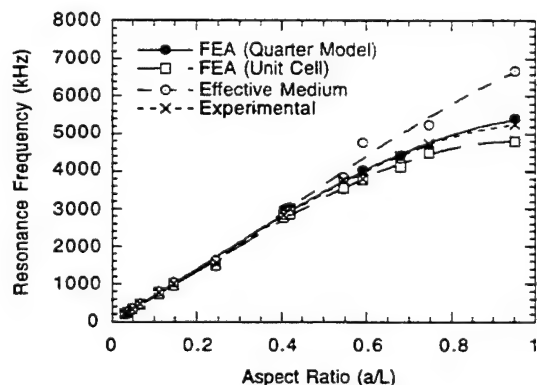


Fig. 6. Comparison of modeling and experimental results for the change of resonance frequency with aspect ratio of the ceramic element, where L and a are the height and width of the ceramic plates in a 2-2 composite transducer.

of the modeling steps. With this simulation procedure, one could virtually design and test composite transducers using computer only. Because of the 3-dimensional nature of the simulation, one could also access the interior of the transducer which could not be obtained experimentally. Such interior information is particularly important to locate the "weak spots" where high mechanical and electrical breakdowns are likely to occur. Compared with those 1-D equivalent circuit models for transducer designs, the 3-D simulation offers much richer information, including the 3-D beam pattern associated with each design. The advantage of computer simulation is the ability to change the design parameters very quickly after a successful base model has been constructed. It is also very cost effective and not limited by the availability of materials. Such virtual designs make it easier to draw scientific conclusions than from experimentally try-and-error approach which are limited by the availability of materials. However, at the current stage, computer simulation does not exclude the necessity of doing some experimental verifications, particularly during the base model construction. As the simulation methods and computer power improve, it is conceivable that in the future completely design and optimize complex transducers, such as the composite transducer, on a computer.

ACKNOWLEDGMENT

This research is sponsored by the Office of Naval Research.

REFERENCES

- [1] R. E. Newnham, D. P. Skinner and L. E. Cross, "Connectivity and piezoelectric-pyroelectric composites" *Mater. Res. Bull.* vol. 13, pp. 525-536 (1978).
- [2] W. A. Smith, "The role of piezocomposites in ultrasonic transducers", *Proc. 1989 IEEE Ultrason. Symp.* PP 755-766 (1989).
- [3] Smith, W.A., Modeling 1-3 composite piezoelectric: thickness-mode oscillations, *IEEE Trans. Ultra. Ferr. and Freq. Contr.*, vol. 38, 40-47(1991).
- [4] Wenwu Cao, Q. M. Zhang and L. E. Cross, "Theoretical study on the static performance of piezoelectric ceramic-polymer composites with 1-3 connectivity", *J. Appl. Phys.*, 72, pp. 5814-5821 (1992).
- [5] Wenwu Cao, Q. M. Zhang and L. E. Cross, "Theoretical study on the static performance of piezoelectric ceramic-polymer composites with 2-2 connectivity", *IEEE Trans. Ultra. Ferr. and Freq. Contr.*, vol. 40, pp. 103-109 (1993).
- [6] Wengkang Qi and Wenwu Cao, "Finite element analysis and experimental studies on piezoelectric composite transducers", *Ultrasonic Imaging*, vol. 18, pp. 1-9 (1996).
- [7] Wengkang Qi and Wenwu Cao, "Finite element analysis of 2-2 piezocomposites", *IEEE Trans. Ultra. Ferr. and Freq. Contr.*, to be appear (1997).
- [8] Wenwu Cao, "Simulation of the dynamic behavior of 1-3 piezocomposites using finite element method", *Ceramic Engineering&Science Proceedings*, vol. 17, pp. 83-90 (1996).
- [9] Wengkang Qi and Wenwu Cao, "Composite and Arrays: Finite element analysis and experimental verifications", to be published (1997).
- [10] Mark R. Draheim and Wenwu Cao, "Finite element and experimental study of impedance matching layer optimization", *Proc. SPIE, Medical Imaging 1997*, vol., 3037, pp 135-139 (1997).
- [11] J. A. Hossack, G. Hayward, "Finite element analysis of 1-3 composite transducers", *IEEE Trans. Ultra. Ferr. and Freq. Contr.*, vol. 38 pp. 618-629 (1991).

Medical Ultrasonic Transducers With Switchable Frequency Bands Centered About f_0 and $2f_0$

T.R. (Raj) Gururaja, Abraham Shurland*, and Jie Chen

Hewlett-Packard Company, Andover, MA 01810

* Currently at University of Pennsylvania, PA 19104

We present a novel type of ultrasonic imaging transducer in which the operating frequency can be switched between two distinct bands centered about f_0 and $2f_0$. In effect, we can achieve greater than 100% transducer bandwidth at the -6dB level. The transducer is based on using DC bias induced piezoelectricity in electrostrictive materials such as lead magnesium niobate - lead titanate (PMN-PT) relaxor ferroelectric materials.

1. INTRODUCTION

Broad operating bandwidth of a transducer is one of the most desirable attributes of current and future ultrasonic transducers used in medical imaging applications. Broad bandwidth in a single transducer offers the advantage of obtaining deep penetration from the low frequency part of the spectrum and fine resolution from the high frequency part of the spectrum. Thus, functions of two or more narrow band transducers are incorporated in one transducer with the combined benefit of more imaging information at a lower cost.

Conventionally, a piezoelectric resonator is provided with a combination of acoustic impedance matching layer(s) and a backing medium to obtain broad band spectral response. The matching layers improve the coupling of acoustic energy from the piezoelectric material (usually a composition of PZT) to the human body and the backing provides additional damping to get smoother spectral response. However, the matching layers are effective only over a narrow band of frequencies. Typically, commercial transducers built with this technology exhibit 50 to 70% bandwidth at the -6dB level (from here on bandwidth will be referred to at the -6dB level unless mentioned otherwise).

Recently, PZT-polymer composites with lower acoustic impedance have been used to improve the acoustic impedance matching. The acoustic impedance of the composites range from 30 to 50% of the value for PZT. Transducer array elements built with composite materials exhibit relatively high electrical impedance compared to the driving electronics. Consequently, bandwidth of composite transducers are also in the 50 to 70% range.

In this paper we describe the theory and experimental results of a transducer in which the operating frequency is switched between two distinct bands centered about frequencies f_0 and $2f_0$. Around each operating frequency, the transducer can be designed to exhibit approximately 60% bandwidth, thereby covering a much wider frequency range than is possible with conventional broad band transducers.

2. THEORY

The design of the transducer is based on using an electrostrictive material. An electrostrictive material is highly polarizable by application of a DC bias voltage, thereby exhibiting piezoelectric properties. The material loses its polarization upon removal of the DC bias voltage and no longer exhibits piezoelectric properties. A classic example of an electrostrictive material is lead magnesium niobate modified with approximately 10 mole% lead titanate, referred to as PMN-PT. This composition exhibits a transition from ferroelectric to a paraelectric phase in the vicinity of room temperature [1].

The dielectric and induced piezoelectric properties of a modified PMN-PT composition at 0 and 5 kV/cm is shown in the Figures 1a and b [2]. Fig. 1b shows that large field-induced coupling constant ($k_t = 0.48$, comparable to that of PZT) can

be obtained in this material near room temperature with a relatively low bias field. The material exhibits zero remnant polarization above 15°C. Thus, the piezoelectric effect can be turned ON or OFF by the presence or absence of a DC bias. The direction of the polarization can also be chosen with the polarity of the DC bias.

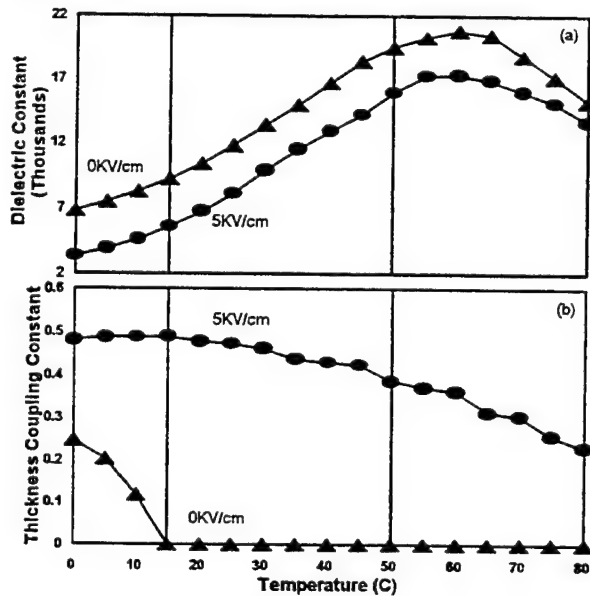


Figure 1 a) Dielectric constant as a function of temperature for PMN-PT at 2 MHz and DC bias levels at 0 and 5kV/cm. b) Thickness coupling constant at 0 and 5kV/cm.

The transducer consists of a stack of two layers of electrostrictive material which are connected electrically in parallel as shown in Figures 2 and 3 [3]. The polarization of each layer can be selected independently with a DC bias of a selected polarity. The structure may be excited to produce two different resonance frequencies. In the first mode, a bias potential of $+V_{\text{bias}}$ with reference to the central electrode is applied to the outer electrodes. Thus, the electric field and consequently polarization in the two layers are opposing each other. An excitation voltage $V_e(t)$ which may be a short rectangular pulse is applied to the central electrode. In this configuration, the fields produced by the excitation voltage in each of the layers are in the same direction relative to the DC bias fields. The structure resonates in the same manner as a single

layer whose thickness is the sum of the thickness of the two layers. The thickness mode resonance frequency f_0 is given by:

$$f_1 = v/4t = f_0,$$

where v is the velocity of sound in the biased electrostrictive material and t is the thickness of each layer.

In a second mode, the outer electrodes are held at opposite polarities $+V_{\text{bias}}$ and $-V_{\text{bias}}$ relative to the central electrode. The electric fields and polarization in the layers are in the same direction. The field produced by the excitation voltage $V_e(t)$ is in the same direction as the DC bias in the lower layer and is in the opposite direction in the upper layer. This structure resonates in the same manner as a single layer whose thickness is equal to thickness of one of the layers. The thickness mode resonance frequency is given by:

$$f_2 = v/2t = 2f_0.$$

Thus, with a single resonator structure, it is possible to produce two distinct resonance at f_0 and $2f_0$. These resonance are high Q in nature with extremely narrow bandwidth. The resonator has to be provided with matching layers and a damping medium to design imaging transducers with bandwidths around 50% or larger. The desired thickness of a matching layer is a quarter wavelength at the frequency of resonance. However, in the current structure, a quarter wavelength matching layer chosen for the resonance at f_0 will be half wavelength for the resonance at $2f_0$. Therefore the acoustic impedance matching at $2f_0$ will be ineffective. A compromise thickness between quarter wavelengths at the two resonance could be chosen.

An ideal scheme for constructing a matching layer for such a structure is the exponentially graded matching layer [4]. In this scheme, the impedance of the matching layer is varied exponentially starting from the impedance of the piezoelectric material (30 MRayl for PZT) to that of the human body (approximately 1.5 MRayl). This can either be constructed by laminating thin layers of materials of various impedance or by varying the packing density of filler in a polymer

matrix. It is estimated that to provide a frequency independent matching layer, the thickness of the matching layer should be at least three quarter wavelengths thick at the lowest frequency of operation. At the higher frequency, the matching layer becomes extremely thick which would result in excessive attenuation through the matching layer and undesirable loss in sensitivity. In the following section, we describe the results of an experiment with two matching layers of compromised thickness between the two resonance.

3. EXPERIMENT AND RESULTS

A modified PMN-PT composition with approximately 10 mole% PT was selected to build frequency switchable transducers. The dielectric and DC bias induced piezoelectric properties for this composition are shown in Figure 1. Thickness of each layer was approximately 0.35 mm to obtain the resonance frequency of the two modes at 2.5 and 5.0 MHz. The design of the transducer with a graded impedance matching layer gave extremely wide band spectral response at both 2.5 and 5 MHz. However, for simplicity of experimentation a two matching layer design was chosen.

As discussed earlier, picking the matching layer thickness appropriate for both resonance modes is critical for the optimal operation of the transducer. At the low frequency mode, the pulse and spectral response was found to be relatively insensitive to the thickness of the two matching layers. A bandwidth in the range of 55 to 60% could be accomplished even when the matching layer thickness varied from 0.25λ to 0.15λ . The sensitivity variation was also limited to 2dB across this range of thickness of the matching layer. However, at the high frequency mode, the sensitivity and bandwidth changed significantly with the variation in matching layer thickness. As the thickness of the matching layer, computed at $2f_0$, increased from 0.25λ to 0.50λ , the bandwidth increased gradually from 50 to 70% while the round trip sensitivity decreased by 8 to 10dB. Thus, a compromise had to be made in selecting the matching layer thickness. A matching layer being a quarter wavelength thick at 3.75 MHz, the mid-point between the two resonance frequencies, was found to be an optimal choice.

Figure 4 shows the spectral response of the transducer operating around f_0 and $2f_0$. Around each frequency, the bandwidth achieved is in the range of

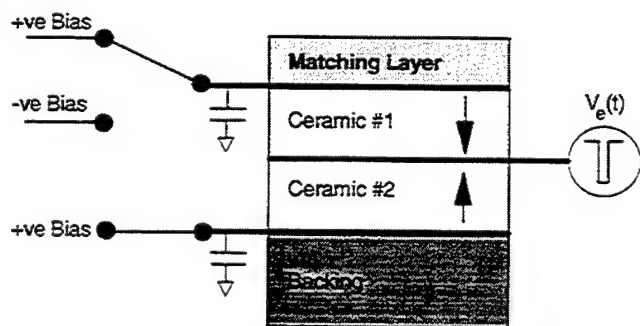


Figure 2. DC biasing circuit for transducer operation at $f_1=f_0$

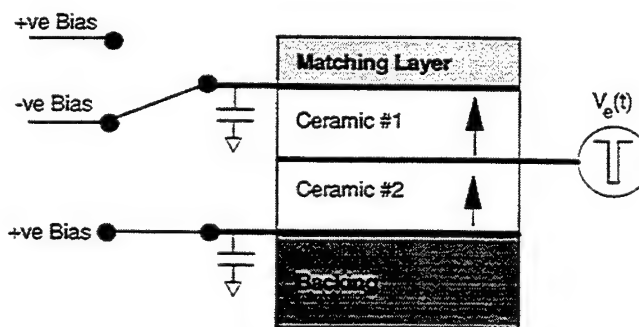


Figure 3. DC biasing circuit for transducer operation at $f_2=2f_0$

55 to 60%. Thus, a single transducer can perform the function of two transducers with center frequencies at 2.7 and 4.6 MHz. Combining the functions of two transducers in this design, the -6dB frequency coverage is from approximately 1.8 to 5.6 MHz. This is equivalent to a conventional transducer with over 100% bandwidth.

Figure 5 compares the pulse response at the f_0 and $2f_0$ modes of operation. The pulse length at $2f_0$ is approximately half of the pulse length at f_0 . The transducer could be operated in the high frequency mode to obtain maximum resolution. The low frequency mode would offer relatively high sensitivity and deep penetration.

4. CONCLUSIONS

We have demonstrated the possibility of combining the functions of two separate transducers in one using a simple two layer electrostrictive stack. The performance at each resonance can be enhanced significantly by choosing more than two matching layers or a graded impedance matching layer that is not frequency dependent. Additionally, each layer of the electrostrictive material could be made of 1-3 or 2-2 composite material to further improve the acoustic impedance matching between the transducer and the human body. In theory it is possible to obtain a bandwidth of 80% at each

mode of resonance and combine the functions of several transducers into one.

5. ACKNOWLEDGMENTS

We would like to acknowledge the work of Linh Pham and Kenny Eng who helped us fabricate and test the transducers, our colleagues for their valuable technical discussions, and our management for support.

6. REFERENCES

- [1] H.Takeuchi, H.Masuzawa, and C. Nakaya, "Relaxor ferroelectric transducers," p697, Proceedings of 1990 IEEE Ultrasonic Symposium.
- [2] J.T. Fielding, T.R. Shrout, and S.J. Jang, "Increased operating temperature range in La modified PMN-PT relaxor ferroelectric-based transducers," p158, Proceedings of 1994 International Symp. on Applns. of Ferroelectrics.
- [3] P.C. Pederson, O. Tretiak, and P.He, "Impedance matching properties of an inhomogeneous matching layer with continuously changing acoustic impedance," J. Acoust. Soc. Am., Vol.72(2), p327 (1982).
- [4] T.R. Gururaja, "Ultrasonic transducer having two or more resonance frequencies," United States Patent, 5,410,205, (1995).

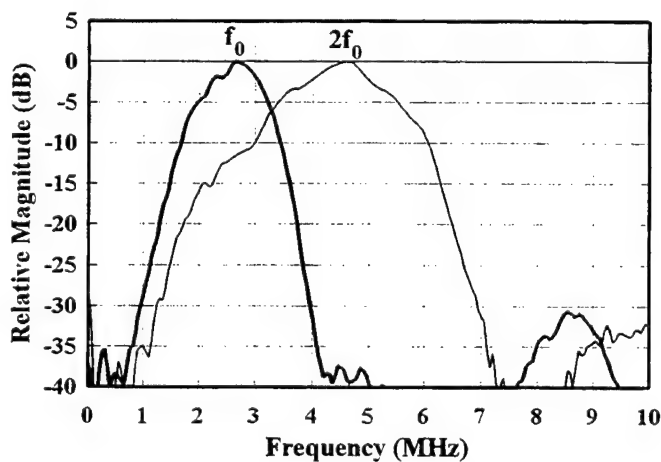


Figure 4. Spectral response at the f_0 and $2f_0$ mode

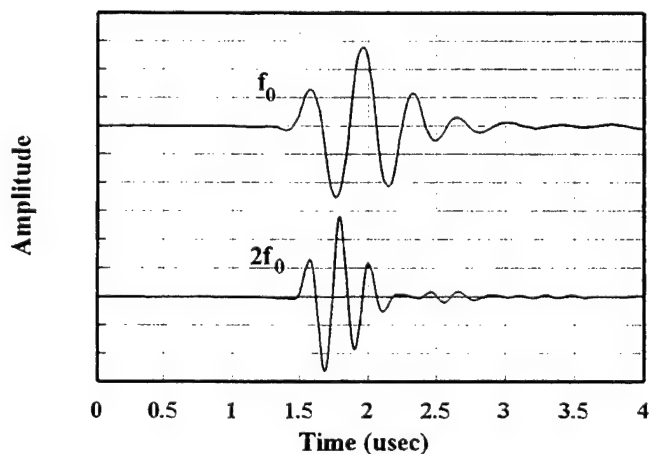


Figure 5. Pulse response at the f_0 and $2f_0$ mode

Bimorph and Pseudo Shear Mode Actuation

L. Eric Cross
Intercollege Materials Research Laboratory
The Pennsylvania State University
University Park, PA 16802-4800 USA

In an earlier meeting we reported preliminary results on a piezoelectric double amplifier concept to provide a light weight high amplitude acoustic source for air acoustic noise control. The continuing development is part of a cooperative program with Dr. Christopher Fuller's group at Virginia Polytechnic Institute (VPI) and Materials Systems Inc (MSI). The original concept (fig. 1) was to use amplified response from two vertical bimorph generators to drive a flexing diaphragm in the orthogonal direction. For the simple unconstrained bimorph the amplification factor over the linear bar displacement

$$A_B = \frac{3}{2} \left(\frac{L}{t} \right) \quad (1)$$

where L is the length and t the thickness. For the flexing element

$$A_F = \frac{w}{h} \quad (2)$$

so that the total amplification

$$A_T = \frac{3}{2} \left(\frac{L}{t} \right) \left(\frac{w}{h} \right) \quad (3)$$

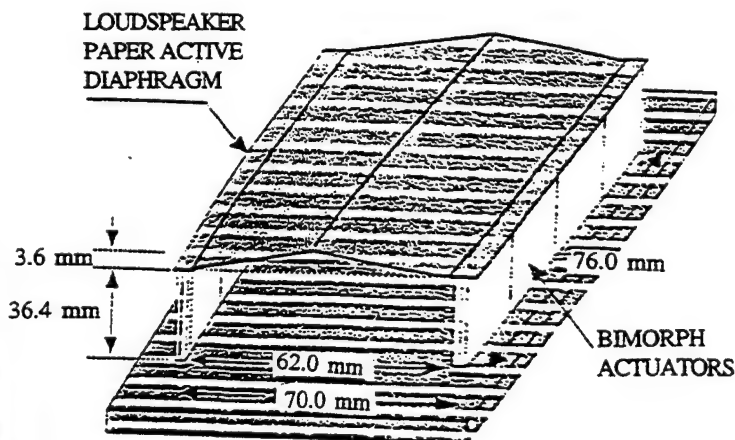


Fig. 1. Bimorph Driven Double Amplifier

some 254 times for the dimensions in Fig. 1 adequate to develop near field sound pressure of 135 dB at 600 Hz with an acoustic impedance ~2000 Rayls.

To improve performance a broad ranging study of the performance of short, end clamped bending mode actuators was undertaken. The configuration used is shown in Fig. 2a, and the simple measuring setup in Fig. 2b. To permit direct comparison all actuators were fabricated from the same piezoceramic, thickness t , length h , and width w of the active ceramic plate was the same, and all were driven by the same electric field. As a figure of merit we chose for our application

$$(\text{Tip displacement} \times \text{Blocking Force}) / \text{Admittance}. \quad (4)$$

Bending Effect

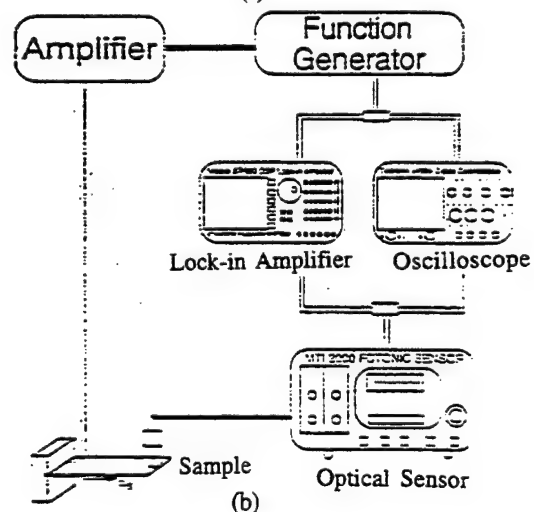
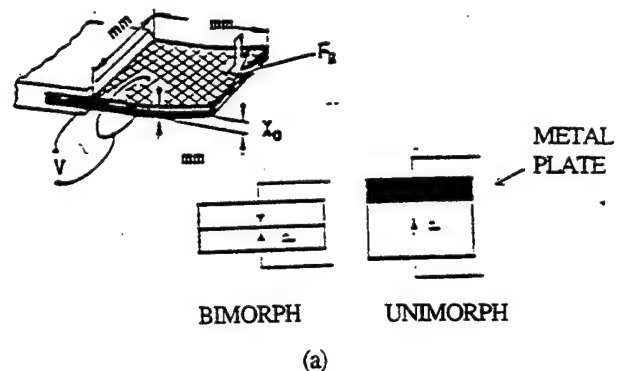



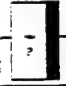

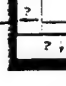






Fig. 2 (a). Typical Bending Mode Actuators.
Fig. 2 (b). Measuring System.

Results for a wide range of bending mode systems are summarized in Table I where performance is scaled to that of a simple bimorph taken as 1 in each category (blocking force, displacement, admittance).

Only the d_{31} driven systems, as expected show significant advantage, although there is a modest improvement with the L-shaped system which is important for the envisaged amplifier configuration.

It should be stressed that the figure of merit chosen does not speak to the robustness of the system or the advantages of slow and benign degradation in performance which are significant advantages for Thunder, Crescent, and Rainbow types.

TABLE I
FIGURE OF MERIT FOR
SEVERAL TYPES OF ACTUATORS

| TYPE OF PIEZOELEMENT | | Displacement | Blocking Force | Admittance | Figure of Merit |
|---|---|--------------|----------------|------------|-----------------|
| d_{31} Bimorph (PK1550) |  | 1 | 1 | 1 | 1 |
| d_{31} Unimorph (SS302-PK1550) |  | 0.41 | 1.8 | 1.0 | 0.74 |
| L-Shape d_{31} Bimorph ($l_1=l_2=0.5l$) |  | 0.75 | 1.5 | 1.0 | 1.15 |
| L-Shape d_{31} Unimorph (SS302-PK1550) |  | 0.51 | 2.7 | 1.0 | 0.84 |
| RAINBOW Aura Ceramics (C1900 ?) |  | 0.19-0.22 | 0.1-1.2 | 0.66 | 0.03-0.40 |
| CRESCENT 250°C (SS302-PK1550) |  | 0.44 | 1.75 | 0.91 | 0.85 |
| THUNDER -500°C (GAUPTISAAI) |  | 0.12 | 0.56-1.0 | 0.90 | 0.05-0.13 |
| Shear-mode (d_{15}) (G203HD) |  | <0.1 | ? | 1 | - |
| d_{32} Bimorph (PK1550) |  | 2.5 | 1.52 | -1 | 3.80 |
| d_{32} Unimorph (SS302-PK1550) |  | 0.72 | 3.5 | -1 | 2.52 |

Based on the L shaped monomorph a new PANEL design has been fabricated using more robust carbon fiber reinforced composite diaphragm (Fig. 3). The expected performance is shown in Fig. 4.

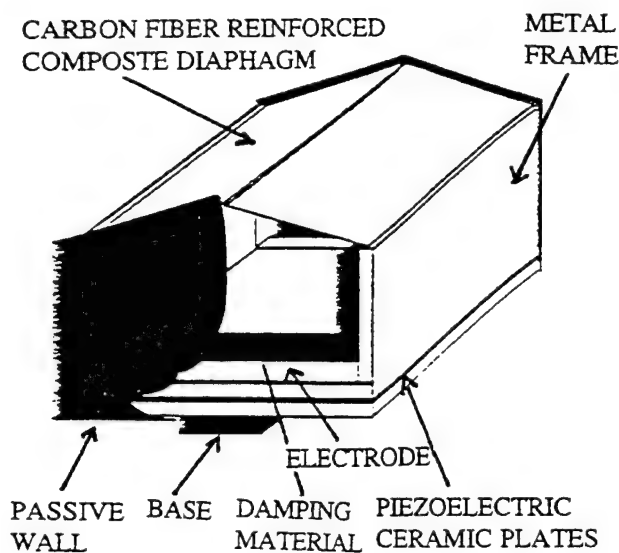


Fig. 3. PANEL: L-shaped Unimorph Driven Double Amplifier

PANEL: Calculated sound pressure of single device based on model of baffled piston

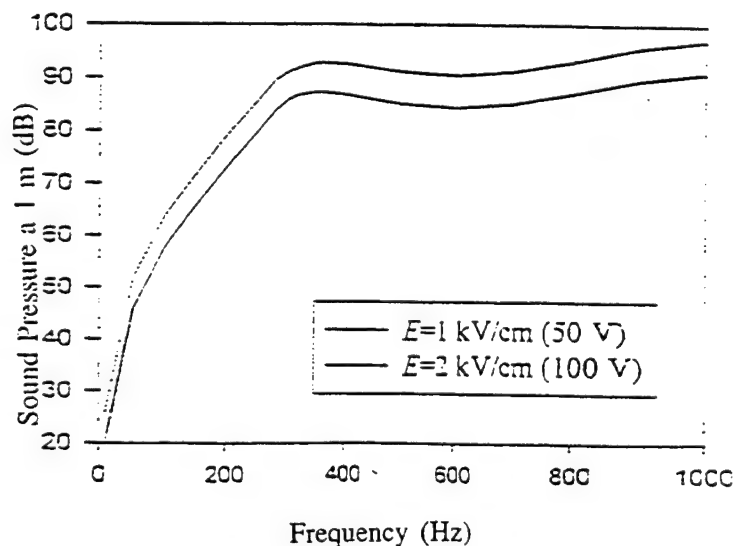
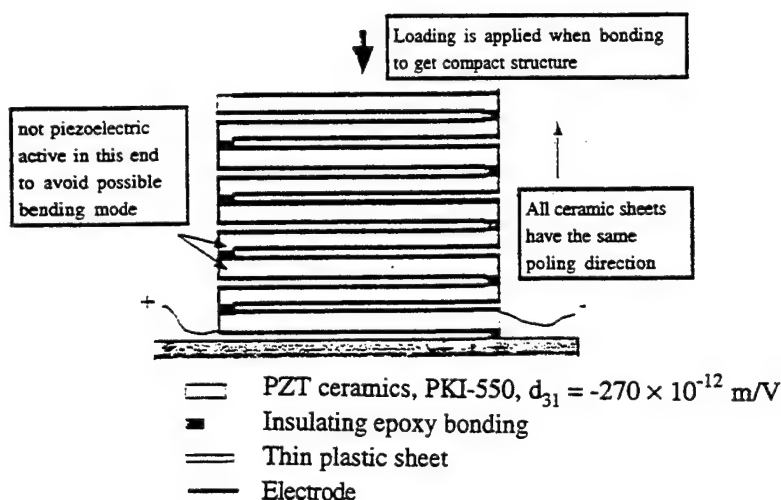


Fig. 4. Expected Performance for PANEL Sound Source.

To enhance lower frequency performance a new type of pseudo shear mode actuator is being explored. The device is essentially a folded d_{11} driven linear actuator (Fig. 5) which develops translation of the upper platen with respect to the base and thus a shearing motion. Performance for a 40 layer structure in PZT5H is given in Fig. 6.

Performance figures for a low frequency sound generator based on the pseudo-shear actuator will be presented.



ADVANTAGES:

1. Only need two connection wires.
2. Eliminate the undersirable low resonance bending modes.
3. Easy fabrication.
4. Blocking force could be larger than bending actuators.
5. Displacement increases with the number of PZT layers.

Fig. 5. Construction of Pseudo-Shear Mode Actuator.

Top Layer Displacement vs. Driving Electric Field for
40 Layers PSEUDO-SHEAR Actuator
(Layer dimensions: 30x10x0.45 mm)

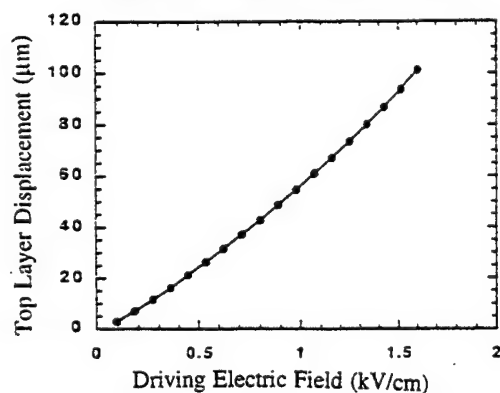


Fig. 6. Transverse Static Displacement for a 40 Layer Pseudo-Shear Device in Soft PZT.

Capped Ceramic Underwater Sound Projector

James F. Tressler, W. Jack Hughes¹, Wenwu Cao, Kenji Uchino, and Robert E. Newnham

Materials Research Laboratory, ¹Applied Research Laboratory

The Pennsylvania State University

University Park, PA 16802 USA

Abstract -- A new type of transducer has been developed for use as a shallow water sound projector at frequencies from 5 kHz to 50 kHz. Dubbed the 'cymbal', it is similar to the more commonly known 'moonie' or class V ring/shell flextensional designs. Prototype cymbal arrays with a radiating area of 14.5 cm² have been developed and tested. Two mounting schemes were examined: unpotted and potted in a 5 mm thick layer of stiff polyurethane. In both cases, a transmitting response comparable to the more widely used tonpilz transducer is attainable. When tested under hydrostatic pressures, the cymbal can withstand pressures of at least 2.5 MPa (which corresponds to 250 m of water depth) without a degradation in its performance.

I. INTRODUCTION

Sound transmission is the single most effective means of directing energy transfer over large distances underwater [1]. The number of applications which utilize some form of acoustic energy is quite large, with frequencies ranging anywhere between 10⁻³ Hz to 10⁹ Hz. There is currently a great interest in the development of shallow water acoustic projectors that operate in the frequency range from 1 kHz to 100 kHz. Ideally, these transducers should be thin, lightweight, exhibit medium to high acoustic output power, be able to conform to a curved surface, and be of simple design such that they are easy and inexpensive to mass produce.

Currently, the predominant underwater projector systems that operate in the 1 kHz to 100 kHz frequency range are the tonpilz transducers and 1-3 composites. The tonpilz transducer consists of a stack of piezoceramic (typically PZT) rings connected mechanically in series and electrically in parallel. The ring stack is sandwiched between two metal masses: a heavy tailmass and a light, flared headmass which serves to transmit the generated acoustic energy into the surroundings. Tonpilz transducers are characterized by their very large acoustic output power, are typically tens of centimeters in thickness, and are designed to operate at frequencies below 100 kHz.

The 1-3 type composites consist of a number of piezoceramic rods separated by a 3-D interconnected polymer matrix. These composites have been manufactured in a number of ways [2]. The current state of the art fabrication method is by injection molding [3]. The performance of 1-3 composites is strongly affected by the elastic properties of both the ceramic and polymer phases, the volume fraction of piezoceramic rods, and most importantly, the aspect ratio of the ceramic rods [4]. Typical 1-3 composites designed for use below 100 kHz are at least 1 cm thick.

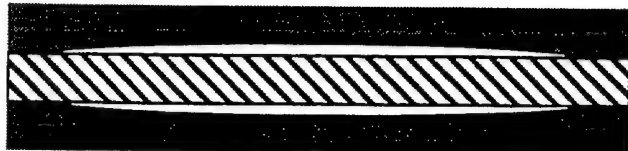
A third type of underwater projector that is seeing a resurgence in interest is the so-called flextensional transducer. Flextensionals have been in existence since the 1920s and have seen use as underwater projectors since the late 1950s [5]. Flextensionals consist of a piezoceramic drive element encapsulated by a metal shell. The shape of the shell has become quite diverse over the years and so a classification system has been established to group the common designs together [6]. Flextensional transducers typically range in size from several centimeters to several meters in length and can weigh up to hundreds of kilograms.

A miniaturized version of the class V flextensional transducer was developed in the late 1980s at the Materials Research Laboratory at The Pennsylvania State University for use as an underwater pressure sensor [7]. This transducer was named the 'moonie' due to the crescent moon shaped cavity on the inner surface of the caps. A second generation moonie-type transducer has recently been developed which consists of a thinner cap with a slightly different shape. This transducer has been dubbed the 'cymbal' due to the similarity in shape of its caps to that of the musical instrument of the same name. The moonie and cymbal designs are compared in Fig. 1.

The moonie and cymbal transducers consist of a piezoceramic (usually PZT) disk poled in the thickness direction which is sandwiched between and mechanically coupled to two metal caps, each of which contains a shallow cavity on its inner surface. The presence of these cavities allows the caps to convert and amplify the small radial displacement and vibration velocity of the piezoceramic disk into a much larger axial displacement and vibration velocity normal to the surface of the caps. This enhanced displacement and vibration velocity from the caps contribute to a much larger acoustic pressure output than would occur in the uncapped ceramic. The dimensions of the standard-size moonie and cymbal transducers are presented in TABLE I.

This work was funded by the Office of Naval Research

(a) moonie structure



(b) cymbal structure

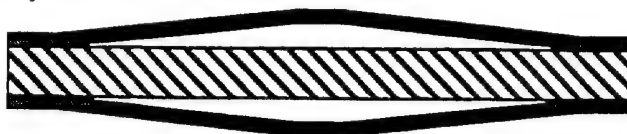


Fig. 1. Cross-sectional views of the (a) moonie-type, and (b) cymbal-type transducers. The dark areas represent the caps and the cross-hatched areas the PZT disk.

TABLE I
DIMENSIONS OF THE STANDARD MOONIE AND CYMBAL TRANSDUCERS

| Moonie Parameter | Dimension |
|---------------------|-----------|
| cap diameter | 12.7 mm |
| cap thickness | 1.0 mm |
| cavity depth | 0.25 mm |
| cavity diameter | 9.0 mm |
| PZT thickness | 1.0 mm |
| PZT diameter | 12.7 mm |
| Cymbal Parameter | Dimension |
| cap diameter | 12.7 mm |
| cap thickness | 0.25 mm |
| cavity depth | 0.30 mm |
| cavity diameter | 9.0 mm |
| dimple diameter | 3.0 mm |
| PZT thickness | 1.0 mm |
| PZT diameter | 12.7 mm |
| weight | ≈ 2 grams |

II. PARAMETERS TO MEASURE

Among the relevant parameters that need to be reported in order to fully characterize an underwater projector, the most important are resonance frequency, mechanical Q , electroacoustic efficiency, electromechanical coupling coefficient (k_{eff}), transmitting voltage response (TVR), source level (SL), and beam patterns. Transmitting voltage response is equal to the sound pressure produced by the projector

referenced (re:) to a distance of one meter from the acoustic center of the transducer when unit voltage is applied across its electrical terminals. It is reported in terms of dB re: 1 $\mu\text{Pa}/\text{V}$ @ 1 m. or as 1 $\mu\text{Pa}\cdot\text{m}/\text{V}$. Source level is the intensity of the radiated sound (i.e. radiated power) relative to the intensity of a plane wave of rms pressure 1 μPa referred to a point one meter from the acoustic center of the projector. Source level is related to the transmitting voltage response through the applied input voltage as:

$$SL = TVR + 20 \cdot \log V_{in, rms} \quad (1)$$

Thus, this parameter has the same units as TVR. In general, a source level of greater than 200 dB re: 1 $\mu\text{Pa}/\text{V}$ @ 1 m is desirable. The beam pattern describes the response of the transducer relative to its main acoustic axis.

III. COMPUTER MODELING

The ANSYS® finite element software program (version 5.1) was used to model the behavior of the cymbal transducer both in-air as well as when it was water-loaded. Modal analysis of a two-dimensional axisymmetric model was performed to obtain vibration mode shapes, resonance frequencies, and the stress distribution within the structure at resonance. Harmonic analysis was utilized to calculate admittance versus frequency curves, from which a theoretical effective coupling coefficient could be derived.

IV. EXPERIMENTAL PROCEDURE

Single element cymbal transducers were fabricated by first simultaneously cutting and shaping the caps in a die press. The caps were then adhered to a poled PZT disk using a very thin layer of epoxy. The bonding quality after curing was characterized by measuring the admittance spectra of the transducer.

Single element cymbal transducers were incorporated into 9-element square arrays, where the single elements were wired together electrically in parallel. Two mounting schemes were investigated: unpotted and potted in a stiff layer of polyurethane approximately 5 mm thick.

Underwater calibration tests were performed in the anechoic water tank at the Applied Research Laboratory at Penn State. The tank measures 5.5 m in depth, 5.3 m in width, and 7.9 m in length. A pure tone sinusoidal pulse signal of 2 msec duration was applied to the test transducer and its acoustic output was subsequently measured by a standard F33 hydrophone. The test transducer and the standard are positioned so that they are at a depth of 2.74 m and separated by a distance of 3.16 m.

V. RESULTS AND DISCUSSION

TABLE II provides some typical experimentally measured values for the parameters described in section II. These are all values for standard-size single element brass-capped cymbals except where otherwise noted. The large shift in the fundamental resonance frequency is due to the mass loading effect of the water. The d_{33} coefficient is really an effective d_{33} coefficient (since it is reported for a device). The PZT type in parenthesis is the type used as the active element in the transducer.

TABLE II
TYPICAL AIR- AND WATER-LOADED CHARACTERISTICS OF THE STANDARD-SIZE BRASS-CAPPED CYMBAL TRANSDUCER

| | air-loading | water-loading |
|--------------------|-------------|---------------|
| f_r | 23.4 kHz | 15.9 kHz |
| k_{tr} | 0.20 | 0.25 |
| Q | 200 | 20 |
| efficiency | | 90% |
| d_{33} (PZT-552) | 12000 pC/N | |
| d_{33} (PZT-5A) | 8000 pC/N | |
| d_{33} (PZT-4) | 6000 pC/N | |
| d_{33} (PZT-8) | 5000 pC/N | |

Fig. 2. shows the first resonance frequency of standard-size cymbal transducers with different cap materials as calculated by FEA both in-air and in-water. The first resonance frequency in-air is proportional to the sonic velocity of the cap material, $\sqrt{E/\rho(1-\sigma)}$, where E is the cap Young's modulus, ρ its density, and σ its Poisson's ratio. When the resonance frequency is measured in-water, the linear trend in the data is no longer observed. This is due to the difference in the density of the caps. Cymbals which have caps with densities closer to that of water, such as titanium, will exhibit a much more marked change in its resonance frequency in going from air to water than cymbals with caps of higher density, e.g. tungsten.

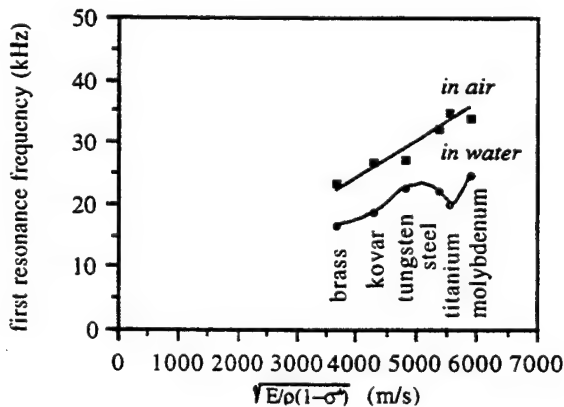


Fig. 2. First resonance frequency of standard-size cymbal transducers with different endcaps measured in-air and in-water.

The transmitting voltage response in the neighborhood of the first resonance frequency for same-size single element brass-capped cymbal transducers utilizing different PZT types is shown in Fig. 3. The transmitting response correlates with the effective d_{33} coefficient of the device, as seen from TABLE II. Single element cymbals are characterized by a relatively high Q_m (≈ 20) and consequently a narrow bandwidth.

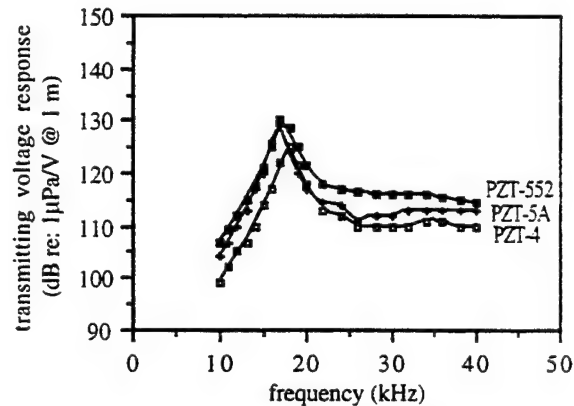


Fig. 3. Transmitting voltage response of a standard-size brass-capped cymbal utilizing different PZT types.

The transmitting voltage response of nine-element arrays of standard-size brass-capped cymbals, both potted and unpotted, are compared in Fig. 4. The fundamental resonance frequency is now strongly damped in both cases, resulting in wideband behavior. This is in part due to the array more closely approaching the idealized 'pc' loading conditions as compared to the single element.

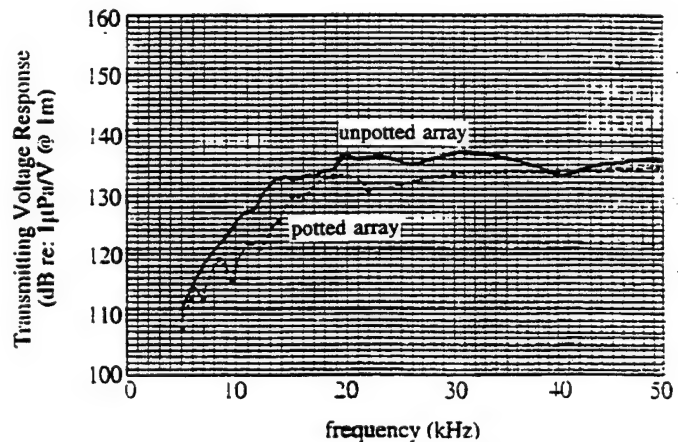


Fig. 4. Comparison of the transmitting voltage response of nine element potted and unpotted arrays of standard-size brass-capped cymbals utilizing PZT-552 driving elements.

A representative beam pattern for the nine-element arrays at 50 kHz is shown in Fig. 5. At frequencies below 50 kHz, the array exhibits near omnidirectionality. Above 50 kHz, the side lobes become more pronounced and grating lobes appear. Thus, 50 kHz is taken to be the upper use frequency for the arrays.

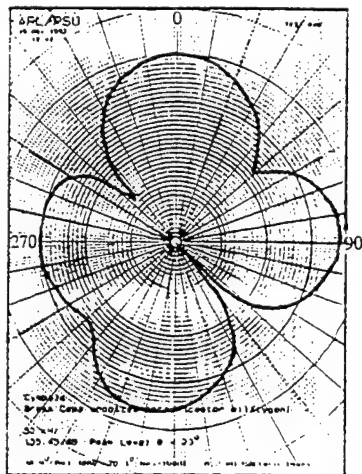


Fig. 5. Beam pattern of the array of brass-capped cymbals at 50 kHz.

Fig. 6. shows the source level as measured for the unpotted array when driven at 52 dBV both before and after failure. A source level of greater than 190 dB is generated by the array between about 18 kHz and at least 25 kHz. Although this is still less than the desired 200 dB, it is important to keep in mind that this is for an array of radiating area of only 14.5 cm². Increasing the radiating area by incorporating more single elements into the array will enhance the source level by a factor of 20•logA, where A is equal to the increase (i.e. multiplication factor) in radiating area.

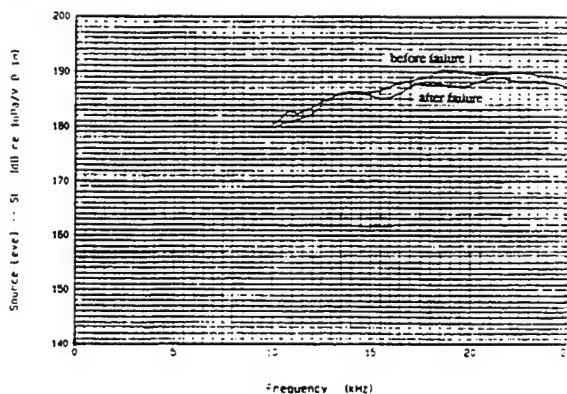


Fig. 6. Source level of the unpotted cymbal array as measured both before and after failure.

Fig. 7. shows the measured pressure dependence of the effective d_h and g_s coefficients of single-element brass-capped

cymbal transducers with different cavity depths. The standard-size cymbal can withstand up to 2.5 MPa without a significant degradation in its properties.

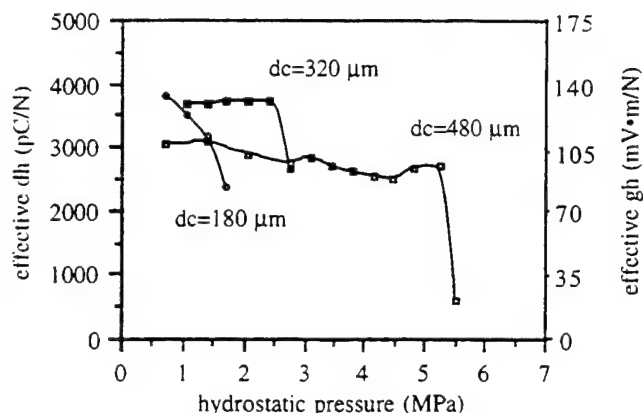


Fig. 7. Measured pressure dependence of the effective d_h and g_s coefficients for standard-size brass-capped single element cymbal transducers.

VI. CONCLUSIONS

The cymbal transducer appears to be a viable candidate for medium- to high-power shallow water acoustic projector applications. Its thin profile when incorporated into arrays makes it ideal for attaching to a curved surface. In addition, its simple design renders it easy and inexpensive to mass produce.

ACKNOWLEDGMENTS

The authors would like to thank Ender Kuntsal of ITC in Santa Barbara, CA, and Robert Dashem of the Applied Research Laboratory at Penn State for their contributions.

REFERENCES

- [1] R.F.W. Coates, *Underwater Acoustic Systems*, Macmillan New Electronics Series, Hong Kong, 1990.
- [2] T.R. Gururaja, A. Safari, R.E. Newnham, and L.E. Cross, "Piezoelectric ceramic-polymer composites for transducer applications," in *Electronic Ceramics: Properties, Devices, and Applications*, L.M. Levinson, Ed., New York: Marcel Dekkar, Inc., 1988, pp. 92-145.
- [3] L. Bowen, R. Gentilman, D. Fiore, H. Pham, W. Serwatka, C. Near, and B. Pazol, "Design, fabrication, and properties of Sonopanel 1-3 piezocomposite transducers," *Ferroelectrics*, vol. 187, pp. 109-120, 1996.
- [4] W. Cao, Q.M. Zhang, and L.E. Cross, "Theoretical study on the static performance of piezoelectric ceramic-polymer composites with 1-3 connectivity," *J. App. Phys.*, vol. 72, pp. 5814-5821, 1992.
- [5] K.D. Rolt, "History of the flexitensional electroacoustic transducer," *J. Acoust. Soc. Am.*, vol. 87, pp. 1340-1349, 1990.
- [6] E.F. Rynne, "innovative approaches for generating high power, low frequency sound," in *Transducers for Sonics and Ultrasonics*, M.D. McCollum, B.F. Hamonic, and O.B. Wilson, Eds., Lancaster, PA: Technomic, 1993, pp. 38-49.
- [7] Q.C. Xu, S. Yoshikawa, J.R. Belsick, and R.E. Newnham, "Piezoelectric composites with high sensitivity and high capacitance for use at high pressures," *IEEE Trans. UFFC*, vol. 38, pp. 634-639, 1991.

Piezocomposite SmartPanels™ for Active Surface Control Applications

D. Fiore, R. Torri, and R. Gentilman,
Materials Systems Inc., 521 Great Road, Littleton, MA 01460

Abstract - Piezocomposite SmartPanels™, capable of performing sensing, actuation, and control functions, have been developed for active surface control applications. These transducers, consisting of 1-3 actuators and pressure sensors and net-shape molded PZT accelerometers in a large area low profile panel, have been fabricated at Materials Systems Inc. (MSI) and evaluated at the Naval Research Laboratory (NRL). Single layer and two-layer 100 x 100 mm SmartPanels have been tested for sensor sensitivities, actuator authority, surface displacement uniformity, and sensor-actuator coupling. Multilayer GRP circuit boards are used both as stiff faceplates and to provide electrical connections and ground planes. SmartPanels draw upon PZT (lead zirconate titanate) ceramic injection molding technology, which is used to produce cost-effective and robust 1-3 piezoelectric ceramic-polymer composite materials. The 1-3 materials are used extensively for SonoPanel™ transducers in a number of sensor and actuator applications and have been qualified for US Navy applications based on the successful completion of pressure and shock tests. Applications for SmartPanels including actively controlled surfaces and vibration reduction mounts are described, along with the results of surface control studies undertaken at NRL.

I. INTRODUCTION

Piezoelectric 1-3 ceramic-polymer composites consist of aligned piezoelectric ceramic rods within a continuous polymer matrix (Figure 1). These materials have been utilized in many advanced underwater transducer applications and offer both fabrication and performance advantages over monolithic ceramic and piezoelectric polymer transducers. Advantages include high receiving sensitivity and transmit response, minimal lateral mode response, high capacitance, low acoustic impedance, and low mass.

Materials Systems' ceramic injection molding capability has made these materials widely available, under the trade name SonoPanel™, for Navy undersea and commercial applications. The manufacturing process, described in detail elsewhere [1], utilizes a heated thermoplastic mix of PZT powder and a wax based binder which is injected into a cooled mold cavity to net shape form the array of ceramic elements. The binder is subsequently removed by thermal decomposition, and the ceramic is conventionally sintered and poled, and then encapsulated in an appropriate polymer matrix to form the composite material.

This paper reviews some of the most recent applications of this technology, including the manufacture of single and double layer SmartPanels, which combine sensing and actuation capabilities in a single device.

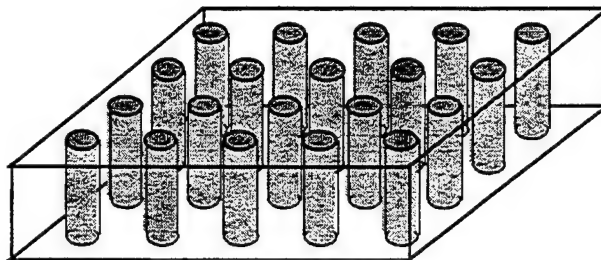


Fig. 1. Schematic description of 1-3 PZT/polymer composite.

II. DISCUSSION

A. SonoPanel Transducers

1-3 piezoelectric ceramic-polymer composite materials are used to make SonoPanel™ transducers for a number of underwater sensor and actuator applications. The wide variety of ceramic and polymer materials available for the fabrication of 1-3 composites means that transducer properties may be tailored to meet the requirements of the user. Ceramic type and volume fraction, matrix stiffness, composite shape and thickness, and electrode patterns are all transducer variables which are optimized for specific applications.

The standard SonoPanel configuration utilizes a compliant composite matrix with stiff, lightweight coverplates bonded to its surfaces to provide efficient stress transfer of incident pressure waves to the ceramic elements. These low profile transducers can be machined to a variety of geometries as shown in Figure 2. Multielement hydrophone arrays for multibeam sonar applications are produced by dicing the coverplate into smaller elements and wiring each one independently (Figure 3). SonoPanel transducers have passed Navy qualification testing for both pressure stability (to 1000 psi) and explosive shock resistance.

An alternate transducer configuration substitutes a stiff, thermoplastic polymer matrix in place of the compliant matrix just described. Stiff matrix transducers do not require coverplates and, although they sacrifice sensitivity slightly, they have the benefit of being conformable to non-planar surfaces. The thermoplastic matrix may be curved, under low heat and pressure, to a cylindrical or spherical radius (Figure 4). Electrode patterns, applied directly to the composite surface, can be apodized to adjust the transducer beam patterns and to reduce side lobes. Multiple electrode patterns can also be applied to the composite to make a constant beamwidth transducer (Figure 5). Constant beamwidth

transducers as large as 685 mm diameter with spherical curvature have been fabricated.

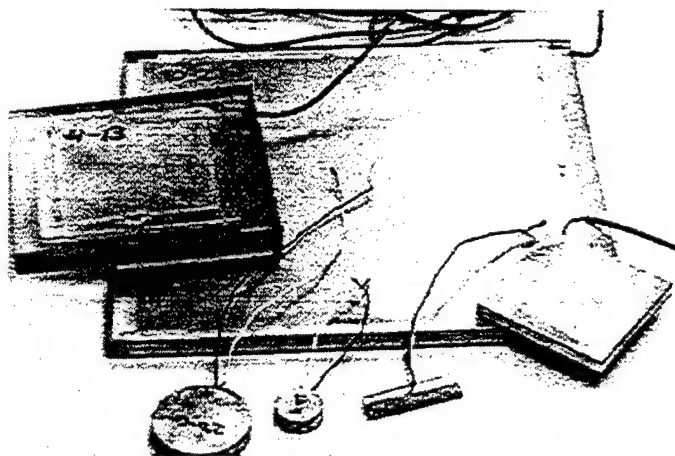


Figure 2. SonoPanel™ transducers in various configurations up to 250 x 250 mm.

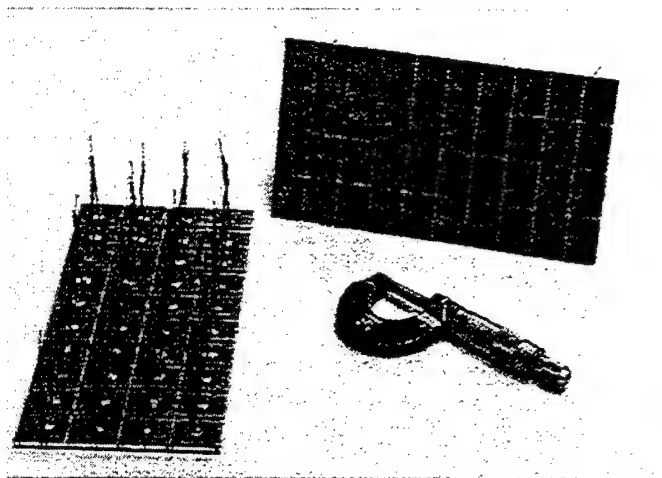


Figure 3. 40 element hydrophone array.

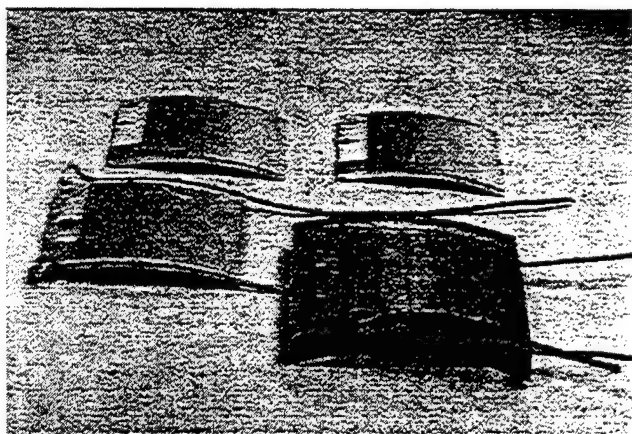


Figure 4. Curved stiff matrix transducers.

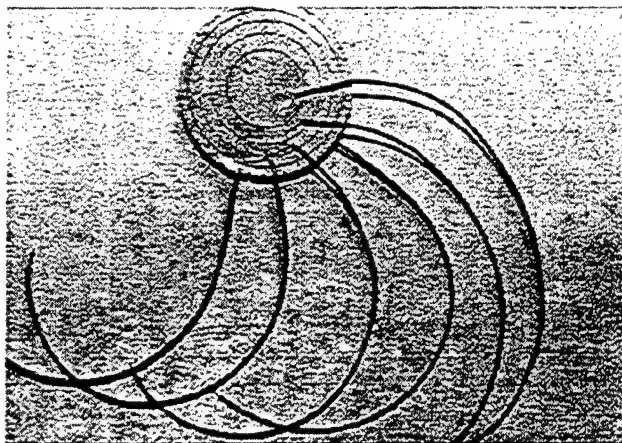


Figure 5. Patterned electrodes can be applied for specific applications.

Very large area SonoPanels, measuring 750mm x 750mm, have been fabricated in both the standard and stiff matrix configurations (Figure 6). The RVS and TVR data for these panels is shown in Figures 7 and 8. RVS for the standard SonoPanel design has been shown to be very flat (± 1 dB) down to 10 Hz [2]. The stiff matrix SonoPanel has a fundamental lateral resonance peak near 500 Hz that is absent in the standard configuration.

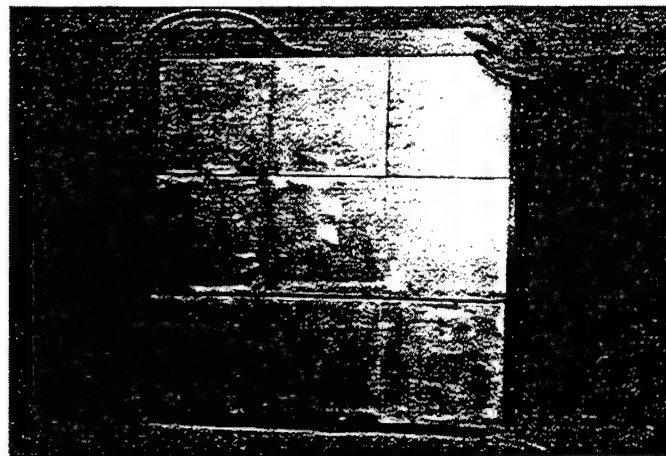


Figure 6. 750 x 750 mm standard SonoPanel.

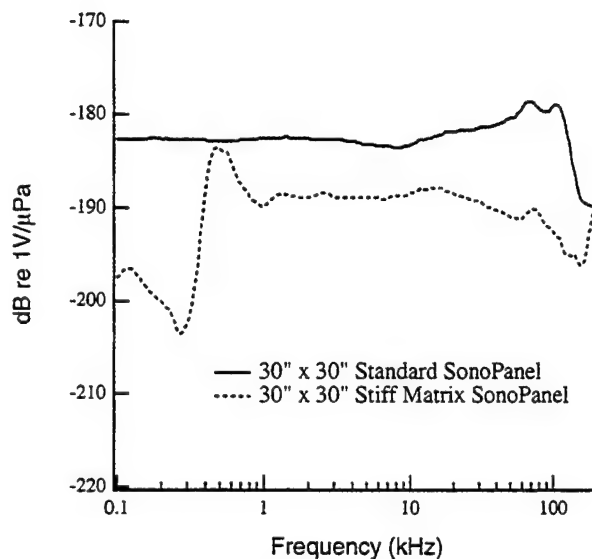


Figure 7. RVS data for 750 mm x 750 mm standard and stiff matrix SonoPanels.

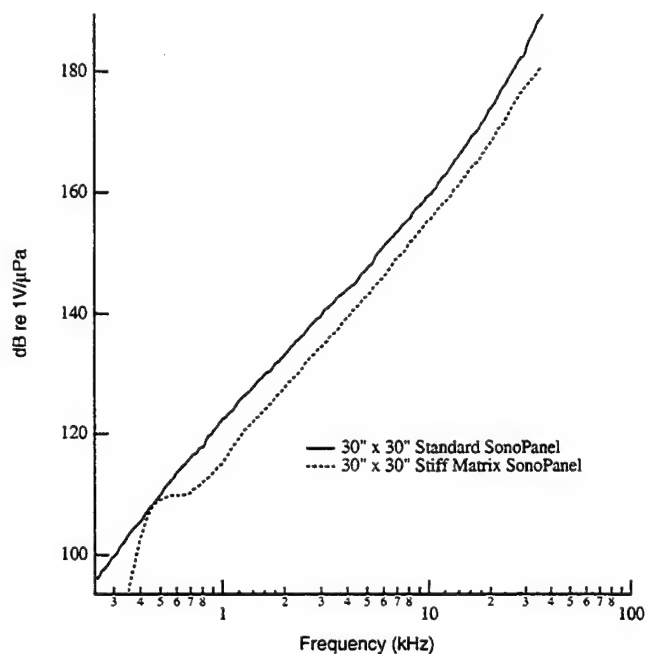


Figure 8. TVR data for 750 mm x 750 mm standard and stiff matrix SonoPanels.

B. SmartPanels™

SmartPanel™ transducers, capable of performing sensing, actuation, and control functions, have been developed for active surface control applications. The velocity sensors are monolithic, net-shape formed, low profile accelerometers (shown in Figure 9) which are uniformly distributed across a SonoPanel transducer (Figure 10). The accelerometers provide feedback to the 1-3 composite which functions as a large area actuator.

A control study was undertaken at NRL to explore the use of a one-layer SmartPanel as a vibration-reduction mount [3]. The mounting surface was vibrated under broadband excitation. Without the control system operating, this vibration transferred to the front surface of the SmartPanel with little loss. The signal from the accelerometer (mounted on the forward or controlled surface) was then connected to the input of a controller. The controller uses this sensor input signal to drive the 1-3 piezocomposite actuator to reduce the motion of the top surface. The controller performance criteria imposed was 20 dB reduction over the frequency range 1 to 4 kHz (limited by EMI at low frequencies and by the cover plate resonance at high frequencies). When the system was then operated in real time, the performance was almost indistinguishable from that predicted, as shown in Figure 11. No instabilities were observed.

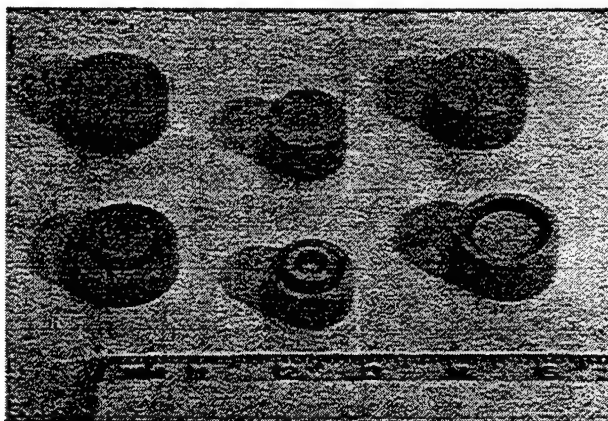


Figure 9. Three versions of net shaped formed PZT accelerometers have been produced.

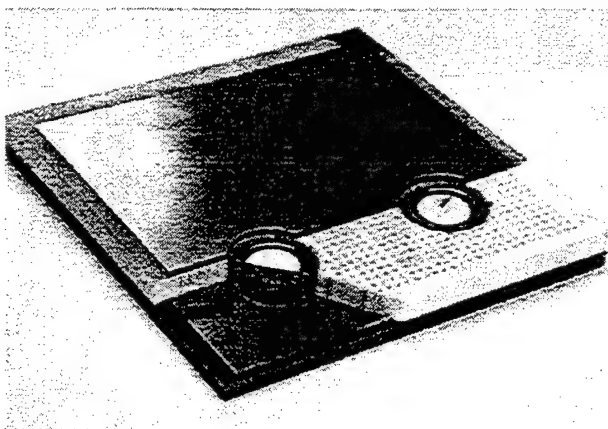


Figure 10. Cutaway view of a SmartPanel transducer.

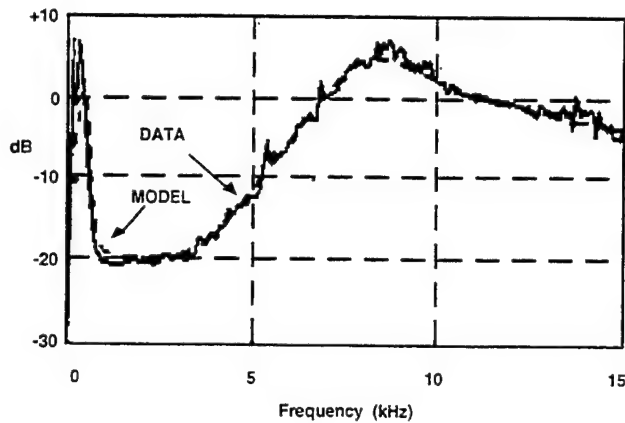


Figure 11. Surface vibration reduction using the single layer SmartPanel [3].

The newest SmartPanel design incorporates a second 1-3 composite layer allowing pressure sensing, velocity sensing, and actuation in a single device (Figure 12). These combination sensor-actuator SmartPanels can be applied to the monitoring and control of sound reflection and radiation from structural surfaces. Two-layer SmartPanels are being scaled to 250 x 250 mm in size, as shown in Figure 13.

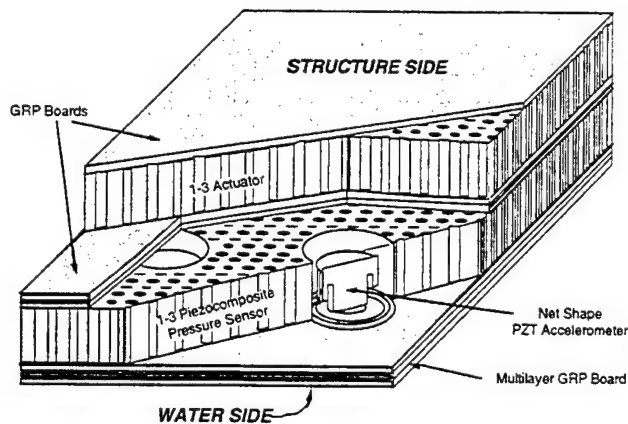


Figure 12. Schematic cut-away of a 2-layer SmartPanel.

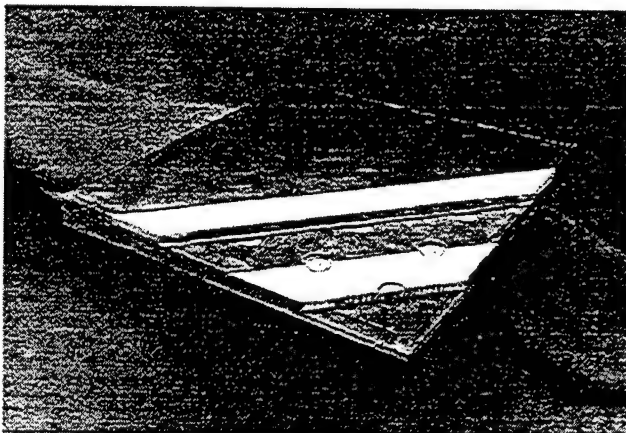


Figure 13. 250 mm 2-layer SmartPanel device.

The next stage of development will involve integrating power and controller electronics into the panel. One approach to integrated electronics is shown schematically in Figure 14. It is believed that excellent performance can be achieved with a local controller for each panel. An array of SmartPanels will soon be fabricated and tested for underwater active surface control.

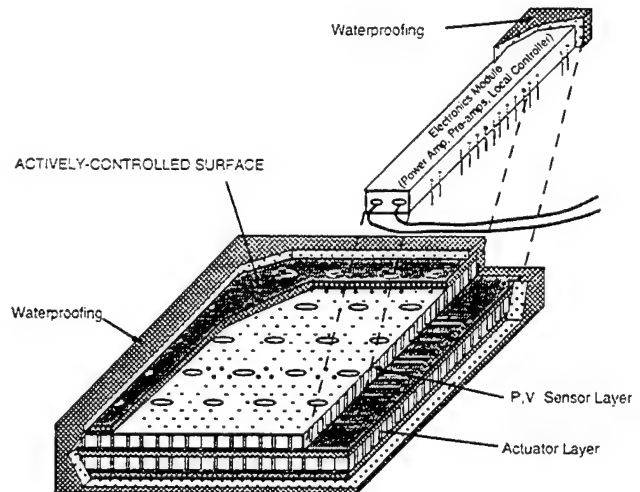


Figure 14. Schematic description of one approach for integrating power and control electronics into a 2-layer SmartPanel.

ACKNOWLEDGMENT

This work is supported by the Office of Naval Research and the Defense Advanced Research Projects Agency. Measurements on transducer materials and devices were made by the Naval Research Laboratory and the Naval Undersea Warfare Center - Underwater Sound Reference Detachment.

REFERENCES

- [1] R. Gentilman, D. Fiore, H. Pham, K. French, L. Bowen, "Fabrication and properties of 1-3 PZT-polymer composites," *Ceramic Transactions* 43, pp. 239-247, 1994.
- [2] Defense Research Agency test data, private communication.
- [3] R. Corsaro, B. Houston, J. Klunder, "Integrated smart actuator containing a monolithic co-formed accelerometer," *Proc. SPIE Smart Materials Conference*, 1997.

Session V—Ferroelectric and Related Materials

Invited Papers

- Piezoelectric Properties of PNN-PT-PZ Ceramics, N. Kamehara, *M. Kondo, M. Hida, and K. Kurihara, Fujitsu Laboratories, Japan* 348
- Structure-Property Relationships of Antiferroelectric Pb(Zr,Ti)O₃ Based Materials: Hydrostatic Depoling Characteristics, B.A. Tuttle, *J. Voigt, D. Zeuch, R. Moore, J. Glass, J. Michael, T. Garino, and W. Olson, Sandia National Laboratory, USA* 353
- Diffusion Phenomena Along Grain and Interphase Boundaries in Electroceramics, H. Haneda, *National Institute for Research in Inorganic Materials, Japan* 359
- Smart Skis and Other Applications of Piezo Control Technology, A. Bogue, *Active Control eXperts, Inc., USA* 366

Piezoelectric Properties of PNN-PT-PZ Ceramics

N. Kamehara, M. Kondo, M. Hida and K. Kurihara
Fujitsu Laboratories Ltd., Materials & Materials Engineering Laboratories
10-1 Morinosato-Wakamiya, Atsugi, Kanagawa 243-01, Japan

Abstract - The electromechanical coupling factor (k_{33}) was investigated as a function of $\text{PbNi}_{1/3}\text{Nb}_{2/3}\text{O}_3\text{-PbTiO}_3\text{-PbZrO}_3$ (PNN-PT-PZ) piezoelectric ceramic compositions close to the morphotropic phase boundary (MPB). The grain size of PNN-PT-PZ ceramics influences k_{33} . The composition of the MPB as determined by k_{33} is slightly different from that of a free permittivity boundary. The maximum value of k_{33} in PNN-PT-PZ systems reached 80.8% with a ceramic composition of 50PNN-34.5PT-15.5PZ. We applied PNN-PT-PZ ceramics to microactuators. We investigated the co-firing metallization of PNN-PT-PZ piezoelectric ceramics and Ag-Pd conductors in an effort to miniaturized them and lower the driving voltage. The PNN-PT-PZ piezoelectric ceramics were manufactured by the green sheet method. Ag-Pd conductors were then screen-printed on the green sheet. We manufactured 10-layered, piezoelectric ceramic Ag-Pd conductors that exhibit a high displacement.

I. INTRODUCTION

Pb-based perovskites have excellent piezoelectric properties. For example, Pb (Zr, Ti) O_3 ceramics have the highest electromechanical coupling factor (k_p) at 77% [1]. PNN-PT-PZ ceramics are a typical soft piezoelectric material known to have high piezoelectric properties. Banno et. al studied PNN-PT-PZ piezoelectric ceramics of various compositions and reported that a morphotropic phase boundary (MPB) of PNN-PT-PZ system [2]. Luff et. al investigated changes in the piezoelectric properties in relation to their composition and reported that the composition offering the highest performance ($d_{33} = 1100$ pC/N) was 0.5PNN-0.35PT-0.15PZ [3]. However, the changes in the electromechanical coupling factor (k_{33}) with respect to the composition has not yet been clearly investigated.

In this paper, we describe the effects of sintering temperature and atmosphere on the density and grain size of PNN-PT-PZ ceramics and on the electromechanical coupling factor (k_{33}). We also investigate the effect of the composition situated close to the morphotropic phase boundary

on k_{33} and free permittivity. Finally, multilayer piezoelectric ceramics with Ag-Pd conductors are also examined.

II. SAMPLE PREPARATION AND EXPERIMENTAL PROCEDURE

We used an oxide powder 99.9% of which was composed of PbO , NiO , Nb_2O_5 , TiO_2 and ZrO_2 . One mole each of NiO and Nb_2O_5 were mixed by ball milling for 20 hours. The mixture was then calcined at 1100°C for 4 hours. The phase of the calcined powder, determined by X-ray diffraction (XRD) was a single phase of NiNb_2O_6 . PbO , TiO_2 and ZrO_2 were added and mixed by ball milling for 20 hours. In this study, the electromechanical coupling factor (k_{33}) with a composition close to 0.5PNN-0.35PT-0.15PZ was investigated. The molar regions of the composition are aPNN-bPT-cPZ ($a + b + c = 1$, $0.495 < a < 0.515$, $0.335 < b < 0.36$, $0.145 < c < 0.17$, hereafter designate as A PNN-B PT-C PZ, A/B/C, A = 100a, B = 100b, C = 100c). The mixtures were dried and calcined at 850°C for 3 hours. The green compacts ($30\text{ mm } \phi \times 1$ to 5 mm) of the calcined powders were die-pressed at 120 to 130 MPa after a binder was added. The binder was burn out at 500°C for 1 to 3 hours. The green compacts were sintered at 970 to 1100°C for 3 hours in a closed container (in air) or in powder of the same composition (in a powder-bed). Then, $4 \times 4 \times 15\text{ mm}$ and $12 \times 3 \times 1\text{ mm}$ specimens were machined from the sintered bodies. The specimens were metallized with Ag paste and poled under a DC field of 2 kV/mm at room temperature in a silicon oil bath.

Multilayered actuators were manufactured by the green sheet method. The thickness of the green sheet was 0.045 mm . Ag-Pd paste was printed on the green sheet. These printed sheets were laminated by 100°C under 45 MPa for 20 min.

The density was measured by the Archimedeam method. The theoretical density of

50/35/15 ceramics, 8.31 g/cm^3 , was calculated from the composition and the lattice parameter. The phase of the surface and the lattice parameters of PNN-PT-PZ ceramics were also determined by XRD. The electromechanical coupling factor (k_{33}) and free permittivity ($\epsilon_{33}^T/\epsilon_0$) of the specimens were measured by the resonance-antiresonance frequency method and with an impedance analyzer, respectively. The microstructure of the fractured surfaces and grain boundaries of the PNN-PT-PZ ceramics were observed with a scanning electron microscope (SEM) and a transmission electron microscope (TEM), respectively. Displacement was measured with a laser vibrometer.

III. RESULTS AND DISCUSSION

Figure 1 shows the microstructure of the fractured surface and the grain boundary of 50/35/15 ceramics. The microstructure observed in Fig. 1(a) is poreless. Secondary reaction phases, such as PbO , Pb-based compound, unreacted oxide and so on, were not observed in the grain boundary (Fig. 1(b)). The microstructures of ceramics under the same sintering conditions were found to be relatively independent of their compositions.

Figure 2 shows the relative density of 50/35/15 ceramics as a function of the sintering temperature. The relative density of 50/35/15 ceramics exceeds 98% at 1050°C , which is larger than that found in a previous study (95%). The 50/35/15 ceramics can be sintered at relatively lower temperatures than other Pb-based perovskite ceramics, such as PMN-PT. The relative density decreases when increasing the temperature above 1100°C . The sintering temperature used in previous studies was around 1150 to 1200°C [3 - 5]. The low densities are due to a slight decomposition of PNN-PT-PZ at high temperature sintering, although the surface of the ceramics at 1150°C was a perovskite single phase.

Figure 3 shows the changes of k_{33} and the relative density as a function of the grain size of PNN-PT-PZ ceramics. The samples were sintered at 1050 or 1100°C and in either air or in a powder-bed. It is well known that grain size increases with an increase of sintering temperature and time. The grain size of the 50/35/15 ceramics sintered in a powder-bed is larger than that in air with equal sintering temperatures. Kudo et. al reported on the partial pressure of oxygen's

influence on the densification and the grain growth of Pb-based ceramics [6]. The partial pressure of PbO also influenced the grain growth of PNN-PT-PZ ceramics.

The microstructure of PNN-PT-PZ ceramics influences the electromechanical coupling factor (k_{33}). This factor (k_{33}) increases with an increase of the grain size of PNN-PT-PZ ceramics. It is supported that the electromechanical coupling factor (k_{33}) of a single crystal is larger than that of ceramics [4]. The highest value of (k_{33}) was obtained with the conditions of sintering at 1100°C in a powder-bed.

Figure 4 shows the change of the electromechanical coupling factor (k_{33}) for PNN-PT-PZ ceramics as a function of the PNN/PT molar ratio. The composition of the PZ component was constant at 15 mol%. The compositions yielding a maximum of k_{33} and free permittivity are not the same. The k_{33} of PNN-PT-PZ ceramics reached 0.8 at around $\text{PNN/PT} = 1.5$, whereas the free permittivity shows a broad maximum at 1.42.

Figure 5 shows the change of k_{33} for piezoelectric ceramics as a function of the PZ/PT molar ratio. The compositions of the PNN component were constant at (a) 50 and (b) 51 mol%. Once again, the compositions that yield the maximum electromechanical coupling factor (k_{33}) and free permittivity are not the same. The value of k_{33} reaches a maximum at $\text{PZ/PT} = 0.45$ (50/34.5/15.5). The electromechanical coupling factor (k_{33}) also reached 0.8. This value is the largest electromechanical coupling factor (k_{33}) which has ever been reported in piezoelectric ceramics [3]. The composition that maximizes the piezoelectric change coefficient (d_{33}) and the electromechanical coupling factor (k_{33}) are the same. The maximum value of the piezoelectric change coefficient (d_{33}) was 900 pC/N .

Figure 6 shows the position of the MPB of electromechanical coupling factor (k_{33}) and the dielectric constant determined by this study. The vertical lines represent the compositions giving the maximum electromechanical coupling factor (k_{33}) and free permittivity. The MPB position in free permittivity coincides with the composition giving the maximum piezoelectric change coefficient (d_{33}). The composition line of the electromechanical coupling factor (k_{33}) in this study shifted to a rich composition of rhombohedral phase (PbZrO_3), since the polarization directions of a rhombohedral phase outnumber those of a tetragonal phase.

Figure 7 shows a cross-sectional view of the 10 - layered piezoelectric ceramics. The thickness

of the PNN-PT-PZ piezoelectric ceramics is $30\text{ }\mu\text{m}$ and the thickness of the Ag-Pd is $2\text{ to }3\text{ }\mu\text{m}$.

Figure 8 shows the relationship between the displacement and the applied voltage of 10 - layered piezoelectric actuators made by the conventional powders of PNN-PT-PZ piezoelectric ceramics and developed powders. The displacement by developed powders is greater than that of conventional powders. The displacement of the piezoelectric actuators can be calculated by the following formula.

$$\Delta l = d_{33} \times E \times n. \quad 1$$

where Δl is the displacement, d_{33} is the piezoelectric strain constant, E is the applied voltage and n is the number of layers.

A greater displacement in the developed powder means a bigger piezoelectric strain constant.

IV. CONCLUSIONS

In this study, the longitudinal electromechanical coupling factor (k_{33}) was investigated as a function of a $\text{PbNi}_{1/3}\text{Nb}_{2/3}\text{O}_3\text{-PbTiO}_3\text{-PbZrO}_3$ (PNN-PT-PZ) piezoelectric ceramic composition close to the morphotropic phase boundary (MPB). The grain size of PNN-PT-PZ ceramics influences k_{33} . The composition

of the MPB as determined by k_{33} is slightly different from that of the free permittivity composition. The maximum value of k_{33} in a PNN-PT-PZ system reached 0.8 with a composition of 0.5PNN-0.345PT-0.155PZ.

REFERENCES

- [1] L. Eyraud, P. Eyraud, P. Gonnard, and M. Troccaz, *Ferroelectrics*, **31**, 113-116, (1981).
- [2] H. Banno, T. Tsunooka, and I. Shimano, *Pro. 1st Meet. Ferroelectric Materials and Their Applications*, Kyoto (1977), Keihin Printing, Tokyo, p.339.
- [3] D. Luff, R. Lane, K. R. Brown, and H. J. Marshallsay, *Trans. J. Brit. Ceram. Soc.*, **73**, 251-264, (1974).
- [4] J. Kuwata, K. Uchino, and S. Nomura, *Jpn. J. Appl. Phys.*, **21**, 1298-1302, (1982).
- [5] N. Ichinose and M. Kimura, *Jpn. J. Appl. Phys.*, **30**, 2220-2223, (1991).
- [6] S. Kudo, S. Tashiro, and H. Igarashi, *Jpn. J. Appl. Phys.*, **34**, 5303-5305, (1995).
- [7] N. Kamehara, Y. Imanaka, M. Hida, M. Tsukada, and K. Kurihara, *Proc. of 1996 Joint Fall Meeting of ACerS*.

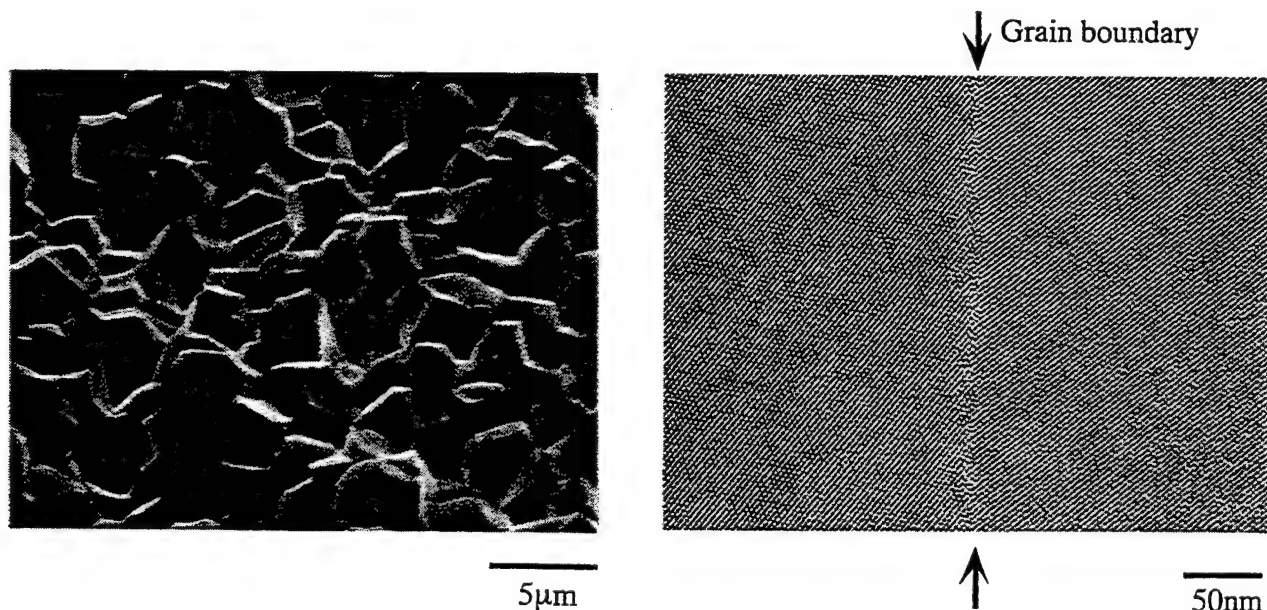


Figure 1. Microstructures of (a) fractured surface and (b) grain boundary of 0.5PNN-0.35PT-0.15PZ (50/35/15) ceramic.

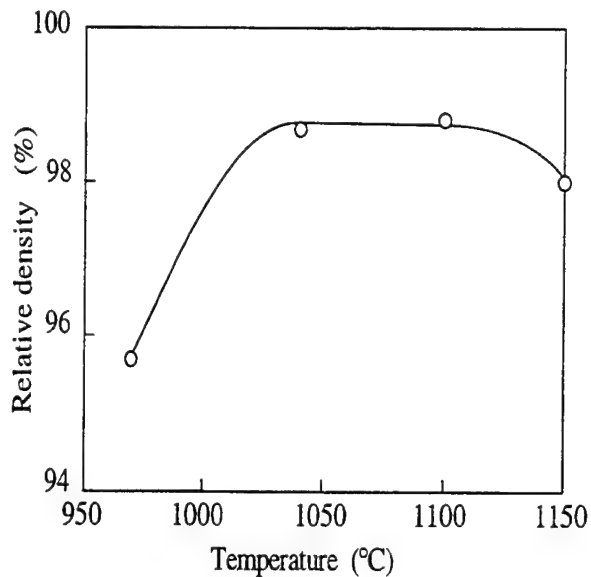


Figure 2. Change of relative density as a function of sintering temperature.

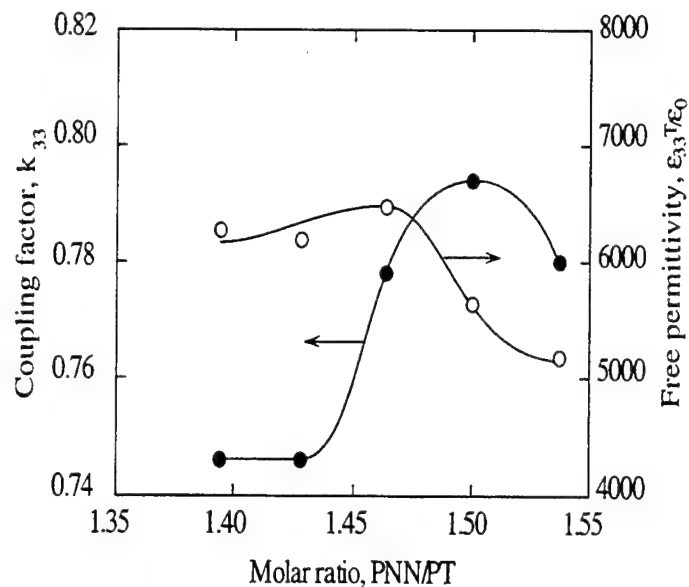


Figure 4. Changes of coupling factor (k_{33}) and free permittivity ($\epsilon_{33}T/\epsilon_0$) for PNN-PT-PZ ceramics (PZ = 15 mol%) as a function of molar ratio, PNN/PT.

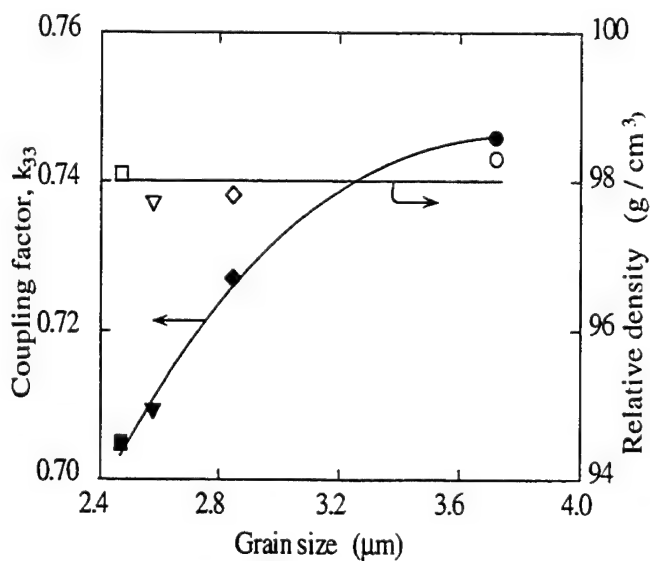


Figure 3. Change of coupling factor (k_{33}) and relative density as a function of grain size of PNN-PT-PZ(50/35/15) ceramics. ○, ●; 1100°C, powder-bed, ◇, ◆; 1100°C, air, ▽, ▼; 1050°C, powder-bed, □, ■; 1050°C, air.

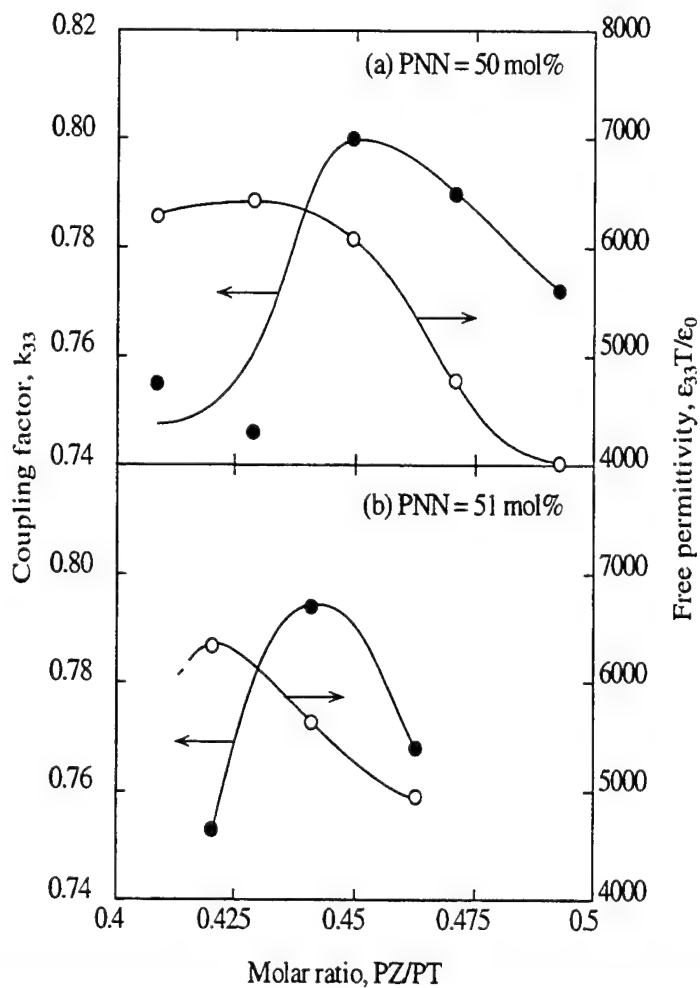


Figure 5. Changes of coupling factor (k_{33}) and free permittivity ($\epsilon_{33}T/\epsilon_0$) for PNN-PT-PZ ceramics (PNN = (a) 50 and (b) 51 mol%) as a function of molar ratio, PZ/PT.

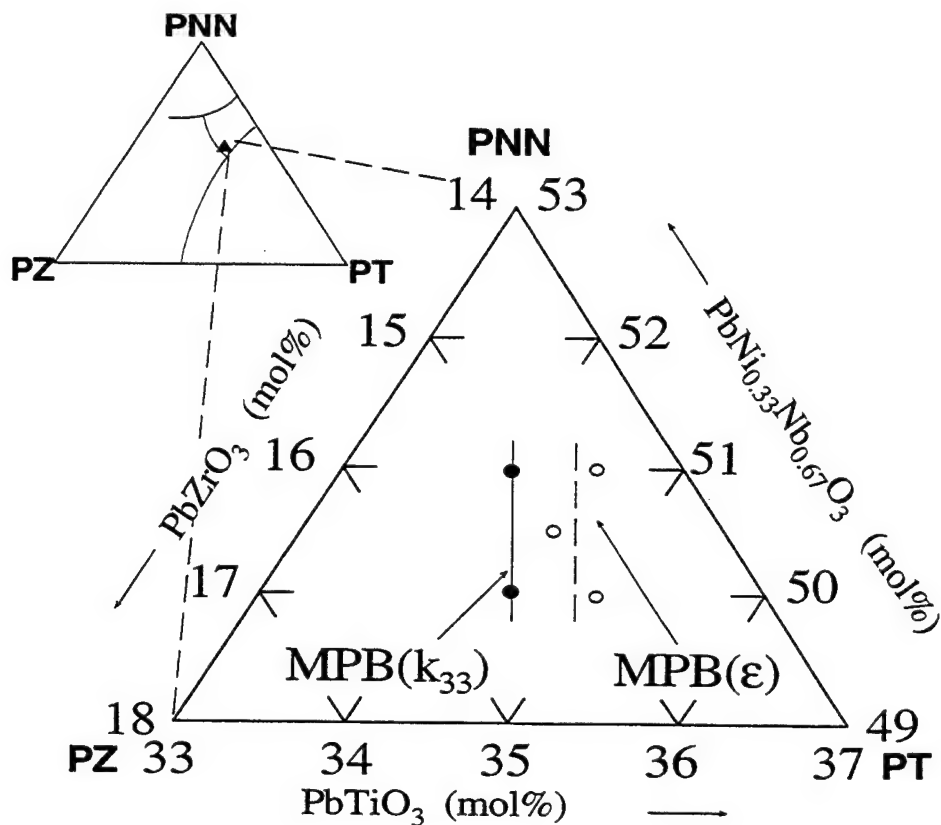


Figure 6. Morphotropic phase boundary of PNN-PT-PZ ceramics. Marks are compositions yielding maximum coupling factor (k_{33}) and free permittivity ($\epsilon_{33}^T/\epsilon_0$) in Figs. 1 and 4. Solid and dashed lines are MPB as determined from k_{33} and $\epsilon_{33}^T/\epsilon_0$ in this study.

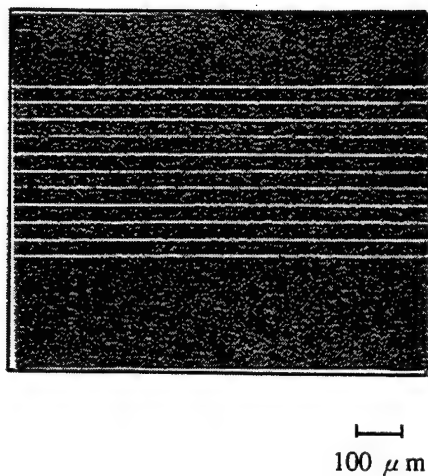


Figure 7. Cross-sectional view of 10-layered piezoelectric ceramics.

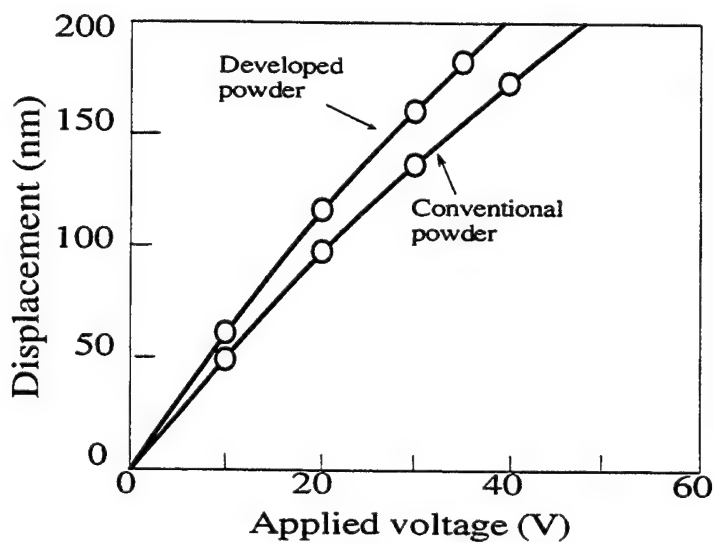


Figure 8. Relationship between displacement and applied voltage of 10-layered piezoelectric actuator

Structure-Property Relationships of Antiferroelectric $\text{Pb}(\text{Zr,Ti})\text{O}_3$ Based Materials: Hydrostatic Depoling Characteristics

Bruce Tuttle, Jim Voigt, David Zeuch, Roger Moore, Jill Glass, Joseph Michael,
Terry Garino and Walter Olson
Sandia National Laboratory
P.O. Box 5800
Albuquerque, NM 87185 USA

Abstract - A novel technique has been developed for the synthesis of homogeneous, weakly agglomerated, highly filterable $\text{Pb}(\text{Zr,Ti})\text{O}_3$ (PZT) powders. PZT 95/5 based ceramics were fabricated from these powders to determine interrelationships among microstructure, dielectric properties and pressure induced ferroelectric (FE) to antiferroelectric (AFE) phase transitions. Initial measurements indicate that microstructure has a substantial effect on hydrostatic depoling characteristics. While smaller grain size materials had higher switching pressures, subtleties in microstructure, which may include entrapped porosity, resulted in a more diffuse depoling characteristic. In addition, greater than 90% dense materials were obtained at process temperatures as low as 900°C. While measured polarizations of the PZT 95/5 ceramics fired at 900°C were only 30% of the values of PZT 95/5 fired at 1345°C, the dielectric constants of the 900°C materials were almost a factor of two higher. Backscattered electron Kikuchi pattern analysis determined that adjacent, nonlinear, irregularly shaped domain structures observed by electron channel imaging were 109° domains.

I. Introduction

$\text{Pb}(\text{Nb,Zr,Ti})\text{O}_3$ (PNZT) 2/95/5 ceramics are the active media for low volume, megawatt explosive power supplies. The basis of operation is the transformation of the PZT 95/5 ceramic from the poled ferroelectric, rhombohedral state to the antiferroelectric, orthorhombic state by application of mechanical pressure. System requirements dictate that the pressure at which the material transforms to the AFE state be very tightly controlled. Specifically, the chemical composition must be controlled to ± 0.05 mole% Ti, to meet

these switching pressure requirements. Another requirement is that substantial current output be obtained. This necessitates excellent chemical uniformity through out the entire ceramic. The requirements of tight stoichiometric control and a high degree of chemical uniformity are reasons why we have initiated one of the first efforts to combine chemical preparation of powders with added pore formers in the PZT 95/5 system. Effects of grain size, initial PbO stoichiometry, density and porosity on dielectric hysteresis and hydrostatic depoling properties of PZT 95/5 ceramics are described in this paper. Our work represents one of the first attempts to correlate microstructure to hydrostatic depoling behavior.

Strict microstructure control is required in addition to chemical uniformity to meet specifications. This is not surprising, in that the energy differences between AFE and FE phases are highly dependent on mechanical stress. Typically, large grains ($> 20 \mu\text{m}$) are desired for three reasons: (1) to minimize the presence of the AFE phase, (2) to obtain high polarization values and (3) to have a quick, uniform release of charge during pressure transformation. Obviously, the presence of the AFE phase in the microstructure diminishes the remanent polarization and thus current output. Larger grains may also reduce localized stress inhomogeneities and thus minimize localized switching pressure distributions. In addition to the above factors, Storz and Dungan [1,2] have shown that addition of pore formers are necessary to prevent high voltage breakdowns at low temperatures (-55°C). Their work has shown that additions of pore formers, such as, avicel and Lucite enhance this low temperature performance. While avicel additions produced acicular pores of approximate 70 μm length and 10 μm width, the Lucite additions resulted in spherical pores of 50 to 100 μm in diameter. Typically, 0.6 wt% of avicel (≈ 4 volume %) addition and densities in the 90% to 93% of theoretical density range result in the best properties. Units that were either hot-pressed to

greater than 98% density or pressureless sintered to greater than 96% density exhibited 100% failure rate for low temperature (-50°C) explosive tests.

The chemical composition used in this study is $\text{Pb}_{0.991}(\text{Zr}_{0.95}\text{Ti}_{0.05})_{0.982}\text{Nb}_{0.018}\text{O}_3$. Niobium is used to allow operation over a wide temperature range (-55°C to 74°C), enhance poling and increase resistivity. The low to high temperature rhombohedral phase transition occurs at 56°C accompanied by an approximate 0.4% change in volume [3]. Slow cooling rates, on the order of 0.1°C/min, are required to prevent larger samples from cracking due to this phase transition. The high temperature rhombohedral phase has space group R3m and the low temperature rhombohedral phase has space group R3c. These phases are distinguished by opposite rotation of the successive oxygen layers along the <111> direction as demonstrated by Dai, Xu and Viehland [4]. No evidence of transformation of the low temperature rhombohedral FE phase to the AFE phase has been observed by Yang [5] by dielectric measurements down to 11K for atmospheric pressure. The pressure / temperature phase diagram by Fritz and Keck [6] indicate that approximately 0.3 MPa hydrostatic pressure is required to transform from the FE to the AFE phase at 25°C for coarse grain, mixed oxide ceramics.

II. Experimental Procedure

PZT powders were synthesized by an alkoxide / oxalic acid technique in this study. This process minimizes waste and produces a readily filterable co-precipitate compared to other chemical preparation techniques, such as the highly regarded Haertling process [7]. In addition, a very uniform, weakly agglomerated, free flowing powder is obtained. At least 99.95% of all of the original chemical constituents were precipitated as determined by ICP analyses. Zirconium, titanium and niobium butoxides are blended with acetic acid in the initial step of the procedure. The butoxides were chosen to minimize moisture sensitivity and undesirable hydrolysis reactions. A lead acetate/acetic acid mixture is then added to the alkoxides. An oxalic acid / propanol solution is used as the precipitating agent and the wet powders are filtered to assist drying. Oxalic acid / propanol was used to stoichiometrically remove constituents, metal species and minimize agglomeration. 1500 gram lots of PZT 95/5 powder were synthesized for this study.

The precursor powder was pyrolyzed at 400°C, ball milled with ZrO_2 media for 16 hours and then calcined at 775°C for 16 hours. While some powders were processed into small 3 gram samples with no binder or pore former additions, for larger samples, polyvinyl alcohol / polyethylene glycol binder was used. The effect of pore former additions were evaluated by adding 0.6 wt% (approximately 4 volume percent) avicel particles, which were uniformly incorporated into the powders by ball milling. The powders were uniaxially pressed at 5 ksi, and then isopressed at 30 ksi, resulting in green densities on the order of 58% theoretical. Firing was performed using a double alumina crucible technique and mixed oxide PZT 95/5 atmosphere powder. Atmosphere powder configurations were modified depending on sample size. Typically, the fired weight of the specimens corresponded to PbO contents within ± 0.4 mol% of stoichiometry, regardless of the initial PbO stoichiometry of the powders. Compositions with 0 mol%, 1 mol%, 3 mol% and 6 mol% excess PbO were investigated. A range of firing temperatures were investigated from 800°C to 1450°C, and a baseline treatment of 1345°C for 6 hours was adopted for this study.

Dielectric hysteresis measurements were made using a HP4284A LCR meter. The majority of the ferroelectric measurements were performed using a Radiant Technologies RT66A ferroelectric tester with 0.5 sec (2 Hz) driving voltages. While pressure application rates for the hydrostatic depoling measurements varied from 0.69 MPa/sec (100 psi / sec) to 5.26 MPa/sec (765 psi/sec), a pressure application rate of 100 psi/sec was most often used. An approximate 4.5% increase in switching pressure was observed for the 765 psi/sec pressure application rate compared to the 100 psi/sec rate. Our baseline electrode deposition procedure was sputter deposition of 20 nm Cr // 100 nm Au electrodes with an 800°C annealing treatment before deposition. While a JEOL 6400 scanning electron microscope was used for BEKP analysis and electron channel imaging, a Hitachi 4500 FEG-SEM was used for conventional secondary electron imaging. Most imaging was performed on polished samples for which a 0.05 μm colloidal silica abrasive was used for the final polishing step.

III. Results and Discussion

A. Density and Grain Size

The effect of the initial PbO stoichiometry of the PZT 95/5 powders on the fired density as a function of temperature is shown in Figure 1. In our studies, excess PbO additions enhanced low temperature densification of the PZT 95/5 materials, similar to that shown by Shrout and coworkers [8] for PNZT 2/52/48 materials. Ceramics containing 6 mol% excess PbO had densities greater than 94% of theoretical for a firing temperature of 900°C. The 0% and 3% excess Pb addition samples fired at 1125°C and above in Figure 1, were all processed using improved powder processing and better PbO atmosphere control than for the 6% excess PbO samples. The improved powder processing consisted of a 400°C pyrolysis procedure and ball milling. An example of the improvement is that ceramics with 0% excess PbO fired at 1200°C were only 65% dense using the old techniques, but had extrapolated densities of 88% using the newer procedures. For the improved process, samples fired at 1345°C for 6 hours are 95% to 97% dense, for all three PbO stoichiometries. Close examination of a number of different batches indicated that statistically both densities and grain sizes increased slightly with higher initial with higher PbO content for ceramics fired at 1345°C. Densities for the improved process powder compacts fired at 1125°C ranged from 82% for the 0% excess PbO powders to 96% for the 6% excess PbO powders.

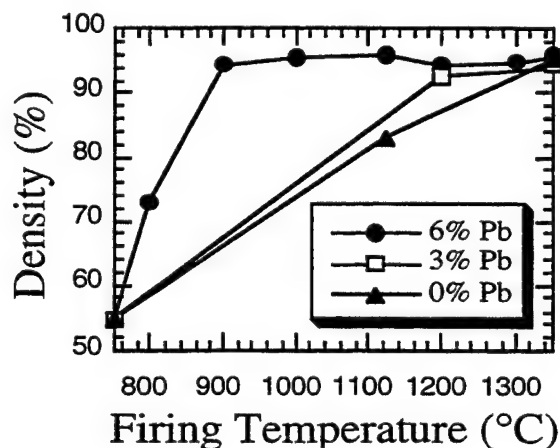


Fig. 1. Density versus firing temperature

B. Dielectric Properties Versus Grain Size

Grain sizes ranging from 0.5 μm to 20 μm were obtained for the chemically prepared PZT 95/5

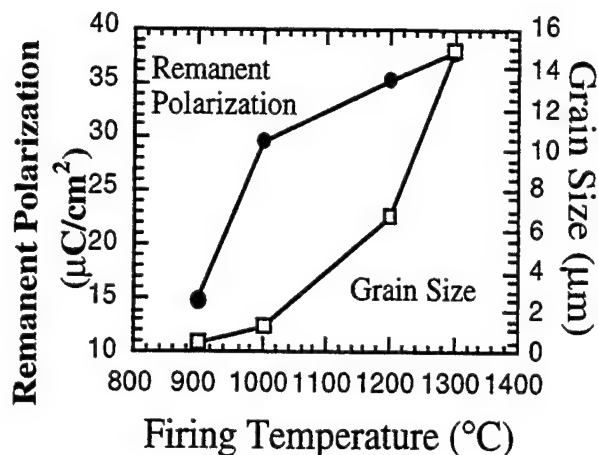


Fig.2. Polarization and grain size versus firing temperature

ceramics in this study. A plot of grain size and remanent polarization versus firing temperature is shown in Figure 2 for samples batched with 6 mol% excess PbO. These samples were all prepared from the same lot of powder and fired at temperatures of 900°C, 1000°C, 1200°C and 1300°C, respectively. A remanent polarization on the order of 38 $\mu\text{C}/\text{cm}^2$ was obtained for the 15 μm grain size sample, while the submicron grain size sample had a remanent polarization of only 15 $\mu\text{C}/\text{cm}^2$. Of potential interest for low fire packaging applications, the 1.5 μm grain size sample had a remanent polarization of 30 $\mu\text{C}/\text{cm}^2$. These grain sizes were calculated using a lineal intercept technique with no three dimensional shape multiplier.

The low field dielectric constants measured at 1 kHz decreased with increasing grain size as shown in Table I. The sample fired at 900°C had a dielectric constant of 511, while the sample fired at 1300°C had a dielectric constant of 281. Dissipation factors were 0.039 and 0.027, respectively. An increase in dielectric constant with decreasing grain size is very common for BaTiO_3 based materials and is attributed to increased internal stress with fine grain size. We have also observed this enhancement of dielectric constant with grain size for chemically prepared PZT 52/48 based ceramics. While the PbO content after firing is close to

stoichiometric for the 1200°C and 1300°C samples, the 900°C sample has the initial 6 mol% excess PbO retained. Because the dielectric constant should decrease with added PbO, the PbO stoichiometry is not a factor in the dielectric constant increase.

TABLE I
Dielectric Properties Versus Grain Size

| Dielectric Constant | Remanent Polarization ($\mu\text{C}/\text{cm}^2$) | Grain Size (μm) | d_{33} (pC/Nt) |
|---------------------|---|------------------------------|------------------|
| 511 | 14.8 | 0.7 | 29 |
| 436 | 29.6 | 1.4 | 61 |
| 335 | 35.2 | 6.7 | 69 |
| 281 | 37.9 | 19.2 | 67 |

C. Hydrostatic Depoling Measurements

The hydrostatic pressure required to invoke the FE to AFE phase transition also appears to be grain size dependent. Depoling curves are shown in Figure 3 for two ceramics (Table I) fired at 1200°C and 1300°C for 1.5 hours, respectively. The pressure necessary to invoke the FE to AFE transition increases from 244 MPa to 360 MPa (35.5 to 52.3 ksi) with decreasing grain size. The even finer grain size sample fired at 1000°C had a switching pressure of 365 MPa (53.1 ksi). In addition, the depoling characteristic is more diffuse for the finer grain size ceramics. The increase in distribution of switching pressures with smaller grain size is consistent with an increase in the heterogeneity of localized mechanical stresses. Since higher levels of internal stress would energetically favor the low volume AFE phase, an increase rather than a decrease in switching pressure with lower grain size at first seems anomalous. However, inhibition of ferroelastic deformation within the finer grain size sample leading to higher transformation pressures may be a factor that influences the depoling pressure.

We have investigated the effects of additions of avicel on dielectric and hydrostatic depoling characteristics of PNZT 1.8/95.4/4.6 chemically prepared ceramics. Ceramics from the same batch

of powder were fabricated with no pore former and with 0.6 wt% avicel. The sample with no pore former additions had a density of 97.3% and those

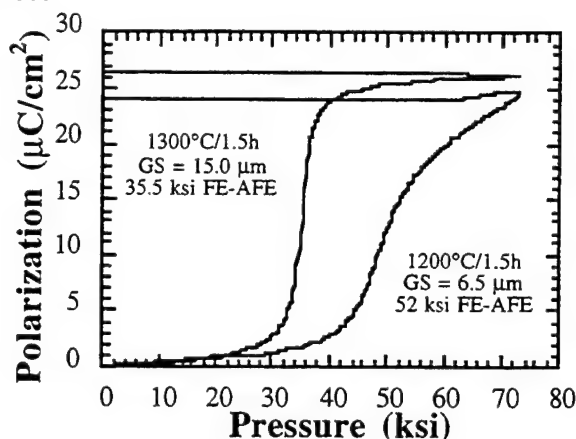


Fig. 3. Hydrostatic depoling characteristics for different grain size ceramics

with pore former had a density of 92.0%. While samples with pore former had a switching pressure of 263 MPa (38.3 ± 0.3 ksi); samples with no pore former had a switching pressure of 282 MPa (41.0 ± 1.0 ksi). Both samples exhibited a sharp hydrostatic depoling characteristic, similar to that shown in Figure 4 for the ceramic with pore former. The amount of charge released was $37.3 \pm 3.6 \mu\text{C}/\text{cm}^2$ for the material with no pore former and $31.8 \mu\text{C}/\text{cm}^2 \pm 1.3 \mu\text{C}/\text{cm}^2$ for samples with avicel additions. Remanent polarization values for 30 kV/cm field applications were 34.3 and 37.0 $\mu\text{C}/\text{cm}^2$, respectively. Piezoelectric d_{33} coefficients were 73 and 72 pC/Nt, respectively. Thus the pore former slightly affected density and released charge, but other properties only marginally.

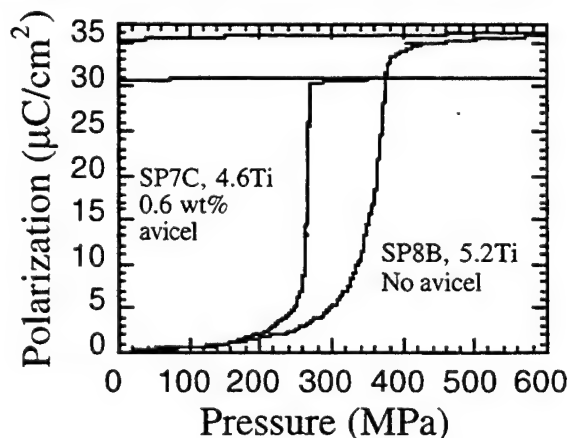


Fig. 4. Hydrostatic depoling curves for chem-prep PZT 95/5 ceramics

Not all chemically prepared samples exhibited sharp depoling characteristics. An example of both a sharp and a more diffuse hydrostatic depoling characteristic are shown in Figure 4. The sharp characteristic is for the previously described 4.6 mol% Ti sample with pore former; whereas the more diffuse characteristic is for a 5.2 mol% Ti sample with no pore former. Some evidence of early charge loss and some slanting of the characteristic above the depoling pressure, both of which are detrimental to device performance, are observed for the 5.2 mol% Ti sample. Evidence from several different batches of material indicates that the presence of pore former is not responsible for the differences in depoling characteristic shape.

Systematic studies were performed to see if the electrode preparation procedure was the cause of the differences in depoling behavior. Three different electrode procedures were used for two different batches of chem-prep 95/5 powders. Batch 8B samples contained 5.2 mol% Ti, while Batch 7C samples had 4.6 mol% Ti. The three different electrode techniques for PZT elements whose surfaces were polished with 600 grit SiC abrasive were:

- (1) ultrasonically clean with acetone, anneal ceramic at 800°C for 30 min and sputter deposit Cr//Au.
- (2) sputter deposit Cr//Au, and
- (3) deposit Dupont 7095 Ag frit paste, anneal at 593°C for 20 min.

Little change was observed in hydrostatic depoling characteristics for the 7C materials prepared with different electrode procedures. Hydrostatic transformation pressures of 275, 282 and 290 MPa (40.0, 41.0 and 42.2 ksi) and released polarizations of 35.2, 41.4 and 35.3 $\mu\text{C}/\text{cm}^2$ were obtained for electrode process 1, 2 and 3, respectively. The variation in properties for the samples containing 5.2 mol% Ti was somewhat greater. Hydrostatic transformation pressures of 335, 365, and 358 MPa (48.7, 53.1 and 52.1 ksi) and charge releases of 38.3, 36.3 and 35.3 $\mu\text{C}/\text{cm}^2$ were obtained for the different electrode procedures. The difference in the average depoling pressure for the two different batches is 10.4 ksi. A value which is close to the expected 12 ksi pressure difference based on the 0.6 mol% change in Ti content. The value of change in depoling pressure with Ti content was determined from measurements of large grain, mixed oxide PZT 95/5 ceramics. Further, some of the variation in switching pressure for the 8B

samples can be attributed to the slanted depoling characteristic. Conversely, all three 7C samples exhibited sharp depoling characteristics similar to that shown in Figure 4.

The aforementioned differences in hydrostatic depoling characteristic shape thus appear to be inherent in the material itself. Microstructural observations of the two different batches of material indicates that to first order grain size and domain configurations are similar. A unique feature is the presence of 1 to 3 μm pores entrapped within the grains of the batch 8b materials. Why these pores would make a substantial change in hydrostatic depoling characteristic, while avicel derived pores with dimensions on the order of 40 μm by 10 μm do not is not understood at this time. While the entrapped porosity may be a factor in the hydrostatic loop shape difference, it is not the sole cause. Ceramics from other batches of material that had very limited entrapped porosity compared to batch 8b samples also exhibited diffuse characteristics.

D. Determination of Domain Orientations on the Microstructural Level

We have used electron channel imaging in conjunction with backscattered electron Kikuchi pattern analysis [9] to positively identify different domain morphologies of the PZT 95/5 materials. Information from a surface layer 30 nm thick is obtained from the electron channel imaging and BEKP analyses. Thus, the condition of the surface of the sample is critical to the quality of the image obtained. We have used 0.05 μm colloidal silica as a final polish to minimize surface damage. From channel imaging micrographs we have accurately determined grain size and have observed two distinctly different types of domain morphology. The first type of domain configuration identified was the conventional straight, lamellar, 90° type domain configurations often observed in distorted, simple perovskite ferroelectrics. BEKP patterns were taken of adjacent, domains separated by a straight domain wall on the micron scale. These images were electronically subtracted from one another, indicating a difference of 71° in (111) orientation between the adjacent domains. Thus, these domains corresponded to a perovskite phase of rhombohedral symmetry and the straight, lamellar domains were conventional 90° type domains.

Investigation of the second type of domain morphology, irregularly shaped structures of roughly 2 μm , was also performed. Initial possibilities as to the origin of these structures included: (1) 180° domains, (2) AFE domain configurations, and (3) 90° type domains. While the irregular domain shapes were very similar to those observed for 180° domains in etched polycrystalline BaTiO₃ and PZT materials, a major difference in diffracted electron intensity for adjacent 180° domains was not expected, BEKP analysis of adjacent domains indicated that the curved domain boundaries separated regions that had (111) directions misoriented by 109°. This result is consistent with these curved structures being 90° type domains of rhombohedral symmetry. While 90° type curved boundaries seem highly unusual, there is previous evidence for this behavior. Randall and coworkers [10] have performed extensive TEM analyses on lead zirconate titanate - lead iron niobate ceramics of rhombohedral symmetry to indicate that curved boundaries were also of the 90° domain type. These domains were not of the same morphology as the domains in our study. Let us caution that this in no way implies that all curved boundaries in etched simple perovskite ferroelectric ceramics are 90° domain type. Indeed, the vast majority of these nonlinear etched structures are 180° type domains, as has been reported by many authors over the last 40 years.

IV. Summary

Chemically prepared PZT 95/5 type ceramics were fabricated and their dielectric properties characterized. Initial studies indicate that pore former additions of approximately 4 volume percent, have only slight impact on dielectric hysteresis behavior, piezoelectric coefficients, and the transformation pressure from the FE to the AFE state during hydrostatic depoling. Some loss in the charge released during hydrostatic depoling was observed for samples with pore former additions compared to samples with no pore former added. Initial investigations of the effects of microstructure on hydrostatic depoling characteristics indicated that depoling pressures increased with decreasing grain size and that entrapped pores may result in more diffuse hydrostatic depoling characteristics.

Backscattered electron Kikuchi pattern analysis was used to positively identify 90° type domains on the microstructural level and to confirm rhombohedral, ferroelectric symmetries of individual grains.

Acknowledgments

Sandia is a multiprogram laboratory, operated by Lockheed Martin Company, for the US Department of Energy under contract DE-ACO4AL85000. The authors acknowledge technical contributions and enlightening discussions from Ben Hoover, Pin Yang, Gary Zender, Bonnie McKenzie, Mike Eatough, Mark Rodriguez, Alice Kilgo, Diana Sipola, Jeff Keck, Steve Lockwood, Tim Scofield and Ted Montoya.

REFERENCES

1. L.J. Storz and R.H. Dungan, "A study of the electrical, mechanical and microstructural properties of 95/5 PZT as function of pore former type and concentration," Sandia Report, SAND85-1612 (1985).
2. R.H. Dungan and L.J. Storz, "Relation between chemical, mechanical and electrical properties of Nb₂O₅ modified 95 mol% PbZrO₃-5 mol% PbTiO₃," *J. Amer. Ceram. Soc.* Vol. 68, pp. 530-33 Oct. 1985
3. H. Jaffe, B. Jaffe and W.R Cook, *Piezoelectric Ceramics*, New York, Academic Press, Inc., 1971, p. 139.
4. X. Dai, Z. Xu and D. Viehland, *J. Amer. Ceram. Soc.*, "Effect of oxygen octahedron rotations on the phase stability, transformational characteristics and polarization behavior in the lead zirconate titanate solid solution series," *J. Amer. Ceram. Soc.*, Vol. 78, pp. 2815-23 Nov. 1995.
5. P. Yang, *Internal Sandia Memo*, May 29, 1997.
6. I. Fritz and J. Keck, "Pressure-temperature phase diagrams for several modified lead zirconate ceramics," *J. Phys. Chem. Solids*, vol. 39, pp. 1163-67, (1978).
7. G.H. Haertling and C.E. Land, "Recent improvements in the optical and electrooptic properties of PLZT ceramics," *Ferroelectrics*, vol. 3, pp. 269-80 (1972).
8. W.S. Hackenberger, T.R. Shrout and D.P. Picerell, "Piezoelectric thick films for ultrasonic transducer arrays," *ISHM '96 Proceedings*, pp71-6 (1996).
9. R.P. Goehner and J. R. "Michael, "Phase identification in a scanning electron microscope using Backscattered electron Kikuchi patterns," *J. of Res. of the Nat. Inst. of Standards and Technology*, vol. 101, pp. 301-8 (1996).
10. C.A. Randall, D.J. Barber, and R.W. Whatmore, "Ferroelectric domain configurations in a modified-PZT ceramic," *J. Matls. Sci.*, vol. 22, pp. 925-31 (1987).

Diffusion Phenomena along Grain and Interphase Boundaries in Electroceramics

Hajime HANEDA

National Institute for Research in Inorganic Materials
1-1 Namiki, Tsukuba-shi, Ibaraki 305 JAPAN

Abstract-Grainboundary diffusion phenomena in several electroceramics were discussed in connection with electric properties, such as varistor characteristics, PTCR, etc. Although the oxide ions diffuse along grainboundaries in some zinc oxide ceramics, values of grainboundary coefficients are almost independent of impurity species. The grainboundary of PTCR-barium titanate ceramics also plays a role of high diffusivity path, while no preferential diffusion along grainboundary was observed in non-PTCR barium titanate. The ions of Ag electrode diffuse at grain boundary and weak bonding strength of grain boundary.

I. INTRODUCTION

Atomic transport along grain and interphase boundaries, being normally orders of magnitude faster than in the bulk, plays a key role in a large number of ceramic processes such as creep, and sintering, etc. Furthermore it is well known that oxygen ions along grain boundary affect grainboundary properties such as PTCR effects. Oxygen diffusion in many oxide systems such as perovskites, spinels, garnets was evaluated by a gas-solid exchange technique. According to the results, oxygen grainboundary diffusion has close relation with PTCR effects. The equilibrium defects are not only important metastable defects are and creation and annihilation of metastable defects in electroceramics. In the recent study, an evidence of grainboundary transformation was found in Bi-doped ZnO varistor system. This phenomenon is analogous to the relation between PTCR and grainboundary diffusivity.

Reactions along interfaces between electrode and electroceramics are interesting, for applications. The reaction and diffusion of Ag electrode were carried out in PLZT ceramics. The grain boundary diffusion of Ag affects the mechanical and chemical properties. These diffusion phenomena along grainboundaries are discussed in the present extended abstract.

II. MEASURING DIFFUSION

A common technique used in measuring diffusion employs a radioactive isotope as a tracer. The tracer is deposited on the desired sample in a fashion that provides

one of the boundary conditions that produce a simple solution to Fick's Second of Law. The diffusion coefficient is then extracted from the concentration profile. This technique is suitable for both self-diffusion and impurity diffusion studies. Unfortunately, many chemical species (including oxygen) do not have suitable radioactive isotopes.

A number of techniques have been developed using a stable isotope tracer to measure self-diffusion. A gas-solid exchange technique has been used in which a sample is annealed in a closed system that contains a gas of the isotopic tracer[1]. In the present study the diffusion coefficients of oxide ions were evaluated by means of this method. The development of the ion probe or secondary mass spectrometer (SIMS) offers a potentially simple technique to measure self-diffusion coefficients using a stable isotope tracer[2].

For measuring the diffusion of a species that is chemically different from the host material, common chemical analysis techniques are suitable. The electron microprobe as well as Auger spectroscopy has been used quite successfully for these types of studies. Chemical techniques are not, by themselves, studied for measuring self-diffusion. SIMS analysis has much dynamic range, so it is one of the best techniques for impurity diffusion analysis. The Ag electrode diffusion characteristics in PLZT ceramics are reported in this paper[3].

III. EXPERIMENTAL

In the present study single crystals, bicrystals and poly crystals were used for oxygen diffusion. Diffusion coefficients of oxide ions were determined by a solid-gas exchange technique[1]. After being cleaned with water, ethanol, acetone, and ethanol, the samples were placed inside a platinum crucible with a platinum susceptor in a vessel of a RF furnace. The system was evacuated, and the ^{18}O -enriched oxygen gas with 5kPa pressure was introduced into vessel that was closed from the gas line. The sample crucible was firstly heated at 700°C for 15 minutes to maintain the constant concentration at sample surface, and then the temperature was elevated to a desired temperature for isotope exchange. The temperature was monitored by an optical pyrometer. Although the temperature accuracy of

pyrometer is in 10K, the temperature variation among samples in a same experimental cycle is believed to be less than few degrees. After isotopic exchange of oxygen between the gaseous phase and the samples during a given time, the furnace was cooled down by switching off the power and ^{18}O -enriched gas was re absorbed back into zeolite storage flask by sold trapping with liquid nitrogen.

The ^{18}O diffusion profiles (concentration versus depth) were measured using SIMS with $^{133}\text{Cs}^+$ as the primary ions, an accelerating voltage 10kV, and beam current of 5 to 20nA. The primary beam scanned at 100 μm area, and signals of secondary ions were detected at 40% central square of a sputtered crater. Intensities for the negative ions ^{16}O and ^{18}O were measured as a function of time. The crater depths were measured using a Dektak 3000 profilometer. For three dimensional analysis, a planar detector was used(Charze Evans, Co.. Resistive anode encoder: RAE). The concentrations of ^{18}O are converted as a function of depth, using sputtering duration.

The concentration ($c(x,t)$) of ^{18}O at any sample depth was determined from the ion intensities:

$$c(x,t) = \frac{I(^{18}\text{O})}{I(^{18}\text{O}) + I(^{16}\text{O})} \quad (1)$$

If the surface is maintained at a constant concentration of ^{18}O , C_g , which is the same concentration as in the gaseous phase, and if the concentration in the solid is initially uniform($C(x,0)=C_0$, natural abundance, 0.204%), the following relation can be used to calculate the diffusion coefficients, D [4]:

$$\frac{c(x,t) - c_0}{c_g - c_0} = \text{erfc} \left(\frac{x}{2\sqrt{D \cdot t}} \right) \quad (2)$$

Where x is the penetration, t the duration of diffusion annealing, and $\text{erfc}=1-\text{erf}$ (erf the Gaussian error function).

In the polycrystalline samples, the tracer diffuses deeper inside than expected from the volume diffusion. This is due to the effect of grain boundary diffusion. Le Claire(4) have proposed the relation between the grain boundary diffusion coefficient and concentration at large depth, which is useful in present case. The value of $(Dt)^{1/2}$ was smaller than the grain size, so a product of oxygen grainboundary coefficient, D' and grainboundary width, δ , is evaluated as follows [6]:

$$D' \cdot \delta = 0.66 (4D/t)^{1/2} \left[-\frac{\partial \log(c(x))}{\partial x^{6/5}} \right]^{-5/3} \quad (3)$$

IV. RESULTS AND DISCUSSION

A ZINC OXIDES

(a) Bulk diffusion

Zinc oxide has a wurtzite structure, where the oxygen ions are in hexagonal closed packing. In hexagonal crystals, it is expected that tensors for diffusion coefficients, $D_{xx}=D_{yy}$ for the two principal axes in the basal plane, and D_{zz} for c-axis direction are different from D_{xx} . Figure 1 shows typical depth profiles of ^{18}O in single crystals with parallel (D_{xx}) and perpendicular (D_{zz}) surfaces to c-axis, respectively.

Typical oxygen diffusion profiles were shown in Figure 1. It is observed that oxygen diffusivity varied with crystal direction. The diffusivity(D_{xx}) in the basal plane is faster than the c-axis direction(D_{zz}). D_{xx} and D_{zz} values are displayed in the Arrhenius diagram of figure 2. Although the values are almost same as Halling's data, the activation energy of present study is slightly larger than Halling's[6]. The D values can be represented by two Arrhenius equation, respectively,

$$D = 1.2 \times 10^8 \cdot \exp(-571(\text{kJ/mol})/RT) \quad (\text{for } D_{zz}) \quad (4)$$

$$D = 1.5 \times 10^5 \cdot \exp(-491(\text{kJ/mol})/RT) \quad (\text{for } D_{xx}) \quad (5)$$

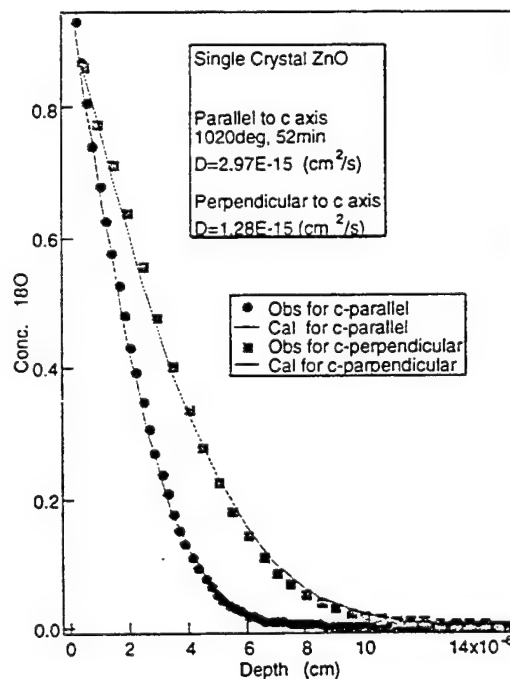


Fig. 1. Typical diffusion profiles in ZnO single crystals.

In the present study, hot-isostatic pressed samples without pores were used[7], because the effects of pores are excluded. Figure 3 shows a typical depth profile of ^{18}O in a ZnO sample. The condition of the constant concentration at the surface for a semi-infinite medium was used. The solid line in Fig.3 indicates the fitted value using data near surface (<1000nm) with a simple error function (Eq.(2)). Lattice diffusion coefficients were obtained, using this equation. The profile had a long tail at larger depth. It is obvious that the long tail was not due to the lattice diffusion but might be caused by the diffusion along grain boundaries. The grainboundary diffusion of oxide ions is discussed later.

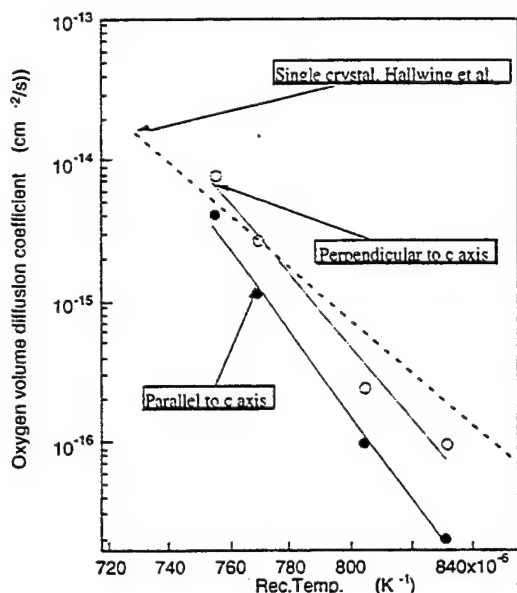
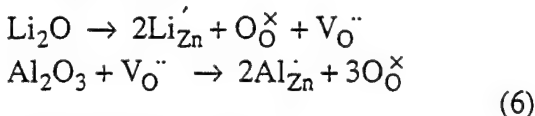


Fig.2. Arrhenius plots of oxygen diffusion in ZnO single crystals

Resultant Arrhenius plots were illustrated in figure 4. The lattice diffusion coefficients of oxygen ions depended on dopants. The Al-doped samples gave the maximum values, and the Li-doped, the minimum values, i.e., the values of the lattice diffusion coefficients with higher valence dopants compare with zinc ions are greater than lower valence dopant such as lithium ions. The values for Al-doped samples are one to twice orders of magnitude larger than Li-doped, so the variation of bulk diffusion coefficients among samples doped with various dopants is not caused by anisotropy diffusion, where the variation factor is less than 4. According to this fact indicates it might be believed that the oxygen ions diffuse with an interstitialcy mechanism as follows,

Vacancy model:



Interstitialcy model:

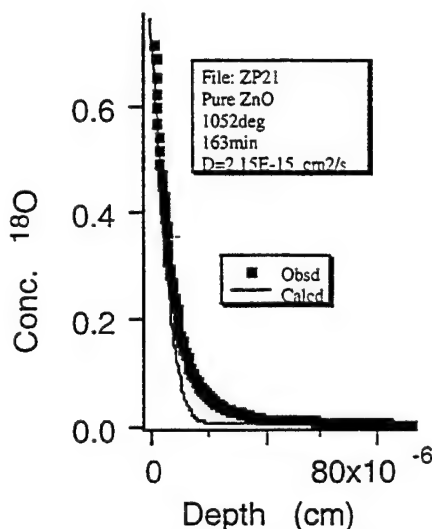
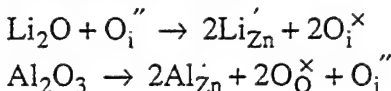


Fig.3. Depth profile of oxygen 18 in zinc oxide ceramics. Closed rectangular, the measured values and solid line, calculated values by a simple error function (Eq.(2)).

A number of measurements of oxygen diffusion in ZnO have been performed[6], [8-10]. The various diffusion coefficients are not in especially good agreement with each other. Because the diffusion occurs by an extrinsic mechanism controlled by impurity, such variation may be observed. To determine the mechanism, some experiments of oxygen partial pressure dependence have been done. Moore[8] has claimed the dependence with the exponent +0.5 had been observed and the power +0.5 has been discussed in terms of oxygen interstitial migration. On the contrary, Hoffman and Lauder[9] have reported the -0.5 and -1.5 of values. The negative exponent was considered to be the result of oxygen vacancy diffusion. Our results support the interstitial mechanism. It is noted that both Moore's data and ours are for polycrystals. Such disagreement would not be unexpected if defect state was in metastable or the diffusion mechanism changed between single and polycrystal. Furthermore, Robin et al. have claimed those highest values for Hoffman and Lauder had been affected by a volatilization of ZnO[10]. Error due to the

vapor pressure of zinc oxide is believed to be increasing with decreasing oxygen partial pressure.

(b) Grainboundary diffusion.

According to ^{18}O ion image about $1\mu\text{m}$ depth, the grain boundary network could be observed in pure ZnO. It is considered to be an evidence of contribution of grainboundary diffusion to the long tail of diffusion profiles. Same high diffusivity paths along grainboundary were appeared in all samples. Using the data at tail parts, one can calculate the products of $D'\delta$ with Eq.(3). Anisotropic oxygen grainboundary diffusion was also observed in polycrystalline samples.

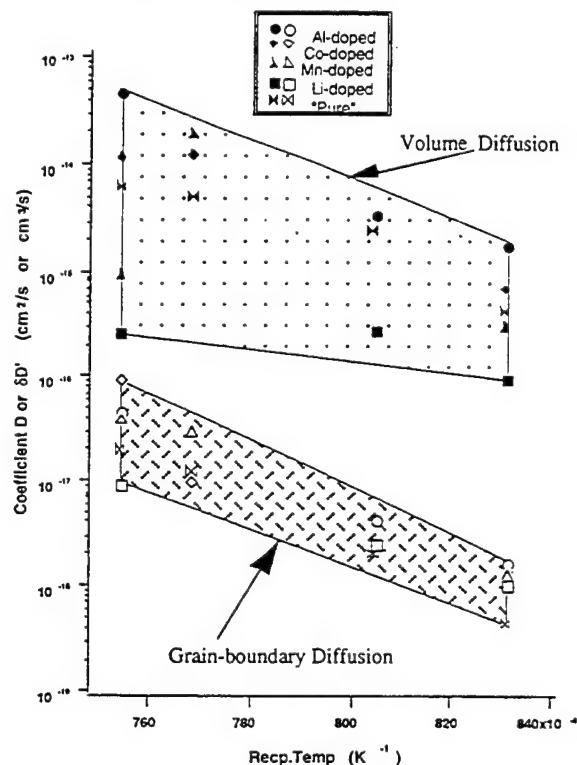


Fig.4. Temperature dependence of volume and grain-boundary diffusion coefficients of multiplied by δ of oxide ions in ZnO ceramics.

Figure 5 shows a typical LeClaire's plots vs. $x^{6/5}$ in a pure ZnO annealed at 1052°C . Using the slope in this figure, the values of grain boundary diffusion coefficients were estimated. As seen in Fig.6, the value of high diffusivity grainboundary is one order of magnitude higher than lower one. The products of grainboundary diffusion, D' , to grainboundary width, δ , are also plotted in Fig.4. The variation range of the grain boundary diffusion coefficients was narrower than that for the lattice diffusion, which indicates that the structure of grain boundaries and mechanism for grain boundary diffusion of oxygen ions little depend on the

characteristics of the dopants, and the values only depend on crystalline orientations between two crystals.

The grainboundary and dislocation diffusion are considered to take a pipe diffusion mechanism. Generally, dopants mainly affect the defect concentration, concerned with dopant valences. It is sure that the pipe structure has a lot of defects, nearly unity, so defect concentration is little influenced by aliovalent dopants. These are reasons that the grainboundary diffusivity is insensitive to the dopant species.

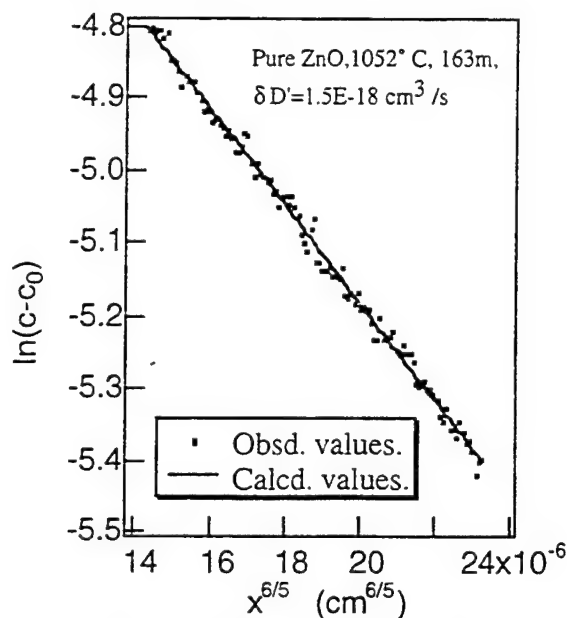


Fig.5. Grainboundary diffusion analysis using Le Claire Eq. Obsd. data, same as Fig.3.

The varistor characteristics are very sensitive to the type of dopant, and then is believed to be related with the preferential oxidation at grainboundary. It is actually lost when annealing in a reduced atmosphere. As for the tendency of dopants and annealing-effects, one can think that they are caused by the difference of grainboundary diffusivity of oxide ions. In the present cases, only Mn-doped samples behaved as varistor[11], and the grainboundary diffusion characteristic is believed to be insensitive to the type of dopants. Therefore, the difference of grainboundary diffusion is not origin of dopant effects. Bi-dopant is well known to give a high non-linearity of V-I characteristics[12], which is caused by the existence of some excess oxygen ions. It is noted that the oxygen interstitial ions exist, above mentioned. If the Bi ions are segregating along grainboundaries, the concentration of interstitial oxide ions (excess oxygen ions) is considered to be increasing.

B STRONTIUM TITANATES

Oxygen defects influence the electric properties in various functional ceramics. It is considered that grain

boundary phenomena such as a PTCR effect relate to the grain boundary structure[13~16]. Therefore, oxygen defect structure and the grain boundary diffusion are important parameters to clarify the electric characteristics and the grain boundary phenomena. It has been already reported at the last US-JAPAN seminar that enhanced oxygen diffusion along grain boundary had been observed in barium titanate ceramics doped with Y or La and the PTCR effects had close related to the oxygen grain boundary diffusion. In this paper, we focus our attention on attempts to investigate the oxygen defects and grain boundary diffusion of oxygen ions in other perovskite compounds particularly as SrTiO_3 .

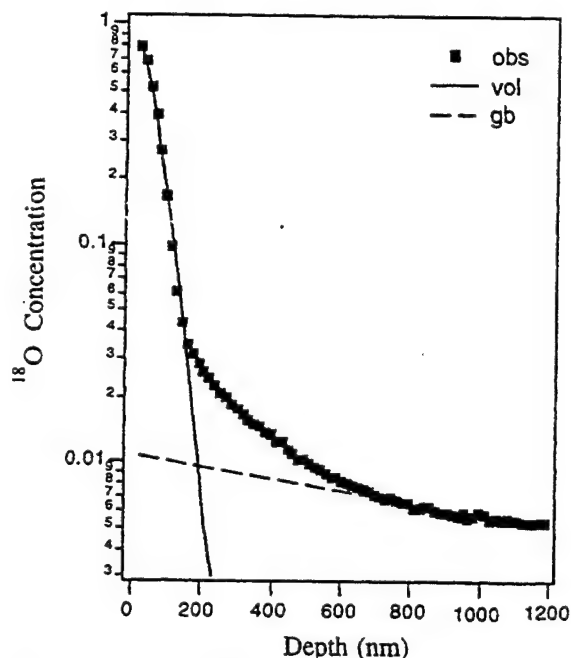


Fig.6. Oxygen diffusion profile obtained by SIMS. The solid squares, the observed oxygen tracer concentration determined by SIMS. The solid line and dashed line, calculated volume diffusion contribution and grain boundary diffusion, respectively.

Figure 6 shows a typical depth profile of ^{18}O in strontium titanate bicrystal, and indicates the surface concentration of ^{18}O was almost same as that of the gaseous phase. The condition of the constant concentration at the surface for a semi-infinite medium can, therefore, be used. The solid line in Fig.6 indicates the fitted value using some data near surface with a simple error function(Eq(2).). Observation of ^{18}O ion image at deeper depth indicated that the joined boundary played the role of a short circuit for oxygen diffusion.

The grain boundary diffusion characteristics (δD_{gb} : δ and D_{gb} , grain boundary width and grain boundary diffusion coefficient, respectively) were obtained by analyzing the grain boundary contribution using the planar

defect model[5], and also shown in Fig.6. as a dashed line. The lattice diffusion coefficients of oxygen ions and the products of grain boundary width to grain boundary diffusion coefficients in strontium titanate bicrystal are plotted in figure 7.

The volume diffusion coefficients in Nb-doped crystals are about three orders of magnitude smaller than undoped crystal. In this region, the activation energy of the oxygen volume diffusion is considered to correspond to that of oxygen migration in oxygen sub-lattice. The value, therefore, indicates the level of oxygen point defect concentration. The dominant oxygen point defect is believed to be vacancy in strontium titanate. Assuming that interstitial ions do not exist, the deviation of cation ratio from unit creates oxygen vacancies and is considered to be a reason of the oxygen high diffusivity in undoped samples. The substitution of Ti ions to Nb ions decreases the oxygen vacancy concentration as following mechanism.

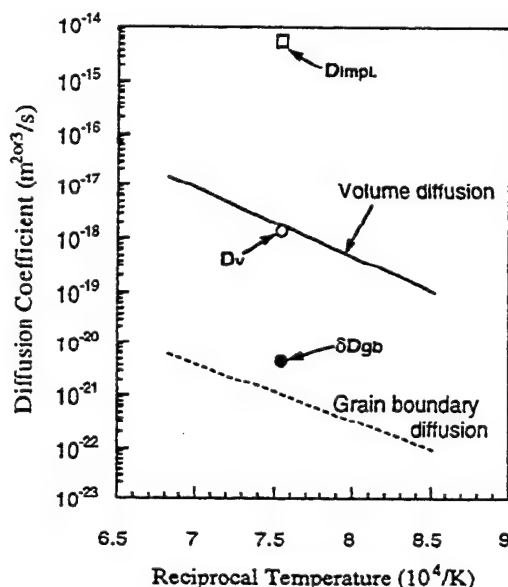
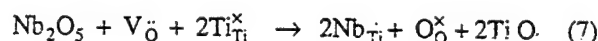


Fig.7. Temperature dependence of oxygen diffusion coefficients for Nb-doped strontium titanate. The solid and dashed lines, volume diffusion and grain boundary diffusion coefficients, respectively. Open and closed circles, volume diffusion coefficient and grain boundary diffusion coefficient in Cu-impanted Nb-SrTiO₃, respectively.

The joined boundaries of un-doped bicrystals do not behave as a high diffusivity path of oxygen ions, as the

lattice diffusion of oxygen is comparable of grain boundary diffusion coefficients. As the boundary width in the strontium titanate is not known, the grain boundary diffusion coefficient can not be obtained. Atkinson and Taylor studied Ni tracer diffusion in nickel oxide ceramics and reported 0.1nm of grain boundary width for the grain boundary diffusion of Ni[17]. If it is same order as strontium titanate, the grain boundary diffusion coefficients are about three orders of magnitude larger than the volume diffusion coefficients. However, the volume diffusion coefficients in undoped crystals are 4 to 5 orders of magnitude larger than Nb-doped crystals, so one can not observe the high diffusivity in undoped crystals.

C. DIFFUSION Ag ELECTRODE IN PLZT CERAMICS

Ferroelectric ceramics of lead-perovskite system are widely used as ceramic capacitors, actuators and so on. Recently, those materials are getting applied to a ferroelectric RAM and a replacement of D-RAM capacitor. These still remain some problem such as leakage current, fatigue, electrical breakdown, decrease of mechanical strength and so on for practical application. To solve them, interaction between ferroelectric materials and electrodes must be studied. Particularly, these problems are in close relation with diffusion behavior. On manufacture processes of the ceramics and thin film, thermal treatments cause the diffusion from electrode to the ceramics and thin films. Here, the diffusion of silver ions in PLZT ceramics was discussed.

In the present study, chemical formulation of PLZT samples was $(\text{Pb}_{0.9}\text{La}_{0.1})(\text{Zr}_{0.65}\text{Ti}_{0.35})\text{O}_3$ (Taki Chemical Co.,Ltd.). The sintered ceramics have a transparent body. One side of the mirror surface was covered with silver paste (Demetron Co.,Ltd.). Isothermal diffusion annealing performed at 700°C for 6h, at 750°C for 4.5h, at 800°C for 3h, at 850°C for 2h, and at 900°C for 1h in an air atmosphere in a furnace. After the diffusion annealing, the silver covering was removed by HNO_3 (1:1). The diffusion profile of silver in the annealed samples was also determined using depth-profile analysis with SIMS (CAMECA IMS-4f).

Figure 8 shows depth profiles of $^{109}\text{Ag}^-$ on various diffusion conditions in PLZT ceramics. Y-axis shows normalized intensities of $^{109}\text{Ag}^-$ calibrated by TiO^- . TiO^- and ZrO^- intensity in PLZT after diffusional annealing corresponded well to those intensity in pure PLZT, and was constant for depth. The profiles of Figure 8 have characteristics the following.

1) On the profile of (e), in spite of the absence of silver in pure PLZT, intensity of $^{109}\text{Ag}^-$ ions is recognized.

2) On diffusional samples not less than 800°C, the profiles of $^{109}\text{Ag}^-$ ions are each composed of a part of high intensity near the surface and a tale part of low intensity far from the surface.

3) On the profile of (d), only the tale part of low intensity is recognized, but a relative intensity is higher than that in pure PLZT sample.

4) On the profile of (a), intensity of $^{109}\text{Ag}^-$ ions is flat on a part from surface to 8000Å of depth.

The characteristic of (1) is caused by obstructive ions as $^{91}\text{Zr}^{18}\text{O}^-$ which mass is nearly 109 amu. The characteristics of (2)–(4) are caused by silver diffusion from electrode to PLZT ceramics.

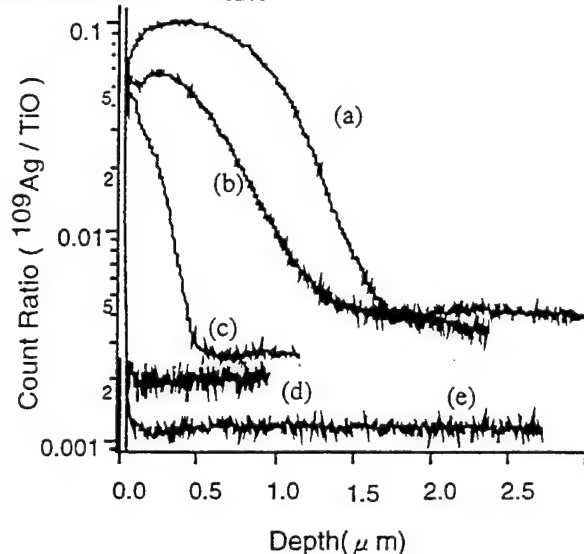


Fig.8. SIMS depth profiles of $^{109}\text{Ag}^-$ -
(a) at 900°C for 1h, (b) at 850°C for 2h,
(c) at 800°C for 3h, (d) at 700°C for 6h, (e) pure

Still, the part of high intensity on depth profile of (a), (b) and (c) is caused by a volume diffusion coefficient (D_v) of silver is described by the Arrhenius law as follows:

$$D_v = 0.12 \exp\{-258(\text{kJ mol}^{-1}) / RT\} (\text{cm}^2\text{s}^{-1}) \quad (8)$$

To clarify the mechanism of the tale part on depth profiles of Figure 8, around 3 mm depth from surface in PLZT polycrystal on the diffusional condition at 900°C for 1h, secondary ion image of $^{109}\text{Ag}^-$ ions was observed by using imaging mode of SIMS (RAE). The silver ions preferentially diffused along grain boundary. Using Eq.(3), one can obtain the grainboundary diffusion coefficients, D_{gb} . In this case, the grainboundary thickness was assumed to be 1nm[17]. D_{gb} is described as follows,

$$D_{gb} = 43.50 \exp\{-236(\text{kJ mol}^{-1}) / RT\} (\text{cm}^2\text{s}^{-1}) \quad (9)$$

Resultant Arrhenius plots are shown in Figure 9.

The silver ions diffuse along grain boundaries, and then weaken bond strength at grainboundary. Figure 10. shows the SEM micrograph of fractured surface in PLZT. Fracture mode at grainboundary with silver ions was intergranular fracture, while transgranular without silver ions.

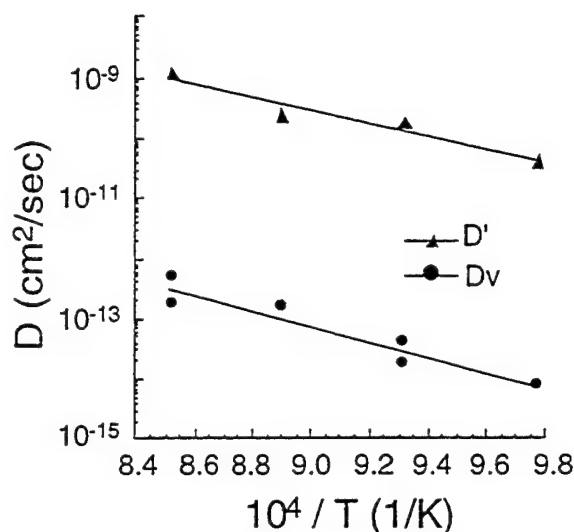


Fig.9. Arrhenius plots of temperature dependence

- (●) volume diffusion coefficient (D_v) of silver in PLZT,
 (▲) grain boundary diffusion coefficient (D') of silver in PLZT.



Fig.10. SEM micrograph of the fracture surface in PLZT.

REFERENCES

- [1] Y.Oishi and W.D.Kingery, *J.Chem.Phys.*, **33**,905 (1960).
- [2] I.Sakaguchi, H.Haneda, J.Tanaka and T.Yanagitani, *J.Am.Ceram.Soc.*, **79**, 1627-1632 (1996).

- [3] H.Nagata, H.Haneda, I.Sakaguchi, T.Takenaka, to be published in *J.Ceram.Soc.JPN*, **105** (1998).
- [4] J. Crank, in "THE MATHEMATICS OF DIFFUSION,"(Oxford University Press, London, 1957) P.30.
- [5] A.D.Le Claire, *Brit. J. Appl. Phys.*, **14**, 351-6 (1963).G.D.Mahan, L.M.Levinson, and H.R.Philipp, *Appl.Phys.Lett.*, **33**, 80 (1978).
- [6] D.Hallwig and H.G.Sockel, *Reactivity of Solids* (Plenum, New York, 1977) p.631.
- [7] A.Watanabe, H.Haneda, T.Ikegami, J.Tanaka, Y.Moriyoshi, S.Shirasaki, and T.Yamamoto, in "Hot isostatic pressing: theory and applications," ed. by M.Koizumi (Els.Sci.Pub. Essex, 1992), p.10
- [8] W.J.Moore and E.L.Williams, *Disc. Faraday Soc.*, **28**, 86 (1959).
- [9] J.W.Hoffman and J.Lauder, *Trans. Faraday Soc.*, **66**, 2346 (1970)
- [10] R.Robin, A.R.Cooper, and A.H.Heuer, *J.Appl.Phys.*, **44**, 3770 (1983).
- [11] A.Watanabe, private communication.
- [12] K.Kostic, O.Milosevic, and D.Uskokovic, *Sinter' 85* (1985) p.301.
- [13] W.Heywang and H.Brauer, *Solid-state Electron.*, **8**, 129-35 (1965).
- [14] C.A.Miller, *J. Phys. D*, **4**, 690-96 (1971).
- [15] J.Daniels and R.Wernicke, *Philips Res. Repts.* **31**, 544-59 (1976).
- [16] I.Ueda and S.Ikegami, *J. Phys. Soc. Japan*, **20**, 546-52 (1965).
- [17] A.Atkinson and R.I.Taylor, *Phil. Mag. A*, **43**, 999-1015 (1981).

Smart Skis and Other Applications of Piezo Control Technology

Adam Bogue
Active Control eXperts, Inc.
215 First Street
Cambridge, MA 02142 USA

Abstract – Recent breakthrough research in the field of piezoelectric technology coupled with innovation in device packaging technology provides opportunity for novel new product applications of piezoceramic materials. This paper describes a few of these new applications, namely: the Smart Ski containing a passive piezo vibration damping device; and the Smart Shock for mountain bikes, containing a piezo bending actuator and active feedback control.

I. INTRODUCTION

Research into piezoelectric “smart” materials and their application to actuators, sensors, and dynamic control systems is opening up doors to innovative new products.

Piezoceramic materials, such as lead zirconium titanate (PZT), are versatile, energy efficient, and cost efficient transducers. However, applications for PZT historically have been limited to a few niche applications, including low fidelity speakers and annunciators, ultrasonic exciters, and charge generators such as those used in ignitors.

Two reasons for the limitation to a few niche applications are device technology and research/education. Piezo device technology historically has not made it easy for PZT materials to be integrated into high-volume manufactured products. By their nature PZT elements are fragile and require special handling during the product assembly process. PZT also requires electrical connection, commonly achieved through soldered wires that, too, are fragile and require special handling.

The other reason PZT applications have been limited is that basic research into piezoelectric properties is still in its infancy relative to other electromechanical coupling technologies. Furthermore, the knowledge-base of piezos amongst the general engineering community is limited. While electro-magnetic theory and the application of solenoids and voice coils are common knowledge, piezos are not well understood by most product designers.

Encouraged by recent advances in piezo device technology and by military and defense investment into “Smart Structures” applications, piezos are now making their way into exciting new application areas. These applications

include: actuators, such as the ultrasonic rotary actuators used in auto-focus cameras; sensors, such as knock detectors used in automobile engines; and dynamic control systems, such as the vibration dampers used in the “Smart Ski.”

This paper describes recently-announced applications of piezoelectric technology in the area of dynamic control, and how the technology application works.

I. SMART SKI APPLICATION

A. Motivations

Vibrations have troubled ski designers and skiers for decades [1]. When people ski at high speed, disturbances caused by terrain dynamically excite the skis causing them to vibrate or chatter. The vibrations cause the edges of the skis to lose contact with the snow, and the skier experiences a loss of stability and control. Increased structural damping helps to limit dynamic excitation in the skis, improving ski edge contact and skier control.

As with most sporting goods, user “feel” is extremely important. Therefore, adding damping to a ski without having a detrimental effect on “feel” becomes a difficult engineering challenge. For this reason, passive piezo damping, which allows electrical tuning of damping characteristics, is attractive for the ski vibration damping application.

Basic research and theory into the mechanics of passive piezo damping is well documented [2] [3]. In passive piezo damping applications, piezoelectric elements are attached on a vibrating structure in order to capture mechanical strain energy and convert it to electrical energy. The electrodes on the piezoelectric elements are shunted with an electrical impedance. The electrical impedance or “shunt circuit” dissipates the electrical energy as heat, providing the loss mechanism for increased structural damping.

Fig. 1 shows a schematic of a system for inducing damping in a structural mode by connecting a passive electrical network across the electrodes of a piezoceramic element bonded to a structure. Fig. 2 shows detail of the electrical schematic of the system.

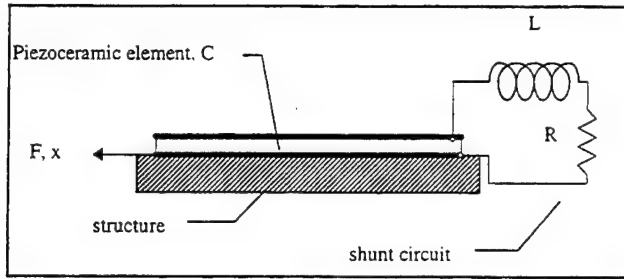


Fig. 1. Schematic of electromechanical system for passive piezo damping.

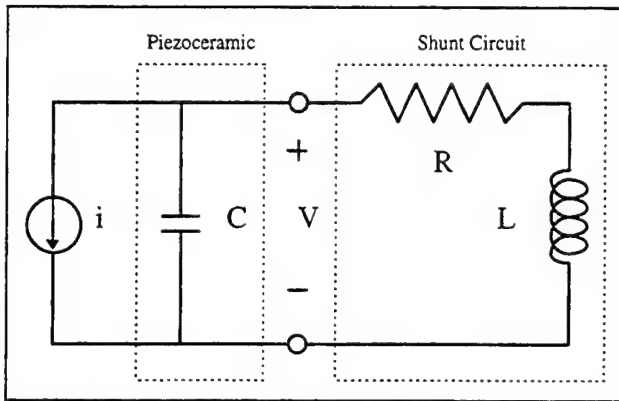


Fig. 2. Schematic of electrical system for passive piezo damping.

The structural and electrical dynamics are related through the coupling parameter, α , where

$$F = \alpha V \quad (1)$$

$$i = \alpha x \quad (2)$$

Passive piezo damping offers distinct advantages over traditional passive damping technologies, such as constrained-layer viscoelastics, foams, and rubber materials. While traditional damping materials provide good performance for narrow ranges of operating temperature, passive piezo dampers are comparatively unaffected by temperature and can perform under extreme conditions. Traditional damping materials cannot perform at low frequencies, while piezo dampers can address broadband vibrations, including the low frequencies. Piezo dampers may also be highly tuned to target specific vibration modes or frequencies. Finally, unlike traditional damping materials, piezo dampers are structural components. Therefore, in composite structures such as skis, the vibration damper can act as a structural element, helping to reduce total system mass.

A. Sizing and Placement of Piezoceramic Elements

To capture the most strain energy in a vibrating structure, and thereby add the most damping, the passive piezo damper should attach to the structure in the area of highest strain for the vibration mode(s) of concern. Detailed structural modeling and modal analysis is required to optimize placement. For applications where modal density is high, a high-fidelity dynamic model of the structural system is necessary to insure that individual piezo dampers are not attached such that they bridge across vibration node lines.

Once the optimal piezo damper location is found, the next issue is to determine what type of piezoelectric material to use and how much piezoelectric material is required. For most commercial applications, including the Smart Ski, a soft piezoceramic such as PZT 5H with a high transverse coupling constant, k_{31} , is most desirable. Using more piezo material will capture more strain energy, which provides high damping. The relationship between added damping, ζ , and strain energy capture, λ , is as follows;

$$\zeta \approx \frac{1}{4} \sqrt{\frac{\lambda k_{31}^2}{1 - k_{31}^2}} \quad (3)$$

As with all practical applications, performance and cost must be balanced. More piezo material provides greater damping, but it also translates to more weight and more cost.

A. Passive Piezo Damping with an RC Shunt Circuit

There are two basic shunt circuit designs used in passive piezo dampers: the RC shunt circuit; and the RLC shunt circuit. In its simplest form, the RC shunt circuit can be a single resistor in parallel with the piezo. (The piezo is modeled electrically as a capacitor, hence the "C" in the RC shunt circuit.) In this case, the value of L in Fig. 2 is set to 0. The RC shunt circuit is relatively broadband, offering damping performance across a wide frequency band. The frequency band can be tuned by choosing an optimal resistor value using the following equation:

$$R = \frac{\sqrt{1 - k_{31}^2}}{C \omega} \quad (4)$$

Most skis that use the Smart Ski technology use the passive piezo damper with an RC shunt circuit. This is because the target mode of vibration for these skis is a first bending mode. The frequency of this mode is a function of boundary conditions that vary during use. If the skier is leaning forward or leaning back, if the skier is light or heavy, and if the skier is turning or jumping, the first resonate mode

varies greatly. Therefore, a broadband damper is required, and the RC shunt circuit is the preferred choice.

A. Passive Piezo Damping with an RLC Shunt Circuit

The RLC shunt can be, in its simplest form, an inductor and a series resistor in parallel with the piezo. With the additional of the inductor, the RLC shunt is a resonant electrical circuit. When this circuit is tuned to the same frequency as that of the targeted vibration mode, the piezo damper acts as the electrical equivalent to a mechanical tuned mass damper. With the RLC shunt circuit, more electrical current passes through the resistor, and the piezo damper provides significantly higher performance but only over a narrow frequency range. The damper can be tuned by choosing optimal inductor and resistor values using the following equations:

$$L = \frac{1}{C\omega^2 \sqrt{1 + \frac{\lambda k_{31}^2}{1 - k_{31}^2}}} \quad (5)$$

$$R = \frac{\sqrt{2}}{C\omega} \frac{\sqrt{\frac{\lambda k_{31}^2}{1 - k_{31}^2}}}{1 + \frac{\lambda k_{31}^2}{1 - k_{31}^2}} \quad (6)$$

Higher-end race skis that use Smart Ski technology use the RLC shunt circuit. This is because the target mode of vibration for these race skis is a higher order bending mode. The frequency of this mode does not vary greatly as a function of boundary conditions seen in actual skiers. Therefore, the RLC shunt circuit provides a means for providing increased damping performance at the single critical frequency.

I. MOUNTAIN BIKE SMART SHOCK APPLICATION

A. Motivations

Full suspension mountain bikes with front and rear shocks are designed to allow bikers to ride in off-road conditions. The characteristics of shock and vibration vary with terrain and rider speed. In addition to causing rider discomfort, shock and vibration can cause the bike to lose contact with the ground, resulting in loss of control and maneuverability.

Traditional mountain bike shocks have a spring-loaded piston that compresses hydraulic fluid, forcing it through a by-pass orifice. Traditional high-end mountain bike shocks have a screw that allows the rider to manually adjust the level

of compression damping in the shock by increasing or decreasing the by-pass orifice size. For example, if the rider expects to be riding over small bumps or at slow speeds, a soft shock would be preferred. Or if the rider expects to hit large rocks or roots, a hard shock is preferred.

Given that rider speed and terrain often vary greatly during the course of a ride, variable performance is desirable. In many cases it is desirable to have variable compression damping forces even within a single compression cycle. For example, if the rider hits a large rock, the shock would ideally soften to absorb the impact force. However, if the shock remained soft through the full compression stroke, the shock would "bottom-out" and transmit an impact to the rider. In this case, the shock would ideally become "hard" toward the end of the compression stroke so that it did not bottom out.

The Smart Shock uses a piezoceramic bending actuator located over the by-pass orifice to control the flow of hydraulic fluid, thus adjusting the compression damping forces in the shock. As the actuator in a closed loop control system, the piezoceramic bending element adjusts the bike's suspension automatically and continuously, adjusting and optimizing performance for all riding conditions on the fly.

A. System Overview

Fig. 3. shows a block diagram of the Smart Shock system. A sensor on the shock (using the giant magnetoresistive effect) reads piston speed and position, sending data to a microprocessor-controlled active feedback circuit. Based on an algorithm described in Fig. 4. that was optimized based on field testing, the circuit sends a command signal to the piezoceramic bending actuator in the valve. The actuator, in turn, regulates the flow of oil through the valve, which adjusts the shock damping. The result is a bike suspension that provides a smoother ride and increased tire-to-ground contact.

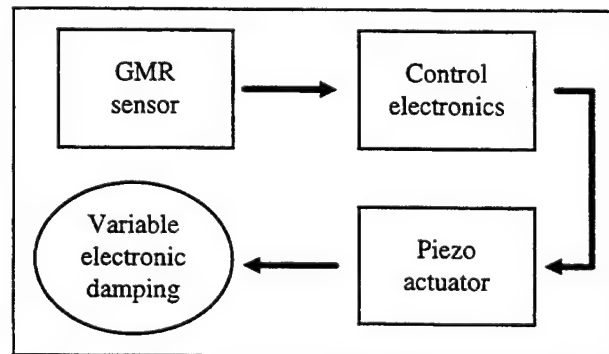


Fig. 3. Block diagram of Smart Shock system.

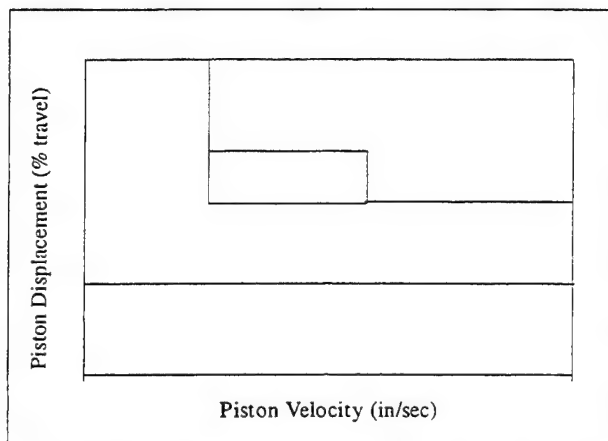


Fig. 4. Smart Shock microprocessor control algorithm for smart mode during the compression stroke.

A. Piezo Bending Element Design Issues

The principles of operation for a piezoelectric bending actuator are well understood and documented [4]. Piezoelectric bending actuators operate by having two independent piezo elements stacked on top of each other. Driving one element to expand while contracting the other causes the actuator to bend, creating an out-of-plane motion. Although many mechanical arrangements are possible, typically a bimorph actuator design has rectangular piezoceramic elements clamped firmly at one end, such as that shown in Fig. 5. Actuation occurs at the free end, away from the clamp.

Force and stroke requirements for the application (e.g., for the Smart Shock application, roughly 300g blocked force and 100 μ m free deflection) drive actuator design parameters including the length, width, and thickness. For example, an increase in actuator length increases the stroke and decreases the force. An increase in width increases the force, but has little effect on stroke. An increase in thickness increases the force and decreases the stroke.

An additional design consideration is bandwidth. Force and stroke are typically specified under quasi-static conditions, meaning that the actuator is operating well below its first resonant mode. If the application requires the actuator to operate at a higher frequency, then the dynamics of the actuator may affect its force and stroke output. For high-bandwidth applications, the actuator is commonly designed so that the first resonant mode is 3x higher than the highest operating frequency for the application.

Along with actuator dimensions, another design variable for the piezoelectric bending actuator is piezoceramic material selection. For most commercial piezoelectric bending actuator applications, the goal is to minimize size

while maximizing force and stroke for a given input voltage. As was the case with the passive piezo damping application, this leads to the use of a soft piezoceramic, such as PZT 5H with a high piezoelectric constant, d_{31} . Other applications where power consumption or stability are more important may indicate a different material selection.

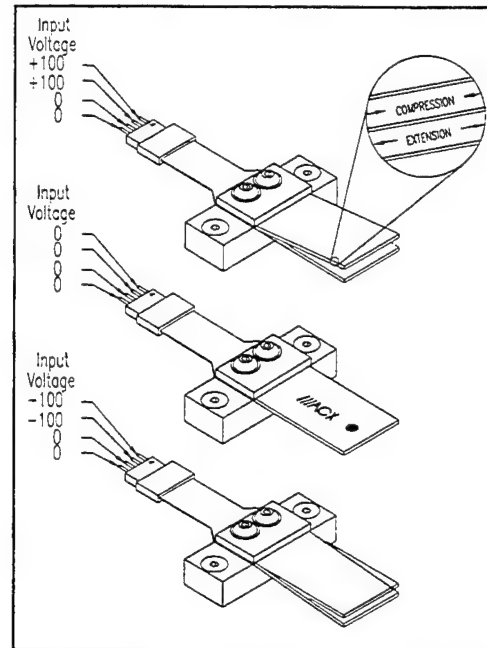


Fig. 5. Piezoelectric bending actuator.

I. FUTURE APPLICATIONS

As basic research into piezoelectric materials opens up opportunities, as this body of knowledge is transferred to the product design and applications engineering community, and as device manufacturers create packaging methods for delivering the piezoelectric technology in a way that is manufacturable and cost-effective, new applications for piezoelectric materials will result. The Smart Ski and the Smart Shock are the first of a new breed application where piezoelectric materials are used to improve every-day products. In addition to sporting goods applications, products in automotive, aerospace, computer, and white goods industries are in the foreseeable future.

- [1] B. Glenn, J. Jorgensen, and J. Chalupnik, "Ski vibrations and damping," *Experimental Mechanics*, 1994(3).
- [2] R. Forward, "Electronic damping of vibrations in optical structures," *Journal of Applied Optics*, vol. 18(2), pp. 690-697, 1979.
- [3] N. Hagood and A. von Flotow, "Damping of structural vibrations with piezoelectric materials and passive electrical networks," *Journal of Sound and Vibration*, vol. 146(2), pp. 243-268, 1991.
- [4] J. Waanders, *Piezoelectric Ceramics: Properties and Applications*, Eindhoven: Philips Components, pp. 26-40, 1991.

8th US-Japan Seminar on Dielectric and Piezoelectric Ceramics
October 15-18, 1997

Participant List (Japan)

Kazunobu Abe
Research Center
Sakai Chemical Ind. Co. Ltd.
5-1 Ebisujima, Sakai
Osaka, 590 Japan
Phone: 81-722-23-4117
Fax: 81-722-27-9796
e-mail:

Katsuhiro Aoki
Texas Instrument Tsukuba
R&D Center Ltd.
17 Miyukigaoka, Tsukuba-shi
Ibaraki, 305 Japan
Phone: 81-298-40-4484
Fax: 81-298-40-4484
e-mail: kaok@dlepl.itg.ti.com

Zhiming Chen
Dept. of Electronics and
Informatics
Toyama Prefectural University
Kosugi-machi, Toyama
939-03 Japan
Phone: 81-766-56-7500
Fax: 81-766-56-8023
e-mail: chen@pu-toyama.ac.jp

Yoshiaki Fuda
Materials Development Labs
Tokin Corporation
6-7-1 Kooriyama, Taihaku-ku
Sendai, 982 Japan
Phone: 81-22-308-0024
Fax: 81-22-308-1143
e-mail: 75008@tokin.co.jp

Masayuki Fujimoto
Research Center
Taiyo Yuden Co., Ltd.
562 Hongo-Tsukanaka
Haruna-machi, Gunma-gun
Gunma, 370-33 Japan
Phone: 81-273-43-1115
Fax: 81-273-44-7210
e-mail: fujimoto@jty.yuden
.co.jp

Yukio Fukuda
Texas Instrument Tsukuba
R&D Center Ltd.
2350 Kihara, Miho
Inashiki, Ibaraki
300-04 Japan
Phone: 81-298-40-4484
Fax: 81-298-40-4484
e-mail: yfuk@msg.ti.com

Hajime Haneda
National Institute for Research
in Inorganic Materials
1-1 Namiki, Tsukuba
Ibaraki, 305 Japan
Phone: 81-298-51-3351
Fax: 81-298-52-7449
e-mail: haneda@nirim.go.jp

Takashi Hayashi
Dept. of Materials Science
Shonan Institute of Technology
1-1-25 Tsujidou-Nishikaigan
Fujisawa, Kanagawa 251 Japan
Phone: 81-466-34-4111
Fax: 81-466-36-1594
e-mail: hayashi@mate.shonan-
it.ac.jp

Noboru Ichinose
Dept. of Materials Sci. & Eng.
Waseda University
Toshiba Corporation
3-4-1 Ohkuba, Shijuku-ku
Tokyo, 169 Japan
Phone: 81-3-5286-3307
Phone: 81-3-3200-2567
e-mail:
ichinose@mn.waseda.ac.jp

Nobuo Kamehara
Inorganic Division
Fujitsu Laboratories Ltd.
10-1 Morinosato-wakamiya
Atsugi, 243-01 Japan
Phone: 81-462-50-8827
Fax: 81-462-48-8812
e-mail:
nkameha@flab.fujitsu.co.jp

Hiroshi Maiwa
Dept. of Materials Science
Shonan Institute of Technology
1-1-25 Tsujidou-Nishikaigan
Fujisawa, Kanagawa 251 Japan
Phone: 81-466-34-4111
Fax: 81-466-36-1594
e-mail: maiwa@mate.shonan-
it.ac.jp

Hiroaki Makino
Ceramics Lab
Toyota Central R&D Lab Inc.
Nagakute-cho, Aichi-gun
Aichi, 480-11 Japan
Phone: 81-561-63-4821
Fax: 81-561-63-6136
e-mail: h-makino@mosk
.tytlabs.co.jp

Yoichiro Masuda
Dept. of Electrical Engineering
Hachinohe Institute of
Technology
88-1 Myoh, Ohbiraki
Hachinohe, Aomori
031 Japan
Phone: 81-178-25-8047
Fax: 81-178-25-1430
e-mail: ymasuda@hi-tech.ac.jp

Kazuo Miyabe
Materials Research Center
TDK Corporation
570-2, Matsugashita
Minamihatori, Narita-shi
Chiba-ken, 286 Japan
Phone: 81-476-37-1637
Fax: 81-476-37-1648
e-mail:
kmiyabe@mbi.tdk.co.jp

Morihito Nishido
R&D Dept.
Fuji Titanium Ind. Co. Ltd.
12-8 Sengen-cho, Hiratsuka
Kanagawa-ken, 280 Japan
Phone: 81-463-32-1266
Fax: 81-463-32-1270
e-mail:

Takeshi Nomura
Materials Research Center
TDK Corporation
570-2, Matsugashita
Minamihatori, Narita-shi
Chiba-ken, 286 Japan
Phone: 81-476-37-1637
Fax: 81-476-37-1648
e-mail: tnomura@mbi.tdk.co.jp

Toshio Ogawa
Dept. of Electronic Engineering
Shizuoka Institute of Science
and Technology
2200-2, Toyosawa
Fukuroi, Shizuoka, 437 Japan
Phone: 81-538-45-0149
Fax: 81-538-45-0154
e-mail: ogawa@ee.sist.ac.jp

Hiromu Ohuchi
Dept. of Materials Science
Shonan Institute of Technology
1-1-25 Tsujido-nishikaigan
Fujisawa 251 Japan
Phone: 81-466-34-4111
Fax: 81-466-36-1594
e-mail: oouchi@mate.shonan-
it.ac.jp

Yukio Sakabe
Materials R&D
Murata Mfg. Co. Ltd.
2288 Oshinohara
Yasu-cho, Shiga
520-23 Japan
Phone: 81-775-86-8275
Fax: 81-775-87-1923
e-mail: sakabe@murata.co.jp

Wataru Sakamoto
Dept. of Applied Chemistry
Nagoya University
Furo-cho, Chikusa-ku
Nagoya, 464-01 Japan
Phone: 81-52-789-3345
Fax: 81-52-789-3182
e-mail: sakamoto@apchem
.nagoya-u.ac.jp

Shigeki Sato
Materials Research Center
TDK Corporation
570-2, Matsugashita
Minamihatori, Narita-shi
Chiba-ken, 286 Japan
Phone: 81-476-37-1637
Fax: 81-476-37-1648
e-mail: ShigekiS@mbi
.tdk.co.jp

Kiyoshi Shimamura
Institute for Materials Research
Tohoku University
Katahira 2-1-1, Aoba-ku
Sendai 980-77 Japan
Phone: 81-22-215-2103
Fax: 81-22-215-2104
e-mail: shimak@lexus.imr
.tohoku.ac.jp

Masaru Shimizu
Dept. of Electronics
Himeji Institute of Technology
Dept. of Electronics
2167 Shosha, Himeji
Hyogo, 671-22 Japan
Phone: 81-792-67-4878
Fax: 81-792-67-4855
e-mail: mshimizu@elnics.eng
.himeji-tech.ac.jp

Tadashi Shiosaki
Dept. of Electrical Science &
Engineering
Kyoto University
Yoshida Honmachi, Sakyo-ku
Kyoto, 606 Japan
Phone: 81-75-753-5327
Fax: 81-75-753-5749
e-mail: tshiosak@kuee
.kyoto-u.ac.jp

Hironari Shoji
R&D Department
Nippon Chemi-con Corp.
1-167-1 Higashioume
Oume, Tokyo, 198 Japan
Phone: 81-428-21-1218
Fax: 81-428-24-1062
e-mail: syoji@nippon.chemi-
con.co.jp

Tomohiro Sogabe
Materials Research Center
TDK Corporation
570-2, Matsugashita
Minamihatori, Narita-shi
Chiba-ken, 286 Japan
Phone: 81-476-37-1637
Fax: 81-476-37-1648
e-mail: tsogabe@mbi.tdk.co.jp

Toshimasa Suzuki
Research Center
Taiyo Yuden Co., Ltd.
562 Hongo, Tsukanaka
Haruna-machi, Gunma-gun
Gunma, 370-33 Japan
Phone: 81-273-44-7207
Fax: 81-273-44-7210
e-mail: suzuki-t@jty.
yuden.co.jp

Masakuni Takahashi
Center Research Institute
Mitsubishi Materials Corp.
1-297 Kitabukuro-cho
Omiya, Saitama
330 Japan
Phone: 81-48-641-9487
Fax: 81-48-642-0545
e-mail: ma-takah@mmc.co.jp

Sadayuki Takahashi
R&D Group
NEC Corporation
4-1-1, Miyazaki
Miyamae-ku, Kawasaki
216 Japan
Phone: 81-44-856-2164
Fax: 81-44-856-2128
e-mail: takahasi@rdg.cl
.nec.co.jp

Tadashi Takenaka
Dept. of Electrical Eng.
Science University of Tokyo
Noda, Chiba-ken, 278 Japan
Phone: 81-471-24-1501
Fax: 81-471-23-0856
e-mail: tadashi@takenaka.ee.
noda.sut.ac.jp

Mitsuo Tamura
Materials Development Lab
Tokin Corporation
6-7-1 Koriyama, Taihaku-ku
Sendai, 982 Japan
Phone: 81-22-308-0028
Fax: 81-22-308-1132
e-mail: 71121@tokin.co.jp

Shinjiro Tashiro
Dept. of Electronic Engineering
National Defense Academy
1-10-20 Hashirimizu
Yokosuka, 239 Japan
Phone: 81-468-41-3810
Fax: 81-468-44-5903
e-mail: tashiro@cc.nda.ac.jp

T. Tsurumi
Dept. of Inorganic Materials
Tokyo Institute of Technology
2-12-1 Ookayama, Meguro-ku
Tokyo, 152 Japan
Phone: 81-3-5734-2517
Fax: 81-3-5734-2514
e-mail: ttsurumi@ceram
.titech.ac.jp

Kikuo Wakino
Murata Manufacturing Co. Ltd.
2-26-10, Tenjin
Nagaokakyo, Kyoto
617 Japan
Phone: 81-75-955-6504
Fax: 81-75-951-1916
email: wakino@murata.co.jp

Takashi Yamamoto
Dept. of Electrical Engineering
National Defense Academy
1-10-20 Hashirimizu
Yokosuka, 239 Japan
Phone: 81-468-41-3810
Fax: 81-468-44-5903
e-mail: ytakashi@cc.nda.ac.jp

John Y. Yamashita
Materials & Devices Res. Lab
Toshiba Corporation
70 Yanagi-cho, Saiwai-ku
Kawasaki, 210 Japan
Phone: 81-44-548-5606
Fax: 81-44-520-5893
e-mail: yohachi.yamashita
@toshiba.co.jp

Hitoshi Yokoi
R&D Center
NGK Spark Plug Co., Ltd.
2808, Iwasaki, Komaki
Aichi 485 Japan
Phone: 81-568-76-1541
Fax: 81-568-76-1295
e-mail: h-yokoi_rd@mg
.ngkntk.co.jp

**8th US-Japan Seminar on Dielectric and Piezoelectric Ceramics
October 15-18, 1997**

Participant List (U.S.)

Hideaki Aburatani
A2 Materials Research
Laboratory
The Pennsylvania State
University
University Park PA 16802
Phone: (814) 865-2434
Fax: (814) 865-2326
email: hxa112@email.psu.edu

Orlando Auciello
Argonne National Laboratory
Materials Science Div/212/C210
9700 Cass Avenue
Argonne IL 60439
Phone: (630) 252-1685
Fax: (630) 252-4798
e-mail:
orlando_auciello@qmgate
.anl.gov

James J. Beeson
Kemet Electronics Corp.
P.O. Box 849
201 Fairview St. Ext.
Fountain Inn, SC 29644
Phone: (864) 409-5615
Fax: (864) 862-6265
e-mail: jimbeeson@kemet.com

Amar S. Bhalla
253 Materials Research
Laboratory
Pennsylvania State University
University Park, PA 16802
Phone: (814) 865 9232
Fax: (814) 865 2326
e-mail: asb1@alpha.mrl.psu.edu

Adam Bogue
Vice President, Marketing
Active Control eXperts, Inc.
215 First Street
Cambridge, MA 02142
Phone: (617) 577-0700 x234
Fax: (617) 577-0656
e-mail: bogue@acx.com

Paul Bridenbaugh
Crystal Associates
31 Farinella Drive
East Hanover, NJ 07936
Phone: (201) 581-1717
Fax: (201) 581-1384
e-mail: crystalassoc
@crystala.com

David Cann
168 Materials Research
Laboratory
The Pennsylvania State
University
University Park PA 16802
Phone: 814 865-9931
Fax: 814 865-2326
email: dpc2@psu.edu

Wenwu Cao
164 Materials Research Lab
Pennsylvania State University
University Park, PA 16802
Phone: (814) 865 4101
Fax: (814) 865 2326
e-mail: cao@math.psu.edu

Chorng Jeon Chen
YTC America Inc.
550 Via Alondra
Camarillo, CA 93012
Phone: (805) 388-9920 x15
Fax: (805) 388-8046
e-mail: cjchen@YTCA.com

Fan Chu
155 Materials Research Lab
Penn State University
University Park, PA 16802
Phone: (814) 863-1953
Fax: (814) 865-2326
e-mail: fxc10@psu.edu

Mike S.H. Chu
TAM Ceramics
4511 Hyde Park Boulevard
P.O. Box 67
Niagara Falls, NY 14305
Phone: (716) 278 9495
Fax: (716) 278 9575
e-mail: Mchu@tamceramics
.com

L. Eric Cross
Pennsylvania State University
187 Materials Research Lab
University Park, PA 16802 4800
Phone: (814) 865 1181
Fax: (814) 863 7846
e-mail: lec3@psu.edu

Dr. Lynn Ewart
NUWC
Code 2131, 1176 Howell Street
Bldg. 1170, Room 214
Newport, RI 02841-1708
Phone: (401) 841-6605 x 35093
Fax: (401) 841-6401
e-mail: ewartlm@code20nl.npt
.nuwc.navy.mil

Daniel Fiore
Materials Systems, Inc.
521 Great Road
Littleton, MA 01460
Phone: (508) 486-0404
Fax: (508) 486-0706
e-mail: MatSystems@aol.com

Jan Fousek
159 Materials Research Lab*
Penn State University
University Park, PA 16802
Phone: (814) 863-2843
Fax: (814) 865-2326
e-mail: janfousek@psu.edu
*on leave from Dept. of
Physics, Technical University,
CZ-46117, Liberec, Czech
Republic

Sandra Fries Carr
US Air Force, WL/POOC
1950 Fifth Street, Bldg. 18
Wright Patterson AFB, OH 45433
Tel: (937) 255-6016
Fax: (937) 255-3211
e-mail: carrsj@wl.wpafb.af.mil

Sri P. Gupta
KEMET Electronics Corporation
PO Box 849, 201 Fairview St. Ext.
Ft. Inn, SC 29644-0849
Phone: (864) 409-5758
Fax: (864) 409-6265
email: srigupta@kemet.com

T.R. (Raj) Gururaja
Hewlett Packard
3000 Minuteman Road
Mail Stop 0095
Andover, MA 01810
Phone: (508) 659-2765
Fax: (508) 687-7265
e-mail: raj_gururaja@hp.com

Martin Harmer
Materials Research Center
Lehigh University
5 East Packer Avenue
Bethlehem, PA 18015
Phone: (610) 758 3850
Fax: (610) 758 4244
e-mail: mph2@Lehigh.edu

John Helgeland
Engineering Manager
TRS Ceramics, Inc.
2820 East College Ave, Suite J
State College, PA 16801
Phone: (814) 238-7485
Fax: (814) 238-7539

Atsushi Hitomi
168 Materials Research Lab.
Pennsylvania State University
University Park PA 16802
Phone: (814) 863-9885
Fax: (814) 865-2326
email: axh33@psu.edu

Wayne Huebner
Ceramic Engineering Dept.
University of Missouri at Rolla
222 McNutt Hall
Rolla, MO 65401
Phone: (573) 341 6129
Fax: (573) 341 6934
e-mail: huebner@umr.edu

Umesh Kumar
AVX Corporation
2200 AVX Drive
Myrtle Beach, S.C. 29577
Phone: (803) 946-0532
Fax: (803) 626-9632

Sean P. Leary
NYS College of Ceramics
Alfred University
Alfred, NY 14802
Phone: (607) 871-2428
Fax: (607) 871-3469
e-mail: learysp@xray-alfred.edu

Galeb H. Maher
MRA Laboratories, Inc.
96 Marshall Street
North Adams, MA 01247
Phone: (413) 664 4524
Fax: (413) 663 5535
email: mralabs@sover.net

John Paul Maria
148 Materials Research Lab.
Pennsylvania State University
University Park PA 16802
Phone: (814) 865-9931
Fax: (814)-865-2326
e-mail: jpm133@psu.edu

Elizabeth A. McLaughlin
NUWC
Code 2131, B-1170
1176 Howell Street
Newport, RI 02841-1708
Phone: (800) 669-6892
Fax: (401) 841-6401 x35103
email: mclaughlin@code20nl
.npt.nuwc.navy.mil

Ming-Jen Pan
259 Materials Research Lab
Penn State University
University Park, PA 16802
Phone: (814) 863-2639
Fax: (814) 865-2326
e-mail: mjpan@psu.edu

Seung-Eek Park
259 Materials Research Lab
Penn State University
University Park, PA 16802
Phone: (814) 863-2639
Fax: (814) 865-2326
e-mail: sxp37@psu.edu

Brian Pazol
Materials Systems Inc.
521 Great Road
Littleton, MA 01460
Phone: (508) 486 0404
Fax: (508) 486 0706
e-mail: MatSystems@aol.com

Dennis Polla
Microtechnology Laboratory
University of Minnesota
1-165 EE/CS
200 Union Street SE
Minneapolis MN 55455
Phone: (612) 624-8005
Fax: (612) 625-5012
e-mail: polla@ee.umn.edu

Alan Rae
TAM Ceramics
4511 Hyde Park Blvd
P.O. Box 67
Niagara Falls NY 14305-0067
Phone: (716) 278-9412
Fax: (716) 285-3026
email: Arae@tamceramics.com

Clive A. Randall
138 Materials Research Lab
Pennsylvania State University
University Park, PA 16802
Phone: (814) 863 1328
Fax: (814) 865 2326
e-mail: carl@alpha.mrl.psu.edu

Richard E. Riman
Rutgers University
Center for Ceramic Research
P.O. Box 909
Piscataway, NJ 08855 0909
Phone: (908) 445 4946
Fax: (908) 445 6264
e-mail:
riman@alumina.rutgers.edu

Rodney Roseman
University of Cincinnati
Dept. of Materials Science &
Engineering, 508 ERC
P.O.Box 210012
Cincinnati OH 45221-0012
Phone: (513) 556-3187
Fax: (513) 556-2569
e-mail: rroseman@uceng.uc.edu

Ahmad Safari
Rutgers University
Center of Ceramic Research
P.O. Box 909
Piscataway, NJ 08855-0909
Phone: (908) 445 4367
Fax: (908) 445 5577
e-mail: safari@safari.rutgers.edu

Walter Schulze
Alfred University, NYSCC
2 Pine Street
Alfred NY 14802
Phone: (607) 871-2471
Fax: (607) 871-2354
email: schulze@bigvax.alfred.edu

Robert W. Schwartz
Sandia National Laboratories,
MTS
P.O., Box 5800, MS 1349
Albuquerque, NM 87185-1349
Phone: (505) 272 7629
Fax: (505) 272 7304
e-mail: rwschwa@sandia.gov

Joseph Shephard
A8 Materials Research Lab.
Pennsylvania State University
University Park PA 16802
Phone: (814) 865-2434
Fax: (814) 865-2326
e-mail: jfs12@email.psu.edu

Thomas R. Shrout
150 Materials Research Lab
Penn State University
University Park, PA 16802
Phone: (814) 865-1645
Fax: (814) 865-2326
e-mail: TShrout@alpha.mrl.psu.edu

Raj Singh
University of Cincinnati
Dept. of Mat. Sci. & Eng.
P.O. Box 210012
Cincinnati OH 45221-0012
Phone: (513) 556-5172
Fax: (513) 556-3773
e-mail: rsingh@uceng.uc.edu

Michael T. Strauss
CeraNova Corporation
14 Menfi Way
Hopedale, MA 01747
Phone: (508) 473-3200
Fax: (508) 473-3200
e-mail: mstrauss@juno.com
or msceanova@aol.com

Scott L. Swartz
NexTech Materials, Ltd.
720-I Lakeview Plaza Blvd.
Worthington, OH 43085
Phone: (614) 842-6606
Fax: (614) 842 6601
email: swartzNTM@aol.com

James Tressler
249 Materials Research Lab
Penn State University
University Park, PA 16802
Phone: (814) 863-0180
Fax: (814) 865-2326
e-mail: jft104@psu.edu

Susan Trolrier-McKinstry
Pennsylvania State University
Dept. of Materials Sci. & Engr.
149 Materials Research Lab
University Park, PA 16802
Phone: (814) 863-9708
Fax: (814) 865-2326
e-mail: stm1@alpha.mrl.psu.edu

Bruce A. Tuttle
Sandia National Laboratories
Electronic Ceramics Department
MS 1405, P.O. Box 5800
Albuquerque, NM 87185
Phone: (505) 845 8026
Fax: (505) 844 2974
e-mail: batuttl@sandia.gov

Peter Van Buskirk
Advanced Technology Materials
Inc.
7 Commerce Drive
Danbury, CT 06810
Phone: (203) 794-1100
Fax: (203) 830-4116
e-mail: pvanb@atmi.com

Venkat S. Venkataramani
General Electric CR&D
K-1: MB167
P.O. Box 8
Schenectady, NY 12301
Phone: (518) 387 5322
Fax: (518) 387 6204
e-mail: Venkata@exc01crdge.crd.ge.com

Dwight Viehland
Univ. of Illinois
at Urbana-Champaign
Dept. of Materials Science
209 Ceramics Building
Urbana, IL 61801
Phone: (217) 333 6837
Fax: (217) 244 6917
e-mail: dviehlan@uiuc.edu

Satoshi Wada
Dept. of Applied Chemistry
Tokyo University of Agriculture
and Technology
24-16, Nakamachi 2-chome
Koganei, Tokyo 184 Japan
Phone: 81-423-88-7040
Fax: 81-423-83-6134
e-mail: swada@cc.tuat.ac.jp

Mr. Jim Wilson
Ferro Corporation
Transelco Division
1789 Transelco Drive
Penn Yan, NY 14527
Phone: (315) 536-3357 x5342
Fax: (315) 536-0376

Shoko Yoshikawa
The Pennsylvania State
University
Current Address:
Director of Materials Research
Active Control eXperts, Inc.
215 First Street
Cambridge, MA 02142-1227
Phone: (617) 577-0700
Fax: (617) 577-0656
e-mail: shoko.acx.com

AUTHOR INDEX

A

Abe, K. - 68
 Aburatani, H. - 28
 Adachi, M. - 61
 Aggarwal, S. - 20
 Alberta, E.F. - 260
 Anderko, A. - 256
 Ando, A. - 303
 Aoki, K. - 74, 88
 Arai, K. - 168, 172
 Arashi, T. - 148
 Auciello, O. - 20

B

Baba, A. - 96
 Bandyopadhyay, A. - 307
 Beeson, J.J. - 180
 Bhalla, A.S. - 260
 Bheemineni, V. - 184
 Bilodeau, S.M. - 80
 Bogue, A. - 366
 Brahmaroutu, B. - 248
 Bridenbaugh, P. - 242
 Bultitude, J. - 155, 165
 Butcher, S. - 155

C

Cann, D. - 36
 Cao, W. - 329, 340
 Callahan, M. - 326
 Carr, S. Fries- - 100
 Chan, H.M. - 244
 Chaudhuri, S.R. - 227
 Chen, C.-J. - 227
 Chen, J. - 333
 Chen, Z. - 61
 Cho, S.B. - 256
 Chu, F. - 24, 120
 Chu, M. - 155, 165
 Clem, P.G. - 92
 Costantino, S.A. - 180
 Cross, L.E. - 11, 337

D

Danforth, S.C. - 307
 Dimos, D. - 92
 Ding, X.M. - 188

E

Ewart, L. - 295

F

Fendler, F. - 24
 Fiore, D. - 344
 Fousek, J. - 6
 Fries-Carr, S. - 100
 Fuda, Y. - 272
 Fujimoto, M. - 168, 172
 Fujisawa, H. - 124
 Fujita, S. - 96
 Fukuda, T. - 57
 Fukuda, Y. - 74, 88
 Furcht, T. - 116

G

Gabriel, K. - 326
 Ganine, V. - 155, 165
 Garino, T. - 353
 Gentilman, R. - 344
 Gersten, B.L. - 256
 Glass, J. - 353
 Gruverman, A. - 20
 Gupta, S.P. - 201
 Gururaja, T.R. - 333

H

Hackenberger, W. - 323
 Haneda, H. - 88, 359
 Hara, T. - 144
 Harada, K. - 197, 252
 Harmer, M.P. - 244
 Hashimoto, T. - 264
 Hayashi, T. - 144, 205
 Helgeland, J. - 323
 Hida, M. - 348
 Hirai, T. - 96
 Hirano, S. - 140
 Hirose, S. - 231
 Hitomi, A. - 44
 Hock, J. - 193
 Hollenbeck, J. - 326
 Hong, S.H. - 248
 Horino, K. - 280
 Horiuchi, T. - 108, 132
 Huebner, W. - 188
 Hughes, W.J. - 340
 Hyodo, S. - 124

I

Ibrahim, R.C. - 108
 Ichinose, N. - 104, 220
 Igarashi, H. - 40
 Ise, O. - 276

J

Jeng, D.-Y. - 227
 Johnston, S.T. - 80

K

Kamehara, N. - 348
 Kamiya, N. - 299
 Kanai, H. - 176
 Katsuno, M. - 272
 Kawabata, A. - 61
 Kawano, K. - 16
 Kawase, A. - 140
 Kimura, H. - 136
 Kimura, M. - 303
 Kobayashi, T. - 252
 Komatsu, R. - 64
 Kondo, M. - 348
 Kumar, U. - 193
 Kurihara, K. - 348

L

Lacey, J.L. - 24
 Leary, S.P. - 292
 Lencka, M.M. - 256
 Li, J.F. - 32
 Li, T. - 244
 Liu, X. - 44, 52
 Loiacono, G.M. - 242

M

Ma, Y. - 136
 Maher, G. - 184
 Maiwa, H. - 104
 Makino, H. - 299
 Mann, L.A. - 180, 201
 Maria, J. P. - 112
 Masuda, Y. - 96
 Masumoto, H. - 96
 Matsushige, K. - 108, 132
 Matsushita, H. - 176
 McCandlish, L.E. - 256
 McCauley, D.L. - 52
 McGlennan, R.C. - 116
 McNulty, T.F. - 307
 Megherhi, M. - 209
 Meschke, F. - 244
 Messing, G.L. - 248
 Meyer, R. - 313
 Michael, J. - 353
 Miyabe, K. - 280
 Miyashita, K. - 61
 Moore, R. - 353

N

Nagata, H. - 284
 Nagata, K. - 96
 Nakashima, S. - 124
 Nakano, Y. - 148, 161, 176
 Newnham, R.E. - 340
 Nishi, Y. - 168, 172
 Nishida, T. - 132
 Nishido, M. - 197
 Nishimura, A. - 74, 88
 Niu, H. - 124
 Nomura, T. - 148, 161
 Numata, K. - 74, 88

O

Ogawa, H. - 176
 Ogawa, T. - 268
 Ogiso, K. - 303
 Ohashi, N. - 136
 Ohbayashi, K. - 212
 Ohuchi, H. - 264
 Okino, H. - 124
 Olson, W. - 353
 Omika, S. - 16
 Onoe, A. - 176
 Osonoi, A. - 40
 Ostrander, S.P. - 48
 Otsuki, E. - 276

P

Pan, M.-J. - 288
 Panda, R.K. - 307
 Park, S.-E. - 11, 235
 Parish, M.V. - 311
 Pazol, B. - 326
 Pennell, M. - 188
 Pham-Nguyen, H. - 326
 Pilgrim, S.M. - 292
 Polla, D. - 116
 Prakash, A.S. - 20
 Prokopowicz, T.I. - 184
 Pruna, P. - 209

R

Rae, A. - 155, 165
 Ramesh, R. - 20
 Randall, C.A. - 36, 44, 52, 323
 Randall, M. - 193
 Rawal, B. - 193
 Rehrig, P. - 248
 Riman, R. - 256
 Roseman, R. - 223
 Rottenberg, J. - 242
 Russell, M.W. - 80

S

Safari, A. - 307
 Saito, M. - 16
 Saito, S. - 252
 Sakabe, Y. - 303
 Sakaguchi, I. - 88
 Sakamoto, W. - 140
 Sanada, T. - 264
 Sasaki, K. - 205
 Sasaki, Y. - 231
 Sato, A. - 148, 161
 Sato, S. - 148, 161
 Satoh, H. - 205
 Satoh, K. - 276
 Satoh, S. - 205
 Schaefer, P.C. - 317
 Schmidt, G. - 326
 Scotch, A.M. - 244
 Schulze, W.A. - 48
 Schwartz, R. - 92
 Shepard, J.F. - 24, 128
 Shimamura, K. - 57
 Shimanuki, S. - 252
 Shimizu, M. - 124
 Shiosaki, T. - 108, 124, 132
 Shoji, H. - 176
 Shurland, A. - 333
 Shrout, T.R. - 11, 44, 84, 235, 313, 323

Singh, R. - 70
 Smith, L.S. - 317
 Sogabe, T. - 216
 Strauss, M. - 311
 Su, T. - 24, 120
 Sunaga, K. - 205
 Suzuki, T. - 168, 172
 Swartz, S. - 84

T

Tachimoto, K. - 280
 Takada, M. - 280
 Takahashi, M. - 64
 Takahashi, S. - 231
 Takada, M. - 280
 Takeda, H. - 57
 Takenaka, T. - 84, 284
 Tamura, M. - 272, 276
 Tan, Q. - 32
 Tanaka, J. - 172
 Tashiro, S. - 40
 Tokumoto, H. - 20
 Torri, R. - 344
 Tosa, A. - 212
 Tressler, J. - 340
 Trolier-McKinstry, S.
 - 24, 112, 120, 128, 248

Tsao, B.H. - 100
 Tsukada, T. - 280
 Tsurumi, T. - 136
 Tuttle, B. - 353

U

Uchino, K. - 28, 340
 Uda, S. - 64
 Ueda, M. - 264
 Ueno, M. - 168
 Ukai, T. - 220

V

Van Buskirk, P. - 80
 Venigalla, S. - 180
 Venkataramani, V.S. - 317
 Venkatesan, T. - 20
 Viehland, D. - 32
 Voigt, J. - 353

W

Wada, S. - 11
 Wakino, K. - 1
 Weimer, J.A. - 100
 Wilson, J. - 209
 Wu, R.L.C. - 100
 Wuttig, M. - 20

X

Xu, F. - 24

Y

Yamada, A. - 268
 Yamamoto, T. - 16
 Yamashita, Y. - 176, 220, 252
 Yang, B. - 20
 Yogo, T. - 140
 Yokoi, H. - 212
 Yoshikawa, S. - 288, 313
 Yu, Y. - 70

Z

Zavala, G. - 24
 Zen, J.R. - 68
 Zeuch, D. - 353
 Zhang, S.C. - 188
 Zipparo, M. - 323

REPORT DOCUMENTATION PAGE

Form Approved
OMB No. 0704-0188

Public reporting burden for this collection of information is estimated to average 1 hour per response, including the time for reviewing instructions, searching existing data sources, gathering and maintaining the data needed, and completing and reviewing the collection of information. Send comments regarding this burden estimate or any other aspect of this collection of information, including suggestions for reducing this burden, to Washington Headquarters Services, Directorate for Information Operations and Reports, 1215 Jefferson Davis Highway, Suite 1204, Arlington, VA 22202-4302, and to the Office of Management and Budget, Paperwork Reduction Project (0704-0188), Washington, DC 20503.

| | | | | |
|--|---|--|---|--|
| 1. AGENCY USE ONLY (Leave blank) | | 2. REPORT DATE 01 April 1999 | 3. REPORT TYPE AND DATES COVERED 01 Feb. 97 - 31 Dec. 97 Proceedings | |
| 4. TITLE AND SUBTITLE 8th US-Japan Seminar of Dielectric and Piezoelectric Ceramics | | | 5. FUNDING NUMBERS ONR: N0014-97-1-0144 | |
| 6. AUTHOR(S) Thomas R. Shrout | | | | |
| 7. PERFORMING ORGANIZATION NAME(S) AND ADDRESS(ES) Materials Research Laboratory Office of Naval Research Penn State University Regional Office Chicago University Park, PA 16802 5363 Clark St. Room 208 Chicago IL 60605-1588 | | | 8. PERFORMING ORGANIZATION REPORT NUMBER | |
| 9. SPONSORING/MONITORING AGENCY NAME(S) AND ADDRESS(ES) Office of Naval Research ONR 254 Ballston Centre Tower One 800 North Quincy Street Arlington, VA 22217-5660 | | | 10. SPONSORING/MONITORING AGENCY REPORT NUMBER | |
| 11. SUPPLEMENTARY NOTES | | | | |
| 12a. DISTRIBUTION/AVAILABILITY STATEMENT | | | 12b. DISTRIBUTION CODE | |
| 13. ABSTRACT (Maximum 200 words) Proceedings of the 8th US-Japan Seminar on Dielectric and Piezoelectric Ceramics held at Plymouth, Massachusetts from October 15-18, 1997 | | | | |
| 14. SUBJECT TERMS | | | 15. NUMBER OF PAGES | |
| | | | 16. PRICE CODE | |
| 17. SECURITY CLASSIFICATION OF REPORT | 18. SECURITY CLASSIFICATION OF THIS PAGE | 19. SECURITY CLASSIFICATION OF ABSTRACT | 20. LIMITATION OF ABSTRACT | |